UNIVERSITÄT BONN

Synthesis, Properties and Application of New Chiral Squaraine Dyes for Optoelectronic Devices

Marvin Frederik Schumacher

Dissertation

Synthesis, Properties and Application of New Chiral Squaraine Dyes for Optoelectronic Devices

Dissertation
zur
Erlangung des Doktorgrades (Dr. rer. nat.)
der
Mathematisch-Naturwissenschaftlichen Fakultät
der
Rheinischen Friedrich-Wilhelms-Universität Bonn

vorgelegt von

Marvin Frederik Schumacher
geboren in Bonn-Bad Godesberg

Bonn
November 2025

Angefertigt mit Genehmigung der Mathematisch-Naturwissenschaftlichen Fakultät der
Rheinischen Friedrich-Wilhelms-Universität Bonn

Gutachter/Betreuer:	Prof. Dr. Arne Lützen
Gutachterin:	apl.-Prof. Dr. Manuela Schiek
Tag der Promotion:	04.03.2026
Erscheinungsjahr:	2026

Affirmation in Lieu of an Oath

I, Marvin Frederik Schumacher, hereby declare that I am the sole author of this dissertation.

The doctoral thesis I submitted is my own work and was prepared without unauthorized outside assistance. I have not included text passages, graphics or other materials from third parties or my own examination papers without identifying them. Only the sources and resources that I have indicated were used. All verbatim and non-verbatim citations from other works are identified in accordance with the citation rules for academic writing. The thesis that I submitted has not been published in full or in part, except as stated in the indicated locations. The thesis that I submitted has not yet been submitted in any form as part of an examination/qualification course. I prepared the doctoral thesis that I submitted in accordance with the principles of good research practice. I am aware of the significance and criminal consequences of a false affirmation in lieu of an oath.

My statements are true to the best of my knowledge and belief.

Place, Date *Signature*

Acknowledgements

Over the past four years, many people have accompanied me on my PhD journey. Before mentioning a few of them, I would like to express how honored I feel to have conducted my doctoral studies in such an inspiring environment, both scientifically and personally.

First and foremost, I would like to thank my supervisor, Prof. Dr. Arne Lützen, to whom I am grateful in many ways. I am deeply thankful for the opportunity to conduct my doctoral research in his group, the exciting and enjoyable research topic, the freedom and opportunities for professional and personal development, and his continuous support in all matters. This includes the chance to participate in the TIDE research training group, as well as his support for my numerous research stays abroad.

I would also like to express my gratitude to apl.-Prof. Dr. Manuela Schiek for her incredible support, as well as for agreeing to be the second reviewer of my thesis. She always took the time to help me whenever I needed it. I am especially thankful for the countless hours she spent teaching me complex topics as well as numerous preparation and measurement techniques. I greatly appreciate our excellent collaboration, which resulted in a wealth of data that enriched this work. I would also like to thank her for the many research stays she has made possible for me and the always open communication style.

I would also like to thank Prof. Dr. Thomas Bredow for our excellent collaboration within the TIDE framework and for participating in my examination board.
My gratitude also extends to Prof. Dr. Ulrich Jaehde for agreeing to be an external member of my examination board.

I gratefully acknowledge the Jürgen Manchot Foundation for supporting my doctoral studies with a scholarship, both financially and ideationally.

I would also like to thank my collaborators: Most of these great collaborations originated from my membership in the TIDE research training group. I would like to thank everyone on the TIDE team. It was a great privilege to be part of this cohort, meet great colleagues, visit interesting places, and learn much more than I would have without this program. In particular, the research residency was a unique opportunity to live in another country and gain scientific experience. I would like to thank Prof. Dr. Seth Marder of the University of Colorado Boulder for being a great host and for allowing me to join his group and learn from him.
Within TIDE, I would especially like to thank Prof. Dr. Klaus Meerholz and his PhD student Otgonbayar Erdene-Ochir for their constant collaboration and for the opportunities to prepare and measure thin films. I would also like to thank Otgo for the friendship that developed and the many *Tatar operations*.

Furthermore, I would like to thank Prof. Dr. Paul H. M. van Loosdrecht and Robin Bernhard for the many interesting projects and numerous questions we were able to address. Outside of TIDE, I would like to thank Prof. Dr. Christoph Lienau of the University of Oldenburg, Prof. Dr. Roland Resel of Graz University of Technology, and Prof. Dr. Anna Painelli for the good collaboration and may interesting projects.

I also wish to thank all the staff members of the analytical departments of the chemical institutes for their numerous measurements, without which this work would not have been possible. My special thanks go to the NMR, mass spectrometry, GC-MS, and elemental analysis departments for their continuous support. I also want to thank Ms. Charlotte Rödde and Dr. Gregor Schnakenburg for measuring and solving the crystal structures.

I would like to express my special thanks to all members of the Lützen group, as well as my bachelor's and master's students, whom I had the pleasure of getting to know along the way, for an unforgettable time. For all the technical discussions, the fun tastings and evenings spent together, and the carefree activities outside of university. I am very grateful to have made so many new friends and truly had a wonderful time with you all.

In addition, I would like to thank my fellow first-semester chemistry friends, with whom I formed wonderful friendships and made many great memories. Thank you for a great time at the university! A special thank you goes to Marcel Müller, with whom I pushed through all exam phases. I am certain that this experience positively impacted us both.

Nicht zuletzt möchte ich mich noch ganz herzlich bei meinen Eltern bedanken, die immer für mich da waren und mich stets in meiner Wissbegierde gefördert haben, auch wenn das bestimmt nicht immer einfach war. Sie unterstützen mich bedingungslos, hatten immer Verständnis und gaben mir immer das Gefühl, dass meine Arbeit viel wert ist und dass sie stolz auf mich sind.

Thank you all!

Publications & Scientific Contributions

Parts of this thesis have been published in peer-reviewed journals:

1. F. Balzer, M. F. Schumacher, S. Mattiello, M. Schulz, J. Zablocki, M. Schmidtmann, K. Meerholz, N. S. Sariciftci, L. Beverina, A. Lützen, and M. Schiek, "The Impact of Chiral Citronellyl-Functionalization on Indolenine and Anilino Squaraine Thin Films," *Israel Journal of Chemistry* **2022**, *62* (7-8), e202100079, DOI: 10.1002/ijch.202100079

2. D. Giavazzi, M. F. Schumacher, L. Grisanti, M. Anzola, F. D. Maiolo, J. Zablocki, A. Lützen, M. Schiek, and A. Painelli, "A marvel of chiral squaraine aggregates: chiroptical spectra beyond the exciton model," *Journal of Materials Chemistry C* **2023**, *11* (24), 8307, DOI: 10.1039/D2TC05555D

3. R. Bernhardt, L. Rieland, T. Wang, M. F. Schumacher, A. Lützen, M. Schiek, and P. H. M. van Loosdrecht, "Ultrafast Excitonic Transitions in Enantiopure and Racemic Squaraine Thin Films," *Aggregate* **2025**, *6* (3), e698, DOI: 10.1002/agt2.698

For the following articles significant contributions have been made:

4. D. Timmer, M. Gittinger, T. Quenzel, S. Stephan, Y. Zhang, M. F. Schumacher, A. Lützen, M. Silies, S. Tretiak, J.-H. Zhong, A. D. Sio, and C. Lienau, "Plasmon mediated coherent population oscillations in molecular aggregates," *Nature Communications* **2023**, *14* (1), 8035, DOI: 10.1038/s41467-023-43578-4

5. C. Wallerius, O. Erdene-Ochir, E. V. Doeselar, R. Alle, A. T. Nguyen, M. F. Schumacher, A. Lützen, K. Meerholz, and S. H. Pun, "Quadruple[6]Helicene Featuring Pyrene Core: Unraveling Contorted Aromatic Core with Larger Effective Conjugation," *Precision Chemistry* **2024**, *2* (9), 488, DOI: 10.1021/prechem.4c00038

The following scientific contributions have been presented at conferences, workshops, and summer schools:

1. 11th Workshop of Ellipsometry, Steyr, Austria, **2021**
   Poster: Ellipsometric Investigation of Chiral Benzothiazole-Derived Squaraine Aggregates in Thin Films.

2. 7th International Winterschool on Bioelectronics, Kirchberg in Tirol, Austria, **2022**
   Poster: Utilizing Circular Dichroism to Study Excitons in Photoactive Semiconductors for Bio-Optoelectronics.

3. 19th International Symposium on Novel Aromatic Compounds, Warsaw, Poland, **2022**
   Poster: Utilizing Circular Dichroism to Study Excitons in Photoactive Semiconductors for Bio-Optoelectronics.

4. KOPO 2022 - Conjungated Polymers and Oligomers, Bad Honnef, Germany, **2022**
   Poster: Investigation of Chiral Benzothiazole-Derived Squaraine Aggregates in Thin Films.

5. 2023 Conference on Excited State Processes, Santa Fe, NM, United States of America, **2023**
   Poster: A Marvel of Chiral Squaraine Aggregates: Chiroptical Spectra beyond the Exciton Model.

6. SupraChem2024, Ulm, Germany, **2024**
   Poster: Chiral Squaraine Aggregates – New Materials for Optoelectronic Devices.

7. 1st TIDE Conference - Template-Designed Organic Electronics & Beyond, Cologne, Germany, **2024**
   Poster: A Novel Class of Chiral Squaraine Dyes – New Materials for Optoelectronic Devices.

8. KOPO 2024 - Conjungated Polymers and Oligomers, Bad Honnef, Germany, **2024**
   Talk: Added Value of Circular Dichroism for Studying Charge Transfer Excitons in Photoactive Organic Thin Films.

9. GDCh/JCF - Young Scientists Introduce Themselves, Bonn, Germany, **2024**
   Talk: Chiral Squaraine Aggregates – New Materials for Optoelectronic Devices.

10. BIGS Summer School 2024 - Modern Electrochmistry, Bonn, Germany, **2024**
    Talk: A Novel Class of Chiral Squaraine Dyes – New Materials for Optoelectronic Devices.

Abstract

The work presented in this thesis investigates a broad range of squaraine dyes, systematically varying their molecular design and terminal *n*-alkyl substituents in order to optimize aggregation behavior and the associated (chir)optical properties. Following their successful synthesis, each squaraine is systematically investigated for their aggregation behaviour in both solution and thin films, with a focus on chiral characteristics where applicable. The results providing important insights into how molecular structure governs supramolecular organisation and, in turn, the observed (chiro)optical properties.

A central question addressed consistently in this work is the underlying arrangement of chromophores and the mechanism responsible for the remarkably strong chiroptical responses observed in these systems. By exploring the added value of chirality, the resulting circular dichroism (CD) response is used to probe these arrangements. This allows their original nature to be identified: bisignate signals were assigned to strongly coupled Coulombic Frenkel excitons, whereas monosignate peaks were linked to intermolecular charge transfer (ICT) interactions. Using this principle on several occasions in combination with other analytical methods, allowed the unimpeachable identification of ICT interactions as a recurring and fundamental element in the aggregation behavior of squaraines.

Together, these results establish a coherent framework for understanding structure-property relationships in squaraines, while demonstrating the practical potential of these materials through their application in an organic photodetector.

Contents

Affirmation in Lieu of an Oath iii

Acknowledgements iv

Publications & Scientific Contributions vi

Abstract viii

1 Introduction 1
- 1.1 Squaraine Dyes: Chemistry's Colorful Surprise – An Overview . . . 1
- 1.2 Aggregation – Induced Optical Changes in Chromophores . . . 7
- 1.3 Chirality and Optical Activity . . . 13
- 1.4 Chirality Meets Optoelectronic Devices – A Short Introduction . . . 18

2 Motivation and Objective 23

Part A – Citronellyl-Functionalized Chiral Squaraines 25

3 The Impact of Chiral Citronellyl-Functionalization on Indolenine and Anilino Squaraine Thin Films 27

4 Citronellyl-Functionalized Chiral Squaraines with Different Alkyl-Substituents 31
- 4.1 The Idea: Modulating ICT Through Steric Hindrance . . . 31
- 4.2 Synthesis of Selected Citronellyl-Functionalized Chiral Squaraines . . . 32
- 4.3 Optical Properties of Aggregated Solutions and Thermally Annealed Thin Films . . . 33
- 4.4 A Preliminary Effort Towards Greater Steric Repulsion . . . 46

5 Synthesis, Structure and Thin Film Optical Properties of a Chiral Benzothiazole-Derived Squaraine 49
- 5.1 Manuscript . . . 50

Part B – Proline-Derived and Extended Chiral Squaraines 65

6 A marvel of chiral squaraine aggregates: chiroptical spectra beyond the exciton model 68

7 Proline-Derived Anilino Squaraines: Impact of Alkyl Chain Reduction to a Methyl Group 71
7.1 Concept and Synthesis . . . 71
7.2 Optical Properties of Aggregated Solutions and Thermally Annealed Thin Films . . . 74
7.3 Single-Crystal X-Ray Structure . . . 77

8 Ultrafast Excitonic Transitions in Enantiopure and Racemic Squaraine Thin Films 81

9 From Proline to Indoline: The Idea of Extending π-Conjugation for Enhancing Optical Properties and π-π-Interactions 84
9.1 The Idea – Enhancing Optical Properties of **ProSQs** even further . . . 84
9.2 Addressing Reduced Nucleophilicity: Initial Attempts . . . 85
9.3 Changing Gears – Octahydro-1H-indole for Restoring Nucleophilicity . . . 90
9.4 Optical Properties of Aggregated Solutions and Thermally Annealed Thin Films . . . 93
9.5 Single-Crystal X-Ray Structure of **(*S*,*S*)-OHI-SQ-C3** . . . 99

Part C – From the Idea to the Device

10 2-Methylbutyl-Derived Anilino Squaraines 103
10.1 The Idea – Strategic Integration of Beneficial Properties for Device Applications . . . 103
10.2 Overcoming Challenges in the Synthesis of Chiral 2-Methylbutyl-Functionalized Squaraines 105
10.3 Single-Crystal X-Ray Structure of **(*S*,*S*)-2mb-SQIB** . . . 111
10.4 Optical Properties of Aggregated Solutions and Thermally Annealed Thin Films . . . 113
10.5 From Vision to Prototype: Final Device Application . . . 123

Part D – Excursus

11 Synthesis of Chiral π-Conjugated Polymers Exhibiting the CISS Effect for Advanced Optoelectronic Applications 129
11.1 Current Research Status of the CISS Effect . . . 129
11.2 The Project Idea – Polymers with Intrinsic Chiral Information . . . 131
11.3 Chiral F8BT derivatives – **(*S*)-c$_x$F8BT** . . . 135

12 Summary and Outlook 142

13 Experimental Section 152
13.1 Materials and Methods . . . 152
13.2 Citronellyl-Functionalized Chiral Squaraines with Different Alkyl-Substituents . . . 156
13.3 Proline-Derived Anilino Squaraines: Impact of Alkyl Chain Reduction to a Methyl Group 168
13.4 From Proline to Indoline: The Idea of Extending π-Conjugation for Enhancing Optical Properties and π-π-Interactions . . . 172
13.5 2-Methylbutyl-Derived Anilino Squaraines . . . 187
13.6 Synthesis of Chiral π-Conjugated Polymers Exhibiting the CISS Effect for Advanced Optoelectronic Applications . . . 202

Bibliography 216

Appendix

A The Impact of Chiral Citronellyl-Functionalization on Indolenine and Anilino Squaraine Thin Films **230**
A.1 Publication . . . 231
A.2 Supplementary Information . . . 244

B Citronellyl-Functionalized Chiral Squaraines with Different Alkyl-Substituents **251**
B.1 Additional Spectra in Solution and Thin Film . . . 251
B.2 Thin Film Preparation of **(*S*,*S*)-nCi-SQIB** by PVD Techniques . . . 259

C Synthesis, Structure and Thin Film Optical Properties of a Chiral Benzothiazole-Derived Squaraine **261**
C.1 Supplementary Information . . . 262

D A marvel of chiral squaraine aggregates: chiroptical spectra beyond the exciton model **284**
D.1 Publication . . . 285
D.2 Supplementary Information . . . 300

E Proline-Derived Anilino Squaraines: Impact of Alkyl Chain Reduction to a Methyl Group **416**
E.1 Additional Spectra in Solution . . . 416
E.2 Additional Information on Single-Crystal Structures . . . 417

F Ultrafast Excitonic Transitions in Enantiopure and Racemic Squaraine Thin Films **424**
F.1 Publication . . . 425
F.2 Supplementary Information . . . 436

G From Proline to Indoline: Extending π-Conjugation for Enhancing Optical Properties and π-π-Interactions **447**
G.1 Additional Spectra in Solution and Thin Film . . . 447
G.2 Additional Information on Single-Crystal Structure . . . 449

H From the Idea to the Device – 2-Methylbutyl-Derived Anilino Squaraines **454**
H.1 Synthesis . . . 454
H.2 Additional Information on Single-Crystal Structures . . . 456
H.3 Additional Spectra in Solution and Thin Film . . . 473
H.4 Additional Information on the Characterisation and Fabrication of the OPVs . . . 477

I Excursus – Synthesis of Chiral π-Conjugated Polymers Exhibiting the CISS Effect for Advanced Optoelectronic Applications **480**
I.1 Equations for gel permeation chromatography (GPC) analysis . . . 480
I.2 Information on Single-Crystal Structure of **(*S*)-Binol-DibromoBT** . . . 481
I.3 Additional Information on Selected Chiral π-Conjugated Polymers . . . 487

J Substance/Reaction-Index + NMR and Mass Spectra **502**

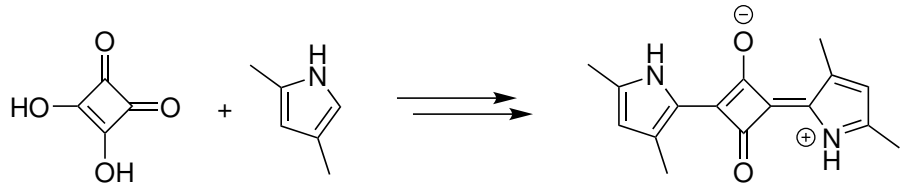
List of Abbreviations and Acronyms **590**

CHAPTER 1

Introduction

1.1 Squaraine Dyes: Chemistry's Colorful Surprise – An Overview

The class of squaraine dyes is on a molecular level understood as the 1,3-condensation product of two equivalents of an electron rich reactant with squaric acid (Figure 1.1, left).[6, 7] The huge variety of different electron rich compound thereby allowing for a sheer unlimited number of different squaraines – emphasizing the structural diversity and easy accessibility of this class of molecules. The initial synthesis of squaraine was reported by *Treibs* and *Jacob* in 1965, when they observed that heating squaric acid with 2,4-dimethyl pyrrole in ethanol yielded the first squaraine compound, as illustrated in Figure 1.1.[8–10]



squaric acid

Figure 1.1: Chemical structure of the first reported squaraine by *Treibs* and *Jacob* in 1965, synthesized from squaric acid and 2,4-dimethyl pyrrole.[8–10]

The name *squaraine* was actually introduced 15 years later by *Schmidt* et al. in 1980, from the combination of ***squar****ic acid* and *bet****aine***.[7] Is it obvious that the first one indicates the origin of the dye, however, the latter one shows the structural similarity of these dyes to betaines. These compounds are on a macroscopic level electronically neutral, but are zwitterionic on the molecular level i.e. have a separated formal charge. Structurally squaraines belong to the class of polymethine dyes and being in addition to cyanine (cationic), oxonol (anionic), and merocyanine (neutral) types, the fourth zwitterionic type.[11, 12] Despite their small chromophore size, these dyes are characterized by an intense light absorption originating from a *push-pull*-system.[13]

This holds true for squaraines as well. The structure of squaraines consists of an oxocyclobutenolate bridge in the center of the molecule, which is quite electron-deficient and acts as an electron-accepting

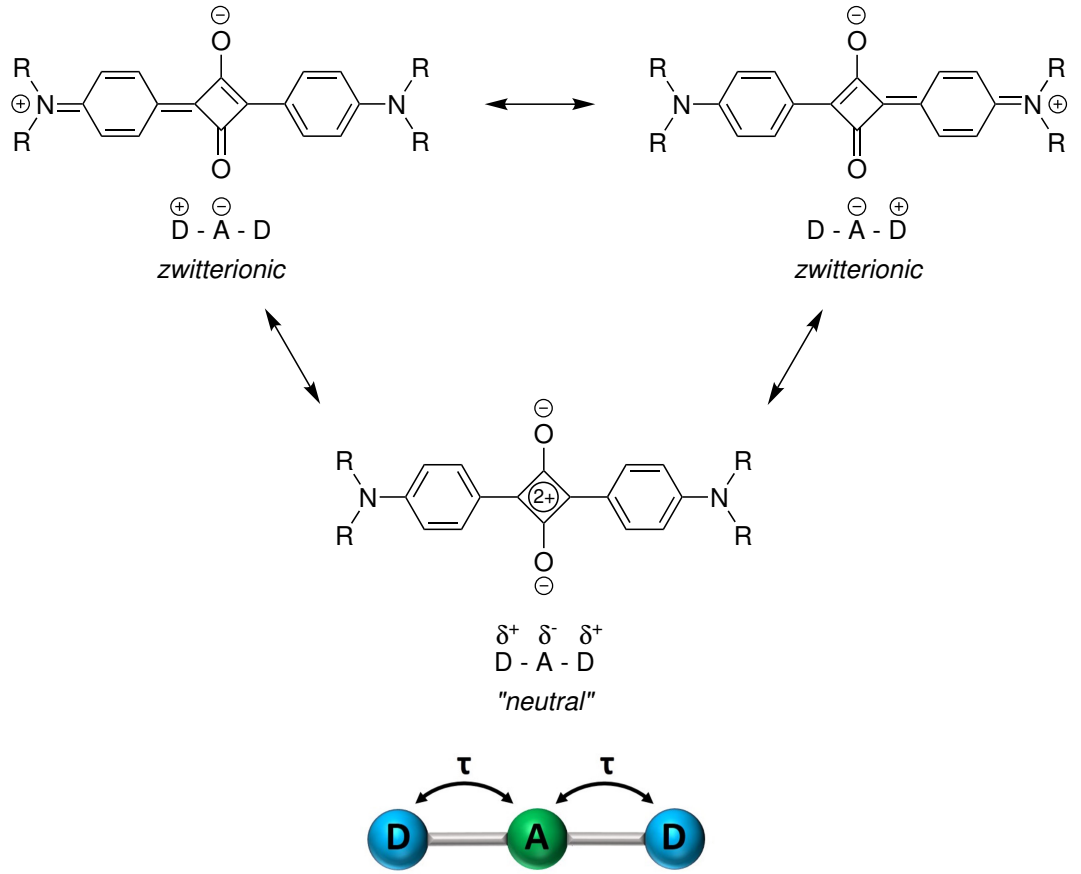
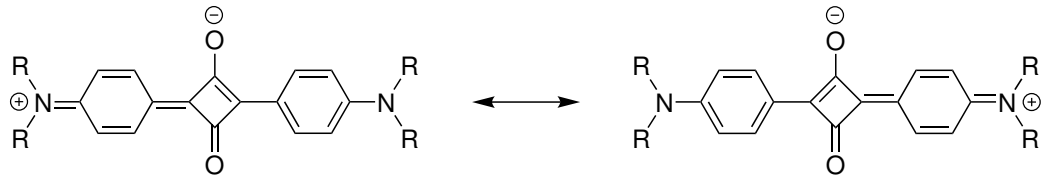


Figure 1.2: Top: Resonance structures of squaraine dyes on the example of anilino squaraines. Bottom: Intramolecular charge transfer (τ) of Donor-Acceptor-Donor type squaraine. Figure reprinted with permission from [2] © The Royal Society of Chemistry 2023.

core. This core is 1,3-substituted with two electron-rich reactants, acting as electron-donating groups and representing together with the core the backbone of squaraines.[6, 7] Since the centered four-membered ring has a aromatic character, the hole molecule fulfills the *Hückel's rule* for aromaticity. This allows delocalization of π-electrons over the entire molecule as it is depicted in the resonance structures on the example of anilino squaraines in Figure 1.2 (top).[11, 14] A further observation from the resonance structures is the molecule's high symmetry, resulting in a dipole moment of nearly zero.[15] By this the squaraine backbone is planar and resonance stabilized, polarized zwitterionic structure with an overall quadrupolar Donor-Acceptor-Donor (D-A-D) arrangement.[16, 17] Due to this special arrangement of the two electron-rich donor groups linked to the electron-accepting core, each squaraine can also be described in terms of three essential diabatic electronic states: one neutral (D-A-D) and two degenerate charge-separated states (D^+-A^--D and D-A^--D^+) as shown in Figure 1.2 (top). This allows for the generation of an *intra*molecular charge transfer complex (not be confused with an *inter*molecular charge transfer – ICT) within the molecule, which is depicted in Figure 1.2 (bottom).[2, 14, 18] All these factors resulting in an extremely strong and sharp absorption (molar extinction coefficients ε of over 10^5 M^{-1} cm^{-1}) in the visible to near infrared (IR) part of the electromagnetic spectrum combined with small Stokes

shifts.[17–21] Furthermore, the planar, zwitterionic D-A-D structure leads to exceptionally high thermal and photochemical stability to these small molecules, making them a highly investigated class of compounds.[6, 15, 17, 22]

1,3-squaraine:



1,3-methine bridged squaraine:

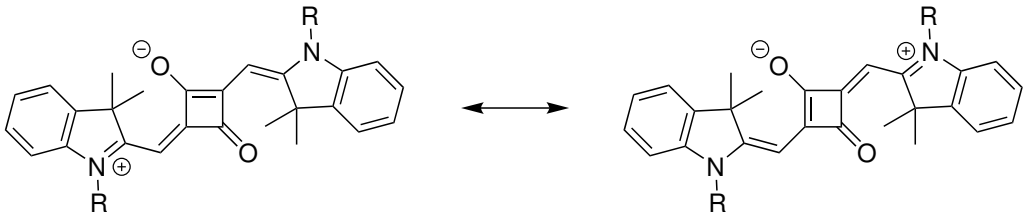


Figure 1.3: Structures of the two relevant squaraine classes discussed in this thesis. Top: Symmetrical 1,3-squaraines (here specific anilino squaraines) synthesized from activated arene precursors. Bottom: Symmetrical 1,3-methine bridged squaraines derived from anhydrobase precursors.

Due to their symmetric framework, squaraines allow to incorporate a vast variety of electron-rich aromatic and heteroaromatic units as donor substituents. Within this family, two structural classes stand out, depending on the precursor employed. The first class comprises symmetrical 1,3-squaraines (Figure 1.3, top), obtained by direct condensation of activated arenes ranging from dialkylanilines to indole, indolizine, and pyrrole derivatives. The second class consists of 1,3-methine-bridged squaraines (Figure 1.3, bottom), derived from activated methylene heterocycles (e.g., Fischer bases) or other methylazinium precursors such as deprotonated anhydrobases.[6, 7, 23] These two structural classes represent by far the most extensively investigated members of the squaraine family, based on their easy accessibility, huge variety of possible compounds, exceptional photophysical properties combined with high thermal and photochemical stability.[15, 17, 22, 24] A direct comparison of 1,3-squaraines and 1,3-methine-bridged squaraines shows that the methine-bridged derivatives generally exhibit higher highest occupied molecular orbital (HOMO) energy levels and smaller HOMO-LUMO gaps (LUMO = lowest unoccupied molecular orbital), resulting in more red-shifted absorption maxima. In terms of photochemical stability, however, they tend to undergo photoisomerization.[6]

During the synthesis of symmetrical 1,3-squaraines (see Figure 1.4), also the 1,2-dicondensation product forms as a side product. From a chemical point also this class is a squaraine, even though the properties differ significantly from those of the 1,3-analogues. However, because of its inferior optoelectronic properties – characterized by weaker absorption intensities, larger HOMO-LUMO gaps, and more demanding synthetic routes – the 1,2-squaraine class has attracted relatively little research interest.[6, 23] With more synthetic effort, unsymmetrical squaraines can be obtained in which the donor units derive from one of the previously introduced classes. By selecting donors of varying electron-donating strength, one can finetune the π-electron delocalisation properties, and thereby, adjust

the dye's charge transfer (CT) character.[25] However, these unsymmetrical systems generally exhibit increased dipole moments and broader absorption bands.[26] Further structural modifications exploit substitution at the squaric acid core,[27] or the synthesis of bis-,[28] oligo-, and polysquaraines.[29–32] All this enables precise control over the HOMO and LUMO energy levels.[33] However, since this thesis focuses exclusively on symmetrical 1,3- and 1,3-methine-bridged squaraines, other structural classes will not be discussed further.

As previously mentioned, the synthesis of squaraines is comparatively straightforward relative to other classes of organic dyes. In fact, it relies of fundamental chemistry, discovered in the early stages of squaraine research and have remained largely unchanged since then. This is especially true for the synthesis of of symmetric 1,3- and 1,3-methine bridged squaraines. The general synthetic strategy is shown in Figure 1.4 using the example of symmetric bis(*N*,*N*-dialkylanilino)-squaraines, and involves the condensation of two equivalents of an electron-rich reactant with squaric acid.[6, 23] Given that the central building block – squaric acid – is commercially available, the primary synthetic challenge lies in the preparation of the activated arene or anhydrobase required for the condensation step. Within this thesis, with the exception of methine-bridged squaraines, only phloroglucinol (1,3,5-trihydroxybenzene) substituted reactant was used. The synthesis of these compounds typically starts with the tautomerization of the commercially available phloroglucinol, followed by nucleophilic attack of a secondary amine, and subsequent elimination of water to yield the electron-rich aniline derivatives (see Figure 1.4, top).[11] By the choice of an suitable secondary amine, different functional groups, certain properties as well as chirality from an ex-chiral pool derivative can be introduced.[1, 2, 34] However, not only the choice of the secondary amine influences the molecular properties but also phloroglucinol was specifically selected due to several benefits. Not only does it increase the solubility of the squaraine but also promotes planarity of the molecular backbone through intramolecular hydrogen bonding, thereby ensuring coplanarity between the phenyl rings and the central core. Another benefit arises from the introduction of hydroxyl groups, which serve as two +M-substituents (positive mesomeric effect). These groups activate the phenyl ring for the subsequent nucleophilic attack on squaric acid or semisquaraine intermediates, thereby improving the regioselectivity of the condensation reaction. Moreover, the +M-effect modulates the absorption/fluorescence characteristics of the final product.[19, 35]

Following the formation of the electron-rich aniline derivative, the next step in the synthetic pathway involves the generation of a semisquaraine (also referred to as emisquaraine) as a key intermediate.[6, 8] Analogous to other α,β-unsaturated carbonyl systems, squaric acid undergoes a 1,4-nucleophilic addition with the dialkylaniline. Subsequent proton transfer restores the aromaticity of the phenyl ring and acid-catalysed water elimination results in the formation of the semisquaraine (ref. Figure 1.4, middle).[37, 38] Next, this semisquaraine intermediate is protonated at the β-carbonyl (3-position) of the squaric acid as most electron-rich carbonyl function, and thus, activated for the next reaction. The catalytic acid milieu for both reaction is thereby created from the squaric acid ($pK_{a,1}$ = 1.5, $pK_{a,2}$ = 3.5) or the semisquaraine itself due to their high acidity. Additionally, Law et al. have demonstrated that squaraine formation does not occur in non-hydroxylic solvents, implying that the presence of alcohols or trace amounts of water is necessary for the reaction.[6, 36] In the final condensation step, a second nucleophilic attack by another electron-rich aniline derivative on the activated carbonyl function takes place, followed by thermally induced water elimination, resulting in the formation of the 1,3-substituted squaraine.[6, 23] At this step of the synthesis, the formation of the previously mentioned side product – the 1,2-regioisomer – can occur. However, this side reaction generally becomes significant only under conditions involving highly reactive, electron-rich substrates, elevated temperatures, or extended reaction times due to the higher

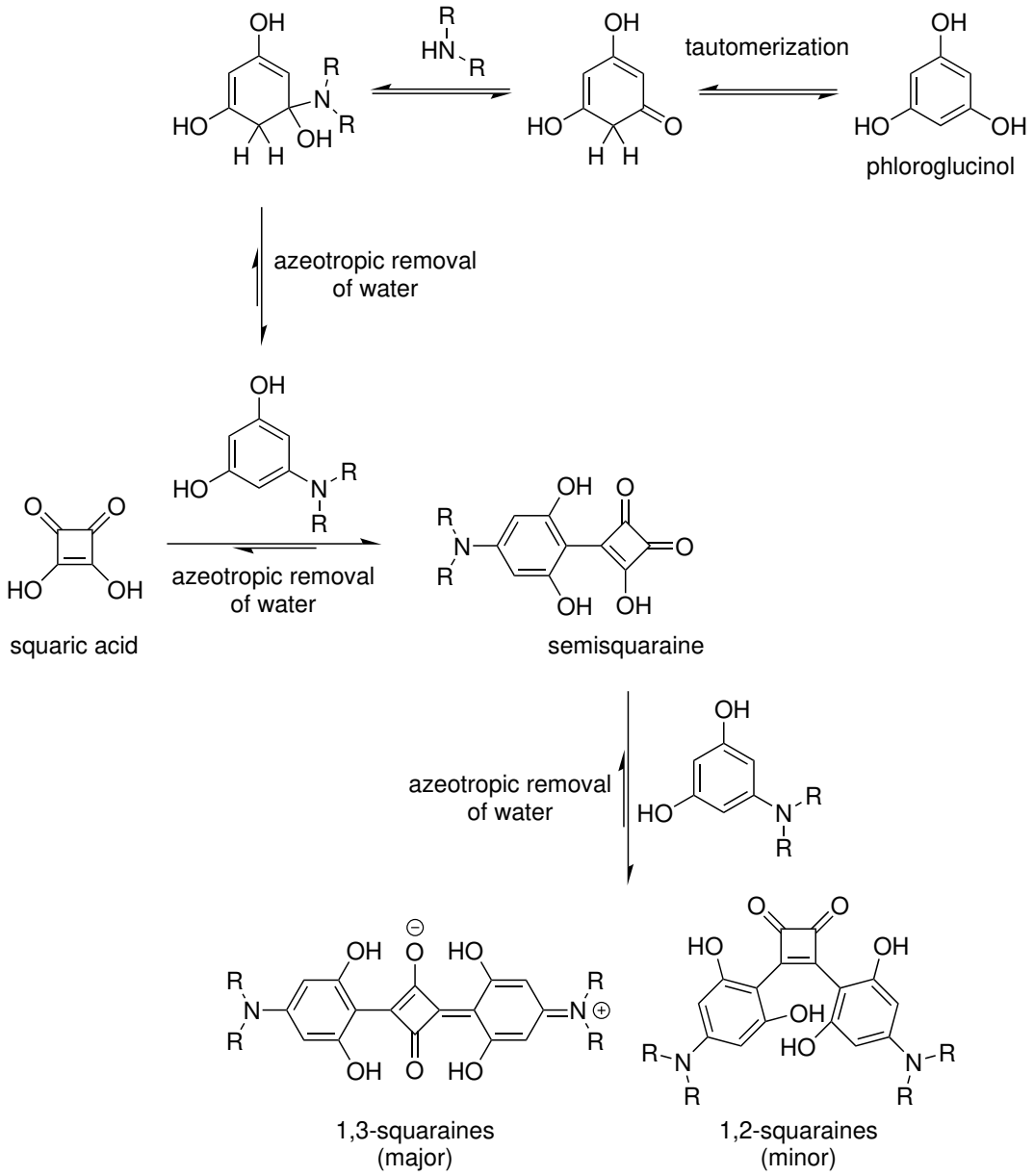


Figure 1.4: General synthesis strategy of symmetrical 1,3-squaraines starting from phloroglucinol and a secondary amine (R = alkyl group).[6, 36]

reactivity of the semisquaraine intermediate as well as squaric acid.[6, 23] Furthermore, phloroglucinol itself contributes to regioselectivity by introducing steric repulsion in the 1,2-arrangement, which likely explains why the 1,2-regioisomer is predominantly observed during the synthesis of methine-bridged squaraines.[6]

As it can be clearly seen from Figure 1.4, a critical aspect to emphasize is that the entire sequence consists of equilibrium reactions. Consequently, a successful synthesis of the desired squaraine and to maximize the product yield, requires consideration of *Le Chatelier's principle*. First, to avoid the

hydrolysis of the formed product, *Sprenger* and *Ziegenbein* improved the synthesis by using an appropriate solvent mixture for the azeotropic removal of water. Historically, a combination of benzene and 1-butanol was used, however, due to health concerns associated with benzene, it is replaced by toluene nowadays.[39] Note, that the addition of 1-butanol serves two purposes: it improves the solubility of the reactants and fulfills the necessity of a protic solvents for the reaction, as described above. Yields can also be affected by the solubility of the formed product. Higher temperatures as well as solubility increasing substituents on the nitrogen leading to higher concentrations in the reaction mixture and consequently favoring the hydrolysis of the product. In general, reported yields are strongly dependent on the specific system and molecular pattern and can vary between 3 and 60%.[40, 41] Typically, the 1,3-squaraine is remarkable less soluble than the corresponding 1,2-regioisomer, displaying another beneficial feature of these molecules. Due to this limited solubility, separation from the 1,2-regioisomer and other reactants is easily possible via simple filtration followed by recrystallization in an appropriate solvent mixture, eliminating the need for costly reagents.[16, 38] On the lab scale, however, column chromatography is still commonly used for convenience. Nevertheless, the absence of expensive metal catalysts and disposal of toxic, halogenated solvents makes this class quite attractive for industrial processes particularly when compared to other organic semiconductors.[42] Furthermore, small molecules have the overall benefit of monodispersity, providing much more control over the synthesis process in comparison to oligomeric or polymeric systems.[43]

All of the above mentioned extraordinary chemical and optoelectronic properties, coupled with the straightforward accessibility and modifiability of squaraine dyes, made them a topic of intense research over the past decades. As *Sreejith* et al. aptly described, squaraines are "*a mine of molecular materials*".[17] Consequently, these dyes have been used in a remarkably diverse set of different applications. This broad interest is reflected in the steadily increasing number of scientific publications per year, as depicted in Figure 1.5. Right after their initial discovery by *Treibs* and *Jacob* in 1965, the geneal interest in this new class of molecules remained rather low for some time.[8–10] One of the earliest applications involved their usage as sensitizers for inorganic ZnO photoconductors.[20] The first "real" attention emerged in the mid-1980s, when the photoconductive properties and the ability to collect static charges were used in the field of xerography.[20, 44, 45] The next wave of publications came in the late 1990s, exploiting the strong hyperpolarizability and two-photon absorption (2PA) of squaraines in the context of non-linear optics.[11, 46–50] Although *Merritt* and *Hovel* first investigated squaraines as active layers in a single-junction Schottky barrier solar cell as early as 1976,[51] widespread interest in this specific application area did not emerge until the mid-2000s. There, a significant increase of the number of publication can be seen due to the advancement in organic- and hybrid-solar cell research with squaraines.[22, 52–54] Given the constant rising in importance and demand for novel materials, squaraines have remained in the focus of scientific research – evidenced by the consistently high number of publications in the past decade.

Currently, all applications can roughly be divided into two main categories.[55] The first category covers all technological applications, including the highly active field of organic- and hybrid-solar cells,[22, 52–54] electroluminescent materials used in organic light-emitting diode (OLED) technologies,[56] and their role as sensors for various analytes.[57–59] The second major category covers all medical-related applications, such as bioimaging[60] as well as in photodynamic therapy (PDT)[61, 62] and photothermal therapy (PTT)[63, 64] by utilizing their 2PA properties,[50] to name a few examples.

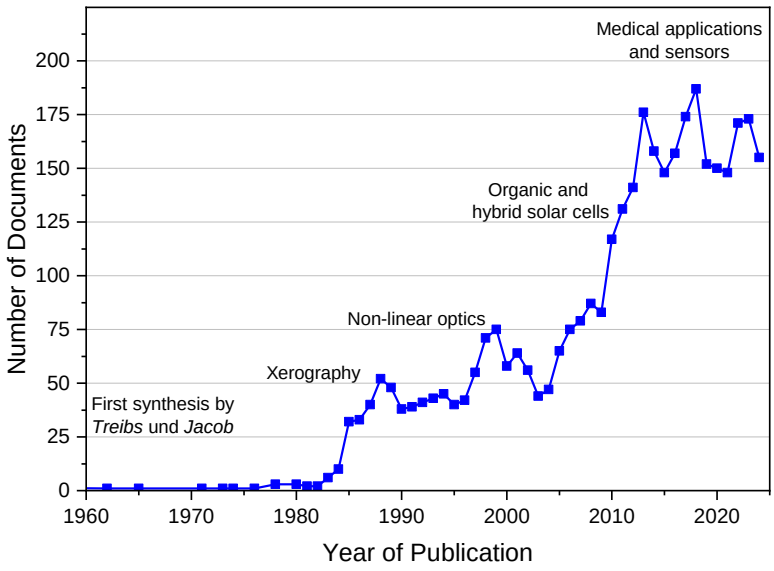


Figure 1.5: Annual number of scientific publications containing the terms “squaraine” or “squarylium” between 1960 and 2024 (Source: SciFinder© , http://www.scifinder.cas.org, retrieved 18. July 2025).

Another indication of the increased significance of squaraines is their appearance beyond the field of academic research. Due to the high demand and broad interdisciplinary interest until today, several squaraine derivatives have become commercially available nowadays. Their primary market is in the field of optoelectronic devices, including photodetectors and organic- and hybrid-solar cells, although other application areas are also promoted by manufacturers.[22, 42, 55, 65–67]

Overall, squaraines represent a remarkably versatile and scientifically interesting class of organic compounds with a diverse range of potential applications and an almost limitless number of structural variations. However, the most interesting property is their pronounced tendency to form aggregates. This influences not only the electronic properties, but also their optical characteristics, thereby offering additional features for tuning performance in materials science and optoelectronic applications.

1.2 Aggregation – Induced Optical Changes in Chromophores

In the early days of dye chemistry, a remarkable phenomenon – aggregation – was observed in certain chromophores. In this context, aggregation refers to the non-covalent, supramolecular assembly of two or more molecules through weak forces e.g., *van-der-Waals* forces, π-π-interactions or hydrogen bonding. Depending on the intermolecular distance and several other factors, such aggregation can give rise to significant electronic interactions between these molecules, and thus, to an energy splitting of the excited states. This often results in pronounced changes of the optical properties, including absorption and fluorescence characteristics. Roughly speaking, a distinction can be made between two types of aggregates: The first type of aggregate is characterized by a hypsochromic shift (blue shift, higher in energy) in the absorption spectra with respect to the monomer absorption. Accordingly, these aggregates are commonly referred to as H-aggregates, with “H” denoting hypsochromic behavior.

In general, H-aggregation leads to a strong fluorescence quenching and a large Stokes shift due to a rapid internal conversion to lower-energy, non-emissive (e.g., dark) exciton states following after photo-excitation.[68–71] The second type of aggregate is characterized by a bathochromic shift (red shift, lower in energy) compared to the monomer absorption. These aggregates are named after their discoverers *E. E. Jelley*[72, 73] and *G. Scheibe*[74, 75] and are sometimes referred to as Scheibe aggregates – though they are way more commonly known as J-aggregates. This type of aggregate is known for its intense fluorescence and small Stokes shifts.[69–71]

Although the optical characteristics of dye aggregates have been recognized since the mid-1930s,[72–75] their theoretical description remains a controversially discussed subject.[2, 3, 14, 76] One of the earliest explanations on this topic emerged in the 1960s by *Davydov*[77] and *Kasha*[70, 78]. Their theoretical groundwork, despite their simplifications, is widely used for the initial interpretation and classification of chromophore aggregates.[79, 80]

1.2.1 The Molecular Exciton Model

To explain the observed changes upon aggregation of chromophores, *Davydov*[77] introduced the molecular exciton model, which was shortly after further refined by *Kasha*[70, 78] in order to obtain a correct description of the resonance coupling between excited states in weakly interacting molecular aggregates. Both considered the excited-states of the chromophores as molecular excitons. This concept was first introduced by *Frenkel* in 1931, where an exciton refers to a coulombically strongly bound pair, consisting of an excited electron and electron hole.[80, 81] This exciton can move in a coherent, particle-like manner and becomes delocalized across adjacent chromophores within an aggregate. In terms of molecular orbital theory, an exciton can be depicted as an light-induced excited electron in the LUMO, accompanied by the corresponding hole in the HOMO. This electron-hole pair stays localized on the same molecule and is bound by coulombic attraction between them.

This results in a redistribution of electron density during the photo-excitation which gives rise to a transition dipole moment $\vec{\mu}$. As a vector quantity, the transition dipole moment has both magnitude and spatial direction. When then two chromophores are brought into close proximity, their respective transition dipole moments can couple through space via strong coulomb forces, resulting in an energy splitting.[77, 78] Utilizing the Born-Oppenheimer approximation,[82] which allows the separation of nuclear and electronic wave functions, and using the point-dipole approximation, the exciton coupling energy J between two identical chromophores aligned in parallel planes can be expressed as:

$$\text{Exciton coupling energy} \quad J = \frac{1}{4\pi\varepsilon_0} \cdot \frac{|\vec{\mu}|^2}{r^3} \left(cos\ \alpha - 3\ cos\ \theta_1\ cos\ \theta_2\right) \tag{1.1}$$

where ε_0 is the vacuum permittivity, r is the center-to-center distance between the chromophores, α the rotational angle, θ_1 and θ_2 are the slip angles of the transition dipole moments as depicted in Figure 1.6.[71, 77, 78] With this, the energy of the transition from the ground state to the exciton state can be calculated by:

$$\text{Transition Energy} \quad E = E_1^* - E_1 + \Delta E_{\text{vdW}} \pm J \tag{1.2}$$

where E_1^* and E_1 refer to excited- and ground-state energy, E_{vdW} is the difference in the *van-der-Waals* energies of the ground and excited-state and J is the exciton coupling energy, as defined above.[71, 77, 78] Since E_1^*, E_1 and E_{vdW} are constant for an specific system, the overall energy splitting only depends

on J. In addition to the magnitude of the transition dipole moment $\vec{\mu}$, the exciton coupling energy J is strongly affected by the spatial arrangement of the chromophores. Even though it is known that the point-dipole approximation dramatically overestimates the exciton coupling energy, this simple explanation of a complex phenomenon is one of the charms of the molecular exciton model.[77, 78, 80]

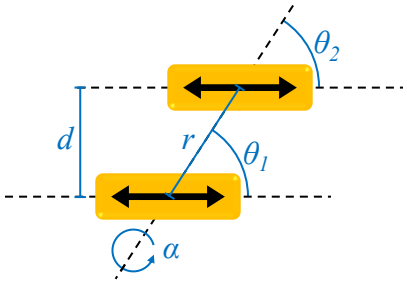


Figure 1.6: Schematic representation of a chromophore dimer highlighting key variables of their spatial arrangement.

Assuming the simplest case – a chromophore dimer – several geometric parameter influence the spatial arrangement and consequently the exciton coupling energy J. As illustrated in Figure 1.6, these parameters include the slip angle θ, the center-to-center distance r, the stacking distance d and the rotational angle α. In the following, four different spatial configurations of chromophore dimers will be discussed, highlighting on how each affects the resulting optical properties.[71, 77, 78]

The first case illustrated in Figure 1.7 (top) presents a coplanar, parallel arrangement (α = 0, $\theta_1 = \theta_2$) of the transition dipole moments $\vec{\mu}$ with a constant center-to-center distance r. Within this configuration, the interaction between the transition dipole moments can be either repulsive or attractive in nature, depending on the relative phase of the coupled dipoles. This coupling gives rise to two non-degenerated excitonic states (refer Equation (1.2)), whose energies lie either above (+J) or below (-J) the monomeric $S_0 \rightarrow S_1$ transition. The energy difference between these two states is 2J and called Davydov splitting. For a transition to be optically allowed, the vector sum (dashed purple arrows) of the individual transition dipole moments (solid purple arrows) must be non-zero $\vec{\mu}_{ges} \neq 0$. This selection rule is only fulfilled in the case of in-phase dipole alignments, as shown by the solid black transition line, whereas the gray transition line represents the forbidden excitation.

Depending on the slip angle θ, this system exhibits two boarder cases that corresponds to two distinct aggregate types. For a slip angle θ = 90°, the chromophores adopt a parallel, face-to-face arrangement. With respect to the selection rule for an optically allowed transition of $\vec{\mu}_{ges} \neq 0$, only the higher-energy excitonic transition is allowed. This results in a hypsochromic (blue) shift of such aggregates in their absorption spectra and are called therefore H-aggregates as mentioned above. As the slip angle θ decreases, the Davydov splitting energy (2J) between the allowed and forbidden exciton states progressively becomes smaller. From Equation (1.1) it is evident that for an angle of 54.7° – commonly referred to as the magic angle – the exciton splitting becomes zero, indication a turning point. When θ approaches 0°, the chromophores adopt a co-linear, head-to-tail arrangement of the chromophores. In this geometry, the lower-energy excitonic transition becomes optically allowed,

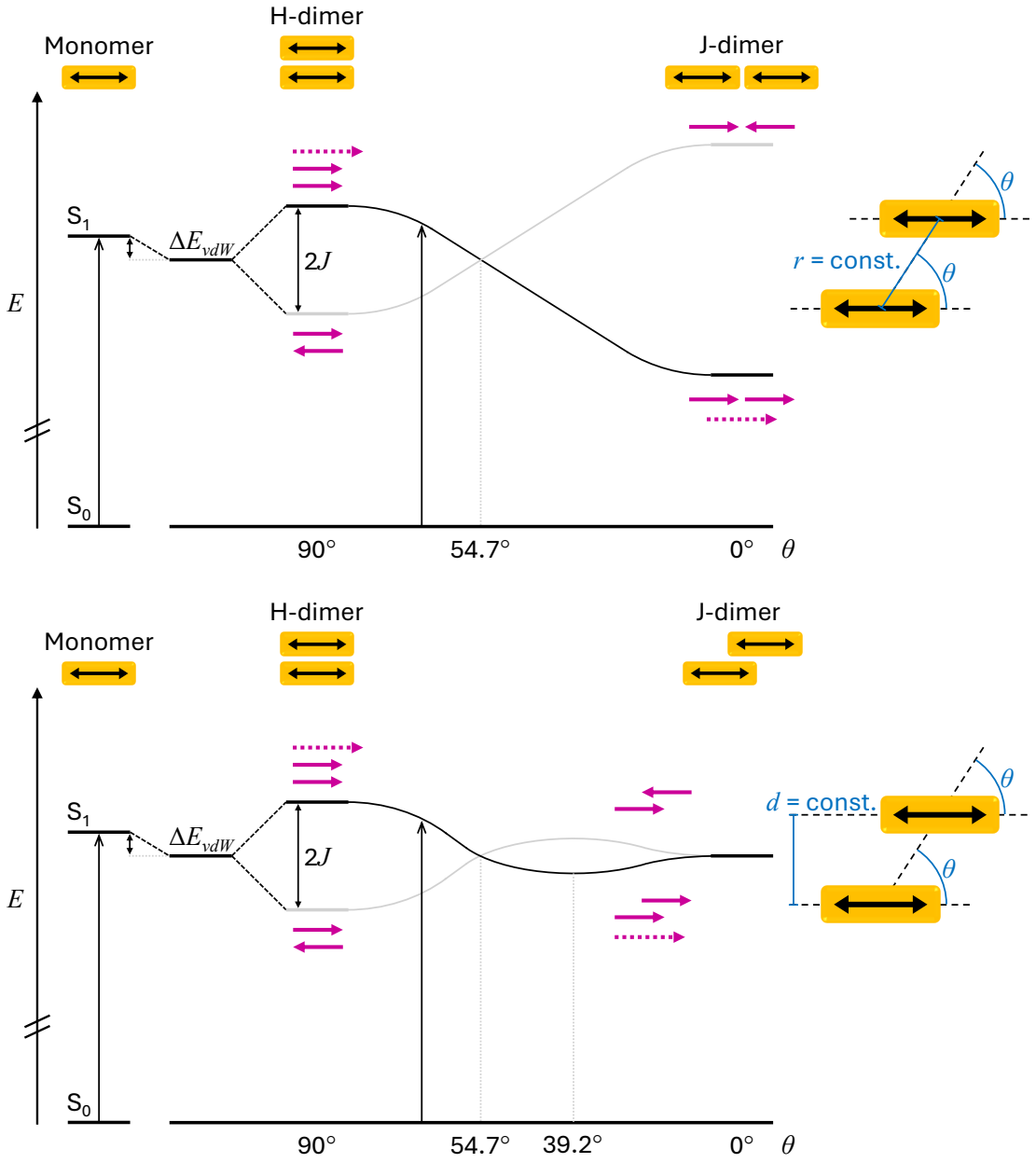


Figure 1.7: Exciton state diagram depending on the slip angle θ for the first two cases: coplanar, parallel arrangement (α = 0, $\theta_1 = \theta_2$) of the transition dipole moments and constant center-to-center distance r (top) or constant stacking distance d (bottom). Individual transition dipole moments are depicted as solid purple arrows, while dashed purple arrows indicate the overall dipole moment derived via vector addition. Allowed and forbidden optical transitions between the electronic states S_0 and S_1 are depicted by black and gray lines, respectively. J denotes the exciton coupling energy and E_{vdW} is the energy stabilization due to *van-der-Waals* interactions.[69, 71]

resulting in a bathochromic (red) shift with respect to the monomer. This behavior is characteristic of J-aggregates, as previously described.[71, 77, 78]

While this simplified explanation is frequently used, it does not consider structural features or differences of the chromophores like the three-dimensional expansion of the molecule itself. A more realistic exciton state diagram of a chromophore dimer is shown in Figure 1.7 (bottom). Here, instead of keeping the center-to-center distance r constant, the stacking distance d is kept constant. A slip angle of θ = 90° corresponds thereby exactly to the previously described H-aggregate, which exhibits the largest excitonic energy splitting (2J). With decreasing θ beyond the magic angle, however, the center-to-center distance r of the chromophores, and thereby, the distance between the transition dipole moments $\vec{\mu}$ steadily increases. Since the exciton coupling energy J is proportional to r^{-3}, the splitting of the exciton states is narrowed and becomes zero at θ = 0°. At this point, instead of considering the system as aggregated dimer, the two chromophores can be seen as non-interacting, isolated molecules.[71, 77, 78]

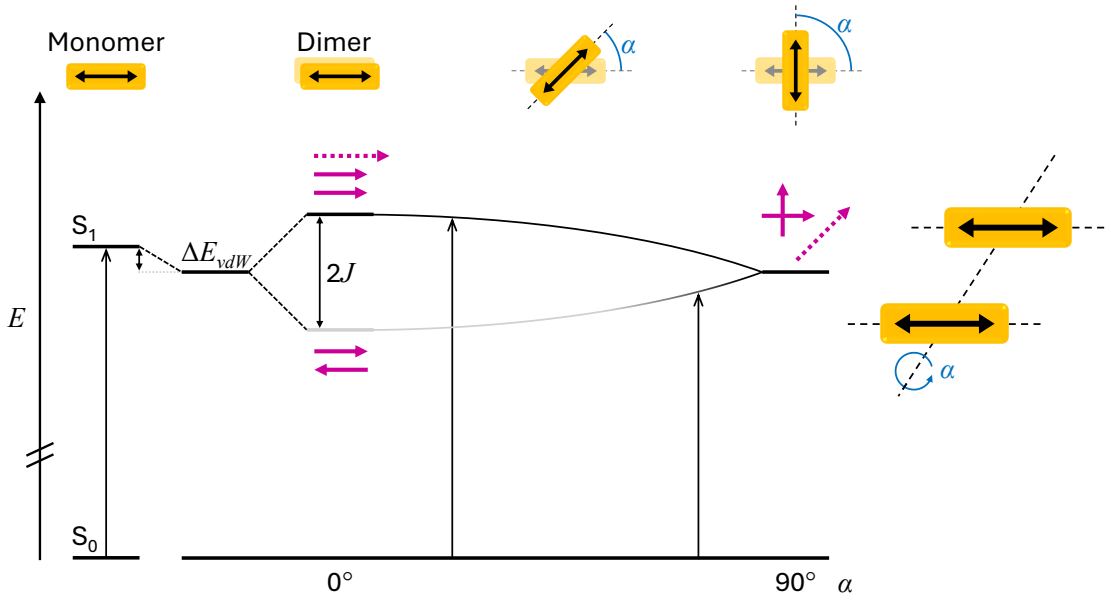


Figure 1.8: Exciton state diagram for the third case: rotation around the angle α with a parallel arrangement (θ_1 = θ_2 = 90°, ideal H-aggregate) of the transition dipole moments. Individual transition dipole moments are depicted as solid purple arrows, while dashed purple arrows indicate the overall dipole moment derived via vector addition. Allowed and forbidden optical transitions between the electronic states S_0 and S_1 are depicted by black and gray lines, respectively. J denotes the exciton coupling energy and E_{vdW} is the energy stabilization due to *van-der-Waals* interactions.[71]

In the upper two cases, only coplanar arrangements with a rotational angle of α = 0° have been discussed. Although this configuration might apply to most chromophore systems, it becomes insufficient when chiral, non-coplanar arrangements are present. Such chiral properties usually arise from helical stacking of the chromophores, which have been reported in the literature several times.[2, 34] The exciton state diagram in Figure 1.8 considers this case, using the example of an ideal H-aggregate (θ_1 = θ_2 = 90°), as function of the rotational angle α. Starting from α = 0°, the largest excitonic energy splitting (2J) of an ideal H-aggregate is observed. As α is continuously increased, the excitonic energy splitting becomes smaller and reaches zero at 90°. Since the vector sum the transition dipole moments for large angles ($\alpha \rightarrow$ 90°) becomes unequal zero, two transitions become optically allowed. Consequently, the

corresponding absorption spectra exhibit two bands – one hypsochromic and one bathochromic shifted relative to the monomer absorption. However, in typical helical stacks, the rotational angle α is usually too small to be spectroscopically resolved, and thus, normally not observed.[71, 77, 78]

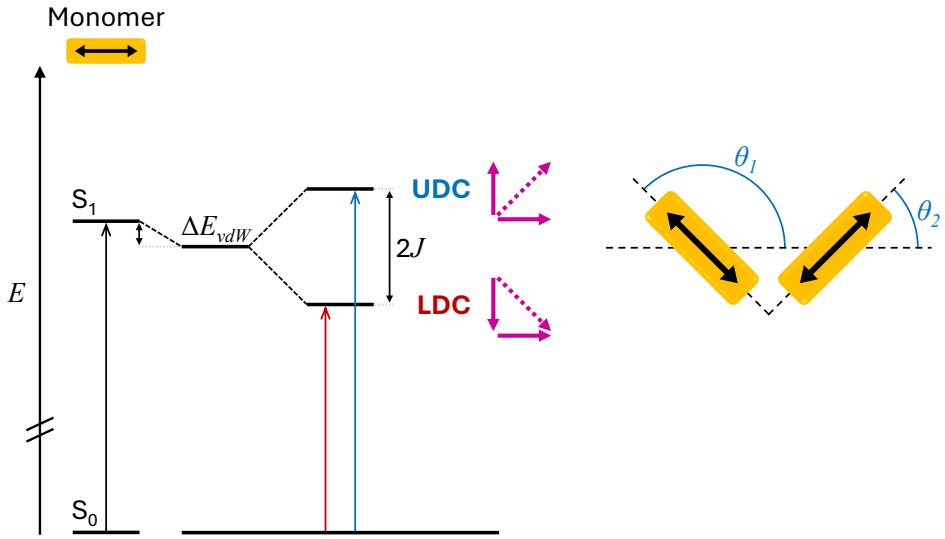


Figure 1.9: Exciton state diagram for the fourth case: coplanar, oblique arrangement (α = 0, $\theta_1 \neq \theta_2$) of the transition dipole moments. Individual transition dipole moments are depicted as solid purple arrows, while dashed purple arrows indicate the overall dipole moment derived via vector addition. Two allowed optical transitions between electronic states S_0 and S_1 are shown as black lines and labeled as UDC (upper Davydov component) and LDC (lower Davydov component), respectively. $2J$ denotes the Davydov splitting energy and E_{vdW} is the energy stabilization due to *van-der-Waals* interactions.[71, 80, 83, 84]

The final case considers a coplanar arrangement of chromophores (α = 0) with non-parallel slip angles ($\theta_1 \neq \theta_2$), resulting in an oblique geometry. In this configuration, the vector sum of the individual transition dipole moments $\vec{\mu}_{ges}$ is non-zero, leading to two optically allowed transitions in the absorption spectrum. Depending on the specific arrangement, the spectrum can exhibit either a pronounced hypsochromic or bathochromic absorption. The energy difference between the two exciton states is called Davydov splitting, a phenomenon only observed in crystal structures of two or more translationally invariant molecules within a unit cell. The higher exciton state is therefore called upper Davydov component (UDC), and the lower exciton state is referred as lower Davydov component (LDC).[77]

1.2.2 Expansion on Intermolecular Charge Transfer

Although the molecular exciton model has clearly its strengths in the simple description of such a complex phenomenon, it is insufficient to account for all observed optical changes upon aggregation. One example are the characteristic double hump spectral signatures in the absorbance spectra of *n*-alkyl anilino-squaraines.[85] In order to achieve a theoretical framework in which the calculated spectra match the experimental observations, incorporation of intermolecular charge transfer (ICT)

interactions was necessary. In this context, the classical Frenkel-like exciton states couple with charge separated (CS) electronic states through an ICT, resulting in mixed electronic states as it is shown in Figure 1.10. Here, the squaraine system is described in terms of three essential diabatic electronic states: one neutral (D-A-D) and two degenerate charge-separated states (D^+-A^--D and D-A^--D^+) as previously depicted in Figure 1.2 (Section 1.1). This concept was originally introduced by *Spano* and *Collison*,[14, 86–88] based on observations made with *n*-alkyl anilino-squaraines. In thin films, these compounds exhibited the characteristic double hump spectral feature. However, the absence of fluorescence and the slip-stacked packing arrangement in single-crystal structures ruled out Davydov splitting, pointing instead to alternative excitonic coupling mechanisms.

Recently, an alternative approach to describing these observations during aggregation was reported, in which linear absorption and pump-probe spectroscopy were used to investigate structural disorder as the underlying cause within the framework of a disordered exciton model.[76] The impact of disorder on the spectral changes, however, is still under discussion.

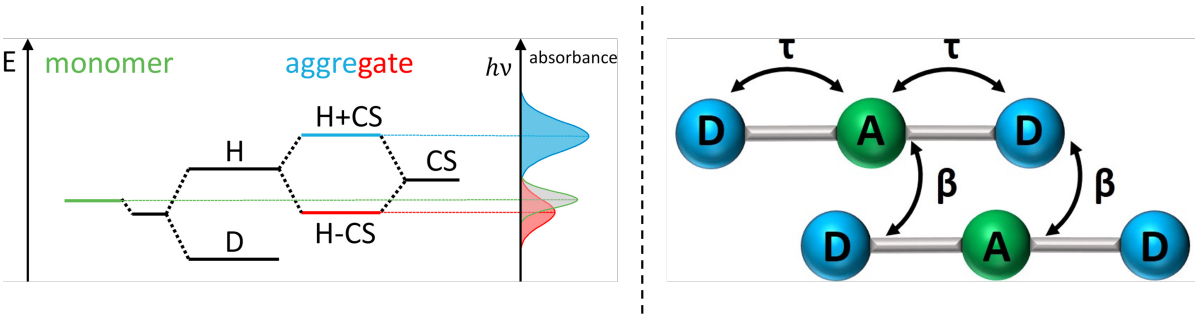


Figure 1.10: Illustration of the origin of double-hump absorbance spectra in *n*-alkyl anilino-squaraines.[85] Coulombic interactions lead to excitonic state splitting within H-aggregates, resulting in a higher-energy, optically allowed (H) state and a lower-energy, optically forbidden (D) state. The donor-acceptor-donor (D-A-D) structure, combined with the slipped π-stacked arrangement of the chromophore dimer, enables both intramolecular (τ) and intermolecular (β) charge transfer interactions (shown on the right). This generated charge-separated (CS) electronic state couples with the H-state, leading to two additional optically allowed transitions (H+CS and H−CS). Left: Figure reprinted with permission from [89] © 2016, Elsevier. Right: Figure reprinted with permission from [2] © The Royal Society of Chemistry 2023.

As several publications included in the main body of this thesis specifically address the aggregation behavior of (chiral) squaraine dyes, this topic was only briefly addressed. For more detailed theoretical and experimental insights, please refer to the following publications in Chapter 3, 6 and 8.

1.3 Chirality and Optical Activity

Chirality is a fundamental concept in chemistry and biology, referring to molecular systems that lack a mirror plane or inversion center and cannot be superimposed onto their mirror image through rotational symmetry. While enantiomers share the same physical properties in achiral environments, their chiral nature becomes only evident when interacting with another chiral object or media – such as polarized light. The entirety of optical properties of chiral molecules are collectively described by the term optical activity. This includes phenomena such as circular birefringence (CB) and circular

dichroism (CD). The latter is defined as the different absorbance between left- and right-circularly polarized light (CPL). In a broader context, also the interaction of linear polarized light occurs since it can be understood as the superposition of left-and right-handed CPL, identical in amplitude and phase. For all chiral compounds, the optical activity – such as CD and CB – occurs within the spectral region corresponding to their normal absorption of electromagnetic radiation. The exploitation of chiral optical properties has recently gained significant attention in the field of optoelectronics.[90] In this context, chirality can serve as a setscrew to control the supramolecular packing and organization within the active layer of a functional device i.e. chirality-dependent organization.[91] In addition, the direct utilization of optical activity is possible as well. This led to the development of unique technologies, including circular dichroic electrochemical sensors, chiroptical switches, electron spin filters (via chiral induced spin selectivity-effect), CPL detectors & emitters, memory & storage devices as well as in spin injection & detection interfaces.[91, 92]

1.3.1 Chiral Dichroism

The most exploited optical activity of matter in chiroptical devices is the electronic circular dichroism (EDC, henceforth just called CD), which requires special techniques – collectively referred to as chiroptical spectroscopies – to measure it.[90] In isotropic media such as solutions, conventional CD spectropolarimeters are used to measure the wavelength-dependent differential absorbance[a] (ΔAbs^{CP}_{sol}) of left- and right- circularly polarized light (Abs_L and Abs_R) to calculate the CD after the following equation:

$$\Delta Abs^{CP}_{sol} = Abs_L - Abs_R \quad \text{with } Abs = \frac{1}{2}(Abs_L + Abs_R) \tag{1.3}$$

Depending on which polarization component is predominantly absorbed, the CD effect can be either positive or negative. For a pair of enantiomers, however, the CD signal is always of opposite sign due to their mirror-image electronic configuration. Analogously to the *Lambert-Beer Law*[b], the molar CD ($\Delta\epsilon$) can be defined based on the molar extinction coefficients of left- and right-CPL (ϵ_L and ϵ_R). This parameter is independent of the optical path length l and concentration c of the sample and is expressed in the same units [M^{-1} cm^{-1}] as the molar extinction coefficient in conventional UV/Vis spectroscopy.[93] Due to historical convention, spectropolarimeters measure the CD as ellipticity θ in millidegree (mdeg),[93] according to the following equation:[40, 94]

$$\theta\,(\text{mdeg}) = 32982 \cdot \Delta Abs^{CP}_{sol} \tag{1.4}$$

This simplified treatment of the CD, however, becomes insufficient when applied to thin films. In solid-state samples, macroscopic anisotropies – such as linear dichroism (LD) and linear birefringence (LB) – often interfere/overlay with the CD signal. These effects, combined with the limitations of conventional spectropolarimeter optics, result in the measurement of a sum of all polarization effects. To certainly distinguish between pseudo-CD signals and the intrinsic CD originating from the anisotropic thin films, another powerful and versatile method – the Mueller matrix spectroscopy, a kind of polarization spectroscopy – is used.[34, 90, 95]

Using a Mueller matrix ellipsometer (to be precise, in this work a J.A. Woollam M2000 variable angle spectroscopic ellipsometer) in normal incidence transmission mode,[34] the first three rows

[a] Please note that absorption $A \neq$ absorbance Abs; with $Abs = -log(T)$, where the transmission T includes contributions from absorption A, reflection $Refl$ and scattering S after $T = 1–A–Refl–S$

[b] Lambert-Beer Law: $Abs_\lambda = \varepsilon_\lambda \cdot l \cdot c$

of the normalized Mueller matrix (see Equation 1.5) can be measured. According to an algebraic method described in the literature,[96] the complete Mueller matrix (MM or M) can be reconstructed for non- or low-depolarizing samples. After calculating the matrix logarithm of M, the reconstructed differential Mueller matrix L is obtained. The physical interpretation of L for transmission of light along a homogeneous medium can be seen in the following equation:[34]

$$ln(M) = L = \begin{pmatrix} 0 & -LD & -LD' & CD \\ -LD & 0 & CB & LB' \\ -LD' & -CB & 0 & -LB \\ CD & -LB' & LB & 0 \end{pmatrix} \tag{1.5}$$

with CD = circular dichroism, CB = circular birefringence, LD = horizontal linear dichroism, LD' = 45° linear dichroism, LB = horizontal linear birefringence and LB' = 45° linear birefringence. To obtain the CD values, the matrix elements l_{03} and l_{30} from the differential Mueller matrix L are averaged[c] and converted into millidegree (mdeg).[34]

Although it is possible to convert the measured CD into ellipticity values θ, the linearity to the optical path length (i.e. the layer thickness) is only given under the small-angle approximation. For this reason, and to improve comparability between different samples and molecules, CD spectra presented in this work are, whenever possible and reasonable, normalized to the thin film thickness (as CD in mdeg/nm) calculated from the ellipsometric analyses.

An even better quantitative assessment of the optical activity is given by the dissymmetry factor g. This dimensionless quantity, independent from the optical path length l (and concentration c in solution), is normalized to the absorbance Abs and defined as:[94, 97]

$$\text{Dissymmetry factor} \quad g = \frac{\Delta Abs^{CP}}{Abs} = \frac{Abs_L - Abs_R}{\frac{1}{2}(Abs_L + Abs_R)} \tag{1.6}$$

The CD[c] can thereby be converted to ΔAbs^{CP} via:[34]

$$\Delta Abs^{CP} = Abs_L - Abs_R = \frac{2}{ln(10)} \cdot CD \tag{1.7}$$

Equation 1.6 allows the dissymmetry factor (g-value) to be between ±2. However, typical g-values for organic small molecules in thin films range from 10^{-4} to 10^{-2}.[90, 97] In contrast, squaraines have been reported with significantly higher g-values – reaching up to 0.75 for proline-derived anilino squaraines (**ProSQs**) – when measured at the wavelength corresponding to the maximum CD signal.[34, 40, 90, 98]

For highly reflective thin film, the measured absorbance Abs^{meas} has to be corrected for reflection losses at the different interfaces. *Schiek* et al. approached this issue by a simple linear fit[d] of the measured absorbance Abs^{meas} at the wavelength of maximum absorbance to the layer thickness d (equivalent to the optical path length l).[34] Multiplying the slope of this linear fit[d] with the layer thickness of interest yields then the reflection-corrected absorbance Abs^{cor}, which replaces the measured absorbance in Equation 1.6 to calculate the true dissymmetry factor g_{true}.[34]

[c] $CD = \frac{l_{03} + l_{30}}{2}$

[d] $-Abs^{meas} = -log(1 - R)^2 + \frac{\alpha}{ln(10)} \cdot d$ where $(1 - R)^2$ summarizes all interface reflection losses and the absorption coefficient α

1.3.2 Interpretation of CD-Spectra

The form and nature of chirality in molecular systems can arise from fundamentally different structural origins. In the case of small molecules, chirality is typically classified into four different types: central chirality, axial chirality, planar chirality and helical chirality.[99] In the case of squaraines, chirality is predominantly introduced via central chirality, typically present on a stereogenic tertiary carbon within one of the nitrogen substituents. The optical activity of this stereocenter, coming from the absorption of C-C and C-H bonds, occurs way below 200 nm – outside the visible range of the electromagnetic spectrum.[93] This is proven by the absence of any signals in the CD spectra within the visible range of monomeric solutions or pristine thin films of, for example, proline-derived anilino squaraines (**ProSQs**).[2, 40] In aggregated solutions or thermally annealed thin films, however, a giant intrinsic excitonic circular dichroism is observed.[2, 34, 100] This phenomena can be attributed to a different level/hierarchy of chirality in these systems, which is obviously expressed by the aggregation. In addition to configurational chirality – arising from stereocenters – chirality of higher order like phase chirality may also be present. In supramolecular chemistry, however, chirality typically arises from conformational chirality, such as the formation of helical arrangements by molecular building blocks. For squaraines, this behavior is based on the unique aggregation behavior of these dyes, where the intrinsic molecular chirality of the molecule is transferred via aggregate formation to a supramolecular, and hence, macroscopically detectable level.[101, 102]

The strength of the CD signal is given by the rotational strength (R), which is defined as the scalar product of the electric ($\vec{\mu}$) and magnetic ($\vec{m}$) transition dipole moments. Considering the simplest case of two coupled chromophores within a supramolecular assembly exhibiting strong exciton coupling (cf. Section 1.2), the rotational strength can be expressed as:[103, 104]

$$\begin{aligned} \text{Rotational strength} \quad R &= \mathrm{Im}(\vec{\mu} \cdot \vec{m}) \\ &= (-\frac{1}{2})\mathrm{Im}(\vec{m}_1 \cdot \vec{\mu}_1 + \vec{m}_2 \cdot \vec{\mu}_2) \pm (-\frac{1}{2})\mathrm{Im}(\vec{m}_1 \cdot \vec{\mu}_2 + \vec{m}_2 \cdot \vec{\mu}_1) \\ &\quad \pm (\frac{\pi}{2\lambda})\vec{r_{21}}(\vec{\mu}_1 \times \vec{\mu}_2) \\ &= R_{\mathrm{mon}} + R_{\mathrm{e-m}} + R_{\mathrm{ex}} \end{aligned} \tag{1.8}$$

where Im stands for the imaginary part and r_{21} is the distance vector between the electric point dipole centers of the monomers. Thereby, the electric transition dipole moment ($\vec{\mu}$) describes the extent of translational motion of the transition charge upon electronic excitation, whereas the magnetic transition dipole moment ($\vec{m}$) describes the extent of transition charge rotation of this excitation process.[90] The term R_{mon} represents the sum of the rotational strengths of the individual monomers. In contrast, the electric-magnetic term $R_{\mathrm{e-m}}$ accounts for the interactions between $\vec{\mu}$ of one chromophore with $\vec{m}$ of the other, and vice versa. The last term R_{ex} is called exciton term, which is the interaction of the two electric transition dipole moments $\vec{\mu}$ of both chromophores in dependence of r_{21}. In order to observe a CD signal, the rotational strength R must be non-zero, which requires a chiral arrangement of the two chromophores (rotational angle $\alpha \neq 0$, see Figure 1.11). Since $\vec{m}$ is typically several orders of magnitude smaller than $\vec{\mu}$ and $\vec{m}$ is often nearly orthogonal to $\vec{\mu}$, R_{mon} becomes usually negligible.[e] In a chiral supramolecular arrangement, however, the angle between $\vec{\mu}_1$ and $\vec{m}_2$ of different chromophores is

[e] The dot product of $\vec{a} \cdot \vec{b}$ with $\vec{a} \perp \vec{b}$ is zero.

no longer orthogonal, giving rise to contributions from the term $R_{\text{e-m}}$. Nevertheless, compared to the other two terms, the excitonic coupling term R_{ex} is by far the largest for excitonically coupled dimers. As a result, this positive/negative excitonic chirality leads to a characteristic bisignated signal in the CD spectra consisting of a positive and negative signal (commonly refereed to as positive or negative Cotton effect), with a zero crossing usually near the absorption maximum and an integral of zero.[94, 103, 104]

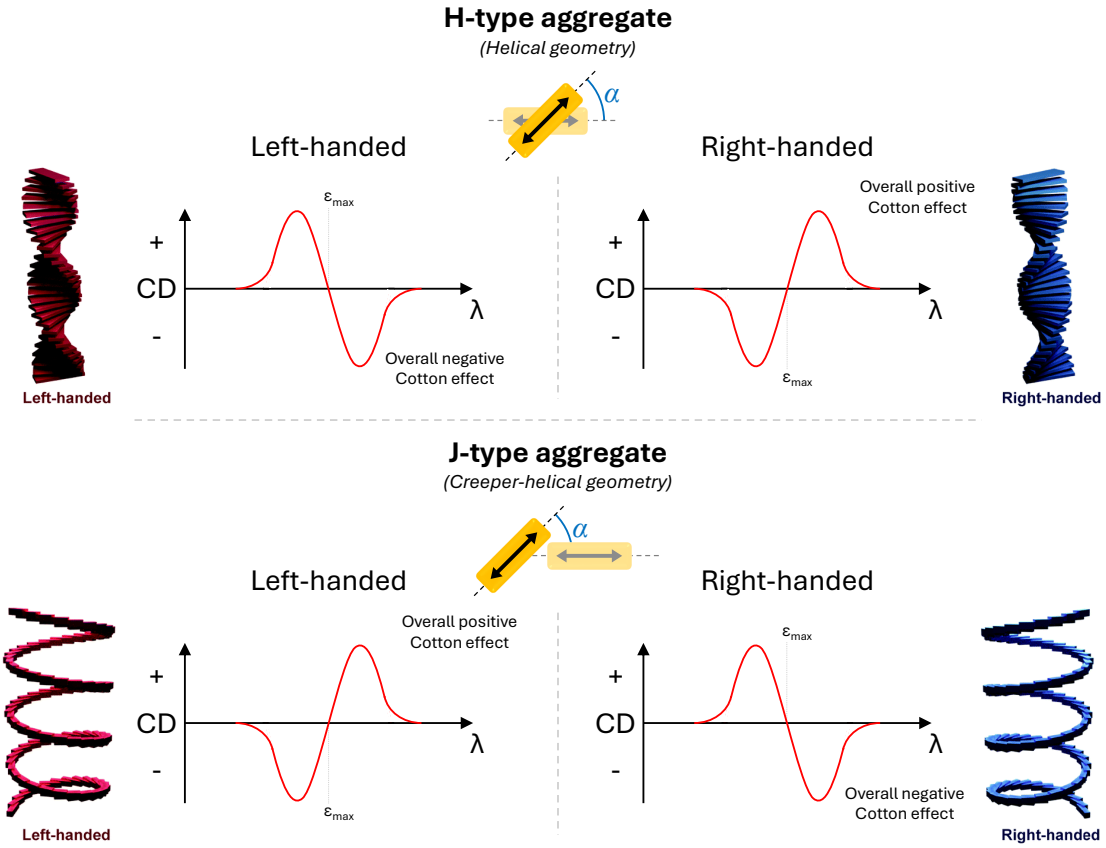


Figure 1.11: Schematic illustration of the relationship between molecular aggregates with a twisted dipole arrangement (rotational angle $\alpha \neq 0$) in a helical geometry (H-type aggregate) or creeper-helical geometry (J-type aggregate) and the bisignate CD signal. Left-handed helices are depicted in blue and right-handed helices in red.[83, 97, 105] Aggregate illustrations adopted with permission from [97] © The Royal Society of Chemistry 2021.

Depending on the sequence of the Cotton effect, the exciton chirality method can be used to give configurational and conformational information of the (supramolecular) arrangement.[106] Figure 1.11 shows the correlation of the overall Cotton effect (positive or negative; attributed to the Cotton effect at longer wavelength) and the aggregate geometry.[97, 105] Considering the first case – a helical stack geometry i.e. H-type aggregate – the overall Cotton effect flips upon changing the handedness of the helix, as expected. This observation was covered by the original exciton chirality method and later extended to creeper-helical stack geometries (i.e. J-type aggregate, henceforth called creeper aggregate).[97, 105, 106] Here, the Cotton effect also flips with a change in the helical handedness. However, an additional inversion of the Cotton effect is observed when transitioning from an H-type to a J-type aggregate.

Although the actual shape and intensity of the observed CD signal is fundamentally governed by positive or negative excitonic chirality, it is also influenced by many other factors. These include the size of the aggregate,[90] the coexistence of different aggregate species,[2, 3] structural disorder,[76] contributions from other coupling effect e.g., vibronic[86] or CT[3] and the presence of superordinate structures – particularly present in thin films.[1, 90] However, the ability to interpret complex CD spectra for configurational or conformational assignments, based simply on the shape of the CD signal is one of the method's greatest strengths. For this reason, circular dichroism spectroscopy is widely employed across both chemistry and biology.[97]

1.4 Chirality Meets Optoelectronic Devices – A Short Introduction

The generation of electrical current upon light exposure is typically associated with energy harvesting such as in conventional solar cells. However, this comprises just a small area of the possible applications. Furthermore, the photogenerated current can also serve as a signal in dedicated photodetectors for certain applications. Although, photovoltaics based on organic materials – ranging from small molecules to polymers – usually have much lower power conversion efficiencies compared to their inorganic counterparts (IPV), their primary function is light detection rather than energy generation. This makes efficiency to a secondary concern since it is only important to distinguish between on and off states in response to the presence or absence of light. The real advantage of organic materials lies in their versatile molecular tunability, allowing structural and functional adaptations for specific applications. In particular, small molecules offer several advantages over oligomeric and polymeric systems, including monodispersity, design flexibility, precise reaction control as well as good processability and reproducibility,[43] making them ideal candidates for tailored devices such as semi-transparent or flexible organic photovoltaics (OPVs).[107, 108] Additionally, purity is of utmost importance for application in OPVs. The much easier purification of small molecules represents another significant advantage.

In the context of this thesis, the chiral functionalization of the squaraines, should allow to create optoelectronic devices with the capability not only to respond to specific wavelengths of light, but also to differentiate between left- and right-handed circularly polarized light (CPL). Remarkably, such a CPL detector is composed solely of a single photodiode, operating without the need for external polarization manipulating optical elements or applied voltage bias.[98, 109] This ability of the squaraines is governed by their extraordinary aggregation behavior, whereby the intrinsic molecular chirality is transferred to a supramolecular level, and thus, usable for such applications, as discussed in Section 1.2 and 1.3. Applications for compact CPL-sensitive optoelectronic devices are still in the early stages of development, but ongoing progress may unlock opportunities in several fields of technology.[40, 98, 109] However, it all starts with the synthesis of new suitable materials, exhibiting extraordinary aggregation properties, while simultaneously meeting electronic performance requirements.

1.4.1 The Photovoltaic Effect

Fundamentally, the generation of an electrical response upon photon absorption is summarized by the photovoltaic effect – an intrinsic property of certain materials. Such an excitation leads to the generation of an Frenkel-exciton (see Section 1.2 - The Molecular Exciton Model), a coulombically strongly bound electron-hole pair.[80, 81] Naturally, there is an attractive Coulomb force – the exciton binding energy – between the negatively charged electron and the positively charged hole. The strengths of this force

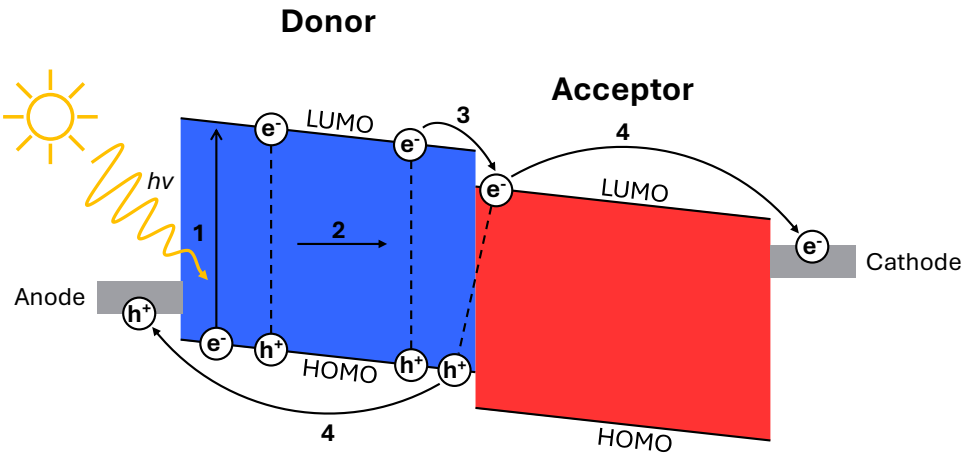


Figure 1.12: Schematic representation of the working principle of a heterojunction organic photovoltaic device with a donor (blue) and an acceptor material (red). Illustration of the four key steps: (1) photon-induced exciton generation, (2) exciton diffusion toward the donor-acceptor interface and (3+4) exciton dissociation into free charge carriers. Figure adopted with permission from [111] © The Royal Society of Chemistry 2015.

depends on the distance between them and the permittivity of the surrounding medium. The latter quantifies the characteristic electric polarizability of a material, relative to the vacuum and is given as the relative permittivity or dielectric constant (ε_r). In inorganic semiconductors, ε_r is relatively high, leading to an efficient shielding, and thus, reduction of the exciton binding energy after the excitation of an electron from the valence to the conduction band.[110] When this binding energy falls below the thermal energy at room temperature, the exciton can spontaneously dissociate into free charge carriers and used in en external circuit.[111]

In contrast to that is the relative permittivity ε_r in organic matter much lower, resulting in an inefficient shielding, and therefore, to coulombically strongly bounded excitons (electron-hole pairs) with a high exciton binding energy, preventing thermal dissociation at room temperature. In order to overcome this issue, OPVs typically use two different organic materials in a heterojunction – functioning analogously to the p- and n-type semiconductors used in IPVs. Depending on whether the material's purpose is to donate or accept the resulting excited electron after photon absorption, it is called donor or acceptor, respectively.[f] Another difference for organic materials is that, in terms of molecular orbital theory, the light-induced excitation of an electron occurs from the highest occupied molecular orbital (HOMO) to the lowest unoccupied molecular orbital (LUMO) of the molecule, rather than from a valence to conduction band. Typically, donor materials have higher HOMO and LUMO levels compared to acceptor materials, resulting in low ionization potentials (IP) for donors and high electron affinitys (E-Aff.) for the acceptor materials. The donor is thereby responsible for absorbing most of the incident light, generating excitons that can be dissociated at the donor-acceptor interface.[111, 112]

Figure 1.12 illustrates the four key steps of the working principle of donor-acceptor heterojunction

[f] Note: The donor and acceptor *materials* in the active layer of an organic photovoltaic should not be confused with the Donor-Acceptor-Donor (D-A-D) *structure* of the squaraine backbone (ref. Section 1.1).

OPVs.[111, 112] Step 1: Electromagnetic radiation of suitable energy is absorbed, leading to the excitation of an electron from the HOMO to the LUMO. This generates a coulombically strongly bounded electron-hole pair i.e. exciton.

Step 2: Once formed, the exciton diffuses towards the donor-acceptor interface. This movement requires a driving force, which typically results from two effects. The first one is based on internal electric fields (generated with and without applied voltage bias), while the second originates from concentration gradients of the respective charge carrier species. Together, these effects generate a net gradient in the electrochemical potentials of electrons and holes, facilitating the diffusion of the excitons.

Step 3: At the donor-acceptor interface, the electron can be transferred from the donor LUMO to the acceptor LUMO, while the hole remains localized on the donors HOMO. This dissociation is primarily driven by the difference in electron affinity (E-Aff.) between the donor and acceptor materials, which corresponds to the energy offset between their respective LUMO levels and occurs when this energy difference overcomes the exciton binding energy. The charge carriers within the resulting charge transfer complex (CT) remain coulombically bound across the donor-acceptor interface and are commonly referred to as geminate pairs. As the separation progresses, the attractive interaction between the electron-hole pair decreases significantly due to the quadratic dependence of Coulombic attraction on their distance. Once the spatial separation between the charge carriers approaches the Coulomb capture radius, the binding energy can be overcome by thermal energy, resulting in the formation of a charge separated (CS) state. The steps leading from the photo absorption to the full CS state must occur within a certain amount of time. If the geminate electron-hole pair cannot overcome their Coulomb attraction during this time, recombination occurs, whereby the electron relaxes back to the ground state and recombines with the hole. This timeframe is known as ”exciton lifetime” and is often given as an average diffusion distance – typically around 10 nm – before recombination occurs. In general, two types of recombination events are typically distinguished and are the primary mechanisms contributing to energy losses in OPVs: geminate recombination, which involves recombination of an initially generated electron-hole pair before their reaching the CS state and non-geminate recombination, which occurs independently of the charge carriers origin.

Step 4: Subsequent to the successful charge separation, the free charge carrier diffuse through the donor or acceptor domains to the corresponding electrodes (electrons to the cathode; positively charged holes to the anode), where they are available for electrical work in the external circuit.[111–113]

1.4.2 Devices

Apart from the molecular properties of the donor and acceptor materials, the overall device architecture has a significant influence on the final device performance. Depending on the desired functional outcome different structural constructions might be beneficial. The actual device, as illustrated in Figure 1.13 (left), consists of multiple functional layers. The two electrodes are the cathode (typically a metal) and the anode, which in academic settings is often a transparent inorganic material such as indium tin oxide (ITO) deposited on a transparent glass substrate. Sandwiched between these electrodes is the active layer, which is responsible for the interaction with electromagnetic radiation. To enhance device performance, this layer is usually put between an electron transporting layer (ETL) and a (hole transporting layer (HTL)), which supports charge carrier mobility.

Thereby, the active layer itself can be constructed differently as shown in Figure 1.13 (right). Nowa-

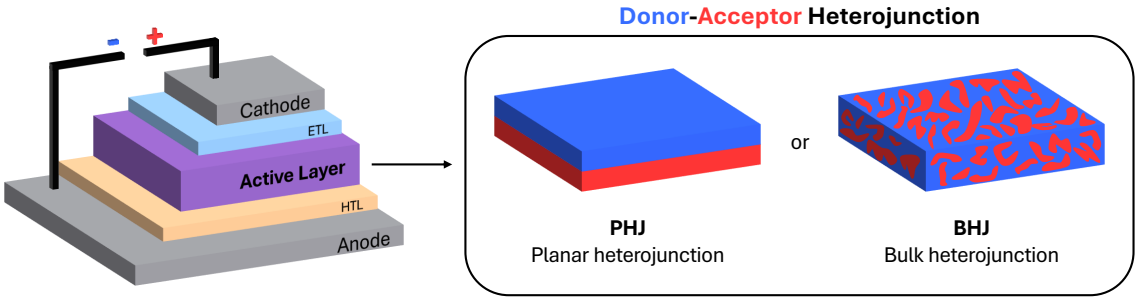


Figure 1.13: Schematic illustration of an organic photovoltaic (OPV) with donor-acceptor heterojunction. Left: Layer construction with ETL and HTL = electron or hole transporting layer. Right: The two most popular active layer construction – planar heterojunction (PHJ) and bulk heterojunction (BHJ).[111]

days, the two most popular active layer architectures are the planar heterojunction (PHJ) and the bulk heterojunction (BHJ). Each type possesses distinct advantages and weaknesses. The PHJ architecture consists of two discrete layers – one donor followed by one acceptor layer – typically achieved by successive vapor deposition of the materials. The key advantage of this architecture is that it allows (precise) control of the morphological and aggregation behavior of the active layer through independent annealing procedures (either during the vaporous deposition or by elaborated post-fabrication). However, the limitation of the PHJ is the low efficiency, attributed to the recombination of the electron-hole pairs. With an exciton lifetime of around 10 nm but a layer thickness of around 100 nm to achieve efficient light absorption, only excitons right at the donor-acceptor interface are capable to dissociate in separated charge carrier.

This problem is tackled by the BHJ, which consists of an intermixed composition with a mostly entropy-driven nanoscale phase separation of the donor and acceptor materials. This architecture allows for short diffusion distances to the interface while still achieving the necessary thickness for efficient light absorption. However, the phase morphology is of essential importance. Highly blended active layers can hinder charge transport by limiting diffusion pathways for separated charge carriers to the electrodes. Conversely, coarsely mixed active layers suffer from the same limitations as the PHJ. Overall, the morphology of the active layer is easier to control and reproduce in PHJ architectures, however, their fabrication is more complicated than that of BHJ layers. Another drawback of the BHJ is that the aggregation of individual molecules is difficult to control, sometimes resulting in dewetting[g] or even in phase separation of the donor and acceptor materials.[111, 112, 114]

1.4.3 Chiroptical Activity in Squaraine Based Optoelectronic Devices

The first investigations into the use of chiral squaraines in optoelectronic devices were conducted by *Schiek* et al. in 2017.[40] In this study, they used proline-derived anilino squaraines – functionalized with either hexyl- or hexadecyl-chains (**ProSQ-C6** or **ProSQ-C16**) – in a conventional BHJ photodiode architecture, using the well-established fullerene [6,6]-phenyl-C_{61}-butyric acid methyl ester (**PCBM**) as acceptor material.[115] Initial results showed that the long-chain compound (**ProSQ-C16**) exhibited signs of phase separation, making the short-chain variant (**ProSQ-C6**), especially in combination with the lower

[g] Dewetting describes the process by which a fluid retracts from a non-wettable surface that it was previously forced to cover.

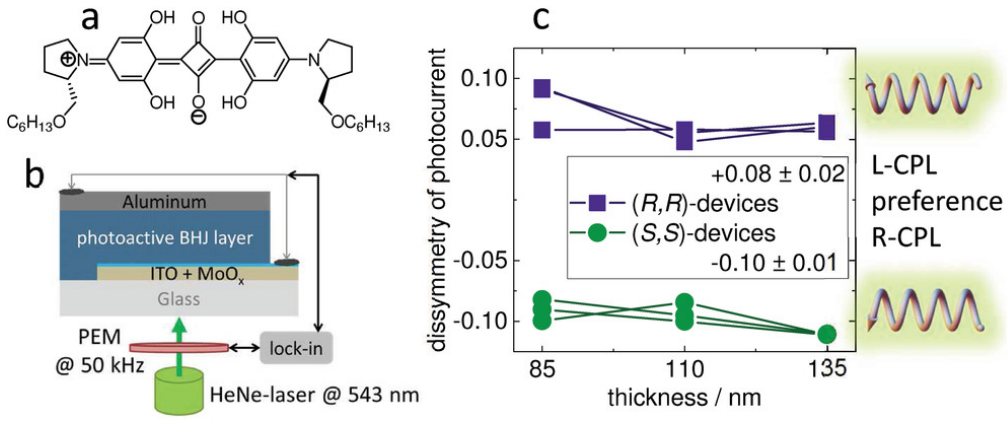


Figure 1.14: Performance of the CPL detector: a) Structural formula of the used proline-derived anilino squaraine – **ProSQ-C6**. b) Schematic illustration of the detector architecture and measuring-setup for the polarization resolved photocurrent. c) Dissymmetry of short circuit current (g_I) under illumination with 543 nm circularly polarized light for both enantiomers of **ProSQ-C6**. Figure reprinted with permission from [98] © 2019 WILEY-VCH Verlag GmbH & Co. KGaA, Weinheim.

annealing temperature to achieve sufficient chiral aggregation, more attractive for further investigations. In 2019 *Schiek* et al. presented a refined chiral excitonic organic photodiode utilizing the two enantiomers of **ProSQ-C6** as donor materials.[98] As shown in Figure 1.14, the circular dichroic photoactive blend of **ProSQ-C6** and **PCBM** exhibited thickness-normalized ellipticity values of +17 and -19 mdeg/nm (averaged across three layer thicknesses), translating to reflection-corrected true optical dissymmetry factors g_{true} (ref. Equation 1.6) of 0.08 and 0.09 for the (*R*,*R*)- and (*S*,*S*)-enantiomers, respectively.[h] The final devices achieved a short-circuit current density (J_{SC}) of approximately 6.5 mAcm^{-2}, fill factor (FF) of around 56% and power conversion efficiency (PCE) near 2.5%. As observed in preliminary studies,[40] the maximum external quantum efficiency (EQE) overlapped well with the CD maximum, reaching values up to 50%. Thereby, the authors showed that the optical dissymmetry of the active layer could be translated into photocurrent dissymmetry via polarization resolved photocurrent measurements. Overall, the devices exhibited a short-circuit photocurrent dissymmetry factor[i] $g_{I_{SC}}$ of up to ±0.1, corresponding to a polarization discrimination efficiency of approximately 5%.

By this *Schiek* et al. successfully fabricated an optoelectronic devices capable not only of responding to green light, but also to differentiate between left- and right-handed circularly polarized light (CPL), operating without external optical elements or applied voltage bias.

[h] The observed differences in the ellipticity and g-values were attributed to variations in the enantiomeric excess (ee) of the starting material.

[i] Calculation similar to Equation 1.6, with I_L and I_R

CHAPTER 2

Motivation and Objective

The extraordinary properties and wide spread application of the unique class of squaraine dyes has already been pointed out several times in this thesis. Here, the class of *n*-alkyl anilino squaraines, showing a characteristic double-hump spectral feature in solution-processed thin films,[85] exhibits excellent properties for the application in optoelectronic devices. The origin of this double-hump, however, has been theorized but never actually supported by experimental data. In terms of chiral squaraines, especially the class of proline-derived anilino squaraines (**ProSQs**) has been given high attention in recent years. Such chiral organic molecules exhibit the potential for the next step in circularly polarized light-sensitive detectors, operating without external optical elements or applied voltage bias.[34, 40, 98] Although the synthetic approach has been steadily developed during the last decades, these dyes are, from a theoretical standpoint, almost unpredictable in terms of the final properties and aggregation behaviour. For example, it has been shown that enantiopure **ProSQs** exhibit structural circular dichroism (CD) via supramolecular self-assembly/aggregation with values several orders of magnitude larger than intrinsic CD. The latter is considered as the molecular chirality introduced via a chiral side chain (which is not directly connected to the conjugated π-system and therefore cannot be seen directly in the normal UV/Vis range), which is transferred to the supramolecular, and thus, measurable level. Spin-coated and thermally annealed thin films lead to the emergence of an exceptionally high optical dissymmetry factor (*g*-value).[2, 34] Even though this class of dyes has been already used in devices, the underlying arrangement of the chromophores and mechanism of this strong chiroptical response, in both solution and the solid state, is still unknown. Thus, empirical and systematic investigations of this and different squaraine systems are required to expand our knowledge and achieve a better understanding of the self-assembly and structure-property relationships of this class of molecules.

The focus of this work was the synthesis of new homochiral proline-, indolenine-derived and chiral-*N*-functionalized anilino squaraines with different substitution patterns, suitable for optoelectronic applications. In addition to exploring different molecular motifs, particular attention was given to the variation of terminal *n*-alkyl groups in order to optimize aggregation behaviour and the associated chiroptical properties. After successful synthesis of specially designed squaraines, all dyes have to be further investigated with respect to their supramolecular organization – i.e. aggregation – and the resulting chiroptical properties, both in solution and in the solid state. Using a wide range of different analytical techniques, a comprehensive characterisation of the individual compounds should

be achieved. Based on the resulting data, structure-property relationships should be analyzed to expand the existing knowledge of this highly interesting class of dyes, thereby mainly focusing on providing new insights into their extraordinary (chiral) aggregation behaviour. This applies in particular to the earlier mentioned emergence of the characteristic double-hump spectral feature via chiral functionalized *n*-alkyl anilino squaraines derivatives as well as to the class of **ProSQs**. Finally, the application and characterisation of a specially designed squaraine in an organic photovoltaic (OPV) device should be accomplished.

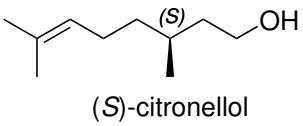
This work can essentially be divided into the following parts:

- **Part A** – including Chapter 3, 4 and 5 – will investigate the impact of *N*-functionalization with enantiopure citronellyl groups on diverse squaraine motifs.
- **Part B** – including Chapter 6, 7, 8 and 9 – covers all studies done on proline-derived and extended (e.g., indoline-derived) chiral squaraines.
- **Part C** – Chapter 10 – is about the strategic integration of beneficial properties from both proline-derived and *n*-alkyl anilino squaraines, for the application in optoelectronic devices.
- **Part D** – Chapter 11 – is an excursus into the synthesis of chiral π-conjugated polymers exhibiting the chiral induced spin selectivity (CISS) effect for advanced optoelectronic applications and summarizes the results of a three-month research stay in 2023 in the group of Prof. Dr. Seth R. Marder at the University of Colorado Boulder, USA.

Part A – Citronellyl-Functionalized Chiral Squaraines

Enantiopure compounds that are either directly obtained from or derived from natural products are commonly referred to as the *chiral pool*. These substances -typically amino acids, carbohydrates or terpenes – allow chemists to introduce chirality into molecular systems in an straightforward, cheap and accessible fashion. Among these, terpenes, a class of natural products consisting of a complex carbon skeleton of isoprene (C_5) units, can be considered as the most versatile contributors to the chiral pool, with over 55,000 known structures. From this isoprenoid group, a wide variety of molecular motifs with various functional groups can be obtained, such as alkenes (e.g., citronellene), alcohols (e.g., citronellol and linalool) and aldehydes (e.g., citronellal). Thereby, (*S*)-citronellol (Figure 2.1) is inexpensive, commercially available and allows for numerous chemical transformations, enabling the introduction of a broad range of different functional groups. All of this contributed to making it one of the most widely used reagents of the chiral pool.[116–118] Over the last decades, functionalization with homochiral citronellyl groups has become one of the most used terpene-based strategies for introducing chirality into molecular systems, particularly in the context of optoelectronic applications.[109, 119]

In the context of squaraines, *N*-functionalization with enantiopure citronellyl groups, is often selected for several reasons. Besides being readily accessible and widely utilized in chiral synthesis, as already mentioned, their branched structure also enhances the solubility of the resulting squaraine, being beneficial for solution-based processing methods. In addition, the alkyl chain can enhance the aggregation tendency via *van-der-Waals* interactions.[1, 120–122]



(*S*)-citronellol

Figure 2.1: Chemical structure of (3*S*)-3,7-dimethyl-1-octanol, commonly known as (*S*)-citronellol.

In the following three chapters, citronellyl-functionalized chiral squaraines will be discussed. The first one – Chapter 3 – comprises the impact of chiral citronellyl-functionalization on indolenine and anilino squaraines applied in solution processed thin films. These results have been published in the peer-reviewed journal *Israel Journal of Chemistry* and is included as a summary in a way that picks up on aspects of the introduction (ref. Chapter 1), allowing the section to be read as a coherent overview. The publication itself is provided in Appendix A.

The second one – Chapter 4 – builds upon the findings of the first by investigating a series of alkyl substituents with increasing steric hindrance in solution and thin films. This approach aims to suppress

the intermolecular charge transfer (ICT) contribution from the proposed hybridization between a Frenkel exciton and a charge transfer exciton.

The last one – Chapter 5 – is about the synthesis and ellipsometric investigation of a chiral benzothiazole-derived squaraine in solution and thin films. By substitution of the CMe_2 group in the indolenine moiety with a sulfur atom, the steric clash is significantly reduced. This resulted, in contrast to the indolenine-derived squaraines from Chapter 3, in pronounced chiral aggregation identified by Mueller matrix polarimetry. This chapter is included in its entirety as it is scheduled for publication in the peer-reviewed journal *ChemPhysChem*.

CHAPTER 3

The Impact of Chiral Citronellyl-Functionalization on Indolenine and Anilino Squaraine Thin Films

F. Balzer,[a] M. F. Schumacher,[b] S. Mattiello,[c] M. Schulz,[b] J. Zablocki,[b] M. Schmidtmann,[d] K. Meerholz,[e] N. Serdar Sariciftci,[f] L. Beverina,[c] A. Lützen,[b] M. Schiek[f,g,h]

Received: July 25, 2021
Published online: November 02, 2021

Reprinted with permission[i] from:
F. Balzer, M. F. Schumacher, S. Mattiello, M. Schulz, J. Zablocki, M. Schmidtmann, K. Meerholz, N. S. Sariciftci, L. Beverina, A. Lützen, and M. Schiek, "The Impact of Chiral Citronellyl-Functionalization on Indolenine and Anilino Squaraine Thin Films," *Israel Journal of Chemistry* **2022**, *62* (7-8), e202100079, doi: 10.1002/ijch.202100079
– Copyright ©The Authors. Israel Journal of Chemistry published by Wiley-VCH GmbH.

Own contributions:

- Preparation of the thin film samples
- Performing and evaluating the ellipsometric/polarimetric measurements
- Writing parts of the manuscript

[a] SDU Centre for Photonics Engineering, Mads Clausen Institute, University of Southern Denmark, Alsion 2, DK-6400 Sønderborg, Denmark
[b] Kekulé-Institute for Organic Chemistry and Biochemistry, University of Bonn, Gerhard-Domagk-Str. 1, D-53121 Bonn, Germany
[c] Department of Materials Chemistry and INSTM, University of Milano-Bicocca, Via R. Cozzi 53, I-20125 Milano, Italy
[d] Department of Chemistry, University of Oldenburg, Carl-von-Ossietzky-Str. 9–11, D-26129 Oldenburg, Germany
[e] Physical Chemistry, University of Cologne, Greinstr. 4–6, D-50939 Cologne, Germany
[f] Linz Institute for Solar Cells, Johannes Kepler University, Altenberger Str. 69, A-4040 Linz, Austria
[g] Center for Surface- and Nanoanalytics and Linz Institute for Solar Cells, Johannes Kepler University, Altenberger Str. 69, A-4040 Linz, Austria
[h] Institute of Physics, University of Oldenburg, Carl-von-Ossietzky-Str. 9–11, D-26129 Oldenburg, Germany
[i] Permission requests to reuse material from this chapter should be directed to Wiley-VCH GmbH.

Squaraine dyes (SQs) are small-molecule Donor-Acceptor-Donor (D-A-D) compounds characterized by zwitterionic resonant structures.[6] This characteristic gives rise to pronounced intramolecular charge-transfer states (not confused with intermolecular charge transfer), which, upon aggregation, result in strong intermolecular excitonic interactions.[86] Such interactions may be of Coulombic nature (e.g., Frenkel excitons)[67] or may involve intermolecular charge transfer (ICT) excitons.[85] This behavior is largely determined by molecular packing, particularly the spatial arrangement of the π-conjugated molecular backbones within the aggregate. One approach to influence the molecular packing involves functionalization with various substituents. For anilino SQs, terminal *N*-functionalization is the most commonly used strategy.[85] There it has been demonstrated that the introduction of bulky substituents can disrupt molecular packing in such a way that only Coulombic interactions are present, resulting in spectra characterized by a Davydov splitting.[67] In contrast, linear alkyl chains allowed for close slip-stack packing and ICT interactions. This resulted in distinct double hump spectral features, which have been interpreted as mixed states involving both Coulombic H-aggregates and charge-separated states.[89] In the case of indolenine-derived squaraines, usually a core substitution is used within the five-membered ring.[122, 123]] However, these systems allow as well for a functionalization of the nitrogen. The usage of chiral substituents offers thereby an essential advantage by implementing excitonic circular dichroism (CD) – another valuable tool for investigation. Here, the exciton chirality emerges from the chiral supramolecular arrangement of SQ transition dipoles, mediated by chiral side chains.[90, 124, 125]

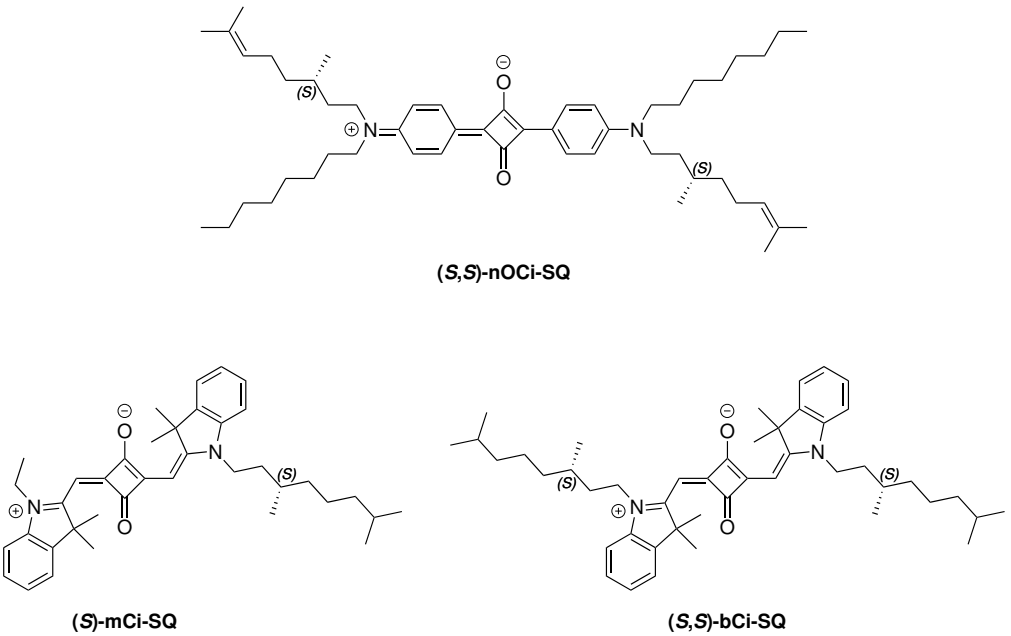


Figure 3.1: Chemical structure of the anilino squaraine **(*S*,*S*)-nOCi-SQ** (top) and the two indolenine-derived squaraines **(*S*,*S*)-mCi-SQ** and **(*S*,*S*)-bCi-SQ** (bottom).

This study aimed to investigate how (*S*)-citronellyl substitution via *N*-alkylation affects aggregation, morphology, optical and chiroptical response of two indolenine-derived squaraines (**(*S*,*S*)-mCi-SQ** and **(*S*,*S*)-bCi-SQ**) and one anilino squaraine (**(*S*,*S*)-nOCi-SQ**) in spin-coated thin films.

First, the two indolenine-derived squaraines, each containing either one or two (*S*)-citronellyl chains

at the indolenic nitrogen, were investigated. Although both dyes showed a pronounced crystallization tendency, solution-processed pristine thin films were perfectly isotropic. The linear absorbance spectra showed one dominant peak at 675 nm with a vibronic shoulder at 615 nm for both compounds. The isotropic refractive index (n) and isotropic extinction coefficients (k) were very similar for both compounds, with notably high k values. As the thin films appeared isotropic without evidence of molecular aggregation, no excitonic CD signals from chiral supramolecular arrangements could be detected. This finding is consistent with previous research in colloidal aggregated solutions, where the (*S*)-citronellyl functionalization at the indolenic nitrogen proved to be inferior for chiral aggregation than the core substitution.[123] To introduce aggregation, subsequent thermal annealing of the spin-coated thin films was performed with mixed results. Both compounds remained isotropic with temperatures up to 90 °C. Above 90 °C, both compounds evaporated off the glass substrate. Notably, for **(*S*,*S*)-bCi-SQ**, one sample with residual crystalline material could be obtained after being removed from the hot plate prior to complete sublimation. The sample showed amoeba-like **(*S*,*S*)-bCi-SQ** residues on the surface. Cross-polarized microscopy imaging confirmed birefringence, indicating crystalline squaraine remains. Spatial and polarization resolved spectroscopy revealed two absorption peaks at 576 nm and 693 nm, with each peak alternating at 90° intervals and repeating every 180°. This pattern is an indication for Davydov splitting, which occurs in molecular aggregates containing at least two translationally invariant molecules per unit cell.[86] Since the overall coverage of the substrate was very low, no X-ray diffraction (XRD) analysis of this sample could be performed. Therefore, a thicker **(*S*,*S*)-bCi-SQ** film suitable for XRD analysis was fabricated by dropcasting followed by thermal annealing. However, the signals differ from the calculated powder pattern of the **(*S*,*S*)-bCi-SQ** pseudo polymorphic crystal structure, indicating that **(*S*,*S*)-bCi-SQ** adopts a different polymorph in processed thin films.

Next, the (*S*)-citronellyl-functionalized anilino squaraine **(*S*,*S*)-nOCi-SQ** was investigated. Samples of this squaraine showed even without thermal annealing a certain degree of molecular aggregation and preferential orientation, probed by optical spectroscopy. The UV/Vis absorbance spectrum showed distinct double-hump spectral features, peaking at 564 nm and 663 nm. The analysis of the ellipsometric data required an anisotropic uniaxial model, yielding two sets for the complex refractive index. The ordinary component (n_o and k_o) within the substrate plane and the extraordinary component (n_e and k_e) perpendicular to the substrate plane. This indicates a preferred orientation of molecules and aggregates parallel to the surface. Studies on other aggregated micro-crystalline anilino squaraine thin films have shown that the molecular stacking direction is within the plane of the thin film, i.e. the molecular backbones are perpendicular (edge-on) to the surface.[16, 67, 85] This assumption was also applied to **(*S*,*S*)-nOCi-SQ** thin films. Although these experiments suggested some level of aggregation or molecular packing, no CD or birefringence was observed at either the macroscopic or microscopic scale. Thermal annealing of the thin films only resulted in minor changes to the absorbance spectrum. However, after trying to fit the ellipsometric data from several samples with different film thicknesses, it turned out that no common uniaxial complex refractive index could be found to exactly describe each sample. So the complex refractive index of annealed **(*S*,*S*)-nOCi-SQ** samples depends on the layer thickness (different processing parameters), rather than representing an intrinsic material property. This was further supported by atomic force microscopy (AFM) images, showing a fibril formation, which – simply said – became more pronounced with increasing layer thickness. The absorbance spectra showed the characteristic double-hump spectral features, typical for *n*-alkyl anilino squaraines in thin films.[85] There, the pattern likely originates from a Coulombic Frenkel exciton having a H-aggregate character with a charge-separated ICT state, which is possible due to close molecular packing.[86] Davydov splitting in this systems is unlikely given the primitive crystallographic unit cell.[85, 86] We assume that the

(*S*)-citronellyl-functionalized anilino squaraine (**(*S*,*S*)-nOCi-SQ**) behaves similarly and therefore consider the ICT-Frenkel hybrid excitons theory as valid. However, given that the **(*S*,*S*)-nOCi-SQ** did show a CD signal, the packing cannot be exactly the same as for the *n*-alkyl anilino squaraines. Using Mueller matrix polarimetry,[95, 126] the CD spectra of the thin film were recorded. For a better comparison between different layer thicknesses, the CD was normalized to the unpolarized absorbance yielding the g-value.[90, 124, 125] The high-energy component of the double hump (in the following called H-band) showed a bisignate CD signal with a zero-crossing coinciding with the maximum peak of the UV/Vis absorbance. According to exciton chirality rules, this observation suggests a right-handed helical arrangement of molecular transition dipole moments and their Coulombic interactions.[86, 90, 124, 125] In contrast, the long-wavelength excitation (in the following called CT-band) gave an additional monosignate signal. Here, the benefit of added chirality is evident. These signals' properties allow their original nature to be assigned: the bisignate shape comes from the Coulombic H-aggregate, while the long-wavelength band produces a monosignate CD peak linked to an ICT, supporting the interpretation of a hybrid Frenkel and charge transfer exciton.[89] However, the g-value was found to depend on layer thickness, a common phenomenon found in molecular or polymeric thin films due to several reasons.[119, 127–130]

Overall, our findings support previous interpretations that the double hump spectral signatures observed in *n*-alkyl anilino SQs emerges from coupling between a Coulombic Frenkel exciton with H-aggregate character and an ICT state. Thereby, citronellyl-functionalization did not result in chiral aggregation in the two indoline systems but was effective for anilino squaraines. This modification introduced another spectroscopic variable that can be investigated and could facilitate the study of more complex systems.

CHAPTER 4

Citronellyl-Functionalized Chiral Squaraines with Different Alkyl-Substituents

4.1 The Idea: Modulating ICT Through Steric Hindrance

The previous work presented in Chapter 3 focused on how chiral (*S*)-citronellyl substituents introduced via *N*-alkylation affect aggregation, morphology, and the optical and chiroptical responses of three squaraines in spin-coated thin films. That study highlighted the added value of chirality for interpreting and assigning the distinct double-humped spectral features observed in *n*-alkyl anilino squaraines. Depending on whether the CD signals originate from Coulombic (Frenkel) excitons or charge-transfer (CT) excitons,[67, 85] the spectral response differs and allows for assignment: the bisignate shape comes from the Coulombic H-aggregate, while the long-wavelength band produces a monosignate CD peak linked to an ICT. This supported the previous proposed interpretation of a hybrid Frenkel and charge

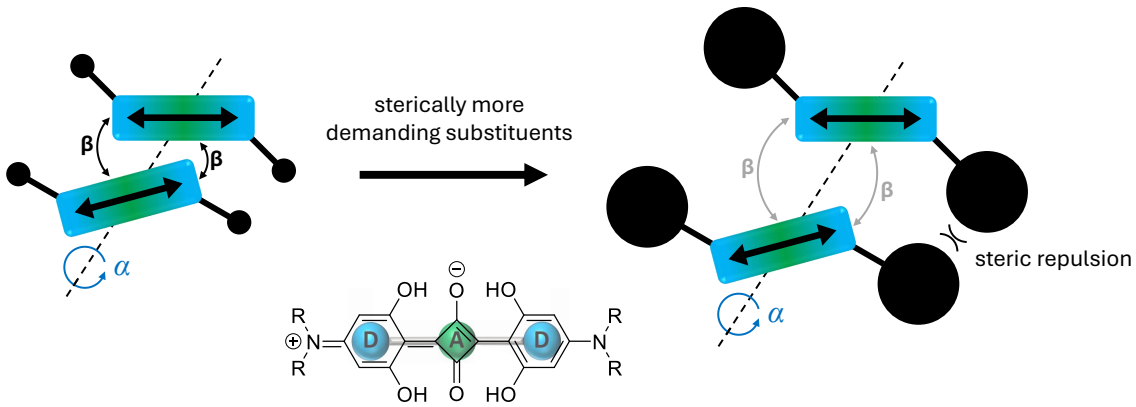


Figure 4.1: General concept of modulating intermolecular charge-transfer interaction (ICT) strength β through the introduction of sterically more demanding substituents. This illustration shows a chiral arrangement of the D-A-D type squaraine dye with $\alpha \neq 0$. The size of the substituents does not correspond to the reality and is only used for illustrative purposes.

transfer exciton.[14, 89] This behavior is largely governed by molecular packing, particularly the spatial arrangement of the π-conjugated molecular backbones within the aggregate. The most common way to influence the molecular packing is – of course – the functionalization with various substituents. Thereby, it has been demonstrated that the introduction of bulky substituents (e.g., anilino squaraine with branched isobutyl side chains – called **SQIB**) can disrupt molecular packing in such a way that only Coulombic interactions are present, resulting in spectra characterized by Davydov splitting.[67] In contrast, linear alkyl chains permit for close slip-stack packing and ICT interactions, resulting in the typical double hump absorbance spectra.[1, 85] Considered as boundary cases, these examples suggest a "sweet spot" or point where the spatial arrangement of the aggregated dyes can be influenced to rebalance the relative signal contributions of Frenkel and ICT excitons.

This idea is picked up and investigated in the following chapter. Figure 4.1 illustrates how the introduction of sterically more demanding substituents should influence the characteristic double hump absorbance spectra by changing the aggregate geometry. Giving that the Coulombic Frenkel exciton coupling energy (ref. Equation 1.1) as well as the ICT interaction strength β are dependent on the overall spacial arrangement of the chromophores, one has to consider which of the two energies are more affected. Based on the literature,[131, 132] I propose that small Ångstrom-level changes in distance, slip or twist can strongly modulate the ICT, while Coulombic coupling – even though the coupling energy scales with the inverse cube of the intermolecular distance ($\frac{1}{r^3}$, see Equation 1.1) – varies more smoothly with distance and orientation. Therefore, the monosignate CD peak (attributed to the ICT interaction) observed in the spectra of *n*-alkyl[85] and citronellyl-functionalized anilino squaraines presented in Chapter 3 is expected to be more strongly affected. The presence of chiral substituents in the molecular structure, and thus, the formation of chiral aggregates with $\alpha \neq 0$, should also allow for utilizing CD spectroscopy to gain deeper insight into the nature of the obtained signals, analogous to the approach described in Chapter 3.

4.2 Synthesis of Selected Citronellyl-Functionalized Chiral Squaraines

With the background that the presence of two branched isobutyl side chains in **SQIB** introduces too much steric repulsion – preventing ICT interactions and leaving only Coulombic coupling,[67] as evidenced by Davydov splitting (Figure 1.9) – a modified squaraine structure was designed. Thereby, it was decided to synthesis a squaraine with just one branched isobutyl side chain and one (*S*)-citronellyl substituent. Additionally, to eliminate/minimize potential effects of the unsaturated double bond in the citronellyl residue, this bond was hydrogenated. The corresponding squaraine is henceforth called **(*S*,*S*)-nCi-SQIB**. For an objective comparison of the substitution effect with a single isobutyl side chain, the hydrogenated analogue of **(*S*,*S*)-nOCi-SQ** from Chapter 3 was also planned – called **(*S*,*S*)-nOnCi-SQ**.

The synthetic route for **(*S*,*S*)-nCi-SQIB** and **(*S*,*S*)-nOnCi-SQ** is depicted in Figure 4.2 and was performed with the help of Tra Giang Nguyen during her bachelor's thesis.[133] Starting with the selected primary amine isobutylamine or octylamine, the first step was a reductive amination with (*S*)-citronellal. After forming the imine by refluxing the mixture 24 h in methanol, sodium borohydride was added as reducting agent, yielding the corresponding secondary amine **(*S*)-Ci-N-IB** and **(*S*)-Ci-N-O** in 65% and 71%, respectively. Next, the double bond on the citronellyl residue was hydrogenated by treatment with palladium on carbon (Pd/C) and elemental hydrogen. Even though the literature reports normally very

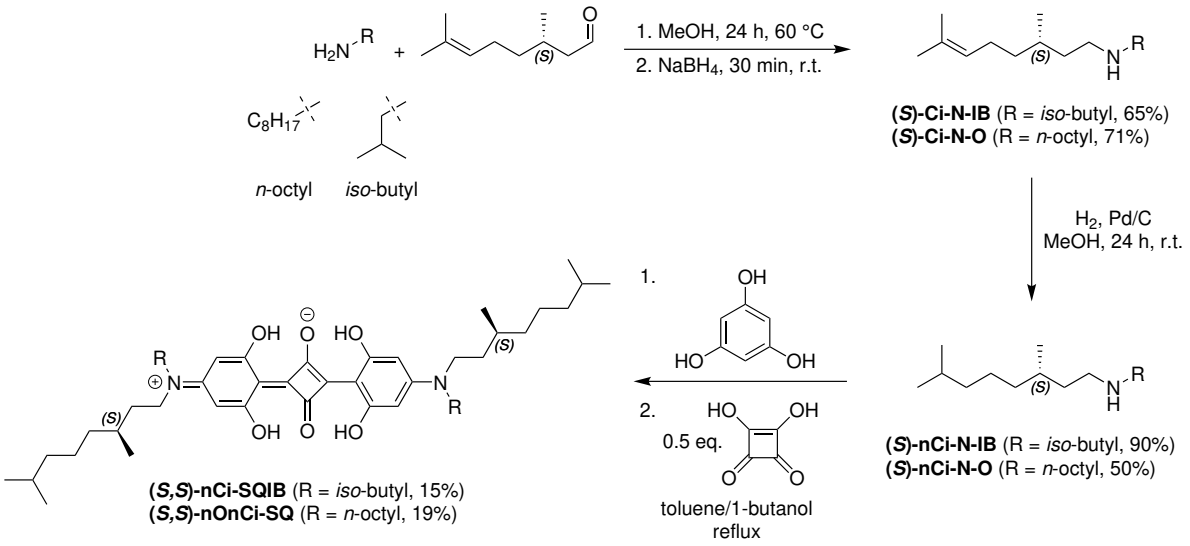


Figure 4.2: Synthesis of **(*S*,*S*)-nCi-SQIB** and **(*S*,*S*)-nOnCi-SQ**, starting from enantiopure (*S*)-citronellal and a selected primary amine (isobutylamine or octylamine).

high or even quantitative yields, in the case of **(*S*)-nCi-N-O** only a conversion of 50% could be achieved. This might be due to the initial difficulties to get the hydrogenation running, as decried in Section 13.2. **(*S*)-nCi-N-IB** on the other hand, was obtained with good yields of 90%.

With a suitable secondary amine on hand, the last step was a literature known two-step, one-pot procedure.[11, 100] Starting by refluxing the corresponding secondary amine **(*S*)-nCi-N-IB** or **(*S*)-nCi-N-O** together with phloroglucinol (1,3,5-trihydroxybenzene) in a mixture of toluene/1-butanol, followed by the subsequent addition of squaric acid. In order to be used in OPVs, achieving high purity is of utmost importance. Accordingly, each squaraine went through purification by column chromatography on silica gel combined with multiple recrystallizations, yielding **(*S*,*S*)-nCi-SQIB** with 15% and **(*S*,*S*)-nOnCi-SQ** with 19%, what can be considered normal as discussed in the introduction (Section 1.1).

4.3 Optical Properties of Aggregated Solutions and Thermally Annealed Thin Films

Aggregated Solutions:

In order to obtain an initial assessment of the aggregation behavior of the two squaraines, a titration experiment was carried out where the water content in a methanol solution was gradually increased. Giving that water is a rather poor solvent for squaraines, this increase should force the dye molecules to aggregated colloidal solutions. The exact procedure for sample preparation is described in Chapter 13.

Starting with **(*S*,*S*)-nOnCi-SQ**, Figure 4.3 shows that with 0% water, the squaraine-typical sharp monomeric absorbance band of the electronic $S_0 \rightarrow S_1$ transition around 650 nm can be observed. Besides this, a small hypsochromic shoulder, originating from the vibronic 0-1 progression, at about 600 nm is detected.[134] A water content of 2% causes a slight broadening of the absorbance band but

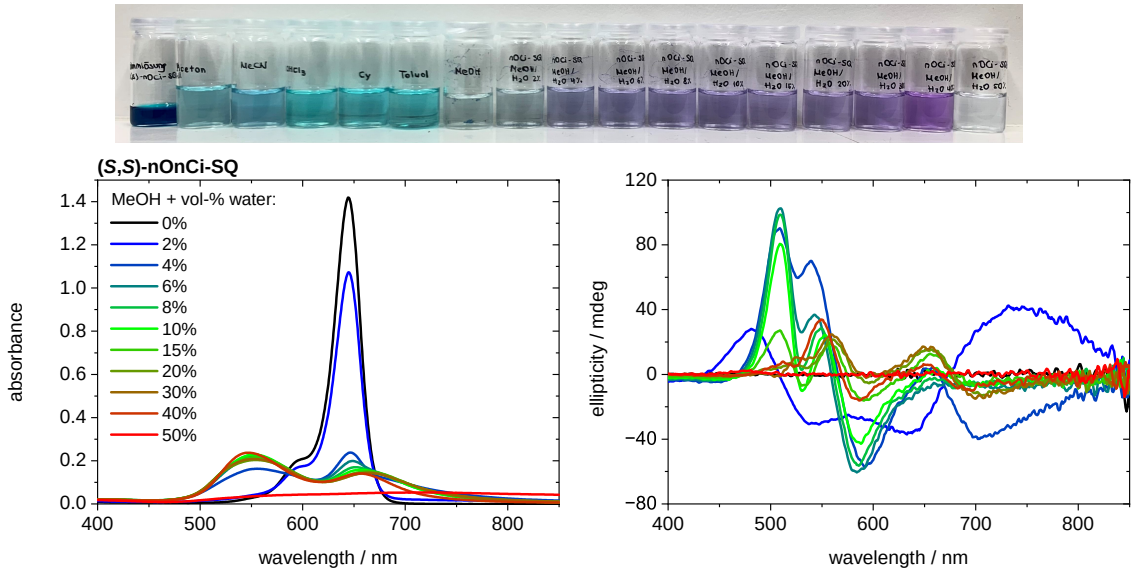


Figure 4.3: Early stage aggregation experiments in solution with UV/Vis absorbance (bottom left), corresponding ellipticity spectra (bottom right) and a picture of the visible changes in color (top) of **(*S*,*S*)-nOnCi-SQ** (c = 3.84 µM). The legend indicates the volume-percentage of water in the methanol-water mixture and applies to all plots. The solutions were prepared from a chloroform stock solution ($c = 2.31 \times 10^{-4}$ M) and therefore contain an additional 1.7% chloroform (50 µL in 3 mL).

at this point very similar to the monomeric absorbance. From a water content of 4%, two absorbance bands form with a hypsochromically shifted band at approximately 550 nm and the bathochromically shifted band at around 650 nm. The intensity of the hypsochromically shifted absorbance band increases with increasing water content, whereas the bathochromically shifted band decreases and broadens. Due to the nonpolar alkyl chains of the squaraine, partial precipitation occurred in the methanol/water mixtures with complete precipitation observed in the 50% methanol/water mixture. As a result, no further spectroscopic investigations could be carried out at this point.

Showing clear evidence of aggregation in these methanol/water mixtures, CD spectroscopy was used to investigate the aggregation behavior in more detail (Figure 4.3, bottom right). Unfortunately, no clear trend in the signals as a function of solvent polarity could be observed, as was the case in the investigation using UV/Vis spectroscopy. As expected, in the monomeric state i.e. 0% water, no ellipticity signal was observed, as the chiral center is not located directly at the chromophore and no chirality transfer via aggregation has occurred thus far.[2, 123] With increasing water content, the ellipticity spectra differ particularly strongly between the 2%, 4–10% and 15–40% ranges. The numerous minima and maxima indicate a very complex aggregation behavior, potentially involving multiple distinct aggregate species, in which the individual chromophores adopt different relative orientations or alignments as explained in Section 1.2. Moreover, even in regions with broadly similar signals (e.g., 4–10% and 15–40%), no isosbestic points are observed. It can be speculated that in these ranges, several bisignate signals overlap, producing the observed complexity. However, as these are only early stage aggregation experiments, no further discussion will be done at this point. The increase in aggregation due to an increasing water content can also be seen with the naked eye by a color change from blue-turquoise to purple-violet or no coloration for 50% water content (Figure 4.3, top).

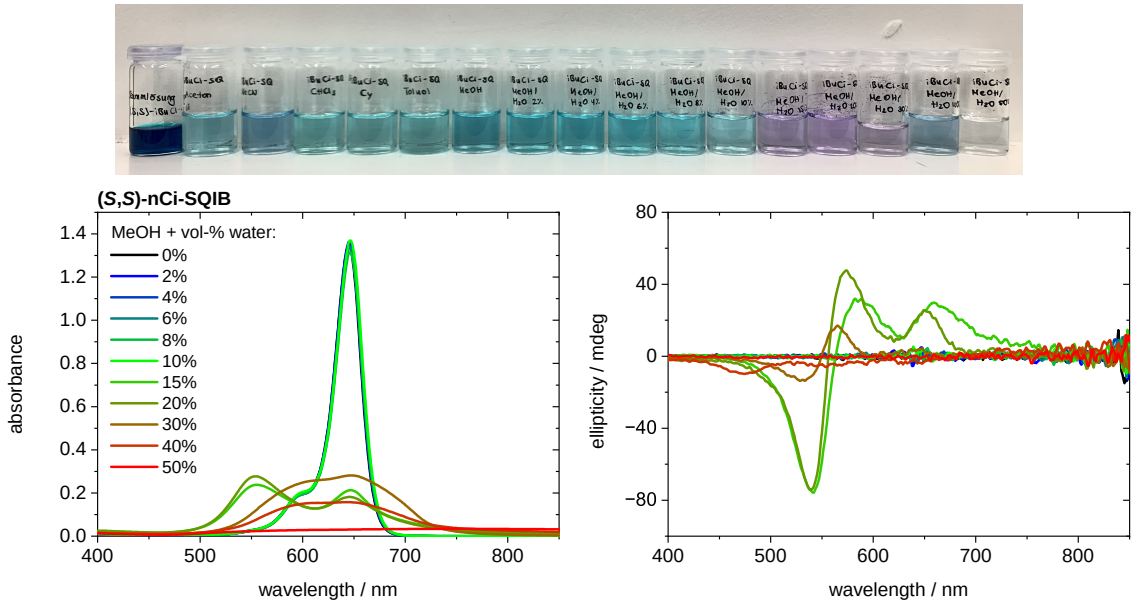


Figure 4.4: Early stage aggregation experiments in solution with UV/Vis absorbance (bottom left), corresponding ellipticity spectra (bottom right) and a picture of the visible changes in color (top) of **(*S*,*S*)-nCi-SQIB** (c = 3.84 µM). The legend indicates the volume-percentage of water in the methanol-water mixture and applies to all plots. The solutions were prepared from a chloroform stock solution ($c = 2.31 \times 10^{-4}$ M) and therefore contain an additional 1.7% chloroform (50 µL in 3 mL).

The early stage aggregation experiments for **(*S*,*S*)-nCi-SQIB** are shown in Figure 4.4. At water contents between 0% and 10%, almost identical absorbance spectra can be seen, showing again the squaraine-ty2pical sharp monomeric absorbance band of the electronic $S_0 \rightarrow S_1$ transition around 650 nm and the small hypsochromic shoulder originating from the vibronic 0-1 progression around 600 nm.[134] At water contents of 15% and 20%, the absorbance spectra show two maxima at around 550 nm and 650 nm with different intensities. At water contents of 30% and 40%, no two clear absorbance maxima can be identified, as the absorbance bands are more widespread and also overlap, resulting in a broad signal over the hole absorbance region. Since the formation of the aggregates is a time-dependent process, this observation may originate from a not completed aggregation process. This could also be observed during sample preparation, where the solution with 30% water initially had a dark blue color. After 10 minutes, however, the solution turned purple. This supports the not completed aggregation assumption and will be investigated at a later stage by means of a time-dependent measurements (ref. Figure 4.5). Due to the precipitation of squaraines out of solution, the overall absorbance of 30% water content is higher than for 40% with nearly complete precipitation observed in the 50% methanol/water mixture.

Also for **(*S*,*S*)-nCi-SQIB**, the aggregation was further investigated by means of CD spectroscopy as shown in Figure 4.4 (bottom right). As expected – and for the same reasons as in monomeric **(*S*,*S*)-nOnCi-SQ** solutions – no ellipticity signal was detected at water contents up to 15%. Compared to the ellipticity spectra of **(*S*,*S*)-nOnCi-SQ**, the spectra of **(*S*,*S*)-nCi-SQIB** is much less complex. At 15% water content, a bisignate CD signal with an overall positive Cotton effect (attributed to the Cotton effect at longer wavelength) with a zero crossing around 550 nm and a monosignate CD signal around 650 nm

can be detected. The Cotton effect allows conclusions to be drawn about the helical arrangement in the aggregates via the exciton chirality method, as discussed in Section 1.3.2 - Interpretation of CD-Spectra. The overall positive Cotton effect, combined with the hypsochromic shift relative to the monomer absorbance, indicates that the squaraine adopts a H-type, right-handed helical arrangement. The same pattern emerges also for 20% water content, even though the overall spectra is slightly hypsochromically shifted, which can be attributed to an increasing slip angles between the chromophores. Increasing the water content to 30% or 40% results in a strong reduction in signal strength (due to stronger precipitation) and a further blue shift to around 380 nm. In this case as well, the aggregation process could be detected by the naked eye as seen in Figure 4.4 (top). In the case of solvents and solvent mixtures in which no aggregation of squaraines was detected, the samples exhibited a cool blue to turquoise coloration. The aggregated samples were clearly distinguishable visually by a purple color and discoloration due to precipitation for 50% water content.

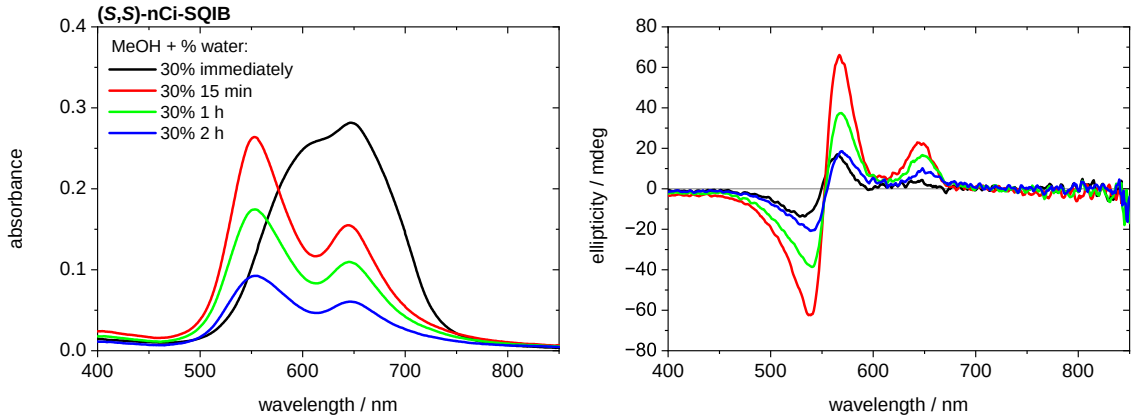


Figure 4.5: Time-dependent UV/Vis absorbance (left) and corresponding ellipticity spectra (right) of **(*S*,*S*)-nCi-SQIB** (c = 3.84 µM) in 30 volume-% of water in the methanol. The solutions were prepared from a chloroform stock solution (c = 2.31 × 10^{-4} M) and therefore contain an additional 1.7% chloroform (50 µL in 3 mL).

Since, in the 30% water-methanol mixture, a gradual color change was observed over time – indicating time-dependent aggregation – this phenomenon was investigated further and is shown in Figure 4.5. The first measurement was taken immediately after sample preparation, with the solution had still a blue color. The absorbance pattern showed two overlapping bands. In the ellipticity spectrum, two low intensity signals could be observed: a bisignate CD signal around 550 nm and signal around 650 nm.[a] The next measurement was taken after 15 minutes, at which point the sample had turned purple. This color change indicated progressive aggregation. The UV/Vis and ellipticity spectra supported this assumption via drastic change in the observed signals. Two distinct absorption bands were now visible in the UV/Vis spectrum around 550 nm and 650 nm, accompanied by the same ellipticity spectra as before, but with markedly higher intensities. Notably, the zero-crossing points of the CD signals in the ellipticity spectra aligned perfectly with the corresponding features in the UV/Vis absorbance

[a] It can be assumed that – due to the measurement setup and the resulting time delay between the UV/Vis measurement (acquired immediately) and the ellipticity measurement (taken roughly three minutes later) – the CD signal does not directly correlate with the linear absorbance spectra.

spectra. After one and two hours, further measurements were taken, revealing a reduction in intensity, originating from the precipitation of the squaraine.

Also for **(*S*,*S*)-nOnCi-SQ**, time-dependent UV/Vis absorbance and corresponding ellipticity spectra of a 30% water-methanol mixture were recorded and are presented in Appendix B-Figure B.2. However, due to the spectral complexity and the absence of significant changes over time, these data are not included in the main body of this chapter.

Notably, the distinct double-humped spectral features observed in **(*S*,*S*)-nOnCi-SQ** (4–40% water in methanol) and **(*S*,*S*)-nCi-SQIB** (15%, 20% and after some time 30% water in methanol) absorbance spectra have significant resemblance with the spectra of *n*-alkyl anilino squaraines in aqueous DMSO solutions[14, 135] and in thin films,[14, 19, 76, 85, 89, 135] as well as thin films of **(*S*,*S*)-nOCi-SQ** from Chapter 3. For non-chiral *n*-alkyl anilino squaraines, *Spano* and *Collison* develop the first theoretical model to describe this spectral feature by mixing Frenkel-like exciton states (Coulombic H-aggregate) and charge-separated states via intermolecular charge transfer (CT) interactions leading to the splitting of the excited state as shown in Section 1.2.2 - *Expansion on Intermolecular Charge Transfer*.[14, 86–88] Whether the double-humped absorbance spectra of **(*S*,*S*)-nOnCi-SQ** and **(*S*,*S*)-nCi-SQIB** in aqueous methanol solutions can also be attributed to intermolecular charge transfer (ICT) was not specifically analyzed for these compounds. However, in Appendix D this concept will be tested and transferred to homochiral proline-derived anilino squaraines (**ProSQs**) with intermediate chain lengths.

Utilizing the added value of chirality for interpreting and assigning the distinct double-humped spectral features by analyzing the corresponding CD response. As noted previously, using the exciton chirality method (see Section 1.3.2) enables the Cotton effect to be used to determine the helical arrangement of the aggregates. For **(*S*,*S*)-nOnCi-SQ**, the high complexity does not allow to draw any conclusions. **(*S*,*S*)-nCi-SQIB**, however, exhibits a nice hypsochromic shifted bisignate signal as well as slightly bathochromic shifted monosignate signal. By this the ellipticity spectra has significant resemblance with the thin film CD spectra of **(*S*,*S*)-nOCi-SQ** (see Chapter 3). Since the overall Cotton effect is positive, with a zero crossing near the absorbance maximum, indicates that the squaraine adopts a right-handed helical arrangement, corresponding to a positive excitonic chirality. The sign reversal around the absorbance maximum is characteristic of exciton-coupled CD effects.[34, 94, 125, 136] The absence of vibronic progression in the aggregate species further suggests strong exciton coupling.[137] Moreover, Davydov splitting from a single aggregate species can be ruled out as the origin of the observed double-humped feature, since it would instead result in a single CD signal across the whole absorbance region.

Additional spectra of **(*S*,*S*)-nCi-SQIB** and **(*S*,*S*)-nOnCi-SQ** in solution, for example in different solvents, can be found in Appendix B.

Thermally Annealed Thin Films:

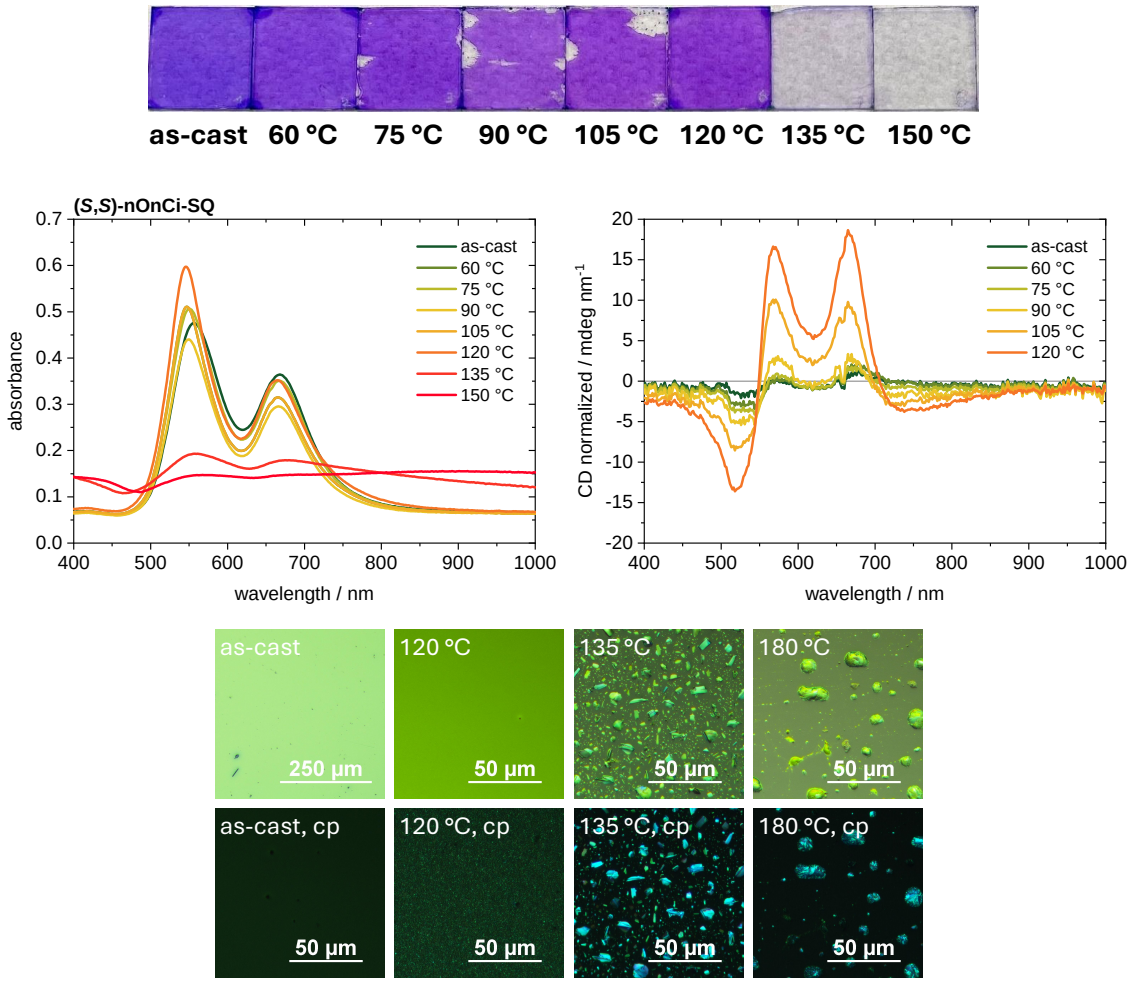


Figure 4.6: UV/Vis absorbance (middle left) and corresponding normalized CD spectra (middle right) of **(*S*,*S*)-nOnCi-SQ**, spin-coated from a chloroform solution under the same conditions and thermally annealed at various temperatures for 30 minutes. CD spectra were recorded only for samples in which a visibly intact thin film was present i.e. up to 120 °C. Top: Picture of thin film samples after annealing at different temperatures. Bottom: Optical microscopy images of spin-coated thin films with corresponding images between crossed polarizers at varying temperatures.

After gaining a preliminary understanding of the aggregation behaviour of the two dyes, their actual aggregation behaviour in the solid state was investigated. Therefore, a series of solution-processed thin films were prepared via spin coating under same conditions, followed by thermal annealing at various temperatures for 30 minutes. Subsequent measurements of the absolute absorbance[b] were carried out, and Mueller matrix ellipsometry was employed to accurately determine the circular

[b] As mentioned in Chapter 1 – Introduction, please note that absorption $A \neq$ absorbance Abs; with $Abs = -log(T)$, where the transmission T includes contributions from absorption A, reflection $Refl$ and scattering S after $T = 1–A–Refl–S$

dichroism (CD) of the samples. By varying the dye concentration (5 or 6 mg squaraine per mL spin-on solution) and the spin-coating parameters (slow, medium and fast), thin films of different thicknesses could be obtained. A detailed fabrication procedure is given in the Experimental Section (Chapter 13). Ellipsometric measurements were furthermore used to determine dielectric material properties – such as optical constants as well as to determine the layer thicknesses of the thin films.

As expected, **(*S*,*S*)-nOnCi-SQ** behaved almost identical to **(*S*,*S*)-nOCi-SQ** from Chapter 3. As shown in Figure 4.6, even the pristine thin film (as-cast) exhibited the characteristic double-hump spectral feature as it is typical for *n*-alkyl anilino squaraines in thin films.[85] This was the case for all other tested temperatures up to 120 °C with only negligible shifts of the absorbance maxima. Although the overall signal intensities did not differ substantially, the ratio of the first to second peak changed after the thermal annealing cycle in favour of the higher-energy component. This is one notable difference between **(*S*,*S*)-nOnCi-SQ** and **(*S*,*S*)-nOCi-SQ**, where as-cast and annealed samples basically looked the same. The strongest absorbance for **(*S*,*S*)-nOnCi-SQ** was thereby observed for the sample annealed at 120 °C. Over this temperature, visible discoloration of the sample could be observed (Figure 4.6, top) in combination with a drastically decrease in the absorbance intensity. Optical microscopy images (Figure 4.6, bottom) of the spin-coated thin films revealed a coarse crystalline and patchy thin film, which can be explained by melting the material at 135 °C and re-solidifying it. This was even more evident for the samples annealed at 180 °C. As the absorbance spectra had already showed a pronounced decrease in intensities, no additional UV/Vis absorbance measurements were performed for this temperature.

Unlike the ellipticity spectra in solution, the normalized thin film CD spectra is much more defined. Also here, a nearly identical behavior compared to **(*S*,*S*)-nOCi-SQ** was observed. Starting with the as-cast thin film, the expected hypsochromically shifted bisignate signal, along with a slightly bathochromically shifted monosignate signal, was detected (schematic modulation due to limited resolution). Both signals increased in intensity upon annealing, reaching a maximum at 120 °C. In comparison to **(*S*,*S*)-nOCi-SQ**, however, the intensity ratio between the bisignate and monosignate signals is shifted more strongly toward the lower-energy signal. If this can purely explained by the absence of the double bond on the citronellyl residue or to slight differences in the fabrication process (e.g., 100 °C vs 120 °C annealing temperature) can not be certainly answered.

Giving the strongest absorbance intensity, CD values of approximately ±15 mdeg/nm and a continuous, smooth, microcrystalline thin film morphology, 120 °C was selected as the optimal annealing temperature for **(*S*,*S*)-nOnCi-SQ**.

Also, **(*S*,*S*)-nCi-SQIB** features the characteristic double-humped spectral feature, already apparent in the as-cast thin film. Thermal annealing resulted in a significant change in the ratio of the first to second peak, favoring the higher-energy component. Notably, while the higher-energy component showed no significant shift in its absorbance maximum, the lower-energy component experienced a hypsochromic shift of approximately 10 nm upon annealing. The highest absorbance for **(*S*,*S*)-nCi-SQIB** was recorded for the sample annealed at 135 °C. Above this temperature, visible discoloration of the sample was observed (Figure 4.7, top), accompanied by a drastic decrease in absorbance intensity. Optical microscopy images (Figure 4.7, bottom) of the spin-coated thin films revealed what appeared to be a molten film with small droplets, which were completely dark between crossed polarizers. Whether these droplets are molten but unsolidified squaraine or a decomposition product was not further investigated. Interestingly, even at room temperature, aggregation could be observed over time, as seen by optical microscopy images between crossed polarizers.

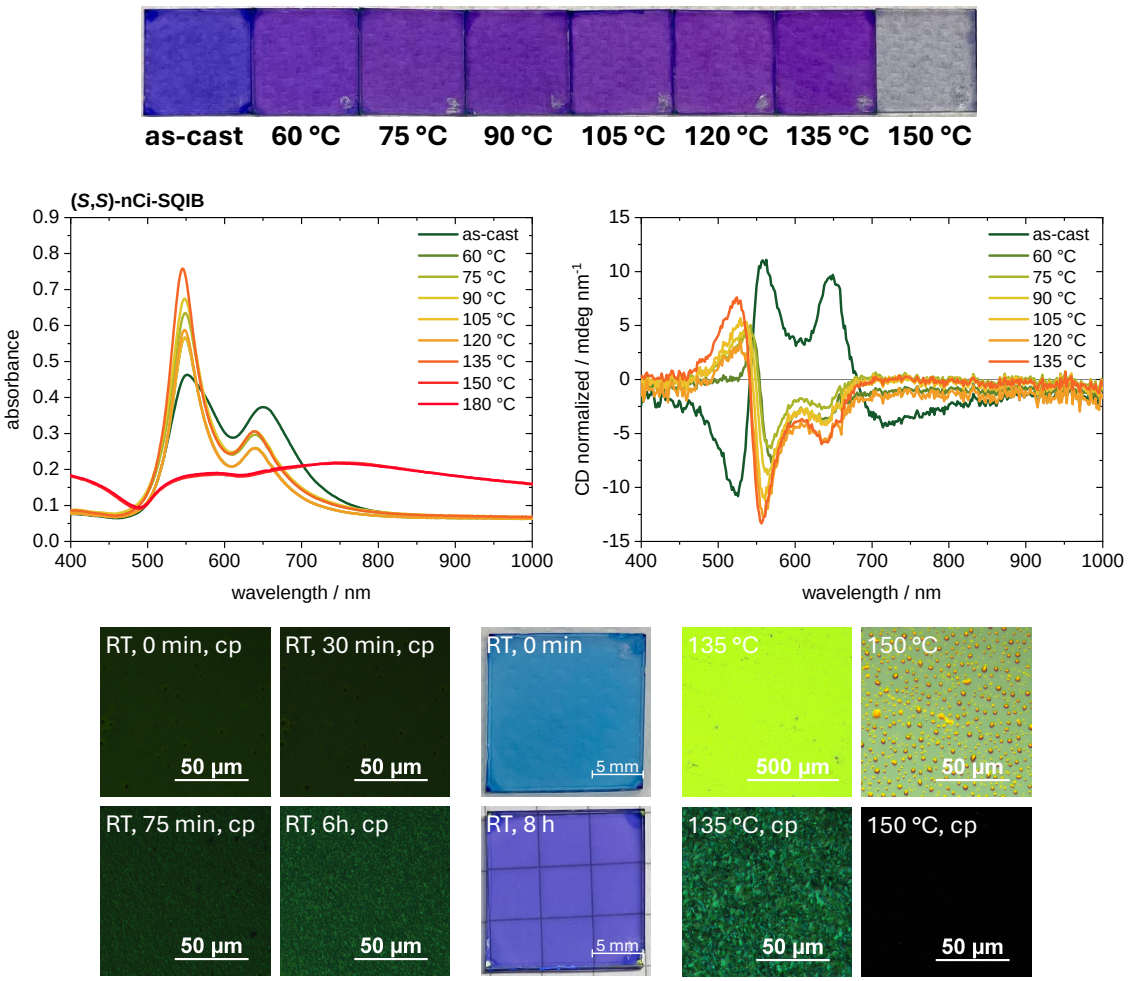


Figure 4.7: UV/Vis absorbance (middle left) and corresponding normalized CD spectra (middle right) of **(*S*,*S*)-nOnCi-SQ**, spin-coated from a chloroform solution under the same conditions and thermally annealed at various temperatures for 30 minutes. CD spectra were recorded only for samples in which a visibly intact thin film was present i.e. up to 135 °C. Top: Picture of thin film samples after annealing at different temperatures. Bottom: Pictures or pptical microscopy images of spin-coated thin films with corresponding images between crossed polarizers at varying times or temperatures.

In the CD spectra, this squaraine showed a substantial degree of chiral aggregation even without thermal annealing. Surprisingly, the as-cast thin film[c] exhibited a hypsochromically shifted bisignate signal together with a slightly bathochromically shifted monosignate signal. The spectral shape matched exactly what was observed in the early stage aggregation experiments in solution (Figure 4.4 and 4.5), although the monosignate signal is much more pronounced in the thin film. Even more surprising were the changes following thermal annealing: although the absorbance maxima showed no significant shifts, the entire CD spectrum reversed in sign. The individual signals remained at roughly the same positions but changed sign, which – according to the exciton chirality method – indicates a helical rearrangement

[c] Due to the time delay between thin film fabrication and measurement, it can be assumed that time-dependent aggregation at room temperature had already occurred.

of the squaraine aggregates to the opposite handedness. With increasing temperature, both signals increased in intensity, reaching a maximum at 135 °C.

Exhibiting the strongest absorbance intensity, CD values of approximately ±10 mdeg/nm (as-cast) and between +8 and -12 mdeg/nm (at 135 °C) and a continuous microcrystalline thin-film morphology (although appearing slightly rougher than for **(*S*,*S*)-nOnCi-SQ**), the sample annealed at 135 °C was selected as the best annealing temperature for **(*S*,*S*)-nCi-SQIB**.

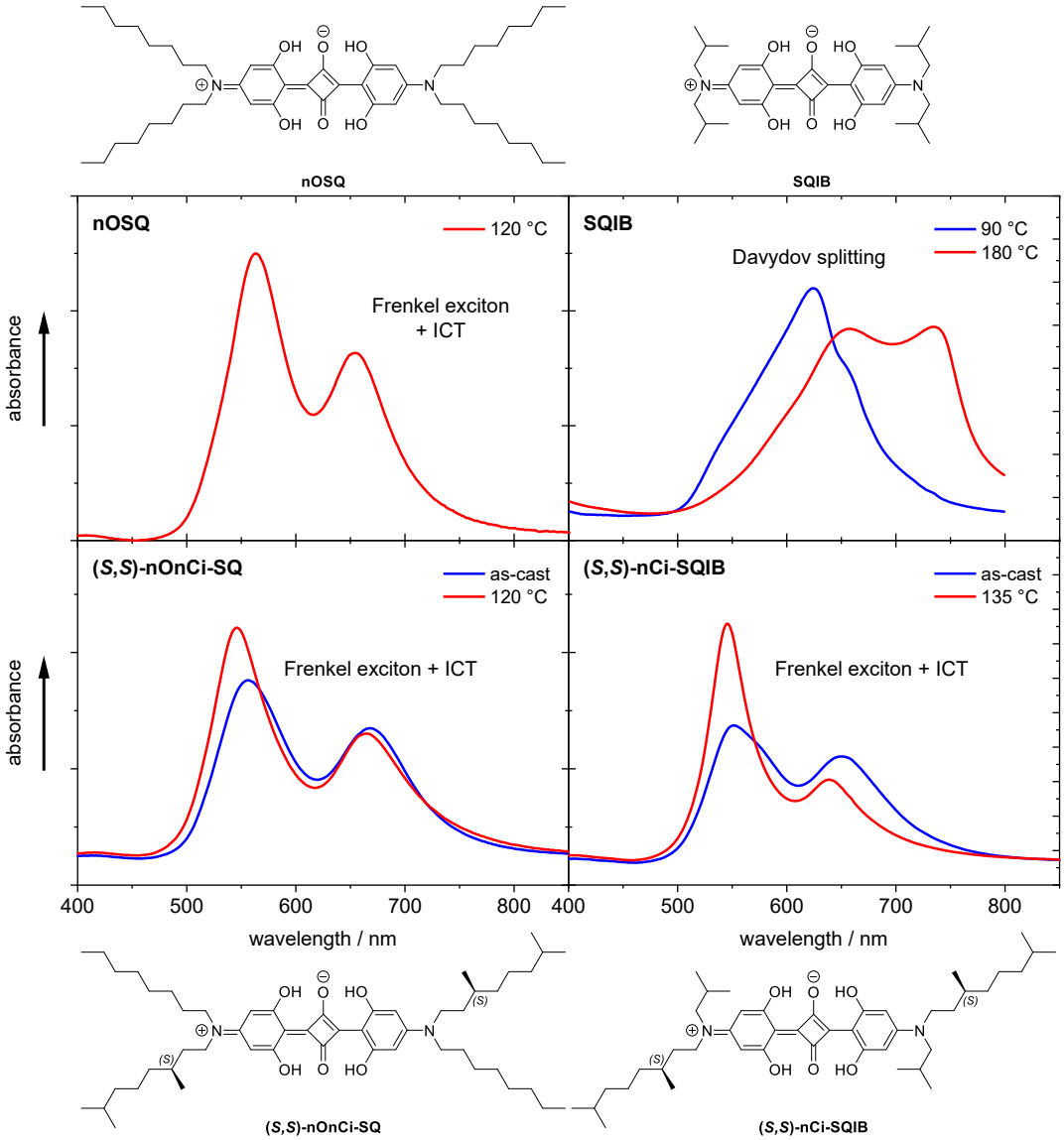


Figure 4.8: Comparison of the UV/Vis absorbance spectra of **nOSQ** (top left), **SQIB** (top right), **(*S*,*S*)-nOnCi-SQ** (bottom left) and **(*S*,*S*)-nCi-SQIB** (bottom right). The data from **nOSQ** and **SQIB** were kindly provided by apl.-Prof. Dr. Manuela Schiek (Johannes Kepler University Linz, Austria) and can be found in the following publications: [85] and [67].

In Figure 4.8, a comparison is shown between the non-chiral *n*-alkyl anilino squaraine **nOSQ**,[d] **SQIB**,[e] and the chiral **(*S*,*S*)-nOnCi-SQ** and **(*S*,*S*)-nCi-SQIB**. The two chiral SQs are essentially identical to the non-chiral **nOSQ**, showing only minor shifts in the absorbance maxima – a trend already observed for other *n*-alkyl anilino squaraines and is due to small changes in the packing of the chromophores.[85] The appearance of the characteristic double-humped feature thereby allows for a direct comparison of the two new chiral derivatives with other *n*-alkyl anilino squaraines. A notable difference is found when comparing these spectra to that of **SQIB**. In **SQIB**, the single-crystal structures of the two polymorphs have Davydov splitting to be identified as the origin of the two interfering peaks observed after annealing at 180 °C. However, because Davydov splitting would produce a single broad CD signal across the entire absorbance region, it can be ruled out for **(*S*,*S*)-nOnCi-SQ** and **(*S*,*S*)-nCi-SQIB**.

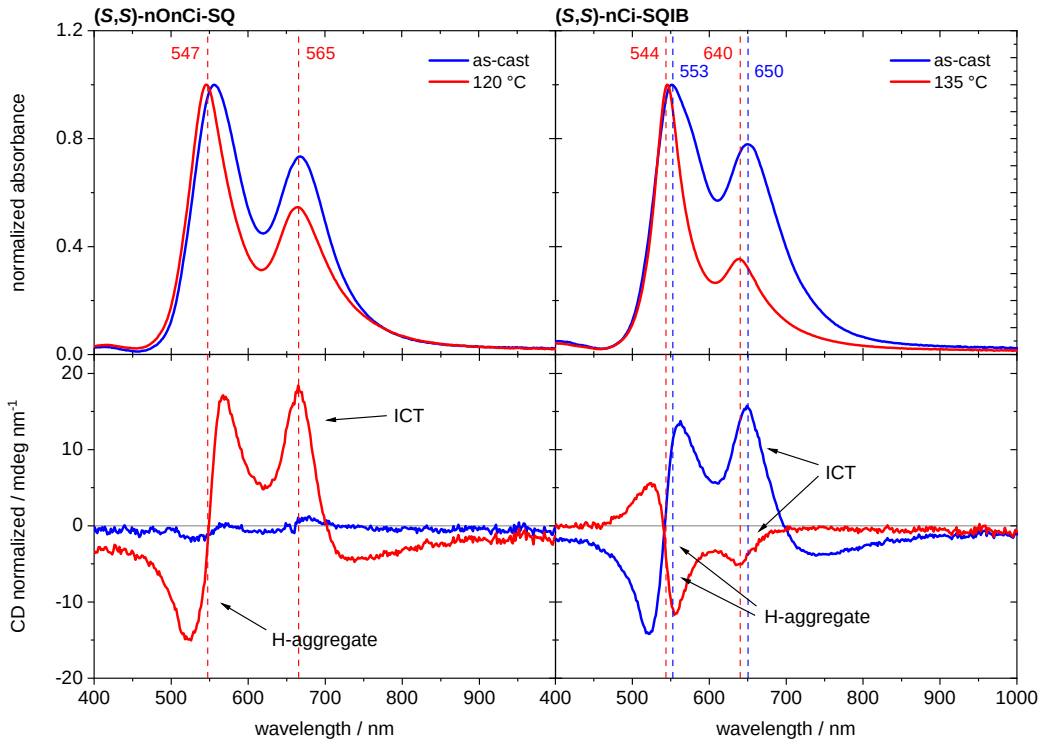


Figure 4.9: Normalized UV/Vis absorbance (top) and corresponding normalized CD spectra (bottom) of **(*S*,*S*)-nOnCi-SQ** (left) and **(*S*,*S*)-nCi-SQIB** (right), as-cast and thermally annealed at the above determined best temperature.

In order to test the hypothesis that the ICT can be modulated through steric hindrance, the UV/Vis absorbance spectra of **(*S*,*S*)-nOnCi-SQ** and **(*S*,*S*)-nCi-SQIB**, normalized to the higher-energy peak, are compared in Figure 4.9. Spectra of both the as-cast thin films and those thermally annealed at the respective optimal temperatures are displayed. In both cases, the characteristic double-humped spectral feature in the UV/Vis region is present regardless of whether annealing was performed. The CD spectra showed, for the high-energy and low-energy components, either a bisignate signal with a zero-crossing

[d] 2,4-bis[4-(*N*,*N*-dioctylamino)-2,6-dihydroxyphenyl]squaraine; molecular structure shown in Figure 4.8.
[e] 2,4-bis[4-(*N*,*N*-diisobutylamino)-2,6-dihydroxyphenyl]squaraine; molecular structure shown in Figure 4.8.

coinciding with the UV/Vis absorbance maximum, or a monosignate signal whose minima/maxima aligns with the absorbance maximum. Looking at the normalized UV/Vis absorbance spectra, it can be seen that for the pristine (as-cast) thin films, no significant differences are detected – apart from a negligible shift and a small bathochromic shoulder on the high-energy peak of **(*S*,*S*)-nCi-SQIB**. Upon annealing, however, the ratio between the previously assigned Coulombic H-aggregate and ICT peaks – (based on the bisignate vs. monosignate shape in the CD spectra) changes substantially. For **(*S*,*S*)-nCi-SQIB**, the ICT peak is markedly reduced in intensity. Since the strength of the ICT signal – simply said – depends on how well the charge transfer between the molecules works, which in turn depends on the packing, i.e., how close the π-conjugated backbones are and how they are shifted or twisted relative to each other. Thereby, this packing depends on the functionalization – increasing chain length or steric bulk alters the degree of steric hindrance at a certain point, thereby influencing the ICT interaction.

From these observations, we provide experimental evidence that the double-humped pattern in (*S*)-citronellyl-functionalized anilino squaraines (**(*S*,*S*)-nOCi-SQ**, **(*S*,*S*)-nOnCi-SQ** and **(*S*,*S*)-nCi-SQIB**) originates indeed from coupling between a Coulombic Frenkel exciton with H-aggregate character and an ICT state.[1–3, 86]

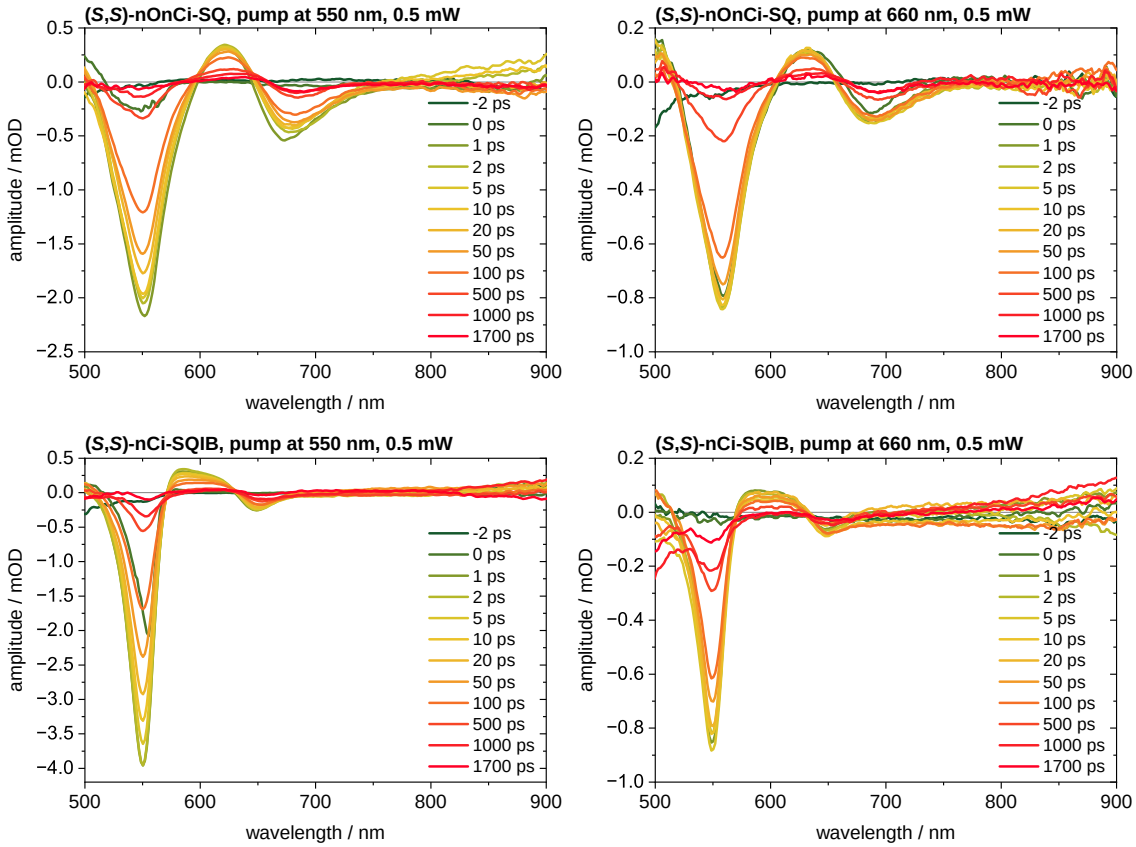


Figure 4.10: Transient absorption spectra of **(*S*,*S*)-nOnCi-SQ** (top) and **(*S*,*S*)-nCi-SQIB** (bottom) thin films, pumped at 550 nm (left) or 660 nm (right) with a pump power of 0.5 mW, recorded over a time window of 1700 ps. Measurements were performed in collaboration with Tianyi Wang (group of Paul H. M. van Loosdrecht, University of Cologne).

Another experimental indication that the double-humped spectral feature originates from the same aggregate was provided by transient absorption (TA) spectroscopy. In collaboration with Tianyi Wang (group of Paul H. M. van Loosdrecht, University of Cologne), thermally annealed thin-film samples were prepared and subsequently measured. Excitation was performed either at the high-energy component (H-band, e.g., 550 nm) or at the low-energy component (ICT-band, e.g., 660 nm). For both squaraines, the spectra were dominated by a strong negative bleach signal around the H-band, together with a red-shifted ICT-band signal. The transient absorption spectral shapes of the two squaraine thin films were highly similar, with the only notable difference being that, for **(*S*,*S*)-nCi-SQIB**, the H-band bleach signal was sharper and did not exhibit a well-defined bisignate form, instead showing a kind of plateau. Compared to direct excitation of the H-band at 550 nm, photo-excitation at the ICT-band at 660 nm produced an almost identical transient response, the only difference being a lower overall signal strength. This strong resemblance indicates that excitation initially corresponding to one of the two bands rapidly relaxes into the other, suggesting strong electronic coupling or exciton delocalization – a phenomena commonly observed in aggregates where the excitation is shared across chromophores.[3] These results strongly suggest that the two absorption bands in the thin films of both squaraines share the same ground state, and thus, originate from the same aggregate species, as it would be in a coupling between a Frenkel exciton with H-aggregate character and an ICT state.

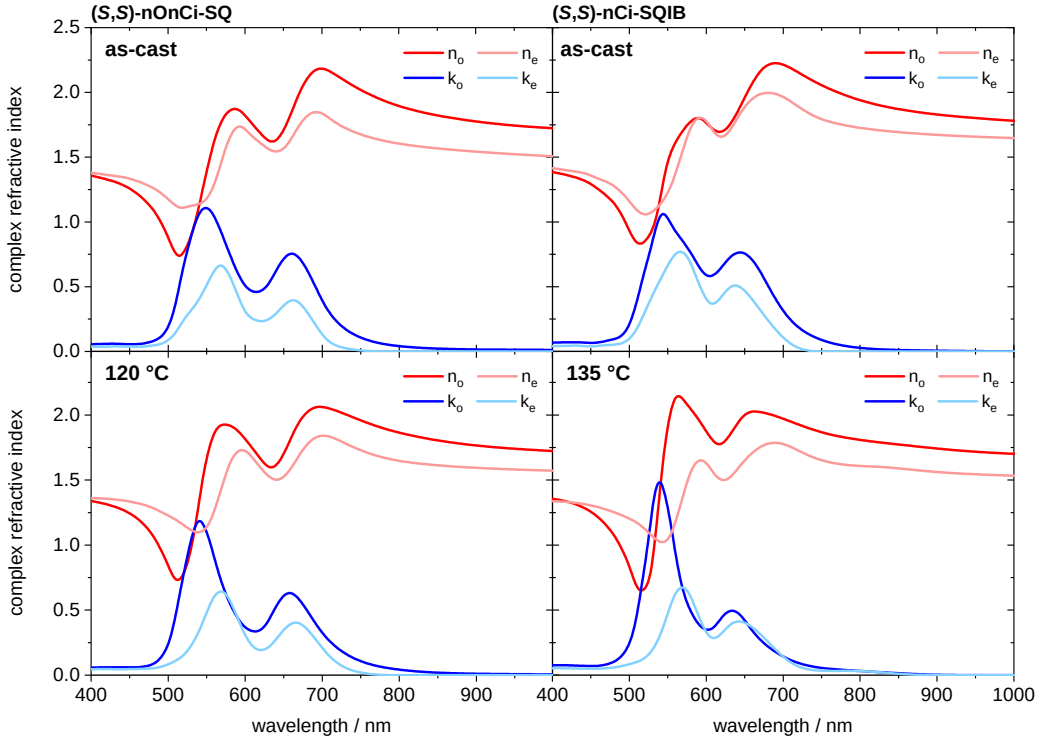


Figure 4.11: Uniaxial anisotropic complex optical constants of as-cast (top) and thermally annealed (bottom) spin coated thin films of **(*S*,*S*)-nOnCi-SQ** (left) and **(*S*,*S*)-nCi-SQIB** (right). Calculations based on a multisample analysis in *CompleteEASE* 6 using B-spline function. The refractive index is denoted as n_o (ordinary, in-plane) and n_e (extraordinary, out-of-plane). The extinction coefficient is denoted as k_o (ordinary, in-plane) and k_e (extraordinary, out-of-plane). The mean-squared error (MSE)[f] for the fits was calculated to: **(*S*,*S*)-nOnCi-SQ** 3.52 (as-cast) and 3.89 (120 °C); **(*S*,*S*)-nCi-SQIB** 5.28 (as-cast) and 5.59 (135 °C). The ellipsometric fitting process determined the layer thicknesses of all samples, yielding values ranging from 3 to 55 nm.

Additionally, the optical constants were calculated for both the as-cast and thermally annealed samples at the optimal temperature by a combined fitting of multiple samples with six different thicknesses, ranging from approximately 3 to 55 nm, as shown in Figure 4.11. Analysis of the measured ellipsometric data required an anisotropic uniaxial model, yielding refractive indices (n) and extinction coefficients (k):[g] the ordinary components (n_o and k_o) and the extraordinary components (n_e and k_e). The overall fit of the ellipsometric data from samples of different thicknesses reproduces the measured absorbance spectra quite good, particularly for the annealed thin films. Very high extinction coefficients[g] were determined, consistent with values typically reported for squaraines.[1, 34, 85] The uniaxial anisotropic complex optical constants thereby indicate a preferred orientation of molecules and aggregates parallel to the surface, as previously observed for **(*S*,*S*)-nOCi-SQ** in Chapter 3. This suggests that the molecular or aggregate organization is random within the substrate plane (ordinary components) of the thin film (at least on length scales smaller than the probing wavelength) while exhibiting a certain degree of preferred alignment perpendicular to the substrate plane (extraordinary components). For other aggregated microcrystalline anilino squaraine thin films, the molecular stacking direction has been reported to lie within the plane of the film,[16, 67, 85] which is also likely for the present **(*S*,*S*)-nOnCi-SQ** and **(*S*,*S*)-nCi-SQIB** samples. However, a chiral arrangement must be present in thermally annealed **(*S*,*S*)-nOnCi-SQ**, as well as in all tested **(*S*,*S*)-nCi-SQIB** samples, since they exhibit a pronounced CD response (ref. Figure 4.9). This arrangement must therefore be slightly different from that of non-chiral *n*-alkyl anilino squaraines. Unfortunately, the present data do not allow further conclusions regarding the molecular packing in detail, and thus, further investigations are necessary.

Additional spectra of **(*S*,*S*)-nCi-SQIB** and **(*S*,*S*)-nOnCi-SQ** spin-coated thin films – e.g., different layer thicknesses, calculated g-values and additional transient absorption (TA) measurements – can be found in Appendix B.

Overall, this chapter demonstrates that ICT interactions can be modulated through steric hindrance. By targeted synthesis, two new chiral (*S*)-citronellyl-functionalized squaraines, **(*S*,*S*)-nOnCi-SQ** and **(*S*,*S*)-nCi-SQIB**, were obtained, both exhibiting moderately complex aggregation behaviour in solution. When applied in solution-processed spin-coated thin films, however, the typical double-humped spectral feature of *n*-alkyl anilino squaraines was observed. Showing that these dyes are eligible to be directly compared to their non-chiral counterparts, the added value of chirality was used to determine the origin of the two peaks. From there, the different intensity ratios in the UV/Vis absorbance and CD spectra between the H-band and ICT-band in **(*S*,*S*)-nOnCi-SQ** and **(*S*,*S*)-nCi-SQIB** revealed an effective reduction of ICT interactions. Additionally, transient absorption measurements further suggested that, by showing that the double-humped feature originates from a single aggregate species. Finally, spectroscopic ellipsometry revealed an effective uniaxial alignment of the molecular aggregates, quantified through their complex refractive indices.

[f] Please note that the MSE reflects the quality of the fit between the experimental and simulated data, rather than the intrinsic variation or dispersion of the actual layer thicknesses. Its magnitude depends on many factors, including surface roughness and model complexity. Although it is difficult to define absolute thresholds for “small” or “large” values, the literature[34, 85, 95] generally considers MSE values below 10 as an excellent fit, while values below 20 are still regarded as acceptable.

[g] Please note that the optical extinction coefficient k is defined as the imaginary component of the complex refractive index $\tilde{n} = n + ik$, and should not be confused with the molar extinction coefficient ϵ commonly used in the context of the Lambert-Beer law.

4.4 A Preliminary Effort Towards Greater Steric Repulsion

Based on this success, an attempt was made to further increase steric repulsion. The aim was either to completely suppress ICT interactions or to entirely hinder aggregation. Obviously the first case is the one I hoped for. To achieve this, the branched isobutyl side chains should be substituted with an adamantanemethyl group. The methylene group was also chosen here for two reasons: first, to allow comparison with the isobutyl system, and second, because the final yields of squaraines are known to be sensitive to the steric effects from the alkyl chains of the secondary amine used.[36, 138]

Equivalent to the synthesis of **(*S*,*S*)-nCi-SQIB** and **(*S*,*S*)-nOnCi-SQ** (Figure 4.2), also here the first step was a reductive amination with (*S*)-citronellal with 1-adamantanemethylamine, yielding the corresponding secondary amine **(*S*)-Ci-N-Ad** in 96%. After hydrogenation of the double bond on the citronellyl residue with palladium on carbon (Pd/C) and elemental hydrogen, the secondary amine **(*S*)-nCi-N-Ad**

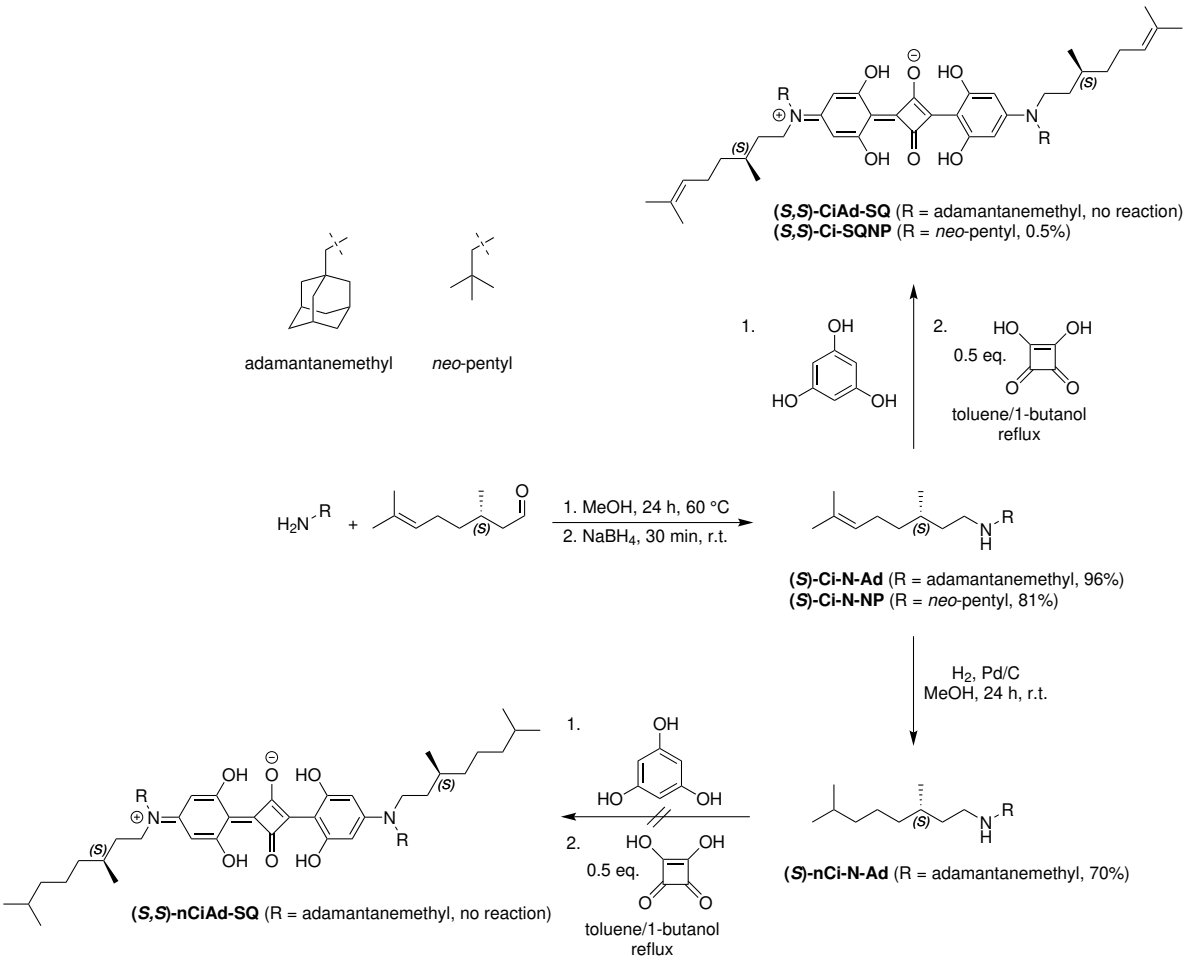


Figure 4.12: Conducted synthetic approaches for **(*S*,*S*)-nCiAd-SQ** and **(*S*,*S*)-Ci-SQNP**, starting from enantiopure (*S*)-citronellal and a selected primary amine (1-adamantanemethylamine or neopentylamine).

was obtained in 70% yield. With the suitable secondary amine in hand, the final step was the double condensation reaction with phloroglucinol (1,3,5-trihydroxybenzene) followed by squaric acid. However, after several attempts varying the toluene/1-butanol solvent ratio, reactant concentrations and reaction times, no successful squaraine synthesis could be achieved. As the issue was clearly with one of the two condensation reactions, it was decided to skip the hydrogenation step to reduce synthetic effort and to focus on refining the condensation reaction first. Using **(*S*)-Ci-N-Ad**, three further attempts were made in which the two-step, one-pot procedure[11, 100] was split into two separate reactions. Although the first condensation with phloroglucinol appeared promising from an thin-layer chromatography (TLC), no squaraine product was detected after the subsequently tried condensation with squaric acid.

Given the background knowledge that the steric effects from the alkyl chains of the secondary amine can significantly influence the reaction[36, 138] – an effect clearly demonstrated here – it was, after six failed attempts, ultimately decided that 1-adamantanemethylamine is likely too sterically demanding for the reaction to occur.

To slightly reduce steric repulsion, but still exceed the size of the isobutyl group, neopentylamine was tried. After the unsuccessful attempts with 1-adamantanemethylamine, the hydrogenation step was again omitted to reduce synthetic effort. With just a single step – the reductive amination of (*S*)-citronellal with neopentylamine – **(*S*)-Ci-N-NP** was obtained in 81% yield, ready for use in the subsequent two condensation reactions. Here, the two-step, one-pot procedure was again divided into two separate reactions, following a method involving a series of solvent changes and varying equivalents of reactants, as it will be described in detail in Chapter 10. At the end, **(*S*,*S*)-Ci-SQNP** was obtained with just 0.5% yield, again highlighting the difficulties associated with sterically demanding secondary amines.

Due to the poor yield of just 0.5% – which was equivalent to 16 mg for the given batch (Section 13.2) – the early stage aggregation experiments in solution were not performed and instead the obtained material was directly used for the fabrication of thin films.[h]

The UV/Vis absorbance and corresponding normalized CD spectra of **(*S*,*S*)-Ci-SQNP**, thermally annealed at different temperatures, are shown in Figure 4.13. The as-cast thin film was perfectly isotropic (see Figure B.13), exhibiting a smooth and continuous layer. Across the entire range of tested temperatures (as-cast, 60 to 220 °C), the absorbance maximum appeared at 675 nm, with a vibronic shoulder at 615 nm. Curiously enough, these positions are identical to those observed for **(*S*,*S*)-mCi-SQ** and **(*S*,*S*)-bCi-SQ**, despite these systems being indolenine-based squaraines. However, all compounds share the typical spectral signature of non-aggregated squaraines.[1, 19, 67, 139, 140] As no distinct molecular aggregation was observed in the UV/Vis absorbance spectra of **(*S*,*S*)-Ci-SQNP**, it is not surprising that the CD spectra also showed no signs of chiral aggregation. Although a potential CD signal was detected at an annealing temperature of 105 °C, this feature was not considered significant, as it appeared only once and the signal-to-noise ratio (S/N ratio) was very low i.e. signals were in the order of instrumental noise level. At annealing temperatures of 200 °C and above, the UV/Vis absorbance intensity decreased significantly, accompanied by a visible loss in color saturation of the thin-film samples (Figure 4.13, top).

[h] In addition, the substrate size was increased from 1 × 1 cm to 1 × 1 inch (1 inch = 2.54 cm), and thus, also the used volume of the spin-on solution. Furthermore, in the case of observed aggregation, a series of thin films with different layer thicknesses equivalent to **(*S*,*S*)-nCi-SQIB** and **(*S*,*S*)-nOnCi-SQ** would have had to be produced. And finally, aggregation in solids is more interesting than in solution in the context of optoelectronic devices. Taken together, these arguments were enough for omitting investigations in solution.

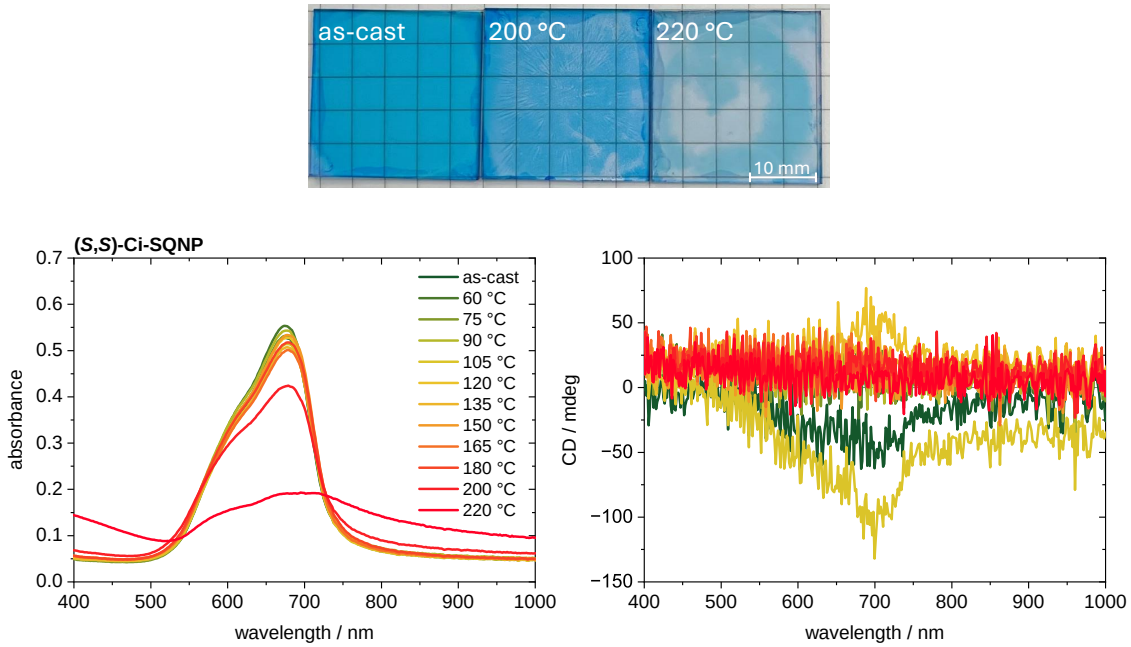


Figure 4.13: UV/Vis absorbance (bottom left) and corresponding normalized CD spectra (bottom right) of **(*S*,*S*)-Ci-SQNP**, spin-coated from a chloroform solution (6 mg squaraine per mL) under the same conditions and thermally annealed at various temperatures for 30 minutes. Top: Picture of thin film samples after annealing at indicated temperatures.

Overall, incorporation of the neopentyl group made the peripheral side groups of **(*S*,*S*)-Ci-SQNP** so sterically demanding that a defined aggregation was entirely hindered. As a result, no changes were observed in either the UV/Vis or CD spectra upon thermal annealing, which remained essentially unchanged until decomposition/evaporation occurred. This demonstrates – once again – that even small changes (isobutyl vs. neopentyl: just one -H is substituted with -CH_3) can lead to significant changes in the aggregation behavior. In the presented case, aggregation is completely suppressed, since the steric repulsion is sufficiently large. These results must, however, be considered preliminary, as **(*S*,*S*)-Ci-SQNP** bears the non-hydrogenated citronellyl residue. In addition to molecular design modifications (moving the steric unit further from the π-conjugated backbone – e.g., ethylene group), alternative annealing techniques such as solvent annealing could be used to allow higher molecular mobility during the annealing process.

With this, a series of new squaraine dyes was presented, allowing for the modulation of ICT interactions up to the complete suppression of aggregation through progressively more sterically demanding substituents.

CHAPTER 5

Synthesis, Structure and Thin Film Optical Properties of a Chiral Benzothiazole-Derived Squaraine

M. F. Schumacher,[a] G. Schnakenburg,[b] N. S. Sariciftci,[c] A. Lützen,[a] M. Schiek,[c,d]

To be published to ChemPhysChem – Please refer to the published article for the final version.

Own contributions:

- Synthesis and purification of the molecules
- Preparation of the thin film samples
- Performing and evaluating the ellipsometric/polarimetric measurements
- Interpretation of the results
- Writing the manuscript

Note: The following chapter is a manuscript[e] intended for submission to the peer-reviewed journal *ChemPhysChem*. Initial parts of this study were subject of my master's thesis.[141] For clarity and coherence, these sections are included here as they will appear in the journal submission. This primarily work comprises parts of the synthesis and UV/Vis absorption experiments in solution, both can be found in the this chapter or in Appendix C.

[a] Kekulé-Institute for Organic Chemistry and Biochemistry, University of Bonn, Bonn, Germany
[b] Institute of Inorganic Chemistry, University of Bonn, Bonn, Germany
[c] Institute for Physical Chemistry (IPC) & Linz Institute for Organic Solar Cells (LIOS), Johannes Kepler University, Linz, Austria
[d] Center for Surface- and Nanoanalytics (ZONA), Johannes Kepler University, Linz, Austria
[e] Preliminary manuscript – subject to change.

Synthesis, Structure and Thin Film Optical Properties of a Chiral Benzothiazole-Derived Squaraine

Marvin F. Schumacher,*[a] Gregor Schnakenburg,[b] N. Serdar Sariciftci,[c] Arne Lützen,[a] and Manuela Schiek*[c,d]

Through functionalization with enantiomerically pure substituents, semiconducting dye molecules such as squaraines can be directed into homo-chiral arrangements in which molecular chirality is transferred to a supramolecular level resulting in an excitonic circular dichroism. Replacing the sterically demanding CMe_2 group in indolenine-derived squaraines with a sulfur atom results in better aggregation in otherwise homogeneous thin films for benzothialzole-derived squaraines. Here, we explore this using solvent-processed and thermally annealed thin films of a benzothialzole-derived squaraine functionalized with homochiral citronellyl groups. The spectral shape of the excitonic circular dichroism depends on the solvent and annealing temperature. Uniaxial anisotropy is evident by X-ray diffraction and spectroscopic ellipsometry, showing a rarely documented spatial separation of what we consider to be Davydov bands into an in-plane and an out-of-plane component. This changes our reading of optical spectra including circular dichroism recorded under standard normal incidence conditions.

1. Introduction

Squaraine dyes are a highly potent class of small semiconducting organic molecules, exhibiting extraordinary optical properties and, thanks to their straightforward synthesis and structural versatility, have driven decades of research.[1–4] Typically described as resonance-stabilized, charge-neutral zwitterions with a donor–acceptor–donor structure, they show remarkable environmental stability and intense visible to near-infrared spectral signatures. Seen as a feature, the self-assembly beneficially influences the optoelectronic characteristics. It is one of the main reasons for the successful application in various fields of optoelectronics such as photovoltaics[5], biomedical applications[6,7], non-linear optics[8–10] and sensor applications[11–13] featuring chiral sensing.[14]

Among the diverse classes of squaraines, Scheme 1, anilino squaraines are the best studied due to their prototypical aggregation patterns.[15–19] Anilino SQs are primarily modified by a terminal substitution at the nitrogen atom, which controls the packing in the aggregated state. For bulky alkyl moieties, Coulomb interactions are prevalent, and the optical spectra are characterized by H- and J-type Frenkel excitons, which are often shaped by a Davydov splitting.[20–22] Linear alkyl chains enable close slip-stack packing and intermolecular charge transfer (ICT) interactions, which result in characteristic spectral double-hump signatures that are interpreted as hybrid Frenkel–ICT excitons.[18,23,24] Chiral functionalization is a powerful molecular design parameter for implementing circular dichroism (CD), which is the differential absorption of circularly polarized light of opposite handedness.[25,26] The chiroptical response is mediated by the chiral supramolecular arrangement of the molecular backbones that carry the optical transition dipole moment, while the chiral groups are not part of the chromophoric unit.[27] ICT interactions appear to play a central role in the giant CD response in thin films of chiral proline-derived anilino SQs.[28,29]

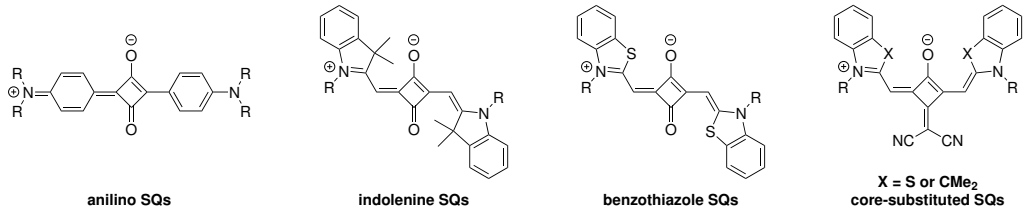
Indolenine-derived SQs have also been extensively discussed in the literature. These can be synthesized on the basis of 2,3,3-trimethylindolenine and provided with various alkyl substituents at the nitrogen.[30,31] Among them are (3*S*)-3,7-dimethyloctyl (citronellyl) chains which can be enantiomerically pure,[17] but typically are racemic and serve solely as solubilizing chains.[32–34] However, chiral functionalization can alternatively target the 3-position of the indolenine subunit by substituting the two methyl groups—either with chiral side chains or by creating a chiral center using two different substituents which is considerably more common.[35–37] Not being part of the aromatic system, the sp^3-hybridized quaternary carbon atom is angled towards the central plane, preventing efficient π-π stacking, which limits research mainly to solution-based experiments. Substitution with even bulkier groups in an attempt to induce chirality amplifies this problem. A strategy to enhance aggregation behavior involves the substitution of the CMe_2 group. Derivatives based on 2-methyl benzoxazole and 2-methyl benzothiazole, incorporating oxygen or sulfur as a secondary heteroatom at the 3-position within the five-membered ring, have been previously reported with various substituents, tremendously enhancing crystallinity

[a] M. F. Schumacher* and Prof. Dr. A. Lützen
Kekulé-Institute for Organic Chemistry and Biochemistry, University of Bonn, Bonn, Germany
E-mail: marvin.schumacher@uni-bonn.de

[b] Dr. Gregor Schnakenburg
Institute of Inorganic Chemistry, University of Bonn, D-53121 Bonn, Germany

[c] Dr. M. Schiek* and Prof. Dr. N. Serdar Sariciftci
Institute for Physical Chemistry (IPC) & Linz Institute for Organic Solar Cells (LIOS), Johannes Kepler University, A-4040 Linz, Austria

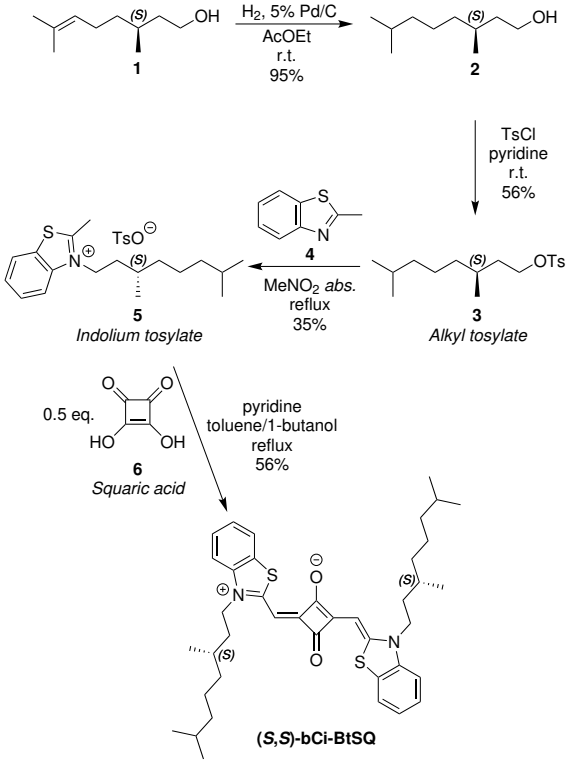
[d] Dr. M. Schiek*
Center for Surface- and Nanoanalytics (ZONA), Johannes Kepler University, A-4040 Linz, Austria
E-mail: manuela.schiek@jku.at



Scheme 1. Structural Motifs of squaraines (SQs): anilino squaraine, indolenine squaraine, benzothiazole squaraine and core-substituted indolenine / benzothiazole squaraines. The terminal N-substitutions R are typically linear, branched, or cyclic alkyl moieties, which may also be chiral. R may also be different within a molecule.

and aggregation behavior.[38–41] Furthermore, an acceptor core substitution is possible, which alters the molecular symmetry and leads to a permanent dipole moment of otherwise quadrupolar SQs.[42,43] This core substitution has a beneficial effect on photovoltaic performance as it promotes packing, which leads to ICT interactions in addition to the otherwise prevailing Frenkel excitons.[12,40,44]

Here, we present the chiral benzothiazole-derived squaraine **(*S*,*S*)-bCi-BtSQ** and discuss its synthesis, structure, and optical properties in thin films processed from various solvents. Compared to previously studied indolenine SQs, firstly, the quaternary carbon atom in position 3 of the five-membered ring (usually a CMe_2 group) is replaced by a sulfur atom as second heteroatom,[17] and second, chirality is introduced into the system by N-functionalization with enantiopure citronellyl substituents.[32,33] A chiral single crystal structure demonstrates the ability to form enantiomerically pure aggregates in the condensed state, even though it differs from the thin film structure. Thin films processed from various solvents and subsequently annealed at different temperatures essentially exhibit uniaxial orientation of molecular aggregates and an excitonic circular dichroism. Remarkably, a solvent and annealing dependent spectral shape of the bisignate excitonic CD signature is observed. In addition to the in-plane component visible in normal incidence transmission spectra, the anisotropic complex refractive index reveals another spectral signature, the out-of-plane component, which is red-shifted relative to the in-plane component. These two signatures are most likely Davydov bands. Such a splitting of Davydov bands into an in-plane and an out-of-plane component is a rarely documented case[45] compared to the usual case of two (effective) Davydov components visible in-plane along certain azimuthal polarization directions.[17,22,46] This changes the possible interpretation of the optical spectra, absorbance and circular dichroism, measured under standard normal incidence conditions.



Scheme 2. Synthesis of **(*S*,*S*)-bCi-BtSQ**, starting from *S*-citronellol (**1**).

2. Results and Discussion

2.1. Synthesis

The complete synthetic pathway of **(*S*,*S*)-bCi-BtSQ**, a benzothiazol SQ with homochrial citronellyl functionalization at the N-atom, is depicted in Scheme 2. The citronellyl group was chosen because it is easily accessible and improves the solubility of the resulting squaraines due to its branched structure, which is advantageous for solution-based processing methods. The synthesis

began with the heterogeneous hydrogenation of (3*S*)-3,7-dimethyloct-6-en-1-ol (*S*-citronellol) **1** using 10% palladium on carbon, yielding **2** in 95%. To activate the alcohol **2** for the following substitution reactions, 4-toluenesulfonyl chloride (TsCl) was added at room temperature under inert gas conditions, yielding the alkyl tosylate **3** in 56%.[47] Next, an S_N2 reaction was performed by refluxing the alkyl tosylate **3** in the presence of 2-methylbenzothiazole **4** in dry nitromethane. The resulting N-alkylated benzothiazolium tosylate species **5** was precipitated from the solution by adding diethyl ether. This alkylation step was reported for similar 2,3,3-trimethylindolenine compounds (CMe_2 group instead of sulfur) with reaction times of approximately 24 hours and yields around 60%.[48] In contrast, the sulfur-containing compound **4** required a reaction time of more than 6 days and produced only 35%. This quite different reaction behavior and the difference in the final yield can be explained by the decreased nucleophilicity of the nitrogen atom as a consequence of changing the system to an aromatic benzothiazole unit. Since enough benzothiazolium tosylate **5** was obtained for the next reaction step, no further reaction optimization and investigation of this phenomenon were performed.

Upon azeotropic removal of water by a 1:1 mixture of toluene and 1-butanol, the benzothiazolium tosylate **5** was converted with 0.5 equivalents of squaric acid **6** in the presence of pyridine to the corresponding squaraine **(*S*,*S*)-bCi-BtSQ**. Once the condensation reaction was completed, the reaction flask was slowly cooled and placed in a freezer overnight. The solvent was subsequently filtered off and the crude product purified by column chromatography on silica gel eluting with a solvent gradient. Initially, pure dichloromethane was used to remove the majority of side products and unreacted starting materials. After 3.5 vol.-% methanol was added to the eluent, the desired benzothiazole-derived squaraine began to elute and could be isolated. Further purification was performed by recrystallization from chloroform/cyclohexane 1:4 (v/v) and yielded the crystalline pure product in 56%. It is interesting to note that although **(*S*,*S*)-bCi-BtSQ** is almost insoluble in cyclohexane, it proved to be crucial that it is present during crystallization. The attempt of recrystallization from chloroform/*n*-hexane 1:4 (v/v) did not result in any crystal formation. However, when cyclohexane was added dropwise to the cooled chloroform/*n*-hexane solution, crystal formation was observed at the drop-in location. This has led to the inclusion of cyclohexane in the crystal structure, which can be seen in the single crystal structure analysis.

2.2. Single Crystal X-ray Structure

The single crystal structure found for **(*S*,*S*)-bCi-BtSQ** is a pseudo-polymorph as it contains cyclohexane solvent molecules. It is depicted in Figure 1 from different perspectives excluding the solvent molecules. A monoclinic unit cell with a chiral $C2$ space group was determined, containing four **(*S*,*S*)-bCi-BtSQ** molecules per unit cell and four cyclohexane molecules. The unit cell parameters are listed in Table 1 together with those of the previously published monoclinic $I2$ pseudo-polymorph of the indolenine SQ **(*S*,*S*)-bCi-SQ**.[17] The space group $C2$ is not primitive but base-centered, so that two of the molecules contained are translationally equivalent, which is analogous to the body-centered space group $I2$. In both cases, two translationally non-equivalent molecules remain whose electrostatic interactions enable a Davydov splitting in optical spectra.[20] See also Figure S2 regarding the possible polarization directions of the Davydov components for the benzothiazole SQ pseudo polymorph.

A view along the crystallographic *b*-axis is given in Figure 1 a), which is the direction of molecular π-stacking. The π-stacking distance of the benzothiazole SQ is slightly increased to about 10.1 Å compared to the indolenine SQ with about 9.4 Å. The π-stacking of anilino SQs can be substantially tighter, about 6.2 Å in case of a monoclinic polymorph of a compound with iso-butyl chains exhibiting Frenkel excitonic spectral signatures,[21] and about 5.2 Å for *n*-alkyl anilino SQs adopting triclinic structures with hybrid Frenkel–ICT excitonic spectral signatures.[15] Anilino SQs maintain complete co-planarity through the presence of intramolecular hydrogen bonds between the hydroxy-functionalized aniline moiety and the central squaric acid core. In contrast, the central squaric acid core of **(*S*,*S*)-bCi-BtSQ** is modestly tilted relative to the two co-planar benzothiazole units, exhibiting a torsion angle of about 11°. The absence of stabilizing hydrogen bonds in the benzothiazole analog introduces steric repulsion, leading to the observed deviation from co-planarity and likely also to an extended molecular stacking distance. Substituting the CMe_2 on the five-membered ring of the indolenine SQ with a sulfur atom to obtain the benzothiazole SQ reduces steric hindrance but only slightly alters the molecular symmetry and packing geometry.

The direction of molecular side-by-side packing without any staircase offset runs along the *c*-axis, as depicted in Figure 1 b). The chiral citronellyl chains at the nitrogen atoms adopt a trans configuration and occupy the interplanar space defined by the $(n\,0\,0)$ series ($n = 1, 2, 3, ...$) of planes. Figure S1 shows how the cyclohexane solvent molecules fit into the cavities between the citronellyl groups. The translationally equivalent molecules organize in interpenetrating columnar stacks tilted with relative to each other. Columnar stacking directions run along $[1\,1\,0]$ and $[1\,\bar{1}\,0]$ within the unit cell. Views along these directions with a slight displacement to better illustrate the stacking are shown in Figure 1 c) and d), respectively. The packing motifs of **(*S*,*S*)-bCi-BtSQ** and the previously published indolenine SQ are very similar overall, including the solvent inclusions, although in the case of the indolenine SQ these are *n*-hexane molecules. The unit cells differ in the choice of lattice centering, which is why the axes of the side-by-side packing are switched. In case of the benzothiazole SQ, the lateral distances are smaller, 17.6 Å compared to 19.1 Å for the indolenine SQ, which is why the unit cell volume of **(*S*,*S*)-bCi-BtSQ** is also smaller even with a slightly extended π-stacking distance.

2.3. Aggregation in Thin Films

A series of **(*S*,*S*)-bCi-BtSQ** thin films were spincasted onto glass substrates from a chloroform solution and subsequently thermally annealed with a stepwise increase of 15 °C per sample, starting at 60 °C and ending at 190 °C and including a non-annealed sample. Each sample was placed individually on a preheated hot plate under ambient conditions but covered with a glass container for this purpose. Unpolarized transmission intensity spectra were recorded at ambient temperature and are shown as absorbance ($-\log(\text{transmission})$) in Figure 2 a). Photos of

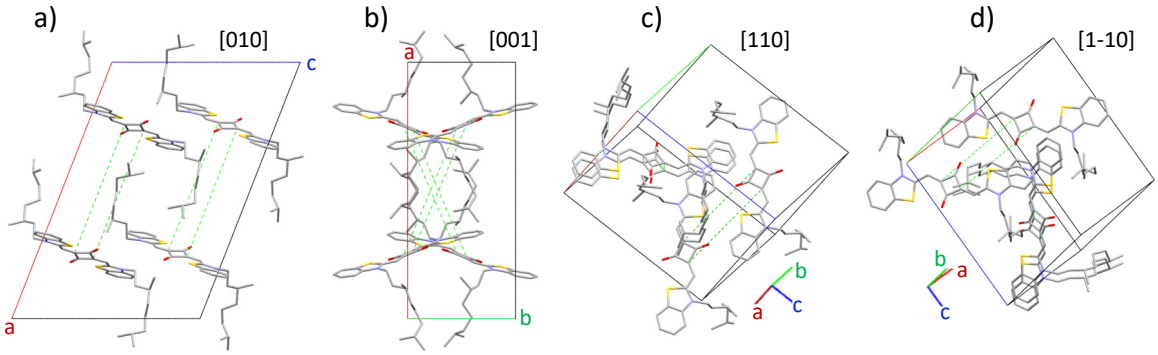


Figure 1. Crystal structure of **(*S*,*S*)-bCi-BtSQ**. Hydrogen atoms and the incorporated cyclohexane solvent molecules have been removed for clarity. Nitrogen is shown in blue, carbon in gray, oxygen in red, and sulfur in yellow. a) View along *b*-axis, the direction of molecular π-stacking. An extended view including solvent molecules can be found in Figure S1. b) View along *c*-axis. c) and d) are views along the two columnar stacking directions $[1\,1\,0]$ and $[1\,\bar{1}\,0]$, respectively, with a slight displacement to illustrate the stacking. Green dashed lines have been added to indicate the stacking squaraic central cores within a columnar stack of translationally equivalent molecules.

Table 1. Unit cell parameters of the pseudo-polymorphs of **(*S*,*S*)-bCi-SQ** with four *n*-hexane molecules and **(*S*,*S*)-bCi-BtSQ** with four cyclohexane molecules (this work).

compound	CCDC	space group	a (Å)	b (Å)	c (Å)	β (°)	Z
(*S*,*S*)-bCi-SQ[17]	2094899	$I2$	19.0769(7)	9.3541(4)	27.3099(13)	108.953(2)	4
(*S*,*S*)-bCi-BtSQ	2494927	$C2$	25.731(2)	10.0986(8)	17.6254(13)	111.379(4)	4

samples at selected annealing temperatures visualize the homogeneous appearance of the thin films and their intense azure blue color changing to turquoise upon annealing, see Figure 2 b).

The spectrum of a non-annealed (r.t.) layer shows broad absorbance with a maximum at around 710 nm and a shoulder at around 640 nm. This is a typical spectrum for condensed but not specifically aggregated SQ molecules, such as anilino SQs and indolenine SQs.[17,21] This is further supported by the absence of an excitonic CD signal, which will be discussed in a later section. Even relatively low annealing temperatures (60 °C, 75 °C, 90 °C) induced molecular aggregation, with the shoulder at 640 nm disappearing in favor of an emerging red-shifted shoulder at around 760 nm. Fortunately, this behavior is different from that of the previously discussed indoneline SQ, which did not show molecular aggregation in thin films upon annealing but evaporated from the substrate already at temperatures above 90 °C.[17] As the annealing temperature was increased (105 °C to 175 °C) for **(*S*,*S*)-bCi-BtSQ** thin films the absorbance sharpened and the peak maximum blue-shifted to around 700 nm, accompanied by the formation of shoulders at shorter and longer wavelengths. Increasing the hot plate temperature further (190 °C) changes the shape of the spectrum significantly, shifting it toward red and blurring the signatures. This is associated with the formation of small crystallites, and thus, a disruption of the homogeneous film structure, which can be seen in microscopy images between crossed polarizer, Figure 2 c). Ultimately, the benzothiazole SQ decomposes at temperatures above 200 °C, leaving small, colorless droplets on the glass surface that appeared completely dark under crossed polarizers.

X-ray diffraction was performed on a **(*S*,*S*)-bCi-BtSQ** thin film sample annealed at 135 °C, see Figure S1. A single diffraction peak is visible, indicating a preferred orientation of one crystallographic plane parallel to the substrate. Since no in-plane crystalline texture can be recognized in the polarized microscope image, Figure 2 c), the thin film can thus be classified as uniaxially anisotropic. A comparison with the calculated powder pattern, Figure S1, of the single crystal structure of the monoclinic $C2$ pseudo-polymorph clearly shows that a thin film spincasted from chloroform adopts a different structure.

At this point, the absorbance spectra of **(*S*,*S*)-bCi-BtSQ** thin films cannot be interpreted conclusively. The spectral profile is reminiscent of an H-aggregate containing vibronic signatures, with the presumed (0-1) transition at around 700 nm having the greatest oscillator strength.[20] The shoulder at 760 nm could be interpreted equally as a (0-0) transition or as a lower Davydov band without information about the polarization characteristics of the signatures. A thin film structure with multiple non-equivalent molecules within an aggregate unit can be assumed, but the domain size of the obtained crystallites, Figure 2 c), is too small to be analyzed by polarized spectro-microscopy.[17,21] However, homogeneous thin films are well suited for determining effective dielectric functions using spectroscopic ellipsometry.

Uniaxial Anisotropic Complex Refractive Indices - Solvent and Annealing Dependence

To better understand the aggregation behavior of **(*S*,*S*)-bCi-BtSQ** in thin films, series of samples were produced from different solvents: chloroform, dichloromethane (DCM) and cyclohexane:dichloromethane 1:1 (CyHex). Pure cyclohexane does not offer sufficient solubility to dissolve the required 5 mg/mL for good film formation in the thickness range of about 15 to 90 nm. In addition, the optical properties of diluted solutions in the selected solvents were characterized. The **(*S*,*S*)-bCi-BtSQ** exhibits a negative solvatochromic effect, whereby the peak maximum

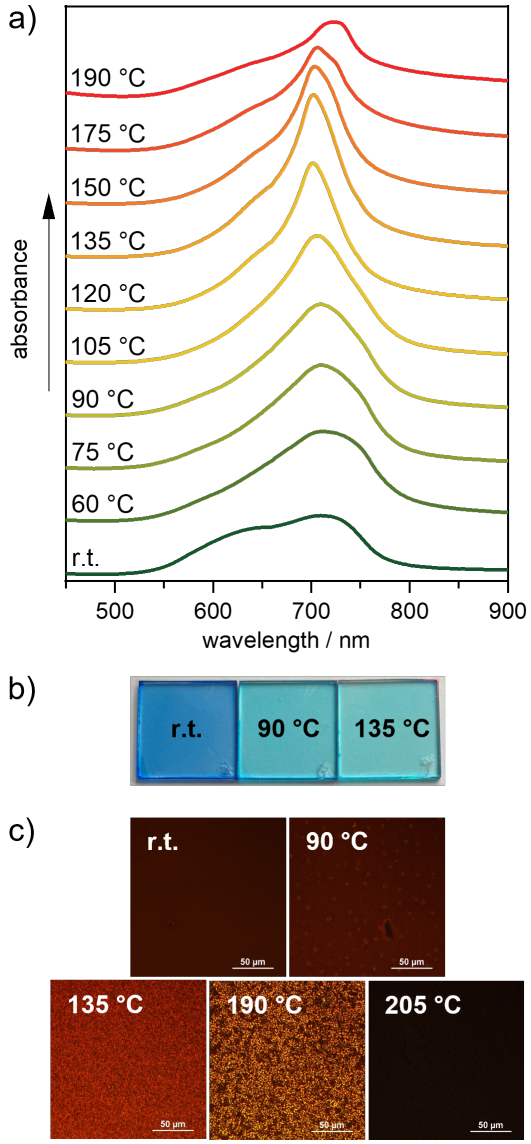


Figure 2. a) Absorbance spectra of **(*S*,*S*)-bCi-BtSQ** thin films, spin-coated from a chloroform solution under the same conditions and thermally annealed for 30 minutes at the specified temperatures (r.t. = room temperature, i.e. no annealing). b) Photos of selected thin film samples. c) Optical microscopy images between crossed polarizers of thin films samples annealed at indicated temperatures.

shifts to shorter wavelengths as the polarity of the solvent increases, see Figure S3. The spectral signatures remain unchanged, consisting of a pronounced maximum with a weak vibronic shoulder. The extinction coefficient in dichloromethane was determined to be $\epsilon = 237000\ \mathrm{M^{-1}cm^{-1}}$ at the peak maximum of 672.5 nm, see Figure S4. While rapid light-induced decomposition occurred in solution, see Figure S5, all spincasted **(*S*,*S*)-bCi-BtSQ** samples remained stable under ambient conditions for several months without any signs of degradation.

For a reliable determination of the uniaxial dielectric function of thin film samples using variable angle spectroscopic ellipsometry (VASE), samples with different layer thicknesses must be evaluated together with transmission spectra in a multi-sample analysis (MSA).[15,49] Additionally, three annealing temperatures were considered: no annealing (as-cast), 90 °C and 135 °C, for a more systematic understanding of temperature-induced aggregation. The importance of considering multiple samples becomes immediately evident when comparing as-cast samples with different layer thicknesses produced by different spin-coating parameters, see Figure S6. The absorbance spectra depend on the layer thickness (or spin-coating parameters), which indicates varying extents of molecular interaction. In case of chloroform, differences were manifested in the position of the peak maximum and its ratio to the shoulder. They were so pronounced that it was not possible to reliably determine a single representative dielectric function, even if uniaxial anisotropy is taken into account. The matrix in Figure 3 shows the complex refractive indices for all other combinations of the three solvents and annealing temperatures, which are all uniaxially anisotropic except for as-cast DCM conditions. Uniaxial anisotropy refers to a set of ordinary refractive index and extinction coefficient within the plane of the thin film, n_o and k_o, as well as a set of extra-ordinary components, n_e and k_e, perpendicular to it (out-of-plane). Note that the spectral signature of the extra-ordinary extinction coefficient is not visible in transmission spectra measured under normal incidence, since the transition dipole moment is perpendicular to the plane of the layer. Also note that transmission spectra of thin films consist of absorption within the layer (Lambert-Beer) as well as reflection at the interfaces and their interference (plus scattering, if applicable).[50] This means that both the real refractive index and the extinction coefficient contribute to the shape of a transmission spectrum, and the exact peak position and peak ratios may differ from those of the extinction coefficient. The representation of a transmission spectrum as absorbance, $-\log(\text{transmission})$, does not change this.[51]

The isotropic layer for the as-cast DCM case shows the typical spectral pattern of a complex refractive index for condensed but not specifically aggregated squaraines, such as anilino SQ with isobutyl chains (SQIB)[21] or the analogous indolenine SQ.[17] The extinction coefficient is slightly exceeds 1 at its maximum and lies within the typical "uniformity range" of extinction coefficients found for conjugated polymers.[52] The same applies to the as-cast CyHex layers, but here there is uniaxial anisotropy, with the extra-ordinary component showing a noticeably red-shifted signature. Annealing at 90 °C induced a noticeable molecular aggregation in the thin films of all three processing solvents and, as a related effect uniaxial anisotropy. At the same

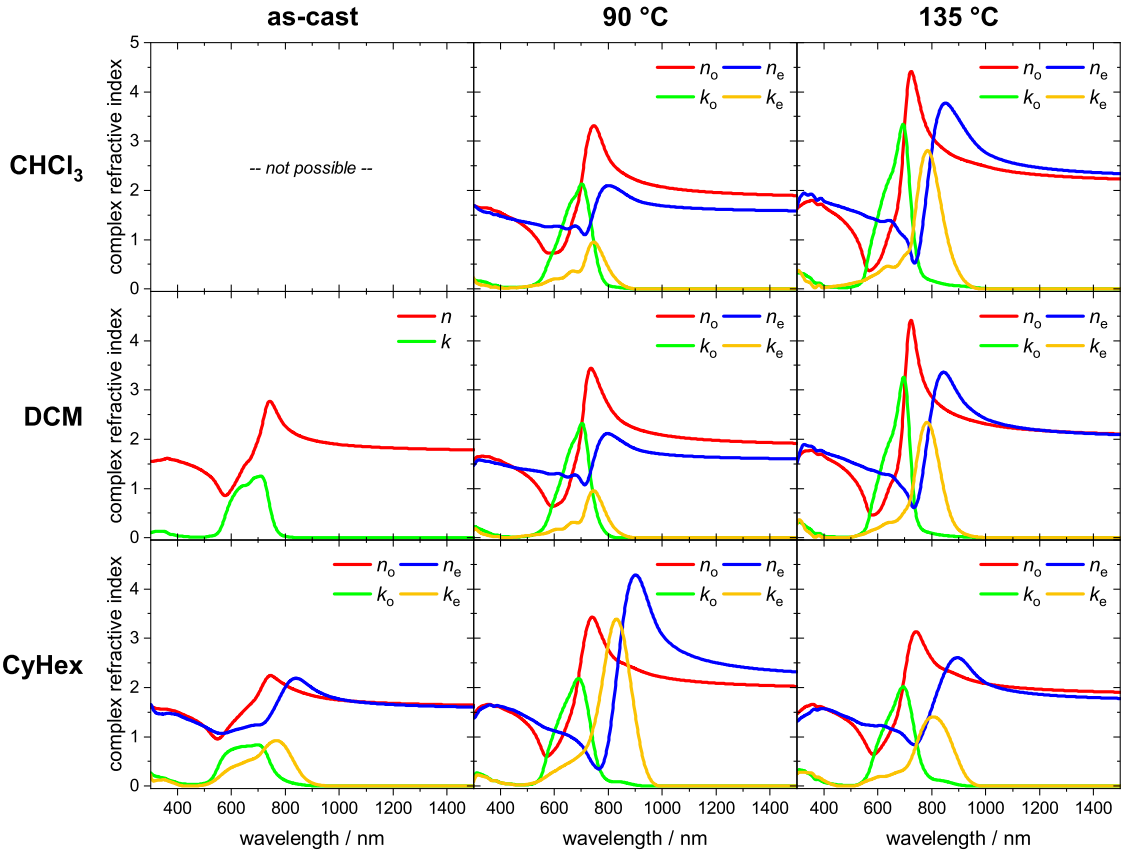


Figure 3. Complex refractive indices of **(*S*,*S*)-bCi-BtSQ** spincasted from various solvents (rows) and annealed at different temperatures (columns) as indicated. In case of uniaxial anisotropy the complex reflective index consists of ordinary (in-plane) and extra-ordinary (out-of plane) components: real refractive indices n_o and n_e, as well as extinction coefficients k_o and k_e. Mean Squared Error (MSE) of the respective fits: $CHCl_3$: 90 °C: MSE = 7.7; 135 °C: MSE = 10.2. DCM as-cast: MSE = 6.4; 90 °C: MSE = 11.0; 135 °C: MSE = 10.0. CyHex (cyclohexane:dichloromthane 1:1) as-cast: MSE = 22.5; 90 °C: MSE = 20.9; 135 °C: MSE = 24.6.

time, the ordinary extinction coefficients increased to values greater than 2 at maximum. The aggregation caused the emergence of an extraordinary spectral signature that is red-shifted compared to the ordinary component. In the case of CyHex-processing, the extra-ordinary component was even dominant and further shifted to the red compared to samples processed from $CHCl_3$ and DCM. An increase in the annealing temperature to 135 °C led to a further amplification of the extinction coefficients in samples processed from $CHCl_3$ and DCM, with the ordinary extinction coefficient now significantly exceeding 3. The extra-ordinary extinction coefficient exhibited a further red shift, as already observed for CyHex processing at 90 °C annealing. 135 °C annealing caused a relative weakening of the extra-ordinary extinction coefficient in CyHex processed samples, but no further enhancement of the ordinary extinction coefficient, compared to the medium annealing temperature.

Aggregation and crystallization can enhance molecular interactions, and thus, excitonic spectral signatures, as already seen in the uniaxial dielectric function of prolinol-derived anilino SQ layers[29] and in the tensor of SQIB orthorhombic micro-crystallites.[53] In case of **(*S*,*S*)-bCi-BtSQ** all layers retained their homogeneity for all processing solvents, even at annealing temperatures of 135 °C. Microscopy images between crossed polarizers displayed sub-micro texturing and, correspondingly, rather uniform birefringence, see Figure 4 a). X-ray diffraction showed, in agreement with ellipsometry, a preferred out-of-plane orientation for all processing solvents with the same interplanar spacing ($2\theta = 8.65°$) for 135 °C annealing, see Figure S1. From this it can be inferred that all three sample types adopt the same thin film structure polymorph, which, however, does not correspond to the resolved single crystal pseudo-polymorph. The use of CyHex processing solvent did not appear to cause the intended inclusion of cyclohexane molecules into the thin film as in the bulk single crystal structure. But this resulted in an increased tendency toward aggregation, as already the as-cast CyHex layers manifested uniaxial anisotropy. Furthermore, the MSE values of the ellipsometric fits were about 20 and with this systematically larger compared to 10 and smaller for the samples processed from the neat chlorinated solvents, see Caption Figure 3 for detailed values. The rise in MSE could be due to increased layer roughness, which in turn could be caused by larger crystallite sizes.

For all three processing solvents, the ordinary extinction coefficient of **(*S*,*S*)-bCi-BtSQ** thin films shows a distinct shoulder at shorter wavelengths, which is mostly pronounced at 135 °C annealing. The energetic difference between the peak maximum and the shoulder is approximately 0.17 meV, which is within the range of a vibronic signature.[20] A shoulder at longer wavelengths could not be resolved here, but can be speculated based on the spectral signatures in the absorbance spectra for $CHCl_3$ processing and annealing temperatures above 135 °C, see Figure 2 a). Nevertheless, we hypothesize that the peak maximum of the ordinary spectral signature is a (0-1) and the shoulder at shorter wavelengths is a (0-2) vibronic progression. The ordinary spectral signature is thus reminiscent of an H-aggregate or the upper Davydov component (UDC) of a Davydov splitting.[20] This determines the extraordinary spectral signature at longer wavelengths for the lower Davydov component (LDC), and the energetic splitting between the two peak maxima for the apparent Davydov splitting. As a reminder: the extra-ordinary spectral signature is not visible in transmission spectra under normal incidence, and therefore neither is the Davydov splitting. The energetic splitting between the maximum values of ordinary and extra-ordinary extinction coefficients (apparent Davydov splitting) is approximately 0.1 eV for $CHCl_3$ and DCM processing solvents at 90 °C annealing and increases to approximately 0.2 eV at 135 °C annealing. For CyHex processing, the apparent Davydov splitting is somewhat larger, amounting to approximately 0.3 eV at both 90 °C and 135 °C annealing temperatures. As a reminder: A transmission spectrum (also in the representation as absorbance) consists of contributions from the real refractive index and extinction coefficient, which means that peak position and energetic separation in an absorbance spectrum and the extinction coefficient may differ from each other. In addition, the extra-ordinary components can be determined with less accuracy than the ordinary ones.[49] Nevertheless, the magnitude of the apparent Davydov splitting in annealed **(*S*,*S*)-bCi-BtSQ** thin films can be classified as typical for pronouncedly interacting small molecules, such as perylene diimide crystallites[54] or pentacene polymorphs.[55] Remarkable is the division of the Davydov components into an ordinary (in-plane) and an extra-ordinary (out-of-plane) component, which is a rarely documented case, such as with a merocyanine dye.[45] In most other examples, both Davydov components show at least a partial projection into the plane of a thin film, making them accessible by polarization resolved spectro-microscopy in normal incidence transmission.[17,22,46]

Circular Dichroism - Solvent and Annealing Dependence

Due to the chirality of **(*S*,*S*)-bCi-BtSQ**, excitonic circular dichroism (CD) can be used as an additional metric to investigate molecular aggregation. The enantiomerically pure terminal citronellyl group directs a homochiral aggregation of the chromophoric SQ backbones, which then exhibit an excitonic CD signal in tandem with the excitonic absorbance. For this purpose, the thin film samples using three different processing solvents (chloroform, dichloromethane, cyclohexane:dichloromethane 1:1) and annealing temperatures (as-cast, 90 °C, 135 °C) were also investigated by Mueller matrix polarimetry. Microscopy images between crossed polarizers reveal a sub-micro texture and a corresponding relatively uniform birefringence in all layers annealed at 135 °C, see Figure 4 a). Mueller matrix polarimetry is particularly advantageous for such thin films, as the obtained CD is free of contributions from linear dichroism.[56] Rotation and flipping of the sample do not influence the measurement result, as is the case with a conventional CD spectrometer.[57,58]

Typical thickness normalized CD together with the corresponding normalized absorbance spectra are shown in Figure 4 b). As discussed in the previous section, the absorbance spectra of the as-cast **(*S*,*S*)-bCi-BtSQ** layers exhibit spectral signatures of condensed but not specifically aggregated molecules.[17,21] For the processing solvents $CHCl_3$ and DCM the spectra looked very similar with a main peak at around 713 nm and a vibronic shoulder at around 638 nm. The CyHex solvent mixture resulted in a slightly broadened absorbance with the main peak at around 695 nm and a shoulder at around 610 nm with an

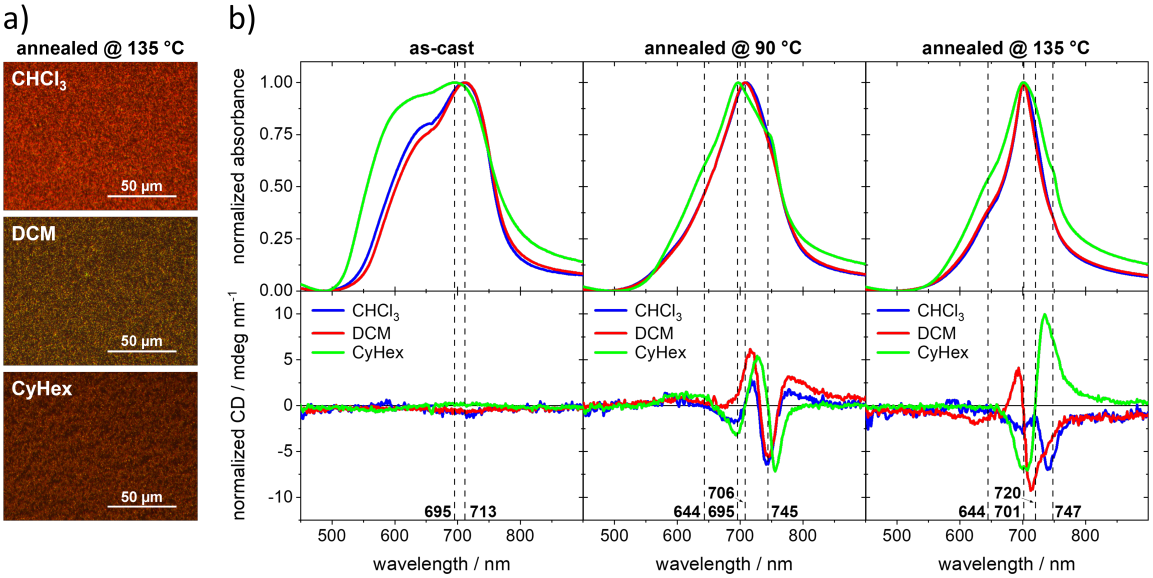


Figure 4. a) Optical microscopy images between crossed polarizers of **(*S*,*S*)-bCi-BtSQ** thin films spincasted from chloroform ($CHCl_3$), dichloromethane (DCM) and cyclohexane:dichloromethane 1:1 (CyHex) after annealing at 135 °C for 30 minutes. b) Normalized absorbance (top) and thickness normalized CD spectra (bottom) of **(*S*,*S*)-bCi-BtSQ** layers processed from the same solutions but with variable annealing temperatures: no annealing (as-cast), 90 °C, 135 °C as indicated from left to right.

increased aspect ratio due to emerging aggregation.[59] A similar tendency toward onset aggregation even without annealing has also been observed in $CHCl_3$-processed layers depending on the spin coating parameters, see Figure S6. As expected with no significant aggregation, none of the as-cast layers showed a detectable CD signal, see left panel in Figure 4 b). To avoid confusion: A single **(*S*,*S*)-bCi-BtSQ** molecule can indeed exhibit a CD signal originating from the enantiomerically pure citronellyl functionalization. This terminal group is not conjugated to the chromophoric SQ backbone and would show a CD signal in the deep UV spectral range regardless of molecular aggregation. However, a non-reproducible special case occurred in an as-cast DCM-processed layer, resulting in pronounced aggregation, so that a clear bisignate excitonic CD signal could be measured, see Figure S7.

Thermal annealing for 30 minutes at 90 °C induced significant changes in the absorbance spectra suggesting aggregation, which is supported by the appearance of CD signals, see middle panel in Figure 4 b). The layers processed from the neat chlorinated solvents showed very similar absorbance spectra with a maximum at around 706 nm and a shoulder at around 745 nm. CyHex-processing resulted in a slightly broader absorbance due to the formation of a second shoulder at a shorter wavelength (644 nm) and a slight blue-shift of the maximum to about 695 nm. Overall, the absorbance spectra of all layers appeared sharper after annealing than without. Based on the results of the uniaxial anisotropic refractive index in the previous section, we interpret this absorbance pattern obtained by aggregation as the upper Davydov component (UDC) of a Davydov splitting.[20] The peak maximum is the vibronic (0-1) transition of the UDC, and the lower Davydov component (LDC) remains invisible in transmission spectroscopy under normal incidence because it is oriented exclusively perpendicular to the layer. Compared to monomer absorbance, which varies between 650 and 680 nm depending on the solvent, see Figure S3, the UDC thin film absorbance is in any case shifted to the red spectral range. This does not match the simple definition of H-like (UDC) and J-like (LDC) transitions based on their spectral blue- and red-shifts, respectively, relative to the monomer transition (Kasha definition). The assignment via vibronic signatures is more robust, as interactions in the solid state can lead to a red shift of both transitions, particularly in quadrupolar molecules such as SQs.[60] However, since Mueller matrix polarimetry was performed in transmission under normal incidence only, all CD signals can be attributed solely to the UDC.

The shape of the CD signals was similar for the layers of all three processing solvents. The CD spectra start with a small negative lobe at around 695 nm, transition to a more pronounced positive lobe at around 720 nm, followed by the most intense negative lobe at around 745 nm, and end with a small positive lobe at around 780 nm. In the case of CyHex-processing, the first positive and second negative peaks are slightly red-shifted, so that in this case the zero crossing is at 745 nm, which corresponds to the presumed (0-0) shoulder in the absorbance spectrum. The magnitude of the first negative signature (695 nm) increases in the following order of processing solvents: DCM, $CHCl_3$, CyHex, while the magnitude of the last positive signature (780 nm) in this sequence decreases. Overall, the CD signals were small: The thickness-normalized CD values range from +6.1 to –7.2 mdeg nm^{-1}, suggesting weak Coulombic intermolecular interactions. Thus, CD spectra took the complex form of a series of vibronic bisignate couplets, as is the case in the weak coupling regime of an H-aggregate or a UDC with pronounced vibronic signatures.[61] Only in the case of strong coupling does a CD spectrum have the simple form of a first derivative of the absorbance spectrum (bisignate Cotton ef-

fect) with a zero crossing at the absorbance maximum.[62,63]

Increasing the annealing temperature further to 135 °C resulted in minor changes in the absorbance and pronounced changes in the CD spectra as shown in Figure 4 b), right panel. Again, the absorbance spectra of the layer processed with neat chlorinated solvents appeared the same, whereas CyHex processing resulted in a broadened absorbance. All three absorbance spectra have sharpened compared to 90° C annealing and exhibited a common main peak at around 701 nm plus two shoulders around 644 nm and 747 nm. The CD spectra still resulted as a series of vibronic bisignate couplets with small CD values, but looked considerably different compared to 90° C annealing and were clearly different from each other. The initial impression was that the increased annealing temperature for the CyHex-processed layer has led to an inversion of the CD signal handedness, and thus possibly to a change in the aggregate structure.

In fact, the exciton chirality method is a common experimental approach to determine the absolute configuration of supramolecular aggregates based on the sign of a bisignate CD couplet.[58,64] However, the method was developed for colloidal aggregates in solution, where anisotropy does not play a role, and only applies to a full extent in the regime of strong coupling, that is, when there is no vibronic coupling involved. In solution, it is comparatively easy to control the handedness of molecular aggregates by using different solvents and additives, which can cause a sign inversion of the CD signal.[65–68] Recent theoretical considerations also indicate that the influence of handedness and coupling energy on the sign of a CD couplet still remains enigmatic.[69]

In case of the **(*S*,*S*)-bCi-BtSQ** thin film samples neither the X-ray diffraction analysis nor all other spectroscopic investigations pointed to any significant structural reorganization comparing the processing solvents. The broadening of the absorbance spectra in the case of CyHex-processing is rather attributed to an increased tendency toward crystallization with the formation of larger crystallites and the associated increased layer roughness. Therefore, we do not consider the variable form of the CD spectra as feature and refrain from drawing further conclusions from it. The peculiar behavior of the CD spectra can be crudely postulated as a sum of multiple bisignate signatures, one for each vibronic progression, which are subject to a change in rotational strength through thermal annealing.[61–63,69] The fact that the CD values were small reinforces the assumption of a weak coupling regime based on electrostatic interactions (Frenkel excitons) only. Contributions from charge transfer interactions have shown a clear and even giant amplification of the CD response in thin films of a homochiral anilino SQ[17] and prolinol-derived SQs,[27,28] respectively. With the prolinol-derived SQs thin films, the dominant in-plane component has a J-like character and, compared to the weaker H-like out-of-plane component, carries the majority of both oscillator and rotational strength.[29] In the **(*S*,*S*)-bCi-BtSQ** thin films, the J-type out-of-plane component (LDC) appears to have an oscillator strength similar to the in-plane component (UDC) based on the uniaxial complex refractive indices, as discussed in the previous section. Unfortunately, we cannot comment on the associated rotational strength of a possible CD signal, as the out-of-plane component (LDC) is not accessible with our experimental methods.

Summary and Conclusion

We successfully synthesized the chiral benzothiazole-derived squaraine **(*S*,*S*)-bCi-BtSQ**, functionalized with enantiomerically pure citronellyl groups, and evaluated its aggregation in solution-processed thin films by means of their uniaxial complex refractive indices and excitonic circular dichroism supported by structural analysis. The resolved single crystal structure is a chiral pseudo-polymorph adopting a monoclinic $C2$ space group, similar to a previously published pseudo-polymorph of a citronellyl-functionalized indolenine SQ, both suffering from the inclusion of solvent molecules. The introduction of the second heteroatom sulfur at the 3-position of the five-membered ring caused planarization of the conjungated π-system, thereby reducing the steric hinderance between neighboring molecules. This enabled the formation of homogeneous layers with distinct molecular aggregation, which was not the case for the indolenine SQ analog.

All thermally annealed **(*S*,*S*)-bCi-BtSQ** layers, regardless of the three processing solvents of choice: chloroform, dichloromethane, and dichloromethane:cyclohexane mixture, exhibit the same uniaxial anisotropic thin film structure, which is different from the single crystal structure. From the uniaxial anisotropic complex refractive index, we learned that, in addition to the in-plane component, there is an out-of-plane component that is invisible in normal incidence transmission spectroscopy. The out-of-plane component is red-shifted relative to the in-plane component, which also has distinct vibronic signatures. Even though we do not know the thin film structure, we assume two or more translationally invariant molecules in the aggregate. Therefore, we interpret the spectral features as Davydov splitting, with the in-plane band being the upper Davydov component (UDC) and the out-of-plane band being the lower Davydov component (LDC). This is a rarely documented case, to the best of our knowledge, to date only for thin films of a merocyanine.

Because the molecular aggregation is chiral, the layers exhibit an excitonic circular dichroism, which unfortunately turns out to be weak. Mueller matrix polarimetry allows us to determine the true CD signal without contributions from linear dichroism and influence from sample orientation. However, since it is a normal incidence transmission measurement, only the CD signals of the in-plane component, that is UDC, can be captured. We observe multifaceted bisignate CD spectra whose shapes depend on the processing solvent and annealing temperature, whereby a sign inversion may mislead to the interpretation of a structural rearrangement. However, the peculiar shape of the CD spectra can rather be interpreted as the sum of several bisignate features, one for each vibronic progression, which are subject to relocation of rotational strength because of processing conditions.

This leaves the splitting of the Davydov bands into an in-plane and an out-of-plane component, compared to the usual case where both Davydov bands are at least partially project into the plane of the thin film, as the most striking feature of the **(*S*,*S*)-bCi-BtSQ** layers.

3. Experimental

3.1. Synthesis and Analytics

The synthetic approach was adapted from the literature-known procedure.[17] All chemicals were purchased from standard suppliers and used as received. Solvents were purified after standard methods and, if necessary, dried according to literature procedures and stored under argon atmosphere over 4 Å molecular sieves. Reactions under inert gas conditions were performed under dry argon atmosphere with dry solvents in dried glassware using *Schlenk* techniques.

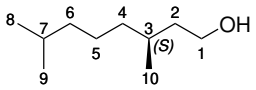
NMR: ^{1}H and ^{13}C NMR were recorded on *Bruker* NMR spectrometer at 298 K at 700 MHz and 176 MHz or 500 MHz and 125 MHz or 400 MHz and 100 MHz, respectively. ^{1}H NMR chemical shifts are reported on the δ scale (ppm) relative to tetramethylsilane. The residual non-deuterated solvent signal was used as the internal standard. ^{13}C NMR chemical shifts are given in δ values (ppm) using to the deuterated solvent as the internal standard.

Mass spectrometry: electrospray ionisation (ESI) and atmospheric pressure chemical ionization (APCI) mass spectra were taken on a Orbitrap XL (*Thermo Fisher Scientific*).

UV/Vis spectroscopy in solution: UV/Vis spectroscopic measurements were carried out at room temperature using a Specord 200 spectrometer (*Analytic Jena*) with 0.5 nm step size and 5 nm/s scanning speed, using 10 mm quartz cuvettes (*Hellma*). The instrument was calibrated with a reference sample in advance. UV/Vis spectra are shown as absorbance $= -\log(\text{transmission})$.

Elemental analysis: The CHNS elemental analyses were carried out after standard methods with "tin-boats" using a Vario EL (*Heraeus*). All compounds were measured two twice and the mean values were compared with the calculated values from ChemDraw 19.1 (PerkinElmer).

(3*S*)-Dihydrocitronellol



Under inert gas conditions, a flame-dried *Schlenk*-flask was charged with (*S*)-citronellol (3.50 g, 22.4 mmol, 1.00 eq.) in 25 mL of ethyl acetate and carefully degassed in three freeze-pump-thaw cycles. After adding 10% palladium on carbon (0.350 g, 1.5mol%), three additional freeze-pump-thaw cycles were performed. A hydrogen gas balloon was connected to the *Schlenk*-flask and the atmosphere was exchanged with hydrogen by three cycles of evacuation and repressurization. After 20 hours of vigorous stirring, the reaction mixture was filtered through *Celite*®, which was afterwards extracted with 75 mL of ethyl acetate. The filtrate was concentrated under reduced pressure to yield the product as a colorless oil that was used without further purification in the next reaction.

Yield: 3.38 g (21.3 mmol, 95%, colorless oil)

Molecular weight: $C_{10}H_{22}O$, 158.29 g/mol

^{1}H-NMR: (500 MHz, Chloroform-*d*, 298 K) δ [ppm] = 3.74 - 3.61 (m, 2H, H-1), 1.64 - 1.56 (m, 1H, H-2a), 1.56 - 1.49 (m, 2H, H-3, H-7), 1.48 (*br* s, 1H, OH), 1.41 - 1.34 (m, 1H, H-2b), 1.34 - 1.18 (m, 3H, H-4a, H-5), 1.19 - 1.06 (m, 3H, H-4b, H-6), 0.89 (d, $^{3}J_{\text{H-6,H-10}} = 6.7$ Hz, 3H, H-10), 0.86 (d, $^{3}J_{\text{H-7,H-8/9}} = 6.6$ Hz, 6H, H-8, H-9)

^{13}C-NMR: (125 MHz, Chloroform-*d*, 298 K) δ [ppm] = 61.4 (C-1), 40.1 (C-2), 39.4 (C-6), 37.5 (C-4), 29.7 (C-3), 28.1 (C-7), 24.8 (C-5), 22.8 (C-8/9), 22.7 (C-8/9), 19.8 (C-10)

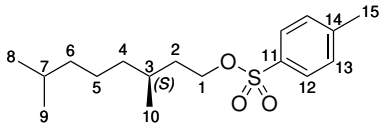
NMR spectra can be found in the SI in Figure S17.

(APCI, Dichloromethane, M = $C_{10}H_{22}O$) *m/z* (Int.) = 157.159 (8) $[M\text{-}H]^-$, 141.164 (100) $[M\text{-}OH]^-$, 99.117 (35) $[M\text{-}C_3H_7O]^-$, 85.101 (82) $[M\text{-}C_4H_9O]^-$, 71.086 (28) $[M\text{-}C_5H_{11}O]^-$, 57.070 (10) $[M\text{-}C_6H_{13}O]^-$

APCI HRMS: $[M\text{-}H]^-$ = $C_{10}H_{21}O^-$, calculated: $m/z = 157.159$, found: $m/z = 157.159$

Mass spectra spectra can be found in the SI in Figure S23.

(3*S*)-3,7-Dimethyloctyl-p-toluolsulfonate



Under inert gas conditions (3*S*)-dihydrocitronellol **13** (3.17 g, 20.0 mmol, 1.00 eq.) was dissolved in 5 mL of *abs.* pyridine in a flame-dried *Schlenk*-flask. The solution was cooled to -10 °C and *p*-toluenesulphonyl chloride (7.50 g, 39.3 mmol, 2.00 eq.) was slowly added over a period of 40 minutes under vigorous stirring. The resulting suspension was allowed to warm up to room temperature over a duration of 24 hours under further stirring. After 24 hours, the mixture was poured into ice-cold 3 M aqueous HCl. The organic layer was separated, the aqueous phase extracted with diethyl ether (3 × 30 mL) and the combined organic phases were washed with water (30 mL) and brine (30 mL). After drying with magnesium sulfate, the solvent was removed under reduced pressure and the pale yellow crude product was purified by column chromatography on silica gel eluting with dichloromethane/cyclohexane 1:1 (v/v). The product was obtained as colorless oil.

Yield: 3.53 g (11.3 mmol, 56%, colorless oil))

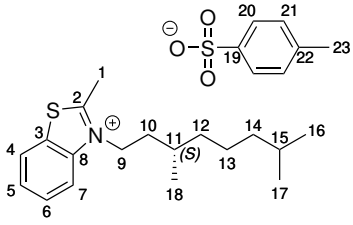
Molecular weight: $C_{17}H_{28}O_3S$, 312.47 g/mol

^{1}H-NMR: (500 MHz, Chloroform-*d*, 298 K) δ [ppm] = 8.2 Hz, 2H, H-12), 7.34 (d,$^{3}J_{\text{H-12,H-13}} = 7.9$ Hz, 2H, H-13), 4.11 - 4.01 (m, 2H, H-1), 2.45 (s, 3H, H-15), 1.70 - 1.61 (m, 1H, H-2a), 1.54 - 1.46 (m, 2H, H-3, H-7), 1.46 - 1.38 (m, 1H, H-2b), 1.33 - 1.22 (m, 1H, H-5a), 1.22 - 1.12 (m, 2H, H-4a, H-5b), 1.12 - 0.99 (m, 3H, H-4b, H-6), 0.85 (d,$^{3}J_{\text{H-7,H-8/9}} = 6.6$ Hz, 6H, H-8, H-9), 0.80 (d,$^{3}J_{\text{H-3,H-10}} = 6.6$ Hz, 3H, H-10))

^{13}C-NMR: (125 MHz, Chloroform-*d*, 298 K) δ [ppm] = 144.8 (C-11), 133.4 (C-14), 129.9 (C-13), 128.0 (C-12), 69.3 (C-1), 39.3 (C-6), 37.0 (C-4), 35.9 (C-2), 29.3 (C-3), 28.1 (C-7), 24.6 (C-5), 22.8 (C-8/9), 22.7 (C-8/9), 21.8 (C-15), 19.3 (C-10)

NMR spectra can be found in the SI in Figure S18.

(*S*)-3-(3,7-dimethyloctyl)-2-methylbenzothiazol-3-ium tosylate - (*S*)-Ci-Bt



Under inert gas conditions, (3*S*)-3,7-dimethyloctyl-p-toluolsulfonate **14** (937 mg, 3.00 mmol, 1.00 eq.) and 2-methylbenzothiazole **16** (448 mg, 3.00 mmol, 1.00 eq.) were dissolved in 5 mL of *abs.* nitromethane in a flame-dried 10 mL single-neck flask with affixed reflux condenser. The reaction mixture was heated to reflux for 18 hours. After cooling to room temperature, the solvent was removed under reduced pressure and 10 mL of diethyl ether was added to the residue. The precipitated quaternary ammonium salt was filtered off and washed generously with diethyl ether. The combined filtrates were concentrated and the residue was again heated to reflux with 5 mL of nitromethane for 5 days. Repeating the isolation process and drying the combined batches yielded the product as a white to pale pink, crystalline powder which was used without further purification in the next reaction step. To obtain an even higher purity, the product can be purified by vapour diffusion crystallization from chloroform with diethyl ether.

Yield: 488 mg (1.06 mmol, 35%, white to pale pink, crystalline powder)

Molecular weight: $C_{25}H_{35}NO_3S_2$, 461.68 g/mol

^{1}H-NMR: (700 MHz, Chloroform-*d*, 298 K) δ [ppm] = 8.16 (d, $^3J_{H\text{-}4,H\text{-}5}$ = 8.1 Hz, 1H, H-4), 7.82 (d, $^3J_{H\text{-}6,H\text{-}7}$ = 8.6 Hz, 1H, H-7), 7.74 (dd, $^3J_{H\text{-}6,H\text{-}7}$ = $^3J_{H\text{-}5,H\text{-}6}$ = 7.8 Hz, 1H, H-6), 7.65 (dd, $^3J_{H\text{-}4,H\text{-}5}$ = $^3J_{H\text{-}5,H\text{-}6}$ = 7.6 Hz, 1H, H-5), 7.57 (d,$^3J_{H\text{-}20,H\text{-}21}$ = 8.1 Hz, 2H, H-20), 6.99 (d,$^3J_{H\text{-}20,H\text{-}21}$ = 7.8 Hz, 2H, H-21), 4.86 - 4.68 (m, 2H, H-9), 3.30 (s, 3H, H-1), 2.26 (s, 3H, H-23), 1.85 - 1.74 (m, 1H, H-10a), 1.68 - 1.56 (m, 2H, H-10b, H-11), 1.54 - 1.46 (m, 1H, H-15), 1.38 - 1.26 (m, 2H, H-12a, H-13a), 1.25 - 1.17 (m, 2H, H-12b, H-13b), 1.17 - 1.08 (m, 2H, H-14), 1.02 (d, $^3J_{H\text{-}11,H\text{-}18}$ = 6.4 Hz, 3H, H-18), 0.85 (d, $^3J_{H\text{-}15,H\text{-}16/17}$ = 6.7 Hz, 6H, H-16, H-17)

^{13}C-NMR: (176 MHz, Chloroform-*d*, 298 K) δ [ppm] = 176.1 (C-2), 143.9 (C-19), 141.0 (C-8), 139.0 (C-22), 129.7 (C-6), 129.5 (C-3), 128.5 (C-5, C-21), 126.0 (C-20), 124.5 (C-4), 116.3 (C-7), 49.1 (C-9), 39.2 (C-14), 37.0 (C-12/13), 35.7 (C-10), 31.1 (C-11), 28.1 (C-15), 24.7 (C-12/13), 22.8 (C-16/17), 22.7 (C-16/17), 21.4 (C-23), 19.5 (C-18), 17.9 (C-1)

NMR spectra can be found in the SI in Figure S19.

(ESI(+), Dichloromethane, M = $C_{18}H_{28}NS^+$ = cation) *m/z* (Int.) = 290.194 $[M]^{\cdot+}$

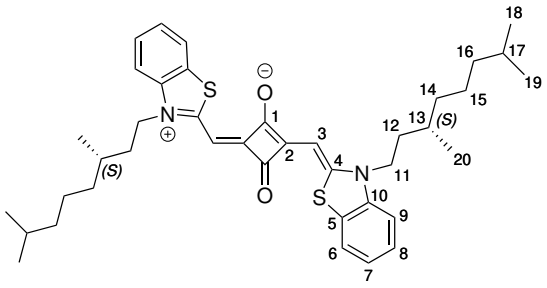
(ESI(-), Dichloromethane, M = $C_7H_7O_3S^-$ = anion) *m/z* (Int.) = 170.9 $[M]^{\cdot-}$

ESI HRMS: $[M]^{\cdot+}$ = $C_{18}H_{28}NS^{+\cdot+}$, calculated: *m/z* = 290.1937, found: *m/z* = 290.1938

Elemental analysis: $C_{25}H_{35}NO_3S_2$ calculated C: 65.04, H: 7.64, N: 3.03, S: 13.89; found C: 65.20, H: 7.73, N: 2.98, S: 13.85

Mass spectra spectra can be found in the SI in Figures S24 and S25.

(*S,S*)-bCi-BtSQ



In a 25 mL single-neck flask, equipped with a Dean-Stark apparatus and reflux condenser, (*S*)-3-(3,7-dimethyloctyl)-2-methylbenzothiazol-3-ium tosylate **16** (457 mg, 0.99 mmol, 1.00 eq.) and squaric acid (56 mg, 0.49 mmol, 0.50 eq.) were suspended in a mixture of toluene/1-butanol 1:1 (v/v, 10 mL/mmol) together with 2 mL of pyridine. The reaction mixture was degassed by evacuation and repressurizing with argon under stirring for 3 cycles and afterwards heated to reflux for 58 hours under argon. Upon boiling, the reactants dissolved and the reaction mixture turned deep green within minutes, which changed to a deep blue over the duration of 24 hours. All volatile compounds were removed under reduced pressure and the crude product was purified by column chromatography on silica gel eluting with dichloromethane/methanol (0 - 3.5%). The obtained deep-blue solid was further purified by recrystallization from chloroform/cyclohexane 1:4 (v/v), filtered off and washed several times with cooled *n*-hexane. The product was obtained after drying for 5 days under reduced pressure as dark-red to green shiny crystals. The crystals obtained contained 0.70 eq. of cyclohexane (C_6H_{12}) in the crystal lattice, which was confirmed via ^{1}H-, ^{13}C-NMR as well as elemental analysis and the single crystal structure.

Please note: The compound undergoes light-induced decomposition in solution, see Figure S5), but it is stable in the solid state.

Yield: 181 mg (0.28 mmol, 56%, dark-red to green shiny crystals)

Molecular weight: $C_{40}H_{52}N_2O_2S_2$, 656.99 g/mol

^{1}H-NMR: (400 MHz, Dichloromethane-d_2, 298 K) δ [ppm] = 7.59 (dd, $^3J_{H\text{-}6,H\text{-}7}$ = 7.9 Hz, $^4J_{H\text{-}6,H\text{-}8}$ = 0.8 Hz, 2H, H-6), 7.39 (ddd, $^3J_{H\text{-}7,H\text{-}8}$ = $^3J_{H\text{-}8,H\text{-}9}$ = 7.9 Hz, $^4J_{H\text{-}6,H\text{-}8}$ = 1.2 Hz, 2H, H-8), 7.21 (ddd, $^3J_{H\text{-}6,H\text{-}7}$ = $^3J_{H\text{-}7,H\text{-}8}$ = 7.4 Hz, $^4J_{H\text{-}7,H\text{-}9}$ = 1.0 Hz 2H, H-7), 7.14 (d, $^3J_{H\text{-}8,H\text{-}9}$ = 8.0 Hz, 2H, H-9), 5.80 (s, 2H, H-3), 4.18 - 4.00 (m, 4H, H-11), 1.89 - 1.73 (m, 2H, H-12a), 1.70 - 1.58 (m, 4H, H-12b, H-13), 1.58 - 1.47 (m, 2H, H-17), 1.42 - 1.32 (m, 4H, H-14a, H-15a), 1.32 - 1.14 (m, 8H, H-14b, H-15b, H-16), 1.06 (d, $^3J_{H\text{-}13,H\text{-}20}$ = 6.3 Hz, 6H, H-20), 0.88 (d, $^3J_{H\text{-}17,H\text{-}18}$ = $^3J_{H\text{-}17,H\text{-}19}$ = 6.4 Hz, 12H, H-18/19)

^{1}H-NMR: (700 MHz, Chloroform-*d*, 298 K) δ [ppm] = 7.43 (d, $^3J_{H\text{-}6,H\text{-}7}$ = 7.6 Hz, 2H, H-6), 7.27 (dd, $^3J_{H\text{-}7,H\text{-}8}$ = $^3J_{H\text{-}8,H\text{-}9}$ = 7.8 Hz, 2H, H-8), 7.10 (dd, $^3J_{H\text{-}6,H\text{-}7}$ = $^3J_{H\text{-}7,H\text{-}8}$ = 7.4 Hz, 2H, H-7), 7.00 (d,

$^{3}J_{\text{H-8,H-9}}$ = 7.6 Hz, 2H, H-9), 5.79 (s, 2H, H-3), 4.17 - 3.77 (m, 4H, H-11), 1.73 - 1.66 (m, 2H, H-12a), 1.58 - 1.47 (m, 4H, H-12b, H-13), 1.47 - 1.39 (m, 2H, H-17), 1.30 - 1.21 (m, 4H, H-14a, H-15a), 1.20 - 1.15 (m, 2H, H-15b), 1.15 - 1.10 (m, 2H, H-14b), 1.10 - 1.03 (m, 4H, H-16), 0.95 (d, $^{3}J_{\text{H-13,H-20}}$ = 6.3 Hz, 6H, H-20), 0.78 (d, $^{3}J_{\text{H-17,H-18/19}}$ = 6.6 Hz, 6H, H-18/19), 0.78 (d, $^{3}J_{\text{H-17,H-18/19}}$ = 6.6 Hz, 6H, H-18/19)

^{13}C-NMR: (176 MHz, Chloroform-*d*, 298 K) *δ* [ppm] = 159.5, 141.1 (C-10), 128.9 (C-5), 127.2 (C-8), 124.1 (C-7), 122.3 (C-6), 111.3 (C-9), 85.4 (C-3), 44.9 (C-11), 39.3 (C-16), 37.2 (C-14), 34.3 (C-12), 31.2 (C-13), 28.1 (C-17), 24.7 (C-15), 22.8 (C-18/19), 22.8 (C-18/19), 19.6 (C-20)

NMR spectra can be found in the SI in Figures S20 and S21.

(ESI(+), Dichloromethane, M = $C_{40}H_{52}N_2O_2S_2$) *m/z* (Int.) = 656.345 $[M]^{\cdot+}$, 276.178 $[C_{17}H_{26}NS]^{\cdot+}$

ESI HRMS: $[M]^{\cdot+}$ = $C_{40}H_{52}N_2O_2S_2{}^{\cdot+}$, calculated: m/z = 656.3465, found: m/z = 656.3458

Mass spectra can be found in the SI in Figure S26.

Elemental analysis: $C_{40}H_{52}N_2O_2S_2 \cdot 0.70\ C_6H_{12}$ calculated C: 74.16, H: 8.50, N: 3.91, S: 8.96; found C: 74.00, H: 8.55, N: 3.77, S: 9.05

3.2. X-ray Single Crystal Structure

Clear blue rhombohedral single crystals of **(*S*,*S*)-bCi-BtSQ** were obtained through crystallization from a dichloromethane and cyclohexane (1:2, (v/(v) mixture applying a temperature gradient by slow cooling from reflux temperature to -18 °C. The single crystal structure was determined using a Bruker D8 Venture diffractometer at 100 K with Cu-Kα radiation (λ = 1.54178 Å). The incorporated solvent molecules (cyclohexane) were removed for clarity in the crystal structure.

Characteristics: clear blue rhombohedral, size 0.16 × 0.14 × 0.09 mm^3, $C_{40}H_{52}N_2O_2S_2 + C_6H_{12}$, M = 741.11 amu, monoclinic, space group $C2$, a = 25.731(2) Å, b = 10.0986(8) Å, c = 17.6254(13) Å, $\alpha = \gamma = 90°$, β = 111.379(4)°, V = 4264.8(6) Å^3, Z = 4, density 1.154 g/cm^3, absorption coefficient 1.414 mm^{-1}, F(000) = 1608.0, 50635 reflections recorded (7596 independent, R_{int} = 0.0563, R_{sigma} = 0.0377), completeness to theta 99.3%, final R indices (I > 2σ(I)), R1 = 0.0896, wR2 = 0.2414, final R indices (all data) R1 = 0.0954, wR2 = 0.2484, GooF = 1.107, maximum and minimum residual electron density 0.63 e·Å^{-3} and -0.47 e·Å^{-3}, Flack parameter = 0.29(5).

Incorporated solvent: cyclohexane. The single crystal structure data were visualized and analyzed using Mercury 2022.3.0 (build 364735). The crystallographic data file can be found at the Cambridge Crystallographic Data Centre under the CCDC code 2494927.

3.3. Thin Film Preparation

Solutions of **(*S*,*S*)-bCi-BtSQ** were prepared in chloroform (HPLC grade, amylene stabilized, *VWR*), dichloromethane (HPLC grade, *Sigma Aldrich*) and cyclohexane/dichloromethane mixtures (1:1, v:v, HPLC grade, *Sigma Aldrich*) at a concentration of 5 mg/mL and stirred under light protection for 24 hours before use. Glass substrates were cut from 1 mm thick float glass objective slides (*VWR*) in 15 × 15 cm or 25 × 25 cm. Thin films were prepared by spin coating 65 µL or 120 µL of the solution for 60 s at different rotation speeds and acceleration 2000 rpm, 400 rpm/s (thick); 3000 rpm, 1000 rpm/s (medium); 4000 rpm, 4000 rpm/s (thin)) onto the glass substrates. The "air" side of the float glass was preselected for coating.[49] Samples were thermally annealed on a preheated hotplate for 30 min at various temperatures (exact temperatures are specified in the main text). Individual sample were fabricated for each annealing temperature. All preparation steps were carried out under ambient conditions.

3.4. Optical Microscopy

A Nikon Eclipse LV100ND equipped with a halogen lamp, XY objectives and a digital camera (XXX) was used to visualize the samples, which were imaged in brightfield reflected light (epi-illumination) between crossed polarizers. Images were captured using the provided NIS-Elements software,

3.5. Optical Characterization

A J.A. Woollam M2000-DI single rotating compensator ellipsometer (PCSA) with a horizontal sample stage and CompleteEASE version 5 software was used for optical data acquisition. The spectral range from 193 nm to 1690 nm is recorded using two CCD detector arrays, which simultaneously offer 705 wavelengths with a bandwidth of 5 nm in the UV/Vis range and 10 nm in the NIR spectral range.

Intensity spectra were recorded in normal incidence transmission mode and are shown as absorbance or optical density, i.e. $-\log$(transmission). The diameter of the light beam is approximately 2 mm, so that possible micro-texture of the thin films is averaged. Transmission in thin films consists of absorption, reflection, and, in the case of textured/rough films, scattering, and includes contributions from absorption and reflection of the glass substrate. Note that absorbance and absorption refer to different quantities.

Variable angle spectroscopic ellipsometry (VASE) in reflection in combination with transmission intensity spectra was used to determine the uniaxial complex refractive indices, while partial Mueller matrix polarimetry in transmission enabled to determine the circular dichroism.

Complex Refractive Index by Variable Angle Spectroscopic Ellipsometry

Using conventional variable angle spectroscopic ellipsometry (VASE) in reflection, Ψ and Δ thin film spectra were measured at different angles of incidence (AOIs) from 45°to 70°in steps of 5°. A multi-sample analysis (MSA) plus transmission intensity strategy, as described in detail previously,[49] was employed to obtain the uniaxial complex refractive indices of **(*S*,*S*)-bCi-BtSQ** samples spincasted from various solvents and subjected to different annealing temperatures. This MSA combines Ψ-Δ-scans of multiple samples prepared in the same way (same solvent and annealing conditions) but with different spincoating conditions, i.e. different layer thicknesses. Adding the transmission intensity to the fitting procedure allows for improved determination of the out-of-plane component of the uniaxial refractive index. Such an anisotropic complex refractive index consist of an ordinary (in-plane) and an extraordinary (out-of-plane) part, within the plane of the thin film, and perpendicular to it, respectively. A B-spline regression, as provided by CompleteEASE version 6, was implemented to accurately model

the ellipsometric data without enforcing a specific physical interpretation through an oscillator model. The optimization criteria of the fitting routine were a "visual best match" of the measured and modeled data, especially the transmission intensity data, and the minimization of the mean square error (MSE). The complex refractive index of the glass substrate was determined beforehand, and care was taken to deposit the **(*S*,*S*)-bCi-BtSQ** layers on the "air" side of the float glass. [49]

Circular Dichroism by Mueller Matrix Polarimetry

The normalized partial Mueller matrix ($m_{11} = 1$, last row missing) was recorded in normal incidence transmission with a custom-made sample holder. The complete Mueller matrix **M** can be reconstructed for non-depolarizing samples using an algebraic method. [56] The physical interpretation of the differential Mueller matrix **L** can be seen in the following equation:

$$\mathbf{L} = \ln(\mathbf{M}) = \begin{pmatrix} 0 & -\mathrm{LD} & -\mathrm{LD}' & \mathrm{CD} \\ -\mathrm{LD} & 0 & \mathrm{CB} & \mathrm{LB}' \\ -\mathrm{LD}' & -\mathrm{CB} & 0 & -\mathrm{LB} \\ \mathrm{CD} & -\mathrm{LB}' & \mathrm{LB} & 0 \end{pmatrix} \quad (1)$$

with CD = circular dichroism, CB = circular birefringence, LD = horizontal linear dichroism, LD' = 45°linear dichroism, LB = horizontal linear birefringence and LB' = 45°linear birefringence.

Selected differential Mueller matrices of **(*S*,*S*)-bCi-BtSQ** thin films for different solvents and annealing temperatures are shown in the SI in Figures S8, S9, S10, S11, S12, S13, S14, S15, S16.

To obtain the circular dichroism (CD) values, the matrix elements l_{14} and l_{41} are averaged and converted from radians to millidegrees (mdeg). For better comparability, all CD spectra shown are normalized to the thin film thicknesses obtained from the ellipsometric analyses.

Note that CD is not identical to the ellipticity θ as the typical output of a conventional CD spectrometer:

$$\theta = \arctan\left(\frac{e^{\mathrm{CD}} - 1}{e^{\mathrm{CD}} + 1}\right) \quad (2)$$

Only for small CD values the following approximation applies: $\theta = \mathrm{CD}/2$. An obvious advantage of the Mueller matrix polarimetry approach for circular dichroism studies is that the CD value provided is free of linear dichroism contributions. This makes this approach particularly suitable for the analysis of thin film samples. No workarounds such as sample rotation or flipping are necessary, as is the case with a conventional CD spectrometer. [57,58] Nevertheless, it is reasonable to average the CD value across measurements at different sample spots to compensate for possible layer thickness inhomogeneities.

Supporting Information

- XRD powder pattern and XRD measurements of spincoated thin films of **(*S*,*S*)-bCi-BtSQ** in Figure S1.
- Calculated polarizations directions of Davydov bands in Figure S2.
- Absorbance spectra of **(*S*,*S*)-bCi-BtSQ** in selected solvent in Figure S3.
- Extinction coefficient of **(*S*,*S*)-bCi-BtSQ** in dichloromethane: Tables S1 and S2, and Figure S4.
- Light-induced decomposition of **(*S*,*S*)-bCi-BtSQ** in chloroform solution in Figure S5.
- Additional as-cast thin film absorbance spectra of **(*S*,*S*)-bCi-BtSQ** processed from $CHCl_3$, DCM and CyHex in Figure S6.
- Additional absorbance and CD spectrum of an as-cast **(*S*,*S*)-bCi-BtSQ** sample processed from DCM in Figure S7.
- Differential Mueller Matrices of **(*S*,*S*)-bCi-BtSQ** thin films spincoated from chloroform solutions without annealing, and annealing at 90°C and 135°C, respectively, in Figures S8, S9, S10.
- Differential Mueller Matrices of **(*S*,*S*)-bCi-BtSQ** thin films spincoated from dichloromethane solutions without annealing, and annealing at 90°C and 135°C, respectively, in Figures S11, S12, S13.
- Differential Mueller Matrices of **(*S*,*S*)-bCi-BtSQ** thin films spincoated from dichloromethane solutions without annealing, and annealing at 90°C and 135°C, respectively, in Figures S14, S15, S16.
- NMR and mass spectra of (3*S*)-Dihydrocitronellol in Figures S17 and S23.
- NMR spectra of 3*S*)-3,7-Dimethyloctyl-p-toluolsulfonate in Figure S18.
- NMR and mass spectra of **(*S*)-Ci-Bt** in Figures S19 and S24, S25.
- NMR and mass spectra of **(*S*,*S*)-bCi-BtSQ** in Figures S20, S21 and S26.

Acknowledgements

MFS and AL acknowledge the financial support from DFG GRK 2591 "Template-designed Organic Electronics – TIDE". MS thanks the Linz Institute of Technology (LIT-2019-7-INC-313 SEAMBIOF and LIT-2023-12-SEE-114 SLIME) for funding. MFS thanks the Manchot Foundation for a doctoral scholarship. Special thanks to Dr. M. Cobet for performing XRD-measurements on thin films. We also thank Prof. K. Hingerl (head of ZONA) for providing access to analytical laboratory facilities.

Conflict of Interest

The authors declare no conflict of interest.

Keywords: X-Ray Diffraction • Uniaxial Anisotropy • Davydov Splitting • Spectroscopic Ellipsometry • Excitonic Circular Dichroism

References

[1] S. Sreejith, P. Carol, P. Chithra, A. Ajayaghosh, *Journal of Materials Chemistry* **2008**, *18*, 264.
[2] L. Beverina, M. Sassi, *Synlett* **2014**, *25*, 477.
[3] G. Xia, H. Wang, *Journal of Photochemistry and Photobiology C: Photochemistry Reviews* **2017**, *31*, 84.

[4] K. Ilina, W. M. MacCuaig, M. Laramie, J. N. Jeouty, L. R. McNally, M. Henary, *Bioconjugate Chemistry* **2020**, *31*, 194.

[5] Y. Chen, W. Zhu, J. Wu, Y. Huang, A. Facchetti, T. J. Marks, *Organic Photonics and Photovoltaics* **2019**, *6*, 1.

[6] J. He, Y. J. Jo, X. Sun, W. Qiao, J. Ok, T. Kim, Z. Li, *Adv. Funct. Mater.* **2020**, *31*, 2008201.

[7] A. Mei, X. He, D. Lei, L. Wang, W. Wang, J. Shao, Q. Shen, F. Jiang, X. Dong, *Coordination Chemistry Reviews* **2025**, *527*, 216419.

[8] M. Pawlicki, H. A. Collins, R. G. Denning, H. L. Anderson, *Angewandte Chemie International Edition* **2009**, *48*, 3244.

[9] E. Michail, M. H. Schreck, M. Holzapfel, C. Lambert, *Phys. Chem. Chem. Phys.* **2020**, *22*, 18340.

[10] G. V. Klishevch, V. O. Hryn, A. O. Kostetskyi, I. B. Kuziv, Y. P. Piryatinski, N. V. Bashmakova, A. M. Dmytruk, V. M. Kadan, I. V. Blonskyi, M. V. Bondar, *J. Lumin.* **2025**, *280*, 121119.

[11] O. S. Abdullaeva, F. Balzer, M. Schulz, J. Parisi, A. Lützen, K. Dedek, M. Schiek, *Advanced Functional Materials* **2019**, *29*, 1805177.

[12] J. H. Kim, A. Liess, M. Stolte, A. Krause, V. Stepanenko, C. Zhong, D. Bialas, F. Spano, F. Würthner, *Adv. Mater.* **2021**, *33*, 2100582.

[13] J. Csucker, E. Didier, J. Pedro Ferreira Assunção, D. Rentsch, R. Kothandaraman, D. Bachmann, I. Shorubalko, F. Nüesch, R. Hany, M. Bauer, *Adv. Sci.* **2025**, *12*, 2502320.

[14] M. Schulz, F. Balzer, D. Scheunemann, O. Arteaga, A. Lützen, S. C. Meskers, M. Schiek, *Advanced Functional Materials* **2019**, *29*, 1900684.

[15] J. Zablocki, M. Schulz, G. Schnakenburg, L. Beverina, P. Warzanowski, A. Revelli, M. Grüninger, F. Balzer, K. Meerholz, A. Lützen, M. Schiek, *The Journal of Physical Chemistry C* **2020**, *124*, 22721.

[16] F. Balzer, H. Kollmann, M. Schulz, G. Schnakenburg, A. Lu, M. Schmidtmann, C. Lienau, M. Silies, M. Schiek, A. Lützen, M. Schmidtmann, C. Lienau, M. Silies, M. Schiek, *Crystal Growth Design* **2017**, *17*, 6455.

[17] F. Balzer, M. F. Schumacher, S. Mattiello, M. Schulz, J. Zablocki, M. Schmidtmann, K. Meerholz, N. S. Sariciftci, L. Beverina, A. Lützen, M. Schiek, *Israel Journal of Chemistry* **2022**, *62*.

[18] F. Balzer, N. J. Hestand, J. Zablocki, G. Schnakenburg, A. Lützen, M. Schiek, *J. Phys. Chem. C* **2022**, *126*, 13802.

[19] S. Brück, C. Krause, R. Turrisi, L. Beverina, S. Wilken, W. Saak, A. Lützen, H. Borchert, M. Schiek, J. Parisi, *Physical Chemistry Chemical Physics* **2014**, *16*, 1067.

[20] N. J. Hestand, F. C. Spano, *Chem. Rev.* **2018**, *118*, 7069.

[21] F. Balzer, T. Breuer, G. Witte, M. Schiek, *Langmuir* **2022**, *38*, 9266.

[22] D. Giavazzi, R. Schwarzl, M. Koch, M. Schiek, A. Painelli, F. C. Spano, *J. Phys. Chem. Lett.* **2025**, *accepted*, NN.

[23] C. Zheng, D. Bleier, I. Jalan, S. Pristash, A. R. Penmetcha, N. J. Hestand, F. C. Spano, M. S. Pierce, J. A. Cody, C. J. Collison, *Sol. Energy Mater. Sol.* **2016**, *157*, 366.

[24] T. J. Wiegand, J. S. Sandoval, J. A. Cody, D. W. McCamant, C. J. Collison, *J. Phys. Chem. C* **2024**, *128*, 4616.

[25] J. R. Brandt, F. Salerno, M. J. Fuchter, *Nature Reviews Chemistry* **2017**, *1*, 0045.

[26] J. S. S. K. Formen, J. R. Howard, E. V. Anslyn, C. Wolf, *Angew. Chem. Int. Ed.* **2024**, *63*, e202400767.

[27] D. Giavazzi, M. F. Schumacher, L. Grisanti, M. Anzola, F. D. Maiolo, J. Zablocki, A. Lützen, M. Schiek, A. Painelli, *Journal of Materials Chemistry C* **2023**, *11*, 8307.

[28] M. Schulz, J. Zablocki, O. S. Abdullaeva, S. Brück, F. Balzer, A. Lützen, O. Arteaga, M. Schiek, *Nature Communications* **2018**, *9*, 2413.

[29] R. Bernhardt, L. Rieland, T. Wang, M. F. Schumacher, A. Lützen, M. Schiek, P. H. M. van Loosdrecht, *Aggregate* **2024**, *6*, e698.

[30] A. L. Tatarets, I. A. Fedyunyaeva, E. Terpetschnig, L. D. Patsenker, *Dyes and Pigments* **2005**, *64*, 125.

[31] Y. Sang Kim, H. Kyu Lee, W. Jin Choi, S. Kim, J. Ho Yoon, W. Kim, J. Pil Kim, *ChemPhotoChem* **2025**, *9*, e202400360.

[32] M. I. S. Röhr, H. Marciniak, J. Hoche, M. H. Schreck, H. Ceymann, R. Mitric, C. Lambert, *J. Phys. Chem. C* **2018**, *122*, 8082.

[33] C. Zhong, D. Bialas, C. J. Collison, F. C. Spano, *J. Phys. Chem. C* **2019**, *123*, 18734.

[34] A. Turkin, M. Holzapfel, M. Agarwal, D. Fischermeier, R. Mitric, R. Schweins, F. Gröhn, C. Lambert, *Chemistry – A European Journal* **2021**, *27*, 8380.

[35] J. Selby, M. Holzapfel, B. K. Lombe, D. Schmidt, A.-M. Krause, F. Würthner, G. Bringmann, C. Lambert, *The Journal of Organic Chemistry* **2020**, *85*, 12227.

[36] J. Selby, M. Holzapfel, K. Radacki, A. K. Swain, H. Braunschweig, C. Lambert, *Macromolecules* **2022**, *55*, 421.

[37] E. Freytag, L. Kreimendahl, M. Holzapfel, J. Petersen, H. Lackinger, M. Stolte, F. Würthner, R. Mitric, C. Lambert, *The Journal of Organic Chemistry* **2023**, *88*, 10777.

[38] K. Ueji, S. Ichimura, Y. Tamaki, K. Miyamura, *CrystEngComm* **2014**, *16*, 10139.

[39] V. V. Kurdyukov, A. I. Tolmachev, *Chemistry of Heterocyclic Compounds* **2009**, *45*, 1283.

[40] U. Mayerhöffer, K. Deing, K. Gruß, H. Braunschweig, K. Meerholz, F. Würthner, *Angewandte Chemie International Edition* **2009**, *48*, 8776.

[41] C.-A. Shen, F. Würthner, *Chemical Communications* **2020**, *56*, 9878.

[42] U. Mayerhöffer, M. Gsänger, M. Stolte, B. Fimmel, F. Würthner, *Chemistry - A European Journal* **2013**, *19*, 218.

[43] C. A. Shen, M. Stolte, J. H. Kim, A. Rausch, F. Würthner, *Journal of the American Chemical Society* **2021**, *143*, 11946.

[44] C. Shen, D. Bialas, M. Hecht, V. Stepanenko, K. Sugiyasu, F. Würthner, *Angew. Chem. Int. Ed.* **2021**, *60*, 11949.

[45] L. Böhner, P. Weitkamp, T. Limböck, N. Gildemeister, D. Fazzi, M. Schiek, R. Bruker, D. Hertel, R. Schäfer, K. Lindfors, K. Meerholz, *Organic Chemistry Frontiers* **2025**, *12*, 1086.

[46] A. M. Valencia, D. Bischof, S. Anhäuser, M. Zeplichal, A. Terfort, G. Witte, C. Cocchi, *Electron. Struct.* **2023**, *5*, 033003.

[47] C. V. Yelamaggad, U. S. Hiremath, S. A. Nagamani, D. S. S. Rao, S. K. Prasad, N. Iyi, T. Fujita, *Liquid Crystals* **2003**, *30*, 681.
[48] A. C. Pardal, S. S. Ramos, P. F. Santos, L. V. Reis, P. Almeida, *Molecules* **2002**, *7*, 320.
[49] A. Kamptner, M. C. Scharber, M. Schiek, *ChemPhysChem* **2024**, *25*, e202400233.
[50] O. Stenzel, *Thick Slabs and Thin Films*, pages 131–161, Springer International Publishing **2024**.
[51] O. Stenzel, *Planar Interfaces*, pages 93–129, Springer International Publishing **2024**.
[52] M. S. Vezie, S. Few, I. Meager, G. Pieridou, B. Dörling, R. S. Ashraf, A. R. Goñi, H. Bronstein, I. McCulloch, S. C. Hayes, M. Campoy-Quiles, J. Nelson, *Nat. Mater.* **2016**, *15*, 746.
[53] S. Funke, M. Duwe, F. Balzer, P. H. Thiesen, K. Hingerl, M. Schiek, *J. Phys. Chem. Lett.* **2021**, *12*, 3053.
[54] A. Austin, N. J. Hestand, I. G. McKendry, C. Zhong, X. Zhu, M. J. Zdilla, F. C. Spano, J. M. Szarko, *J. Phys. Chem. Lett.* **2017**, *8*, 1118.
[55] C. Cocchi, T. Breuer, G. Witte, C. Draxl, *Phys. Chem. Chem. Phys.* **2018**, *20*, 29724.
[56] O. Arteaga, R. Ossikovski, *Journal of the Optical Society of America A* **2019**, *36*, 416.
[57] G. Albano, M. Lissia, G. Pescitelli, L. A. Aronica, L. D. Bari, *Materials Chemistry Frontiers* **2017**, *1*, 2047.
[58] G. Albano, G. Pescitelli, L. D. Bari, *Chemical Reviews* **2020**, *120*, 10145.
[59] C. Zheng, M. F. Mark, T. Wiegand, S. A. Diaz, J. Cody, F. C. Spano, D. W. McCamant, C. J. Collison, *J. Phys. Chem. C* **2020**, *124*, 4032.
[60] C. Zheng, C. Zhong, C. J. Collison, F. C. Spano, *J. Phys. Chem. C* **2019**, *123*, 3203.
[61] F. C. Spano, *JACS* **2009**, *131*, 4267.
[62] K. A. Kistler, C. M. Pochas, H. Yamagata, S. Matsika, F. C. Spano, *J. Phys. Chem. B* **2011**, *116*, 77.
[63] Y. Xu, Y. Zhao, W. Liang, *J. Phys. Chem. C* **2024**, *128*, 20253.
[64] G. Pescitelli, *Chirality* **2021**, *34*, 333.
[65] H. von Berlepsch, S. Kirstein, C. Böttcher, *J. Phys. Chem. B* **2003**, *107*, 9646.
[66] Y. Nagata, T. Nishikawa, M. Suginome, *Chemical Communications* **2012**, *48*, 11193, solvent-dependent.
[67] V. F. Ximenes, N. H. Morgon, A. R. de Souza, *Chirality* **2018**, *30*, 1049.
[68] S. Hattori, S. Vandendriessche, T. Hirano, F. Sato, G. Koeckelberghs, T. Verbiest, K. Ishii, *J. Phys. Chem. B* **2019**, *123*, 2925.
[69] M. Sujith, E. Aiswarya, M. Mohankumar, M. Anzola, A. Painelli, C. Sissa, L. Grisanti, K. G. Thomas, *J. Phys. Chem. Lett.* **2025**, *16*, 7481.

Part B – Proline-Derived and Extended Chiral Squaraines

In contrast to the citronellyl substituents used to introduce chirality (see Part A – Citronellyl-Functionalized Chiral Squaraines), amino acids can also serve as sources of chirality. Among them, especially the amino acid proline – shown in Figure 5.1 – has been widely used due to its low cost, commercial availability and cyclic nature as well as the close proximity of the stereogenic center to the π-conjugated backbone. These advantages have led to the development of the class of proline-derived anilino squaraines (abbreviated as **ProSQs**).[2, 34, 100]

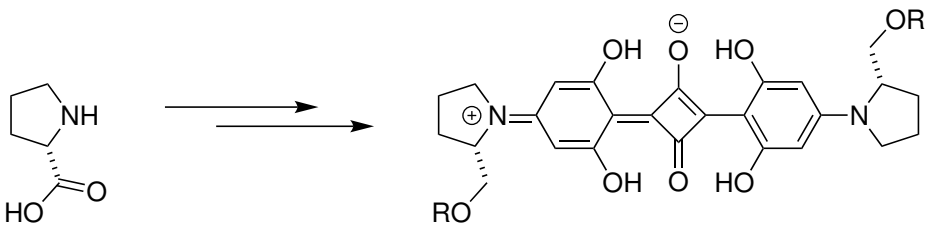


Figure 5.1: Chemical structure of proline and proline-derived anilino squaraines (**ProSQs**).

The first representative of this class of homochiral, symmetrical anilino squaraines – **ProSQ-C10** – was synthesized by *Stoll* et al. in 2006.[100] This was achieved via the condensation of an L-prolinol-based secondary amine with phloroglucinol (1,3,5-trihydroxybenzene) and a subsequent reaction with squaric acid. Remarkably, even this single compound revealed an unique aggregation behavior in solution and in self-assembled monolayers, highlighting the potential in optoelectronic applications.[100] In their search for a suitable materials that exhibiting strong optical activity combined with high performance in organic optoelectronic devices, our groups revisited the class of **ProSQs** nearly a decade later.[34, 38, 40, 98] In these investigations, the exceptional aggregation behavior of both longer- and shorter-chain proline-based anilino squaraine derivatives were explored, examining their self-assembly in solution and thin films. This renewed interest laid the groundwork for several projects in the *Lützen* group, including this thesis.

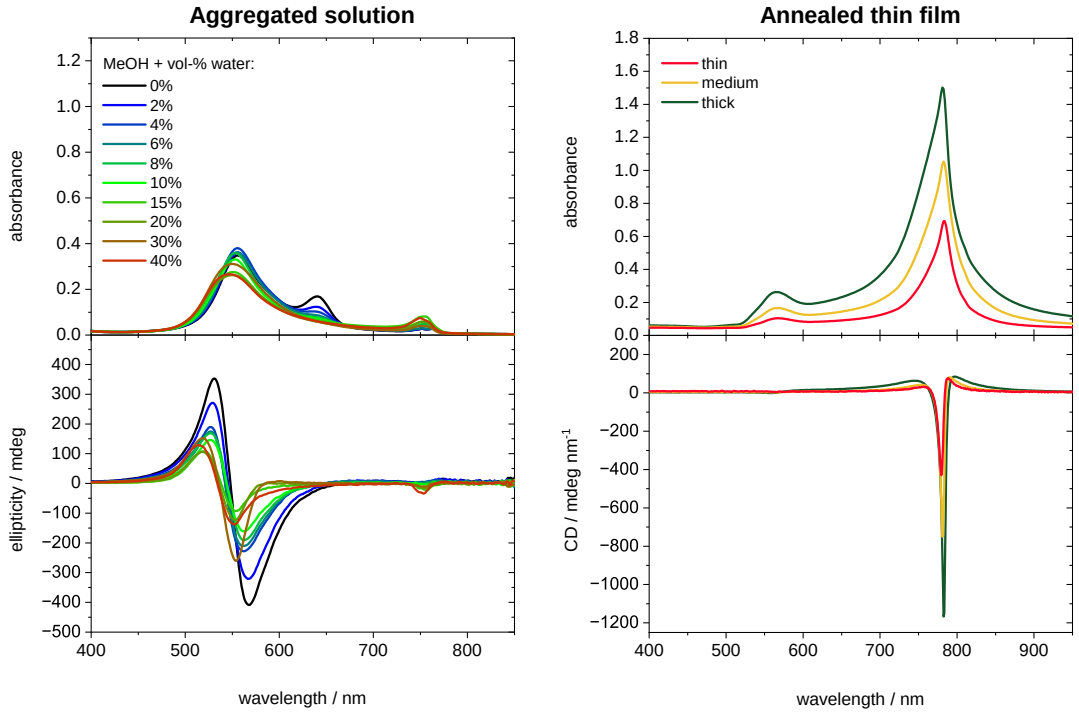


Figure 5.2: Exemplary UV/Vis absorbance and ellipticity/circular dichroism (CD) spectra highlighting the extraordinary aggregation behavior of proline-derived anilino squaraines (**ProSQs**) in both aggregated solution (left) and thermally annealed thin films (right), using **(*S*,*S*)-ProSQ-C12** as an example.

The exceptional aggregation behavior in both aggregated solution[a] and thermally annealed thin films is shown in Figure 5.2, using **(*S*,*S*)-ProSQ-C12** as a representative. Characterized by strong absorption combined with a remarkable high chiral aggregation tendency resulting in exceptionally high dissymmetry factors (g-value) and strong circular dichroism (CD).[34, 100] Despite their intriguing properties and even though this class of dyes has been already used successfully in optoelectronic devices,[98] the nature of the aggregates as well as the underlying mechanism of the strong chiroptical response, remains a mystery.

In the following four chapters, proline-derived and proline-extended chiral squaraines will be discussed. The first one – Chapter 6 – focuses on a **ProSQs** with intermediate chain lengths, which exhibit two bisignate CD signals in solution. The goal was to uncover whether these signals result from a single aggregate type or multiple species. The paper introduced the first model to explain the aggregation behavior of chiral squaraines in solution, providing valuable insights into their structure. These results have been published in the peer-reviewed *Journal of Materials Chemistry C* and is included as a summary in a way that picks up on aspects of the introduction (ref. Chapter 1), allowing the section to be read as a coherent overview. The publication itself is provided in Appendix D.

The second one – Chapter 7 – addresses the challenge of obtaining a single-crystal structure of

[a] Achieved by so-called *poor-solvent titration experiments*, in which water is gradually added to a solution of the squaraine dye in methanol to induce aggregation.

proline-derived anilino squaraines by further shortening the alkyl chain to the minimal case of a methyl group. This modification was intended to help crystallization while hoping of preserving the exceptional aggregation behavior.

After exploring aggregation in solution (Chapter 6), the third one – Chapter 8 – focused on the structure-to-property relationship of enantiopure and racemic **ProSQ** thin films, using steady-state and ultrafast transient absorption spectroscopy to investigate the nature and dynamics of excitons in aggregates. These results have been published in the peer-reviewed journal *Aggregate* and is included as a summary in a way that picks up on aspects of the introduction (ref. Chapter 1), allowing the section to be read as a coherent overview. The publication itself is provided in Appendix F.

The last one – Chapter 9 – builds upon the success of **ProSQs** by attempting to tune the absorption maxima and enhance π-π stacking interactions through targeted structural modification. In particular, this involves extending the π-conjugated system by replacing the proline- with an indoline-derived unit, thereby introducing greater planarity and electronic delocalization.

CHAPTER 6

A marvel of chiral squaraine aggregates: chiroptical spectra beyond the exciton model

D. Giavazzi,[‡a] M. F. Schumacher,[‡b] L. Grisanti,[c] M. Anzola,[a] F. Di Maiolo,[a] J. Zablocki,[b] A. Lützen,[b] M. Schiek,[d] A. Painelli[a]

Received: December 31, 2022
Published online: May 15, 2023

Reprinted with permission[e] from:
D. Giavazzi, M. F. Schumacher, L. Grisanti, M. Anzola, F. D. Maiolo, J. Zablocki, A. Lützen, M. Schiek, and A. Painelli, "A marvel of chiral squaraine aggregates: chiroptical spectra beyond the exciton model," *Journal of Materials Chemistry C* **2023**, *11* (24), 8307, doi: 10.1039/D2TC05555D
– Copyright ©Journal of Materials Chemistry C, The Royal Society of Chemistry 2023.

Own contributions:

- Synthesis and purification of the investigated molecules as well as performing analytical data (NMR, MS and EA)
- Performing and evaluating the experimental spectroscopic measurements (UV/Vis and CD)
- Interpretation of the results
- Writing of the manuscript

[‡] These authors contributed equally to this work.
[a] Department of Chemistry, Life Science and Environmental Sustainability, Parma University, Parco Area delle Scienze 17/A, 43124 Parma, Italy
[b] Kekulé-Institute for Organic Chemistry and Biochemistry, University of Bonn, Gerhard-Domagk-Str. 1, D-53121 Bonn, Germany
[c] Division of Theoretical Physics, Ruđer Bošković Institute, Bijenička cesta 54, 10000 Zagreb, Croatia
[d] Center for Surface- and Nano-Analytics (ZONA), Institute for Physical Chemistry (IPC) and Linz Institute for Organic Solar Cells (LIOS), Johannes Kepler University, Altenberger Str. 69, A-4040 Linz, Austria.
[e] Permission requests to reuse material from this chapter should be directed to The Royal Society of Chemistry

Chiral squaraines are a fascinating and well-studied class of organic chromophores with a zwitterionic Donor-Acceptor-Donor (D-A-D) structure.[6, 19, 22] A specific subgroup derived from the amino acid proline (**ProSQs**) stands out due to its extraordinary optoelectronic properties such as a remarkable high chiral aggregation tendency resulting in exceptionally high g-values and strong circular dichroism (CD), observed in both solution and thin films.[34, 40, 98, 100] Despite their intriguing properties, the nature of the aggregates remains a mystery. The first model to describe the aggregation behavior of non-chiral squaraines was performed by *Spano* and *Collison*.[14, 86–88] Their approach was to model the linear absorption spectrum of the aggregates by mixing Frenkel-like exciton states (Coulombic H-aggregate) and charge-separated states via intermolecular charge transfer (CT) interactions. This hypothesis was recently supported by a detailed study of spectroscopic measurements in non-chiral squaraine crystals.[142] An alternative approach to describing the spectroscopic changes during aggregation was recently reported, in which linear absorption and pump-probe spectroscopy were used to investigate structural disorder as the underlying cause within the framework of a disordered exciton model.[76] All these studies, however, just looked at non-chiral squaraines. Understanding the nature of the chiral aggregates and unraveling whether the aggregates are H-/J-type or something else is crucial for designing new squaraines and applying them as active compounds in optoelectronic devices.

To address this question, this study focuses on poor-solvent-titration experiments of proline-derived anilino squaraines (**ProSQs**) with intermediate chain lengths (C6 - C10) in solution. By stepwise increasing the water content in a methanol solution, a dispersed colloidal aggregated **ProSQ** solution was obtained. Thereby, the monomer absorbance band at 640 nm vanishes as signals from aggregates become more dominant. For **ProSQs** with alkyl chains up to *pentyl* (C5), a hypsochromic absorption band to around 550 nm is observed. At the same time, a strong bisignate CD signal corresponding to this shifted signal emerges. A similar pattern is observed for **ProSQs** with longer alkyl chains (beginning with dodecane, i.e., C12+), with the primary difference being the required water concentration for introducing aggregation. It is self-explanatory that water, being a poor solvent, increases aggregation tendency with longer alkyl-chains. In contrast to **ProSQs** aggregates with either short (C3 - C5) or long chain lengths (C11 - C16) – whose spectral features are consistent with conventional H-type aggregation theories – **ProSQs** with intermediate chain lengths (C6-C11) exhibit two spectral features in both, the UV/Vis absorbance and CD spectrum in aggregated solutions. These features consist of a hypsochromically shifted signal at approximately 550 nm and a more intense bathochromically shifted signal near 750 nm. Interestingly, both features exhibit a distinct bisignate CD signal with the same Cotton effect. These observations suggest an alternative mode of supramolecular organization.[83, 97, 105] The goal was to uncover whether these signals result from a single aggregate type or multiple species.

However, modeling these aggregates remains challenging due to the complex interplay of electrostatic (ES) forces and both intra- and intermolecular CT interactions. To explain the experimental findings, two essential state models (ESM) were developed. The first model being an essential state model accounting for just electrostatic intermolecular interactions (ESM-ES), describing each squaraine (SQ) in terms of three essential diabatic electronic states (one neutral and two degenerate charge-separated states). This results in a base set that has 3^N states per dye molecule in the aggregate, consequently currently limiting the practical computations to aggregates with size of $N \leq 9$. Simulations of aggregates with predefined geometries comprising up to eight SQ units using the ESM-ES, can reproduce the experimentally observed two spectral features in the UV/Vis absorption spectra, but only when two distinct aggregate types coexist. This means that both H- and J-type aggregates need to coexist in

solution to simulate the observed spectra. When looking at the CD spectra, however, the ESM-ES failed to reproduce the correct sign of the Cotton effect associated with the bisignate signal at longer wavelengths. Interestingly, the dimeric model alone provided a reasonably accurate description of the linear absorption properties. The second model was a charge-transfer-inclusive model (ESM-CT) extending the ESM-ES by adding explicit intermolecular CT couplings. Being even computational more demanding, the ESM-CT was limited to just tetrameters. However, this was the first time an explicit calculation of the CD-effect including intermolecular CT was performed. Remarkably, in this case, the two spectral features could be reproduced by a single aggregate geometry when modeled using the ESM-CT, matching experimental UV/Vis absorption and CD spectra without invoking multiple aggregate species. Even the signs of both Cotton effects of the two bisignate signals could be correctly reproduced. ESM-CT also delivered the first explicit expressions for CD rotational strengths in electronically delocalized aggregates.

Overall, these findings show that the classical exciton approach cannot accurately describe the complex aggregation behavior of squaraines in solution. While dimeric models may sufficiently explained the linear spectral characteristics of aggregates, they were insufficient for an accurate description of the chiroptical properties. In comparison to that, mixing Frenkel-like exciton states (Coulombic H-aggregate) and charge-separated states via intermolecular charge transfer (CT) interactions, accurately described the linear and CD spectral characteristics of aggregated solutions for **ProSQs** with intermediate alkyl-chain lengths. Molecular dynamics (MD) simulations, despite inherent size limitations, indicated that kinetic trapping can potentially invert aggregate helicity relative to the equilibrium structure. Both ESM-ES and ESM-CT models predicted a superlinear enhancement of circular dichroism (CD) intensity with increasing aggregate size, consistent with the exceptionally strong chiroptical responses observed in **ProSQ-C16** films.[34] Although a definitive structural assignment for squaraine aggregates in solution could not been done, this comprehensive investigation provided valuable insights into the chiral optical responses of molecular aggregates beyond the scope of the traditional exciton model.

CHAPTER 7

Proline-Derived Anilino Squaraines: Impact of Alkyl Chain Reduction to a Methyl Group

7.1 Concept and Synthesis

The exceptional chiroptical properties of **ProSQs** have been demonstrated repeatedly in the literature,[4, 34, 40, 98] as well as in Chapter 6 and (forthcoming) Chapter 8 of this thesis. Even though the applications and resulting properties are therefore well investigated, the exact molecular arrangement has so far only been theorised.[34, 40] In the previous chapter (Chapter 6), insight was gained into the aggregation behavior, resulting chiroptical properties, and special arrangements of proline-derived anilino squaraines (**ProSQs**) with intermediate alkyl-chain lengths in solution. There, a theoretical model was developed and applied. In the solid state, however, the most direct approach would be to obtain a single-crystal structure of the substance of interest and compare it with X-ray diffraction (XRD) measurements of the corresponding thin film. Moreover, an experimentally determined single-crystal structure enables or makes theoretical modelling of the chiroptical properties much easier, providing a deeper understanding of the underlying processes.

In the context of **ProSQs**, however, it was not possible to acquire a *real* single-crystal structure. These compounds are more difficult to crystallise than *n*-alkyl-anilino squaraines,[85] whereby long terminal alkyl groups generally hinder crystallisation. In her dissertation, *J. Zablocki* synthesised several **ProSQs** with varying alkyl-chain lengths with the smallest representative being a propyl-chain i.e. **(*S*,*S*)-ProSQ-C3**.[143] Although a single-crystal structure was obtained for this squaraine, the unit cell – containing eight **(*S*,*S*)-ProSQ-C3** molecules – also incorporated eight cyclohexane molecules (anti-solvent from the crystallisation method). This made the presented single crystal structure to a pseudo-polymorph, which can cause significant differences in molecular packing and calculated properties. The issue became more clear when the calculated powder XRD pattern of the single-crystal structure did not match the measured XRD patterns of pristine and annealed thin films. The interpretation was that inclusion of cyclohexane molecules in the single crystal increased the lattice-plane spacing along the crystallographic c-axis. In the absence of cyclohexane, a similar crystal structure with smaller spacings is likely adopted. However, the possibility of entirely different polymorphs cannot be excluded and appears more probable.

During this work, I attempted to address this issue by crystallising **(*S*,*S*)-ProSQ-C3** without cyclohexane,

testing several methods (e.g., layer- and vapour-diffusion, slow solvent evaporation, temperature gradients, etc.). Although crystals of reasonable size were obtained (see Appendix Figure E.3), several attempts to measure or resolve the crystal structure were unsuccessful. In some cases, the crystals did not provide sufficient diffraction signals; in others – especially when using synchrotron X-ray diffraction (SXRD) methods – the crystals decomposed due to their exceptionally high interaction with light, as quantified by the (effective) uniaxial complex refractive indices (see Appendix F.2, Supporting Information of [3]).

It was therefore decided to further shorten the alkyl chain length to the minimal case of a methyl group. This should favour the formation of single crystals without incorporated solvent. However, as the chiroptical properties are known to depend strongly on alkyl-chain length,[2, 40] it must first be shown that the thin film properties remain the same or at least sufficiently similar to allow conclusions to be drawn.

As it is shown in Figure 7.1, **(*S*,*S*)-ProSQ-C1** was synthesized after the literature known procedure, starting from enantiopure *N*-Boc-L-prolinol and methyl iodide.[2] Yields were in the range of the reported once.

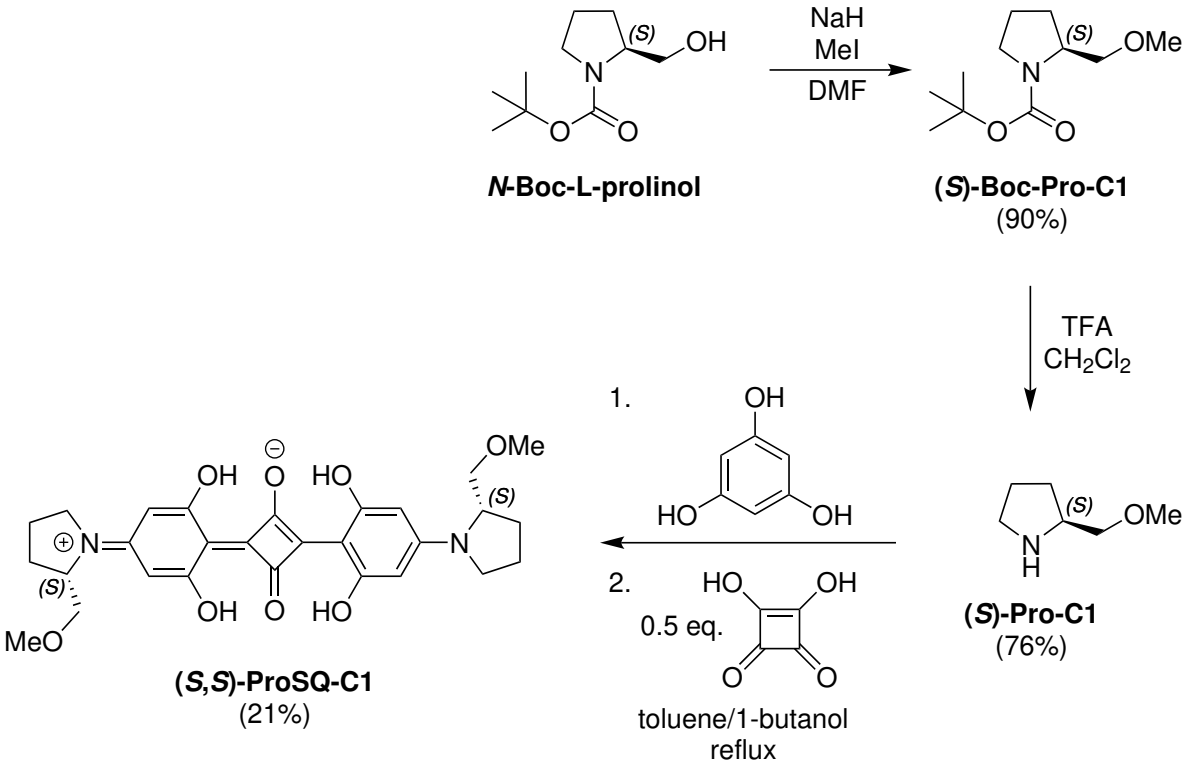


Figure 7.1: Synthesis of **(*S*,*S*)-ProSQ-C1** after [2], starting from enantiopure *N*-Boc-L-prolinol and methyl iodide.

As the investigations by *Schulz* and *Schiek* et al. show, the enantiomeric purity of the synthesized materials has a significant influence on the chiroptical properties and thin film aggregation.[34, 38] Therefore, here and in addition to Chapter 6, chiral high-performance liquid chromatography (HPLC) analysis was conducted.

HPLC analysis of the starting material:[a]

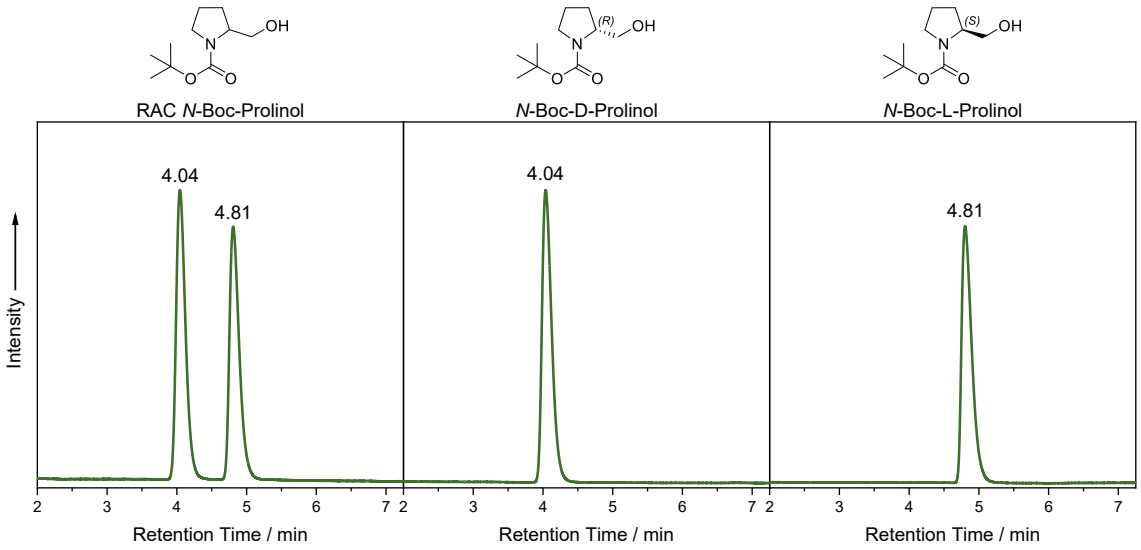


Figure 7.2: Analytical chromatograms of the chiral HPLC analysis of the starting material *N*-Boc-prolinol of the squaraine synthesis. (left) 1:1 mixture of *N*-Boc-D-prolinol and *N*-Boc-L-prolinol; (middle) pure *N*-Boc-D-prolinol (integral area 100%); (right) pure *N*-Boc-L-prolinol (integral area 100%). Parameters: stationary phase: DAICEL Chiralpak IA-U, 1.6 µm, 3.0 mm × 100 mm; mobile phase: *n*-hexane/2-propanol (98:2, v/v); flow rate: 0.85 mL/min; pressure: 288 bar; Detection: UV/Vis at 205 nm and Ri-detector: range: 50 Hz / 0,02 s – target-temp: 35 °C.

In order to determine the enantiopurity of the synthesized squaraine, chiral HPLC analysis was initially considered. However, the zwitterionic nature of the squaraine dye combined with its high extinction coefficient raised concerns regarding potential staining or damage to the stationary phase, direct analysis of the squaraine dye was avoided. As an alternative, the enantiomeric purity of the commercially available starting material, *N*-Boc-prolinol, was analysed. Figure 7.2 shows the chiral HPLC chromatograms for racemic *N*-Boc-prolinol (left), *N*-Boc-D-prolinol (middle), and *N*-Boc-L-prolinol (right), with intensity plotted as a function of retention time in minutes. The racemic mixture of *N*-Boc-prolinol was prepared by combining equimolar amounts of *N*-Boc-D-prolinol and *N*-Boc-L-prolinol, as confirmed by a chiral HPLC ratio of 52:48. Using *n*-hexane/2-propanol (98:2, v/v) mobile phase yielded two sharp, well-resolved peaks at retention times of 4.04 and 4.81 minutes, corresponding to the two enantiomers. The observed resolution was good enough to not further adjustment the mobile phase composition. Subsequent analysis of the individual *N*-Boc-D-prolinol and *N*-Boc-L-prolinol components confirmed the expected retention times of 4.04 and 4.81 minutes, respectively, with the integration areas of 100%, indicating high enantiomeric purity for each enantiomeric starting material. Since the synthetic route (shown in Figure 7.1) does not interact or affect the stereocenter, it is reasonable to assume that the enantiopurity of the squaraine directly depends on the enantiopurity of the starting material, thus proofing a high enantiomeric purity of the squaraine.

[a] Text is intended for publication in a peer-reviewed journal – no specific details available.

7.2 Optical Properties of Aggregated Solutions and Thermally Annealed Thin Films

Aggregated Solutions:

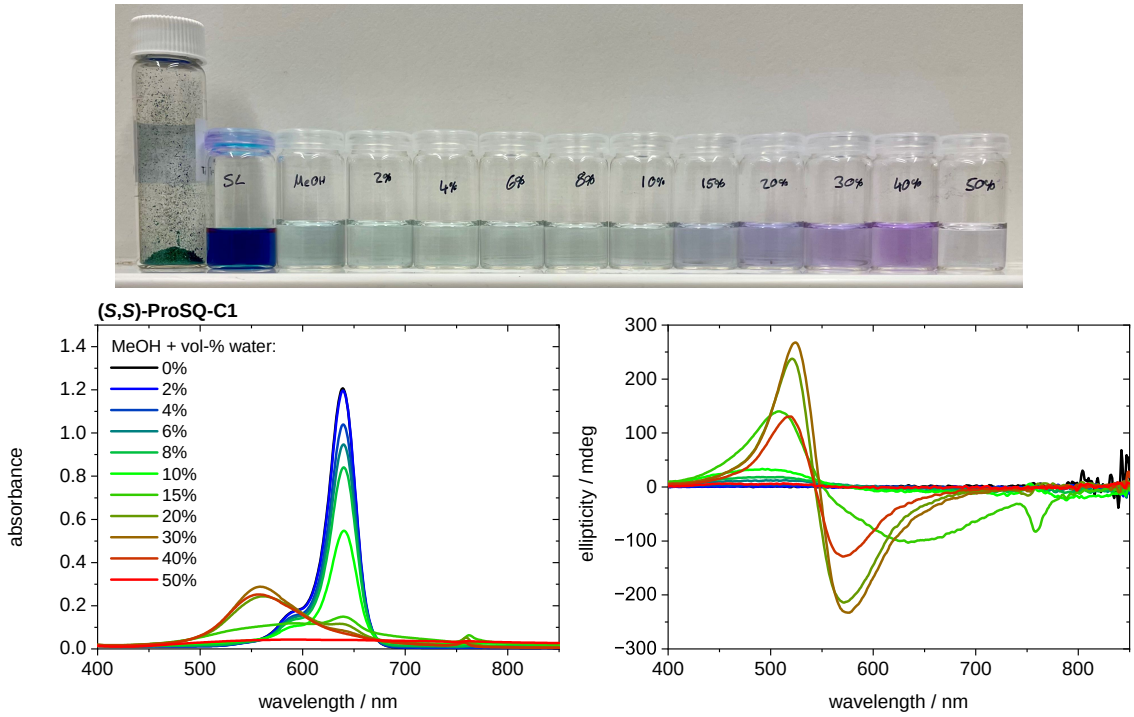


Figure 7.3: Early stage aggregation experiments in solution with UV/Vis absorbance (bottom left), corresponding ellipticity spectra (bottom right) and a picture of the visible changes in color (top) of **(*S*,*S*)-ProSQ-C1** (c = 3.85 µM). The legend indicates the volume-percentage of water in the methanol-water mixture and applies to all plots. The solutions were prepared from a chloroform stock solution (c = 2.31 × 10^{-4} M) and therefore contain an additional 1.7% chloroform (50 µL in 3 mL).

The early-stage aggregation experiments in solution revealed a nearly identical aggregation behaviour to that of **(*S*,*S*)-ProSQ-C3** (see Appendix D.2, Supporting Information of [2]). As shown in Figure 7.3,[b] at 0% water the characteristic sharp monomeric absorbance band of the electronic $S_0 \rightarrow S_1$ transition appears at 654 nm, together with a small hypsochromic shoulder at around 600 nm arising from the vibronic 0-1 progression.[134] Increasing the water content let initially to a reduced intensity of the monomeric band. At 15% water, a broad signal spanning 480–800 nm emerged, with the monomer band still visible alongside a small feature around 760 nm. At this stage, a visible colour change from blue to purple was also observed (Figure 7.3, top). In addition, the previously featureless ellipticity spectra displayed a broad signal over the same range. This signal appeared as a distorted bisignate CD signal with an overall negative Cotton effect, overlapping with a feature at around 760 nm. Based

[b] The UV/Vis absorbance spectra of **(*S*,*S*)-ProSQ-C1** in different solvents can be found in Figure E.1.

on this observation, the formation of two aggregate species can be proposed, yielding the measured spectral shape. This may indicate a time-dependent aggregation process – similar to that observed for **(*S*,*S*)-nCi-SQIB** in Chapter 4 – where he formation of the thermodynamically more favored species is not yet completed. In concentrations between 20 and 40% water content, an intense hypsochromically shifted absorbance band at around 550 nm appeared, with minimal residual monomer signal. The corresponding ellipticity spectra exhibited a well-resolved bisignate CD signal, peaking at 30 vol-% water, with an overall negative Cotton effect, similar to **(*S*,*S*)-ProSQ-C3**. Thereby, the negative Cotton effect for the hypsochromic band, with a zero-crossing near the absorbance maximum, indicates a H-type, left-handed helical arrangement corresponding to a negative excitonic chirality, as discussed in Section 1.3.2 - Interpretation of CD-Spectra. The sign reversal around the absorbance maximum is characteristic of exciton-coupled CD effects,[34, 94, 125, 136] while the absence of vibronic progression further indicates strong exciton coupling.[137] Compared with **(*S*,*S*)-ProSQ-C3**, **(*S*,*S*)-ProSQ-C1** appeared to be less affected by increased water content and polarity, as indicated by later observed aggregation and tolerance to higher water fractions. This behaviour is consistent with the expectation of the shorter, non-polar alkyl chains of **(*S*,*S*)-ProSQ-C1** compared to its C3 analogue, consistent with the observations in Chapter 6.[2] Also in this water content region, a high similarity with the UV/Vis absorbance and ellipticity spectra of **ProSQs** with long alkyl chains (e.g., C12 or C16 – shown in Appendix D, manuscript and Supporting Information of [2]) can be noted. This is evident by the same spectral shape and position as for **(*S*,*S*)-ProSQ-C3**. Nevertheless, complete precipitation was observed in the 50% methanol/water mixture, prohibit further spectroscopic investigations at this point.

Thermally Annealed Thin Films:

After showing the same characteristics in aggregated solutions as **(*S*,*S*)-ProSQ-C3**,[2] the aggregation behaviour in the solid state was investigated. Therefore, a series of solution-processed thin films were prepared via spin coating under same conditions, followed by thermal annealing at various temperatures for 30 minutes. Subsequent measurements of the absolute absorbance were carried out and Mueller matrix ellipsometry was used to accurately determine the circular dichroism (CD) of the samples.

As for **(*S*,*S*)-ProSQ-C3** and other **ProSQs**,[34, 40, 143] untempered films of **(*S*,*S*)-ProSQ-C1** (Figure 7.4, left side) are fully aggregated. The broad absorption band with a hypsochromically shifted maximum at 550 nm (henceforth referred to as the H-band) and a small bathochromically shifted feature around 755 nm remain unchanged up to 180 °C. The spectrum of the annealed thin film has a striking resemblance to that measured in aqueous methanol solutions containing 20–40% water (see Figure 7.3), both in the positions of the absorption maxima (H-band: 550 nm vs. 558 nm; J-band: ~755 nm vs. ~760 nm) and in the overall spectral shape. By contrast, thin films tempered at 230 °C display marked changes: the intensity of the H-band decreases significantly, while a broad J-band develops, peaking at around 760 nm. This transformation can be explained by a kinetically controlled transition from metastable H-type aggregates to a new, thermodynamically more stable molecular arrangement. In the corresponding CD spectra (Figure 7.4, right side), the response was, unfortunately, most often insignificant, with signals at the level of instrumental noise. Between 120 °C and 160 °C, at the wavelength region of the H-band maximum, a broad positive CD signal was observed, accompanied by two weaker negative peaks shifted to shorter and longer wavelengths. In early-stage aggregation experiments, by contrast, a nicely resolved bisignate CD signal is observed. Thereby, the strongest response was obtained at a

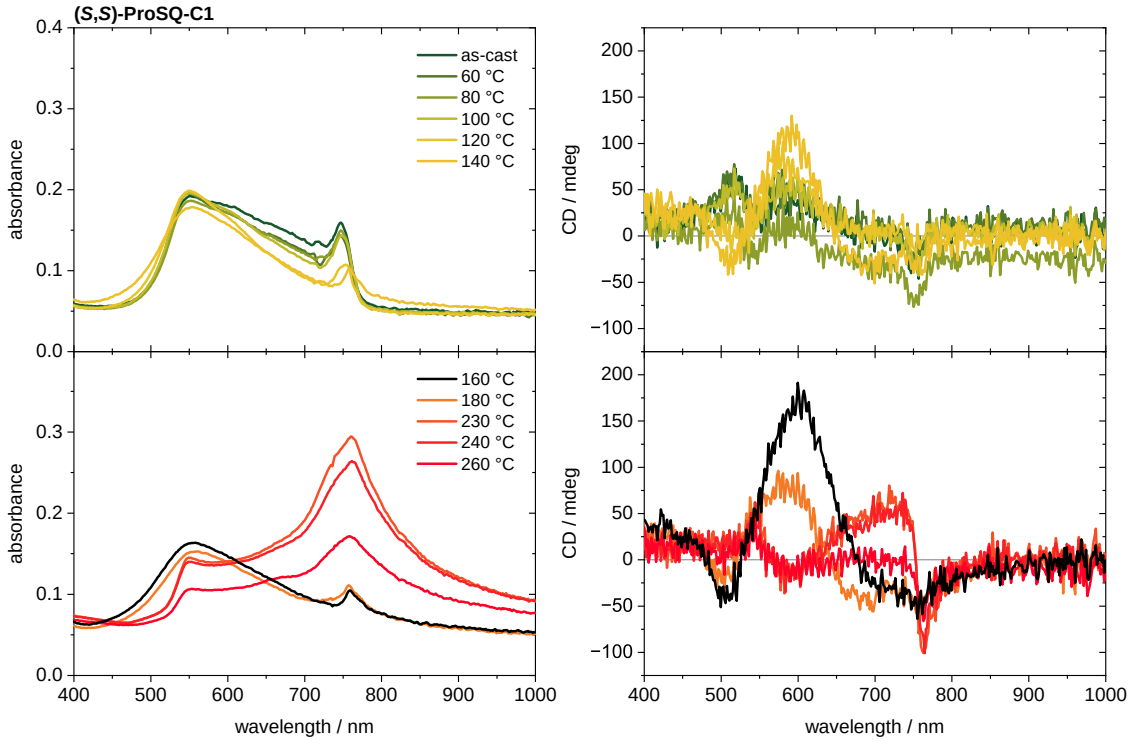


Figure 7.4: UV/Vis absorbance (left side) and corresponding CD spectra (right side) of **(*S*,*S*)-ProSQ-C1**, spin-coated from a chloroform solution under the same conditions and thermally annealed at various temperatures for 30 minutes. Measurements were performed in collaboration with Otgonbayar Erdene-Ochir (group of Prof. Klaus Meerholz, University of Cologne).

temperature of 160 °C. For samples tempered at 230 °C and 240 °C, two small bisignate CD features with the same overall negative Cotton effect were present in the absorption regions of both the H- and J-bands. Based on analogies to aggregated solutions (Chapter 6), this behaviour could be interpreted as mixing of Frenkel-like exciton states (Coulombic H-aggregates) and charge-separated states via intermolecular charge transfer (CT) interactions, despite the short side chain in this squaraine. However, given the relatively poor signal-to-noise ratio (S/N ratio) and the possibility that the spectrum results from superposition of CD contributions from thermodynamic and kinetic species, no final conclusion can be made without further experiments.

Overall, the linear absorption spectrum of **(*S*,*S*)-ProSQ-C1** is quite similar to that of **(*S*,*S*)-ProSQ-C3**, although the CD spectra differ significantly. Furthermore, the UV/Vis absorbance spectra of other **ProSQs**s with longer alkyl chain, up to an annealing temperature of 120 °C – such as **ProSQ-C6** and **ProSQ-C16** – show a strong resemblance to that of **(*S*,*S*)-ProSQ-C1** in both peak positions and overall shape. Above this temperature, however, the longer alkyl-chain derivatives exhibit a significantly more pronounced J-band. In addition, their CD spectra are completely different, displaying well-resolved spectral features.[34, 40] However, the similarity of the UV/Vis absorbance spectra still allows a comparison between these squaraines with **(*S*,*S*)-ProSQ-C1** – at least with **(*S*,*S*)-ProSQ-C3**. Another proline-derived squaraine with an even shorter side chain is **(*R*,*R*)-PyrSQ-C1** (2-methylpyrrolidine-derived anilino squaraine), which lacks the alkoxy chain entirely. This dye, however, exhibits UV/Vis

absorbance and CD spectra dominated by Davydov splitting and shows no significant resemblance to **(*S*,*S*)-ProSQ-C1**.[16] Therefore, no further comparison of the optical properties will be made.

7.3 Single-Crystal X-Ray Structure

Started with the idea that the reduction of the alkyl chain length to the minimal case of a methyl group, would favour the formation of single crystals without incorporated solvent, it was then tried to get single crystals from **(*S*,*S*)-ProSQ-C1**. By layer-diffusion crystallization using chloroform as good solvent and methanol as poor solvent, clear bluish green flat rhombus-shaped crystals of **(*S*,*S*)-ProSQ-C1** were obtained (a picture of the crystals is shown in Figure E.3). The single crystal structure is depicted in Figure 7.5. Detailed characteristics and additional figures of the single-crystal X-ray structure can be found in Appendix E.2.

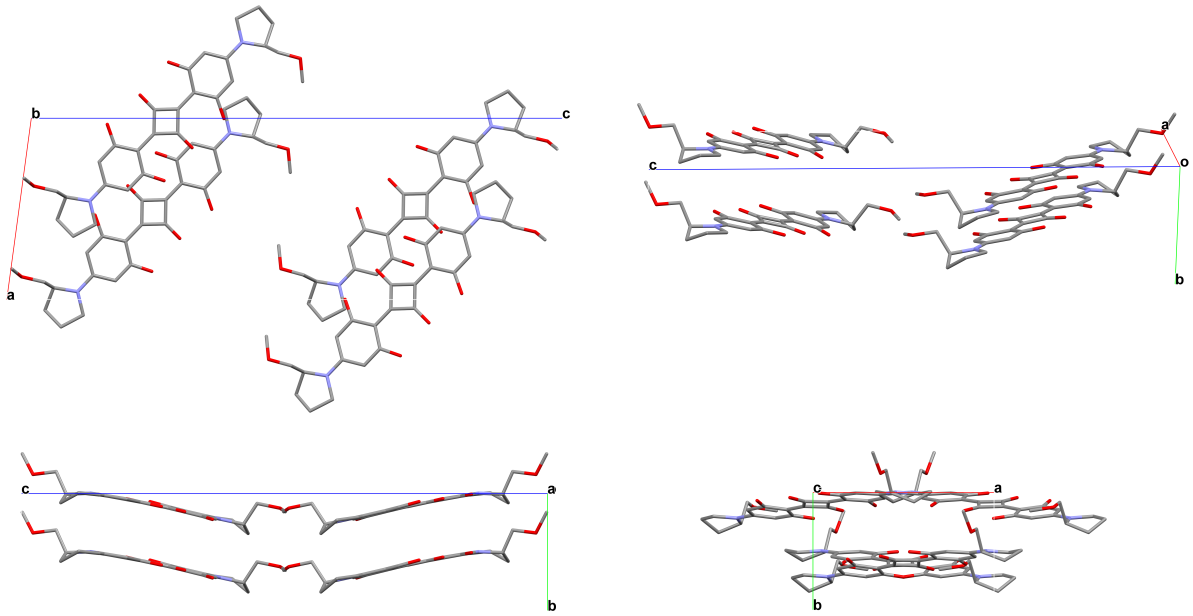


Figure 7.5: Crystal structure of **(*S*,*S*)-ProSQ-C1** (monoclinic, space group = *C*2, a = 11.0261(8) Å, b = 7.0320(8) Å, c = 32.0206(20) Å, α = 90°, β = 97.576(6)°, γ = 90° and Z = 4). Hydrogen was removed for clarity. Nitrogen is represented by blue, carbon by gray and oxygen by red. Top left image: View of the unit cell along the b-axis. Top right image: View of the unit cell along no specific axis. Bottom left image: View of the unit cell along the a-axis. Bottom right image: View of the unit cell along the c-axis. Detailed characteristics and additional figures of the single-crystal X-ray structure can be found in Appendix E.2.

A monoclinic unit cell with a chiral *C2* space group was determined, containing four **(*S*,*S*)-ProSQ-C1** molecules per unit cell. With this – for the first time – a single crystal structure with no incorporated solvent is present. Within the unit cell, the prolinyl groups of the squaraine molecules adopt a trans-conformation, resulting in an “up-up” orientation of the methoxymethyl groups.

The unit cell comprises two shifted-π-stacked dimers whose molecular axes are tilted relative to each other and to the crystallographic axes. These dimers stack along the crystallographic b-axis, with all molecules within a stack coplanar (better visible in Appendix Figure E.4). The central squaric acid core is co-planar with the resorcinol units, with a torsion angle below 5°. This co-planarity is maintained by intramolecular hydrogen bonds between the hydroxy-functionalized aniline moiety (resorcinol units) and the central core.[85] A herringbone packing motif is observed when viewed along the [100] direction (a-axis) (Figure 7.5, bottom left), with an inter-dimer angle of approximately 160°. Since the crystal structure contains two or more translationally invariant molecules per unit cell, it fulfills the criteria for Davydov splitting.[67]

Additionally, the spatial proximity of the donor and acceptor groups within the shifted-π-stacked dimers (visible in Figure 7.5, top left) can give rise to intermolecular charge transfer (ICT) interactions. The actual distance between the π-stacking molecules in fractional coordinates is [0.5, ±0.5, 0.0]. Furthermore, the projected charge-transfer length (ctL, illustrated in Figure 7.6) was calculated to be 5.81 Å, placing it in the "long-range" CT regime, according to the procedure published by *Zablocki* and *Schiek* et al.[85] Coupling between Frenkel-excitonic Coulomb interactions and ICT resonances results in energetic splitting of the allowed exciton state, and thus, can give rise to two distinct bands in the corresponding absorption spectra, as shown in the Introduction (Section 1.2.2). This could explain the two features observed in the absorption spectra (ref. Figure 7.4), however, without further investigation, any conclusion would be purely hypothetical, even though the spatial arrangement in the crystal structure of **(*S*,*S*)-ProSQ-C1** would allow such an interpretation. In the following chapter (Chapter 8), the optical response of thin films of **ProSQ-C16**-which exhibit a dominant J-band and a weaker H-band-is examined by steady-state and ultrafast transient absorption spectroscopy, suggesting hybridisation of a Frenkel exciton with a charge-transfer exciton in these systems. Without XRD measurements of thin films to determine whether the single-crystal structure of **(*S*,*S*)-ProSQ-C1** corresponds to that in the thin film – and without complementary transient-absorption spectroscopy – no definitive conclusion can be drawn at this point.

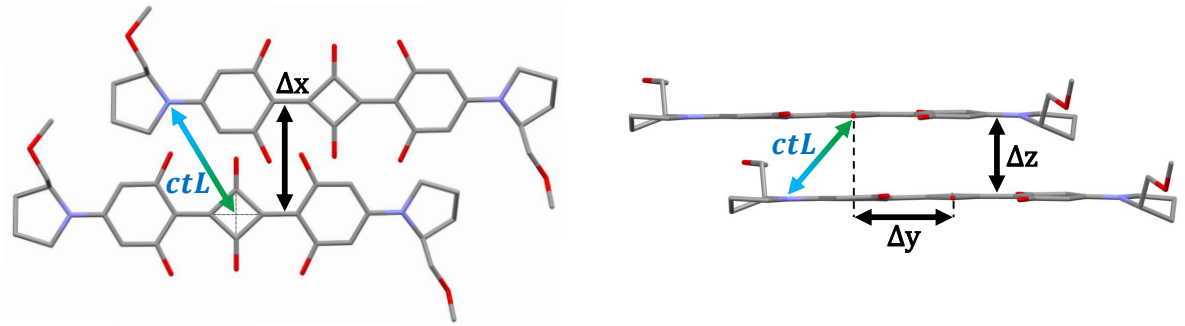


Figure 7.6: Illustration of two stacked nearest-neighbor donor-acceptor-donor (D-A-D) molecules, highlighting the geometric parameters determined at Δx = 3.9002 Å, Δy = 3.9976 Å, Δz = 3.4059 Å, ctL = 5.8065 Åand the shortest translational stacking distance = 6.5388 Å, according to the procedure outlined in [85].

A direct comparison between **(*S*,*S*)-ProSQ-C1**, **(*S*,*S*)-ProSQ-C3**[143] and **(*R*,*R*)-PyrSQ-C1**[16] is shown in Figure 7.7. Both **(*S*,*S*)-ProSQ-C1** and **(*R*,*R*)-PyrSQ-C1** crystallise in a monoclinic unit cell with the space group *C*2 and Z = 4, whereas **(*S*,*S*)-ProSQ-C3** crystallises in an orthorhombic unit cell with the space group $P2_12_12_1$ and Z = 8. It must be noted that for **(*S*,*S*)-ProSQ-C3** the reported single-crystal

structure corresponds to a pseudo-polymorph, which can cause significant differences in molecular packing. This makes a direct structural comparison more difficult, if not impossible. On the other hand, **(*R*,*R*)-PyrSQ-C1** itself is known to exist in two polymorphs – one monoclinic and one orthorhombic.

Whether **(*S*,*S*)-ProSQ-C1** can also crystallise in the orthorhombic polymorph remains an open question – multiple attempts to obtain this polymorph yielded only the monoclinic one. In general, **(*S*,*S*)-ProSQ-C1** shares more similarities with the monoclinic crystal structure of **(*R*,*R*)-PyrSQ-C1** than with **(*S*,*S*)-ProSQ-C3**. In particular, **(*S*,*S*)-ProSQ-C1** exhibits a notably long c-axis, such that the molecules are arranged not in the "zig-zag" (herringbone) pattern of **(*R*,*R*)-PyrSQ-C1** (85°) but almost in a straight row (160°). The presence of two shifted-π-stacked dimers, whose molecular axes are tilted relative to each other and to the crystallographic axes within the unit cell, is also observed in **(*R*,*R*)-PyrSQ-C1**. Based on these findings, it is conceivable that **(*S*,*S*)-ProSQ-C3** – in the absence of incorporated solvent – would also adopt a chiral *C*2 monoclinic unit cell.

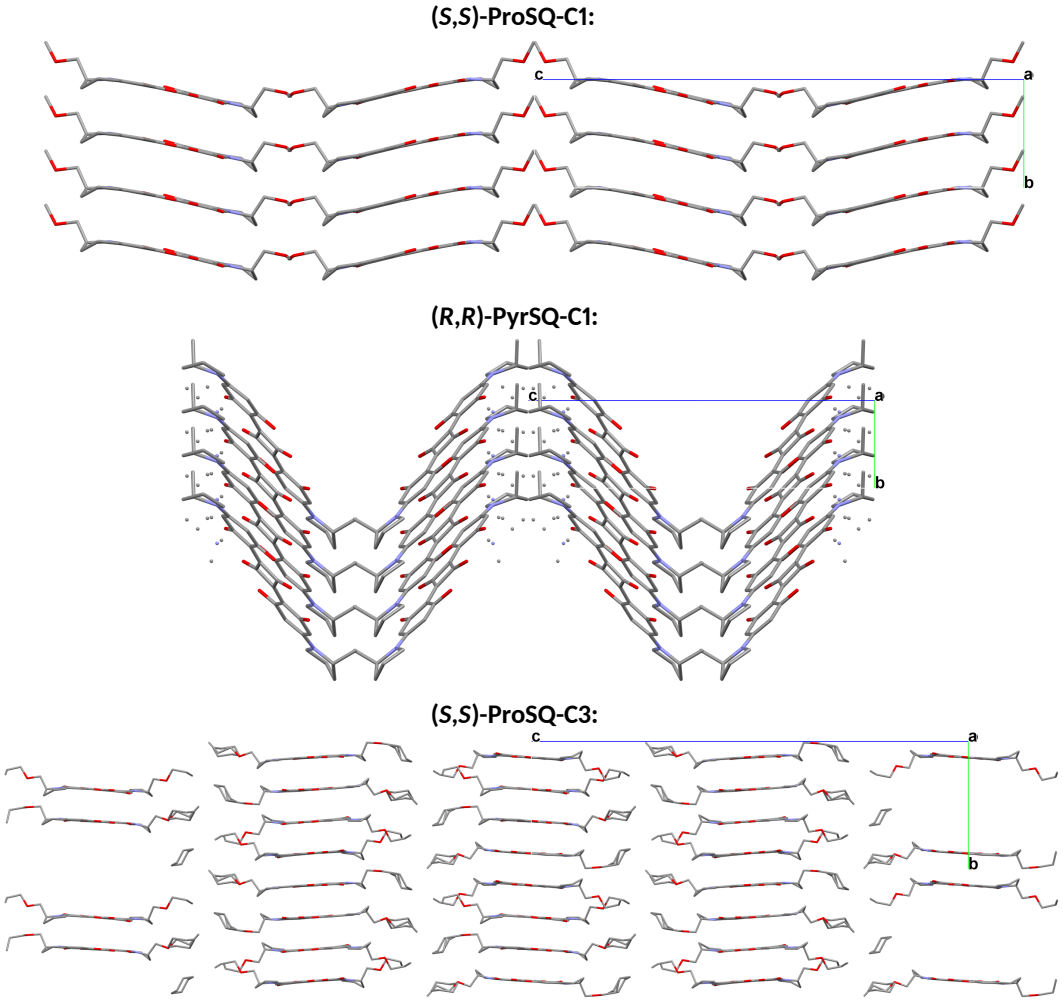


Figure 7.7: Comparison between the single crystal structure viewing the unit cell along the a-axis. Top: **(*S*,*S*)-ProSQ-C1** (monoclinic); Middle: **(*R*,*R*)-PyrSQ-C1** (monoclinic); Bottom: **(*S*,*S*)-ProSQ-C3** (orthorhombic). Hydrogen was removed for clarity. Nitrogen is represented by blue, carbon by gray and oxygen by red. Single crystal structures of **(*R*,*R*)-PyrSQ-C1** and **(*S*,*S*)-ProSQ-C3** have been published earlier in [16] and [143], respectively.

Overall, this chapter examined the first crystal structure of a **ProSQs** – using **(*S*,*S*)-ProSQ-C1** – with no incorporated solvent, which found that it crystallizes in a monoclinic unit cell with space group *C*2. By this the idea of reduction of the alkyl chain length to a minimal case, would favour the formation of single crystals without incorporated solvent worked as attended. **(*S*,*S*)-ProSQ-C1** is based on the crytsal structure much more similar to **(*R*,*R*)-PyrSQ-C1** but exhibits a much longer c-axis and an almost straight molecular chain and no zigzag arrangement. The early-stage aggregation experiments in solution of **(*S*,*S*)-ProSQ-C1** revealed a nearly identical aggregation behaviour to that of **(*S*,*S*)-ProSQ-C3** and – within a certain water-content range of 20 to 40% – even a similar behaviour to long-chain **ProSQs** such as C12 and C16. The linear optical properties of solution-processed **(*S*,*S*)-ProSQ-C1** thin films were comparable to those of **(*S*,*S*)-ProSQ-C3**. Moreover, depending on the annealing temperature, similarities with longer alkyl-chain **ProSQs**, such as **ProSQ-C6** and **ProSQ-C16**, were observed in both peak positions and overall spectral shape. In contrast, the CD spectra revealed significant differences, highlighting the influence of the alkyl-chain lengths.

In order to reach a final conclusion and ensure transferability to other **ProSQs**, further experiments (e.g., XRD on thin films, transient absorption spectroscopy, supporting theoretical calculations, etc.) are necessary.

CHAPTER 8

Ultrafast Excitonic Transitions in Enantiopure and Racemic Squaraine Thin Films

R. Bernhardt,[a] L. Rieland,[a] T. Wang,[a] M. F. Schumacher,[b] A. Lützen,[b] M. Schiek,[c] P. H. M. van Loosdrecht[a]

Received: August 20, 2024
Published online: October 16, 2024

Reprinted with permission[d] from:
R. Bernhardt, L. Rieland, T. Wang, M. F. Schumacher, A. Lützen, M. Schiek, and P. H. M. van Loosdrecht, "Ultrafast Excitonic Transitions in Enantiopure and Racemic Squaraine Thin Films," *Aggregate* **2025**, *6* (3), e698, doi: 10.1002/agt2.698
– Copyright ©The Author(s). Aggregate published by SCUT, AIEI, and John Wiley & Sons Australia, Ltd.

Own contributions:

- Synthesis and purification of the squaraine molecules
- Preparation of the thin film samples
- Performing and evaluating the ellipsometric/polarimetric measurements
- Interpretation of the results
- Writing parts of the manuscript

[a] Institute of Physics II, University of Cologne, Cologne, Germany
[b] Kekulé-Institute for Organic Chemistry and Biochemistry, University of Bonn, Bonn, Germany
[c] Centerfor Surface- and Nanoanalytics (ZONA), Institute for Physical Chemistry (IPC) & Linz Institute for Organic Solar Cells (LIOS), Johannes Kepler University, Linz, Austria
[d] Permission requests to reuse material from this chapter should be directed to SCUT, AIEI, and John Wiley & Sons Australia, Ltd.

Chirality is omnipresent in natural and synthetic molecules and governs many properties of them. One property of special interest is the interaction with light such as the different absorption of circularly polarized light, widely known as circular dichroism (CD).[94] This interaction, however, is usually quite small due to the weak interaction between magnetic and electric dipoles. In the literature, a few examples of extraordinarily high CD values can be found. In these cases, structural CD is often present which is several orders of magnitude larger than intrinsic CD. One class of such molecules are the enantiopure proline-derived anilino squaraines (**ProSQs**). Spin-coated and thermally annealed thin films lead to the emergence of an exceptionally high optical dissymmetry factor (g-value).[2, 34] Even though this class of dyes have been already used in devices, the underlying arrangement of the chromophores and mechanism of this strong chiroptical response is not yet known. Decorated with a sixteen-carbon atom long terminal alkyl chains (**ProSQ-C16**), annealed thin film approaches an extraordinary high excitonic g-value of 0.75 with both red-shifted (J-like) and blue-shifted (H-like) spectroscopic features. What can be said is that the photophysical properties of such an aggregated material is highly influenced by their excitonic states.[144, 145] These states are a result of intermolecular interactions and therefore depend on the spatial alignment of the π-conjugated molecular backbones within the aggregate.[78] To describe these interactions traditional molecular exciton theory uses Coulombic interactions (Frenkel excitons) with the formation of H- or J-type,[78] and oblique aggregates (Davydov splitting).[77] Vibronic coupling and intermolecular charge transfer, however, can hybridize Frenkel excitons, influencing spectral signatures.

In this work we combined steady-state absorption, CD, and ultrafast transient absorption spectroscopy to probe the nature of excitons in enantiopure (both enantiomers) and racemic thin films of **ProSQ-C16**. The leading question was whether a single aggregate type underlies both red-shifted (J-like) and blue-shifted (H-like) transitions in these films. Samples were prepared by spin-coating on glass substrates from a spin-on solution, followed by thermal annealing at 180 °C for 30 min, resulting in film thicknesses between 19 and 29 nm. Steady-state absorption of the enantiomeric pure samples showed a strong asymmetric J-band at 780 nm (1.6 eV) and a weak H-band at 550 nm (2.2 eV). The CD spectra of both enantiomers showed mirror image peaks centered at the J-band and scaling linearly with thickness. In contrast, the racemic samples showed two J-type sub-bands at 740 nm (1.675 eV) and 770 nm (1.615 eV) with long absorptive tail to higher energies which suppressed the H-band. Since the performed CD measurements were an integral method, no CD signal could be detected. This expected result was interpreted as a heterogeneous racemic packing rather than discrete enantiopure aggregate domains with opposite chirality.[146] Transient absorption measurements were performed by selectively exciting (called *pumping*) either the J-band (750 nm, 1.65 eV) or H-band (550 nm, 2.25 eV) of each sample. Excitation of the J-band yielded strong negative bleach (ground-state bleach plus stimulated emission), which is a well-known footprint of J-aggregates,[147] as well as a blue-shifted photo-induced absorption (PIA). Excitation of the H-band, however, produced an almost identical transient response around the J-band. The pronounced similarity observed suggests that the initially excited exciton state associated with the H-band undergoes ultrafast relaxation, within sub-picoseconds, to the excitonic state linked to the J-band. This finding implies that both absorption features in the enantiopure thin films originate from a single type of aggregate with a common ground state. In contrast to the enantiopure thin films, the transient response of the racemic thin films was quite complex. Pumping the J-band led to a complex PIA substructure with multiple peaks between 690–750 nm (1.65–1.80 eV). H-band excitation alters PIA amplitudes and resulted in a different spectral shape. All these findings for the racemic mixture

pointing towards multiple excitonic environments, showing that the thermal annealing does not lead to a resolution of the racemic mixture into enantiopure aggregate domains. Instead, multiple types of racemic aggregates with comparable stability can be assumed, supporting the observations from the CD measurements.[146] Nevertheless, the overall transient response is remarkably high, further highlighting the exceptionally strong light-matter interaction observed in **ProSQ-C16** aggregates.[76, 88, 148] Looking at the transient absorption dynamics of individual bleach and PIA signals and their fluence dependence, revealed further insights in the excitonic nature of the **ProSQ-C16** aggregates. Overall, the PIA decayed consistently faster that the bleach, implying an exciton transition into an intermediate state. Further investigation using singular value decomposition (SVD) suggested the presence of multiple relaxation channels and sub-populations of the initially excited states occurring over various time scales.

In conclusion, our findings strongly suggest a "single-type-of-aggregate" in thermally annealed enantiopure thin films of **ProSQs**, proven by **ProSQ-C16**. This single aggregate species is therefore responsible for the strong light-matter interactions at visible-light frequencies. Based on the theoretical groundwork of Painelli and coworkers on dispersed colloidal **ProSQ** solutions, a single enantiopure aggregate can produce two peaks in the UV/Vis absorbance and CD spectra due to intermolecular charge transfer hybridization of excitons.[2] Recent theoretical and experimental studies have also confirmed the existence of charge transfer (CT) Frenkel hybrid excitons in non-chiral anilino-squaraine thin films.[14, 142] Furthermore, transient absorption dynamics, in combination with the dynamics obtained from SVD, indicate that multiple relaxation channels of the exited enantiopure **ProSQ-C16** aggregate must be considered. This relaxation is dominated by a transition of the photoexcited exciton band minimum within the J-type aggregate into an optically dark intermediate state, which explains the quenched fluorescence observed in **ProSQ** thin films. The nature of this observed intermediate state exceeded the scope of this study and could not be resolved. However, an intermolecular charge transfer (ICT) state, which is optically non-radiative,[14, 149] has been proposed as a possible candidate based on theoretical research by Painelli and coworker.[2] Such a dark state from charge-transfer Frenkel hybrid excitons has been recently experimentally proven by transient absorption spectroscopy in non-chiral anilino-squaraine thin films. Thus, we conclude this intermediate state involves an ICT. Due to the short exciton lifetimes and rapid transition to the dark state, we propose a conical intersection towards the intermediate CT as an efficient non-radiative relaxation pathway.

Our findings show that chiral supramolecular order governs the linear UV/Vis absorbance and strong excitonic CD as well as ultrafast exciton dynamics in squaraine aggregates. Compared to enantiopure samples, racemic ones show several racemic aggregate species without consistent chiroptical or exciton dynamics signatures. Additionally, these results pave the way for tuneable chiral excitonic materials for circularly polarized light emitters and spintronic applications.

CHAPTER 9

From Proline to Indoline: The Idea of Extending π-Conjugation for Enhancing Optical Properties and π-π-Interactions

9.1 The Idea – Enhancing Optical Properties of ProSQs even further

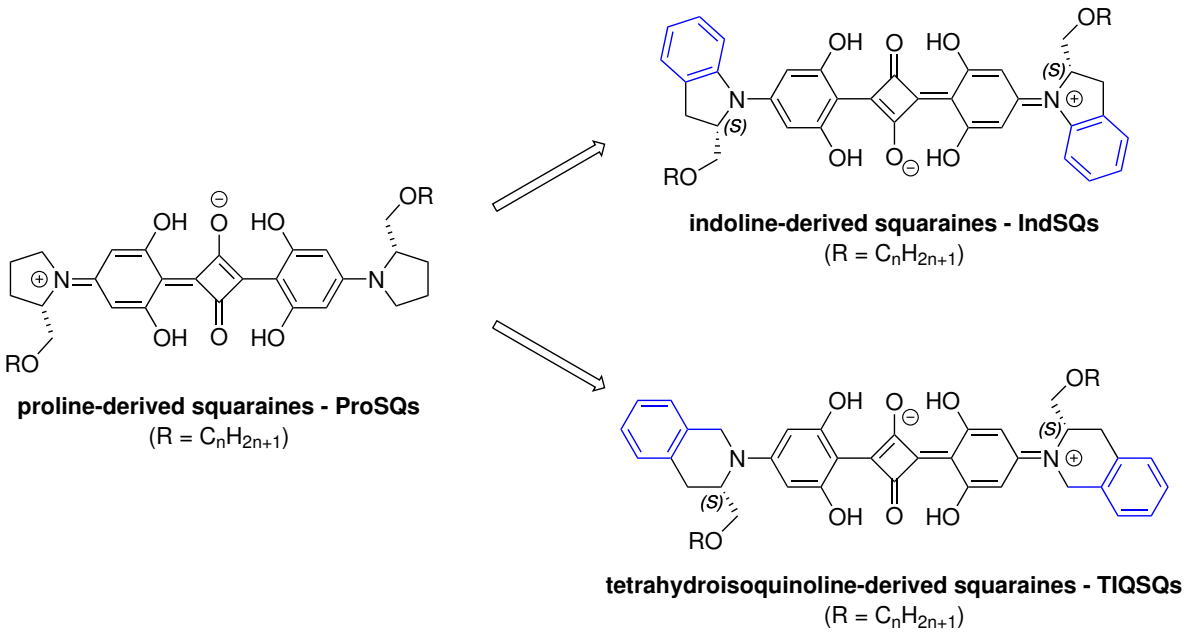


Figure 9.1: Overall targeted structural modifications and design concept, building upon the success of the **ProSQ** class.

This chapter builds upon the success of proline-derived anilino squaraines by attempting to tune the absorption maxima and enhance π-π stacking interactions through targeted structural modification. In

particular, the idea involves extending the π-conjugated system through introduction of an additional aryl unit at the proline substituent, resulting in an indoline- and a tetrahydroisoquinoline-derived unit. It is hoped that this will positively influence the (chiral) aggregation behaviour of the compounds by introducing more efficient π-π-interactions and electronic delocalisation, which should enhance the CD-effect. Following the precedent set by the **ProSQs**, the new squaraines will also incorporate alkoxy chains, as these are generally known to have a beneficial effect on aggregation behaviour by providing stabilising *van-der-Waals* interactions between the chromophores and their side chains. The overall targeted structural modifications and design concept can be seen in Figure 9.1.

(*S*,*S*)-IndSQ-C10 was thereby the primary target structure based on an indoline-substituent. In addition to the previously mentioned benefits, it was anticipated that the extended π-system would induce a bathochromic shift of the absorption maximum, and subsequently of the aggregate absorption. As noted in the Introduction, squaraine dyes feature a relatively small HOMO-LUMO band gap combined with a high stability against light and heat compared to other photoactive chromophores. Since molecules with small band gaps are often unstable under prolonged illumination, difficult to synthesise or unsuitable for manufacturing processes in OPVs, the range of suitable materials for red-to-near-IR detectors is rather limited. To distinguish which properties arise from the extended $\pi-$system and which originate from additional π-π interactions, **(*S*,*S*)-TIQSQ-C10** was also selected as a target as well.

9.2 Addressing Reduced Nucleophilicity: Initial Attempts

During the bachelor's thesis of Fraz Azarnousha, where the practical work was supervised by me, we explored a synthetic route starting from **(*S*)-Ind-COOH** and **(*S*)-TIQ-OH**, in analogy with the previously reported synthesis of **ProSQs**.[2, 34] Although individual intermediates were successfully obtained, the target squaraines could not be produced via the synthetic route shown in Figure 9.2 and 9.3.

Starting with the indoline derivative, the target secondary amine **(*S*)-Ind-C10** was successfully prepared and subjected to the typical two-step, one-pot condensation procedure for the synthesis of anilino squaraines.[2, 11, 34, 100] Surprisingly, instead of the anticipated **(*S*,*S*)-IndSQ-C10**, the reaction yielded the corresponding semi-squaraine precursor **(*S*)-Semi-IndSQ-C10** in negligible amounts, along with an interesting chiral 1,3-squaramide **(*S*,*S*)-IndSQAm-C10**, in which the indoline derivative is directly linked to the squaric acid. Both compounds were clearly characterized by NMR spectroscopy, mass spectrometry and UV/Vis spectroscopy for their absorption behaviour. Since the 1,3-squaramide **(*S*,*S*)-IndSQAm-C10** was unfortunately a viscous oil at room temperature, no further solid-state studies were conducted. Nevertheless, its potential use in transferring chirality from the molecular to the supramolecular level – i.e. as a chiral dopant – could be considered.

The unsuccessful synthesis of the desired (*S*,*S*)-IndSQ-C10 squaraine can be explained by the reduced nucleophilicity of **(*S*)-Ind-C10**, as the nitrogen lone pair can delocalize into the aromatic π-system. This possible obstacle was already known for this synthetic approach and was later confirmed by an additional attempt be me using the C16-indoline derivative, which yielded the same products. In my attempt, the reactant concentrations were increased and the reaction time after the addition of squaric acid was shortened, since in the C10 batch a gradual colour change from an intense deep-red to dark-brown had been observed.[150] The reaction was therefore stopped while the solution still exhibited the deep-red colour. However, as said above, no **(*S*,*S*)-IndSQ** was obtained.

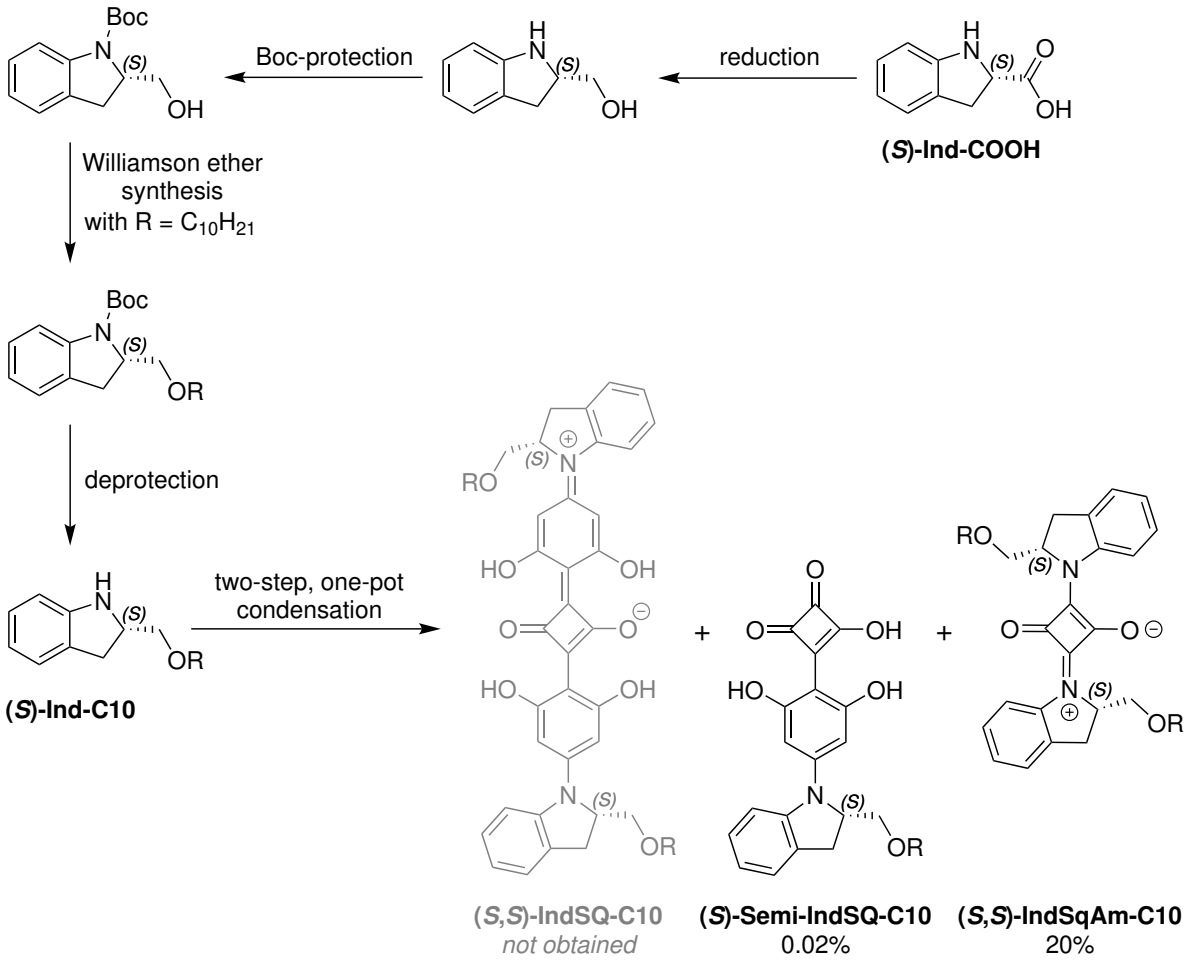


Figure 9.2: Initial synthetic approach for **(*S*,*S*)-IndSQ-C10**, developed and tried during Fraz Azarnousha's bachelor's thesis [150].

The same synthetic route was applied to the tetrahydroisoquinoline derivatives, as shown in Figure 9.3. Unfortunately, the synthesis of the squaraine was again unsuccessful, although it failed at a different stage. Instead of running into difficulties during the condensation reaction, the Williamson ether synthesis failed, and **(*S*)-Boc-TIQ-C10** could not be obtained via this route. NMR and mass analysis suggested an intramolecular cyclisation, initiated by nucleophilic attack of the alkoxide ion ($R\text{-}O^-$) on the Boc group, leading to what appears to be a hydroxyl-mediated transcarbamoylation.[151] Since the reaction was unsuccessful, no further structural analysis of the product was carried out and this remains an unproven hypothesis.

To tackle this problem, I adapted and modified the literature procedure by skipping the entire Boc-protection step, as shown in Figure 9.4. By adjusting the equivalents of the used reactants from 1.5 eq. of sodium hydride (NaH) and alkyl iodide (R-I) to 1.05 eq. each and extending the deprotonation period to 1 h relative to the traditional conditions, **(*S*)-TIQ-C10** was obtained in good yields of 58%. With the secondary amine in hand, the two-step, one-pot condensation could be carried out. Despite using

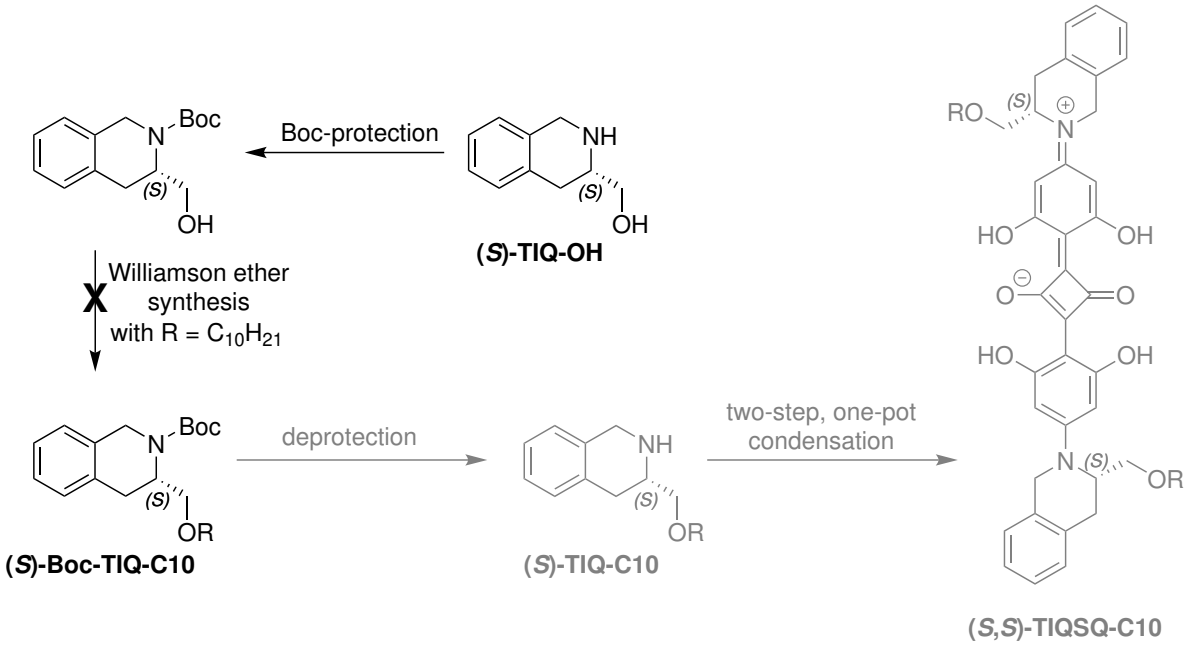


Figure 9.3: Initial synthetic approach for **(*S*,*S*)-THISQ-C10**, developed and tried during Fraz Azarnousha's bachelor's thesis [150].

roughly 630 mg of **(*S*)-TIQ-C10** in this step, the condensation procedure largely failed: after precipitation in the fridge or the reaction mixture, only a small amount of bluish amorphous material (around 10 mg, corresponding to roughly 1% yield based on the amine) was isolated. No additional squaraines were detected in the mother liquor, as evidenced by the absence of any blue spots on the TLC, which indicates that all squaraines formed during the reaction have been completely precipitated. However, the TLC of the isolated solid indicated three different squaraine species (Figure 9.4, bottom right). Separation of the three squaraines was attempted by column chromatography on silica gel eluting with DCM. Mass spectrometry suggested that the first and second flasks (Figure 9.4, bottom left) contained the desired squaraines but the signals were very weak. Although mass spectrometry does not allow conclusions to be drawn about the quantity of a substance in a sample, in combination with the terrible yield, the formation of three different squaraines (despite the ^{1}H- and ^{13}C-NMR showing no significant amounts of other secondary amines alongside **(*S*)-TIQ-C10**) and the separation difficulties led to the decision not to try further synthesis attempts at this stage. Instead, it must first be clarified why the synthesis of the two anticipated squaraines (**(*S*,*S*)-IndSQ-C10** and **(*S*,*S*)-TIQSQ-C10**) is so difficult, whether its due to reduced nucleophilicity, steric hindrance or other factors.

Next, in order to preserve the additional aromatic ring, the synthesis of an isoindole derivative (2,3-dihydro-1H-isoindol-4-ol) was attempted. The idea and goal with this molecular structure was that, due to the position of the nitrogen atom in the molecule, the isoindole should be sterically more accessible, leading to higher overall reactivity, and thus, improved formation of the desired squaraine. In addition, the almost linear arrangement of the aromatic systems could promote aggregation (e.g., H-type), with the chiral side chains pointing outwards and introducing a helical arrangement, as discussed in Section 1.3 - Chirality and Optical Activity.

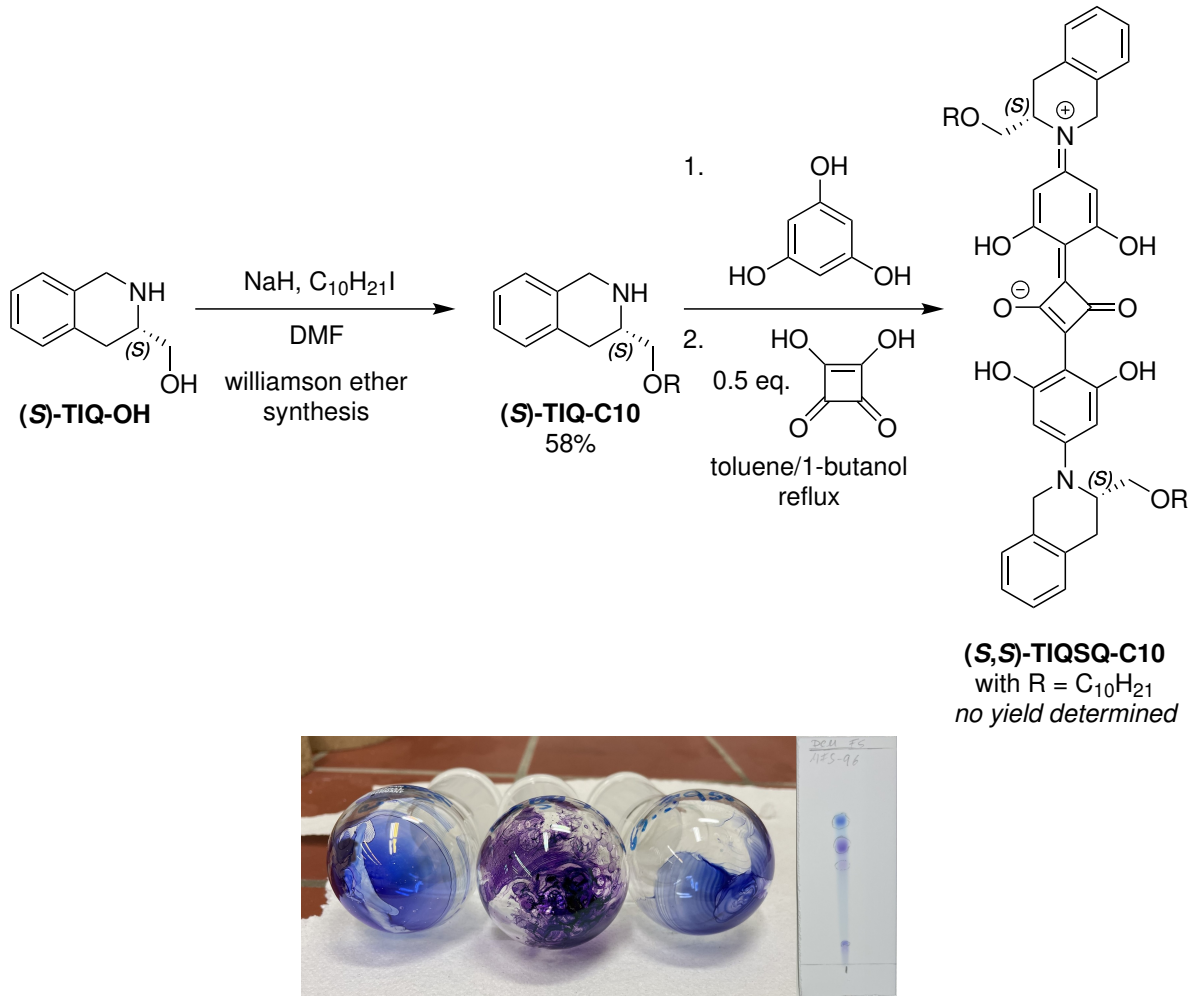


Figure 9.4: Top: Synthetic approach for **(*S*,*S*)-TIQSQ-C10**, starting from enantiopure **(*S*)-TIQ-OH** and omiting the Boc-protection step. Bottom: Picture of the obtained squaraine species after separation by column chromatography on silica gel eluting with DCM (left) and corresponding TLC (right).

The synthetic approach, shown in Figure 9.5, started from **Boc-isoindole** and enantiopure (*S*)-2-methylbutyl *p*-toluenesulfonate as the chiral side chain. In the first step – a Williamson ether synthesis- the corresponding ether **Boc-(*S*)-2mb-isoindole** was obtained in great yields of 88%. Subsequent deprotection of **Boc-(*S*)-2mb-isoindole** with trifluoroacetic acid afforded **(*S*)-2mb-isoindole** in acceptable yield 62%. The significantly lower yield of this step compared to literature values (the majority reported with 90% to quantitative)[2, 34] can be attributed to the additional purification by column chromatography on silica gel eluting with ethyl acetate containing 5% methanol. Here, the retention factor (R_f-value) depends strongly on the concentration of the amine in solution, which is typical for free primary and secondary amines. This leads always to small product losses during purification. The addition of triethylamine was not considered, based on previous experience.

With the secondary amine in hand, a modified two-step condensation procedure was applied for the synthesis of the squaraine, which will be described in detail in Chapter 10 – 2-Methylbutyl-Derived

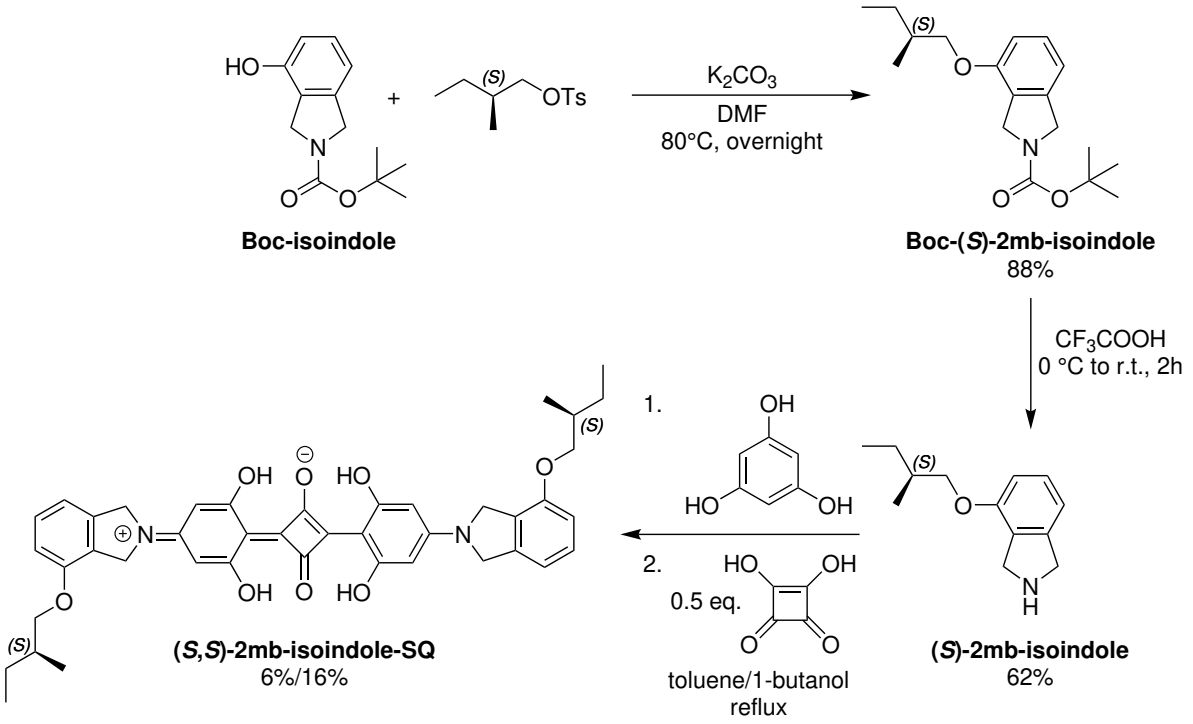


Figure 9.5: Synthetic approach for **(*S*,*S*)-2mb-isoindole-SQ**, starting from **Boc-isoindole** (2,3-dihydro-1H-isoindol-4-ol) and enantiopure (*S*)-2-methylbutyl *p*-toluenesulfonate.

Anilino Squaraines. Although the first condensation step proceeded without any significant differences compared to other squaraines, the second step was unusual. Upon addition of squaric acid and heating, the initially slightly reddish-brown solution rapidly turned blue, as expected. However, after a few additional minutes, the color changed again – this time to purple. Such a purple color is typically observed only upon aggregation or due to solvatochromic effects. Both explanations are reasonable: On the one hand, the reaction was carried out in a highly polar solvent mixture (toluene and 1-butanol, 1:1, v/v) at high concentration (2.2 mL/mmol vs. the usual 10 mL/mmol), favoring solvatochromic effects. On the other hand, the purple color change was accompanied by precipitation of a dark-green, fine solid, indicating poor solubility of the product, and thus, favoring aggregation. At the end 83 mg, corresponding to 16% yield, of this dark solid were isolated after chilling the crude reaction mixture in the freezer overnight.

Although a solid could be isolated from this reaction, further purification proved challenging. Attempts to dissolve the product were unsuccessful due to its extremely poor solubility. At room temperature, dichloromethane, chloroform, acetonitrile, dimethylformamide and trifluoroacetic acid were tested, but no visible dissolution was observed. Stirring the solid overnight at 100 °C in toluene, 1,2-dichlorobenzene or dimethyl sulfoxide dissolved only trace amounts – as judged by faint coloration (see Figure 9.6) – corresponding to concentrations far below the NMR detection limit and below typical UV/Vis concentrations. Consequently, no NMR or UV/Vis analyses were performed. Using APCI(+) mass spectrometry, however, confirmed the presence of the desired squaraine **(*S*,*S*)-2mb-isoindole-SQ**. Although the color of the dissolved squaraine in Figure 9.6 matched the expected one, the elemental

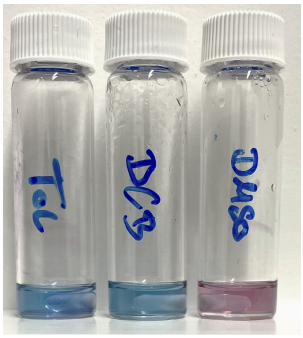


Figure 9.6: Attempts to dissolve the obtained product from the squaraine condensation step shown in Figure 9.5 for further purification, NMR or UV/Vis analysis. The picture showed the solutions of toluene, 1,2-dichlorobenzene and dimethyl sulfoxide (left to right) after stirring at 100 °C overnight, directly after taken from the oil bath (i.e. still at elevated temperatures). Only trace amounts – as judged by faint coloration – were dissolved, corresponding to concentrations far below the NMR detection limit and below typical UV/Vis concentrations.

analysis (EA) (ref. Section 13.4) indicated that the isolated solid was not pure. As possible contaminants the semi-squaraine intermediate and 1-butanol where considered, providing an acceptable fit to the measured EA. Accounting for these impurities, however, would reduce the actual product yield from 83 mg → 33 mg (16% → 6%). Given the uncertain purity of the product and its extremely poor solubility, no further investigations were conducted – such as purification by sublimation or substitution of the (*S*)-2-methylbutyl group with an solubility enhancing but still chiral side chain like (*S*)-citronellyl.

Since the incorporation of an additional aromatic ring into the synthesis evidently alters the system to such an extent that no traditional, easily accessible condensation procedures are suitable anymore, more drastic measures had to be applied.

9.3 Changing Gears – Octahydro-1H-indole for Restoring Nucleophilicity

As clearly evidenced by the previous experiments, incorporation of an additional aromatic ring leads to the failure of the traditional condensation reaction with phloroglucinol and squaric acid. This is particularly true for **(*S*,*S*)-IndSQs** but the synthesis of the other two squaraines presented here also proved to be challenging. For **(*S*,*S*)-IndSQs**, the reduced reactivity can be theoretically explained by the decreased nucleophilicity of the nitrogen atom, as the lone pair on nitrogen can delocalize into the aromatic π-system, thereby diminishing its availability for nucleophilic attack. As a result, the attack on the carbonyl group (keto-enol tautomerism, keto-form of phloroglucinol as shown in the Introduction – Figure 1.4) becomes more difficult. Even though it has been shown that with squaric acid – which is highly electron-deficient and acts as a strong electron-accepting agent – a reaction does occur, forming a 1,3-squaramide (**(*S*,*S*)-IndSQAm-C10**, Figure 9.2). To really chemically verify this hypothesis that the reduced nucleophilicity alone is responsible for the lack of reactivity with phloroglucinol and to exclude steric effects as the cause, a control experiment was designed. As illustrated in Figure 9.7, the idea was to synthesise a squaraine based on an octahydro-1H-indole-derived precursor, basically the hydrogenated analogue of the indoline-derived precursor. This molecular structure should therby result in a steric hindrance comparable to that of the indoline-derived precursor but with higher nucleophilicity

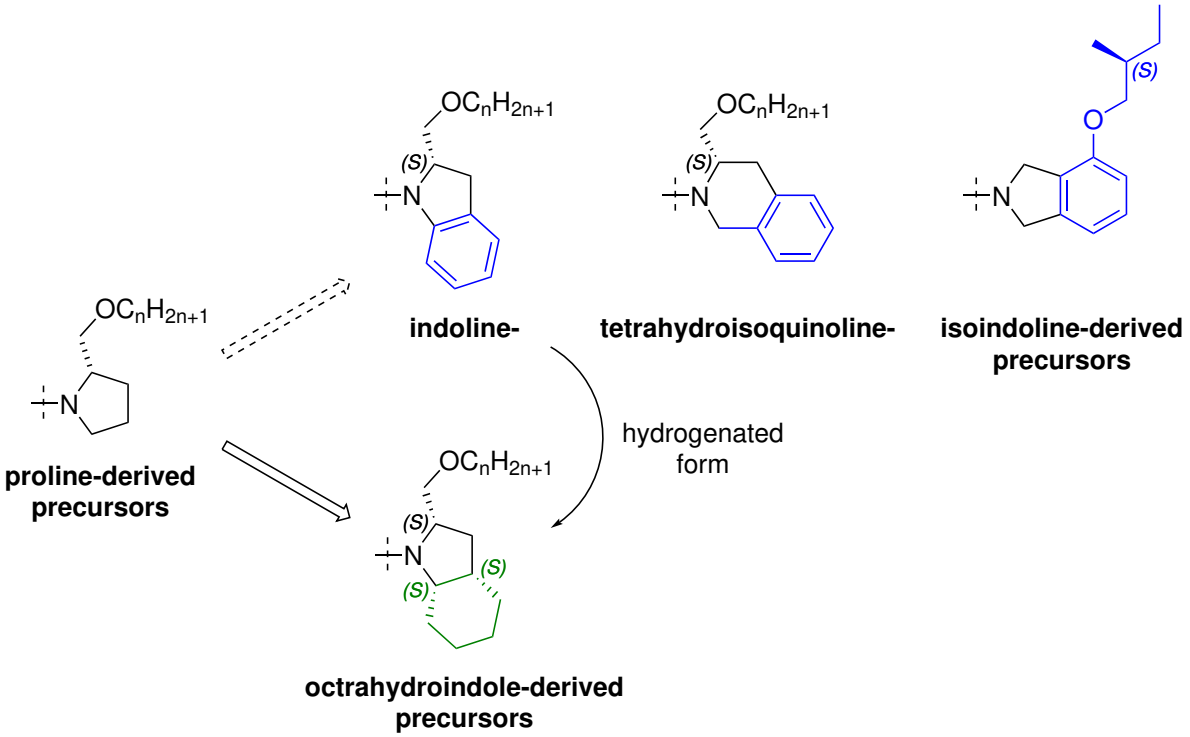


Figure 9.7: Idea of changing the system to the hydrogenated indoline form (i.e. octahydro-1H-indole) to restore the nucleophilicity.

due to the absence of the aromatic π-system. Please note that in the following, the stereochemical information of the (*S*,*S*,*S*)-octahydro-1H-indole-derived precursor will be abbreviated with a single (*S*) and consequently the (*S*,*S*,*S*,*S*,*S*)-octahydro-1H-indole-derived squaraine – one of eight possible stereoisomers – just as (*S*,*S*)-squaraine, consistent with the notation used for the other squaraines in this thesis.

The synthesis of **(*S*,*S*)-OHI-SQ-C3** and **(*S*,*S*)-OHI-SQ-C10** is depicted in Figure 9.8 and followed the same overall strategy as for the **(*S*,*S*)-IndSQs** (see Figure 9.2). Staring with the reduction of **(*S*)-OHI-COOH** to the corresponding alcohol **(*S*)-OHI-OH** in excellent yield of 97%. Subsequently, **(*S*)-OHI-OH** was Boc-protected in 86% yield, preparing it for the Williamson ether synthesis. In this step, **(*S*)-Boc-OHI-OH** was treated with sodium hydride (NaH) and the chosen alkyl iodide (C3: 1-iodopropane; C10: 1-iododecane) to afford the corresponding Boc-protected ethers in good yields – 79% for the C3 and 66% for the C10 derivative. Deprotection of **(*S*)-Boc-OHI-C3/C10** with trifluoroacetic acid yielded the corresponding secondary amines **(*S*)-OHI-C3** and **C10** in 74% and 95%, respectively. The yield for **(*S*)-OHI-C3** is at the lower end of the range reported in the literature but still within an acceptable margin.[2] With the secondary amines in hand, the classical two-step, one-pot condensation procedure was followed, affording **(*S*,*S*)-OHI-SQ-C3** in 9% and **(*S*,*S*)-OHI-SQ-C10** in 29% yield and excellent purity.

This successful reaction, in which **(*S*,*S*)-OHI-SQ-C3** and **(*S*,*S*)-OHI-SQ-C10** were obtained in good yields, supports the previously stated hypothesis. It can therefore be concluded that the reaction of – at

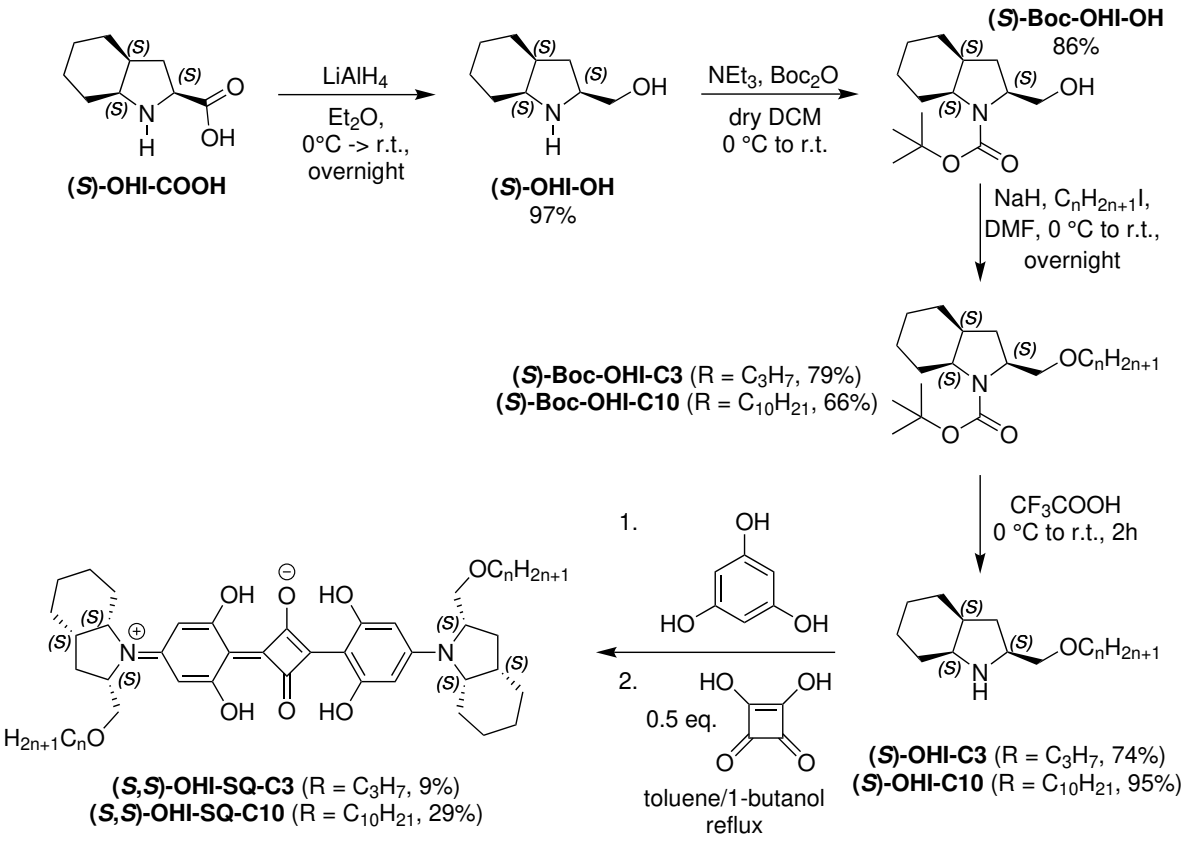


Figure 9.8: Synthesis of **(*S*,*S*)-OHI-SQ-C3** and **(*S*,*S*)-OHI-SQ-C10**, starting from enantiopure **(*S*)-OHI-COOH**, adapted from the synthesis of **(*S*,*S*)-IndSQ-C10** (Figure 9.2).

least – the **(*S*,*S*)-IndSQs** does not occur due to reduced nucleophilicity rather than steric hindrance. Extrapolating these findings to **(*S*,*S*)-TIQSQs** is somewhat more tricky, since the nitrogen atom is not directly conjugated with the aromatic π-system and no strong driving force, such as precipitation of the squaraine as observed for **(*S*,*S*)-2mb-isoindole-SQ**, is present. However, it has been shown that benzylamine exhibits significantly reduced nucleophilic reactivity – actually comparable to that of aniline, although slightly higher – relative to aliphatic cyclic amines, due to the electronic effect of the benzyl group.[152] Transferred to the **(*S*,*S*)-TIQSQ** system, in combination with the extremely poor yields obtained for this type of squaraine, the same conclusion can be drawn here: the reduced nucleophilicity is the primary cause of the diminished reactivity.

To tackle the problem of the C-N bond formation, harsher conditions must be employed. One promising approach is a palladium-catalysed *Buchwald-Hartwig* cross-coupling reaction, which offers a higher driving force compared to the conventional condensation reaction. Preliminary tests between 1-iodo-3,5-dimethoxybenzene and indoline showed promising results. This strategy was further investigated and successfully developed in Fraz Azarnousha's master's thesis.[153]

Even though the initial aim of this chapter was to extend the π-conjugation by introducing an additional aryl unit – thereby enhancing the optical properties (e.g., red-shifting the absorption spectrum)

and increasing π-π-interactions – this goal could not be achieved within this work and was handed over as a master's thesis topic. However, during the course of this thesis, two new chiral octahydro-1H-indole-derived squaraines, **(*S*,*S*)-OHI-SQ-C3** and **(*S*,*S*)-OHI-SQ-C10**, were obtained. Although these compounds lack the extended π-system, the introduction of multiple stereogenic centres in close proximity to the π-conjugated backbone represents an interesting structural feature. Therefore, in the following section, the optical properties of these two squaraines will be investigated both in solution and in solution processed thin films.

9.4 Optical Properties of Aggregated Solutions and Thermally Annealed Thin Films

Aggregated Solutions:

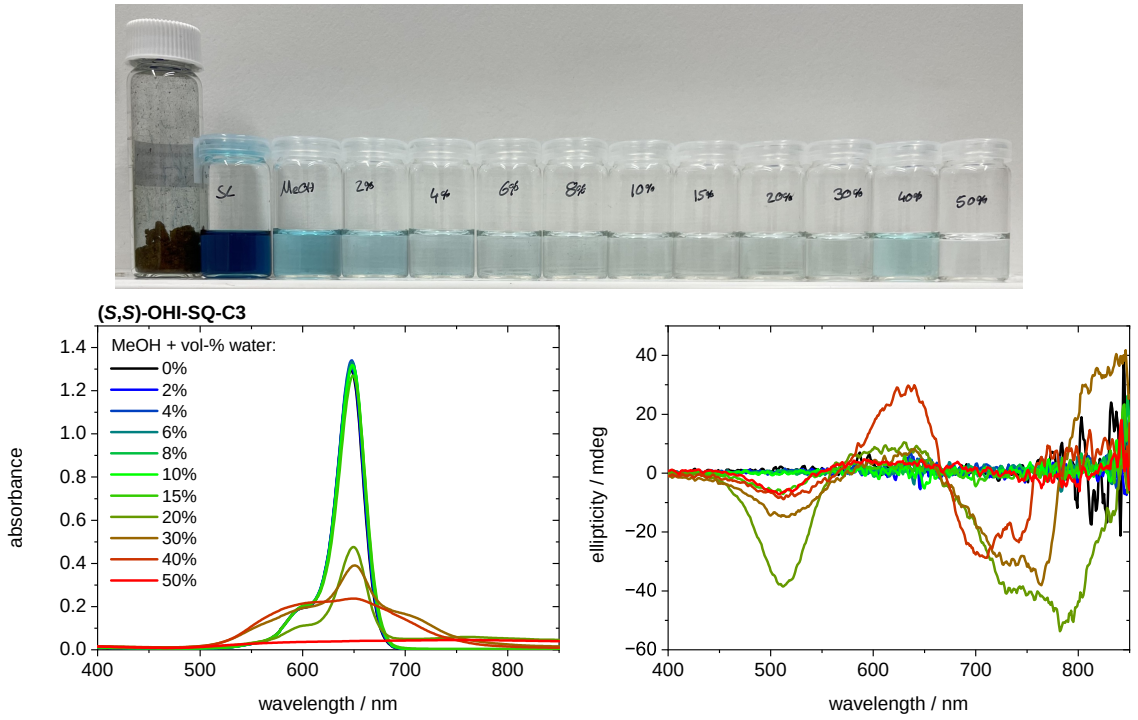


Figure 9.9: Early stage aggregation experiments in solution with UV/Vis absorbance (bottom left), corresponding ellipticity spectra (bottom right) and a picture of the probed samples (top) of **(*S*,*S*)-OHI-SQ-C3** (c = 3.84 µM). The legend indicates the volume-percentage of water in the methanol-water mixture and applies to all plots. The solutions were prepared from a chloroform stock solution ($c = 2.31 \times 10^{-4}$ M) and therefore contain an additional 1.7% chloroform (50 µL in 3 mL).

As usual, in order to obtain an initial assessment of the aggregation behavior of the two squaraines, a titration experiment was carried out where the water content in a methanol solution was gradually

increased. Giving that water is a rather poor solvent, this increase should force the squaraines to aggregated colloidal solutions. The exact procedure for sample preparation is described in Chapter 13.

Staring with **(*S*,*S*)-OHI-SQ-C3**, the UV/Vis absorbance spectra depicted in Figure 9.9 shows that between 0% and 15%water, no signs of aggregation can be detected and the squaraine shows the typical sharp monomeric absorbance band of the electronic $S_0 \rightarrow S_1$ transition around 650 nm. Besides this, a small hypsochromic shoulder, originating from the vibronic 0-1 progression, at about 600 nm is detected.[134] A change can only be observed from over 15% water content onwards. At 20% water content the signal intensity is significantly reduced and an extremely broad signal – more like an offset of the baseline – can be observed over 680 nm. At 30% and 40%, a broad and undefined absorbance band around the still visible monomer absorption is detected. As seen from the picture (Figure 9.9, top) partial precipitation occurred in the methanol/water mixtures over 8% with complete precipitation observed in the 50% methanol/water mixture. As a result, no further spectroscopic investigations could be carried out at this point.

In addition, CD spectroscopy was used to investigate the aggregation behaviour in more detail (Figure 9.9, bottom right). In the monomeric state, i.e. at 0–15% water content, no ellipticity signal was expected or observed, as the chiral center is not located directly at the chromophore and thus no chirality transfer via aggregation had occurred so far.[2, 123] Upon increasing the water content to 20%, the ellipticity spectra displayed two signals: a hypsochromically shifted, monosignate negative band around 520 nm and an additional bathochromically shifted, monosignate negative band around 780 nm. Further increasing the water content led to a reduction in the intensity of the hypsochromic band, while the bathochromic band not only decreased slightly in intensity but also shifted to shorter wavelengths, from approximately 780 nm at 20% →725 nm at 40% warter content. Although a small positive signal around 640 nm was observed at 20% and 30%, it became only significant in the 40% sample. Even though the UV/Vis absorbance spectra suggested complete precipitation of the squaraine at higher water content, a small CD signal at 520 nm was still detectable. Whether this originates from colloidal aggregates or from macroscopic particles suspended in the solution cannot be distinguished. It can, however, be speculated that in this range several signals overlap, producing the observed spectral complexity. As these are only early stage aggregation experiments, no further interpretation will be attempted at this point.

The early stage aggregation experiments for **(*S*,*S*)-OHI-SQ-C10** are shown in Figure 9.10 and differ significantly from those of **(*S*,*S*)-OHI-SQ-C3**. The UV/Vis absorbance spectra for water contents between 0% and 4% shows the typical monomeric absorption band observed for other anilino squaraines. However, due to the longer alkyl chain, **(*S*,*S*)-OHI-SQ-C10** exhibits a stronger aggregation tendency or rather reduced solubility in polar solvents. This is evident from the pictures of the probed samples (Figure 9.10, top), where significant precipitation occurred even in pure methanol (i.e. 0% water). Interestingly, starting at 8% water content, no precipitation was observed. Whether this is a kinetic effect or simply due to the time difference between the preparation of the first and last samples was not investigated in detail. However, based on experience, I would suspect the latter reason. At 6% water content, the first signs of aggregation appeared, indicated by the emergence of a bathochromically shifted band around 760 nm. Between 8% and 20% water content, the monomer band disappeared and the spectrum became dominated by two absorption bands at approximately 675 nm and 755 nm. The spectral shape is strongly reminiscent of the “double-hump” spectral feature observed for citronellyl-functionalized chiral squaraines (Chapter 4) but in reversed order of the signal intensities. Increasing

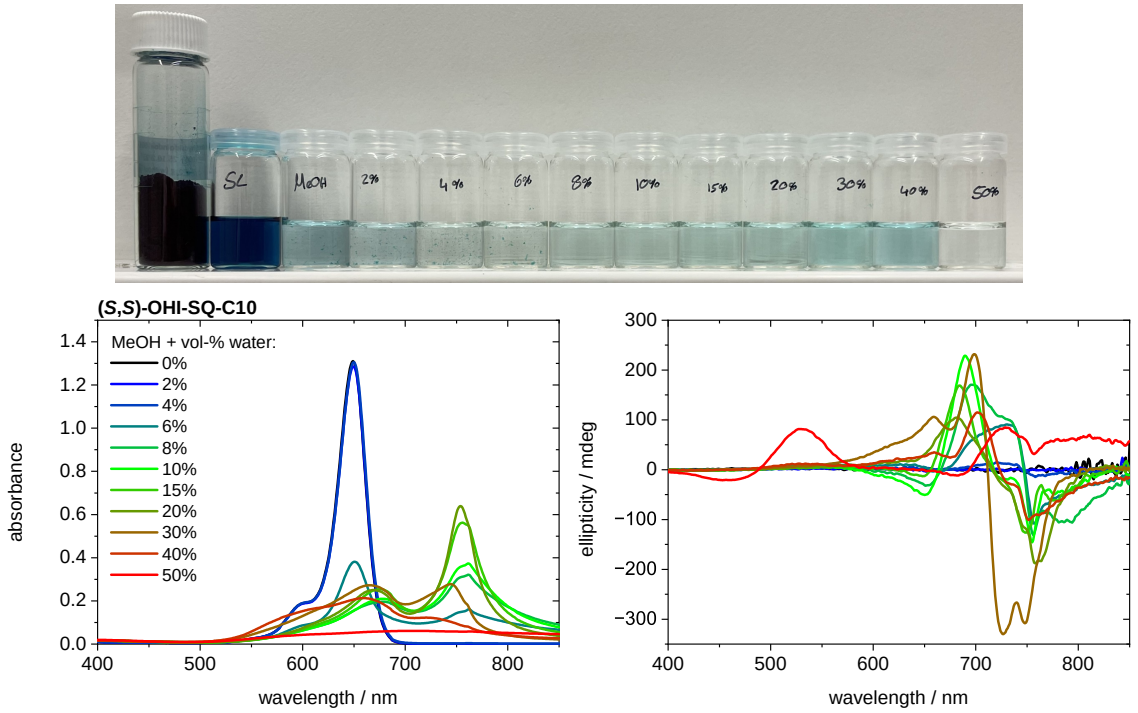


Figure 9.10: Early stage aggregation experiments in solution with UV/Vis absorbance (bottom left), corresponding ellipticity spectra (bottom right) and a picture of the probed samples (top) of **(*S*,*S*)-OHI-SQ-C10** (c = 3.84 µM). The legend indicates the volume-percentage of water in the methanol-water mixture and applies to all plots. The solutions were prepared from a chloroform stock solution ($c = 2.31 \times 10^{-4}$ M) and therefore contain an additional 1.7% chloroform (50 µL in 3 mL).

the water content to 30% and above led to a shift and eventual disappearance of this ”reversed double hump”, with no significant absorption signal detectable in the 50% methanol/water mixture. Consequently, no further spectroscopic investigations could be carried out at this point.

Showing clear evidence of aggregation in these methanol/water mixtures, CD spectroscopy was used to investigate the aggregation behaviour in more detail (Figure 9.10, bottom right). For this squaraine, however, the aggregation behaviour also proved to be rather complex with overlapping contributions from potentially several aggregate species. Although significant precipitation of **(*S*,*S*)-OHI-SQ-C10** occurred, no pronounced ellipticity signal was observed for water contents between 0% and 4%. In the 6% to 20% methanol/water mixtures, overlapping signals produced an overall ellipticity profile with three distinct features: a small negative band, followed by a strong positive band with a zero crossing at around 675 nm and a subsequent negative band around 755 nm, containing several local maxima and minima. The spectral shifts correspond to the higher- and lower-energy components of the “reversed double-hump” feature observed in the UV/Vis absorbance spectra. Interpreting this spectral signature in the context of the coupling between a Coulombic Frenkel exciton and an intermolecular charge transfer (ICT) – as explored and investigated in Chapter 3, 4, 6 and 8, within this thesis, would be particularly interesting, since in contrast to other anilino squaraines (except the **ProSQs**), the Coulombic Frenkel exciton here appears to have J-type rather than H-type character. Unfortunately, the apparent

overlap of multiple aggregate species makes a comprehensive conclusion difficult, just based on these early stage aggregation experiments in solution. At 30% water content, a strong bisignate signal with two maxima and two minima was observed (again likely originating from the overlap of multiple signals) with an overall negative Cotton effect and a zero crossing around 710 nm. The spectrum for the 40% methanol/water mixture resembled those of the 6–20% samples, but with reduced intensity. At 50% water content – despite the UV/Vis absorbance spectra indicating complete precipitation – a hypsochromically shifted bisignate signal around 500 nm, accompanied by a complex bathochromic feature between 680 nm and 850 nm[a] was observed.

Overall, both new squaraines (OHI-SQ-C3 and OHI-SQ-C10) exhibited distinctly different, yet still complex, aggregation behaviours during the early stage aggregation experiments in solution. Additional spectra of **(*S*,*S*)-OHI-SQ-C3** and **(*S*,*S*)-OHI-SQ-C10** in solution, for example in different solvents, can be found in Appendix G.

Thermally Annealed Thin Films:

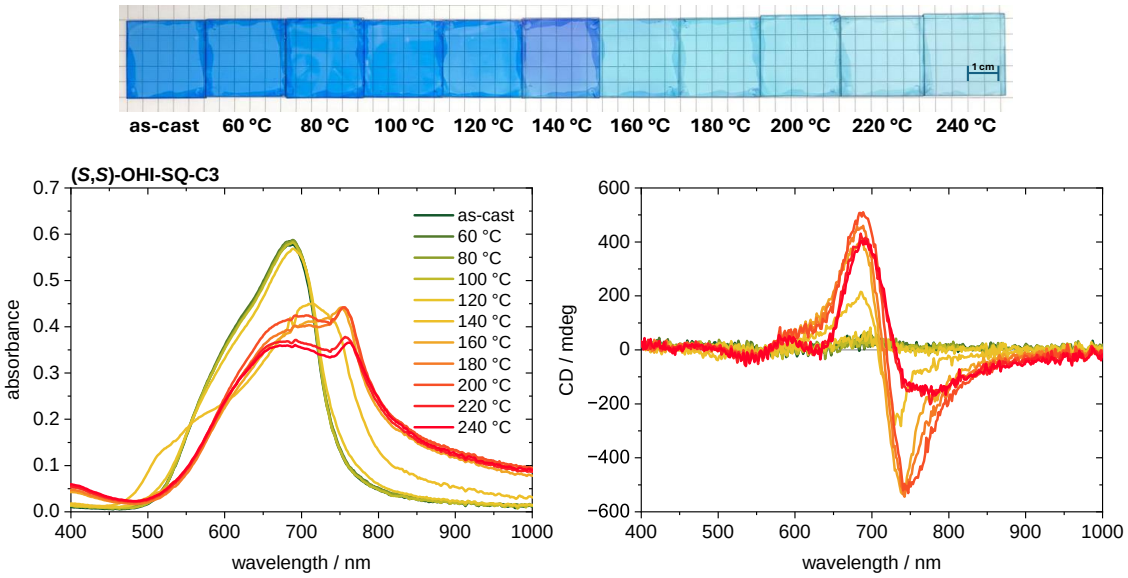


Figure 9.11: UV/Vis absorbance (bottom left) and corresponding CD spectra (bottom right) of **(*S*,*S*)-OHI-SQ-C3**, spin-coated from a chloroform solution under the same conditions and thermally annealed at various temperatures for 30 minutes. The legend indicates the annealing temperature and applies to all plots. Top: Picture of thin film samples after annealing at different temperatures.

After gaining a preliminary understanding of the aggregation behaviour of the two dyes, their actual aggregation behaviour in the solid state was investigated. Therefore, a series of solution-processed thin films were prepared via spin coating under same conditions, followed by thermal annealing at various

[a] Please note that the spectrum was only recorded up to 850 nm. It is therefore not possible to evaluate whether the signal extends further into the near-infrared region.

temperatures for 30 minutes. Subsequent measurements of the absolute absorbance[b] were carried out, and Mueller matrix ellipsometry was employed to accurately determine the circular dichroism (CD) of the samples. A detailed fabrication procedure is given in Chapter 13.

The UV/Vis absorbance and corresponding CD spectra of **(*S*,*S*)-OHI-SQ-C3**, thermally annealed at different temperatures, are shown in Figure 9.11. Up to an annealing temperature of 120 °C, no molecular aggregation was observed. Here, only the typical spectral signature of non-aggregated squaraines is detected – as it has been seen for **(*S*,*S*)-Ci-SQNP** (Section 4.4) – with an absorption maximum at 685 nm and a vibronic shoulder at 615 nm.[1, 19, 67, 139, 140] At 140 °C, both a slight color change in the thin film, from dark blue to blue with a purple hue (Figure 9.11, top) and a change in the UV/Vis spectra were observed. This temperature appears to be the transition between the non-aggregated and aggregated state of the this dye. Further heating caused the films to become lighter blue, accompanied by the emergence of two bathochromically shifted bands: a broad band around 690 nm and a sharp band at 755 nm, which partially overlap. The maximum intensity of these bands was reached at 200 °C, at which further heating led to a gradual decrease in intensity. For comparison, fully thermally annealed proline-derived anilino squaraines (**ProSQs**) with long alkyl chains reach their maximum intensity in the UV/Vis absorbance spectra at around 780 nm, as shown in Figure 5.2. This stronger bathochromic shift can be interpreted as resulting from a different slip angle between the individual dyes, as discussed in Section 1.2 - Aggregation – Induced Optical Changes in Chromophores. Notably, **(*S*,*S*)-OHI-SQ-C3** exhibits exceptional thermal stability. Although the absorbance band intensities diminished at higher temperatures, no evidence of dye decomposition or evaporation was detected, neither in the UV/Vis spectra nor in the visual appearance of the thin films, even after heating up to 240 °C. At this already very high temperature, it was decided not to heat any further.

In the CD spectra, this squaraine showed a substantial degree of chiral aggregation starting at 140 °C. Below this temperature, only a very small signal – on the order of the instrumental noise level – was detectable and therefore cannot be considered a reliable feature. Above 140 °C, however, a well-resolved symmetrical bisignate signal emerged with an overall negative Cotton effect and a zero-crossing at approximately 715 nm. Notably, this zero-crossing does not align directly with a maximum in the UV/Vis absorbance spectra. The signal intensity increased with annealing temperature, reaching values of approximately ±510 mdeg at 200 °C, in agreement with the UV/Vis absorbance trends. Over this temperature, the negative band of the bisignate signal decreased in intensity to around -200 mdeg. As discussed in Section 1.3.2 – Interpretation of CD-Spectra, the Cotton effect can be used to draw conclusions on the helical arrangement of aggregates via the exciton chirality method. Here, the overall negative Cotton effect, combined with the bathochromic shift relative to the monomer absorption, indicates that the squaraine adopts a J-type (Coulombic Frenkel exciton), right-handed helical arrangement – a characteristic of a creeper-aggregate.

For the long-chain equivalent, **(*S*,*S*)-OHI-SQ-C10**, the UV/Vis absorbance and corresponding CD spectra of thermally annealed thin films at different temperatures are presented in Figure 9.12. The as-cast sample also displayed the typical spectral signature of non-aggregated squaraines, but hypsochromically shifted compared to **(*S*,*S*)-OHI-SQ-C3**, with an absorption maximum at 675 nm and a vibronic shoulder at 580 nm.[1, 19, 67, 139, 140] Upon increasing the annealing temperature to 60 °C, visible aggregation was evident in the UV/Vis spectra through the emergence of two new absorption bands: an intense,

[b] As mentioned in Chapter 1 – Introduction, please note that absorption $A \neq$ absorbance Abs; with $Abs = -log(T)$.

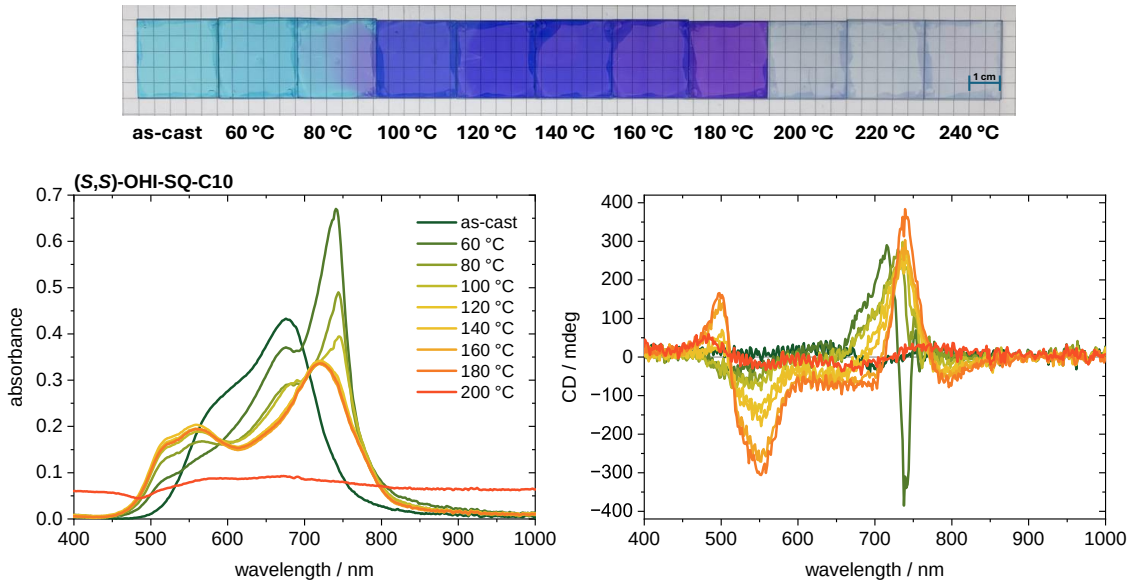


Figure 9.12: UV/Vis absorbance (bottom left) and corresponding CD spectra (bottom right) of **(*S*,*S*)-OHI-SQ-C10**, spin-coated from a chloroform solution under the same conditions and thermally annealed at various temperatures for 30 minutes. The legend indicates the annealing temperature and applies to all plots. Top: Picture of thin film samples after annealing at different temperatures.

bathochromically shifted band around 740 nm and a less intense, hypsochromically shifted feature – more akin to a shoulder – at 515 nm, accompanied by the still-visible absorption at 675 nm. Further heating resulted in a gradual blue shift and decrease in intensity of the 740 nm band, alongside an increase in intensity of the 515 nm band. This resulted finally at 120 °C to a spectrum featuring three absorption bands: a bathochromically shifted band at around 720 nm (relative to the monomer) and two hypsochromically shifted features at 560 nm and 515 nm. Whether the latter is a distinct band or simply a shoulder cannot be determined from the UV/Vis spectrum alone. Over this temperature range, a visible color change of the thin films was also observed, from light blue (as-cast) to an intense purple at 120 °C (Figure 9.11, top). Between 120 °C and 180 °C, no significant spectral changes occurred, although the color of the sample became less bluish purple. At 200 °C, a significant decrease in absorbance intensity was observed, accompanied by discoloration of the sample. Due to the clear signs of squaraine decomposition or something like that, no further measurements were made above this temperature.

As with the complete different UV/Vis absorbance spectra, the CD spectra of **(*S*,*S*)-OHI-SQ-C10** also differ completely from those of **(*S*,*S*)-OHI-SQ-C3**. At 60 °C, a single, non-symmetrical bisignate signal appeared, with a zero-crossing at 730 nm. With increasing temperature (60 °C to 180 °C), this signal gradually evolved into two distinct spectral features: a symmetrical bisignate signal with an overall negative Cotton effect and a zero-crossing at approximately 515 nm, alongside a positive monosignate signal at 740 nm. The asymmetry of the bisignate feature is clearly evident from the intensities at 180 °C: +160 mdeg at 500 nm and -305 mdeg at 550 nm. Meanwhile, the monosignate signal exhibited an intensity of +380 mdeg. At 200 °C, a significant decrease in the CD values was observed, reducing them to essentially insignificant levels.

What is highly interesting is that these two spectral features closely resemble those previously

observed in chiral anilino squaraines such as **(*S*,*S*)-nOCi-SQ** (Chapter 3) or **(*S*,*S*)-nCi-SQIB** and **(*S*,*S*)-nOnCi-SQ** (Chapter 4). Transferring the knowledge gained from Chapter 3, 4, 6 and 8, it can be assumed that in this case the spectral signature originates as well from coupling between a Coulombic Frenkel exciton with H-aggregate character and an intermolecular charge transfer (ICT). One key difference, however, is the relative sign of the overall Cotton effect of the hypsochromically shifted band (H-band) compared to the bathochromically shifted monosignate ICT-band. Whereas in the above mentioned chiral anilino squaraines, the sign of the overall Cotton effect of the H-band matches that of the ICT signal – either both positive, as in **(*S*,*S*)-nOCi-SQ** (annealed), **(*S*,*S*)-nOnCi-SQ** (annealed) and **(*S*,*S*)-nCi-SQIB** (as-cast) or both negative, as in **(*S*,*S*)-nCi-SQIB** (annealed). In contrast, **(*S*,*S*)-OHI-SQ-C10** exhibits a negative H-band and a positive ICT-band. Additionally, the relative intensities in the UV/Vis absorbance spectra are reversed: in **(*S*,*S*)-nOCi-SQ**, **(*S*,*S*)-nOnCi-SQ** and **(*S*,*S*)-nCi-SQIB**, the H-band is more intense than the ICT-band, whereas in **(*S*,*S*)-OHI-SQ-C10** the H-band is less intense (and split into two signals) compared to the ICT-band. By means of the exciton chirality method, the H-band suggests a left-handed helical arrangement of the chromophores. This interesting finding is, however, quite complex and the exact spatial arrangement of the chromophores will need to be confirmed through theoretical calculations and modelling.

Overall, the two new squaraine dyes, **(*S*,*S*)-OHI-SQ-C3** and **(*S*,*S*)-OHI-SQ-C10**, exhibit completely different behaviours – not only between the early stage aggregation experiments in solution and in the solid state, but also when compared to each other. This once again highlights the influence of alkyl chain length, as previously observed for the **ProSQs** in solution (Chapter 6) and spin-coated thin films.[143] It is proposed that **(*S*,*S*)-OHI-SQ-C3** in thermally annealed thin films adopts a right-handed creeper-aggregate geometry, as evidenced by its symmetrical bisignate CD signal, origination from an Coulombic Frenkel exciton with a J-type character. In contrast, **(*S*,*S*)-OHI-SQ-C10** shows a more complex aggregation behaviour, indicating a coupling between a Coulombic Frenkel exciton with H-aggregate character and an intermolecular charge transfer (ICT), similar to that observed for other chiral anilino squaraines. However, drawing definitive conclusions on the actual spatial arrangement of the chromophores is rather challenging and will require further investigation through *in silico* methods (e.g., molecular dynamics simulations or related approaches).

By varying the spin-coating parameters (slow, medium and fast; same dye concentration of 6 mg squaraine per mL spin-on solution), thin films of different thicknesses could be obtained and can be found in Appendix G.

A single-crystal structure of **(*S*,*S*)-OHI-SQ-C3** was successfully obtained and will be presented in the following section.

9.5 Single-Crystal X-Ray Structure of (*S*,*S*)-OHI-SQ-C3

Based on the combination of a short alkyl chain (-C_3H_7) with a cyclohexane-derived substituent (overall octahydro-1H-indole motif), the molecular structure offers several advantages. The short alkyl chains clearly benefits crystallisation, as it has been seen in the case of the **ProSQs** (especially **(*S*,*S*)-ProSQ-C1**, Chapter 7), while the additional cyclohexane-derived residue – adopting the typical chair conformation – gives greater rigidity, and thus, reduces conformational diversity. This increased

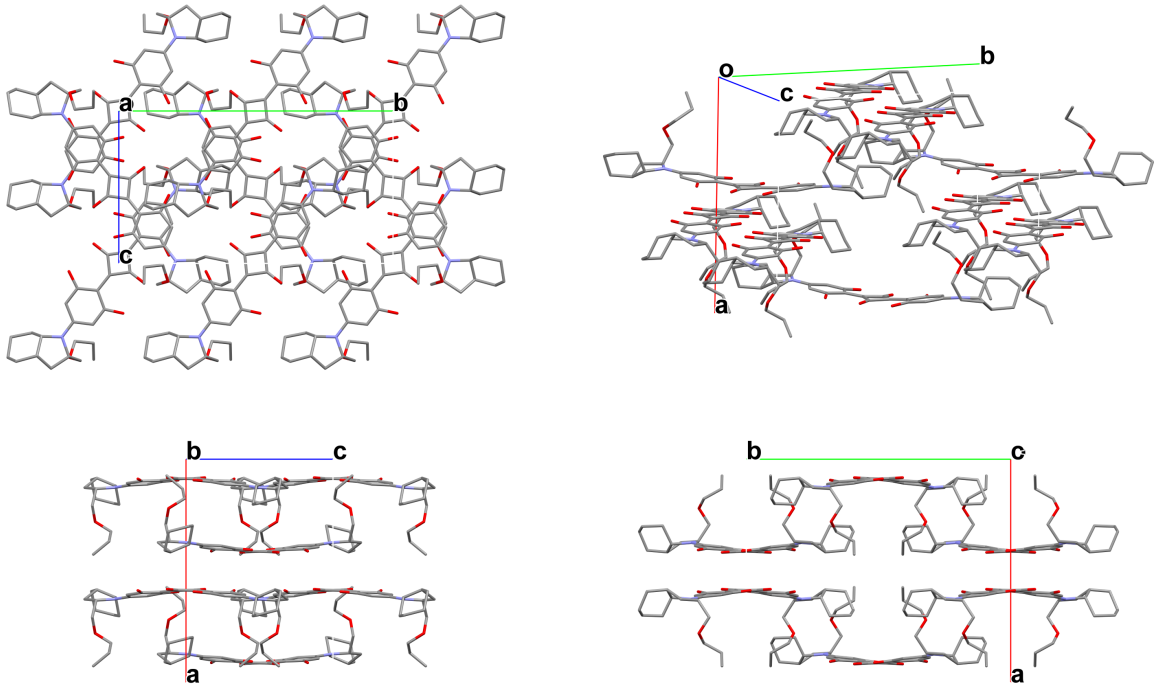


Figure 9.13: Crystal structure of **(*S*,*S*)-OHI-SQ-C3** (orthorhombic, space group = $C222_1$, a = 16.4987(6) Å, b = 19.5419(7) Å, c = 10.8616(3) Å, α = 90°, β = 90°, γ = 90° and Z = 4). Hydrogen was removed for clarity. Nitrogen is represented by blue, carbon by gray and oxygen by red. Top left image: View of the unit cell along the a-axis. Top right image: View of the unit cell along no specific axis. Bottom left image: View of the unit cell along the b-axis. Bottom right image: View of the unit cell along the c-axis. Detailed characteristics and additional figures of the single-crystal X-ray structure can be found in Appendix E.2.

rigidity enables the molecules to arrange themselves more readily in a regular manner, resulting in higher crystallinity. This property of cyclohexyl residues to stabilise crystal structures has already been demonstrated in the literature.[154–156] Accordingly, from the crude reaction mixture (solvent mixture: toluene/1-butanol, 1:1, v/v, 10 mL/mmol) obtained after the second condensation step, slow cooling to room temperature followed by further chilling in the freezer to promote precipitation yielded metallic yellowish-brown plank-shaped single crystals suitable for single-crystal X-ray diffraction. The single crystal structure of **(*S*,*S*)-OHI-SQ-C3** is depicted in Figure 9.13. Detailed characteristics and additional figures of the single-crystal X-ray structure can be found in Appendix G.2.

An orthorhombic unit cell (a = 16.4987(6) Å, b = 19.5419(7) Å, c = 10.8616(3) Å, α = 90°, β = 90°, γ = 90°) with a chiral $C222_1$ space group was determined, containing four **(*S*,*S*)-OHI-SQ-C3** molecules per unit cell. Within the unit cell, the (2*S*,3*S*,9*S*)-2-(propyloxymethyl)-octahydro-1H-indole groups of the squaraine molecules adopt a trans-conformation, resulting in an “up-up” orientation of the propyloxymethyl residues. The unit cell consists of two planes (Appendix G.2, bottom left; hereafter referred to as “planes”), stacked along the crystallographic a-axis. Each plane consists of two sub-planes (henceforth referred to as ”sub-planes”), with the propyloxymethyl chains pointing inwards (into the plane). The molecule itself adopts a slight “banana-like” curvature, bending outward from the

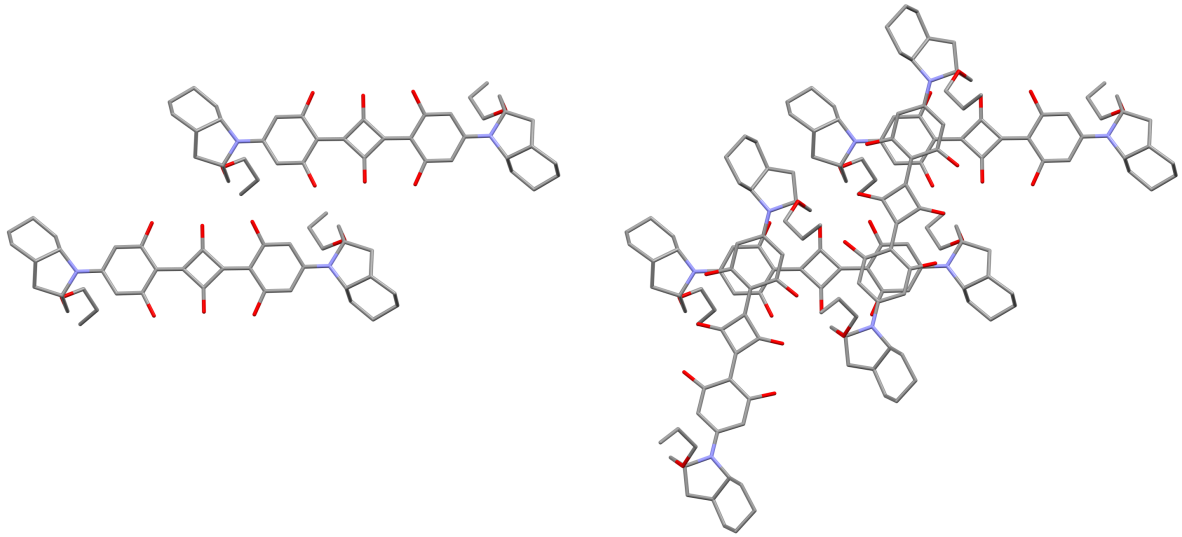


Figure 9.14: Dimer arrangement (left) vs. two dimers pairs rotated to each other (right) between to planes (i.e. from two adjacent sub-planes which are from two different planes) from the crystal structure of **(*S*,*S*)-OHI-SQ-C3** (orthorhombic, space group = $C222_1$, a = 16.4987(6) Å, b = 19.5419(7) Å, c = 10.8616(3) Å, α = 90°, β = 90°, γ = 90° and Z = 4). Hydrogen was removed for clarity. Nitrogen is represented by blue, carbon by gray and oxygen by red.

plane, with the two resorcinol substituents of the squaraic acid core forming an angle of approximately 173.5° (more clearly seen in Figure G.5). This near co-planarity is stabilised by intramolecular hydrogen bonds between the hydroxy-functionalized aniline moieties (resorcinol units) and the central core.[85] Squaraine molecules within the two sub-planes of a common plane, as well as molecules from adjacent sub-planes belonging to different planes, are rotated by 76°/104°[c] relative to each other. Within each sub-plane, all molecules are parallel to each other. This is more clearly visible in Figure 9.14 (left), where two parallel molecules within a sub-plane arrange with a slip angle of around $\theta \approx 38.5°$ and a stacking distance or around $d \approx 6.7$ Å.[d] According to the *Molecular Exciton Model* (Section 1.2), such an arrangement would be expected to produce a bathochromic shift in the absorbance spectrum (i.e. a Coulombic Frenkel exciton with J-type character), as illustrated in Figure 1.7. This redshift is indeed observed in the UV/Vis absorbance and CD spectra of thermally annealed thin films of **(*S*,*S*)-OHI-SQ-C3** (Figure 9.11).

Additionally, the spatial proximity and overlap of donor and acceptor units between molecules from two dimer pairs located in adjacent sub-planes of different planes (Figure 9.14, right) should, in principle, allow for intermolecular charge transfer (ICT) interactions. Such interactions could lead to an energetic splitting of the allowed exciton state, potentially giving rise to two distinct bands in the UV/Vis absorbance and CD spectra (discussed and illustrated in Section 1.2.2). While the Coulombic Frenkel exciton with J-type character is clearly observed, no additional band is detected in the UV/Vis absorbance or CD spectra up to 1600 nm. The absence of this second feature could be explained by differences in morphology/spatial arrangements between the crystal structure of **(*S*,*S*)-OHI-SQ-C3** and the thermally annealed thin films.

[c] Depending on whether the acute or obtuse angle is measured.
[d] Determined from the angle or distance between the molecular axes, defined as the straight line connecting the two nitrogens within the squaraine motif.

Comparing the crystal structure of **(*S*,*S*)-OHI-SQ-C3** with those of other chiral squaraines – e.g., **(*S*,*S*)-ProSQ-C1** (Chapter 7), **(*S*,*S*)-ProSQ-C3**[143] or **(*R*,*R*)-PyrSQ-C1** (two polymorphs)[16] – is challenging. While **(*S*,*S*)-OHI-SQ-C3** does adopt an orthorhombic structure, similar to the pseudo-crystal structure of **(*S*,*S*)-ProSQ-C3** and one of the **(*R*,*R*)-PyrSQ-C1** polymorphs, its actual spatial arrangement of molecules is unique, making a direct comparison not feasible.

Overall, this chapter explored the concept of extending π-conjugation to enhance optical properties and π-π-interactions. Unfortunately, the initially targeted molecular design could not be achieved via the traditional condensation method. This was demonstrated through three distinct molecular designs, which, despite their differences, still retained key features of the original concept – namely, the incorporation of an additional aromatic ring with a nitrogen atom in close proximity. The unsuccessful reactions/reduced reactivity was attributed to the reduced nucleophilicity of the nitrogen atom, either in the indolenine-derivative (structurally similar to aniline) or in the tetrahydroisoquinoline/isoindole-derivatives (structurally similar to benzylamine). Rather than leaving this explanation as an assumption and discontinue the research at this point, it was decided to acquire a chemical proof. For this, the system was modified to the hydrogenated indoline form (i.e. octahydro-1H-indole) to investigate the reason why the previous attempts of incorporating an additional aromatic ring failed.

This approach led to the synthesis of two new squaraine dyes, **(*S*,*S*)-OHI-SQ-C3** and **(*S*,*S*)-OHI-SQ-C10**, in substantial quantities. Their successful preparation not only confirmed the previous hypothesis of reduced nucleophilicity in the earlier systems but also allowed the investigation of a highly interesting molecular design, featuring multiple stereogenic centres in close proximity to the π-conjugated backbone.

Both squaraines proved to be highly interesting, exhibiting markedly different behaviours – not only between early stage aggregation in solution and in the solid state, but also when compared directly to each other. Such a strong influence of alkyl chain length was already previously observed for the **ProSQs** in both solution (Chapter 6) and spin-coated thin films[143] and is once again shown here. For **(*S*,*S*)-OHI-SQ-C3**, the observations suggest a Coulombic Frenkel exciton with J-type character, supported by the single-crystal X-ray structure. While the crystal packing also opens the possibility for ICT interactions, no such feature was detected in the UV/Vis absorbance or CD spectra. In contrast, **(*S*,*S*)-OHI-SQ-C10** exhibits an aggregation behaviour similar to that observed for other chiral anilino squaraines (e.g., **(*S*,*S*)-nOCi-SQ**, **(*S*,*S*)-nOnCi-SQ** and **(*S*,*S*)-nCi-SQIB**), indicating coupling between a Coulombic Frenkel exciton with H-aggregate character and an intermolecular charge transfer (ICT).

Although **(*S*,*S*)-OHI-SQ-C3** and **(*S*,*S*)-OHI-SQ-C10** were thoroughly investigated for their aggregation behaviour, drawing definitive conclusions on the precise spatial arrangement of the chromophores remains challenging. Further insight will require computer based, *in silico* studies, such as molecular dynamics simulations or related approaches.

CHAPTER 10

From the Idea to the Device – 2-Methylbutyl-Derived Anilino Squaraines

10.1 The Idea – Strategic Integration of Beneficial Properties for Device Applications

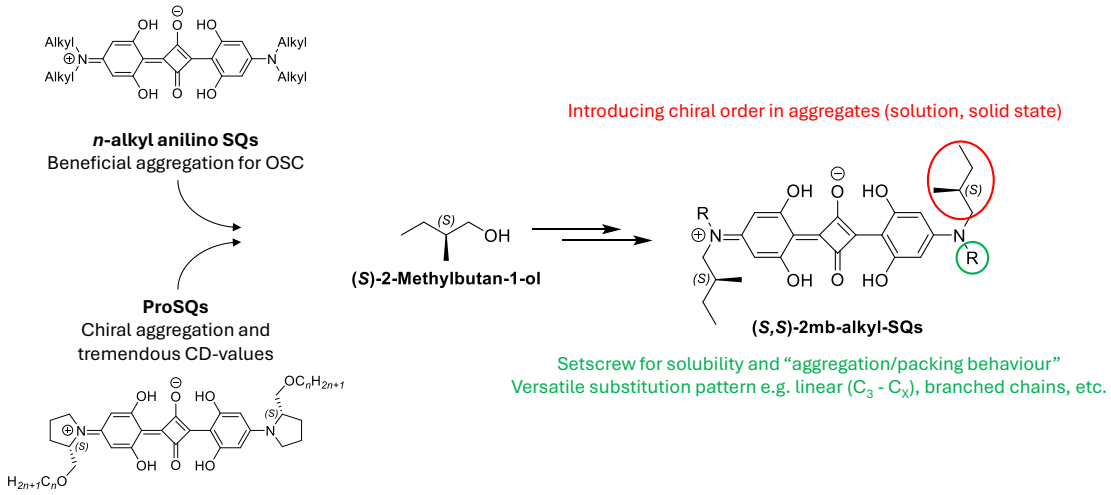


Figure 10.1: Design concept of the **2mb-SQs** – illustrating the strategic combination of the key properties of the **ProSQ** and ***n*-alkyl anilino squaraine** classes.

This final squaraine chapter focuses on the concept, design, synthesis and finally the application of a new class of squaraine dyes in optoelectronic devices. The design concept is illustrated in Figure 10.1, which, on the right, shows the molecular structure of this new class: (*S*)-2-methylbutyl-derived anilino squaraines. Thereby, this design attempt to combine key aspects from two already well-studied squaraine classes.

On one hand, the long alkyl chains (green circle) are inspired by the *n*-alkyl anilino squaraines, known to exhibit favorable aggregation behaviour in organic photovoltaics (OPVs).[85, 142] Their effective orbital

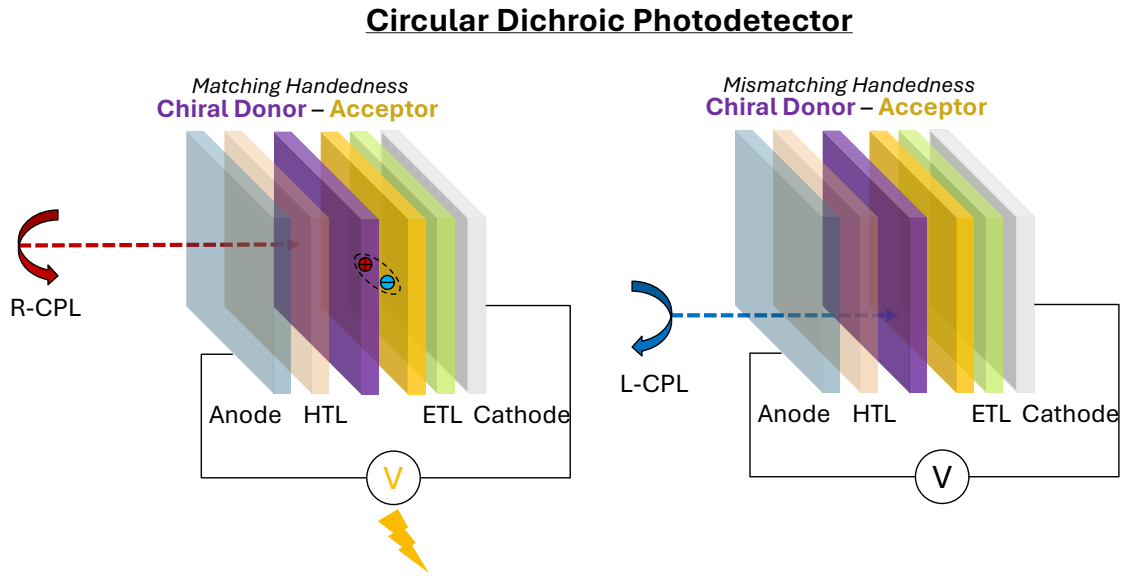


Figure 10.2: Concept of a circular dichroic photodetector, capable not only of responding to a specific wavelengths of light, but also to differentiate between left- and right-handed circularly polarized light (L-CPL and R-CPL), operating without external optical elements or applied voltage bias. Planar heterojunction layer construction with ETL and HTL = electron or hole transporting layer.

overlap and electron transfer are evidenced by the characteristic double-humped absorbance spectra, originating from coupling between a Coulombic Frenkel exciton and an ICT state, as discussed extensively in this thesis. Thereby, this residue not only enables versatile substitution patterns but also governs the overall aggregation and packing behaviour.

On the other hand, the chiral aggregation properties and exceptionally high CD values of the **ProSQs** class, should be introduced via chiral 2-methylbutyl residues (red circle). This substituent offers two main advantages. First, compared to the citronellyl-functionalized chiral squaraines investigated in this work (see Chapter 3 and 4), the stereogenic center is positioned one carbon closer to the π-conjugated backbone, which should enhance chirality transfer to the aggregate, resulting in more pronounced chiroptical properties e.g., higher CD values. Second, its smaller size addresses a limitation observed in previous applications of **ProSQs** in circular dichroic photodetectors by *Schiek* et al. (see Section 1.4.3)[40, 98], where high annealing temperatures promoted phase separation of donor and acceptor materials. By reducing the side-chain size in combination with the presence of two side chains, the design aims to significantly lower the required annealing temperature for complete aggregation of the material.

The overall goal is to use dyes with this molecular design in circular dichroic photodetectors, as depicted in Figure 10.2. In such devices, the optical dissymmetry of the active layer should be translated into photocurrent dissymmetry, enabling operation that not only responds to specific wavelengths but also distinguishes between left- and right-handed circularly polarized light (CPL), without the need for external optical elements or an applied voltage bias.

10.2 Overcoming Challenges in the Synthesis of Chiral 2-Methylbutyl-Functionalized Squaraines

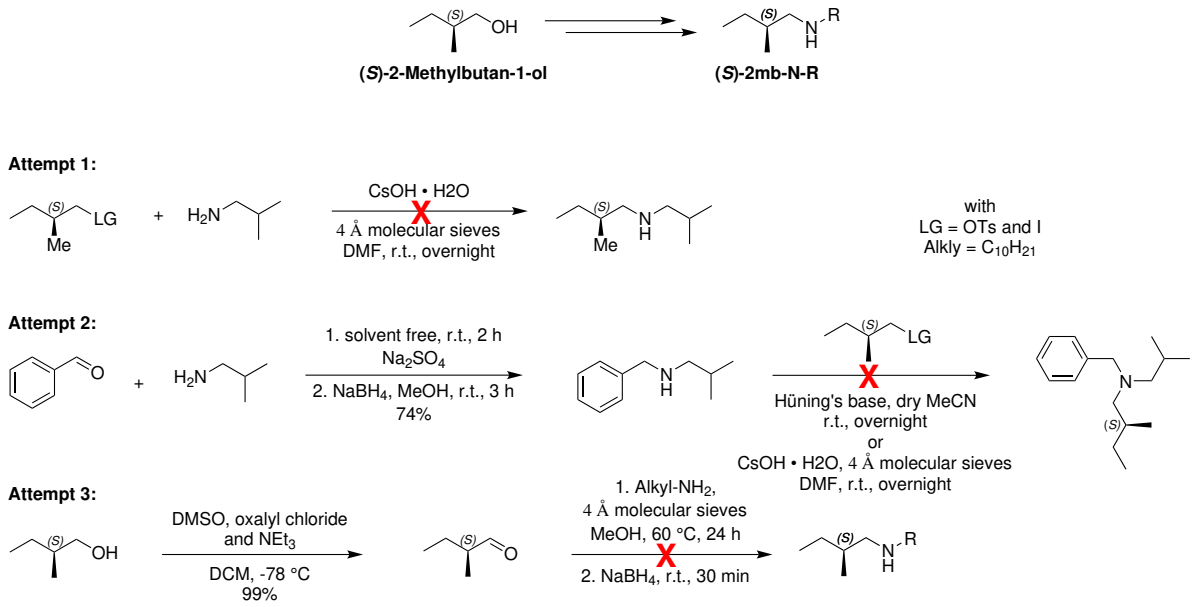


Figure 10.3: Attempted but unsuccessful syntheses of different secondary amines **(*S*)-2mb-N-R**, starting from (*S*)-2-methylbutan-1-ol.

As with most squaraine syntheses, the first step was to obtain the secondary amine, which could then be used in the subsequent condensation reaction. For the **(*S*,*S*)-2mb-SQs**, this secondary amine is **(*S*)-2mb-N-R**, targeted to produce from the commercially available and cheap (*S*)-2-methylbutan-1-ol (see Figure 10.3, top). Unfortunately, the synthesis of **(*S*)-2mb-N-R** proved to be challenging. Figure 10.3 summaries the initial synthetic attempts.

The first approach involved direct alkylation of isobutylamine with (*S*)-2-methylbutyl tosylate or iodide, which yielded only the tertiary amine due to double alkylation. This outcome was somehow expected, as the formed secondary amine is more nucleophilic than the starting primary amine, leading to the well-known problem of over-alkylation. The second approach aimed to avoid this by benzyl-protecting the starting primary amine. Introduction of the protecting group via reductive amination with benzaldehyde afforded the benzylamine derivative in 74% yield. However, subsequent alkylation attempts under two different conditions were unsuccessful. The third approach started with the oxidation of (*S*)-2-methylbutan-1-ol to the corresponding aldehyde via a Swern-oxidation. The aldehyde was obtained in near-quantitative yield but proved to be highly volatile. During work-up, dichloromethane was used for extraction, but could not be completely removed – even with a 45 cm Vigreux column and very slow heating. This volatility and separation difficulty has also been reported in the literature.[157] Aware of this issue, the subsequent reductive amination with decylamine was carried out in a sealed, pressure-resistant vessel. Nevertheless, the reaction failed and no desired secondary amine could be isolated.

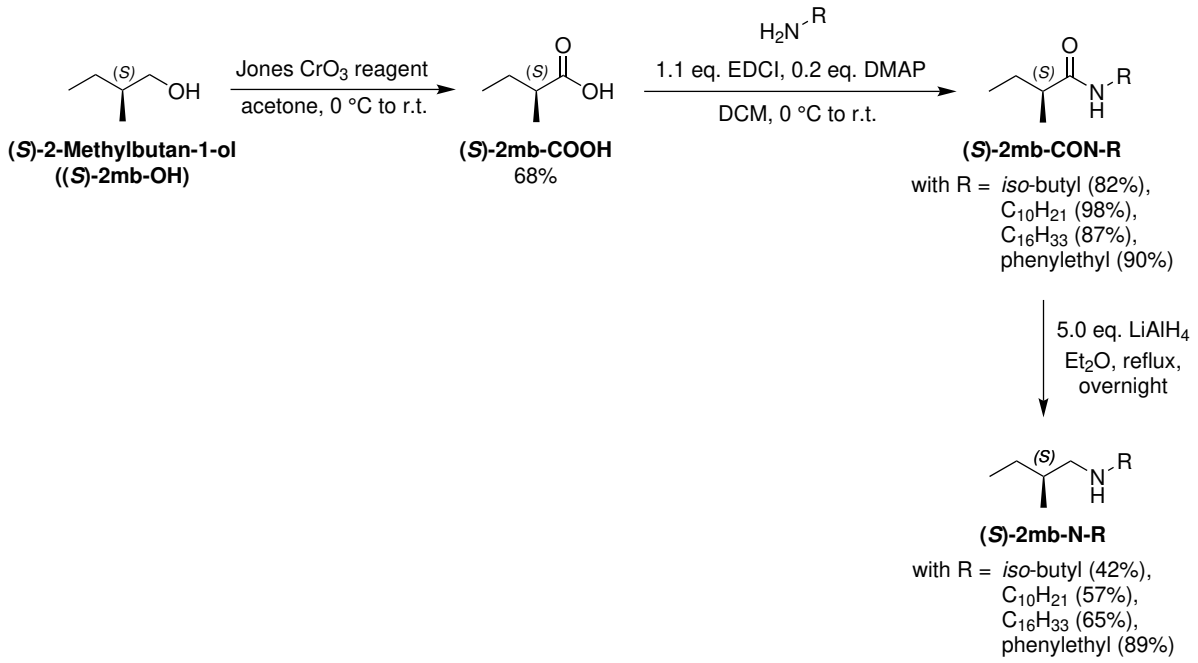


Figure 10.4: Successful synthesis of the secondary amines **(*S*)-2mb-N-R**, starting from (*S*)-2-methylbutan-1-ol.

After several unsuccessful attempts, the synthesis was finally achieved using the approach shown in Figure 10.4. The initial step involved oxidation of (*S*)-2-methylbutan-1-ol to the corresponding carboxylic acid **(*S*)-2mb-COOH** using Jones CrO_3 reagent. The product was obtained in 68% yield after fractional distillation under reduced pressure. Although the yield was not quantitative – due to acid-catalysed ester formation between the carboxylic acid and the starting alcohol – it was sufficient, as all starting materials were inexpensive and readily available. The subsequent EDCI-mediated (a carbodiimide reagent) coupling of **(*S*)-2mb-COOH** with a selected primary amine afforded the corresponding amides **(*S*)-2mb-CON-R** in good yields between 82 and 98%. Variations in yield were attributed to losses during work-up and purification. The more expensive EDCI (1-ethyl-3-(3-dimethylaminopropyl)carbodiimide) reagent was specifically chosen over DCC (*N*,*N*'-dicyclohexylcarbodiimide) to allow a straightforward aqueous work-up, and thus, an easy separation of the coupling reagent. The final and most critical step was the reduction of the amides **(*S*)-2mb-CON-R** to the corresponding secondary amines **(*S*)-2mb-N-R** using lithium aluminium hydride. Even with a large excess of 5.00 equivalents, the reduction proceeded only with moderate yields of 42–65%. The reduction of **(*S*)-2mb-CON-PE** to **(*S*)-2mb-N-PE** was an exception, giving a good yield of 89%, attributed to the change in the solvent system for the purification step – column chromatography on silica gel eluting with acetone + 1% triethylamine → ethyl acetate + 5% methanol. Nevertheless, all secondary amines were obtained in sufficient quantity and with excellent purity for the subsequent squaraine synthesis.

As mentioned above, the reduction of the amides to the corresponding secondary amines represents the most critical step in the sequence. This is not only based on the lowest-yielding reaction, but also to the potential risk of racemization due to the highly basic nature of lithium aluminium hydride. As schematically illustrated in Figure 10.5, **(*S*)-2mb-CON-R** can, in principle, be deprotonated at the

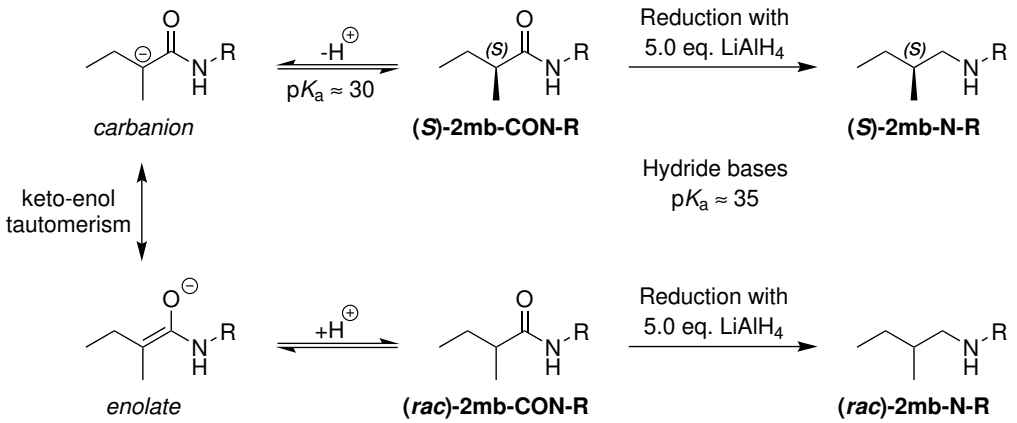


Figure 10.5: Potential problem of the racemization of enantiopure **(*S*)-2mb-N-R** to racemic **(*rac*)-2mb-N-R**

α-position to form the corresponding carbanion (pK_a = 30) by lithium aluminium hydride (hydride bases: pK_a ≈ 35). The resulting carbanion then undergos keto-enol tautomerism, during which the stereogenic information is lost at the enolate stage. Subsequent protonation would then yield the racemic amide **(*rac*)-2mb-CON-R**, which, upon reduction, affords the racemic secondary amine **(*rac*)-2mb-N-R**. Given that the reduction does not proceed in high yields, such a racemization pathway is a plausible concern.

In order to verify that this reduction step proceeds without racemisation, **(*S*)-2mb-N-PE** and its racemic analogue **(*rac*)-2mb-N-PE** were synthesised according to the procedure described in the experimental section (Section 13.5). The phenylethyl residue was specifically chosen for several reasons. First, the additional phenyl ring allows for an easier detection during chiral high-performance liquid chromatography (HPLC) analysis. However, having the aromatic system too close to the nitrogen – e.g., in a benzylic position – could influence the reaction outcome. On the other hand, an excessively long alkyl chain might result in differences too small for effective chiral HPLC separation. Conversely, phenylethylamine was selected as an optimal compromise. The reaction conditions – i.e. equivalents, concentration, time and temperature – for the enantiopure and racemic **2mb-N-PE** syntheses, were identical of those used for the other reductions.

Although both **(*S*)-2mb-N-PE** and **(*rac*)-2mb-N-PE** were obtained in good yields and high purity, direct separation of **(*S*)-2mb-N-PE** and **(*R*)-2mb-N-PE** by chiral HPLC was not possible due to identical retention times. To overcome this issue, it was decided to convert the enantiomers into diastereomers using enantiopure (+)-camphor-10-sulfonyl chloride, as it is shown in Figure 10.6 (top). The resulting camphor-sulfonamides, being diastereomers, possess different chemical properties, making an efficient separation by HPLC much easier to achieve. The chromatograms (Figure 10.6, bottom) show that the camphor-sulfonamides from the racemic **(*rac*)-2mb-N-PE** exhibited as expected two peaks at 12.97 and 13.90 min, corresponding to two diastereomers. In contrast, the camphor-sulfonamide from the presumed enantiopure **(*S*)-2mb-N-PE** showed only a single peak at 13.01 min, consistent with the presence of a single diastereomer. In addition, the formation of diastereomers was confirmed by ^{1}H-NMR spectroscopy. As shown in Figure 10.6 (middle), the spectrum of the racemic camphor-sulfonamide exhibits a duplicated set of signals in the selected region, whereas the enantiopure derivative shows only one set.

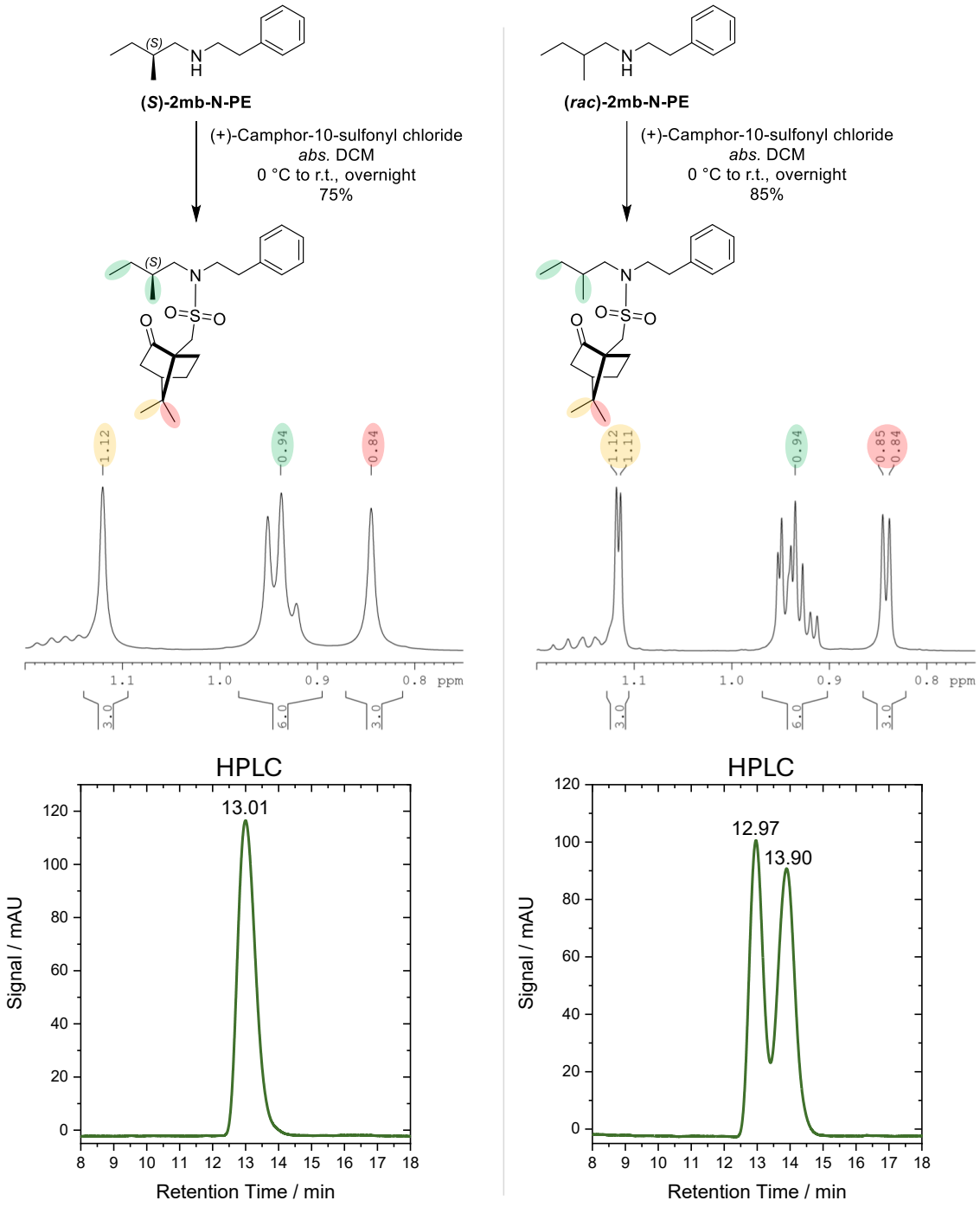


Figure 10.6: Top: Syntheses of the two diastereomeric camphor-sulfonamides, starting from **(*S*)-2mb-N-PE** and **(*rac*)-2mb-N-PE**, both synthesised following the procedure shown in Figure 10.4. Middle: Selected ^{1}H-NMR spectral region highlighting the signal splitting observed for **(*rac*)-2mb-N-PE** compared to the singlet spectrum of enantiomerically pure **(*S*)-2mb-N-PE** (700 MHz, chloroform-*d*, 298 K, 64 scans). Bottom: Analytical chromatograms of the chiral HPLC analysis of the camphor-sulfonamides batches. Parameters: integral area in both cases 100%; stationary phase: DAICEL Chiralpak IC-U, 1.6 µm, 3.0 mm × 100 mm; mobile phase: *n*-hexane/2-propanol (93.1:6.9, v/v); flow rate: 0.85 mL/min; pressure: 324 bar; Detection: UV/Vis at 205 nm.

Taken together, the HPLC and ^{1}H-NMR data confirm that the reduction proceeds indeed without racemization. It can therefore be concluded that the enantiopurity of the amides **(*S*)-2mb-CON-R** directly reflects the enantiopurity of the corresponding secondary amines **(*S*)-2mb-N-R**.

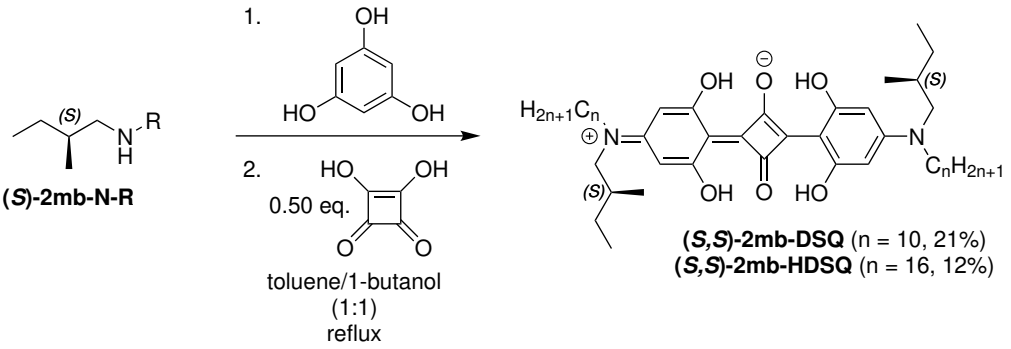


Figure 10.7: Synthesis of **(*S*,*S*)-2mb-DSQ** and **(*S*,*S*)-2mb-HDSQ** following the literature known two-step, one-pot procedure,[2, 100] starting from **(*S*)-2mb-N-C10** and **(*S*)-2mb-N-C16**.

With the enantiopurity of the secondary amines confirmed, **(*S*,*S*)-2mb-DSQ** and **(*S*,*S*)-2mb-HDSQ** were synthesised following the literature-known two-step, one-pot procedure, affording yields typical for squaraines of 21 and 16%, respectively.[2, 100] In contrast, repeated usage of the same reaction conditions with **(*S*)-2mb-N-IB** failed to produce the desired squaraine at all. Instead, only the yellow

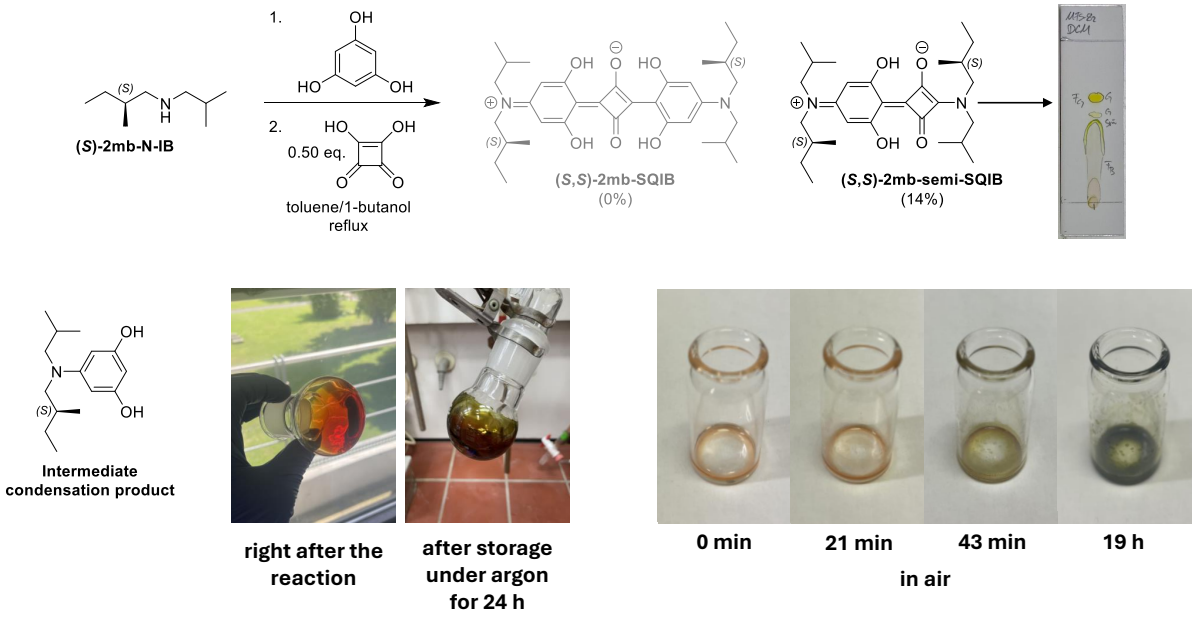


Figure 10.8: Challenges during the synthesis of **(*S*,*S*)-2mb-SQIB**. Top: Results of the literature-reported two-step, one-pot procedure, yielding exclusively the semi-squaraine. Bottom: Pictures of the visual decomposition of the intermediate condensation product by time and upon contact to air.

semi-squaraine was obtained (Figure 10.8, top). A ^{1}H-NMR comparison of the semi-squaraine and the fully condensed squaraine is provided in Figure H.1, together with an ESI(+) mass spectrum of the semi-squaraine in Figure H.2. Multiple variations of the reaction parameters – e.g., reaction time, concentration and total substrate amount – were tested without success. Even separating the synthesis into two steps proved unsuccessful. Thereby, the first condensation was carried out in a toluene/1-butanol (4:1, v/v) mixture to reduce solvation of the secondary amine, and thus, increase its nucleophilicity.[1] During these attempts, it became evident that the intermediate condensation product was unstable under ambient conditions or upon prolonged storage. As shown in Figure 10.8 (bottom), the initially orange-to-red oily intermediate turned dirty yellow when stored under argon for extended periods or rapidly became olive green upon exposure to oxygen or moisture. These observations led to an optimised synthetic approach: The first condensation was performed with a slight excess of secondary amine (1.25 eq.) at a higher concentration (2.2 mL/mmol versus the standard 10 mL/mmol) in a 4:1 toluene/1-butanol mixture (v/v). After the first condensation, all volatiles were removed under high vacuum at 60 °C. This step often required several hours due to the high viscosity of the product and the persistent formation of bubbles. It is hypothesised that the small excess of secondary amine may act as a solvent, driving the equilibrium further toward the condensation product, which could explain the prolonged bubbling. However, this hypothesis has not been proven by any means. The resulting residue was then taken up in a 1:1 (v/v) mixture of toluene and 1-butanol and squaric acid was added for the second condensation step. Given the instability of the intermediate, it was essential to maintain the inert-gas conditions at all time and to initiate the second condensation on the same day. All subsequent work-up and purification steps followed standard squaraine protocols.[2] Using this improved method, **(*S*,*S*)-2mb-SQIB** and **(*S*,*S*)-2mb-SQPE** were obtained in good yields for squaraines of 21% and 16%, respectively, as shown in Figure 10.9.

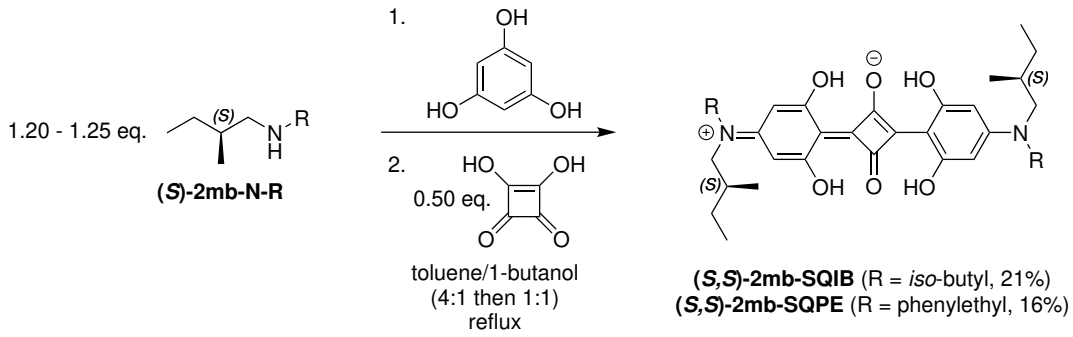


Figure 10.9: Synthesis of **(*S*,*S*)-2mb-SQIB** and **(*S*,*S*)-2mb-SQPE** after the new procedure, starting from **(*S*)-2mb-N-C10** and **(*S*)-2mb-N-C16**.

For both squaraines, **(*S*,*S*)-2mb-SQIB** and **(*S*,*S*)-2mb-SQPE**, single-crystal X-ray diffraction (SC-XRD) structure data were successfully obtained. The structure of **(*S*,*S*)-2mb-SQIB** will be discussed in detail in the following section, while the structure of **(*S*,*S*)-2mb-SQPE** is presented in Appendix H.2. Since the primary purpose of synthesizing **(*S*)-2mb-N-PE** was to verify the enantiopurity of the secondary amines after the reduction step, no further detailed investigations have been conducted on this substance – just the condensation to **(*S*,*S*)-2mb-SQPE**. Combined with the lack of suitable opportunities, this resulted in the absence of any thin-film application studies for **(*S*,*S*)-2mb-SQPE**. Consequently, this new squaraine will only be mentioned briefly in the following.

10.3 Single-Crystal X-Ray Structure of (*S*,*S*)-2mb-SQIB

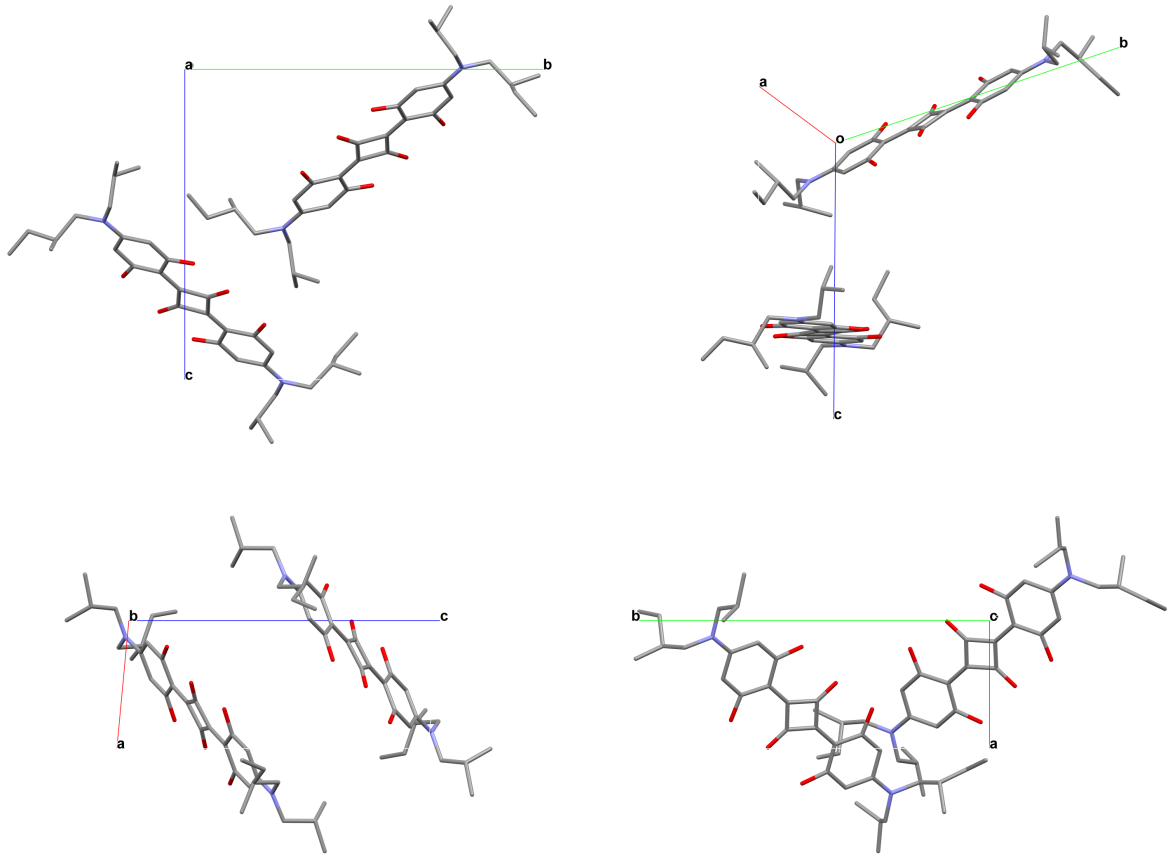


Figure 10.10: Crystal structure of **(*S*,*S*)-2mb-SQIB** (monoclinic, space group = $P2_1$, a = 6.1340(2) Å, b = 17.1614(4) Å, c = 14.9058(5) Å, α = 90°, β = 95.361(2)°, γ = 90° and Z = 2). Hydrogen was removed for clarity. Nitrogen is represented by blue, carbon by gray and oxygen by red. Top left image: View of the unit cell along the a-axis. Top right image: View of the unit cell along no specific axis. Bottom left image: View of the unit cell along the b-axis. Bottom right image: View of the unit cell along the c-axis. Detailed characteristics and additional figures of the single-crystal X-ray structure can be found in Appendix H.2.

The idea behind the synthesis of **(*S*,*S*)-2mb-SQIB** was its close structural similarity to the well-known and extensively studied squaraine **SQIB**[a].[19, 53, 67, 158] The only structural difference being the presence of an additional methyl group, which, however, introduces chirality as intended. Thereby, **SQIB** is one of the most prominent squaraines due to its broad range of potential applications and straightforward accessibility – highlighted by the fact that it is one of the few anilino squaraines commercially available. The achiral **SQIB** is known to crystallise in two polymorphic forms (monoclinic and orthorhombic) both in the bulk and in spin-coated thin films, as reported in the literature.[67]

[a] 2,4-bis[4-(*N*,*N*-dibutylamino)-2,6-dihydroxyphenyl]squaraine

For **(*S*,*S*)-2mb-SQIB**, clear greenish-violet needles were obtained via layer-diffusion crystallisation, using chloroform as the good solvent and methanol as the poor solvent. The resulting single-crystal structure is shown in Figure 10.10, with detailed crystallographic data and additional figures provided in Appendix H.2. Single-crystal X-ray diffraction (SC-XRD) analysis revealed that **(*S*,*S*)-2mb-SQIB** crystallises as well in a monoclinic system with the chiral space group $P2_1$. Overall, the structure exhibits remarkable similarity to the monoclinic form of **SQIB**,[67] with only a minor distortion effects of the additional methyl group, as summarised by the most important single-crystal cell parameters in Table 10.1. Of course, the monoclinic space group $P2_1/c$ contains, in addition to the 2_1 screw axis, a c-glide plane and an inversion center, making it centrosymmetric and therefore non-chiral, in contrast to the non-centrosymmetric $P2_1$.

Table 10.1: Comparison of the most important single-crystal cell parameters of monoclinic **SQIB**[67] and **(*S*,*S*)-2mb-SQIB**.

	space group	a / Å	b / Å	c / Å	$\alpha = \gamma$ / °	β / °	Z
SQIB[67]	$P2_1/c$	6.1979(2)	16.4874(6)	15.4762(5)	90	111.248(2)	2
(*S*,*S*)-2mb-SQIB	$P2_1$	6.1340(2)	17.1614(4)	14.9058(5)	90	95.361(2)	2

The central squaraine core is stabilized by hydrogen bonding, resulting in a coplanar arrangement of the squaric and anilino rings, as shown more clearly in Appendix H.2 – Figure H.4. The primitive crystallographic unit cell, containing two translationally invariant molecules with obliquely aligned transition dipole moments (oriented along the long molecular axis of the squaraine core), enables Coulombic excitonic coupling and could give rise to spectral features with Davydov splitting. A similar molecular arrangement has been reported for monoclinic **SQIB**, where both Davydov components appear simultaneously in the absorption spectra, interpreted as a "Davydov-split H-aggregate characteristic of the monoclinic phase".[67]

As shown in Figure 10.11, the monoclinic **(*S*,*S*)-2mb-SQIB** adopts, like the monoclinic **SQIB**, a herringbone packing motif within the crystallographic *bc*-plane, combined with slipped $\pi - \pi$ stacking along the crystallographic *a*-axis, resulting in two sandwich stacks. The non-projected slip angle θ[b] of an isolated dimer sandwich is 59°. For 54.7° < θ ≤ 90°, blue-shifted spectral signature of an H-aggregate is expected as discussed and illustrated in Figure 1.7. All molecules within a stack display parallel and coplanar ordering (Figure 10.11, bottom) with an interplanar distance of 2.95 Å. In this geometry, partial overlap of the donor and acceptor units of the D-A-D chromophore is observed.

Based solely on this crystal structure, the UV/Vis absorption spectrum would be expected to exhibit a Davydov-split H-aggregate signature, producing a broad CD signal across the entire absorption region. However, given the high structural similarity to **SQIB**, it is reasonable to assume that chiral **(*S*,*S*)-2mb-SQIB** may also form an orthorhombic polymorph – a hypothesis supported by observations in solution-processed thin films (see next section). Attempts to crystallise **(*S*,*S*)-2mb-SQIB** in the orthorhombic form are ongoing but have so far been turned out to be challenging. From a stereochemical perspective, such a polymorphic change could be highly interesting: While the monoclinic form is expected to exhibit a Davydov-split UV/Vis and CD profile dominated by H-type aggregation pattern, the orthorhombic

[b] Border cases: slip angle θ = 90° → chromophores adopt a parallel, face-to-face arrangement; slip angle θ = 0° → chromophores adopt a co-linear, head-to-tail arrangement – see Section 1.2.

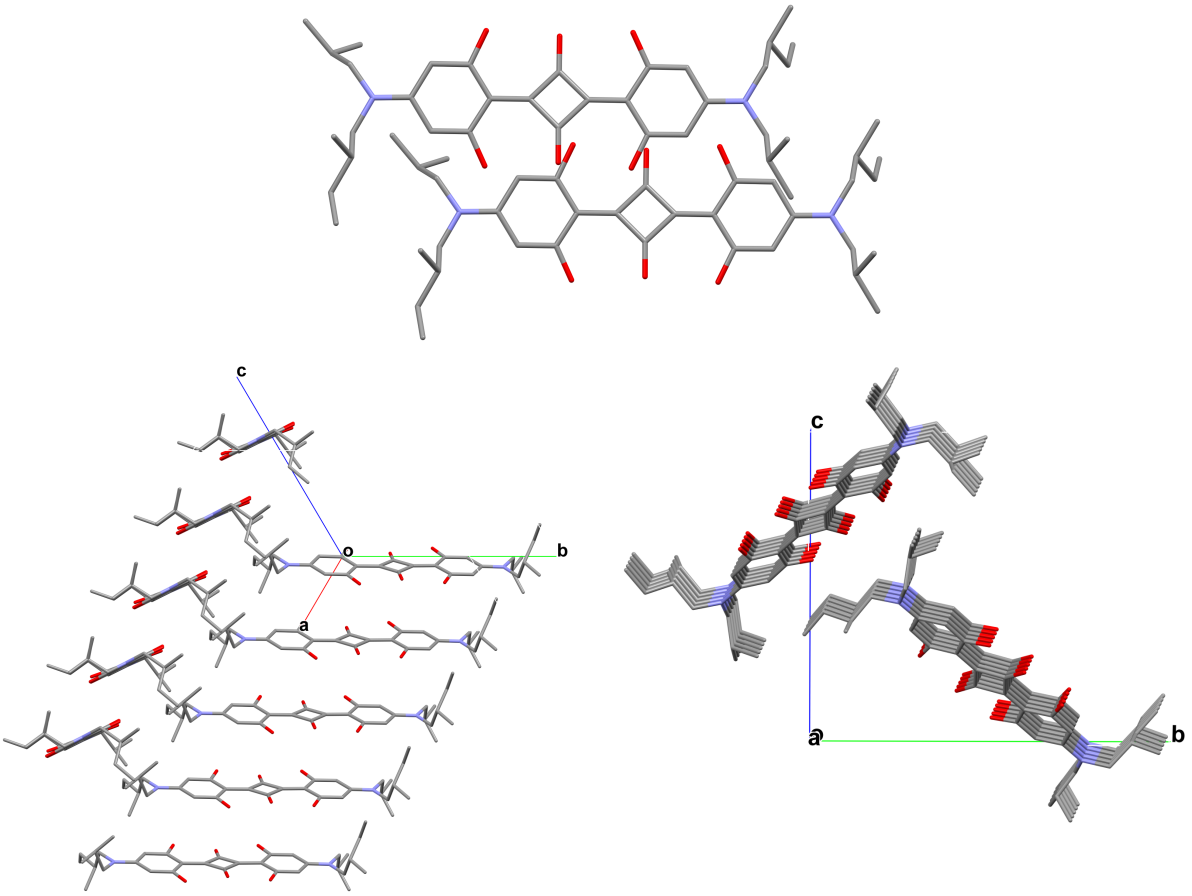


Figure 10.11: Visualization of the sandwich stacks along the a-axis in the crystal structure of monoclinic **(*S*,*S*)-2mb-SQIB** with an isolated dimer sandwich (top) and the two independent stacks in a 5×1×1 unit cell (bottom). Hydrogen was removed for clarity. Nitrogen is represented by blue, carbon by gray and oxygen by red. The non-projected slip angle θ (see Section 1.2 – The Molecular Exciton Model) of a dimer sandwich is 59° and the interplanar distance of 2.95 Å.

polymorph, based on observations for **SQIB**, could instead lead to spectral features dominated by J-type aggregation. This would provide deeper insight into the relationship between molecular structure, micromorphology and the optical properties of polymorphic squaraine thin-film samples.

10.4 Optical Properties of Aggregated Solutions and Thermally Annealed Thin Films

Aggregated Solutions:

As usual, in order to obtain an initial assessment of the aggregation behavior of all four squaraines – **(*S*,*S*)-2mb-SQIB**, **(*S*,*S*)-2mb-DSQ**, **(*S*,*S*)-2mb-HDSQ** and **(*S*,*S*)-2mb-SQPE** – titration experiments were

carried out where the water content in a methanol solution was gradually increased. Giving that water is a rather poor solvent, this increase should force the squaraines to aggregated colloidal solutions. The exact procedure for sample preparation is described in Chapter 13.

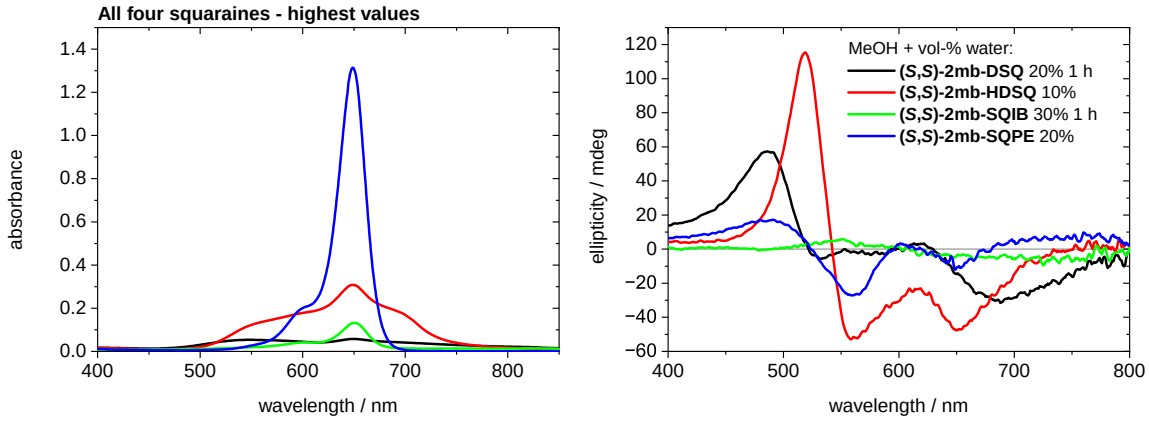


Figure 10.12: Best-performing early stage aggregation experiments in solution for all four new squaraines – **(*S*,*S*)-2mb-SQIB**, **(*S*,*S*)-2mb-DSQ**, **(*S*,*S*)-2mb-HDSQ** and **(*S*,*S*)-2mb-SQPE** – with UV/Vis absorbance (left) and corresponding ellipticity spectra (right). The legend specifies the squaraine derivative, volume-percentage of water in the methanol-water mixture as well as the time point and applies to all plots. The solutions were prepared from a chloroform stock solution (c = 2.31 × 10^{-4} M) and therefore contain an additional 1.7% chloroform (50 µL in 3 mL). The full spectra are provided in Appendix H.3.

Since none of the four squaraines were found to significantly aggregate in solution, all UV/Vis absorbance and ellipticity spectra from the early-stage aggregation experiments, as well as measurements in different solvents, are provided in Appendix H.3. However, a short summary together with an overview of the best results (see Figure 10.12) is given in the following:

For **(*S*,*S*)-2mb-SQIB** (Figure H.9), no significant signs of aggregation were observed at any water content until complete precipitation occurred at 40%. In a 30% methanol/water mixture, a very weak ellipticity signal appeared after the sample stand for one hour indicating a time-dependent aggregation behaviour. However, the signal-to-noise ratio (S/N ratio) was poor with intensities on the order of the instrumental noise level.

Similarly, **(*S*,*S*)-2mb-DSQ** (Figure H.10) showed initially no clear evidence of aggregation. Although the longer alkyl chains caused precipitation at lower water contents, yet apart from a broadening of the absorption band, no aggregation features were detected. In the 20% water mixture, a signal in the ellipticity spectra emerged after one hour, but UV/Vis data indicated that the squaraine was already almost completely precipitated. Based solely on the ellipticity spectra, this signal can be interpreted as a hypsochromically shifted, non-symmetrical bisignate feature with an overall negative Cotton effect, accompanied by a bathochromically shifted monosignate band. This pattern has a high resemblance with the characteristic “double-hump” signature arising from coupling between a Coulombic Frenkel exciton with H-aggregate character and an ICT state,[1–3, 86] as previously reported for chiral anilino squaraines in solution and thermally annealed thin films (Chapter 3 and 4). According to exciton chirality rules, this suggests a left-handed helical (H-type) arrangement of the chromophores and their transition dipole moments within the formed aggregate.[86, 90, 124, 125]

A comparable observation was made for **(*S*,*S*)-2mb-HDSQ** (Figure H.11), where the even longer alkyl chains led to pronounced precipitation at only 10% water content, evident from changes in UV/Vis absorbance intensity. At 2% water and even more dominantly at 10%, the same hypsochromically shifted, non-symmetrical bisignate signal with an overall negative Cotton effect and a bathochromically shifted monosignate band was detected. Compared to **(*S*,*S*)-2mb-DSQ**, the spectral splitting was smaller, indicating a similar left-handed helical H-type arrangement but with a slightly different packing geometry and/or altered ICT or Coulombic coupling strength.

For **(*S*,*S*)-2mb-SQPE** (Figure H.12), an ellipticity signal was observed only at 20% water in methanol, despite no detectable changes in the UV/Vis spectra at this concentration. A similar spectral pattern as for **(*S*,*S*)-2mb-DSQ** and **(*S*,*S*)-2mb-HDSQ** was observed, although the proposed ICT contribution was at the level of instrumental noise.

Overall, none of the four squaraines in this new series exhibited pronounced aggregation behaviour in solution. When ellipticity signals were detected, they consistently indicated a left-handed helical (H-type) arrangement of the chromophores within the aggregates.

Thermally Annealed Thin Films:

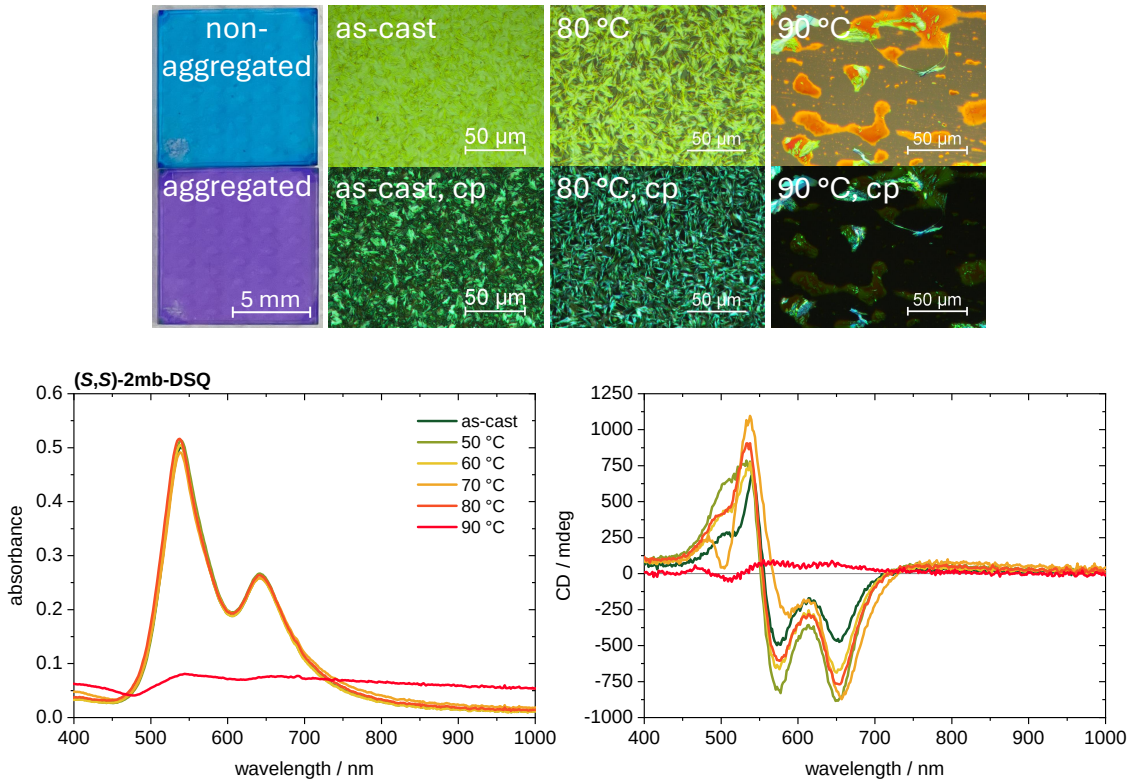


Figure 10.13: UV/Vis absorbance (bottom left) and corresponding CD spectra (bottom right) of **(*S*,*S*)-2mb-DSQ**, spin-coated from a chloroform solution under the same conditions and thermally annealed at various temperatures for 30 minutes. The legend indicates the annealing temperature and applies to all plots. Top: Picture of thin film samples before and after annealing and optical microscopy images of spin-coated thin films with corresponding images between crossed polarizers at indicated temperatures.

After the preliminary testing of the aggregation behaviour of the new dyes, their actual aggregation behaviour in the solid state was investigated. Therefore, a series of solution-processed thin films were prepared via spin coating under same conditions, followed by thermal annealing at various temperatures for 30 minutes. Subsequent measurements of the absolute absorbance[c] were carried out, and Mueller matrix ellipsometry was employed to accurately determine the circular dichroism (CD) of the samples. A detailed fabrication procedure is given in Chapter 13.

Starting with **(*S*,*S*)-2mb-DSQ**, the UV/Vis absorbance and corresponding CD spectra of thin films thermally annealed at different temperatures are shown in Figure 10.13. As expected from the early stage aggregation experiments in solution, **(*S*,*S*)-2mb-DSQ** behaved similar to other chiral (e.g., **(*S*,*S*)-nOCi-SQ** – Chapter 3, **(*S*,*S*)-nOnCi-SQ** or **(*S*,*S*)-nCi-SQIB** – Chapter 4) and non-chiral *n*-alkyl anilino squaraines.[85] Thereby featuring the characteristic double-hump spectral features in the UV/Vis absorbance spectra at

[c] As mentioned in Chapter 1 – Introduction, please note that absorption $A \neq$ absorbance Abs; with $Abs = -log(T)$.

538 and 642 nm. This was the case for all tested temperatures from the as-cast thin film up to 80 °C with negligible changes in the intensities of the two absorbance maxima. As seen from the pictures of the thin films (Figure 10.13, top), a clear color change is visible between the non-aggregated (blue) and aggregated (purple) samples. This aggregation also occurs over time as depicted in Appendix H.3.2 – Figure H.15. Over 80 °C, visible discoloration of the sample could be observed in combination with a drastically decrease in the absorbance intensity. Thus, no additional UV/Vis absorbance measurements were performed over 90 °C. Optical microscopy images (Figure 10.13, top) of the spin-coated samples (as-cast and thermally annealed at 80 °C) revealed a highly crystalline and micro-structured thin film. The images of the samples annealed at 90 °C clearly exhibited signs of melting and re-solidifying of the material. However, no signs of actual decomposition were observed.

Unlike the ellipticity spectra in solution, the thin film CD spectra (Figure 10.13, bottom right) actually exhibits defined signals. Also here, a similar behavior compared to **(*S*,*S*)-nOCi-SQ**, **(*S*,*S*)-nOnCi-SQ** and **(*S*,*S*)-nCi-SQIB** was observed. Starting with the as-cast thin film, the expected hypsochromically shifted bisignate signal with a zero-crossing at 552 nm and an overall negative Cotton effect, along with a slightly bathochromically shifted monosignate signal with a maximum at 651 nm and a negative cotton effect as well was observed. Both signals increased in intensity upon annealing, accomplished by the appearance of different low-intensity shoulders, indicating the presence of different arrangements of the chromophores. However, the characteristic double spectral feature persisted under all annealing conditions with only minor shifts of the minima/maxima. At 80 °C, a nicest looking bisignate and monosignate signal was obtained, even though a – as well as in all other annealing temperatures observed – shoulder at around 495 nm was visible. In comparison to the as-cast thin film the ratio of the two signals shifted towards a more intense monosignate signal.

Given the slightly higher absorbance intensity, the well-defined spectral shape in both the UV/Vis absorbance and CD spectra, CD values of approximately +900 to -700 mdeg and the formation of a continuous, highly microcrystalline thin-film morphology, 80 °C was selected as the optimal annealing temperature for **(*S*,*S*)-2mb-DSQ**.

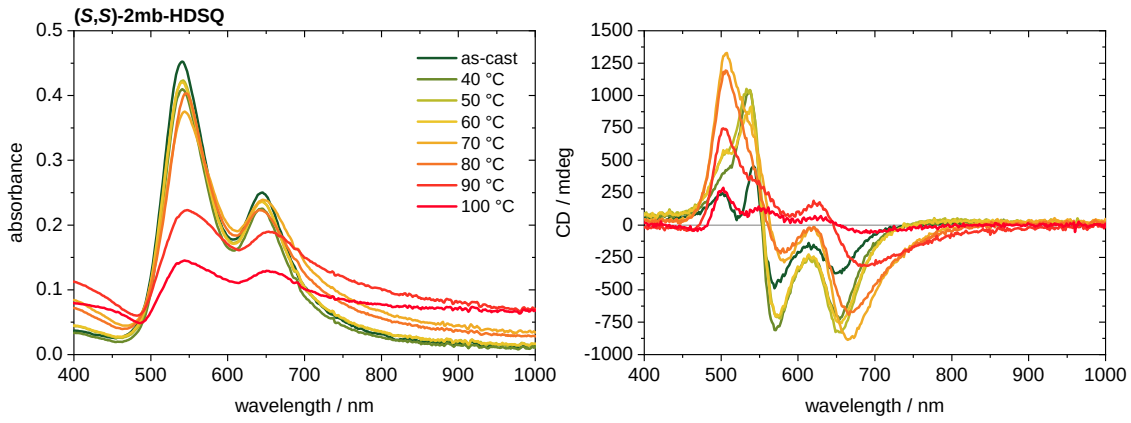


Figure 10.14: UV/Vis absorbance (left) and corresponding CD spectra (right) of **(*S*,*S*)-2mb-HDSQ**, spin-coated from a chloroform solution under the same conditions and thermally annealed at various temperatures for 30 minutes. The legend indicates the annealing temperature and applies to all plots.

The long alkyl-chain analogue **(*S*,*S*)-2mb-HDSQ** behaves, as expected, almost identically to **(*S*,*S*)-2mb-DSQ**, and thus, similarly to other chiral and non-chiral *n*-alkyl anilino squaraines in the UV/Vis absorbance spectrum (Figure 10.14, left). For all tested annealing temperatures up to 80 °C, the characteristic double-hump spectral features at approximately 540 nm and 645 nm were observed. The as-cast thin film exhibited the highest overall absorbance intensity, while films annealed at other temperatures showed only minor variations in the relative intensities of the two maxima, with no clear trend. Annealing at 90 °C or 100 °C caused a pronounced decrease in absorbance intensity accompanied by visible decolouration of the films. Therefore, no further measurements were performed over these temperatures.

The CD spectra of **(*S*,*S*)-2mb-HDSQ** are shown in Figure 10.14 (right). While the UV/Vis absorbance spectra are nearly identical to those of **(*S*,*S*)-2mb-DSQ**, the CD spectra differ markedly. In the as-cast sample, in addition to the expected hypsochromically shifted bisignate signal with a zero-crossing at 552 nm and an overall negative Cotton effect, and a slightly bathochromically shifted monosignate signal with a maximum at around 650 nm (also with a negative Cotton effect), an additional monosignate band with a maximum at 500 nm and a positive Cotton effect is observed. This feature appeared only as a weak shoulder in **(*S*,*S*)-2mb-DSQ** but is more distinctly separated here. Upon annealing up to 60 °C, the spectra resemble those of **(*S*,*S*)-2mb-DSQ**, with the 500 nm feature only appearing as a shoulder. At 70 °C and 80 °C, however, this monosignate band becomes significantly more intense and dominates the CD spectrum, producing a highly asymmetric bisignate profile with only a small residual negative contribution from the overlapping signals. Annealing at 90 °C or 100 °C led as for the UV/Vis absorbance spectra to a pronounced loss of intensity and distortion of the spectral shape.

Following the narrative of this thesis, that the characteristic double-hump spectral features originates from coupling between a Coulombic Frenkel exciton with H-aggregate character (bisignate signal) with an ICT state (monosignate signal), the spectral signatures of **(*S*,*S*)-2mb-DSQ** and **(*S*,*S*)-2mb-HDSQ** can be assigned accordingly. Furthermore, using the exciton chirality method, the overall negative Cotton effect combined with the hypsochromic shift relative to the monomer absorbance, indicates that both squaraines adopt a H-type, left-handed helical arrangement. It remains unclear, however, what the origin of the additional monosignate signal around 500 nm, particularly pronounced for **(*S*,*S*)-2mb-HDSQ**, might be. Interestingly, compared to the citronellyl-functionalized chiral squaraines from Chapter 3 and 4, the overall Cotton effect actually inverts. Whether this observation arises from the positional shift of the stereogenic centre – e.g., an odd-even effect – from the third carbon atom (citronellyl) to the second carbon atom (2-methylbutyl) of the chiral side chain, or from other factors, cannot be conclusively determined based solely on the two investigated chiral side chains. However, the absolute CD values are in the same order of magnitude as those of the two presented dyes.

In comparison to **(*S*,*S*)-2mb-DSQ** and **(*S*,*S*)-2mb-HDSQ**, the chiral **SQIB** analogue **(*S*,*S*)-2mb-SQIB** exhibits a completely different behaviour in its UV/Vis absorbance and CD spectra (Figure 10.15, bottom). In the as-cast state and after thermal annealing up to 90 °C, the UV/Vis spectra display a broad band with a maximum at 700 nm and a shoulder at 620 nm, indicative of an amorphous film – i.e. no noticeable aggregation/crystallization is initiated. At 120 °C, two distinct maxima emerge at 650 nm and 730 nm, which decrease in intensity upon annealing at 180 °C. Further heating to 210 °C produces a pronounced spectral change to a broad absorbance band peaking around 670 nm. In addition to the very similar single-crystal X-ray diffraction (SC-XRD) data, this behaviour closely resembles that of **SQIB** in solution-processed thin films.[67] Optical microscopy images between crossed polarizers of

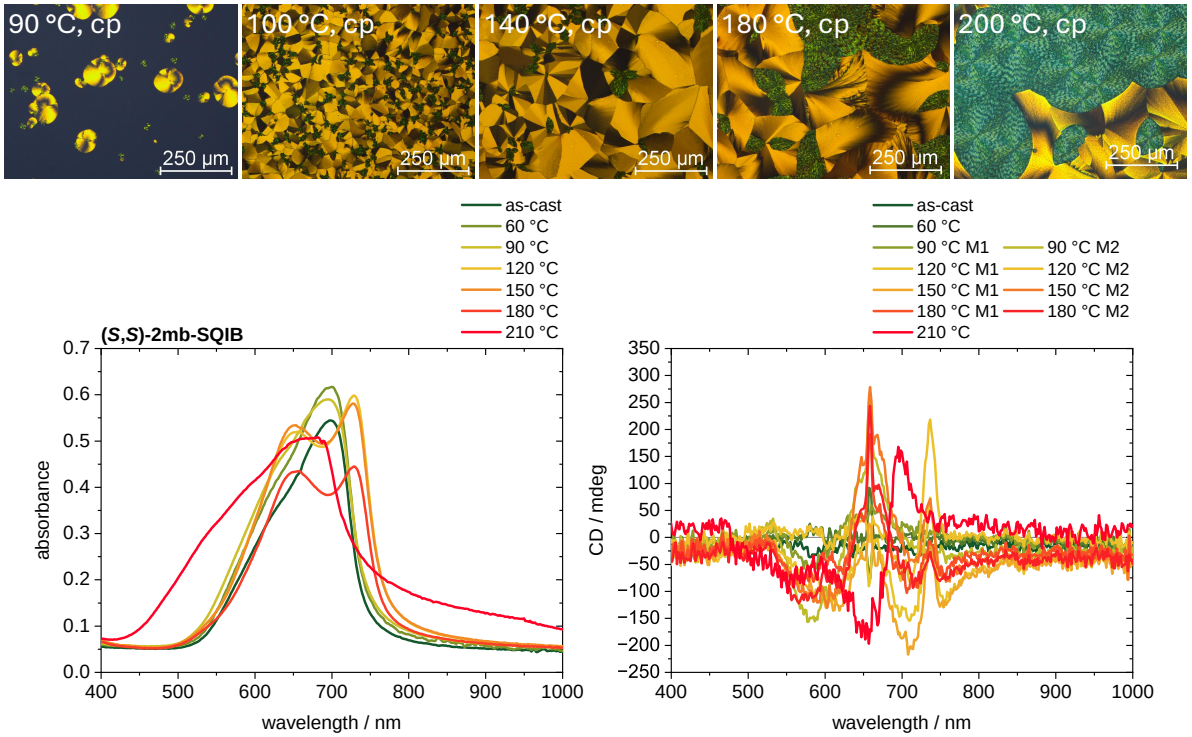


Figure 10.15: UV/Vis absorbance (bottom left) and corresponding CD spectra (bottom right) of **(*S*,*S*)-2mb-SQIB**, spin-coated from a chloroform solution under the same conditions and thermally annealed at various temperatures for 30 minutes. M1/M2 indicates sample which where measured twice at approximately the same position, with a 90° rotation between measurements. Top: Optical microscopy images between crossed polarizers of spin-coated thin films at indicated temperatures.

spin-coated films (Figure 10.15, top) provide further insight. Two distinct polymorphs can be identified: golden platelets and green microcrystalline regions, visually identical to **SQIB**. Using **SQIB** as reference substance, the golden platelets are likely the orthorhombic polymorph (structure not yet determined), while the green microcrystalline regions correspond to the known monoclinic polymorph (chiral $P2_1$ space group). For **SQIB**, the orthorhombic polymorph produces two absorbance maxima as well, matching the observations of **(*S*,*S*)-2mb-SQIB** at 120 °C with 650 nm and 730 nm. This strongly supports the presence of an orthorhombic polymorph in **(*S*,*S*)-2mb-SQIB**. I therefore propose that the UV/Vis spectra of films annealed between 120 °C and 180 °C are dominated by the orthorhombic polymorph, whereas the spectrum at 210 °C is dominated by the monoclinic form. This hypothesis is partially consistent with **SQIB**, where the monoclinic polymorph was predominant at lower temperatures, e.g., 90 °C.

However, from the optical microscopy images between crossed polarizers two other conclusion can be drawn. On the one hand, it is evident that thermal annealing at 90 °C does not initiate noticeable crystallisation of the film. On the other hand, regardless of the annealing temperature, a mixture of the two polymorphs is always obtained, as evidenced by the observation of golden platelets and greenish microcrystalline regions. While temperature appears to influence the ratio of the two polymorphs (as for **SQIB**),[67] selective formation of a single polymorph was not achieved. Given the macroscopic beam size

of the instrument used (J.A. Woollam M2000-DI ellipsometer, beam diameter approximately 2 - 3 mm), the measured spectra inevitably contain contributions from both polymorphs. This overlap also explains why the corresponding CD spectra (Figure 10.15, bottom right) are difficult – if not impossible – to interpret, especially with the background of expected Davydov splitting. Even repeated measurements of the same film yield different spectra (M1 and M2), as particuallry highlighted in Figure H.16. Without specialized equipment such as an imaging ellipsometer with an appropriately small beam size, separation of the two contributions is not feasible.

For this reason, the CD spectra will not be discussed further. It should be noted, however, that the overall CD intensities do not initially appear particularly strong, possibly due to cancellation effects

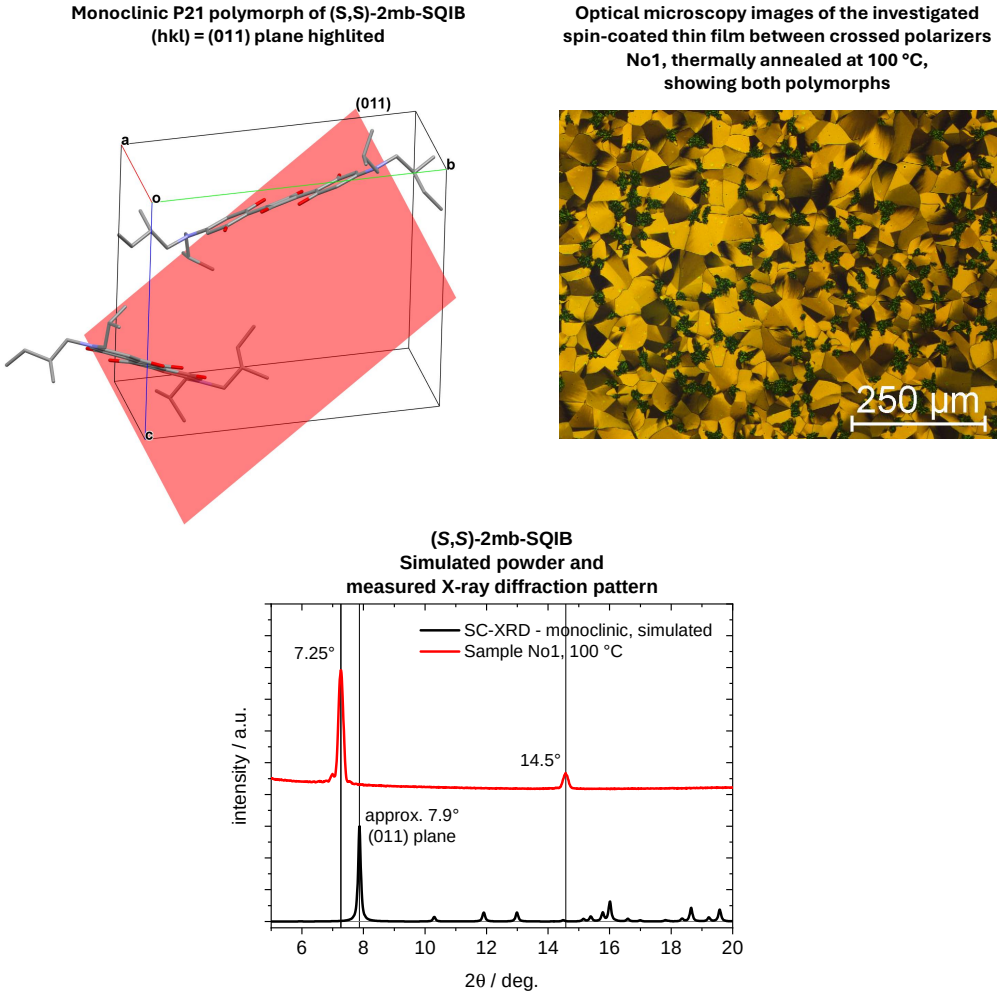


Figure 10.16: Top left: Crystal structure of **(*S*,*S*)-2mb-SQIB** with the plane for the Miller index (*hkl*) = (011) depicted in red. Top right: Optical microscopy images of the investigated spin-coated thin film (No1, thermally annealed at 100 °C) between crossed polarizers, showing two different polymorphs. Bottom: Simulated powder diffraction pattern (in black) obtained from the monoclinic single crystal structure and the XRD measurement (in red) of the thin film. Measurements were performed in collaboration with apl.-Prof. Dr. Manuela Schiek (Johannes Kepler University Linz, Austria) and Anmol Andotra (group of Prof. Roland Resel, Graz University of Technology, Austria).

between the two polymorphs or to microtexturing of the film. However, obtaining spatially resolved data via imaging ellipsometry, in combination with SC-XRD structure of the orthorhombic polymorph, would enable determination of both the dielectric tensor and the chiral tensor of this material.

To gain molecular-level insights into the thin-film morphology, XRD measurements were performed in collaboration with Anmol Andotra (group of Prof. Roland Resel, Graz University of Technology). Six samples were prepared following the normal procedure described in Chapter 13 with different annealing temperatures (90 °C, 100 °C, 120 °C, 140 °C, 160 °C and short heating at 180 °C). The measurements were carried out using a PANalytical Empyrean diffractometer. The primary side was equipped with a sealed copper tube and a multilayer mirror for monochromatization (wavelength = 1.5418 Å) to produce a parallel beam. The secondary side has an anti-scatter slit, a 0.02 rad Soller slit and a PANalytical PIXcel 3D detector operating as a point detector.

Since all six samples exhibited the same diffraction pattern, it was decided to show and describe only one representative example here – thermally annealed at 100 °C. An optical microscopy image of the investigated spin-coated thin film between crossed polarizers is presented in Figure 10.16 (top right). Figure 10.16 (top left) shows the monoclinic unit cell of **(*S*,*S*)-2mb-SQIB**, with the (hkl) = (011) plane is highlighted in red. This plane was selected based on the reference compound **SQIB**, for which this plane is observed in XRD measurements of the monoclinic phase, as well as the powder diffraction pattern was based on SC-XRD data of **(*S*,*S*)-2mb-SQIB**. The assignment of Miller planes and calculated powder diffraction pattern was based on SC-XRD data using Mercury 3.10.3 (build 206425). The simulated pattern (Figure 10.16, bottom, black line) shows a pronounced peak at approximately 7.9°, attributed to the (011) reflection – comparable to the (011) reflection of monoclinic **SQIB** at 8.1°.[67] Several additional, low-intensity peaks are also present in the simulated pattern. In contrast, the experimentally measured XRD pattern of the thin films (Figure 10.16, bottom, red line) differs considerably from the simulated SC-XRD-derived pattern. In all six samples, regardless of annealing temperature, a new phase was identified. The primary diffraction peak for this phase appears at 2θ = 7.25°, corresponding to an interplanar spacing d_{hkl} = 12.128 Å. A second-order reflection is observed at 2θ = 14.5°, with a corresponding d_{hkl} value of 12.128/2 = 6.064 Å, confirming the presence of this phase. According to Bragg's law, a shift to smaller 2θ values indicates an increased lattice spacing and, consequently, a looser molecular packing. Using **SQIB** as reference substance (again), this suggests that the measured XRD pattern originates from the orthorhombic polymorph. For **SQIB**, the monoclinic peak is found at 8.1° (for (hkl) = (011), $P2_1/c$) with much lower intensity than the orthorhombic peak at 7.6° (for (hkl) = (110), *Pbcn*). The predominance of the orthorhombic polymorph in optical microscopy images (Figure 10.16, top right) and in the UV/Vis absorbance spectra (Figure 10.15) for the investigated annealing temperatures supports this assignment. Further evidence comes from the observation of the higher-order (220) reflection in the XRD measurements – seen for **SQIB** only in the orthorhombic phase – which is also present for **(*S*,*S*)-2mb-SQIB**. While the orthorhombic form can be detected relatively easily, the monoclinic polymorph has proven far more challenging to identify in XRD measurements, which remains an ongoing task.

[d] Please note that the MSE reflects the quality of the fit between the experimental and simulated data, rather than the intrinsic variation or dispersion of the actual layer thicknesses. Its magnitude depends on many factors, including surface roughness and model complexity. Although it is difficult to define absolute thresholds for "small" or "large" values, the literature[34, 85, 95] generally considers MSE values below 10 as an excellent fit, while values below 20 are still regarded as acceptable.

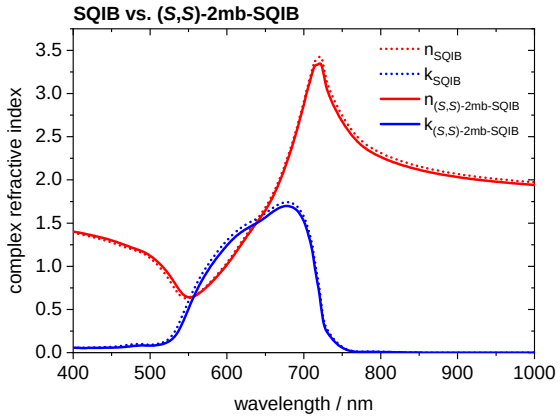


Figure 10.17: Isotropic optical constants of as-cast spin coated thin films of **SQIB** (dotted line, kindly provided by apl.-Prof. Dr. Manuela Schiek, Johannes Kepler University Linz, Austria) and **(*S*,*S*)-2mb-SQIB** (solid line). Calculations based on a multisample analysis in *CompleteEASE 6* using B-spline function. The refractive index is denoted as *n* and the extinction coefficient is denoted as *k*. The mean-squared error (MSE)[d] for the fits was calculated to: **SQIB** → 5.94 and for **(*S*,*S*)-2mb-SQIB** → 5.85. The ellipsometric fitting process determined the layer thicknesses of all samples, yielding values ranging from 22 to 42 nm.

The high similarity of **(*S*,*S*)-2mb-SQIB** to the non-chiral **SQIB** can be also seen if looked at the optical constants, presented in Figure 10.17. Since integral (macroscopic) standard ellipsometry only works for amorphous/isotropic layers and uniaxial anisotropic layers, i.e. they may have different properties perpendicular to the layer, but they must be uniform throughout the layer. This is only fulfilled for non-annealed samples of the chiral **(*S*,*S*)-2mb-SQIB**, however, not for the microtextured samples – even if they would only one consist of one polymorph. Therefore, the optical properties of only non-annealed thim film samples of **(*S*,*S*)-2mb-SQIB** and **SQIB** were analyzed, using variable angle spectroscopic ellipsometry (VASE). For this a series of thin films of the two dyes were produced on UV-transparent glass with varying thickness, ranging from approximately 22 to 42 nm. Note that the simple absorbance spectrum (Abs), calculated from the transmission (T) spectrum with $Abs = -log(T)$ does not represent the extinction coefficient in a simple way. Since the measured transmission does include contributions from absorption (A), reflection (R) and scattering (S), defined as $T = 1–A–R–S$. Therefore, a multisample analysis in *CompleteEASE 6* using B-spline function was used to yield the final optical constants. The data used included VASE measured in reflection as well as normal incidence transmission intensity data. Furthermore, because the samples had not undergone thermal annealing, surface-roughness modelling was not required.

The obtained isotropic complex refractive index ("optical constants") of **(*S*,*S*)-2mb-SQIB** closely matches, in both magnitude and spectral shape, that of the non-chiral **SQIB** (data kindly provided by apl.-Prof. Dr. Manuela Schiek, Johannes Kepler University Linz, Austria), thereby reproduces the measured absorbance spectra well (ref. Figure 10.15). The extinction coefficients *k*[e] are remarkably high – on the order of 1.7 for both dyes – reflecting their exceptionally strong interaction with light and consistent with values typically reported for squaraines.[1, 34, 85] The spectral shape corresponds to

[e] Please note that the optical extinction coefficient *k* is defined as the imaginary component of the complex refractive index $\tilde{n} = n + ik$, and should not be confused with the molar extinction coefficient ϵ commonly used in the context of the Lambert-Beer law.

the typical signature of non-aggregated squaraines,[1, 19, 67, 139, 140] consistent with the absence of any distinct molecular aggregation, as indicated by the lack of any signals in the CD spectra of the as-cast sample. This overall shows that, in the isotropic thin film, the molecular or aggregate organization is random.

Overall, **(*S*,*S*)-2mb-SQIB** is a highly interesting dye, exhibiting properties closely matching those of the structurally related **SQIB** molecule. While the presumably orthorhombic form can be detected relatively easily, UV/Vis absorbance, CD, and thin film XRD measurements of the monoclinic polymorph in thin films (even though a SC-XRD structure was obtained) have proven far more challenging and remain an ongoing task. However, as it was not possible to reliably reproduce a single polymorph and consistently achieve identical characteristics, a different dye was ultimately selected for the OPV application, which is presented in the next section.

10.5 From Vision to Prototype: Final Device Application

To finalize this chapter, one newly synthesised squaraine dye was incorporated into an organic photovoltaic (OPV) device in collaboration with Otgonbayar Erdene-Ochir (group of Prof. Klaus Meerholz, University of Cologne) within the framework of TIDE. The first step was to select the most suitable candidate from three options: **(*S*,*S*)-2mb-SQIB**, **(*S*,*S*)-2mb-DSQ** or **(*S*,*S*)-2mb-HDSQ**. Due to the previously discussed challenges in consistently achieving identical Thin film characteristics, **(*S*,*S*)-2mb-SQIB** was ruled out. A direct comparison between **(*S*,*S*)-2mb-HDSQ** and **(*S*,*S*)-2mb-DSQ** clearly indicated that the latter was the better option. Not only does **(*S*,*S*)-2mb-DSQ** exhibiting well-defined UV/Vis absorbance and CD spectra (Figure 10.13) that align perfectly with the findings and narrative of this thesis, but also forms highly crystalline, micro-structured thin films. The latter can especially enhance charge transport within the active layer. Furthermore, **(*S*,*S*)-2mb-DSQ** has an optimal annealing temperature of only 80 °C, which is considerably low for squaraines and much lower than that of previously tested **ProSQs**.[40, 98]

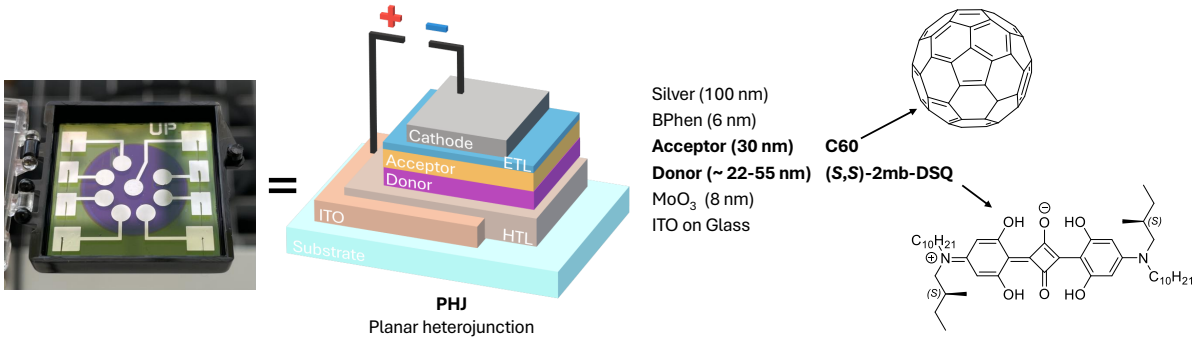


Figure 10.18: Illustration and actual picture of the fabricated device based on the newly synthesised dye **(*S*,*S*)-2mb-DSQ** as the donor material and C60-fullerene as the acceptor material in a planar heterojunction device architecture. The electron-transporting layer (ETL) consists of BPhen (bathophenanthroline) and the hole-transporting layer (HTL) consists of MoO_3 (molybdenum trioxide). Device fabrication performed in collaboration with Otgonbayar Erdene-Ochir (group of Prof. Klaus Meerholz, University of Cologne).

For the actual application, a series of OPVs were fabricated with three different squaraine layer thicknesses (each thickness several times). The chosen device architecture (see Section 1.4) was a planar heterojunction (PHJ), consists of two discrete layers – one donor followed by one acceptor layer. The key advantage of this architecture is that it allows (precise) control over the morphological and aggregation behavior of the active layer through independent annealing procedures. Although PHJ devices typically exhibit lower efficiencies than BHJ devices due to recombination of electron-hole pairs – where only excitons generated close to the donor-acceptor interface can dissociate into free charge carriers – efficiency was not the primary concern in this work. Since our overall goal was to develop a circular dichroic photodetector, capable not only of responding to a specific wavelengths of light, but also to differentiate between left- and right-handed CPL, thereby operating without external optical elements or applied voltage bias, low efficiency is not as important as controlling aggregation. In fact, since such photodiodes have only to detect the presence or absence of light (alongside the polarization state) and not to generate energy, efficiency is really a secondary aspect. Moreover, mixing donor and acceptor materials – as in a bulk heterojunction (BHJ) – can affect aggregation properties and may lead to dewetting[f] or even phase separation of the donor and acceptor domains. The PHJ architecture avoids these issues, making it the preferred choice for this application.

An illustration of the fabricated device is shown in Figure 10.18. As basis a indium tin oxide (ITO)-coated glass substrate 1 × 1 inch (1 inch = 2.54 cm) was used. Onto this substrate, first an 8 nm thick HTL – in this case MoO_3 (molybdenum trioxide) – was deposited via physical vapor deposition (PVD). All relevant physical vapor deposition (PVD) parameters are listed in Appendix H.4 – Table H.1. An additional series combining 8 nm MoO_3 with a subsequent 6 nm layer of QUPD[g] was fabricated, however, this configuration did not yield significant improvements and will therefore not further discussed. On top of the HTL, **(*S*,*S*)-2mb-DSQ** was spin-coated from 180 µL of a chloroform spin-on solution (6 mg/mL). Three different film thicknesses were obtained by varying the spin-coating parameters: thick = 1500 rpm, 750 rpm/s (∅ 45–55 nm); medium = 3000 rpm, 3000 rpm/s (∅ 35–40 nm) and thin = 6000 rpm, 6000 rpm/s (∅ 22–26 nm). Subsequent thermal annealing at 80 °C for 30 min induced chiral aggregation in the thin film, visible by a color change from blue to lila (Figure 10.13). The acceptor material, C_{60} fullerene, was then deposited as a 30 nm layer via PVD, followed by a 6 nm layer of BPhen (bathophenanthroline) serving as the ETL, also applied via PVD. Additional tests using calcium as the ETL failed due to degradation issues. Finally, shadow masks (allowing for complex structures on the surface) were used to pattern multiple silver electrodes onto the device prototype with a thickness of 100 nm. This layer served as the back electrode (cathode) and was applied in this pattern to allow multiple data points to be collected from a single device. Using this procedure, several PHJ-OPV devices were fabricated. In the following, one representative device from each squaraine layer thickness will be discussed in detail.

First, it was checked whether the squaraine layer remained aggregated in the desired manner – i.e. as observed in the spin-coated and thermally annealed thin film (Figure 10.13). For this, as with the other thin films, the UV/Vis absorbance and corresponding CD spectra of the final **(*S*,*S*)-2mb-DSQ** device were measured, shown in Figure 10.19. The macroscopic beam size of approximately 2 - 3 mm of the instrument used (J.A. Woollam M2000-XI variable-angle spectroscopic ellipsometer), was small enough

[f] Dewetting describes the process by which a fluid retracts from a non-wettable surface that it was previously forced to cover.

[g] *N*4,*N*4'-Bis(4-(6-((3-ethyloxetan-3-yl)methoxy)hexyloxy)phenyl)-*N*4,*N*4'-bis(4-methoxyphenyl)biphenyl-4,4'-diamine

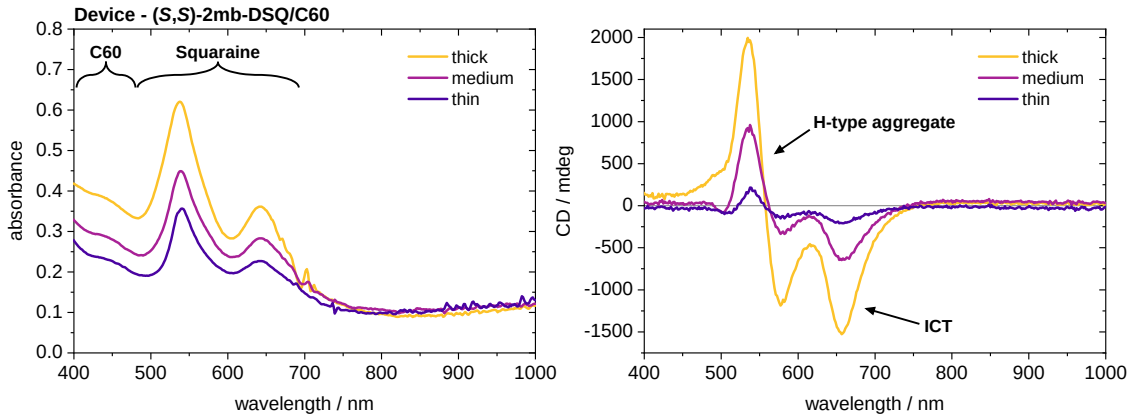
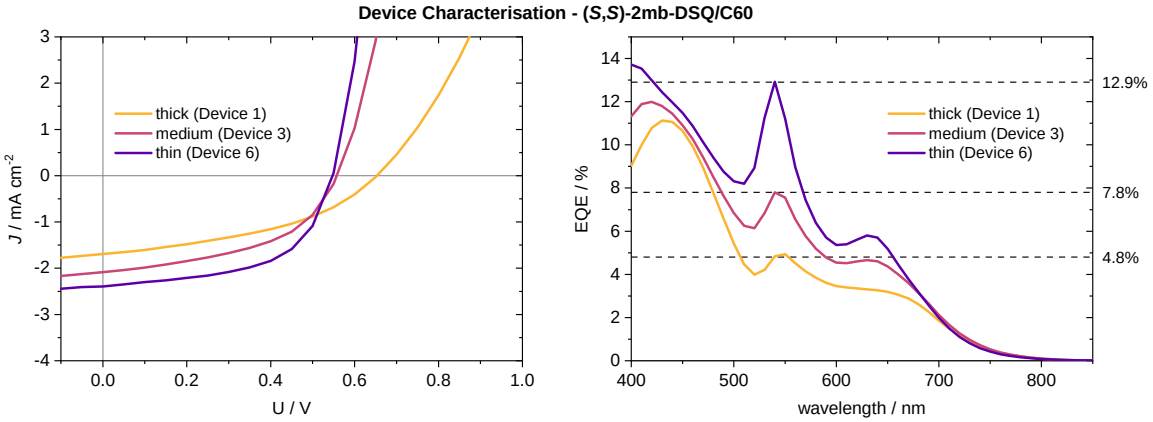


Figure 10.19: UV/Vis absorbance (left) and corresponding CD spectra (right) of final **(*S*,*S*)-2mb-DSQ** based PHJ-OPV with different donor layer thickness, fabricated as described in the main text. Measurement were done at a light-permeable – i.e. at a spot where no silver was deposited (ref. purple areas in picture fo the device in Figure 10.18).

to pass unrestricted between the deposited silver electrodes, but still passing though all other layers of the device. For this, the measurements took place at a purple areas seen in picture of the device (Figure 10.18).As clearly seen in Figure 10.19, the aggregated **(*S*,*S*)-2mb-DSQ** layer survived indeed the device fabrication process without noticeable changes. This is evidenced by the characteristic double-humped absorbance spectrum at 538 nm and 642 nm, together with the corresponding hypsochromically shifted bisignate CD signal with a zero-crossing at around 560 nm and an overall negative Cotton effect, as well as a slightly bathochromically shifted monosignate signal with a maximum at 656 nm and a negative Cotton effect. This spectral pattern originates from coupling between a Coulombic Frenkel exciton and an ICT state, as discussed and proven extensively in this thesis. Compared to the pristine thin film, the zero-crossing of the bisignate signal and the maximum of the monosignate signal are slightly shifted (552 → 560 nm and 651 → 656 nm), which is attributed to the presence of other device components. These, but most notably the C_{60} fullerene influence is visible in the spectra below 500 nm. Additional features, such as the non-zero baseline, the slight increase in absorbance over 800 nm and the slightly worse signal-to-noise ratio (S/N ratio), are likewise attributed to these components. Nevertheless, **(*S*,*S*)-2mb-DSQ** retained the desired chiral aggregation properties even within the complete device structure.

Next, the so fabricated devices were tested for their photovoltaic characteristics. For more information on the general characterization procedures for photovoltaic (PV) devices, please refer to Appendix H.4. For this, current density-voltage (*J*-*V*) curves under unpolarised, simulated sunlight (*AM 1.5 G*) were recorded, along with external quantum efficiency (EQE) measurements, both shown in Figure 10.20. From these data, the device performance parameters were calculated and are presented in the table below the figure. Overall, device performance was found to depend on the thickness of the squaraine donor layer. Thereby, the open-circuit voltage (V_{OC}) increased as the layer thickness decreased, while the short-circuit current density (J_{SC}) decreased with decreasing thickness. The increase in open-circuit voltage (V_{OC}) can be attributed to reduced recombination and voltage losses in thinner layers, as well as minimised leakage and shunt pathways. The jump from 0.55 V (thick) to



Thickness	V_{OC} / V	J_{SC} / mAcm^{-2}	FF / %	PCE / %
thick (Device 1)	0.55 ± 0.0068	2.39 ± 0.0180	56 ± 0.0001	0.74 ± 0.0036
medium (Device 3)	0.56 ± 0.0051	2.08 ± 0.0653	49 ± 0.0030	0.57 ± 0.0182
thin (Device 6)	0.65 ± 0.0126	1.69 ± 0.0459	42 ± 0.0152	0.47 ± 0.0370

Figure 10.20: Top: Current density-voltage (J-V) curves of a **(*S*,*S*)-2mb-DSQ** based PHJ-OPV under illumination (left) and the corresponding external quantum efficiency (EQE, left) for three different thicknesses. Bottom: Calculated device performance characteristics from the J-V diagram as well as the equations given in Appendix H.4.

0.65 V (thin) is substantial, indicating recombination-limited open-circuit voltage (V_{OC}) in thicker films. The decrease in short-circuit current density (J_{SC}) with decreasing thickness can be explained by lower optical absorption and, consequently, fewer generated excitons/charge carriers. The fill factor (FF) was calculated to range between 56% and 42%, decreasing with thinner layers. Notably, a fill factor of around 56% is remarkably high for solution-processed, squaraine-based photodiodes.[35, 40, 42, 98] Also power conversion efficiency (PCE) peaked for the thick-layer device, where the thick device's higher short-circuit current density (J_{SC}) and fill factor (FF) values more than compensated for the lower open-circuit voltage (V_{OC}), resulting in the best overall efficiency.

In Figure 10.20 (top, right), the external quantum efficiency (EQE) was measured across the entire absorbance region. The spectra were recorded without any background illumination and under short-circuit conditions. Notably, the EQE spectrum closely resembles the UV/Vis absorbance spectrum (Figure 10.19), exhibiting the characteristic double-humped feature at approximately 540 nm and 640 nm. The slight misalignment with the absorbance spectrum is attributed to the limited resolution of the measurement setup, which operated in just 10 nm steps. The EQE values range from 4.8% to 12.9%, increasing as the squaraine layer gets thinner. Since the EQE – in simple terms – does not account for the number of photons absorbed, but rather how effectively the device uses those that are absorbed. In combination with that thinner layers have most excitons within a diffusion length of the donor-acceptor interface, leads to a higher proportion being harvested, and thus, resulting in higher EQE values. In thicker layers, many excitons are generated far from the interface and recombine before dissociation, a typical limitation of PHJs.

Compared to other devices, and specifically to the one presented in 2019 by *Schiek* et al. (see

Introduction – Section 1.4.3),[98] the EQE values obtained here are actually lower than the reported once. However, given the primary purpose of this device – to respond not only to specific wavelengths but also to distinguish between left- and right-handed circularly polarized light (CPL) without the need for external optical elements or an applied voltage bias – makes these rather low values of the **(*S*,*S*)-2mb-DSQ**-based OPV in comparison to other organic devices secondary when used as photodetectors and not for light-harvesting purposes. In such devices, it is only important to distinguish between ON and OFF state according to presence or absence of light. In addition, this was just an preliminary application without any significant work done on device optimization. It is reasonable to expect that, with sufficient fine-tuning, the overall performance could be substantially improved, as demonstrated for the device reported by *Schiek* et al. from 2017 → 2019.[40, 98] Thus, the most important takeaway is the preservation of the spectral signature from the double-humped feature, resulting in good spectral overlap between the maximum absorbance and, most importantly, the CD response (Figure 10.19, right) with the photocurrent response, i.e. the EQE.

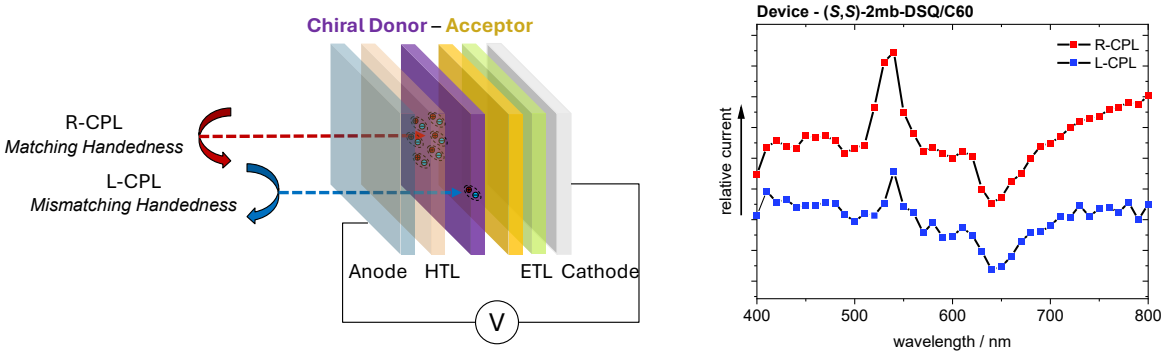


Figure 10.21: Preliminary data from chirality-resolved photocurrent measurements of a **(*S*,*S*)-2mb-DSQ**-based PHJ-OPV device with a thin donor layer thickness (Device 6). Please note that the number of generated excitons depicted in the left-hand illustration is intentionally exaggerated for visualisation purposes. Performed in collaboration with Otgonbayar Erdene-Ochir (group of Prof. Klaus Meerholz, University of Cologne).

As the final experiment, one device was tested to determine whether the observed optical dissymmetry could be translated into a photocurrent dissymmetry. Due to the highest EQE value, device 6 with the thinnest **(*S*,*S*)-2mb-DSQ** donor layer was selected. It should be emphasised that the following results represent preliminary data obtained from a single device and were conducted only as a proof of concept. As noted above, no significant optimization of the device or measurement setup has been done. In this experiment, the photocurrent was measured as a function of wavelength under illumination with left- and right-handed CPL. The CPL was generated using a standard spectropolarimeter setup with a photoelastic modulator (PEM) and a lock-in amplifier.

The resulting spectra (Figure 10.21) clearly indicated a distinction between left- and right-handed CPL. Relative to each other, the device (based on the (*S*,*S*)-enantiomer) preferentially absorbed the right-handed CPL (R-CPL), resulting in a higher measured current that for the left-handed CPL (L-CPL), thus demonstrating a photocurrent dissymmetry of the device. This means that more charge carriers are generated when the preferential/matching CPL interacts with the active layer compared to the mismatching polarisation, as also illustrated in Figure 10.21 (left). However, to provide a more accurate comparison, the optical and photocurrent dissymmetry factors should be considered. This was beyond

the scope of this thesis, but will be continued by Otgonbayar Erdene-Ochir (group of Prof. Klaus Meerholz, University of Cologne). It should also be considered that incomplete absorption of light can lead to back-reflection at the silver electrode, causing a handedness-reversion. This effect can introduce opposite contributions to photocurrent generation within the CD-active spectral range, potentially compensating (or even reversing) the polarization-selective response.[159]

However, even though this chirality-resolved photocurrent experiment must be considered preliminary, the obtained data clearly shows the translation of optical dissymmetry – evident by the strong excitonic CD effect – into a relative photocurrent dissymmetry, which allows for the direct detection of CPL.

In summary, this chapter follows the development of an initial molecular design concept, beneficial for the application in optoelectronic devices, all the way to the fabrication and testing of the functional device. Starting with the synthetic approach and their challenges, a suitable route for the preparation of 2-methylbutyl-derived anilino squaraines was established. Concerns regarding possible racemisation in the final step toward the secondary amine were resolved by the targeted synthesis of a diastereomeric compound, which could be separated via HPLC. Once the enantiomeric purity of the secondary amines was confirmed, the classical two-step, one-pot procedure was applied, yielding two new squaraines: **(*S*,*S*)-2mb-DSQ** and **(*S*,*S*)-2mb-HDSQ**. Although this standard method proved effective for these two compounds, the synthesis of the chiral **SQIB**-derivative **(*S*,*S*)-2mb-SQIB** turned out be be challenging. After the observation of the instability of the product of the first condensation between the secondary amine and phloroglucinol (1,3,5-trihydroxybenzene), the reaction could be fine tuned regarding the used equivalents and conditions. Thus another two squaraines were accessible: **(*S*,*S*)-2mb-SQIB** and **(*S*,*S*)-2mb-SQPE**. Given the frequent use of the non-chiral squaraine **SQIB** in the literature, there was particular interest in **(*S*,*S*)-2mb-SQIB**. With these four uniquely structured squaraines in hand, their chiral aggregation behaviour was systematically investigated. While early-stage aggregation experiments in solution revealed only negligible aggregation tendencies, solution-processed thin films exhibited the opposite behaviour. Here, **(*S*,*S*)-2mb-DSQ**, **(*S*,*S*)-2mb-HDSQ** and **(*S*,*S*)-2mb-SQIB** exhibited strong aggregation tendencies even at low temperatures. **(*S*,*S*)-2mb-DSQ** and **(*S*,*S*)-2mb-HDSQ** showed the characteristic double-humped absorbance spectra – arising from coupling between a Coulombic Frenkel exciton and an ICT state – together with the corresponding bisignate and monosignate signals in the CD spectra, indicative of supramolecular aggregation. In contrast, **(*S*,*S*)-2mb-SQIB** closely resembled the non-chiral **SQIB** in almost all respects. The occurrence of two distinct polymorphs, a monoclinic and a presumably orthorhombic form, as well as other similarities to **SQIB**, were intensively investigated. At the end, **(*S*,*S*)-2mb-DSQ** was selected for application as the donor material in a PHJ-OPV, paired with C_{60} fullerene as the acceptor material. Device fabrication used a combination of solution-processed spin-coating and PVD techniques. The resulting devices, prepared with varying squaraine layer thicknesses, were characterized using standard methods. Although the overall performance was relatively low compared to other squaraine-based devices, this was considered secondary, as the primary aim was to function as a detector. This ability of the device to distinguish between left- and right-handed CPL, was finally tested as a proof of concept. Thus demonstrating the successful progression of the project from the initial molecular design concept to the fabrication of a working circular dichroic photodetector.

CHAPTER 11

Excursus – Synthesis of Chiral π-Conjugated Polymers Exhibiting the CISS Effect for Advanced Optoelectronic Applications

The following chapter is primarily based on work carried out during a three-month research stay in 2023 in the group of Prof. Dr. Seth R. Marder at the University of Colorado Boulder, USA. This stay was made possible through the support and efforts of Prof. Dr. Arne Lützen and Prof. Dr. Seth R. Marder, as well as financially funded by the Research Training Group TIDE – Template-Designed Organic Electronics. I would like to take this opportunity to once again express my gratitude to all who contributed – particularly the persons mentioned above – for making this exceptional experience possible.

Being mainly an excursus, this chapter will provide only a brief introduction to the topic of chiral π-conjugated polymers exhibiting the chiral induced spin selectivity (CISS) effect for advanced optoelectronic applications and briefly go over the motivation of this work. Further details can be found in the cited literature.

11.1 Current Research Status of the CISS Effect

The chiral induced spin selectivity (CISS) effect, which describes the phenomenon of how electron transmission through chiral materials can be spin selective, was first discovered over two decades ago.[160] Since then this effect has been observed in a number of organic, inorganic and hybrid materials. Even studies of how the CISS effect plays an important role in biology (e.g., chemical reactions involving redox chemistry with chiral molecules in a chiral environment) have been performed.[161] In general, this effect holds promise for numerous applications, such as enhancing the fluorescent singlet yields in light-emitting diodes, creating detectors for circularly polarized light (CPL), and influencing the outcome of chemical reactions. The latter is often referred to as ”Spin Chemistry” and studies the effect of reaction kinetics by affecting electron spin dynamics.[162] Additionally, future applications in spintronics, memory, and quantum computing may arise as our understanding of this phenomenon deepens.

Despite significant research and studies in this area, the precise mechanisms behind the CISS effect and the factors contributing to its magnitude are not fully revealed, yet.

A schematic illustration of the CISS effect can be seen in Figure 11.1. The most common explanation for this phenomenon is that electrons moving through a chiral potential such as a chiral arrangement tend to align their spin orientation either parallel or antiparallel to their direction of motion (velocity *v*, see Figure 11.1). This alignment occurs because the electron experiences an effective magnetic field generated by the interaction between its velocity and the chiral electric potential of the environment. The effective magnetic field then breaks the degeneracy of the electron spin levels, allowing to distinguish between spin-up and spin down electrons and leading to spin polarizations of over 80% in some systems.[163–166]

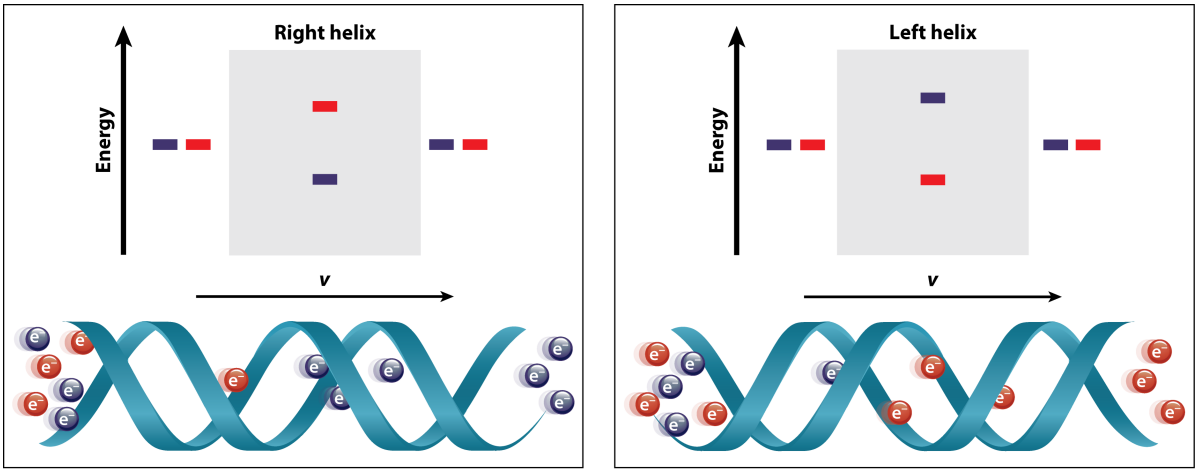


Figure 11.1: Schematic illustration of the CISS effect, with spin up (red) and spin down (blue) electrons passing a right and left handed helix. Figure reprinted with permission from [163] © 2015, Annual Reviews, Inc.

As for the material of interest – polymers – mainly three different ways of incorporating chirality and the CISS effect in optoelectronic devices have been described in the literature.[166] First, semiconducting pristine (i.e. undoped and non-chiral) materials have been used, in which the chiral charge carriers are primarily injected from neighbouring materials (e.g., a spin-selective hole transporting layer, ref. Figure 11.2a). In these cases, the polymer is either used as a chiral injection layer or as an emission layer only depending on whether the polymer is chiral (intrinsically chiral or chirality-induced) or non-chiral, respectively.[167, 168]

Although this is an interesting approach, this chapter focus more on the other two, far more established approaches to achieve this goal, namely the use of polymers with intrinsic chiral information (Figure 11.2b), which can be achieved by implementing chiral side groups on the polymer chain or by the addition of chiral dopants/additives[a] (Figure 11.2c). No matter which approach is used, both cases resulting in helicity in the polymer main chain, and thus, chirality-related properties such as CD, CISS etc.

[a] Defined here as neutral chiral molecules that can be mixed with the semiconductor but do not undergo electron transfer reactions with it – not be confused with electrical dopants

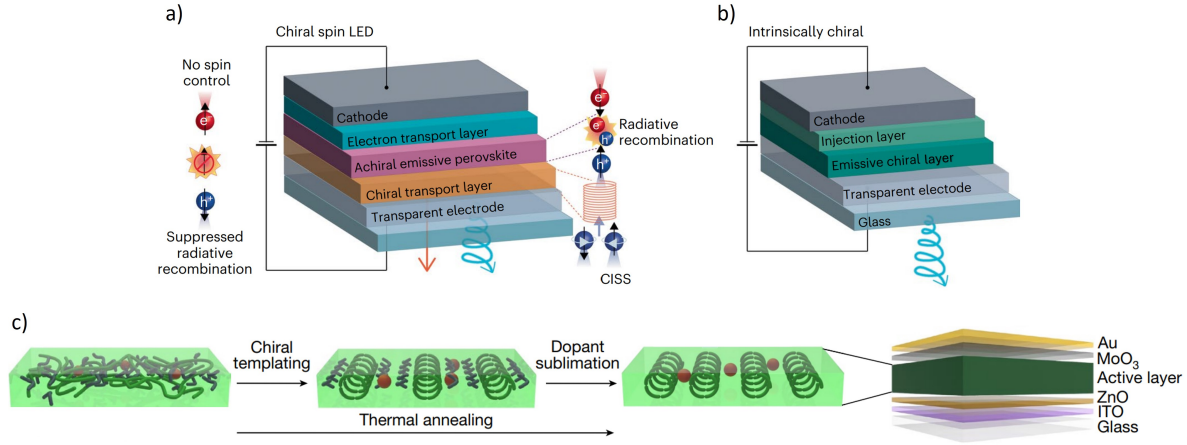


Figure 11.2: a) CLP-LED based on a spin-selective hole transporting layer where the recombination occurs in a layer of achiral perovskite; b) CLP-LED with a intrinsically chiral emissive layer; c) OPV with a chiral photoactive layer initiated by chiral dopants. Figures reprinted with permission from [166] (a and b) and [169] (c) © 2023 and 2024, Springer Nature.

These strategies usually require a careful design of the chiral moieties/dopants used, to ensure relatively strong interactions with the semiconductor, such as with a polymer chain. Generally, it is assumed that stronger supramolecular interactions will transfer the chirality of the side group/additive to the polymer better, i.e. lead to a more pronounced chiral chain conformation.[119, 169] Examples for these approaches are, e.g., blends of **F8BT** (poly(9,9-dioctylfluorene-*alt*-benzothiadiazole)) and PFO (poly(9,9'-dioctylfluorene-2,7-diyl)) with chiral helicene derivative,s which have already been proven to exhibit large CD responses on the order of hundreds or even thousands of millidegree (mdeg) as well as circularly polarized photoluminescence (CP-PL) and electroluminescence of several percentage.[166, 170–172] Such compounds may therefore serve as active layer of circularly polarized OLED (CP-OLED) in the future. However, until now blending of achiral conjugated polymers with chiral dopants is much more investigated than decorating conjugated polymer backbones with chiral side-chains. Although chiral derivatives of many known high performing polymers have been reported in the literature, none of them have been systematically studied in the context of CISS.[173–175] Overall, a clear understanding of the mechanism behind CISS is still missing and many fundamental questions remain to be answered, particularly regarding how the CISS effect is related to other properties of chiral matter, such as CD and other novel optical, spintronic, and opto-electronic properties of chiral organic (semi)conductors.[176]

11.2 The Project Idea – Polymers with Intrinsic Chiral Information

During my research stay, I focused on the synthesis of conjugated chiral polymers and their application and investigation in solution processed thin films. The approach I took there was to only partially add a chiral monomer during the synthesis to obtain a chiral random copolymer with different percentages of chiral building blocks. In fact, this approach has barely been investigated, so far. Apart from a hand full of examples, the more common way is to perform the synthesis with only chiral monomers or, in

a co-polymerisation, with one chiral monomeric species.[177] The resulting polymers can subsequent either used directly or in a blend with an achiral polymer.[119]

Until now, the incorporation of intrinsic chiral information has largely been a side topic in research over the past decades. In most cases, chirality has been introduced via chiral side chains – for example, 9,9-dioctylfluorene-derived building blocks functionalized with citronellyl groups.[119] In such cases, the overall molecular structure remains largely undisturbed, as replacing an octyl-chain with a citronellyl group does not introduce significant steric hindrance. The resulting polymers, although exhibiting chiral properties, behave similarly to their achiral counterparts, allowing their properties to be predicted. The drawback, however, is that the stereocenter – bearing only a methyl substituent – belongs to the central chirality and does not strongly transfer its chirality to the substrate. Moreover, the stereocenter is not directly connected to the π-conjugated polymer backbone.

For this project, the goal was therefore to increase the "transfer of chirality" by attaching the stereogenic information directly to the π-conjugated backbone and going from central to axial chirality. As a logical choice, BINOL was selected for this purpose, as it combines all the desired properties and allows for a broad spectrum of chemical reactions.

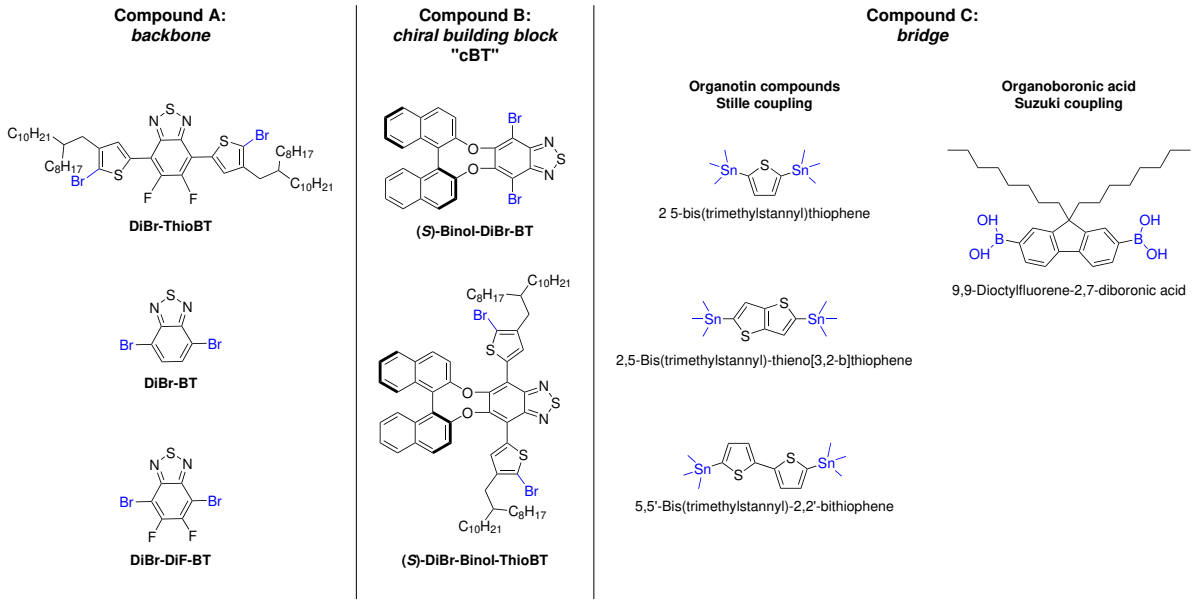


Figure 11.3: Molecular library of building blocks which were available for the chiral π-conjugated polymer synthesis with **Compound A** – the achiral backbone, **Compound B** – the chiral building block and **Compound C** – the achiral bridge.

Focusing on the approach of only partially add a chiral monomer during the synthesis to obtain a chiral random copolymer with different percentages of chiral building blocks, the initial task was to create a molecular library of different compounds that could subsequently be used in a polymerisation reaction. As illustrated in Figure 11.3, a distinction was made between three different categories of components: **Compound A** – an achiral polymer backbone, typically employed in other high-performance second- or third-generation polymers; **Compound B** – the chiral building block, designed to partially substitute the achiral backbone and introduce intrinsic chiral information; and **Compound C** – an achiral "bridge",

serving as the counterpart in the co-polymerisation via cross-coupling polymerisations. Thereby **Compound A** and **B** are considered electron-acceptor (A) molecules, whereas **Compound C** functions as an electron-donor (D). This arrangement results in an alternating D-A sequence during co-polymerisation. Such donor-acceptor systems are well known for their strong interaction with light – analogous to the D-A-D system in squaraine dyes – and therefore a primary topic in current research.[119, 166]

The majority of molecules in this library, including all **Compound C** species, were commercially available. In contrast, the remaining monomers were either synthesised by me or supplied by the host laboratory (Group of Prof. Seth Marder).

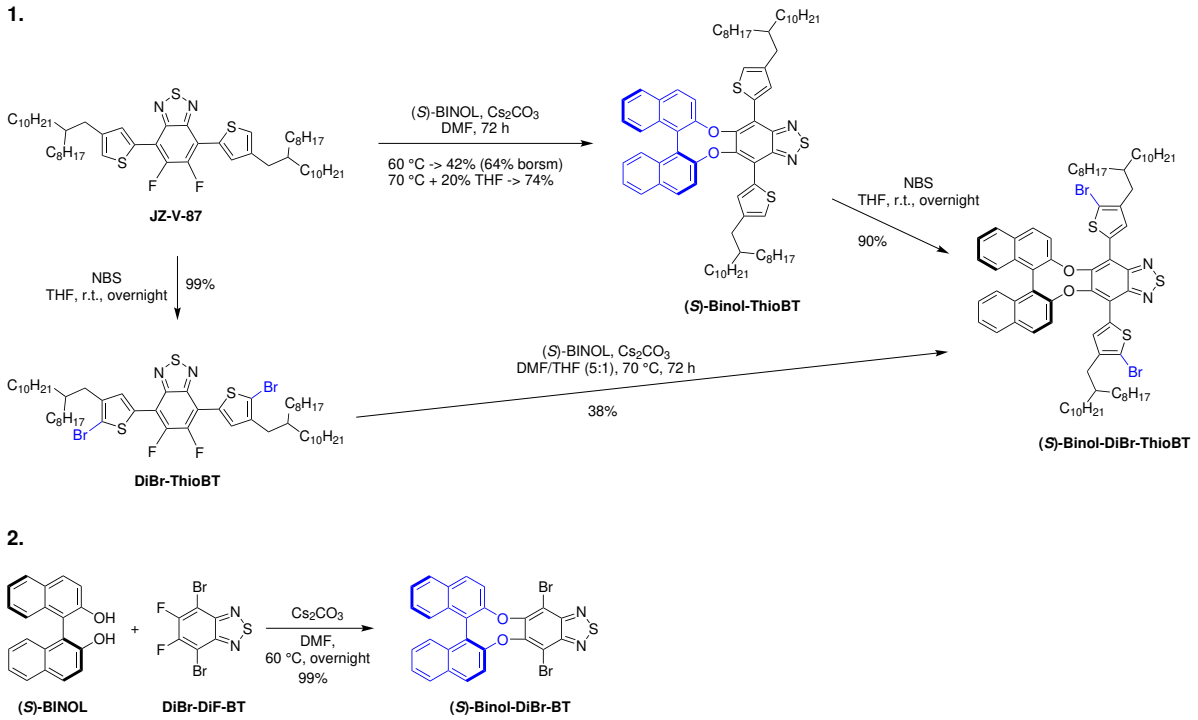


Figure 11.4: Synthesis of the monomers **(*S*)-BINOL-DiBr-ThioBT**, **DiBr-ThioBT**, and **(*S*)-Binol-DiBr-BT** starting from **JZ-V-87** or 4,7-dibromo-5,6-difluoro-2,1,3-benzothiadiazole. Non-commercially available precursors were provided by Dr. Junxiang Zhang – Group of Seth Marder, University of Colorado Boulder (USA).

The synthetic approach for the selected monomers is shown in Figure 11.4. As an example, benzothiadiazole (**BT**) is a commonly used building block in conjugated polymers, such as **F8BT** and various donor-acceptor polymers utilized in organic photovoltaics. In particular, difluoro-BT (**DiF-BT**) exhibits high reactivity towards nucleophiles. I demonstrated that **DiF-BT** derivatives can react with enantiopure 1,1'-bi-2-naphthol (**BINOL**) to yield chiral benzothiadiazole-derived monomers (**cBT**) – representing the chiral scaffold used in all chiral building blocks (**Compound B**).

The synthesis of **DiBr-ThioBT** and **(*S*)-Binol-DiBr-ThioBT** started from **JZ-V-87** (provided by Dr. Junxiang Zhang, Group of Seth Marder). The achiral backbone **DiBr-ThioBT** was obtained in excellent yield of 99% via bromination of **JZ-V-87** using *N*-bromosuccinimide (**NBS**) and was later used as a backbone (**Compound A**) in the polymerisation. Subsequent functionalization with **(*S*)-BINOL** to obtain the chiral building block **(*S*)-Binol-DiBr-ThioBT** via a nucleophilic aromatic substitution (S_NAr) reaction, using

caesium carbonate as base, unfortunately afforded only a poor yield of 38%. Based on these disappointing results, an alternative synthetic route was explored in which **JZ-V-87** was first functionalized with **(*S*)-BINOL**. Initially, **JZ-V-87**, **(*S*)-BINOL** and caesium carbonate were reacted at 60 °C in DMF for 72 h, yielding the intermediate **(*S*)-Binol-ThioBT** in 42% yield (64% based on recovered starting material (borsm)). Increasing the reaction temperature to 70 °C and adding 20% THF to the DMF – addressing solubility issues with **JZ-V-87** in pure DMF – resulted in an acceptable yield of 74%. Subsequent bromination with **NBS** afforded the final chiral building block **(*S*)-Binol-DiBr-ThioBT** in 90% yield.

For the chiral version of benzothiadiazole, 4,7-dibromo-5,6-difluoro-2,1,3-benzothiadiazole (**DiBr-DiF-BT**) was functionalized with **(*S*)-BINOL** via a nucleophilic aromatic substitution (S_NAr) reaction, giving **(*S*)-Binol-DiBr-BT** in excellent yield of 99%.

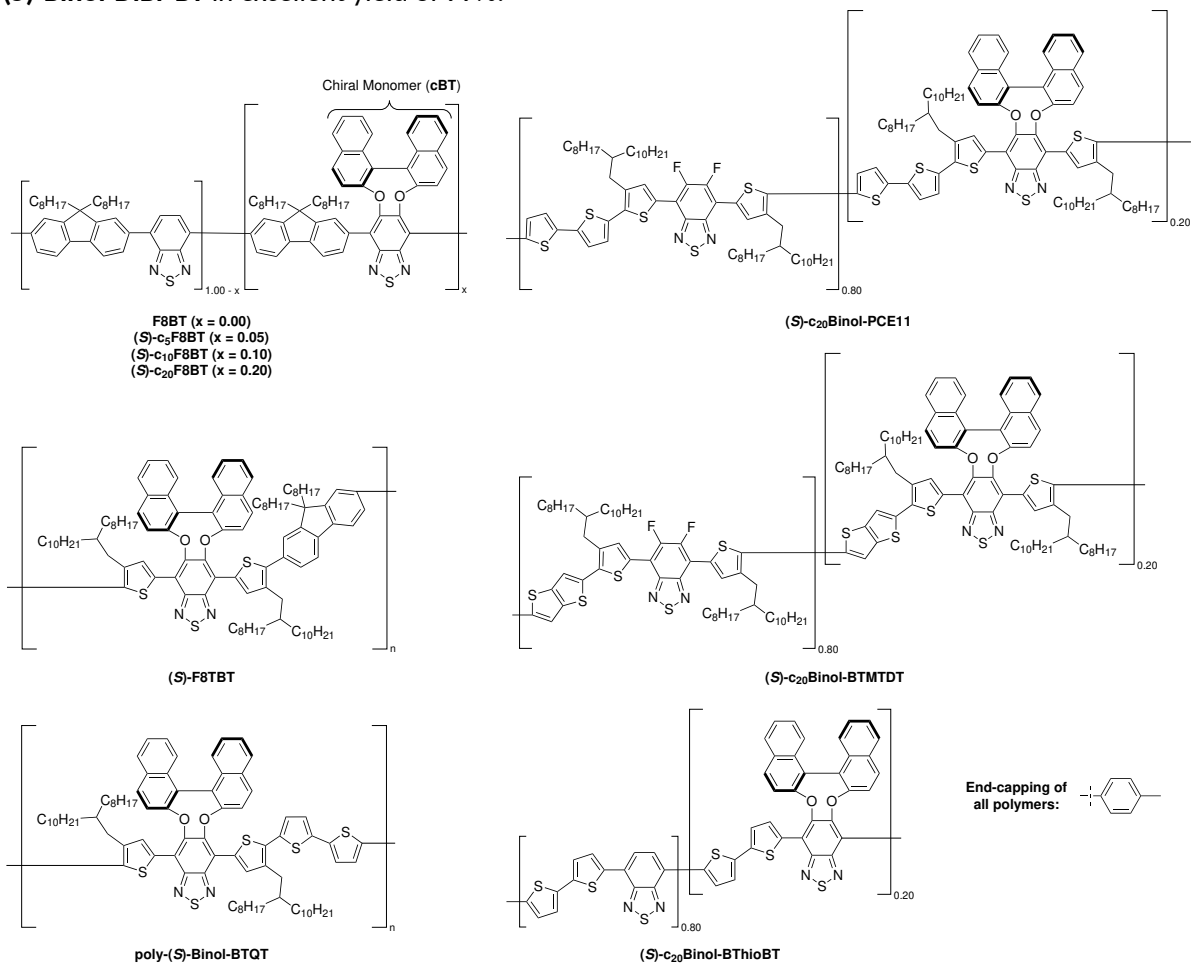


Figure 11.5: Overview of all synthesized polymers either by a Suzuki or Stille cross-coupling reaction. Detailed information can be found in Appendix I or Section 13.6.

With these syntheses completed, all molecules in the molecular library were available for the subsequent polymerisation reactions, which were carried out via either a Suzuki (organoboron compound) or Stille (organotin compounds) cross-coupling reaction. An overview of all synthesized polymers can be seen in Figure 11.5. In total, nine different polymers with intrinsic chiral information from incorporated **cBT** derived monomers and featuring diverse molecular designs were successfully synthesised.

Thereby, the **cBT** derived monomer (**Compound B** – the chiral building block) was incorporated in varying amounts of 0, 5, 10, 20 or 100%, depending on the specific polymer.

As this section is just an excursus, the following discussion will focus only on the most surprising and interesting polymer class – the chiral **F8BT** derivatives, **(*S*)-c$_x$F8BT**. Since **F8BT** with chiral additives or incorporating chiral alkyl substituents on the fluorene unit exhibit some of the largest CD values reported to date,[119, 171] we were interested in comparing the impact of the chiral **BINOL** substituent to that of chiral additives or alkyl chains and so incorporated **cBT** into **F8BT** with mol%-fractions ranging from 0 to 20 mol% (Figure 11.5,top left side, abbreviated as e.g., **(*S*)-c$_{20}$F8BT** for 20 mol%). For further information on the other polymers or for additional details on **(*S*)-c$_x$F8BTs**, including synthesis procedures, compound images, thermogravimetric analysis (TGA), differential scanning calorimetry (DSC), and investigations of spin-coated thin films (thermally annealed, solvent vapour annealed and used as chiral dopants in achiral **F8BT**), refer to Appendix I and Section 13.6.

11.3 Chiral F8BT derivatives – (*S*)-c$_x$F8BT

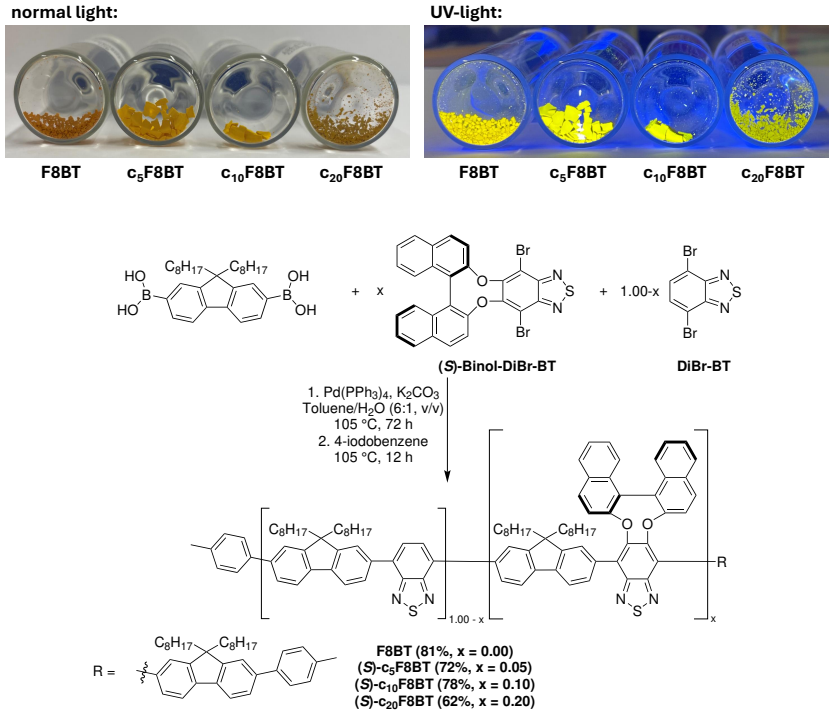


Figure 11.6: Bottom: Synthesis of **(*S*)-c$_x$F8BT**, starting from **DiBr-BT**, enantiopure **(*S*)-Binol-DiBr-BT** and 9,9-dioctylfluorene-2,7-diboronic acid. x stands for the different amount of **(*S*)-Binol-DiBr-BT** and ranges from 0.00, 0.05, 0.10 to 0.20. Top: Picture of the four obtained **(*S*)-c$_x$F8BTs** under normal (left) and UV-light (right).

The chiral **F8BT** derivatives, **(*S*)-c$_x$F8BT**, were synthesised via a Suzuki cross-coupling reaction, as shown in Figure 11.6. For this, **DiBr-BT**, enantiopure **(*S*)-Binol-DiBr-BT** and 9,9-dioctylfluorene-2,7-diboronic acid were polymerised using Pd(PPh$_3$)$_4$ as the catalyst in a toluene/water mixture (6:1, v/v).

To terminate the polymerisation and to end-cap the polymer chains, 4-iodotoluene was added in excess. After the reaction mixture was cooled to room temperature, the polymer was precipitated in methanol. The crude product was redissolved in toluene, and sodium diethyldithiocarbamate was added as a Pd-scavenger, forming a water-soluble transition-metal dithiocarbamate complex. The polymer was recovered by reprecipitation in methanol and further purified by Soxhlet extraction with methanol, acetone, and *n*-hexane. A final dissolution in toluene followed by precipitation in methanol afforded the desired polymer in good yields of 62–81%. These yields are actually comparable to those reported in the literature,[178] indicating that incorporation of **cBT** did not negatively affected the reaction efficiency. Interestingly, a slight colour difference between the solid polymer samples was observed (Figure 11.6, top), despite, if dissolved, all solutions exhibiting the same colour as well as exhibiting the same UV/Vis absorbance spectra in spin coated thin films. Therefore it was attributed to different morphologies of the amorphous powders.

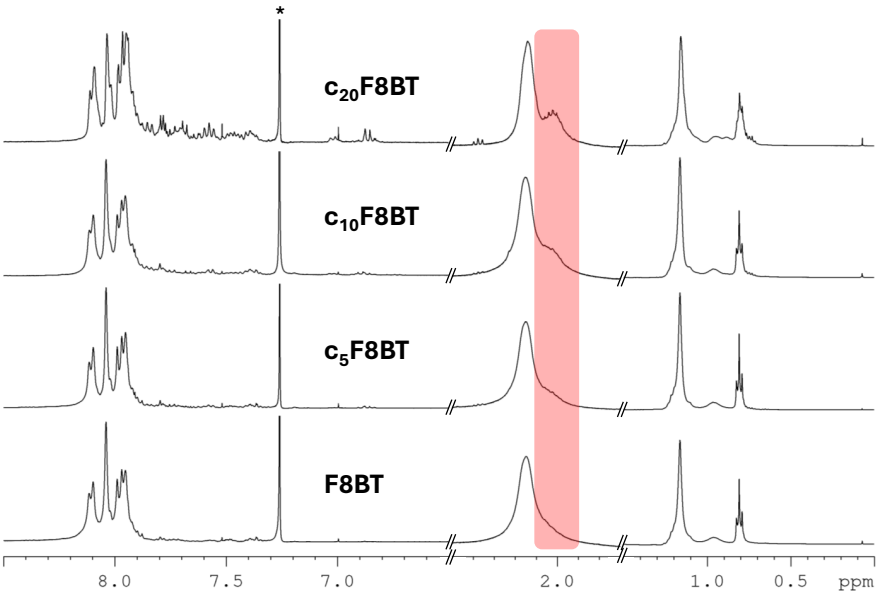


Figure 11.7: Selected region of the ^{1}H-NMR spectrum (400 MHz, chloroform-*d*, 298 K, 1024 scans) of the precipitated and purified polymers, illustrating the spectral changes observed with increasing **cBT** content in **(*S*)-c$_x$F8BT**. The deuterated solvent signals are marked with an "*".

As is typical for polymers, a precisely defined chemical composition cannot be given as for small molecules. Therefore, it is impossible to determine the relative position and exactly how much **(*S*)-Binol-DiBr-BT** was actually incorporated into the polymer during polymerisation. Interestingly, however, the ^{1}H-NMR spectra of the polymers, shown in Figure 11.7, revealed distinct changes with increasing **cBT** content. Most notably, a shoulder emerged at around 2 ppm, which can be attributed to the first CH_2 group of the octyl-chain from the 9,9-dioctylfluorene building block. This shift can be rationalized with a change in the chemical environment when a **BINOL** unit is in close spatial proximity. In addition, also other signals showed emerging splitting in both the aliphatic and aromatic regions of the spectrum. Due to significant signal overlap, however, the exact quantification of **(*S*)-Binol-DiBr-BT** units within the polymer backbone based on NMR integrals is unfortunately not feasible – especially for those with

Table 11.1: GPC characteristics of synthesised **(*S*)-c$_x$F8BTs** – measured against polystyrene standards. Definitions and equations are provided in Appendix I.1 and values are rounded to the nearest thousand. All GPC measurements were carried out with the assistance of the group of Prof. Sigurd Höger, University of Bonn.

Polymer	M_n [g/mol]	M_w [g/mol]	M_z [g/mol]	PDI	DP
F8BT	18000	24000	32000	1.35	≈35
(*S*)-c$_5$F8BT	15000	21000	28000	1.41	≈27
(*S*)-c$_{10}$F8BT	15000	22000	29000	1.47	≈26
(*S*)-c$_{10}$F8BT	6000	10000	14000	1.62	≈10

low percentages. While these observations do not constitute absolute proof, they strongly suggest the successful incorporation of **(*S*)-Binol-DiBr-BT** during the polymerisation.

This observation was further supported by gel permeation chromatography (GPC) measurements of the obtained polymers, performed against polystyrene standards. As shown by the calculated gel permeation chromatography (GPC) characteristics in Table 11.1 for the synthesised **(*S*)-c$_x$F8BTs**, the degree of polymerisation (DP) for all samples lies between 35 and 10. A clear trend is observed in which increasing the **cBT** content leads to a decrease in DP, suggesting reduced reactivity during polymerisation – likely due to steric or electronic effects. Nevertheless, for all polymers, the average chain length would statistically include at least two **cBT** units. It should be mentioned, however, that these values are not optimized and should be interpreted with caution, as the molecular structures of polystyrene and the synthesised chiral **F8BT** derivatives differ significantly. Therefore, it should be considered a hint rather than a proof.

Optical Properties of Thermally Annealed Thin Films:

The normalised thin-film UV/Vis absorbance spectra of **(*S*)-c$_x$F8BTs** are shown in Figure 11.8 (left). These measurements were obtained from samples spin-coated from equally concentrated spin-on solutions under identical conditions, followed by thermal annealing at the respective optimal annealing temperature for 10 minutes. This optimal temperatures were determined to be 160 °C for **F8BT** and **(*S*)-c$_5$F8BT** or 180 °C for **(*S*)-c$_{10}$F8BT** and **(*S*)-c$_{20}$F8BT**. Measurements at different annealing temperatures, used to determine these optima, are provided in Appendix I.3.1. By this, the optimal annealing temperatures are well below the thermal racemisation threshold of enantiopure **BINOL** – reported as a minimum of 190 °C with $t_{1/2}$ = 180 h, 210 °C with $t_{1/2}$ = 29 h and 250 °C with $t_{1/2}$ = 1.15 h.[179]

All spectra of **(*S*)-c$_x$F8BTs**, regardless of the **cBT** content, display almost identical absorption profiles, with only slightly different intensities – except for **(*S*)-c$_{20}$F8BT**, which exhibits a clear deviation. Being normalized to the peak at approximately 210 nm, an overlap with the absorption of **BINOL** has to be taken into account for the polymers with higher **cBT** unit content. Like most organic materials, polymers exhibit a characteristic strong deep-UV absorption, caused by higher-energy π-π^* and σ-σ^* transitions in the aromatic backbone. Although the overlap with the **BINOL** adsorption is not noticeable for the lower **cBT** unit content, it can be assumed that for **(*S*)-c$_{20}$F8BT** this results in a more intense signal than what would be expected from the pure achiral polymer alone, leading to a negativ offset of the other absorbance bands in the spectra.

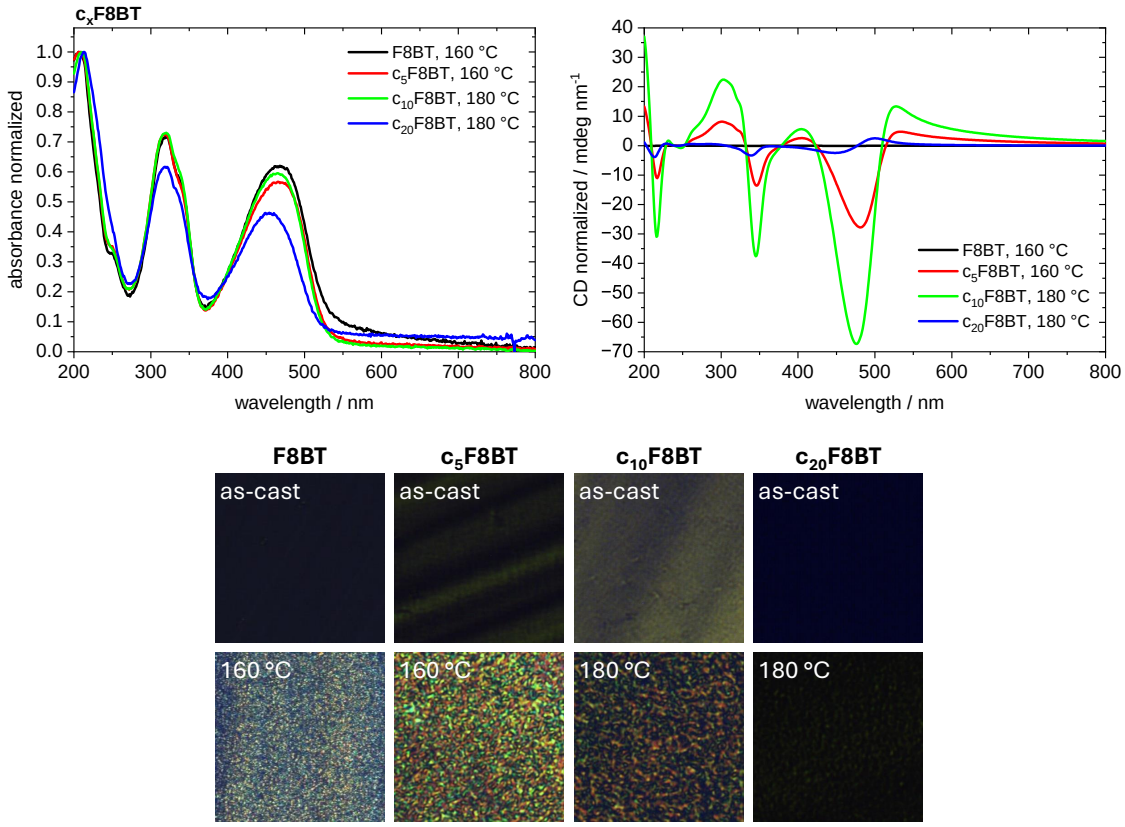


Figure 11.8: Comparison of the normalized UV/Vis absorbance (top, left) and corresponding normalized CD spectra (top, right) of **(*S*)-c$_x$F8BTs**, spin-coated from equally concentrated toluene/chloroform 5:3 (v/v) solutions under the same conditions and thermally annealed at the optimal annealing temperature (corresponding to the highest CD values – see Appendix I.3.1) for 10 minutes. Bottom: Optical microscopy images of spin-coated thin films of **(*S*)-c$_x$F8BTs** between crossed polarizers at indicated temperatures (same magnification for all images).

In addition, all UV/Vis absorbance spectra exhibit two further expected maxima: one at around 320 nm, corresponding to the dioctylfluorene donor unit, and another at 466 nm, corresponding to the benzothiadiazole (**BT**) acceptor unit.[180]

The normalized thin film CD spectra of **(*S*)-c$_x$F8BTs**[b] are shown in Figure 11.8 (right). As expected, the spectrum of **F8BT** (i.e. **(*S*)-c$_0$F8BT**) is completely CD-silent, as no intrinsic chiral information from **cBT** units is present. In contrast, the spectra of the polymers containing 5%, 10%, or 20% of the **(*S*)-Binol-DiBr-BT** building block during polymerisation exhibit several pronounced CD signals. Specifically, two asymmetric bisignate signals with zero-crossings at approximately 210 nm and 330 nm, as well as a monosignate signal at 466 nm, are observed. The latter two features correspond to the **BT** and dioctylfluorene units, respectively, and align closely with the UV/Vis absorbance bands. The slight shift between the UV/Vis maximum at 320 nm and the CD feature at 330 nm can be rationalized by the asymmetry of the bisignate signal. In addition, although the signal at 466 nm of the **BT** (acceptor unit)

[b] Absolute values (i.e. unnormalised) are shown in Figure 11.9.

shows features of an extremely asymmetric bisignate shape, it is declared here as a monosignate signal, as it is likely to originate from a transfer mechanism (either CT or Förster resonance energy transfer (FRET))[181] within the donor-acceptor polymer system. On the one hand, intermolecular charge transfer (ICT) represents a single allowed electronic transition with inherent chirality, thus producing (even if coupled with a Coulombic Frenkel exciton) a monosignate band, as observed for squaraines (see Chapter 3, 9, 6). On the other hand, Förster resonance energy transfer (FRET) with excitonic coupling – i.e. when donor and acceptor transitions are strongly coupled in a chiral arrangement – can lead to exciton splitting, resulting in a bisignate CD signal. Therefore, the observed asymmetry of the feature at 466 nm could origin from two different mechanisms. Interestingly, this asymmetry appears to vanish when 20% of the **(*S*)-Binol-DiBr-BT** building block is incorporated, resulting in a symmetrical bisignate signal with a zero-crossing shifted to approximately 475 nm. However, a detailed investigation of these two phenomena lies beyond the scope of this chapter and was therefore not further intensified.

The actual observation of a chiral response from the dioctylfluorene units – despite the absence of directly attached chiral groups – indicates the formation of a chiral (supra)molecular arrangements in the polymer thin films. Furthermore, strong exciton coupling (arising from the donor-acceptor system) between chromophores within the polymer aggregate can be assumed, due to the bisignate nature of the high-energy band of the fluorene transitions. In this way, the primary goal of transferring chiral information to the polymer backbone via polymers with intrinsic chiral information was successfully achieved.

Although the exciton chirality method (discussed in Section 1.3.2 - Interpretation of CD-Spectra) for interpretation of the bisignate CD signal, is based on the through-space coupling of two or more chromophores in discrete chiral arrangements rather than polymers, it can also be applied to such systems. Given the overall negative Cotton effect of the dioctylfluorene-related signal and its obvious interpretation as a J-type aggregate due to the nature of the polymer, a right-handed arrangement with a creeper-helical geometry can be assumed.

In terms of absolute values, a clear correlation between the intensity of the CD signal and the incorporated amount of **cBT** units is visible. For the monosignate **BT**-related lower-energy band at 466 nm, **(*S*)-c$_5$F8BT** exhibits values of approximately -30 mdeg/nm. Increasing the **cBT** content to 10 mol% in **(*S*)-c$_{10}$F8BT** results in a drastic increase to around -70 mdeg/nm. However, a further increase to 20 mol% leads actually to a decrease rather than a further increase. This unusual behaviour suggests the existence of a “sweet spot” in chiral additive content, where the transfer of chiral information is most efficient. This effect may be linked to the crystallinity of the samples: if the **cBT** content is too high, the formation of crystalline domains is hindered, resulting in an amorphous thin film with no macroscopic CD effect. This hypothesis is actually supported by optical microscopy images of spin coated **(*S*)-c$_x$F8BT** thin films between crossed polarizers (Figure 11.8, bottom). For 0, 5, and 10 mol%, highly crystalline films are obtained after proper thermal annealing, whereas for 20 mol% **cBT** only minor crystallinity is observed. Without ordered structures, chiral information cannot be effectively transferred to the polymer backbone, and thus, no macroscopic CD effect can be observed. This sweet spot of incorporated chiral **cBT** units was further investigated during Marc-Laurent Mende’s master’s thesis which I supervised and was determined to lie between 10 and 20 mol%.[182] Further studies on this topic will be conducted by him during his PhD in the group of Prof. Arne Lützen (University of Bonn).

In order to actually proof the superiority of the intrinsic chirality approach, non-chiral **F8BT** was doped with 10 mol% of chiral additives based on structurally similar molecules, as shown in Figure 11.9. Three different dopants were tested: **(*S*)-Binol-DiBr-BT** (the chiral building block partially incorporated

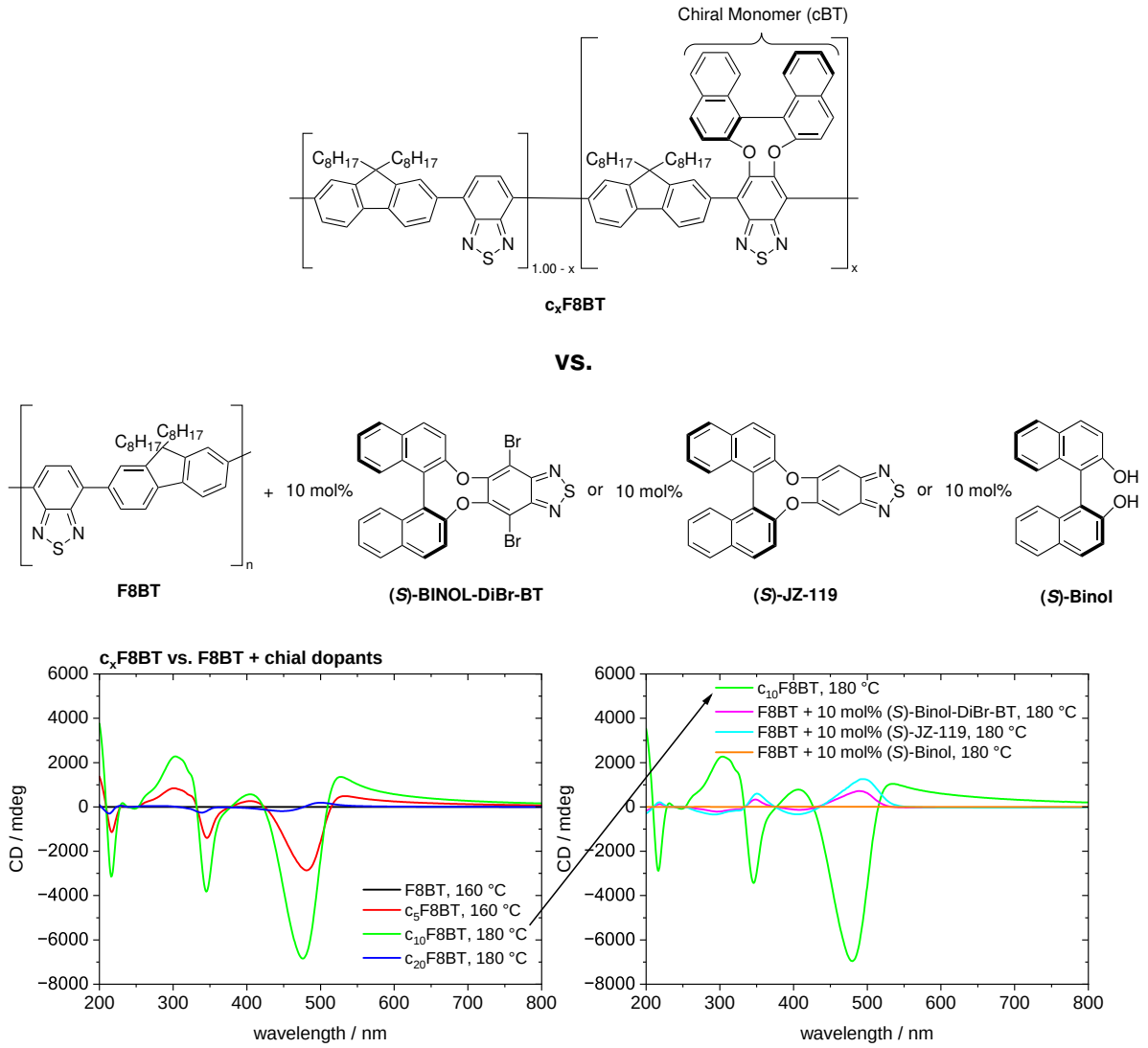


Figure 11.9: Comparison of the unnormalised CD spectra between **(*S*)-c$_x$F8BTs** (left) and **F8BT** mixed with 10 mol% of different chiral dopants (same stereogenic configuration) based on structurally similar molecules (right), both thermally annealed at the optimal annealing temperatures (see Figure I.5, I.6, I.7 and Figure I.11). Spin-coated from equally concentrated toluene/chloroform 5:3 (v/v) solutions under the same conditions. Top: Molecular structures of the polymers and used dopants.

during polymerisation), **(*S*)-JZ-119** (the "naked" **cBT** unit, provided by Dr. Junxiang Zhang) and **(*S*)-BINOL**. Detailed investigations of the optimal thermal annealing temperatures and times for maximizing the CD response can be found in Figure I.11.

As can be clearly seen from the left CD spectra, no chiral dopant achieves values closely to those obtained via the intrinsic chirality approach. **(*S*)-BINOL** produced no detectable CD signal at all, whereas **(*S*)-Binol-DiBr-BT** and **(*S*)-JZ-119** yielded values of approximately 730 mdeg and 1200 mdeg, respectively, measured at the monosignate **BT**-related lower-energy band at 466 nm. In contrast, the **(*S*)-c$_{10}$F8BT**

achieves values of over -7000 mdeg (the values for **(*S*)-c$_5$F8BT** and **(*S*)-c$_{20}$F8BT** can be found in Figure 11.9). Interestingly, the CD signals of the doped systems exhibited an inverted sign compared to the intrinsically chiral polymers, despite the same stereogenic configuration. This interesting observation is still under active investigation, so a definitive explanation cannot be provided at this point.

These results highlight several advantages of partially incorporating chiral building blocks into the polymer backbone over traditional post-synthetic doping. One key benefit is that, as part of the molecular structure, the chiral units do not disrupt the overall arrangement of the polymer chains. In fact, the presence of some **cBT** units can enhance the aggregation properties of the material. However, excessive incorporation, on the other hand, can actually hinder aggregation, as observed for **(*S*)-c$_{20}$F8BT**. A particularly highly interesting concept emerging from this work is the use of chiral polymers themselves as scaffolds or additives to induce chiral aggregation in otherwise non-chiral polymers in the sense of a "sergeant and soldier" approach to reduce the total **cBT** content to a minimum of under 1% – a strategy currently being explored in collaboration with Prof. Seth Marder (University of Colorado Boulder, USA).

Overall, the research stay can be considered as highly successful, yielding several uniquely structured polymers whose chiral aggregation behaviour was systematically investigated. Thereby, the group of **(*S*)-c$_x$F8BTs** stood out with the most striking and promising aggregation behaviour. These polymers showed pronounced chiroptical properties in properly processed and annealed thin films, with huge CD-values peaking at ca. -70 mdeg/nm for **(*S*)-c$_{10}$F8BT**. Even though this system is not optimized yet and the best mol%-fraction of incorporated **cBT** into **F8BT** has to be still figured out, these values are in the same order of magnitude as those of the best performing chiral materials reported today. In direct comparison to traditional thin films of achiral **F8BT** with chiral dopants/additives based on structurally similar molecules, the intrinsic chirality approach has already been proven to be superior and surpasses the performance of films with chiral additives many times over. Previous approaches to synthesizing chiral polymers typically involved exclusively on chiral monomers, which generally exhibited inferior overall chirality-related properties, as it was also demonstrated during the research stay (see Appendix I.3.2 and I.3.3). However, our approach in which chiral and achiral monomers (**cBT** and **BT**) are copolymerized, which we have found to be profitable in at least some cases, has barely been investigated so far and requires more systematical research. The most promising materials were selected for further investigations into chirality-related optical and electronic properties – for example, to determine whether they exhibit the CISS effect – in collaboration with Prof. Seth Marder (University of Colorado Boulder, USA), Prof. Valy Vardeny (University of Utah, USA) and Prof. Ying Diao (University of Illinois at Urbana-Champaign, USA). However, as this is an ongoing project and goes beyond the scope of the research stay, it will not be discussed further at this point.

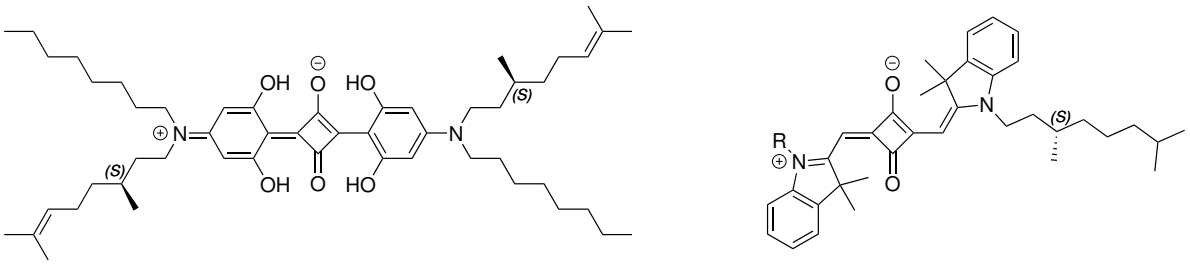
CHAPTER 12

Summary and Outlook

The objective of this thesis was to design, synthesize, and characterize new classes of homochiral squaraine dyes – including proline- and indolenine-derived as well as chiral *N*-functionalized anilino squaraines – with tailored substitution patterns for optoelectronic applications. By combining different synthetic approaches with a broad range of spectroscopic and structural techniques, the work aimed to contribute to the structure-property relationship understanding and uncover the mechanisms behind the extraordinary chiroptical responses of these dyes. Thereby, a subdivision into roughly four distinct parts was made:

Part A – including Chapter 3, 4 and 5 – investigated the impact of *N*-functionalization with enantiopure citronellyl groups on diverse squaraine motifs.

Thereby, Chapter 3 support previous interpretations, that the double hump spectral signatures observed in *n*-alkyl anilino SQs, emerge from coupling between a Coulombic Frenkel exciton with H-aggregate character and an ICT state. Thereby, the citronellyl-functionalization did not result in chiral aggregation in the two indoline systems but was effective for anilino squaraines (molecular structure shown in Figure 12.1). This modification introduced another spectroscopic variable that can be investigated and could be used in the study of more complex systems.



(*S*,*S*)-nOCi-SQ

(*S*,*S*)-bCi-SQ (R = (*S*)-3,7-dimethyloctyl)
(*S*,*S*)-mCi-SQ (R = ethyl)

Figure 12.1: Molecular structure of the investigated squaraines **(*S*,*S*)-nOCi-SQ**, **(*S*,*S*)-mCi-SQ** and **(*S*,*S*)-bCi-SQ**

Based on these results, two new chiral (*S*)-citronellyl-functionalized squaraines, **(*S*,*S*)-nOnCi-SQ** and **(*S*,*S*)-nCi-SQIB**, were designed and investigated in Chapter 4. Thereby, it could be demonstrated that

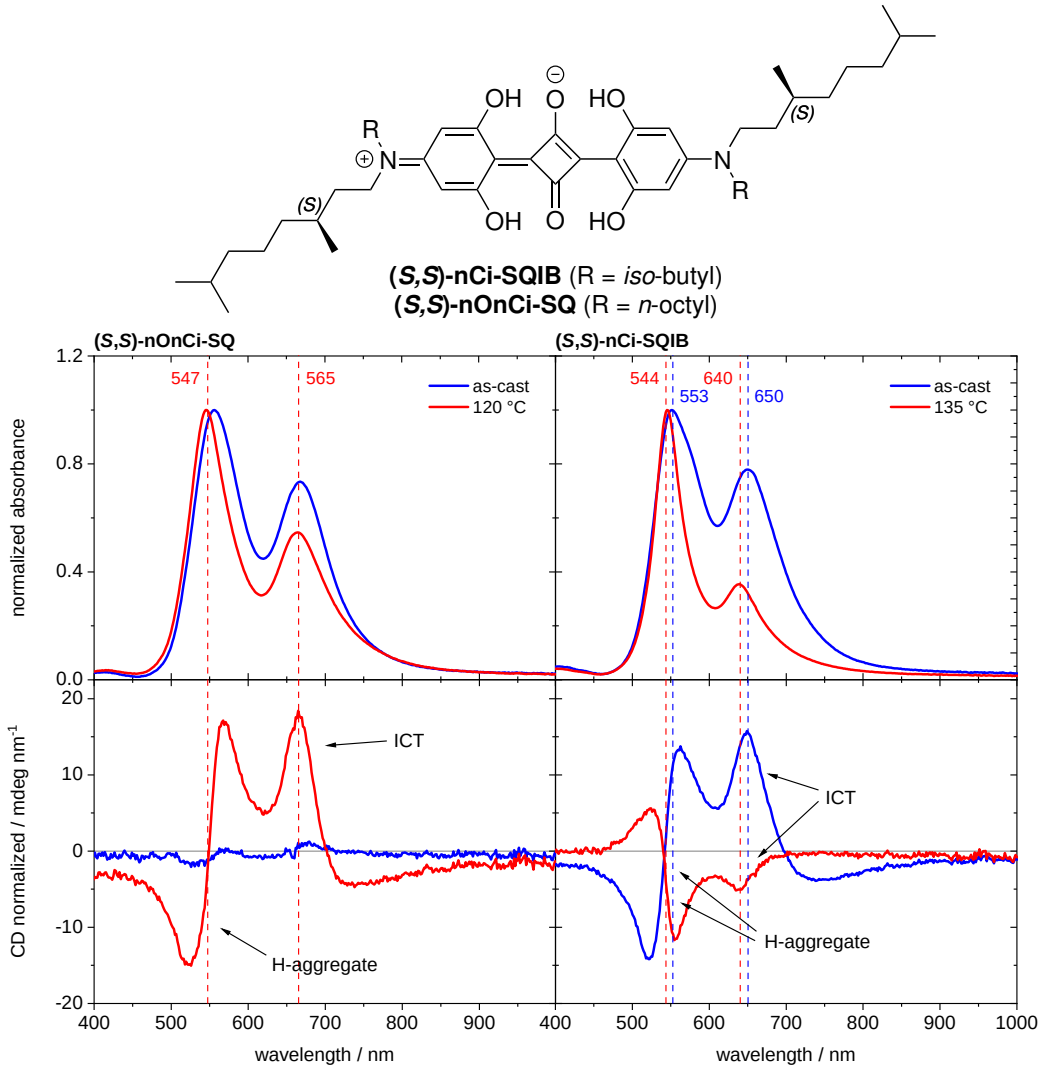


Figure 12.2: Top: Molecular structure of the investigated squaraines **(*S*,*S*)-nOnCi-SQ** and **(*S*,*S*)-nCi-SQIB**. Bottom: Summary of the modulation of the ICT through steric hindrance.

the ICT interactions can be modulated through steric hindrance, as summarized in Figure 12.2. This was possible due to the exhibition of the characteristic double-humped spectral feature when applied in solution-processed spin-coated thin films, similar to non-chiral *n*-alkyl anilino squaraines. Showing that these dyes are eligible to be directly compared to their non-chiral counterparts, the added value of chirality was used to determine the origin of the two peaks. From there, the different intensity ratios in the UV/Vis absorbance and CD spectra between the H-band and ICT-band in **(*S*,*S*)-nOnCi-SQ** and **(*S*,*S*)-nCi-SQIB** revealed an effective reduction of ICT interactions. This was further supported by transient absorption measurements, by showing that the double-humped feature originates from a single aggregate species. Finally, spectroscopic ellipsometry revealed an effective uniaxial alignment of the molecular aggregates, quantified through their complex refractive indices.

In addition, the incorporation of a neopentyl group (**(*S*,*S*)-Ci-SQNP**) was successfully attempted to

maximize steric hindrance. As a result, aggregation was entirely hindered and no changes were observed in either the UV/Vis or CD spectra upon thermal annealing, which remained essentially unchanged until decomposition/evaporation occurred. This demonstrates – once again – that even small changes (isobutyl vs. neopentyl: just one -H is substituted with -CH_3) can lead to significant changes in the aggregation behavior. In the presented case, aggregation is completely suppressed, since the steric repulsion is sufficiently large. However, design modifications (like moving the steric unit further from the π-conjugated backbone – e.g., ethylene group) or alternative annealing techniques such as solvent annealing should be attempted to allow higher molecular mobility during the annealing process.

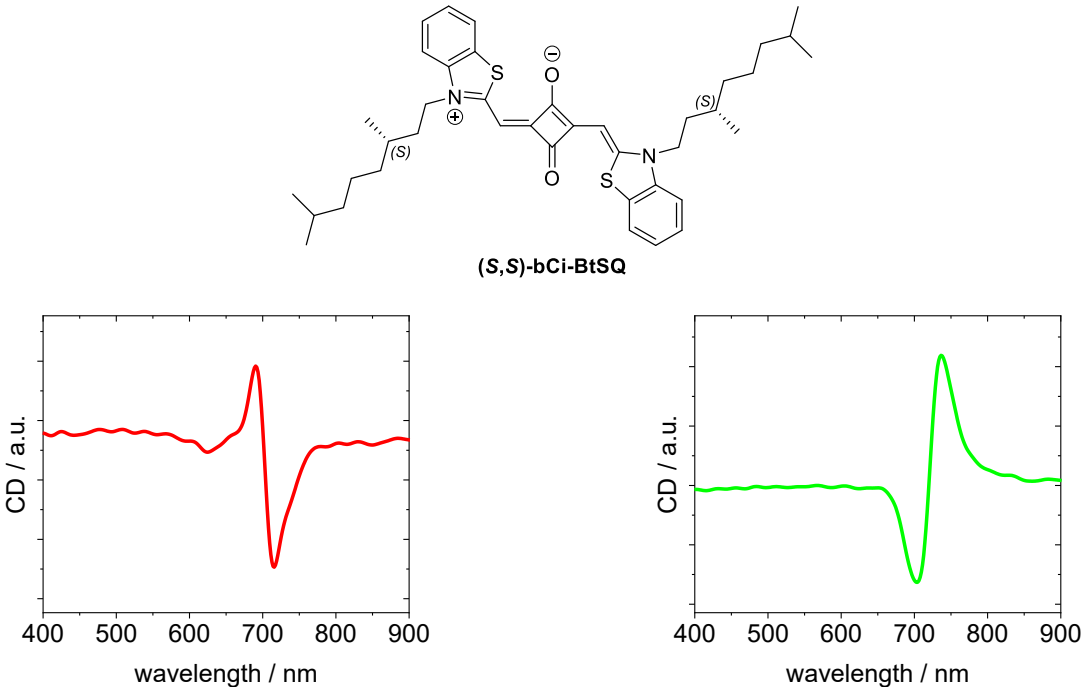


Figure 12.3: Molecular structure of the chiral benzothiazole-derived squaraine **(*S*,*S*)-bCi-BtSQ** and the illustrated change in chiroptical repose of thin films produced from different solvents.

In Chapter 5, we successfully synthesized and characterized the chiral benzothiazole-derived squaraine (*S*,*S*)-bCi-BtSQ, and investigated its aggregation behavior as well as optical constants in solution-processed thin films. The introduction of the second heteroatom sufur in the five-membered ring significantly enhanced the aggregation properties of the squaraine, by planarisation of the conjungated π-system, and thus, reducing the steric bulk between molecules. Through this approach, the previously encountered challenges associated with the aggregation of **(*S*,*S*)-mCi-SQ** and **(*S*,*S*)-bCi-SQ** (Chapter 3) were successfully resolved. All thermally annealed **(*S*,*S*)-bCi-BtSQ** layers, regardless of the three processing solvents of choice: chloroform, dichloromethane, and dichloromethane:cyclohexane mixture, exhibit the same uniaxial anisotropic thin film structure, which is different from the single crystal structure. From the uniaxial anisotropic complex refractive index, we learned that, in addition to the in-plane component, there is an out-of-plane component that is invisible in normal incidence transmission spectroscopy. The out-of-plane component is red-shifted relative to the in-plane component, which also has distinct vibronic signatures. Even though we do not know the thin film

structure, we assume two or more translationally invariant molecules in the aggregate. Therefore, we interpret the spectral features as Davydov splitting, with the in-plane band being the upper Davydov component (UDC) and the out-of-plane band being the lower Davydov component (LDC). This is a rarely documented case. Because the molecular aggregation is chiral, the layers exhibit an excitonic circular dichroism which was determined using Mueller matrix polarimetry. However, since it is a normal incidence transmission measurement, only the CD signals of the in-plane component, that is UDC, can be captured. We observe multifaceted bisignate CD spectra whose shapes depend on the processing solvent and annealing temperature, whereby a sign inversion may mislead to the interpretation of a structural rearrangement. However, the peculiar shape of the CD spectra can rather be interpreted as the sum of several bisignate features, one for each vibronic progression, which are subject to relocation of rotational strength because of processing conditions.

This leaves the splitting of the Davydov bands into an in-plane and an out-of-plane component, compared to the usual case where both Davydov bands are at least partially project into the plane of the thin film, as the most striking feature of the **(*S*,*S*)-bCi-BtSQ** layers.

Part B – including Chapter 6, 7, 8 and 9 – covered all studies done on proline-derived and extended (e.g., indoline-derived) chiral squaraines.

First, the underlying arrangement of **ProSQs** with intermediate alkyl-chain lengths in aggregated solutions, as well as the origin of the strong chiroptical response, were investigated. Overall, the findings show that the classical exciton approach cannot accurately describe the complex aggregation behavior

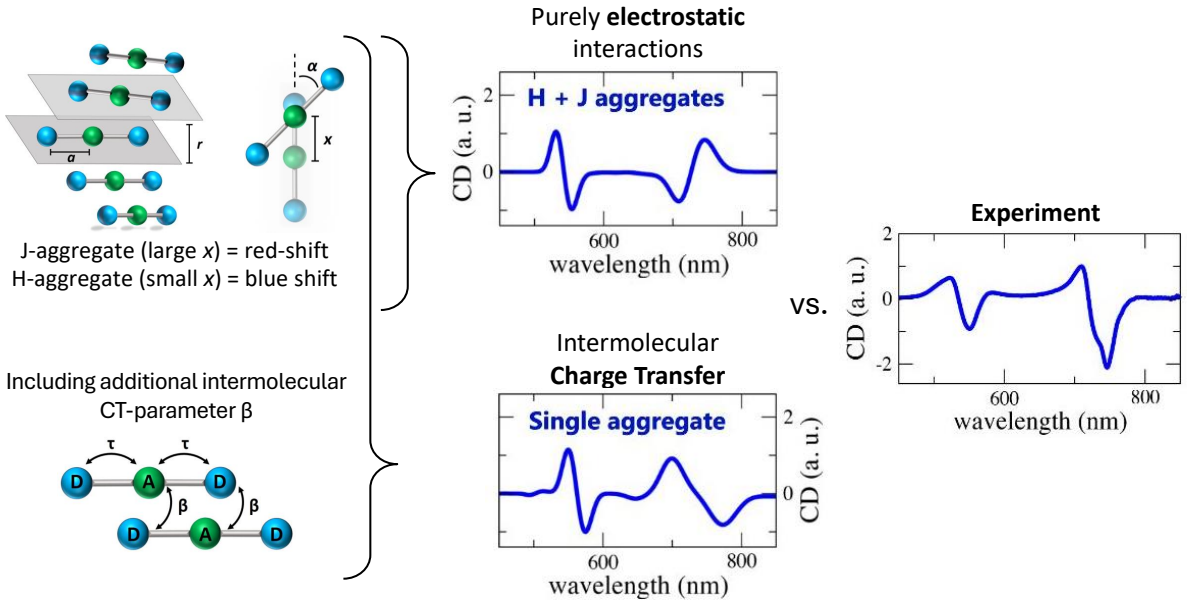


Figure 12.4: Summary of the aggregation behavior of chiral **ProSQs** with intermediate alkyl-chain lengths. The classical exciton model alone cannot account for the observed complexity. Instead, a description involving mixing Frenkel-like exciton states (Coulombic H-aggregates) and charge-separated states mediated by ICT interactions provides an accurate explanation of the CD spectral characteristics. Figure adapted with permission from [2] © The Royal Society of Chemistry 2023.

of squaraines in solution. While dimeric models may sufficiently explain the linear spectral characteristics of aggregates, they are insufficient for an accurate description of the chiroptical properties. In comparison to that, mixing Frenkel-like exciton states (Coulombic H-aggregate) and charge-separated states via intermolecular charge transfer (ICT) interactions, accurately describes the linear and CD spectral characteristics, as depicted in Figure 12.4. Molecular dynamics (MD) simulations, despite inherent size limitations, indicate that kinetic trapping can potentially invert aggregate helicity relative to the equilibrium structure. Both ESM-ES and ESM-CT models predict a superlinear enhancement of the CD intensity with increasing aggregate size, consistent with the exceptionally strong chiroptical responses observed in **ProSQ-C16** films.[34] Although a definitive structural assignment for squaraine aggregates in solution could not been done, this comprehensive investigation provides valuable insights into the chiral optical responses of molecular aggregates beyond the scope of the traditional exciton model.

Next, by following the idea that the reduction of the alkyl chain lengths to a minimal case would favour the formation of single crystals without incorporated solvent, worked as attended and led to the synthesis and investigation of **(*S*,*S*)-ProSQ-C1**. With this the first crystal structure of a **ProSQ** – with no incorporated solvent – was achieved. Thereby the crytsal structure of **(*S*,*S*)-ProSQ-C1** is similar to the one of **(*R*,*R*)-PyrSQ-C1**, with a monoclinic unit cell in the *C*2 space group but exhibits a much longer c-axis and an almost straight molecular chain and no zigzag arrangement. The early-stage aggregation experiments in solution of **(*S*,*S*)-ProSQ-C1** revealed a nearly identical aggregation behaviour to that of **(*S*,*S*)-ProSQ-C3** and – within a certain water-content range of 20 to 40% – even a similar behaviour to long-chain **ProSQs** such as C12 and C16. The linear optical properties of solution-processed **(*S*,*S*)-ProSQ-C1** thin films were comparable to those of **(*S*,*S*)-ProSQ-C3**. Moreover, depending on the annealing temperature, similarities with longer alkyl-chain **ProSQs**, such as **ProSQ-C6** and **ProSQ-C16**, were observed in both peak positions and overall spectral shape. In contrast, the CD spectra revealed significant differences, highlighting the influence of the alkyl-chain lengths.

Following the study of **ProSQs** in aggregated solutions, attention was turned to their behavior in the solid state. Spin-coated and thermally annealed thin films of **ProSQs** exhibit exceptionally high optical g-values. Although this class of compounds has been known about for over a decade, the precise chromophore arrangement and the underlying mechanism responsible for their pronounced chiroptical response remained unresolved for a long time. Our findings strongly suggest a “single-type-of-aggregate” in thermally annealed enantiopure thin films of **ProSQs**, proven by **ProSQ-C16**. This single aggregate species is therefore responsible for the strong light-matter interactions at visible-light frequencies. Based on the theoretical groundwork presented in Chapter 6, a single enantiopure aggregate can produce two peaks in the UV/Vis absorbance and CD spectra due to intermolecular charge transfer hybridization of excitons. Recent theoretical and experimental studies have also confirmed the existence of charge transfer Frenkel hybrid excitons in non-chiral anilino-squaraine thin films.[14, 142] Furthermore, transient absorption dynamics, in combination with the dynamics obtained from SVD, indicate that multiple relaxation channels of the exited enantiopure **ProSQ-C16** aggregate must be considered. As shown in Figure 12.5, this relaxation is dominated by a transition of the photoexcited exciton band minimum within the J-type aggregate into an optically dark intermediate state, which explains the quenched fluorescence observed in **ProSQ** thin films. The nature of this observed intermediate state exceeded the scope of this study and could not be resolved. However, an ICT state, which is optically non-radiative,[14, 149] has been proposed as a possible candidate based on theoretical research by Painelli and coworker.[2]

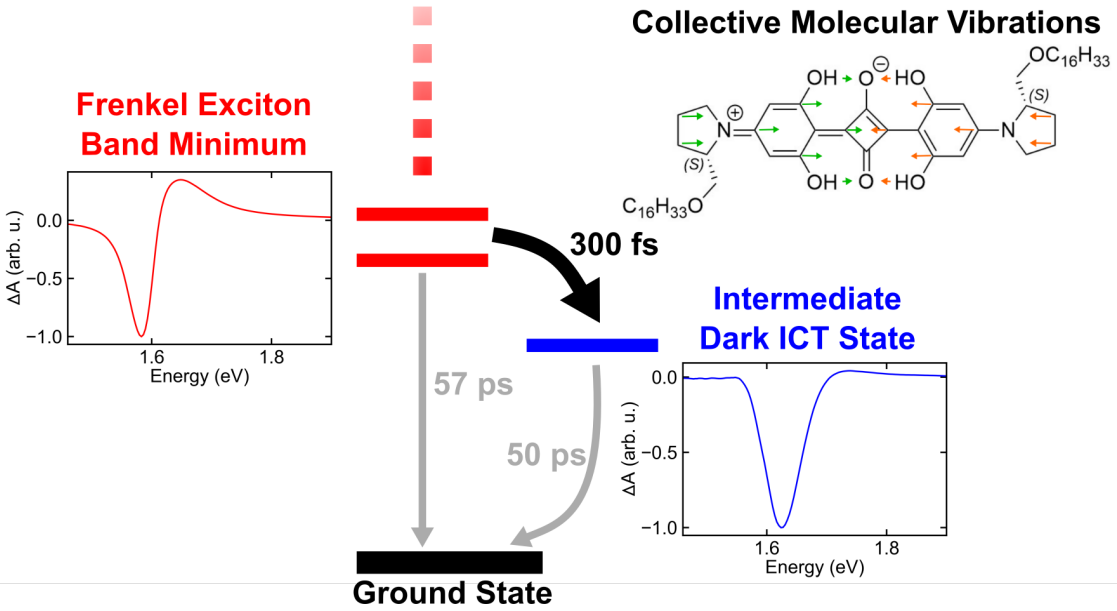


Figure 12.5: Sketch of the exciton relaxation channels in enantiopure **ProSQ-C16** aggregates. The fastest dynamics correspond to a transition from the initially excited state (red platforms) into an intermediate state (blue platform), potentially mediated by vibronic coupling to collective molecular vibrational modes (indicated by arrows on the molecular structure). This migration occurs on ultrafast timescales, whereas relaxation to the ground state is significantly slower. Figure adapted with permission from [3] © 2024 SCUT, AIEI, and John Wiley & Sons Australia, Ltd.

Such a dark state from charge-transfer Frenkel hybrid excitons has been recently experimentally proven by transient absorption spectroscopy in non-chiral anilino-squaraine thin films. Thus, we concluded this intermediate state involves an ICT. Due to the short exciton lifetimes and rapid transition to the dark state, we propose a conical intersection towards the intermediate CT as an efficient non-radiative relaxation pathway.

Building on the success of **ProSQs**, next it was attempted to tune the absorption maxima and enhance π-π stacking interactions through targeted structural modification. In particular, in the beginning the idea consisted of extending the π-conjugated system through introduction of an additional aryl unit at the proline substituent, resulting in an indoline- and a tetrahydroisoquinoline-dervied unit (Figure 12.6). Unfortunately, the initially targeted molecular design could not be achieved via the traditional condensation method. This was demonstrated through three distinct molecular designs, which, despite their differences, still retained key features of the original concept – namely, the incorporation of an additional aromatic ring with a nitrogen atom in close proximity. The unsuccessful reactions/reduced reactivity was attributed to the reduced nucleophilicity of the nitrogen atom, either in the indolenine-derivative (structurally similar to aniline) or in the tetrahydroisoquinoline/isoindole-derivatives (structurally similar to benzylamine). Rather than leaving this explanation as an assumption and discontinue the research at this point, it was decided to acquire a chemical proof. For this, the system was modified to the hydrogenated indoline form (i.e. octahydro-1H-indole) to investigate the reason why the previous attempts of incorporating an additional aromatic ring failed.

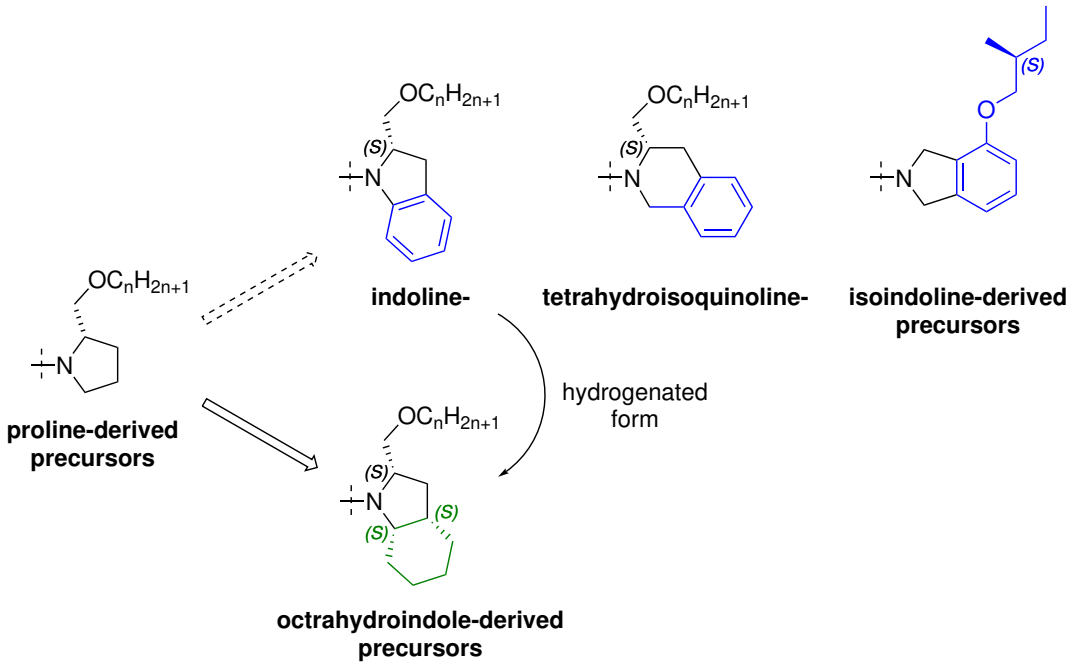


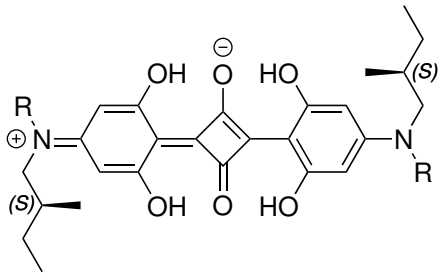
Figure 12.6: Idea of changing the system to the hydrogenated indoline form (i.e. octahydro-1H-indole) to restore the nucleophilicity as previous attempts of incorporation of an additional aromatic ring (blue) failed.

This approach led to the synthesis of two new squaraine dyes, **(*S*,*S*)-OHI-SQ-C3** and **(*S*,*S*)-OHI-SQ-C10**, in substantial quantities. Their successful preparation not only confirmed the previous hypothesis of reduced nucleophilicity in the earlier systems but also allowed the investigation of a highly interesting molecular design, featuring multiple stereogenic centres in close proximity to the π-conjugated backbone.

Both squaraines proved to be highly interesting, exhibiting markedly different behaviours – not only between early stage aggregation in solution and in the solid state, but also when compared directly to each other. Such a strong influence of alkyl chain length was already previously observed for the **ProSQs** and once again shown here. For **(*S*,*S*)-OHI-SQ-C3**, the observations suggest a Coulombic Frenkel exciton with J-type character, supported by the single-crystal X-ray structure. While the crystal packing also opens the possibility for ICT interactions, no such feature was detected in the UV/Vis absorbance or CD spectra. In contrast, **(*S*,*S*)-OHI-SQ-C10** exhibits an aggregation behaviour similar to that observed for other chiral anilino squaraines (e.g., **(*S*,*S*)-nOCi-SQ**, **(*S*,*S*)-nOnCi-SQ** and **(*S*,*S*)-nCi-SQIB**), indicating coupling between a Coulombic Frenkel exciton with H-aggregate character and an ICT. Although **(*S*,*S*)-OHI-SQ-C3** and **(*S*,*S*)-OHI-SQ-C10** were thoroughly investigated for their aggregation behaviour, drawing definitive conclusions on the precise spatial arrangement of the chromophores was not possible without supporting *in silico* methods.

Part C – Chapter 10 – was the attempt of the strategic integration of beneficial properties from both proline-derived and *n*-alkyl anilino squaraines, for the application in optoelectronic devices.

2-Methylbutyl-Derived Anilino Squaraines:



(*S*,*S*)-2mb-SQIB (R = *iso*-butyl)
(*S*,*S*)-2mb-DSQ (R = $C_{10}H_{21}$)
(*S*,*S*)-2mb-HDSQ (R = $C_{16}H_{33}$)
(*S*,*S*)-2mb-SQPE (R = phenylethyl)

Figure 12.7: Molecular structure of the investigated (*S*)-2-methylbutyl-derived anilino squaraines.

In summary, this chapter follows the development of an initial molecular design concept, beneficial for the application in optoelectronic devices, all the way to the fabrication and testing of the functional device. Starting with the synthetic approach and their challenges, a suitable route for the preparation of 2-methylbutyl-derived anilino squaraines was established. Concerns regarding possible racemisation in the final step toward the secondary amine were resolved by the targeted synthesis of a diastereomeric compound, which could be separated via HPLC. Once the enantiomeric purity of the secondary amines was confirmed, the classical two-step, one-pot procedure was applied, yielding two new squaraines: **(*S*,*S*)-2mb-DSQ** and **(*S*,*S*)-2mb-HDSQ**. Although this standard method proved effective for these two compounds, the synthesis of the chiral **SQIB**-derivative **(*S*,*S*)-2mb-SQIB** turned out be be challenging. After the observation of the instability of the product of the first condensation between the secondary amine and phloroglucinol, the reaction could be fine tuned regarding the used equivalents and conditions. Thus, another two squaraines were accessible: **(*S*,*S*)-2mb-SQIB** and **(*S*,*S*)-2mb-SQPE**.

With these four uniquely structured squaraines (Figure 12.7) in hand, their chiral aggregation be-

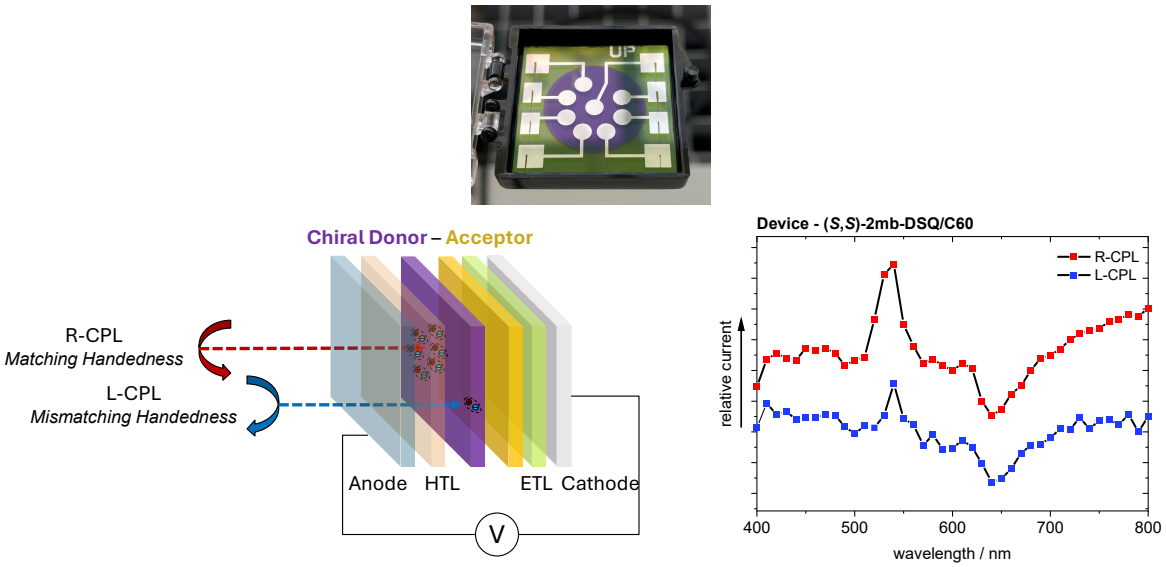


Figure 12.8: Actual picture, illustration and preliminary data from chirality-resolved photocurrent measurements of a **(*S*,*S*)-2mb-DSQ**-based PHJ-OPV device.

haviour was systematically investigated. While early-stage aggregation experiments in solution revealed only negligible aggregation tendencies, solution-processed thin films exhibited the opposite behaviour. Here, **(*S*,*S*)-2mb-DSQ**, **(*S*,*S*)-2mb-HDSQ** and **(*S*,*S*)-2mb-SQIB** exhibited strong aggregation tendencies even at low temperatures. **(*S*,*S*)-2mb-DSQ** and **(*S*,*S*)-2mb-HDSQ** showed the characteristic double-humped absorbance spectra – arising from coupling between a Coulombic Frenkel exciton and an ICT state – together with the corresponding bisignate and monosignate signals in the CD spectra, indicative of supramolecular aggregation. In contrast, **(*S*,*S*)-2mb-SQIB** closely resembled the non-chiral **SQIB** in almost all respects. The occurrence of two distinct polymorphs, a monoclinic and a presumably orthorhombic form, as well as other similarities to **SQIB**, were intensively investigated.

At the end, **(*S*,*S*)-2mb-DSQ** was selected for application as the donor material in a PHJ-OPV, paired with C_{60} fullerene as the acceptor material. Device fabrication used a combination of solution-processed spin-coating and PVD techniques. The resulting devices, prepared with varying squaraine layer thicknesses, were characterized using standard methods. Although the overall performance was relatively low compared to other squaraine-based devices, this can be considered secondary, as the primary aim was to function as a detector. This ability of the device to distinguish between left- and right-handed CPL, was finally tested as a proof of concept, as shown in Figure 12.8. Thus demonstrating the successful progression of the project from the initial molecular design concept to the fabrication of a working circular dichroic photodetector.

The **Part D** – Chapter 11 – was an excursus into the synthesis of chiral π-conjugated polymers exhibiting the chiral induced spin selectivity (CISS) effect for advanced optoelectronic applications and summarized the results of a three-month research stay in 2023 in the group of Prof. Dr. Seth R. Marder at the University of Colorado Boulder, USA.

Expanding the acquired knowledge regarding chiral materials and their characterization, the research stay turned out to be highly successful, yielding several uniquely structured polymers. Thereby, the

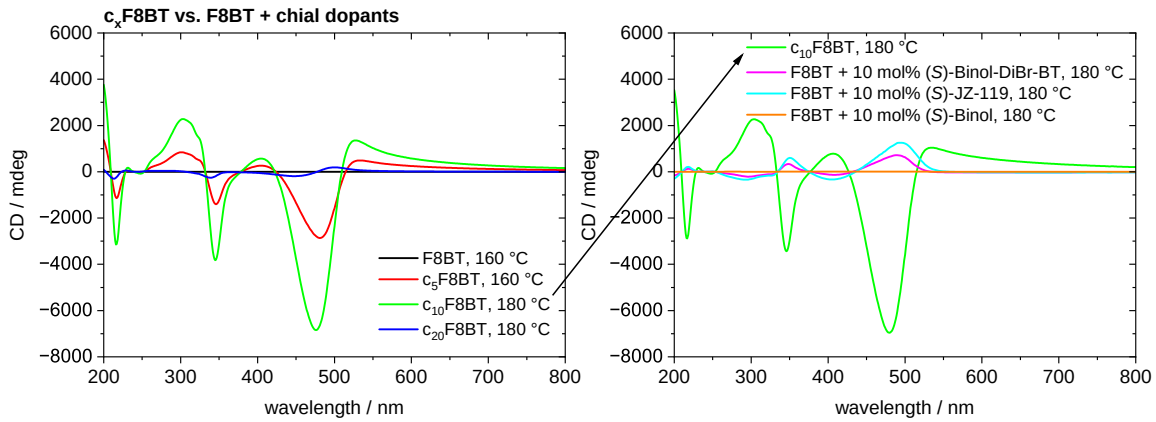


Figure 12.9: Comparison of the CD spectra between the best performing polymer **(*S*)-c$_x$F8BTs** (left, normalised) and non-chiral **F8BT** mixed with 10 mol% of different chiral dopants based on structurally similar molecules (right, unnormalised), proofing the superiority of the intrinsic chirality approach.

group of **(*S*)-c$_x$F8BTs** stood out with the most striking and promising aggregation behaviour. These polymers showed pronounced chiroptical properties in properly processed and annealed thin films, with huge CD-values peaking at ca. -70 mdeg/nm for **(*S*)-c$_{10}$F8BT**. Even though this system is not optimized yet and the best mol%-fraction of incorporated **cBT** into **F8BT** has still to be figured out, these values are in the same order of magnitude as those of the best performing chiral materials reported today. In direct comparison to traditional thin films of achiral **F8BT** with chiral dopants/additives based on structurally similar molecules, the intrinsic chirality approach has already been proven to be superior and surpasses the performance of films with chiral additives many times over (Figure 12.9). Previous approaches to synthesizing chiral polymers typically involved exclusively on chiral monomers, which generally exhibited inferior overall chirality-related properties, as it was also demonstrated during the research stay (see Appendix I.3.2 and I.3.3). However, our approach in which chiral and achiral monomers (**cBT** and **BT**) are copolymerized, which we have found to be profitable in at least some cases, has barely been investigated so far and requires more systematical research.

Final Remarks

In conclusion, the work presented in this thesis has investigated a broad range of squaraine dyes, systematically varying their molecular design and terminal *n*-alkyl substituents in order to optimize aggregation behavior and the associated chiroptical properties. While not every derivative exhibited exceptional chiral aggregation, most of them did and their study provided valuable insights into the interaction of molecular structure, supramolecular organization, and (chir)optical response. A central question addressed consistently this work was the underlying arrangement of chromophores and the mechanism responsible for the remarkably strong chiroptical responses observed in these systems. By exploding the added value of chirality, the resulting CD response was used to probe these arrangements. This allowed their original nature to be identified: bisignate signals were assigned to strongly coupled Coulombic Frenkel excitons, whereas monosignate peaks were linked to ICT interactions. Using this principle on several occasions in combination with other analytical methods, allowed the unimpeachable identification of ICT interactions as a recurring and fundamental element in the aggregation behavior of squaraines.

Together, these results establish a coherent framework for understanding structure-property relationships in squaraines, while demonstrating the practical potential of these materials through their application into a organic photovoltaic device. However, this works shows well that even small molecular modifications can have significant consequences for aggregation and optical behavior. Thus, the fine-tuning of these systems remains an ongoing challenge. Considerable work is still required, both on the synthetic and on the theoretical side. Latter are essential to fully capture the interplay between excitonic coupling, charge transfer, and supramolecular organization.

CHAPTER 13

Experimental Section

13.1 Materials and Methods

General Remarks

Reactions under inert gas conditions were performed under dry argon atmosphere with dry solvents in flame-dried glassware using common *Schlenk* techniques. As inert gas, Argon (99.996% purity) was obtained commercially and further purified by passage through a gas purification system to remove residual traces of water prior to use.

Chemicals

All chemicals used were directly purchased from common chemical suppliers or taken from the stock of the *Lützen* group. Unless otherwise described, all chemicals were used without further purification.

Solvents

All solvents used for reactions were commercially obtained and purified by standard methods. Solvents for column chromatography were previously distilled. Dry solvents were previously dried by standard methods and stored over 4 Å molecular sieves under dry argon atmosphere or dried by a *MP-SPS 800* (*MBRAUN*) solvent purification system.

Chromatography

Flash column chromatographic purifications were performed using silica gel 60 (40 - 63 μm, 230 - 400 mesh, ASTM, *Merk*) and pre-purified solvents. Reaction processes and column chromatographic separations were monitored by thin-layer chromatography (TLC) using silica gel 60 F_{254} TLC-aluminum plates by *Mercl* as stationary phase and proper solvent/solvent mixtures as mobile phase. Fluorescent and fluorescent quenching substances were detected under UV light at the wavelengths of λ = 254 nm and λ = 366 nm. For the detection of non-UV-active compounds, TLC plates were developed either with ethanolic ninhydrin (2,2-dihydroxyindane-1,3-dione) solution or by oxidation using an aqueous potassium permanganate solution, followed, when required, by gentle heating with a heat gun. Analytical high-performance liquid chromatography (HPLC) separations were performed in the HPLC pool of the

Kekulé Institute for Organic Chemistry and Biochemistry at the University of Bonn using equipment from Knauer. Specific parameters are indicated in the relevant sections.

NMR-Spectroscopy

All NMR-spectroscopic measurements were performed at a ^{1}H-Larmor frequency of around 300 MHz, 400 Mhz, 500 MHz or 700 MHz using *Bruker Avance I 300*, *frequency = 300.13 MHz*, *Bruker Avance I 400*, *frequency = 400.13 MHz*, *Bruker Avance I 500*, *frequency = 499.13 MHz*, *Bruker Avance III 500*, *frequency = 500.13 MHz* or *Bruker Avance III 700*, *frequency = 700.41 MHz* spectrometers. The samples were prepared with commercially obtained deuterated solvent. The spectra were calibrated against the proton and natural abundance of ^{13}C resonance of $CDCl_3$ (δ(^{1}H) = singlet, 7.26 ppm; δ(^{13}C) = triplet, 77.16 ppm) or CD_2Cl_2 (δ(^{1}H) = triplet, 5.32 ppm; δ(^{13}C) = triplet, 53.84 ppm) relative to tetramethylsilane.[183] Evaluation and plotting of the spectra were performed using *TopSpin 4.07* (*BrukerBioSpin*). The assignment of the ^{1}H and ^{13}C signals (all measured proton decoupled) was possible by different 1D and 2D-NMR-experiments (COSY, HMBC, HSQC). The following abbreviations were used to describe the nature of the signals: s = singlet, d = doublet, t = triplet, m = multiplet, *br* = broad.

Elemental Analysis

The CHNS elemental analyses were carried out after standard methods with either tin of silver ”boats” using a *Vario EL* (*Heraeus*). All compounds were measured at least two times and the mean values were compared with the calculated values from *ChemDraw* (*PerkinElmer*).

Mass-Spectrometry

All mass spectrometric ESI and APCI experiments were performed on an *Orbitrap XL* mass spectrometer (*Thermo Fischer Scientific*).

Single-Crystal X-Ray Diffraction

All SC-XRD measurements were carried out in the Central analytics department of the Chemical Institutes of University of Bonn. The single crystal structure data were visualized and analyzed using Mercury 3.10.3 (build 206425). Detailed parameters for each measurement and determination are given in the respective sections.

UV/Vis-Spectroscopy in Solution

UV/Vis spectroscopic measurements in solution were carried out using a *Specord 200* spectrometer (*Analytic Jena*) with 10 mm glass cuvettes (*Hellma*). A previous measurement of the pure solvent or solvent mixture was used for a baseline correction.

CD-Spectroscopy in Solution

CD spectroscopic measurements in solution were performed using a *J-810* spectrometer (*JASCO Corporation*) with 10 mm glass cuvettes (*Hellma*). A previous measurement of the pure solvent or solvent mixture was used for a baseline correction.

Early Stage Aggregation Experiments in Solution

A detailed generl procedure for the early-stage aggregation experiments in solution can be found in [2] (included paper of this thesis found in Appendix D) and [141].

Thin Film Preparation

If not otherwise noted: Solutions of the desired squaraine were prepared in chloroform (HPLC grade, amylene stabilized, *VWR*), dichloromethane (HPLC grade, *Sigma Aldrich*) and cyclohexane/dichloromethane mixtures (1:1, *v*:*v*, HPLC grade, *Sigma Aldrich*) at a concentration of 4, 5 or 6 mg/mL and stirred under light protection for 24 hours before use. Glass substrates were cut from 1 mm thick float glass objective slides (*VWR*) in 15 × 15 cm or 1 × 1 inch (1 inch = 2.54 cm). Thin films were prepared by spin coating 65 µL or 120 µL of the prepared spin-on solution for 60 s at different rotation speeds and acceleration (2000 rpm, 400 rpm/s (slow); 3000 rpm, 1000 rpm/s (medium); 4000 rpm, 4000 rpm/s (fast)) onto the glass substrates. The ”air” side of the float glass was preselected for coating. Samples were thermally annealed on a preheated hotplate for 30 min at various temperatures (exact temperatures are specified in the respective sections). Individual sample were fabricated for each annealing temperature. All preparation steps were carried out under ambient conditions.

Ellipsometry, Mueller Matrix Polarimetry and Absorbance of Thin Films

A J.A. Woollam M2000-DI or M2000XI single rotating compensator variable-angle spectroscopic ellipsometer a with a horizontal sample stage and CompleteEASE software version 5 (evaluation version 6) were used for optical data acquisition. The spectral range from 193 nm to 1690 nm is recorded using two CCD detector arrays, which simultaneously offer 705 wavelengths with a bandwidth of 5 nm in the UV/Vis range and 10 nm in the NIR spectral range. Intensity spectra are recorded in normal incidence transmission mode and are shown as absorbance, i.e. $-\log(\text{transmission})$. The diameter of the light beam is approximately 2–3 mm, so that possible microtexture of the thin films is averaged.

Using conventional variable angle spectroscopic ellipsometry (VASE) in reflection, Ψ and Δ thin film spectra were measured at different angles of incidence (AOIs) from 45°to 70°in steps of 5°. A multi-sample analysis (MSA) plus was employed to obtain the uniaxial complex refractive indices of several squaraines. This MSA combines Ψ-Δ-scans of multiple samples prepared in the same way (same solvent and annealing conditions) but with different spincoating conditions, i.e. different layer thicknesses. Adding the transmission intensity to the fitting procedure allows for improved determination of the out-of-plane component of the uniaxial refractive index. A B-spline regression, as provided by CompleteEASE version 6, was implemented to accurately model the ellipsometric data without enforcing a specific physical interpretation through an oscillator model. The optimization criteria of the fitting routine were a “visual best match” of the measured and modeled data, especially the transmission intensity data, and the minimization of the mean square error (MSE).

The detailed procedures of the general approach, as well as the method by which the CD spectra of the samples were extracted from Mueller matrix recordings, are described in detail in [34], [96] and [3] (included paper of this thesis found in Appendix F).

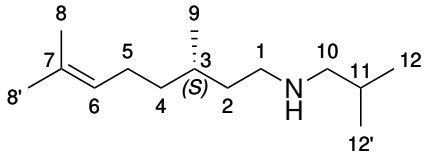
Fabrication of Photodiodes

The organic photovoltaic device of **(*S*,*S*)-2mb-DSQ** were fabricated during a research stay and in collaboration with Otgonbayar Erdene-Ochir in the group of Prof. Klaus Meerholz at the University of Cologne.

13.2 Experimental Section for Citronellyl-Functionalized Chiral Squaraines with Different Alkyl-Substituents

Synthesis of Precursors for Squaraine Dyes

_N_-(_S_)-(3,7-dimethyl-6-octenyl)-_N_-isobutylamine - (_S_)-Ci-N-IB



(_S_)-Ci-N-IB

Synthesis adopted and modified from the literature.[1]
Under inert gas conditions, (_S_)-(-)-3,7-dimethyl-6-octenal (2.31 g, 15.0 mmol, 1.00 eq.) and isobutylamine (1.10 g, 15.0 mmol, 1.00 eq.) were dissolved in 60 mL of dry methanol. The colorless solution was stirred at 65 °C under minor reflux and light exclusion overnight. Sodium borohydride (993 mg, 26.3 mmol, 1.75 eq.) was added portionwise to the ice cooled solution and stirred at r.t. for 24 h. The mixture was then poured in 15 mL of 1 M sodium hydroxide solution and subsequent extracted with diethylether (3 × 15 mL). The combined organic phases were washed with water (2 × 50 mL) and dried with magnesium sulfate. The solvent was removed under reduced pressure to obtain the product as a light yellow oil.

Yield: 2.05 g (9.69 mmol, 65%, light yellow oil)

Molecular weight: $C_{14}H_{29}N$, 211.39 g/mol

^{1}H-NMR: **(500 MHz, Chloroform-*d*, 298 K) δ [ppm] =**
5.09 (t, $^3J_{6,5}$ = 7.2 Hz, 1H, H-6), 2.68-2.54 (m, 2H, H-1), 2.43 (d, $^3J_{10,11}$ = 6.8 Hz, 2H, H-10), 2.03-1.90 (m, 2H, H-5), 1.82-1.73 (m, 1H, H-11), 1.68 (s, 3H, H-8'), 1.60 (s, 3H, H-8), 1.57-1.43 (m, 2H, H-2^a, H-3), 1.38-1.28 (m, 2H, H-2^b, H-4^a), 1.21-1.12 (m, 1H, H-4^b), 0.91 (d, $^3J_{12,11}$ = 6.6 Hz, 6H, H-12, H-12'), 0.89 (d, $^3J_{9,3}$ = 6.6 Hz, 3H, H-9)

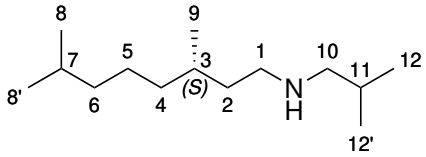
^{13}C-NMR: **(125 MHz, Chloroform-*d*, 298 K) δ [ppm] =**
131.3 (C-7), 125.0 (C-6), 58.2 (C-10), 48.2 (C-1), 37.4 (C-4), 37.2 (C-2), 30.9 (C-3), 28.3 (C-11), 25.9 (C-8'), 25.6 (C-5), 20.9 (C-12, C-12'), 19.8 (C-9), 17.8 (C-8)

MS: **(ESI(+), Dichloromethane, M = $C_{14}H_{29}N$) *m/z* =**
212.236 $[M+H]^+$

ESI HRMS: $[M+H]^+ = C_{14}H_{29}NH$
Calculated: *m/z* = 212.2373
Found: *m/z* = 212.2373

R_f-value: 0.40 (ethyl acetate)

***N*-(*S*)-(3,7-dimethyloctyl)-*N*-isobutylamine - (*S*)-nCi-N-IB**



(*S*)-nCi-N-IB

Synthesis adopted and modified from the literature.[141]
Under inert gas conditions, **(*S*)-Ci-N-IB** (2.05 g, 9.70 mmol, 1.00 eq.) was dissolved in 25 mL of dry methanol and carefully degassed in three freeze-pump-thaw cycles. After adding 10% palladium on carbon (514 mg, equal to 5 mol%), three additional freeze-pump-thaw cycles were performed. A hydrogen gas balloon was connected to the Schlenk-flask and the atmosphere was exchanged with hydrogen by three cycles of evacuation and repressurization. Complete conversion was tested by NMR and after 72 hours of vigorous stirring, the reaction mixture was filtered through a glass fibber filter. The filtrate was concentrated under reduced pressure and the yielded slightly yellow oil was used without further purification in the next reaction step.

Yield: 1.87 g (8.75 mmol, 90%, slightly yellow oil)

Molecular weight: $C_{14}H_{31}N$, 213.41 g/mol

^{1}H-NMR: **(500 MHz, Chloroform-*d*, 298 K) δ [ppm] =**
2.72-2.59 (m, 2H, H-1), 2.48 (d, $^3J_{10,11}$ = 7.0 Hz, 2H, H-10), 1.83 (sept, 1H, H-11), 1.62-1.44 (m, 3H, H-2^a, H-3, H-7), 1.40-1.24 (m, 5H, NH, H-2^b, H-4^a, H-5), 1.19-1.13 (m, 3H, H-4^b, H-6), 0.95 (d, $^3J_{12,11}$ = 6.6 Hz, 6H, H-12, H-12'), 0.92-0.87 (m, 9H, H-8, H-8', H-9)

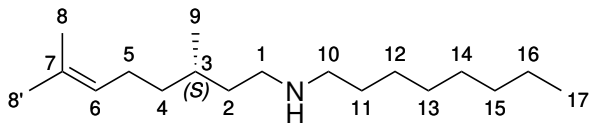
^{13}C-NMR: **(125 MHz, Chloroform-*d*, 298 K) δ [ppm] =**
58.1 (C-10), 48.2 (C-1), 39.4 (C-6), 37.5 (C-4), 37.1 (C-2), 31.2 (C-3), 28.2 (C-11), 28.1 (C-7), 24.9 (C-5), 22.9 (C-8'), 22.8 (C-8), 20.9 (C-12, C-12'), 19.9 (C-9)

MS: **(ESI(+), Dichloromethane, M = $C_{14}H_{31}N$) *m/z* =**
214.253 $[M+H]^+$

ESI HRMS: $[M+H]^+ = C_{14}H_{31}NH$
Calculated: *m/z* = 214.2529
Found: *m/z* = 214.2527

R_f-value: 0.06 (acetone + 1% triethylamine)

***N*-(*S*)-(3,7-dimethyl-6-octenyl)-*N*-octylamine - (*S*)-Ci-N-O**



(*S*)-Ci-N-O

(*S*)-Ci-N-O was synthesized according to the literature.[1]

Yield: 1.91 g (7.13 mmol, 71%, slightly yellow oil)

Molecular weight: $C_{18}H_{37}N$, 267.50 g/mol

^{1}H-NMR: **(500 MHz, Chloroform-*d*, 298 K) δ [ppm] =**
5.08 (t, $^3J_{6,5}$ = 7.2 Hz, 1H, H-6), 2.67-2.56 (m, 4H, H-1, H-10), 2.11-1.89 (m, 3H, NH, H-5), 1.67 (s, 3H, H-8'), 1.59 (s, 3H, H-8), 1.54-1.42 (m, 4H, H-2^a, H-3, H-11), 1.36-1.20 (m, 13H, H-2^b, H-4, H-12-16), 0.88 (d, $^3J_{9,3}$ = 6.3 Hz 3H, H-9), 0.87 (t, $^3J_{17,16}$ = 7.1 Hz, 3H, H-17)

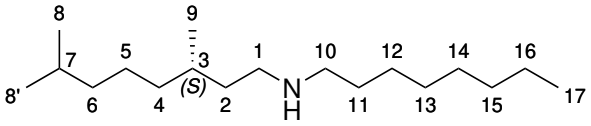
^{13}C-NMR: **(125 MHz, Chloroform-*d*, 298 K) δ [ppm] =**
131.3 (C-7), 124.9 (C-6), 50.2 (C-10), 48.0 (C-1), 37.3 (C-4), 37.2 (C-2), 32.0 (C-11), 30.8 (C-3), 30.1 (C-12), 29.7 (C-13), 29.4 (C-14), 27.5 (C-15), 25.8 (C-8'), 25.6 (C-5), 22.8 (C-16), 19.8 (C-9) 17.8 (C-8), 14.2 (C-17)

MS: **(ESI(+), Dichloromethane, M = $C_{18}H_{37}N$) *m/z* =**
268.298 $[M+H]^+$

ESI HRMS: $[M+H]^+ = C_{18}H_{37}NH$
Calculated: *m/z* = 268.2999
Found: *m/z* = 268.2999

R_f-value: 0.26 (ethyl acetate)

***N*-(*S*)-(3,7-dimethyloctyl)-*N*-octylamine - (*S*)-nCi-N-O**



(*S*)-nCi-N-O

Synthesis adopted and modified from the literature.[141]
Under inert gas conditions, **(*S*)-Ci-N-O** (1.90 g, 7.04 mmol, 1.00 eq.) was dissolved in 20 mL of dry ethyl acetate and carefully degassed in three freeze-pump-thaw cycles. After adding 10% palladium on carbon (38.3 mg, equal to 1.5 mol%), three additional freeze-pump-thaw cycles were performed. A hydrogen gas balloon was connected to the Schlenk-flask and the atmosphere was exchanged with hydrogen by three cycles of evacuation and repressurization. Complete conversion was tested by NMR and after 24 hours of vigorous stirring. Since only trace amounts of **(*S*)-Ci-N-O** were hydrated, the solvent was exchanged to 15 mL of dry methanol. After again performing freeze-pump-thaw cycles and adding additional 10% palladium on carbon (40.0 mg, equal to 15 mol%[a]), the atmosphere was exchanged with hydrogen. After 24 hours of vigorous stirring, NMR analysis showed complete hydrogenated of the amine **(*S*)-Ci-N-O**. The reaction mixture was filtered through Celite® and the filtrate was concentrated under reduced pressure to yield the product as yellow oil, which was used without further purification in the next reaction step.

Yield:	948 mg (3.52 mmol, 50%, yellow oil)
Molecular weight:	$C_{18}H_{39}N$, 269.52 g/mol
^{1}H-NMR:	**(700 MHz, Chloroform-*d*, 298 K) δ [ppm] =** 2.68-2.63 (m, 2H, H-1), 2.63-2.58 (m, 2H, H-10), 1.58-1.48 (m, 4H, H-2^a, H-7, H-11), 1.47-1.43 (m, 1H, H-3), 1.37- 1.20 (m, 12H, H-2^b, H-4^a, H-5, H-13-16), 1.15-1.09 (m, 3H, H-4^b, H-6) 0.89-0.85 (m, 12H, H-8, H-8', H-9, H-17)
^{13}C-NMR:	**(176 MHz, Chloroform-*d*, 298 K) δ [ppm] =** 50.1 (C-10), 48.0 (C-1), 39.4 (C-6), 37.5 (C-4), 37.0 (C-2), 32.0 (C-15), 31.2 (C-3), 29.9 (C-11), 29.7 (C-13), 29.4 (C-14), 28.1 (C-7), 27.5 (C-12), 24.9 (C-5), 22.8 (C-16), 22.8 (C-8'), 22.7 (C-8), 19.8 (C-9), 14.2 (C-17)
MS:	**(ESI(+), Dichloromethane, M = $C_{18}H_{39}N$) *m/z* =** 270.315 $[M+H]^+$

[a] 15 mol-% based on the amount of the non-hydrogenated amine, as determined by NMR analysis.

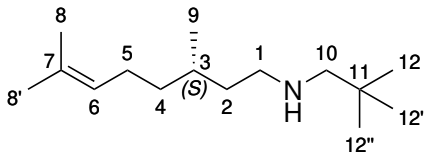
ESI HRMS: $[M+H]^+ = C_{18}H_{39}NH$
Calculated: *m/z* = 270.3155
Found: *m/z* = 270.3153

Elemental analysis: $C_{18}H_{39}N$

Calculated:	C: 80.22	H: 14.59	N: 5.20
Found:	C: 79.02	H: 14.00	N: 4.92

R_f-value: 0.24 (acetone + 1% triethylamine)

_N_-(_S_)-(3,7-dimethyl-6-octenyl)-_N_-neopentylamine - (_S_)-Ci-N-NP



(_S_)-Ci-N-NP

Synthesis adopted and modified from the literature.[1]
Under inert gas conditions, (*S*)-(-)-3,7-dimethyl-6-octenal (3.86 g, 25.0 mmol, 1.10 eq.) and neopentylamine (1.98 g, 22.7 mmol, 1.00 eq.) were dissolved in 50 mL of dry methanol. To the colorless solution, 3Å activated molecular sieves were added and the mixture kept at 65 °C under minor reflux and light exclusion overnight. Sodium borohydride (1.50 g, 39.77 mmol, 1.75 eq.) was added portionwise to the ice cooled solution and stirred at r.t. for 90 min. The mixture was then filtered off, poured in 25 mL of 1 M sodium hydroxide solution and subsequent extracted with diethylether (3 × 50 mL). The combined organic phases were washed with water (2 × 200 mL) and dried with magnesium sulfate. The solvent was removed under reduced pressure and the crude product purified by column chromatography on silica gel eluting with ethyl acetate + 5% methanol to obtain the product as a yellow oil.

Yield: 4.16 g (18.5 mmol, 81%, yellow oil)

Molecular weight: $C_{15}H_{31}N$, 225.42 g/mol

^{1}H-NMR: **(400 MHz, Chloroform-*d*, 298 K) δ [ppm] =**
5.08 (t, $^3J_{6,5}$ = 7.2 Hz, 1H, H-6), 2.71-2.53 (m, 2H, H-1), 2.35 (s, 2H, H-10), 2.06-1.88 (m, 2H, H-5), 1.67 (s, 3H, H-8'), 1.59 (s, 3H, H-8), 1.57-1.39 (m, 2H, H-2^a, H-3), 1.38-1.26 (m, 2H, H-2^b, H-4^a), 1.16 (m, 1H, H-4^b), 0.91 (s, 9H, H-12, H-12', H-12"), 0.88 (d, $^3J_{9,3}$ = 6.6 Hz, 3H, H-9)

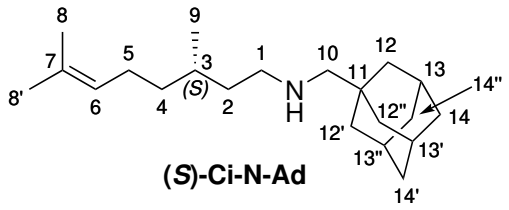
^{13}C-NMR: **(125 MHz, Chloroform-*d*, 298 K) δ [ppm] =**
131.3 (C-7), 125.0 (C-6), 62.6 (C-10), 49.1 (C-1), 37.4 (C-4), 37.1 (C-2), 31.5 (C-11), 30.9 (C-3), 28.0 (C-12, C-12', C-12"), 25.8 (C-8'), 25.6 (C-5) , 19.8 (C-9), 17.8 (C-8)

MS: **(ESI(+), Dichloromethane, M = $C_{15}H_{31}N$) *m/z* =** 226.254 $[M+H]^+$

ESI HRMS: $[M+H]^+ = C_{15}H_{31}NH$
Calculated: *m/z* = 226.2531
Found: *m/z* = 226.2529

***R*$_f$-value:** 0.50 (ethyl acetate + 5% methanol)

***N*-(*S*)-(3,7-dimethyl-6-octenyl)-*N*-adamantanemethylamine - (*S*)-Ci-N-Ad**



(*S*)-Ci-N-Ad

Synthesis adopted and modified from the literature.[1]
Under inert gas conditions, (*S*)-(-)-3,7-dimethyl-6-octenal (2.31 g, 15.0 mmol, 1.10 eq.) and 1-adamantanemethylamine (2.25 g, 13.64 mmol, 1.00 eq.) were dissolved in 30 mL of dry methanol. To the colorless solution, 3Å activated molecular sieves were added and the mixture kept at 65 °C under minor reflux and light exclusion overnight. Sodium borohydride (903 mg, 23.9 mmol, 1.75 eq.) was added portionwise to the ice cooled solution and stirred at r.t. for 90 min. The mixture was then filtered off, poured in 20 mL of 1 M sodium hydroxide solution and subsequent extracted with diethylether (3 × 50 mL). The combined organic phases were washed with water (2 × 200 mL) and dried with magnesium sulfate. The solvent was removed under reduced pressure and the crude product purified by column chromatography on silica gel eluting with ethyl acetate + 5% methanol to obtain the product as a white solid.

Yield: 3.79 g (12.5 mmol, 92%, white solid)

Molecular weight: $C_{21}H_{37}N$, 303.53 g/mol

^{1}H-NMR: **(400 MHz, Chloroform-*d*, 298 K) δ [ppm] =**
5.09 (t, $^3J_{6,5}$ = 7.2 Hz, 1H, H-6), 2.67-2.50 (m, 2H, H-1), 2.25 (s, 2H, H-10), 2.07-1.86 (m, 6H, NH, H-5, H-13, H-13', H-13"), 1.73-1.58 (m, 6H, H-14, H-14', H-14") 1.67 (s, 3H, H-8), 1.59 (s, 3H, H-8'), 1.56-1.42 (m, 8H, H-2^a, H-3, H-12, H-12', H-12"), 1.37-1.27 (m, 2H, H-2^b, H-4^a), 1.21-1.09 (m, 1H, H-4^b), 0.88 (d, $^3J_{9,3}$ = 6.5 Hz 3H, H-9)

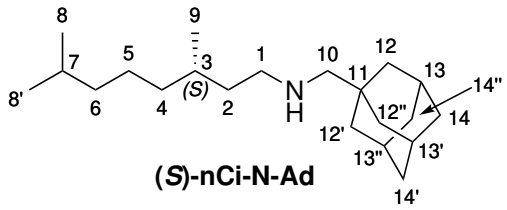
^{13}C-NMR: **(125 MHz, Chloroform-*d*, 298 K) δ [ppm] =**
131.3 (C-7), 125.0 (C-6), 63.0 (C-10), 49.1 (C-1), 41.0 (C-12, C-12', C-12"), 37.3 (C-2, C-14, C-14', C-14"), 36.8 (C-3), 33.4 (C-11), 30.8 (C-4), 28.6 (C-13, C-13', C-13"), 25.9 (C-8), 25.6 (C-5), 19.8 (C-9), 17.8 (C-8')

MS: **(ESI(+), Dichloromethane, M = $C_{21}H_{37}N$) *m/z* =**
304.299 $[M+H]^+$

ESI HRMS: $[M+H]^+ = C_{21}H_{37}NH$
Calculated: *m/z* = 304.2999
Found: *m/z* = 304.2994

R_f-value: 0.40 (ethyl acetate + 5% methanol)

_N_-(_S_)-(3,7-dimethyloctyl)-_N_-adamantanemethylamine - (_S_)-nCi-N-Ad



(*S*)-nCi-N-Ad

Synthesis adopted and modified from the literature.[141]
Under inert gas conditions, **(*S*)-Ci-N-Ad** (1.12 g, 3.69 mmol, 1.00 eq.) was dissolved in 25 mL of dry methanol and carefully degassed in three freeze-pump-thaw cycles. After adding 10% palladium on carbon (196 mg, equal to 5 mol%), three additional freeze-pump-thaw cycles were performed. A hydrogen gas balloon was connected to the Schlenk-flask and the atmosphere was exchanged with hydrogen by three cycles of evacuation and repressurization. Complete conversion was tested by NMR and after 72 hours of vigorous stirring, the reaction mixture was filtered filtered through Celite®. The filtrate was concentrated under reduced pressure and the crude product purified by column chromatography on silica gel eluting with acetone + 5% methanol to obtain the product as an oily yellow solid.

Yield: 785 mg (2.57 mmol, 70%, oily yellow solid)

Molecular weight: $C_{21}H_{39}N$, 305.55 g/mol

^{1}H-NMR: **(400 MHz, Chloroform-*d*, 298 K) δ [ppm] =**
2.70-2.56 (m, 2H, H-1), 2.48 (s, 2H, H-10), 2.06-1.88 (m, 3H, H-13, H-13', H-13"), 1.75-1.58 (m, 6H, H-14, H-14', H-14"), 1.57-1.39 (m, 9H, H-2^a, H-3, H-7, H-12, H-12', H-12") 1.38-1.18 (m, 4H, H-2^b, H-4^a, H-5) 1.18-1.02 (m, 3H, H-4^b, H-6) 0.88-0.80 (m, 9H, H-8, H-8', H-9)

^{13}C-NMR: **(125 MHz, Chloroform-*d*, 298 K) δ [ppm] =**
62.6 (C-10), 49.0 (C-1), 41.0 (C-12, C-12', C-12"), 39.4 (C-6), 37.4 (C-4), 37.2 (C-2), 37.2 (C-14, C-14', C-14"), 33.3 (C-11), 31.2 (C-3), 28.5 (C-13, C-13', C-13"), 28.1 (C-7), 24.8 (C-5), 22.8 (C-8'), 22.7 (C-8), 19.8 (C-9)

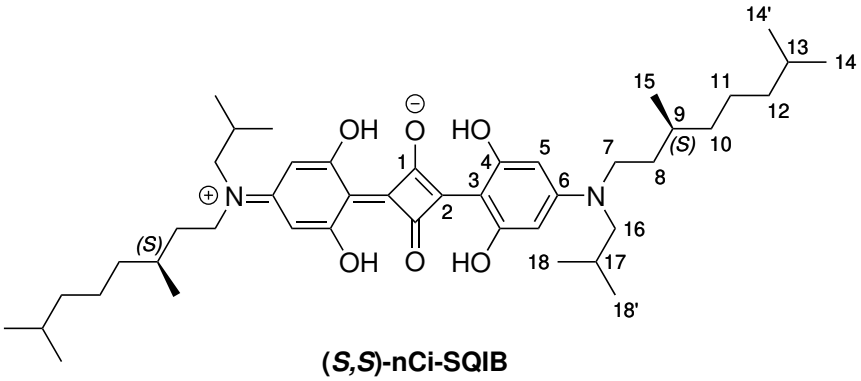
MS: **(ESI(+), Dichloromethane, M = $C_{21}H_{39}N$) *m/z* =**
306.315 $[M+H]^+$

ESI HRMS: $[M+H]^+ = C_{21}H_{39}NH$
Calculated: *m/z* = 306.3155
Found: *m/z* = 306.3155

R_f-value: 0.80 (acetone + 5% methanol)

Synthesis of Squaraine Dyes

2,4-bis[4-(*N*-(*S*)-(3,7-dimethyloctyl)-*N*-isobutylamine)-2,6-dihydroxyphenyl]squaraine - (*S*,*S*)-nCi-SQIB



(*S*,*S*)-nCi-SQIB

A single-neck flask, equipped with a Dean-Stark apparatus and reflux condenser, was charged with **(*S*)-nCi-N-IB** (1.00 g, 4.69 mmol, 1.00 eq.) and phloroglucinol (579 mg, 4.59 mmol, 0.98 eq.). The reactants were suspended in a mixture of toluene/1-butanol (1:1, v/v, 10 mL/mmol), evacuated 5 times under vigorous stirring and repressurized with argon. The reaction mixture was refluxed under argon atmosphere for 24 hours. After cooling to room temperature, squaric acid (267 mg, 2.34 mmol, 0.50 eq.) was added and the reaction mixture was heated to reflux. With the beginning of boiling, a sudden color change from slightly reddish over dark-green to dark-blue could be observed within minutes. Over the course of 12 hours, the reaction mixture gradually turned more and more green, suggesting possible hydrolysis of the formed squaraine. This caused me to stop the reaction prematurely, despite the fact that a reflux time of 24 hours is normally attempted. The mixture was slowly cooled to room temperature and chilled further in the freezer to promote precipitation of the raw product. The solid was collected via filtration and washed with methanol until the filtrate was colorless. Further purification was done by column chromatography on silica gel eluting with dichloromethane, followed by recrystallization from dichloromethane/methanol (1:1, v/v) and dichloromethane/cyclohexane (1:2,

v/v). The precipitated solid was each time filtered off and washed several times with methanol. After drying the collected solid under reduced pressure, the pure squaraine was obtained as a green solid.

Yield: 255 mg (0.35 mmol, 15%, green solid)

Molecular weight: $C_{44}H_{68}N_2O_6$, 721.04 g/mol

^{1}H-NMR: **(400 MHz, Chloroform-*d*, 298 K) δ [ppm] =**
10.97 (s, 4H, OH), 5.80 (s, 4H, H-5), 3.46-3.29 (m, 4H, H-7), 3.16 (d, $^3J_{16,17}$ = 7.7 Hz, 4H, H-16), 2.16-2.04 (m, 2H, H-17), 1.66-1.57 (m, 2H, H-8^a), 1.56-1.50 (m, 2H, H-13), 1.49-1.39 (m, 4H, H-8^b, H-9), 1.36-1.22 (m, 6H, H-10^a, H-11), 1.20-1.11 (m, 6H, H-10^b, H-12), 0.98-0.93 (m, 18H, H-15, H-18, H-18'), 0.87 (d, $^3J_{14,13}$ = 6.7 Hz, 12H, H-14, H-14')

^{13}C-NMR: **(176 MHz, Chloroform-*d*, 298 K) δ [ppm] =**
181.4 (C-1), 162.7 (C-4), 161.2 (C-2), 158.1 (C-6), 102.5 (C-3), 94.0 (C-5), 58.7 (C-16), 50.8 (C-7), 39.2 (C-12), 37.1 (C-10), 34.4 (C-8), 31.1 (C-9), 28.0 (C-17), 27.9 (C-13), 24.6 (C-11), 22.7 (C-14'), 22.6 (C-14), 20.2 (C-18, C-18'), 19.6 (C-15)

MS: **(ESI(+), Dichloromethane, M = $C_{44}H_{68}N_2O_6$) *m/z* =**
721.513 $[M+H]^+$

ESI HRMS: $[M+H]^+ = C_{44}H_{68}N_2O_6H$
Calculated: *m/z* = 721.5150
Found: *m/z* = 721.5135

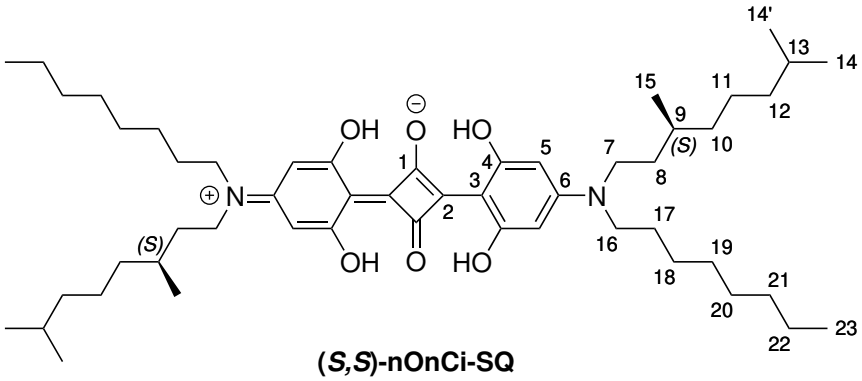
Elemental analysis: $C_{44}H_{68}N_2O_6$

Calculated:	C: 73.30	H: 9.51	N: 3.89
Found:	C: 73.16	H: 9.59	N: 3.85

UV/Vis: λ_{max} = 652.0 nm, ϵ = 401000 $M^{-1}cm^{-1}$ in chloroform

***R*$_f$-value:** 0.85 (dichloromethane)

2,4-bis[4-(*N*-(*S*)-(3,7-dimethyloctyl)-*N*-octylamine)-2,6-dihydroxyphenyl]squaraine - (*S,S*)-nOnCi-SQ



(*S,S*)-nOnCi-SQ

A single-neck flask, equipped with a Dean-Stark apparatus and reflux condenser, was charged with **(*S*)-nCi-N-O** (700 mg, 2.60 mmol, 1.00 eq.) and phloroglucinol (328 mg, 2.60 mmol, 1.00 eq.). The reactants were suspended in a mixture of toluene/1-butanol (1:1, v/v, 10 mL/mmol), evacuated 5 times under vigorous stirring and repressurized with argon. The reaction mixture was refluxed under argon atmosphere for 24 hours. After cooling to room temperature, squaric acid (145 mg, 1.27 mmol, 0.49 eq.) was added and the reaction mixture was heated to reflux for additional 24 hours. With the beginning of boiling, a sudden color change from slightly reddish over dark-green to dark-blue could be observed within minutes. The mixture was slowly cooled to room temperature and chilled further in the freezer to promote precipitation of the raw product. The solid was collected via filtration and washed with methanol until the filtrate was colorless. Further purification was done by recrystallization from dichloromethane/methanol (3:4, v/v), dichloromethane/cyclohexane (1:2, v/v) and *n*-hexane. The precipitated solid was each time filtered off and washed several times with methanol. After drying the collected solid under reduced pressure, the pure squaraine was obtained as a green solid.

Yield: 208 mg (0.25 mmol, 19%, green solid)

Molecular weight: $C_{52}H_{84}N_2O_6$, 833.25 g/mol

^{1}H-NMR: **(700 MHz, Chloroform-*d*, 298 K) δ [ppm] =**
10.97 (s, 4H, OH), 5.77 (s, 4H, H-5), 3.40-3.34 (m, 2H, H-7^a), 3.34-3.26 (m, 6H, H-7^b, H-16), 1.67-1.58 (m, 6H, H-8^a, H-17), 1.56-1.51 (m, 2H, H-13), 1.50-1.42 (m, 4H, H-8^b, H-9), 1.35-1.23 (m, 26H, H-10^a, H-11, H-18, H-19, H-20, H-21, H-22), 1.19-1.12 (m, 6H, H-10^b, H-12), 0.95 (d, $^3J_{15,9}$ = 6.4 Hz, 6H, H-15), 0.91-0.86 (m, 18H, H-14, H-14', H-23)

^{13}C-NMR: **(176 MHz, Chloroform-*d*, 298 K) δ [ppm] =**
181.5 (C-1), 162.9 (C-4), 161.1 (C-2), 157.8 (C-6), 102.7 (C-3), 93.8 (C-5), 51.7 (C-16), 50.1 (C-7), 39.3 (C-12), 37.2 (C-10), 34.9 (C-8), 31.3 (C-9), 28.1 (C-13), 28.1 (C-17), 22.8 (C-14'), 22.7 (C-14), 19.7 (C-15), 14.2 (C-23), 31.9 + 29.5 + 29.4 + 27.1 + 24.8 + 22.8 (C-11, C-18, C-19, C-20, C-21, C-22)

MS: **(ESI(+), Dichloromethane, M = $C_{52}H_{84}N_2O_6$) *m/z* =** 833.693 $[M+H]^+$, 762.558 $[M+H-C_5H_{11}]^{\cdot+}$

ESI HRMS: $[M+H]^+ = C_{52}H_{84}N_2O_6H$
Calculated: *m/z* = 833.6402
Found: *m/z* = 833.6396

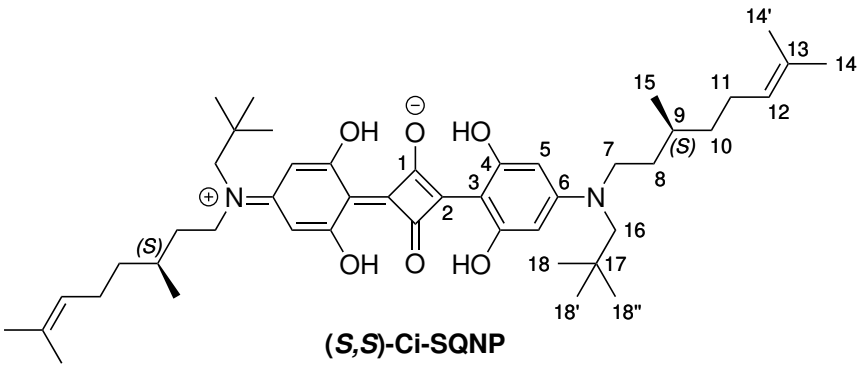
Elemental analysis: $C_{52}H_{84}N_2O_6$

Calculated:	C: 74.96	H: 10.16	N: 3.36
Found:	C: 74.86	H: 10.22	N: 3.40

UV/Vis: λ_{max} = 651.5 nm, ϵ = 421000 $M^{-1}cm^{-1}$ in chloroform

R_f-value: 0.84 (dichloromethane)

2,4-bis[4-(*N*-(*S*)-(3,7-dimethyl-6-octenyl)-*N*-neopentylamine)-2,6-dihydroxyphenyl]squaraine - (*S*,*S*)-Ci-SQNP



(*S*,*S*)-Ci-SQNP

A single-neck flask, equipped with a Dean-Stark apparatus and reflux condenser, was charged with **(*S*)-Ci-N-NP** (2.00 g, 8.87 mmol, 2.00 eq.) and phloroglucinol (559 mg, 4.44 mmol, 1.00 eq.). The reactants were suspended in a mixture of toluene/1-butanol (4:1, v/v, 2.2 mL/mmol), evacuated 5 times under vigorous stirring and repressurized with argon. The reaction mixture was refluxed under argon atmosphere for 24 hours. After cooling to room temperature, all volatile substances were removed and the solid was taken up with a mixture of toluene/1-butanol (1:1, v/v, 2.2 mL/mmol). Squaric acid (253 mg, 2.22 mmol, 0.50 eq.) was added and the reaction mixture was heated to reflux for additional 24 hours. No sudden color change could be observed, however, over the course of 24 hours the color changed slowly from reddish brown to dark-green. After cooling the reaction mixture to room temperature, the solvent mixture was removed and the remaining solid was purified by column chromatography on silica gel eluting with dichloromethane/cyclohexane (1:1, v/v). Further purification was done by recrystallization from dichloromethane/methanol (1:2, v/v). The precipitated solid was washed several times with methanol and after drying under reduced pressure, the pure squaraine was obtained as a green solid.

Yield: 16.5 mg[b] (0.02 mmol, 0.5%, green solid)

Molecular weight: $C_{46}H_{68}N_2O_6$, 745.05 g/mol

^{1}H-NMR: **(500 MHz, Chloroform-*d*, 298 K) δ [ppm] =**
10.93 (s, 4H, OH), 5.87 (s, 4H, H-5), 5.08 (t, $^3J_{12,11}$ = 7.2 Hz, 2H, H-12), 3.51-3.37 (m, 4H, H-7), 3.22 (s, 4H, H-16), 2.06-1.92 (m, 4H, H-11), 1.69 (s, 6H, H-14), 1.61 (s, 8H, H-10[a], H-14'), 1.49-1.41 (m, 4H, H-9, H-10[b]), 1.38-1.32 (m, 2H, H-8[a]), 1.24-1.16 (m, 2H, H-8[b]), 1.00 (s, 18H, C-18, C-18', C-18"), 0.95 (d, $^3J_{15,9}$ = 6.4 Hz, 6H, C-15)

^{13}C-NMR: **(125 MHz, Chloroform-*d*, 298 K) δ [ppm] =**
181.5 (C-1), 162.7 (C-4), 161.5 (C-2), 159.3 (C-6), 131.8 (C-13), 124.5 (C-12), 102.7 (C-3), 95.1 (C-5), 61.2 (C-16), 51.2 (C-7), 37.0 (C-10), 35.3 (C-17), 33.9 (C-8), 30.8 (C-9), 28.9 (C-18, C-18', C-18"), 25.9 (C-14'), 25.6 (C-11), 19.6 (C-15) 17.8 (C-14)

MS: **(ESI(+), Dichloromethane, M = $C_{46}H_{68}N_2O_6$) *m/z* =**
745.516 $[M+H]^+$

ESI HRMS: $[M+H]^+ = C_{46}H_{68}N_2O_6H$
Calculated: *m/z* = 745.5150
Found: *m/z* = 745.5149

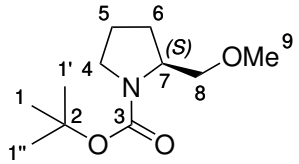
R_f-value: 0.80 (dichloromethane/cyclohexane (1:1, v/v))

[b] Due to the low yield, no elemental analysis was performed.

13.3 Experimental Section for Proline-Derived Anilino Squaraines: Impact of Alkyl Chain Reduction to a Methyl Group

Synthesis of Precursors for Squaraine Dyes

N-Boc-L-prolinyl methyl ether - (*S*)-Boc-Pro-C1



(*S*)-Boc-Pro-C1

(*S*)-Boc-Pro-C1 was synthesized according to the literature.[2]

Yield: 2.91 g (13.5 mmol, 90%, yellow oil)

Molecular weight: $C_{11}H_{21}NO_3$, 215.29 g/mol

^{1}H-NMR: **(500 MHz, Chloroform-*d*, 298 K) δ [ppm] =**
3.90 (*br* s, 1H, H-7), 3.48 (*br* s, 1H, H8[a]), 3.34 (s, 3H, H-9), 3.34-3.19 (m, 3H, H-4, H-8[b]), 1.94-1.82 (m, 3H, H-5[a], H-6), 1.81-1.74 (m, 1H, H-5[b]), 1.45 (s, 9H, H-1, H-1', H-1")

^{13}C-NMR: **(125 MHz, Chloroform-*d*, 298 K) δ [ppm] =**
154.7 (C-3), 79.31 (C-2), (73.46 (C-8)[x], 59.14 (C-9), 56.40 (C-7), 46.76 (C-4)[x], 28.65 (C-1), 28.43 (C-6), 23.47 (C-5)[x]

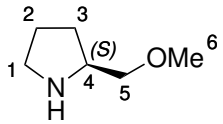
MS: **(ESI(+), Dichloromethane, M = $C_{11}H_{21}NO_3$) *m/z* =**
238.141 $[M+Na]^+$

ESI HRMS: $[M+Na]^+ = C_{11}H_{21}NO_3Na$
Calculated: *m/z* = 238.1414
Found: *m/z* = 238.1412

R_f-value: 0.25 (ethyl acetate/cyclohexane (1:9, v/v))

[x] A broad signal with splitting was identified, due to rotamers.

L-prolinyl methyl ether - (*S*)-Pro-C1



(*S*)-Pro-C1

(*S*)-Pro-C1 was synthesized according to the literature.[2]

Yield: 1.16 g (10.1 mmol, 76%, colorless oil)

Molecular weight: $C_6H_{13}NO$, 115.18 g/mol

^{1}H-NMR: **(500 MHz, Chloroform-*d*, 298 K) δ [ppm] =**
3.63 (*br* s, 1H, NH), 3.37-3.26 (m, 6H, H-4, H-5, H-6), 3.02-2.84 (m, 2H, H-1^a, H-1^b), 1.88-1.77 (m, 1H, H-3^a), 1.77-1.64 (m, 2H, H-2), 1.47-1.35 (m, 1H, H-3^b).

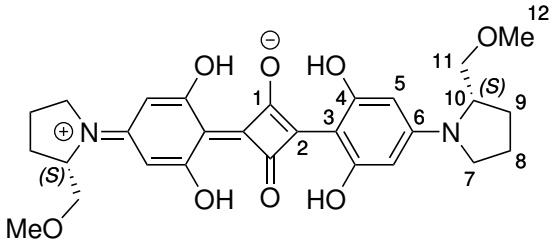
^{13}C-NMR: **(125 MHz, Chloroform-*d*, 298 K) δ [ppm] =**
75.53 (C-5), 59.02 (C-6), 57.90 (C-4), 46.32 (C-1), 27.80 (C-3), 25.18 (C-2)

MS: **(ESI(+), Dichloromethane, M = $C_6H_{13}NO$) *m/z* =**
231.207 $[2M+H]^+$, 116.107 $[M+H]^+$, 84.081 $[M-CH3]^\cdot$

ESI HRMS: $[M+Na]^+ = C_6H_{13}NOH$
Calculated: *m/z* = 116.1070
Found: *m/z* = 116.1070

Synthesis of the Squaraine Dye

2,4-bis[4-(*N*)-(*S*)-2-(methoxymethyl)-pyrrolidone-2,6-dihydroxyphenyl]squaraine - (*S*,*S*)-ProSQ-C1



(*S*,*S*)-ProSQ-C1

Synthesis adopted and modified from the literature.[2]
A single-neck flask, equipped with a Dean-Stark apparatus and reflux condenser, was charged with **(*S*)-Pro-C1** (1.06 g, 9.24 mmol, 1.10 eq.) and phloroglucinol (1.06 g, 8.40 mmol, 1.00 eq.). The reactants were suspended in a mixture of toluene/1-butanol (1:1, v/v, 10 mL/mmol), evacuated 5 times under vigorous stirring and repressurized with argon. The reaction mixture was refluxed under argon atmosphere for 24 hours. After cooling the red solution to room temperature, squaric acid (479 mg, 4.20 mmol, 0.50 eq.) was added and the reaction mixture was heated to reflux for additional 24 hours. With the beginning of boiling, a sudden color change from slightly reddish over dark-green to dark-blue could be observed within minutes. The mixture was slowly cooled to room temperature and chilled further in the freezer to promote precipitation of the raw product. The solid was collected via filtration and washed with a minimal amount of methanol, since **(*S*,*S*)-ProSQ-C1** is soluble in methanol. Further purification was done by column chromatography on silica gel eluting with dichloromethane, followed by recrystallization from dichloromethane/methanol (3:1, v/v), followed by recrystallization via layer-diffusion with dichloromethane as solvent and cyclohexane as anti-solvent (ratio 1:10, v/v). The precipitated solid was each time filtered off and washed carefully with chilled methanol. After drying the collected solid under reduced pressure, the pure squaraine was obtained as a bluish green crystalline solid.

Yield: 505 mg (0.96 mmol, 21%, bluish green crystalline solid)

Molecular weight: $C_{28}H_{32}N_2O_8$, 524.57 g/mol

^{1}H-NMR: **(400 MHz, Chloroform-*d*, 298 K) δ [ppm] =**
11.03 (s, 4H, OH), 5.79 (s, 4H, H-5), 4.07 (s, 2H, H-10), 3.58-3.51 (m, 2H, H-7_a), 3.51-3.46 (m, 2H, H-11_a), 3.42-3.34 (m, 8H, H-7_b, H-12), 3.34-3.28 (m, 2H, H-11_b), 2.16-1.98 (m, 8H$_a$, H-8_b, H-9_a, H-9_b)

^{13}C-NMR: **(176 MHz, Chloroform-*d*, 298 K) δ [ppm] =**
181.5 (C-1), 162.9 (C-4), 162.0 (C-2), 157.0 (C-6), 103.0 (C-3), 94.8 (C-5), 72.4 (C-11), 59.4 (C-12), 58.9 (C-10), 49.1 (C-7), 28.5 (C-9), 22.9 (C-8)

MS: **(EI, Dichloromethane, M = $C_{28}H_{32}N_2O_8$) *m/z* =**
524,2 [M], 479.1 [M-C_2H_5O]$^{\cdot-}$

EI HRMS: $[M+H]^+ = C_{28}H_{32}N_2O_8H$
Calculated: *m/z* = 524.2158
Found: *m/z* = 524.2151 (average value over 40 points)

Elemental analysis: $C_{28}H_{32}N_2O_8$

Calculated:	C: 64.11	H: 6.15	N: 5.34
Found:	C: 64.18	H: 6.19	N: 5.33

UV/Vis: λ_{max} = 654 nm, ϵ = 375000 $M^{-1}cm^{-1}$ in chloroform

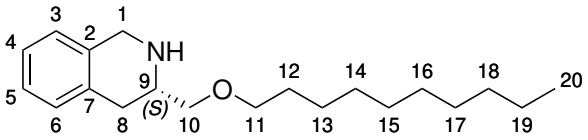
***R*$_f$-value:** 0.20 (dichloromethane)

SC-XRD: see Section 7.3 and Appendix E.2

13.4 Experimental Section for From Proline to Indoline: The Idea of Extending π-Conjugation for Enhancing Optical Properties and π-π-Interactions

Synthesis of Precursors for Squaraine Dyes

(*S*)-2-(decyloxymethyl)-tetrahydroisoquinoline - (*S*)-TIQ-C10



(*S*)-TIQ-C10

Synthesis adopted and modified from the literature.[2]
Under inert gas conditions, (*S*)-1,2,3,4-tetrahydro-3-isoquinolinemethanole (816 mg, 5.00 mmol, 1.00 eq.) was suspended in *abs.* DMF (1.00 mL/mmol) and cooled to under -15 °C in a flame-dried Schlenk-flask. Under vigorous stirring, sodium hydride (126 mg, 5.25 mmol, 1.05 eq., 60% in mineral oil) was slowly added in portions to the solution. The reaction mixture is further stirred at this temperature for 60 minutes until no further hydrogen formation can be observed. Afterwards 1-iodododecane (1.41 g, 5.25 mmol, 1.05 eq.) was added dropwise. The resulting suspension was stirred overnight during which the reaction mixture is allowed to warm up to room temperature. The obtained solution (all dissolved over night) was quenched by adding 3 M NaOH solution (30 mL) and diluted with DCM (30 mL). The organic phase separated and the aqueous phase was extracted with DCM (4 × 50 mL). The combined organic phases are washed with brine (100 mL) and dried with magnesium sulfate. All volatile compound were removed under reduced pressure and the crude product purified by column chromatography on Alox (neutral) eluting with DCM + 5% MeOH (v/v), yielding the product as colorless oil.

Yield: 874 mg (2.88 mmol, 58%, colorless oil)

Molecular weight: $C_{20}H_{33}NO$, 303.49 g/mol

^{1}H-NMR: **(500 MHz, Dichloromethane-d_2, 298 K) δ [ppm] =**
7.18-7.02 (m, 4H, H-3, H-4, H-5, H-6), 4.11-3.99 (m, 2H, H-1), 3.60-3.38 (m, 4H, H-10, H-11), 3.18-3.06 (m, 1H, H-9), 2.81 (*br* s, 1H, NH), 2.73-2.66 (m, 1H, H-8^a), 2.64-2.55 (m, 1H, H-8^b), 1.66-1.54 (m, 2H, H-12), 1.40-1.27 (m, 14H, H-13 - H-19), 0.92 (t, $^3J_{20,19}$ = 7.2 Hz, 3H, H-20)

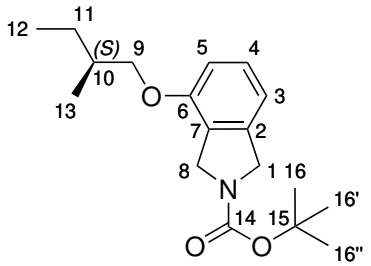
^{13}C-NMR: **(125 MHz, Dichloromethane-d_2, 298 K) δ [ppm] =**
136.1 (C-2), 134.8 (C-7), 129.6 (C-6), 126.6, 126.4, 126 (C-3, C-4, C-5), 74.9 (C-10), 71.9 (C-11), 53.8 (C-9), 48.5 (C-1), 32.0 (C-8), 32.4, 30.2, 30.1, 30.1, 30.0, 29.8, 26.6, 23.2 (C-12 , C-13 , C-14 , C-15 , C-16 , C-17 , C-18 , C-19), 14.4 (C-20).

MS: **(ESI(+), Dichloromethane, M = $C_{20}H_{33}NO$) *m/z* =** 304.235 $[M+H]^+$, 146.096 $[M\text{-}OC_{10}H_{22}]^+$

ESI HRMS: $[M+H]^+ = C_{20}H_{33}NOH$
Calculated: *m/z* = 304.2635
Found: *m/z* = 304.2632

R_f-value: 0.50 (dichloromethane + 5% methanol (v/v))

_N_-Boc-4-((_S_)-2-methylbutyloxymethyl)-isoindole - Boc-(_S_)-2mb-isoindole



Boc-(*S*)-2mb-isoindole

Under inert gas conditions, the isoindole-derivative - *N*-Boc-protected-2,3-dihydro-1H-isoindol-4-ol (835 mg, 3.55 mmol, 1.00 eq.) and potassium carbonate (981 mg, 7.10 mmol, 2.00 eq.) were dissolved in *abs.* DMF (5 mL/mmol) in a flame-dried Schlenk-flask and heated to 80 °C for 30 min. Afterwards, (*S*)-2-methylbutyl *p*-toluenesulfonate (1.29 g, 5.32 mmol, 1.50 eq.) was added and the resulting suspension was stirred for 24 h at 80 °C. Since TLC analysis showed still significant amounts of starting materials, additional 0.75 eq. of (*S*)-2-methylbutyl *p*-toluenesulfonate (645 mg, 2.66 mmol) were added and stirred again for 24 h at 80 °C. The reaction was quenched by adding a saturated aqueous ammonium chloride solution (50 mL) and diluted with ethyl acetate (10 mL/mmol). The organic phase was separated, and the aqueous phase extracted with ethyl acetate (3 × 5 mL/mmol). The combined organic phases were washed with water (2 × 10 mL/mmol), brine (10 mL/mmol) and dried with magnesium sulfate. The solvent was removed under reduced pressure and the crude product purified by column chromatography on silica gel eluting with DCM. The product[c] was obtained as colorless oil.

Yield: 449 mg (3.14 mmol, 88%, colorless oil)

Molecular weight: $C_{18}H_{27}NO^3$, 305.418 g/mol

[c] NMR-analysis of the product showed small amounts of (*S*)-2-methylbutyl *p*-toluenesulfonate. Reported yields were corrected according to the ^{1}H-NMR.

^{1}H-NMR: **(500 MHz, Chloroform-*d*, 298 K) δ [ppm] =**
7.21 (dd, $^{3}J_{4,3}$ = 8.0 Hz, $^{3}J_{4,5}$ = 7.8 Hz, 1H, H-4), 6.81 (*br* s, 1H, H-5), 6.72 (d, $^{3}J_{3,4}$ = 8.0 Hz 1H, H-3), 4.65/4.59 (two s, 4H, H-1, H-8), 3.88-3.75 (m, 2H, H-9), 1.86 (*br* s, 1H, H-10), 1.58-1.50 (m, 10H, H-11^{a}, H-16, H-16', H-16"), 1.32-1.24 (m, 1H, H-11^{b}), 1.01 (d, $^{3}J_{13,10}$ = 6.6 Hz, 3H, H-13), 0.98-0.91 (m, 3H, H-12)

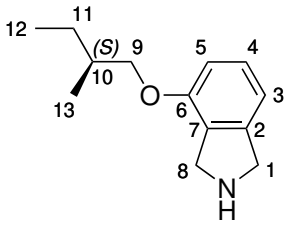
^{13}C-NMR: **(125 MHz, Chloroform-*d*, 298 K) δ [ppm] =**
154.8 (C-14), 154.6 (C-6), 139.1 (C-2), 129.1 (C-4), 125.9 (C-7), 114.6 (C-5), 109.6 (C-3), 79.7 (C-15), 72.9 (C-9), 52.8/50.3 (C-1, C-8), 34.8 (C-10), 28.7 (C-16, C-16', C-16"), 26.3 (C-11), 16.7 (C-13), 11.5 (C-12)

MS: **(ESI(+), Dichloromethane, M = $C_{18}H_{27}NO^{3}$) *m/z* =**
328.188 $[M+Na]^{+}$, 250.143 $[M\text{-}Boc_{\cdot}]^{+\cdot}$

ESI HRMS: $[M+Na]^{+} = C_{18}H_{27}NO^{3}Na$
Calculated: *m/z* = 328.1883
Found: *m/z* = 328.1878

R_f-value: 0.6 (dichloromethane)

2,3-dihydro-4-((*S*)-2-methylbutyloxymethyl)-1H-isoindol - (*S*)-2mb-isoindole



(*S*)-2mb-isoindole

Boc-(*S*)-2mb-isoindole (449 mg, 1.47 mmol, 1.00 eq.) was deprotected with trifluoroacetic acid (1.68 g, 14.7 mmol, 10.0 eq.) according to the literature.[2]
Variation from the literature: The crude product was purified by column chromatography on silica gel eluting with ethyl acetate + 5% methanol (v/v). The product was obtained as a yellow oil and showed signs of decomposition during storage in the freezer visible by color change to dark brown after one week.

Yield: 181 mg (0.88 mmol, 62%, yellow oil)

Molecular weight: $C_{13}H_{19}NO$, 205.301 g/mol

^{1}H-NMR: **(500 MHz, Chloroform-*d*, 298 K) δ [ppm] =**
7.19 (t, $^{3}J_{4,3}$ = 8.0 Hz, $^{3}J_{4,5}$ = 7.8 Hz, 1H, H-4), 6.83 (d, $^{3}J_{5,4}$ = 7.8 Hz, 1H, H-5), 6.72 (d, $^{3}J_{3,4}$ = 8.0 Hz, 1H, H-3), 4.35/4.33 (two s, 4H, H-1, H-8), 3.87-3.74 (m, 2H, H-9), 3.57 (*br* s, 1H, NH), 1.90-1.80 (m, 1H, H-10), 1.59-1.49 (m, 1H, H-11^{a}), 1.32-1.22 (m, 1H, H-11^{b}), 1.00 (d, $^{3}J_{13,9}$ = 6.9 Hz, 3H, H-13), 0.96-0.92 (m, 3H, H-12)

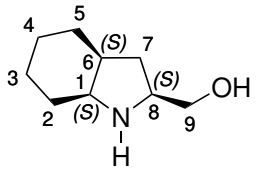
^{13}C-NMR: **(125 MHz, Chloroform-*d*, 298 K) δ [ppm] =**
154.9 (C-6), 141.8 (C-2), 129.1 (C-4), 128.5 (C-7), 114.5 (C-5), 109.8 (C-3), 73.0 (C-9), 53.1/50.4 (C-1, C-8), 34.9 (C-10), 26.3 (C-11), 16.7 (C-13), 11.5 (C-12)

MS: **(ESI(+), Dichloromethane, M = $C_{13}H_{19}NO$) *m/z* =**
206.153 $[M+H]^{+}$

ESI HRMS: $[M+H]^{+} = C_{13}H_{19}NOH$
Calculated: *m/z* = 206.1539
Found: *m/z* = 206.1537

***R*$_f$-value:** 0.01 - 0.35[d](ethyl acetate + 5% methanol (v/v))

(2*S*,3*S*,9*S*)-2-(hydroxymethyl)-octahydro-1H-indol - (*S*)-OHI-OH



(*S*)-OHI-OH

Octahydro-1H-indol (3.38 g, 20.0 mmol, 1.00 eq.) was reduced with lithium aluminium hydride (1.14 g, 30.0 mmol, 1.50 eq.) according to the literature.[184, 185]
The product was obtained as a yellow oil with the tendency to solidify.

Yield: 3.02 g (19.5 mmol, 97%, yellow oil or white solid)

Molecular weight: $C_9H_{17}NO$, 155.24 g/mol

[d] As typical for free primary and secondary amines, the retention factor depends strongly on the concentration.

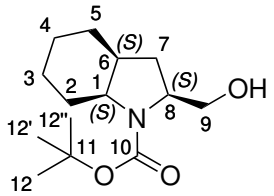
^{1}H-NMR: **(500 MHz, Chloroform-*d*, 298 K) δ [ppm] =**
3.61 (dd, $^{2}J_{9^a,9^b}$ = 4.2 Hz, $^{3}J_{9,8}$ = 10.8 Hz, 1H, H-9^a), 3.42 (dd, $^{2}J_{9^b,9^a}$ = 4.2 Hz, $^{3}J_{9,8}$ = 10.8 Hz, 1H, H-9^b), 3.35-3.27 (m, 1H, H-8), 3.21-3.03 (m, 2H, NH, H-1), 2.06-1.96 (m, 1H, H-6), 1.92-1.81 (m, 1H, H-7^a), 1.67-1.57 (m, 1H, H-5^a), 1.57-1.40 (m, 5H, H-2, H-3^a, H-4^a, H-5^b), 1.36-1.20 (m, 3H, H-3^b, H-4^b, H-7^b)

^{13}C-NMR: **(125 MHz, Chloroform-*d*, 298 K) δ [ppm] =**
65.8 (C-9), 59.0 (C-8), 57.5 (C-1), 38.4 (C-6), 33.1 (C-7), 29.8 (C-2), 28.2 (C-5), 23.6 (C-3), 22.4 (C-4)

MS: **(ESI(+), Dichloromethane, M = $C_9H_{17}NO$) *m/z* =**
293.258 $[2M-H]^+$, 156.138 $[M+H]^+$, 138.128 $[M-H_2O]^{\cdot}$

ESI HRMS: $[M+H]^+ = C_9H_{17}NOH$
Calculated: *m/z* = 156.1383
Found: *m/z* = 156.1381

_N_-Boc-(2_S_,3_S_,9_S_)-2-(hydroxymethyl)-octahydro-1H-indol - (_S_)-Boc-OHI-OH



(*S*)-Boc-OHI-OH

To a at 0 °C cooled solution of **(*S*)-OHI-OH** (3.00 g, 19.31 mmol, 1.00 eq.) in DCM (2.5 mL/mmol) with triethylamine (5.86 g, 57.9 mmol, 3.00 eq.), Boc_2O (4.63 g, 21.24 mmol, 1.10 eq.) dissolved in DCM (0.4 mL/mmol) was slowly added and stirred overnight. The reaction was quenched with the addition of water (25 mL). The organic phase is separated and washed with water (2 × 25 mL), again separated and dried with magnesium sulfate. The solvent was removed under reduced pressure and the crude product purified by column chromatography on silica gel eluting with ethyl acetate/cyclohexane (1:1, v/v), yielding the product as colorless oil.

Yield: 4.23 g (16.6 mmol, 86%, colorless oil)

Molecular weight: $C_{14}H_{25}NO_3$, 255.36 g/mol

^{1}H-NMR: **(500 MHz, Chloroform-*d*, 298 K) δ [ppm] =**
4.92 (*br* s, 1H, OH), 4.01-3.85 (m, 1H, H-1), 3.79-3.65 (m, 2H, H-8, H-9^{a}), 3.64-3.50 (m, 1H, H-9^{b}), 2.26-2.15 (m, 1H, H-6), 1.94-1.88 (m, 1H, H-7^{a}), 1.88-1.80 (m, 1H, H-2^{a}), 1.75-1.68 (m, 1H, H-5^{a}), 1.68-1.51 (m, 3H, H-2^{b}, H-3^{a}, H-5^{b}), 1.50-1.38 (m, 10H, H-4^{a}, H-12, H-12', H-12"), 1.29-1.18 (m, 1H, H-4^{b}), 1.18-1.02 (m, 2H, H-3^{b}, H-7^{b})

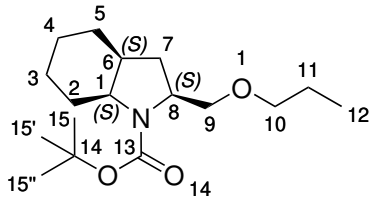
^{13}C-NMR: **(125 MHz, Chloroform-*d*, 298 K) δ [ppm] =**
157.2 (C-10), 80.2 (C-11), 69.5 (C-9), 61.0 (C-1), 58.5 (C-8), 35.8 (C-6), 30.6 (C-2), 29.4 (C-7), 28.6 (C-12), 26.0 (C-5), 24.2 (C-3), 20.6 (C-4)

MS: **(ESI(+), Dichloromethane, M = $C_{14}H_{25}NO_3$) *m/z* =**
278.172 $[M+Na]^+$, 256.190 $[M+H]^+$, 178.120 $[M-Boc+HNa]^+$, 156.138 $[M-Boc+2H]^+$

ESI HRMS: $[M+Na]^+ = C_{14}H_{25}NO_3Na$
Calculated: *m/z* = 278.1727
Found: *m/z* = 278.1723

***R*$_f$-value:** 0.45 (ethyl acetate/cyclohexane (1:1, v/v))

***N*-Boc-(2*S*,3*S*,9*S*)-2-(propyloxymethyl)-octahydro-1H-indol - (*S*)-Boc-OHI-C3**



(*S*)-Boc-OHI-C3

(*S*)-Boc-OHI-OH (1.22 g, 4.76 mmol, 1.00 eq.) was reacted with sodium hydride (171 mg, 7.14 mmol, 1.50 eq., 60% in mineral oil) and 1-iodopropane (1.21 g, 7.14 mmol, 1.50 eq.) according to the literature.[2]

Yield: 1.12 g (3.77 mmol, 79%, colorless oil)

Molecular weight: $C_{17}H_{31}NO_3$, 297.439 g/mol

^{1}H-NMR: **(500 MHz, Chloroform-*d*, 298 K) δ [ppm] =**
3.92-3.60 (m, 3H, H-1, H-8, H-9^{a}), 3.56-3.32 (m, 3H, H-9^{b}, H-10), 2.24-2.12 (m, 1H, H-6), 2.02-1.93 (m, 1H), 1.93-1.79 (m, 1H, H-7^{a}), 1.76-1.52 (m, 2H, H-11), 1.76-1.52 (m, 4H), 1.44 (s, 9H, H-15, H-15', H-15"), 1.48-1.41 (m, 1H), 1.36-1.20 (m, 2H, H-7^{b}), 1.17-1.05 (m, 1H), 0.90 (t, $^{3}J_{12,11}$ = 7.3 Hz, 3H, H-12)

^{13}C-NMR: **(125 MHz, Chloroform-*d*, 298 K) δ [ppm] =**
154.6 (C-13), 78.9 (C-14), 73.1 (C-9), 71.9 (C-10), 57.8 (C-8), 57.0 (C-1), 36.0 (C-6), 32.2 (C-5), 31.2 (C-2), 28.7 (C-15, C-15', C-15"), 28.6 (C-7), 26.2 (C-), 24.2, 23.0 (C-11), 20.6, 10.6 (C-12)

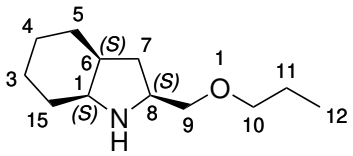
MS: **(ESI(+), Dichloromethane, M = $C_{17}H_{31}NO_3$) *m/z* =**
320.219 $[M+Na]^+$, 198.185 $[M-Boc+H]^+$

ESI HRMS: $[M+Na]^+ = C_{17}H_{31}NO_3Na$
Calculated: *m/z* = 320.2196
Found: *m/z* = 320.2192

ESI HRMS: $[M+H]^+ = C_{14}H_{25}NO_3H$
Calculated: *m/z* = 298.2377
Found: *m/z* = 298.2374

R_f-value: 0.45 (cyclohexane/ethyl acetate (9:1, v/v))

(2*S*,3*S*,9*S*)-2-(propyloxymethyl)-octahydro-1H-indol - (*S*)-OHI-C3



(*S*)-OHI-C3

(*S*)-Boc-OHI-C3 (1.12 g, 3.77 mmol, 1.00 eq.) was deprotected with trifluoroacetic acid (4.30 g, 37.7 mmol, 10.0 eq.) according to the literature.[2]

Yield: 553 mg (2.80 mmol, 74%, colorless oil)

Molecular weight: $C_{12}H_{23}NO$, 197.322 g/mol

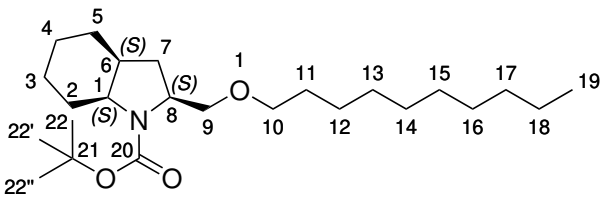
^{1}H-NMR: **(500 MHz, Chloroform-*d*, 298 K) δ [ppm] =**
5.81 (*br* s, 1H, NH), 3.74-3.67 (m, 1H, H-8), 3.67-3.61 (m, 1H, H-9^{a}), 3.59-3.52 (m, 1H, H-9^{a}), 3.52-3.41 (m, 3H, H-1, H-10), 2.33-2.22 (m, 1H, H-6), 1.97-1.81 (m, 1H, H-7^{a}), 1.97-1.81 (m, 1H), 1.77-1.67 (m, 2H), 1.67-1.51 (m, 2H, H-11), 1.67-1.51 (m, 3H), 1.50-1.19 (m, 1H H-7^{b}), 1.50-1.19 (m, 2H), 0.91 (t, $^{3}J_{12,11}$ = 7.5 Hz, 3H, H-12)

^{13}C-NMR: **(125 MHz, Chloroform-*d*, 298 K) δ [ppm] =**
73.2 (C-9), 71.01 (C-10), 58.2 (C-8), 57.9 (C-1), 37.4 (C-6), 31.5 (C-7), 26.9/26.7 (C-2/C-5), 22.9/22.7 (C-3/C-4), 22.1 (C-11), 10.7 (C-12)

MS: **(ESI(+), Dichloromethane, M = $C_{12}H_{23}NO$) *m/z* =**
198.185 $[M+H]^{+}$

ESI HRMS: $[M+H]^{+} = C_{12}H_{23}NOH$
Calculated: *m/z* = 198.1852
Found: *m/z* = 198.1849

_N_-Boc-(2_S_,3_S_,9_S_)-2-(decyloxymethyl)-octahydro-1H-indol - (_S_)-Boc-OHI-C10



(*S*)-Boc-OHI-C10

(*S*)-Boc-OHI-OH (2.09 g, 8.20 mmol, 1.00 eq.) was reacted with sodium hydride (295 mg, 12.3 mmol, 1.50 eq., 60% in mineral oil) and 1-iododecane (3.30 g, 12.3 mmol, 1.50 eq.) according to the literature.[2]

Yield: 2.14 g (5.40 mmol, 66%, colorless oil)

Molecular weight: $C_{24}H_{45}NO_3$, 297.439 g/mol

^{1}H-NMR: **(500 MHz, Chloroform-*d*, 298 K) δ [ppm] =**
3.93-3.59 (m, 3H, H-1, H-8, H-9^{a}), 3.59-3.31 (m, 3H, H-9^{b}, H-10), 2.23-2.12 (m, 1H, H-6), 2.03-1.92 (m, 1H), 1.92-1.79 (m, 1H, H-7^{a}), 1.77-1.50 (m, 2H, H-11), 1.77-1.50 (m, 3H), 1.44 (s, 9H, H-15, H-15', H-15"), 1.49-1.39 (m, 1H), 1.37-1.19 (m, 2H, H-7^{b}), 1.37-1.19 (m, 16H), 1.17-1.08 (m, 1H), 0.90 (t, $^{3}J_{19,18}$ = 7.1 Hz, 3H, H-19)

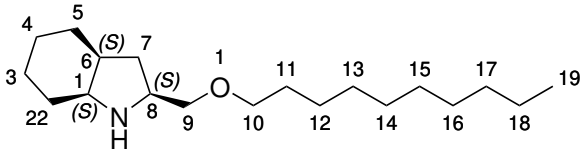
^{13}C-NMR: **(125 MHz, Chloroform-*d*, 298 K) δ [ppm] =**
154.5 (C-20), 78.9 (C-21), 73.5, 72.0, 71.5, 57.7 (C-8), 57.0 (C-1), 36.0 (C-6), 32.2 (C-5), 31.9, 31.1 (C-2), 29.8, 29.6, 29.5, 29.4, 29.3, 28.6 (C-22, C-22', C-22"), 28.5, 26.2, 26.1, 24.1, 22.7, 20.6, 14.1 (C-19)

MS: **(ESI(+), Dichloromethane, M = $C_{24}H_{45}NO_3$) *m/z* =**
813.671 $[2M+Na]^+$, 434.304 $[M+K]^+$, 418.329 $[M+Na]^+$, 396.348 $[M+H]^+$, 318.277 $[M\text{-}Boc+Na+H]^+$, 296.295 $[M\text{-}Boc+2H]^+$

ESI HRMS: $[M+Na]^+ = C_{24}H_{45}NO_3Na$
Calculated: *m/z* = 418.3292
Found: *m/z* = 418.3297

R_f-value: 0.40 (cyclohexane/ethyl acetate (9:1, v/v))

(2*S*,3*S*,9*S*)-2-(decyloxymethyl)-octahydro-1H-indol - (*S*)-OHI-C10



(*S*)-OHI-C10

(*S*)-Boc-OHI-C10 (1.99 g, 5.03 mmol, 1.00 eq.) was deprotected with trifluoroacetic acid (5.73 g, 50.3 mmol, 10.0 eq.) according to the literature.[2]

Yield: 1.41 g (4.76 mmol, 95%, yellow oil)

Molecular weight: $C_{19}H_{37}NO$, 295.511 g/mol

^{1}H-NMR: **(500 MHz, Chloroform-*d*, 298 K) δ [ppm] =**
3.98 (*br* s, 1H, NH), 3.54-3.49 (m, 1H, H-9^a), 3.48-3.41 (m, 4H, H-8, H-9^b, H-10), 3.20-3.14 (m, 1H, H-1), 2.13-2.03 (m, 1H, H-6), 1.95-1.86 (m, 1H, H-7^a), 1.72-1.61 (m, 2H, H-11), 1.59-1.54 (m, 2H), 1.53-1.45 (m, 4H), 1.43-1.36 (m, 1H, H-7^b), 1.36-1.19 (m, 16H), 0.87 (t, $^3J_{19,18}$ = 7.2 Hz 3H, H-19)

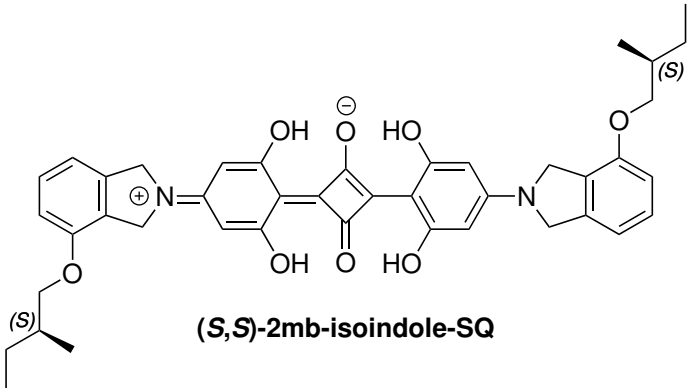
^{13}C-NMR: **(125 MHz, Chloroform-*d*, 298 K) δ [ppm] =**
73.9 (C-9), 71.5 (C-10), 58.0 (C-1), 57.6 (C-8), 37.9 (C-6), 33.5 (C-7), 32.0, 29.8, 29.8, 29.7, 29.6, 29.5, 28.5 (C-11), 28.0, 26.3, 23.5, 22.8, 22.2, 14.2 (C-19)

MS: **(ESI(+), Dichloromethane, M = $C_{19}H_{37}NO$) *m/z* =** 337.320 $[M+H+MeCN]^+$, 296.294 $[M+H]^+$

ESI HRMS: $[M+H]^+ = C_{19}H_{37}NOH$
Calculated: *m/z* = 296.2948
Found: *m/z* = 296.2945

Synthesis of Squaraine Dyes

2,4-bis[4-(2,3-dihydro-4-((*S*)-2-methylbutyloxymethyl)-1H-isoindol)-2,6-dihydroxyphenyl]squaraine - (*S*,*S*)-2mb-isoindole-SQ



(*S*,*S*)-2mb-isoindole-SQ

A single-neck flask, equipped with a Dean-Stark apparatus and reflux condenser, was charged with **(*S*)-2mb-isoindole** (181 mg, 0.881 mmol, 1.2 eq.) and phloroglucinol (92.7 mg, 0.734 mmol, 1.00 eq.). The reactants were suspended in a mixture of toluene and 1-butanol (4:1, v/v, 4.0 mL/mmol), evacuated 5 times under vigorous stirring and repressurized with argon. The reaction mixture was refluxed under argon atmosphere for 24 hours. After cooling to room temperature, all volatile substances were removed and the solid was taken up with a mixture of toluene/1-butanol (1:1, v/v, 2.2 mL/mmol). Squaric acid (253 mg, 2.22 mmol, 0.50 eq.) was added and the reaction mixture was heated to reflux for additional 24 hours. With the beginning of boiling, a sudden color change from slightly reddish brown over blue to purple could be observed within minutes, accompanied by the precipitation of a dark green, fine solid. The mixture was slowly cooled to room temperature and chilled further in the freezer to promote precipitation of the product. The solid was collected via filtration and washed generously with methanol and dichloromethane. The product was obtained as a nearly non-soluble very fine green powder.

Attempts to dissolve the obtained product for further purification, NMR or UV/Vis analysis were unsuccessful due to very poor solubility. At room temperature, the solvents tested were dichloromethane, chloroform, acetonitrile, dimethylformamide and trifluoroacetic acid - at 100 °C with overnight stirring, toluene, 1,2-dichlorobenzene and dimethyl sulfoxide. Only the latter three dissolved trace amounts - as judged by faint coloration - corresponding to concentrations far below the NMR detection limit and below typical UV/Vis concentrations (see Figure 9.6).

Yield: 33 mg[e]/83 mg (0.12 mmol, 6%[e]/16%, green solid)

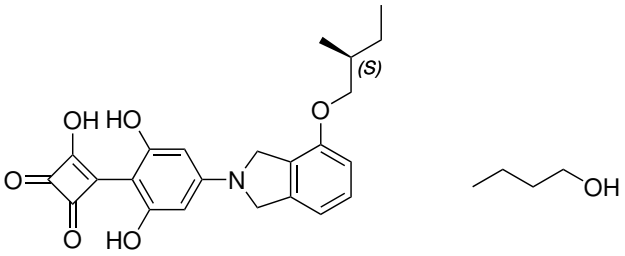
Molecular weight: $C_{42}H_{44}N_2O_8$, 704.820 g/mol

MS: **(APCI(+), Dichloromethane, M = $C_{42}H_{44}N_2O_8$) *m/z* (Int.) =** 705.317 (5) $[M+H]^+$

APCI HRMS: $[M+H]^+ = C_{42}H_{44}N_2O_8$ H
Calculated: *m/z* = 705.3170
Found: *m/z* = 705.3166

Elemental analysis: $C_{42}H_{44}N_2O_8$
Calculated: C: 71.57 H: 6.29 N: 3.97
Found: C: 68.91 H: 6.27 N: 3.63

Elemental analysis: $C_{42}H_{44}N_2O_8 \cdot 2.45\ C_{23}H_{23}NO_6 \cdot 0.8\ C_4H_{10}O$ (see molecules below)
Calculated: C: 69.91 H: 6.18 N: 3.53
Found: C: 68.91 H: 6.27 N: 3.63

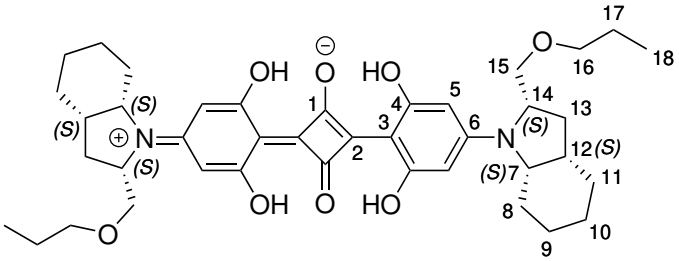


(*S*)-semi-2mb-isoindole-SQ Chemical Formula: $C_{23}H_{23}NO_6$

1-butanol Chemical Formula: $C_4H_{10}O$

[e] Calculated yield, based on the elemental analysis.

2,4-bis[4-((2*S*,3*S*,9*S*)-2-(propyloxymethyl)-octahydro-1H-indol)-2,6-dihydroxyphenyl]squaraine - (*S*,*S*)-OHI-SQ-C3



(*S*,*S*)-OHI-SQ-C3

Synthesis adopted and modified from the literature.[2]
A single-neck flask, equipped with a Dean-Stark apparatus and reflux condenser, was charged with **(*S*)-OHI-C3** (539 mg, 2.73 mmol, 1.05 eq.) and phloroglucinol (328 mg, 2.60 mmol, 1.00 eq.). The reactants were suspended in a mixture of toluene/1-butanol (1:1, v/v, 10 mL/mmol), evacuated 5 times under vigorous stirring and repressurized with argon. The reaction mixture was refluxed under argon atmosphere for 48 hours. After cooling the red solution to room temperature, squaric acid (148 mg, 1.30 mmol, 0.50 eq.) was added and the reaction mixture was heated to reflux for additional 24 hours. With the beginning of boiling, a sudden color change from slightly reddish over dark-green to dark-blue could be observed within minutes. The mixture was slowly cooled to room temperature and chilled further in the freezer to promote precipitation of the crystalline raw product. The solid was collected via filtration and washed with methanol. Further purification was done by column chromatography on silica gel eluting with dichloromethane, followed by recrystallization from dichloromethane/methanol (2:1, v/v). The precipitated solid was filtered off and washed carefully with chilled methanol. After drying the collected solid under reduced pressure, the pure squaraine was obtained as a golden solid.

Yield: 166 mg (0.24 mmol, 9%, golden solid)

Molecular weight: $C_{40}H_{52}N_2O_8$, 688.682 g/mol

^{1}H-NMR: **(700 MHz, Chloroform-*d*, 298 K) δ [ppm] =**
10.97 (s, 4H, OH), 5.78 (s, 4H, H-5), 4.09-4.00 (m, 2H, H-14), 3.81-3.73 (m, 2H, H-7), 3.73 (dd, $^2J_{15^a,15^b}$ = 3.6 Hz, $^3J_{15,14}$ = 10.1 Hz, 2H, H-15^a), 3.46 (dd, $^2J_{15^b,15^a}$ = 6.5 Hz, $^3J_{15,14}$ = 10.1 Hz, 2H, H-15^b), 3.43-3.35 (m, 4H, H-16), 2.32-2.24 (m, 2H, H-12), 2.19-2.06 (m, 4H, H-13), 2.01-1.94 (m, 2H, H-8^a), 1.83-1.77 (m, 2H, H-11^a), 1.76-1.71 (m, 2H, H-9^a), 1.70-1.64 (m, 2H, H-11^b), 1.61-1.52 (m, 6H, H-10^a, H-17), 1.46-1.39 (m, 2H, H-8^b), 1.39-1.32 (m, 2H, H-10^b), 1.25-1.15 (m, 2H, H-9^b), 0.92 (t, $^3J_{18,17}$ = 7.5 Hz, 6H, H-18)
Around 14% of the incorporated solvent DCM can be seen at 5.30 ppm in accordance with the elemental analysis.

^{13}C-NMR: **(176 MHz, Chloroform-*d*, 298 K) δ [ppm] =**
181.5 (C-1), 162.8 (C-4), 161.1 (C-2), 156.8 (C-6), 102.8 (C-3), 94.4 (C-5), 73.4 (C-16), 72.3 (C-15), 61.4 (C-7), 58.8 (C-14), 36.3 (C-12), 31.5 (C-13), 27.7 (C-8), 26.0 (C-11), 24.1 (C-9), 23.0 (C-17), 20.4 (C-10), 10.7 (C-18)
The incorporated solvent DCM can be seen at 53.5 ppm.

MS: **(APCI(+), Dichloromethane, M = $C_{40}H_{52}N_2O_8$) *m/z* (Int.) =**
689.379 (100) $[M+H]^+$
(ESI(+), Dichloromethane, M = $C_{40}H_{52}N_2O_8$) *m/z* =
689.3803 $[M+H]^+$

APCI HRMS: $[M+H]^+ = C_{40}H_{52}N_2O_8H$
Calculated: *m/z* = 689.3796
Found: *m/z* = 689.3794

ESI HRMS: $[M+H]^+ = C_{40}H_{52}N_2O_8H$
Calculated: *m/z* = 689.3796
Found: *m/z* = 689.3803

Elemental analysis: $C_{40}H_{52}N_2O_8 \cdot 14\%\ CH_2Cl_2$ (in accordance with ^{1}H-NMR analysis.)

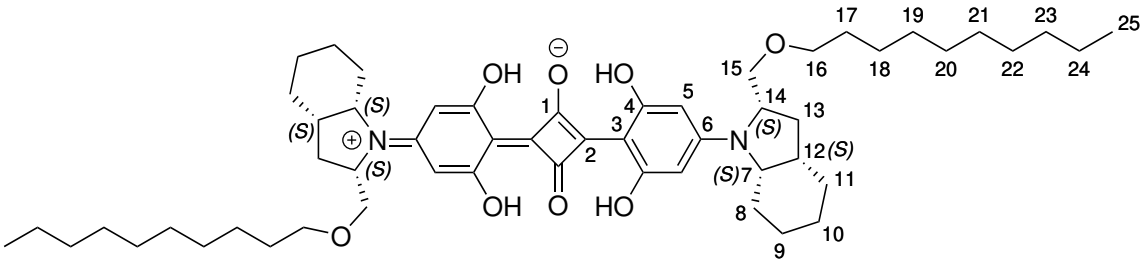
Calculated:	C: 68.65	H: 7.51	N: 3.99
Found:	C: 68.71	H: 7.34	N: 3.96

UV/Vis: λ_{max} = 654 nm, ϵ = 376000 $M^{-1}cm^{-1}$ in chloroform

R_f-value: 0.35 (dichloromethane)

SC-XRD: see Section 9.5 and Appendix G.2

2,4-bis[4-((2*S*,3*S*,9*S*)-2-(decyloxymethyl)-octahydro-1H-indol)-2,6-dihydroxyphenyl]squaraine - (*S*,*S*)-OHI-SQ-C10



(*S*,*S*)-OHI-SQ-C10

Synthesis adopted and modified from the literature.[2]
A single-neck flask, equipped with a Dean-Stark apparatus and reflux condenser, was charged with **(*S*)-OHI-C10** (1.40 g, 4.74 mmol, 1.05 eq.) and phloroglucinol (569 mg, 4.51 mmol, 1.00 eq.). The reactants were suspended in a mixture of toluene/1-butanol (1:1, v/v, 10 mL/mmol), evacuated 5 times under vigorous stirring and repressurized with argon. The reaction mixture was refluxed under argon atmosphere for 24 hours. After cooling the orange solution to room temperature, squaric acid (257 mg, 2.26 mmol, 0.50 eq.) was added and the reaction mixture was heated to reflux for additional 24 hours. With the beginning of boiling, a sudden color change from orange to green could be observed within minutes, which changed to dark-blue over the course of 3 hours. The mixture was slowly cooled to room temperature and chilled further in the freezer to promote precipitation of the raw product. The solid was collected via filtration and washed with methanol. Further purification was done by column chromatography on silica gel eluting with dichloromethane, followed by recrystallization from dichloromethane/methanol (1:1, v/v). The precipitated solid was filtered off and washed carefully with chilled methanol. After drying the collected solid under reduced pressure, the pure squaraine was obtained as a red solid.

Yield: 610 mg (0.69 mmol, 29%, red solid)

Molecular weight: $C_{54}H_{80}N_2O_8$, 885.240 g/mol

^{1}H-NMR: **(500 MHz, Chloroform-*d*, 298 K) δ [ppm] =**
10.97 (s, 4H, OH), 5.77 (s, 4H, H-5), 4.09-3.98 (m, 2H, H-14), 3.81-3.72 (m, 2H, H-7), 3.68 (dd, $^2J_{15^a,15^b}$ = 3.4 Hz, $^3J_{15,14}$ = 9.9 Hz, 2H, H-15^a), 3.49-3.37 (m, 6H, H-15^b, H-16), 2.33-2.23 (m, 2H, H-12), 2.19-2.11 (m, 2H, H-13^a), 2.11-2.05 (m, 2H, H-13^b), 2.02-1.92 (m, 2H, H-8^a), 1.84-1.76 (m, 2H, H-11^a), 1.76-1.71 (m, 2H, H-9^a), 1.71-1.63 (m, 2H, H-11^b), 1.59-1.50 (m, 6H, H-10^a, H-17), 1.48-1.34 (m, 4H, H-8^b, H-10^b), 1.34-1.18 (m, 30H, H-9^b, H-18-H-24), 1.22-1.16 (m, 2H, H-9^b), 0.87 (t, $^3J_{25,24}$ = 6.8 Hz, 6H, H-25)

^{13}C-NMR: **(125 MHz, Chloroform-*d*, 298 K) δ [ppm] =**
181.5 (C-1), 162.8 (C-4), 161.1 (C-2), 156.8 (C-6), 102.8 (C-3), 94.4 (C-5), 72.2 (C-15), 71.9 (C-16), 61.5 (C-7), 58.8 (C-14), 36.4 (C-12), 32.1 (C-23), 31.5 (C-13), 29.8/29.8/29.7/29.6/29.5/26.3 (C-17 - C-22), 27.7 (C-8), 26.0 (C-11), 24.1 (C-9), 22.8 (C-24), 20.4 (C-10), 14.3 (C-25)

MS: **(APCI(+), Dichloromethane, M = $C_{54}H_{80}N_2O_8$) *m/z* (Int.) =**
885.598 (100) $[M+H]^+$

APCI HRMS: $[M+H]^+ = C_{54}H_{80}N_2O_8H$
Calculated: *m/z* = 885.5987
Found: *m/z* = 885.5990

Elemental analysis: $C_{54}H_{80}N_2O_8$

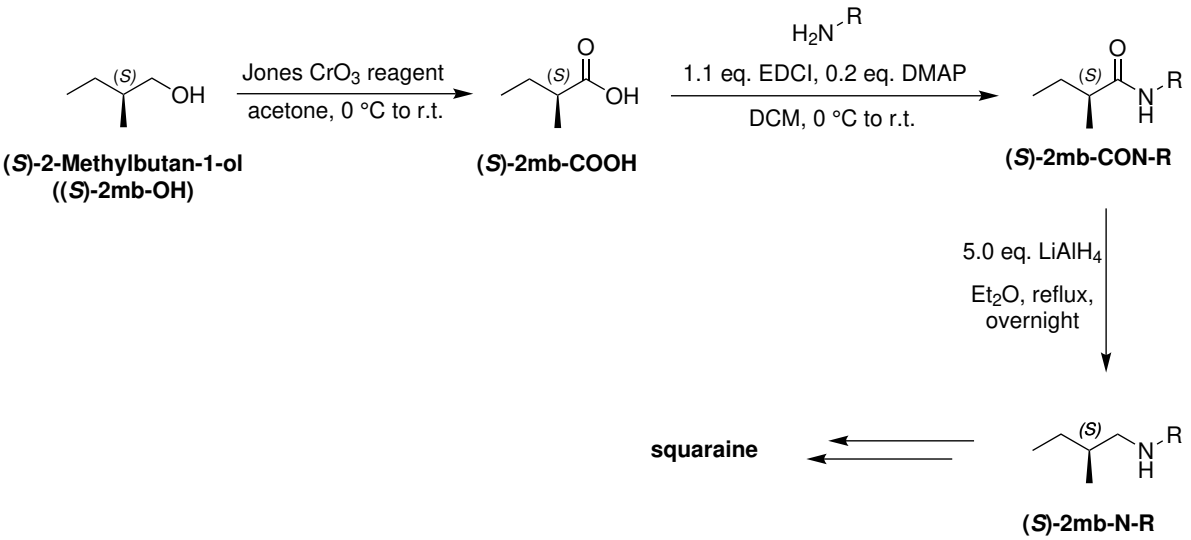
Calculated:	C: 73.27	H: 9.11	N: 3.16
Found:	C: 73.32	H: 9.18	N: 3.12

UV/Vis: λ_{max} = 654 nm, ϵ = 373000 $M^{-1}cm^{-1}$ in chloroform

***R*$_f$-value:** 0.55 (dichloromethane)

13.5 Experimental Section for 2-Methylbutyl-Derived Anilino Squaraines

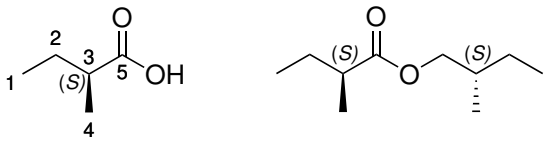
Synthesis of Precursors for Squaraine Dyes



(*S*)-2-Methylbutan-1-ol ((*S*)-2mb-OH) | **(*S*)-2mb-COOH** | **(*S*)-2mb-CON-R** | **(*S*)-2mb-N-R**

Figure 13.1: Overview of the synthesis sequence of precursors for **(*S*,*S*)-2mb-SQs**.

(*S*)-2-methylbutanoic acid - (*S*)-2mb-COOH



(*S*)-2mb-COOH | **side product (ester)**

Synthesis adopted from the literature.[186]
To prepare the Jones CrO_3 reagent, chromium trioxide (11.1 g, 111 mmol, 1 part) was dissolved in water (33.3 mL, 3 parts). To the stirred and ice-cooled solution, 95% sulfuric acid (11.1 mL, 1 part) was added dropwise.
A round-bottom flask was loaded with (*S*)-2-methylbutan-1-ol (7.50 g, 9.248 mL, 85.1 mmol, 1.00 eq.) in acetone (10 mL/g). The solution was stirred and cooled to 0 °C. The ice-cooled Jones CrO_3 reagent was added dropwise, during which a color change of the solution from colorless to green to green-blue and finally to slightly yellow/brown accomplished by a blue precipitation was observed. The reaction mixture was stirred at 0 °C for 30 min and at room temperature for 1.5 h. The reaction was quenched by the addition of 2-propanol and a few drops of sulfuric acid until a discolored solution was obtained. All volatile compounds were removed under reduced pressure. The residue was diluted with water and extracted three times with diethyl ether (same volume as the concentrated reaction mixture). The combined organic phases were washed with dilute HCl (10%), brine, dried with magnesium sulfate and concentrated in vacuum. The crude product was purified by distillation under reduced pressure

(22-23 mbar, b.p. 89-90 °C) to give the carboxylic acid as a colorless oil.
The ^{1}H-NMR spectrum indicates formation of 21% of a side product (the corresponding ester, determined by the ^{1}H-NMR signal at 3.91 ppm), which was considered in the calculation of the yield. The product was used in the subsequent reaction without further purification, as the ester does not react during the following EDC-mediated coupling step. Even after this stage, the subsequent reduction simply converts the ester to the corresponding alcohols, making further purification unnecessary.

Yield: 6.59 g (57.4 mmol, 68%, colorless oil)

Molecular weight: $C_5H_{10}O_2$, 102.13 g/mol

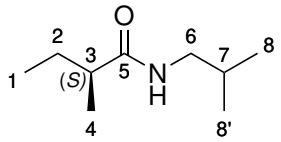
^{1}H-NMR: **(300 MHz, Chloroform-*d*, 298 K) δ [ppm] =**
11.5 (*br* s, 1H, COOH), 2.46-2.30 (h, $^{3}J_{3,2}$ = 7.0 Hz, $^{3}J_{3,4}$ = 7.0 Hz, 1H, H-3), 1.79-1.68 (m, 1H, H-2^{a}), 1.57-1.41 (m, 1H, H-2^{b}), 1.17 (d, $^{3}J_{4,3}$ = 7.0 Hz, 3H, H-4), 0.95 (t, $^{3}J_{1,2}$ = 7.5 Hz, 3H, H-1)

^{13}C-NMR: **(176 MHz, Chloroform-*d*, 298 K) δ [ppm] =**
183.2 (C-5), 41.0 (C-3), 26.7 (C-2), 16.5 (C-4), 11.7 (C-1)

General Procedure of the Amide Formation

Under inert gas conditions, a flame-dried Schlenk-flask is loaded with **(*S*)-2mb-COOH** (1.00 eq.) in dry dichloromethane (30 mL/g) and the solution is cooled to -10 °C. After addition of DMAP (0.20 eq.), the reaction mixture is stirred at -10 °C for 5 min and the amine (1.00 eq.) is added subsequently. The solution is stirred at -10 °C for another 5 min and a solution of EDCl (1-ethyl-3-(3-dimethylaminopropyl)carbodiimide, 1.10 eq.) in dry DCM (30 mL/g) is added dropwise. The reaction mixture is slowly warmed up to room temperature overnight, washed with dilute HCl (10%, same volume as the reaction mixture) and saturated aqueous $NaHCO_3$ solution (same volume as the concentrated reaction mixture). The combined organic phases are dried with magnesium sulfate. All volatile compounds are removed under reduced pressure and the crude product is purified by column chromatography on silica gel eluting with ethyl acetate/cyclohexane (1:1, v/v) to give the corresponding amide.

(*S*)-*N*-isobutyl-2-methylbutanamide - (*S*)-2mb-CON-IB



(*S*)-2mb-CON-IB

(*S*)-2mb-COOH (1.28 g, 12.5 mmol, 1.00 eq.), DMAP (305 mg, 2.50 mmol, 0.20 eq.), isobutylamine (914 mg, 12.5 mmol, 1.00 eq.) and EDCl (2.64 g, 13.8 mmol, 1.10 eq.) were reacted according to the

general procedure.

Yield: 1.61 g (10.2 mmol, 82%, colorless oil)

Molecular weight: $C_9H_{19}NO$, 157.26 g/mol

^{1}H-NMR: **(500 MHz, Chloroform-*d*, 298 K) δ [ppm] =**
5.47 (*br* s, 1H, NH), 3.16-2.96 (m, 2H, H-6), 2.15-2.00 (m, 1H, H-3), 1.84-1.72 (m, 1H, H-7), 1.72-1.60 (m, 1H, H-2^a), 1.48-1.37 (m, 1H, H-2^b), 1.14 (d, $^3J_{4,3}$ = 6.0 Hz, 3H, H-4), 0.96-0.87 (m, 9H, H-1, H-8, H-8')

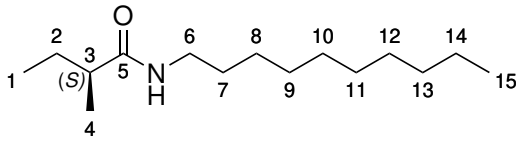
^{13}C-NMR: **(125 MHz, Chloroform-*d*, 298 K) δ [ppm] =**
176.6 (C-5), 46.8 (C-6), 43.7 (C-3), 28.7 (C-7), 27.6 (C-2), 20.3 (C-8, C-8'), 17.8 (C-4), 12.1 (C-1)

MS: **(ESI(+), Dichloromethane, M = $C_9H_{19}NO$) *m/z* =**
158.154 $[M+H]^+$

ESI HRMS: $[M+H]^+ = C_9H_{19}NOH$
Calculated: *m/z* = 158.1539
Found: *m/z* = 158.1537

***R*$_f$-value:** 0.40 (ethyl acetate/cyclohexane (1:1, v/v))

(*S*)-*N*-decyl-2-methylbutanamide - (*S*)-2mb-CON-C10



(*S*)-2mb-CON-C10

(*S*)-2mb-COOH (1.11 g, 10.9 mmol, 1.00 eq.), DMAP (265 mg, 2.17 mmol, 0.20 eq.), decylamine (1.71 g, 10.9 mmol, 1.00 eq.) and EDCI (2.20 g, 11.5 mmol, 1.06 eq.) were reacted according to the general procedure.

Yield: 2.59 g (10.7 mmol, 98%, colorless oil)

Molecular weight: $C_{15}H_{31}NO$, 241.24 g/mol

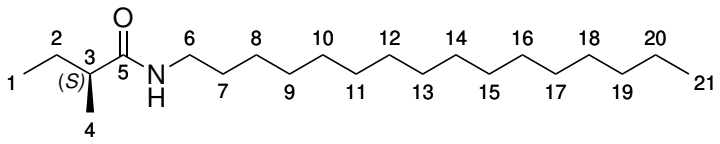
^{1}H-NMR: **(400 MHz, Chloroform-*d*, 298 K) δ [ppm] =**
5.37 (*br* s, 1H, NH), 3.32-3.17 (m, 2H, H-6), 2.13-2.01 (m, 1H, H-3), 1.73-1.58 (m, 1H, H-2^{a}), 1.52-1.36 (m, 3H, H-2^{b}, H-7), 1.36-1.22 (m, 14H, H-8 to H-14), 1.13 (d, $^{3}J_{4,3}$ = 6.9 Hz, 3H, H-4), 0.92 - 0.84 (m, 6H, H-1, H-15)

MS: **(ESI(+), Dichloromethane, M = $C_{15}H_{31}NO$) *m/z* =**
242.247 $[M+H]^{+}$

ESI HRMS: $[M+H]^{+} = C_{15}H_{31}NOH$
Calculated: *m/z* = 242.2478
Found: *m/z* = 242.2475

R_f-value: 0.45 (ethyl acetate/cyclohexane (1:1, v/v))

(*S*)-*N*-hexadecyl-2-methylbutanamide - (*S*)-2mb-CON-C16



(*S*)-2mb-CON-C16

(*S*)-2mb-COOH (1.50 g, 14.7 mmol, 1.00 eq.), DMAP (358 mg, 2.94 mmol, 0.20 eq.), hexadecylamine (3.55 g, 14.7 mmol, 1.00 eq.) and EDCl (3.10 g, 16.2 mmol, 1.10 eq.) were reacted according to the general procedure.

Yield: 4.18 g (12.8 mmol, 87%, white solid)

Molecular weight: $C_{21}H_{43}NO$, 325.58 g/mol

^{1}H-NMR: **(500 MHz, Chloroform-*d*, 298 K) δ [ppm] =**
5.64 (*br* s, 1H, NH), 3.31-3.18 (m, 2H, H-6), 2.17-2.06 (m, 1H, H-3), 1.71-1.60 (m, 1H, H-2^{a}), 1.54-1.46 (m, 2H, H-2, H-7), 1.46-1.38 (m, 1H, H-2^{b}), 1.36-1.18 (m, 26H, H-8 to H-20), 1.13 (d, $^{3}J_{4,3}$ = 6.6 Hz, 3H, H-4), 0.93 - 0.83 (m, 6H, H-1, H-21)

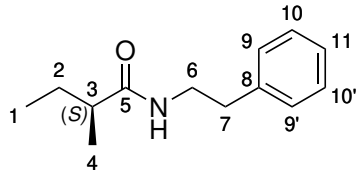
^{13}C-NMR: **(125 MHz, Chloroform-*d*, 298 K) δ [ppm] =**
176.7 (C-5), 46.4 (C-3), 39.6 (C-6), 32.1 (C-20), 29.8, 29.8, 29.8, 29.8, 29.8, 29.8, 29.7, 29.7, 29.5, 29.4, 27.5, 27.1, 22.8 (C-7 to C-19), 17.7 (C-4), 14.3 (C-21), 12.1 (C-1)

MS: **(ESI(+), Dichloromethane, M = $C_{21}H_{43}NO$) *m/z* =**
326.341 $[M+H]^{+}$

ESI HRMS: $[M+H]^+ = C_{21}H_{43}NOH$
Calculated: *m/z* = 326.3417
Found: *m/z* = 326.3414

R_f-value: 0.75 (ethyl acetate/cyclohexane (1:1, v/v))

(*S*)-*N*-phenylethyl-2-methylbutanamide - (*S*)-2mb-CON-PE



(*S*)-2mb-CON-PE

(*S*)-2mb-COOH (919 mg, 9.00 mmol, 1.00 eq.), DMAP (220 mg, 1.80 mmol, 0.20 eq.), phenylethylamine (1.09 g, 9.00 mmol, 1.00 eq.) and EDCl (1.90 g, 9.90 mmol, 1.10 eq.) were reacted according to the general procedure.

Yield: 1.66 g (8.07 mmol, 90%, colorless oil)

Molecular weight: $C_{13}H_{19}NO$, 205.30 g/mol

^{1}H-NMR: **(500 MHz, Chloroform-*d*, 298 K) δ [ppm] =**
7.31 (dd, $^3J_{10,9}$ = 7.4 Hz, $^3J_{10,11}$ = 7.4 Hz, 2H, H-10, H-10') 7.24 (d, $^3J_{11,10}$ = 7.4 Hz, 1H, H-11), 7.21-7.17 (m, 2H, H-9, H-9'), 5.43 (*br* s, 1H, NH), 3.63-3.45 (m, 2H, H-6), 2.90-2.75 (m, 2H, H-7), 2.10-1.96 (m, 1H, H-3), 1.68-1.57 (m, 1H, H-2^a), 1.45-1.33 (m, 1H, H-2^b), 1.09 (d, $^3J_{4,3}$ = 6.8 Hz, 3H, H-4), 0.86 (t, $^3J_{1,2}$ = 7.4 Hz, 3H, H-1)

^{13}C-NMR: **(125 MHz, Chloroform-*d*, 298 K) δ [ppm] =**
176.6 (C-5), 139.1 (C-8), 128.9 (C-9), 128.8 (C-10), 126.6 (C-11), 43.4 (C-3), 40.5 (C-6), 36.0 (C-7), 27.4 (C-2), 17.7 (C-4), 12.1 (C-1)

MS: **(ESI(+), Dichloromethane, M = $C_{13}H_{19}NO$) *m/z* =**
411.300 $[2M+H]^+$, 206.154 $[M+H]^+$

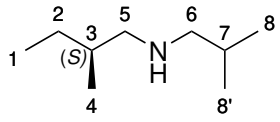
ESI HRMS: $[M+H]^+ = C_{13}H_{19}NOH$
Calculated: *m/z* = 206.1539
Found: *m/z* = 206.1536

R_f-value: 0.40 (ethyl acetate/cyclohexane (1:1, v/v))

General Procedure of the Amide Reduction

Under inert gas conditions, dry diethyl ether (20 mL/g) is placed in a flame dried two neck flask equipped with a flame dried reflux condenser, to which lithium aluminium hydride (5.00 eq.) is carefully added. The amide (1.00 eq.) is dissolved in dry diethyl ether (15-20 mL/g) and the solution is added dropwise to the flask. The reaction mixture is heated to refluxed for 16 h. The reaction is cooled to 0 °C and carefully (!) quenched with water until a complete white suspension is obtained. To this suspension, an excess of magnesium sulfate is added, filtered off and generously washing with diethyl ether. All volatile compounds are removed under reduced pressure and the crude product is purified by column chromatography on silica gel eluting with acetone + 1% triethylamine to give the corresponding amine.

(*S*)-*N*-isobutyl-2-methylbutanamine - (*S*)-2mb-N-IB



(*S*)-2mb-N-IB

(*S*)-2mb-CON-IB (1.81 g, 11.5 mmol, 1.00 eq.) was reduced with lithium aluminium hydride (2.19 g, 57.6 mmol, 5.00 eq.) according to the general procedure. Please note: This amine is quite volatile and therefore caution must be taken when removing the solvent.

Yield: 696 mg (4.86 mmol, 42%, yellow oil)

Molecular weight: $C_9H_{21}N$, 143.27 g/mol

^{1}H-NMR: **(500 MHz, Chloroform-*d*, 298 K) δ [ppm] =**
2.54-2.48 (m, 1H, H-5^a), 2.42-2.37 (m, 2H, H-6), 2.37-2.33 (m, 1H, H-5^b), 1.80-1.70 (m, 1H, H-7), 1.57-1.49 (m, 1H, H-3), 1.47-1.35 (m, 2H, NH, H-2^a), 1.18-1.08 (m, 1H, H-2^b), 0.93-0.84 (m, 12H, H-1,H-4, H-8, H-8')

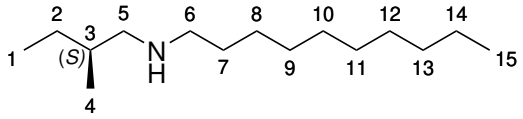
^{13}C-NMR: **(125 MHz, Chloroform-*d*, 298 K) δ [ppm] =**
58.4 (C-6), 56.4 (C-5), 34.9 (C-3), 28.3 (C-7), 27.7 (C-2), 20.8, 20.8 (C-8, C-8'), 17.8 (C-4), 11.5 (C-1)

MS: **(ESI(+), Dichloromethane, M = $C_9H_{21}N$) *m/z* =**
144.175 $[M+H]^+$

ESI HRMS: $[M+H]^+ = C_9H_{21}NH$
Calculated: *m/z* = 144.1747
Found: *m/z* = 144.1744

R_f-value: 0.35-0.05[f](acetone + 1% triethylamine)

(*S*)-*N*-decyl-2-methylbutanamine - (*S*)-2mb-N-C10



(*S*)-2mb-N-C10

(*S*)-2mb-CON-C10 (2.59 g, 10.7 mmol, 1.00 eq.) was reduced with lithium aluminium hydride (2.03 g, 53.5 mmol, 5.00 eq.) according to the general procedure.

Yield: 1.39 g (6.11 mmol, 57%, colorless oil)

Molecular weight: $C_{15}H_{33}N$, 227.44 g/mol

^{1}H-NMR: **(500 MHz, Chloroform-*d*, 298 K) δ [ppm] =**
2.62-2.56 (m, 2H, H-6), 2.55-2.50 (m, 1H, H-5^a), 2.41-2.35 (m, 1H, H-5^b), 1.58-1.52 (m, 1H, H-3), 1.52-1.47 (m, 2H, H-7), 1.43-1.36 (m, 1H, H-2^a), 1.32-1.22 (m, 14H, H-8 to H-14), 1.17-1.09 (m, 1H, H-2^b), 0.92-0.85 (m, 9H, H-1, H-4, H-15)

^{13}C-NMR: **(125 MHz, Chloroform-*d*, 298 K) δ [ppm] =**
56.3 (C-5), 50.4 (C-6), 34.8 (C-3), 32.0 (C-14), 30.2 (C-7), 29.8, 29.7, 29.5, 27.6, 22.8 (C8 to C14), 27.7 (C-2), 17.8 (C-4), 14.3 (C-15), 11.5 (C-1)

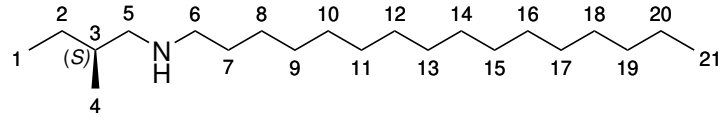
MS: **(ESI(+), Dichloromethane, M = $C_{15}H_{33}N$) *m/z* =**
228.268 $[M+H]^+$

ESI HRMS: $[M+H]^+ = C_{15}H_{33}NH$
Calculated: *m/z* = 228.2686
Found: *m/z* = 228.2684

R_f-value: 0.15-0.05[f] (acetone + 1% triethylamine)

[f] As typical for free primary and secondary amines, the retention factor depends strongly on the concentration.

(*S*)-*N*-hexadecyl-2-methylbutanamine - (*S*)-2mb-N-C16



(*S*)-2mb-N-C16

(*S*)-2mb-CON-C16 (4.00 g, 12.3 mmol, 1.00 eq.) was reduced with lithium aluminium hydride (2.33 g, 61.4 mmol, 5.00 eq.) according to the general procedure. Please note: Due to the poor solubility of **(*S*)-2mb-CON-C16** in diethyl ether, dry THF was added to the reaction mixture (overall 60 mL diethyl ether + 150 mL THF).

Yield: 2.48 g (7.97 mmol, 65%, white solid)

Molecular weight: $C_{21}H_{45}N$, 311.60 g/mol

^{1}H-NMR: **(500 MHz, Chloroform-*d*, 298 K) δ [ppm] =**
2.62-2.55 (m, 2H, H-6), 2.54-2.49 (m, 1H, H-5^{a}), 2.41-2.33 (m, 1H, H-5^{b}), 1.57-1.51 (m, 1H, H-3), 1.51-1.44 (m, 2H, H-7), 1.44-1.35 (m, 1H, H-2^{a}), 1.32-1.22 (m, 26H, H-8 to H-20), 1.17-1.09 (m, 1H, H-2^{b}), 0.92-0.84 (m, 9H, H-1, H-4, H-21)

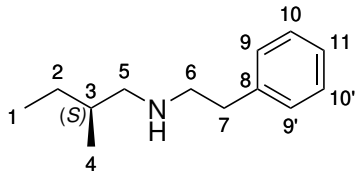
^{13}C-NMR: **(125 MHz, Chloroform-*d*, 298 K) δ [ppm] =**
56.4 (C-5), 50.4 (C-6), 34.9 (C-3), 32.1 (C-20), 30.2 (C-7), 29.8, 29.8, 29.8, 29.8, 29.7, 29.5, 27.6, 22.8 (C-8 to C-19), 27.7 (C-2) 17.8 (C-4), 14.3 (C-21), 11.5 (C-1)

MS: **(ESI(+), Dichloromethane, M = $C_{21}H_{45}N$) *m/z* =**
312.362 $[M+H]^+$

ESI HRMS: $[M+H]^+ = C_{21}H_{45}NH$
Calculated: *m/z* = 312.3625
Found: *m/z* = 312.3621

R_f-value: 0.20-0.01^{f} (acetone + 1% triethylamine)

(*S*)-*N*-phenylethyl-2-methylbutanamine - (*S*)-2mb-N-PE



(*S*)-2mb-N-PE

(*S*)-2mb-CON-PE (1.61 g, 7.83 mmol, 1.00 eq.) was reduced with lithium aluminium hydride (1.49 g, 39.2 mmol, 5.00 eq.) according to the general procedure. Please note: Purification was done by column chromatography on silica gel eluting with ethyl acetate + 5% methanol.

Yield: 1.34 g (6.98 mmol, 89%, white waxy solid)

Molecular weight: $C_{13}H_{21}N$, 191.32 g/mol

^{1}H-NMR: **(500 MHz, Chloroform-*d*, 298 K) δ [ppm] =**
7.32-7.26 (m, 2H, H-10, H-10'), 7.25-7.18 (m, 3H, H-9, H-9', H-11), 2.92-2.81 (m, 4H, H-6, H-7), 2.60-2.53 (m, 1H, H-5^{a}), 2.46-2.37 (m, 1H, H-5^{b}), 1.94 (*br* s, 1H, NH), 1.60-1.47 (m, 1H, H-3), 1.44-1.33 (m, 1H, H-2^{a}), 1.18-1.06 (m, 1H, H-2^{b}), 0.90-0.85 (m, 6H, H-1, H-4)

^{13}C-NMR: **(125 MHz, Chloroform-*d*, 298 K) δ [ppm] =**
140.1 (C-8), 128.8 (C-9), 128.6 (C-10), 126.3 (C-11), 56.0 (C-5), 51.5 (C-6), 36.3 (C-7), 34.8 (C-3), 27.6 (C-2), 17.8 (C-4), 11.4 (C-1)

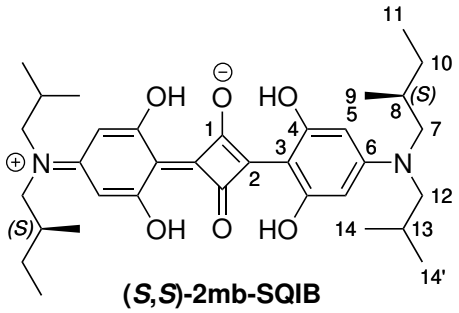
MS: **(ESI(+), Dichloromethane, M = $C_{13}H_{21}N$) *m/z* =**
192.174 $[M+H]^+$

ESI HRMS: $[M+H]^+ = C_{13}H_{21}NH$
Calculated: *m/z* = 192.1747
Found: *m/z* = 192.1743

R_f-value: 0.10-0.01^{f} (ethyl acetate + 5% methanol)

Synthesis of Squaraine Dyes

2,4-bis[4-((*S*)-*N*-isobutyl-2-methylbutanamine)-2,6-dihydroxyphenyl]squaraine - (*S*,*S*)-2mb-SQIB



(*S*,*S*)-2mb-SQIB

A single-neck flask, equipped with a Dean-Stark apparatus and reflux condenser, was charged with **(*S*)-2mb-N-IB** (528 mg, 3.69 mmol, 1.20 eq.) and phloroglucinol (387 mg, 3.07 mmol, 1.00 eq.). The reactants were suspended in a mixture of toluene/1-butanol (4:1, v/v, 2.2 mL/mmol), evacuated 5 times under vigorous stirring and repressurized with argon. The reaction mixture was refluxed under argon atmosphere for 24 hours. After cooling to room temperature, all volatile substances were removed (at 60 °C, high vacuum) and the orange/red oil was taken up with a mixture of toluene/1-butanol (1:1, v/v, 2.2 mL/mmol). For a successful synthesis, it is crucial to minimize the intermediate product's exposure to air, as it tends to decompose either upon contact with atmospheric oxygen or after prolonged storage, as discussed in the main part. Squaric acid (175 mg, 1.54 mmol, 0.50 eq.) was added and the reaction mixture was heated to reflux for additional 18 hours. With the beginning of boiling, a sudden color change from slightly reddish over green to dark-blue could be observed within minutes. The mixture was slowly cooled to room temperature and chilled further in the freezer to promote precipitation of the raw product. The solid was collected via filtration and washed with a minimal amount of methanol. Further purification was done by column chromatography on silica gel eluting with dichloromethane, followed by recrystallization from dichloromethane/methanol (1:1.5, v/v). The precipitated solid was filtered off and washed carefully with chilled methanol. After drying the collected solid under reduced pressure, the pure squaraine was obtained as a golden green crystalline solid.

Yield: 365 mg (0.63 mmol, 21%, golden green solid)

Molecular weight: $C_{34}H_{48}N_2O_8$, 580.77 g/mol

^{1}H-NMR: **(500 MHz, Chloroform-*d*, 298 K) δ [ppm] =**
10.96 (s, 4H, OH), 5.81 (s, 4H, H-5), 3.41-3.32 (m, 2H, H-7^a), 3.31-3.23 (m, 2H, H-12^a), 3.23-3.11 (m, 4H, H-7^b, H-12^b), 2.19-2.07 (m, 2H, H-13), 1.96-1.85 (m, 2H, H-8), 1.48-1.37 (m, 2H, H-10^a), 1.19-1.07 (m, 2H, H-10^b), 0.96-0.90 (m, 18H, H-11, H-14, H-14'), 0.89 (d, $^3J_{9,8}$ = 7.0 Hz, 6H, H-9)

^{13}C-NMR: **(125 MHz, Chloroform-*d*, 298 K) δ [ppm] =**
181.5 (C-1), 162.8 (C-4), 161.5 (C-2), 158.4 (C-6), 102.6 (C-3), 94.6 (C-5), 60.5 (C-12), 59.2 (C-7), 34.2 (C-8), 27.8 (C-13), 27.3 (C-10), 20.3, 20.3 (C-14, C-14'), 17.1 (C-9), 11.4 (C-11)

MS: **(ESI(+), Dichloromethane, M = $C_{34}H_{48}N_2O_8$) *m/z* =**
580.351 $[M+H]^+$

ESI HRMS: $[M+H]^+ = C_{34}H_{48}N_2O_8H$
Calculated: *m/z* = 580.3507
Found: *m/z* = 580.3507

Elemental analysis: $C_{34}H_{48}N_2O_8$

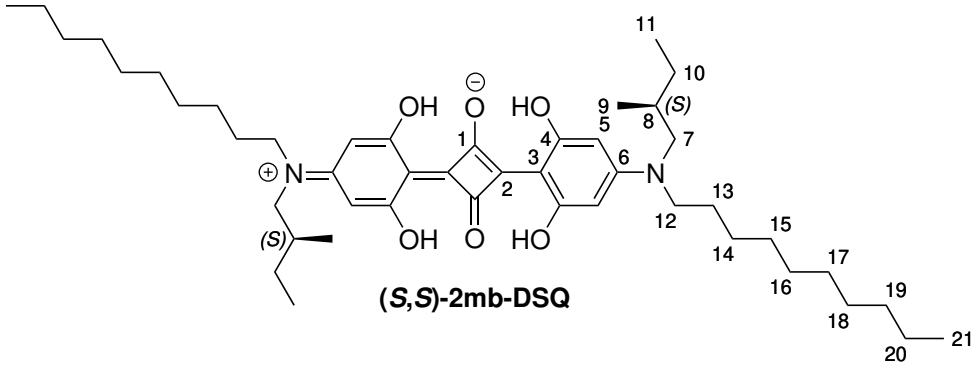
Calculated:	C: 70.32	H: 8.33	N: 4.82
Found:	C: 70.65	H: 8.24	N: 4.83

UV/Vis: λ_{max} = 654 nm, ϵ = 380000 $M^{-1}cm^{-1}$ in chloroform

R_f-value: 0.90 (dichloromethane)

SC-XRD: see Chapter 10 and Appendix H.2

2,4-bis[4-((*S*)-*N*-decyl-2-methylbutanamine)-2,6-dihydroxyphenyl]squaraine - (*S*,*S*)-2mb-DSQ



(*S*,*S*)-2mb-DSQ

A single-neck flask, equipped with a Dean-Stark apparatus and reflux condenser, was charged with **(*S*)-2mb-N-C10** (1.39 g, 6.12 mmol, 1.00 eq.) and phloroglucinol (772 mg, 6.12 mmol, 1.00 eq.). The reactants were suspended in a mixture of toluene/1-butanol (1:1, v/v, 10 mL/mmol), evacuated 5 times under vigorous stirring and repressurized with argon. The reaction mixture was refluxed under argon atmosphere for 24 hours. After cooling to room temperature, squaric acid (349 mg, 3.06 mmol, 0.50 eq.) was added and the reaction mixture was heated to reflux for additional 24 hours. With the beginning of boiling, a sudden color change from red over green to dark-blue could be observed within minutes. The

mixture was slowly cooled to room temperature and chilled further in the freezer to promote precipitation of the raw product. The solid was collected via filtration and washed generously with methanol. Further purification was done by column chromatography on silica gel eluting with dichloromethane, followed by two recrystallizations from dichloromethane/methanol (1:2, v/v). The precipitated solid was each time filtered off and washed with chilled methanol. After drying the collected solid under reduced pressure, the pure squaraine was obtained as a green solid.

Yield: 491 mg (0.65 mmol, 21%, green solid)

Molecular weight: $C_{46}H_{74}N_2O_8$, 751.11 g/mol

^{1}H-NMR: **(700 MHz, Chloroform-*d*, 298 K) δ [ppm] =**
10.97 (s, 4H, OH), 5.80 (s, 4H, H-5), 3.39-3.32 (m, 4H, H-12), 3.31-3.26 (m, 2H, H-7^a), 3.16-3.12 (m, 2H, H-7^b), 1.90-1.83 (m, 2H, H-8), 1.63-1.59 (m, 4H, H-13), 1.47-1.41 (m, 2H, H-10^a), 1.33-1.22 (m, 28H, H-14 to H-20), 1.18-1.11 (m, 2H, H-10^b), 0.93 (t, $^3J_{21,20}$ = 7.4 Hz, 6H, H-21), 0.91 (d, $^3J_{10,9}$ = 6.7 Hz, 6H, H-9), 0.88 (t, $^3J_{12,11}$ = 7.1 Hz, 6H, H-11)

^{13}C-NMR: **(176 MHz, Chloroform-*d*, 298 K) δ [ppm] =**
181.5 (C-1), 162.8 (C-4), 161.2 (C-2), 158.3 (C-6), 102.7 (C-3), 94.3 (C-5), 57.9 (C-7), 52.8 (C-12), 34.4 (C-8), 32.0 (C-20), 29.7, 29.7, 29.5, 29.4, 27.1, 22.8 (C-14 to C-19), 27.7 (C-13), 27.3 (C-10), 17.1 (C-9), 14.3 (C-21), 11.5 (C-11)

MS: **(ESI(+), Dichloromethane, M = $C_{46}H_{74}N_2O_8$) *m/z* =**
749.547 $[M+H]^+$

ESI HRMS: $[M+H]^+ = C_{46}H_{74}N_2O_8H$
Calculated: *m/z* = 749.5463
Found: *m/z* = 749.5462

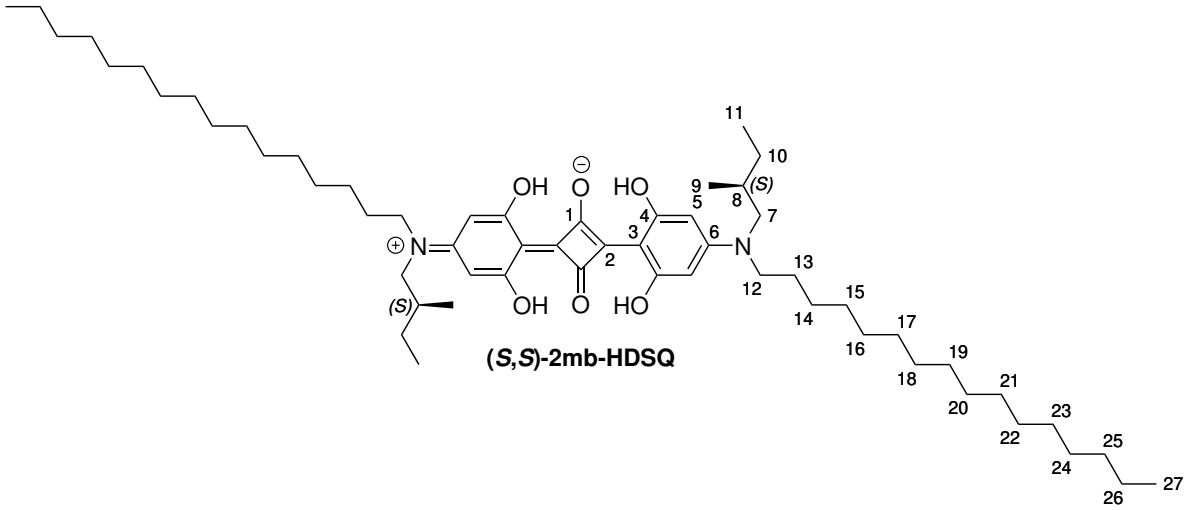
Elemental analysis: $C_{46}H_{74}N_2O_8$

Calculated:	C: 73.76	H: 9.69	N: 3.74
Found:	C: 73.67	H: 9.78	N: 3.74

UV/Vis: λ_{max} = 652.5 nm, ϵ = 391000 $M^{-1}cm^{-1}$ in chloroform

R_f-value: 0.95 (dichloromethane)

2,4-bis[4-((*S*)-*N*-hexadecyl-2-methylbutanamine)-2,6-dihydroxyphenyl]squaraine - (*S*,*S*)-2mb-HDSQ



A single-neck flask, equipped with a Dean-Stark apparatus and reflux condenser, was charged with **(*S*)-2mb-N-C16** (2.46 g, 7.52 mmol, 1.00 eq.) and phloroglucinol (948 mg, 7.52 mmol, 1.00 eq.). The reactants were suspended in a mixture of toluene/1-butanol (1:1, v/v, 10 mL/mmol), evacuated 5 times under vigorous stirring and repressurized with argon. The reaction mixture was refluxed under argon atmosphere for 24 hours. After cooling to room temperature, squaric acid (429 mg, 3.76 mmol, 0.50 eq.) was added and the reaction mixture was heated to reflux for additional 24 hours. With the beginning of boiling, a sudden color change from red over green to dark-blue could be observed within minutes. The mixture was slowly cooled to room temperature and chilled further in the freezer to promote precipitation of the raw product. The solid was collected via filtration and washed generously with methanol. Crude purification was done recrystallization from dichloromethane/methanol (1:3, v/v). Further purification was done by column chromatography on silica gel eluting with dichloromethane, followed by two recrystallization from dichloromethane/methanol (1:2, v/v). The precipitated solid was filtered off and washed with chilled methanol. After drying the collected solid under reduced pressure, the pure squaraine was obtained as a green solid.

Yield: 415 mg (0.45 mmol, 12%, green solid)

Molecular weight: $C_{58}H_{96}N_2O_8$, 917.41 g/mol

^{1}H-NMR: **(500 MHz, Chloroform-*d*, 298 K) δ [ppm] =**
10.97 (s, 4H, OH), 5.80 (s, 4H, H-5), 3.41-3.31 (m, 4H, H-12), 3.31-3.25 (m, 2H, H-7^a), 3.18-3.10 (m, 2H, H-7^b), 1.94-1.81 (m, 2H, H-8), 1.65-1.57 (m, 4H, H-13), 1.48-1.40 (m, 2H, H-10^a), 1.35-1.20 (m, 52H, H-14 to H-26), 1.19-1.10 (m, 2H, H-10^b), 0.96-0.86 (m, 18H, H-9, H-11, H-27)

^{13}C-NMR: **(125 MHz, Chloroform-*d*, 298 K) δ [ppm] =**
181.5 (C-1), 162.8 (C-4), 161.3 (C-2), 158.4 (C-6), 102.5 (C-3), 94.1 (C-5), 57.8 (C-7), 52.7 (C-12), 34.4 (C-8), 32.1 (C-26), 29.9, 29.9 ,29.8, 29.8, 29.8, 29.7, 29.7, 29.5, 27.1, 22.9 (C-14 to C-25), 27.7 (C-13), 27.2 (C-10), 17.1 (C-9), 14.3 (C-27), 11.5 (C-11)

MS: **(ESI(+), Dichloromethane, M = $C_{58}H_{96}N_2O_8$) *m/z* =**
1834.463 $[2M+H]^+$, 917.732 $[M+H]^+$

ESI HRMS: $[M+H]^+ = C_{58}H_{96}N_2O_8H$
Calculated: *m/z* = 917.7341
Found: *m/z* = 917.7340

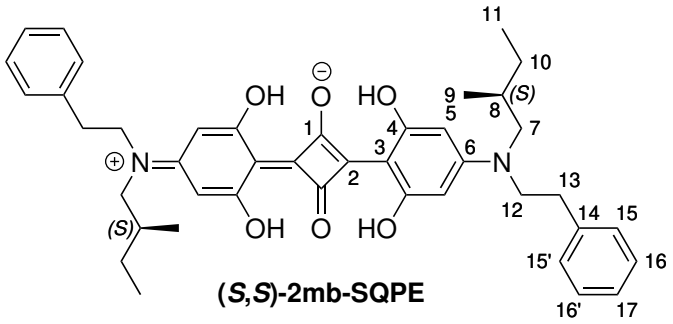
Elemental analysis: $C_{58}H_{96}N_2O_8$

Calculated:	C: 75.93	H: 10.55	N: 3.05
Found:	C: 75.78	H: 10.30	N: 3.07

UV/Vis: λ_{max} = 652.5 nm, ϵ = 380000 $M^{-1}cm^{-1}$ in chloroform

***R*$_f$-value:** 0.95 (dichloromethane)

2,4-bis[4-((*S*)-*N*-phenylethyl-2-methylbutanamine)-2,6-dihydroxyphenyl]squaraine - (*S*,*S*)-2mb-SQPE



(*S*,*S*)-2mb-SQPE

A single-neck flask, equipped with a Dean-Stark apparatus and reflux condenser, was charged with **(*S*)-2mb-N-PE** (568 mg, 2.97 mmol, 1.25 eq.) and phloroglucinol (300 mg, 2.38 mmol, 1.00 eq.). The reactants were suspended in a mixture of toluene/1-butanol (4:1, v/v, 4.0 mL/mmol), evacuated 5 times under vigorous stirring and repressurized with argon. The reaction mixture was refluxed under argon atmosphere for 24 hours. After cooling to room temperature, all volatile substances were removed (at 60 °C, high vacuum) and the orange/red oil was taken up with a mixture of toluene/1-butanol (1:1, v/v, 9.3 mL/mmol). Squaric acid (136 mg, 1.19 mmol, 0.50 eq.) was added and the reaction mixture was heated to reflux for additional 24 hours. With the beginning of boiling, a sudden color change from slightly reddish over green to dark-blue with a green hint could be observed within minutes. The mixture was slowly cooled to room temperature and chilled further in the freezer to promote precipitation of the raw product. The solid was collected via filtration and washed generously with methanol. Further

purification was done by column chromatography on silica gel eluting with dichloromethane, followed by recrystallization from dichloromethane/methanol (1:0.74, v/v). The precipitated solid was filtered off and washed with chilled methanol. After drying the collected solid under reduced pressure, the pure squaraine was collected as a green crystalline solid.

Yield: 263 mg (0.39 mmol, 16%, green solid)

Molecular weight: $C_{42}H_{48}N_2O_8$, 676.85 g/mol

^{1}H-NMR: **(500 MHz, Chloroform-*d*, 298 K) δ [ppm] =**
11.02 (s, 4H, OH), 7.35-7.30 (m, 2H, H-16, H-16'), 7.28-7.22 (m, 2H, H-17), 7.21-7.16 (m, 4H, H-15, H-15'), 5.88 (s, 4H, H-5), 3.71-3.56 (m, 4H, H-12), 3.18-3.08 (m, 2H, H-7^a), 3.03-2.96 (m, 2H, H-7^b), 2.92 (t, $^3J_{13,12}$ = 7.4 Hz, 4H, H-13), 1.91-1.76 (m, 2H, H-8), 1.45-1.33 (m, 2H, H-10^a), 1.17-1.05 (m, 2H, H-10^b), 0.90 (t, $^3J_{11,10}$ = 7.4 Hz, 6H, H-11), 0.87 (d, $^3J_{9,8}$ = 6.8 Hz, 6H, H-9)

^{13}C-NMR: **(125 MHz, Chloroform-*d*, 298 K) δ [ppm] =**
181.5 (C-1), 163.1 (C-4), 161.9 (C-2), 158.3 (C-6), 138.3 (C-14), 129.0 (C-15), 128.9 (C-16), 127.0 (C-17), 102.9 (C-3), 94.3 (C-5), 58.1 (C-7), 54.3 (C-12), 34.4 (C-8), 34.0 (C-13), 27.2 (C-10), 17.1 (C-9), 11.4 (C-11)

MS: **(ESI(+), Dichloromethane, M = $C_{42}H_{48}N_2O_8$) *m/z* =**
676.350 $[M+H]^+$

ESI HRMS: $[M+H]^+ = C_{42}H_{48}N_2O_8H$
Calculated: *m/z* = 676.3507
Found: *m/z* = 676.3504

Elemental analysis: $C_{42}H_{48}N_2O_8$

Calculated:	C: 74.53	H: 7.15	N: 4.14
Found:	C: 74.29	H: 6.95	N: 4.18

UV/Vis: λ_{max} = 652.5 nm, ϵ = 380000 $M^{-1}cm^{-1}$ in chloroform

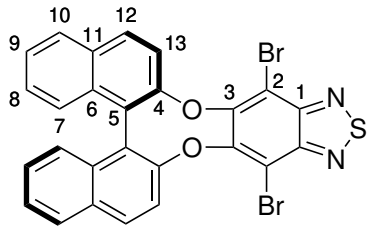
R_f-value: 0.90 (dichloromethane)

SC-XRD: see Appendix H.2.1

13.6 Experimental Section for Synthesis of Chiral π-Conjugated Polymers Exhibiting the CISS Effect for Advanced Optoelectronic Applications

Synthesis of Precursors for Chiral π-Conjugated Polymers

4,7-dibromo-5,6-[(*S*)-1,1'-bi-2-naphthoxy]-2,1,3-benzothiadiazole - (*S*)-Binol-DiBr-BT



(*S*)-Binol-DiBr-BT

Under inert gas conditions, dry DMF (13 mL/mmol) was added to a solid mixture of 4,7-dibromo-5,6-difluoro-2,1,3-benzothiadiazole[g] (340 mg, 1.03 mmol, 1.00 eq.). Caesium carbonate (1.01 g, 3.09 mmol, 3.00 eq.) and (*S*)-(-)-1,1'-bi(2-naphthol) (295 mg, 1.03 mmol, 1.00 eq.) were added and the reaction mixture is stirred at 60 °C overnight. The reaction was diluted with DCM and quenched by the addition of water (same volume as the reaction mixture) An aqueous ammonium chloride solution was added dropwise to the obtained suspension until all white precipitate was dissolved. The organic phase was separated, and the aqueous phase was extracted with DCM (3 × 20 mL/mmol). The combined organic phases were washed with brine (2 × 20 mL/mmol) and dried with magnesium/sodium sulfate. The solvent was removed under reduced pressure and the crude product purified by column chromatography on silica gel eluting with a solvent gradient from dichloromethane/cyclohexane 3:7 → 8:2 (v/v). The product was obtained as an off white solid.

Yield:	588 mg (1.02 mmol, 99%, off white solid)
Molecular weight:	$C_{26}H_{12}Br_2N_2O_2S$, 576.26 g/mol
^{1}H-NMR:	**(400 MHz, Chloroform-*d*, 298 K) δ [ppm] =** 8.01 (d, $^3J_{12,13}$ = 8.9 Hz, 2H, H-12), 7.96 (d, $^3J_{10,9}$ = 8.2 Hz, 2H, H-10), 7.69-7.60 (m, 4H, H-7, H-13), 7.59-7.50 (m, 2H, H-9), 7.46-7.39 (m, 2H, H-8)
^{13}C-NMR:	**(100 MHz, Chloroform-*d*, 298 K) δ [ppm] =** 150.6 (C-4), 150.6 (C-3), 150.2 (C-1), 132.3 (C-11), 132.0 (C-6), 131.2 (C-12), 128.6 (C-10), 127.3 (C-8), 126.9 (C-7), 126.1 (C-9), 125.3 (C-5), 120.8 (C-13), 105.3 (C-2)

[g] Provided by Dr. Junxiang Zhang - Group of Prof. Seth Marder, University of Colorado Boulder (USA).

MS: **(ESI(+), Dichloromethane, M = $C_{26}H_{12}Br_2N_2O_2S$) *m/z* =**
596.8817 $[M+Na]^+$, 574.9096 $[M+H]^+$, 573.895 $[M]^{\cdot+}$

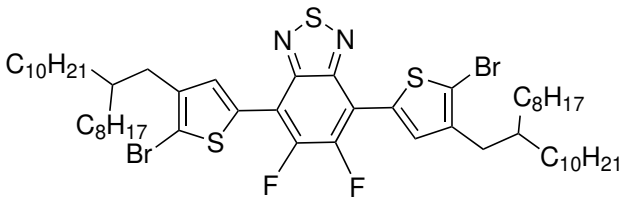
ESI HRMS: $[M+H]^+ = C_{26}H_{12}Br_2N_2O_2SH$
Calculated: *m/z* = 574.9064
Found: *m/z* = 574.9096

Elemental analysis: $C_{26}H_{12}Br_2N_2O_2S$

Calculated:	C: 54.19	H: 2.10	N: 4.86	S: 5.56
Found:	C: 54.20	H: 2.32	N: 4.86	S: 5.96

SC-XRD: see Appendix I.2

4,7-bis[5-bromo-4-(2-octyldodecyl)thiophen-2-yl]-5,6-difluoro-2,1,3-benzothiadiazole - DiBr-ThioBT



DiBr-ThioBT

To a solution of 5,6-difluoro-4,7-bis(4-(2-octyldodecyl)thiophen-2-yl)benzo[c][1,2,5]thiadiazole (JZ-V-87[h]) (449 mg, 0.50 mmol, 1.00 eq.) in THF (50 mL/mmol), *N*-bromosuccinimide (267 mg, 1.50 mmol, 3.00 eq.) was added portionwise and stirred at room temperature overnight. The solvent was removed under reduced pressure, water (20 mL) and *n*-hexane (20 mL) were added (side products are not soluble in *n*-hexane), separated and the aqueous phase extracted with *n*-hexane (3 × 20 mL). The combined organic phases were washed once with brine (30 mL) and the solvent was removed under reduced pressure. The crude product was purified by column chromatography on silica gel eluting with *n*-hexane to yield the product as bright orange solid.

Yield: 522 mg (0.49 mmol, 99%, bright orange solid)

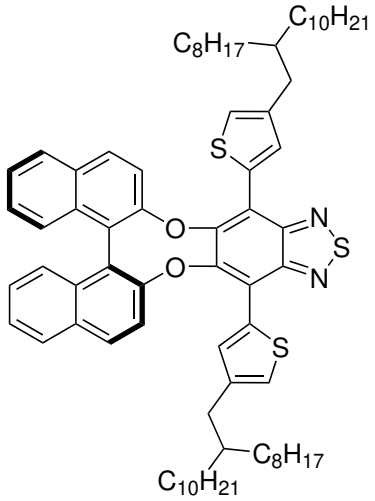
Molecular weight: $C_{54}H_{84}Br_2F_2N_2S_3$, 1055.27 g/mol

^{1}H-NMR: **(400 MHz, Chloroform-*d*, 298 K) δ [ppm] =**
7.91 (s, 2H), 2.58 (d, *J* = 7.2 Hz, 4H), 1.74 (*br* s, 2H), 1.51-1.11 (m, 64H), 0.87 (t, *J* = 6.7 Hz, 6H), 0.86 (t, *J* = 6.8 Hz, 6H)

[h] Provided by Dr. Junxiang Zhang - Group of Seth Marder, University of Colorado Boulder (USA).

^{13}C-NMR: **(100 MHz, Chloroform-*d*, 298 K) δ [ppm] =**
151.1, 148.6, 141.9, 132.5, 131.2, 115.2, 111.2, 38.7, 34.3, 33.5, 33.5, 32.1, 30.2, 30.2, 29.9, 29.8, 29.8, 29.5, 26.7, 26.7, 22.8, 14.3

4,7-bis[5-bromo-4-(2-octyldodecyl)thiophen-2-yl]-5,6-[(*S*)-1,1'-bi-2-naphthoxy]-2,1,3-benzothiadiazole - (*S*)-Binol-ThioBT



(*S*)-Binol-ThioBT

Under inert gas conditions, a mixture of dry DMF (50.00 mL/mmol) and dry THF (20 mL/mmol) was added to a mixture of 5,6-difluoro-4,7-bis(4-(2-octyldodecyl)thiophen-2-yl)benzo[c][1,2,5]thiadiazole (JZ-V-87[i]) (395 mg, 0.44 mmol, 1.00 eq.), caesium carbonate (430 mg, 1.32 mmol, 3.00 eq.) and (*S*)-(-)-1,1'-bi(2-naphthol) (126 mg, 0.44 mmol, 1.00 eq.). After stirring at 70 °C for 48 hours, the reaction mixture (orange solution) was diluted with DCM (50 mL) and quenched by the addition of water (same volume as the reaction mixture). An aqueous ammonium chloride solution was added dropwise to the suspension until all white precipitate was dissolved. The organic phase was separated and the aqueous phase was extracted with DCM (2 × samle volume as reaction mixture). The combined organic phases were washed once with water (50 mL), brine (50 mL) and dried with magnesium sulfate. The solvent was removed under reduced pressure and the crude product purified by column chromatography on silica gel eluting with *n*-hexane and DCM with a gradient from 0 → 15% (v:v) to yield the product as orange solid.

Yield: 371 mg (0.32 mmol, 74%, orange solid)

Molecular weight: $C_{74}H_{98}N_2O_2S_3$, 1143.79 g/mol

[i] Provided by Dr. Junxiang Zhang - Group of Seth Marder, University of Colorado Boulder (USA).

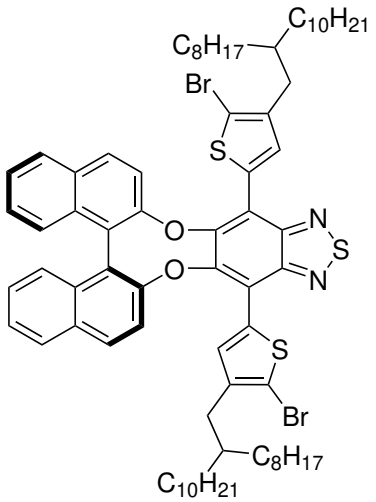
^{1}H-NMR: **(400 MHz, Chloroform-*d*, 298 K) δ [ppm] =**
8.48 (d, *J* = 1.4 Hz, 2H), 7.95 (t, *J* = 9.2 Hz, 4H), 7.79 (d, *J* = 8.6 Hz, 2H), 7.56-7.51 (m, 2H), 7.51-7.44 (m, 4H), 7.08 (d, *J* = 1.4 Hz, 2H), 2.65 (d, *J* = 6.8 Hz, 4H), 1.78-1.61 (m, 2H), 1.44-1.12 (m, 64H), 0.97-0.78 (m, 12H)

^{13}C-NMR: **(100 MHz, Chloroform-*d*, 298 K) δ [ppm] =**
151.1, 150.7, 148.2, 141.9, 133.5, 133.3, 132.1, 132.1, 130.7, 128.6, 127.0, 126.9, 125.9, 125.7, 124.0, 121.0, 116.7, 39.1, 35.1, 33.5, 33.5, 32.1, 30.2, 30.2, 29.9, 29.8, 29.8, 29.5, 26.9, 29.8, 22.8, 14.3

MS: **(ESI(+), Dichloromethane, M = $C_{74}H_{98}N_2O_2S_3$) *m/z* =**
1143.6804 $[M+H]^+$, 1142.678 $[M]^{\cdot+}$

ESI HRMS: $[M+H]^+ = C_{74}H_{98}N_2O_2S_3H$
Calculated: *m/z* = 1143.6869
Found: *m/z* = 1143.6804

4,7-bis[5-bromo-4-(2-octyldodecyl)thiophen-2-yl]-5,6-[(*S*)-1,1'-bi-2-naphthoxy]-2,1,3-benzothiadiazole - (*S*)-Binol-DiBr-ThioBT



(*S*)-Binol-DiBr-ThioBT

To a solution of **(*S*)-Binol-ThioBT** (354 mg, 0.31 mmol, 1.00 eq.) in THF (50 mL/mmol), *N*-bromosuccinimide (165 mg, 0.93 mmol, 3.00 eq.) was added portionwise and stirred at room temperature overnight. The solvent was removed under reduced pressure, water (15 mL) and *n*-hexane (15 mL) were added (side products are not soluble in *n*-hexane), separated and the aqueous phase extracted with *n*-hexane (3 × 15 mL). The combined organic phases were washed once with brine (30 mL) and the solvent was removed under reduced pressure. The crude product was purified by column chromatography on silica

gel eluting with *n*-hexane to yield the product as bright orange solid.

Yield: 373 mg (0.29 mmol, 93%, orange solid)

Molecular weight: $C_{74}H_{96}Br_2N_2O_2S_3$, 1301.58 g/mol

^{1}H-NMR: **(400 MHz, Chloroform-*d*, 298 K) δ [ppm] =**
8.46 (s, 2H), 7.98 (d, *J* = 8.8 Hz, 4H), 7.81 (d, *J* = 8.5 Hz, 2H), 7.58-7.53 (m, 2H), 7.53-7.45 (m, 4H), 2.59 (d, *J* = 6.9 Hz, 4H), 1.85-1.70 (m, 2H), 1.43-1.13 (m, 64H), 0.95-0.80 (m, 12H)

^{13}C-NMR: **(100 MHz, Chloroform-*d*, 298 K) δ [ppm] =**
150.4, 150.2, 148.1, 141.3, 133.3, 133.2, 132.2, 132.1, 130.9, 128.7, 127.1, 127.0, 125.9, 125.8, 120.9, 116.0, 114.2, 38.6, 34.3, 33.6, 33.5, 32.1, 32.1, 30.2, 30.2, 29.9, 29.9, 29.8, 29.5, 29.5, 26.8, 26.7, 22.8, 14.3

Synthesis of Chiral π-Conjugated Polymers

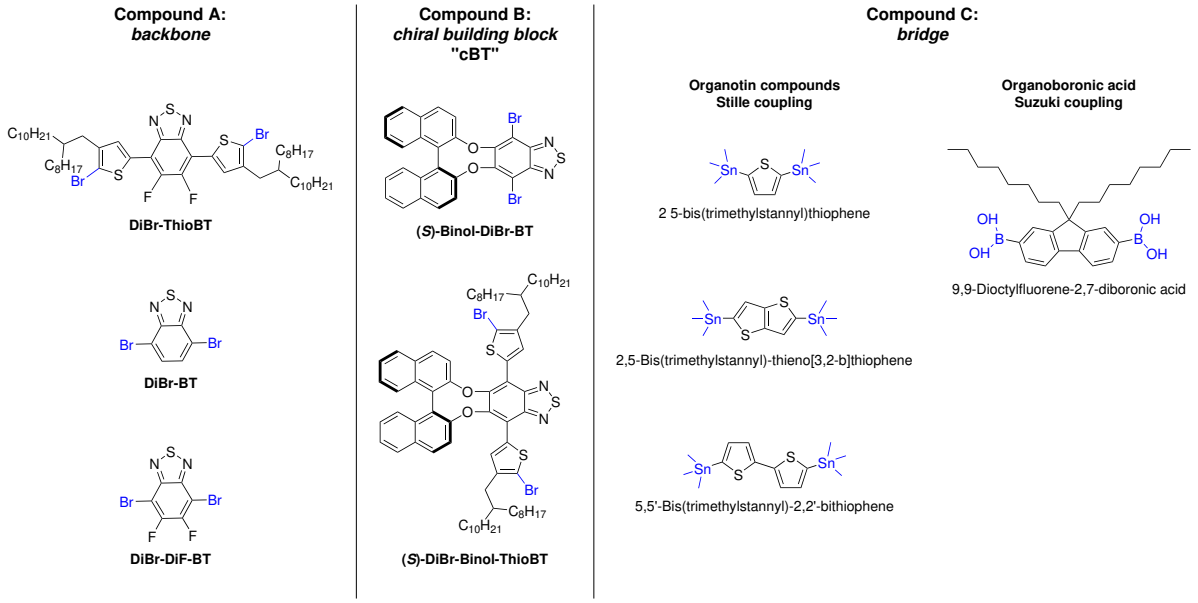


Figure 13.2: Molecular library of building blocks which were available for the chiral π-conjugated polymer synthesis with **Compound A** - the achiral backbone, **Compound B** - the chiral building block and **Compound C** - the achiral bridge.

General Procedure for the Polymerization - Suzuki or Stille Cross-Coupling Reaction

Suzuki Cross-Coupling Reaction for (*S*)-c$_x$F8BT and (*S*)-F8TBT:

Synthesis adopted and modified from the literature.[178, 187]
A mixture of 9,9-dioctylfluorene-2,7-diboronic acid (1.01 eq.), 4,7-dibromo-2,1,3-benzothiadiazole (**DiBrBT**) (1.00-x eq.), **(*S*)-Binol-DiBr-BT** (x eq.; x = 0.00, 0.05, 0.10 or 0.20),[j] K_2CO_3 (10.0 eq.), and $Pd(PPh_3)_4$ (0.03 eq.) is placed in a dried round-bottom flask under inert gas conditions. Degassed toluene (12 mL/mmol) and degassed H_2O (2 mL/mmol) are injected into the flask using a syringe, followed by stirring at 105 °C for 72 h under inert gas. 4-Iodotoluene (in excess) is added and the reaction is stirred at 105 °C for additional 12 h to cap the polymer.

Stille Cross-Coupling Reaction for poly-(*S*)-Binol-BTQT, (*S*)-c$_{20}$Binol-PCE11 and (*S*)-c$_{20}$Binol-BTMTDT:

Synthesis adopted and modified from the literature.[188]
A mixture of **Compound C**[k] (bridge, 1.01 eq.), **Comound A**[k] (backbone, 1.00-x eq.), **Compound B**[k] (chiral building block, x eq.; x = 0.00 or 0.20), $Pd_2(dba)_3$ (0.04 eq.), and P(*o*-tol)$_3$ (0.08 eq.) is placed in a dried round-bottom flask under inert gas conditions. Degassed toluene (12 mL/mmol) is injected into the

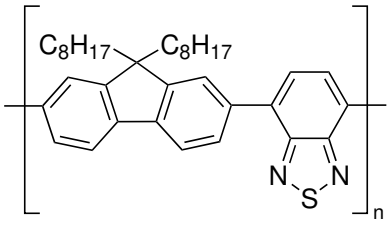
[j] In the case of (*S*)-F8TBT only **(*S*)-Binol-DiBr-ThioBT** was used instead of **DiBrBT** and **(*S*)-Binol-DiBr-BT**
[k] See Figure 13.2

flask using a syringe, followed by stirring at 105 °C for 72 h under inert gas. 4-Iodotoluene (in excess) is added and the reaction is stirred at 105 °C for additional 12 h to cap the polymer.

General Work-Up of the polymerisation Reaction:

The mixture is cooled down to room temperature, and the polymer is precipitated in methanol and filtered off. The solid residue is dissolved in toluene (200 mL/mmol), sodium diethyldithiocarbamate solution (excess, 10 wt-% in H_2O) is added and stirred at 80 °C for 6 hours. The solid is recovered by precipitation in methanol and purified by Soxhlet extraction with methanol, acetone, *n*-hexane and toluene successively. The desired polymer (in the toluene fraction) is precipitated in methanol and obtained as colorful solid.

Poly[9,9-dioctylfluorene-*alt*-benzothiadiazole] - F8BT



F8BT

9,9-Dioctylfluorene-2,7-diboronic acid (145 mg, 0.30 mmol, 1.01 eq.), 4,7-dibromo-2,1,3-benzothiadiazole (**DiBrBT**) (88.2 mg, 0.30 mmol, 1.00 eq.), K_2CO_3 (415 mg, 3.00 mmol, 10.0 eq.), and $Pd(PPh_3)_4$ (10.4 mg, 0.09 mmol, 0.03 eq.) were reacted according to the general procedure for the polymerization.

Yield: 127 mg (0.24 mmol, 81%, yellow solid)

Molecular weight of the repeating unit: $C_{35}H_{42}N_2S$, 522.80 g/mol

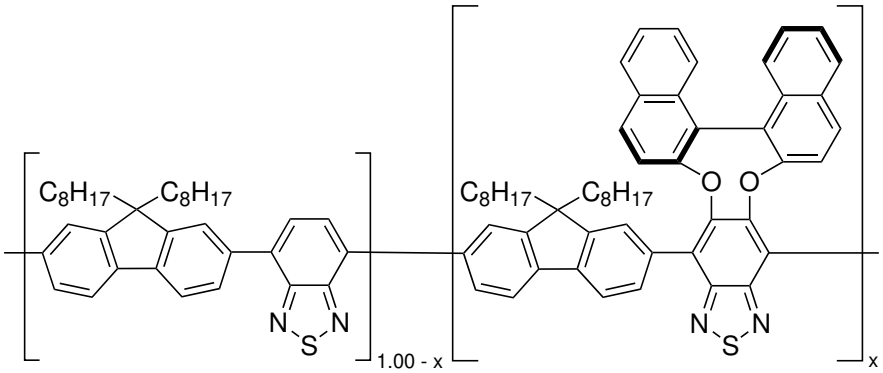
^{1}H-NMR: **(400 MHz, Chloroform-*d*, 298 K, 1024 scans) δ [ppm] =**
8.11 (m), 8.04 (m), 7.97 (m), 2.15 (*br* s), 1.16 (m), 0.96 (m), 0.81 (t)
Due to the complexity of the signal set, it is impractical to define distinct areas. For further details, please refer to the spectra itself provided in Appendix J.

GPC:[I]

M_n [g/mol]	M_w [g/mol]	M_z [g/mol]	PDI	DP
18000	24000	32000	1.35	≈35

[I] Definitions and equations are given in Appendix I.1; Measured against polystyrene standards; Values rounded to the nearest thousand.

Poly[9,9-dioctylfluorene-*alt*-(2,1,3-benzothiadiazole-*ran*-(5,6-[(*S*)-1,1'-bi-2-naphthoxy]-2,1,3-benzothiadiazole))] (1.00:0.95:0.05 mass-%) - (*S*)-c_5F8BT



(*S*)-c_5F8BT (x = 0.05)

9,9-Dioctylfluorene-2,7-diboronic acid (145 mg, 0.30 mmol, 1.01 eq.), 4,7-dibromo-2,1,3-benzothiadiazole (**DiBrBT**) (83.8 mg, 0.285 mmol, 0.95 eq.), **(*S*)-Binol-DiBr-BT** (8.64 mg, 0.015 mmol, 0.05 eq.), K_2CO_3 (415 mg, 3.00 mmol, 10.0 eq.), and $Pd(PPh_3)_4$ (10.4 mg, 0.09 mmol, 0.03 eq.) were reacted according to the general procedure for the polymerization.

Yield: 117 mg (0.22 mmol, 72%, yellow solid)

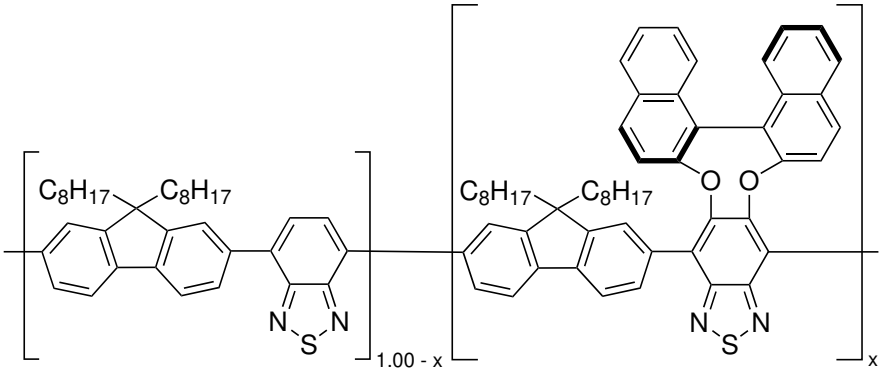
Molecular weight of the repeating unit: $C_{36}H_{43.5}N_2O_{0.1}S$, 537.92 g/mol

^{1}H-NMR: **(400 MHz, Chloroform-*d*, 298 K, 1024 scans) δ [ppm] =**
8.11 (m), 8.04 (m), 7.97 (m), 2.15 (*br* s), 1.16 (m), 0.96 (m), 0.81 (t)
Due to the complexity of the signal set, it is impractical to define distinct areas. For further details, please refer to the spectra itself provided in Appendix J.

GPC:[l]

M_n [g/mol]	M_w [g/mol]	M_z [g/mol]	PDI	DP
15000	21000	28000	1.41	≈27

Poly[9,9-dioctylfluorene-*alt*-(2,1,3-benzothiadiazole-*ran*-(5,6-[(*S*)-1,1'-bi-2-naphthoxy]-2,1,3-benzothiadiazole))] (1.00:0.90:0.10 mass-%) - (*S*)-c_{10}F8BT



(*S*)-c_{10}F8BT (x = 0.10)

9,9-Dioctylfluorene-2,7-diboronic acid (145 mg, 0.30 mmol, 1.01 eq.), 4,7-dibromo-2,1,3-benzothiadiazole (**DiBrBT**) (79.4 mg, 0.27 mmol, 0.90 eq.), **(*S*)-Binol-DiBr-BT** (17.3 mg, 0.03 mmol, 0.10 eq.), K_2CO_3 (415 mg, 3.00 mmol, 10.0 eq.), and $Pd(PPh_3)_4$ (10.4 mg, 0.09 mmol, 0.03 eq.) were reacted according to the general procedure for the polymerization.

Yield: 129 mg (0.23 mmol, 78%, yellow solid)

Molecular weight of the repeating unit: $C_{37}H_{44}N_2O_{0.2}S$, 552.04 g/mol

^{1}H-NMR: **(400 MHz, Chloroform-*d*, 298 K, 1024 scans) δ [ppm] =**
8.11 (m), 8.04 (m), 7.96 (m), 2.15 (*br* s), 1.16 (m), 0.96 (m), 0.81 (t)
Due to the complexity of the signal set, it is impractical to define distinct areas. For further details, please refer to the spectra itself provided in Appendix J.

GPC:[l]

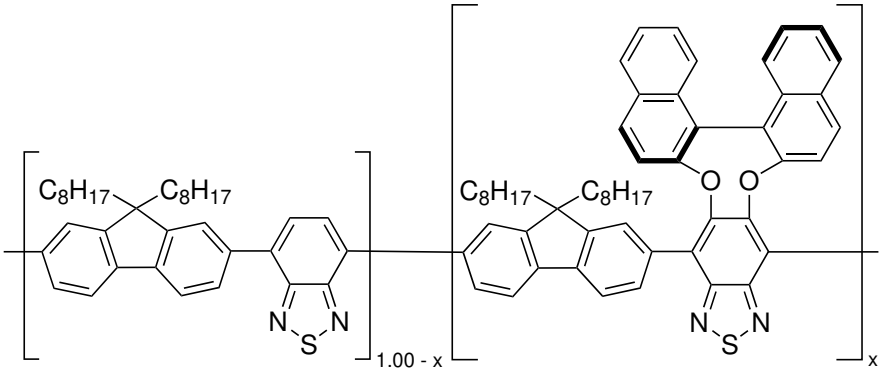
M_n [g/mol]	M_w [g/mol]	M_z [g/mol]	PDI	DP
15000	22000	29000	1.47	≈26

Elemental analysis:[m] $C_{37}H_{44}N_2O_{0.2}S$

Calculated:	C: 80.50	H: 8.03	N: 5.07	S: 5.81
Found:	C: 80.35	H: 8.03	N: 5.00	S: 5.86

[m] Measured from a different batch.

Poly[9,9-dioctylfluorene-*alt*-(2,1,3-benzothiadiazole-*ran*-(5,6-[(*S*)-1,1'-bi-2-naphthoxy]-2,1,3-benzothiadiazole))] (1.00:0.80:0.20 mass-%) - (*S*)-c$_{20}$F8BT



(*S*)-c$_{20}$F8BT (x = 0.20)

9,9-Dioctylfluorene-2,7-diboronic acid (145 mg, 0.30 mmol, 1.01 eq.), 4,7-dibromo-2,1,3-benzothiadiazole (**DiBrBT**) (70.6 mg, 0.24 mmol, 0.80 eq.), **(*S*)-Binol-DiBr-BT** (34.6 mg, 0.06 mmol, 0.20 eq.), K_2CO_3 (415 mg, 3.00 mmol, 10.0 eq.), and $Pd(PPh_3)_4$ (10.4 mg, 0.09 mmol, 0.03 eq.) were reacted according to the general procedure for the polymerization.

Yield: 108 mg (0.19 mmol, 62%, yellow solid)

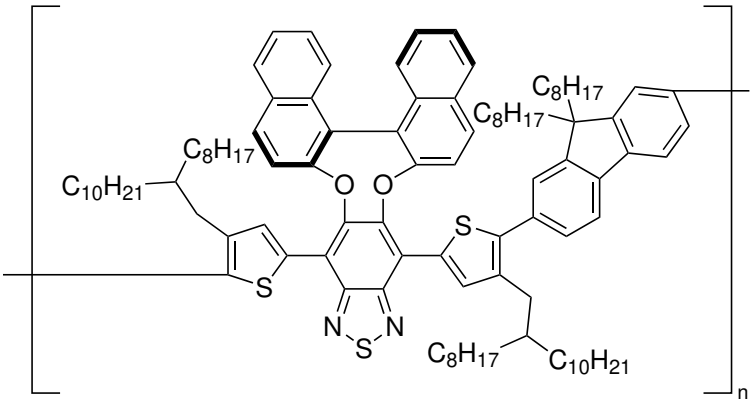
Molecular weight of the repeating unit: $C_{39}H_{45}N_2O_{0.4}S$, 580.26 g/mol

^{1}H-NMR: **(400 MHz, Chloroform-*d*, 298 K, 1024 scans) δ [ppm] =**
8.10 (m), 8.04 (m), 7.97 (m), 2.14 (m), 1.16 (m), 0.95 (m), 0.88 (m), 0.81 (m)
Due to the complexity of the signal set, it is impractical to define distinct areas. For further details, please refer to the spectra itself provided in Appendix J.

GPC:[m]

M_n [g/mol]	M_w [g/mol]	M_z [g/mol]	PDI	DP
6000	10000	14000	1.62	≈10

Poly[9,9-dioctylfluorene-*alt*-[4,7-bis[4-(2-octyldodecyl)thiophen-2-yl]-5,6-[(*S*)-1,1'-bi-2-naphthoxy]-2,1,3-benzothiadiazole]] - (*S*)-F8TBT



(*S*)-F8TBT

9,9-Dioctylfluorene-2,7-diboronic acid (48.3 mg, 0.10 mmol, 1.01 eq.), **(*S*)-Binol-DiBr-ThioBT** (130 mg, 0.10 mmol, 1.00 eq.), K_2CO_3 (138 mg, 1.00 mmol, 10.0 eq.), and $Pd(PPh_3)_4$ (3.47 mg, 0.03 mmol, 0.03 eq.) were reacted according to the general procedure for the polymerization.

Yield: 129 mg (0.08 mmol, 84%, red solid)

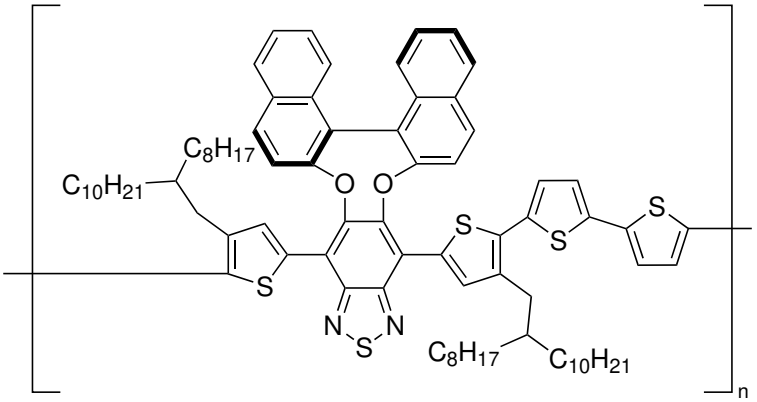
Molecular weight of the repeating unit: $C_{103}H_{136}N_2O_2S_3$, 1530.41 g/mol

^{1}H-NMR: **(400 MHz, Chloroform-*d*, 298 K, 1024 scans) δ [ppm] =**
8.54 (m), 7.95 (m), 7.78 (m), 7.65 (m), 7.52 (m), 2.72 (m), 1.97 (m), 1.71 (m), 1.15 (m), 0.82 (m), 0.67 (m)
Due to the complexity of the signal set, it is impractical to define distinct areas. For further details, please refer to the spectra itself provided in Appendix J.

GPC:[m]

M_n [g/mol]	M_w [g/mol]	M_z [g/mol]	PDI	DP
9000	13000	18000	1.44	≈6

Poly[2,2'-bithiophene-*alt*-[4,7-bis[4-(2-octyldodecyl)thiophen-2-yl]-5,6-[(*S*)-1,1'-bi-2-naphthoxy]-2,1,3-benzothiadiazole]] - poly-(*S*)-Binol-BTQT



poly-(*S*)-Binol-BTQT

5,5'-Bis(trimethylstannyl)-2,2'-bithiophene (45.9 mg, 0.093 mmol, 1.01 eq.), **(*S*)-Binol-DiBr-ThioBT** (120 mg, 0.092 mmol, 1.00 eq.), $Pd_2(dba)_3$ (3.38 mg, 0.004 mmol, 0.04 eq.), and $P(o\text{-tol})_3$ (2.25 mg, 0.007 mmol, 0.08 eq.) were reacted according to the general procedure for the polymerization.

Yield: 89 mg (0.07 mmol, 74%, dark red solid)

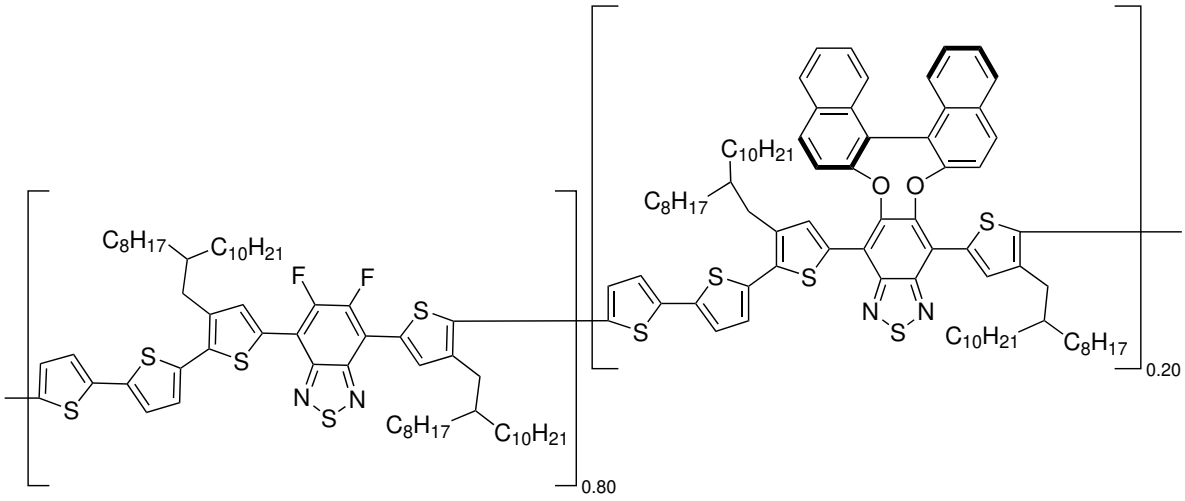
Molecular weight of the repeating unit: $C_{82}H_{100}N_2O_2S_5$, 1306.01 g/mol

^{1}H-NMR: **(400 MHz, Chloroform-*d*, 298 K, 1024 scans) δ [ppm] =**
8.52 (*br* s, 2H), 8.03-7.88 (m, 4H), 7.88-7.75 (m, 2H), 7.63-7.38 (m, 6H), 7.06 (*br* s, 4H), 2.94-2.63 (m, 4H), 1.78 (*br* s, 2H), 1.40-1.07 (m, 64H), 0.89-0.75 (m, 12H)

GPC:[m]

M_n [g/mol]	M_w [g/mol]	M_z [g/mol]	PDI	DP
46000	69000	92000	1.49	≈35

Poly[2,2'-bithiophene-*alt*-((4,7-bis[4-(2-octyldodecyl)thiophen-2-yl]-5,6-difluoro-2,1,3-benzothiadiazole)-*ran*-(4,7-bis[4-(2-octyldodecyl)thiophen-2-yl]-5,6-[(*S*)-1,1'-bi-2-naphthoxy]-2,1,3-benzothiadiazole))] (1.00:0.80:0.20 mass-%) - (*S*)-c_{20}Binol-PCE11



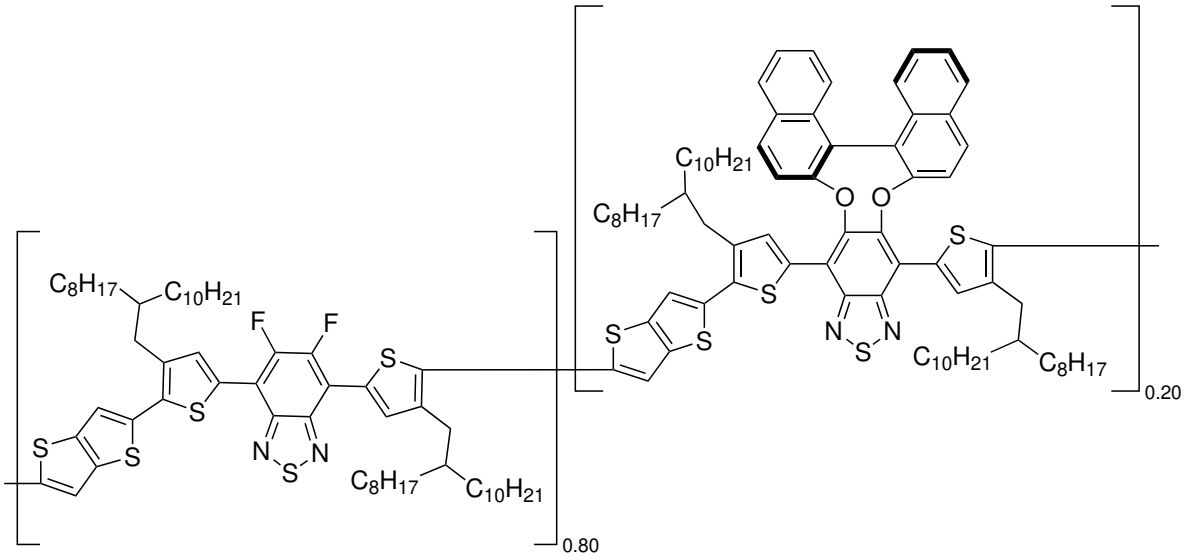
(*S*)-c_{20}Binol-PCE11

5,5'-Bis(trimethylstannyl)-2,2'-bithiophene (133 mg, 0.270 mmol, 1.01 eq.), **DiBr-ThioBT** (226 mg, 0.214 mmol, 0.80 eq.), **(*S*)-Binol-DiBr-ThioBT** (69.7 mg, 0.054 mmol, 0.20 eq.), $Pd_2(dba)_3$ (9.81 mg, 0.011 mmol, 0.04 eq.), and P(*o*-tol)$_3$ (6.52 mg, 0.021 mmol, 0.08 eq.) were reacted according to the general procedure for the polymerization.

Due to the low solubility at room temperature, it was not possible to obtain any analytical data.

Yield:	248 mg (0.22 mmol, 83%, dark red to black solid)
Molecular weight of the repeating unit:	$C_{66}H_{92.4}F_{1.6}N_2O_{0.4}S_5$, 1110.98 g/mol

Poly[thieno[3,2-*b*]thiophene-*alt*-((4,7-bis[4-(2-octyldodecyl)thiophen-2-yl]-5,6-difluoro-2,1,3-benzothiadiazole)-*ran*-(4,7-bis[4-(2-octyldodecyl)thiophen-2-yl]-5,6-[(*S*)-1,1'-bi-2-naphthoxy]-2,1,3-benzothiadiazole))] (1.00:0.80:0.20 mass-%) - (*S*)-c$_{20}$Binol-BTMTDT



(*S*)-c$_{20}$Binol-BTMTDT

2,5-Bis(trimethylstannyl)-thieno[3,2-*b*]thiophene (141 mg, 0.303 mmol, 1.01 eq.), **DiBr-ThioBT** (253 mg, 0.240 mmol, 0.80 eq.), **(*S*)-Binol-DiBr-ThioBT** (78.1 mg, 0.060 mmol, 0.20 eq.), $Pd_2(dba)_3$ (11.1 mg, 0.012 mmol, 0.04 eq.), and P(*o*-tol)$_3$ (7.38 mg, 0.024 mmol, 0.08 eq.) were reacted according to the general procedure for the polymerization.

Due to the low solubility at room temperature, it was not possible to obtain any analytical data.

Yield:	317 mg (0.29 mmol, 97%, dark red to black solid)
Molecular weight of the repeating unit:	$C_{64}H_{90.4}F_{1.6}N_2O_{0.4}S_5$, 1084.94 g/mol

Bibliography

[1] F. Balzer, M. F. Schumacher, S. Mattiello, M. Schulz, J. Zablocki, M. Schmidtmann, K. Meerholz, N. S. Sariciftci, L. Beverina, A. Lützen, and M. Schiek, "The Impact of Chiral Citronellyl-Functionalization on Indolenine and Anilino Squaraine Thin Films," *Israel Journal of Chemistry* **2022**, *62* (7-8), e202100079, doi: 10.1002/ijch.202100079.

[2] D. Giavazzi, M. F. Schumacher, L. Grisanti, M. Anzola, F. D. Maiolo, J. Zablocki, A. Lützen, M. Schiek, and A. Painelli, "A marvel of chiral squaraine aggregates: chiroptical spectra beyond the exciton model," *Journal of Materials Chemistry C* **2023**, *11* (24), 8307, doi: 10.1039/D2TC05555D.

[3] R. Bernhardt, L. Rieland, T. Wang, M. F. Schumacher, A. Lützen, M. Schiek, and P. H. M. van Loosdrecht, "Ultrafast Excitonic Transitions in Enantiopure and Racemic Squaraine Thin Films," *Aggregate* **2025**, *6* (3), e698, doi: 10.1002/agt2.698.

[4] D. Timmer, M. Gittinger, T. Quenzel, S. Stephan, Y. Zhang, M. F. Schumacher, A. Lützen, M. Silies, S. Tretiak, J.-H. Zhong, A. D. Sio, and C. Lienau, "Plasmon mediated coherent population oscillations in molecular aggregates," *Nature Communications* **2023**, *14* (1), 8035, doi: 10.1038/s41467-023-43578-4.

[5] C. Wallerius, O. Erdene-Ochir, E. V. Doeselar, R. Alle, A. T. Nguyen, M. F. Schumacher, A. Lützen, K. Meerholz, and S. H. Pun, "Quadruple[6]Helicene Featuring Pyrene Core: Unraveling Contorted Aromatic Core with Larger Effective Conjugation," *Precision Chemistry* **2024**, *2* (9), 488, doi: 10.1021/prechem.4c00038.

[6] L. Beverina and M. Sassi, "Twists and Turns Around a Square: The Many Faces of Squaraine Chemistry," *Synlett* **2014**, *25* (4), 477, doi: 10.1055/s-0033-1340482.

[7] A. H. Schmidt, "Reaktionen von Quadratsäure und Quadratsäure-Derivaten," *Synthesis* **1980**, *1980* (12), 961, doi: 10.1055/s-1980-29291.

[8] A. Treibs and K. Jacob, "Cyclotrimethine Dyes Derived from Squaric Acid," *Angewandte Chemie International Edition in English* **1965**, *4* (8), 694, doi: 10.1002/anie.196506941.

[9] A. Treibs and K. Jacob, "Über Tetracyclotrimethin-Farbstoffe. Cyclobutenderivate der Pyrrolreihe," *Justus Liebigs Annalen der Chemie* **1966**, *699* (1), 153, doi: 10.1002/jlac.19666990116.

[10] A. Treibs and K. Jacob, "Cyclobutenderivate der Pyrrolreihe, II 1) Über Vierring-trimethin-Farbstoffe," *Justus Liebigs Annalen der Chemie* **1968**, *712* (1), 123, doi: 10.1002/jlac.19687120116.

[11] C. W. Dirk, W. C. Herndon, F. Cervantes-Lee, H. Selnau, S. Martinez, P. Kalamegham, A. Tan, G. Campos, and M. Velez, "Squarylium Dyes: Structural Factors Pertaining to the Negative Third-Order Nonlinear Optical Response," *Journal of the American Chemical Society* **1995**, *117* (8), 2214, doi: 10.1021/ja00113a011.

[12] A. Mishra, R. K. Behera, P. K. Behera, B. K. Mishra, and G. B. Behera, "Cyanines during the 1990s: A Review," *Chemical Reviews* **2000**, *100* (6), 1973, doi: 10.1021/cr990402t.

[13] S. Dähne, "Systematik und Begriffserweiterung der Polymethinfarbstoffe," *Zeitschrift für Chemie* **1965**, *5* (12), 441, doi: 10.1002/zfch.19650051202.

[14] N. J. Hestand, C. Zheng, A. R. Penmetcha, B. Cona, J. A. Cody, F. C. Spano, and C. J. Collison, "Confirmation of the Origins of Panchromatic Spectra in Squaraine Thin Films Targeted for Organic Photovoltaic Devices," *The Journal of Physical Chemistry C* **2015**, *119* (33), 18964, doi: 10.1021/acs.jpcc.5b05095.

[15] S. Pascal, A. Haefele, C. Monnereau, A. Charaf-Eddin, D. Jacquemin, B. L. Guennic, O. Maury, and C. Andraud, "On the versatility of electronic structures in polymethine dyes," ed. by D. Burgess, G. Owen, H. Rana, R. Zamboni, F. Kajzar, and A. A. Szep, **2014** 92531A, doi: 10.1117/12.2072624.

[16] J. Zablocki, O. Arteaga, F. Balzer, D. Hertel, J. J. Holstein, G. Clever, J. Anhäuser, R. Puttreddy, K. Rissanen, K. Meerholz, A. Lützen, and M. Schiek, "Polymorphic chiral squaraine crystallites in textured thin films," *Chirality* **2020**, *32* (5), 619, doi: 10.1002/chir.23213.

[17] S. Sreejith, P. Carol, P. Chithra, and A. Ajayaghosh, "Squaraine dyes: a mine of molecular materials," *J. Mater. Chem.* **2008**, *18* (3), 264, doi: 10.1039/B707734C.

[18] R. W. Bigelow and H.-J. Freund, "An MNDO and CNDO / S(S + DES CI) study on the structural and electronic properties of a model squaraine dye and related cyanine," *Chemical Physics* **1986**, *107* (2-3), 159, doi: 10.1016/0301-0104(86)85001-7.

[19] G. Chen, H. Sasabe, Y. Sasaki, H. Katagiri, X.-F. Wang, T. Sano, Z. Hong, Y. Yang, and J. Kido, "A Series of Squaraine Dyes: Effects of Side Chain and the Number of Hydroxyl Groups on Material Properties and Photovoltaic Performance," *Chemistry of Materials* **2014**, *26* (3), 1356, doi: 10.1021/cm4034929.

[20] K. Y. Law, "Organic photoconductive materials: recent trends and developments," *Chemical Reviews* **1993**, *93* (1), 449, doi: 10.1021/cr00017a020.

[21] K. Y. Law, "Squaraine chemistry: effects of structural changes on the absorption and multiple fluorescence emission of bis[4-(dimethylamino)phenyl]squaraine and its derivatives," *The Journal of Physical Chemistry* **1987**, *91* (20), 5184, doi: 10.1021/j100304a012.

[22] M. Tian, M. Furuki, I. Iwasa, Y. Sato, L. S. Pu, and S. Tatsuura, "Search for Squaraine Derivatives That Can Be Sublimed without Thermal Decomposition," *The Journal of Physical Chemistry B* **2002**, *106* (17), 4370, doi: 10.1021/jp013698r.

[23] E. Ronchi, R. Ruffo, S. Rizzato, A. Albinati, L. Beverina, and G. A. Pagani, "Regioselective Synthesis of 1,2- vs 1,3-Squaraines," *Organic Letters* **2011**, *13* (12), 3166, doi: 10.1021/ol201093t.

[24] E. Terpetschnig, "Synthesis and characterization of unsymmetrical squaraines: a new class of cyanine dyes," *Dyes and Pigments* **1993**, *21* (3), 227, doi: 10.1016/0143-7208(93)85016-S.

[25] L. Beverina, R. Ruffo, G. Patriarca, F. D. Angelis, D. Roberto, S. Righetto, R. Ugo, and G. A. Pagani, "Second harmonic generation in nonsymmetrical squaraines: tuning of the directional charge transfer character in highly delocalized dyes," *Journal of Materials Chemistry* **2009**, *19* (43), 8190, doi: 10.1039/b914716k.

[26] B. Schrader, ed., *Infrared and Raman Spectroscopy*, Wiley, **1995**, https://doi.org/10.1002/9783527615438.

[27] U. Mayerhöffer, M. Gsänger, M. Stolte, B. Fimmel, and F. Würthner, "Synthesis and Molecular Properties of Acceptor-Substituted Squaraine Dyes," *Chemistry – A European Journal* **2013**, *19* (1), 218, doi: 10.1002/chem.201202783.

[28] V. Rapozzi, L. Beverina, P. Salice, G. A. Pagani, M. Camerin, and L. E. Xodo, "Photooxidation and Phototoxicity of π-Extended Squaraines," *Journal of Medicinal Chemistry* **2010**, *53* (5), 2188, doi: 10.1021/jm901727j.

[29] Q. Xiao, F. Wu, M. Han, Z. Li, L. Zhu, and Z. Li, "A pseudo-two-dimensional conjugated polysquaraine: an efficient p-type polymer semiconductor for organic photovoltaics and perovskite solar cells," *Journal of Materials Chemistry A* **2018**, *6* (28), 13644, doi: 10.1039/C8TA05026K.

[30] Q. Xiao, Y. Li, M. Han, F. Wu, X. Leng, D. Zhang, X. Zhang, S. Yang, Y. Zhang, Z. Li, H. Zhou, and Z. Li, "Rational Design of 2D p–π Conjugated Polysquaraines for Both Fullerene and Nonfullerene Polymer Solar Cells," *Macromolecular Chemistry and Physics* **2020**, *221* (2), doi: 10.1002/macp.201900439.

[31] G. Garbay, T. Tailliez, E. Pavlopoulou, J. Oriou, M. Bezirdjoglou, G. Hadziioannou, E. Cloutet, and C. Brochon, "Triaryl-1,4-diamine-based polysquaraines: effect of co-solvent and monomer insertion on optoelectronic properties," *Polymer Chemistry* **2018**, *9* (11), 1288, doi: 10.1039/C7PY02056B.

[32] A. Ajayaghosh, V. K. Praveen, and C. Vijayakumar, "Organogels as scaffolds for excitation energy transfer and light harvesting," *Chem. Soc. Rev.* **2008**, *37* (1), 109, doi: 10.1039/B704456A.

[33] L. Beverina, R. Ruffo, M. M. Salamone, E. Ronchi, M. Binda, D. Natali, and M. Sampietro, "Panchromatic squaraine compounds for broad band light harvesting electronic devices," *Journal of Materials Chemistry* **2012**, *22* (14), 6704, doi: 10.1039/c2jm16240g.

[34] M. Schulz, J. Zablocki, O. S. Abdullaeva, S. Brück, F. Balzer, A. Lützen, O. Arteaga, and M. Schiek, "Giant intrinsic circular dichroism of prolinol-derived squaraine thin films," *Nature Communications* **2018**, *9* (1), 2413, doi: 10.1038/s41467-018-04811-7.

[35] S. Brück, C. Krause, R. Turrisi, L. Beverina, S. Wilken, W. Saak, A. Lützen, H. Borchert, M. Schiek, and J. Parisi, "Structure-property relationship of anilino-squaraines in organic solar cells," *Phys. Chem. Chem. Phys.* **2014**, *16* (3), 1067, doi: 10.1039/C3CP54163K.

[36] K.-Y. Law and F. C. Bailey, "Squaraine chemistry. Synthesis of bis(4-dimethylaminophenyl)squaraine from dialkyl squarates. Mechanism and scope of the synthesis," *Canadian Journal of Chemistry* **1986**, *64* (12), 2267, doi: 10.1139/v86-372.

[37] L. Hu, Z. Yan, and H. Xu, "Advances in synthesis and application of near-infrared absorbing squaraine dyes," *RSC Advances* **2013**, *3* (21), 7667, doi: 10.1039/c3ra23048a.

[38] M. P. Schulz, "Synthese, Eigenschaften und Anwendung von Squarainen als Komponente in Photodioden," PhD thesis: Rheinischen Friedrich-Wilhems-Universität Bonn, **2018**.

[39] H.-E. Sprenger and W. Ziegenbein, "Condensation Products of Squaric Acid and Tertiary Aromatic Amines," *Angewandte Chemie International Edition in English* **1966**, *5* (10), 894, doi: 10.1002/anie.196608941.

[40] M. Schulz, M. Mack, O. Kolloge, A. Lützen, and M. Schiek, "Organic photodiodes from homochiral L-proline derived squaraine compounds with strong circular dichroism," *Physical Chemistry Chemical Physics* **2017**, *19* (10), 6996, doi: 10.1039/C7CP00306D.

[41] K. Ueji, S. Ichimura, Y. Tamaki, and K. Miyamura, "Effects of alkyl chain substitution on the crystal structure of benzothiazole-derived squarylium dyes," *CrystEngComm* **2014**, *16* (43), 10139, doi: 10.1039/C4CE01571A.

[42] G. Chen, H. Sasabe, T. Igarashi, Z. Hong, and J. Kido, "Squaraine dyes for organic photovoltaic cells," *Journal of Materials Chemistry A* **2015**, *3* (28), 14517, doi: 10.1039/C5TA01879J.

[43] A. Mishra and P. Bäuerle, "Small Molecule Organic Semiconductors on the Move: Promises for Future Solar Energy Technology," *Angewandte Chemie International Edition* **2012**, *51* (9), 2020, doi: 10.1002/anie.201102326.

[44] R. B. Champ and M. D. Shattuck, *U.S. Patent 3,824,099*.

[45] D. Pai, "Organic photoconductors in electrophotography," *Journal of Non-Crystalline Solids* **1983**, *59-60* 1255, doi: 10.1016/0022-3093(83)90396-4.

[46] C.-T. Chen, S. R. Marder, and L.-T. Cheng, "Syntheses and Linear and Nonlinear Optical Properties of Unsymmetrical Squaraines with Extended Conjugation," *Journal of the American Chemical Society* **1994**, *116* (7), 3117, doi: 10.1021/ja00086a049.

[47] C.-T. Chen, S. R. Marder, and L.-T. Cheng, "Molecular first hyperpolarizabilities of a new class of asymmetric squaraine dyes," *Journal of the Chemical Society, Chemical Communications* **1994**, (3), 259, doi: 10.1039/c39940000259.

[48] G. J. Ashwell, G. S. Bahra, C. R. Brown, D. G. Hamilton, C. H. L. Kennard, and D. E. Lynch, "2,4-Bis[4-(N,N-dibutylamino)phenyl] squaraine: X-ray crystal structure of a centrosymmetric dye and the second-order non-linear optical properties of its non-centrosymmetric Langmuir–Blodgett films," *J. Mater. Chem.* **1996**, *6* (1), 23, doi: 10.1039/JM9960600023.

[49] G. J. Ashwell, M. P. S. Roberts, N. D. Rees, G. S. Bahra, and C. R. Brown, "2,4-Bis[4-(N-methyl-N-alkylamino)phenyl]squaraines: Structure−Property Relationship and Dependence of the Type of Aggregate upon the Hydrophobicity of the Alkyl Group," *Langmuir* **1998**, *14* (18), 5279, doi: 10.1021/la9805591.

[50] M. Pawlicki, H. A. Collins, R. G. Denning, and H. L. Anderson, "Two-Photon Absorption and the Design of Two-Photon Dyes," *Angewandte Chemie International Edition* **2009**, *48* (18), 3244, doi: 10.1002/anie.200805257.

[51] V. Y. Merritt and H. J. Hovel, "Organic solar cells of hydroxy squarylium," *Applied Physics Letters* **1976**, *29* (7), 414, doi: 10.1063/1.89101.

[52] F. Silvestri, M. D. Irwin, L. Beverina, A. Facchetti, G. A. Pagani, and T. J. Marks, "Efficient Squaraine-Based Solution Processable Bulk-Heterojunction Solar Cells," *Journal of the American Chemical Society* **2008**, *130* (52), 17640, doi: 10.1021/ja8067879.

[53] S. Wang, L. Hall, V. V. Diev, R. Haiges, G. Wei, X. Xiao, P. I. Djurovich, S. R. Forrest, and M. E. Thompson, "N,N-Diarylanilinosquaraines and Their Application to Organic Photovoltaics," *Chemistry of Materials* **2011**, *23* (21), 4789, doi: 10.1021/cm2020803.

[54] G. Wei, S. Wang, K. Sun, M. E. Thompson, and S. R. Forrest, "Solvent-Annealed Crystalline Squaraine: PC70BM (1:6) Solar Cells," *Advanced Energy Materials* **2011**, *1* (2), 184, doi: 10.1002/aenm.201100045.

[55] J. He, Y. J. Jo, X. Sun, W. Qiao, J. Ok, T.-i. Kim, and Z. Li, "Squaraine Dyes for Photovoltaic and Biomedical Applications," *Advanced Functional Materials* **2021**, *31* (12), doi: 10.1002/adfm.202008201.

[56] B. Stender, S. F. Völker, C. Lambert, and J. Pflaum, "Optoelectronic Processes in Squaraine Dye-Doped OLEDs for Emission in the Near-Infrared," *Advanced Materials* **2013**, *25* (21), 2943, doi: 10.1002/adma.201204938.

[57] W. Wang, A. Fu, J. You, G. Gao, J. Lan, and L. Chen, "Squaraine-based colorimetric and fluorescent sensors for Cu2+-specific detection and fluorescence imaging in living cells," *Tetrahedron* **2010**, *66* (21), 3695, doi: 10.1016/j.tet.2010.03.070.

[58] Y. Xu, M. J. Panzner, X. Li, W. J. Youngs, and Y. Pang, "Host–guest assembly of squaraine dye in cucurbit[8]uril: its implication in fluorescent probe for mercury ions," *Chemical Communications* **2010**, *46* (23), 4073, doi: 10.1039/c002219p.

[59] Y. Xu, B. Li, W. Li, J. Zhao, S. Sun, and Y. Pang, ""ICT-not-quenching" near infrared ratiometric fluorescent detection of picric acid in aqueous media," *Chemical Communications* **2013**, *49* (42), 4764, doi: 10.1039/c3cc41994k.

[60] J. Karpenko, A. S. Klymchenko, S. Gioria, R. Kreder, I. Shulov, P. Villa, Y. Mély, M. Hibert, and D. Bonnet, "Squaraine as a bright, stable and environment-sensitive far-red label for receptor-specific cellular imaging," *Chemical Communications* **2015**, *51* (14), 2960, doi: 10.1039/C4CC09113B.

[61] R. R. Avirah, D. T. Jayaram, N. Adarsh, and D. Ramaiah, "Squaraine dyes in PDT: from basic design to in vivo demonstration," *Org. Biomol. Chem.* **2012**, *10* (5), 911, doi: 10.1039/C1OB06588B.

[62] M. Soumya, K. Shafeekh, S. Das, and A. Abraham, "Symmetrical diiodinated squaraine as an efficient photosensitizer for PDT applications: Evidence from photodynamic and toxicological aspects," *Chemico-Biological Interactions* **2014**, *222* 44, doi: 10.1016/j.cbi.2014.08.006.

[63] F.-P. Gao, Y.-X. Lin, L.-L. Li, Y. Liu, U. Mayerhöffer, P. Spenst, J.-G. Su, J.-Y. Li, F. Würthner, and H. Wang, "Supramolecular adducts of squaraine and protein for noninvasive tumor imaging and photothermal therapy invivo," *Biomaterials* **2014**, *35* (3), 1004, doi: 10.1016/j.biomaterials.2013.10.039.

[64] P. Sun, Q. Wu, X. Sun, H. Miao, W. Deng, W. Zhang, Q. Fan, and W. Huang, "J-Aggregate squaraine nanoparticles with bright NIR-II fluorescence for imaging guided photothermal therapy," *Chemical Communications* **2018**, *54* (95), 13395, doi: 10.1039/C8CC08096H.

[65] C. Qin, W.-Y. Wong, and L. Han, "Squaraine Dyes for Dye-Sensitized Solar Cells: Recent Advances and Future Challenges," *Chemistry – An Asian Journal* **2013**, *8* (8), 1706, doi: 10.1002/asia.201300185.

[66] J.-Q. Jiang, C.-L. Sun, Z.-F. Shi, and H.-L. Zhang, "Squaraines as light-capturing materials in photovoltaic cells," *RSC Adv.* **2014**, *4* (62), 32987, doi: 10.1039/C4RA03972F.

[67] F. Balzer, H. Kollmann, M. Schulz, G. Schnakenburg, A. Lützen, M. Schmidtmann, C. Lienau, M. Silies, and M. Schiek, "Spotlight on Excitonic Coupling in Polymorphic and Textured Anilino Squaraine Thin Films," *Crystal Growth and Design* **2017**, *17* (12), 6455, doi: 10.1021/acs.cgd.7b01131.

[68] A. Herz, "Aggregation of sensitizing dyes in solution and their adsorption onto silver halides," *Advances in Colloid and Interface Science* **1977**, *8* (4), 237, doi: 10.1016/0001-8686(77)80011-0.

[69] F. Würthner, T. E. Kaiser, and C. R. Saha-Möller, "J-Aggregates: From Serendipitous Discovery to Supramolecular Engineering of Functional Dye Materials," *Angewandte Chemie International Edition* **2011**, *50* (15), 3376, doi: 10.1002/anie.201002307.

[70] M. Kasha, "Energy Transfer Mechanisms and the Molecular Exciton Model for Molecular Aggregates," *Radiation Research* **1963**, *20* (1), 55, doi: 10.2307/3571331.

[71] D. Bialas, "Exciton Coupling in Homo- and Heterostacks of Merocyanine and Perylene Bisimide Dyes," PhD thesis: Julius-Maximilians-Universität Würzburg, **2017**.

[72] E. E. Jelley, "Spectral Absorption and Fluorescence of Dyes in the Molecular State," *Nature* **1936**, *138* (3502), 1009, doi: 10.1038/1381009a0.

[73] E. E. Jelley, "Molecular, Nematic and Crystal States of I: I-Diethyl–Cyanine Chloride," *Nature* **1937**, *139* (3519), 631, doi: 10.1038/139631b0.

[74] G. Scheibe, "Über die Veränderlichkeit der Absorptionsspektren in Lösungen und die Nebenvalenzen als ihre Ursache," *Angewandte Chemie* **1937**, *50* (11), 212, doi: 10.1002/ange.19370501103.

[75] G. Scheibe, L. Kandler, and H. Ecker, "Polymerisation und polymere Adsorption als Ursache neuartiger Absorptionsbanden von organischen Farbstoffen," *Die Naturwissenschaften* **1937**, *25* (5), 75, doi: 10.1007/BF01493278.

[76] R. Bernhardt, M. Manrho, J. Zablocki, L. Rieland, A. Lützen, M. Schiek, K. Meerholz, J. Zhu, T. L. C. Jansen, J. Knoester, and P. H. M. van Loosdrecht, "Structural Disorder as the Origin of Optical Properties and Spectral Dynamics in Squaraine Nano-Aggregates," *Journal of the American Chemical Society* **2022**, *144* (42), 19372, doi: 10.1021/jacs.2c07064.

[77] A. S. Davydov, "The Theory of Molecular Excitons," *Soviet Physics Uspekhi* **1964**, *7* (2), 145, doi: 10.1070/PU1964v007n02ABEH003659.

[78] M. Kasha, H. R. Rawls, and M. A. El-Bayoumi, "The exciton model in molecular spectroscopy," *Pure and Applied Chemistry* **1965**, *11* (3-4), 371, doi: 10.1351/pac196511030371.

[79] S. Ma, S. Du, G. Pan, S. Dai, B. Xu, and W. Tian, "Organic molecular aggregates: From aggregation structure to emission property," *Aggregate* **2021**, *2* (4), doi: 10.1002/agt2.96.

[80] S. C. J. Meskers, "The Exciton Model for Molecular Materials: Past, Present and Future?" *ChemPhysChem* **2023**, *24* (24), doi: 10.1002/cphc.202300666.

[81] J. Frenkel, "On the Transformation of light into Heat in Solids. I," *Physical Review* **1931**, *37* (1), 17, doi: 10.1103/PhysRev.37.17.

[82] M. Born and R. Oppenheimer, "Zur Quantentheorie der Molekeln," *Annalen der Physik* **1927**, *389* (20), 457, doi: 10.1002/andp.19273892002.

[83] F. Bertocchi, C. Sissa, and A. Painelli, "Circular dichroism of molecular aggregates: A tutorial," *Chirality* **2023**, *35* (10), 681, doi: 10.1002/chir.23565.

[84] F. C. Spano, "The Spectral Signatures of Frenkel Polarons in H- and J-Aggregates," *Accounts of Chemical Research* **2010**, *43* (3), 429, doi: 10.1021/ar900233v.

[85] J. Zablocki, M. Schulz, G. Schnakenburg, L. Beverina, P. Warzanowski, A. Revelli, M. Grüninger, F. Balzer, K. Meerholz, A. Lützen, and M. Schiek, "Structure and Dielectric Properties of Anisotropic n-Alkyl Anilino Squaraine Thin Films," *The Journal of Physical Chemistry C* **2020**, *124* (41), 22721, doi: 10.1021/acs.jpcc.0c07498.

[86] N. J. Hestand and F. C. Spano, "Expanded Theory of H- and J-Molecular Aggregates: The Effects of Vibronic Coupling and Intermolecular Charge Transfer," *Chemical Reviews* **2018**, *118* (15), 7069, doi: 10.1021/acs.chemrev.7b00581.

[87] C. Zheng, C. Zhong, C. J. Collison, and F. C. Spano, "Non-Kasha Behavior in Quadrupolar Dye Aggregates: The Red-Shifted H-Aggregate," *The Journal of Physical Chemistry C* **2019**, *123* (5), 3203, doi: 10.1021/acs.jpcc.8b11416.

[88] C. Zheng, M. F. Mark, T. Wiegand, S. A. Diaz, J. Cody, F. C. Spano, D. W. McCamant, and C. J. Collison, "Measurement and Theoretical Interpretation of Exciton Diffusion as a Function of Intermolecular Separation for Squaraines Targeted for Bulk Heterojunction Solar Cells," *The Journal of Physical Chemistry C* **2020**, *124* (7), 4032, doi: 10.1021/acs.jpcc.9b11816.

[89] C. Zheng, D. Bleier, I. Jalan, S. Pristash, A. R. Penmetcha, N. J. Hestand, F. C. Spano, M. S. Pierce, J. A. Cody, and C. J. Collison, "Phase separation, crystallinity and monomer-aggregate population control in solution processed small molecule solar cells," *Solar Energy Materials and Solar Cells* **2016**, *157* 366, doi: 10.1016/j.solmat.2016.05.060.

[90] G. Albano, G. Pescitelli, and L. D. Bari, "Chiroptical Properties in Thin Films of π-Conjugated Systems," *Chemical Reviews* **2020**, *120* (18), 10145, doi: 10.1021/acs.chemrev.0c00195.

[91] J. R. Brandt, F. Salerno, and M. J. Fuchter, "The added value of small-molecule chirality in technological applications," *Nature Reviews Chemistry* **2017**, *1* (6), 0045, doi: 10.1038/s41570-017-0045.

[92] S.-H. Ham, M. J. Han, and M. Kim, "Chiral Materials for Optics and Electronics: Ready to Rise?" *Micromachines* **2024**, *15* (4), 528, doi: 10.3390/mi15040528.

[93] M. Hesse, H. Meier, and B. Zeeh, *Spektroskopische Methoden in der organischen Chemie*, ed. by M. Hesse, H. Meier, and B. Zeeh, Georg Thieme Verlag, **2005**, https://doi.org/10.1055/b-002-46985.

[94] N. Berova, L. D. Bari, and G. Pescitelli, "Application of electronic circular dichroism in configurational and conformational analysis of organic compounds," *Chemical Society Reviews* **2007**, *36* (6), 914, doi: 10.1039/b515476f.

[95] S. Funke, M. Duwe, F. Balzer, P. H. Thiesen, K. Hingerl, and M. Schiek, "Determining the Dielectric Tensor of Microtextured Organic Thin Films by Imaging Mueller Matrix Ellipsometry," *The Journal of Physical Chemistry Letters* **2021**, *12* (12), 3053, doi: 10.1021/acs.jpclett.1c00317.

[96] O. Arteaga and R. Ossikovski, "Complete Mueller matrix from a partial polarimetry experiment: the 12-element case," *Journal of the Optical Society of America A* **2019**, *36* (3), 416, doi: 10.1364/JOSAA.36.000416.

[97] N. S. S. Nizar, M. Sujith, K. Swathi, C. Sissa, A. Painelli, and K. G. Thomas, "Emergent chiroptical properties in supramolecular and plasmonic assemblies," *Chemical Society Reviews* **2021**, *50* (20), 11208, doi: 10.1039/D0CS01583K.

[98] M. Schulz, F. Balzer, D. Scheunemann, O. Arteaga, A. Lützen, S. C. J. Meskers, and M. Schiek, "Chiral Excitonic Organic Photodiodes for Direct Detection of Circular Polarized Light," *Advanced Functional Materials* **2019**, *29* (16), 1900684, doi: 10.1002/adfm.201900684.

[99] M. Tang and X. Yang, "Catalytic Enantioselective Synthesis of Inherently Chiral Molecules: Recent Advances," *European Journal of Organic Chemistry* **2023**, *26* (42), doi: 10.1002/ejoc.202300738.

[100] R. S. Stoll, N. Severin, J. P. Rabe, and S. Hecht, "Synthesis of a Novel Chiral Squaraine Dye and Its Unique Aggregation Behavior in Solution and in Self-Assembled Monolayers," *Advanced Materials* **2006**, *18* (10), 1271, doi: 10.1002/adma.200502094.

[101] E. Yashima, N. Ousaka, D. Taura, K. Shimomura, T. Ikai, and K. Maeda, "Supramolecular Helical Systems: Helical Assemblies of Small Molecules, Foldamers, and Polymers with Chiral Amplification and Their Functions," *Chemical Reviews* **2016**, *116* (22), 13752, doi: 10.1021/acs.chemrev.6b00354.

[102] K. Jyothish, M. Hariharan, and D. Ramaiah, "Chiral supramolecular assemblies of a squaraine dye in solution and thin films: concentration-, temperature-, and solvent-induced chirality inversion," *Chemistry - A European Journal* **2007**, *13* (20), 5944, doi: 10.1002/chem.200700130.

[103] E. Freytag, L. Kreimendahl, M. Holzapfel, J. Petersen, H. Lackinger, M. Stolte, F. Würthner, R. Mitric, and C. Lambert, "Chiroptical Properties of Planar Benzobisthiazole-Bridged Squaraine Dimers," *The Journal of Organic Chemistry* **2023**, *88* (15), 10777, doi: 10.1021/acs.joc.3c00821.

[104] W. W. Parson, *Modern Optical Spectroscopy*, Springer Berlin Heidelberg, **2007**, https://doi.org/10.1007/978-3-540-37542-5.

[105] K. Swathi, C. Sissa, A. Painelli, and K. G. Thomas, "Supramolecular chirality: a caveat in assigning the handedness of chiral aggregates," *Chemical Communications* **2020**, *56* (59), 8281, doi: 10.1039/D0CC01922D.

[106] N. Harada and K. Nakanishi, "Exciton chirality method and its application to configurational and conformational studies of natural products," *Accounts of Chemical Research* **1972**, *5* (8), 257, doi: 10.1021/ar50056a001.

[107] H. S. Ryu, S. Y. Park, T. H. Lee, J. Y. Kim, and H. Y. Woo, "Recent progress in indoor organic photovoltaics," *Nanoscale* **2020**, *12* (10), 5792, doi: 10.1039/D0NR00816H.

[108] Y. Cui, L. Hong, and J. Hou, "Organic Photovoltaic Cells for Indoor Applications: Opportunities and Challenges," *ACS Applied Materials & Interfaces* **2020**, *12* (35), 38815, doi: 10.1021/acsami.0c10444.

[109] J. Ahn, S. H. Lee, I. Song, P. Chidchob, Y. Kwon, and J. H. Oh, "Chiral organic semiconducting materials for next-generation optoelectronic sensors," *Device* **2023**, *1* (5), 100176, doi: 10.1016/j.device.2023.100176.

[110] W. Brütting, ed., *Physics of Organic Semiconductors*, Wiley, **2005**, https://doi.org/10.1002/3527606637.

[111] K. A. Mazzio and C. K. Luscombe, "The future of organic photovoltaics," *Chemical Society Reviews* **2015**, *44* (1), 78, doi: 10.1039/C4CS00227J.

[112] H. Hoppe and N. S. Sariciftci, "Organic solar cells: An overview," *Journal of Materials Research* **2004**, *19* (7), 1924, doi: 10.1557/JMR.2004.0252.

[113] S. M. Menke, N. A. Ran, G. C. Bazan, and R. H. Friend, "Understanding Energy Loss in Organic Solar Cells: Toward a New Efficiency Regime," *Joule* **2018**, *2* (1), 25, doi: 10.1016/j.joule.2017.09.020.

[114] G. de la Torre, G. Bottari, and T. Torres, "Phthalocyanines and Subphthalocyanines: Perfect Partners for Fullerenes and Carbon Nanotubes in Molecular Photovoltaics," *Advanced Energy Materials* **2017**, *7* (10), 1601700, doi: 10.1002/aenm.201601700.

[115] A. Pivrikas, N. S. Sariciftci, G. Juška, and R. Österbacka, "A review of charge transport and recombination in polymer/fullerene organic solar cells," *Progress in Photovoltaics: Research and Applications* **2007**, *15* (8), 677, doi: 10.1002/pip.791.

[116] A. J. Pacuła-Miszewska, M. Obieziurska-Fabisiak, and J. Ścianowski, "Monoterpenes as Chiral Building Blocks," *Chiral Building Blocks in Asymmetric Synthesis*, Wiley, **2022** 235, doi: 10.1002/9783527834204.ch8.

[117] M. Hirama, T. Noda, and S. Ito, "Convenient synthesis of (S)-citronellol of high optical purity," *The Journal of Organic Chemistry* **1985**, *50* (1), 127, doi: 10.1021/jo00201a027.

[118] T. Yamamoto, A. Shimada, T. Ohmoto, H. Matsuda, M. Ogura, and T. Kanisawa, "Olfactory study on optically active citronellyl derivatives," *Flavour and Fragrance Journal* **2004**, *19* (2), 121, doi: 10.1002/ffj.1280.

[119] J. Wade, J. N. Hilfiker, J. R. Brandt, L. Liirò-Peluso, L. Wan, X. Shi, F. Salerno, S. T. J. Ryan, S. Schöche, O. Arteaga, T. Jávorfi, G. Siligardi, C. Wang, D. B. Amabilino, P. H. Beton, A. J. Campbell, and M. J. Fuchter, "Natural optical activity as the origin of the large chiroptical properties in pi-conjugated polymer thin films," *Nature Communications* **2020**, *11* (1), 6137, doi: 10.1038/s41467-020-19951-y.

[120] S. F. Völker, T. Dellermann, H. Ceymann, M. Holzapfel, and C. Lambert, "Synthesis, electrochemical, and optical properties of low band gap homo- and copolymers based on squaraine dyes," *Journal of Polymer Science Part A: Polymer Chemistry* **2014**, *52* (7), 890, doi: 10.1002/pola.27073.

[121] S. F. Völker and C. Lambert, "Exciton Coupling Effects in Polymeric cis -Indolenine Squaraine Dyes," *Chemistry of Materials* **2012**, *24* (13), 2541, doi: 10.1021/cm301109u.

[122] C. Zhong, D. Bialas, C. J. Collison, and F. C. Spano, "Davydov Splitting in Squaraine Dimers," *The Journal of Physical Chemistry C* **2019**, *123* (30), 18734, doi: 10.1021/acs.jpcc.9b05297.

[123] J. Selby, M. Holzapfel, B. K. Lombe, D. Schmidt, A.-M. Krause, F. Würthner, G. Bringmann, and C. Lambert, "Chiroptical Properties of Indolenine Squaraines with a Stereogenic Center at Close Proximity," *The Journal of Organic Chemistry* **2020**, *85* (19), 12227, doi: 10.1021/acs.joc.0c01422.

[124] G. Pescitelli, L. D. Bari, and N. Berova, "Conformational aspects in the studies of organic compounds by electronic circular dichroism," *Chemical Society Reviews* **2011**, *40* (9), 4603, doi: 10.1039/c1cs15036g.

[125] M. Liu, L. Zhang, and T. Wang, "Supramolecular Chirality in Self-Assembled Systems," *Chemical Reviews* **2015**, *115* (15), 7304, doi: 10.1021/cr500671p.

[126] A. Mendoza-Galván, E. Muñoz-Pineda, S. J. L. Ribeiro, M. V. Santos, K. Järrendahl, and H. Arwin, "Mueller matrix spectroscopic ellipsometry study of chiral nanocrystalline cellulose films," *Journal of Optics* **2018**, *20* (2), 024001, doi: 10.1088/2040-8986/aa9e7d.

[127] G. Lakhwani, G. Koeckelberghs, S. Meskers, and R. Janssen, "The chiroptical properties of chiral substituted poly[3-((3S)-3,7-dimethyloctyl)thiophene] as a function of film thickness," *Chemical Physics Letters* **2007**, *437* (4-6), 193, doi: 10.1016/j.cplett.2007.02.031.

[128] R. Abbel, A. P. H. J. Schenning, and E. Meijer, "Fluorene-based materials and their supramolecular properties," *Journal of Polymer Science Part A: Polymer Chemistry* **2009**, *47* (17), 4215, doi: 10.1002/pola.23499.

[129] G. Lakhwani and S. C. J. Meskers, "Insights from Chiral Polyfluorene on the Unification of Molecular Exciton and Cholesteric Liquid Crystal Theories for Chiroptical Phenomena," *The Journal of Physical Chemistry A* **2012**, *116* (4), 1121, doi: 10.1021/jp209893h.

[130] C. Kulkarni, D. D. Nuzzo, E. Meijer, and S. C. Meskers, "Pitch and Handedness of the Cholesteric Order in Films of a Chiral Alternating Fluorene Copolymer," *The Journal of Physical Chemistry B* **2017**, *121* (51), 11520, doi: 10.1021/acs.jpcb.7b10236.

[131] P. Cudazzo, M. Gatti, A. Rubio, and F. Sottile, "Frenkel versus charge-transfer exciton dispersion in molecular crystals," *Physical Review B* **2013**, *88* (19), 195152, doi: 10.1103/PhysRevB.88.195152.

[132] S. Canola, G. Bagnara, Y. Dai, G. Ricci, A. Calzolari, and F. Negri, "Addressing the Frenkel and charge transfer character of exciton states with a model Hamiltonian based on dimer calculations: Application to large aggregates of perylene bisimide," *The Journal of Chemical Physics* **2021**, *154* (12), doi: 10.1063/5.0045913.

[133] T. G. Nguyen, "Synthese und Aggregation von Citronellyl funktionalisierten Anilinosquarainen," Bachelor's Thesis: Rheinische Friedrich-Wilhelms-Universität Bonn, **2022**.

[134] A. Köhler and H. Bässler, *Electronic Processes in Organic Semiconductors*, Wiley, **2015**, https://doi.org/10.1002/9783527685172.

[135] C. Zheng, I. Jalan, P. Cost, K. Oliver, A. Gupta, S. Misture, J. A. Cody, and C. J. Collison, "Impact of Alkyl Chain Length on Small Molecule Crystallization and Nanomorphology in Squaraine-Based Solution Processed Solar Cells," *The Journal of Physical Chemistry C* **2017**, *121* (14), 7750, doi: 10.1021/acs.jpcc.7b01339.

[136] G. Pescitelli, L. D. Bari, and N. Berova, "Application of electronic circular dichroism in the study of supramolecular systems," *Chem. Soc. Rev.* **2014**, *43* (15), 5211, doi: 10.1039/C4CS00104D.

[137] F. C. Spano, "Analysis of the UV/Vis and CD Spectral Line Shapes of Carotenoid Assemblies: Spectral Signatures of Chiral H-Aggregates," *Journal of the American Chemical Society* **2009**, *131* (12), 4267, doi: 10.1021/ja806853v.

[138] M. A. Smith, R. J. D. Kang, R. Kumar, B. Roy, and M. J. Gaunt, "Modular synthesis of α-branched secondary alkylamines via visible-light-mediated carbonyl alkylative amination," *Chemical Science* **2024**, *15* (36), 14888, doi: 10.1039/D4SC03916E.

[139] D. Yang, T. Sano, H. Sasabe, and J. Kido, "A novel pi-D1-A-D2 type low bandgap squaraine dye for efficient small molecular organic solar cells," *Dyes and Pigments* **2019**, *163* 564, doi: 10.1016/j.dyepig.2018.12.044.

[140] S. Wang, E. I. Mayo, M. D. Perez, L. Griffe, G. Wei, P. I. Djurovich, S. R. Forrest, and M. E. Thompson, "High efficiency organic photovoltaic cells based on a vapor deposited squaraine donor," *Applied Physics Letters* **2009**, *94* (23), doi: 10.1063/1.3152011.

[141] M. F. Schumacher, "Proline- and Indolenine-derived Chiral Squaraines- Synthesis and Characteristics," Master's Thesis: Rheinischen Friedrich-Wilhelms-Universität Bonn, **2021**.

[142] F. Balzer, N. J. Hestand, J. Zablocki, G. Schnakenburg, A. Lützen, and M. Schiek, "Spotlight on Charge-Transfer Excitons in Crystalline Textured n-Alkyl Anilino Squaraine Thin Films," *The Journal of Physical Chemistry C* **2022**, *126* (32), 13802, doi: 10.1021/acs.jpcc.2c03665.

[143] J. Zablocki, "Synthese, Eigenschaften und Anwendung symmetrischer Anilinosquaraine als Komponente in Photodioden," PhD thesis: Rheinische Friedrich-Wilhelms-Universität Bonn, **2022**.

[144] S. K. Saikin, A. Eisfeld, S. Valleau, and A. Aspuru-Guzik, "Photonics meets excitonics: natural and artificial molecular aggregates," *Nanophotonics* **2013**, *2* (1), 21, doi: 10.1515/nanoph-2012-0025.

[145] A. M. Valencia, D. Bischof, S. Anhäuser, M. Zeplichal, A. Terfort, G. Witte, and C. Cocchi, "Excitons in organic materials: revisiting old concepts with new insights," *Electronic Structure* **2023**, *5* (3), 033003, doi: 10.1088/2516-1075/acf2d4.

[146] R. K. Hylton, G. J. Tizzard, T. L. Threlfall, A. L. Ellis, S. J. Coles, C. C. Seaton, E. Schulze, H. Lorenz, A. Seidel-Morgenstern, M. Stein, and S. L. Price, "Are the Crystal Structures of Enantiopure and Racemic Mandelic Acids Determined by Kinetics or Thermodynamics?" *Journal of the American Chemical Society* **2015**, *137* (34), 11095, doi: 10.1021/jacs.5b05938.

[147] L. D. Bakalis and J. Knoester, "Pump−Probe Spectroscopy and the Exciton Delocalization Length in Molecular Aggregates," *The Journal of Physical Chemistry B* **1999**, *103* (31), 6620, doi: 10.1021/jp990354g.

[148] T. J. Wiegand, J. S. Sandoval, J. A. Cody, D. W. McCamant, and C. J. Collison, "Directional Exciton Diffusion, Measured by Subpicosecond Transient Absorption as an Explanation for Squaraine Solar Cell Performance," *The Journal of Physical Chemistry C* **2024**, *128* (11), 4616, doi: 10.1021/acs.jpcc.3c06361.

[149] C.-A. Shen, D. Bialas, M. Hecht, V. Stepanenko, K. Sugiyasu, and F. Würthner, "Polymorphism in Squaraine Dye Aggregates by Self-Assembly Pathway Differentiation: Panchromatic Tubular Dye Nanorods versus J-Aggregate Nanosheets," *Angewandte Chemie* **2021**, *133* (21), 12056, doi: 10.1002/ange.202102183.

[150] F. Azarnousha, "Beiträge zur Synthese von Indolin und Tetrahydroisoquinolin funktionalisierten Squarainen," Bachelor's Thesis: Rheinischen Friedrich-Wilhelms-Universität Bonn, **2022**.

[151] Y. Tao, X. Liang, J. Zhang, I. M. Lei, and J. Liu, "Polyurethane vitrimers: Chemistry, properties and applications," *Journal of Polymer Science* **2023**, *61* (19), 2233, doi: 10.1002/pol.20220625.

[152] F. Brotzel, "Nucleophilicities of Amines, Amino Acids and Pyridines," PhD thesis: Ludwig-Maximilians-Universität München, **2008**.

[153] F. Azarnousha, "Synthesis and Investigation of new Chiral Anilinosquaraines," Master's Thesis: Rheinischen Friedrich-Wilhelms-Universität Bonn, **2024**.

[154] N. S. Begum, D. E. Vasundhara, C. R. Girija, G. D. Kolavi, V. S. Hegde, and I. M. Khazi, "Synthesis, spectroscopic and crystal structure analysis of a compound with pharmocophoric substituent: 2-cyclohexyl-6-(2-oxo-2H-chromen-3-yl)- imidazo[2,1-b][1,3,4]thiadiazole-5-carbaldehyde," *Journal of Chemical Crystallography* **2007**, *37* (3), 193, doi: 10.1007/s10870-006-9159-4.

[155] K. Szwaczko, D. M. Kamiński, and A. E. Koziol, "Coumarin Derivatives: The Influence of Cycloalkyl Groups at the C-3 Position on Intermolecular Interactions - Synthesis, Structure and Spectroscopy," *Crystals* **2024**, *14* (2), 196, doi: 10.3390/cryst14020196.

[156] F. Sun, X. Wang, M. Wan, Z. Liu, Y. Luo, J. Ren, X. Zheng, T. Rath, C. Xiao, T. Hu, G. Trimmel, and R. Yang, "High Miscibility-Induced Reduction of Trap Density in All-Polymer Solar Cells Using Hybrid Cyclohexyl-Hexyl Side Chains," *Advanced Functional Materials* **2023**, *33* (40), doi: 10.1002/adfm.202306791.

[157] I. Burkhardt and J. S. Dickschat, "Synthesis and Absolute Configuration of Natural 2-Pyrones," *European Journal of Organic Chemistry* **2018**, *2018* (24), 3144, doi: 10.1002/ejoc.201800621.

[158] A. Viterisi, N. F. Montcada, C. V. Kumar, F. Gispert-Guirado, E. Martin, E. Escudero, and E. Palomares, "Unambiguous determination of molecular packing in crystalline donor domains of small molecule solution processed solar cell devices using routine X-ray diffraction techniques," *Journal of Materials Chemistry A* **2014**, *2* (10), 3536, doi: 10.1039/c3ta13116e.

[159] J. Gilot, R. Abbel, G. Lakhwani, E. W. Meijer, A. P. H. J. Schenning, and S. C. J. Meskers, "Polymer Photovoltaic Cells Sensitive to the Circular Polarization of Light," *Advanced Materials* **2010**, *22* (20), E131, doi: 10.1002/adma.200903995.

[160] K. Ray, S. P. Ananthavel, D. H. Waldeck, and R. Naaman, "Asymmetric Scattering of Polarized Electrons by Organized Organic Films of Chiral Molecules," *Science* **1999**, *283* (5403), 814, doi: 10.1126/SCIENCE.283.5403.814.

[161] R. Naaman and D. H. Waldeck, "Chiral-induced spin selectivity effect," *Journal of Physical Chemistry Letters* **2012**, *3* (16), 2178, doi: 10.1021/JZ300793Y/ASSET/IMAGES/LARGE/JZ-2012-00793Y_0007.JPEG.

[162] P. J. Hore, K. L. Ivanov, and M. R. Wasielewski, "Spin chemistry," *Journal of Chemical Physics* **2020**, *152* (12), 120401, doi: 10.1063/5.0006547/953744.

[163] R. Naaman and D. H. Waldeck, "Spintronics and chirality: Spin selectivity in electron transport through chiral molecules," *Annual Review of Physical Chemistry* **2015**, *66* (1), 263, doi: 10.1146/ANNUREV-PHYSCHEM-040214-121554/CITE/REFWORKS.

[164] B. P. Bloom, Y. Paltiel, R. Naaman, and D. H. Waldeck, "Chiral Induced Spin Selectivity," *Chemical Reviews* **2024**, *124* (4), 1950, doi: 10.1021/acs.chemrev.3c00661.

[165] R. Naaman, Y. Paltiel, and D. H. Waldeck, "Chiral Molecules and the Spin Selectivity Effect," *The Journal of Physical Chemistry Letters* **2020**, *11* (9), 3660, doi: 10.1021/acs.jpclett.0c00474.

[166] F. Furlan, J. M. Moreno-Naranjo, N. Gasparini, S. Feldmann, J. Wade, and M. J. Fuchter, "Chiral materials and mechanisms for circularly polarized light-emitting diodes," *Nature Photonics 2024* **2024** 1, doi: 10.1038/s41566-024-01408-z.

[167] Y.-H. Kim, Y. Zhai, H. Lu, X. Pan, C. Xiao, E. A. Gaulding, S. P. Harvey, J. J. Berry, Z. V. Vardeny, J. M. Luther, and M. C. Beard, "Chiral-induced spin selectivity enables a room-temperature spin light-emitting diode," *Science* **2021**, *371* (6534), 1129, doi: 10.1126/science.abf5291.

[168] H. Lu, J. Wang, C. Xiao, X. Pan, X. Chen, R. Brunecky, J. J. Berry, K. Zhu, M. C. Beard, and Z. V. Vardeny, "Spin-dependent charge transport through 2D chiral hybrid lead-iodide perovskites.," *Science advances* **2019**, *5* (12), eaay0571, doi: 10.1126/sciadv.aay0571.

[169] I. Song, J. Ahn, H. Ahn, S. H. Lee, J. Mei, N. A. Kotov, and J. H. Oh, "Helical polymers for dissymmetric circularly polarized light imaging.," *Nature* **2023**, *617* (7959), 92, doi: 10.1038/s41586-023-05877-0.

[170] L. Wan, X. Shi, J. Wade, A. J. Campbell, and M. J. Fuchter, "Strongly Circularly Polarized Crystalline and β-Phase Emission from Poly(9,9-dioctylfluorene)-Based Deep-Blue Light-Emitting Diodes," *Advanced Optical Materials* **2021**, *9* (19), 2100066, doi: 10.1002/adom.202100066.

[171] L. Wan, J. Wade, F. Salerno, O. Arteaga, B. Laidlaw, X. Wang, T. Penfold, M. J. Fuchter, and A. J. Campbell, "Inverting the Handedness of Circularly Polarized Luminescence from Light-Emitting Polymers Using Film Thickness," *ACS Nano* **2019**, *13* (7), 8099, doi: 10.1021/acsnano.9b02940.

[172] D.-M. Lee, J.-W. Song, Y.-J. Lee, C.-J. Yu, and J.-H. Kim, "Control of Circularly Polarized Electroluminescence in Induced Twist Structure of Conjugate Polymer," *Advanced Materials* **2017**, *29* (29), 1700907, doi: 10.1002/adma.201700907.

[173] G. Koeckelberghs, M. Vangheluwe, C. Samyn, A. Persoons, and T. Verbiest, "Regioregular Poly(3-alkoxythiophene)s: Toward Soluble, Chiral Conjugated Polymers with a Stable Oxidized State," *Macromolecules* **2005**, *38* (13), 5554, doi: 10.1021/ma050731p.

[174] D. Amsallem, A. Bedi, F. Tassinari, and O. Gidron, "Relation between Morphology and Chiroptical Properties in Chiral Conducting Polymer Films: A Case Study in Chiral PEDOT," *Macromolecules* **2020**, *53* (21), 9521, doi: 10.1021/acs.macromol.0c01731.

[175] L. D. Cremer, S. Vandeleene, M. Maesen, T. Verbiest, and G. Koeckelberghs, "Chiroptical Properties of Cyclopentadithiophene-Based Conjugated Polymers," *Macromolecules* **2008**, *41* (3), 591, doi: 10.1021/ma7023304.

[176] F. Evers et al., "Theory of Chirality Induced Spin Selectivity: Progress and Challenges," *Advanced Materials* **2022**, *34* (13), 2106629, doi: 10.1002/adma.202106629.

[177] Y. Sanada, K. Terao, and T. Sato, "Double screw-sense inversions of helical chiral-achiral random copolymers of fluorene derivatives in phase separating solutions," *Polymer Journal* **2011**, *43* (10), 832, doi: 10.1038/pj.2011.75.

[178] W. Zhong, J. Liang, S. Hu, X.-F. Jiang, L. Ying, F. Huang, W. Yang, and Y. Cao, "Effect of Monofluoro Substitution on the Optoelectronic Properties of Benzo[c][1,2,5]thiadiazole Based Organic Semiconductors," *Macromolecules* **2016**, *49* (16), 5806, doi: 10.1021/acs.macromol.6b00185.

[179] D. C. Patel, R. M. Woods, Z. S. Breitbach, A. Berthod, and D. W. Armstrong, "Thermal racemization of biaryl atropisomers," *Tetrahedron: Asymmetry* **2017**, *28* (11), 1557, doi: 10.1016/j.tetasy.2017.09.006.

[180] M. Axelsson, Z. Xia, S. Wang, M. Cheng, and H. Tian, "Role of the Benzothiadiazole Unit in Organic Polymers on Photocatalytic Hydrogen Production," *JACS Au* **2024**, *4* (2), 570, doi: 10.1021/jacsau.3c00681.

[181] M. A. Stevens, C. Silva, D. M. Russell, and R. H. Friend, "Exciton dissociation mechanisms in the polymeric semiconductors poly(9,9-dioctylfluorene) and poly(9,9-dioctylfluorene-co-benzothiadiazole)," *Physical Review B* **2001**, *63* (16), 165213, doi: 10.1103/PhysRevB.63.165213.

[182] M.-L. Mende, "Synthesis of Chiral π-Conjugated Polymers for Optoelectronic Devices," Master's Thesis: Rheinischen Friedrich-Wilhelms-Universität Bonn, **2024**.

[183] G. R. Fulmer, A. J. M. Miller, N. H. Sherden, H. E. Gottlieb, A. Nudelman, B. M. Stoltz, J. E. Bercaw, and K. I. Goldberg, "NMR Chemical Shifts of Trace Impurities: Common Laboratory Solvents, Organics, and Gases in Deuterated Solvents Relevant to the Organometallic Chemist," *Organometallics* **2010**, *29* (9), 2176, doi: 10.1021/om100106e.

[184] S. Sakamuri, D. Liu, L. Eltepu, B. Liu, L. J. Reboton, R. Preston, and C. W. Bradshaw, "Identification of a Tricyclic P III Chiral Auxiliary for Solid-Supported Synthesis of Stereopure Phosphorothioate-Containing Oligonucleotides," *ChemBioChem* **2020**, *21* (9), 1298, doi: 10.1002/cbic.201900631.

[185] X. Hu, Y.-F. Wei, N. Wu, Z. Jiang, C. Liu, and R.-S. Luo, "Indolinol-catalyzed asymmetric Michael reaction of aldehydes to nitroalkenes in brine," *Tetrahedron: Asymmetry* **2016**, *27* (9-10), 420, doi: 10.1016/j.tetasy.2016.03.006.

[186] H. Ohmukai, Y. Sugiyama, A. Hirota, M. Kirihata, and S. Tanimori, "Total synthesis of (S)-(+)-ent-phomapyrones B and surugapyrone B," *Journal of Heterocyclic Chemistry* **2020**, *57* (3), 1090, doi: 10.1002/jhet.3845.

[187] L. Wang, C. Pan, A. Liang, X. Zhou, W. Zhou, T. Wan, and L. Wang, "The effect of the backbone structure on the thermoelectric properties of donor-acceptor conjugated polymers," *Polymer Chemistry* **2017**, *8* (32), 4644, doi: 10.1039/C7PY01005B.

[188] T. Olla, O. A. Ibraikulov, S. Ferry, O. Boyron, S. Méry, B. Heinrich, T. Heiser, P. Lévêque, and N. Leclerc, "Benzothiadiazole Halogenation Impact in Conjugated Polymers, a Comprehensive Study," *Macromolecules* **2019**, *52* (21), 8006, doi: 10.1021/acs.macromol.9b01760.

[189] K. Anagnostou, M. M. Stylianakis, K. Petridis, and E. Kymakis, "Building an Organic Solar Cell: Fundamental Procedures for Device Fabrication," *Energies* **2019**, *12* (11), 2188, doi: 10.3390/en12112188.

APPENDIX A

The Impact of Chiral Citronellyl-Functionalization on Indolenine and Anilino Squaraine Thin Films

F. Balzer,[a] M. F. Schumacher,[b] S. Mattiello,[c] M. Schulz,[b] J. Zablocki,[b] M. Schmidtmann,[d] K. Meerholz,[e] N. Serdar Sariciftci,[f] L. Beverina,[c] A. Lützen,[b] M. Schiek[f,g,h]

Received: July 25, 2021
Published online: November 02, 2021

Reprinted with permission[i] from:
F. Balzer, M. F. Schumacher, S. Mattiello, M. Schulz, J. Zablocki, M. Schmidtmann, K. Meerholz, N. S. Sariciftci, L. Beverina, A. Lützen, and M. Schiek, "The Impact of Chiral Citronellyl-Functionalization on Indolenine and Anilino Squaraine Thin Films," *Israel Journal of Chemistry* **2022**, *62* (7-8), e202100079, doi: 10.1002/ijch.202100079
– Copyright ©The Authors. Israel Journal of Chemistry published by Wiley-VCH GmbH.

Own contributions:

- Preparation of the thin film samples
- Performing and evaluating the ellipsometric/polarimetric measurements
- Writing parts of the manuscript

[a] SDU Centre for Photonics Engineering, Mads Clausen Institute, University of Southern Denmark, Alsion 2, DK-6400 Sønderborg, Denmark
[b] Kekulé-Institute for Organic Chemistry and Biochemistry, University of Bonn, Gerhard-Domagk-Str. 1, D-53121 Bonn, Germany
[c] Department of Materials Chemistry and INSTM, University of Milano-Bicocca, Via R. Cozzi 53, I-20125 Milano, Italy
[d] Department of Chemistry, University of Oldenburg, Carl-von-Ossietzky-Str. 9–11, D-26129 Oldenburg, Germany
[e] Physical Chemistry, University of Cologne, Greinstr. 4–6, D-50939 Cologne, Germany
[f] Linz Institute for Solar Cells, Johannes Kepler University, Altenberger Str. 69, A-4040 Linz, Austria
[g] Center for Surface- and Nanoanalytics and Linz Institute for Solar Cells, Johannes Kepler University, Altenberger Str. 69, A-4040 Linz, Austria
[h] Institute of Physics, University of Oldenburg, Carl-von-Ossietzky-Str. 9–11, D-26129 Oldenburg, Germany
[i] Permission requests to reuse material from this chapter should be directed to Wiley-VCH GmbH.

Research Article

Israel Journal of Chemistry
www.ijc.wiley-vch.de

doi.org/10.1002/ijch.202100079

The Impact of Chiral Citronellyl-Functionalization on Indolenine and Anilino Squaraine Thin Films

Frank Balzer,[a] Marvin F. Schumacher,[b] Sara Mattiello,[c] Matthias Schulz,[b] Jennifer Zablocki,[b] Marc Schmidtmann,[d] Klaus Meerholz,[e] N. Serdar Sariciftci,[f] Luca Beverina,[c] Arne Lützen,[b] and Manuela Schiek*[f, g, h]

Dedicated to Prof. N.S. Sariciftci on the occasion of his 60th birthday.

Abstract: The impact on chiral aggregation in solution processed and thermally annealed thin films of two indolenine and one anilino squaraines with chiral (*S*)-citronellyl functionalization at the nitrogen of the squaraine backbone is investigated. A pseudo polymorphic crystal structure is obtained for one of the indolenine squaraines, but thin films of both compounds are basically non-aggregated and truly isotropic as evidenced by spectroscopic ellipsometry. The anilino squaraine coalesces and readily aggregates to circular dichroic but discontinuous thin films. The extent of circular dichroism correlates with the morphology of the samples, which is quantified by Mueller matrix polarimetry in combination with atomic force microscopy. The shape of the CD spectra reinforces the hybrid Frenkel and charge-transfer excitonic nature of the characteristic double hump signatures within unpolarized absorbance spectra of previously investigated non-chiral anilino squaraines with linear alkyl chain functionalization. Such excitonic CD offers an additional design parameter for next-generation opto-electronic devices.

Keywords: squaraine · circular dichroism · micro-morphology · charge-transfer excitons

1. Introduction

Squaraine dyes are attractive due to their intense interactions with visible to near-infrared light combined with environmental robustness and friendliness as well as convenient chemical accessibility.[1–4] This results in a wide-spread application potential covering photovoltaics, photocatalysis, biomedicine and sensing devices.[5–11] Squaraines (SQs) can adopt different structural motifs such as anilino or indolenine type SQs, Figure 1. Both types are donor-acceptor-donor small molecular compounds with zwitterionic resonant structures causing pronounced *intra*molecular charge-transfer states. These in turn give rise to strong *inter*molecular excitonic interactions[12] that can be of Coulombic nature (Frenkel excitons)[13] or involve *inter*molecular charge-transfer (ICT) excitons.[14] This is basically depending on molecular packing geometry steered by terminal *N* or acceptor-core substitution in case of indolenine SQs.[15]

Acceptor-core substitution changes the molecular symmetry and installs a permanent dipole moment to the otherwise

[a] *F. Balzer*
SDU Centre for Photonics Engineering, Mads Clausen Institute, University of Southern Denmark, Alsion 2, DK-6400 Sønderborg, Denmark
[b] *M. F. Schumacher, M. Schulz, J. Zablocki, A. Lützen*
Kekulé-Institute for Organic Chemistry and Biochemistry, University of Bonn, Gerhard-Domagk-Str. 1, D-53121 Bonn, Germany
[c] *S. Mattiello, L. Beverina*
Department of Materials Chemistry and INSTM, University of Milano-Bicocca, Via R. Cozzi 53, I-20125 Milano, Italy
[d] *M. Schmidtmann*
Department of Chemistry, University of Oldenburg, Carl-von-Ossietzky-Str. 9–11, D-26129 Oldenburg, Germany
[e] *K. Meerholz*
Physical Chemistry, University of Cologne, Greinstr. 4–6, D-50939 Cologne, Germany
[f] *N. Serdar Sariciftci, M. Schiek*
Linz Institute for Solar Cells, Johannes Kepler University, Altenberger Str. 69, A-4040 Linz, Austria
E-mail: manuela.schiek@jku.at
[g] *M. Schiek*
Center for Surface- and Nanoanalytics and Linz Institute for Solar Cells, Johannes Kepler University, Altenberger Str. 69, A-4040 Linz, Austria
[h] *M. Schiek*
Institute of Physics, University of Oldenburg, Carl-von-Ossietzky-Str. 9–11, D-26129 Oldenburg, Germany

Supporting information for this article is available on the WWW under https://doi.org/10.1002/ijch.202100079

© 2021 The Authors. Israel Journal of Chemistry published by Wiley-VCH GmbH. This is an open access article under the terms of the Creative Commons Attribution License, which permits use, distribution and reproduction in any medium, provided the original work is properly cited.

© 2021 The Authors. Israel Journal of Chemistry published by Wiley-VCH GmbH.

Research Article

Israel Journal of Chemistry

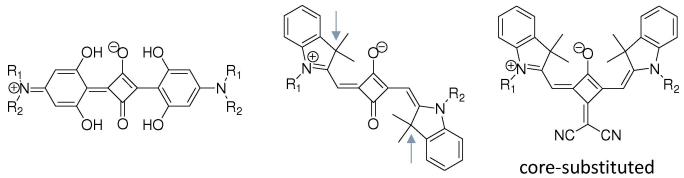


Figure 1. Structural motifs of squaraines (SQs): anilino SQ, indolenine SQ and acceptor-core substituted indolenine SQ. Terminal *N* substitutions ($R_1 \neq R_2$ or $R_1 = R_2$) are typically linear, branched or cyclic alkyl rests, that can also be chiral. The arrows indicate further optional positions for structural variations of indolenine SQs.

quadrupolar SQs.[16] This core-substitution was found to be beneficial for photovoltaic performance[17] since it inhibits photophysical dark-states[18] and fosters packing leading to ICT interactions.[19,20] Further variations of the indolenine SQ motif are replacing the carbon at the indicated ring position in Figure 1 with a sulfur or selenium atom to increase charge mobility for transistor applications.[21] Anilino SQs are basically modified by terminal *N* substitution. In case of bulky rests Coulombic interactions prevail and the optical spectra are shaped by a Davydov splitting.[13] Linear alkyl chains allow close slip-stack packing and ICT interactions that result in marked spectral double hump signatures, which are interpreted as mixed states of a Coulombic H-aggregate and a charge separated state.[22]

Chiral substitution adds another molecular design parameter to implement excitonic circular dichroism (CD), which is the differential absorption of circular polarized light of opposite handedness. The chiroptical response is mediated by the chiral supramolecular arrangement of the molecular backbones carrying the optical transition dipole moment, i.e. by the excitonic coupling of the molecules.[23–25] The chiral groups typically act as steering agent for the packing, but not directly cause the chiroptical response. For indolenine SQs there has also been an approach to integrate the chiral center into the backbone at the indicated position in Figure 1.[26] Terminal chiral functionalization, such as cyclic pyrrol-[27] and prolinol-derived[28] groups, has proven feasibility for anilino squaraines to induce an excitonic circular dichroic response in aggregated thin film samples. Actually, the prolinol moiety successfully generated a largely enhanced CD response, more than a factor of 100 larger than generic chiral organic thin films, solely based on the nature of the excitonic coupling. Yet, the critical role of ICT for the enhancement is under debate.[29] However, such a strong excitonic CD effect has proven to be functional in circular polarized light detectors without the need for further external polarization manipulating elements.[30]

Selective sensitivity to – and emissivity of – circular polarized light is a central theme for the development of advanced photonic and optoelectronic devices as well as novel spectroscopic and imaging tools. Rational design of molecular materials is a key to success.[31,32] A strategy that avoids costly separation of racemic mixtures is to start with abundant chiral pool reactants such as terpenes and in particular citronellol. Citronellyl (3,7-dimethyloctyl) substituents are widely used in racemic form to enhance solubility of a compound.[15,33–36] Basically the *S*-enantiomeric form was shown to efficiently imprint supramolecular chirality to graphitic nanotubes,[37] perylene bisimides,[38] and poly-thiophenes[39,40] as well as poly-fluorenes.[41–45]

In this work, we study the impact on chiral aggregation in solution processed and thermally annealed thin films of two indolenine and one anilino SQs with chiral (*S*)-citronellyl *N* terminal functionalization. Even though we could resolve a crystal structure for one of indolenine SQs, crystallization in thin films was barely obtained due to volatility of the material. For the anilino SQ we could quantify its circular dichroic response in thin films, which was strongly affected by the morphology of the samples. However, the shape of the CD spectra is significant and reinforces the interpretation of the characteristic double hump signatures of unpolarized absorbance spectra of previously investigated non-chiral anilino squaraines with linear alkyl chain functionalization.[14,22]

2. Mono- and Bis-Citronellyl Functionalized Indolenine Squaraines mCi-SQ and bCi-SQ

The synthesis of the two indolenine compounds (***S***)-**mCi-SQ** and (***S,S***)-**bCi-SQ**, carrying one or two (*S*)-citronellyl chiral groups at the indolenic nitrogen, respectively, has been facilitated following the scheme presented in Figure 2.

Directly from the purification procedure, single crystals of **bCi-SQ** suitable for X-ray analysis have been obtained. Unfortunately, this was a pseudo-polymorph structure including four *n*-hexane solvent molecules together with four **bCi-SQ** molecules within the body-centered monoclinic unit cells with a chiral *I*2 space group. Details on the unit cell parameters can be found in Table 1. The structure can be seen in Figure 3 omitting the solvent molecules for clarity of presentation. The molecules organize in two columnar π stacks tilted with respect to each other, with an inclination angle of 20° with respect to the crystallographic *c*-axis in the projection viewing along the *a*-axis, Figure 3(a). Along the *b*-axis, the molecules are arranged side-by-side, no staircase-shape, Figure 3(b). In (c) and (d) views slightly offset from the

© 2021 The Authors. Israel Journal of Chemistry published by Wiley-VCH GmbH.

Research Article

Israel Journal of Chemistry

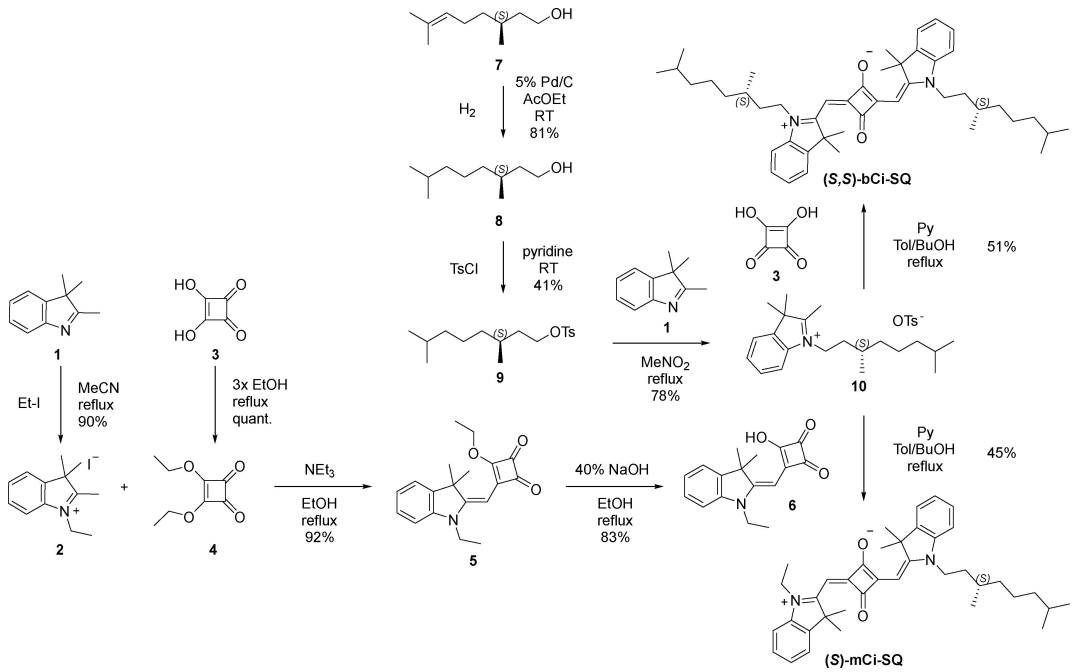


Figure 2. Schematic synthesis protocol for the two indolenine compounds **(*S*)-mCi-SQ** (or shortly **mCi-SQ**) and **(*S,S*)-bCi-SQ** (or shortly **bCi-SQ**). For this, 1-ethyl-2,3,3-trimethyl-3H-indoliumiodide **2**,[46] 3,4-diethoxycyclobut-3-ene-1,2-dione **4**,[46] 3-ethoxy-4-((1-ethyl-3,3-dimethylindolin-2-ylidene)methyl)cyclobut-3-ene-1,2-dione **5**[46,47] and 3-((1-ethyl-3,3-dimethyl-indolin-2-ylidene)methyl)-4-hydroxy-cyclobut-3-ene-1,2-dione **6**[46,47] were synthesized according to the cited references. The other syntheses were done by modified versions of previously reported protocols in the literature as indicated in the experimental section.

Table 1. Unit cell parameters of **(*S,S*)-bCi-SQ** (CCDC 2094899).

space group	*a* (Å)	*b* (Å)	*c* (Å)	*α* (°)	*β* (°)	*γ* (°)	*Z*
*I*2 (5)	19.0769(7)	9.3541(4)	27.3099(13)	90	108.953(2)	90	4

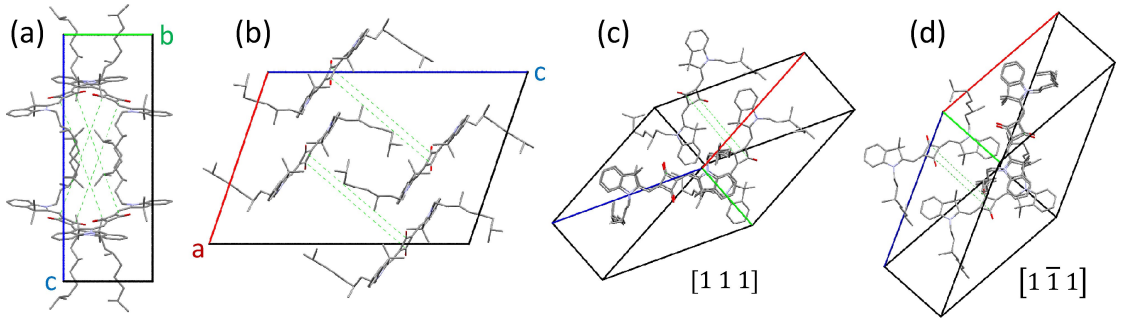


Figure 3. Visualization of the monoclinic pseudo crystal structure with space group *I*2 of **bCi-SQ** (CCDC code 2094899) omitting the *n*-hexane solvent molecules. (a) View along the *a*-axis, (b) view along the *b*-axis. (c) and (d) are views along the two molecular stacking directions [*u v w*]=[1 1 1] and [1 $\bar{1}$ 1], respectively, with a slight offset to show the stacking molecules. Green dashed lines are added to indicate the stacking squaraic central cores. The angle between the stacking directions is 40° in the projection viewing along the crystallographic a-axis in (a). The *c*-axis is the angle bisector.

© 2021 The Authors. Israel Journal of Chemistry published by Wiley-VCH GmbH.

Research Article

Israel Journal of Chemistry

perspective along the columnar stack axis pointing in [*u v w*] = [1 1 1] and [1 $\bar{1}$ 1] directions, respectively, are presented.

Despite the readiness to crystallize in the bulk, spincasted thin films were perfectly isotropic for both indolenine SQs. The layers are also reasonably smooth and continuous, see atomic force microscopy images in the Supporting Information Figure S1. The normalized absorbance spectra and the complex refractive index of **mCi-SQ** and **bCi-SQ** without thermal post-treatment are shown in Figure 4. The absorbance peaks at the same spectral position 675 nm with a vibronic shoulder at 615 nm for both compounds as shown in Figure 4(a). The energetic difference is roughly 180 meV, which is typical for C=C stretching and ring breathing vibrations of conjugated organic molecules.[12] The vibronic progression is slightly more pronounced for the **mCi-SQ**, relative peak height 0.62 versus 0.56 for **bCi-SQ**. This results already in a slightly different color impression of the thin films as illustrated by the insets showing photographs of the samples on a white background. Consequently, the isotropic complex refractive index is very similar for the indolenine compounds, Figure 4(b). The extinction coefficients *k* are remarkably large being on the order of 1.6 to 1.7 at maximum for **mCi-SQ** and **bCi-SQ**, respectively. This is among the highest values of

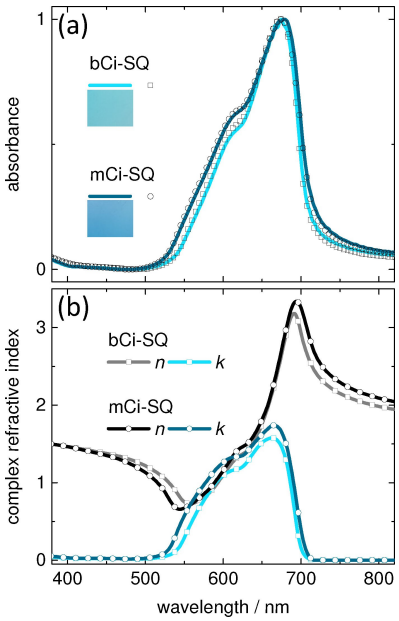


Figure 4. (a) Normalized absorbance of **bCi-SQ** (squares) and **mCi-SQ** (circles) spincasted thin films without thermal post-treatment. Solid lines are measured spectra and symbols show fit data obtained from the simultaneous fitting of ellipsometric and transmission intensity data. Insets display photos of samples on white background. (b) Isotropic real refractive index *n* and extinction coefficient *k* of **bCi-SQ** (squares) and **mCi-SQ** (circles) obtained by spectroscopic ellipsometry.

conjugated polymers typically used for highly efficient solar cells,[48] but yet is exceeded by crystalline anilino squaraine thin films.[49] Since no distinct molecular aggregation could be evidenced for the isotropic **mCi-SQ** and **bCi-SQ** it is self-explaining that neither excitonic CD signals, which would arise from chiral molecular aggregation or crystallization, could be detected. This is in line with a study, that compares chiral functionalization at the backbone of indolenine SQ with chiral terminal substitution.[26] This study utilized an acceptor-core substituted indolenine and covered only colloidal aggregation in solution, however, the chiral (*S*)-citronellyl at the nitrogen atom showed inferior (chiral) aggregation behavior.

Subsequent thermal annealing of thin films after solution processing is a common strategy to induce aggregation and even crystallization, but not for the present compounds **mCi-SQ** and **bCi-SQ**. They remained isotropic for annealing temperatures up to 90 °C, and for slightly higher temperatures then suddenly coalesced and evaporated off the substrate. In case of **bCi-SQ** we could capture a sample, which was covered with residual crystalline material by timed removal from the hotplate before all material was sublimed. The result can be seen in Figure 5(a), which shows the amoeba-like shape remains of **bCi-SQ** on the substrate. The yellow rectangle and the yellow square mark the areas, that have been imaged by intermittent contact mode AFM and displayed in (b) and (c), respectively. Cross-polarized microscopy imaging, Figure 5(d), revealed birefringence, and thus, crystallinity of the remaining **bCi-SQ**. The AFM measured the edges to be taller than the core area, which finds its expression in different interference colors: greenish for the taller rim and brownish for the core area. There were also shallow droplet-like features imaged by AFM in (b) that certainly were amorphous and consequently are invisible between crossed polarizers.

In the next step, a sufficiently homogeneous core area was selected as marked by the white circle in Figure 5(d) for spatially and polarization resolved spectroscopy. In (e) linear polarized absorbance spectra for a full rotation of the linear polarizer are shown as two-dimensional contour plot. Two absorption maxima at 576 nm and at 693 nm became visible that peak alternately at 90° and repeat themselves every 180°. Figure 5(f) shares the wavelength scale with (e) and displays the absorbance spectra in one dimensional representation for a 90° rotation of the linear polarizer. Starting and ending points were at a position where the short and long wavelength peaks were at maximum, respectively. Such spectral polarization course is typical for a Davydov splitting arising from molecular aggregates with at minimum two translationally invariant molecules per primitive unit cell interacting.[12] The short wavelength peak is the upper (UDC) and the long wavelength peak the lower Davydov component (LDC). The Davydov splitting amounts to 0.36 eV which is large, indicative for strong intermolecular interactions, but yet typical for squaraine compounds.[13,15,49]

The overall coverage with **bCi-SQ** material of the above discussed sample was very low, therefore the sample appeared

© 2021 The Authors. Israel Journal of Chemistry published by Wiley-VCH GmbH.

Research Article

Israel Journal of Chemistry

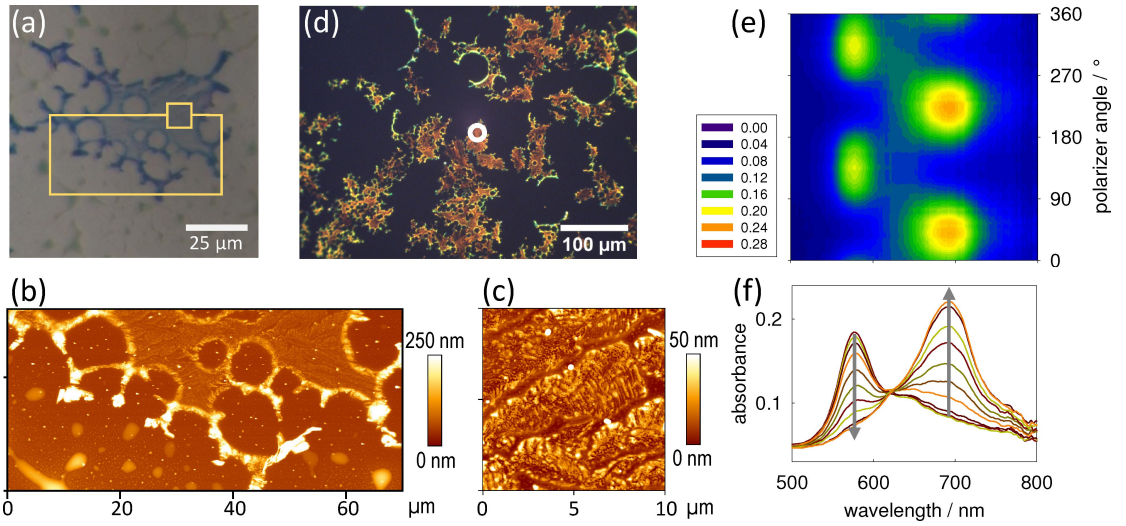


Figure 5. (a) Unpolarized brightfield microscopy image of a textured and discontinuous, micro-crystalline **bCi-SQ** sample. The yellow rectangle and the yellow square mark the areas imaged by AFM in (b) and (c), respectively. The edges of the amoeba-like shape **bCi-SQ** structure were taller and appeared greenish in cross-polarized microscopy imaging (d) while the core areas were flatter and seemed brownish. Shallow droplet-like amorphous aggregates were dark between crossed polarizers. The white circle in (d) indicates the core area, where polarized transmission spectra have been recorded. These spectra are shown as absorbance (= −log(T)) in the two-dimensional contour plot (e) for a full rotation of the linear polarizer. Horizontal axis: wavelength in nanometers (same scale as in (f)), vertical axis = polarizer angle in degrees. (f) displays the absorbance spectra versus wavelength for 90° rotation of the linear polarizer starting at maximum UDC and ending at maximum LDC. The arrows guide the eye to illustrate the evolution of peaks.

silent in thin film XRD analysis. But we could generate by dropcasting and thermal annealing a thick, crystalline **bCi-SQ** sample, which returned a signal in thin film XRD analysis, Figure S2 in the Supporting Information. For optical spectroscopy in transmission, such dropcasted samples were too thick. The single diffraction peak obtained by XRD is characteristic for a single crystallographic plane being parallel to the substrate. However, this signal does not match at all with the calculated powder pattern of the **bCi-SQ** pseudo-polymorph found for bulk crystals. Thus, the **bCi-SQ** adopts a different crystal polymorph in processed thin films.

3. *n*-Octyl Citronellyl Functionalized Anilino Squaraine nOCi-SQ

The synthesis scheme for the anilino SQ compound (***S,S***)-**nOCi-SQ** can be seen in Figure 6 following adopted, previously reported protocols.[2]

Even for spincasted **nOCi-SQ** samples without thermal treatment a certain molecular aggregation and preferential orientation became evident by optical spectroscopy. A normalized absorbance spectrum can be seen in Figure 7(a) displaying two spectral signatures peaking at 564 nm and 663 nm. Fitting of ellipsometric data required an anisotropic uniaxial model giving two data sets for the complex refractive index: ordinary, n_o and k_o, within the plane, and extra-ordinary, n_e and k_e, perpendicular to the plane of the thin film, Figure 7(b). This means that the organization of molecules or aggregates is random within the plane of the thin film, at least on a dimensional scale that is smaller than the wavelength of the probing light. The samples showed no linear dichroism or birefringence on a macroscopic or microscopic scale under typical normal incidence optical inspection. But there is a certain preferred orientation of molecules and aggregates parallel to the surface. For other aggregated micro-crystalline anilino squaraine thin films it was found, that the molecular stacking direction lies within the plane of the thin film,[13,14,27] which is also a likely case for the present **nOCi-SQ** samples. The fitted uniaxial complex refractive index serves well to calculate the absorbance spectra. In Figure 4(a) the solid line shows a measured absorbance spectrum together with a fitted spectrum (squares) from the ellipsometric data analysis procedure.

This was different for spincasted **nOCi-SQ** thin films with subsequent annealing, here at 100 °C. The absorbance spectra for as cast and annealed samples basically looked the same, only a slight blue-shift of the short wavelength peak to 557 nm was noticeable. The solid lines in Figure 7(c) show measured absorbance spectra for variable layer thicknesses of annealed samples. But the uniaxal complex refractive index determined for such samples, Figure 7(d) reproduces the measured absorbance spectra rather poorly. The fitted absorbance spectra

© 2021 The Authors. Israel Journal of Chemistry published by Wiley-VCH GmbH.

Research Article

Israel Journal of Chemistry

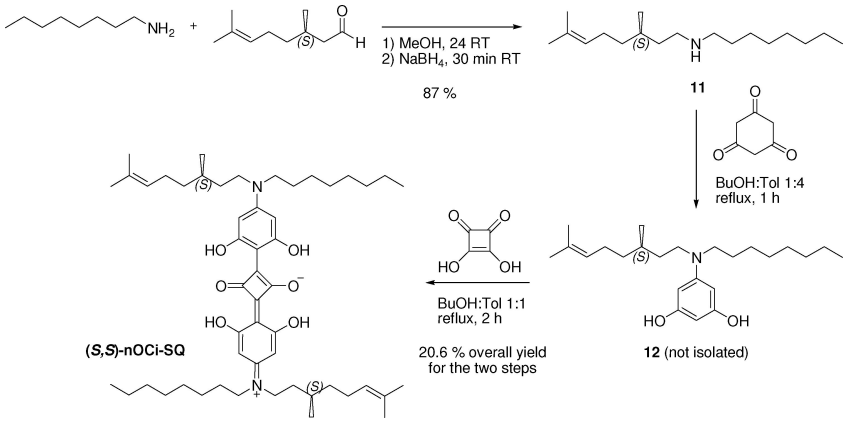


Figure 6. Schematic synthesis protocol for the anilino squaraine compound (***S,S***)**-nOCi-SQ** (shortly **nOCi-SQ**). Note that the (*S*)-citronellyl group has not been hydrated for this compound.

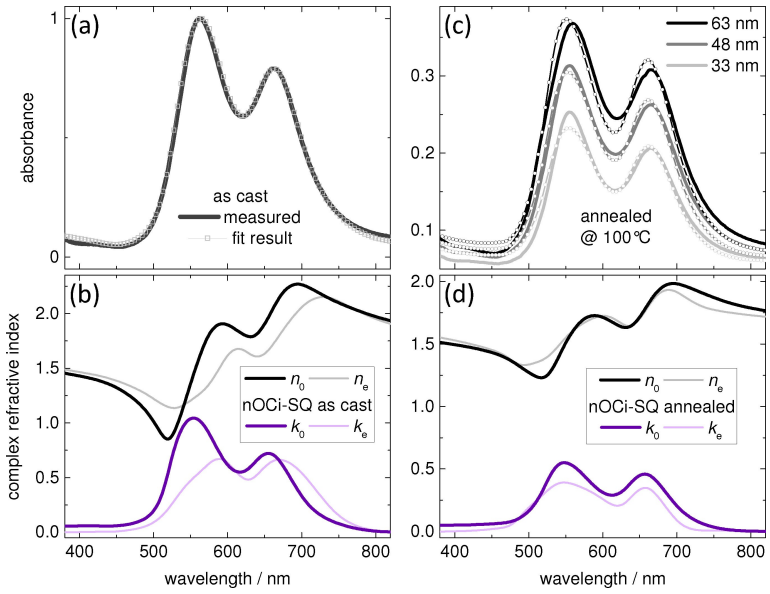


Figure 7. (a) Normalized absorbance of spincasted **nOCi-SQ** without thermal post-treatment. Solid line is the measured spectrum and symbols show fit data obtained from the simultaneous fitting of ellipsometric and transmission intensity data. (b) Uniaxial anisotropic complex refractive index of a **nOCi-SQ** thin film without annealing. Thick and thin lines denote the ordinary components n_o and k_o and the extra-ordinary components n_e and k_e, respectively. (c) Absorbance as measured (solid lines) of spincasted and subsequently annealed at 100 °C **nOCi-SQ** samples having three different coverages. Note that the thickness values indicated in the graph are nominal estimates as obtained from ellipsometric fitting. Symbols show fit data obtained from the simultaneous fitting of ellipsometric and transmission intensity data. (d) Averaged uniaxial anisotropic complex refractive index of spincasted **nOCi-SQ** samples annealed at 100 °C. Thick and thin lines denote the ordinary components n_o and k_o and the extra-ordinary components n_e and k_e, respectively.

from the ellipsometric data analysis procedure are shown as thin lines with circles in Figure 7(c). Three layer thicknesses and a non-normalized representation are chosen to illustrate that the deviation between measured and fitted absorbance spectra depends on sample parameters, here variable layer thickness. It is also conspicuous that the extinction coefficients for the annealed samples are significantly reduced (d) compared to the non-annealed samples (b). Since we conducted a combined fitting of multiple samples with six different thicknesses ranging roughly from 30 nm to 80 nm,

© 2021 The Authors. Israel Journal of Chemistry published by Wiley-VCH GmbH.

Research Article

Israel Journal of Chemistry

this means that there was no common uniaxial complex refractive index to describe all samples sufficiently. In other words, the complex refractive index of annealed **nOCi-SQ** samples varies with layer thickness. Thus, they describe no longer a material property but a sample property depending on processing parameters.

This is supported by inspection of the **nOCi-SQ** sample's morphology. Figure 8 displays intermittent contact mode atomic force microscopy (AFM) images of a sample without annealing in (a) and two samples annealed at 100 °C in (b) and (c). The as cast **nOCi-SQ** sample consisted of a continuous and smooth thin film with an average surface roughness *R*a just below 2 nm. Exact values are given in the caption of Figure 8. Upon thermal annealing, here 100 °C, microsized fibril-shaped aggregates emerged making the samples discontinuous. With this, it becomes problematic to define an accurate layer thickness. The values given for the annealed samples can be rather understood as nominal layer thicknesses or as indicator for a certain coverage with material. The fibril formation became more pronounced with increasing material coverage. Figures 8(b) and (c) show samples with 44 nm and 79 nm nominal thicknesses, respectively, and the average surface roughness *R*a increased from almost 9 nm to almost 12 nm. Such samples can only poorly be analyzed with standard spectroscopic ellipsometry. Therefore, the uniaxial complex refractive index given for the annealed **nOCi-SQ** samples in Figure 7(d) have only an estimative character.

Coming back to the absorbance spectra, the spectral shape is very much reminiscent of the characteristic double hump spectral signatures of *n*-alkyl anilino SQ thin films.[14] The physical origin of these peaks is mixing of a Coulombic Frenkel exciton with a charge separated state from ICT and redistribution of the shared oscillator strength.[22] The Frenkel exciton has the character of an H-aggregate, and the ICT is possible because of closely π-stacked molecular backbones as evidenced by the single crystal structures. Based on the primitive crystallographic unit cell containing only a single molecule, a Davydov splitting can be ruled out as reason for the double peaks.[12] For simplicity we name the two peaks the H-band (shorter wavelength) and the CT-band (longer wavelength). We assume that the (*S*)-citronellyl chain, even though it is not fully linear, does not disturb tight slip-stacked π-stacking of the **nOCi-SQ** backbones enabling ICT interactions. Therefore, we consider the hybrid Frenkel-ICT-exciton theory as valid also for the **nOCi-SQ**. However, the packing motif cannot be the same as in case of the *n*-alkyl anilino SQs,[14] which show fully parallel alignment of the backbones carrying the transition dipole moment. For the **nOCi-SQ** a chiral arrangement must be realized at least for the temperature treated samples since they show a pronounced circular dichroic response. Unfortunately, we cannot say more about the molecular packing here. All **nOCi-SQ** samples were silent in thin film XRD investigation, and no bulk single crystals could be obtained from the powder.

By Mueller matrix polarimetry[50,51] in normal incidence transmission we have analyzed the circular dichroism of the **nOCi-SQ** samples. Note that our instrumentation did not provide spatial resolution, and consequently we obtained only effective or averaged spectra in case of micro-structured samples. While the as cast samples were CD-silent, the thermally annealed samples showed a significant CD-response, Figure 9(a). The CD signal has been normalized to the unpolarized absorbance of the samples to give the dissymmetry factor *g*,[23–25] which is plotted for varying nominal layer thicknesses. The shape of the CD-spectra was the same for all sample coverages. The H-band showed a bisignate CD signal with a negative lobe at 515 nm and a positive lobe peaking at 575 nm. The zero-crossing of this bisignate signal is at the maximum peak position of the H-band of the unpolarized **nOCi-SQ** absorbance. According to exciton chirality rules, this hints to a right-handed helical organization of the molecular transition dipole moments and their Coulombic coupling.[12,23–25] The long wavelength CT-band gave another CD signal, which was monosignate, positive only and peaked slightly red-shifted compared to the unpolarized absorbance at 670 nm. The characteristic shape of the **nOCi-SQ** CD-spectrum reinforces the interpretation of the double hump spectral signatures of the unpolarized absorbance spectra as hybrid Frenkel and charge transfer exciton.[22] Furthermore, the humps reveal their original nature in the CD-spectrum: the

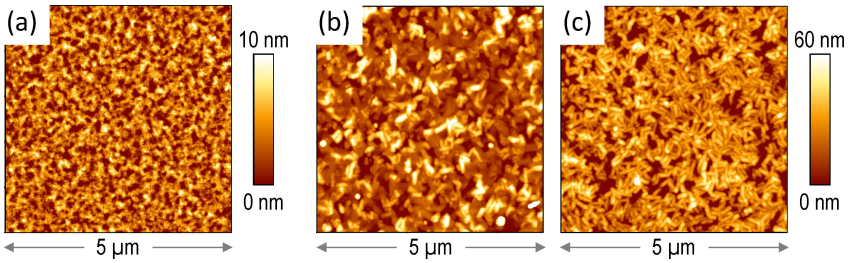


Figure 8. Intermittent contact mode AFM images of spincasted **nOCi-SQ** samples (a) without thermal treatment (layer thickness 32 nm, *Ra* = 1.89(2) nm and *Rq* = 2.37(2) nm) and thermally annealed at 100 °C with (b) 44 nm (*Ra* = 8.7(2) nm, *Rq* = 14.0(5) nm) and (c) 79 nm (*Ra* = 11.8(2) nm and *Rq* = 16.1(3) nm) nominal film thickness. Scan range is the same for all images being 5 µm × 5 µm, but height scale is six times smaller for the non-annealed sample in (a).

© 2021 The Authors. Israel Journal of Chemistry published by Wiley-VCH GmbH.

Research Article

Israel Journal of Chemistry

short wavelength band retains the bisignate shape originating from the Coulombic H-aggregate, while the long wavelength band returns a monosignate CD peak shape arising from the ICT. However, the impact of ICT on CD spectra is a largely underexplored topic, and deserves further theoretical analysis in the future.

Another striking aspect of the **nOCi-SQ** CD spectra is their dependence on nominal layer thickness. Figure 9(b) illustrate the evolution of the dissymmetry factor g of CD peak extrema with coverage. All three g peaks, both negative and positive lobe of the H-band, 515 nm and 575 nm, respectively, and the positive CT-band peak at 670 nm first increased in magnitude with layer thickness up to 60 nm and saturated for the largest nominal layer thickness close to 80 nm. The bisignate signal was asymmetric with a more pronounced negative lobe than positive lobe. For the highest value, the negative lobe resulted in a value of more than 0.2 for $|g|$, which was twice as much as the corresponding positive lobe maximum at around 0.1. The CT-band maximum was lagging behind with approximately 0.07 for the larger coverages. Actually, the g value better correlated with surface roughness of the samples, Figure 9(c), rather than with the nominal layer thickness. Note that even though the thickness values need to be considered with care, the g value solely depends on measured data, that is CD (ΔAbs^{CP}) and absorbance ($Abs = -\log(T)$) spectra: $g = \frac{\Delta Abs^{CP}}{Abs}$. However, CD spectra normalized to the nominal film thickness showed the same trend in coverage dependence, see Supporting Information Figure S3.

Nevertheless, the dissymmetry factor g per definition is an intensive quantity not depending on dimensional parameters such as layer thickness. The original definition is valid for dissolved molecules or small colloidal aggregates not accounting for scatter or reflection which is inherent to the nature of thin films. Actually it is commonly found, that g depends on layer thickness for molecular or polymeric thin films.[39,41–43, 45] A suitable correction for reflection losses can overcome this issue,[28] but this holds true only for smooth and continuous thin layers. For very thick layers like several hundreds of nanometers a cholesteric ordering and Bragg reflection could be found as explanation.[42,43] For thinner but macroscopically ordered samples liquid crystalline blue phases have been proposed to cause the thickness dependent g.[45] For the annealed **nOCi-SQ** samples we can say that the thickness or better roughness dependent g is not an intrinsic material property but an effect caused by the rotationally random micro-morphology of the samples convoluted with the macroscopic probe beam.[52] The impact of such intermediate supra-chiral coupling of likewise chiral supra-molecular aggregates on the chiroptical response of thin film samples is largely underexplored – despite the emerging interest in chiral organic opto-electronics – and deserves further quantitative assessment in the future.

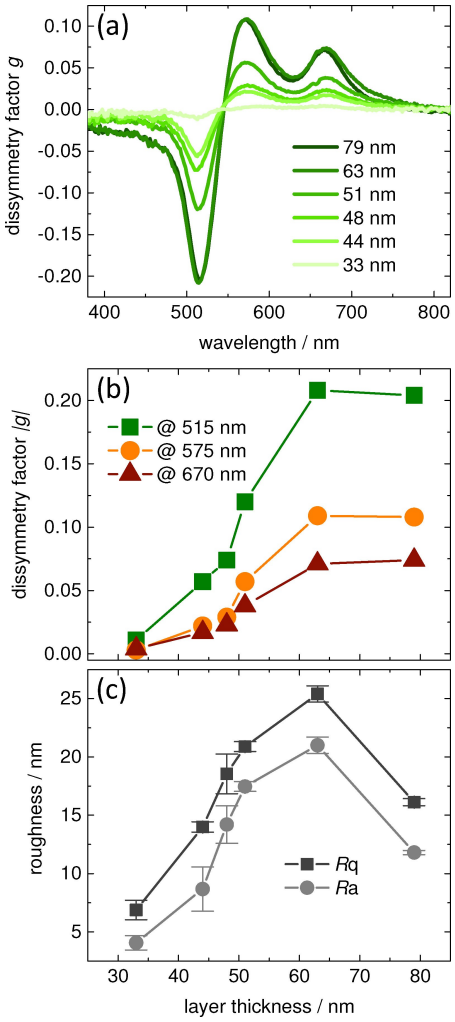


Figure 9. (a) Calculated dissymmetry factor g of spincasted and subsequently at 100 °C annealed **nOCi-SQ** samples with varying coverage. Note that the layer thickness values as indicated in the graph are only nominal estimates as obtained from the ellipsometric fitting procedure due to the micro-morphology of the samples. (b) Dissymmetry factor g peak values versus nominal film thickness for the minimum at 515 nm (squares) and the maximum (circles) at 575 nm of the bisignate CD signal, and for the second peak maximum at 670 nm (triangles). (c) Corresponding average surface roughness *Ra* and root mean square surface roughness *Rq* taken from 5 μm×5 μm AFM scans versus nominal layer thickness of the temperature treated **nOCi-SQ** samples.

4. Summary and Conclusion

We have prepared squaraine compounds with indolenine and anilino backbone motifs functionalized with chiral (*S*)-citronellyl groups at the terminal *N* position. Only in case of

© 2021 The Authors. Israel Journal of Chemistry published by Wiley-VCH GmbH.

Research Article

Israel Journal of Chemistry

the anilino SQ we could obtain chiral aggregation in spincasted and subsequently thermally annealed samples. Their chiroptical response was clearly impacted by morphology: condensation of **nOCi-SQ** into micro-fibrils with random distribution caused the dissymmetry factor g to depend on material coverage. The shape of the **nOCi-SQ** CD spectra is characteristic and independent of micro-texture. It reinforces the interpretation of the double hump spectral signatures previously found for *n*-alkyl anilino SQs to consist of a Coulomb-ICT-hybrid exciton. The exploration of both aspects, impact of charge transfer excitons and micro-morphology on the chiroptical response of organic thin film samples, is still at its infancy. And that is despite the emerge of chiral organic opto-electronics for next-generation devices. We hope to stimulate further basic research in this direction after having introduced a suitable model system.

5. Experimental

5.1 Synthesis

All chemicals were purchased from standard suppliers and used without further purification, all syntheses were done in standard glassware. NMR: ^{1}H and ^{13}C NMR spectra were recorded at 299 K at 500 MHz and 125 MHz. ^{1}H NMR chemical shifts are reported on the δ scale (ppm) relative to the residual non-deuterated solvent as the internal standard. ^{13}C NMR chemical shifts are given in δ values (ppm) relative to the deuterated solvent as the internal standard. Mass spectrometry: ESI mass spectra were taken on Thermo Fisher Scientific Orbitrap XL and Bruker Daltonik micrOTOF–Q spectrometers. UV-vis: UV-vis absorbance spectra were recorded on Analytik Jena Specord 200 using 1 cm Hellma quartz cuvettes. Elemental Analysis: elemental analysis was conducted on Heraeus Vario EL.

(*S*)-3,7-Dimethyloctan-1-ol ((*3S*)-dihydrocitronellol) (8)[53] Under argon atmosphere, 4.3 g (27.5 mmol, 1 eq.) (*S*)-citronellol (7) were dissolved in 30 mL ethyl acetate in a 100 mL Schlenk flask and the mixture was degassed by three freeze-pump-thaw cycles. 430 mg palladium 10 % on carbon (1.5 mol%) were added and the mixture was again degassed three times. The argon atmosphere was replaced by a hydrogen atmosphere and the mixture was stirred vigorously. After 16 hours, the mixture was filtrated through Celite® and the residue was extracted with ethyl acetate. The filtrates were combined and the solvent was removed under reduced pressure to obtain the product as a colorless liquid, which was used without further purification (3.54 g, yield: 81 %). ORD: $[\alpha]_D^{20} = -3.4°$ ($c = 2$ in $CHCl_3$). The other analytical data are in accordance with the literature.[53]

(*S*)-3,7-Dimethyloctyl-*p*–toluenesulfonate (9)[33] Under argon atmosphere, 1.5 g (9.5 mmol, 1 eq.) (*S*)-3,7-dimethyl-1-octanol (**8**) were suspended in 5 mL pyridine abs. and cooled to 10 °C. To the reaction mixture, 3.62 g (19.0 mmol, 2 eq.) tosyl chloride were added in portions under stirring over 30 minutes. After warming to room temperature and stirring for additional 24 hours, the mixture was poured into ice-cold 3 N hydrochloric acid and extracted with diethyl ether. The combined organic phases were washed with water and brine and dried over sodium sulphate. After removal of the solvents under reduced pressure, the raw product was obtained as a yellow oil and purified by column chromatography (silica gel) with dichloromethane/cyclohexane (1 : 1, v/v) as the eluent. The purified product was obtained as a colourless oil (1.24 g, yield: 41 %). ORD: $[\alpha]_D^{20} = -2.6°$ ($c = 1$ in $CHCl_3$). The other analytical data are in accordance with the reported values of the racemic mixture.[33]

(*S*)-1-(3,7-Dimethyloctyl)-2,3,3-trimethyl-3*H*-indole-1-iumtosylate (10)[34] Under argon atmosphere, 478 mg (3 mmol, 1 eq.) 2,3,3-trimethyl-3*H*-indole (**1**) and 937 mg (3 mmol, 1 eq.) (*S*)-3,7-dimethyloctyl-p-toluenesulfonate (**9**) were dissolved in 5 mL nitromethane abs. and refluxed for 16 hours. The mixture was cooled to room temperature and the solvents were partially removed under reduced pressure. The residue was mixed with diethyl ether and the precipitate was collected, washed with diethyl ether, and dried under vacuum. The product was obtained as a wine-red solid. (1.10 g, yield: 78 %) The analytical data are in accordance with the reported values of the racemic mixture.[34]

(*S,S*)-1,3-Bis[(1-(3,7-dimethyloctyl)-2,3-dihydro-3,3-dimethyl-1H-indol-2-yl)methyl]-squaraine ((*S,S*)-bCi-SQ)[35] In a flask with affixed Dean-Stark apparatus and reflux condenser 500 mg (1.06 mmol, 2 eq.) (*S*)-1-(3,7-dimethyloctyl)-2,3,3-trimethyl-3*H*-indol-1-iumtosylate (10) and 60 mg (0.53 mmol, 1 eq.) squaric acid (3) were suspended in a mixture of 5 mL butanol, 5 mL toluene and 2 mL pyridine. The mixture was refluxed under argon atmosphere for 18 hours. After removal of the solvents under reduced pressure the raw product was purified by column chromatography (silica gel) with cyclohexane/ethyl acetate (gradient elution, 3 : 1 to 2 : 1, v/v) as the eluent. The product was dissolved in small amounts of dichloromethane, diluted in an excess of *n*-hexane, and stored at 2 °C. The precipitate was collected and washed with cold *n*-hexane. The purified product was obtained as green-golden crystals (184 mg, yield: 51 %). ^{1}H NMR: (500 MHz, chloroform-*d*) δ [ppm] = 7.35 (dd, ^{3}J = 7.4 Hz, ^{4}J = 1.2 Hz, 2H), 7.30 (ddd, ^{3}J = 7.7 Hz, ^{4}J = 1.2 Hz, 2H), 7.14 (ddd, ^{3}J = 7.5 Hz, ^{4}J = 0.9 Hz, 2H), 6.96 (d, ^{3}J = 7.9 Hz, 2H), 5.98 (s, 2H), 4.08–3.93 (m, 4H), 1.79 (s, 14H), 1.65–1.58 (m, 4H), 1.56–1.48 (m, 2H), 1.43–1.29 (m, 4H), 1.30–1.18 (m, 4H), 1.18–1.11 (m, 4H), 1.04 (d, ^{3}J = 6.0 Hz, 6H), 0.86 (d, ^{3}J = 6.6 Hz, 12H). ^{13}C NMR: (126 MHz, chloroform-*d*) δ [ppm] = 182.4, 170.1, 142.5, 127.9, 123.8, 122.4, 109.4, 86.7, 49.4, 42.3, 39.3, 37.3, 34.0, 31.3, 28.1, 27.2, 24.8, 22.8, 22.7, 19.7. MS (ESI+): m/z = 677.5 $[M+H]^+$. MS (ESI HRMS): m/z calcd for $C_{46}H_{64}N_2O_2H$ $[M+H]^+$: 677.5041, found: 677.5047. m/z calcd for $C_{46}H_{64}N_2O_2$ $M^{\bullet+}$: 676.4962, found: 676.4969. UV/vis: (toluene) λ_{max} = 644 nm. Elemental Analysis: calcd for $C_{46}H_{64}N_2O_2 \cdot 0.1\ CH_2Cl_2 \cdot 0.5\ C_6H_{14}$: C: 80.94; H: 9.85; N: 3.84, found: C: 80.95; H: 9.87; N: 3.53.

© 2021 The Authors. Israel Journal of Chemistry published by Wiley-VCH GmbH.

Research Article

Israel Journal of Chemistry

(*S*)-[(1-(3,7-dimethyloctyl)-2,3-dihydro-3,3-dimethyl-1*H*-indol-2-yl)methyl]-squaraine ((*S*)-mCi-SQ) In a flask with affixed Dean-Stark apparatus and reflux condenser 250 mg (0.51 mmol, 1 eq.) (*S*)-1-(3,7-dimethyloctyl)-2,3,3-trimethyl-3H-indol-1-iumtosylate (**10**) and 150 mg (0.53 mmol, 1 eq.) 3-((1-ethyl-3,3-dimethylindolin-2-ylidene) methyl)-4-hydroxycyclobut-3-ene-1,2-dione (**6**) were suspended in a mixture of 5 mL butanol, 5 mL toluene and 2 mL pyridine. The mixture was refluxed under argon atmosphere for 18 hours. After removal of the solvents under reduced pressure the raw product was purified by column chromatography (silica gel) with cyclohexane/acetone (2 : 1, v/v) as the eluent. The product was dissolved in small amounts of dichloromethane, diluted in an excess of *n*-hexane, and stored at 2 °C. The precipitate was collected and washed with cold *n*-hexane. The purified product was obtained as a green powder (134 mg, yield: 41 %). ^{1}H NMR: (500 MHz, acetone-d_6) δ [ppm] = 7.54–7.46 (m, 2H), 7.42–7.34 (m, 2H), 7.28 (d, ^{3}J = 7.9 Hz, 1H), 7.24 (d, ^{3}J = 7.9 Hz, 1H), 7.22–7.15 (m, 2H), 5.96 (s, 1H), 5.94 (s, 1H), 4.21 (d, ^{3}J = 7.2 Hz, 2H), 4.25–4.13 (m, 2H), 1.89–1.80 (m, 1H), 1.77 (s, 12H, H-6), 1.73–1.66 (m, 1H), 1.66–1.59 (m, 1H), 1.59–1.49 (m, 1H), 1.49–1.42 (m, 1H), 1.39 (t, ^{3}J = 7.2 Hz, 3H), 1.42–1.22 (m, 3H, H-30b), 1.22–1.16 (m, 2H), 1.08 (d, ^{3}J = 6.4 Hz, 3H), 0.86 (2x d, ^{3}J = 6.6 Hz, 6H). ^{13}C NMR: (126 MHz, acetone-d_6) δ [ppm] = 182.3, 182.1, 181.8, 170.1, 169.9, 143.4, 143.1, 142.9, 142.9, 128.8, 128.8, 124.5, 124.4, 123.1, 110.6, 110.5, 87.3, 87.0, 49.9, 49.9, 42.5, 39.9, 38.9, 37.8, 34.4, 28.7, 27.4, 27.3, 27.3, 25.5, 23.0, 22.9, 20.1, 12.2. MS (ESI+): m/z = 564.4 $M^{\bullet+}$, 1129.8 $[2\,M+H]^{+}$. MS (ESI HRMS): m/z calcd for $C_{38}H_{48}N_2O_2$ $M^{\bullet+}$: 564.3710, found: 564.3705. UV/vis: (toluene) λ_{max} = 642 nm. Elemental Analysis: calcd for $C_{38}H_{48}N_2O_2 \cdot 0.05\ CH_2Cl_2 \cdot 0.05\ C_6H_{14}$: C: 80.34; H: 8.58; N: 4.89, found: C: 80.16; H: 8.47; N: 4.75.

***N*-(*S*)-(3,7-Dimethyl-6-octenyl)-*N*-octylamine (11)** (*S*)-(-)-3,7-Dimethyl-6-octenal (7.01 g, 45.38 mmol) and octylamine (6.07 g, 47.00 mmol) are dissolved in 30 ml of MeOH. The colorless solution is stirred at r.t. overnight. $NaBH_4$ (3.00 g, 79.30 mmol) is added portion wise to the solution and the mixture is stirred at r.t. for 30 min. The solution is then poured in 400 ml of 1 M NaOH and the resulting mixture is extracted with Et_2O (3 × 150 ml). Combined organic phase was washed with water (2 × 200 ml), dried over powdered KOH and evaporated to dryness to give alight yellow oil (10.5 g, 39.25 mmol, yield 87 %). ^{1}H NMR ($CDCl_3$) δ 5.05 (m, 1H), 3.14 (t, J = 7.5 Hz, 2H), 3.12 (t, J = 7.5 Hz, 2H), 2.84 (s, 3H), 1.96 (m, 2H), 1.65 (s, 3H), 1.61 (s, 3H), 1.70-1.09 (m, 17H), 0.90 (d, J = 6.6 Hz, 3H), 0.87 (t, J = 7.2 Hz, 3H).

1,3-bis[4-(*N*-(*S*)-3,7-Dimethyl-6-octenyl)-*N*-octylamine)-2,6-dihydroxyphenyl]-squaraine ((*S,S*)-nOCi-SQ) *N*-(*S*)-(3,7-Dimethyl-6-octenyl)-*N*-octylamine (6.00 g, 22.43 mmol) and phloroglucinol (1.50 g, 11.90 mmol) are suspended in a 1 : 4 vol mixture of nBuOH:toluene (50 ml). Mixture is refluxed under a Dean-Stark trap until no more water is collected (about 1 h). Volatiles are removed and the solid residue is taken up with a 1 : 1 vol mixture of nBuOH:toluene (50 ml). Squaric acid (0.68 g, 5.95 mmol) is added, and mixture refluxed under a Dean-Stark trap for 2 h. All volatiles are removed, and the dark oily residue is taken up with MeOH (60 ml) to give a golden green precipitated that is collected by filtration and crystallized from EtOH to give the pure title compound as a dark green solid with a metallic luster (1.02 g, 1.23 mmol, 20.7 % yield). ^{1}H NMR (CD_2Cl_2) δ 10.88 (s, 4H), 5.80 (s, 4H), 5.15 (t, J = 7.2 Hz, 2H), 3.45-3.35 (m, 8H), 2.10-1.95 (m, 4H), 1.73 (s, 6H), 1.66 (s, 12H), 1.56-1.48 (m, 4H), 1.40-1.30 (m, 24H), 1.00 (d, J = 6.0 Hz, 6H), 0.93 (t, J = 6.0 Hz, 6H); ^{13}C NMR (CD_2Cl_2) δ 181.3, 162.6, 160.5, 157.8, 131.4, 124.4, 102.1, 93.4, 51.5, 49.8, 36.9, 34.6, 31.8, 30.7, 29.3, 29.2, 28.0, 27.0 25.4, 25.3, 22.6, 19.2, 17.4, 13.9. Anal Calcd For $C_{52}H_{80}N_2O_6$: C, 75.32; H, 9.72; N, 3.38. Found: C, 75.08; H, 9.83; N, 3.29.

5.2 Single Crystal Structure Analysis

Single crystals of **(*S,S*)-bCi-SQ** suitable for X-ray diffraction analysis were directly obtained from the purification procedure. A selected crystal was measured with a Bruker AXS Kappa Apex II CCD diffractometer at 100 K using graphite-monochromated Mo-Kα radiation (λ = 0.71073 Å).

Crystal dimensions 0.300 mm × 0.200 mm × 0.150 mm, metallic-green-blue block, empirical formula $C_{52}H_{78}N_2O_2$ and weight 763.16 amu, monoclinic, space group I2, a = 19.0769(7) Å, b = 9.3541(4) Å, c = 27.3099(13) Å, $\alpha = \gamma = 90°$, β = 108.953(2)°, V = 4609.2(3) Å^3, Z = 4, density 1.100 g/cm^3, absorption coefficient 0.065 mm^{-1}, F(000) = 1680, theta range for data collection 1.753° to 30.032°, index ranges $-26 \le h \le 26, -13 \le k \le 13, -38 \le l \le 38$, 173568 reflections collected (13500 unique, $R_{(int)}$ = 0.0390, observed reflections ($I > 2(I)$) 12474, completeness to theta = 30.032° 100 %, semi-empirical from equivalents absorption correction, max and min transmission 1.0000 and 0.9624, final R indices ($I > 2\sigma(I)$) $R1 = 0.0410$, $wR2 = 0.1055$, R induces (all data) $R1 = 0.0464$, $wR2 = 0.1093$, full-matrix least-squares on F^2 refinement, GOF on F^2 = 1.083 for 13500 data and 1 restraint and 526 parameters, largest diff. peak and hole 0.396 eÅ^{-3} and −0.240 eÅ^{-3}.

The structures were solved with SHELXS-2013/1 and then refined with the SHELXL 2018/3.[54] The crystallographic data file can be found online at the Cambridge Crystallographic Data Centre under the CCDC code 2094899. The single crystal structure data were analyzed with VESTA 3.5.7[55] and are visualized with Mercury 4.2.0.[56]

5.3 Thin Film Sample Preparation

The molecular compounds were dissolved on amylene-stabilized chloroform at concentrations of 4 mg/mL, 5 mg/mL, or 6 mg/mL and spincoated onto float glass substrates (15 mm × 15 mm) cut from float glass objectives slides (VWR) at variable rotation speeds to obtain layers of varying thick-

© 2021 The Authors. Israel Journal of Chemistry published by Wiley-VCH GmbH.

Research Article

Israel Journal of Chemistry

ness. Optional subsequent thermal annealing typically for 30 minutes on a preheated hot plate (temperatures as indicated in the text) was applied to induce controlled aggregation of the molecular compounds. Preparation was either conducted in inert nitrogen atmosphere or under ambient conditions, which had no effect on the sample quality.

5.4 Spatially Resolved Optical and Morphological Characterization

The morphology of the thin film samples was obtained by atomic force microscopy (AFM, JPK NanoWizard) in intermittent contact mode. Tap300-G cantilevers from BudgetSensors were used for imaging. AFM images were analyzed either by Gwyddion 2.59[57] or by the JPK SPM data processing software, version 5.0.133.

The optical micro-structure of the samples was characterized using a Leica DMRME polarization microscope. Both, images in reflection with a single or two crossed polarizers as well as images in transmission were taken. The microscope was coupled to a miniature spectrometer (Ocean Optics Maya2000) through a 200 µm optical fiber, allowing to take local transmission spectra from a spot size of about 30 µm diameter. A simple polarization analysis was obtained by adding a linear polarizer behind the sample and rotating the sample by a computer controlled rotation stage (Thorlabs PRM1Z8).

5.5 Ellipsometry and Mueller Matrix Polarimetry

Standard spectroscopic ellipsometric scans to obtain Ψ and Δ in reflection (45°–75° in steps of 5°) have been obtained with a J.A. Woollam M-2000 DI or XI rotating compensator instrument with horizontal sample stage. The spectral range from 193 nm or 245 nm to 1690 nm containing 690 or 660 wavelengths is recorded with a CCD-array detector. For unpolarized normal incidence transmission intensity spectra a custom-made sample holder was used. The complex refractive index was fitted using the vendor provided software CompleteEASE version 6. The multiple sample analysis feature was used for combined fitting of samples with variable layer thickness and to include transmission intensity data (1000 % fit weighting).[58] Incoherent backside reflections from the glass substrate and depolarization data have been included in the fit routine. The Kramers Kronig consistent B-spline with spectral node spacing of 0.1 eV was used to obtain a best match of fitted and experimental data. Optionally, anisotropic fitting (type uniaxial, difference mode off) was applied to obtain two sets of the complex refractive index: ordinary (in-plane) within the thin film plane, and extra-ordinary (out-of-plane) perpendicular to the extended thin film.[14] Note that the collimated beam diameter of approximately 3 mm does not provide spatial resolution but returns effective or averaged dielectric properties of textured thin films.

To extract the circular dichroism from the thin films, Mueller matrix recording in normal incidence transmission were performed with the J.A. Woollam DI or XI using a custom-made sample holder. Due to the polarizer-compensator-sample-analyzer (PCSA) configuration of the instruments, only the first three rows (12 elements out of 16) of the normalized Mueller matrix could be obtained. The complete normalized Mueller matrix **M** (all 16 elements with $m11 = 1$) is recovered by an algebraic procedure, which is applicable due to reasonably low depolarization effects.[59] The differential, recovered non-depolarizing Mueller matrix **L** provides the following physical interpretation of the matrix elements in case of normal incidence transmission recording:[28,60]

$$\mathbf{L} = \ln(\mathbf{M}) = \begin{pmatrix} 0 & -\mathrm{LD} & -\mathrm{LD}' & \mathrm{CD} \\ -\mathrm{LD} & 0 & \mathrm{CB} & \mathrm{LB}' \\ -\mathrm{LD}' & -\mathrm{CB} & 0 & -\mathrm{LB} \\ \mathrm{CD} & -\mathrm{LB}' & \mathrm{LB} & 0 \end{pmatrix} \quad (1)$$

with CD: circular dichroism, CB: circular birefringence, LD: horizontal linear dichroism, LB: horizontal linear birefringence, LD': 45° linear dichroism, LB': 45° linear birefringence.

Differential, recovered Mueller matrix data for selected **nOCi-SQ** samples can be seen in the Supporting Information in Figure S4.

The circular dichroism value CD is then taken as the average of the $l14$ and $l41$ elements. Note that CD is not the same as the ellipticity θ as typical output of a conventional CD-spectrometer:

$$\theta = \arctan\left(\frac{e^{\mathrm{CD}} - 1}{e^{\mathrm{CD}} + 1}\right) \quad (2)$$

Only for small CD quantities the following approximation $\theta = \mathrm{CD}/2$ holds true. An obvious benefit of the Mueller matrix polarimetry approach to circular dichroism studies is, that the provided CD value is free from linear dichroism contribution. This makes the approach most suitable for the analysis of thin film samples.

The dissymmetry factor g[23–25] is defined as the circular dichroism in "units of absorbance" $\Delta Abs^{\mathrm{CP}} = Abs^{\mathrm{LCP}} - Abs^{\mathrm{RCP}} = \frac{2}{\ln(10)} \cdot \mathrm{CD}$ normalized to the unpolarized absorbance $Abs = -\log(T)$ calculated from the transmission T:

$$g = \frac{\Delta Abs^{\mathrm{CP}}}{Abs} \quad (3)$$

This definition applies for spectroscopy of samples in solution, where the absorbance basically does not include contributions from reflection, scatter and thin film interference. Therefore, a true dissymmetry factor is supposed to be

© 2021 The Authors. Israel Journal of Chemistry published by Wiley-VCH GmbH.

Research Article

Israel Journal of Chemistry

an intensive quantity, a unique measure for the material property, not depending on dimensional aspects of the sample. For thin film samples, the dissymmetry factor requires cumbersome refinement accounting for inherent reflection, interference, scatter, and in case of discontinuous micro-structured samples–as in case of spincasted and thermally annealed **nOCi-SQ** also other morphology related aspects. Especially the latter would require spatially resolved CD analysis, and therefore, is beyond the scope of the present study. Thus, we adhere to the original definition of the dissymmetry factor *g*.

Acknowledgements

MS*, MS and JZ are obliged to the DFG for funding within GRK 1885 “Molecular Basis of Sensory Biology”. MS* thanks the PRO RETINA Stiftung for personal funding. MS*, NSS and MFS acknowledge the Linz Institute of Technology (LIT-2019-7-INC-313 SEAMBIOF) for funding. MFS, AL and KM are obliged to the DFG GRK 2591 “Template-designed Organic Electronics – TIDE” for financial support. MS* is grateful to Prof. Kurt Hingerl and the ZONA team for inspiration and support as well as Dr. Munise Cobet from the LIOS team.

References

[1] S. Sreejith, P. Carol, P. Chithra, A. Ajayaghosh, *J. Mater. Chem.* **2008**, *18*, 264–274.
[2] L. Beverina, M. Sassi, *Synlett* **2014**, *25*, 477–490.
[3] G. Xia, H. Wang, *J. Photochem. Photobiol. C* **2017**, *31*, 84–113.
[4] K. Ilina, W. M. MacCuaig, M. Laramie, J. N. Jeouty, L. R. McNally, M. Henary, *Bioconjugate Chem.* **2019**, *31*, 194–213.
[5] C. Qin, W. Y. Wong, L. Han, *Chem. Asian J.* **2013**, *8*, 1706–1719.
[6] G. Chen, H. Sasabe, T. Igarashi, Z. Hong, J. Kido, *J. Mater. Chem. A* **2015**, *3*, 14517–14534.
[7] M. Jo, S. Choi, J. H. Jo, S. Y. Kim, P. S. Kim, C. H. Kim, H. J. Son, C. Pac, S. O. Kang, *ACS Omega* **2019**, *4*, 14272–14283.
[8] Y. Chen, W. Zhu, J. Wu, Y. Huang, A. Facchetti, T. J. Marks, *Org. Photonics Photovolt.* **2019**, *6*, 1–16.
[9] J. He, Y. J. Jo, X. Sun, W. Qiao, J. Ok, T. il Kim, Z. Li, *Adv. Funct. Mater.* **2020**, *31*, 2008201.
[10] E. Lima, O. Ferreira, J. F. Silva, A. O. Santos, R. E. Boto, J. R. Fernandes, P. Almeida, S. M. Silvestre, L. V. Reis, *Dyes Pigm.* **2020**, *174*, 108024.
[11] K. Strassel, W. H. Hu, S. Osbild, D. Padula, D. Rentsch, S. Yakunin, Y. Shynkarenko, M. Kovalenko, F. Nüesch, R. Hany, M. Bauer, *Sci. Technol. Adv. Mater.* **2021**, *22*, 194–204.
[12] N. J. Hestand, F. C. Spano, *Chem. Rev.* **2018**, *118*, 7069–7163.
[13] F. Balzer, H. Kollmann, M. Schulz, G. Schnakenburg, A. Lützen, M. Schmidtmann, C. Lienau, M. Silies, M. Schiek, *Cryst. Growth Des.* **2017**, *17*, 6455–6466.
[14] J. Zablocki, M. Schulz, G. Schnakenburg, L. Beverina, P. Warzanowski, A. Revelli, M. Grüninger, F. Balzer, K. Meerholz, A. Lützen, M. Schiek, *J. Phys. Chem. C* **2020**, *124*, 22721–22732.
[15] C. Zhong, D. Bialas, C. J. Collison, F. C. Spano, *J. Phys. Chem. C* **2019**, *123*, 18734–18745.
[16] U. Mayerhöffer, M. Gsänger, M. Stolte, B. Fimmel, F. Würthner, *Chem. Eur. J.* **2012**, *19*, 218–232.
[17] U. Mayerhöffer, K. Deing, K. Gruß, H. Braunschweig, K. Meerholz, F. Würthner, *Angew. Chem. Int. Ed.* **2009**, *48*, 8776–8779; *Angew. Chem.* **2009**, *121*, 8934–8937.
[18] G. M. Paternò, N. Barbero, S. Galliano, C. Barolo, G. Lanzani, F. Scotognella, R. Borrelli, *J. Mater. Chem. C* **2018**, *6*, 2778–2785.
[19] C. A. Shen, D. Bialas, M. Hecht, V. Stepanenko, K. Sugiyasu, F. Würthner, *Angew. Chem. Int. Ed.* **2021**, *60*, 11949–11958.
[20] J. H. Kim, A. Liess, M. Stolte, A. M. Krause, V. Stepanenko, C. Zhong, D. Bialas, F. Spano, F. Würthner, *Adv. Mater.* **2021**, *33*, 2100582.
[21] T. Maeda, A. Liess, A. Kudzus, A. M. Krause, M. Stolte, H. Amitani, S. Yagi, H. Fujiwara, F. Würthner, *Chem. Commun.* **2020**, *56*, 9890–9893.
[22] C. Zheng, D. Bleier, I. Jalan, S. Pristash, A. R. Penmetcha, N. J. Hestand, F. C. Spano, M. S. Pierce, J. A. Cody, C. J. Collison, *Sol. Energy Mater. Sol. Cells* **2016**, *157*, 366–376.
[23] G. Pescitelli, L. D. Bari, N. Berova, *Chem. Soc. Rev.* **2011**, *40*, 4603.
[24] M. Liu, L. Zhang, T. Wang, *Chem. Rev.* **2015**, *115*, 7304–7397.
[25] G. Albano, G. Pescitelli, L. D. Bari, *Chem. Rev.* **2020**, 120, 10145–10243.
[26] J. Selby, M. Holzapfel, B. K. Lombe, D. Schmidt, A. M. Krause, F. Würthner, G. Bringmann, C. Lambert, *J. Org. Chem.* **2020**, *85*, 12227–12242.
[27] J. Zablocki, O. Arteaga, F. Balzer, D. Hertel, J. J. Holstein, G. Clever, J. Anhäuser, R. Puttreddy, K. Rissanen, K. Meerholz, A. Lützen, M. Schiek, *Chirality* **2020**, *32*, 619–631.
[28] M. Schulz, J. Zablocki, O. S. Abdullaeva, S. Brück, F. Balzer, A. Lützen, O. Arteaga, M. Schiek, *Nat. Commun.* **2018**, *9*, 2413.
[29] A. Painelli, University di Parma, Italy, private communication.
[30] M. Schulz, F. Balzer, D. Scheunemann, O. Arteaga, A. Lützen, S. C. J. Meskers, M. Schiek, *Adv. Funct. Mater.* **2019**, *29*, 1900684.
[31] J. R. Brandt, F. Salerno, M. J. Fuchter, *Nat. Chem. Rev.* **2017**, 1, 0045.
[32] J. L. Greenfield, J. Wade, J. R. Brandt, X. Shi, T. J. Penfold, M. J. Fuchter, *Chem. Sci.* **2021**, *12*, 8589–8602.
[33] C. V. Yelamaggad, U. S. Hiremath, S. A. Nagamani, D. S. Rao, S. K. Prasad, N. Iyi, T. Fujita, *Liq. Cryst.* **2003**, *30*, 681–690.
[34] S. F. Voelker, C. Lambert, *Chem. Mater.* **2012**, *24*, 2541–2553.
[35] S. F. Völker, T. Dellermann, H. Ceymann, M. Holzapfel, C. Lambert, *J. Polym. Sci. Part A* **2014**, *52*, 890–911.
[36] H. Ceymann, M. Balkenhohl, A. Schmiedel, M. Holzapfel, C. Lambert, *Phys. Chem. Chem. Phys.* **2016**, 18, 2646–2657.
[37] W. Jin, T. Fukushima, M. Niki, A. Kosaka, N. Ishii, T. Aida, *Proc. Nat. Acad. Sci.* **2005**, *102*, 10801–10806.
[38] T. Seki, A. Asano, S. Seki, Y. Kikkawa, H. Murayama, T. Karatsu, A. Kitamura, S. Yagai, *Chem. Eur. J.* **2011**, *17*, 3598–3608.
[39] G. Lakhwani, G. Koeckelberghs, S. Meskers, R. Janssen, *Chem. Phys. Lett.* **2007**, *437*, 193–197.
[40] J. Gilot, R. Abbel, G. Lakhwani, E. W. Meijer, A. P. H. J. Schenning, S. C. J. Meskers, *Adv. Mater.* **2010**, *22*, E131–E134.
[41] R. Abbel, A. P. H. J. Schenning, E. Meijer, *J. Polym. Sci. Part A* **2009**, *47*, 4215–4233.
[42] G. Lakhwani, S. C. J. Meskers, *J. Phys. Chem. A* **2011**, *116*, 1121–1128.
[43] C. Kulkarni, D. D. Nuzzo, E. Meijer, S. C. Meskers, *J. Phys. Chem. B* **2017**, *121*, 11520–11527.

© 2021 The Authors. Israel Journal of Chemistry published by Wiley-VCH GmbH.

Research Article

Israel Journal of Chemistry

[44] T. Yamada, K. Nomura, M. Fujiki, *Macromolecules* **2018**, *51*, 2377–2387.
[45] J. Wade, J. N. Hilfiker, J. R. Brandt, L. Liirò-Peluso, L. Wan, X. Shi, F. Salerno, S. T. J. Ryan, S. Schöche, O. Arteaga, T. Jávorfi, G. Siligardi, C. Wang, D. B. Amabilino, P. H. Beton, A. J. Campbell, M. J. Fuchter, *Nat. Commun.* **2020**, *11*, 6137.
[46] J. H. Yum, P. Walter, S. Huber, D. Rentsch, T. Geiger, F. Nüesch, F. D. Angelis, M. Grätzel, M. K. Nazeeruddin, *J. Am. Chem. Soc.* **2007**, *129*, 10320–10321.
[47] C. H. Chang, Y. C. Chen, C. Y. Hsu, H. H. Chou, J. T. Lin, *Org. Lett.* **2012**, *14*, 4726–4729.
[48] M. S. Vezie, S. Few, I. Meager, G. Pieridou, B. Dörling, R. S. Ashraf, A. R. Goñi, H. Bronstein, I. McCulloch, S. C. Hayes, M. Campoy-Quiles, J. Nelson, *Nat. Mater.* **2016**, *15*, 746–753.
[49] S. Funke, M. Duwe, F. Balzer, P. H. Thiesen, K. Hingerl, M. Schiek, *J. Phys. Chem. Lett.* **2021**, *12*, 3053–3058.
[50] J. H. Freudenthal, E. Hollis, B. Kahr, *Chirality* **2009**, *21*(1E), E20–E27.
[51] A. Mendoza-Galván, E. Muñoz-Pineda, S. J. L. Ribeiro, M. V. Santos, K. Järrendahl, H. Arwin, *J. Opt.* **2018**, *20*, 024001.
[52] M. H. Kim, L. Ulibarri, D. Keller, M. F. Maestre, C. Bustamante, *J. Chem. Phys.* **1986**, *84*, 2981–2989.
[53] T. Yamamoto, A. Shimada, T. Ohmoto, H. Matsuda, M. Ogura, T. Kanisawa, *Flavour Fragrance J.* **2004**, *19*, 121–133.
[54] G. M. Sheldrick, *Acta Crystallogr. Sect. C* **2015**, *71*, 3–8.
[55] K. Momma, F. Izumi, *J. Appl. Crystallogr.* **2011**, *44*, 1272–1276.
[56] C. F. Macrae, I. Sovago, S. J. Cottrell, P. T. Galek, P. Mc–Cabe, E. Pidcock, M. Platings, G. P. Shields, J. S. Stevens, M. Towler et al., *J. Appl. Crystallogr.* **2020**, *53*, 226–235.
[57] D. Necas, P. Klapetek, *Cent. Eur. J. Phys.* **2012**, *10*, 181–188.
[58] J. N. Hilfiker, N. Singh, T. Tiwald, D. Convey, S. M. Smith, J. H. Baker, H. G. Tompkins, *Thin Solid Films* **2008**, *516*, 7979–7989.
[59] O. Arteaga, R. Ossikovski, *J. Opt. Soc. Amer. A* **2019**, *36*, 416.
[60] O. Arteaga, B. Kahr, *Opt. Lett.* **2013**, *38*, 1134.

Manuscript received: July 25, 2021
Version of record online: November 2, 2021

© 2021 The Authors. Israel Journal of Chemistry published by Wiley-VCH GmbH.

Israel Journal of Chemistry

Supporting Information

The Impact of Chiral Citronellyl-Functionalization on Indolenine and Anilino Squaraine Thin Films

Frank Balzer, Marvin F. Schumacher, Sara Mattiello, Matthias Schulz, Jennifer Zablocki, Marc Schmidtmann, Klaus Meerholz, N. Serdar Sariciftci, Luca Beverina, Arne Lützen, and Manuela Schiek*© 2021 The Authors. Israel Journal of Chemistry published by Wiley-VCH GmbH. This is an open access article under the terms of the Creative Commons Attribution License, which permits use, distribution and reproduction in any medium, provided the original work is properly cited.

Supporting Information

The Impact of Chiral Citronellyl-Functionalization on Indolenine and Anilino Squaraine Thin Films

Frank Balzer,[†] Marvin F. Schumacher,[‡] Sara Mattiello,[¶] Matthias Schulz,[‡] Jennifer Zablocki,[‡] Marc Schmidtmann,[§] Klaus Meerholz,[‖] N. Serdar Sariciftci,[⊥] Luca Beverina,[¶] Arne Lützen,[‡] and Manuela Schiek[*,#,@]

†*Centre for Photonics Engineering, University of Southern Denmark, Alsion 2, DK-6400 Sønderborg, Denmark.*

‡*Kekulé-Institute for Organic Chemistry and Biochemistry, University of Bonn, Gerhard-Domagk-Str. 1, D-53121 Bonn, Germany.*

¶*Department of Materials Chemistry and INSTM, University of Milano-Bicocca, Via R. Cozzi 53, I-20125 Milano, Italy*

§*Department of Chemistry, Carl-von-Ossietzky-Str. 9-11, University of Oldenburg, D-26129 Oldenburg, Germany.*

‖*Physical Chemistry, Greinstr. 4-6, University of Cologne, D-50939 Cologne, Germany.*

⊥*Linz Institute for Solar Cells, Johannes Kepler University, Altenberger Str. 69, A-4040 Linz, Austria.*

#*Center for Surface- and Nanoanalytics and Linz Institute for Solar Cells, Johannes Kepler University, Altenberger Str. 69, A-4040 Linz, Austria.*

@*Institute of Physics, University of Oldenburg, Carl-von-Ossietzky-Str. 9-11, D-26129 Oldenburg, Germany.*

E-mail: manuela.schiek@jku.at

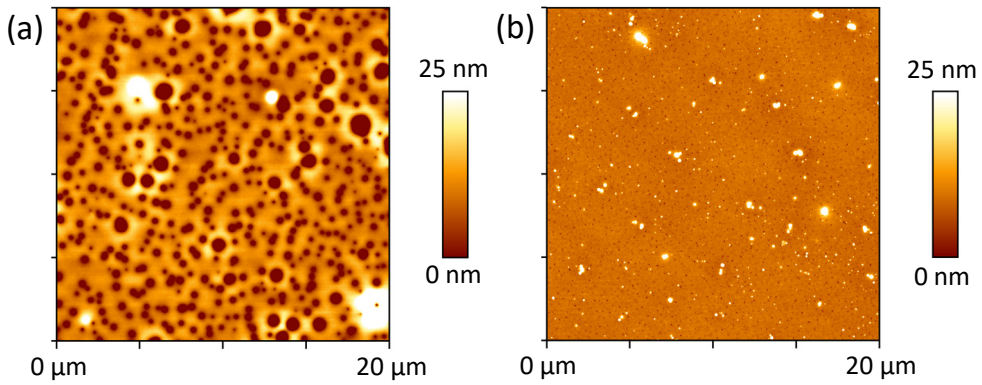


Figure S1: Intermittent contact mode AFM images (20 µm×20 µm, height scale 25 nm) of spincasted indolenine SQ samples without thermal treatment: (a) **bCi-SQ**, surface roughness Ra = 5.5 nm and Rq = 8.6 nm). (b) **mCi-SQ**, surface roughness Ra = 1.0 nm, Rq = 4.0 nm.

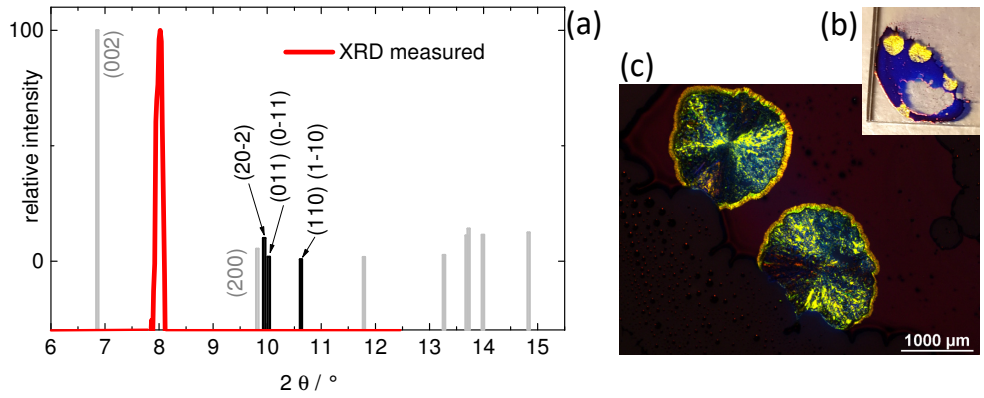


Figure S2: (a) X-ray diffraction pattern (monochromated Cu-$K\alpha$-radiation) of a dropcasted and thermally annealed **bCi-SQ** sample. The single diffraction peak at $2\theta = 8°$ plotted in red was obtained from the sample. The calculated powder pattern (Mercury) based on the monoclinic $I2$ single crystal structure (CCDC 2094899) is shown as bars. The bars colored black instead of grey are from crystallographic planes (Miller indices are given in the graph) that have the molecular stacking direction being parallel to the substrate surface. Since this is a typical preferred orientation theme for anilino squaraines[1–3] such planes can be expected to be realized for **bCi-SQ**. This presupposes that the determined single crystal structure is adopted in the thin film sample, which obviously is not the case. The resolved structure is a pseudo-polymorph containing an equal amounts of solvent and SQ molecules within the unit cell. A photograph of the **bCi-SQ** sample is shown in (b) and a microscopy image between crossed polarizers in (c). We thank Dorian Ziss and Julian Stangl, Semiconductor Physics Johannes Kepler University, for access to the X-ray diffractometer (PANalytical X'Pert PRO, PIXcel 1D detector).

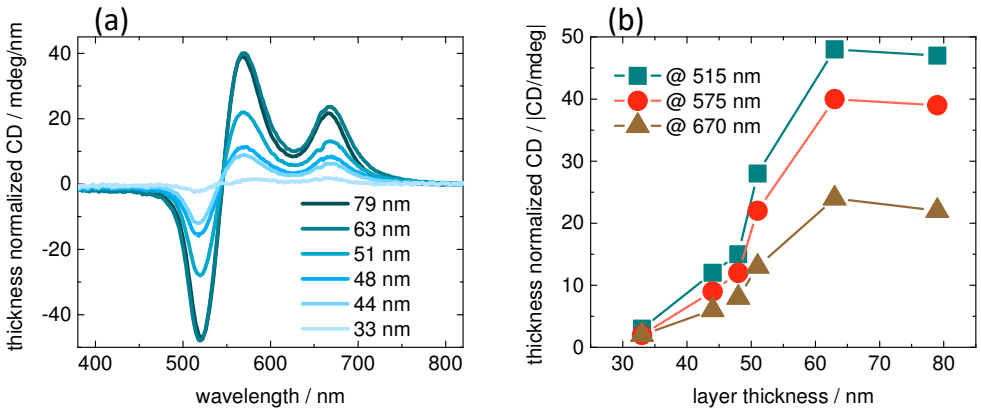


Figure S3: (a) Thickness-normalized CD spectra of **nOCi-SQ** samples. The peak maxima versus thickness of the bisignate signal and the additional peak at longer wavelength are plotted in (b). Note that these are only nominal thickness values due to the micro-structured nature of the samples.

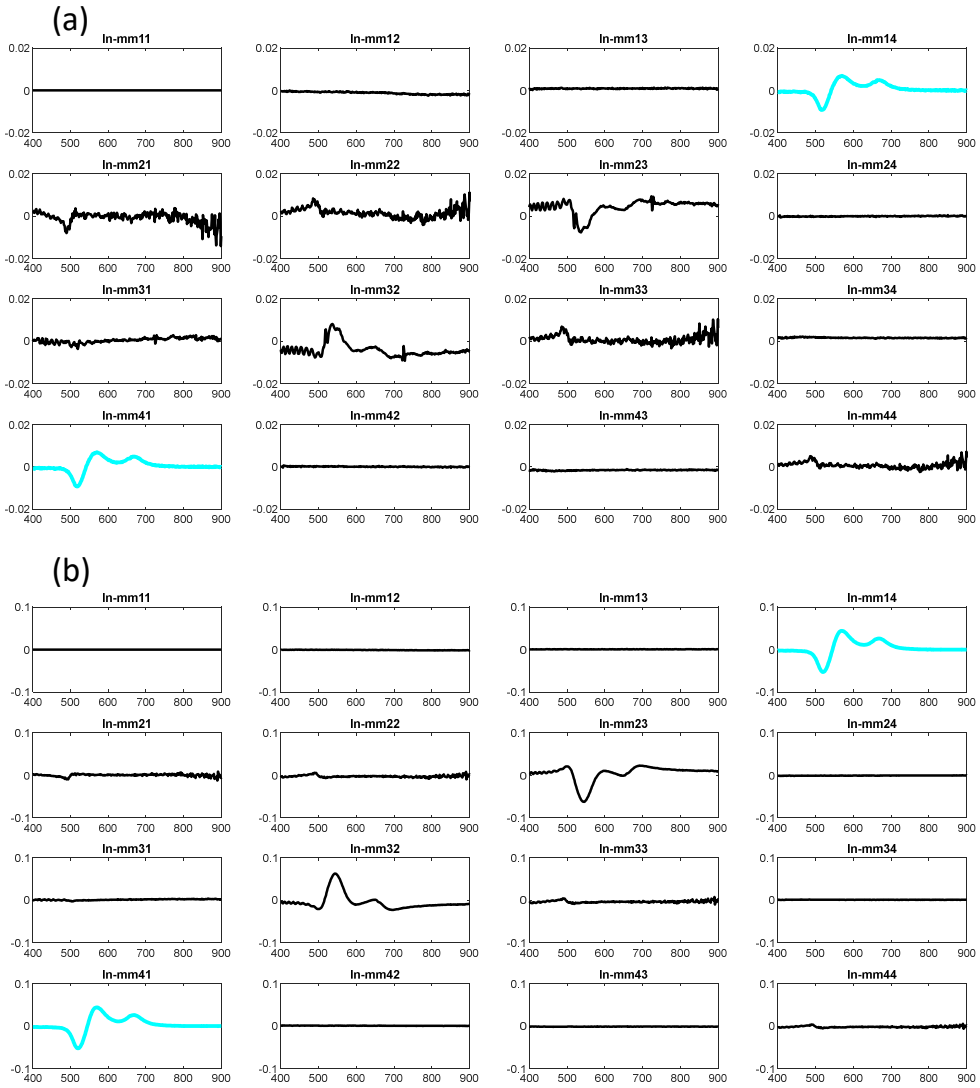


Figure S4: Recovered differential Mueller matrices[4,5] of **nOCi-SQ** samples for (a) 44 nm and (b) 63 nm nominal film thickness. x-axes: wavelength in nanometers, y-axes: signal in radians.

References

(1) Balzer, F.; Kollmann, H.; Schulz, M.; Schnakenburg, G.; Lützen, A.; Schmidtmann, M.; Lienau, C.; Silies, M.; Schiek, M. Spotlight on Excitonic Coupling in Polymorphic and Textured Anilino Squaraine Thin Films. *Cryst. Growth Des.* **2017**, *17*, 6455–6466.

(2) Zablocki, J.; Schulz, M.; Schnakenburg, G.; Beverina, L.; Warzanowski, P.; Revelli, A.; Grüninger, M.; Balzer, F.; Meerholz, K.; Lützen, A. et al. Structure and Dielectric Properties of Anisotropic n-Alkyl Anilino Squaraine Thin Films. *J. Phys. Chem. C* **2020**, *124*, 22721–22732.

(3) Zablocki, J.; Arteaga, O.; Balzer, F.; Hertel, D.; Holstein, J. J.; Clever, G.; Anhäuser, J.; Puttreddy, R.; Rissanen, K.; Meerholz, K. et al. Polymorphic chiral squaraine crystallites in textured thin films. *Chirality* **2020**, *32*, 619–631.

(4) Arteaga, O.; Ossikovski, R. Complete Mueller matrix from a partial polarimetry experiment: the 12-element case. *J. Opt. Soc. Amer. A* **2019**, *36*, 416.

(5) Schulz, M.; Zablocki, J.; Abdullaeva, O. S.; Brück, S.; Balzer, F.; Lützen, A.; Arteaga, O.; Schiek, M. Giant intrinsic circular dichroism of prolinol-derived squaraine thin films. *Nat. Commun.* **2018**, *9*, 2413.

APPENDIX **B**

Citronellyl-Functionalized Chiral Squaraines with Different Alkyl-Substituents

B.1 Additional Spectra in Solution and Thin Film

Aggregated Solutions:

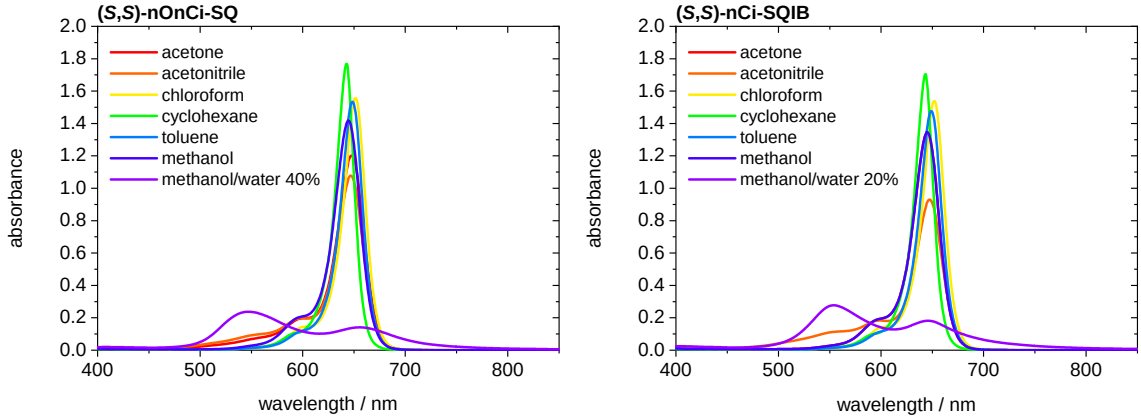


Figure B.1: UV/Vis absorbance spectra of **(*S*,*S*)-nOnCi-SQ** (left) and **(*S*,*S*)-nCi-SQIB** (right) in different solvents. The solutions were prepared from a chloroform stock solution (c = 2.31 × 10^{-4} M) and therefore contain an additional 1.7% chloroform (50 µL in 3 mL) with an final concentration of the sample of c = 3.84 µM.

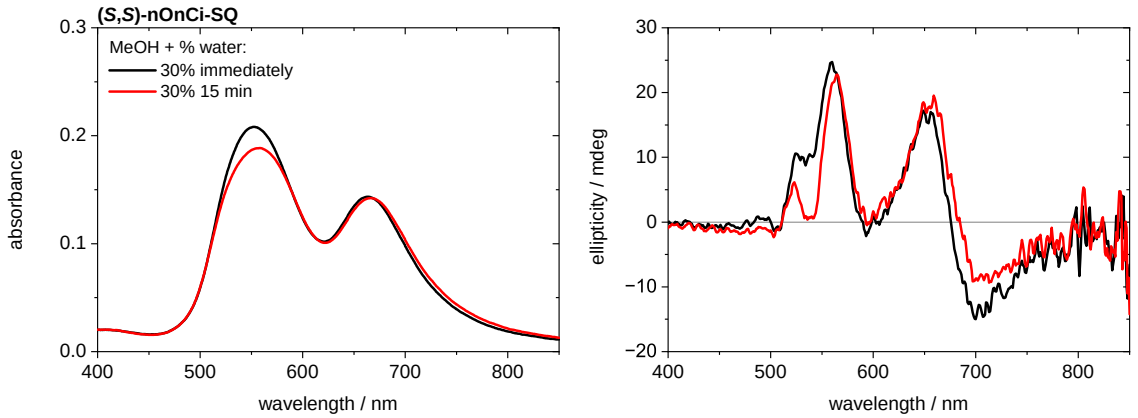


Figure B.2: Time-dependent UV/Vis absorbance (left) and corresponding ellipticity spectra (right) of **(*S*,*S*)-nOnCi-SQ** (c = 3.84 µM) in 30 volume-% of water in the methanol. The solutions were prepared from a chloroform stock solution (c = 2.31 × 10^{-4} M) and therefore contain an additional 1.7% chloroform (50 µL in 3 mL).

Thermally Annealed Thin Films:

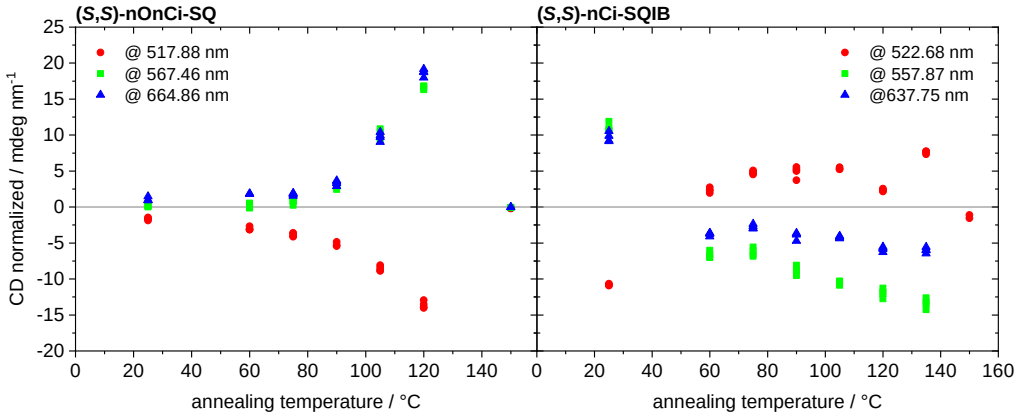


Figure B.3: Normalized CD values plotted against the annealing temperature of **(*S*,*S*)-nOnCi-SQ** (left) and **(*S*,*S*)-nCi-SQIB** (right), spin-coated from a chloroform solution under the same conditions and thermally annealed at given temperatures for 30 minutes.

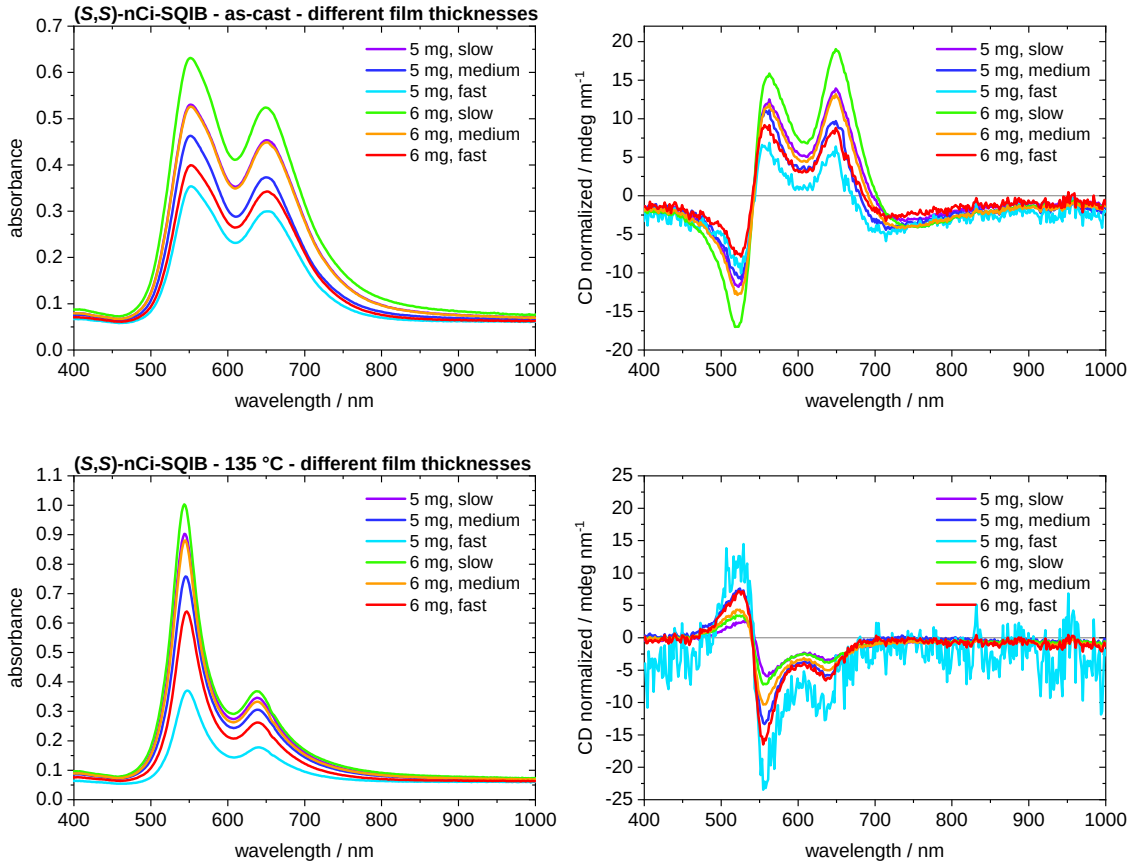


Figure B.4: UV/Vis absorbance (left) and corresponding normalized CD spectra (right) of as-cast (top) and thermally annealed (bottom) **(*S*,*S*)-nCi-SQIB** thin films with varying thickness. Thin films were prepared by spin coating 65 µL of a chloroform solution with a dye concentration of either 5 or 6 mg squaraine per mL, for 60 s at different rotation speeds and acceleration (2000 rpm, 400 rpm/s (slow); 3000 rpm, 1000 rpm/s (medium); 4000 rpm, 4000 rpm/s (fast)) on the glass substrate and – if noted – subsequent thermally annealed at 135 °C for 30 minutes.

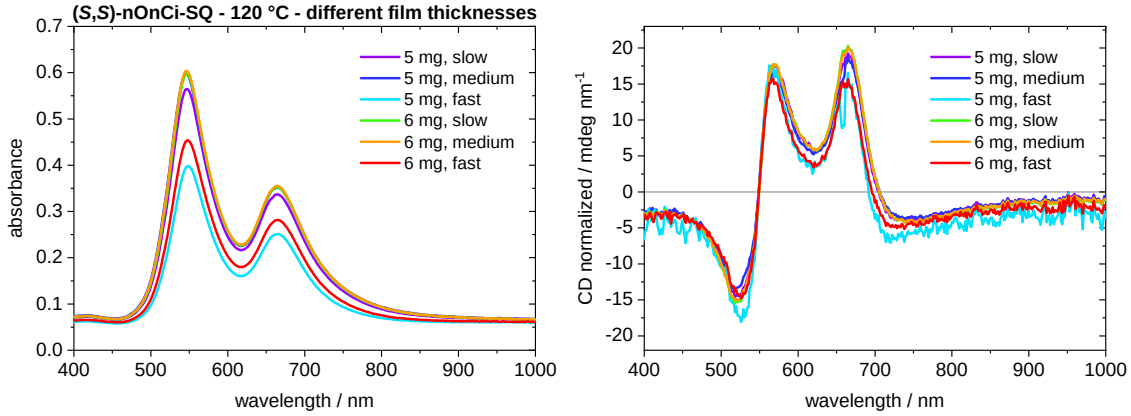


Figure B.5: UV/Vis absorbance (left) and corresponding normalized CD spectra (right) of **(*S*,*S*)-nOnCi-SQ** thin films with varying thickness. Thin films were prepared by spin coating 65 µL of a chloroform solution with a dye concentration of either 5 or 6 mg squaraine per mL, for 60 s at different rotation speeds and acceleration (2000 rpm, 400 rpm/s (slow); 3000 rpm, 1000 rpm/s (medium); 4000 rpm, 4000 rpm/s (fast)) on the glass substrate and subsequent thermally annealed at 120 °C for 30 minutes.

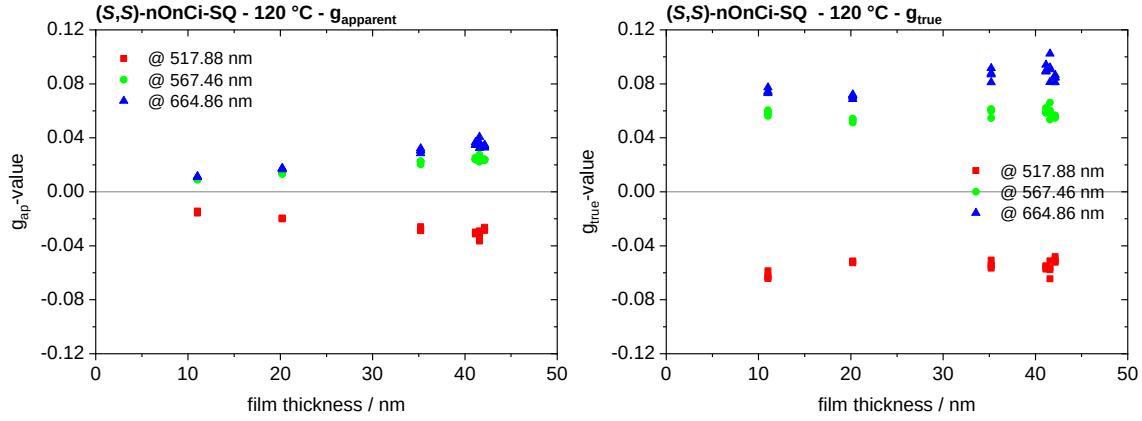


Figure B.6: Maximum apparent (g_{ap}) and true (g_{true}) dissymmetry factors of **(*S*,*S*)-nOnCi-SQ** (thermally annealed at 120 °C for 30 minutes) for different wavelengths according to the procedure given in Section 1.3.

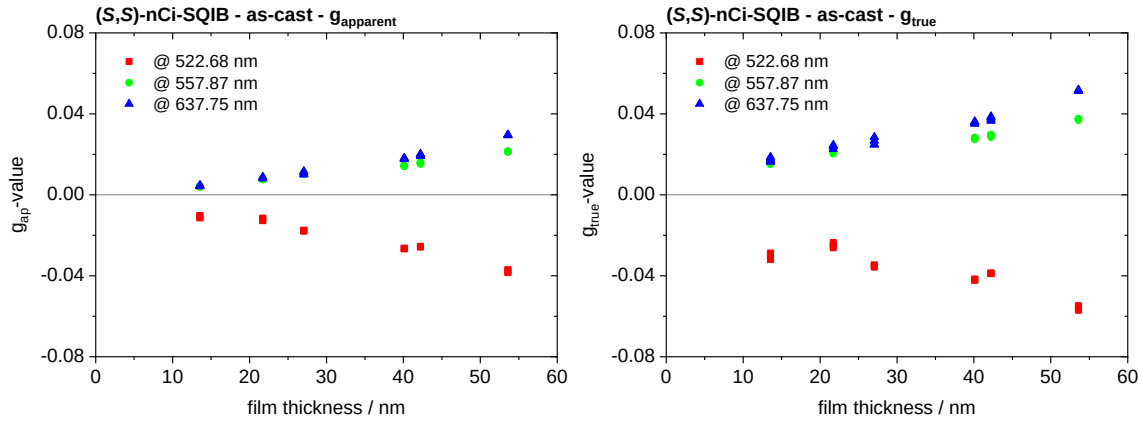


Figure B.7: Maximum apparent (g_{ap}) and true (g_{true}) dissymmetry factors of **(*S*,*S*)-nCi-SQIB** (as-cast) for different wavelengths according to the procedure given in Section 1.3.

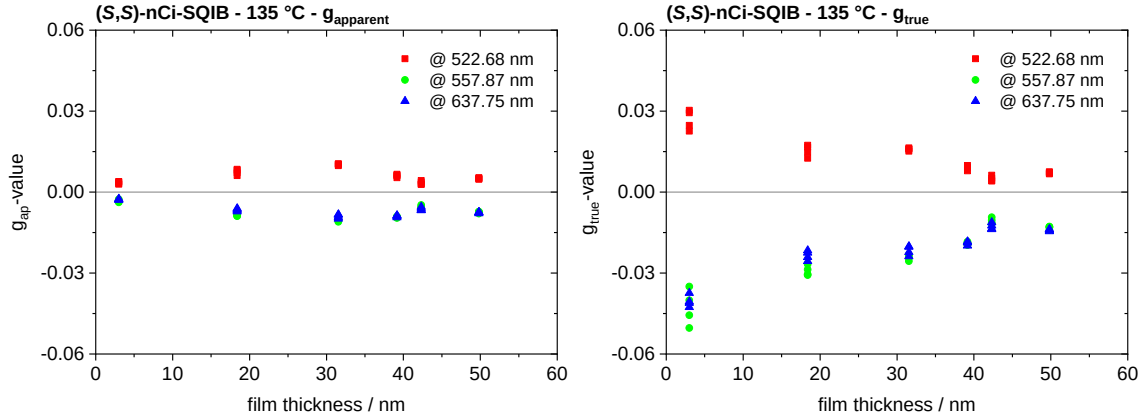


Figure B.8: Maximum apparent (g_{ap}) and true (g_{true}) dissymmetry factors of **(*S*,*S*)-nCi-SQIB** (thermally annealed at 135 °C for 30 minutes) for different wavelengths according to the procedure given in Section 1.3.

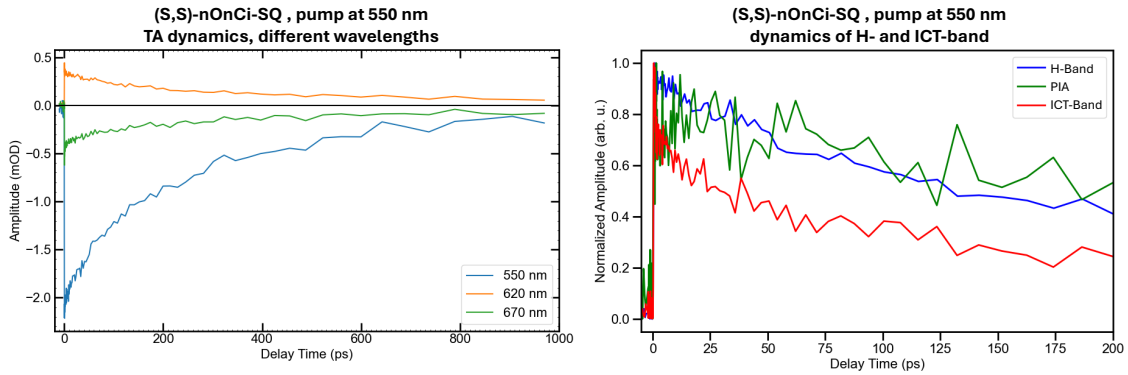


Figure B.9: Transient absorption spectroscopy data of thermally annealed (120 °C) **(*S*,*S*)-nOnCi-SQ** thin films, pumped at 550 nm with a pump power of 0.5 mW. Left: Transient absorption dynamics for different wavelengths. Right: Dynamics of the H-band (550 nm), photo-induced absorption (PIA) and ICT-band (660 nm).

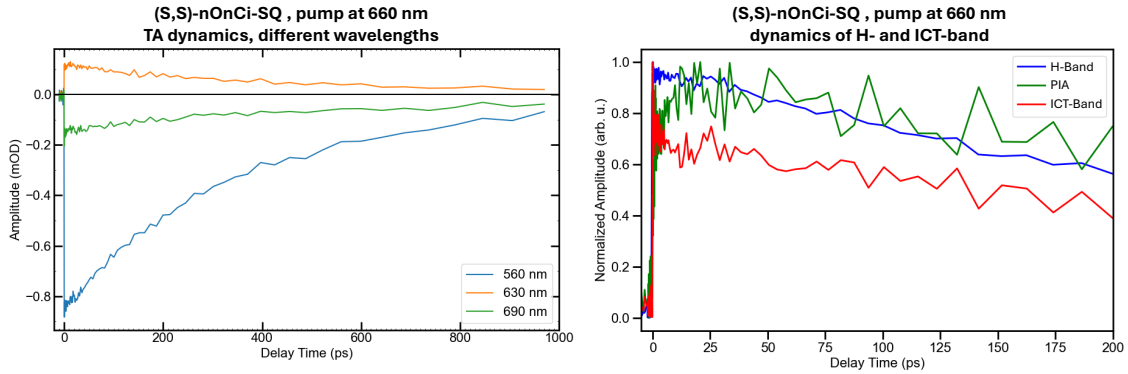


Figure B.10: Transient absorption spectroscopy data of thermally annealed (120 °C) **(*S*,*S*)-nOnCi-SQ** thin films, pumped at 660 nm with a pump power of 0.5 mW. Left: Transient absorption dynamics for different wavelengths. Right: Dynamics of the H-band (550 nm), photo-induced absorption (PIA) and ICT-band (660 nm).

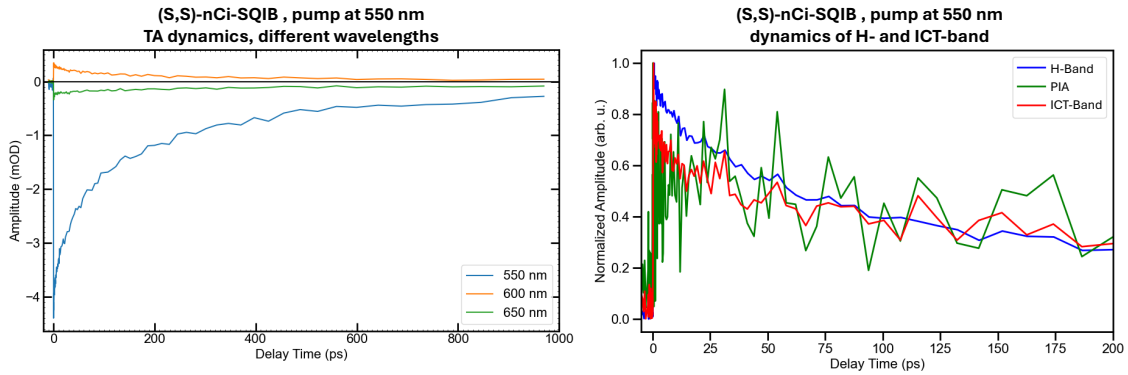


Figure B.11: Transient absorption spectroscopy data of thermally annealed (135 °C) **(*S*,*S*)-nCi-SQIB** thin films, pumped at 550 nm with a pump power of 0.5 mW. Left: Transient absorption dynamics for different wavelengths. Right: Dynamics of the H-band (550 nm), photo-induced absorption (PIA) and ICT-band (660 nm).

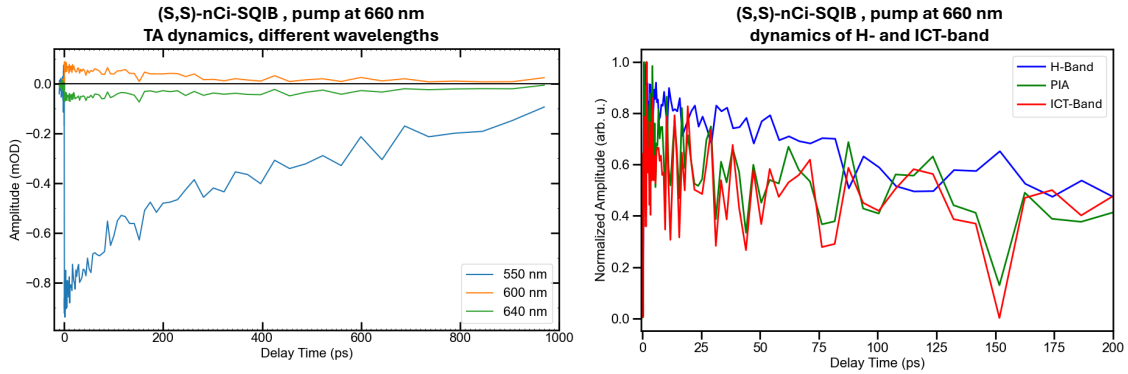


Figure B.12: Transient absorption spectroscopy data of thermally annealed (135 °C) **(*S*,*S*)-nCi-SQIB** thin films, pumped at 660 nm with a pump power of 0.5 mW. Left: Transient absorption dynamics for different wavelengths. Right: Dynamics of the H-band (550 nm), photo-induced absorption (PIA) and ICT-band (660 nm).

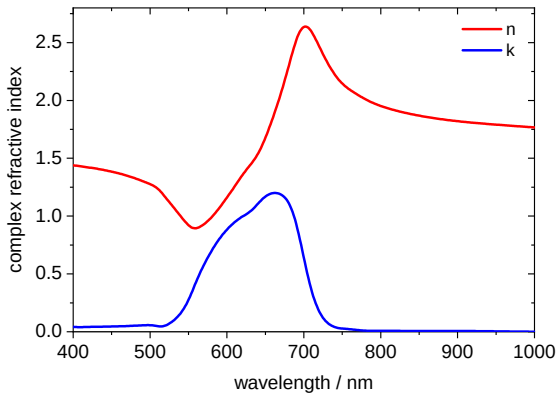


Figure B.13: Isotropic optical constants of as-cast spin coated thin films of **(*S*,*S*)-Ci-SQNP**. Calculations based on a multisample analysis in *CompleteEASE 6* using B-spline function. The refractive index is denoted as *n*, the extinction coefficient is denoted as *k*. The mean-square error (MSE) for the fits was calculated to: 4.75. The ellipsometric fitting process determined the layer thicknesses of all samples, yielding values around 40 nm.

B.2 Thin Film Preparation of (*S*,*S*)-nCi-SQIB by PVD Techniques

In collaboration with the group of Roland Resel (Graz University of Technology, Austria), physical vapor deposition (PVD) was carried out on **(*S*,*S*)-nCi-SQIB** to evaluate its capability for thin-film applications beyond solution-based spin-coating. **(*S*,*S*)-nCi-SQIB** was specifically chosen for its shorter isobutyl side chain compared to **(*S*,*S*)-nOnCi-SQ**.

The thin film preparation of the squaraine molecule was tried in two different evaporation units. The two evaporators have unique specifications in terms of vacuum conditions and evaporating conditions. The following table represents the classification of evaporators.

Evaporator	Base Pressure	Evaporating Source	Target to Substrate Distance	Remarks
Evaporator 1 (HV)	1×10^{-6} mbar	Tungsten filament with quartz insert	25 cm	Moderate control over the filament current
Evaporator 2 (UHV)	3×10^{-10} mbar	Kentax 3 cell evaporator with quartz crucible	16 cm	Precise control over the filament current

Evaporator 1: The evaporation of the **(*S*,*S*)-nCi-SQIB** was attempted in evaporator 1 and unfortunately did not yield any results. The compound was loaded to the deposition chamber with help of a quartz insert and heated up using a tungsten filament. The compound was evaporated by slowly increasing the heating current thereby increasing the filament temperature. The pressure started increasing from 1×10^{-6} mbar to 6×10^{-5} mbar during the evaporation. There was not any deflection on quartz crystal microbalance even at higher temperatures (or currents). The evaporator does not have a facility to measure the real time temperature of the filament. However, by indirect method we calculated the maximum temperature that was tried for the molecule and it was found to be around 300 °C. The quartz insert and glass substrates were examined after the evaporation. There was no traces of deposition on the glass substrate. Also the quartz insert had turned black after the heating which also revealed that the molecule had undergone some decomposition by the heating. This also explains why the molecule did not evaporate. The molecule undergoes chemical changes while applying heat under vacuum conditions. Figure B.14 (left) represents the image of the quartz insert loaded with the compound before the heating and Figure B.14 (right) represents the image of the quartz insert after the heating.

Evaporator 2: The evaporation of **(*S*,*S*)-nCi-SQIB** was tried in an ultra high vacuum evaporation unit. The compound was loaded into the quartz crucible and was inserted into the Kentax three cell evaporator. The bake out for the evaporator was done for 12 hours at 120 °C. After the bakeout the evaporator was subjected to slow degassing and during the degassing a sudden rise in the pressure was observed. The pressure increased from 9×10^{-9} mbar to 6×10^{-6} mbar within short periods of time. The evaporation at this pressure would cause serious damage to the deposition chamber and due to this the experiment was terminated.

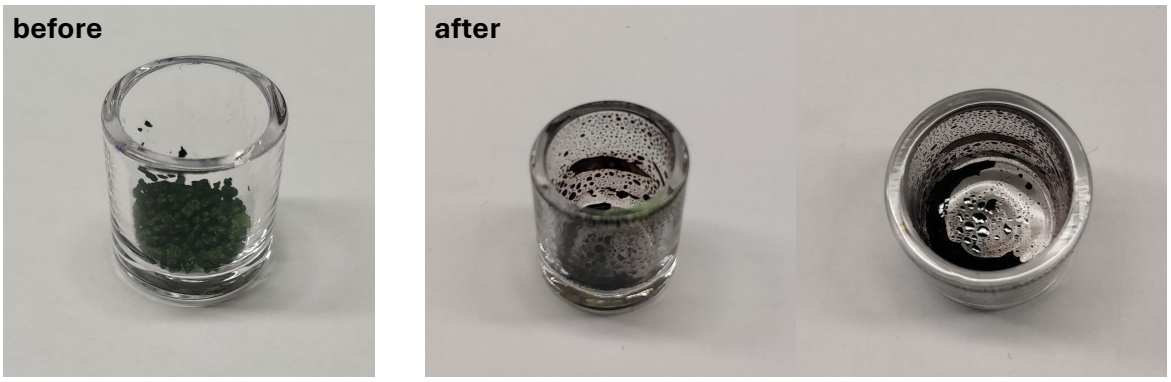


Figure B.14: Crucible with **(*S*,*S*)-nCi-SQIB** before (left) and after (right) heating the source.

Conclusion: The evaporation of **(*S*,*S*)-nCi-SQIB** on two different evaporation units was tried and turned out to be not successful. It has been observed that the molecule decomposes while heating under vacuum conditions, making it not suitable for PVD.

APPENDIX C

Synthesis, Structure and Thin Film Optical Properties of a Chiral Benzothiazole-Derived Squaraine

M. F. Schumacher,[a] G. Schnakenburg,[b] N. S. Sariciftci,[c] A. Lützen,[a] M. Schiek,[c,d]

To be published to ChemPhysChem – Please refer to the published article for the final version.

Own contributions:

- Synthesis and purification of the molecules
- Preparation of the thin film samples
- Performing and evaluating the ellipsometric/polarimetric measurements
- Interpretation of the results
- Writing the manuscript

Note: The following chapter is a manuscript[e] intended for submission to the peer-reviewed journal *ChemPhysChem*. Initial parts of this study were subject of my master's thesis.[141] For clarity and coherence, these sections are included here as they will appear in the journal submission. This primarily work comprises parts of the synthesis and UV/Vis absorption experiments in solution, both can be found in the main chapter (Chapter 5) or in following appendix.

[a] Kekulé-Institute for Organic Chemistry and Biochemistry, University of Bonn, Bonn, Germany
[b] Institute of Inorganic Chemistry, University of Bonn, Bonn, Germany
[c] Institute for Physical Chemistry (IPC) & Linz Institute for Organic Solar Cells (LIOS), Johannes Kepler University, Linz, Austria
[d] Center for Surface- and Nanoanalytics (ZONA), Johannes Kepler University, Linz, Austria
[e] Preliminary manuscript – subject to change.

Supporting Information: Synthesis, Structure and Thin Film Optical Properties of a Chiral Benzothiazole-Derived Squaraine

Marvin F. Schumacher,*[a] Gregor Schnakenburg,[b] N. Serdar Sariciftci,[c] Arne Lützen,[a] and Manuela Schiek*[c,d]

[a] M. F. Schumacher* and Prof. Dr. A. Lützen
Kekulé-Institute for Organic Chemistry and Biochemistry, University of Bonn, Bonn, Germany
E-mail: marvin.schumacher@uni-bonn.de

[b] Dr. Gregor Schnakenburg
Institute of Inorganic Chemistry, University of Bonn, D-53121 Bonn, Germany

[c] Dr. M. Schiek* and Prof. Dr. N. Serdar Sariciftci
Institute for Physical Chemistry (IPC) & Linz Institute for Organic Solar Cells (LIOS), Johannes Kepler University, A-4040 Linz, Austria

[d] Dr. M. Schiek*
Center for Surface- and Nanoanalytics (ZONA), Johannes Kepler University, A-4040 Linz, Austria
E-mail: manuela.schiek@jku.at

1. XRD Powder Pattern and Measurements of Spincoated Thin Films

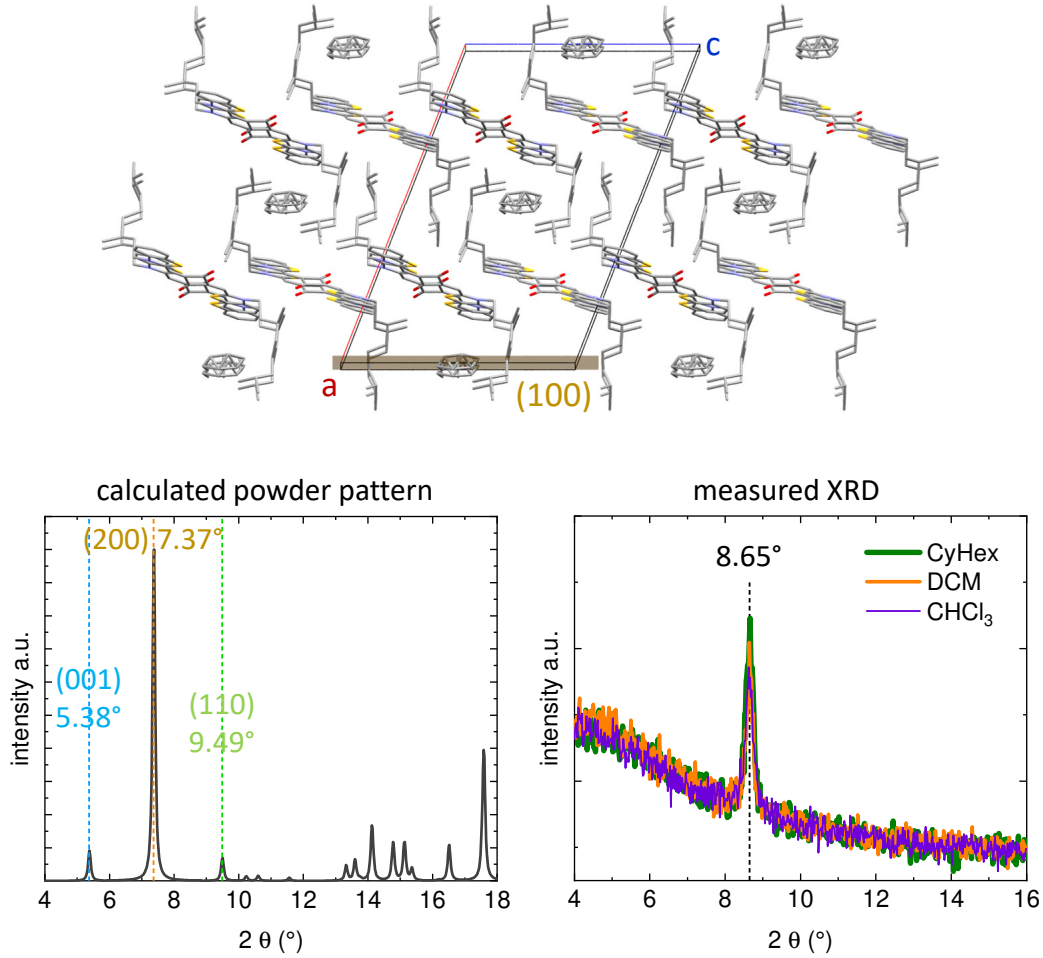


Figure S1. Top: The single crystal structure of **(*S*,*S*)-bCi-BtSQ**, including the cyclohexane solvent molecules it contains, is shown with horizontal alignment of the $(1\,0\,0)$ plane and a view along the slightly inclined b-axis to illustrate the molecular π-stacking along the b-axis. Hydrogen atoms have been removed. Nitrogen is shown in blue, carbon in gray, oxygen in red, and sulfur in yellow. Bottom left: Calculated X-ray ($\lambda = 1.54056$ Å) diffraction powder pattern in steps of $2\theta = 0.2°$ using CCDC Mercury 2022.3.0 of the **(*S*,*S*)-bCi-BtSQ** single crystal structure. Main crystallographic planes are indicated in the plot. Bottom right: Measured X-ray diffraction pattern of **(*S*,*S*)-bCi-BtSQ** thin films, which were spincasted from cyclohexane (CyHex; green), dichloromethane (DCM; orange) and chloroform ($CHCl_3$; lilac) and then annealed at 135°C. Patterns were acquired with monochromated Cu-$K\alpha$ radiation using an integration time of 3 seconds per data point, a step resolution of 0.02° and a fixed divergence slit of 1/4° using a PANalytical X'Pert PRO diffractometer with PIXcel 1D detector.

2. Calculated Polarization Directions of Davydov Bands

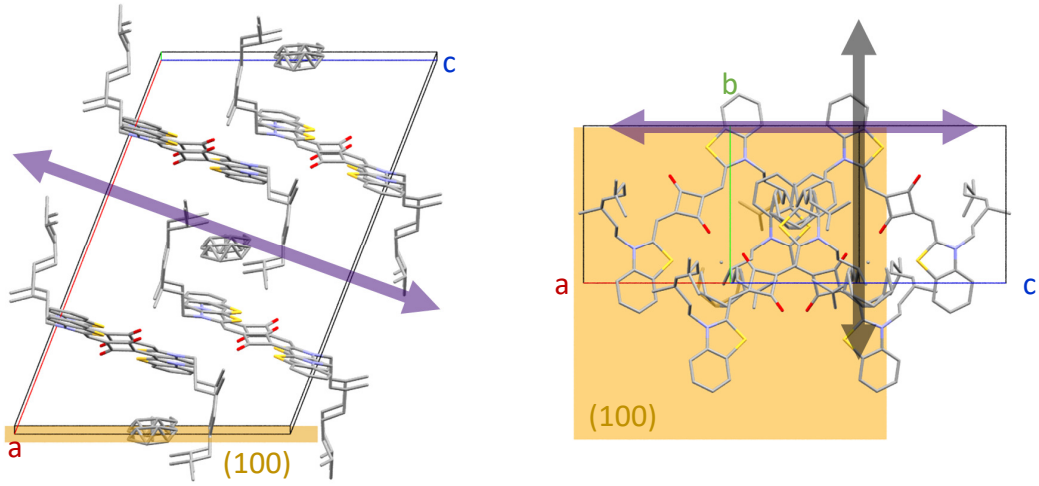


Figure S2. The single crystal structure of **(*S*,*S*)-bCi-BtSQ**, including the cyclohexane solvent molecules it contains, is shown with (left) horizontal alignment of the (1 0 0) plane and a view along the slightly inclined *b*-axis to illustrate the molecular π-stacking along the *b*-axis, and with (right) view normal onto the (1 0 0) plane. Hydrogen atoms have been removed. Nitrogen is shown in blue, carbon in gray, oxygen in red, and sulfur in yellow. The arrows of arbitrary lengths depict the polarization directions of the Davydov bands calculated based on vector geometry.

The polarization directions of the Davydov bands are calculated based on vector geometry using the pseudo single crystal structure of **(*S*,*S*)-bCi-BtSQ** including cyclohexane solvent molecules. The transition dipole moment (TDM) of an individual molecule is considered to lie along the long molecular axis, i.e. along the vector connecting the nitrogen atoms.[1] The actual orientation of the TDM may differ slightly from this, which would need to be verified using quantum chemical calculations. Atomic fractional coordinates of the nitrogen atoms are extracted using VESTA version 3.5.8.[2] The vector sum and difference of the TDM vectors of the two translationally non-equivalent molecules are calculated in cartesian coordinates using MATLAB version R2022b. One of the excitonic transitions (Davydov bands) is polarized along the crystallographic *b*-axis, which is logical since the *b*-axis is the unique axis in monoclinic crystals. It is shown in Figure S2 as dark grey arrow. The second Davydov band is polarized along a direction that is perpendicular to the first Davydov band, and consequently it is not along a crystallographic axis. It is shown in Figure S2 as lilac arrow. The inclination angle of the lilac arrow relative to the (1 0 0) plane is about 20°. In the projection with view normal to the (1 0 0) plane, the two Davydov bands appear polarized along the *b*-axis (dark grey arrow) and along the projected *a*- and *c*-axes (lilac arrow). The lengths of the arrows are arbitrary. Approximately 22% of the excitonic transition depicted by the lilac arrow projects into the (1 0 0) plane and approximately 78% along the normal to the (1 0 0) plane. Assuming a uniaxial orientation with the (1 0 0) plane parallel to the substrate, it follows that the Davydov band along the *b*-axis is completely polarized in-plane, while the second Davydov band is only polarized out-of-plane to a small extent. This means that both Davydov bands are clearly visible in transmission spectra under normal incidence, based on the pseudo crystal structure and a (1 0 0) orientation. This contrasts with the results obtained experimentally for the **(*S*,*S*)-bCi-BtSQ** thin films, which means that they must adopt a different crystal structure from the one determined here.

3. Optical properties in Solution

3.1. Absorbance Spectra in Selected Solvents

The transmission spectra shown as absorbance of **(*S*,*S*)-bCi-BtSQ** in selected solvents can be seen in Figure S3. They are dominated by an intense and narrow of the $S_0 \rightarrow S_1$ transition and are accompanied by a vibronic sholder. The peak maximum shifted with increasing solvent/solvent mixture polarity from cyclohexane at around 679.5 nm to dichloromethane at around 672.5 nm to 651.0 nm for the methanol/water mixture. Such negative solvatochromism is typical for squaraines.[3] It means that the ground state is better stabilized in polar solvents because it is more polar than the excited state. These maxima are shifted to longer wavelengths by about 50 nm compared to the corresponding 2,3,3-trimethylindolenine compounds. This bathochromic tendency is usually observed to a different extend when the CMe_2 group is exchanged for sulphur.[4]

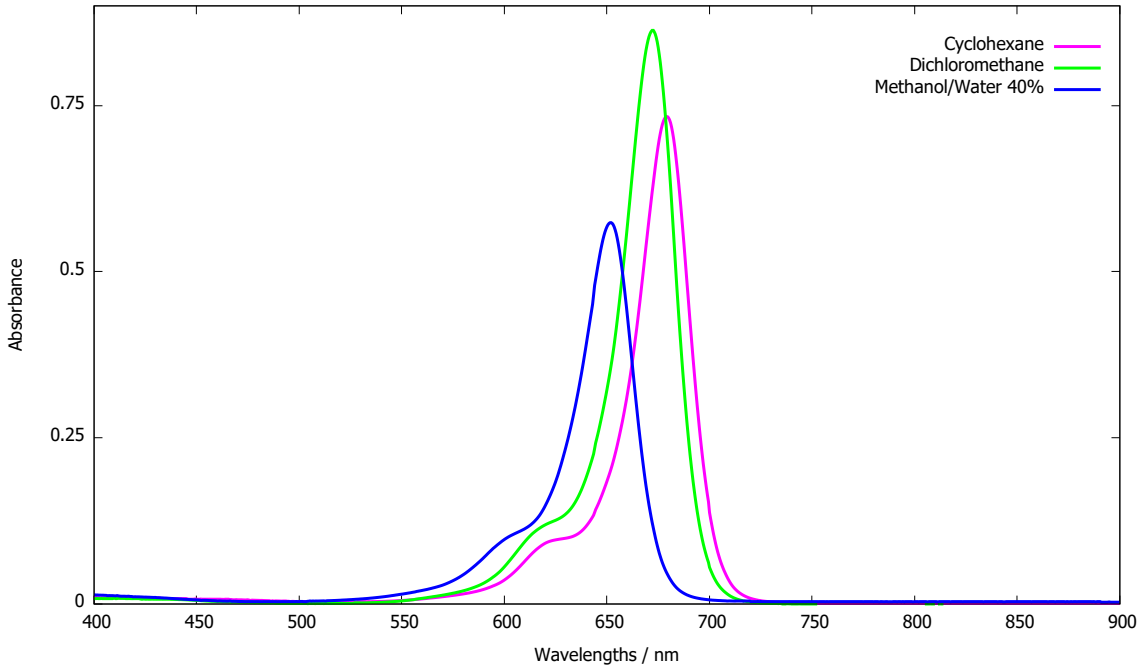


Figure S3. Transmission spectra shown as absorbance of **(*S*,*S*)-bCi-BtSQ** in cyclohexane, dichloromethane and methanol with 40 vol-% water content.

3.2. Extinction Coefficient in Dichloromethane

For determination of the extinction coefficient a stock solution of the squaraine **(*S*,*S*)-bCi-BtSQ** in dichloromethane was prepared. The weight-in of the solid squaraine and the final concentration can be seen in Table S1.

Table S1. Weight-in ($m_{\text{squaraine}}$), added solvent volume (V_{solvent}) and resulting concentration ($c_{\text{stock solution}}$) of the stock solution of **(*S*,*S*)-bCi-BtSQ**. c_{sample} represents the final concentration of the measured sample after diluting 50 µL stock solution with 2950 µL of the desired solvent or solvent mixture.

$m_{\text{squaraine}}$ / mg	V_{solvent}	$c_{\text{stock solution}}$ / 10^{-4} M	c_{sample} / µM
3.79	25 mL CH_2Cl_2	2.31	3.85

The stock solution as well as all used solvents and solvent mixtures were prepared and stored at 19 °C for 1 days before use. For the measurement, 50 µL of the stock solution was diluted with 2950 µL of the desired solvent or solvent mixture and transferred after good mixing with a pipette to a 10 mm glass cuvette (final concentration is given in Table S1). Samples prepared in this manner were immediately measured unless otherwise described. For each measurement a baseline correction was performed by referencing to the solvent/solvent mixture used at the same conditions.

For determination of the extinction coefficient ϵ, a dilution series with a total of six different samples of known concentrations were prepared based on the stock solution. The absorbance from each sample was measured at the peak maxima of 672.5 nm. From this dilution series (detailed information and exact concentrations are given in Table S2) the extinction coefficient could be calculated to $\epsilon = 237000\ \mathrm{M^{-1}cm^{-1}}$ according to the *Lambert-Beer Law* from a linear regression, see Figure S4. Compared to other documented values for squaraines, this value is smaller but is in the range of other benzothiazole-derived squaraines.[5,6]

Table S2. Detailed information about the preparation of the dilution series of **(*S*,*S*)-bCi-BtSQ** for the determination of the extinction coefficient ϵ. With volume and origin of the squaraine solution (V_{SQ}), the added dichloromethane volume ($V_{\mathrm{CH_2Cl_2}}$), the total volume (V_{total}) and the final concentration of the sample (c_{final}) as well as the dilution factor (DF).

Sample	V_{SQ} / µL	from	$V_{\mathrm{CH_2Cl_2}}$ / µL	V_{total} / µL	DF	c_{final}
1	240	stock solution	11760	12000	0.020	$4.62 \cdot 10^{-6}$
2	2400	sample 1	600	3000	0.800	$3.69 \cdot 10^{-6}$
3	1800	sample 1	1200	3000	0.600	$2.77 \cdot 10^{-6}$
4	1200	sample 1	1800	3000	0.400	$1.85 \cdot 10^{-6}$
5	600	sample 1	2400	3000	0.200	$9.23 \cdot 10^{-7}$
6	60	sample 1	2940	3000	0.020	$9.23 \cdot 10^{-8}$

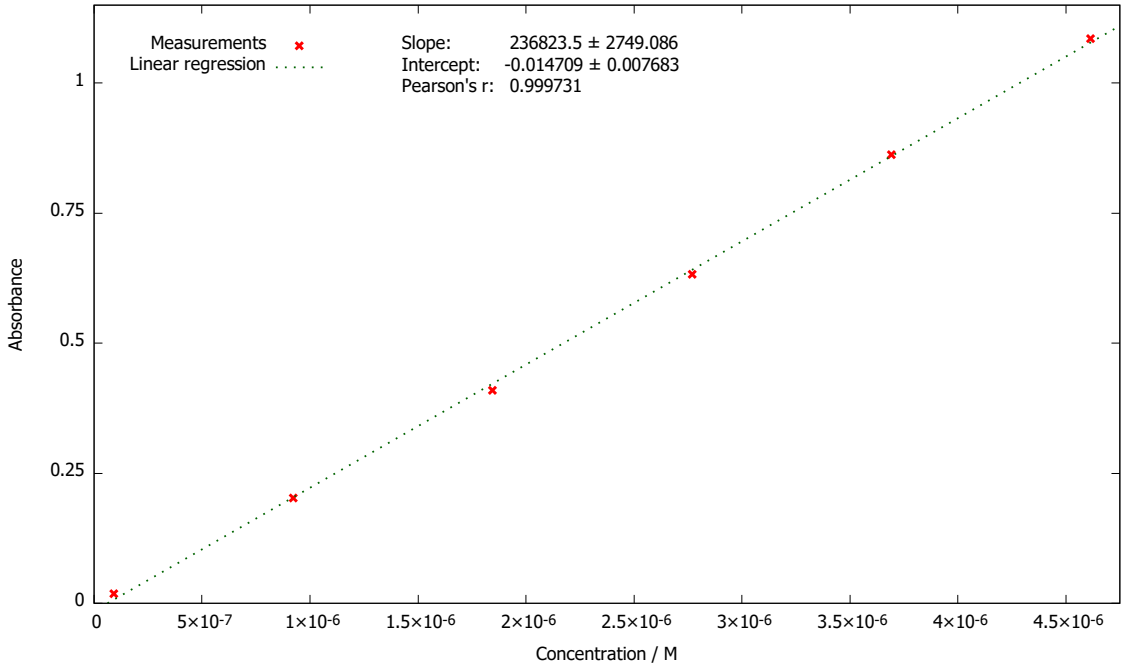


Figure S4. Measured absorbance at the peak maxima of 672.5 nm vs. concentration (red crosses). According to the *Lambert-Beer Law*, the extinction coefficient could be calculated to $\epsilon = 237000\ \mathrm{M^{-1}cm^{-1}}$ via linear regression (dotted green line).

3.3. Light-Induced Decomposition in Chloroform Solution

Unfortunately, a light-induced decomposition of **(*S*,*S*)-bCi-BtSQ** in a chloroform solution was observed. As shown in Figure S5, the absorbance band of **(*S*,*S*)-bCi-BtSQ** completely vanished within 4 hours in favor of an unknown side product with an absorbance band at around 440 nm. This decomposition process could be stopped entirely and preserved in the current state when the sample was kept under light exclusion. The initial idea of a photooxidation of the sulphur with the elemental oxygen present in the solvent could not be confirmed by ESI(+) mass spectroscopy. According to the mass spectrum of the decomposed compound, only one signal with $m/z = 276.178$ in a significant intensity occurred. This signal could be assigned to $[\mathrm{C_{17}H_{26}NS}]^{\cdot+}$, a citronellyl

functionalized benzothiazole radical ion species. This unusual behavior was only observed in the stock solution and could not be observed when stored as solid or spin-coated thin films, which both have good shelf life similar to other squaraines. However, photodegradation by UV light in solution has also been documented for anilino SQs.[7]

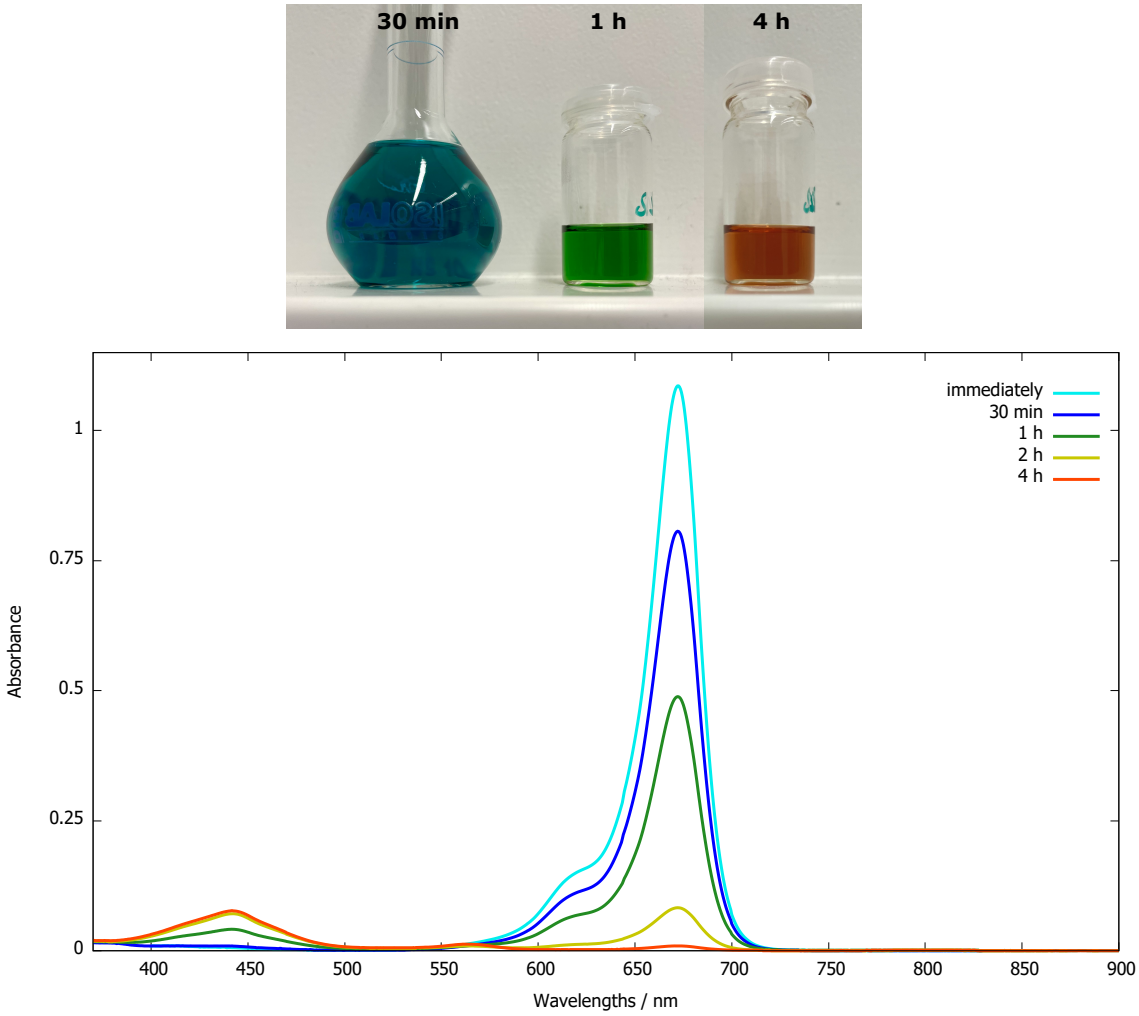


Figure S5. Photos document the Visual change of the **(*S*,*S*)-bCi-BtSQ** stock solution over time when exposed to light (top) and the corresponding absorbance spectra (bottom).

4. Additional Thin Film Absorbance and CD Spectra

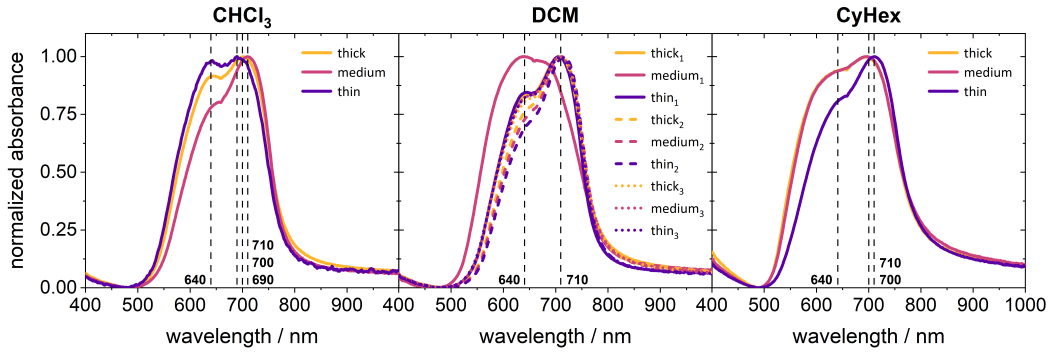


Figure S6. Normalized absorbance spectra of as-cast **(*S*,*S*)-bCi-BtSQ** thin films, which were spin-coated in three different layer thicknesses and from three different solvents are shown. The thickness variation was achieved using different spincoating parameters: "thin" = 4000 rpm acceleration 4000 rpm/sec; "medium" = 3000 rpm acceleration 1000 rpm/sec; "thick" = 2000 rpm acceleration 400 rpm/sec. **Left:** Thin films were spin-coated from $CHCl_3$. The spectra exhibit two features: the primary absorbance around 700 nm, which varies slightly by $\pm$ 10 nm depending on the film thickness. The signature at 640 nm appears as a shoulder for medium-thickness films but is almost equal in intensity to the main peak for thin and thick films. This demonstrates the critical influence of layer thickness / spin-coating parameters on the resulting thin film. **Middle:** Thin films were spin-coated from DCM. The subscripts denote different batches of thin films. All batches and thicknesses display coherence, with the main peak at 710 nm and a shoulder at 640 nm. The only anomaly observed is the medium thickness from the first batch, see Figure S7 for further details. **Right:** Thin films were spin-coated from CyHex. The thick and medium films are well-aligned with each other, showing a main peak at 700 nm and a shoulder at 640 nm. Compared to the thinnest film, the shoulder is more pronounced. Additionally, the main peak of the thinnest film is slightly red-shifted by 10 nm. Overall, all solvents resulted in as-cast layers with similar spectral profiles typical for condensed but not specifically aggregated molecules. However, the layers obtained from CyHex systematically showed broader spectra. This may be attributed to the slower evaporation rate of CyHex, leading to a more ordered structure in the layers compared to those from faster evaporating chlorinated solvents, as evidenced by the anisotropic nature of the CyHex thin film.

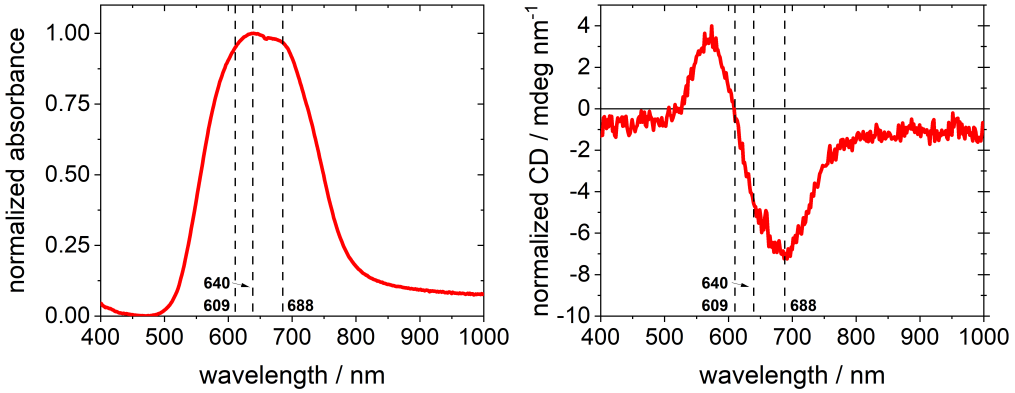


Figure S7. Normalized absorbance (left) and thickness normalized CD (right) spectra of a DCM-processed layer using "medium" spincoating parameters. Despite identical conditions, equipment, and solutions, only this sampleshowed a CD signal without thermal annealing. The bisignate shape with a zero crossing at 609 nm indicates a classical Frenkel exciton, i.e. the formation of an H- or J-aggregate. The absorbance spectrum differs from other DCM samples, Figure S6 middle, with a shift in aspect ration towards a broad absorbance maximum at around 640 nm and a blue-shifted shoulder at around 688 nm. Since this sample could not be reproduced, we refrain from further discussion.

5. Mueller Matrix Polarimetry – Selected Differential Mueller Matrices

Recorded were normalized partial Mueller matrices ($m_{11} = 1$, last row missing) in normal incidence transmission with a J.A. Woollam M2000-DI ellipsometer. The complete Mueller matrix $\mathbf{M}$ was reconstructed assuming non-depolarizing samples using an algebraic method.[8] The CD values were obtained according to CD $= (l_{14} + l_{41})/2$ from the elements of the differential Mueller matrix $\mathbf{L} = \ln(\mathbf{M})$.

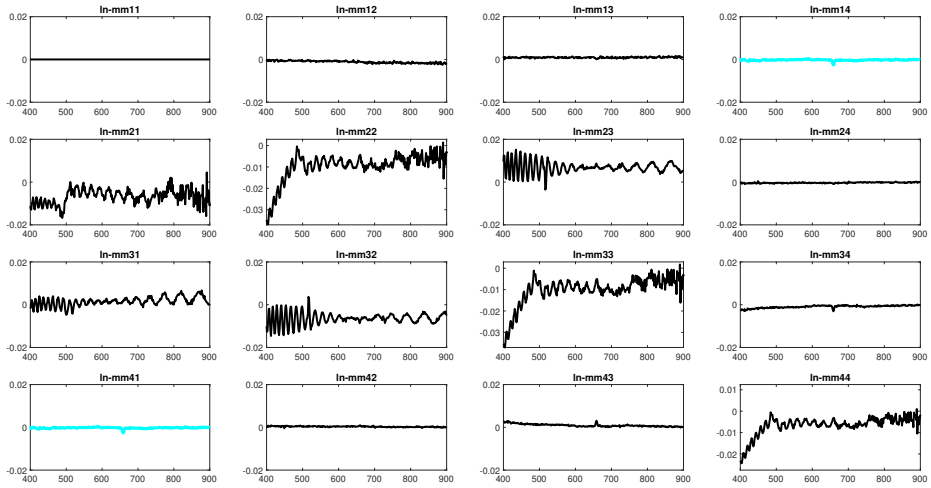


Figure S8. Calculated differential Mueller matrix of **(*S*,*S*)-bCi-BtSQ** spincoated from chloroform without subsequent annealing (as-cast). x-axes: wavelength in nanometer; y-axes: signal in radians.

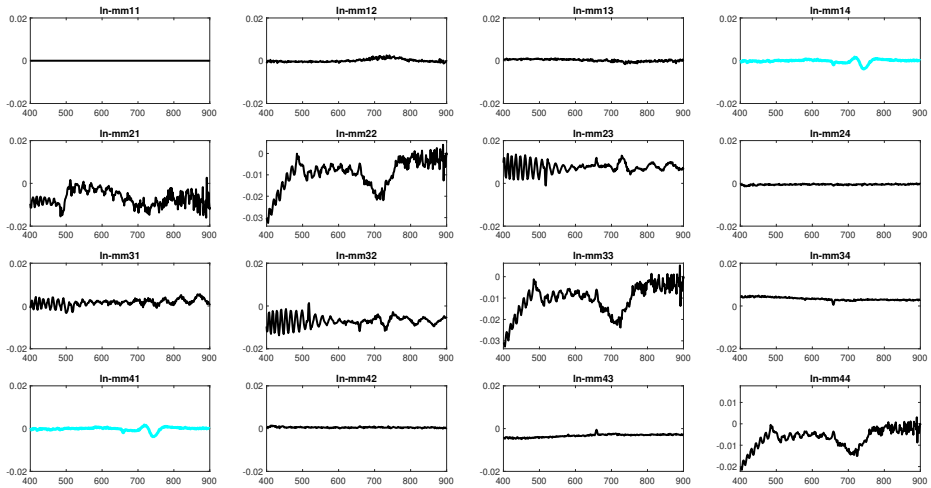


Figure S9. Calculated differential Mueller matrix of **(*S*,*S*)-bCi-BtSQ** spincasted from chloroform with subsequent annealing at 90 °C for 30 min. x-axes: wavelength in nanometer; y-axes: signal in radians.

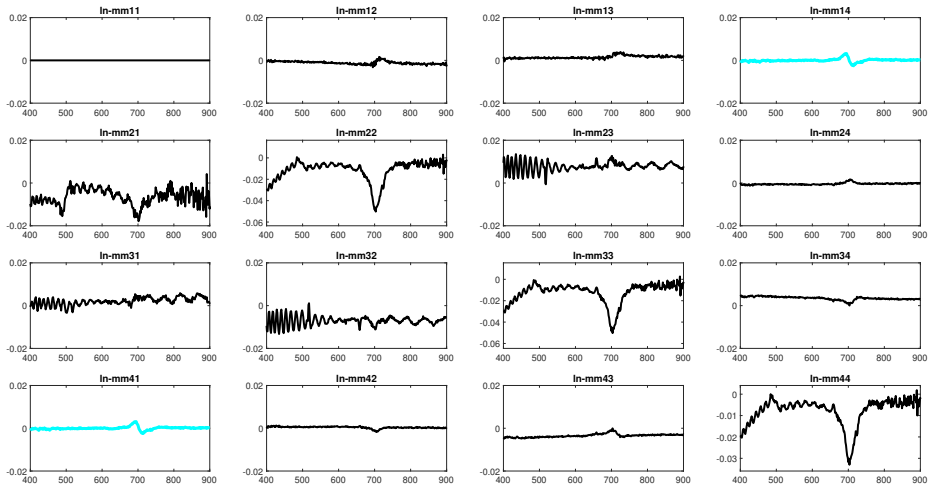


Figure S10. Calculated differential Mueller matrix of **(*S*,*S*)-bCi-BtSQ** spincasted from chloroform with subsequent annealing at 135 °C for 30 min. x-axes: wavelength in nanometer; y-axes: signal in radians.

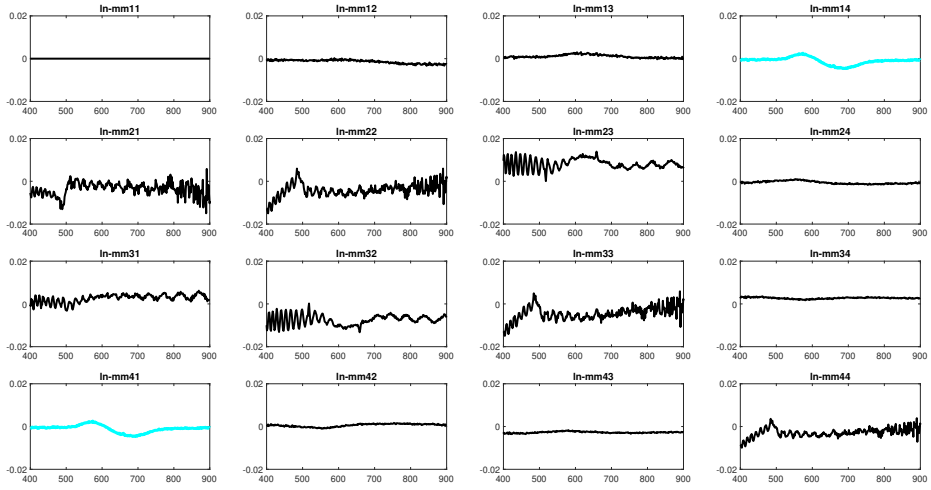


Figure S11. Calculated differential Mueller matrix of **(*S*,*S*)-bCi-BtSQ** spincasted from dichloromethane without subsequent annealing (as-cast). x-axes: wavelength in nanometer; y-axes: signal in radians.

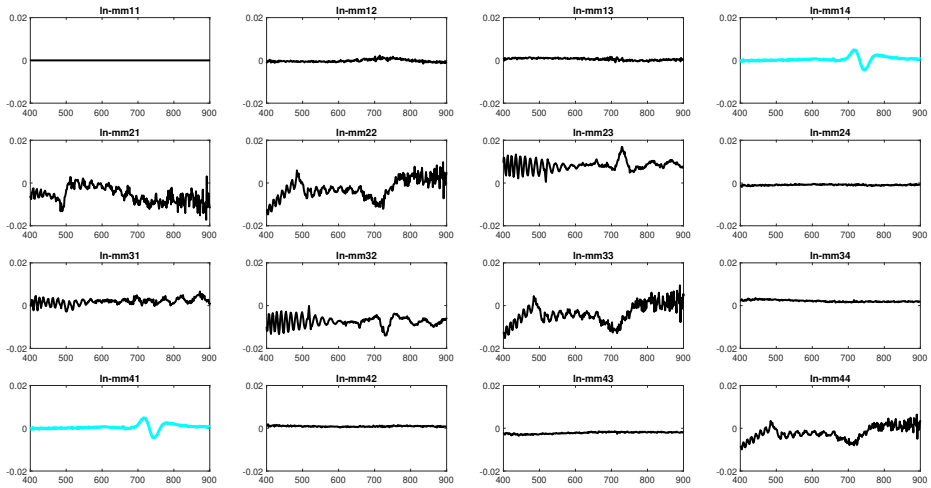


Figure S12. Calculated differential Mueller matrix of ***(S,S)*-bCi-BtSQ** spincasted from dichloromethane with subsequent annealing at 90 °C for 30 min. x-axes: wavelength in nanometer; y-axes: signal in radians.

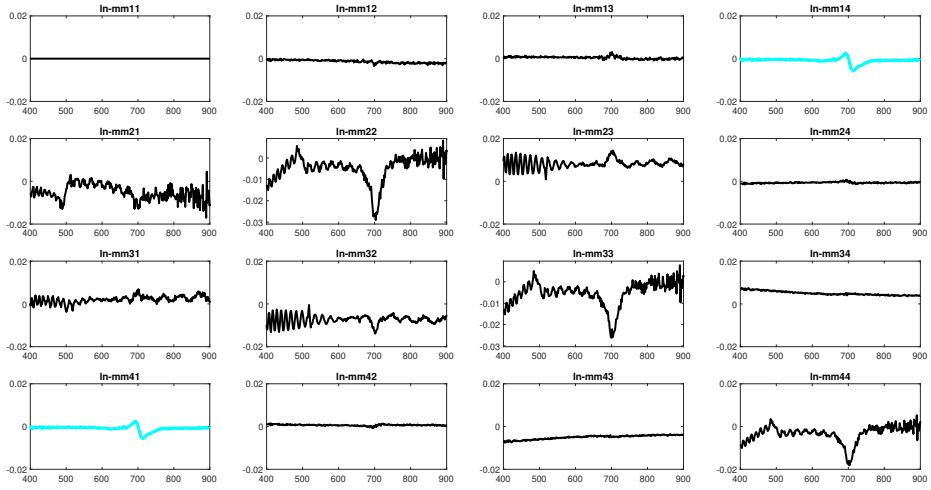


Figure S13. Calculated differential Mueller matrix of ***(S,S)*-bCi-BtSQ** spincasted from dichloromethane with subsequent annealing at 135 °C for 30 min. x-axes: wavelength in nanometer; y-axes: signal in radians.

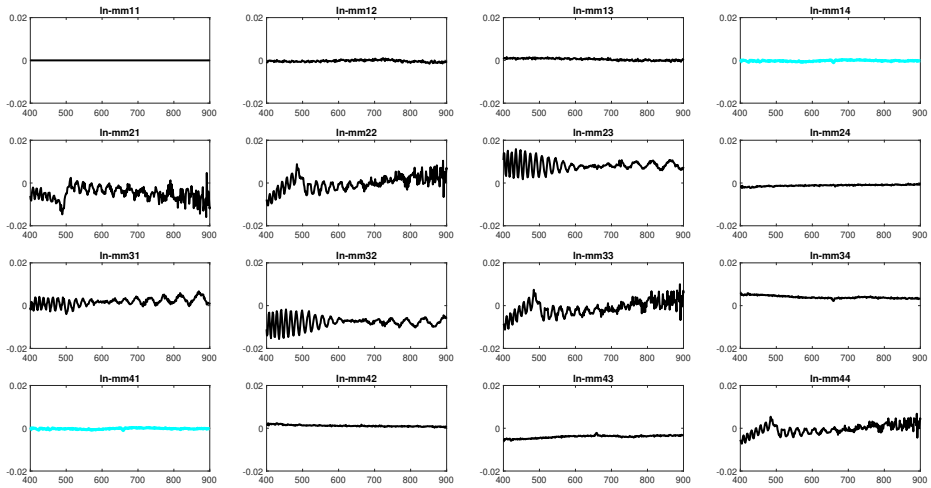


Figure S14. Calculated differential Mueller matrix of **(*S*,*S*)-bCi-BtSQ** spincasted from CyHex (cyclohexane:dichloromethane mixture, 1:1, *v*:*v*) without subsequent annealing (as-cast). x-axes: wavelength in nanometer; y-axes: signal in radians.

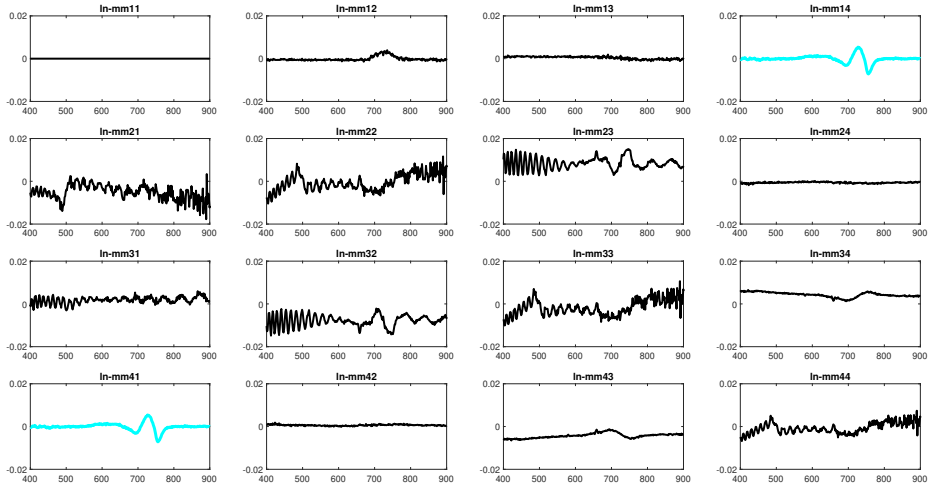


Figure S15. Calculated differential Mueller matrix of **(*S*,*S*)-bCi-BtSQ** spincasted from CyHex (cyclohexane:dichloromethane mixture, 1:1, *v*:*v*) with subsequent annealing at 90 °C for 30 min. x-axes: wavelength in nanometer; y-axes: signal in radians.

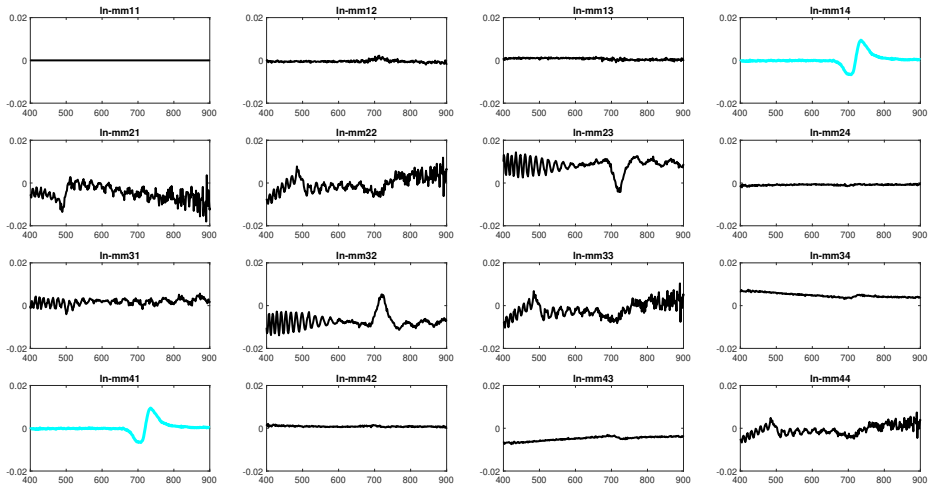


Figure S16. Calculated differential Mueller matrix of **(*S*,*S*)-bCi-BtSQ** spincasted from CyHex (cyclohexane:dichloromethane mixture, 1:1, *v*:*v*) with subsequent annealing at 135 °C for 30 min. x-axes: wavelength in nanometer; y-axes: signal in radians.

6. NMR and Mass Spectra

6.1. NMR spectra

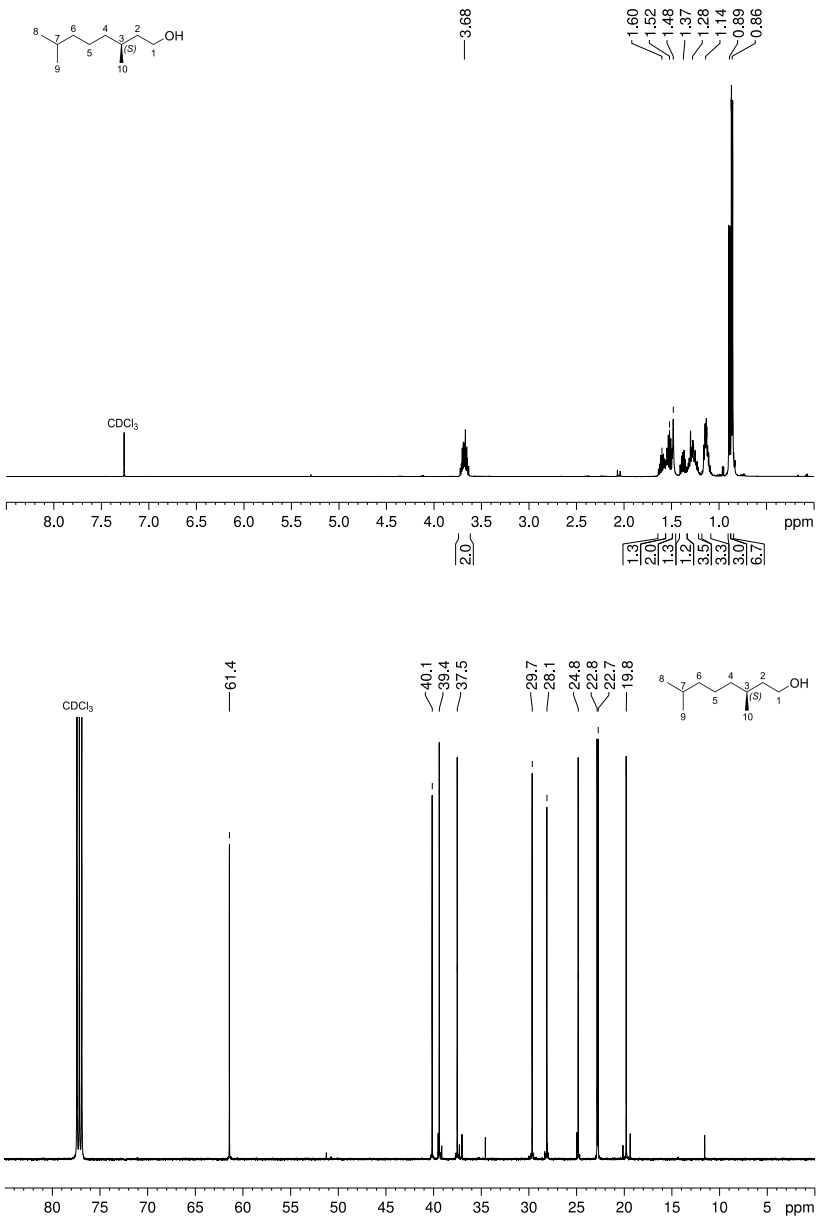


Figure S17. ^{1}H- (top, 500 MHz) and ^{13}C-NMR (bottom, 125 MHz) spectrum of (3*S*)-dihydrocitronellol; $CDCl_3$, 298 K.

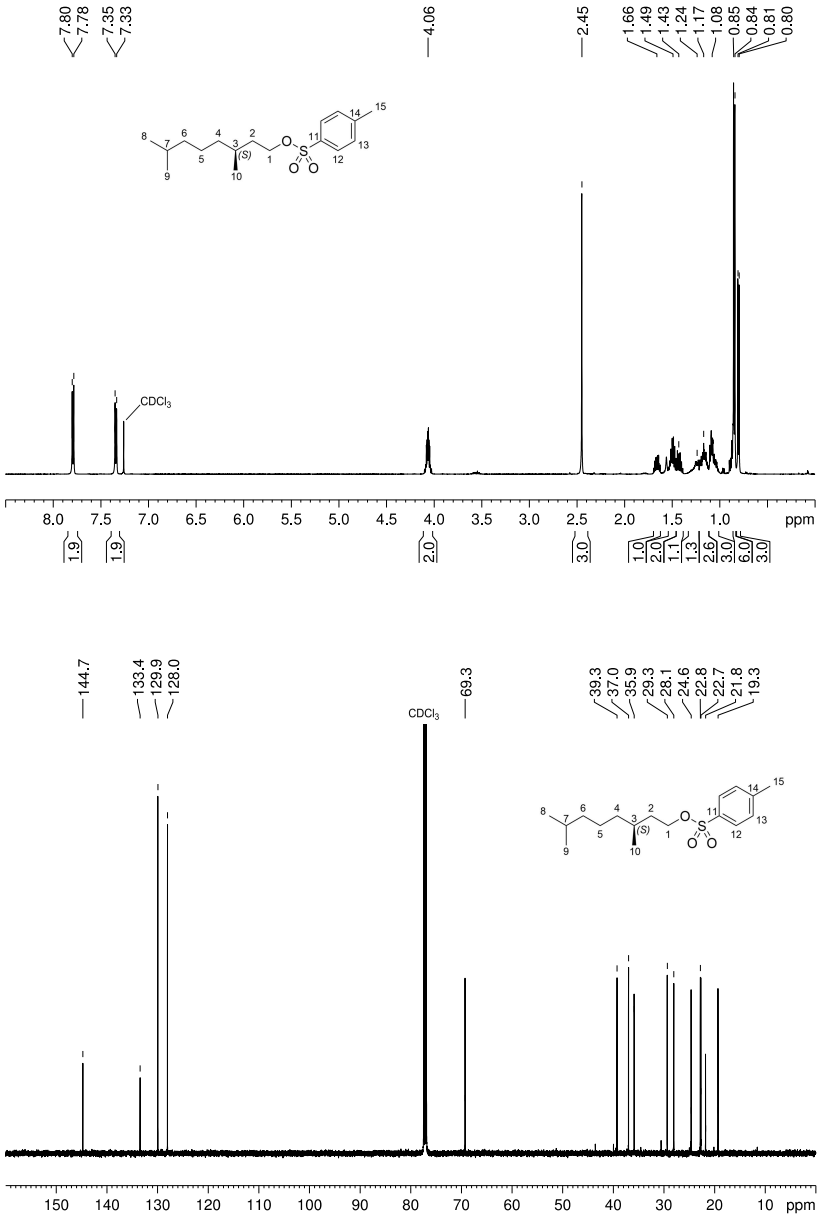


Figure S18. ^{1}H- (top, 500 MHz) and ^{13}C-NMR (bottom, 125 MHz) spectrum of (3*S*)-3,7-dimethyloctyl-p-toluolsulfonate; $CDCl_3$, 298 K.

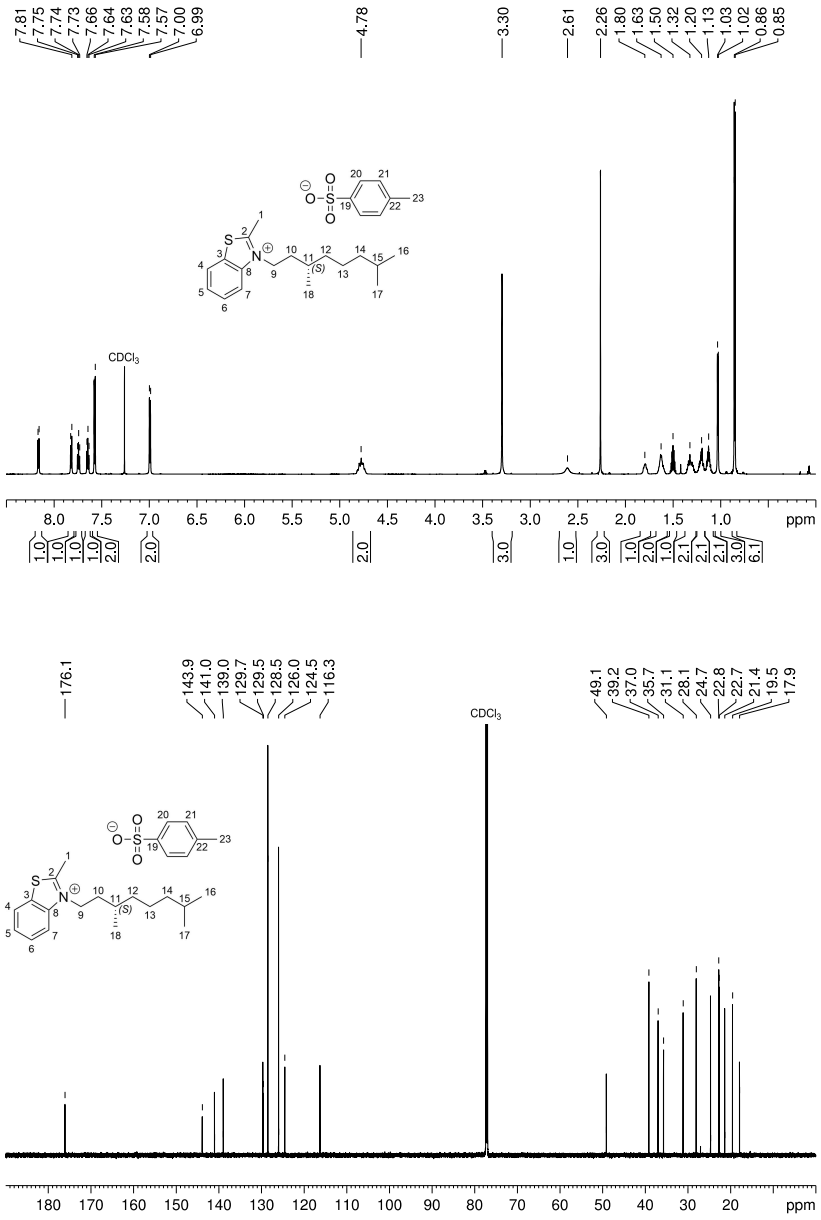


Figure S19. ^{1}H- (top, 700 MHz) and ^{13}C-NMR (bottom, 176 MHz) spectrum of **(*S*)-Ci-Bt**; $CDCl_3$, 298 K.

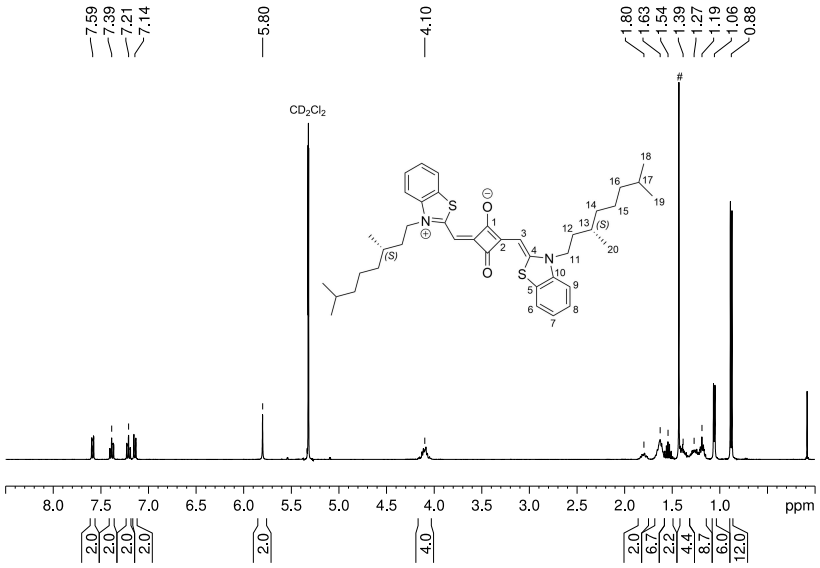


Figure S20. ^{1}H-NMR spectrum of **(*S*,*S*)-bCi-BtSQ**; CD_2Cl_2, 400 MHz, 298 K. The signal denoted with an "#" corresponds to cyclohexane (C_6H_{12}) - see Chapter 3.1.

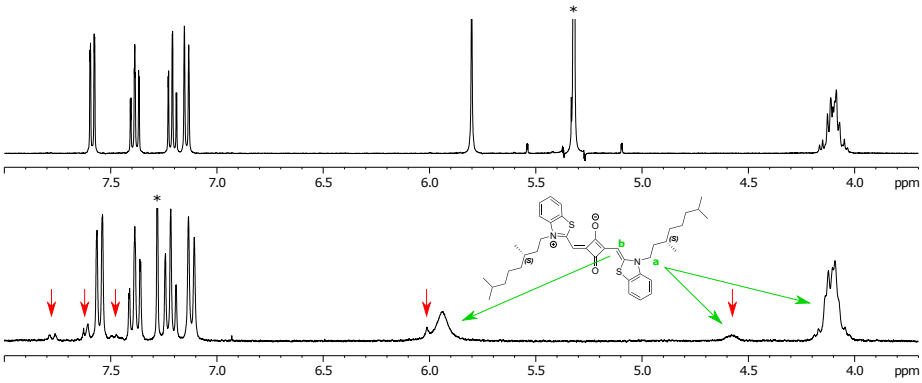


Figure S21. ^{1}H-NMR spectrum section of **(*S*,*S*)-bCi-BtSQ** in CD_2Cl_2 (top) and $CDCl_3$ (bottom) from the very same sample. The deuterated solvent signals are marked with an "*". The signals denoted with the red arrows are assumed to be the protonated **(*S*,*S*)-bCi-BtSQ** form by $CDCl_3$.

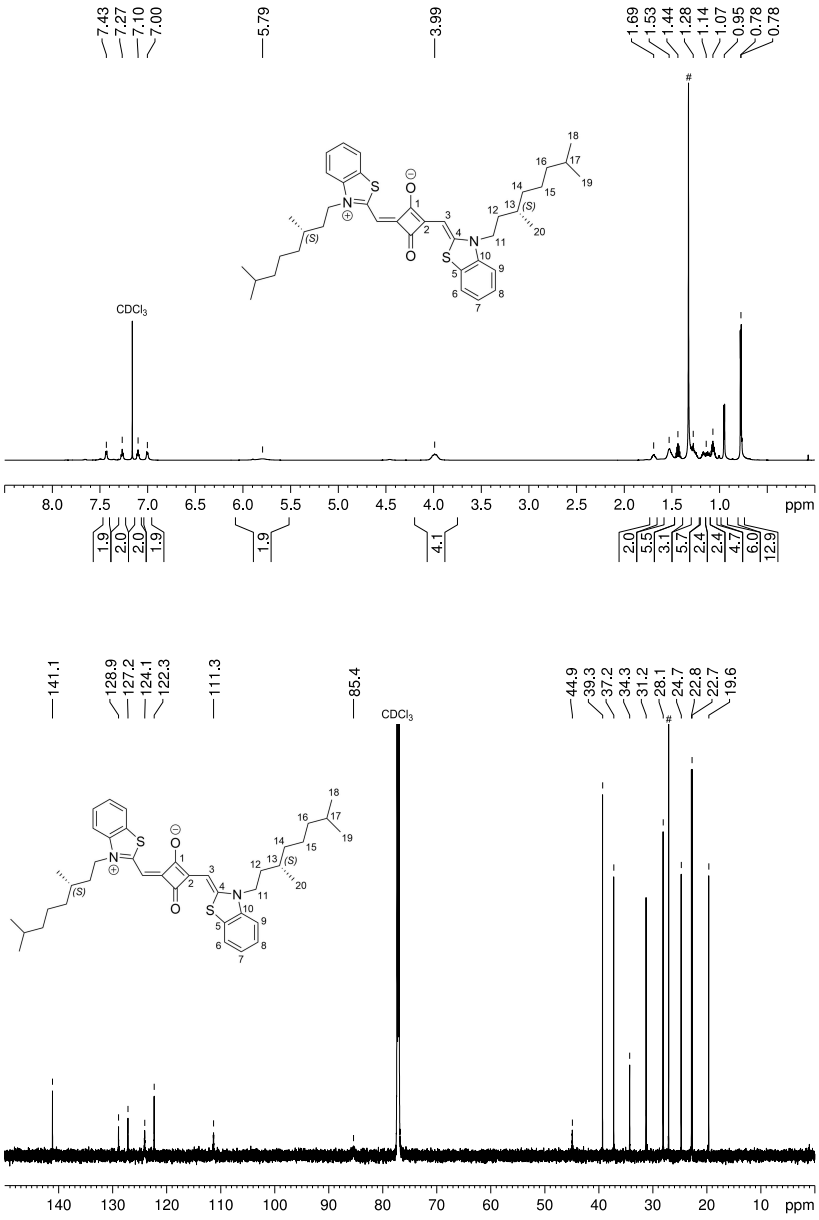


Figure S22. ^{1}H- (top, 700 MHz) and ^{13}C-NMR (bottom, 176 MHz) spectrum of **(*S*,*S*)-bCi-BtSQ**; $CDCl_3$, 298 K. The signal denoted with an "#" corresponds to cyclohexane (C_6H_{12}) - see Chapter 3.1.

6.2. Mass spectra

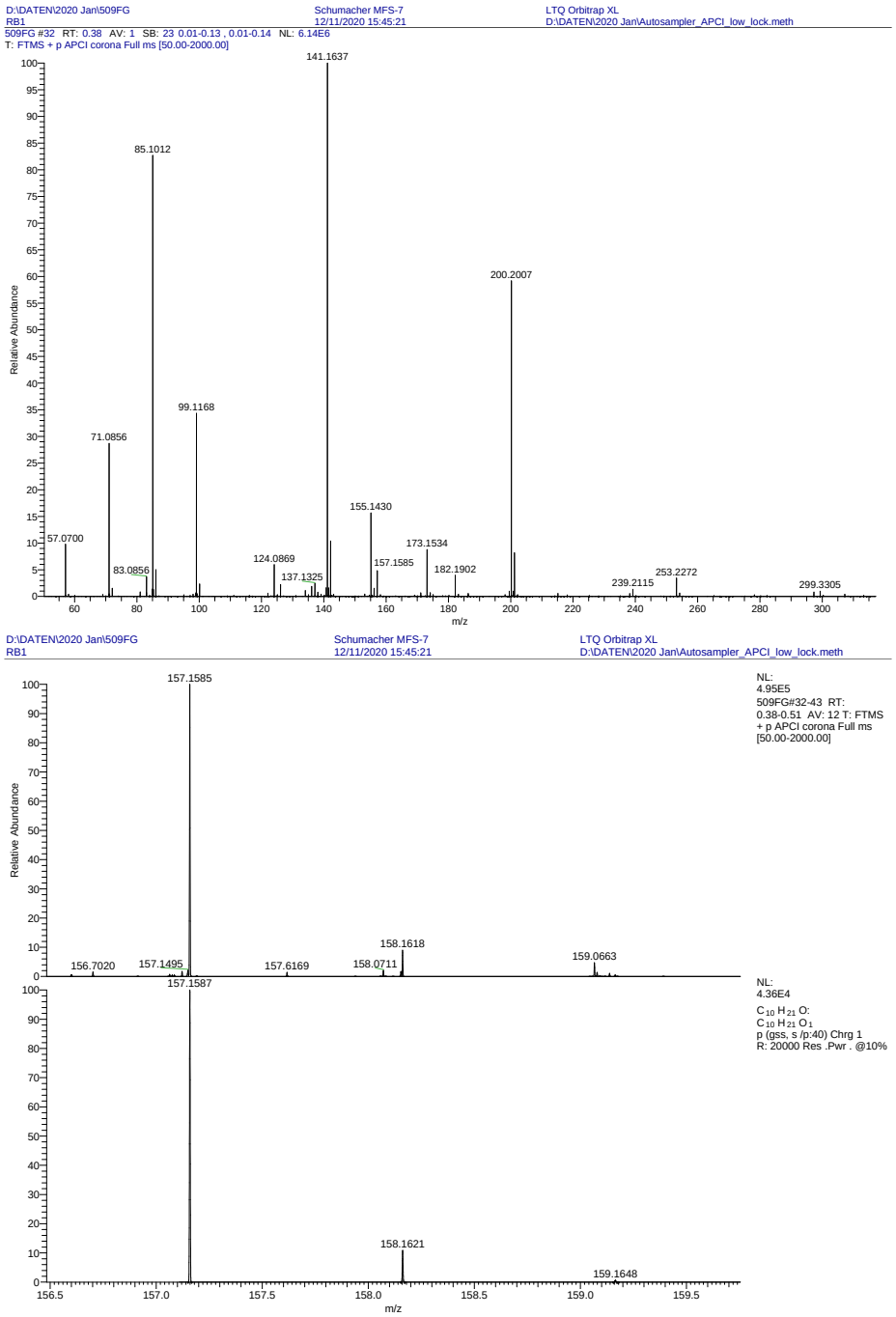


Figure S23. APCI Mass spectra of (3*S*)-dihydrocitronellol.

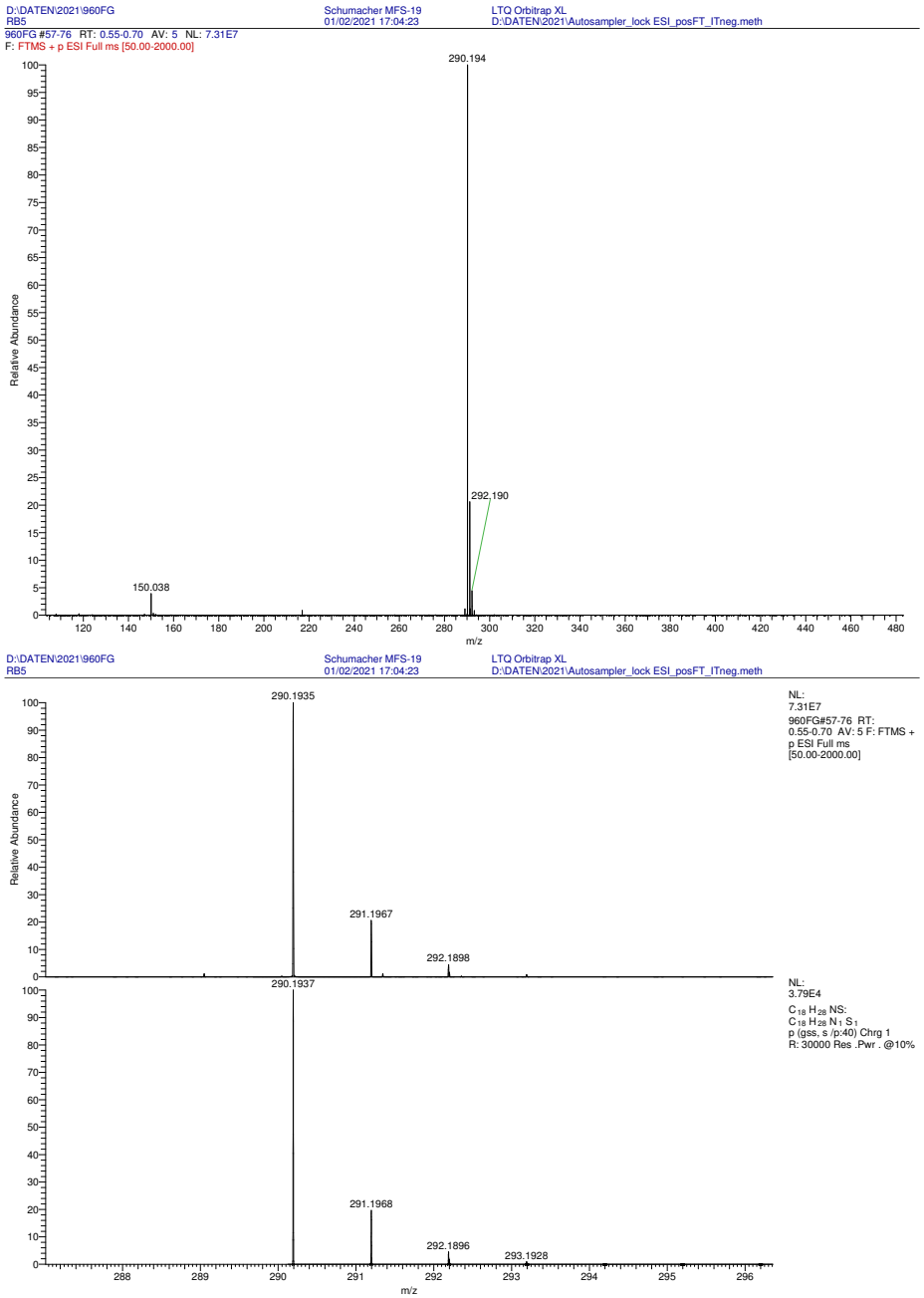


Figure S24. ESI(+) Mass spectra of **(*S*)-Ci-Bt**.

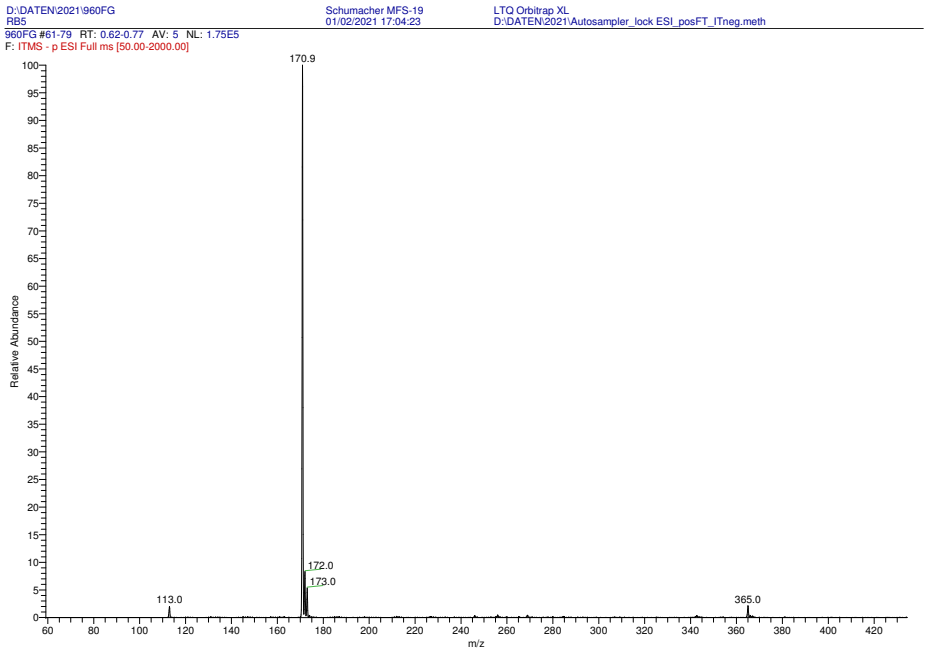


Figure S25. ESI(-) Mass spectra of **(*S*)-Ci-Bt**.

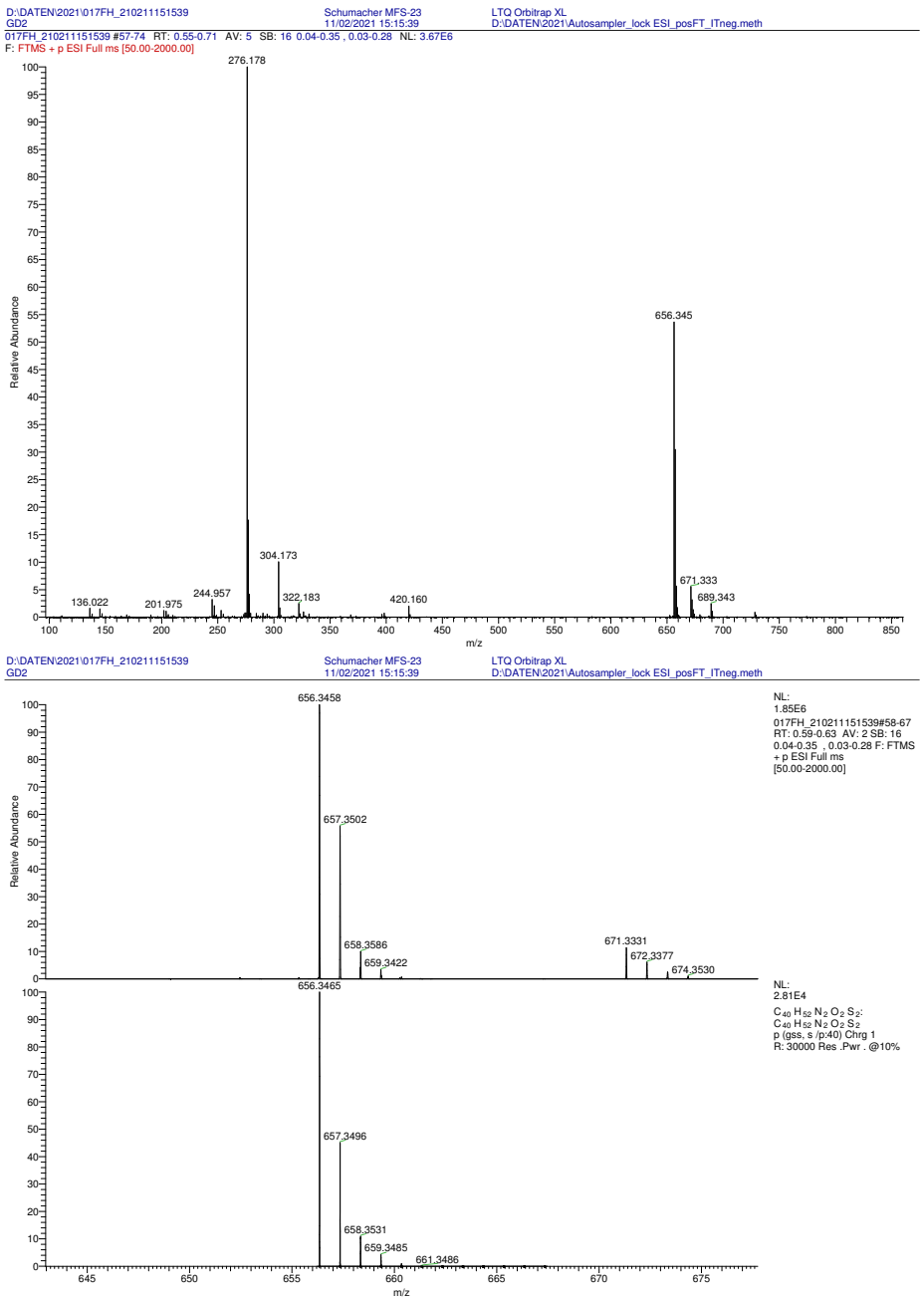


Figure S26. ESI(+) Mass spectra of **(*S*,*S*)-bCi-BtSQ**.

References

[1] E. Freytag, L. Kreimendahl, M. Holzapfel, J. Petersen, H. Lackinger, M. Stolte, F. Würthner, R. Mitric, C. Lambert, *The Journal of Organic Chemistry* **2023**, *88*, 10777.

[2] K. Momma, F. Izumi, *J. Appl. Crystallogr.* **2011**, *44*, 1272.

[3] V. Stamentović, D. Collado, E. Perez-Inestrosa, *Spectrochim. Acta, Part A* **2022**, *267*, 120546.

[4] U. Mayerhöffer, M. Gsänger, M. Stolte, B. Fimmel, F. Würthner, *Chemistry - A European Journal* **2013**, *19*, 218.

[5] D. Giavazzi, M. F. Schumacher, L. Grisanti, M. Anzola, F. D. Maiolo, J. Zablocki, A. Lützen, M. Schiek, A. Painelli, *Journal of Materials Chemistry C* **2023**, *11*, 8307.

[6] K. Ueji, S. Ichimura, Y. Tamaki, K. Miyamura, *CrystEngComm* **2014**, *16*, 10139.

[7] A. K. Kędziera, M. Ziegler-Borowska, D. Chełminiak, P. Kuchnicki, H. Kaczmarek, *J. Photochem. Photobiol., A* **2016**, *318*, 77.

[8] O. Arteaga, R. Ossikovski, *Journal of the Optical Society of America A* **2019**, *36*, 416.

APPENDIX D

A marvel of chiral squaraine aggregates: chiroptical spectra beyond the exciton model

D. Giavazzi,[‡a] M. F. Schumacher,[‡b] L. Grisanti,[c] M. Anzola,[a] F. Di Maiolo,[a] J. Zablocki,[b] A. Lützen,[b] M. Schiek,[d] A. Painelli[a]

Received: December 31, 2022
Published online: May 15, 2023

Reprinted with permission[e] from:
D. Giavazzi, M. F. Schumacher, L. Grisanti, M. Anzola, F. D. Maiolo, J. Zablocki, A. Lützen, M. Schiek, and A. Painelli, "A marvel of chiral squaraine aggregates: chiroptical spectra beyond the exciton model," *Journal of Materials Chemistry C* **2023**, *11* (24), 8307, doi: 10.1039/D2TC05555D
– Copyright ©Journal of Materials Chemistry C, The Royal Society of Chemistry 2023.

Own contributions:

- Synthesis and purification of the investigated molecules as well as performing analytical data (NMR, MS and EA)
- Performing and evaluating the experimental spectroscopic measurements (UV/Vis and CD)
- Interpretation of the results
- Writing of the manuscript

[‡] These authors contributed equally to this work.
[a] Department of Chemistry, Life Science and Environmental Sustainability, Parma University, Parco Area delle Scienze 17/A, 43124 Parma, Italy
[b] Kekulé-Institute for Organic Chemistry and Biochemistry, University of Bonn, Gerhard-Domagk-Str. 1, D-53121 Bonn, Germany
[c] Division of Theoretical Physics, Ruđer Bošković Institute, Bijenička cesta 54, 10000 Zagreb, Croatia
[d] Center for Surface- and Nano-Analytics (ZONA), Institute for Physical Chemistry (IPC) and Linz Institute for Organic Solar Cells (LIOS), Johannes Kepler University, Altenberger Str. 69, A-4040 Linz, Austria.
[e] Permission requests to reuse material from this chapter should be directed to The Royal Society of Chemistry

Journal of Materials Chemistry C

ROYAL SOCIETY OF CHEMISTRY

PAPER

View Article Online
View Journal | View Issue

Check for updates

Cite this: *J. Mater. Chem. C*, 2023, **11**, 8307

A marvel of chiral squaraine aggregates: chiroptical spectra beyond the exciton model†

Davide Giavazzi, ‡[a] Marvin F. Schumacher, ‡[b] Luca Grisanti, [c] Mattia Anzola,[a] Francesco Di Maiolo, [a] Jennifer Zablocki,[b] Arne Lützen, [b] Manuela Schiek *[d] and Anna Painelli *[a]

Squaraines are quadrupolar molecular dyes forming aggregates with remarkable structure-correlated excitonic properties within the visible to near-infrared spectral range. Upon chiral functionalization a chiroptical response such as circular dichroism is an additional spectroscopic feature. We provide a combined experimental and theoretical survey on chiral aggregates dispersed in a solution of proline-derived anilino squaraines (ProSQs) with varying terminal alkyl chain length (C3 to C12 and C16) directing the aggregation. Different aggregation scenarios with characteristic spectroscopic features appear, intricately depending on the alkyl chain length: concomitant blue- and red-shifted spectroscopic signatures both within the linear and circular absorption for intermediate chain length, and a scenario with dominating blue-shifted signatures for shorter and longer alkyl chain length. Molecular dynamics (MD) simulations on the aggregate structure return the opposite handedness suggesting kinetic control in the experiments. Two modified essential state models (ESM) are applied to calculate the optical spectra with prescribed geometric parameters: a model accounting for just electrostatic intermolecular interactions (ESM-ES) suggests two concomitant aggregates to explain the simultaneous blue- and red-shifted spectral signatures while a model including intermolecular charge transfer (ESM-CT) returns both features for a single aggregate. Due to the complexity of the calculation this is the first time an explicit expression for calculating circular dichroism including intermolecular charge transfer is rendered. However, the ESM-CT model is still limited to tetramers, so finite size effects such as disorder are not fully captured. This could be the reason why the ESM-CT does not reproduce the scenario with dominant blue-shifted spectral signatures. We demonstrate that a dimeric model is sufficient to describe linear absorption but fails for chiroptical properties. Furthermore, a superlinear amplification of circular dichroism intensity with increasing aggregate size is noted for both models. This adds value to the application potential for chiral squaraine aggregates.

Received 31st December 2022,
Accepted 15th May 2023

DOI: 10.1039/d2tc05555d

rsc.li/materials-c

Published on 18 May 2023. Downloaded on 6/27/2025 6:42:25 PM.

10th Anniversary Statement

It is a pleasure to contribute a paper to the special issue dedicated to the 10th anniversary of the *Journal of Materials Chemistry C*, a journal that offers a vibrant publication environment for outstanding papers in materials science. The journal has a wide reader audience, reaching chemists and physicists, as well as *bona fide* materials scientists. A pool of distinguished authors and reviewers contributes to maintaining high standards. Interactions with Editors are easy and rewarding in several respects. Overall, our experiences with the *Journal of Materials Chemistry C* as authors, reviewers and special issue Editors have been pleasant and fruitful. Many happy returns!

[a] *Department of Chemistry, Life Science and Environmental Sustainability, Parma University, Parco Area delle Scienze 17/A, 43124 Parma, Italy. E-mail: anna.painelli@unipr.it*
[b] *Kekulé-Institute for Organic Chemistry and Biochemistry, University of Bonn, Gerhard-Domagk-Str. 1, D-53121 Bonn, Germany*
[c] *Division of Theoretical Physics, Ruđer Bošković Institute, Bijenička cesta 54, 10000 Zagreb, Croatia*
[d] *Center for Surface- and Nano-Analytics (ZONA), Institute for Physical Chemistry (IPC) and Linz Institute for Organic Solar Cells (LIOS), Johannes Kepler University, Altenberger Str. 69, A-4040 Linz, Austria. E-mail: manuela.schiek@jku.at*
† Electronic supplementary information (ESI) available. See DOI: https://doi.org/10.1039/d2tc05555d
‡ These authors contributed equally to this work.

View Article Online

Paper

Journal of Materials Chemistry C

Published on 18 May 2023. Downloaded on 6/27/2025 6:42:25 PM.

1 Introduction

Squaraine dyes represent a well known and widely investigated family of organic chromophores with unique spectral properties.[1–10] They are characterized by a rigid inner core, a squaraine ring, with a strong electron affinity and, typically, two equivalent electron-donating groups are attached to the inner core in a centrosymmetric D–A–D structure. Asymmetrically substituted squaraines also have interesting properties,[11,12] but will not be discussed here. So called quadrupolar DAD (or ADA) dyes are often unstable towards symmetry breaking either in the excited state (class I quadrupolar dyes) or in the ground state (class III quadrupolar dyes), a phenomenon that shows up most clearly in fluorescence or absorption solvatochromism, respectively.[4] Squaraines are the most famous representative of the elusive family of quadrupolar dyes of class II, and resist symmetry breaking in either the ground or excited state, as a result of strong conjugation among the D and A molecular moieties. They show intense, narrow and marginally solvatochromic absorption and fluorescence bands, typically in the red portion of the spectrum, that can be moved to the near infrared region by a judicious choice of the D groups.[13–16] Moreover, at roughly twice the energy of linear absorption, a state is found, dark to linear absorption, but with a large (resonantly enhanced) two photon cross-section.[4] Squaraine dyes are investigated and exploited for NLO applications,[2] bioimaging,[17] biosensing[18] and photodynamic therapy.[19,20] Another interesting applicative field for squaraine dyes is found in solar cells,[21–23] where, however, most interesting results are obtained with squaraine aggregates that show an amazing panchromatic absorbance spectrum.[16,24–31]

Squaraine aggregates are fascinating systems, attracting interest not just for their panchromatic spectrum, but also for amplified NLO responses,[32] and for large chiral responses.[33–35] Modeling squaraine aggregates is challenging as the intertwined role of electrostatic (ES) intermolecular interactions, intra and intermolecular charge transfer (CT) and disorder must be taken into account. In a series of papers,[30,36–38] Spano and Collison first proposed that the panchromatic absorption spectrum of squaraine aggregates is due to intermolecular CT interactions, a hypothesis recently supported by detailed spectroscopic measurements in squaraine crystals.[39] The same hypothesis was very recently challenged in a paper where linear absorption and pump–probe spectra of squaraine aggregates are discussed in the framework of a disordered exciton model.[40]

In this complex and intriguing scenario, we address chiroptical properties of chiral aggregates of squaraine dyes. Specifically, the next chapter describes experimental data collected on a family of anilino squaraine dyes decorated with chiral pendants bearing alkyl chains of different length. The dyes aggregate in solution forming chiral superstructures that, depending on the length of the terminal alkyl chain, show distinctively different behavior. Aggregates of dyes decorated with alkyl chains with intermediate length (from C6 to C10) show two features in the absorbance spectra: the first one at 500–550 nm is located towards the blue with respect to the monomer absorption (at 640 nm) the second one, in the 700–800 spectral region, is strongly red-shifted *vs.* the monomer absorption. Quite interestingly, a bisignated signal appears in the CD spectrum in the proximity of both absorption features. In aggregates formed by dyes with either shorter (C3–C5) or longer (C11, C12, and C16) pendants, instead, the absorption and CD features at long wavelength become extremely weak and almost disappear.

This complex experimental scenario will be discussed adopting an essential state model (ESM) approach,[4] describing each SQ dye in terms of three basis states, leading to a molecular model that reliably describes the spectral properties of the isolated dye.[4,41] A first model for the aggregate, the ESM-ES, is then built accounting just for ES interactions among the dyes, much as in the standard exciton model. In the ESM-ES approach, experimental data can be accounted for in terms of the coexistence of H and J aggregates in the system.

Following the original suggestion from Spano and Collison,[30,36–38] the model is extended, in the ESM-CT version, to also account for intermolecular CT interactions, leading to the highly non-trivial problem of calculating CD spectra in an aggregate with electrons delocalized among different molecular units. Towards this aim, we release the spinless-Fermion approximation adopted by Spano and Collison and propose an explicit expression for the rotational strengths in aggregates with delocalized electrons. To the best of our knowledge, this is the first attempt in this direction. In the ESM-CT approach, the experimental observation of two features in absorption spectra and two exciton couplets in CD spectra can be rationalized accounting for a single aggregate structure, an appealing result, as it does not require the somewhat *ad hoc* hypothesis of two families of aggregates. However, the model cannot easily describe the behavior of systems with short or very long alkylic chains that show a single dominant feature either in absorption or CD spectra.

Extensive molecular dynamics (MD) simulations were run to shed light on these intriguing systems, with somewhat disappointing results: in the process we learned that reliable aggregate structures for these systems may require simulations accounting for a very large number of molecules, with computational efforts well beyond the scope of this work. While we hardly reach a firm conclusion on the structure of the chiral aggregates of squaraine dyes, our discussion sets the basis for a thorough understanding of the physics of chiral aggregates. Moreover, we can definitely exclude the origin of the two bands as related to a Davydov splitting. This result on colloidal aggregates is interesting as it also suggests that the panchromatic spectrum observed in SQ films cannot be ascribed to the Davydov splitting but requires a different explanation.

2 Data and experiment

2.1 Titration experiments

The different proline-derived squaraine dyes (ProSQs), which differ in the terminal alkyl chain length (C3 to C12 and C16),

This journal is © The Royal Society of Chemistry 2023

View Article Online

Published on 18 May 2023. Downloaded on 6/27/2025 6:42:25 PM.

were investigated for their aggregation behavior in poor solvent titration experiments. The general synthesis approach and analytical details are given in the ESI,† and for both enantiomers of C6 and C16 compounds can be found in ref. 34. For a titration experiment, a 2.30×10^{-4} M stock solution of each squaraine in a good solvent, here chloroform, is prepared. Afterwards, 50 μL of the stock solution is diluted by 2950 μL of poor solvent mixtures consisting of methanol with various water concentrations, varying from 0–40%. The colloidal solutions are mixed thoroughly and transferred to a 10 mm quartz cuvette (*Hellma*). UV/Vis transmission measurements were subsequently carried out using a Specord 200 spectrometer (*Analytic Jena*) with 0.5 nm step size and 5 nm s^{-1} scanning speed. Followed immediately by CD-spectroscopic measurements on a J-810 spectro-polarimeter (*JASCO Corporation*) with 1 nm step size, a scanning speed of 200 nm min^{-1}, and a 1 nm bandwidth. An initial measurement of the pure solvent or solvent mixture was used for baseline correction. UV/Vis spectra are shown as absorbance = −log(transmission), which is for (colloidal) solution basically equivalent to absorption. The circular dichroism (CD) spectra are shown as ellipticity in units of milli degree (mdeg) as outputted from the spectro-polarimeter. Note that CD and ellipticity are not the same values but for small quantities ellipticity = CD/2.[35]

2.2 UV/Vis and CD measurements in solution

Experimental absorbance and CD spectra of colloidal (*S,S*)-ProSQ aggregates having an alkyl chain length of C5, C10 and C12 in varying ratios of the poor solvent methanol–water mixture are plotted in Fig. 1. These compounds are representative for the different aggregation regimes. Fig. S1 (ESI†) contains both enantiomers of the C7 compound to illustrate the inverted sign of the CD spectra, but otherwise identical spectral features. The spectra of all other available compounds (C3, C4, C6–C9, C11, C12 and C16) are given in the ESI† in Fig. S2 and S3. The C10 compound has an intermediate alkyl chain length and expresses two pronounced aggregate absorbance bands with two corresponding bisignate CD bands to the same extent, Fig. 1(c) and (d). These aggregate absorbance bands are blue- and redshifted with respect to the monomer absorbance band peaking at 640 nm. Both for the C5 and the C12 compound, the blue-shifted aggregate absorbance and CD features within the green spectral range are dominant, Fig. 1(a), (b), (e) and (f), respectively. The overall aggregation tendency increases with increasing chain length, which is indicated by the reduction of the molecular absorbance band already in the initial pure methanol solvent. Therefore, the predominant expression of blue-shifted spectral features is neither simply correlated with alkyl chain length nor with aggregation tendency. The dissolved molecular compounds do not have a corresponding CD feature since the stereogenic carbon atom is located on the pyrrolidine ring carrying the alkyl chain, and is not conjugated with the chromophoric squaraine backbone. The circular dichroism of the aggregate bands has an excitonic character and arises from the chiral arrangement of the squaraine backbones directed by the chiral alkyl chains.

The two-dimensional representation of absorbance and CD spectra for all (*S,S*)-ProSQ compounds for two selected methanol–water mixing ratios are shown in Fig. 2 to give a better impression of the different aggregation regimes. For a lower water fraction of 4 vol% as plotted in Fig. 2(a) and (b) there is a dominant blue-shifted bisignate CD response for both the shorter (C3 to C5) and the longer (C11, C12, C16) alkyl chain compounds, while the intermediate alkyl chain length (C6 to C10) compounds form a more pronounced red-shifted bisignate CD response. Interestingly, the red-shifted CD

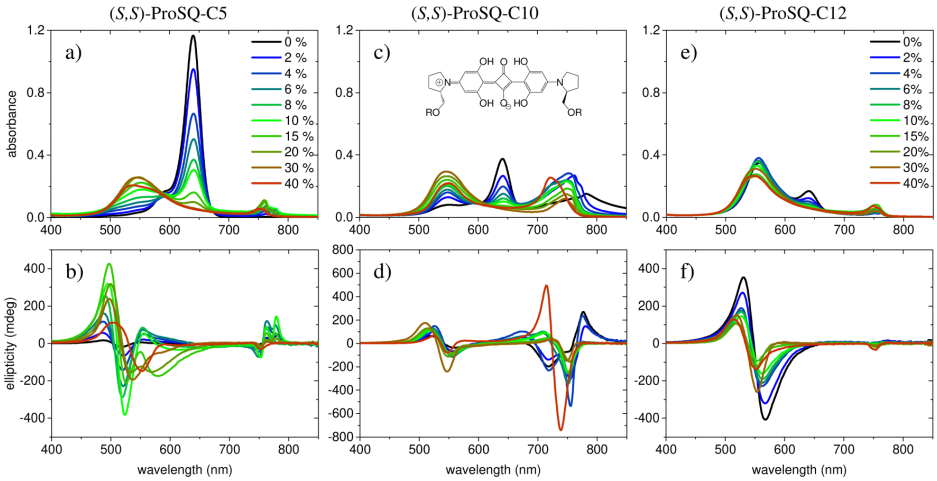


Fig. 1 Experimental UV/Vis absorbance spectra (top row) and corresponding ellipticity spectra (bottom row) for selected (*S,S*)-ProSQ compounds with varying alkyl chain lengths: C5 in (a and b), C10 in (c and d), and C12 in (e and f). The inset in (c) sketches the molecular structure where R denotes the varying alkyl chain. The legend indicates the volume-percentage of water in the methanol–water mixture and applies to all plots.

View Article Online

Published on 18 May 2023. Downloaded on 6/27/2025 6:42:25 PM.

signatures are not smoothly bisignate in shape but express more detailed spectral features. For a higher water fraction of 40 vol% as plotted in Fig. 2(c) and (d) nearly no molecular dissolved compounds are left. The bisignate blue-shifted CD response for the shorter and longer alkyl chain compounds gain signal strength while maintaining the signs of the band, *i.e.* positive at around 520 nm and negative at around 550 nm. The increased share of water in the solvent mixture has certainly more impact on the red-shifted CD feature, and consequently affects the intermediate alkyl chain length compounds more. The red-shifted CD features become less detailed so the spectral width is reduced and the bisignate shape becomes more evident. Additionally, the signs of the bisignate bands appear to be inverted, *i.e.* the most red-shifted band (here at around 750 nm) is negative while the band at around 710 nm is positive.

The absorption spectra of the colloidal suspensions of SQ aggregates shown in Fig. 1 and Fig. S13 (ESI†) share some similarity with the extensively studied spectra of SQ-films.[16,26–31,42] Specifically, much as in the films, our aggregates show absorption features both to the red and to the blue of the monomer band. Our study may then offer some valuable information to shed light on the puzzling photophysics of SQ films. However, a major difference must be highlighted. In films, the absorbance spectrum is extremely broad, suggesting a fairly disordered structure with the coexistence of aggregates with different nature and/or dimension as well as of monomeric species. Our spectra, instead, show much sharper spectral features, suggesting more ordered structures, as also confirmed by the consistency of the spectra obtained from different batches.

The experimental absorbance spectra of our samples show a negligible amount of scattering, indicating the formation of tiny colloids in highly diluted suspensions. Consequently, these colloids could not be dried out on a solid support for microscopic or X-ray diffraction investigations, hindering the possibility to collect reliable experimental data on the aggregate geometry.

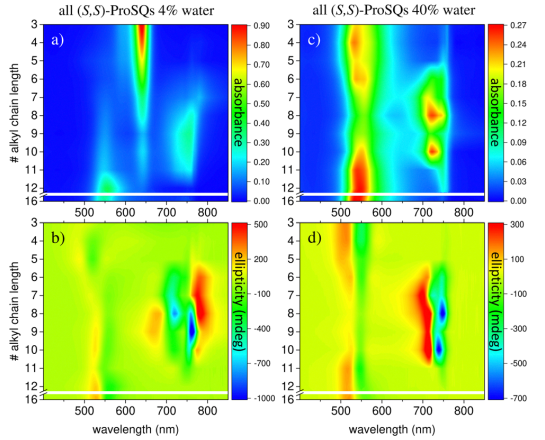


Fig. 2 UV/Vis absorbance spectra (top row) and corresponding ellipticity spectra (bottom row) in a 2D representation of all (*S*,*S*)-ProSQ compounds with varying alkyl chain lengths (C3 to C12 and C16) for two selected volume-percentages of water in the methanol–water: 4% in (a) and (b) and 40% in (c) and (d).

3 Simulations of the spectral properties of aggregates

All molecules of interest have the same chromophoric core, and only differ for the different lengths of the alkylic pendants. The spectral properties of the isolated molecules in the visible region are not affected by the length of the pendants, as best recognized looking at the absorption spectrum, where the monomer absorption is seen in all cases as a narrow band at 640 nm. Similarly, the chiral groups, while instrumental to guide the aggregates into chiral supramolecular structures, do not affect the spectral properties of the isolated (non-aggregated) molecules, that do not show any CD response in the visible spectral region. We will therefore adopt a bottom-up modeling strategy:[32] in this subsection we will define and parametrize a model for the isolated (solvated) molecule, only accounting for the main chromophoric part. In the next two subsections, the molecular model will be exploited to build two concurrent models to describe the interacting dyes in the aggregates.

Low-energy spectral properties of squaraine dyes are well-captured by an ESM approach that only accounts for three electronic states.[4,41] The three basis (diabatic) states correspond to the main resonating structures, a neutral (DAD) state, $|N\rangle$, and two degenerate zwitterionic states (D^+A^-D and DA^-D^+) $|Z_1\rangle$ and $|Z_2\rangle$. The zwitterionic states are separated from the neutral state by an energy gap $2z$ and are coupled to the neutral state by a mixing matrix element $-\tau$. Vibronic coupling is marginally relevant in squaraines, so that, in view of the complexity of the aggregation problem, we will not address it. Polar solvation will not be discussed either, as it does not affect the spectral properties of squaraines that have and maintain a centrosymmetric (hence non-polar) structure both in the ground and excited states.[4] The molecular Hamiltonian reads:

$$\hat{h} = 2z\hat{\rho} - \tau\hat{\sigma} \tag{1}$$

with

$$\begin{aligned} \hat{\rho} &= \sum_{k=1,2} |Z_k\rangle\langle Z_k| \\ \hat{\sigma} &= \sum_{k=1,2} (|N\rangle\langle Z_k| + |Z_k\rangle\langle N|) \end{aligned} \tag{2}$$

Finally, the molecular dipole moment is aligned with the long molecular axis and its magnitude is measured by the operator:

$$\hat{d} = \mu_0(|Z_1\rangle\langle Z_1| - |Z_2\rangle\langle Z_2|) \tag{3}$$

where μ_0 is the equal and opposite permanent dipole moment associated with the zwitterionic forms, $|Z_1\rangle$ and $|Z_2\rangle$.

 This journal is © The Royal Society of Chemistry 2023

View Article Online

Published on 18 May 2023. Downloaded on 6/27/2025 6:42:25 PM.

Accounting for symmetry helps to understand the photophysics of squaraines:[4] the two zwitterionic states can in fact be mixed into a symmetric $|Z_+\rangle$ and an antisymmetric $|Z_-\rangle$ combination. The $|N\rangle$ and $|Z_+\rangle$ states are mixed into a ground $|g\rangle$ and a symmetric excited $|e\rangle$ state, while $|Z_-\rangle$ stays unmixed. The lowest energy excitation $|g\rangle \rightarrow |Z_-\rangle$ is active in one-photon absorption, while the higher energy excitation $|g\rangle \rightarrow |e\rangle$ is seen in two-photon absorption. The model parameters for squaraines can be fixed to best reproduce the position of one and two photon absorption band. Specifically, the one and two photon transition energies $\hbar\omega_c$ = 1.93 eV and $\hbar\omega_e$ = 3.04 eV, respectively,[41] allow us to fix τ = 1.04 eV and z = 0.4 eV. Finally, the experimental transition dipole moment, μ_c = 12.5 D,[41] fixes μ_0 = 20.83 D. This corresponds to a dipole length $a \sim 4.33$ Å, that we assign as the effective length of each D–A arm (*cf.* Fig. 3). We underline that the parametrization of the electronic Hamiltonian against solution data ensures that it implicitly accounts for the effect of the medium refractive index:[43] the marginal variability of the refractive index in common organic solvents and, more generally, in organic media, allows us to adopt environment independent model parameters to describe dyes in organic media.[43–45]

3.1 Squaraine aggregates: the ESM-ES approach

Having a reliable description of the solvated dyes, we are now in the position to develop a model that, accounting for intermolecular interactions, will describe the spectral properties of the aggregate. The alkylic pendant and the chiral groups play a fundamental and specific role in guiding the geometry of the supramolecular assemblies formed upon aggregation in poor solvents. This specific role is recognized in the distinctively different spectral properties of the aggregates formed by dyes with alkyl chains of different length (Fig. 1, 2 and Fig. S2, S3, ESI†), and by the opposite sign of the CD spectra collected from aggregates formed by enantiomeric species (Fig. S1, ESI†). As stated above, we observe that the tendency to aggregate is amplified in systems with longer chains. Specifically, signatures of aggregation are seen already in pure methanol solvent for pendants longer than C7, while for C16 only the aggregated form is observed. In any case, the spectral properties of the aggregates in the visible region are dominated by the chromophoric cores and their interactions. In this and in the following subsections we will therefore build two concurrent models for the aggregates, only accounting for the chromophoric species and their interactions.

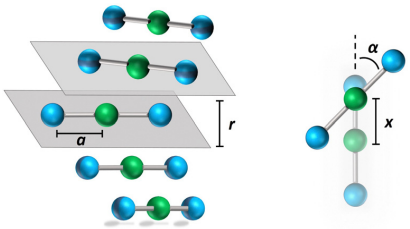


Fig. 3 Schematic representation of the aggregate geometry. The blue and green spheres represent the electron donor (D) and acceptor (A) sites, respectively. Geometrical parameters are also shown: *a* is the length of the D–A arm, *r* is the interplanar distance, *x* is the displacement along the long molecular axis, and α is the angle formed by adjacent molecules. Positive and negative α describes left and right handed helices, respectively. The figure a pentamer, bigger aggregates are constructed maintaining the same arrangement along the stack (one molecule per unit cell).

The exciton model[46,47] is widely and successfully applied to describe linear spectral properties of molecular aggregates. The basic assumption of the exciton model is that electrons are localized on each molecular unit, so that only ES intermolecular interactions are accounted for and are usually dealt with in the dipolar approximation. In the standard version of the exciton model, molecules are described in terms of a single excited state. Moreover, the interactions between non-degenerate states are neglected, so that the exciton Hamiltonian is defined on the N degenerate states bearing a single excitation. This approximation amounts to neglect the molecular polarizability.[48–50] In other terms, when the molecules are brought together in the aggregate, the exciton model neglects any effect of the interaction with the surrounding molecules apart from the exciton delocalization. This is a good approximation for poorly polarizable molecules or, equivalently, when the excitation energy is much larger than the intermolecular interactions, but is expected to fail for aggregates of largely polarizable molecules with low-lying excitations, like squaraines.[37,48–52] A short description of the exciton model and its application to SQ aggregates can be found in the ESI,† Section 3.1.

ESMs for polar and multipolar dyes lend themselves quite naturally to address ES intermolecular interactions in molecular aggregates, releasing the main approximations of the exciton model.[32,48,50,53,54] Specifically, modeling SQ aggregates we release the dipolar approximation and describe each molecule in terms of a ground and two excited states. More interestingly, however, since intermolecular interactions are defined on the diabatic basis, the resulting model fully accounts for the molecular polarizability, allowing the charge distribution on each dye to readjust in response to the ES potential generated by the surrounding molecule.[48–50]

As in the exciton model[46,47] (see the ESI,† Section 3.1), in this subsection we neglect the overlap between frontiers molecular orbitals of different molecules, so that electrons are fully localized on each squaraine unit and intermolecular interactions are just ES in origin. The basis set relevant to the aggregate is then the direct product of the three basis states of each dye, for a grand-total of 3^N states. This limits the dimension of aggregates that can be reasonably dealt with to $\sim$9. The Hamiltonian for the aggregate reads:

$$H = \sum_i \hat{h}_i + \sum_{i>j} \sum_{p,q} V_{ip,jq} \hat{q}_{i,p} \hat{q}_{j,q} \qquad (4)$$

where the first term is the sum of the molecular Hamiltonians in eqn (1), with i running on the molecules. The second term accounts for ES intermolecular interactions, with i and j running on the molecules, and p and q on the three (D, A, D) sites

Published on 18 May 2023. Downloaded on 6/27/2025 6:42:25 PM.

of each molecule. The three operators measuring the charge on each site of the i-th molecule are:

$$\hat{q}_{i,1} = |Z_1^i\rangle\langle Z_1^i|$$

$$\hat{q}_{i,2} = -|Z_1^i\rangle\langle Z_1^i| - |Z_2^i\rangle\langle Z_2^i|$$

$$\hat{q}_{i,3} = |Z_2^i\rangle\langle Z_2^i| \quad (5)$$

Finally, the ES interaction between unit charges residing in site p of molecule i and site q of molecule j is

$$V_{ip,jq} = \frac{1}{4\pi\varepsilon_0\eta^2}\frac{e^2}{|\vec{r}_{ip} - \vec{r}_{jq}|} \quad (6)$$

where e is the electron charge, $\vec{r}_{ip}$ is the vector that defines the position of the i, p site and η is the effective refractive index, accounting for the medium refractive index and for the screening due to electrons not explicitly accounted for in the model. In the following, results are shown for $\eta^2 = 2$ (results for different values are shown in the ESI,† Section 3). Fig. 3 shows a schematic view of the aggregate geometry with the definition of the main geometrical parameters: a is the length of the D–A arm, r is the distance between adjacent molecular planes, α is the rotation angle between adjacent molecules, and x is the displacement of the dyes along the long molecular axis.

The diagonalization of the Hamiltonian in eqn (4) leads to the aggregate eigenstates ψ_i. To calculate absorption spectra, the dipole moment operator $\hat{\vec{D}}$ for the aggregate is defined as the vectorial sum of molecular dipole moments $\hat{\vec{d}}_n$. The transition dipole moment from the ground state $|\psi_0\rangle$ to state $|\psi_i\rangle$ is finally obtained, as needed to calculate the linear absorption spectrum (ESI,† Section 2.4).

The rotational strength, defining the intensity and sign of each feature in the CD spectrum, is:

$$R_i = \Im\left\{\left\langle\psi_0\middle|\hat{\vec{M}}\middle|\psi_i\right\rangle \cdot \left\langle\psi_i\middle|\hat{\vec{D}}\middle|\psi_0\right\rangle\right\} \quad (7)$$

where $\Im\{\ldots\}$ takes the imaginary part and $\hat{\vec{M}}$ is the magnetic dipole moment operator. Since electrons are localized on each molecular unit, following Condon,[55,56] the rotational strength can be evaluated as:

$$R_i \propto \sum_{m\neq n}(\vec{r}_n - \vec{r}_m) \cdot \left\langle\psi_0\middle|\hat{d}_n\middle|\psi_i\right\rangle \wedge \left\langle\psi_i\middle|\hat{d}_m\middle|\psi_0\right\rangle \quad (8)$$

where $\vec{r}_m$ is the position vector of the m-th molecular site.

The color maps in Fig. 4 show absorption and CD spectra calculated for aggregates of $N = 2$, 4 and 8 molecules, with r = 3.5 Å, $\alpha = 20^\circ$ and variable x. Results for different geometries, reported in the ESI,† demonstrate that different aggregate geometries leads to marginally different spectra, maintaining the general picture unaffected.

Comparing results for 4 and 8 sites, one recognizes that the spectra become cleaner, as expected, due to the progressive reduction of finite size effects. Moreover, the splitting between the positive and negative peaks in the CD spectrum reduces when going from 4 to 8 sites, an effect that is more pronounced at small x. But, the overall picture is only marginally altered. On the opposite, the dimer spectrum leads to a qualitatively different picture. Indeed, the dimeric model qualitatively captures the behavior of the linear absorption spectra. Specifically, and in close analogy with the exciton model (Fig. S6, ESI†), a single band largely dominates the absorption spectrum, located to the blue of the monomer absorption spectrum for small x (H-aggregate geometry) and progressively moving to the red at larger x (J-aggregate geometry). But looking at the CD spectra, Fig. 4 lower panels, the situation changes. Qualitatively, and again in line with the exciton model (*cf.* Fig. S6, ESI†), in all cases a bisignated feature appears. As expected for a left-handed H-aggregate, at small x the positive CD feature is observed at higher frequency (shorter wavelength), while at large x, when moving to a J-aggregate structure, the sign of the CD doublet reverses.[57] However, the CD signal for the dimer is qualitatively different from what we get for longer aggregates. For a dimer in fact the positive and negative CD signatures are seen at the frequencies of the upper and lower exciton states, so that the distance between the two peaks amounts to twice the exciton coupling. In bigger aggregates, instead, the exciton couplet involves nearby states close in energy to either the highest energy states in the exciton band (H-aggregates) or to the lowest energy states in the exciton band (J-aggregates). The distance between the positive and negative peaks is not a measure of the exciton splitting in aggregates with $N > 2$.[57] A lesson is learned here: dimeric models work reasonably well to describe linear absorption spectra, but they may be misleading when applied to CD spectra, a conclusion that holds true for both the standard exciton model (Fig. S6, ESI†) and the ESM-ES model (Fig. 4).

Another interesting observation concerns the intensity of the spectra. Absorption and CD intensities in Fig. 4 are normalized to the number of sites. As expected, the normalized absorption intensity is roughly constant upon increasing the aggregate size. On the other hand, the normalized intensity of the CD signals increases fast with N, a result that could explain the very large chiroptical responses reported recently for annealed thin films of proline-derived squaraines with C16 alkyl chain (ProSQ-C16).[35]

It is instructive to compare results from the ESM-ES model in Fig. 4 with the results obtained in the standard exciton model, shown in Fig. S6 (ESI†). The two sets of results share some similarity, with a single main absorption peak and a single main bisignated CD feature. Moreover, as expected, in both models the absorption peak is located to the blue of the monomer absorption for superimposed or almost so molecules (small x in Fig. 3, H-like aggregates) while it is located to the red of the monomer absorption for largely displaced molecules (large x in Fig. 3, J-like aggregates). However, some important differences between the two models is observed.

In the exciton model, the switch from H to J-aggregate behavior occurs for $x \sim 2.5$ Å, while much larger $x \sim 4$ Å values are needed in the ESM-ES model. Even more interesting is the comparison of absorption and CD spectra. In the exciton model, the molecular polarizability is disregarded, so that the

 This journal is © The Royal Society of Chemistry 2023

View Article Online

Published on 18 May 2023. Downloaded on 6/27/2025 6:42:25 PM.

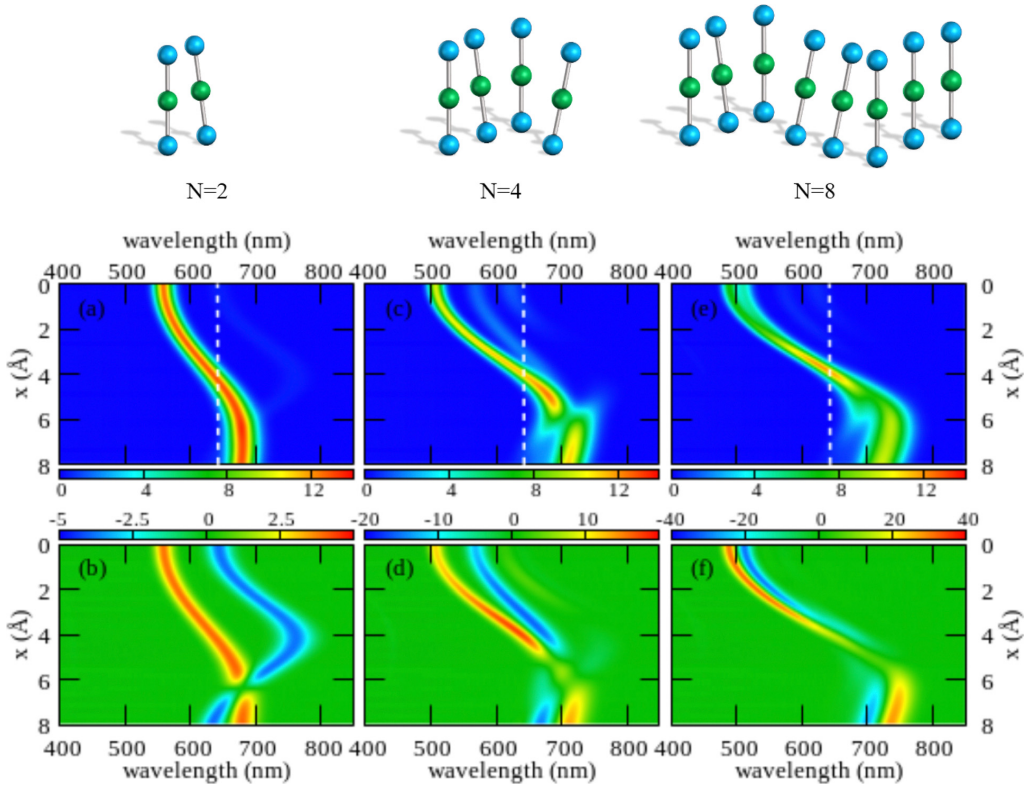


Fig. 4 Spectral properties of squaraine aggregates described in the ESM-ES approach (model Hamiltonian in eqn (4)). Molecular parameters: z = 0.4 eV, τ = 1.04 eV, a = 4.33 Å. Results are shown for aggregates of 2, 4 and 8 molecules with r = 3.5 Å and α = 20°. The color maps show the absorption intensity (top panels) and the CD intensity (bottom panels) plotted against the wavelength (horizontal axis) upon varying x (vertical axis). All intensities, in arbitrary units, are normalized to the number of molecules. Notice the different scale adopted for the CD intensity in the three bottom panels to account for the superlinear amplification of CD intensity with aggregate size.

position of the absorption band vs the monomer absorption is determined by the sign of the intermolecular electrostatic interactions, positive for H-aggregates, negative for J-aggregates. Since, as recently discussed,[57,58] for fixed helicity the sign of the CD doublet depends on the sign of intermolecular interactions, in the exciton model the sign of the bisignated signature in the CD spectrum reverses precisely at the same x value where the system crosses from H to J-behavior. The situation is more complex in the ESM-ES model, where the molecular polarizability is fully accounted for so that the charge distribution on each molecular unit rearranges in response to the presence of surrounding molecules. Accordingly, the reference absorption frequency of the monomer does not coincide with the one observed for the isolated dye and the position of the absorption peak of the aggregate cannot be only ascribed to the sign of the interaction. Just for the sake of simplicity, let's focus on the dimer case (left panels of Fig. 4): the sign of the CD spectrum reverses at $x \sim 6$ Å, unambiguously suggesting that the sign of the intermolecular interaction is positive for $x < 6$ Å, and negative for $x > 6$ Å. This apparently contrasts with the observation of a red-shifted absorption in the region of x comprised between 4 and 6 Å. Indeed this is the strange region of non-fluorescent J-aggregates, corresponding to a region where the blue-shift associated with repulsive intermolecular interactions is overcompensated by the red-shift of the monomer absorption as due to the rearrangement of the charge distribution occurring in each polarizable molecule in response to the electric potential generated by the surrounding molecules.[48,52,59,60]

As noticed above, both the exciton model and the ESM-ES model predict for the dimer a bisignated CD signal whose positive and negative peaks are close to the position of the two Davydov components, so that the CD spectrum is centered at the position of the monomer absorption. For larger aggregates instead, the main CD features are seen in the close proximity of the main absorption band, so that the CD bisignated signal is centered either to the blue or to the red of the monomer absorption in H or J-aggregates, respectively.[57] These results teach us another important lesson: as long as the electrons stay localized in each molecular unit, a single main

View Article Online

Published on 18 May 2023. Downloaded on 6/27/2025 6:42:25 PM.

bisignated CD signal is expected for each aggregate geometry. The experimental observation of two bisignated peaks in SQ aggregates therefore rules out the possibility that the red and blue spectral features observed in the absorption spectra are related to two Davydov components, which would imply a single bisignated signal in the CD spectrum. This is an important observation as it excludes at least one of the possible scenarios invoked to explain the spectra of SQ films.[29]

Having a general picture of the spectral properties of an aggregate of squaraine dyes described in the ESM-ES approach (Fig. 3 and Fig S7 and S8 in the ESI†) we can relate this picture to experimental data. The observation of two spectral features in both absorption and CD spectra, can be rationalized within ESM-ES due to the formation of aggregates (larger than dimers) where structures with x = 6–8 Å, responsible for the feature in the red region of the spectrum, coexists with structures with x ~ 2 Å, responsible for the spectral feature at ~500 nm. Quite interestingly, the feature in the red portion of the spectrum is located very close to the region where the simulated CD feature changes its sign, possibly explaining the large variability of the experimental CD spectrum in this region. Of course, the different intensities of the two spectral features in the aggregates formed by dyes with different side chains could be rationalized in terms of different relative amounts of the two aggregates in the different systems.

3.2 Introducing intermolecular charge resonance: the ESM-CT approach

In recent years, squaraine aggregates have been extensively investigated by Collison and Spano[28,30,36–38] who ascribed the fairly complex absorbance spectra of (non-chiral) squaraine films to the presence of CT interactions among adjacent molecules. Specifically, a sizable overlap between two D–A pairs in nearby molecules, as schematically shown in Fig. 5, was proposed to justify the experimental observations. The films of (non-chiral) anilino squaraine with linear terminal alkyl chains investigated by Collison and Spano show two bands in the absorption spectrum, one to the blue and one to the red of the monomer absorption band, much as in our case, even if with much broader bandshapes. It is therefore interesting to see if a model accounting for intermolecular CT interactions (ESM-CT) does apply to our aggregates in colloidal suspensions.

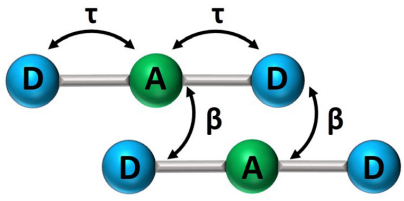


Fig. 5 A sketch of intramolecular (τ) and intermolecular (β) charge resonance interactions, shown as double-sided arrows, for a pair of adjacent molecules.

If electrons can hop among different molecules, the number of states needed to describe the aggregate increases fast. In a dimer, accounting only for charge degrees of freedom, the number of states increases from 9 in the case of localized electrons to 15.[36] However, 15 states are not enough if the electron spin is appropriately accounted for, leading to much larger basis, as discussed in the ESI† (Section 2.3). The Hamiltonian for N molecules is constructed as a modified Hubbard Hamiltonian accounting on each molecule for three sites, D–A–D, and four electrons. The Hamiltonian reads (eqn (9)):

$$\begin{aligned}\hat{H} &= \sum_{i,p}\varepsilon_p\hat{n}_{ip} + \frac{U}{2}\sum_{i,p}\hat{n}_{ip}\left(\hat{n}_{ip}-1\right) + \frac{1}{2}\sum_{ip,jq}V_{ip,jq}\hat{q}_{ip}\hat{q}_{jq} \\ &- \frac{\tau}{\sqrt{2}}\sum_i\left(\hat{b}_{i1,i2}+\hat{b}_{i2,i1}+\hat{b}_{i2,i3}+\hat{b}_{i3,i2}\right) \\ &- \frac{\beta}{\sqrt{2}}\sum_i\left(\hat{b}_{i2,(i+1)1}+\hat{b}_{(i+1)1,i2}+\hat{b}_{i3,(i+1)2}+\hat{b}_{(i+1)2,i3}\right)\end{aligned} \tag{9}$$

where i,j run on the N molecules (in the third term $i \neq j$ and in the last term the sum is truncated to $N-1$), and p,q run on the three sites on each molecule. The operator that counts the electrons on the p site of the ith molecule is $\hat{n}_{i,p} = \sum_\sigma a^\dagger_{i,p,\sigma}a_{i,p,\sigma}$, where $a_{i,p,\sigma}$ and $a^\dagger_{i,p,\sigma}$ annihilate and create, respectively, an electron with spin σ on the relevant site. We also define the auxiliary operator $\hat{b}_{ip,jq} = \sum_\sigma a^\dagger_{i,p,\sigma}a_{j,q,\sigma}$. The energy of the p site on each molecule is ε_p, while U (site-independent for the sake of simplicity) is the energy required to put two electrons on the same site. The intra and intermolecular electron hopping are described by τ and β, respectively. Finally, ES interactions are described by the last term in the first row: the operators measuring the charge on each site are $\hat{q}_{i,p} = 2 - \hat{n}_{i,p}$ for p = 1,3 (D site) and $\hat{q}_{i,p} = \hat{n}_{i,p}$ for p = 2 (A site) and $V_{ip,jq}$ is defined as in eqn (6).

The ESM-CT must describe exactly the same physics as the ESM-ES in Section 3.1 when β = 0, provided that model parameters are appropriately selected. On-site energies are defined as $\varepsilon_p = -\Delta$ for p = 1,3 (D site) and $\varepsilon_p = +\Delta$ for p = 2 (A site). To limit the basis dimension, states with D sites bearing a negative charge or A sites bearing a positive charge or with sites bearing double charges (D^{2+} or A^{2-}) are excluded setting their energy to very large values. To this aim, we set U and Δ to very large values while maintaining their difference finite. Specifically, for direct comparison with the molecular essential state model, the energy difference between D^+A^-D and DAD configurations is $2z = 2\Delta - U - V$, where

$$V = V_{i1,i2} = V_{i2,i3} = \frac{e^2}{4\pi\varepsilon_0\eta^2 a} \tag{10}$$

is the ES interaction energy between two charges on adjacent D and A sites in the same molecule. In the calculations we will set U to a very large value (as to make its precise value irrelevant) and, for fixed z and V, we estimate $\Delta = z + (U+V)/2$.

 This journal is © The Royal Society of Chemistry 2023

View Article Online

Published on 18 May 2023. Downloaded on 6/27/2025 6:42:25 PM.

We adopt the real-space basis, *i.e.* the basis where the $4N$ electrons are distributed on the different sites and only consider the subspace with an equal number of spins up and down (see the ESI,† Section 2.3). Even discarding high energy states (with doubly charged sites or with negatively charged D or positively charged A), the dimension of the basis increases very fast with N, from 53 states in a dimer, to 707 in a trimer and 10 453 in a tetramer. In any case, the relevant Hamiltonian matrix can be diagonalized to get the lowest eigenstates of interest for spectral properties.

To calculate the absorption spectrum we need the dipole moment operator that, due to the intermolecular CT, cannot be written as the sum of molecular dipoles. Its definition, in terms of site charges and positions, is however very simple:

$$\hat{\vec{D}} = \sum_{ip} \hat{q}_{ip} \vec{r}_{ip} \qquad (11)$$

The eigenstates of the Hamiltonian in eqn (9) can then be used to calculate transition dipole moments, as needed to obtain the absorption spectra (see the ESI,† Section 2.3).

Addressing CD spectra is much more delicate. The Condon approach[55–57,61] only applies to aggregates where electrons are confined inside each molecular unit and, to the best of our knowledge, approaches to evaluate CD spectra in aggregates also accounting for intermolecular CT interactions are not available. To calculate rotational strengths (eqn (7)) we need an explicit expression for the electric dipole moment operator, given in eqn (11), and for the magnetic dipole moment operator. The derivation of the magnetic dipole moment operator is non-trivial and is addressed in the ESI† (Section 2.2), where the somewhat clumsy expressions for the rotational strength are also explicitly reported.

The large dimension of the real space basis and the large number of matrices to be stored in the computer memory for the calculation of rotational strengths make ESM-CT calculations extremely demanding, limiting the dimension of the aggregate we could address to 4 molecules. The ESM-ES results shown in Section 3.1 for aggregates of 4 and 8 molecules suggest that, while finite size effects are sizable, reliable information can already be obtained for 4 sites. Fig. 6 shows ESM-CT spectra calculated for 4-site aggregates, with the same model parameters as in Fig. 4, but with intermolecular CT interactions switched on to β = 0.2, 0.4 and 0.6 eV. Results for other aggregate geometries and other parameter values are shown in the ESI† (Section 3.2).

As first recognized by Collison and Spano,[36] when intermolecular CT interactions are accounted for, two major peaks appear in the absorption spectrum whose separation increases with increasing β. Indeed, two predominant bands are seen for a dimer (see Fig. S11 and S12, ESI†) but, upon increasing the

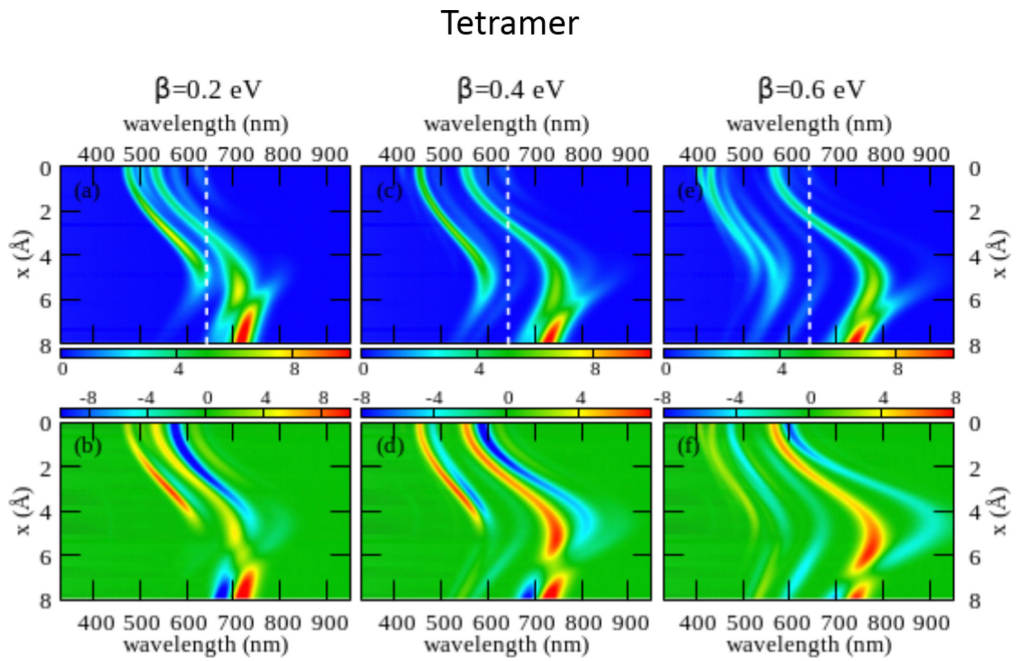


Fig. 6 Spectral properties of squaraine aggregates described in the ESM-CT approach (model Hamiltonian in eqn (4)). Results are shown for tetramers adopting the same geometry and the same molecular parameters as in Fig. 4. The color maps show the absorption intensity (top panels) and the CD intensity (bottom panels) plotted against the wavelength (horizontal axis) and x (vertical axis). Left panels refer to β = 0.2 eV, middle panels to β = 0.4 eV and right panels to β = 0.6 eV.

Published on 18 May 2023. Downloaded on 6/27/2025 6:42:25 PM.

number of molecules, additional weak bands are also seen that, being most probably related to finite size effects, could disappear in larger aggregates. Quite interestingly, two bisignate features appear in the CD spectra in the same spectral regions as the two main absorption peaks (again the spectrum is somewhat more complex with additional small features appearing, most probably related to finite size effects). The superlinear increase of the intensity of the CD signal, observed for the model with localized electrons, is also confirmed in the presence of intermolecular CT interactions (see Fig. S12 in the ESI† where results of the ESM-CT model are shown for aggregates with N = 2, 3 and 4).

We are now in the position to discuss experimental results in the framework of the ESM-CT approach. Experimental spectra collected for aggregates of dyes with pendants of intermediate size (C6, C7 or C10) could be roughly accounted for in terms of aggregates with β = 0.4 eV and $x \sim$ 3–4 Å. So a single aggregate type can explain the observation of double features in both absorption and CD spectra. Simulating absorption and CD spectra accounting for a single form of aggregates is fairly appealing if compared with the need to postulate the presence of two different types of aggregates in the ESM-ES approach. However, the ESM-CT approach hardly applies to aggregates of dyes with short (C3, C5) or long (C11, C12, C16) chains. In these aggregates in fact the red-most feature observed in either absorption or CD spectra has a dramatically reduced intensity if compared with the blue-most features. In our model, irrespective of the strength of the CT interaction, and of the details of the aggregate geometry (see the ESI,† Section 3.2) it is not possible to simulate a spectrum where the red-most features have negligible intensity.

4 The helicity of the aggregate: a difficult case study for MD

In the previous section, we have seen how the complex experimental behavior of chiral squaraine aggregates can be rationalized in terms of (a) a model accounting for only ES intermolecular interactions in the hypothesis of the coexistence of both H-type and J-type aggregates or (b) due to the presence of a single type of aggregate if intermolecular CT interactions are present. As for the sign of the CD spectrum, in line with experimental results, some variability is expected for the red-most feature, while, as for the high energy feature, a consistent sign of the exciton doublet is observed experimentally that can be reproduced imposing a left-handed helix for aggregates of (*S,S*)-ProSQ compounds and a right-handed helix for aggregates of (*R,R*)-ProSQ compounds. In an effort to get independent information on the supramolecular arrangement of the dyes in the aggregates, as needed to assist the interpretation of experimental data, we performed extensive MD simulations on ProSQ-C10 aggregates.

All simulations were run in Gromacs.[62] First, a generalized Amber Force Field (GAFF)[63] potential in its standard implementation with restrained ES potential (RESP) charges[64] was adopted starting from the isolated molecules with constrained planarity of the conjugated framework. A first set of enhanced-sampling simulations with fixed number of molecules, pressure and temperature (NPT) were run on tetramers in explicit solvent, adopting the Hamiltonian replica exchange MD (HREMD) approach.[65] Details about the method and the sample preparation can be found in the ESI,† Section 4. These simulations consistently returned a right-handed helix for the (*S,S*)-enantiomer, in contrast with the handedness requested to simulate the experimental CD spectra. Similar results were obtained using pure methanol as the solvent or methanol–water (60 : 40) mixtures, with marginal fluctuations around equilibrium structures (see Fig. S15, ESI†). A shorter simulation on (*R,R*)-ProSQ-C10 in water–methanol (60 : 40) produced a left-handed helix, as expected.

In an attempt to improve the description and move towards larger aggregates, a second round of simulations were run employing a modified version of the GAFF potential by (i) fixing some of the C–C–C–C dihedrals for the conjugated core, and (ii) improving the description of long alkyl chains, as suggested in the context of liquid crystal by Boyd and Wilson[66] (more details in the ESI† – Section 4). We dubbed these simulations as mod.GAFF + LCFF MDs. Unbiased simulations on tetramers still returned similar structures as in the original GAFF, suggesting that, at least for small N, this family of force fields robustly predicts at the thermodynamic equilibrium the same type of helical aggregates (compare Fig. 7 with Fig. S15 in the ESI†).

In a very relevant work[33] Hariharan and coworkers reported some interesting findings on chiral aggregates of a different family of squaraine dyes. They observed an astounding inversion of the sign of CD spectra of the aggregate after thermal treatment, suggesting that the helicity of the aggregate may reverse for aggregates formed under thermodynamic control vs kinetic control. Inspired by these results, we have exploited MD in an attempt to probe configurations not necessarily corresponding to the equilibrium. To this aim, two extra sets of simulations were run on 12-mer and 24-mer of (*S,S*)-ProSQ-C10 aggregates. In all cases, simulations started with the molecules arranged with their center of mass on a regular 3D grid and in random orientation. We prepared 6 different 12-mer samples and two different 24-mer samples in 60 : 40 MeOH : water. After relaxation and equilibration, we finally run unbiased NPT simulation for 45 ns (full details in the ESI,† Section 4). In this approach, several ''disordered'' large aggregates are investigated, in an effort to mimic conditions of kinetic control, while keeping a balance between satisfactory sampling and representative structures. With the aim of understanding the fundamental interactions assisting the optical signatures, we have limited our analysis by extracting from the dynamics the information related to molecular pairs. Specifically, for each aggregate size we collected distributions of pairwise geometric parameters (see the ESI,† Section 4). Fig. 7 show relevant results, with the colormaps showing as 2D histograms the distribution of the distance between two molecular centers of mass *versus* the rotation angle as defined

 This journal is © The Royal Society of Chemistry 2023

View Article Online

Published on 18 May 2023. Downloaded on 6/27/2025 6:42:25 PM.

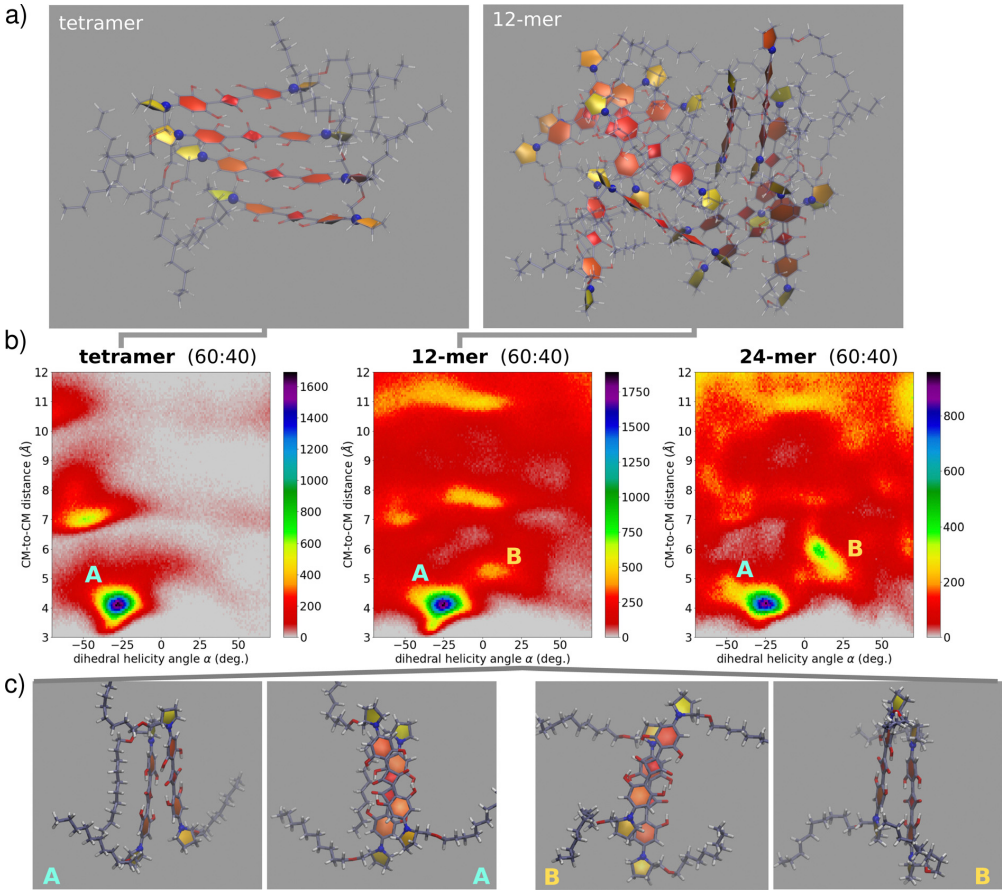


Fig. 7 Snapshots and pairwise information extracted from MD trajectories. (a) Snapshots from the MD trajectories of tetramer (left) and 12-mer (right), with highlighted rings and N atoms in blue; (b) heatmaps showing the distribution of α (x-axis, in degree) and of the distance between two centers of mass (y-axis, in Å). Results refer to a tetramer (left panel), a 12-mer (middle panel) and a 24-mer (right panel) of (*S,S*)-ProSQ-C10 simulated with mod.GAFF + LCFF MDs; (c) selected representative dimer structure extracted from the 12-mer trajectory belonging to the A domain (on the left) and to the B domain (on the right), both in the top view (middle) and side view (external).

in Fig. 3. We observe the presence of at least two basins among the first-neighbour close-distance region: the first basin, largely dominating, is located at negative α and hence corresponds to the right-handed helix of (*S,S*)-ProSQ-C10, expected to give rise to the wrong sign of the CD spectrum. The second basin, located at positive α, corresponds to a left-handed helix, the structure in line with the observed sign of the CD spectrum. Quite interestingly, this secondary basin becomes more prominent with increasing aggregate size, suggesting that MDs on larger aggregates could better reproduce the experiment. Moreover, as clear from Fig. 7, upon increasing the aggregate size a more diverse configurational landscape is obtained, with dimer structures exhibiting several possibilities of geometrical orientations. These maps include non-nearest-neighbor molecular pairs as well. From MD trajectories in mod.GAFF + LCFF, we can obtain an average value of such geometrical parameters (see also S19, ESI†). For the 12-mer in the B domain we obtain $\bar{\alpha} = 8^{\circ}$, $\bar{d}_{\mathrm{CM-CM}} = 5.2$ Å, $\bar{r} = 3.5$ Å, $\bar{x} = 3.9$ Å. For the sake of comparison, we also report the corresponding values for A domain: $\bar{\alpha} = -28^{\circ}$, $\bar{d}_{\mathrm{CM-CM}} = 4.0$ Å, $\bar{r} = 3.5$ Å, $\bar{x} = 2.3$ Å.

While MD simulations suggest the opposite helix handedness to be the dominant, the above values of the geometrical parameters provide us a valuable flavour of the typical nearest-neighbour intermolecular pair motifs. These values compare well with those employed to simulate optical spectra in the previous Section. Besides critical aspects typically associated with simulations obtained with standard classical force fields, including assuming fixed charges and fixed parameters in spite of the large polarizability of the conjugated molecular structure, the presence of hydrogen bonds *etc.*, it is likely that wrong

Published on 18 May 2023. Downloaded on 6/27/2025 6:42:25 PM.

handedness prediction for these systems may be caused by a free energy surface that strongly depends on the number of molecules, rendering its full exploration very challenging from the computational point of view. MD simulations on 12-mers were also exploited to select representative dimeric structures through clustering (see the ESI,† Section 4.4 for the adopted protocol). As expected, the largest abundance of the representative dimers refers to the right handedness. After carefully transferring these representative structures through constrained relaxations, we have run TD-DFT calculations on these representative dimers to calculate absorption and CD spectra (computational details in the ESI,† Section 4.5). Preliminary results obtained with two common functionals (B3LYP and CAM-B3LYP) are shown in Fig. S20 (ESI†). First, it is worth noticing that the calculated TD-DFT spectra predict CD features in agreement with the exciton or ESM-ES/CT models. Secondly, even for such simple dimers, the resulting spectra obtained with either functional have complex shapes, manifesting two spectral features and hence possibly supporting the presence of intermolecular CT interactions. Neither functional reproduces satisfactorily the experimental results: in both cases the blue-shifted spectral feature is too close to the monomer absorption peak, if compared with the experiment. As it is often the case, calculated spectra largely depend on the choice of the functional, suggesting that a more careful inspection of the electronic structure method is needed. Moreover, as discussed above, larger aggregates than dimers must be studied in order to extract reliable information. This may further complicate the spectra, making the TD-DFT calculations and the analysis of relevant results a very demanding task, definitely beyond the scope of this work.

5 Discussion and conclusions

An extensive experimental and theoretical study is presented on a large family of squaraine dyes in an effort to shed light on the structure of these fascinating systems showing astounding spectral features. The investigated proline-derived anilino squaraines have a similar chemical structure, bearing a chiral terminal group in each one of the two D moieties. The only difference among the investigated squaraine dyes is the length of the alkyl pendant attached to each D moiety: we were able to synthesize and characterize dyes with alkyl chains with a number of carbon atoms ranging from 3 to 12, as well as a dye bearing C16 chains. These alkyl chains are not part of the chromophoric system but steer the aggregation pattern. Upon aggregation, induced in solution by poor solvent titration, the different compounds show distinctively different spectral properties, suggesting different aggregation behavior. Specifically, the tendency to aggregate increases with the length of the alkyl chains. On the contrary, the nature of the formed aggregates, as demonstrated by the spectra, has a more complex and intriguing behavior. Specifically, dyes decorated with alkyl chains with intermediate length show two distinct and intense features in either the absorption and CD spectra, one located at longer wavelength *vs*. the monomer absorption the other one at shorter wavelengths. In aggregates of dyes with very short or very long alkyl chains, instead, the spectral features located at long wavelengths lose intensity and become almost irrelevant, while the spectral position of the two features is basically the same in all samples.

The spectra of our colloidal suspensions of chiral aggregates, showing features appearing both to the blue and to the red of the monomer absorption, while much narrower, do share some similarity with the panchromatic spectra of squaraine films, then offering some useful hints about the origin of this technologically relevant and highly debated feature. Specifically, the consistent observation of two bisignated features in the CD spectrum of our aggregates, occurring at the frequencies of the red and blue-shifted absorption bands, allows to definitely exclude that the two signals are due to the two Davydov components of the relevant exciton, as expected in aggregates with oblique arrangement of the dyes. This conclusion definitely applies to our colloidal aggregates, but it can be very reasonably extended to squaraine aggregates in films. Other alternative scenarios are presently considered in the literature to explain the observation of two peaks in the spectra of non-chiral anilino squaraine films. In the first scenario, the observation of the two peaks is ascribed to intermolecular CT interactions, while an alternative view relies on the presence of disorder. Of course, the aggregation behavior can be markedly different in aggregates obtained from different squaraine dyes, however the chiroptical responses of our aggregates give precious additional information to shed light on this intriguing issue. Indeed, the presence of the two spectral features in our aggregates can be justified either in terms of a system where intermolecular interactions are purely ES in nature but two types of aggregation are present, or in terms of a single aggregation type in the presence of sizable intermolecular CT. On one side, the ESM-CT model hardly applies to systems where the feature to the blue is largely dominant, suggesting that most probably the specific case disorder is more important than intermolecular CT. However, due to the complexity of the calculation, the ESM-CT model could only be applied to systems not larger than a tetramer, leaving the doubt that finite size effects may alter the conclusion. While MD simulations do not fully unveil all structural details, they suggest an evolution of accessible configurations with the increase of the aggregate size. So, even if a direct comparison with the experiment remains a critical step, the atomistic information, *i.e.* the structure prediction by MD and the evaluation of the electronic structure with (TD)-DFT, can complement the information obtained with ESM and resize the boundary of the problem. Sizable intermolecular CT interactions are supported by preliminary TD-DFT results, that however require additional efforts to validate the functional choice and to extend the analysis to larger aggregates than dimers. At this stage, a definite conclusion is hardly reached. Additional and demanding simulations are needed to fully solve these issues.

In this study, we propose for the first time an explicit expression for the calculation of CD spectra of aggregates in

 This journal is © The Royal Society of Chemistry 2023

Published on 18 May 2023. Downloaded on 6/27/2025 6:42:25 PM.

the presence of intermolecular CT interactions, a highly non-trivial result. We learned that dimeric models may be adequate to describe linear spectral properties of aggregates, but fail for chiroptical properties. Moreover, we recognized an impressive superlinear amplification of the CD response with the aggregate dimension that survives both in the presence or in the absence of intermolecular CT interactions. While a firm conclusion about the structure of squaraine aggregates is hardly reached, we consider that this extensive study gives important information on chiral responses of molecular aggregates beyond the exciton model.

Conflicts of interest

There are no conflicts to declare.

Acknowledgements

MS thanks the Linz Institute of Technology (LIT-2019-7-INC-313 SEAMBIOF) for funding and is grateful to Franz Badura from the PRO RETINA foundation. MFS and AL are obliged to the DFG GRK 2591 ''Template-designed Organic Electronics – TIDE'' for financial support. MFS thanks the Manchot Foundation for a doctoral scholarship. Work in Parma was funded by PNRR MUR project ECS-00000033-ECOSISTER, and benefited from the HPC center and from the equipment and framework of the COMP-HUB and COMP-R Initiatives, funded by the 'Departments of Excellence program of the Italian Ministry for University and Research (MIUR, 2018–2022 and MUR, 2023–2027). MD simulations were run in Zagreb at the HPC (High Performance Computing) unit of the Division of Theoretical Physics of Ruer Bošković Institute. L. G. acknowledges the Croatian science foundation (HrZZ) through the project HYMO4EXNOMOMA (IP-2020-02-7262) and thanks Prof. Mark Wilson and Jane Boyd for the help with GAFF-LCFF. A. P. thanks Suresh Das for interesting discussion on the spectral properties of squaraine films. The authors thank Cristina Sissa for useful discussions.

References

1 S. Das, K. G. Thomas, R. Ramanathan, M. V. George and P. V. Kamat, Photochemistry of squaraine dyes. 6. Solvent hydrogen bonding effects on the photophysical properties of bis(benzothiazolylidene)squaraines, *J. Phys. Chem.*, 1993, **97**, 13625–13628.

2 S.-J. Chung, S. Zheng, T. Odani, L. Beverina, J. Fu, L. A. Padilha, A. Biesso, J. M. Hales, X. Zhan, K. Schmidt, A. Ye, E. Zojer, S. Barlow, D. J. Hagan, E. W. V. Stryland, Y. Yi, Z. Shuai, G. A. Pagani, J.-L. Brédas, J. W. Perry and S. R. Marder, Extended Squaraine Dyes with Large Two-Photon Absorption Cross-Sections, *J. Am. Chem. Soc.*, 2006, **128**, 14444–14445.

3 V. S. Jisha, K. T. Arun, M. Hariharan and D. Ramaiah, Site-Selective Binding and Dual Mode Recognition of Serum Albumin by a Squaraine Dye, *J. Am. Chem. Soc.*, 2006, **128**, 6024–6025.

4 F. Terenziani, A. Painelli, C. Katan, M. Charlot and M. Blanchard-Desce, Charge instability in quadrupolar chromophores: Symmetry breaking and solvatochromism, *J. Am. Chem. Soc.*, 2006, **128**, 15742–15755.

5 S. Sreejith, P. Carol, P. Chithra and A. Ajayaghosh, Squaraine dyes: a mine of molecular materials, *J. Mater. Chem.*, 2008, **18**, 264–274.

6 L. Beverina and P. Salice, Squaraine Compounds: Tailored Design and Synthesis towards a Variety of Material Science Applications, *Eur. J. Org. Chem.*, 2010, 1207–1225.

7 C. Sissa, F. Terenziani, A. Painelli, R. B. K. Siram and S. Patil, Spectroscopic Characterization and Modeling of Quadrupolar Charge-Transfer Dyes with Bulky Substituents, *J. Phys. Chem. B*, 2012, **116**, 4959–4966.

8 T. Liu, X. Liu, W. Wang, Z. Luo, M. Liu, S. Zou, C. Sissa, A. Painelli, Y. Zhang, M. Vengris, M. V. Bondar, D. J. Hagan, E. W. Van Stryland, Y. Fang and K. D. Belfield, Systematic Molecular Engineering of a Series of Aniline-Based Squaraine Dyes and Their Structure-Related Properties, *J. Phys. Chem. C*, 2018, **122**, 3994–4008.

9 F. J. AvilaFerrer, C. Angeli, J. Cerezo, S. Coriani, A. Ferretti and F. Santoro, The Intriguing Case of the One-Photon and Two-Photon Absorption of a Prototypical Symmetric Squaraine: Comparison of TDDFT and Wave-Function Methods, *ChemPhotoChem*, 2019, **3**, 778–793.

10 J. He, Y. J. Jo, X. Sun, W. Qiao, J. Ok, T. Il Kim and Z. Li, Squaraine Dyes for Photovoltaic and Biomedical Applications, *Adv. Funct. Mater.*, 2020, **31**, 2008201.

11 K. M. Shafeekh, S. Das, C. Sissa and A. Painelli, Asymmetric Squaraine Dyes: Spectroscopic and Theoretical Investigation, *J. Phys. Chem. B*, 2013, **117**, 8536–8546.

12 G. M. Somashekharappa, C. Govind, V. Pulikodan, M. Paul, M. A. G. Namboothiry, S. Das and V. Karunakaran, Unsymmetrical Squaraine Dye-Based Organic Photodetector Exhibiting Enhanced Near-Infrared Sensitivity, *J. Phys. Chem. C*, 2020, **124**, 21730–21739.

13 M. Basheer, U. Santhosh, S. Alex, K. G. Thomas, C. H. Suresh and S. Das, Design and synthesis of squaraine based near infrared fluorescent probes, *Tetrahedron*, 2007, **63**, 1617–1623.

14 H.-Y. Ahn, S. Yao, X. Wang and K. D. Belfield, Near-Infrared-Emitting Squaraine Dyes with High 2PA Cross-Sections for Multiphoton Fluorescence Imaging, *ACS Appl. Mater. Interfaces*, 2012, **4**, 2847–2854.

15 C. Magistris, S. Martiniani, N. Barbero, J. Park, C. Benzi, A. Anderson, C. Law, C. Barolo and B. ORegan, Near-infrared absorbing squaraine dye with extended conjugation for dye-sensitized solar cells, *Renewable Energy*, 2013, **60**, 672–678.

16 K. Strassel, W.-H. Hu, S. Osbild, D. Padula, D. Rentsch, S. Yakunin, Y. Shynkarenko, M. Kovalenko, F. Nüesch, R. Hany and M. Bauer, Shortwave infrared-absorbing squaraine dyes for all-organic optical upconversion devices, *Sci. Technol. Adv. Mater.*, 2021, **22**, 194–204.

Published on 18 May 2023. Downloaded on 6/27/2025 6:42:25 PM.

17 S. Sreejith, J. Joseph, M. Lin, N. V. Menon, P. Borah, H. J. Ng, Y. X. Loong, Y. Kang, S. W.-K. Yu and Y. Zhao, Near-Infrared Squaraine Dye Encapsulated Micelles for *in Vivo* Fluorescence and Photoacoustic Bimodal Imaging, *ACS Nano*, 2015, **9**, 5695–5704.

18 O. S. Abdullaeva, F. Balzer, M. Schulz, J. Parisi, A. Lützen, K. Dedek and M. Schiek, Organic Photovoltaic Sensors for Photocapacitive Stimulation of Voltage-Gated Ion Channels in Neuroblastoma Cells, *Adv. Funct. Mater.*, 2019, **29**, 1805177.

19 R. R. Avirah, D. T. Jayaram, N. Adarsh and D. Ramaiah, Squaraine dyes in PDT: from basic design to in vivo demonstration, *Org. Biomol. Chem.*, 2012, **10**, 911–920.

20 P. S. S. Babu, P. M. Manu, T. J. Dhanya, P. Tapas, R. N. Meera, A. Surendran, K. A. Aneesh, S. J. Vadakkancheril, D. Ramaiah, S. A. Nair and M. R. Pillai, Bis(3,5-diiodo-2,4,6-trihydroxyphenyl) squaraine photodynamic therapy disrupts redox homeostasis and induce mitochondria-mediated apoptosis in human breast cancer cells, *Sci. Rep.*, 2017, **7**, 42126.

21 G. Chen, H. Sasabe, W. Lu, X.-F. Wang, J. Kido, Z. Hong and Y. Yang, J-aggregation of a squaraine dye and its application in organic photovoltaic cells, *J. Mater. Chem. C*, 2013, **1**, 6547.

22 T. Maeda, T. V. Nguyen, Y. Kuwano, X. Chen, K. Miyanaga, H. Nakazumi, S. Yagi, S. Soman and A. Ajayaghosh, Intramolecular Exciton-Coupled Squaraine Dyes for Dye-Sensitized Solar Cells, *J. Phys. Chem. C*, 2018, **122**, 21745–21754.

23 Y. Chen, W. Zhu, J. Wu, Y. Huang, A. Facchetti and T. J. Marks, Recent Advances in Squaraine Dyes for Bulk-Heterojunction Organic Solar Cells, *Org. Photonics Photovoltaics*, 2019, **6**, 1–16.

24 S. Das, K. G. Thomas, K. J. Thomas, V. Madhavan, D. Liu, P. V. Kamat and M. V. George, Aggregation Behavior of Water Soluble Bis(benzothiazolylidene)squaraine Derivatives in Aqueous Media*sup*/sup, *J. Phys. Chem.*, 1996, **100**, 17310–17315.

25 S. Alex, M. C. Basheer, K. T. Arun, D. Ramaiah and S. Das, Aggregation Properties of Heavy Atom Substituted Squaraine Dyes: Evidence for the Formation of J-Type Dimer Aggregates in Aprotic Solvents, *J. Phys. Chem. A*, 2007, **111**, 3226–3230.

26 S. D. Spencer, C. Bougher, P. J. Heaphy, V. M. Murcia, C. P. Gallivan, A. Monfette, J. D. Andersen, J. A. Cody, B. R. Conrad and C. J. Collison, The effect of controllable thin film crystal growth on the aggregation of a novel high panchromaticity squaraine viable for organic solar cells, *Sol. Energy Mater. Sol. Cells*, 2013, **112**, 202–208.

27 S. Brück, C. Krause, R. Turrisi, L. Beverina, S. Wilken, W. Saak, A. Lützen, H. Borchert, M. Schiek and J. Parisi, Structure–property relationship of anilino-squaraines in organic solar cells, *Phys. Chem. Chem. Phys.*, 2014, **16**, 1067–1077.

28 C. Zheng, I. Jalan, P. Cost, K. Oliver, A. Gupta, S. Misture, J. A. Cody and C. J. Collison, Impact of Alkyl Chain Length on Small Molecule Crystallization and Nanomorphology in Squaraine-Based Solution Processed Solar Cells, *J. Phys. Chem. C*, 2017, **121**, 7750–7760.

29 G. M. Paternò, L. Moretti, A. J. Barker, C. DAndrea, A. Luzio, N. Barbero, S. Galliano, C. Barolo, G. Lanzani and F. Scotognella, Near-infrared emitting single squaraine dye aggregates with large Stokes shifts, *J. Mater. Chem. C*, 2017, **5**, 7732–7738.

30 C. Zheng, M. F. Mark, T. Wiegand, S. A. Diaz, J. Cody, F. C. Spano, D. W. McCamant and C. J. Collison, Measurement and Theoretical Interpretation of Exciton Diffusion as a Function of Intermolecular Separation for Squaraines Targeted for Bulk Heterojunction Solar Cells, *J. Phys. Chem. C*, 2020, **124**, 4032–4043.

31 T. Wiegand, J. Godoy, S. Gupta, J. Cody, T. Coffey and C.-J. Collison, Optimal morphology, H-aggregation, and ternary blend excited state disruption in equilibrated squaraine-based all small molecule solar-cells, *Thin Solid Films*, 2022, 139623.

32 G. D'Avino, F. Terenziani and A. Painelli, Aggregates of quadrupolar dyes: Giant two-photon absorption from biexciton states, *J. Phys. Chem. B*, 2006, **110**, 25590–25592.

33 K. Jyothish, M. Hariharan and D. Ramaiah, Chiral Supramolecular Assemblies of a Squaraine Dye in Solution and Thin Films: Concentration-, Temperature-, and Solvent-Induced Chirality Inversion, *Chem. – Eur. J.*, 2007, **13**, 5944–5951.

34 M. Schulz, M. Mack, O. Kolloge, A. Lützen and M. Schiek, Organic photodiodes from homochiral L-proline derived squaraine compounds with strong circular dichroism, *Phys. Chem. Chem. Phys.*, 2017, **19**, 6996–7008.

35 M. Schulz, J. Zablocki, O. S. Abdullaeva, S. Brück, F. Blazer, A. Lützen, O. Arteaga and M. Schiek, Giant intrinsic circular dichroism of prolinol-derived squaraine thin films, *Nat. Commun.*, 2018, **9**, 2413.

36 N. J. Hestand, C. Zheng, A. R. Penmetcha, B. Cona, J. A. Cody, F. C. Spano and C. J. Collison, Confirmation of the origins of panchromatic spectra in squaraine thin films targeted for organic photovoltaic devices, *J. Phys. Chem. C*, 2015, **119**, 18964–18974.

37 C. Zheng, C. Zhong, C. J. Collison and F. C. Spano, Non-Kasha behavior in quadrupolar dye aggregates: The red-shifted h-aggregate, *J. Phys. Chem. C*, 2019, **123**, 3203–3215.

38 N. J. Hestand and F. C. Spano, Expanded Theory of H- and J-Molecular Aggregates: The Effects of Vibronic Coupling and Intermolecular Charge Transfer, *Chem. Rev.*, 2018, **118**, 7069–7163.

39 F. Balzer, N. J. Hestand, J. Zablocki, G. Schnakenburg, A. Lützen and M. Schiek, Spotlight on Charge-Transfer Excitons in Crystalline Textured *n*-Alkyl Anilino Squaraine Thin Films, *J. Phys. Chem. C*, 2022, **126**, 13802–13813.

40 R. Bernhardt, M. Manrho, J. Zablocki, L. Rieland, A. Lützen, M. Schiek, K. Meerholz, J. Zhu, T. L. C. Jansen, J. Knoester and P. H. M. van Loosdrecht, Structural Disorder as the Origin of Optical Properties and Spectral Dynamics in Squaraine Nano-Aggregates, *J. Am. Chem. Soc.*, 2022, **144**, 19372–19381.

 This journal is © The Royal Society of Chemistry 2023

Published on 18 May 2023. Downloaded on 6/27/2025 6:42:25 PM.

41 D. Timmer, F. Zheng, M. Gittinger, T. Quenzel, D. C. Lünemann, K. Winte, Y. Zhang, M. E. Madjet, J. Zablocki, A. Lützen, J.-H. Zhong, A. D. Sio, T. Frauenheim, S. Tretiak and C. Lienau, Charge Delocalization and Vibronic Couplings in Quadrupolar Squaraine Dyes, *J. Am. Chem. Soc.*, 2022, **144**, 19150–19162.
42 K. C. Deing, U. Mayerhöffer, F. Würthner and K. Meerholz, Aggregation-dependent photovoltaic properties of squaraine/PC61BM bulk heterojunctions, *Phys. Chem. Chem. Phys.*, 2012, **14**, 8328.
43 A. Painelli, Amplification of NLO responses: vibronic and solvent effects in push-pull polyenes, *Chem. Phys.*, 1999, **245**, 185–197.
44 D. K. A. P. Huu, C. Sissa, F. Terenziani and A. Painelli, Optical spectra of organic dyes in condensed phases: the role of the medium polarizability, *Phys. Chem. Chem. Phys.*, 2020, **22**, 25483–25491.
45 D. K. A. P. Huu, S. Saseendran and A. Painelli, Effective models for TADF: the role of the medium polarizability, *J. Mater. Chem. C*, 2022, 4620–4628.
46 M. Kasha, Energy Transfer Mechanism and the Molecular Exciton Model for Molecular Aggregates, *Radiat. Res.*, 1964, **3**, 317–331.
47 F. C. Spano, The Spectral Signatures of Frenkel Polarons in H- and J-Aggregates, *Acc. Chem. Res.*, 2010, **43**, 429–439.
48 F. Terenziani and A. Painelli, Supramolecular interactions in clusters of polar and polarizable molecules, *Phys. Rev. B: Condens. Matter Mater. Phys.*, 2003, **68**, 165405.
49 M. Anzola, F. D. Maiolo and A. Painelli, Optical spectra of molecular aggregates and crystals: testing approximation schemes, *Phys. Chem. Chem. Phys.*, 2019, **21**, 19816–19824.
50 M. Anzola and A. Painelli, Aggregates of polar dyes: beyond the exciton model, *Phys. Chem. Chem. Phys.*, 2021, **23**, 8282–8291.
51 B. Bardi, C. Dall'Agnese, M. Tassé, S. Ladeira, A. Painelli, K. I. Moineau-Chane Ching and F. Terenziani, Multistimuli-Responsive Materials from Benzothiadiazole-Based Charge-Transfer Chromophores: Interdependence of Optical Properties and Aggregation, *ChemPhotoChem*, 2018, **2**, 1027–1037.
52 C. Zhong, D. Bialas and F. C. Spano, Unusual Non-Kasha Photophysical Behavior of Aggregates of Push–Pull Donor–Acceptor Chromophores, *J. Phys. Chem. C*, 2020, **124**, 2146–2159.
53 S. Sanyal, C. Sissa, F. Terenziani, S. K. Pati and A. Painelli, Superlinear amplification of the first hyperpolarizability of linear aggregates of DANS molecules, *Phys. Chem. Chem. Phys.*, 2017, **19**, 24979–24984.
54 D. Giavazzi, S. Saseendran, F. Di Maiolo and A. Painelli, A Comprehensive Approach to Exciton Delocalization and Energy Transfer, *J. Chem. Theory Comput.*, 2023, **19**, 436–447.
55 E. U. Condon, Theories of Optical Rotatory Power, *Rev. Mod. Phys.*, 1937, **9**, 432–457.
56 D. P. Craig and T. Thirunamachandran, *Molecular Quantum Electrodynamics*, Academic Press, 1984.
57 K. Swathi, C. Sissa, A. Painelli and K. G. Thomas, Supramolecular chirality: a caveat in assigning the handedness of chiral aggregates, *Chem. Commun.*, 2020, **56**, 8281–8284.
58 F. Bertocchi, C. Sissa and A. Painelli, Circular dichroism of molecular aggregates: A tutorial, *Chirality*, 2023, DOI: **10.1002/chir.23565**.
59 B. Bardi, C. DallAgnese, K. I. Moineau-Chane Ching, A. Painelli and F. Terenziani, Spectroscopic Investigation and Theoretical Modeling of Benzothiadiazole-Based Charge-Transfer Chromophores: From Solution to Nanoaggregates, *J. Phys. Chem. C*, 2017, **121**, 17466–17478.
60 C. Zheng, C. Zhong, C. J. Collison and F. C. Spano, Non-Kasha Behavior in Quadrupolar Dye Aggregates: The Red-Shifted H-Aggregate, *J. Phys. Chem. C*, 2019, **123**, 3203–3215.
61 S. Kar, K. Swathi, C. Sissa, A. Painelli and K. G. Thomas, Emergence of Chiroptical Properties in Molecular Assemblies of Phenyleneethynylenes: The Role of Quasi-degenerate Excitations, *J. Phys. Chem. Lett.*, 2018, **9**, 4584–4590.
62 D. Van Der Spoel, E. Lindahl, B. Hess, G. Groenhof, A. E. Mark and H. J. C. Berendsen, GROMACS: Fast, flexible, and free, *J. Comput. Chem.*, 2005, **26**, 1701–1718.
63 J. Wang, R. M. Wolf, J. W. Caldwell, P. A. Kollman and D. A. Case, Development and Testing of a General Amber Force Field, *J. Comput. Chem.*, 2004, **25**, 1157.
64 C. I. Bayly, P. Cieplak, W. Cornell and P. A. Kollman, A Well-Behaved Electrostatic Potential Based Method Using Charge Restraints for Deriving Atomic Charges: the RESP Model, *J. Phys. Chem.*, 1993, **97**, 10269.
65 G. Bussi, Hamiltonian replica exchange in GROMACS: a flexible implementation, *Mol. Phys.*, 2014, **112**, 379–384.
66 N. J. Boyd and M. R. Wilson, Validating an optimized GAFF force field for liquid crystals: TNI predictions for bent-core mesogens and the first atomistic predictions of a dark conglomerate phase, *Phys. Chem. Chem. Phys.*, 2018, **20**, 1485–1496.

Supporting information

A Marvel of Chiral Squaraine Aggregates: Chiroptical Spectra beyond the Exciton Model

Davide Giavazzi, Marvin F. Schumacher, Luca Grisanti,
Mattia Anzola, Francesco Di Maiolo, Jennifer Zablocki, Arne Lützen,
Manuela Schiek, Anna Painelli

April 25, 2023

Note: citation numbers refer to the specific bibliography of this document

Contents

1 Additional UV/Vis absorbance and ellipticity spectra **4**

2 Aggregate models: further details **7**

2.1 The Exciton Model 7
2.2 Rotational strength in ESM-CT 8
2.3 The real space basis for the ESM-CT model 9
2.4 Calculation of absorption and CD spectra 10

3 Calculated spectra: additional results **13**

3.1 Standard exciton model 13
3.2 ESM-ES model 14
3.3 ESM-CT model 16

4 Molecular dynamics simulations and time-dependent Density Functional Theory 22

4.1 GAFF HREMDs 22
4.2 Modified GAFF+LCFF MDs 23
4.3 Analysis of MD trajectories 25
4.4 Selection of representative dimer structures: clustering 29
4.5 Structure refinement and TDDFT calculations 30

5 Synthesis 32

5.1 General synthesis of *N*-Boc-L-prolinyl ethers 33
5.1.1 Synthesis of *N*-Boc-L-prolinyl *n*-propyl ether 33
5.1.2 Synthesis of *N*-Boc-L-prolinyl *n*-butyl ether 34
5.1.3 Synthesis of *N*-Boc-L-prolinyl *n*-pentyl ether 35
5.1.4 Synthesis of *N*-Boc-L-prolinyl *n*-hexyl ether 35
5.1.5 Synthesis of *N*-Boc-L-prolinyl *n*-heptyl ether 36
5.1.6 Synthesis of *N*-Boc-D-prolinyl *n*-heptyl ether 36
5.1.7 Synthesis of *N*-Boc-L-prolinyl *n*-octyl ether 37
5.1.8 Synthesis of *N*-Boc-L-prolinyl *n*-nonyl ether 38
5.1.9 Synthesis of *N*-Boc-L-prolinyl *n*-decyl ether 38
5.1.10 Synthesis of *N*-Boc-L-prolinyl *n*-undecyl ether 39
5.1.11 Synthesis of *N*-Boc-L-prolinyl *n*-dodecyl ether 40
5.1.12 Synthesis of *N*-Boc-L-prolinyl *n*-hexadecyl ether 41
5.2 General method for the Boc deprotection 41
5.2.1 Synthesis of L-prolinyl *n*-propyl ether 42
5.2.2 Synthesis of L-prolinyl *n*-butyl ether 42
5.2.3 Synthesis of L-prolinyl *n*-pentyl ether 43
5.2.4 Synthesis of L-prolinyl *n*-hexyl ether 44
5.2.5 Synthesis of L-prolinyl *n*-heptyl ether 44
5.2.6 Synthesis of D-prolinyl *n*-heptyl ether 45
5.2.7 Synthesis of L-prolinyl *n*-octyl ether 45
5.2.8 Synthesis of L-prolinyl *n*-nonyl ether 46
5.2.9 Synthesis of L-prolinyl *n*-decyl ether 46

5.2.10 Synthesis of L-prolinyl *n*-undecyl ether 47
5.2.11 Synthesis of L-prolinyl *n*-dodecyl ether 48
5.2.12 Synthesis of L-prolinyl *n*-hexadecyl ether 48
5.3 General synthesis of squaraines 49
5.3.1 Synthesis of 2,4-Bis[4-(*S*)-(-)-2-(propyloxymethyl)-pyrrolidone-2,6-dihydroxyphenyl]squaraine (*S*,*S*)-ProSQ-C3 49
5.3.2 Synthesis of 2,4-Bis[4-(*S*)-(-)-2-(butyloxymethyl)-pyrrolidone-2,6-dihydroxyphenyl]squaraine (*S*,*S*)-ProSQ-C4 50
5.3.3 Synthesis of 2,4-Bis[4-(*S*)-(-)-2-(pentyloxymethyl)-pyrrolidone-2,6-dihydroxyphenyl]squaraine (*S*,*S*)-ProSQ-C5 51
5.3.4 Synthesis of 2,4-Bis[4-(*S*)-(-)-2-(hexyloxymethyl)-pyrrolidone-2,6-dihydroxyphenyl]squaraine (*S*,*S*)-ProSQ-C6 52
5.3.5 Synthesis of 2,4-Bis[4-(*S*)-(-)-2-(heptyloxymethyl)-pyrrolidone-2,6-dihydroxyphenyl]squaraine (*S*,*S*)-ProSQ-C7 52
5.3.6 Synthesis of 2,4-Bis[4-(*R*)-(-)-2-(heptyloxymethyl)-pyrrolidone-2,6-dihydroxyphenyl]squaraine (*R*,*R*)-ProSQ-C7 53
5.3.7 Synthesis of 2,4-Bis[4-(*S*)-(-)-2-(octyloxymethyl)-pyrrolidone-2,6-dihydroxyphenyl]squaraine (*S*,*S*)-ProSQ-C8 54
5.3.8 Synthesis of 2,4-Bis[4-(*S*)-(-)-2-(nonyloxymethyl)-pyrrolidone-2,6-dihydroxyphenyl]squaraine (*S*,*S*)-ProSQ-C9 55
5.3.9 Synthesis of 2,4-Bis[4-(*S*)-(-)-2-(decyloxymethyl)-pyrrolidone-2,6-dihydroxyphenyl]squaraine (*S*,*S*)-ProSQ-C10 56
5.3.10 Synthesis of 2,4-Bis[4-(*S*)-(-)-2-(undecyloxymethyl)-pyrrolidone-2,6-dihydroxyphenyl]squaraine (*S*,*S*)-ProSQ-C11 57
5.3.11 Synthesis of 2,4-Bis[4-(*S*)-(-)-2-(dodecyloxymethyl)-pyrrolidone-2,6-dihydroxyphenyl]squaraine (*S*,*S*)-ProSQ-C12 58
5.3.12 Synthesis of 2,4-Bis[4-(*S*)-(-)-2-(hexadecyloxymethyl)-pyrrolidone-2,6-dihydroxyphenyl]squaraine (*S*,*S*)-ProSQ-C16 59

References **59**

6 NMR and mass spectra **63**

6.1 NMR spectra 63
6.2 Mass spectra 90

1 Additional UV/Vis absorbance and ellipticity spectra

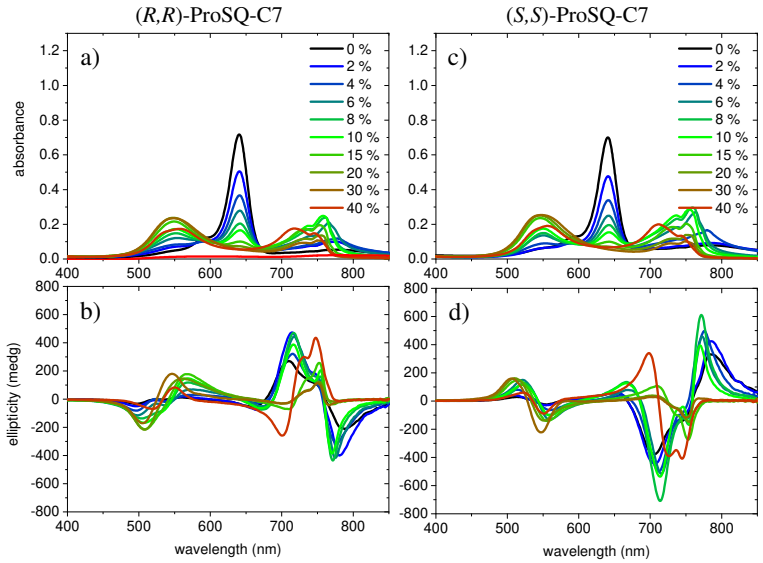


Figure S1: Experimental UV/Vis absorbance spectra a), c), and corresponding ellipticity spectra b), d) for the (*R*,*R*)-ProSQ-C7 (a) and b)) and (*S*,*S*)-ProSQC7 compounds (b) and c)). The legend indicates the volume-percentage of water in the methanol-water mixture and applies for all plots.

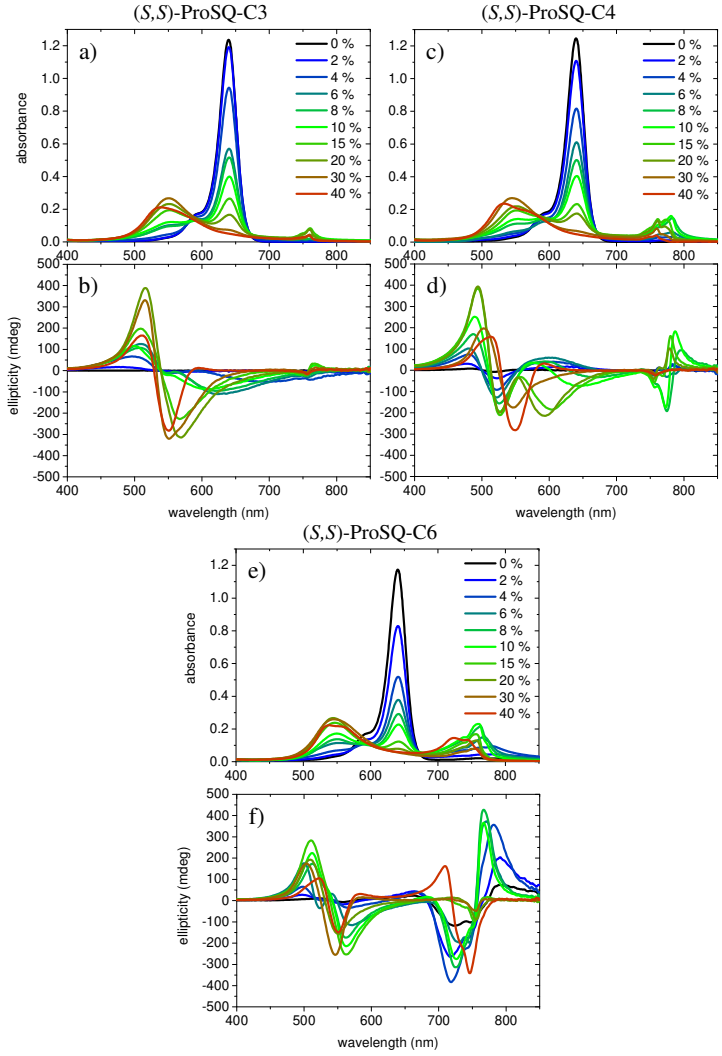


Figure S2: Experimental UV/Vis absorbance spectra a), c), e), and ellipticity spectra b), d), f) for the(*S,S*)-ProSQ compounds with varying alkyl chains: C3 in a) and b), C4 in c) and d), and C6 in e) and f). The legend indicates the volume-percentage of water in the methanol-water mixture and applies for all plots.

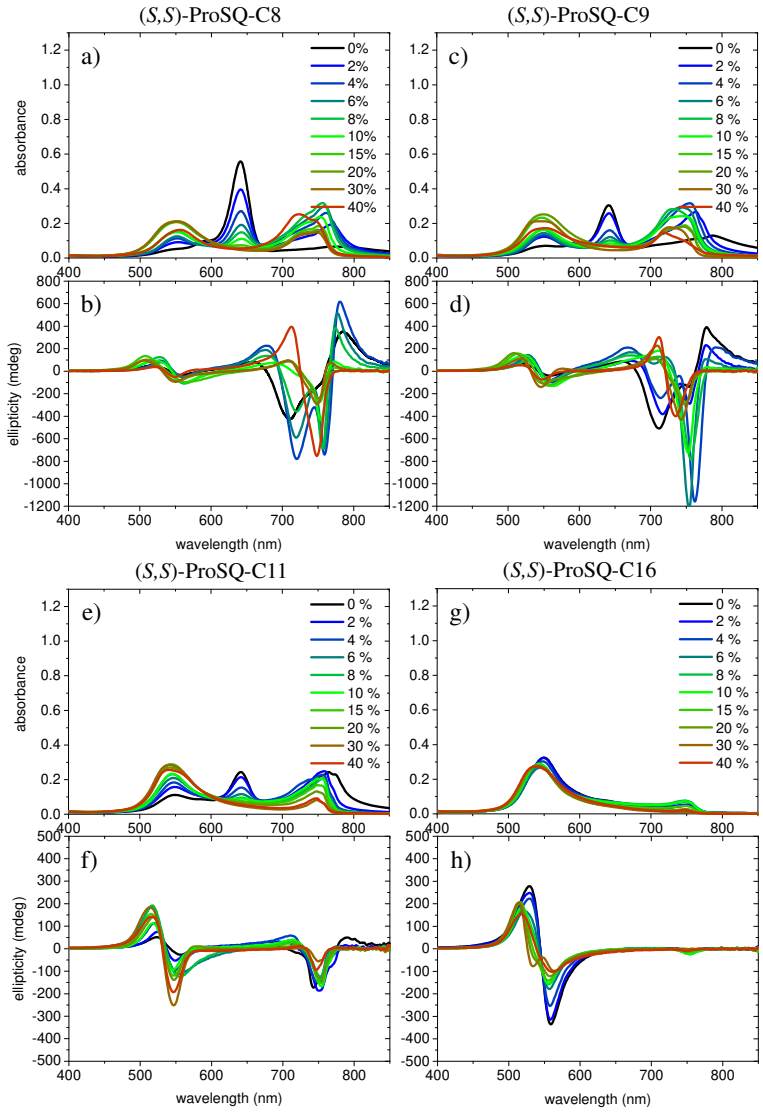


Figure S3: Experimental UV/Vis absorbance spectra a), c), e), g) and corresponding ellipticity spectra b), d), f), h) for the(*S*,*S*)-ProSQ compounds with varying alkyl chain lengths: C8 in a) and b), C9 in c) and d), C11 in e) and f), and C16 in g) and h). The legend indicates the volume-percentage of water in the methanol-water mixture and applies for all plots. For both enantiomers of the C16 compound titration experiments with acetonitrile as poor solvent can be found in reference [1].

2 Aggregate models: further details

2.1 The Exciton Model

The simplest model to account for electrostatic intermolecular interactions in molecular aggregates is the celebrated exciton model.[2, 3, 4] In this very simple model, a single transition is considered on each molecule with frequency ω_c (the correction of the excitation energy of the monomer due to the inclusion of the molecule in the aggregate is often neglected or phenomenologically introduced as a correction to ω_c). In the hypothesis that intermolecular interactions are small if compared with the excitation energies, only degenerate states are mixed up. Specifically, if interested to linear spectral properties, it is enough to diagonalize the Hamiltonian written on the basis of the states bearing a single excited molecule (single exciton subspace). Accordingly, for an aggregate of N molecules the relevant basis is comprised of the states where the i molecule (i runs from 0 to N) is in the excited state, while all other molecules are in the ground state state. Electrostatic intermolecular interactions are typically introduced in the dipolar approximation so that the interaction between the two states where either molecule i or j is in the excited state reads:

$$J_{ij} = \frac{\mu_c^2}{4\pi\epsilon_0\eta^2 d_{ij}^3}\mu_c^2 G_{ij} \tag{1}$$

where μ_c is the transition dipole moment (as experimentally estimated for the isolated dye), ϵ_0 is the vacuum dielectric constant, η is the medium refractive index and G_{ij} is a purely geometric factor that only depends on the distance and relative orientation of the transition dipole moments on the two molecules:

$$G_{ij} = \vec{e}_i \cdot \vec{e}_j - 3(\vec{e}_i \cdot \vec{e}_{ij})(\vec{e}_j \cdot \vec{e}_{ij}) \tag{2}$$

where $\vec{e}_i$ is the unit vector parallel to the dipole moment on molecule i and $\vec{e}_{ij}$ is the unit vector associated with the $i-j$ direction. The diagonalization of the $N \times N$ exciton Hamiltonian gives the excitonic eigenstates ϕ_k, with energies ϵ_k as linear combitations of the basis states.

To address absorption spectra, transition dipole moments must be calculated from the ground state (the state where all molecules are not excited) and the ϕ_k

eigenstates. To do so, the total dipole moment operator is defined as the vectorial sum of the molecular dipole moment operators, so that the transition dipole moment and the rotational strength for the k-th exciton transition are easily expressed on the basis of the transition dipole moments on each dye and their relative orientation and positions.[5] Since in the exciton model the dimension of the relevant subspace is equal to N, the number of dyes in the aggregates, very large aggregates, easily up to thousands of dyes, can be addressed.

2.2 Rotational strength in ESM-CT

The magnetic dipole is proportional to the total angular momentum:

$$\hat{\vec{M}} \propto -\hat{\vec{L}} = -\sum_k \hat{\vec{l}}_k \tag{3}$$

where k runs on all electrons and the angular momentum of k electron is related to its linear momentum $\hat{\vec{p}}_k$ by

$$\hat{\vec{l}}_k = \vec{r}_k \wedge \hat{\vec{p}}_k \tag{4}$$

Finally the linear momentum can be obtained as

$$\hat{\vec{p}}_k = -\frac{i}{\hbar}[\hat{\vec{\mu}}_k, H] \tag{5}$$

The problem is that in a real-space description we cannot address the properties of a single electron.

To overcome the problem we start evaluating the total linear momentum. For the sake of clarity, we address only its x component:

$$\hat{P}_x = -\frac{i}{\hbar}[\hat{D}_x, H] \tag{6}$$

where $\hat{D}_x$ is the x component of the total dipole moment, defined in Eq. 11. The dipole moment operator commutes with all terms in the Hamiltonian in Eq. 9 but the intra- and inter-molecular hopping terms. Accordingly:

$$\begin{aligned} \hat{P}_x &= \frac{i}{\hbar} t \sum_{i=1}^{N} [(x_{i2} - x_{i1})\hat{v}_{i1,i2} + (x_{i3} - x_{i2})\hat{v}_{i2,i3}] \\ &+ \frac{i}{\hbar}\beta \sum_{i=1}^{N-1} \left[(x_{(i+1)1} - x_{i2})\hat{v}_{i2,(i+1)1} + (x_{(i+1)2} - x_{i3})\hat{v}_{i3,(i+1)2}\right] \end{aligned} \tag{7}$$

where the bond velocity is the antiHermitian operator

$$\hat{v}_{ip,jq} = \hat{b}_{ip,jq} - \hat{b}^{\dagger}_{ip,jq} = \hat{b}_{ip,jq} - \hat{b}_{jq,ip} \tag{8}$$

The vectorial product $\hat{\vec{D}} \wedge \hat{\vec{P}}$ is not the total angular momentum in Eq. 3. Indeed $\hat{\vec{L}}$ and hence the magnetic dipole operator is a one-electron operator, while $\hat{\vec{R}} \wedge \hat{\vec{P}}$ does contain both one-electron and two-electron terms. We then define for our purposes $\hat{\vec{L}}$ selecting out of the $\hat{\vec{D}} \wedge \hat{\vec{P}}$ operator only the one-electron terms. Accordingly:

$$\begin{aligned}
\hat{L}_x \;=\; & -\frac{i}{\hbar} t \sum_{i=1}^{N} \Big[(z_{i2} - z_{i1})(y_{i1}\hat{b}_{i1,i2} - y_{12}\hat{b}_{i2,i1}) + (z_{i3} - z_{i2})(y_{i2}\hat{b}_{i23} - y_3\hat{b}_{32}) \Big] \\
& -\frac{i}{\hbar} \beta \sum_{i=1}^{N-1} \Big[(z_{(i+1)1} - z_{i,2})(y_{i,2}\hat{b}_{i2,(i+1)1} - y_{(i+1)1}\hat{b}_{(i+1)1,i2}) \\
& +(z_{(i+1)2} - z_{i3})(y_{i3}\hat{b}_{i3,(i+1)2} - y_{(i+1)2}\hat{b}_{(i+1)2,i3}) \Big] \\
& +\frac{i}{\hbar} t \sum_{i=1}^{N} \Big[(y_{i2} - y_{i1})(z_{i1}\hat{b}_{i1,i2} - z_{12}\hat{b}_{i2,i1}) + (y_{i3} - y_{i2})(z_{i2}\hat{b}_{i23} - z_3\hat{b}_{32}) \Big] \\
& +\frac{i}{\hbar} \beta \sum_{i=1}^{N-1} \Big[(y_{(i+1)1} - y_{i,2})(z_{i,2}\hat{b}_{i2,(i+1)1} - z_{(i+1)1}\hat{b}_{(i+1)1,i2}) \\
& +(y_{(i+1)2} - y_{i3})(z_{i3}\hat{b}_{i3,(i+1)2} - z_{(i+1)2}\hat{b}_{(i+1)2,i3}) \Big]
\end{aligned} \tag{9}$$

Analogous expressions for $\hat{L}_y$ and $\hat{L}_z$ can be obtained upon cyclic permutation of x, y, z indices. Remembering that $-\hat{\vec{L}} \propto \hat{\vec{M}}$ we are now in the position to calculate rotational strengths using Eq. 7.

2.3 The real space basis for the ESM-CT model

The definition of the basis relevant to the Hamiltonian in Eq. 9 describing delocalized electrons in the aggregate is a delicate issue. The basis selected by Spano and coworkers[6] that comprises only 15 states for a dimer is not complete. Specifically, only the charge distribution is accounted for, neglecting spin degrees of freedom, or, in more technical terms, electrons are approximated as spinless fermions. If electronic spin is accounted for the smallest basis is the valence-bond basis, that limit attentions to subspaces with the total spin quantum number S is conserved. Just as an example, fig. S4 shows how a single diagram in the

spinless fermion representation, corresponding to a specific charge distribution, actually corresponds to two valence bond-diagrams in the singlet states $S = 0$.

The valence bond basis is very convenient in terms of reduced dimension of the subspaces, but it has the main disadvantage of being non-orthonormal, leading to a somewhat cumbersome calculation of the matrix elements. We therefore adopt the much simpler real-space basis where electrons are located in the site orbitals and only states with the total projection of the spin operator equal to zero are considered, S_z=0. This leads to a much larger basis set than in valence bond, since it also includes S_z=0 components from triplet and higher spin states, but with the advantage of working with an orthonormal basis. Specifically, fig. S4 shows that the spinless Fermion state in panel (a) corresponds to 6 real space states in panel (c).

We use a bit representation for the real space basis, assigning 2 bits to each site, the first bit refers to the α spin, the second bit to β spin. An, of course 0/1 means that the specific spin state is void/occupied. Considering a single squaraine, just as an example, the $|N\rangle$ state is represented as 110011, while $|Z1\rangle$ is a singlet state, represented as a linear combination of 100111 and 011011. For the SQ dimer the real space basis is composed of 53 diagrams, listed in Fig 2. The diagonalization of the Hamiltonian matrix written on the real space basis gives relevant eigenstates $\psi_i\rangle$ and energies E_i.

2.4 Calculation of absorption and CD spectra

Irrespective of the specific model adopted for the calculation, spectra are calculated from the eigenstates, $|\psi_i\rangle$, where $|\psi_0\rangle$ is the ground states (the lowest energy states). Specifically absorption spectra are calculated as:

$$Abs(\omega) = \frac{1}{N}\hbar\omega \sum_i e^{-\frac{\hbar\omega-\hbar\omega_i}{2\sigma^2}} |\langle\psi_i|\hat{\vec{D}}|\psi_0\rangle|^2 \tag{10}$$

where N is the number of molecules in the aggregate, $\hbar\omega_i$ is the energy of the $|\psi_0\rangle \rightarrow |\psi_0\rangle$ transition and $\hat{\vec{D}}$ is the aggregate dipole moment as defined in the main text according to the specific model. A Gaussian bandshape with standard deviation σ is assigned to each absorption transition.

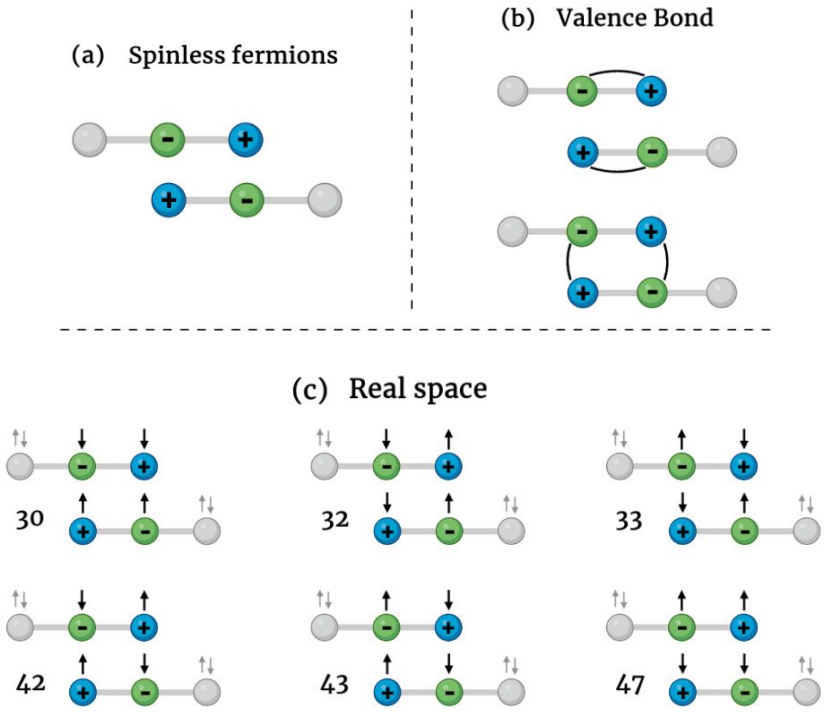


Figure S4: (a) Specific charge distribution for a dimer, corresponding to a single basis state in the spinless fermion approximation adopted in ref. [6]. (b) The two valence bond states corresponding to the same charge distribution as in (a) where the black lines mark two electrons paired in a singlet state, in the standard representation by Pauling. (c) The six real space diagrams corresponding to the charge distribution in (a), the numbers assigned to each diagram correspond to the labels in Fig. S5

1	1275	110111 110010	28	3318	011011 110011
2	1467	110111 011010	29	3321	100111 110011
3	1515	110101 111010	30	3435	110101 101011
4	1530	010111 111010	31	3450	010111 101011
5	1659	110111 100110	32	3483	110110 011011
6	1719	111011 010110	33	3495	111001 011011
7	1755	110110 110110	34	3507	110011 011011
8	1767	111001 110110	35	3510	011011 011011
9	1779	110011 110110	36	3513	100111 011011
10	1782	011011 110110	37	3546	010110 111011
11	1785	100111 110110	38	3555	110001 111011
12	2295	111011 110001	39	3558	011001 111011
13	2427	110111 101001	40	3561	100101 111011
14	2487	111011 011001	41	3570	010011 111011
15	2523	110110 111001	42	3675	110110 100111
16	2535	111001 111001	43	3687	111001 100111
17	2547	110011 111001	44	3699	110011 100111
18	2550	011011 111001	45	3702	011011 100111
19	2553	100111 111001	46	3705	100111 100111
20	2679	111011 100101	47	3735	111010 010111
21	2775	111010 110101	48	3765	101011 010111
22	2805	101011 110101	49	3795	110010 110111
23	3195	110111 100011	50	3798	011010 110111
24	3255	111011 010011	51	3801	100110 110111
25	3291	110110 110011	52	3813	101001 110111
26	3303	111001 110011	53	3825	100011 110111
27	3315	110011 110011			

Figure S5: The 53 diagrams composing the real state basis of a dimer. The first column numbers the diagrams, the second column is the integer number representative of each state, the third column is the corresponding bit representation

Similarly, CD spectra are calculated as:

$$CD(\omega) = \frac{1}{N} \sum_i e^{-\frac{\hbar\omega - \hbar\omega_i}{2\sigma^2}} R_i \tag{11}$$

where for a system with localized electrons the rotational strenghts R_i are calculated following eq. 8 in the main text, while for a system with delocalized electrons the more general equation 7 (main text) is used, where $\vec{\hat{M}}$ is evaluated according to equations S4 and S10.

3 Calculated spectra: additional results

In the following we report additional calculated spectra (absorption in the top panels and CD in the bottom panels) obtained in different approximations and varying the parameters entering the calculation (the number of molecules N, the angle α, the refractive index η and the amount of intermolecular charge transfer β; parameter values are specified in the figures).

3.1 Standard exciton model

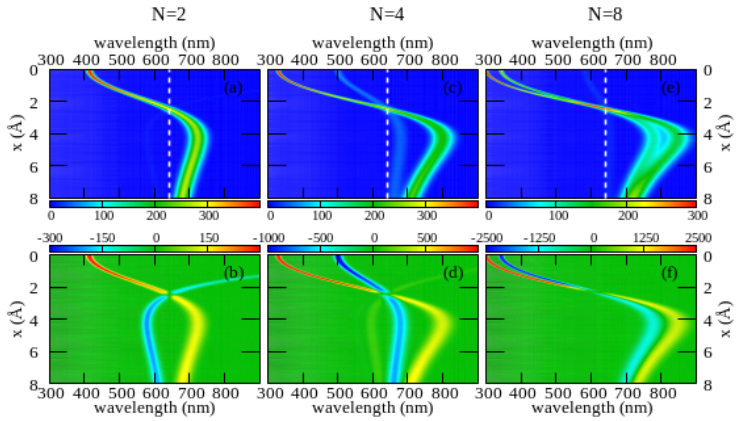


Figure S6: Results for aggregates of 2, 4 and 8 molecules obtained in the standard exciton model for the same geometries as in Fig. 4 (main text) and setting the molecular parameters entering the model as ω_c=1.93 eV, μ_c=12.5 D (values from ref. 41 in main text). Same quantities as in main text fig. 4. All intensities, in arbitrary units, are normalized to the number of molecules.

3.2 ESM-ES model

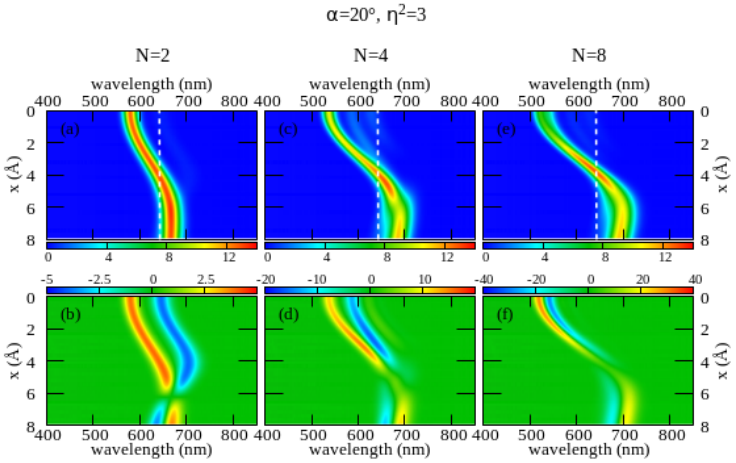


Figure S7: Results for aggregates of 2, 4 and 8 molecules with the same molecular parameters as in Fig. 4 (main text) and r=3.5 Å, α=20° and $\eta^2 = 3$.

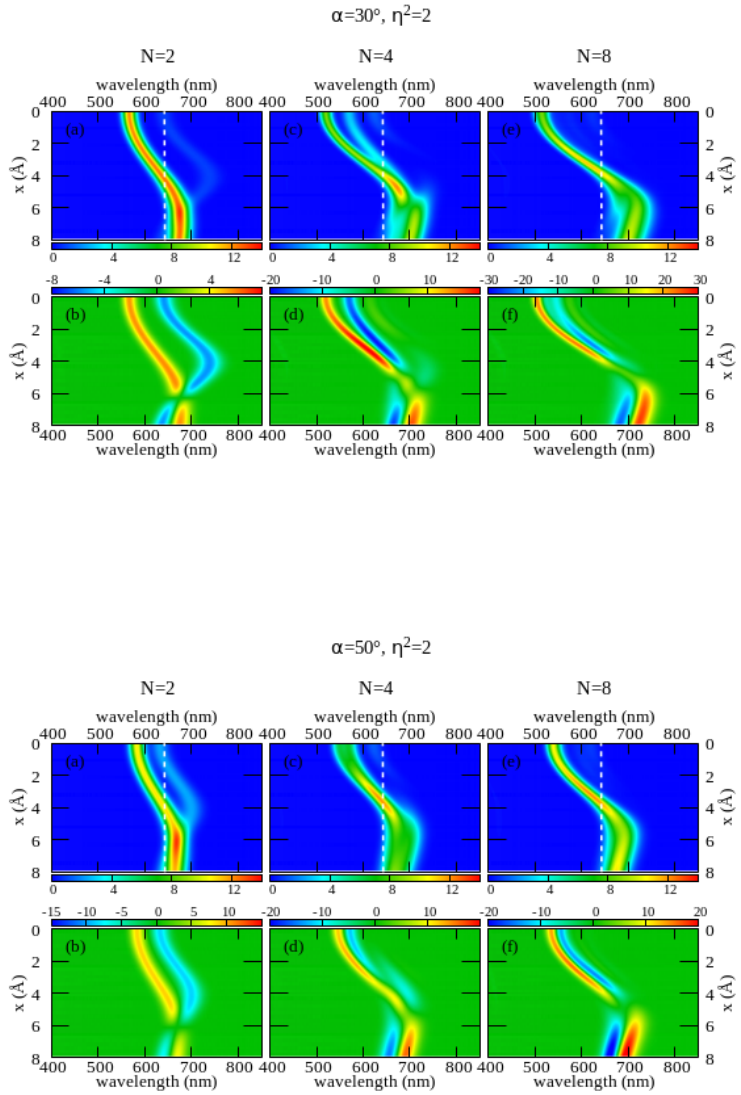


Figure S8: Results for aggregates of 2, 4 and 8 molecules with with the same molecular parameters as in Fig. 4 (main text) and r=3.5 Å, $\eta^2 = 2$, α=30° (topmost panels) and α=50° (bottom panels).

3.3 ESM-CT model

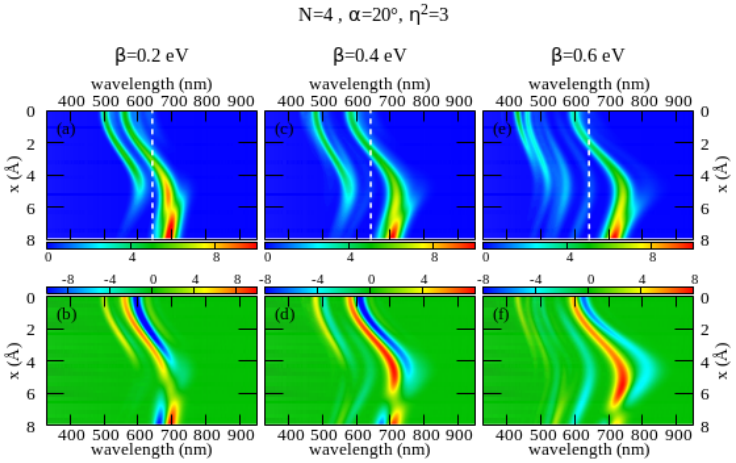


Figure S9: Results for aggregates of 4 molecules with the same molecular parameters as in Fig. 4 (main text) and for β =0.2, 0.4 and 0.6 eV with r=3.5 Å, α=20° and $\eta^2 = 3$.

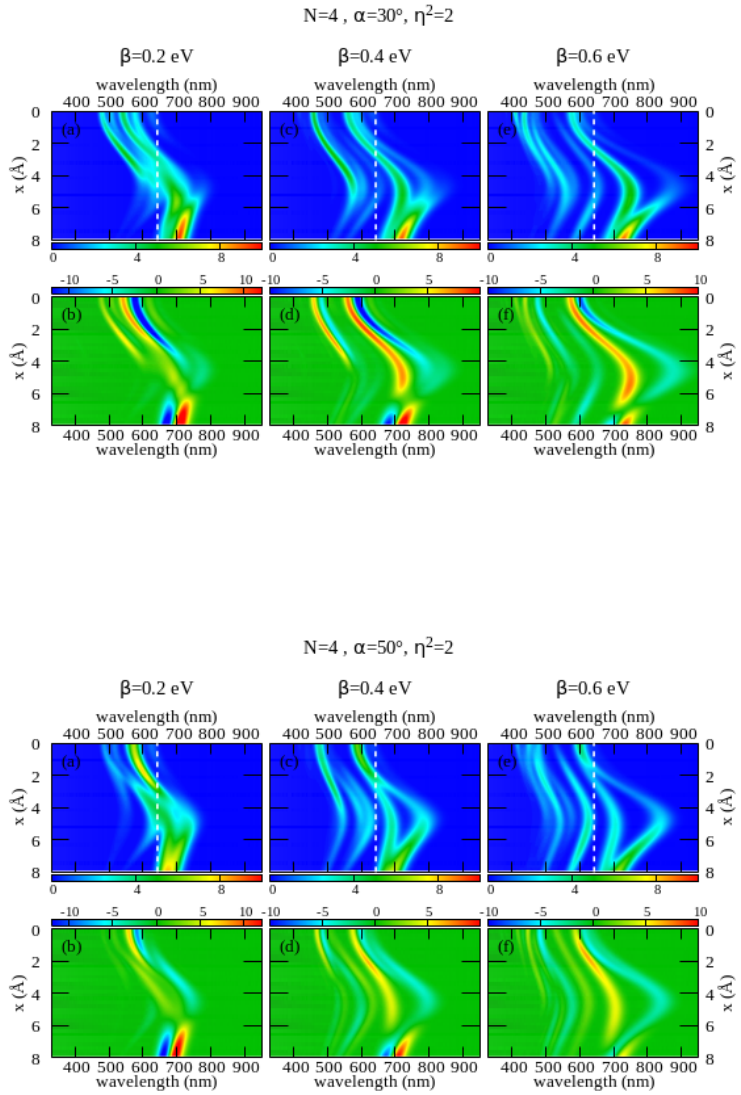


Figure S10: Results for aggregates of 4 molecules with the same molecular parameters as in Fig. 4 (main text) and for β =0.2, 0.4 and 0.6 eV with r=3.5 Å, $\eta^2 = 2$, α=30° (topmost panels) and α=50° (bottom panels).

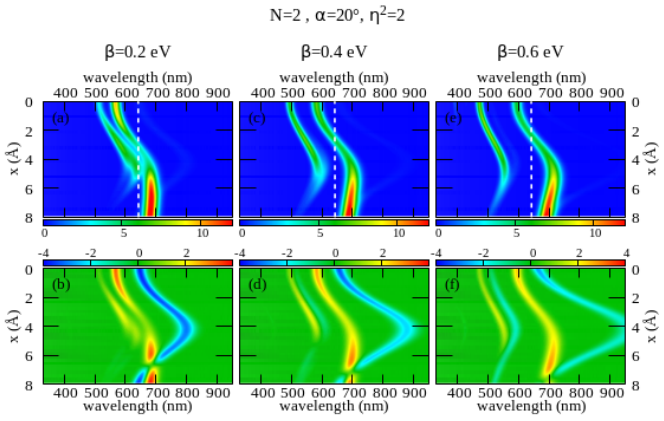


Figure S11: Results for aggregates of 2 molecules with the same molecular parameters as in Fig. 4 (main text) and for β =0.2, 0.4 and 0.6 eV with r=3.5 Å, α=20° and $\eta^2 = 2$.

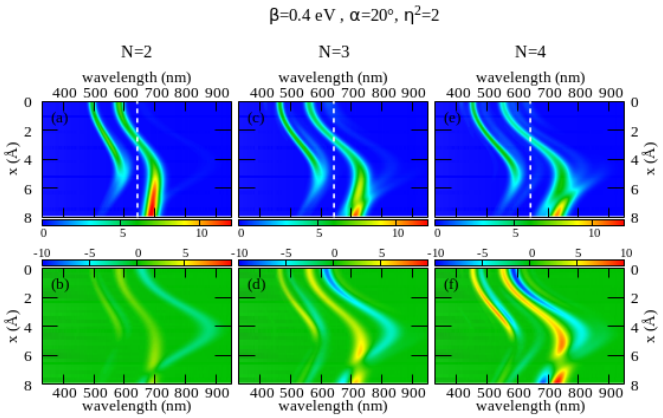


Figure S12: Results for aggregates of 2, 3 and 4 molecules with with the same molecular parameters as in Fig. 4 (main text) and for β =0.4 eV, r=3.5 Å, α=20° and $\eta^2 = 2$.

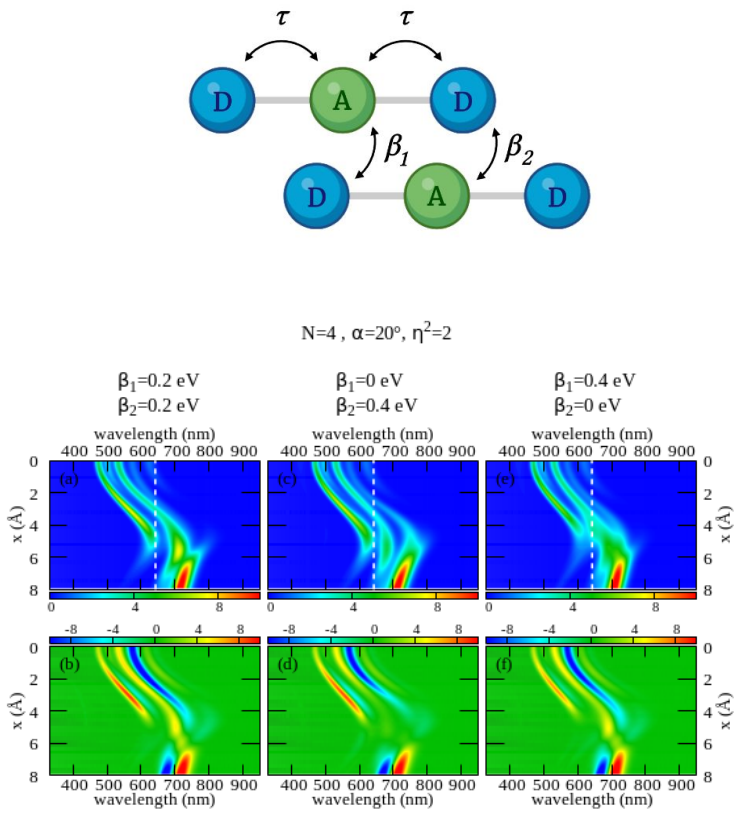


Figure S13: Results for aggregates of 4 molecules with with the same molecular parameters as in Fig. 4 (main text) and r=3.5 Å, α=20°, $\eta^2 = 2$ and imposing $\beta_1 = \beta_2 = 0.2$ eV (left panels), $\beta_1 = 0$ eV and $\beta_2 = 0.4$ eV (middle panels) and $\beta_1 = 0.4$ eV and $\beta_2 = 0$ eV (left panels).

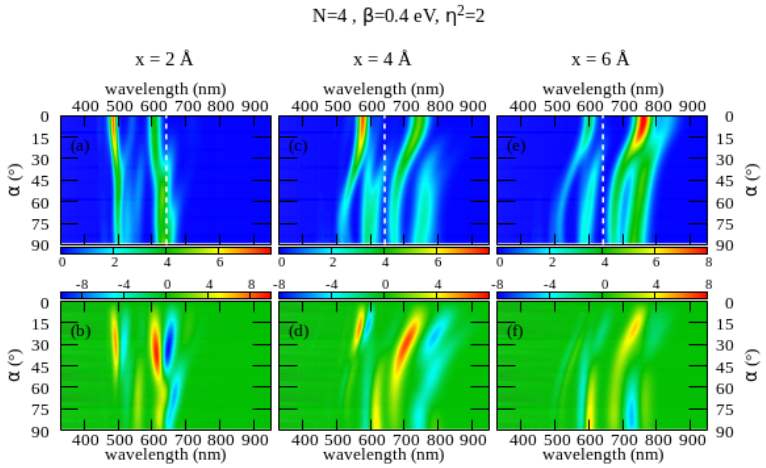


Figure S14: Results as a function of the angle α for aggregates of 4 molecules with with the same molecular parameters as in Fig. 4 (main text) and β =0.4 eV, r=3.5 Å, $\eta^2 = 2$ for different values of x.

4 Molecular dynamics simulations and time-dependent Density Functional Theory

Explicit solvent boxes were prepared as pure methanol [7] and 60:40 v/v mixture of methanol and water [8]. Simulation boxes in the two compositions were prepared and equilibrated and used as a starting point for the insertion of ProSQ-C10 according to the simulation set-up described below. For production runs in the NPT ensemble (300 K, 1 atm) Velocity Verlet algorithm was used and time step was set to 1fs, with v-rescale and Berendsen algorithms for temperature and pressure couplings, respectively, and with all bonds constrained using LINCS[9]. All simulations were pre-equilibrated for 4ns using Berendsen for both pressure and temperature coupling.

4.1 GAFF HREMDs

MD Hamiltonian replica exchange (HREMD) [10] simulations were were run using GROMACS 2020 [11] and its PLUMED plugin [12]. General AMBER Force Field (GAFF) [13] parameters were assigned using the antechamber module of AmberTools. QM calculations in g16 [14] were run to obtain RESP charges [15] at the HF/6-31G* level, calculated on previously optimized geometries at DFT-B3LYP [16] obtained by constraining planarity on the conjugated molecular core. The following simulations were run for ProSQ-C10: (a) 140ns of HREMD (12 replicas) of ProSQ-C10(S,S) tetramer in 60:40 MeOH:water (b) 140ns of HREMD (12 replicas) of ProSQ-C10(S,S) tetramer in pure MeOH (c) 60ns of HREMD (12 replicas) of ProSQ-C10(R,R) tetramer in pure MeOH. Results for ProSQ-C10 (S,S) tetramers are shown as 2D heatmaps of the center of mass (CM) distances vs. dihedral helical angle α in Fig. S15.

Simulation box size amounts to $\sim$ 50 Å corresponding to $\sim$ 1750 MeOH molecules (pure methanol simulation) or $\sim$ 1050 MeOH and 1550 water molecules (for the methanol-water 60:40 mixture), under fully periodic boundary conditions. In all cases only the trajectory of the first replica, at 300 K, was retained. In the above simulations, molecules were placed along an approximate stack in

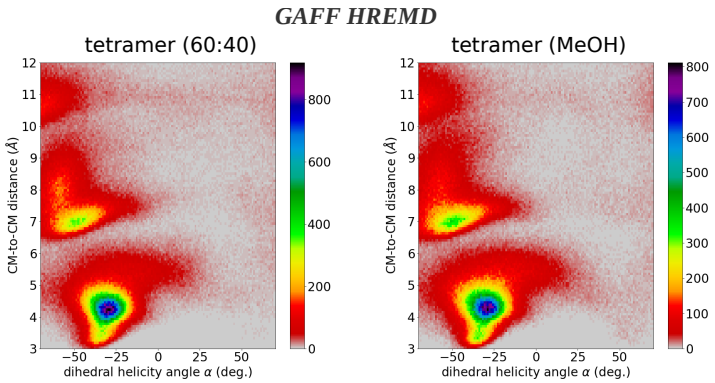


Figure S15: Results of two GAFF HREMDs on ProSQ-C10 (S,S) in methanol-water 60:40 mixtures (left) and pure methanol (right). Color plots showing the distribution of α (x axis, in degree), defined as in Fig. 3, main text) and of the distance between two center of mass (y-axis, in Å).

the starting geometry, before relaxation and equilibration. Further simulations in pure water (tot extra HREMD simulation time: 220 ns), as well as starting from different input structures (tot extra HREMD simulation time: $\sim$ 130 ns) were attempted searching for different type of aggregates and to ensure there is no bias due to the starting structure. In all cases, the same kind of helices as dominating structures were obtained (results not shown).

4.2 Modified GAFF+LCFF MDs

We manually edited some of the GAFF parameters to fix two critical issues, deriving the mod.GAFF+LCFF. First, in an attempt to improve the description of the conjugated core, we set to values for sp^2 carbon (differently from smaller value assigned automatically). This choice was motivated by the observation of several structures featuring a twisted molecular plane, not expected in term of chemical intuition. Moreover, we identify limitation of GAFF when systems exhibit long alkyl chains, as in our case. This was specifically addressed in the work by Boyd and Wilson on liquid crystals [17]. Starting from the above standard GAFF for ProSQ-C10 molecule with RESP charges, topologies were

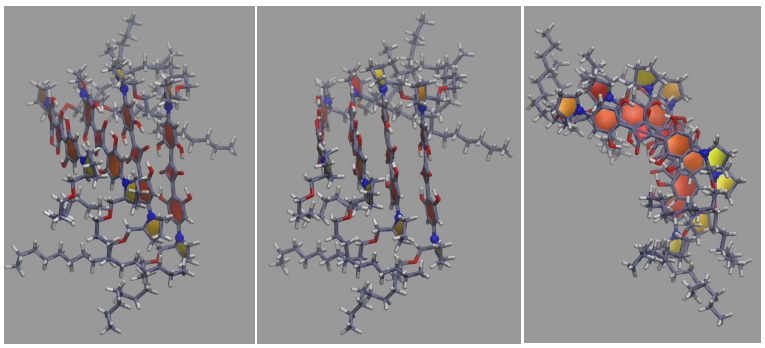


Figure S16: Sketches of a representative configuration selected along the tetramer simulated with mod. GAFF+LCFF MDs from the main right-hand helix (domain marked as A in Fig. 7 in the main text), view in three different perspectives. Rings are highlighted in colors, and nitrogen atoms represented as blue spheres.

modified accordingly, so that these mod.GAFF+LCFF MDs simulations were run of ProSQ-C10 (S,S): a) 200 ns for tetramer in Methanol:water 60:40, b1-b6) 6× 45 ns of 12-mer aggregate in 60:40 MeOH:water, c1-c2) 2× 45 ns of 24-mer aggregate in 60:40 MeOH:water.

Under fully periodic boundary conditions simulation boxes were considered with size $\sim$ 50 Å for tetramers (see above), $\sim$ 100 Å for 12-mer (9000 MeOH and 13000 water molecules approx), and $\sim$ 150 Å for 24-mer (30000 MeOH and 45000 water molecules approx). The starting structures were obtained placing the molecules onto a 2x2x3 cubic grid for 12-mer and on a 3x3x3 -3 grid for 24-mer MDs. The spacing in the grids amonted to 20 Å and moelcules where random orientated in each point of the grid. In all cases, a single aggregate is obtained after the first few ns of dynamics, often already between the minimization and the pre-equilibration phase.

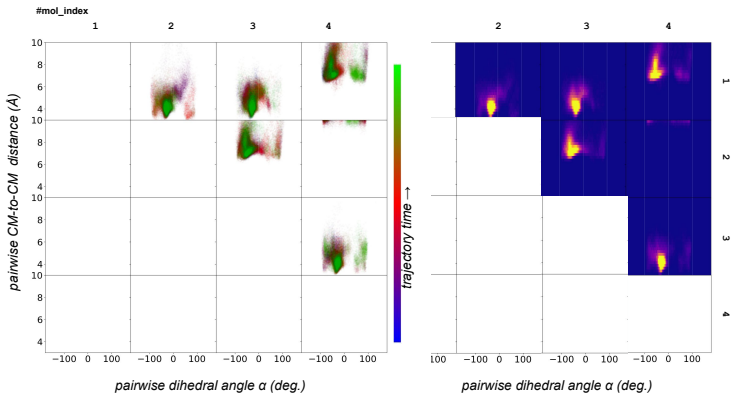


Figure S17: 2D distributions along dihedral angle α (x axis) and distance between two center of masses (y-axis) from the tetramer mod.GAFF+LCFF MDs for each molecular pair separately. Left: datapoints are shown according to the their time-occurrence during the simulation. Right, distributions of the same pairwise quantities shown as 2D color-maps on the overall trajectory.

4.3 Analysis of MD trajectories

Analysis on MDs trajectories obtained by Gromacs [11] were performed by employing python module MDAnalysis [18, 19]. The geometrical parameters were extracted, as schematically shown in Fig. S18, by selecting 4 atoms that represent the shape of the system: two carbon atoms of the squarainic core connected to oxygens (C1 and C3) and the two carbons Ca on the external vertex of the aromatic rings, connected to the two nitrogens (C14 and C8). By representing with $\vec{R}_A$ the coordinates of atom/point A, we can then define a set of geometrical derived quantities. Specifically, we define the molecular center of mass (CM) $\vec{R}_{CM} = \frac{1}{2}(\vec{R}_{C1} + \vec{R}_{C3})$, and the average plane, defined by the normal to the two axis: $\vec{a}(C1, C3)$ and $\vec{a}(C8, C14)$ as a proxy for the average molecular plane A. We also define the two molecular arms as vector connecting molecular CM to the Ca atoms: $\vec{v}(CM, C8)$ and $v(\vec{CM}, C14)$. Moreover, for the dimer we can define the angle *alpha*, defined in Fig. 3 main text, as the dihedral angle (Ca,CM,CM',Ca') where primed index refers to the second molecule, and Ca and Ca' refer to the either C8 or C14 atoms that determines the closest inter-

molecular Ca pair. All other quantities appearing in Fig. S19, including x and r (see Fig. 3, main text) were derived from the above quantisties, implementing point-to-plane distances and projections. Dealing with dimers, it is possible to compute two values for x and r, the employed value is then the average of the two. In figure S18 a sketch of some of these quantities is shown. In all cases, the first 10 ns of simulations were excluded from the analysis.

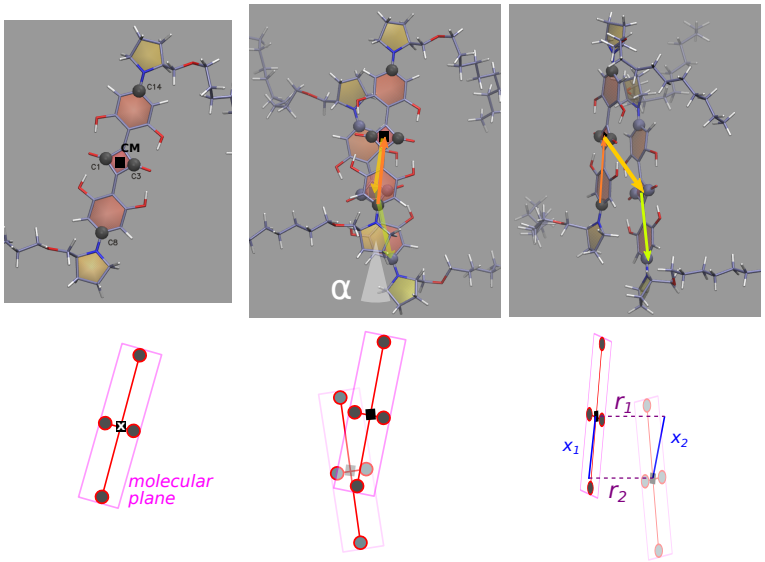


Figure S18: Top panels: example of a molecular structure of squaraine with highlighted atoms used for references and the center of mass (CM) marked as black square (left), molecular structure of a dimer with 3 vectors highlighted used to compute the dihedral angle α: $\vec{v}(Ca, CM)$ (orange), $\vec{v}(CM, CM')$ (yellow) and $\vec{v}(CM', Ca')$ (lime green), from top (middle) and side view (right). Bottom panels: sketch of the molecular frame used to define the molecular plane (left), and a possible dimer arrangement from top (middle). Side view of the same dimer with the definition of distances between CM and projection of CM', labeled as x_1 and x_2 and used to compute the displacement $x = \frac{1}{2}(x_1 + x_2)$ and the distance between the plane and such projection r_1 and r_2, used to define the plane distance $r = \frac{1}{2}(r_1 + r_2)$.

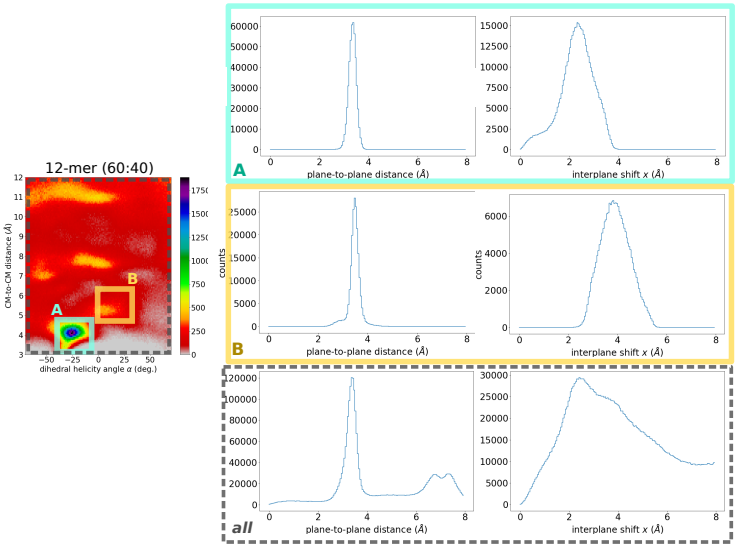


Figure S19: Panel on the right: distributions of geometrical quantities according to the region A of the right-handed helix (cyan contour), the region B of the left-handed helix (orange contour) vs. the whole region (dashed gray contour). The heatmaps on the left, is the same as Fig. T1: pairwise helical dihedral angle equivalent to α (x axis) and distance between two center of masses (y-axis) in ProSQ-C10 (S,S) 12-mer simulated with mod.GAFF+LCFF MDs.

4.4 Selection of representative dimer structures: clustering

The selection of representative dimers was only performed on MD simulations of 12-mers. From the complete pairwise information across all the 6 replicas (excluding the first portion of the trajectories as above), we first identify nearest-neighbours (i.e. pairs of molecules that spend in contact at least a fraction of the trajectory). On this ensemble of dimeric structures, the following four pairwise geometrical variables were used for clustering: r (CM-to-CM distance: same of Fig. 7b - central panel, y-axis), α (dihedral helicity: same of Fig. 7b - central panel, x-axis), angle between two average planes $\pi(A, A')$ as well as the shift x. The large numbers of point was then filtered based on the r distance by setting a cut-off at 8 Å, and 1 point each 4 was sampled in order to further reduce the number of points to 310206. On such 4-dimensional space we applied a density-peak based clustering [20], as to select the most representative dimeric structures across all 12-mers simulations. We set the threshold for merging clusters to Z =2.8, as to obtain 66 clusters. Only the 20 clusters having at least 3000 points were further considered - accounting for 90 % of the total sample. Among these, 5 were identified having a population p larger than 5%: Table S1 lists also the geometric properties of each of the representative dimers Dj - as selected by clustering to be the most representative from the sample of MD trajectory snapshots.

	p	r (d_{CM}) Å	α deg.	π deg.	x Å
D3	6.59050	5.3514	7.00	0.95	3.8990
D9	29.25685	4.3529	-25.24	-8.29	2.5778
D13	8.50822	6.3853	-50.42	177.6	5.5300
D14	8.92582	4.5537	29.47	170.44	2.9849
D19	11.60745	4.1436	-19.90	170.54	2.0967

Table S1: Populations and geometrical parameters relevant to the five representative dimers

4.5 Structure refinement and TDDFT calculations

The representative dimeric structures were then processed in order to compute excitation energies with (Time Dependent) Density functional Theory, (TD)-DFT. The 5 dimers (D3, D9, D13, D14 and D19) as extracted from above procedure rely on a classical potential and hence must be refined. We then processed the 5 dimers using `orca 5.0.2` [21] structures according to the following protocol:

1. from both molecules of dimer structures Dj the C10 chains were pruned, as to leave only a methyl group connected to oxygens at each molecular end
2. HF-3c [22] optimization (in vacuum) restraining intermolecular contacts between pairs of C atoms (`Connectfragment` option). We selected the two intermolecular pairs of aromatic ring C atoms (that are bonded to the N atoms) as a connector for the restraint
3. PBEh-3c [23] optimization (in vacuum) with the same restraint as above
4. def2-TZVP B3LYP-D3BJ [16, 24] optimization (in vacuum) with the same restraint as above
5. final TDDFT calculations at either i. B3LYP [16] or ii. CAM-B3LYP [25] functionals. We did not take advantage of Tamm-Dancoff approximation (TDA) as we realized the simulated spectra were not reliable when employing TDA. Basis set: def2-TZVP.

Simulated absorption and CD spectra for these two functionals are reported in figure S20. In our calculations 8 excited states are included. Spectra were simulated modeling each electronic transition with a Gaussian lineshape with $\sigma = 0.05$eV.

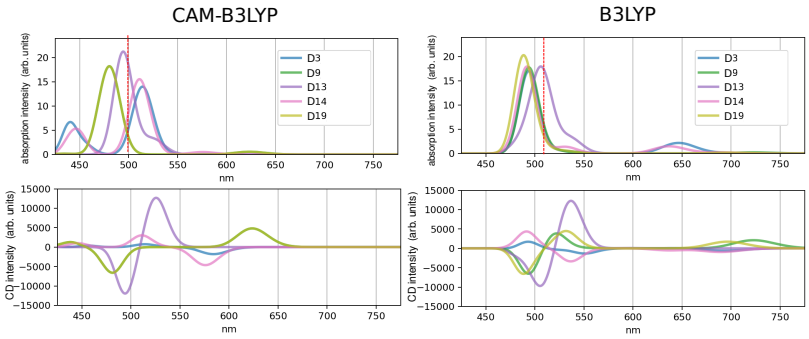


Figure S20: Simulated spectra on dimer representative structures with TDDFT at CAM-B3LYP functional (left) and B3LYP functional (right) with def2-TZVP basis set. Refined structure according to the procedure in section 4.5. Top: absorption spectra, bottom: CD spectra. Red dashed lines in the absorption spectra mark the average position of absorption maximum for corresponding monomers structures.

5 Synthesis

The synthetic route of the proline-derived squaraines (ProSQ) was adopted from the literature-known two-step, one-pot procedure.[26] As staring material, *N*-Boc-L-prolinol ((*S*)-1-Boc-2-pyrrolidinemethanol) was used as received, which was purchased from TCI, Fluorochem or chemPUR in >98 % purity and *ee* > 98 %. All other chemicals were purchased from standard suppliers and used without further purification. Solvents were purified with standard methods and, if necessary, dried according to literature procedures and stored under argon atmosphere over 4 Å molecular sieves. Reactions under inert gas conditions were performed under dry argon atmosphere with dry solvents in flame-dried glassware using *Schlenk* techniques.

NMR: ^{1}H and ^{13}C NMR were recorded at 298 K at 700 MHz and 176 MHz or 500 MHz and 125 MHz, respectively. ^{1}H NMR chemical shifts are reported on the δ scale (ppm) relative to tetramethylsilane. The residual non-deuterated solvent signal was used as the internal standard. ^{13}C NMR chemical shifts are given in δ values (ppm) relative to the deuterated solvent as the internal standard.

Mass spectrometry: electrospray ionisation (ESI) mass spectra were taken on a Orbitrap XL (*Thermo Fisher Scientific*).

UV/Vis spectroscopy: UV/Vis spectra were recorded at room temperature on a Specord 200 spectrometer (*Analytic Jena*) with 0.5 nm step size and 5 nm/s scanning speed, using 10 mm quartz cuvettes (*Hellma*). The instrument was calibrated with a reference sample in advance. UV/Vis spectra are shown as absorbance $=-\log(\text{transmission})$.

CD spectroscopy: Ellipsticity spectra were recorded on a J-810 spectro-polarimeter (*JASCO Corporation*) with 1 nm step size, a scanning speed of 200 nm/min, and a 1 nm bandwidth. An initial measurement of the pure solvent or solvent mixture was used for baseline correction. The circular dichroism (CD) spectra are shown as ellipticity in units of milli degree (mdeg) as outputted from the spectro-polarimeter. Note that CD and ellipticity are not the same values but for small quantities ellipticity = CD/2.[1]

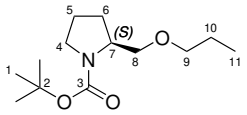
Elemental analysis: elemental analysis was performed on a Vario EL (*Heraeus*).

All compounds were measured at least two times.

5.1 General synthesis of *N*-Boc-L-prolinyl ethers

The synthesis is based on the procedure published by *Lützen* et al. in 2017.[26] Under inert gas conditions, *N*-Boc-L-prolinol (1.00 eq.) is dissolved in *abs.* DMF (1 mL/mmol) and cooled to -15 °C in a flame-dried *Schlenk*-flask. Under vigorous stirring, sodium hydride (1.50 eq., 60 % in mineral oil) is slowly added in portions to the solution. The reaction mixture is further stirred at this temperature for 45 minutes and afterwards, the appropriate alkyl iodide (1.50 eq.) is added dropwise. The resulting suspension is stirred for 16 h during which the reaction mixture is allowed to warm up to room temperature. After complete consumption of the starting material (TLC monitoring), the reaction is quenched by adding a saturated aqueous ammonium chloride solution and diluted with ethyl acetate. The organic phase is separated and the aqueous phase is extracted three times with ethyl acetate. The combined organic phases are washed with water, brine and dried with magnesium sulfate. The solvent is removed under reduced pressure and the crude product is purified by column chromatography on silica gel (eluent cyclohexane/ethyl acetate 9:1 (v:v)). The *N*-Boc-L-prolinyl ethers are obtained as colorless oils.

5.1.1 Synthesis of *N*-Boc-L-prolinyl *n*-propyl ether



N-Boc-L-prolinol (2.01 g, 10.0 mmol) was reacted with 1-iodopropane (2.55 g, 15.0 mmol) according to the general procedure.

Yield: 1.21 g (4.98 mmol, 50 %, colorless oil)

Molecular weight: $C_{13}H_{25}NO_3$, 243.35 g/mol

^{1}H-NMR: (500 MHz, Chloroform-*d*, 298 K) δ [ppm] = 4.02-3.78 (m, 1H, H-7), 3.62-3.46 (m, 1H, H-8a), 3.46-3.11 (m, 5H, H-4, H-8b, H-9), 1.99-1.83

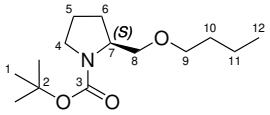
(m, 3H, H-5a, H-6), 1.83-1.72 (m, 1H, H-5b), 1.61-1.51 (m, 2H, H-10), 1.45 (s, 9H, H-1), 0.90 (t, 3H, H-11, $^3J_{10,11}$ = 7.4 Hz).

^{13}C-NMR: (125 MHz, Chloroform-*d*, 298 K) δ [ppm] = 154.7 (C-3), 79.3, 79.2 (C-2)*, 73.1 (C-9), 71.7, 71.0 (C-8)*, 56.6 (C-7), 47.0, 46.5 (C-4)*, 28.9, 28.1 (C-6)*, 28.7 (C-1), 23.9, 23.1 (C-5)*, 23.1 (C-10), 10.7 (C-11). Two signals can be identified that are due to rotamers.

MS (ESI(+), Dichloromethane, M = $C_{13}H_{25}NO_3$) *m/z* = 266.17 $[M+Na]^+$, 244.19 $[M+H]^+$, 188.13 $[M\text{-}C_4H_8+H]^+$, 144.14 $[M\text{-Boc}+H]^+$.

ESI HRMS: $[M+H]^+ = C_{13}H_{25}NO_3H^+$, calculated: m/z = 244.1907, found: m/z = 244.1902.

5.1.2 Synthesis of *N*-Boc-L-prolinyl *n*-butyl ether



N-Boc-L-prolinol (4.06 g, 20.0 mmol) was reacted with 1-iodobutane (5.52 g, 30.0 mmol) according to the general procedure.

Yield: 2.43 g (9.43 mmol, 47 %, colorless oil)

Molecular weight: $C_{14}H_{27}NO_3$, 257.37 g/mol

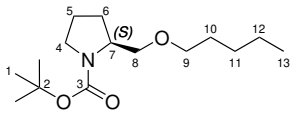
^{1}H-NMR: (700 MHz, Chloroform-*d*, 298 K) δ [ppm] = 4.00-3.80 (m, 1H, H-7), 3.60-3.48 (m, 1H, H-8a), 3.48-3.37 (m, 2H, H-9), 3.37-3.17 (m, 3H, H-4, H-8b), 1.98-1.82 (m, 3H, H-5a, H-6), 1.82-1.72 (m, 1H, H-5b), 1.57-1.48 (m, 2H, H-10), 1.45 (s, 9H, H-1), 1.39-1.29 (m, 2H, H-11), 0.90 (t, 3H, H-12, $^3J_{11,12}$ = 7.5 Hz).

^{13}C-NMR: (176 MHz, Chloroform-*d*, 298 K) δ [ppm] = 154.7 (C-3), 79.3, 79.2 (C-2)*, 71.7, 71.1 (C-8)*, 71.2 (C-9), 56.6 (C-7), 47.0, 46.5 (C-4)*, 32.0 (C-10), 28.9, 28.1 (C-6)*, 28.7 (C-1), 23.9, 23.0 (C-5)*, 19.4 (C-11), 14.0 (C-12). Two signals can be identified that are due to rotamers.

MS (ESI(+), Dichloromethane, M = $C_{14}H_{27}NO_3$) *m/z* = 280.19 $[M+Na]^+$, 258.21 $[M+H]^+$, 202.14 $[M\text{-}C_4H_8+H]^+$, 144.14 $[M\text{-Boc}+H]^+$.

ESI HRMS: $[M+H]^+ = C_{14}H_{27}NO_3H^+$, calculated: $m/z = 258.2064$, found: $m/z = 258.2065$.

5.1.3 Synthesis of *N*-Boc-L-prolinyl *n*-pentyl ether



N-Boc-L-prolinol (2.02 g, 10.0 mmol) was reacted with 1-iodopentane (2.97 g, 15.0 mmol) according to the general procedure.

Yield: 1.96 g (7.22 mmol, 72 %, colorless oil)

Molecular weight: $C_{15}H_{29}NO_3$, 271.40 g/mol

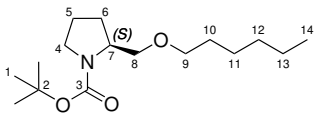
^{1}H-NMR: (500 MHz, Chloroform-*d*, 298 K) δ [ppm] = 3.96-3.85 (m, 1H, H-7), 3.56-3.50 (m, 1H, H-8a), 3.49-3.35 (m, 2H, H-9), 3.35-3.23 (m, 3H, H-4, H-8b), 1.98-1.83 (m, 3H, H-5a, H-6), 1.83-1.74 (m, 1H, H-5b), 1.59-1.50 (m, 2H, H-10), 1.45 (s, 9H, H-1), 1.36-1.27 (m, 4H, H-11, H-12), 0.89 (t, 3H, H-13, $^3J_{12,13} = 7.0$ Hz).

^{13}C-NMR: (125 MHz, Chloroform-*d*, 298 K) δ [ppm] = 154.7 (C-3), 79.3 (C-2), 71.5 (C-9), 71.4 (C-8), 56.6 (C-7), 46.7 (C-4), 29.6 (C-10), 28.7 (C-1), 28.6 (C-6), 28.5 (C-11), 23.4 (C-5), 22.7 (C-12), 14.2 (C-13).

MS (ESI(+), Dichloromethane, M = $C_{15}H_{29}NO_3$) *m/z* = 565.42 $[2M+Na]^+$, 294.20 $[M+Na]^+$, 272.22 $[M+H]^+$, 216.16 $[M\text{-}C_4H_8+H]^+$, 172.17 $[M\text{-Boc}+H]^+$.

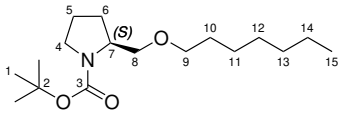
ESI HRMS: $[M+H]^+ = C_{15}H_{29}NO_3H^+$, calculated: $m/z = 272.2220$, found: $m/z = 272.2218$.

5.1.4 Synthesis of *N*-Boc-L-prolinyl *n*-hexyl ether



N-Boc-L-prolinyl *n*-hexyl ether was synthesized according to the literature.[26]

5.1.5 Synthesis of *N*-Boc-L-prolinyl *n*-heptyl ether



N-Boc-L-prolinol (1.01 g, 5.00 mmol) was reacted with 1-iodoheptane (3.40 g, 7.50 mmol) according to the general procedure.

Yield: 896 mg (2.99 mmol, 60 %, colorless oil)

Molecular weight: $C_{17}H_{33}NO_3$, 299.46 g/mol

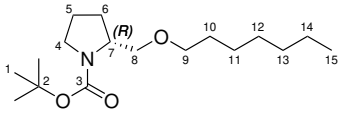
^{1}H-NMR: (500 MHz, Chloroform-*d*, 298 K) δ [ppm] = 3.95-3.85 (m, 1H, H-7), 3.57-3.49 (m, 1H, H-8a), 3.48-3.36 (m, 2H, H-9), 3.36-3.22 (m, 3H, H-4, H-8b), 1.98-1.83 (m, 3H, H-5a, H-6), 1.83-1.74 (m, 1H, H-5b), 1.57-1.49 (m, 2H, H-10), 1.46 (s, 9H, H-1), 1.35-1.20 (m, 8H, H-11 to H-14), 0.87 (t, 3H, H-15, $^3J_{14,15}$ = 6.8 Hz).

^{13}C-NMR: (125 MHz, Chloroform-*d*, 298 K) δ [ppm] = 154.7 (C-3), 79.3 (C-2), 71.5 (C-9), 71.4 (C-8), 56.6 (C-7), 46.7 (C-4), 32.0, 29.3, 26.2, 22.8 (C-11 to C-14), 29.9 (C-10), 28.7 (C-1), 28.6 (C-6), 23.3 (C-5), 14.3 (C-15).

MS (ESI(+), Dichloromethane, M = $C_{17}H_{33}NO_3$) *m/z* = 621.48 $[2M+Na]^+$, 322.24 $[M+Na]^+$, 300.25 $[M+H]^+$, 244.19 $[M-C_4H_8+H]^+$, 200.20 $[M-Boc+H]^+$.

ESI HRMS: $[M+H]^+ = C_{17}H_{33}NO_3H^+$, calculated: m/z = 300.2533, found: m/z = 300.2537.

5.1.6 Synthesis of *N*-Boc-D-prolinyl *n*-heptyl ether



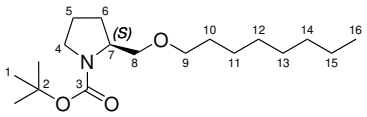
N-Boc-D-prolinol (2.01 g, 10.0 mmol) was reacted with 1-iodoheptane (1.70 g, 15.0 mmol) according to the general procedure.

Yield: 754 mg (2.52 mmol, 25 %, colorless oil)

Molecular weight: $C_{17}H_{33}NO_3$, 299.46 g/mol

All other analytical data of the (*R*,*R*)-enantiomer are in agreement with those of the (*S*,*S*)-enantiomer.

5.1.7 Synthesis of *N*-Boc-L-prolinyl *n*-octyl ether



N-Boc-L-prolinol (1.01 g, 5.00 mmol) was reacted with 1-iodooctane (1.80 g, 7.50 mmol) according to the general procedure.

Yield: 997 mg (3.18 mmol, 64 %, colorless oil)

Molecular weight: $C_{18}H_{35}NO_3$, 313.48 g/mol

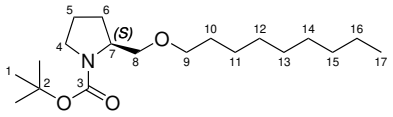
^{1}H-NMR: (500 MHz, Chloroform-*d*, 298 K) δ [ppm] = 3.89 (m, 1H, H-7), 3.52 (d, 1H, H-9a, $^3J_{9a,9b}$ = 7.9 Hz), 3.47-3.35 (m, 2H, H-9), 3.35-3.20 (m, 3H, H-4, H-8b), 1.97-1.82 (m, 3H, H-5a, H-6), 1.82-1.73 (m, 1H, H-5b), 1.58-1.48 (m, 2H, H-10), 1.45 (s, 9H, H-1), 1.34-1.18 (m, 10H, H-11 to H-15), 0.87 (t, 3H, H-1, $^3J_{15,16}$ = 7.1 Hz).

^{13}C-NMR: (125 MHz, Chloroform-*d*, 298 K) δ [ppm] = 154.7 (C-3), 79.2 (C-2), 71.5 (C-9), 71.5 (C-8), 56.6 (C-7), 46.7 (C-4), 32.0, 29.5, 29.4, 26.3, 23.4 (C-1 to C-15), 29.9 (C-10), 28.7 (C-1), 28.7 (C-6), 22.8 (C-5), 14.2 (C-16).

MS (ESI(+), Dichloromethane, M = $C_{18}H_{35}NO_3$) *m/z* = 336.250 $[M+Na]^+$, 314.268 $[M+H]^+$, 280.187 $[M\text{-}C_4H_8+Na]^+$, 258.206 $[M\text{-}C_4H_8+H]^+$, 214.216 $[M\text{-Boc}+H]^+$.

ESI HRMS: $[M+H]^+ = C_{18}H_{35}NO_3H^+$, calculated: m/z = 314.2690, found: m/z = 314.2685.

5.1.8 Synthesis of *N*-Boc-L-prolinyl *n*-nonyl ether



N-Boc-L-prolinol (3.02 g, 15.0 mmol) was reacted with 1-iodononane (5.72 g, 22.5 mmol) according to the general procedure.

Yield: 2.88 g (8.78 mmol, 59 %, colorless oil)

Molecular weight: $C_{19}H_{37}NO_3$, 327.51 g/mol

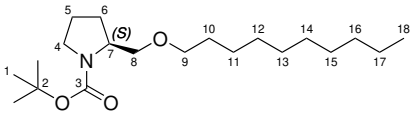
^{1}H-NMR: (700 MHz, Chloroform-*d*, 298 K) δ [ppm] = 3.94-3.85 (m, 1H, H-7), 3.56-3.50 (m, 1H, H-8a), 3.47-3.37 (m, 2H, H-9), 3.35-3.23 (m, 3H, H-4, H-8b), 1.97-1.83 (m, 3H, H-5a, H-6), 1.83-1.75 (m, 1H, H-5b), 1.56-1.50 (m, 2H, H-10), 1.46 (s, 9H, H-1), 1.35-1.21 (m, 12H, H-11 to H-16), 0.87 (t, 3H, H-17, $^3J_{16,17}$ = 7.1 Hz).

^{13}C-NMR: (176 MHz, Chloroform-*d*, 298 K) δ [ppm] = 154.7 (C-3), 79.3 (C-2), 71.5 (C-9), 71.4 (C-8), 56.6 (C-7), 46.7 (C-4), 32.0, 29.7, 29.6, 29.4, 26.3, 22.8 (C-11 to C-16), 29.9 (C-10), 28.7 (C-1), 28.6 (C-6), 23.3 (C-5), 14.2 (C-17).

MS (ESI(+), Dichloromethane, M = $C_{19}H_{37}NO_3$) *m/z* = 366.24 $[M+K]^+$, 350.27 $[M+Na]^+$, 328.28 $[M+H]^+$, 294.20 $[M\text{-}C_4H_8+Na]^+$, 272.22 $[M\text{-}C_4H_8+H]^+$, 228.23 $[M\text{-Boc}+H]^+$.

ESI HRMS: $[M+H]^+ = C_{19}H_{37}NO_3H^+$, calculated: m/z = 328.2846, found: m/z = 328.2833.

5.1.9 Synthesis of *N*-Boc-L-prolinyl *n*-decyl ether



N-Boc-L-prolinol (2.01 g, 10.0 mmol) was reacted with 1-iododecane (4.02 g, 15.0 mmol) according to the general procedure.

Yield: 2.23 g (6.82 mmol, 65 %, colorless oil)

Molecular weight: $C_{20}H_{39}NO_3$, 341.54 g/mol

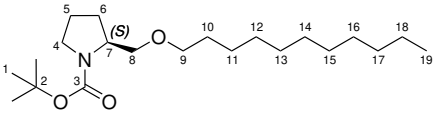
^{1}H-NMR: (700 MHz, Chloroform-*d*, 298 K) δ [ppm] = 3.95-3.86 (m, 1H, H-7), 3.56-3.50 (m, 1H, H-8a), 3.47-3.36 (m, 2H, H-9), 3.35-3.23 (m, 3H, H-4, H-8b), 1.97-1.83 (m, 3H, H-5a, H-6), 1.83-1.75 (m, 1H, H-5b), 1.57-1.50 (m, 2H, H-10), 1.46 (s, 9H, H-1), 1.34-1.21 (m, 14H, H-11 to H-17), 0.89 (t, 3H, H-18, $^3J_{17,18}$ = 7.1 Hz).

^{13}C-NMR: (176 MHz, Chloroform-*d*, 298 K) δ [ppm] = 154.7 (C-3), 79.3 (C-2), 71.5 (C-9), 71.4 (C-8), 56.6 (C-7), 46.8 (C-4), 32.1, 29.8, 29.7, 29.6, 29.5, 26.3 (C-11 to C-16), 29.9 (C-10), 28.7 (C-1), 28.6 (C-6), 23.4 (C-5), 22.8 (C-17), 14.3 (C-18).

MS (ESI(+), Dichloromethane, M = $C_{20}H_{39}NO_3$) *m/z* = 705.58 $[2M+Na]^+$, 364.28 $[M+Na]^+$, 342.30 $[M+H]^+$, 286.24 $[M\text{-}C_4H_8+H]^+$, 242.25 $[M\text{-Boc}+H]^+$.

ESI HRMS: $[M+H]^+ = C_{20}H_{39}NO_3H^+$, calculated: m/z = 342.3003, found: m/z = 342.3006.

5.1.10 Synthesis of *N*-Boc-L-prolinyl *n*-undecyl ether



N-Boc-L-prolinol (3.02 g, 15.0 mmol) was reacted with 1-iodoundecane (6.35 g, 22.5 mmol) according to the general procedure.

Yield: 2.18 g (6.14 mmol, 41 %, colorless oil)

Molecular weight: $C_{21}H_{41}NO_3$, 355.56 g/mol

^{1}H-NMR: (500 MHz, Chloroform-*d*, 298 K) δ [ppm] = 3.94-3.85 (m, 1H, H-7), 3.55-3.49 (m, 1H, H-8a), 3.47-3.35 (m, 2H, H-9), 3.34-3.23 (m, 3H, H-4, H-8b), 1.97-1.82 (m, 3H, H-5a, H-6), 1.82-1.73 (m, 1H, H-5b), 1.57-1.49 (m, 2H, H-10), 1.45 (s, 9H, H-1), 1.34-1.18 (m, 16H, H-11 to H-18), 0.87 (t, 3H, H-19,

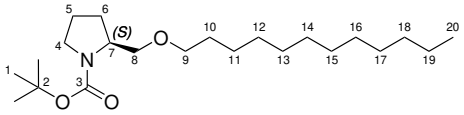
$^3J_{18,19}$ = 6.9 Hz).

^{13}C-NMR: (125 MHz, Chloroform-*d*, 298 K) δ [ppm] = 154.7 (C-3), 79.2 (C-2), 71.5 (C-9), 71.4 (C-8), 56.6 (C-7), 46.7 (C-4), 32.1, 29.8, 29.6, 29.5, 26.3, 22.8 (C-11 to C-18), 29.9 (C-10), 28.7 (C-1), 28.6 (C-6), 23.4 (C-5), 14.2 (C-19).

MS (ESI(+), Dichloromethane, M = $C_{21}H_{41}NO_3$) *m/z* = 394.27 $[M+K]^+$, 378.30 $[M+Na]^+$, 356.32 $[M+H]^+$, 322.24 $[M-C_4H_8+Na]^+$, 300.25 $[M-C_4H_8+H]^+$, 256.26 $[M-Boc+H]^+$.

ESI HRMS: $[M+H]^+ = C_{21}H_{41}NO_3H^+$, calculated: m/z = 356.3159, found: m/z = 356.3158.

5.1.11 Synthesis of *N*-Boc-L-prolinyl *n*-dodecyl ether



N-Boc-L-prolinol (1.01 g, 5.00 mmol) was reacted with 1-iododododecane (2.22 g, 7.50 mmol) according to the general procedure.

Yield: 2.18 g (6.14 mmol, 41 %, colorless oil, with the tendency to solidify)

Molecular weight: $C_{22}H_{43}NO_3$, 369.59 g/mol

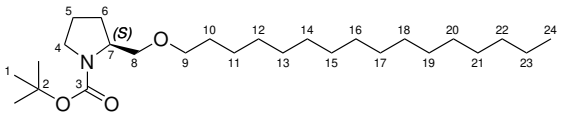
^{1}H-NMR: (500 MHz, Chloroform-*d*, 298 K) δ [ppm] = 3.90 (m, 1H, H-7), 3.53 (dd, 1H, H-8a, $^3J_{13a,14}$ = 3.2 Hz, $^3J_{13a,13b}$ = 9.5 Hz), 3.49-3.35 (m, 2H, H-9), 3.35-3.23 (m, 3H, H-8b, H-4), 1.99-1.83 (m, 3H, H-5a, H-6), 1.83-1.73 (m, 1H, H-5b), 1.57-1.49 (m, 2H, H-10), 1.46 (s, 9H, H-1), 1.36-1.19 (m, 18H, H-11 to H-19), 0.87 (t, 3H, H-20, $^3J_{19,20}$ = 6.8 Hz).

^{13}C-NMR: (125 MHz, Chloroform-*d*, 298 K) δ [ppm] = 154.7 (C-3), 79.3 (C-2), 71.5 (C-9), 71.1 (C-8), 56.6 (C-7), 46.7 (C-4), 32.1, 29.9, 29.8, 29.8, 29.7, 29.6, 29.5, 28.9, 28.1, 26.3, 23.0 (C-6, C-10 to C-19), 28.7 (C-1), 22.8 (C-5), 14.2 (C-20).

MS (ESI(+), Dichloromethane, M = $C_{22}H_{43}NO_3$) *m/z* = 392.314 $[M+Na]^+$, 370.332 $[M+H]^+$, 314.269 $[M-C_4H_8+H]^+$, 270.279 $[M-Boc+H]^+$.

ESI HRMS: $[M+H]^+ = C_{22}H_{43}NO_3H^+$, calculated: $m/z = 370.3316$, found: $m/z = 370.3321$.

5.1.12 Synthesis of *N*-Boc-L-prolinyl *n*-hexadecyl ether

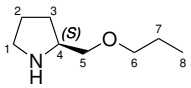


N-Boc-L-prolinyl *n*-hexadecyl ether was synthesized according to the literature.[26, 1]

5.2 General method for the Boc deprotection

The synthesis is based on the procedure published by *Lützen* et al. in 2017.[26] Under inert gas conditions and flame-dried glassware, the corresponding *N*-Boc-L-prolinyl ether (1.00 eq.) is dissolved in *abs.* dichloromethane (1 mL/mmol) and cooled to 0 °C. Under stirring, trifluoroacetic acid (10.0 eq.) is added dropwise to the solution. The reaction mixture is stirred for additional 30 minutes at 0 °C and after removing the cooling bath for 2 hours at room temperature. After dilution with dichloromethane, the mixture is poured into the same volume of ice-cold aqueous 10 % NaOH. The organic phase is separated and the aqueous phase is extracted with dichloromethane. The combined organic phases are washed with brine and dried with magnesium sulfate. The solvent is removed under reduced pressure and the obtained residue is used without further purification in the next reaction step. The products are obtained as pale yellow oils.

5.2.1 Synthesis of L-prolinyl *n*-propyl ether



N-Boc-L-prolinyl *n*-propyl ether (1.02 g, 4.18 mmol) was deprotected according to the general procedure.

Yield: 590 mg (4.12 mmol, 99 %, pale yellow oil)

Molecular weight: $C_8H_{17}NO$, 143.23 g/mol

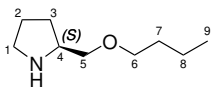
^{1}H-NMR: (500 MHz, Chloroform-*d*, 298 K) δ [ppm] = 6.20 (br s, 1H, NH), 3.57-3.48 (m, 2H, H-4, H-5a), 3.48-3.36 (m, 3H, H-5b, H-6), 3.18-3.03 (m, 2H, H-1), 2.00-1.78 (m, 3H, H-2, H-3a), 1.65-1.52 (m, 3H, H-3b, H-7), 0.89 (t, 3H, H-8, $^3J_{7,8}$ = 7.4 Hz).

^{13}C-NMR: (125 MHz, Chloroform-*d*, 298 K) δ [ppm] = 73.2 (C-6), 71.9, (C-5), 58.4 (C-4), 46.1 (C-1), 27.7 (C-3), 24.8 (C-2), 22.9 (C-7), 10.6 (C-8).

MS (ESI(+), Dichloromethane, M = $C_8H_{17}NO$) *m/z* = 287.27 $[2M+H]^+$, 144.14 $[M+H]^+$.

ESI HRMS: $[M+H]^+ = C_8H_{17}NOH^+$, calculated: m/z = 144.1383, found: m/z = 144.1384.

5.2.2 Synthesis of L-prolinyl *n*-butyl ether



N-Boc-L-prolinyl *n*-butyl ether (2.43 g, 9.43 mmol) was deprotected according to the general procedure.

Yield: 1.01 g (6.42 mmol, 68 %, pale yellow oil)

Molecular weight: $C_9H_{19}NO$, 157.26 g/mol

^{1}H-NMR: (500 MHz, Chloroform-*d*, 298 K) δ [ppm] = 8.34 (br s, 1H, NH), 3.82-3.74 (m, 1H, H-4), 3.71-3.58 (m, 2H, H-5), 3.55-3.42 (m, 2H, H-6),

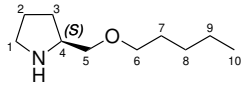
3.34-3.27 (m, 2H, H-1), 2.12-1.90 (m, 3H, H-2, H-3a), 1.88-1.77 (m, 1H, H-3b), 1.58-1.50 (m, 2H, H-7), 1.38-1.28 (m, 2H, H-8), 0.89 (t, 3H, H-9, $^3J_{8,9} = 7.4$ Hz).

^{13}C-NMR: (125 MHz, Chloroform-*d*, 298 K) δ [ppm] = 71.5 (C-6), 69.7, (C-5), 58.6 (C-4), 45.8 (C-1), 31.7 (C-7), 27.4 (C-3), 24.3 (C-2), 19.4 (C-8), 14.0 (C-9).

MS (ESI(+), Dichloromethane, M = $C_9H_{19}NO$) *m/z* = 351.28 $[2M+HCl+H]^+$, 315.30 $[2M+H]^+$, 158.15 $[M+H]^+$.

ESI HRMS: $[M+H]^+ = C_9H_{19}NOH^+$, calculated: $m/z = 158.1539$, found: $m/z = 158.1533$.

5.2.3 Synthesis of L-prolinyl *n*-pentyl ether



N-Boc-L-prolinyl *n*-pentyl ether (1.72 g, 6.34 mmol) was deprotected according to the general procedure.

Yield: 1.08 g (6.30 mmol, 99 %, pale yellow oil)

Molecular weight: $C_{10}H_{21}NO$, 171.28 g/mol

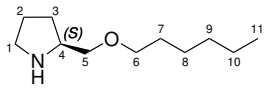
^{1}H-NMR: (500 MHz, Chloroform-*d*, 298 K) δ [ppm] = 3.45-3.40 (m, 3H, H-5a, H-6), 3.36-3.29 (m, 2H, H-4, H-5b), 3.30-3.21 (br s, 1H, NH), 3.05-2.88 (m, 2H, H-1), 1.90-1.80 (m, 1H, H-3a), 1.80-1.68 (m, 2H, H-2), 1.60-1.51 (m, 2H, H-7), 1.49-1.40 (m, 1H, H-3b), 1.36-1.26 (m, 4H, H-8, H-9), 0.88 (t, 3H, H-10, $^3J_{9,10} = 7.0$ Hz).

^{13}C-NMR: (125 MHz, Chloroform-*d*, 298 K) δ [ppm] = 73.7 (C-5), 71.6, (C-6), 58.1 (C-4), 46.4 (C-1), 29.5 (C-7), 28.4 (C-8), 28.0 (C-3), 25.2 (C-2), 22.7 (C-9), 14.2 (C-10).

MS (ESI(+), Dichloromethane, M = $C_{10}H_{21}NO$) *m/z* = 172.17 $[M+H]^+$.

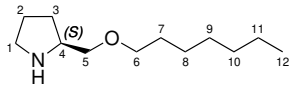
ESI HRMS: $[M+H]^+ = C_{10}H_{21}NOH^+$, calculated: $m/z = 172.1696$, found: $m/z = 172.1693$.

5.2.4 Synthesis of L-prolinyl *n*-hexyl ether



L-prolinyl *n*-hexyl ether was synthesized according to the literature.[26]

5.2.5 Synthesis of L-prolinyl *n*-heptyl ether



N-Boc-L-prolinyl *n*-heptyl ether (0.72 g, 2.40 mmol) was deprotected according to the general procedure.

Yield: 478 mg (2.40 mmol, quant., pale yellow oil)

Molecular weight: $C_{12}H_{25}NO$, 199.34 g/mol

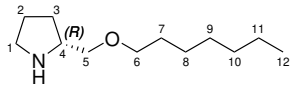
^{1}H-NMR: (500 MHz, Chloroform-*d*, 298 K) δ [ppm] = 3.45-3.38 (m, 3H, H-5a, H-6), 3.36-3.28 (m, 3H, H-4, H-5b, NH), 3.05-2.87 (m, 2H, H-1), 1.93-1.80 (m, 1H, H-3a), 1.80-1.65 (m, 2H, H-2), 1.59-1.51 (m, 2H, H-7), 1.49-1.40 (m, 1H, H-3b), 1.35-1.20 (m, 8H, H-8 to H-11), 0.87 (t, 3H, H-12, $^3J_{11,12} = 6.8$ Hz).

^{13}C-NMR: (125 MHz, Chloroform-*d*, 298 K) δ [ppm] = 73.8 (C-5), 71.6, (C-6), 58.1 (C-4), 46.5 (C-1), 32.9, 29.3, 26.2, 22.8 (C-8 to C-11), 29.8 (C-7), 28.0 (C-3), 25.2 (C-2), 14.2 (C-12).

MS (ESI(+), Dichloromethane, M = $C_{12}H_{25}NO$) *m/z* = 435.37 $[2M+HCl+H]^+$, 200.20 $[M+H]^+$.

ESI HRMS: $[M+H]^+ = C_{12}H_{25}NOH^+$, calculated: $m/z = 200.2009$, found: $m/z = 200.2008$.

5.2.6 Synthesis of D-prolinyl *n*-heptyl ether



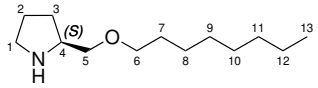
N-Boc-D-prolinyl *n*-heptyl ether (1.80 g, 6.00 mmol) was deprotected according to the general procedure.

Yield: 1.31 mg (6.00 mmol, quant., pale yellow oil)

Molecular weight: $C_{12}H_{25}NO$, 199.34 g/mol

All other analytical data of the (*R*,*R*)-enantiomer are in agreement with those of the (*S*,*S*)-enantiomer.

5.2.7 Synthesis of L-prolinyl *n*-octyl ether



N-Boc-L-prolinyl *n*-octyl ether (888 mg, 2.83 mmol) was deprotected according to the general procedure.

Yield: 444 mg (2.08 mmol, 74 %, pale yellow oil)

Molecular weight: $C_{13}H_{27}NO$, 213.37 g/mol

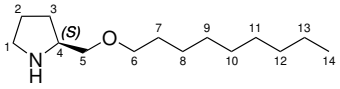
^{1}H-NMR: (500 MHz, Chloroform-*d*, 298 K) δ [ppm] = 3.46-3.36 (m, 3H, H-5a, H-6), 3.36-3.28 (m, 2H, H-4, H-5b), 3.26 (br s, 1H, NH), 3.05-2.96 (m, 1H, H-1a), 2.94-2.86 (m, 1H, H-1b), 1.90-1.80 (m, 1H, H-3a), 1.80-1.67 (m, 2H, H-2), 1.60-1.49 (m, 2H, H-7), 1.49-1.38 (m, 1H, H-3b), 1.36-1.18 (m, 10H, H-8 to H-12), 0.86 (t, 3H, H-13, $^3J_{12,13}$ = 7.0 Hz).

^{13}C-NMR: (125 MHz, Chloroform-*d*, 298 K) δ [ppm] = 73.7 (C-5), 71.6 (C-6), 58.1 (C-4), 46.4 (C-1), 31.9, 29.8, 29.6, 29.4, 26.5, 22.8 (C-7 to C-12), 27.9 (C-3), 25.2 (C-2), 14.2 (C-13).

MS (ESI(+), Dichloromethane, M = $C_{13}H_{27}NO$) *m/z* = 172.17 $[M+H]^+$.

ESI HRMS: $[M+H]^+ = C_{13}H_{27}NOH^+$, calculated: m/z = 214.2165, found: m/z = 214.2165.

5.2.8 Synthesis of L-prolinyl *n*-nonyl ether



N-Boc-L-prolinyl *n*-nonyl ether (1.96 g, 5.50 mmol) was deprotected according to the general procedure.

Yield: 1.53 g (6.74 mmol, 84 %, pale yellow oil)

Molecular weight: $C_{14}H_{29}NO$, 227.39 g/mol

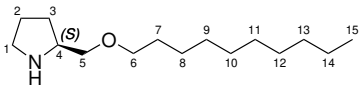
^{1}H-NMR: (400 MHz, Chloroform-*d*, 298 K) δ [ppm] = 4.80 (br s, 1H, NH), 3.77-3.69 (m, 1H, H-4), 3.62-3.49 (m, 2H, H-5), 3.49-3.37 (m, 2H, H-6), 3.30-3.20 (m, 2H, H-1), 2.13-1.90 (m, 3H, H-2, H-3a), 1.83-1.73 (m, 1H, H-3b), 1.57-1.49 (m, 2H, H-7), 1.34-1.19 (m, 12H, H-8 to H-13), 0.87 (t, 3H, H-14, $^3J_{13,14}$ = 6.9 Hz).

^{13}C-NMR: (125 MHz, Chloroform-*d*, 298 K) δ [ppm] = 71.8 (C-5), 70.0, (C-6), 58.7 (C-4), 45.7 (C-1), 32.0, 29.7, 29.6, 29.5, 29.4, 26.1, 22.8 (C-7 to C-13), 27.3 (C-3), 24.3 (C-2), 14.2 (C-14).

MS (ESI(+), Dichloromethane, M = $C_{14}H_{29}NO$) *m/z* = 455.46 $[2M+H]^+$, 228.23 $[M+H]^+$.

ESI HRMS: $[M+H]^+ = C_{14}H_{29}NOH^+$, calculated: m/z = 228.2322, found: m/z = 228.2310.

5.2.9 Synthesis of L-prolinyl *n*-decyl ether



N-Boc-L-prolinyl *n*-decyl ether (1.97 g, 5.76 mmol) was deprotected according to the general procedure.

Yield: 1.39 g (5.76 mmol, quant., pale yellow oil)

Molecular weight: $C_{15}H_{31}NO$, 241.42 g/mol

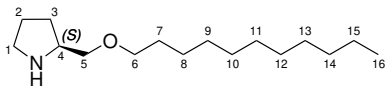
^{1}H-NMR: (700 MHz, Chloroform-*d*, 298 K) δ [ppm] = 3.48-3.41 (m, 3H, H-5a, H-6), 3.41-3.33 (m, 2H, H-4, H-5b), 3.08-2.92 (m, 2H, H-1), 1.91-1.84 (m, 1H, H-3a), 1.84-1.73 (m, 1H, H-2), 1.59-1.53 (m, 2H, H-7), 1.53-1.45 (m, 1H, H-3b), 1.34-1.21 (m, 14H, H-8 to H-14), 0.87 (t, 3H, H-15, $^3J_{14,15}$ = 7.1 Hz).

^{13}C-NMR: (176 MHz, Chloroform-*d*, 298 K) δ [ppm] = 73.5 (C-5), 71.7 (C-6), 58.2 (C-4), 46.4 (C-1), 32.1, 29.8, 29.8, 29.7, 29.6, 29.5, 26.3, 22.8 (C-7 to C-14), 27.9 (C-3), 25.2 (C-2), 14.3 (C-15).

MS (ESI(+), Dichloromethane, M = $C_{15}H_{31}NO$) *m/z* = 242.25 $[M+H]^+$.

ESI HRMS: $[M+H]^+ = C_{15}H_{31}NOH^+$, calculated: m/z = 242.2478, found: m/z = 242.2480.

5.2.10 Synthesis of L-prolinyl *n*-undecyl ether



N-Boc-L-prolinyl *n*-undecyl ether (1.96 g, 5.50 mmol) was deprotected according to the general procedure.

Yield: 1.27 g (4.96 mmol, 90 %, pale yellow oil)

Molecular weight: $C_{16}H_{33}NO$, 255.45 g/mol

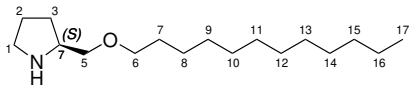
^{1}H-NMR: (500 MHz, Chloroform-*d*, 298 K) δ [ppm] = 4.00-3.87 (m, 1H, NH), 3.46-3.38 (m, 3H, H-5a, H-6), 3.38-3.30 (m, 2H, H-4, H-5b), 3.06-2.88 (m, 2H, H-1), 1.90-1.69 (m, 3H, H-2, H-3a), 1.58-1.50 (m, 2H, H-7), 1.50-1.42 (m, 1H, H-3b), 1.34-1.18 (m, 16H, H-8 to H-15), 0.86 (t, 3H, H-16, $^3J_{15,16}$ = 6.9 Hz).

^{13}C-NMR: (125 MHz, Chloroform-*d*, 298 K) δ [ppm] = 73.5 (C-5), 71.6 (C-6), 58.2 (C-4), 46.4 (C-1), 32.0, 29.8, 29.7, 29.7, 29.6, 29.5, 26.3, 22.8 (C-7 to C-15), 27.9 (C-3), 25.1 (C-2), 14.2 (C-16).

MS (ESI(+), Dichloromethane, M = $C_{16}H_{33}NO$) *m/z* = 256.265 $[M+H]^+$.

ESI HRMS: $[M+H]^+ = C_{16}H_{33}NOH^+$, calculated: m/z = 256.2635, found: m/z = 256.2623.

5.2.11 Synthesis of L-prolinyl *n*-dodecyl ether



N-Boc-L-prolinyl *n*-dodecyl ether (1.09 g, 2.96 mmol) was deprotected according to the general procedure.

Yield: 787 mg (2.92 mmol, 99 %, pale yellow oil)

Molecular weight: $C_{17}H_{35}NO$, 269.47 g/mol

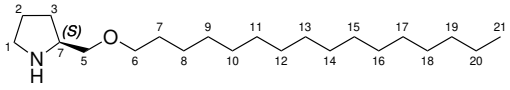
^{1}H-NMR: (500 MHz, Chloroform-*d*, 298 K) δ [ppm] = 4.07 (br s, 1H, NH), 3.54-3.33 (m, 5H, H-4, H-5, H-6) 3.16-2.98 (m, 2H, H-1), 2.00-1.65 (m, 3H, H-2, H-3a), 1.63-1.49 (m, 3H, H-3b, H-7), 1.36-1.17 (m, 18H, H-8 to H-16), 0.87 (t, 3H, H-17, $^3J_{16,17}$ = 6.9 Hz).

^{13}C-NMR: (125 MHz, Chloroform-*d*, 298 K) δ [ppm] = 72.5 (C-5), 71.7 (C-6), 58.3 (C-4), 46.3 (C-1), 32.1, 29.8, 29.8, 29.8, 29.8, 29.7, 29.6, 29.5, 26.2, 22.8 (C-7 to C-16), 27.8 (C-3), 25.0 (C-2), 14.3 (C-17).

MS (ESI(+), Dichloromethane, M = $C_{17}H_{35}NO$) *m/z* = 270.279 $[M+H]^+$.

ESI HRMS: $[M+H]^+ = C_{17}H_{35}NOH^+$, calculated: m/z = 270.2791, found: m/z = 270.2790.

5.2.12 Synthesis of L-prolinyl *n*-hexadecyl ether

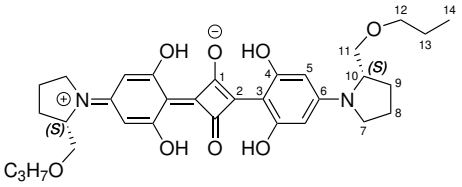


L-prolinyl *n*-hexadecyl ether was synthesized according to the literature.[26, 1]

5.3 General synthesis of squaraines

A round-bottom flask, equipped with a Dean-Stark apparatus and reflux condenser, is charged with the corresponding L-prolinyl *n*-alkyl ether (1.0 eq.) and phloroglucinol (1.00 eq.). The reactants are suspended in a mixture of toluene/1-butanol 1:1 (v/v, 10 mL/mmol) followed by degassing the mixture by 5 evacuation cycles under vigorous stirring and repressurizing with argon. The reaction mixture is refluxed under argon atmosphere for 16 hours. After cooling to room temperature, squaric acid (0.50 eq.) is added and the reaction mixture is heated to reflux for additional 16 hours. With the beginning of boiling, a sudden color change from slightly reddish over dark-green to dark-blue could be observed within minutes. The reaction mixture was slowly cooled to room temperature and stored at 4 °C overnight to promote crystallization. The intensely blue precipitate is filtered off and generously washed with methanol. The crude product is purified by column chromatography on silica gel (eluent: dichloromethane). The so-obtained deep blue solid is further purified by recrystallization from dichloromethane/methanol 1:2 (v/v) and dichloromethane/cyclohexane 1:2 (v/v). The precipitated solid was each time filtered off and washed several times with methanol. After drying under vacuum overnight, the squaraine dye is obtained as an intensively colored solid.

5.3.1 Synthesis of 2,4-Bis[4-(*S*)-(-)-2-(propyloxymethyl)-pyrrolidone-2,6-dihydroxyphenyl]squaraine (*S*,*S*)-ProSQ-C3



L-prolinyl *n*-propyl ether (500 mg, 3.50 mmol) was reacted according to the general procedure.

Yield: 132 mg (0.23 mmol, 13 %, deep-green solid with golden shine)

Molecular weight: $C_{32}H_{40}N_2O_8$, 580.68 g/mol

^{1}H-NMR: (700 MHz, Chloroform-*d*, 298 K) δ [ppm] = 11.01 (s, 4H, OH), 5.78 (br s, 4H, H-5), 4.09-4.04 (m, 2H, H-10), 3.55-3.49 (m, 4H, H-7a, H-11a), 3.44-3.31 (m, 8H, H-7b, H-11b, H-12), 2.17-2.06 (m, 4H, H-8a, H-9a), 2.06-1.96 (m, 4H, H-8b, H-9b), 1.61-1.54 (m, 4H, H-13), 0.92 (t, 6H, H-14, $^3J_{13,14}$ = 7.4 Hz).

^{13}C-NMR: (176 MHz, Chloroform-*d*, 298 K) δ [ppm] = 181.4 (C-2), 162.9 (C-4), 161.8 (C-1), 156.9 (C-3), 103.0 (C-6), 94.7 (C-5), 73.4 (C-12), 70.4 (C-11), 59.0 (C-10), 49.1 (C-7), 28.6 (C-9), 23.0 (C-13), 22.9 (C-8), 10.7 (C-14).

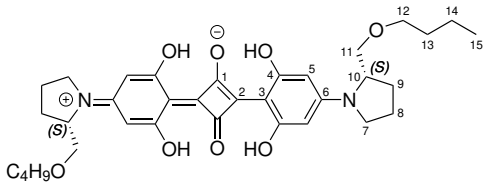
MS (ESI(+), Dichloromethane, M = $C_{32}H_{40}N_2O_8$) *m/z* = 580.28 $[M]^{\cdot+}$.

ESI HRMS: $[M]^{\cdot+}$ = $C_{32}H_{40}N_2O_8{}^{\cdot+}$, calculated: m/z = 580.2779, found: m/z = 580.2776.

UV/Vis: (Chloroform) λ_{max} = 646 nm, ε = 380800 $M^{-1}cm^{-1}$

Elemental analysis: $C_{32}H_{40}N_2O_8$ calculated C: 66.19, H: 6.94, N: 4.82; found C: 65.99, H: 7.06, N: 4.74.

5.3.2 Synthesis of 2,4-Bis[4-(*S*)-(-)-2-(butyloxymethyl)-pyrrolidone-2,6-dihydroxyphenyl]squaraine (*S*,*S*)-ProSQ-C4



L-prolinyl *n*-butyl ether (865 mg, 5.50 mmol) was reacted according to the general procedure.

Yield: 38.2 mg (0.06 mmol, 2.3 %, ochre-brown solid)

Molecular weight: $C_{34}H_{44}N_2O_8$, 608.73 g/mol

^{1}H-NMR: (500 MHz, Chloroform-*d*, 298 K) δ [ppm] = 11.00 (s, 4H, OH), 5.77 (br s, 4H, H-5), 4.09-4.02 (m, 2H, H-10), 3.56-3.49 (m, 4H, H-7a, H-11a), 3.49-3.42 (m, 2H, H-12a), 3.42-3.35 (m, 4H, H-7b, H-12b), 3.35-3.29 (m, 2H,

H11b), 2.17-2.06 (m, 4H, H-8a, H-9a), 2.06-1.96 (m, 4H, H-8b, H-9b), 1.57-1.50 (m, 4H, H-13), 1.40-1.32 (m, 4H, H-14), 0.92 (t, 6H, H-15, $^3J_{14,15}$ = 7.4 Hz).

^{13}C-NMR: (125 MHz, Chloroform-*d*, 298 K) δ [ppm] = 181.4 (C-2), 162.8 (C-4), 161.7 (C-1), 156.9 (C-3), 103.0 (C-6), 94.7 (C-5), 71.6 (C-12), 70.4 (C-11), 59.0 (C-10), 49.1 (C-7), 31.9 (C-13), 28.6 (C-9), 22.9 (C-8), 19.5 (C-14), 14.1 (C-15).

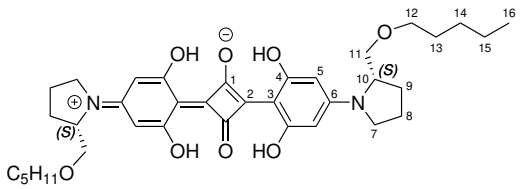
MS (ESI(+), Dichloromethane, M = $C_{34}H_{44}N_2O_8$) *m/z* = 609.32 $[M+H]^+$.

ESI HRMS: $[M+H]^+ = C_{34}H_{44}N_2O_8H^+$, calculated: m/z = 609.3170, found: m/z = 609.3166.

UV/Vis: (Chloroform) λ_{max} = 646 nm, ε = 383400 $M^{-1}cm^{-1}$

Elemental analysis: $C_{34}H_{44}N_2O_8$ calculated C: 67.09, H: 7.29, N: 4.60; found C: 66.86, H: 7.36, N: 4.55.

5.3.3 Synthesis of 2,4-Bis[4-(*S*)-(-)-2-(pentyloxymethyl)-pyrrolidone-2,6-dihydroxyphenyl]squaraine (*S*,*S*)-ProSQ-C5



L-prolinyl *n*-pentyl ether (995 mg, 5.82 mmol) was reacted according to the general procedure.

Yield: 42 mg (0.07 mmol, 3 %, brown solid)

Molecular weight: $C_{36}H_{48}N_2O_8$, 636.79 g/mol

^{1}H-NMR: (500 MHz, Chloroform-*d*, 298 K) δ [ppm] = 11.02 (s, 4H, OH), 5.78 (br s, 4H, H-5), 4.10-4.03 (m, 2H, H-10), 3.57-3.48 (m, 4H, H-7a, H-11a), 3.48-3.42 (m, 2H, H-12a), 3.42-3.29 (m, 6H, H-7b, H-11b, H-12b), 2.18-2.06 (m, 4H, H-8a, H-9a), 2.06-1.94 (m, 4H, H-8b, H-9b), 1.61-1.50 (m, 4H, H-13), 1.38-1.26 (m, 8H, H-14, H-15), 0.90 (t, 6H, H-16, $^3J_{15,16}$ = 7.0 Hz).

^{13}C-NMR: (125 MHz, Chloroform-*d*, 298 K) δ [ppm] = 181.5 (C-2),

162.9 (C-4), 161.8 (C-1), 156.9 (C-3), 103.0 (C-6), 94.8 (C-5), 71.9 (C-12), 70.4 (C-11), 59.0 (C-10), 49.1 (C-7), 29.5 (C-13), 28.6 (C-9), 28.4 (C-14), 22.9 (C-8), 22.7 (C-15), 14.2 (C-16).

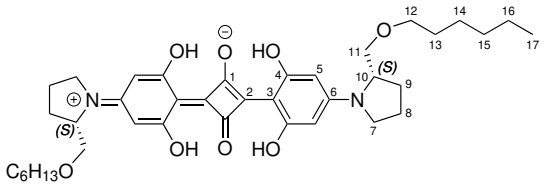
MS (ESI(+), Dichloromethane, M = $C_{36}H_{48}N_2O_8$) ***m/z*** **=** 637.35 $[M+H]^+$.

ESI HRMS: $[M+H]^+ = C_{36}H_{48}N_2O_8H^+$, calculated: $m/z = 637.3483$, found: $m/z = 637.3482$.

UV/Vis: (Chloroform) $\lambda_{max} = 646$ nm, $\varepsilon = 389300$ $M^{-1}cm^{-1}$

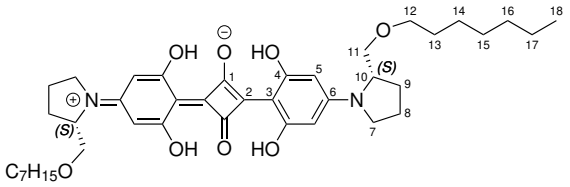
Elemental analysis: $C_{36}H_{48}N_2O_8 \cdot 0.3$ MeOH calculated C: 67.45, H: 7.67, N: 4.33; found C: 67.42, H: 7.68, N: 4.33.

5.3.4 Synthesis of 2,4-Bis[4-(*S*)-(-)-2-(hexyloxymethyl)-pyrrolidone-2,6-dihydroxyphenyl]squaraine (*S*,*S*)-ProSQ-C6



(*S*,*S*)-ProSQ-C6 was synthesized according to the literature.[26]

5.3.5 Synthesis of 2,4-Bis[4-(*S*)-(-)-2-(heptyloxymethyl)-pyrrolidone-2,6-dihydroxyphenyl]squaraine (*S*,*S*)-ProSQ-C7



L-prolinyl *n*-heptyl ether (399 mg, 2.00 mmol) was reacted according to the general procedure.

Yield: 147 mg (0.21 mmol, 21 %, red solid)

Molecular weight: $C_{40}H_{56}N_2O_8$, 692.89 g/mol

^{1}H-NMR: (500 MHz, Chloroform-*d*, 298 K) δ [ppm] = 11.00 (s, 4H, OH), 5.77 (br s, 4H, H-5), 4.08-4.03 (m, 2H, H-10), 3.55-3.48 (m, 4H, H-7a, H-11a), 3.47-3.42 (m, 2H, H-12a), 3.40-3.34 (m, 4H, H-7b, H-12b), 3.34-3.30 (m, 2H, H-11b), 2.16-2.05 (m, 4H, H-8a, H-9a), 2.05-1.95 (m, 4H, H-8b, H-9b), 1.59-1.51 (m, 4H, H-13), 1.35-1.23 (m, 16H, H-14 to H-17), 0.88 (t, 6H, H-18, $^3J_{17,18}$ = 7.0 Hz).

^{13}C-NMR: (125 MHz, Chloroform-*d*, 298 K) δ [ppm] = 181.4 (C-2), 162.8 (C-4), 161.7 (C-1), 156.9 (C-3), 103.0 (C-6), 94.7 (C-5), 71.9 (C-12), 70.4 (C-11), 59.0 (C-10), 49.0 (C-7), 32.0, 29.8, 29.3, 26.2, 22.8 (C-13 to C-17), 28.6 (C-9), 22.9 (C-8), 14.2 (C-18).

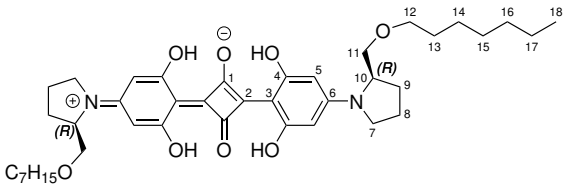
MS (ESI(+), Dichloromethane, M = $C_{40}H_{56}N_2O_8$) *m/z* = 692.40 $[M]^{\cdot+}$.

ESI HRMS: $[M]^{\cdot+}$ = $C_{40}H_{56}N_2O_8H^+$, calculated: m/z = 692.4031, found: m/z = 692.4033.

UV/Vis: (Chloroform) λ_{max} = 646 nm, ε = 375400 $M^{-1}cm^{-1}$

Elemental analysis: $C_{40}H_{56}N_2O_8$ calculated C: 69.34, H: 8.15, N: 4.04; found C: 69.37, H: 8.15, N: 4.06.

5.3.6 Synthesis of 2,4-Bis[4-(*R*)-(-)-2-(heptyloxymethyl)-pyrrolidone-2,6-dihydroxyphenyl]squaraine (*R*,*R*)-ProSQ-C7



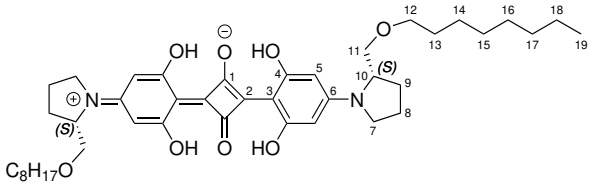
D-prolinyl *n*-heptyl ether (923 mg, 5.00 mmol) was reacted according to the general procedure.

Yield: 254 mg (0.37 mmol, 15 %, red solid)

Molecular weight: $C_{40}H_{56}N_2O_8$, 692.89 g/mol

All other analytical data of the (*R*,*R*)-enantiomer are in agreement with those of the (*S*,*S*)-enantiomer.

5.3.7 Synthesis of 2,4-Bis[4-(*S*)-(-)-2-(octyloxymethyl)-pyrrolidone-2,6-dihydroxyphenyl]squaraine (*S*,*S*)-ProSQ-C8



L-prolinyl *n*-octyl ether (411 mg, 1.93 mmol) was reacted according to the general procedure.

Yield: 105 mg (0.15 mmol, 17 %, red solid)

Molecular weight: $C_{42}H_{60}N_2O_8$, 720.95 g/mol

^{1}H-NMR: (500 MHz, Chloroform-*d*, 298 K) δ [ppm] = 11.02 (s, 4H, OH), 5.78 (br s, 4H, H-5), 4.12-4.00 (m, 2H, H-10), 3.61-3.48 (m, 4H, H-7a, H-11a), 3.48-3.41 (m, 2H, H-12a), 3.41-3.34 (m, 4H, H-7b, H-12b), 3.34-3.27 (m, 2H, H-11b), 2.22-2.07 (m, 4H, H-8a, H-9a), 2.07-1.91 (m, 4H, H-11b, H-8b), 1.63-1.47 (m, 4H, H-13), 1.40 1.14 (m, 20H, H-14 to H-18), 0.88 (t, 6H, H-19, $^3J_{18,19}$ = 6.6 Hz).

^{13}C-NMR: (125 MHz, Chloroform-*d*, 298 K) δ [ppm] = 181.5 (C-2), 162.9 (C-4), 161.8 (C-1), 156.9 (C-3), 103.0 (C-6), 94.8 (C-5), 71.9 (C-12), 70.4 (C-11), 59.0 (C-10), 49.1 (C-7), 32.0 (C-17), 29.8, 29.6, 29.4 (C-13, C-15, C-16), 28.6 (C-9), 26.3 (C-14), 22.9 (C-8), 22.8 (C-18), 14.3 (C-19).

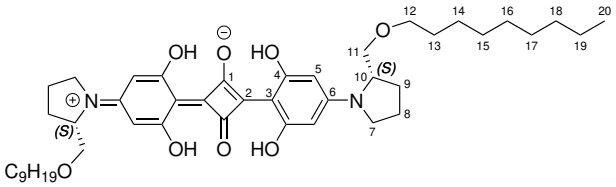
MS (ESI(+), Dichloromethane, M = $C_{42}H_{60}N_2O_8$) *m/z* = 720.434 $[M]^{\cdot+}$, 577.291 $[M\text{-}C_9H_{19}O]^{\cdot+}$.

ESI HRMS: $[M]^{\cdot+} = C_{42}H_{60}N_2O_8H^{\cdot+}$, calculated: m/z = 720.4344, found: m/z = 720.4345.

UV/Vis: (Chloroform) λ_{max} = 646 nm, ε = 438000 $M^{-1}cm^{-1}$

Elemental analysis: $C_{42}H_{60}N_2O_8$ calculated C: 69.97, H: 8.39, N: 3.89; found C: 69.47, H: 8.44, N: 3.85.

5.3.8 Synthesis of 2,4-Bis[4-(*S*)-(-)-2-(nonyloxymethyl)-pyrrolidone-2,6-dihydroxyphenyl]squaraine (*S*,*S*)-ProSQ-C9



L-prolinyl *n*-nonyl ether (1.08 g, 4.75 mmol) was reacted according to the general procedure.

Yield: 456 mg (0.61 mmol, 26 %, red solid)

Molecular weight: $C_{44}H_{64}N_2O_8$, 749.00 g/mol

^{1}H-NMR: (500 MHz, Chloroform-*d*, 298 K) δ [ppm] = 11.01 (s, 4H, OH), 5.77 (br s, 4H, H-5), 4.09-4.03 (m, 2H, H-10), 3.56-3.48 (m, 4H, H-7a, H-11a), 3.48-3.42 (m, 2H, H-12a), 3.40-3.35 (m, 4H, H-7b, H-12b), 3.34-3.30 (m, 2H, H-11b), 2.16-2.06 (m, 4H, H-8a, H-9a), 2.06-1.96 (m, 4H, H-8b, H-9b), 1.57-1.51 (m, 6H, H-13), 1.36-1.19 (m, 24H, H-14 to H-19), 0.88 (t, 6H, H-20, $^3J_{19,20}$ = 7.0 Hz).

^{13}C-NMR: (125 MHz, Chloroform-*d*, 298 K) δ [ppm] = 181.4 (C-2), 162.8 (C-4), 161.7 (C-1), 156.9 (C-3), 103.0 (C-6), 94.8 (C-5), 71.9 (C-12), 70.4 (C-11), 59.0 (C-10), 49.1 (C-7), 32.0 (C-18), 29.8, 29.7, 29.6, 29.4 (C-13, C-15 to C-17), 28.6 (C-9), 26.3 (C-14), 22.9 (C-8), 22.8 (C-19), 14.3 (C-20).

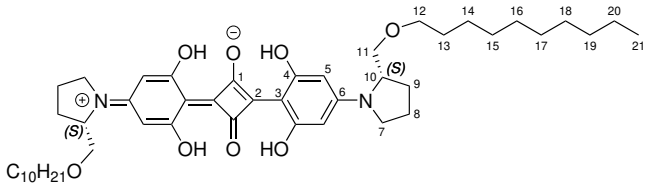
MS (ESI(+), Dichloromethane, M = $C_{44}H_{64}N_2O_8$) *m/z* = 749.47 $[M]^+$

ESI HRMS: $[M]^+ = C_{44}H_{64}N_2O_8H^+$, calculated: m/z = 749.4737, found: m/z = 749.4735.

UV/Vis: (Chloroform) λ_{max} = 646 nm, ε = 367700 $M^{-1}cm^{-1}$

Elemental analysis: $C_{44}H_{64}N_2O_8$ calculated C: 70.56, H: 8.61, N: 3.74; found C: 70.73, H: 8.69, N: 3.72.

5.3.9 Synthesis of 2,4-Bis[4-(*S*)-(-)-2-(decyloxymethyl)-pyrrolidone-2,6-dihydroxyphenyl]squaraine (*S*,*S*)-ProSQ-C10



L-prolinyl *n*-decyl ether (1.10 g, 4.55 mmol) was reacted according to the general procedure.

Yield: 271 mg (0.35 mmol, 15 %, red solid)

Molecular weight: $C_{46}H_{68}N_2O_8$, 777.06 g/mol

^{1}H-NMR: (500 MHz, Chloroform-*d*, 298 K) δ [ppm] = 11.02 (s, 4H, OH), 5.78 (br s, 4H, H-5), 4.10-4.03 (m, 2H, H-10), 3.57-3.48 (m, 4H, H-7a, H-11a), 3.48-3.41 (m, 2H, H-12a), 3.41-3.29 (m, 6H, H-7b, H-11b, H-12b), 2.17-2.06 (m, 4H, H-8a, H-9a), 2.06-1.96 (m, 4H, H-8b, H-9b), 1.59-1.50 (m, 4H, H-13), 1.36-1.20 (m, 28H, H-14 to H-20), 0.88 (t, 6H, H-21, $^3J_{20,21}$ = 7.0 Hz).

^{13}C-NMR: (125 MHz, Chloroform-*d*, 298 K) δ [ppm] = 181.5 (C-2), 162.9 (C-4), 161.8 (C-1), 156.9 (C-3), 103.0 (C-6), 94.8 (C-5), 71.9 (C-12), 70.4 (C-11), 59.0 (C-10), 49.1 (C-7), 32.1, 29.8, 29.8, 29.7, 29.6, 29.5, 26.3, 22.9 (C-13 to C-20), 28.6 (C-9), 22.9 (C-8), 14.3 (C-21).

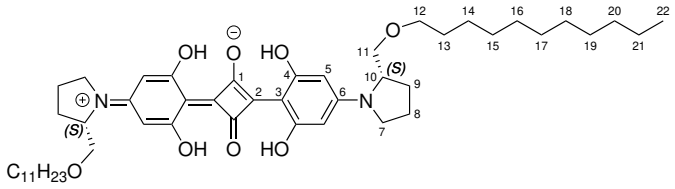
MS (ESI(+), Dichloromethane, M = $C_{46}H_{68}N_2O_8$) *m/z* = 777.50 $[M+H]^+$

ESI HRMS: $[M]^+ = C_{46}H_{68}N_2O_8H^+$, calculated: m/z = 777.5048, found: m/z = 777.5049.

UV/Vis: (Chloroform) λ_{max} = 646 nm, ε = 361000 $M^{-1}cm^{-1}$

Elemental analysis: $C_{46}H_{68}N_2O_8$ calculated C: 71.10, H: 8.82, N: 3.61; found C: 71.27, H: 8.95, N: 3.60.

5.3.10 Synthesis of 2,4-Bis[4-(*S*)-(-)-2-(undecyloxymethyl)-pyrrolidone-2,6-dihydroxyphenyl]squaraine (*S*,*S*)-ProSQ-C11



L-prolinyl *n*-undecyl ether (1.02 g, 4.00 mmol) was reacted according to the general procedure.

Yield: 165 mg (0.20 mmol, 5 %, red solid)

Molecular weight: $C_{48}H_{72}N_2O_8$, 805.11 g/mol

^{1}H-NMR: (700 MHz, Chloroform-*d*, 298 K) δ [ppm] = 11.02 (s, 4H, OH), 5.78 (br s, 4H, H-5), 4.09-4.04 (m, 2H, H-10), 3.56-3.49 (m, 4H, H-7a, H-11a), 3.47-3.42 (m, 2H, H-12a), 3.41-3.35 (m, 4H, H-7b, H-12b), 3.35-3.30 (m, 2H, H-11b), 2.16-2.07 (m, 4H, H-8a, H-9a), 2.06-1.96 (m, 4H, H-8b, H-9b), 1.58-1.52 (m, 4H, H-13), 1.34-1.23 (m, 32H, H-14 to H-21), 0.88 (t, 6H, H-22, $^3J_{21,22}$ = 7.0 Hz).

^{13}C-NMR: (176 MHz, Chloroform-*d*, 298 K) δ [ppm] = 181.5 (C-2), 162.9 (C-4), 161.8 (C-1), 156.9 (C-3), 103.0 (C-6), 94.8 (C-5), 71.9 (C-12), 70.4 (C-11), 59.0 (C-10), 49.1 (C-7), 32.1 (C-20), 29.8, 29.8, 29.8, 29.6, 29.5 (C-13, C-15 to C-19), 28.6 (C-9), 26.3 (C-14), 22.9 (C-8), 22.9 (C-21), 14.3 (C-22).

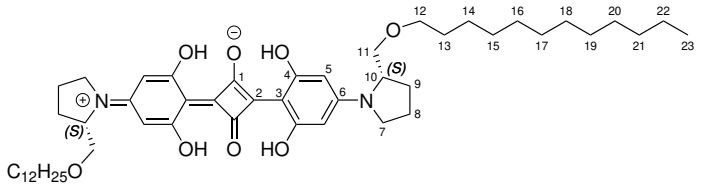
MS (ESI(+), Dichloromethane, M = $C_{48}H_{72}N_2O_8$) *m/z* = 804.53 $[M]^{\cdot+}$, 619.34 $[M\text{-}C_{12}H_{25}O]^{\cdot+}$

ESI HRMS: $[M]^+ = C_{48}H_{72}N_2O_8{}^{\cdot+}$, calculated: m/z = 804.5283, found: m/z = 804.5283.

UV/Vis: (Chloroform) λ_{max} = 646 nm, ε = 382000 $M^{-1}cm^{-1}$

Elemental analysis: $C_{48}H_{72}N_2O_8$ calculated C: 71.61, H: 9.01, N: 3.48; found C: 71.35, H: 9.05, N: 3.33.

5.3.11 Synthesis of 2,4-Bis[4-(*S*)-(-)-2-(dodecyloxymethyl)-pyrrolidone-2,6-dihydroxyphenyl]squaraine (*S*,*S*)-ProSQ-C12



L-prolinyl *n*-dodecyl ether (719 mg, 2.67 mmol) was reacted according to the general procedure.

Yield: 226 mg (0.27 mmol, 22 %, violet solid)

Molecular weight: $C_{50}H_{76}N_2O_8$, 833.17 g/mol

^{1}H-NMR: (500 MHz, Chloroform-*d*, 298 K) δ [ppm] = 11.02 (s, 4H, OH), 5.78 (br s, 4H, H-5), 4.10-4.01 (m, 2H, H-10), 3.57-3.48 (m, 4H, H-7a, H-11a), 3.48-3.41 (m, 2H, H-12a), 3.41-3.35 (m, 4H, H-7b, H-12b), 3.35-3.29 (m, 2H, H-11b), 2.20-2.07 (m, 4H, H-8a, H-9a), 2.07-1.94 (m, 4H, H-7b, H-9b), 1.61-1.48 (m, 4H, H-13), 1.37-1.16 (m, 36H, H-14 to H-22), 0.88 (t, 6H, H-23, $^3J_{22,23}$ = 7.0 Hz).

^{13}C-NMR: (125 MHz, Chloroform-*d*, 298 K) δ [ppm] = 181.5 (C-2), 162.9 (C-4), 161.8 (C-1), 156.9 (C-3), 103.0 (C-6), 94.8 (C-5), 71.9 (C-12), 70.4 (C-11), 59.0 (C-10), 49.1 (C-7), 32.1 (C-21), 29.8, 29.8, 29.8, 29.8, 29.8, 29.6, 29.5 (C-13, C-16 to C-20), 28.6 (C-9), 26.3 (C-14), 22.9 (C-8), 22.8 (C-22), 14.3 (C-23).

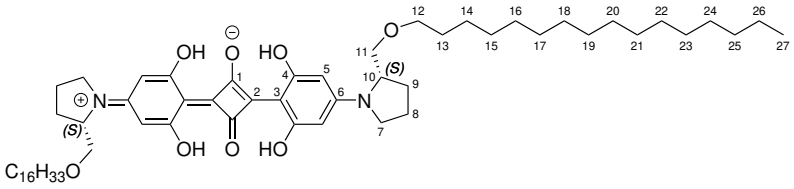
MS (ESI(+), Dichloromethane, M = $C_{50}H_{76}N_2O_8$) *m/z* = 832.56 $[M]^{\cdot+}$

ESI HRMS: $[M]^+ = C_{50}H_{76}N_2O_8{}^{\cdot+}$, calculated: m/z = 832.5596, found: m/z = 832.5597.

UV/Vis: (Chloroform) λ_{max} = 646 nm, ε = 408000 $M^{-1}cm^{-1}$

Elemental analysis: $C_{50}H_{76}N_2O_8$ calculated C: 72.08, H: 9.19, N: 3.36; found C: 71.92, H: 9.30, N: 3.22.

5.3.12 Synthesis of 2,4-Bis[4-(*S*)-(-)-2-(hexadecyloxymethyl)-pyrrolidone-2,6-dihydroxyphenyl]squaraine (*S*,*S*)-ProSQ-C16



(*S*,*S*)-ProSQ-C16 was synthesized according to the literature.[26, 1]

References

[1] Matthias Schulz et al. "Giant intrinsic circular dichroism of prolinol-derived squaraine thin films". In: *Nat. Commun.* 9.2413 (2018), p. 2413.

[2] Kasha, M. "Energy Transfer Mechanism and the Molecular Exciton Model for Molecular Aggregates". In: *Radiat. Res.* 3 (1964), pp. 317–331.

[3] Spano, F. C. "The Spectral Signatures of Frenkel Polarons in H- and J-Aggregates". In: *Acc. Chem. Res.* 43.3 (2010), pp. 429–439. DOI: 10.1021/ar900233v.

[4] M. Anzola, F. Di Maiolo, and A. Painelli. "Optical spectra of molecular aggregates and crystals: testing approximation schemes". In: *Phys. Chem. Chem. Phys.* 21.36 (2019), pp. 19816–19824. DOI: 10.1039/c9cp03122g.

[5] Sabnam Kar et al. "Emergence of Chiroptical Properties in Molecular Assemblies of Phenyleneethynylenes: The Role of Quasi-degenerate Excitations". In: *J. Phys. Chem. Lett.* 9.16 (2018), pp. 4584–4590. DOI: 10.1021/acs.jpclett.8b01988.

[6] Nicholas J Hestand et al. "Confirmation of the origins of panchromatic spectra in squaraine thin films targeted for organic photovoltaic devices". In: *J. of Phys. Chem. C* 119.33 (2015), pp. 18964–18974.

[7] C. Caleman et al. "Force field benchmark of organic liquids: density, enthalpy of vaporization, heat capacities, surface tension, isothermal compressibility, volumetric expansion coefficient, and dielectric constant". In: *J. Chem. Theory Comput.* 8 (2012), p. 61.

[8] William L. Jorgensen et al. "Comparison of simple potential functions for simulating liquid water". In: *J. Chem. Phys.* 79.2 (1983), pp. 926–935. DOI: 10.1063/1.445869. eprint: https://doi.org/10.1063/1.445869. URL: https://doi.org/10.1063/1.445869.

[9] Berk Hess et al. "LINCS: A linear constraint solver for molecular simulations". In: *J. Comp. Chem.* 18.12 (1997), pp. 1463–1472.

[10] Giovanni Bussi. "Hamiltonian replica exchange in GROMACS: a flexible implementation". In: *Molecular Physics* 112.3-4 (2014), pp. 379–384. DOI: 10.1080/00268976.2013.824126. eprint: https://doi.org/10.1080/00268976.2013.824126. URL: https://doi.org/10.1080/00268976.2013.824126.

[11] David Van Der Spoel et al. "GROMACS: Fast, flexible, and free". In: *J. Comp. Chem.* 26.16 (2005), pp. 1701–1718. DOI: https://doi.org/10.1002/jcc.20291. eprint: https://onlinelibrary.wiley.com/doi/pdf/10.1002/jcc.20291. URL: https://onlinelibrary.wiley.com/doi/abs/10.1002/jcc.20291.

[12] Gareth A. Tribello et al. "PLUMED 2: New feathers for an old bird". In: *Computer Physics Communications* 185.2 (2014), pp. 604–613. ISSN: 0010-4655. DOI: https://doi.org/10.1016/j.cpc.2013.09.018. URL: https://www.sciencedirect.com/science/article/pii/S0010465513003196.

[13] J. Wang et al. "Development and Testing of a General Amber Force Field". In: *J. Comput. Chem.* 25 (2004), p. 1157.

[14] M. J. Frisch et al. *GaussianË16 Revision C.01*. Gaussian Inc. Wallingford CT. 2016.

[15] C. I. Bayly et al. "A Well-Behaved Electrostatic Potential Based Method Using Charge Restraints for Deriving Atomic Charges: the RESP Model". In: *J. Phys. Chem.* 97 (1993), p. 10269.

[16] P. J. Stephens et al. “Ab Initio Calculation of Vibrational Absorption and Circular Dichroism Spectra Using Density Functional Force Fields”. In: *J. Phys. Chem.* 98.45 (1994), pp. 11623–11627. DOI: 10.1021/j100096a001. eprint: https://doi.org/10.1021/j100096a001. URL: https://doi.org/10.1021/j100096a001.

[17] Nicola Jane Boyd and Mark R. Wilson. “Validating an optimized GAFF force field for liquid crystals: TNI predictions for bent-core mesogens and the first atomistic predictions of a dark conglomerate phase”. In: *Phys. Chem. Chem. Phys.* 20 (3 2018), pp. 1485–1496. DOI: 10.1039/C7CP07496D. URL: http://dx.doi.org/10.1039/C7CP07496D.

[18] Naveen Michaud-Agrawal et al. “MDAnalysis: A toolkit for the analysis of molecular dynamics simulations”. In: *J. Comp. Chem.* 32.10 (2011), pp. 2319–2327. DOI: https://doi.org/10.1002/jcc.21787. eprint: https://onlinelibrary.wiley.com/doi/pdf/10.1002/jcc.21787. URL: https://onlinelibrary.wiley.com/doi/abs/10.1002/jcc.21787.

[19] Richard J. Gowers et al. “MDAnalysis: A Python Package for the Rapid Analysis of Molecular Dynamics Simulations”. In: *Proceedings of the 15th Python in Science Conference*. Ed. by Sebastian Benthall and Scott Rostrup. 2016, pp. 98–105. DOI: 10.25080/Majora-629e541a-00e.

[20] Maria dâErrico et al. “Automatic topography of high-dimensional data sets by non-parametric density peak clustering”. In: *Information Sciences* 560 (2021), pp. 476–492. ISSN: 0020-0255. DOI: https://doi.org/10.1016/j.ins.2021.01.010. URL: https://www.sciencedirect.com/science/article/pii/S0020025521000116.

[21] Frank Neese. “Software update: The ORCA program systemâVersion 5.0”. In: *WIREs Computational Molecular Science* 12.5 (2022), e1606. DOI: https://doi.org/10.1002/wcms.1606. eprint: https://wires.onlinelibrary.wiley.com/doi/pdf/10.1002/wcms.1606. URL: https://wires.onlinelibrary.wiley.com/doi/abs/10.1002/wcms.1606.

[22] Rebecca Sure and Stefan Grimme. “Corrected small basis set Hartree-Fock method for large systems”. In: *Journal of Computational Chemistry* 34.19

(2013), pp. 1672–1685. DOI: https://doi.org/10.1002/jcc.23317. eprint: https://onlinelibrary.wiley.com/doi/pdf/10.1002/jcc.23317. URL: https://onlinelibrary.wiley.com/doi/abs/10.1002/jcc.23317.

[23] Stefan Grimme et al. "Consistent structures and interactions by density functional theory with small atomic orbital basis sets". In: *The Journal of Chemical Physics* 143.5 (2015), p. 054107. DOI: 10.1063/1.4927476. eprint: https://doi.org/10.1063/1.4927476. URL: https://doi.org/10.1063/1.4927476.

[24] Stefan Grimme, Stephan Ehrlich, and Lars Goerigk. "Effect of the damping function in dispersion corrected density functional theory". In: *Journal of Computational Chemistry* 32.7 (2011), pp. 1456–1465. DOI: https://doi.org/10.1002/jcc.21759. eprint: https://onlinelibrary.wiley.com/doi/pdf/10.1002/jcc.21759. URL: https://onlinelibrary.wiley.com/doi/abs/10.1002/jcc.21759.

[25] Takeshi Yanai, David P Tew, and Nicholas C Handy. "A new hybrid exchangeâcorrelation functional using the Coulomb-attenuating method (CAM-B3LYP)". In: *Chemical Physics Letters* 393.1 (2004), pp. 51–57. ISSN: 0009-2614. DOI: https://doi.org/10.1016/j.cplett.2004.06.011. URL: https://www.sciencedirect.com/science/article/pii/S0009261404008620.

[26] Matthias Schulz et al. "Organic photodiodes from homochiral L-proline derived squaraine compounds with strong circular dichroism". In: *Phys. Chem. Chem. Phys.* 19.10 (2017), pp. 6996–7008.

6 NMR and mass spectra

6.1 NMR spectra

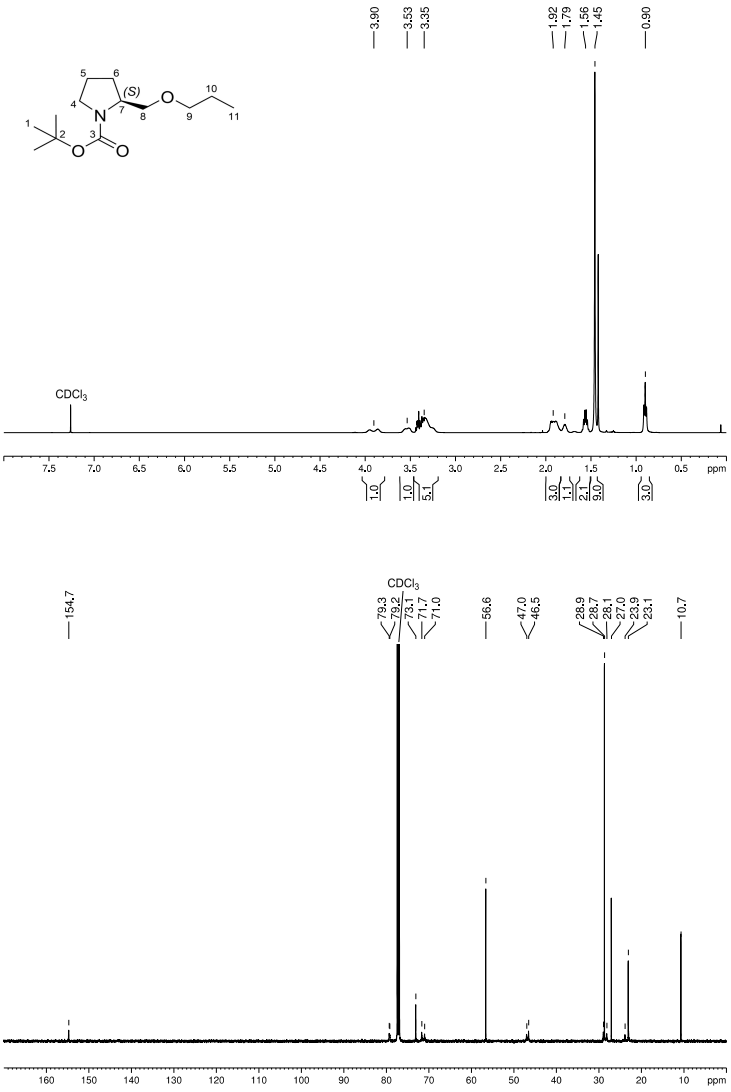


Figure S21: ^{1}H- (top, 500 MHz) and ^{13}C-NMR (bottom, 125 MHz) spectrum of *N*-Boc-L-prolinyl *n*-propyl ether; $CDCl_3$, 298 K.

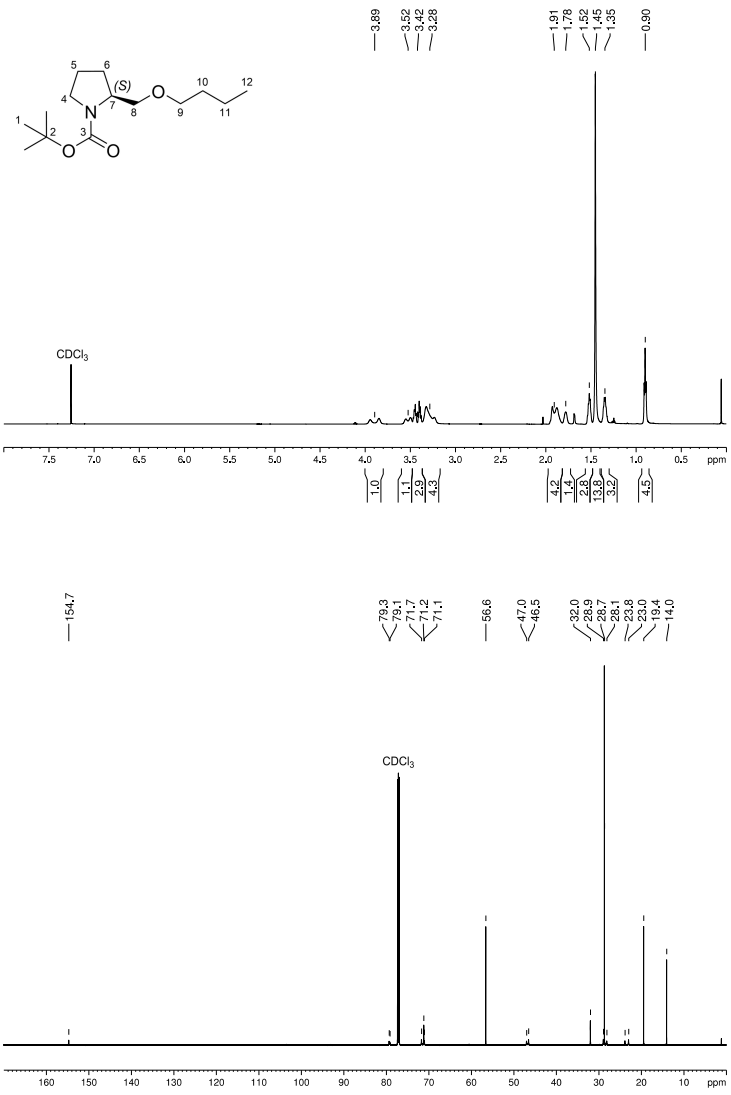


Figure S22: ^{1}H- (top, 700 MHz) and ^{13}C-NMR (bottom, 176 MHz) spectrum of *N*-Boc-L-prolinyl *n*-butyl ether; $CDCl_3$, 298 K.

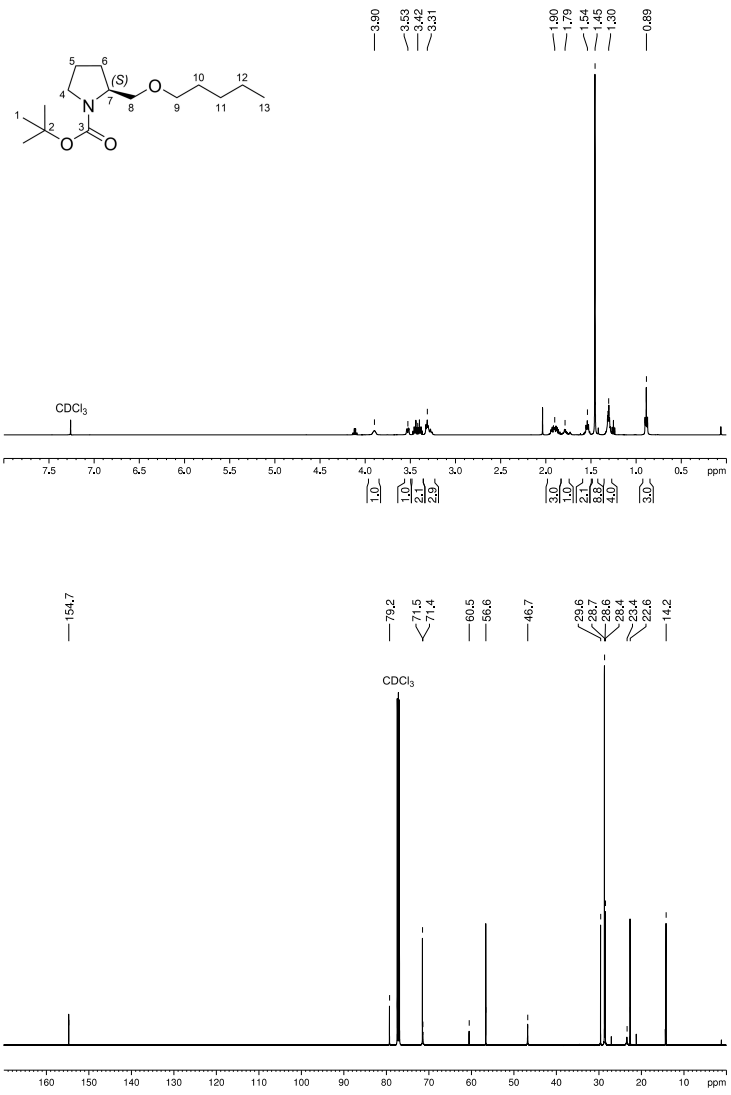


Figure S23: ^{1}H- (top, 500 MHz) and ^{13}C-NMR (bottom, 125 MHz) spectrum of *N*-Boc-L-prolinyl *n*-pentyl ether; $CDCl_3$, 298 K.

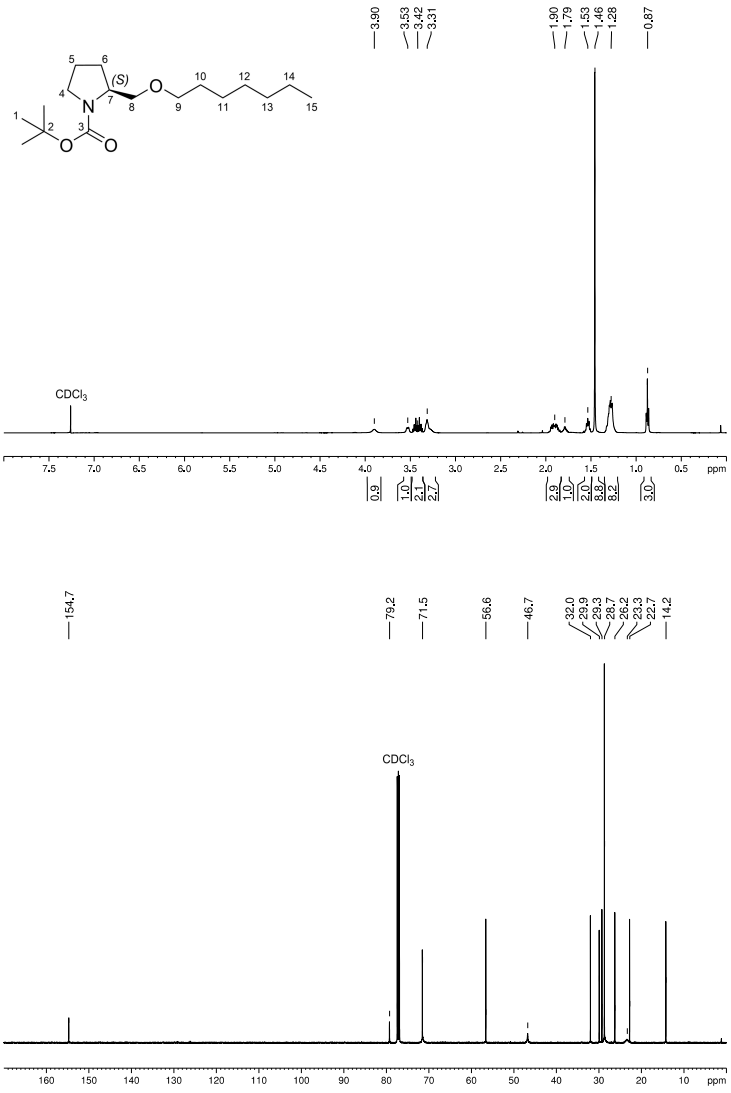


Figure S24: ^{1}H- (top, 500 MHz) and ^{13}C-NMR (bottom, 125 MHz) spectrum of *N*-Boc-L-prolinyl *n*-heptyl ether; $CDCl_3$, 298 K.

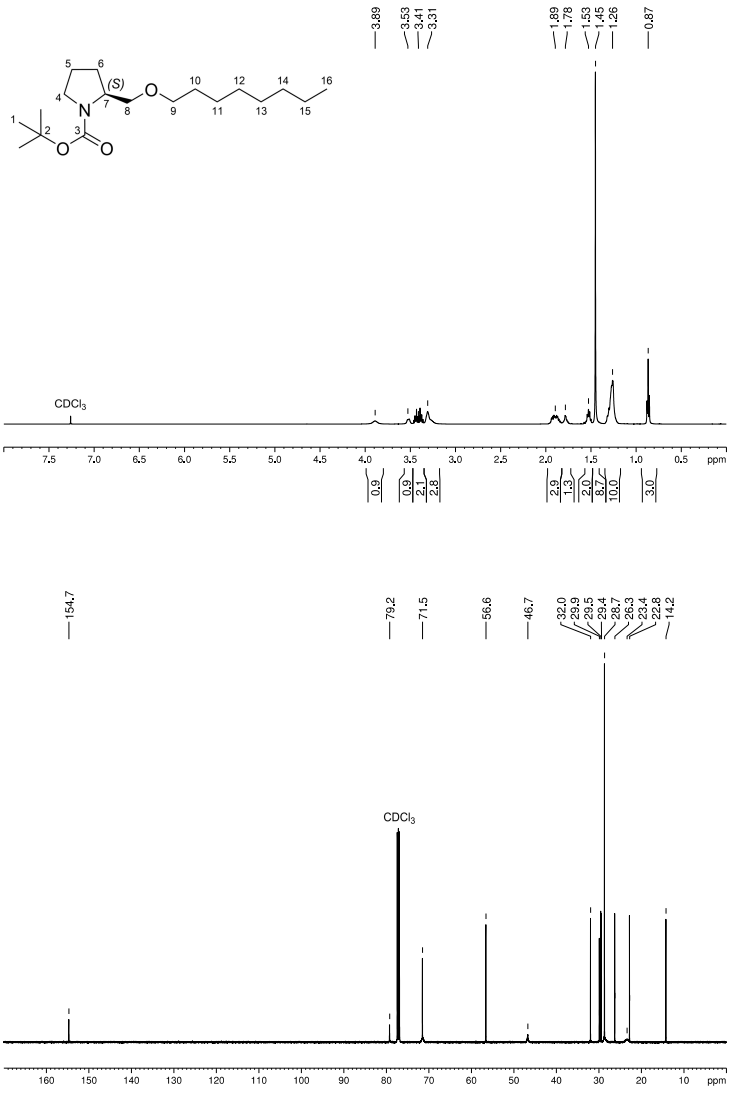


Figure S25: ^{1}H- (top, 500 MHz) and ^{13}C-NMR (bottom, 125 MHz) spectrum of *N*-Boc-L-prolinyl *n*-octyl ether; $CDCl_3$, 298 K.

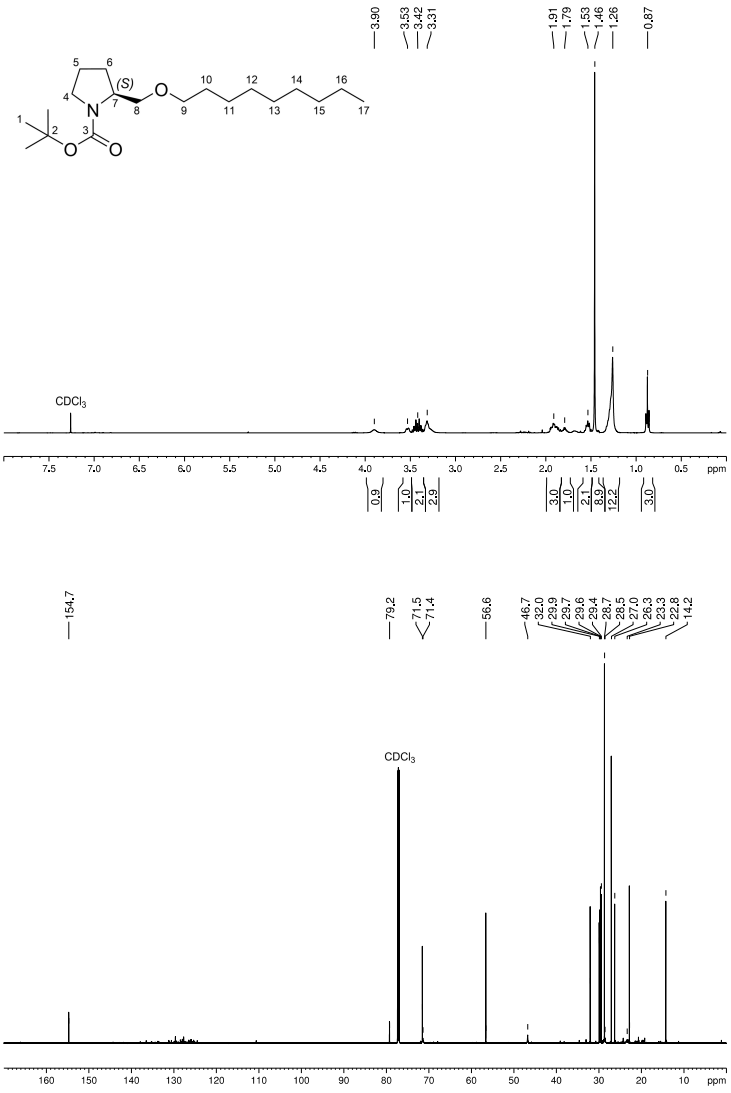


Figure S26: ^{1}H- (top, 700 MHz) and ^{13}C-NMR (bottom, 176 MHz) spectrum of *N*-Boc-L-prolinyl *n*-nonyl ether; $CDCl_3$, 298 K.

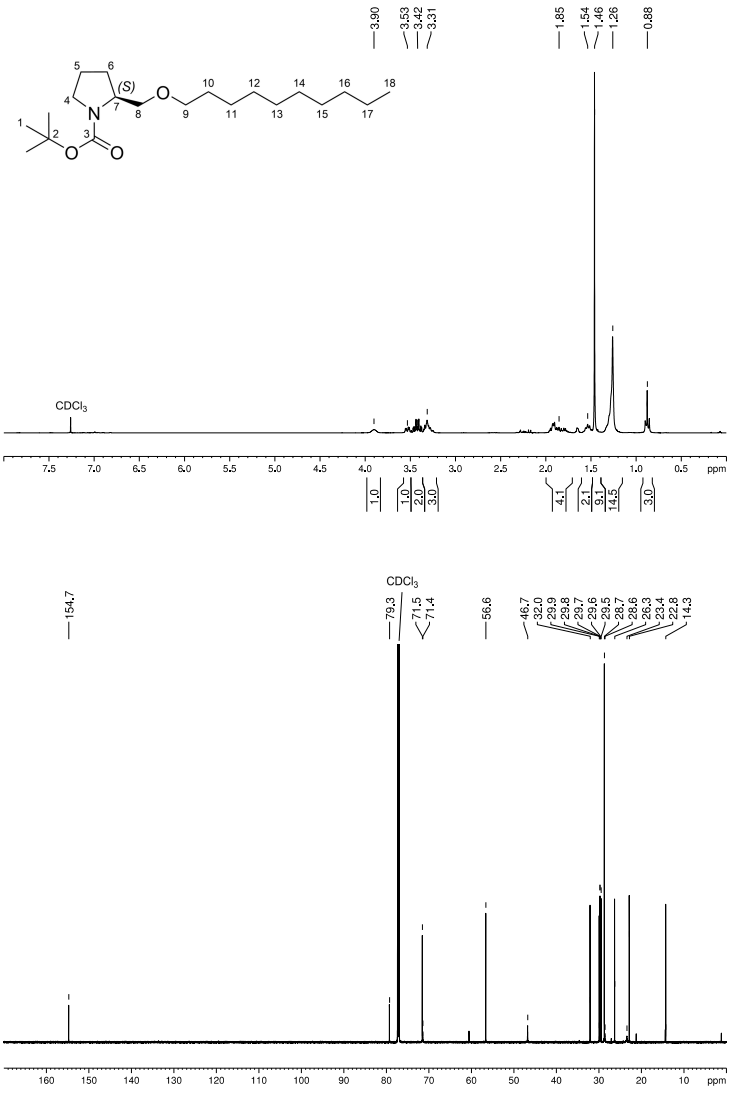


Figure S27: ^{1}H- (top, 700 MHz) and ^{13}C-NMR (bottom, 176 MHz) spectrum of *N*-Boc-L-prolinyl *n*-decyl ether; $CDCl_3$, 298 K.

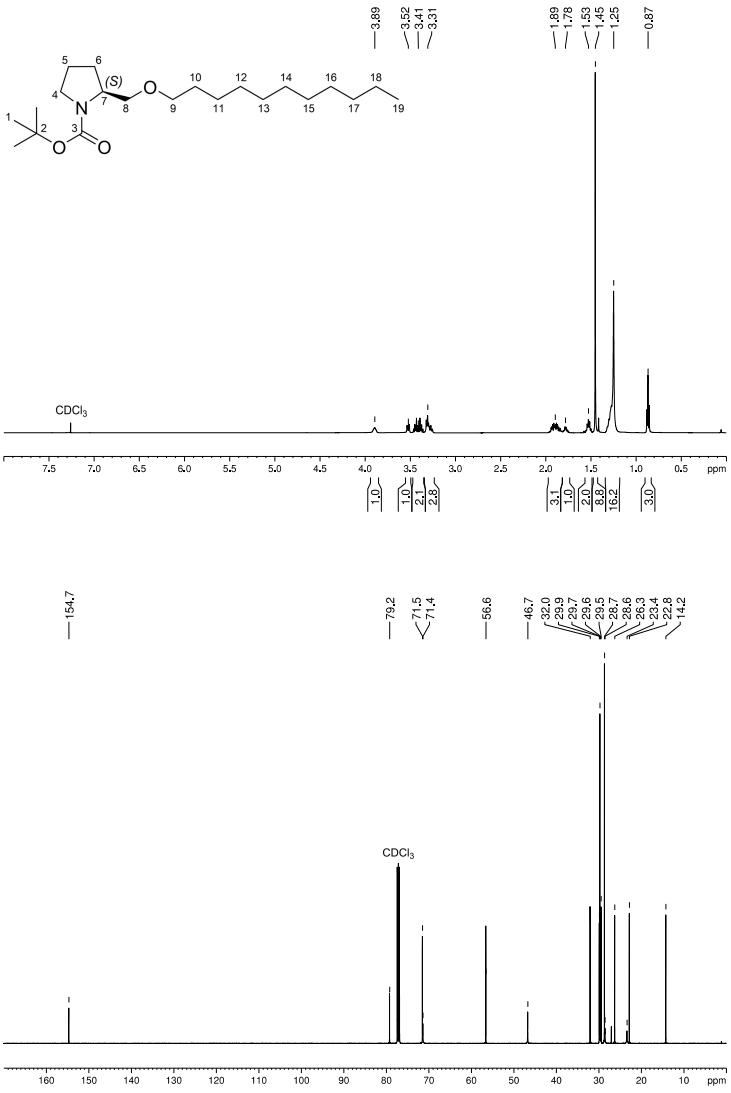


Figure S28: ^{1}H- (top, 500 MHz) and ^{13}C-NMR (bottom, 125 MHz) spectrum of *N*-Boc-L-prolinyl *n*-undecyl ether; $CDCl_3$, 298 K.

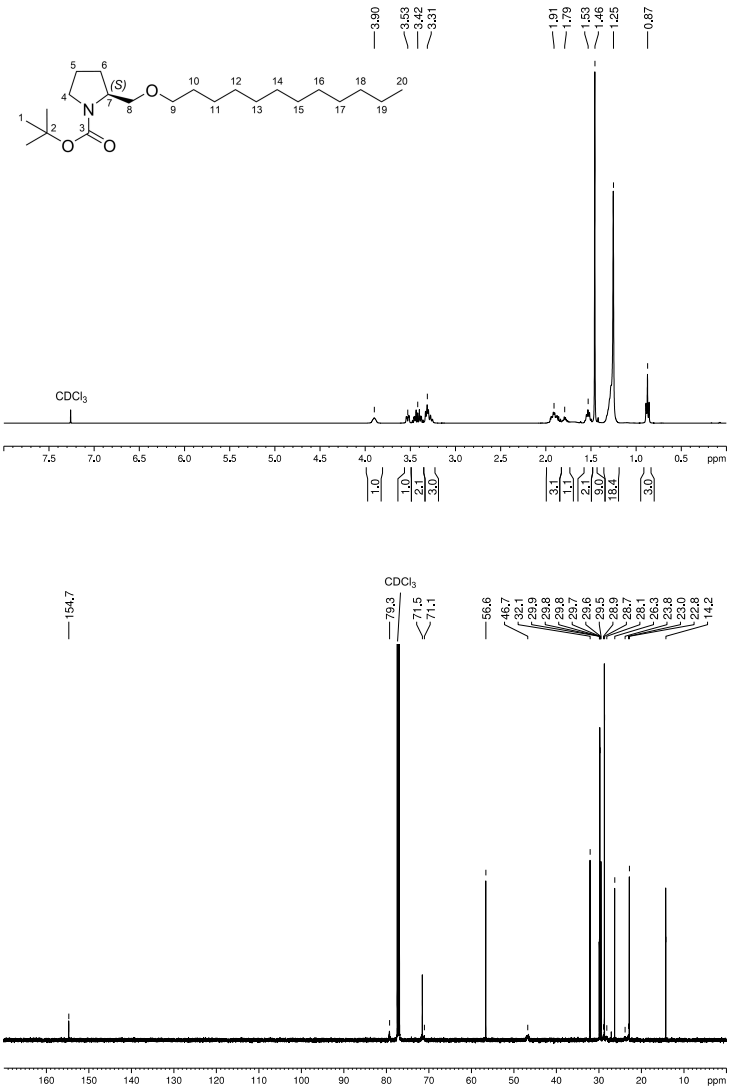


Figure S29: ^{1}H- (top, 400 MHz) and ^{13}C-NMR (bottom, 125 MHz) spectrum of *N*-Boc-L-prolinyl *n*-dodecyl ether; $CDCl_3$, 298 K.

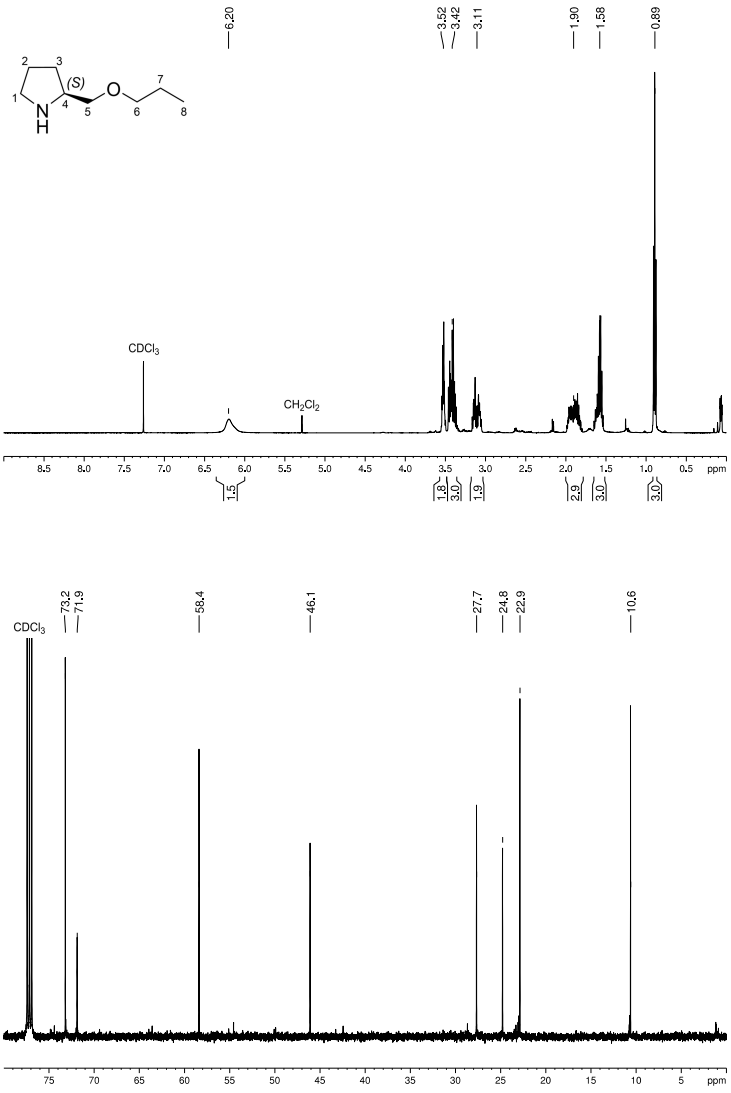


Figure S30: ^{1}H- (top, 500 MHz) and ^{13}C-NMR (bottom, 125 MHz) spectrum of L-prolinyl *n*-propyl ether; $CDCl_3$, 298 K.

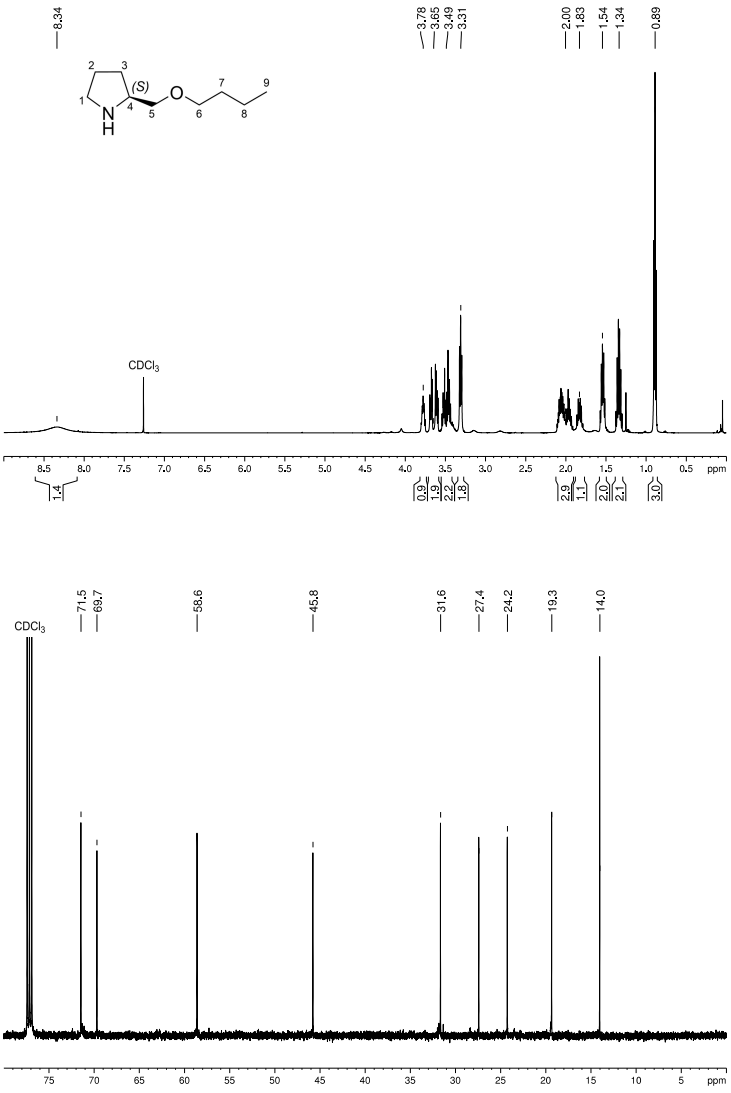


Figure S31: ^{1}H- (top, 500 MHz) and ^{13}C-NMR (bottom, 125 MHz) spectrum of L-prolinyl *n*-butyl ether; $CDCl_3$, 298 K.

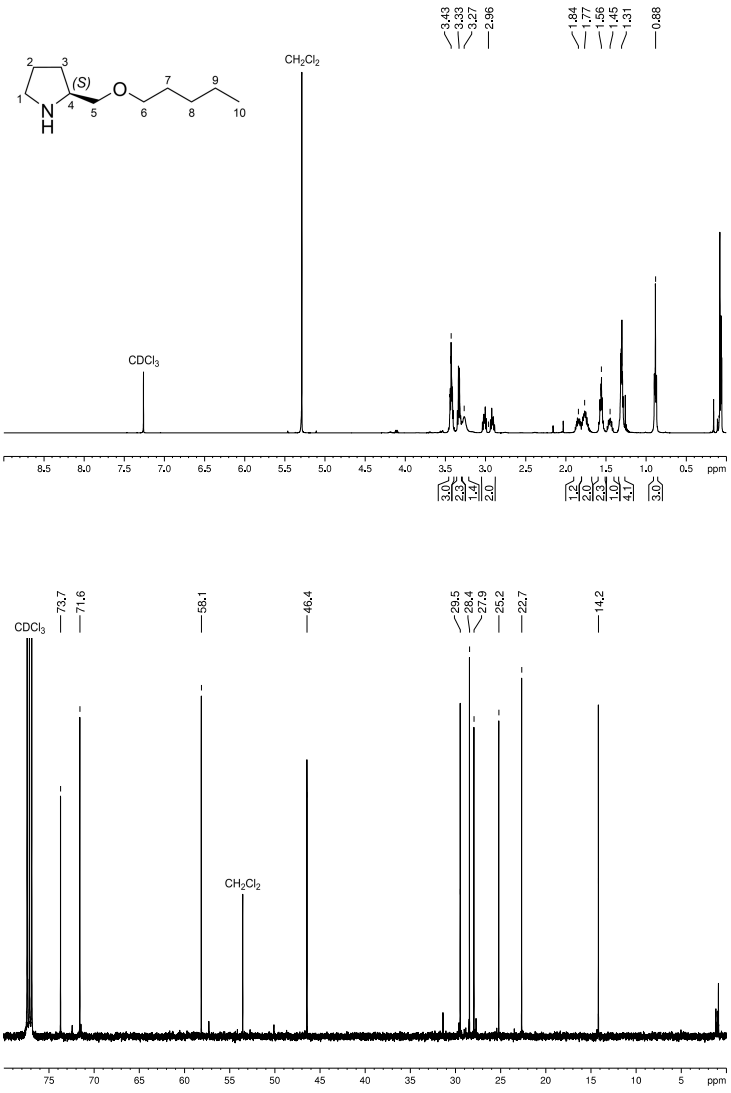


Figure S32: ^{1}H- (top, 500 MHz) and ^{13}C-NMR (bottom, 125 MHz) spectrum of L-prolinyl *n*-pentyl ether; $CDCl_3$, 298 K.

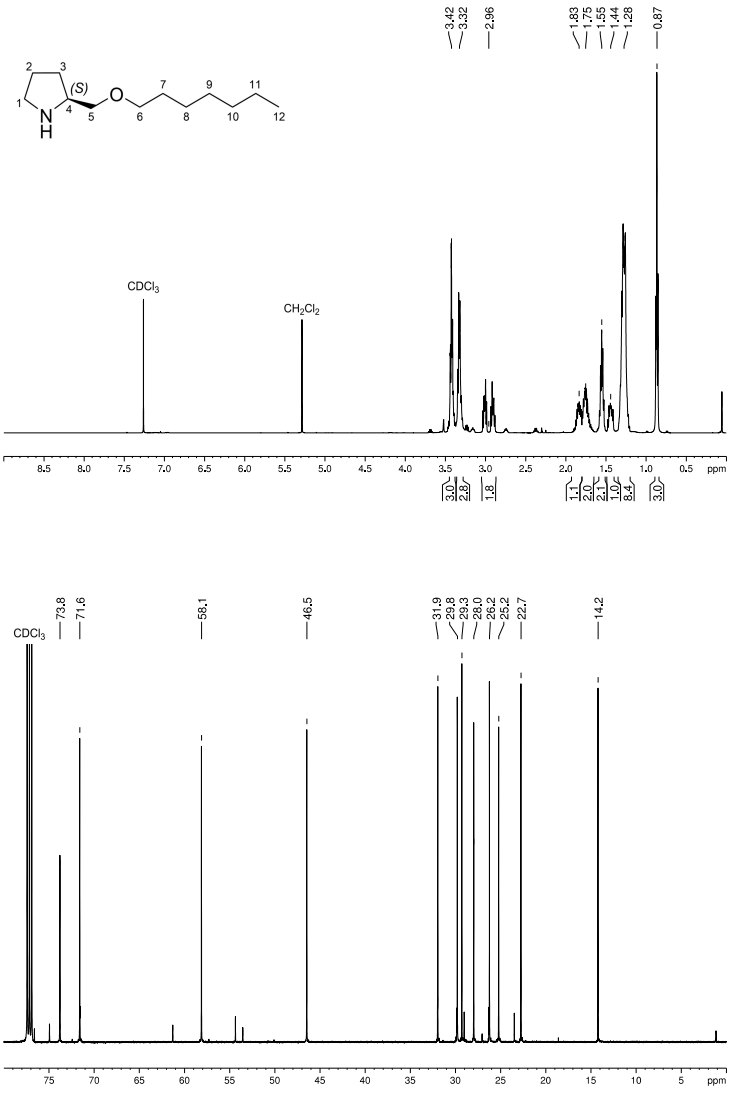


Figure S33: ^{1}H- (top, 500 MHz) and ^{13}C-NMR (bottom, 125 MHz) spectrum of L-prolinyl *n*-heptyl ether; $CDCl_3$, 298 K.

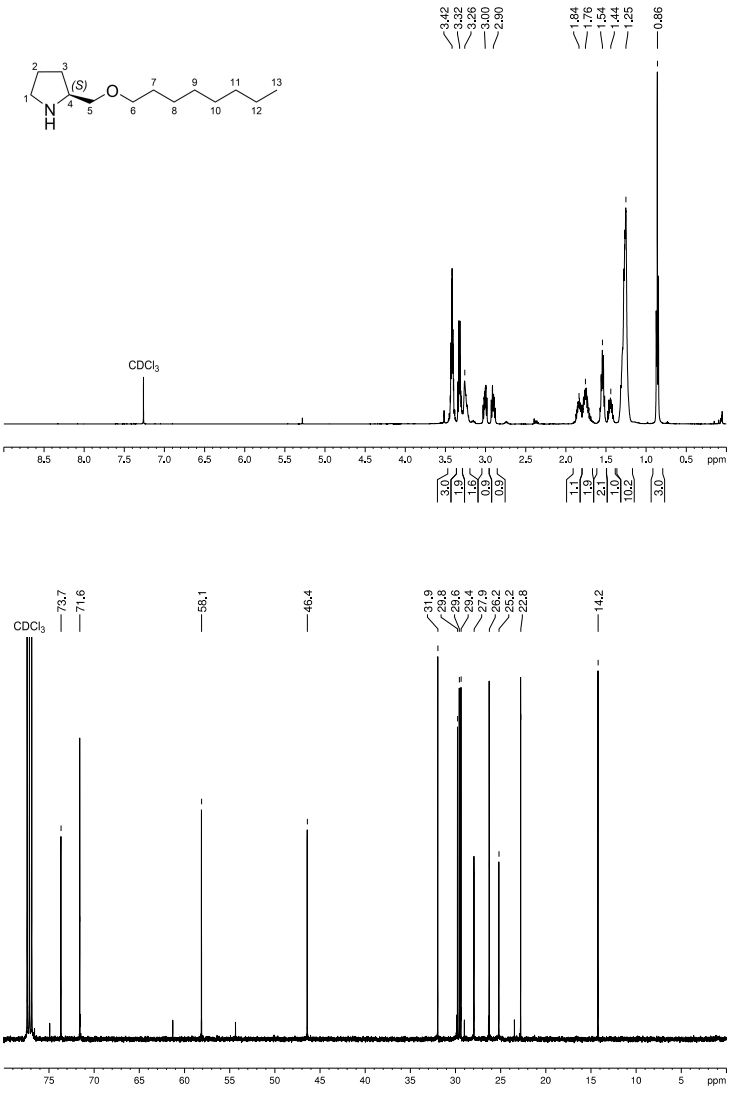


Figure S34: ^{1}H- (top, 500 MHz) and ^{13}C-NMR (bottom, 125 MHz) spectrum of L-prolinyl *n*-octyl ether; $CDCl_3$, 298 K.

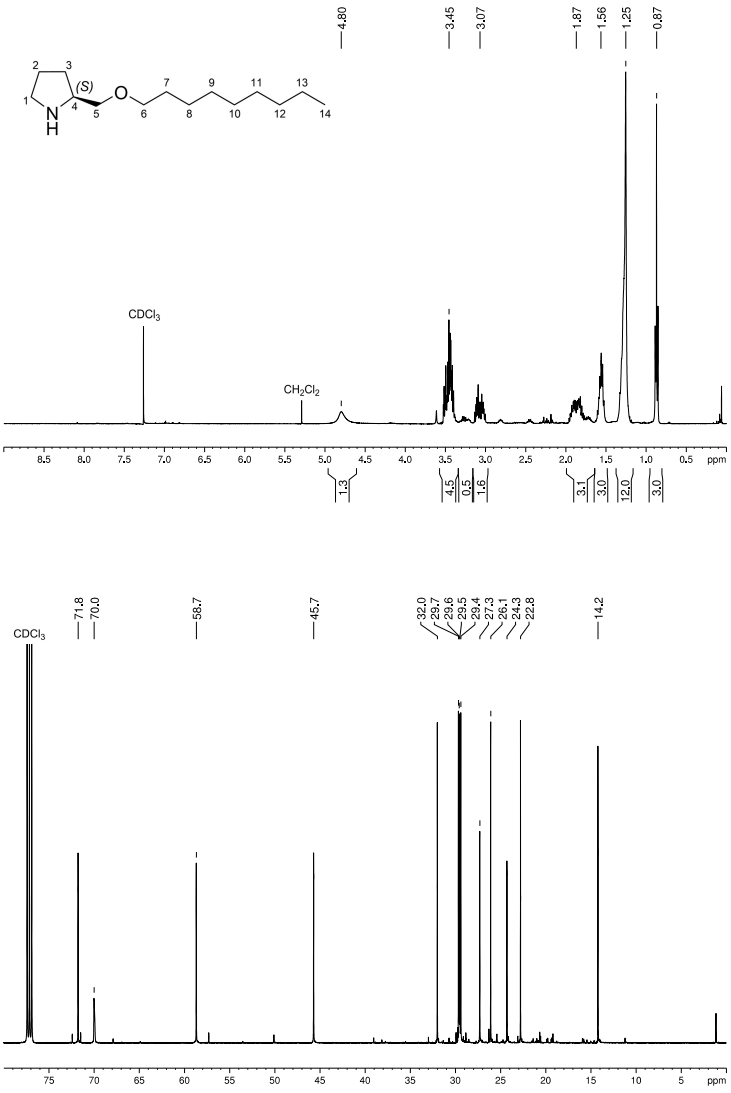


Figure S35: ^{1}H- (top, 400 MHz) and ^{13}C-NMR (bottom, 176 MHz) spectrum of L-prolinyl *n*-nonyl ether; $CDCl_3$, 298 K.

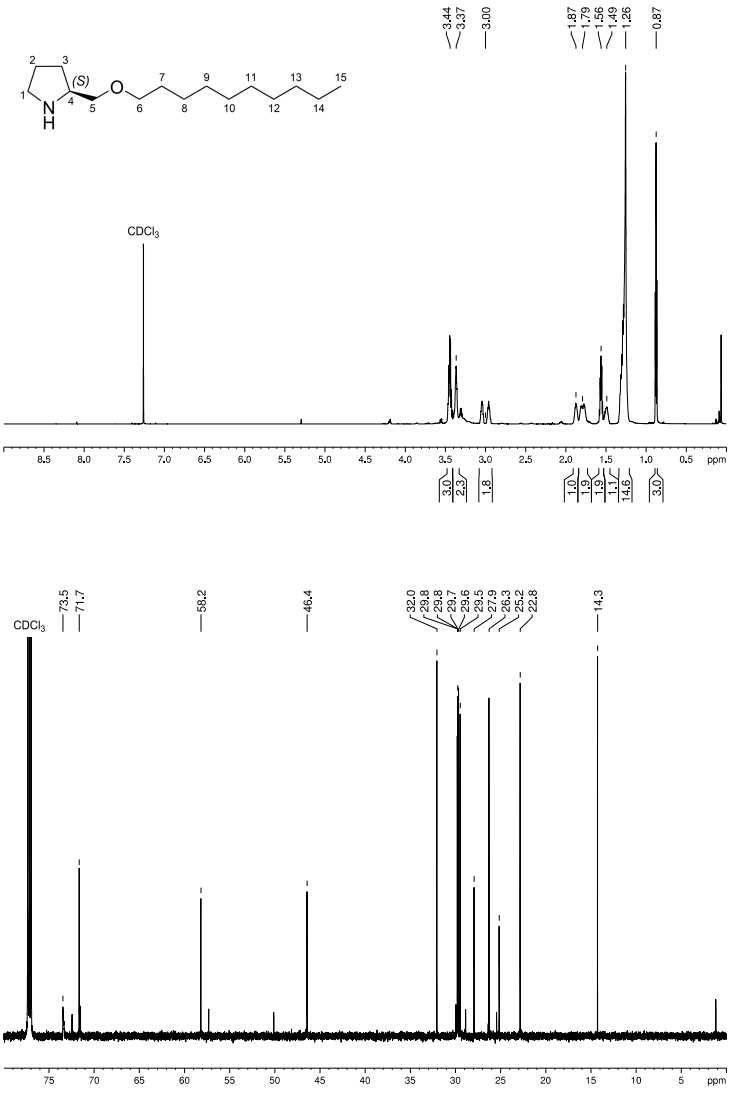


Figure S36: ^{1}H- (top, 700 MHz) and ^{13}C-NMR (bottom, 176 MHz) spectrum of L-prolinyl *n*-decyl ether; $CDCl_3$, 298 K.

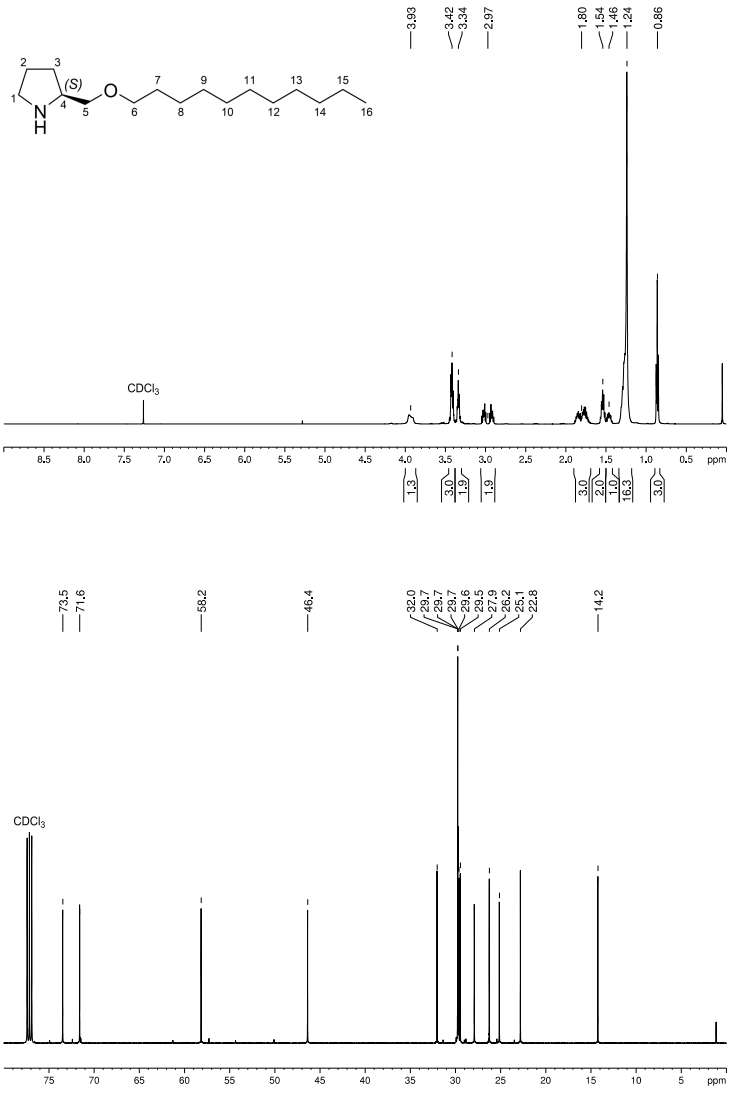


Figure S37: ^{1}H- (top, 500 MHz) and ^{13}C-NMR (bottom, 125 MHz) spectrum of L-prolinyl *n*-undecyl ether; $CDCl_3$, 298 K.

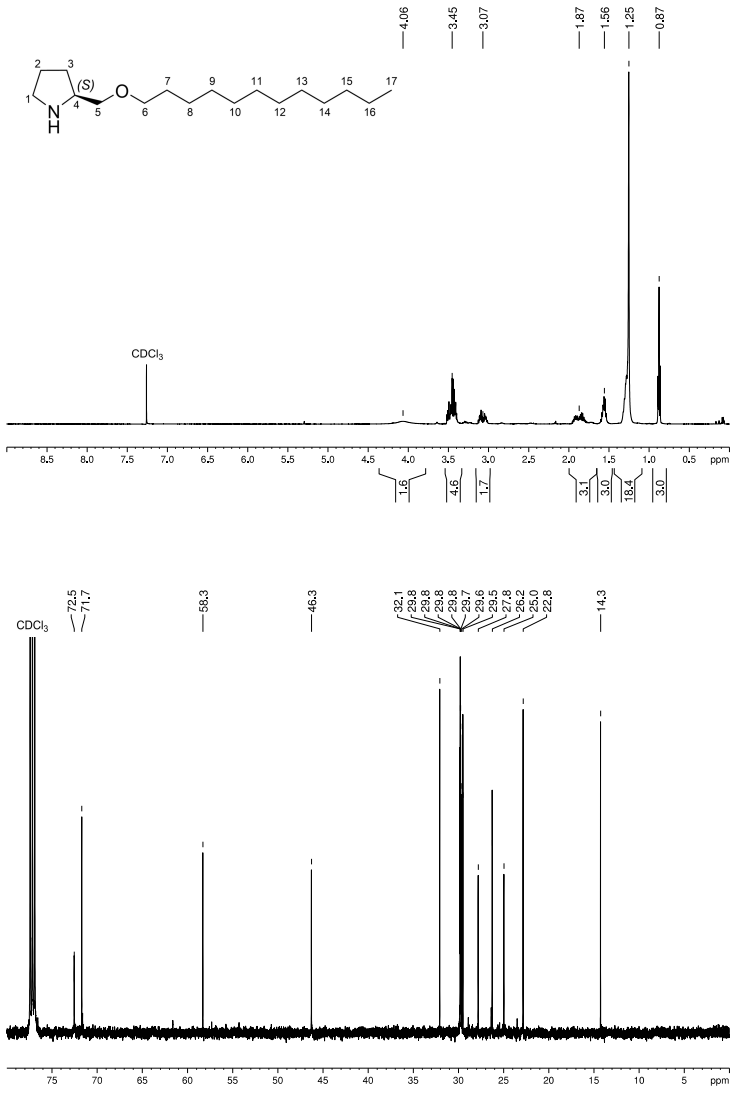


Figure S38: ^{1}H- (top, 500 MHz) and ^{13}C-NMR (bottom, 125 MHz) spectrum of L-prolinyl *n*-dodecyl ether; $CDCl_3$, 298 K.

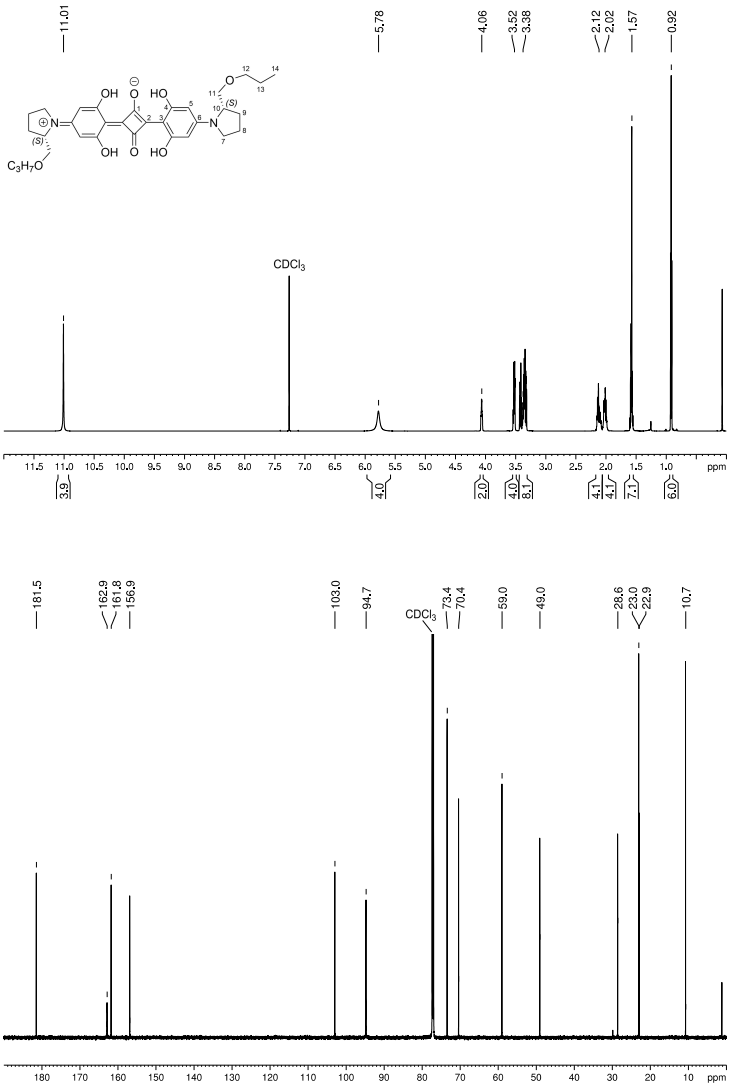


Figure S39: ^{1}H- (top, 700 MHz) and ^{13}C-NMR (bottom, 176 MHz) spectrum of (*S*,*S*)-ProSQ-C3; $CDCl_3$, 298 K.

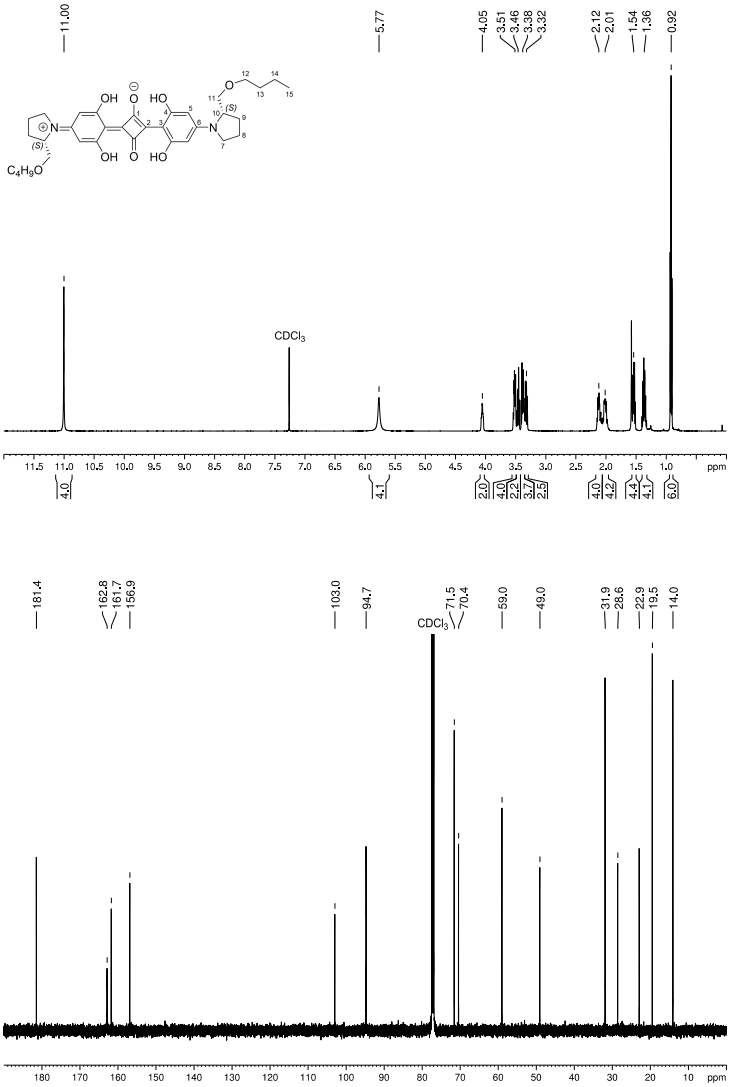


Figure S40: ^{1}H- (top, 500 MHz) and ^{13}C-NMR (bottom, 125 MHz) spectrum of (*S*,*S*)-ProSQ-C4; $CDCl_3$, 298 K.

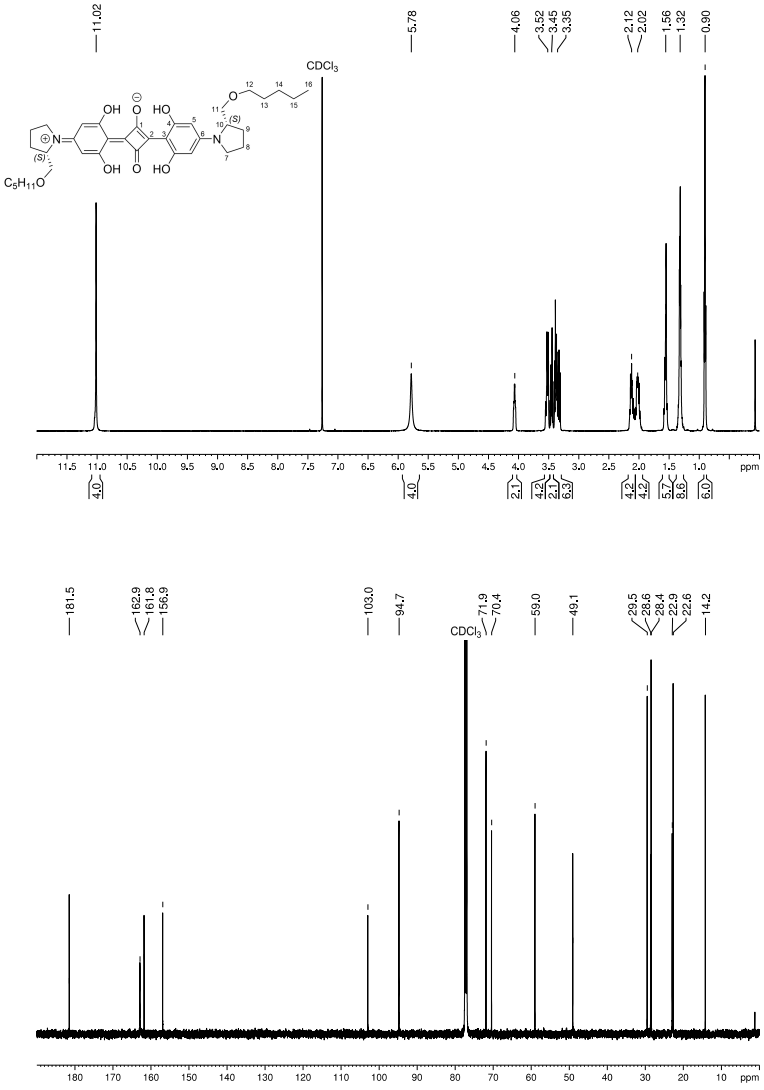


Figure S41: ^{1}H- (top, 500 MHz) and ^{13}C-NMR (bottom, 125 MHz) spectrum of (*S*,*S*)-ProSQ-C5; $CDCl_3$, 298 K.

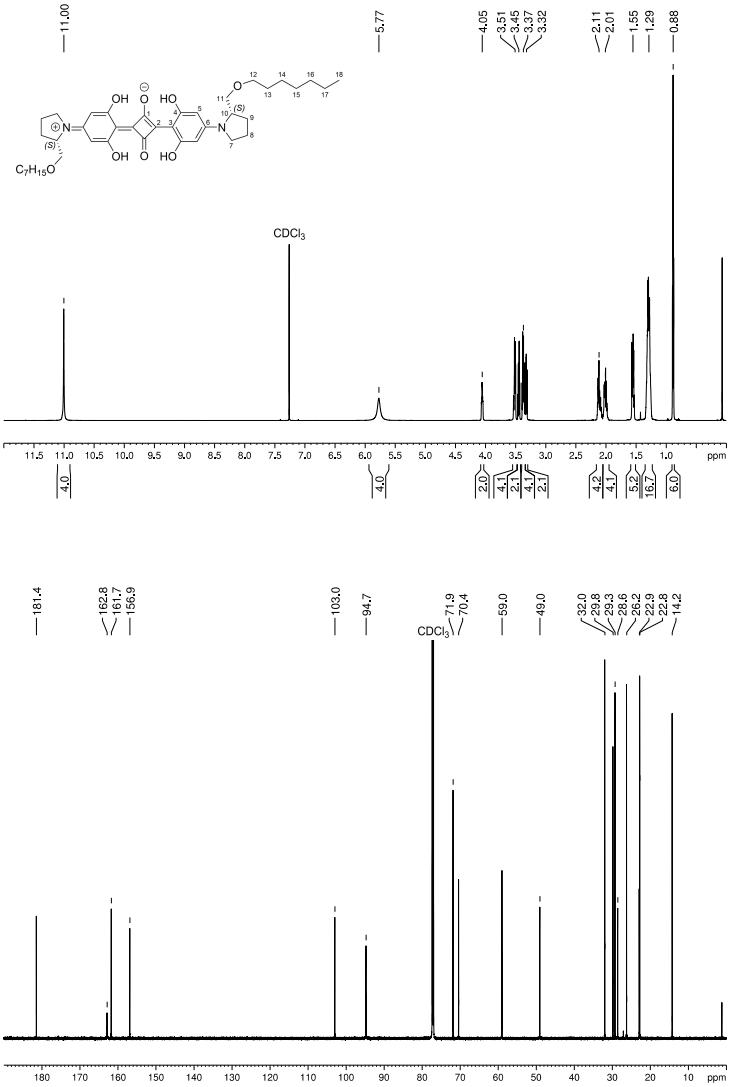


Figure S42: ^{1}H- (top, 500 MHz) and ^{13}C-NMR (bottom, 125 MHz) spectrum of (*S*,*S*)-ProSQ-C7; $CDCl_3$, 298 K.

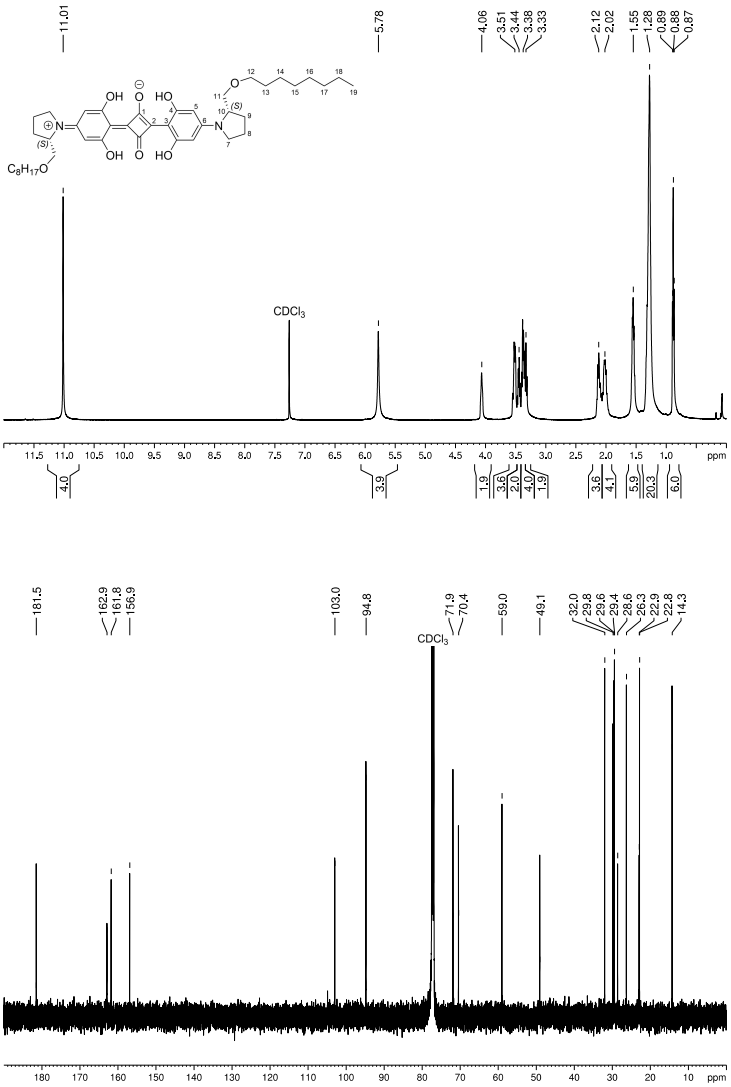


Figure S43: ^{1}H- (top, 500 MHz) and ^{13}C-NMR (bottom, 125 MHz) spectrum of (*S*,*S*)-ProSQ-C8; $CDCl_3$, 298 K.

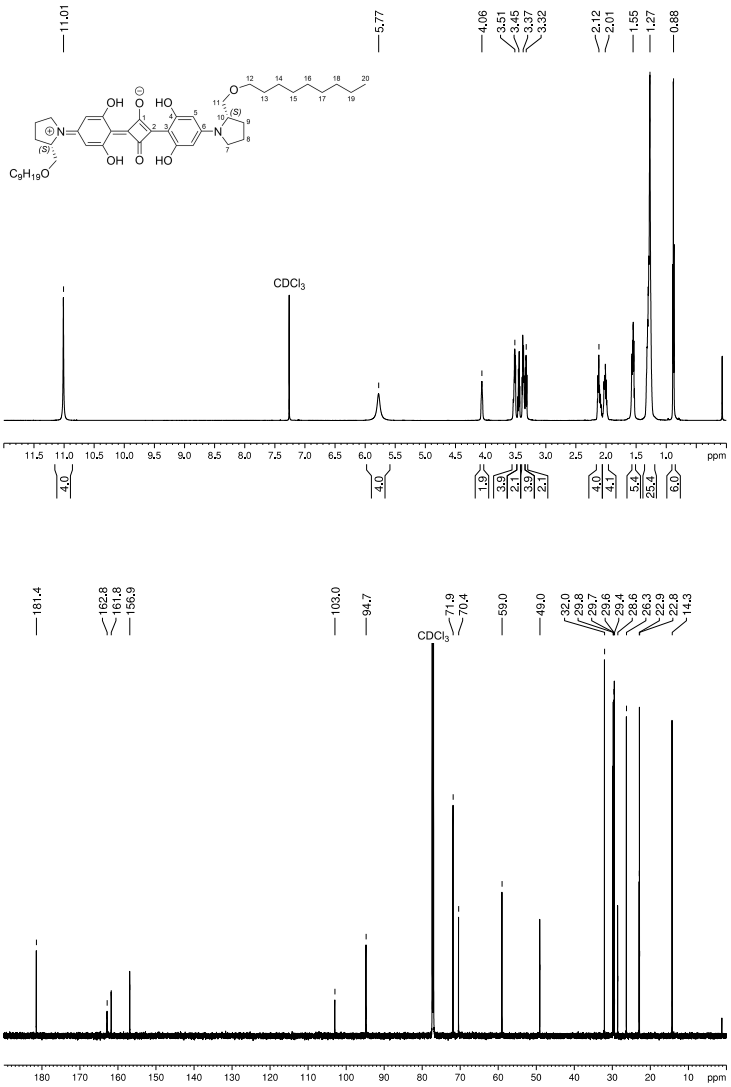


Figure S44: ^{1}H- (top, 500 MHz) and ^{13}C-NMR (bottom, 176 MHz) spectrum of (*S*,*S*)-ProSQ-C9; $CDCl_3$, 298 K.

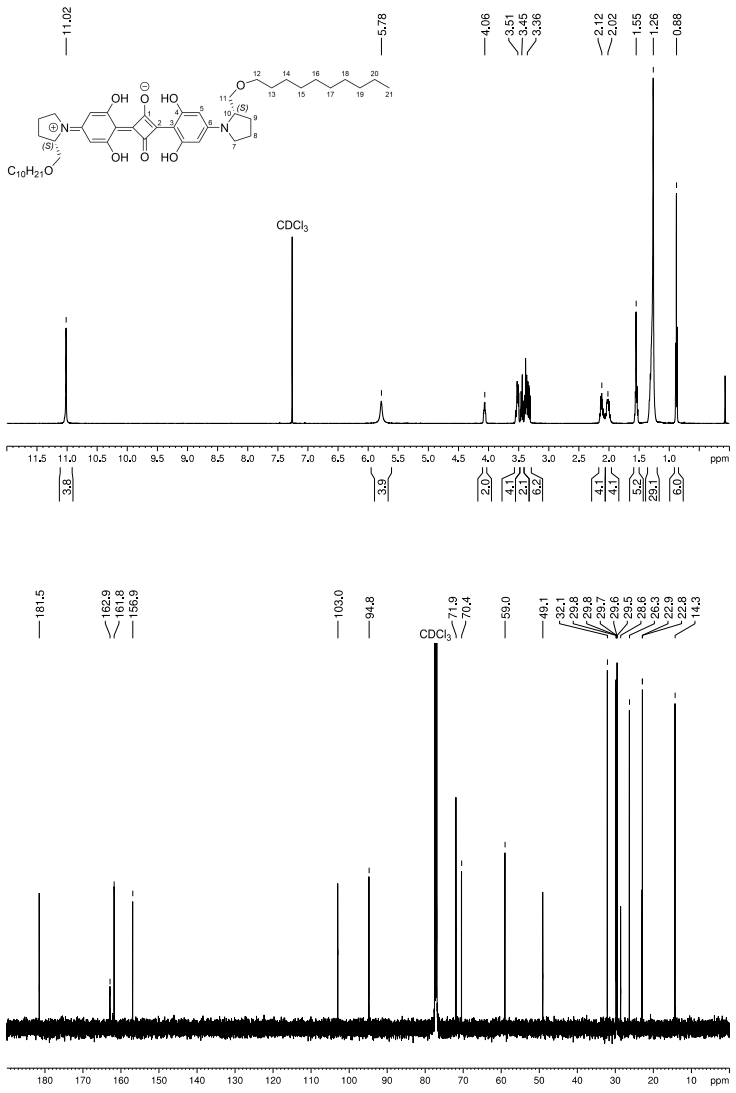


Figure S45: ^{1}H- (top, 500 MHz) and ^{13}C-NMR (bottom, 125 MHz) spectrum of (*S*,*S*)-ProSQ-C10; $CDCl_3$, 298 K.

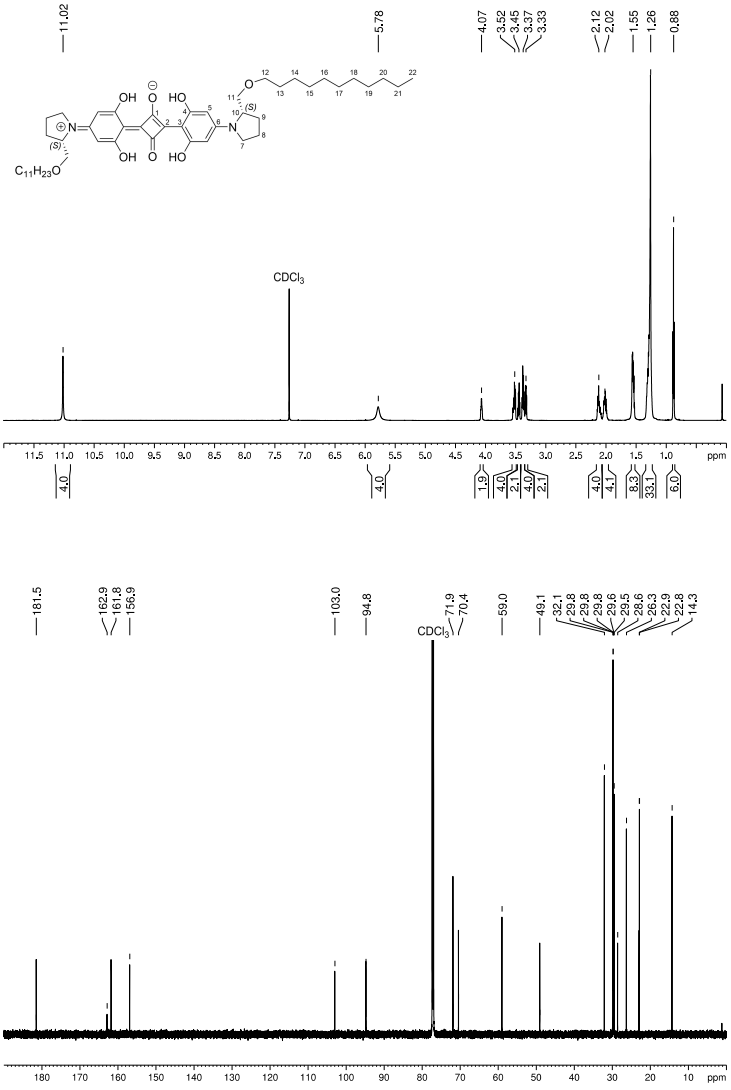


Figure S46: ^{1}H- (top, 700 MHz) and ^{13}C-NMR (bottom, 176 MHz) spectrum of (*S*,*S*)-ProSQ-C11; $CDCl_3$, 298 K.

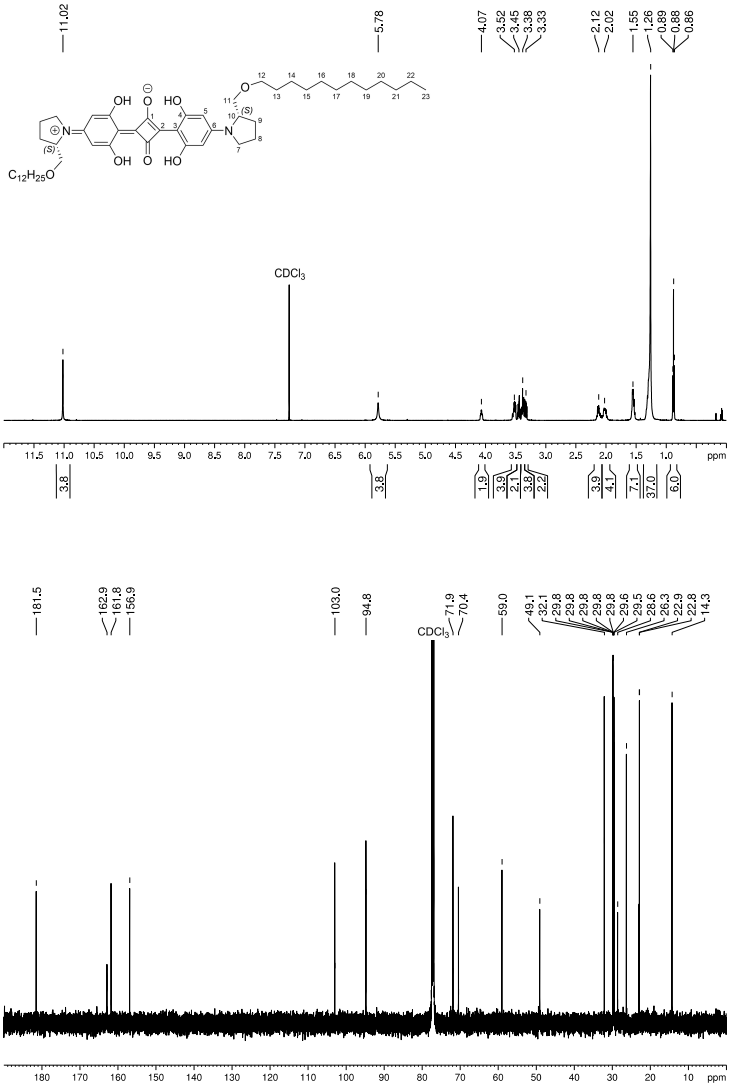


Figure S47: ^{1}H- (top, 500 MHz) and ^{13}C-NMR (bottom, 125 MHz) spectrum of (*S*,*S*)-ProSQ-C12; $CDCl_3$, 298 K.

6.2 Mass spectra

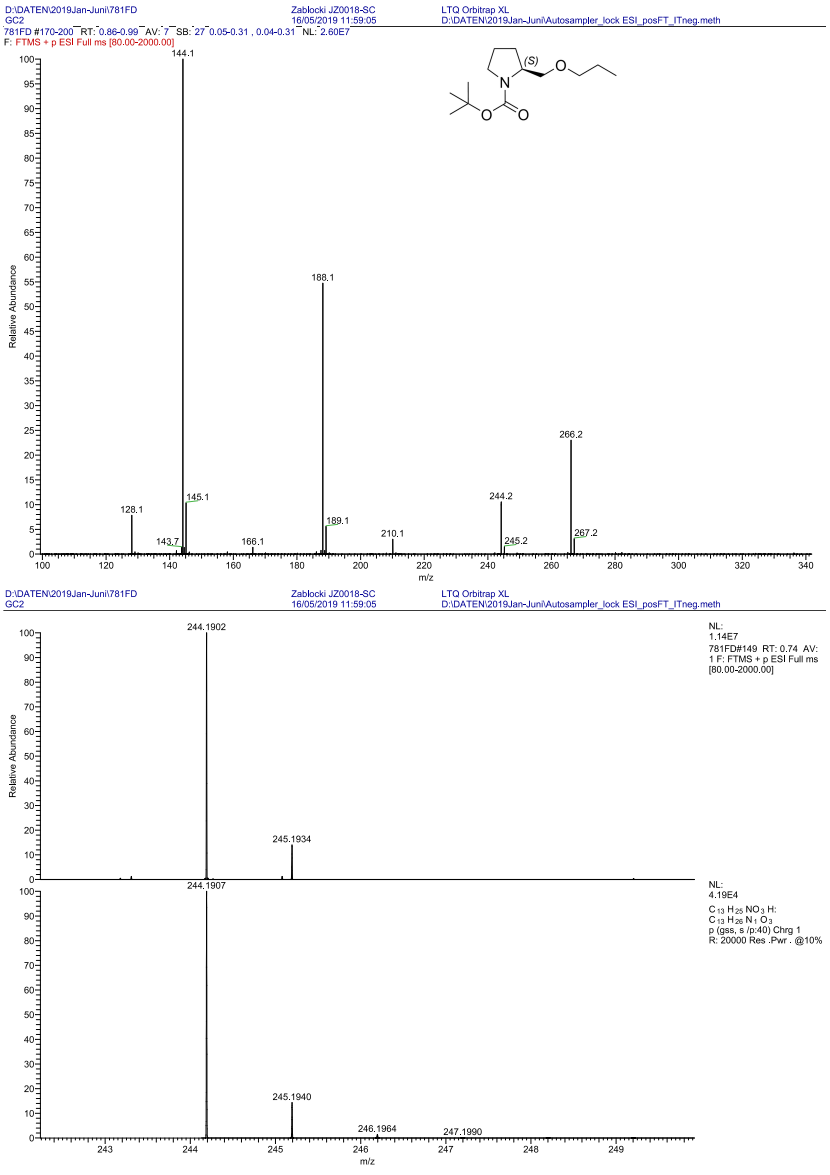


Figure S48: ESI(+) Mass spectra of *N*-Boc-L-prolinyl *n*-propyl ether

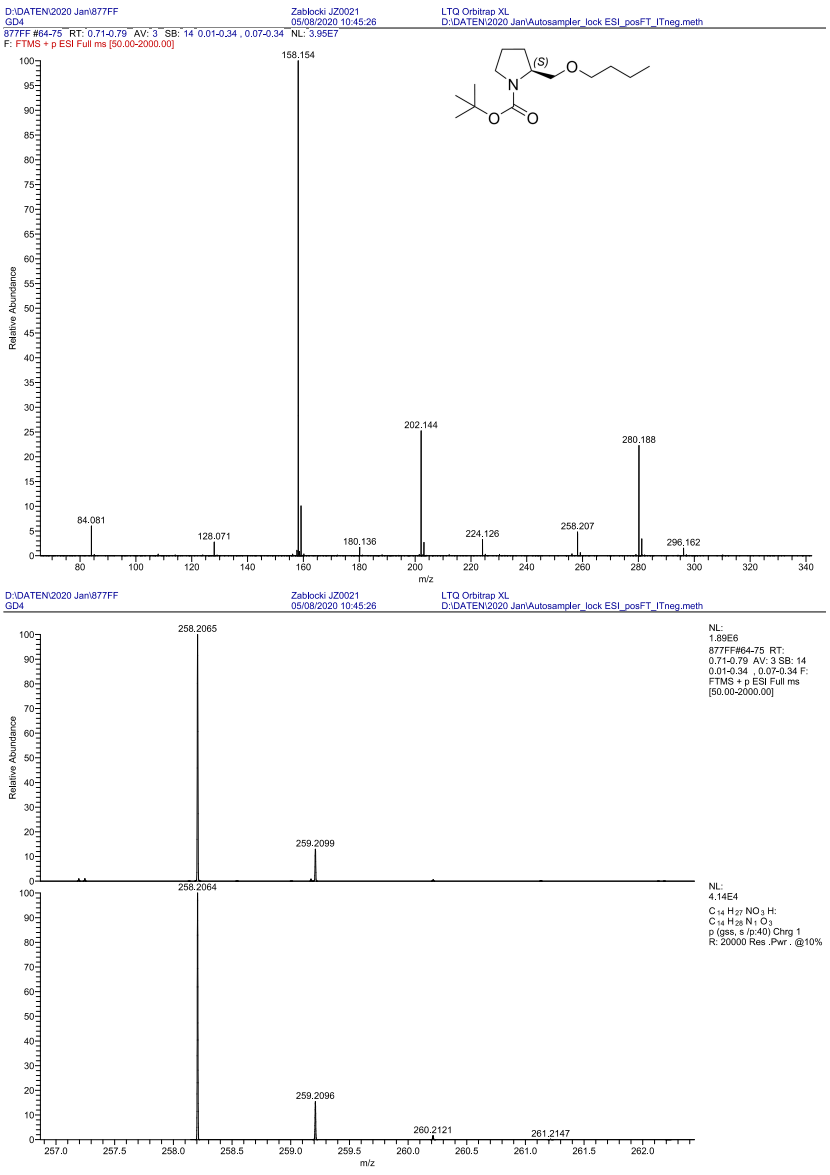


Figure S49: ESI(+) Mass spectra of *N*-Boc-L-prolinyl *n*-butyl ether

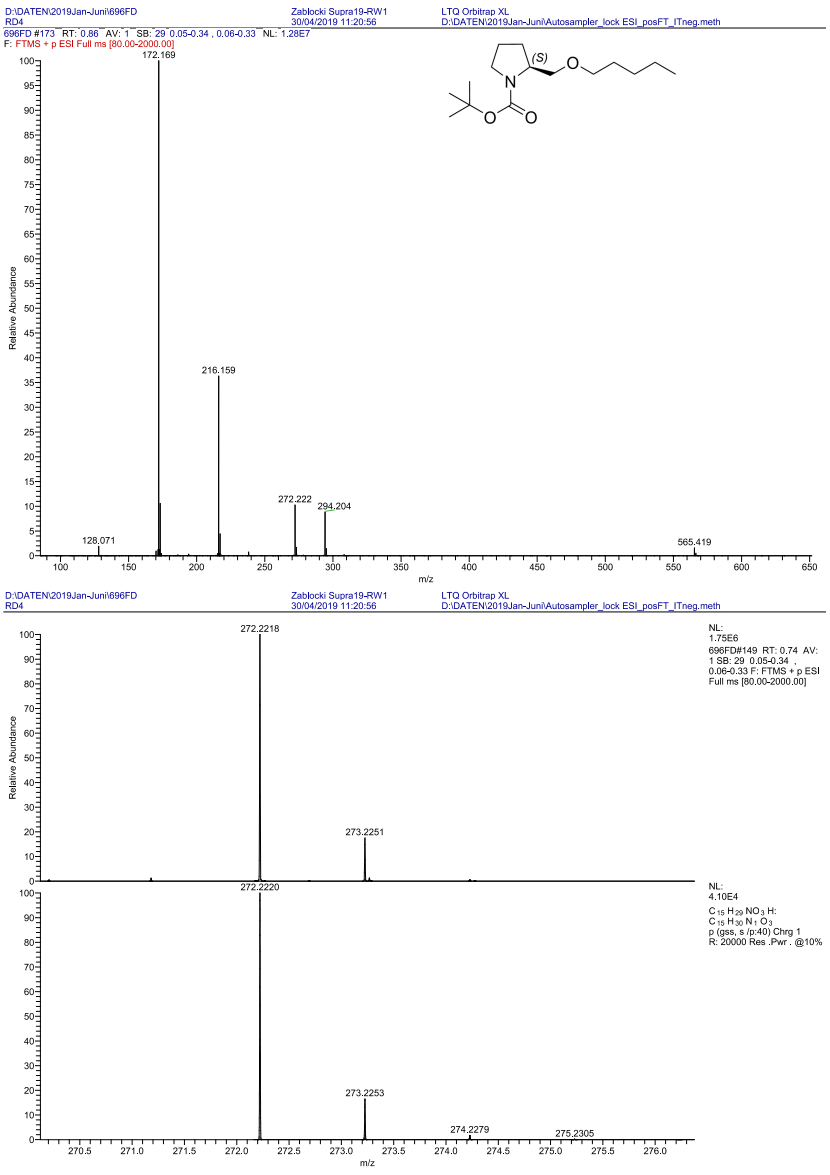


Figure S50: ESI(+) Mass spectra of *N*-Boc-L-prolinyl *n*-pentyl ether

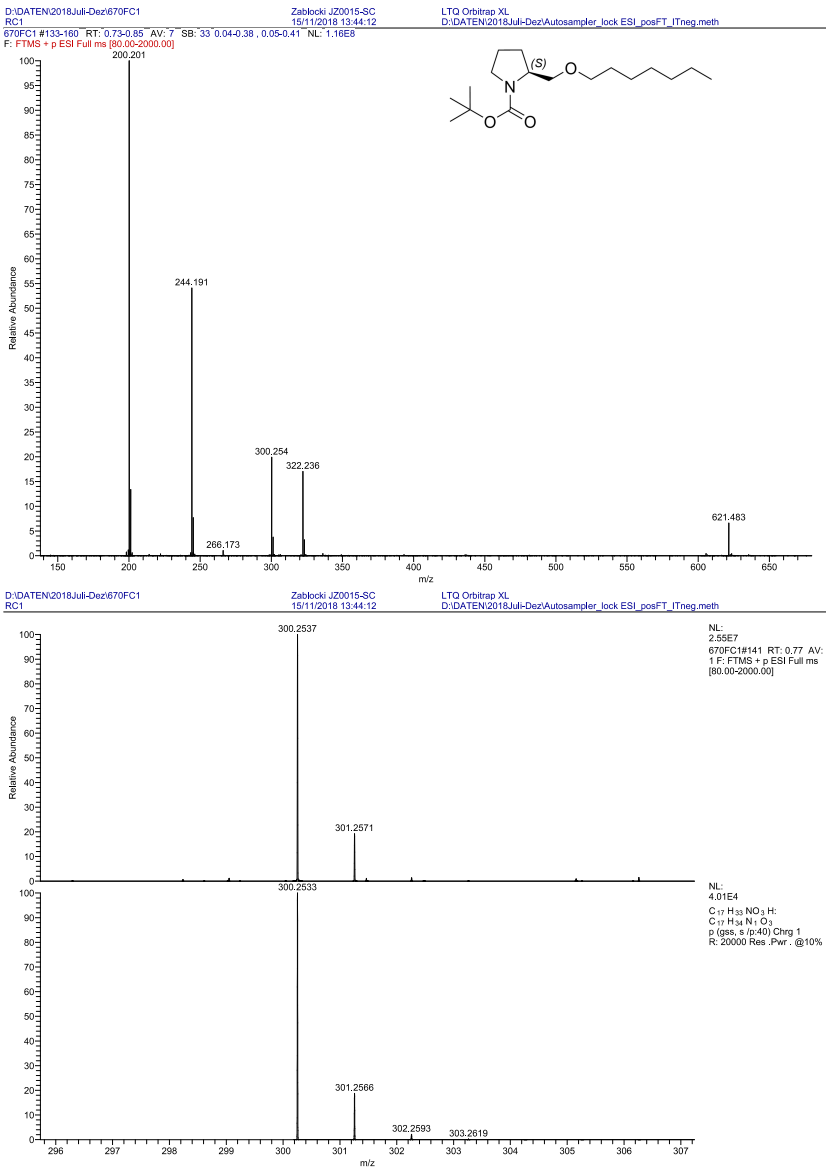


Figure S51: ESI(+) Mass spectra of *N*-Boc-L-prolinyl *n*-heptyl ether

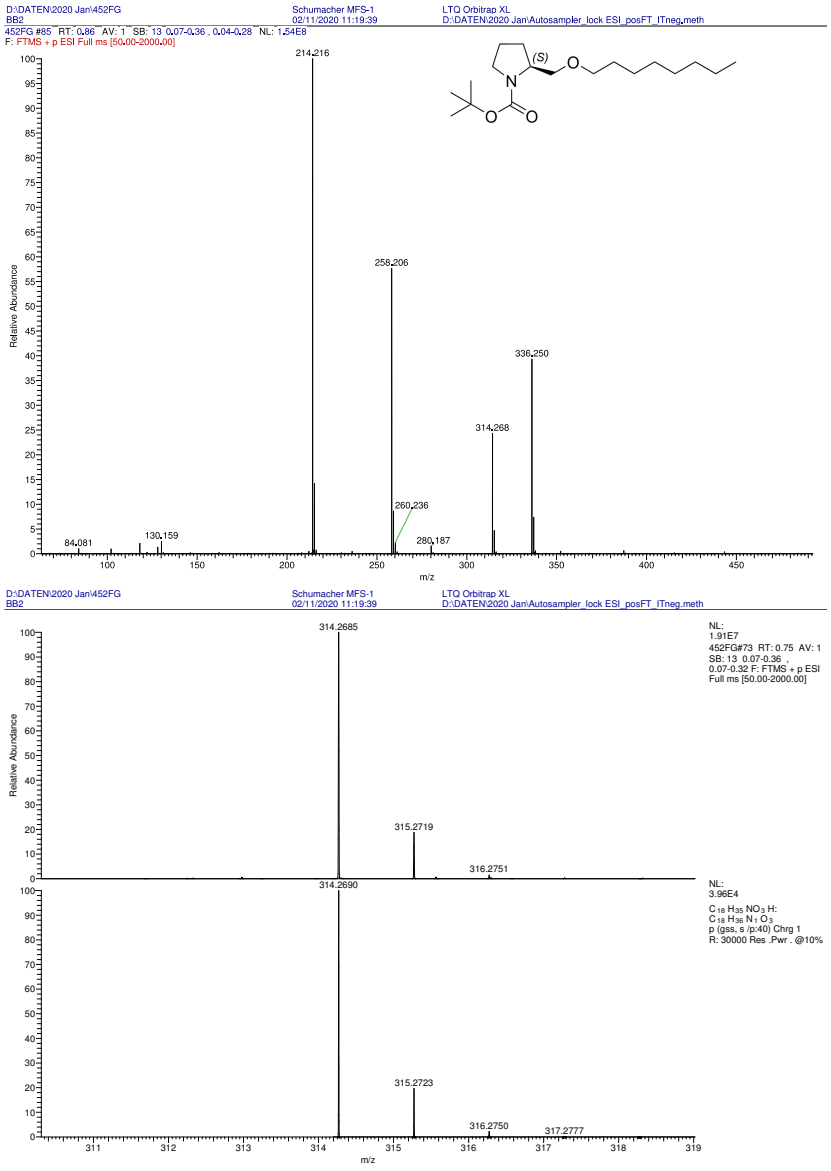


Figure S52: ESI(+) Mass spectra of *N*-Boc-L-prolinyl *n*-octyl ether

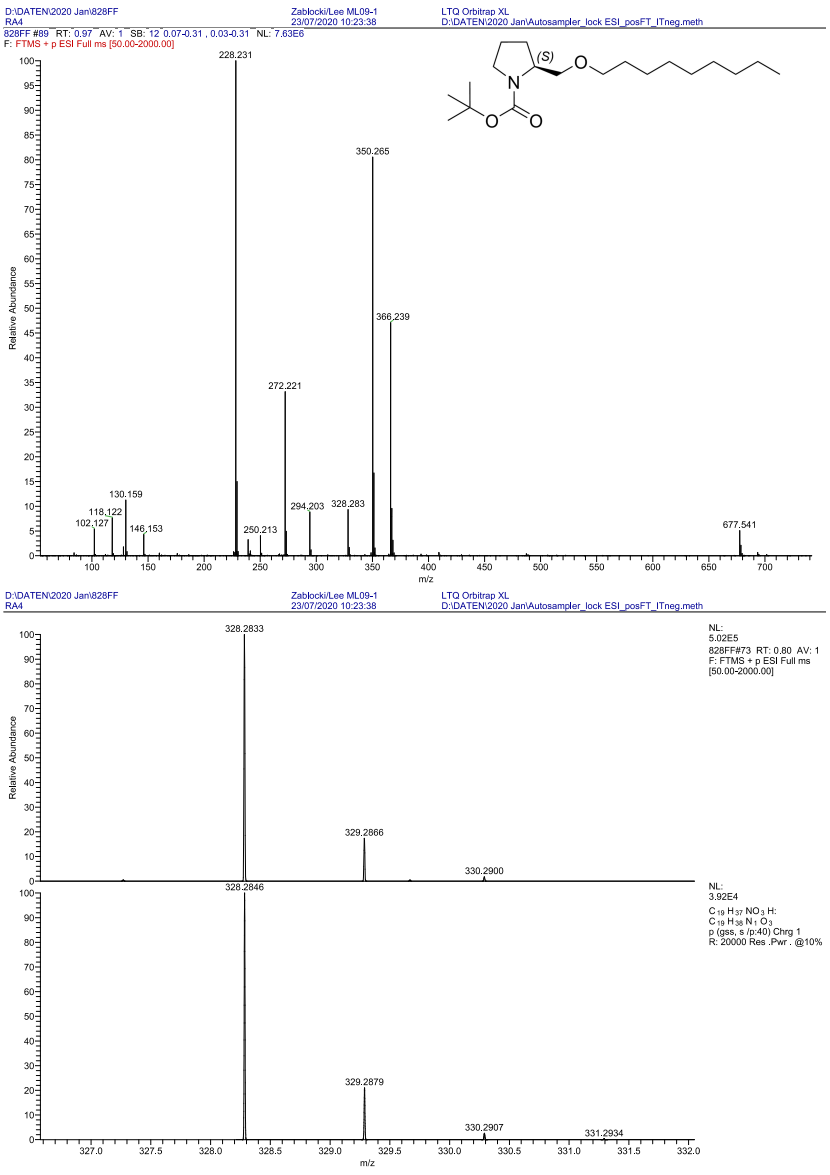


Figure S53: ESI(+) Mass spectra of *N*-Boc-L-prolinyl *n*-nonyl ether

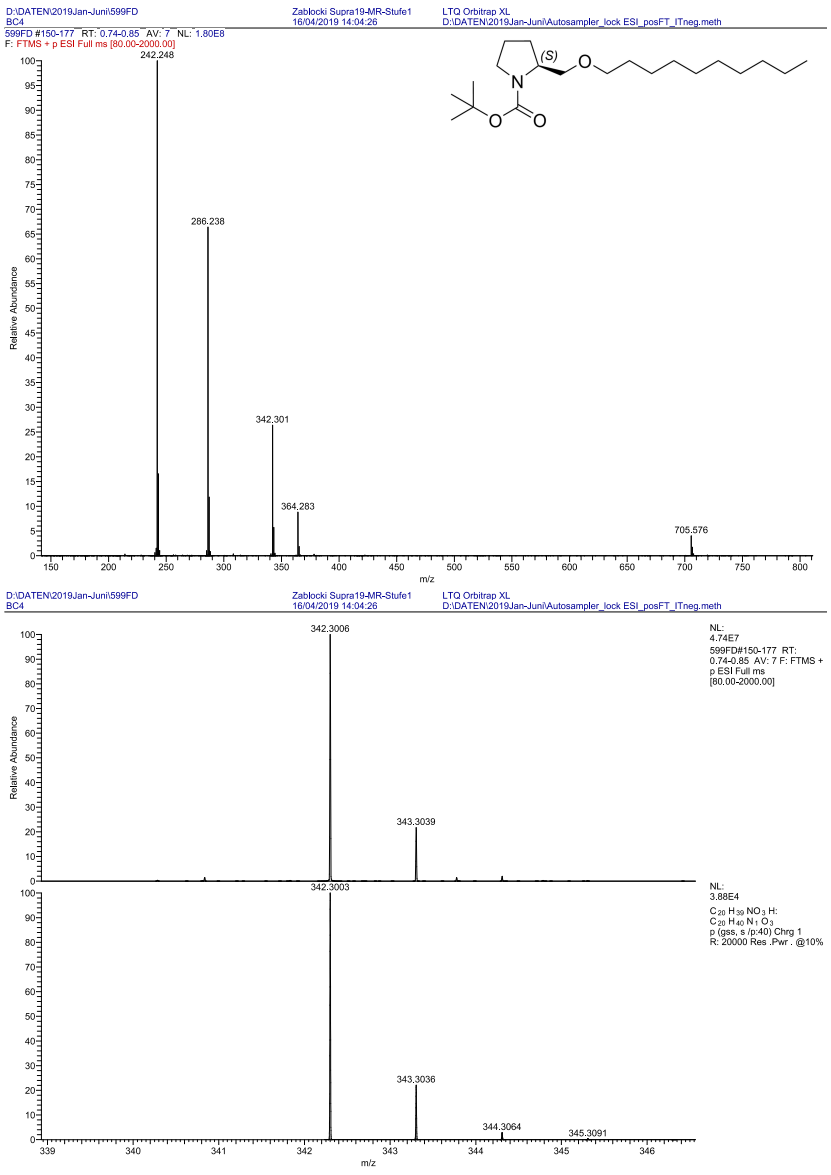


Figure S54: ESI(+) Mass spectra of *N*-Boc-L-prolinyl *n*-decyl ether

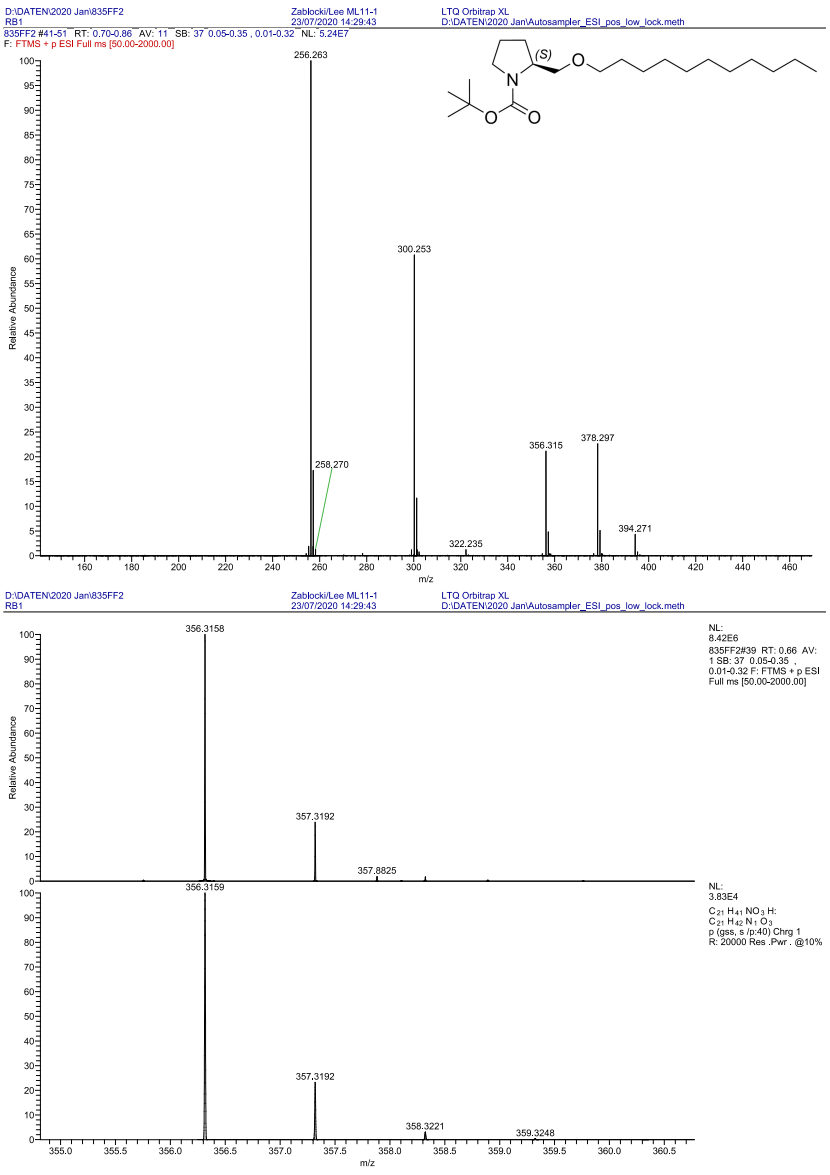


Figure S55: ESI(+) Mass spectra of *N*-Boc-L-prolinyl *n*-undecyl ether

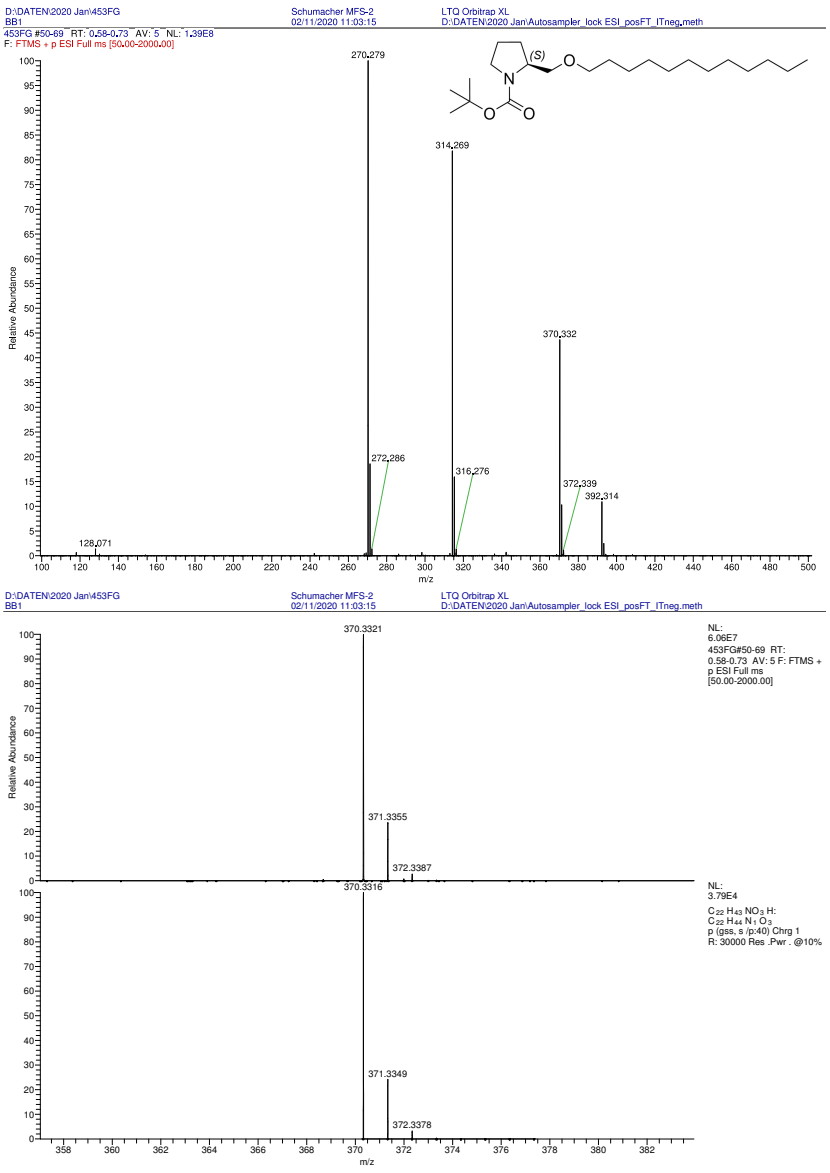


Figure S56: ESI(+) Mass spectra of *N*-Boc-L-prolinyl *n*-dodecyl ether

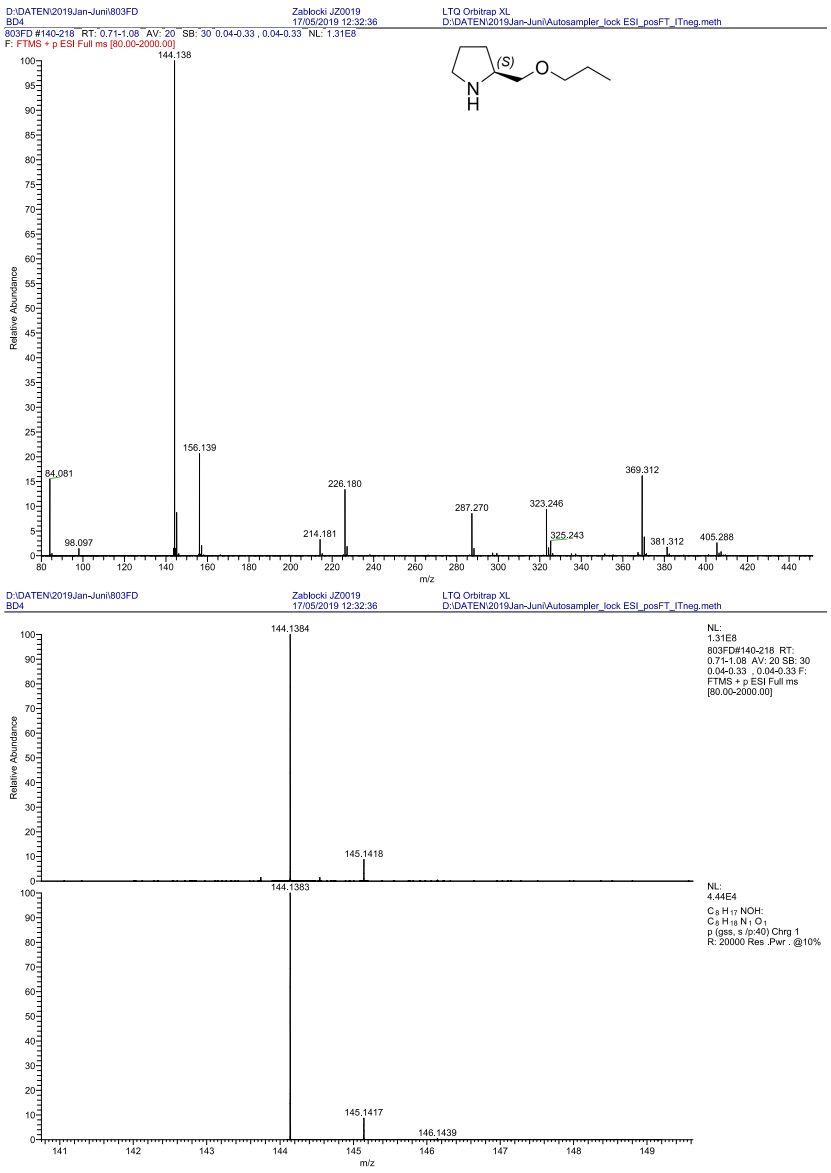


Figure S57: ESI(+) Mass spectra of L-prolinyl *n*-propyl ether

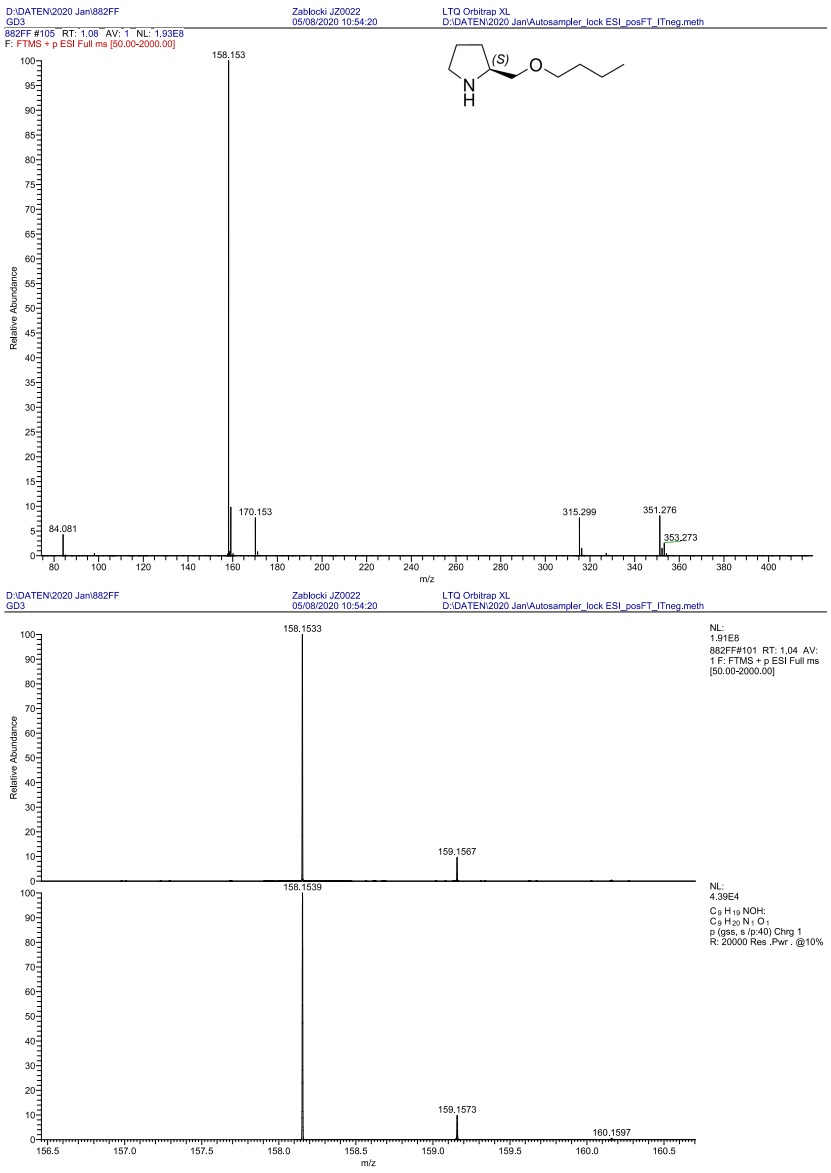


Figure S58: ESI(+) Mass spectra of L-prolinyl *n*-butyl ether

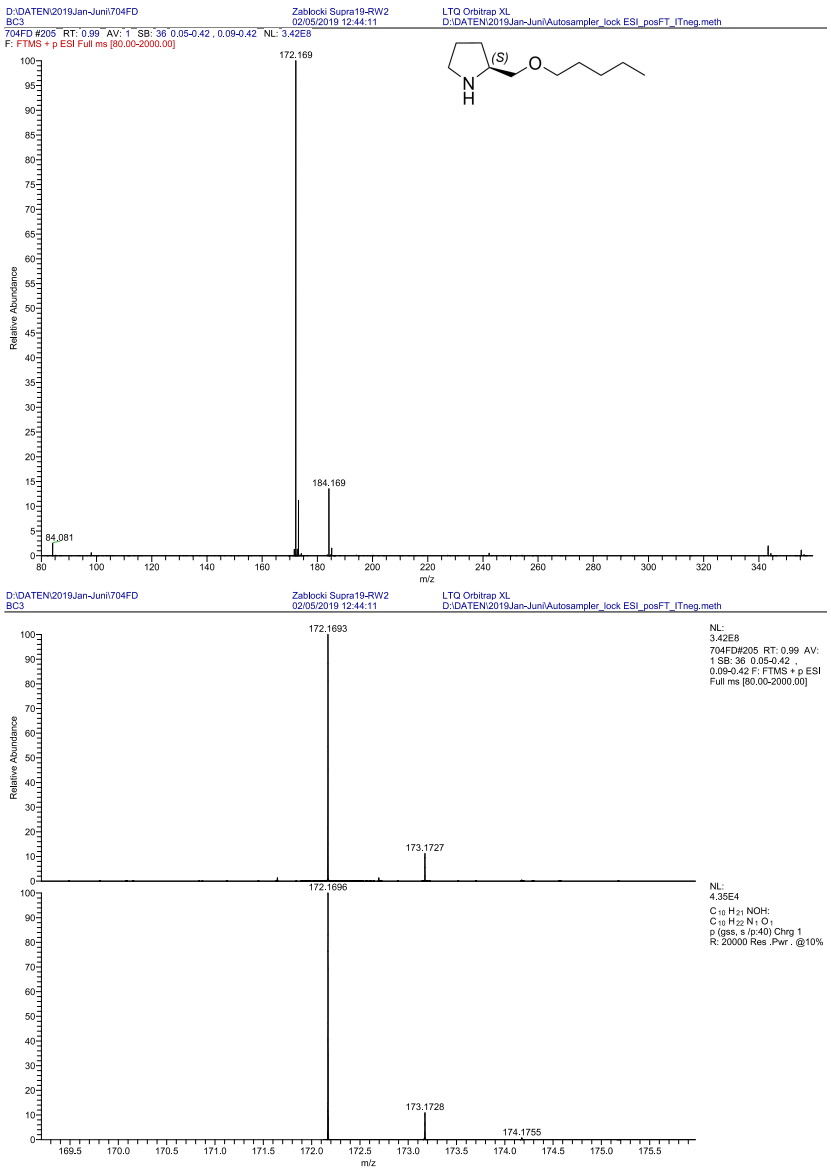


Figure S59: ESI(+) Mass spectra of L-prolinyl *n*-pentyl ether

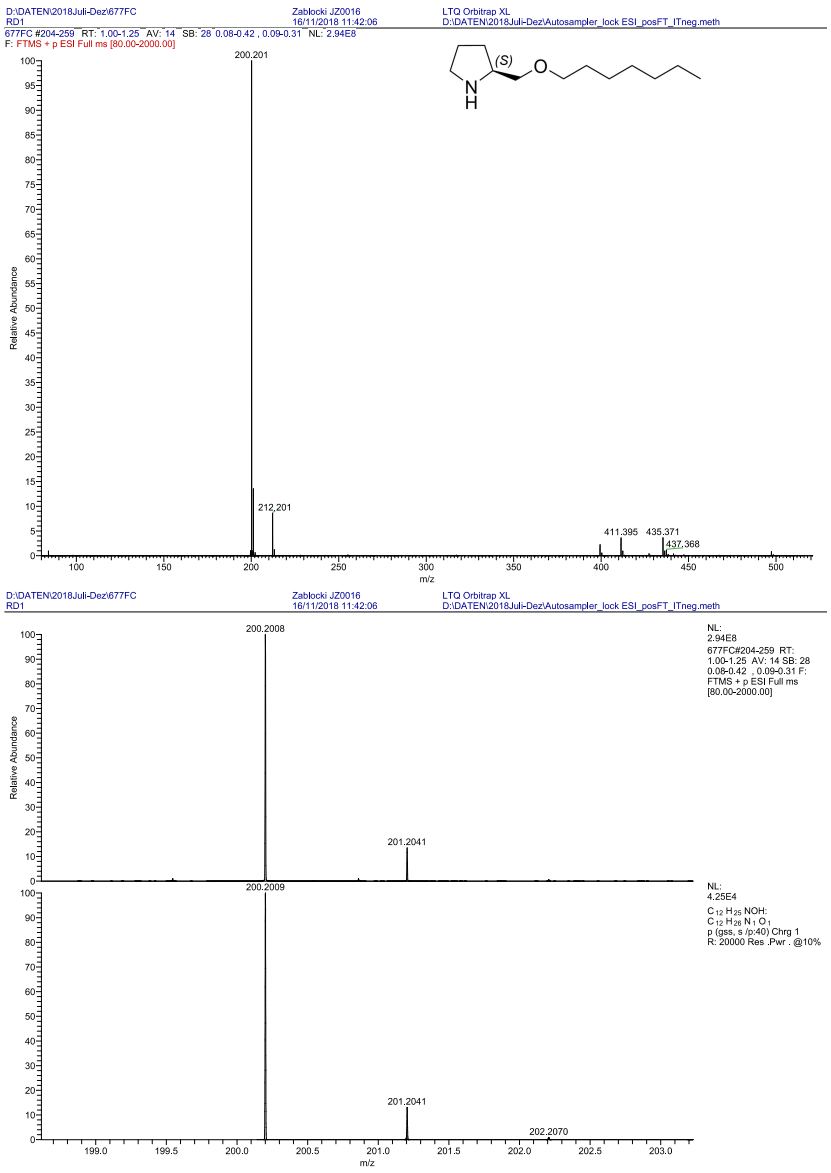


Figure S60: ESI(+) Mass spectra of L-prolinyl *n*-heptyl ether

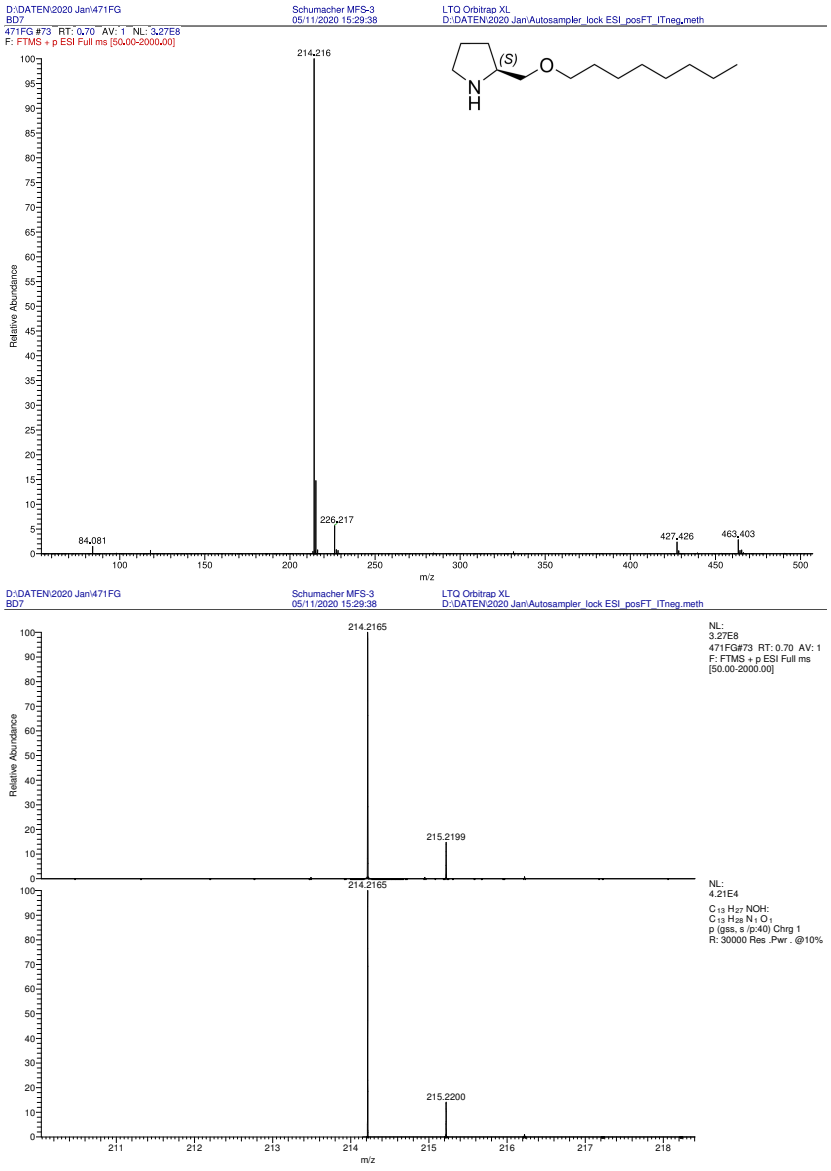


Figure S61: ESI(+) Mass spectra of L-prolinyl *n*-octyl ether

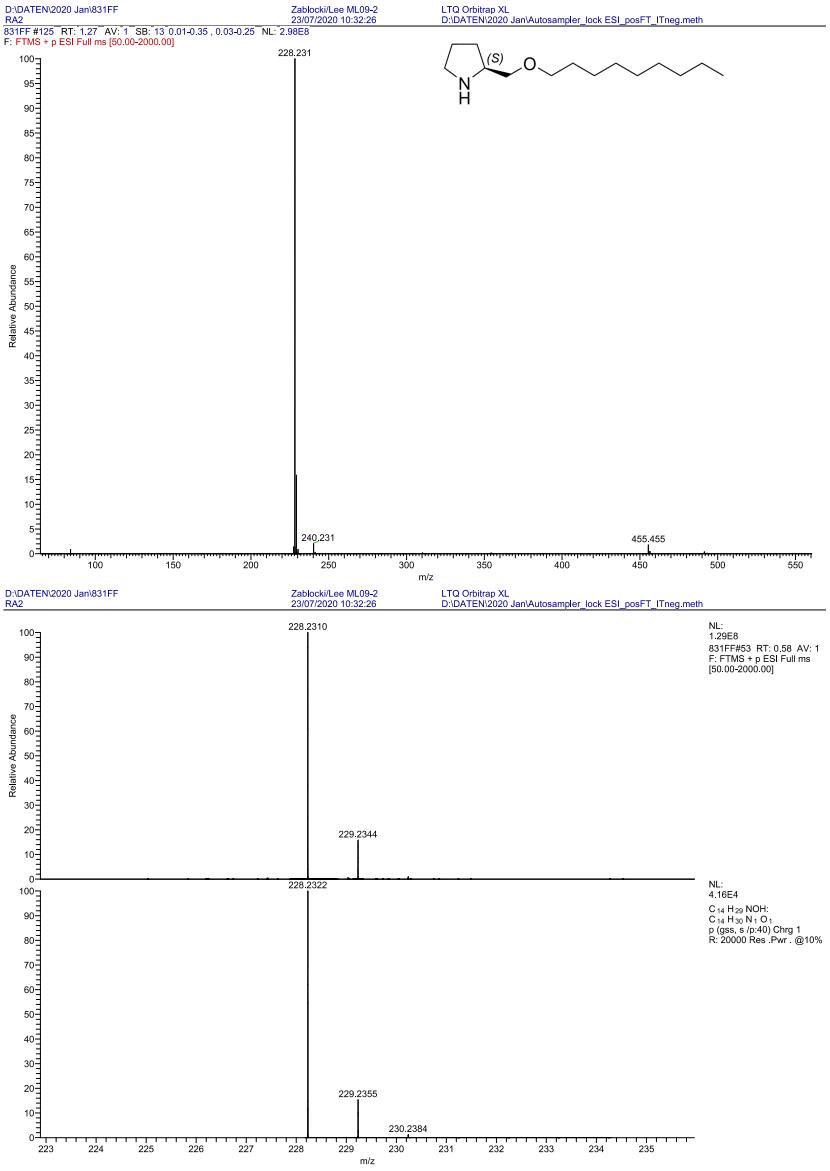


Figure S62: ESI(+) Mass spectra of L-prolinyl *n*-nonyl ether

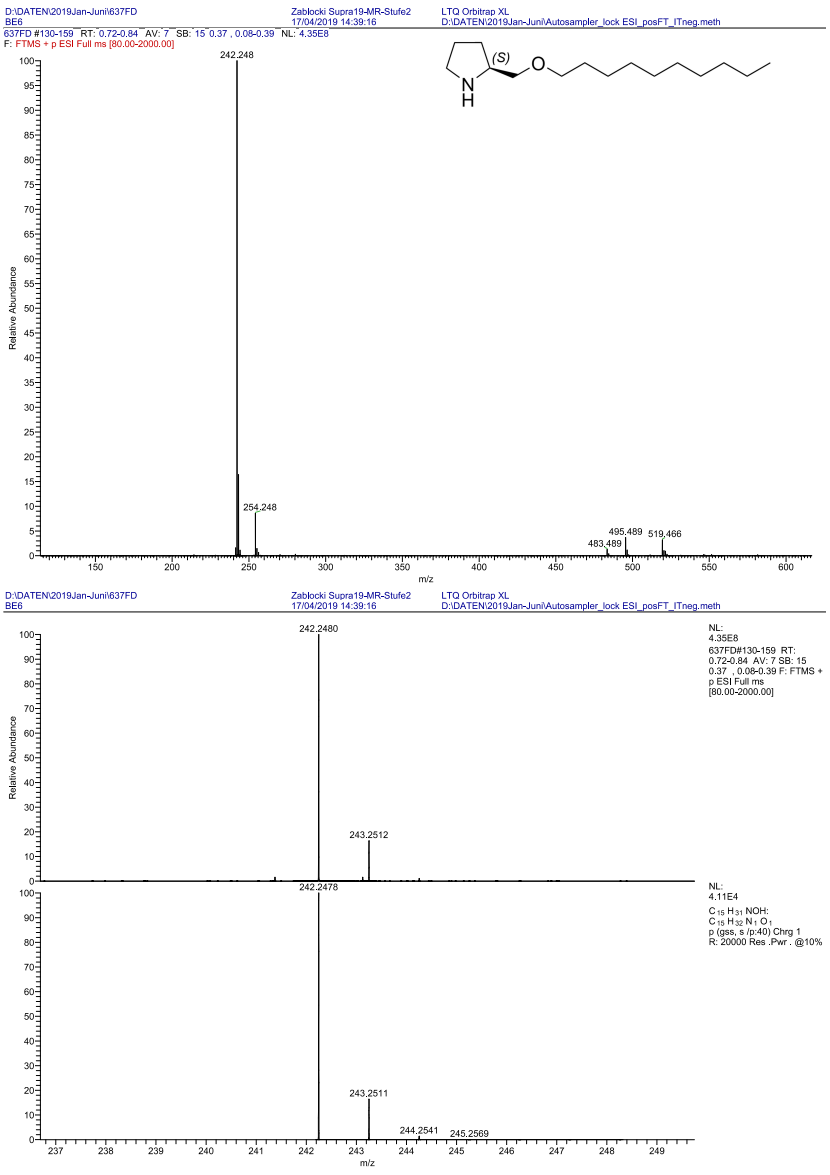


Figure S63: ESI(+) Mass spectra of L-prolinyl *n*-decyl ether

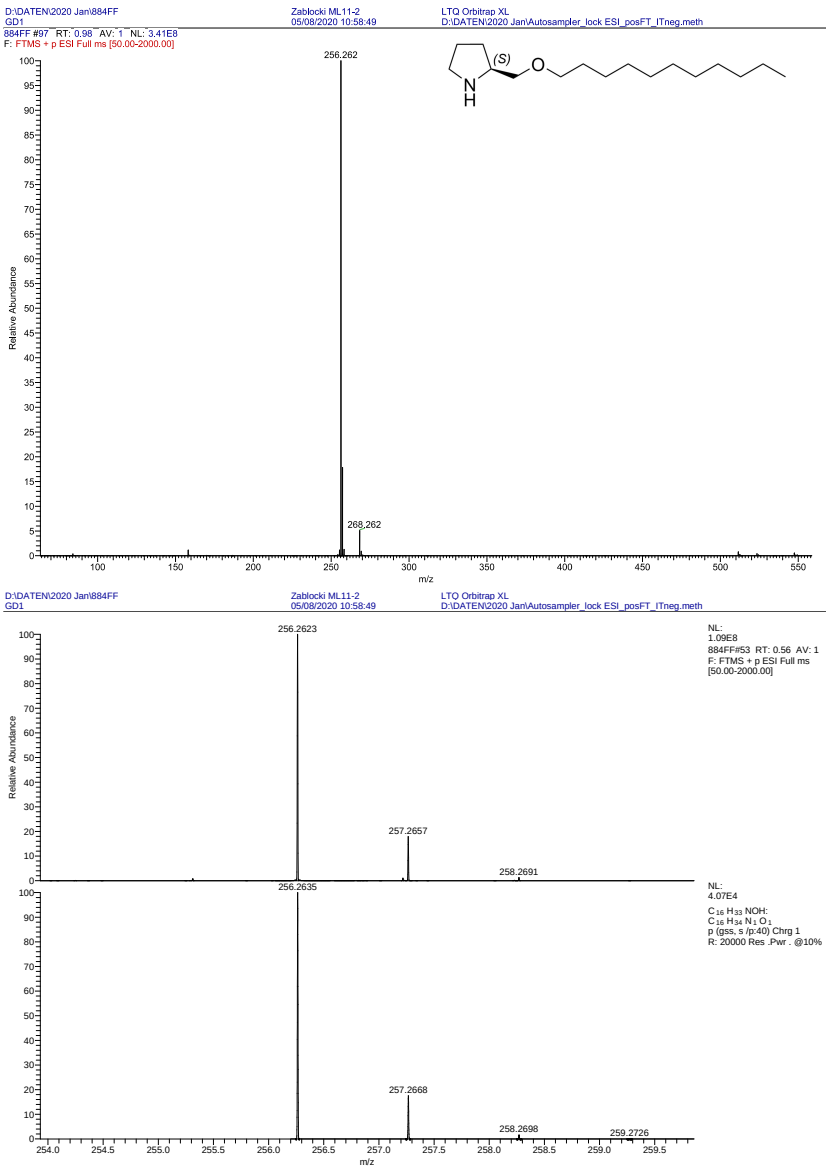


Figure S64: ESI(+) Mass spectra of L-prolinyl n-undecyl ether

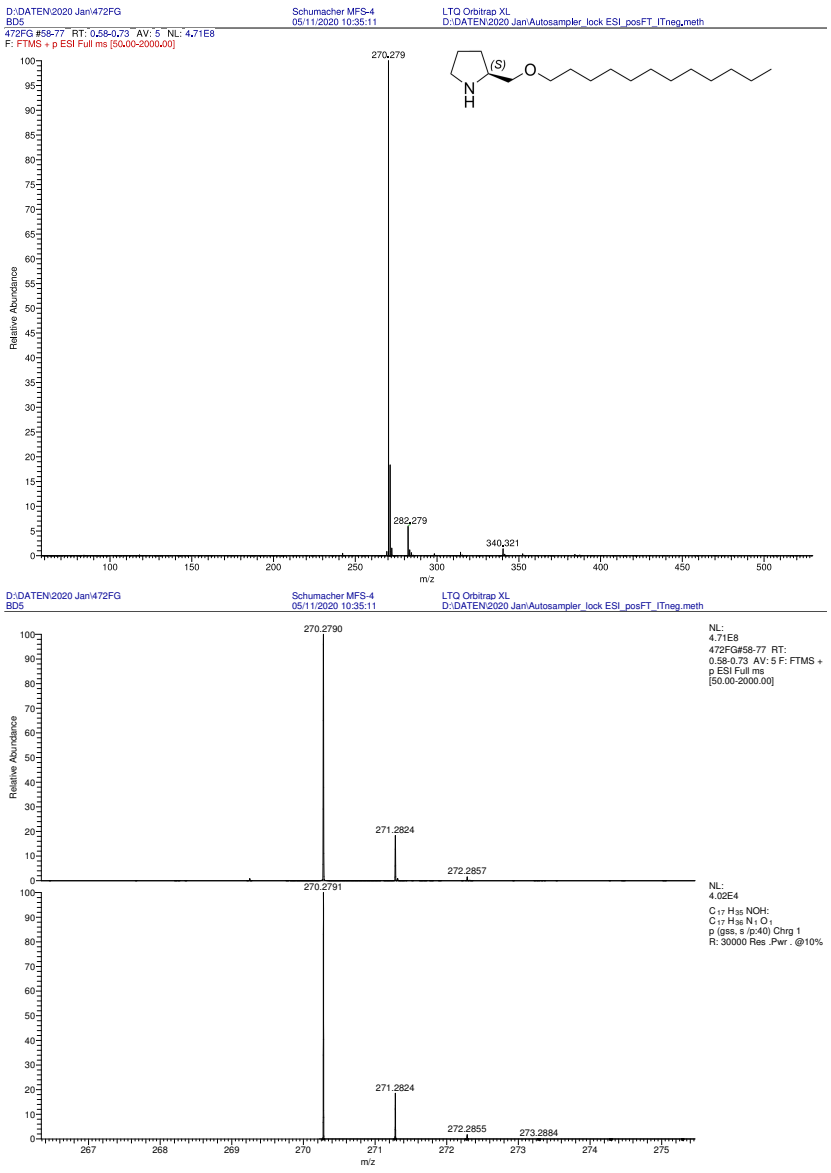


Figure S65: ESI(+) Mass spectra of L-prolinyl *n*-dodecyl ether

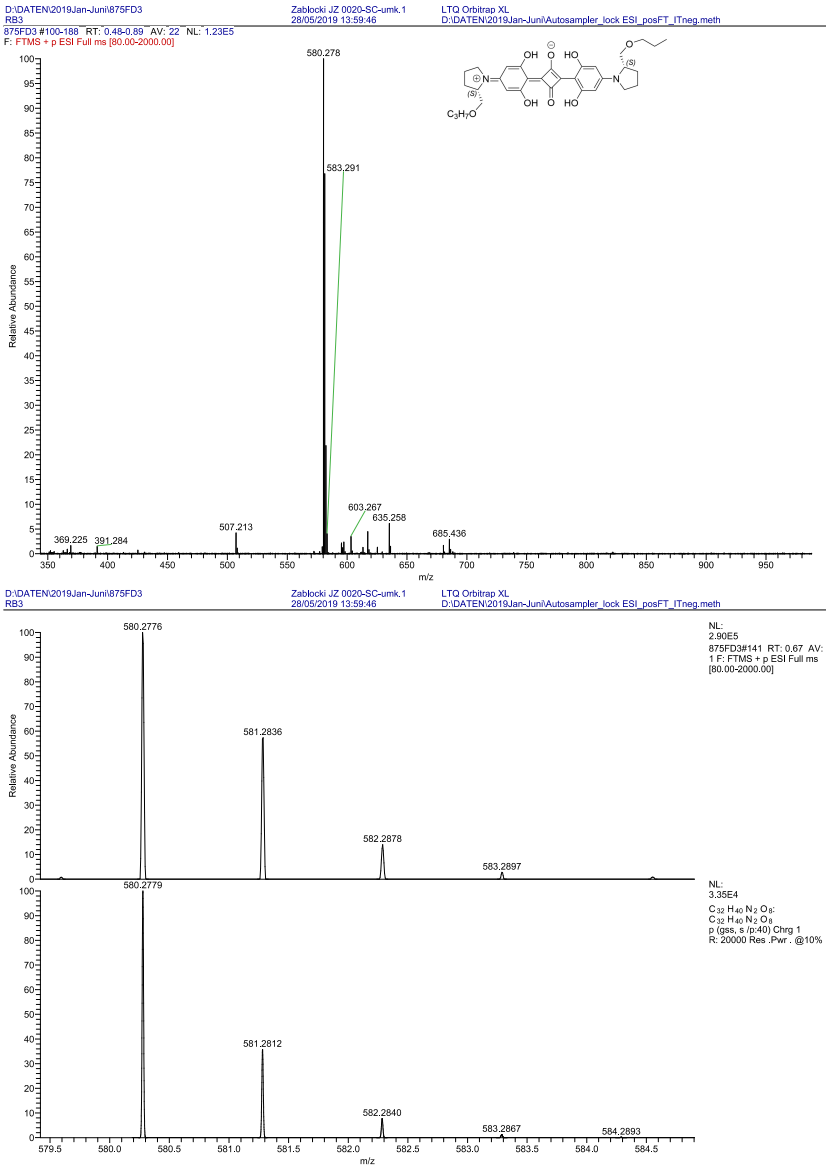


Figure S66: ESI(+) Mass spectra of (*S*,*S*)-ProSQ-C3

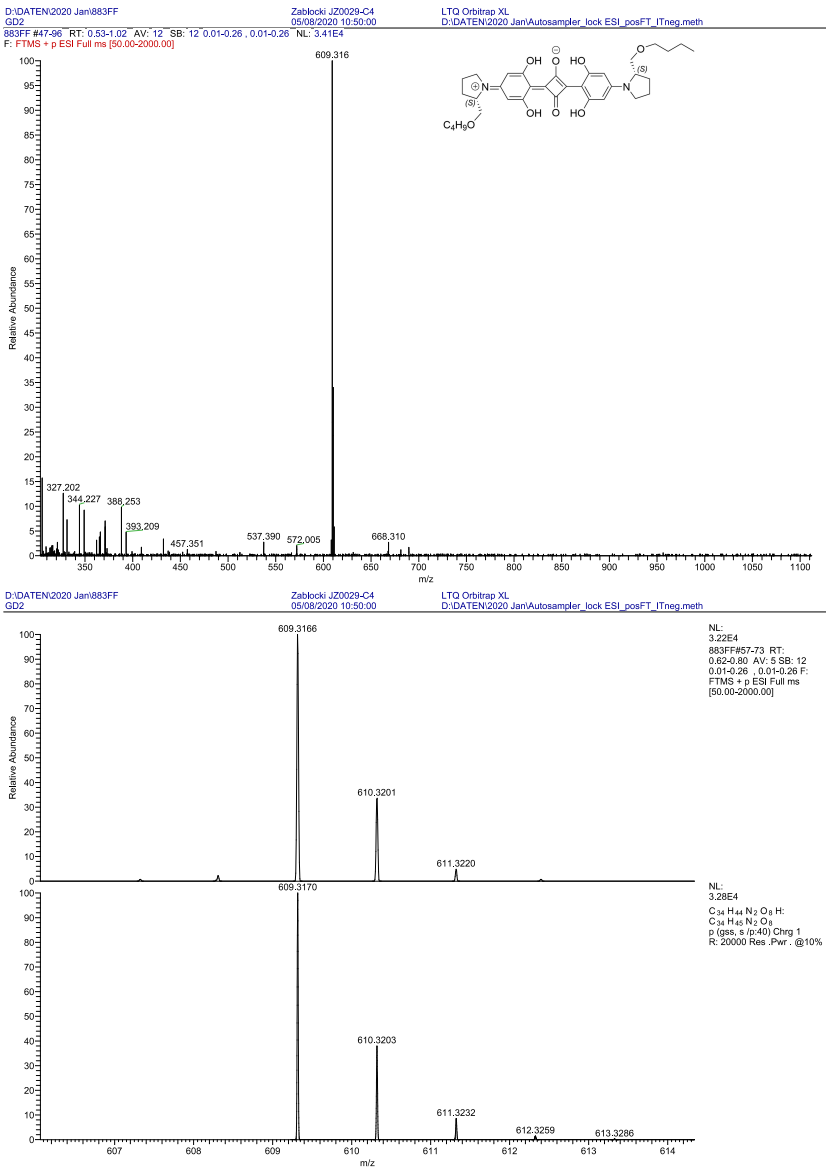


Figure S67: ESI(+) Mass spectra of (*S*,*S*)-ProSQ-C4

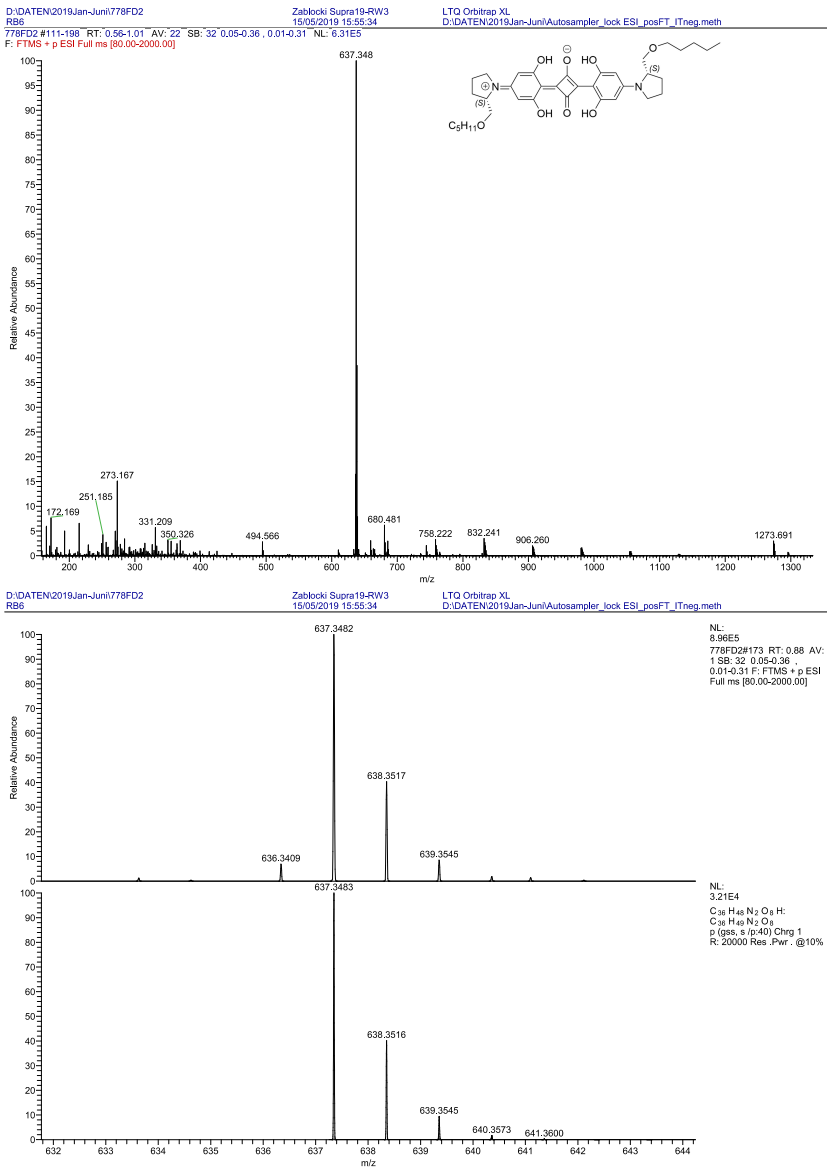


Figure S68: ESI(+) Mass spectra of (*S*,*S*)-ProSQ-C5

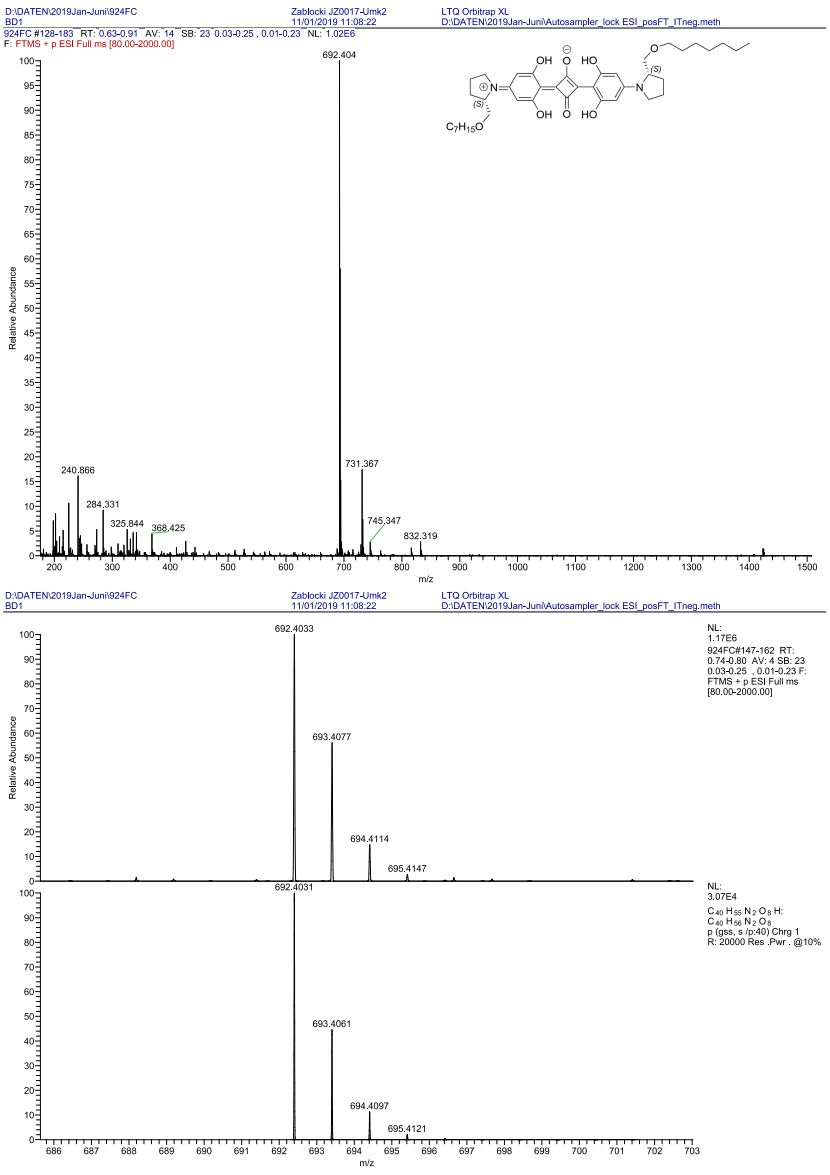


Figure S69: ESI(+) Mass spectra of (*S*,*S*)-ProSQ-C4

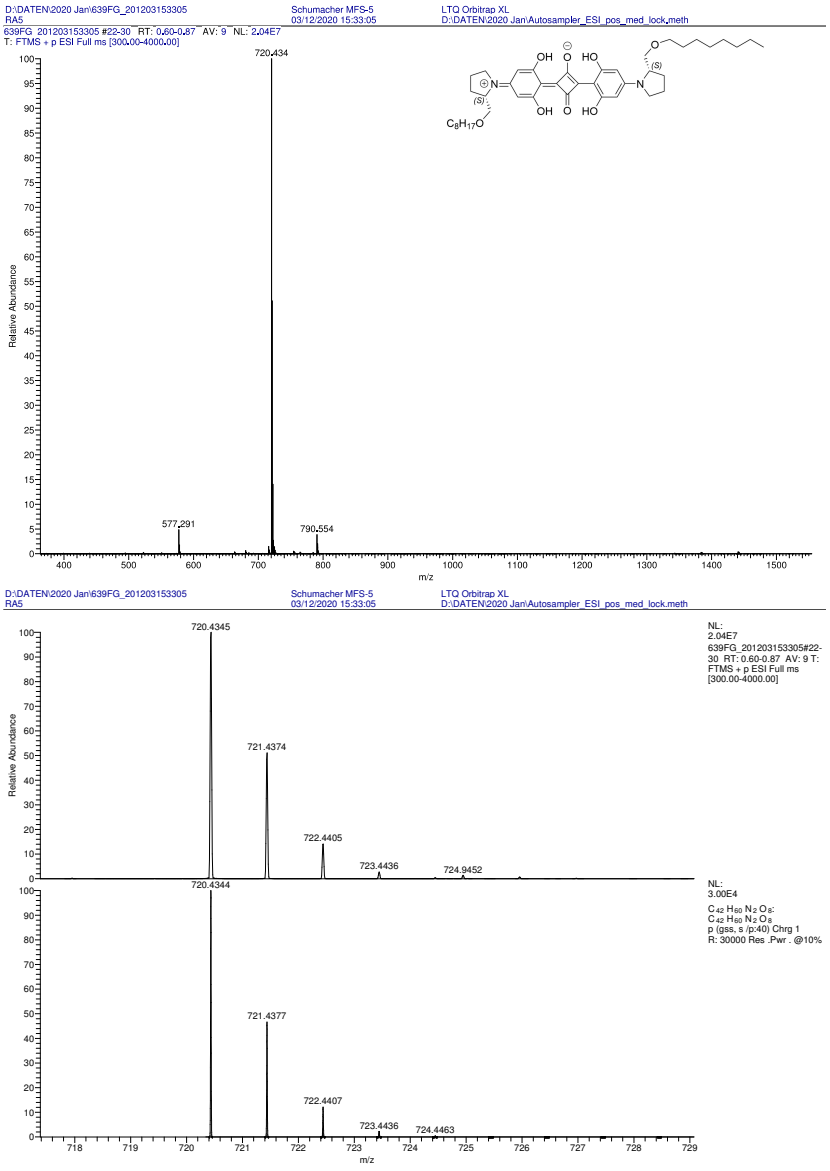


Figure S70: ESI(+) Mass spectra of (*S*,*S*)-ProSQ-C8

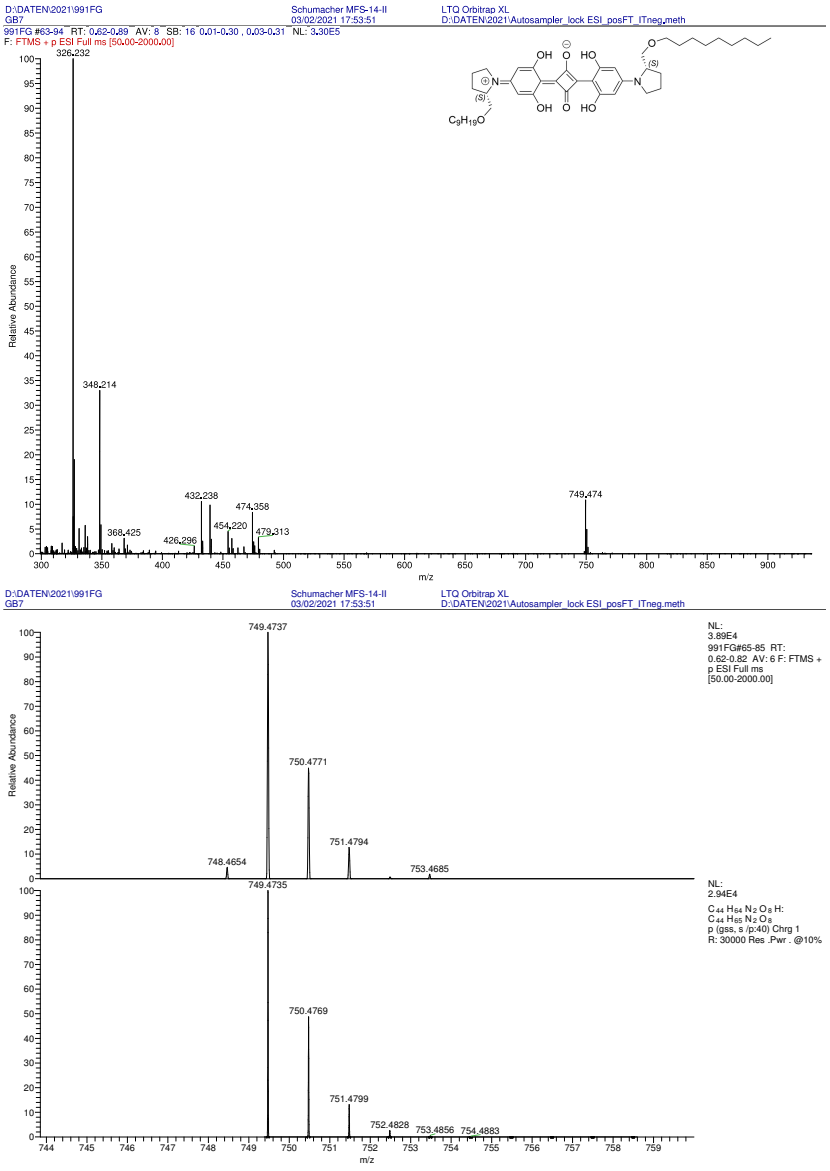


Figure S71: ESI(+) Mass spectra of (*S*,*S*)-ProSQ-C9

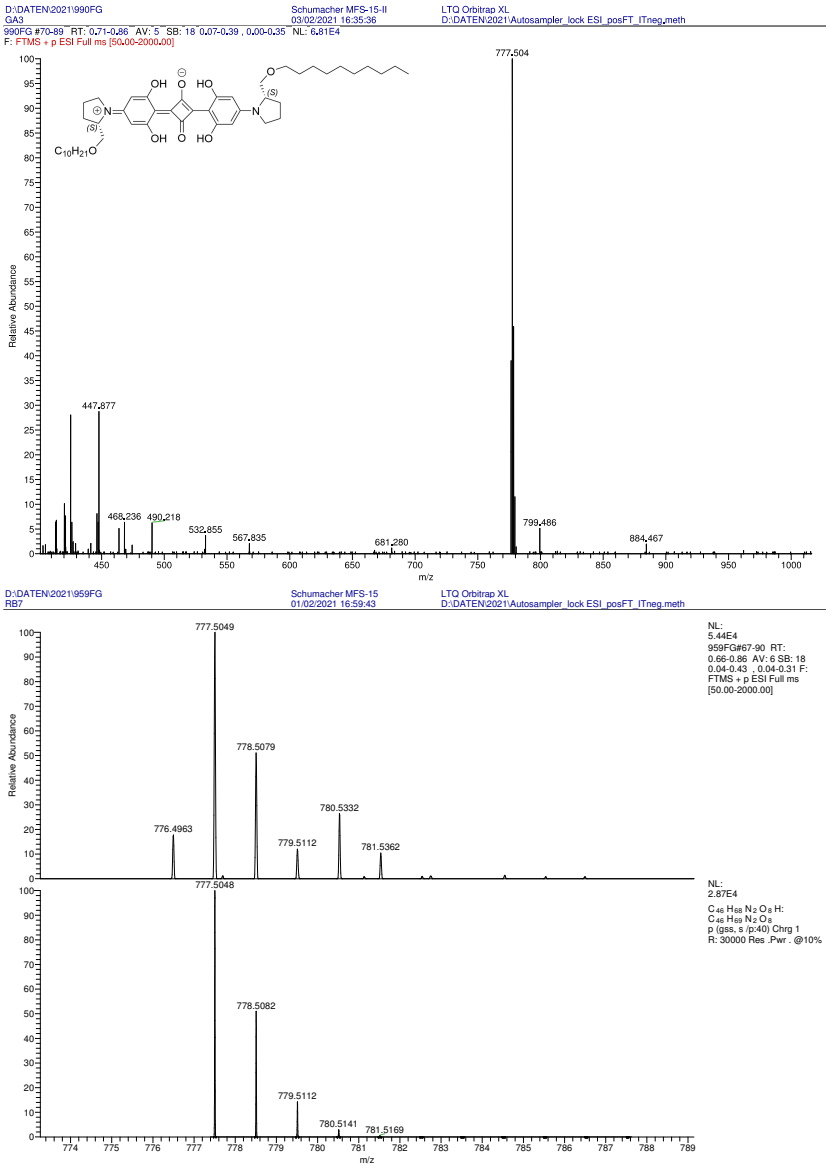


Figure S72: ESI(+) Mass spectra of (*S*,*S*)-ProSQ-C10

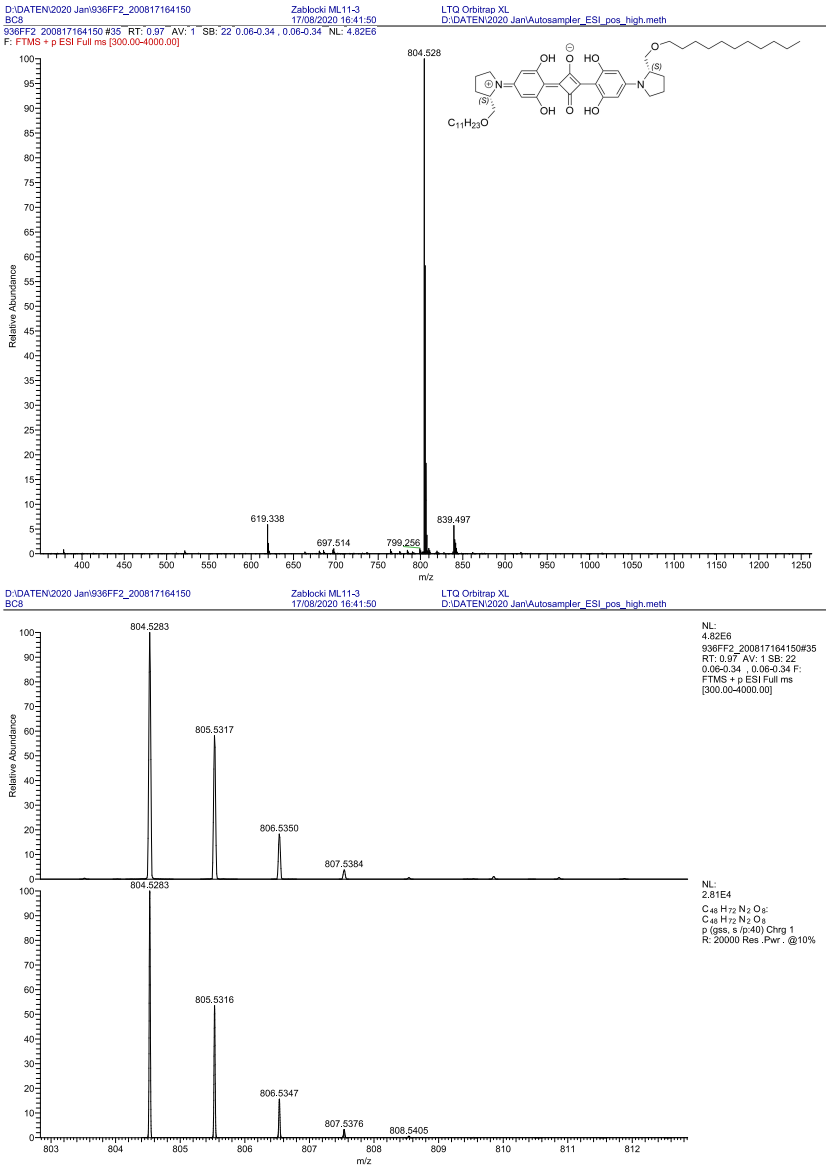


Figure S73: ESI(+) Mass spectra of (*S*,*S*)-ProSQ-C11

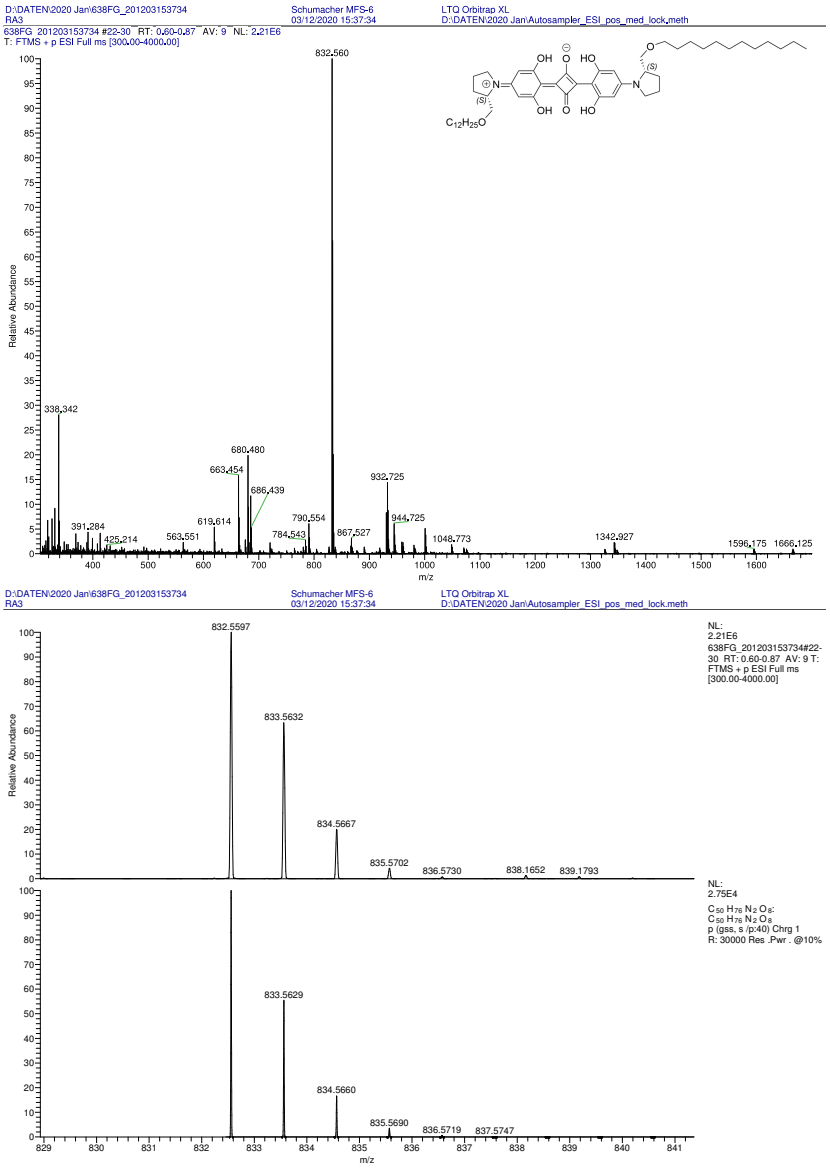


Figure S74: ESI(+) Mass spectra of (*S*,*S*)-ProSQ-C12

APPENDIX **E**

Proline-Derived Anilino Squaraines: Impact of Alkyl Chain Reduction to a Methyl Group

E.1 Additional Spectra in Solution

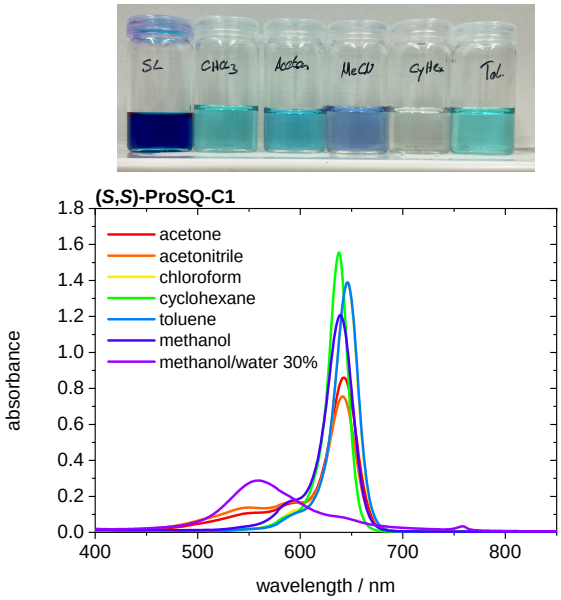


Figure E.1: UV/Vis absorbance spectra of **(*S*,*S*)-ProSQ-C1** in different solvents (bottom) and a picture of the visible changes in color (top). The solutions were prepared from a chloroform stock solution (c = 2.31 × 10^{-4} M) and therefore contain an additional 1.7% chloroform (50 µL in 3 mL) with an final concentration of the sample of c = 3.85 µM.

E.2 Additional Information on Single-Crystal Structures

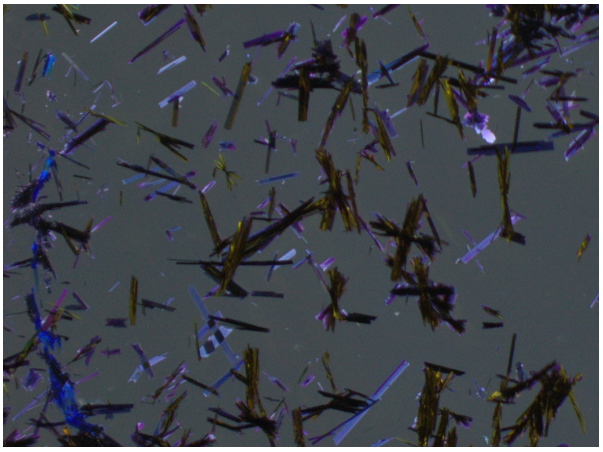


Figure E.2: Picture of the clear purple crystals of **(*R*,*R*)-ProSQ-C3** obtained by layer-diffusion crystallization using chloroform (good solvent) and methanol (poor solvent). Several attempts to measure or resolve the crystal structure were unfortunately unsuccessful.

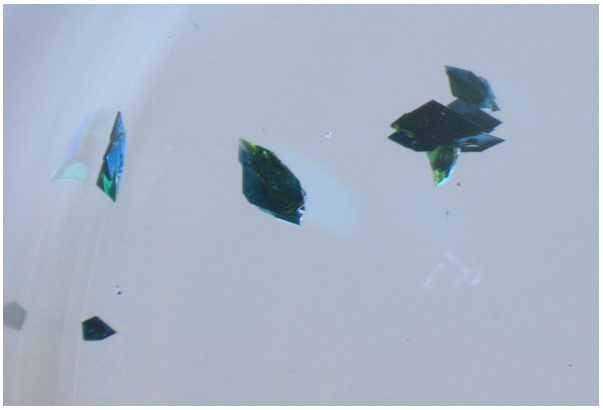


Figure E.3: Picture of the obtained clear bluish green flat rhombus-shaped crystals of **(*S*,*S*-ProSQ-C1** obtained by layer-diffusion crystallization using chloroform (good solvent) and methanol (poor solvent).

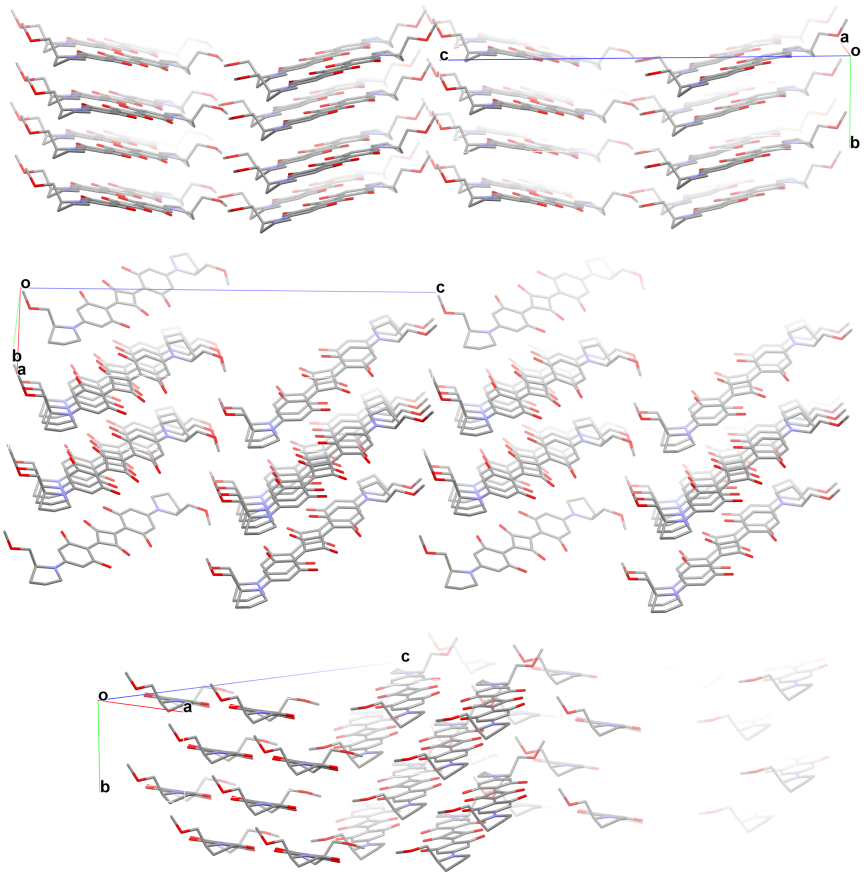


Figure E.4: Crystal structure of **(*S*,*S*)-ProSQ-C1** in a 2×2×2 unit cell (monoclinic, space group = *C*2, a = 11.0261(8) Å, b = 7.0320(8) Å, c = 32.0206(20) Å, α = 90°, β = 97.576(6)°, γ = 90° and Z = 4). Hydrogen was removed and depth perception was activated for clarity. Nitrogen is represented by blue, carbon by gray and oxygen by red.

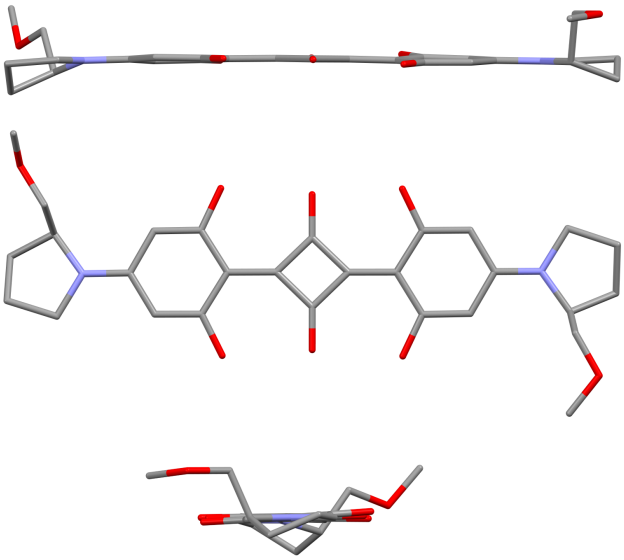


Figure E.5: Molecular geometry of **(*S*,*S*)-ProSQ-C1** from the monoclinic crystal structure.

7463

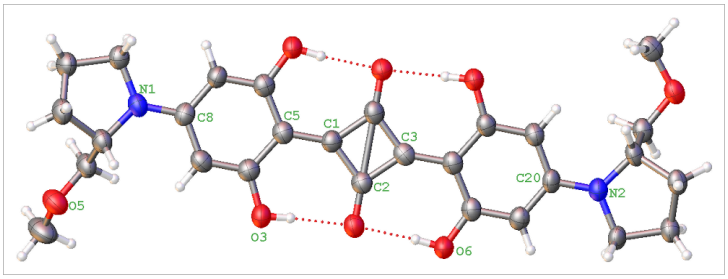


Table 1 Crystal data and structure refinement for 7463.

Identification code	GLUE256, MFS-95 // GXray7463
Crystal Habitus	clear bluish green plate
Device Type	STOE STADIVARI
Empirical formula	$C_{28}H_{32}N_2O_8$
Moiety formula	C28 H32 N2 O8
Formula weight	524.55
Temperature/K	100
Crystal system	monoclinic
Space group	C2
a/Å	11.0261(8)
b/Å	7.0320(8)
c/Å	32.0206(20)
α/°	90.00
β/°	97.576(6)
γ/°	90.00
Volume/Å^3	2461.1(4)
Z	4
ρ_{calc}g/cm^3	1.413
μ/mm^{-1}	0.864
F(000)	1112.0
Crystal size/mm^3	0.21 × 0.11 × 0.03
Absorption correction	multi-scan
Tmin; Tmax	0.0003; 0.9671
Radiation	CuKα (λ = 1.54186)
2Θ range for data collection/°	8.35 to 135.5°
Completeness to theta	0.994
Index ranges	$-13 \le h \le 4$, $-8 \le k \le 8$, $-37 \le l \le 38$
Reflections collected	18870
Independent reflections	18870 [R_{int} = ?, R_{sigma} = 0.0269]
Data/restraints/parameters	18870/1/349
Goodness-of-fit on F^2	1.808
Final R indexes [I>=2σ (I)]	R_1 = 0.1494, wR_2 = 0.3858
Final R indexes [all data]	R_1 = 0.1613, wR_2 = 0.3996
Largest diff. peak/hole / e Å^{-3}	0.77/-0.61
Flack parameter	0.0(8)

Table 2 Bond Lengths for 7463.

Atom	Atom	Length/Å	Atom	Atom	Length/Å
O1	C2	1.254(13)	C3	C17	1.403(15)
O2	C4	1.250(13)	C5	C6	1.449(15)
O3	C6	1.347(14)	C5	C10	1.437(15)
O4	C10	1.350(13)	C6	C7	1.370(16)
O5	C15	1.415(13)	C7	C8	1.413(16)
O5	C16	1.45(2)	C8	C9	1.404(14)
O6	C18	1.348(13)	C9	C10	1.365(15)
O7	C22	1.345(13)	C11	C12	1.540(17)
O8	C27	1.421(12)	C11	C15	1.510(17)
O8	C28	1.408(14)	C12	C13	1.516(18)
N1	C8	1.369(14)	C13	C14	1.523(14)
N1	C11	1.469(13)	C17	C18	1.434(15)
N1	C14	1.452(15)	C17	C22	1.450(14)
N2	C20	1.354(13)	C18	C19	1.390(15)
N2	C23	1.470(14)	C19	C20	1.405(15)
N2	C26	1.456(13)	C20	C21	1.414(16)
C1	C2	1.448(15)	C21	C22	1.394(15)
C1	C4	1.460(14)	C23	C24	1.526(13)
C1	C5	1.419(15)	C24	C25	1.530(16)
C2	C3	1.456(14)	C25	C26	1.529(15)
C2	C4	2.018(14)	C26	C27	1.518(15)
C3	C4	1.457(16)			

Table 3 Bond Angles for 7463.

Atom	Atom	Atom	Angle/°	Atom	Atom	Atom	Angle/°
C15	O5	C16	111.0(10)	N1	C8	C9	120.1(9)
C28	O8	C27	112.1(7)	C9	C8	C7	119.0(9)
C8	N1	C11	123.7(10)	C10	C9	C8	120.9(9)
C8	N1	C14	122.3(9)	O4	C10	C5	121.6(9)
C14	N1	C11	112.8(8)	O4	C10	C9	116.4(9)
C20	N2	C23	122.1(9)	C9	C10	C5	122.0(9)
C20	N2	C26	125.2(9)	N1	C11	C12	101.6(9)
C26	N2	C23	112.7(8)	N1	C11	C15	112.0(9)
C2	C1	C4	87.8(8)	C15	C11	C12	111.7(10)
C5	C1	C2	136.4(9)	C13	C12	C11	103.6(9)
C5	C1	C4	135.7(10)	C12	C13	C14	102.7(9)
O1	C2	C1	133.7(9)	N1	C14	C13	103.9(8)
O1	C2	C3	133.8(10)	O5	C15	C11	107.7(10)
O1	C2	C4	179.0(9)	C3	C17	C18	121.9(9)
C1	C2	C3	92.5(8)	C3	C17	C22	121.7(9)
C1	C2	C4	46.3(6)	C18	C17	C22	116.4(9)
C3	C2	C4	46.2(6)	O6	C18	C17	122.2(9)
C2	C3	C4	87.7(8)	O6	C18	C19	115.6(9)
C17	C3	C2	136.2(10)	C19	C18	C17	122.2(9)
C17	C3	C4	136.1(9)	C18	C19	C20	120.3(10)
O2	C4	C1	134.0(10)	N2	C20	C19	120.3(10)
O2	C4	C2	179.2(10)	N2	C20	C21	120.4(10)
O2	C4	C3	134.0(9)	C19	C20	C21	119.3(9)
C1	C4	C2	45.8(6)	C22	C21	C20	121.1(10)
C3	C4	C1	92.0(8)	O7	C22	C17	123.1(9)
C3	C4	C2	46.1(6)	O7	C22	C21	116.3(9)
C1	C5	C6	122.0(10)	C21	C22	C17	120.6(10)
C1	C5	C10	122.0(9)	N2	C23	C24	103.4(8)
C10	C5	C6	115.9(9)	C23	C24	C25	104.6(9)
O3	C6	C5	122.4(9)	C26	C25	C24	102.8(8)
O3	C6	C7	116.3(9)	N2	C26	C25	103.1(8)
C7	C6	C5	121.3(10)	N2	C26	C27	110.9(9)
C6	C7	C8	120.8(10)	C27	C26	C25	111.7(8)
N1	C8	C7	120.9(10)	O8	C27	C26	112.5(8)

Table 4 Torsion Angles for 7463.

A	B	C	D	Angle/°	A	B	C	D	Angle/°
O1	C2	C3	C4	178.6(13)	C8	N1	C11	C12	153.1(11)
O1	C2	C3	C17	-3(2)	C8	N1	C11	C15	-87.6(13)
O3	C6	C7	C8	-178.6(10)	C8	N1	C14	C13	-177.5(10)
O6	C18	C19	C20	177.5(10)	C8	C9	C10	O4	-176.7(10)
N1	C8	C9	C10	177.3(10)	C8	C9	C10	C5	2.7(17)
N1	C11	C12	C13	32.9(12)	C10	C5	C6	O3	180.0(10)
N1	C11	C15	O5	175.2(9)	C10	C5	C6	C7	-1.0(16)
N2	C20	C21	C22	-179.0(10)	C11	N1	C8	C7	12.4(16)
N2	C23	C24	C25	24.9(11)	C11	N1	C8	C9	-166.2(10)
N2	C26	C27	O8	173.7(8)	C11	N1	C14	C13	-10.0(13)
C1	C2	C3	C4	0.4(9)	C11	C12	C13	C14	-39.5(12)
C1	C2	C3	C17	178.8(12)	C12	C11	C15	O5	-71.6(12)
C1	C5	C6	O3	0.0(17)	C12	C13	C14	N1	30.4(12)
C1	C5	C6	C7	179.0(10)	C14	N1	C8	C7	178.6(10)
C1	C5	C10	O4	-2.1(16)	C14	N1	C8	C9	0.0(16)
C1	C5	C10	C9	178.5(10)	C14	N1	C11	C12	-14.3(13)
C2	C1	C4	O2	-178.9(13)	C14	N1	C11	C15	105.0(11)
C2	C1	C4	C3	0.4(9)	C15	C11	C12	C13	-86.6(11)
C2	C1	C5	C6	0(2)	C16	O5	C15	C11	-174.1(11)
C2	C1	C5	C10	179.9(12)	C17	C3	C4	O2	0(2)
C2	C3	C4	O2	178.9(13)	C17	C3	C4	C1	-178.8(12)
C2	C3	C4	C1	-0.4(9)	C17	C3	C4	C2	-178.5(17)
C2	C3	C17	C18	6(2)	C17	C18	C19	C20	-4.4(17)
C2	C3	C17	C22	-177.2(11)	C18	C17	C22	O7	178.9(10)
C3	C17	C18	O6	-1.4(16)	C18	C17	C22	C21	-1.1(15)
C3	C17	C18	C19	-179.4(10)	C18	C19	C20	N2	-178.7(11)
C3	C17	C22	O7	1.6(16)	C18	C19	C20	C21	2.9(16)
C3	C17	C22	C21	-178.4(10)	C19	C20	C21	C22	-0.7(16)
C4	C1	C2	O1	-178.6(13)	C20	N2	C23	C24	176.3(10)
C4	C1	C2	C3	-0.4(9)	C20	N2	C26	C25	161.2(10)
C4	C1	C5	C6	-177.5(12)	C20	N2	C26	C27	-79.1(14)
C4	C1	C5	C10	3(2)	C20	C21	C22	O7	179.8(9)
C4	C2	C3	C17	178.5(17)	C20	C21	C22	C17	-0.2(16)
C4	C3	C17	C18	-176.5(11)	C22	C17	C18	O6	-178.6(10)
C4	C3	C17	C22	1(2)	C22	C17	C18	C19	3.4(15)
C5	C1	C2	O1	3(2)	C23	N2	C20	C19	-1.2(17)
C5	C1	C2	C3	-178.5(12)	C23	N2	C20	C21	177.2(9)
C5	C1	C2	C4	-178.1(17)	C23	N2	C26	C25	-18.6(12)
C5	C1	C4	O2	-1(2)	C23	N2	C26	C27	101.1(10)
C5	C1	C4	C2	178.2(17)	C23	C24	C25	C26	-36.2(11)
C5	C1	C4	C3	178.5(12)	C24	C25	C26	N2	33.1(10)
C5	C6	C7	C8	2.3(18)	C24	C25	C26	C27	-86.1(10)
C6	C5	C10	O4	177.9(10)	C25	C26	C27	O8	-71.9(11)
C6	C5	C10	C9	-1.5(16)	C26	N2	C20	C19	179.0(10)
C6	C7	C8	N1	-179.7(10)	C26	N2	C20	C21	-2.6(17)
C6	C7	C8	C9	-1.1(17)	C26	N2	C23	C24	-3.9(12)
C7	C8	C9	C10	-1.4(17)	C28	O8	C27	C26	-92.1(10)

APPENDIX F

Ultrafast Excitonic Transitions in Enantiopure and Racemic Squaraine Thin Films

R. Bernhardt,[a] L. Rieland,[a] T. Wang,[a] M. F. Schumacher,[b] A. Lützen,[b] M. Schiek,[c] P. H. M. van Loosdrecht[a]

Received: August 20, 2024
Published online: October 16, 2024

Reprinted with permission[d] from:
R. Bernhardt, L. Rieland, T. Wang, M. F. Schumacher, A. Lützen, M. Schiek, and P. H. M. van Loosdrecht, "Ultrafast Excitonic Transitions in Enantiopure and Racemic Squaraine Thin Films," *Aggregate* **2025**, *6* (3), e698, doi: 10.1002/agt2.698
– Copyright ©The Author(s). Aggregate published by SCUT, AIEI, and John Wiley & Sons Australia, Ltd.

Own contributions:

- Synthesis and purification of the squaraine molecules
- Preparation of the thin film samples
- Performing and evaluating the ellipsometric/polarimetric measurements
- Interpretation of the results
- Writing parts of the manuscript

[a] Institute of Physics II, University of Cologne, Cologne, Germany
[b] Kekulé-Institute for Organic Chemistry and Biochemistry, University of Bonn, Bonn, Germany
[c] Centerfor Surface- and Nanoanalytics (ZONA), Institute for Physical Chemistry (IPC) & Linz Institute for Organic Solar Cells (LIOS), Johannes Kepler University, Linz, Austria
[d] Permission requests to reuse material from this chapter should be directed to SCUT, AIEI, and John Wiley & Sons Australia, Ltd.

Aggregate

WILEY
Aggregate

RESEARCH ARTICLE OPEN ACCESS

Ultrafast Excitonic Transitions in Enantiopure and Racemic Squaraine Thin Films

Robin Bernhardt[1] | Lukas Rieland[1] | Tianyi Wang[1] | Marvin F. Schumacher[2] | Arne Lützen[2] | Manuela Schiek[3] | Paul H. M. van Loosdrecht[1]

[1]Institute of Physics II, University of Cologne, Cologne, Germany | [2]Kekulé-Institute for Organic Chemistry and Biochemistry, University of Bonn, Bonn, Germany | [3]Center for Surface- and Nanoanalytics (ZONA), Institute for Physical Chemistry (IPC) & Linz Institute for Organic Solar Cells (LIOS), Johannes Kepler University, Linz, Austria

Correspondence: Robin Bernhardt (bernhardt@ph2.uni-koeln.de) | Tianyi Wang (twang@ph2.uni-koeln.de) | Manuela Schiek (manuela.schiek@jku.at) | Paul H. M. van Loosdrecht (pvl@ph2.uni-koeln.de)

Received: 20 August 2024 | **Revised:** 24 September 2024 | **Accepted:** 16 October 2024

Funding: This study was supported by the Deutsche Forschungsgemeinschaft (DFG, RTG-2591, and Template-designed Organic Electronics-TIDE), and Linz Institute of Technology (LIT-2019-7-INC-313 SEAMBIOF, LI1013770001- 2D3M).

Keywords: chirality | excitons | molecular aggregation | transient absorption | ultrafast dynamics

ABSTRACT

While chirality is a prevalent character of numerous biological and synthetic organic molecules, its selective absorption of circularly polarized light, known as circular dichroism (CD), is typically small due to intrinsically weak coupling between magnetic and electric dipoles. However, thin films of aggregated, enantiopure prolinol-derived squaraine molecules (ProSQ-C16) exhibit an unusually large excitonic CD signal, although the underlying mechanism is not yet known. In this study, we employ steady-state and ultrafast transient absorption spectroscopy to investigate the nature and dynamics of excitons in aggregates of enantiopure and racemic ProSQ-C16 thin films. Highly resembling transient responses of enantiopure thin films under excitations at different photon energies strongly indicate that a single type of aggregate dominates the linear optical response, that is, a strong red-shifted (J-like) and weak blue-shifted (H-like) absorption band. On the other hand, the transient properties of the racemic thin film deviate from this pattern and remain largely ambiguous. The short lifetime of excited states and coherent oscillations present in the dynamics of the transient absorption signal indicate that the early time dynamics are governed by a transition towards a dark intermediate state, which might arise from intermolecular charge transfer with potential contributions from the coupling of excitons to the vibrations. This non-radiative relaxation pathway explains the unusually weak fluorescence of the predominately J-like behaving aggregate. Our findings conclusively show that the chiral aggregate structure has a strong impact on the optical and dynamic response of the excitons and underline the significance of non-Frenkel exciton states for the optical properties of anilino squaraine dyes.

1 | Introduction

The photophysical properties of aggregated natural and synthetic molecular dyes in many cases are governed by their excitonic states [1, 2]. These excitonic states are a result of intermolecular interactions [3], which are controlled by the packing of the chromophores in an aggregate. Traditional molecular exciton theory [3] covers Coulombic interactions (Frenkel excitons) and the formation of archetypical H- and J-aggregates as well as "oblique" aggregates (Davydov splitting [4]). However, both vibronic coupling and intermolecular charge transfer can significantly impact the photophysical properties [5]. Aggregates

This is an open access article under the terms of the Creative Commons Attribution License, which permits use, distribution and reproduction in any medium, provided the original work is properly cited.

© 2024 The Author(s). *Aggregate* published by SCUT, AIEI, and John Wiley & Sons Australia, Ltd.

26924560, 2025, 3, Downloaded from https://onlinelibrary.wiley.com/doi/10.1002/agt2.698, Wiley Online Library on [27/06/2025]. See the Terms and Conditions (https://onlinelibrary.wiley.com/terms-and-conditions) on Wiley Online Library for rules of use; OA articles are governed by the applicable Creative Commons License

of quadrupolar anilino squaraine dyes exhibit distinct excitonic absorption signatures within the visible to deep-red spectral range [6]. These exciton states depend on the spatial alignment of the π-conjugated molecular backbones, which can be facilitated by non-chromophoric terminal functionalization patterns [7]. They can be predominately of Frenkel-excitonic nature [8–12] or are hybridized with intermolecular charge transfer states [11, 13, 14] and exhibit excitonic CD upon chiral functionalization [7, 15–19].

Chirality is a symmetry property primarily referring to the structural non-superimposability of an object with its mirror image, which can give rise to optical activity (circular birefringence (CB) and circular dichroism (CD)), as well as circularly polarized light emission and spin polarization effects (e.g., chirality-induced spin selectivity (CISS)) [20, 21]. For natural chiral molecular and supramolecular systems, CD is typically a weak effect because it arises from coupling of magnetic and electric dipoles, which is inherently weak in molecular materials [22, 23]. The chiroptical response of engineered materials such as liquid crystals [24], periodic nanostructures [25] and chiral metamaterials [26] is spectroscopically almost indistinguishable from intrinsic CD, even though it emerges from a different physical origin, as it is based on spatial dispersion rather than interactions of magnetic and electric dipoles [25]. Structural CD is often several orders of magnitude larger than intrinsic CD. Nevertheless, the development of strongly intrinsically CD-active organic semiconductors for chiroptical applications is an undauntedly active field of research [27–31].

In this context, a group of prolinol-derived anilino squaraines (ProSQs) were developed, demonstrating a giant intrinsic excitonic CD in dispersed aggregates and thin films [32, 33]. In particular, annealed thin films of enantiopure ProSQ carrying a sixteen carbon atom long terminal alkyl chain (ProSQ-C16) showed an optical dissymmetry factor of ± 0.75—by far the highest value for small molecule assemblies [33]. Moreover, the linear absorbance of enantiopure ProSQ-C16 thin films is beyond archetypical H- and J-aggregation. While a strong J-like redshift of the main absorption band compared to the monomer is observed for this thin film, the fluorescence is surprisingly weak. Furthermore, the line shape of this main absorption band is not symmetric, and a low-amplitude absorbing continuum extending to the weaker blue-shifted absorption band is observed. These optical and excitonic properties of aggregated enantiopure ProSQ-C16 thin films can further be tuned by interaction with a gold substrate layer, leading to exciton-plasmon coupling which strongly enhances delocalization of the excitons [34]. Due to the lack of a conclusive structural model, the underlying structure-property relationship responsible for these optical properties has not been resolved so far. Two different scenarios have been proposed via theoretical modeling for dispersed aggregates involving either intermolecular charge transfer or a network of coexisting aggregates [32], which asks for more experimental evidence.

In this study, we conduct ultrafast transient absorption spectroscopy on enantiopure and racemic thin films of ProSQ-C16 on glass substrates to provide a deeper insight into the excitonic properties and the structural nature of their aggregation. Using transient absorption spectroscopy we confirm a J-aggregate-like character of the main absorption band and the connection of the J- and H-like absorption bands via a common ground state, indicating a single type of aggregate for both enantiopure thin films. It has already been shown that intermolecular charge transfer must be accounted for if the absorption pattern originates from a single aggregate [32].

The transient absorption dynamics reveal that inside this aggregate, an efficient non-radiative decay channel exists that converts the first excited singlet state into an optically dark intermediate state. This transition might explain the lack of fluorescence, potentially due to a conical intersection between the initially excited and an intermediate dark state, as is hinted by the coherent oscillations observed in the early transient dynamics. As expected, the racemic thin film does not exhibit excitonic CD, but the linear and transient absorption properties are also influenced by the heterogeneity of the aggregation. Our study highlights the importance of linear and transient excitonic properties in understanding the structure-property relationship of these extraordinary chiral molecular aggregates, as well as the significance of charge transfer interactions for the linear, chiral and transient optical properties.

2 | Results

2.1 | Steady-State Absorption

The molecular structure of one of the enantiopure ProSQ-C16, (*S,S*)-ProSQ-C16, is shown in Figure 1a. Thermal annealing of the spincasted enantiopure and racemic ProSQ-C16 thin films ensures molecular aggregation, which leads to absorbance spectra as shown in Figure 1b. The enantiopure thin films exhibit the already-known spectral signatures of a single asymmetric and strong red-shifted transition (J-band) centered around 1.6 eV (about 780 nm) and a weaker blue-shifted transition (H-band) at 2.2 eV (about 550 nm) with respect to the absorbance spectrum of the monomer [33, 34]. While the shapes and spectral positions of the main features are the same in both enantiopure thin films, differences between the enantiopure and racemic films become evident. The racemic film absorbs with two closely spaced sub-bands at 1.615 eV and 1.675 eV, which both are blue-shifted with respect to the much sharper absorption band in the enantiopure films. In addition, the weaker H-band has almost disappeared in the racemic film. Instead, a long absorptive tail emerges, extending from the two J-bands to higher energies. These clearly visible differences in the absorbance spectra are the first indications of a different aggregate packing in the racemic thin film with respect to the enantiopure films. The intermolecular arrangement must be significantly altered on the nanometer scale, which makes the existence of discrete chiral domains of (*R,R*) and (*S,S*) moieties in the racemic film unlikely.

The overall interaction with light is remarkably high, as quantified by the (effective) uniaxial complex refractive indices for the chiral and racemic thin films shown in Figures S1a and S1c, respectively. The maxima of the ordinary extinction coefficients of the J-band range from 3.0 for the chiral thin films to 2.0 for the racemic thin films. Although the value for the racemic thin film is significantly lower compared to the chiral thin films, it still by far exceeds the typical range for conjugated polymer thin films, which often appears to be limited to 1.0 [35]. From the uniaxial anisotropy of both the enantiopure and racemic

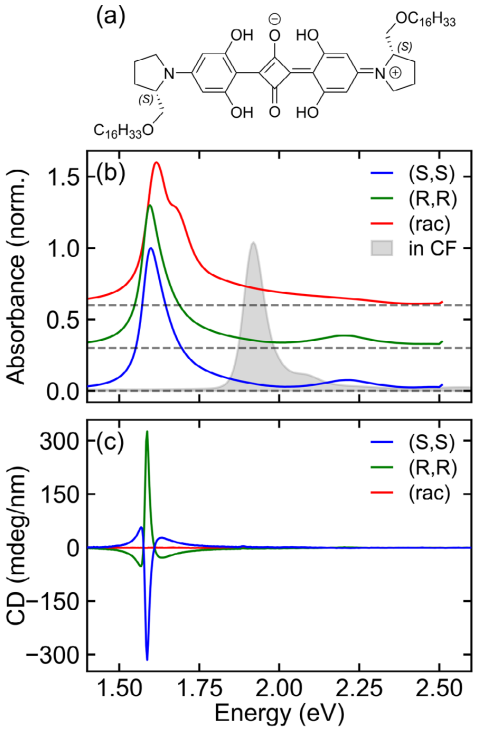


FIGURE 1 | (a) Molecular structure of (*S,S*)-ProSQ-C16 with the stereogenic C atom marked with "*(S)*". (b) Normalized steady-state absorbance spectra of the ProSQ-C16 thin films examined in this study, as well as monomeric (*S,S*)-ProSQ-C16 in a chloroform (CF) solution as reference (grey spectrum). (*S,S*)/(*R,R*) denotes the enantiopure thin film only containing (*S,S*)- or (*R,R*)-ProSQ-C16, and (rac) the racemic thin film. The absorbance baseline is offset by 0.3 and 0.6 for the (*R,R*) and (*rac*) thin film, respectively. (c) Thickness normalized circular dichroism (CD) spectra extracted from the matrix logarithm of reconstructed normal incidence transmission Mueller matrix measurements of spincasted and annealed thin films of (*R,R*)- and (*S,S*)-ProSQ-C16 as well as (*rac*)-ProSQ-C16.

thin films, it is evident that the H-like transition is basically oriented perpendicular to the plane of the thin films (extraordinary components of the complex refractive index). Therefore, this H-band appears only weakly in all normal incidence steady-state and transient transmission measurements discussed in this study, while the J-like transition is mainly oriented within the plane of the thin films (ordinary components of the complex refractive index) and dominates the spectra.

Circular dichroism (CD) spectra of the enantiopure and the racemic thin films are shown in Figure 1c. The enantiopure thin films feature sharp conservative excitonic CD signals of opposite sign, peaking at about 1.6 eV. Thus, almost all of the CD rotational strength has relocated to the J-band transition. This CD signal scales linearly with layer thickness (see Figure S1b), as expected for an intrinsic excitonic circular dichroism [33]. From this it can be inferred that aggregate morphology and dimensions are consistent for the enantiopure thin film samples under investigation. In contrast, the racemic layer shows no CD regardless of the layer

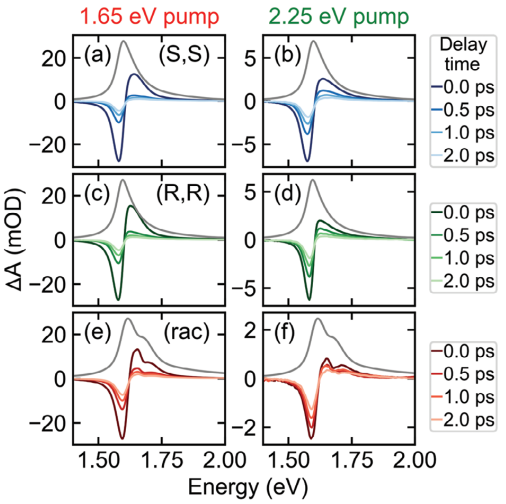


FIGURE 2 | Transient absorption spectra upon photoexcitation at 1.65 eV (750 nm) (a,c,e) and at 2.25 eV (550 nm) (b,d,f) for selected delay times as indicated in the legend for a fluence of 400 W/cm^2. Blue colors show the transient absorption spectra of (*S,S*)-ProSQ-C16 thin film (a,b), green colors the (*R,R*)-ProSQ-C16 thin film (c,d), and red colors the racemic film (e,f). The grey line shows the steady-state absorbance spectrum of the given sample for reference in arbitrary units.

thickness (see also Figure S1d). Since the steady-state absorbance spectrum of the racemic thin film differs significantly from that of the enantiopure films, it seems unlikely that enantiopure aggregate domains with opposite chirality would be formed [36]. Even if there were discrete S-S and R-R interactions that cause resolution of the racemic mixture into chiral subdomains, they would be of equal number. As long as the CD measurement is an integral method like in this case, racemic samples will always be CD-silent.

2.2 | Transient Absorption

To investigate the nature of excitons within the thin film more thoroughly, transient absorption measurements are carried out by selectively exciting either the J-band or the H-band of each thin film. The spectral transient response of the respective thin films, (*S,S*), (*R,R*), (*rac*), can be seen in Figure 2a,c,e for J-band excitation and Figure 2b,d,f for H-band excitation, along with the steady-state absorbance of the corresponding thin films. In all measurements, the amplitude of the transient response is outstandingly high, further emphasizing the extremely strong light-matter interaction in ProSQ-C16 aggregates [12, 37, 38].

The transient response of the enantiopure films to J-band excitation (Figure 2a,b) is dominated by strong negative bleach signal around the J-band, coupled to blue-shifted photo-induced absorption (PIA) signals, as observed before [34]. This is in line with the well-established footprint of J-aggregates [39], where the negative bleach signal carries both ground-state bleach (GSB) and stimulated emission (SE) contributions. It is important to note that the spectral shape of each sample does not depend on the fluence of the photoexcitation. The amplitude of the initial

26924560, 2025, 3, Downloaded from https://onlinelibrary.wiley.com/doi/10.1002/agt2.698, Wiley Online Library on [27/06/2025]. See the Terms and Conditions (https://onlinelibrary.wiley.com/terms-and-conditions) on Wiley Online Library for rules of use; OA articles are governed by the applicable Creative Commons License

26924560, 2025, 3, Downloaded from https://onlinelibrary.wiley.com/doi/10.1002/agt2.698, Wiley Online Library on [27/06/2025]. See the Terms and Conditions (https://onlinelibrary.wiley.com/terms-and-conditions) on Wiley Online Library for rules of use; OA articles are governed by the applicable Creative Commons License

transient response remains proportional to the fluence even at very high excitation densities (see Figure S2).

The shapes of the transient absorption spectra of the two enantiopure thin films are highly similar, with the only difference being the slightly sharper low-energy shoulder of the PIA signal in the (*R,R*)-ProSQ-C16 thin film. The residual difference in the spectra could be due to a minimal difference in enantiomeric purity and the experimental uncertainty in the thin film preparation [33], which could lead to a different extent of aggregation and disorder in the films. The film thickness of the (*R,R*) and (*S,S*) samples is approximately 28 nm and 22 nm, respectively, and is thus a variable parameter related to processing.

Compared to direct excitation of the J-band at 1.65 eV, photoexcitation at the H-band at 2.25 eV reveals an almost identical transient response around the J-band for both enantiopure films, with an amplitude consistent with the weaker absorbance of the H-band compared to the J-band. This strong resemblance suggests that the initially excited exciton state corresponding to the H-band rapidly relaxes into the excitonic state corresponding to the J-band. This strongly suggests that the two absorption lines of the enantiopure thin films originate from the same type of aggregate and share the same ground state.

In contrast, the transient response of the racemic thin film is more complicated. While both the bleach and PIA signals can be identified as for the enantiopure thin films, a substructure between 1.65 eV and 1.8 eV arises in the PIA signal. At least two peaks can be recognized in the PIA signal, whose peak energies correspond to one of the optical bright states seen in the steady-state absorbance spectrum. A proper assignment of these peaks is difficult, as bleach signals and PIA signals from different excitonic states might overlap.

Exciting the weakly absorbing H-band of the racemic thin film results in distinct changes to the transient spectra compared to direct excitation of the J-bands. The relative amplitude of the PIA features is significantly reduced when the H-band is excited, and the spectral shape of the PIA sub-peaks does not match the transient response of J-band excitation either. The bleach signal, on the other hand, appears to be consistent in both sets of measurements. This implies to some extent an efficient transition from the H-band to the J-bands, while the exact distribution of populated excitonic states differs between the 1.65 eV and 2.25 eV photoexcitation conditions. In contrast to the enantiopure thin films, the transient response of the racemic thin film cannot be unambiguously assigned as J-aggregate-like. The thermal annealing process does not seem to cause resolution of the racemic mixture into an equivalent number of enantiopure aggregate domains. Instead, multiple types of equally stable racemic aggregates are most likely formed [36].

2.3 | Transient Absorption Dynamics

Further insights into the excitonic nature of the enantiopure and racemic ProSQ-C16 aggregates are revealed by the dynamics of individual bleach and PIA signals and their fluence dependence, as is shown in Figure 3. Overall, the dynamics in all thin films are rather fast when compared to other SQ aggregates [8, 12, 15]. Within this fast response window (<4 ps), the bleach and PIA signals show different dynamics across all measurements.

All PIA signals decay faster than their bleach counterparts under the same measurement condition. This holds true for all samples, fluences and photoexcitation energies, and can be seen most clearly by the different remaining signals at a delay time of 4 ps in Figure 3. In the context of two exciton absorption [39], the PIA and SE signals persist as long as the exciton band minimum (J-band) is occupied, while the ground-state bleach persists until the ground-state is occupied again. The mismatch between PIA and bleach dynamics therefore requires an intermediate state, into which excitons can transition.

As expected, the dynamics of two enantiopure thin films are almost identical to each other, which again demonstrates that they adopt the same (mirror-imaged) aggregate structure. On the contrary, the racemic thin film shows much slower dynamics at lower fluences, which are accelerating significantly with increasing fluence. Even though all thin films exhibit fluence-dependent dynamics, it is much more pronounced in the racemic sample.

Further insights can be gained by fitting of the bleach dynamics of the racemic thin film with multi-exponential decay functions (see Section S3 for all fit functions used and Tables S1–S6 and Figure S3 for the fit results of all samples). The fitting results suggest multiple dynamic contributions with different decay times. The apparent acceleration of the dynamics for higher fluences seems to be caused by an increase in the relative amount of excitons undergoing fast decay at the expense of the slower decay channels. A consistent trend is observable only for the racemic thin film, but not for the enantiopure films, which might indicate different relaxation mechanisms.

Additionally to the decay observed for the PIA and bleach dynamics, coherent oscillations can be found in the spectral region between PIA and bleach signals. These coherent oscillations are visible for all thin films, but only when the J-band is directly excited at 1.65 eV. After careful subtraction of the exponentially decaying population signal using a fitted single exponential decay function, the clearly visible coherent oscillations are presented in Figure 4a,c,e, for all three samples. The Fourier-transform of the residuals (Figure 4b,d,f) shows that the oscillations occur at a frequency of 4.3 THz or approximately 144 cm^{-1}, which applies to all films and suggests a molecular origin. Similar coherent oscillations at 147 cm^{-1} were found in monomeric ProSQ-C16 in solution also on ps-timescale, and were identified as a collective molecular backbone vibration [40] of a single molecule of ProSQ-C16. The fact that this mode is observed in both enantiopure and racemic thin films further suggests that this vibrational mode is insensitive to the aggregate structure, and is intrinsic to a single molecule. The lack of coherent oscillations under H-band excitation can be caused by incoherent relaxation of the excitons from the H-band to the J-band—therefore coherence is lost before the J-band excitons can couple to vibrational degrees of freedom.

2.4 | Singular Value Decomposition

In order to disentangle different correlated spectral and dynamical contributions, singular value decomposition (SVD) is

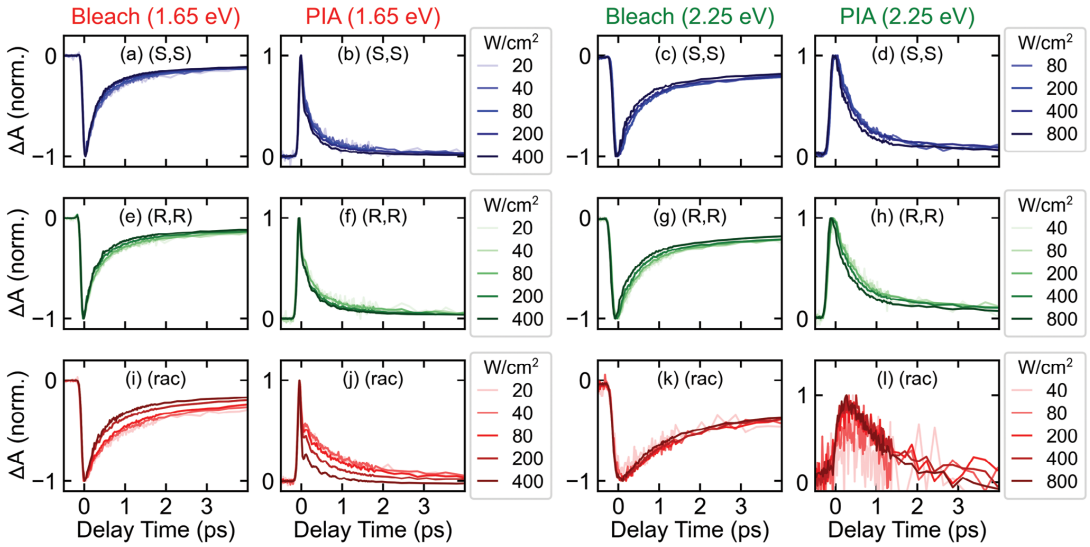


FIGURE 3 | Fluence-dependent dynamics of bleach (a,c,e,g,i,k) and photoinduced absorption (b,d,f,h,j,l) signals. Data from (*S,S*) enantiopure thin films are shown in blue, (*R,R*) in green, and racemic in red. Left side spectra represent a photoexcitation at 1.65 eV (750 nm), right side 2.25 eV (550 nm) photoexcitation.

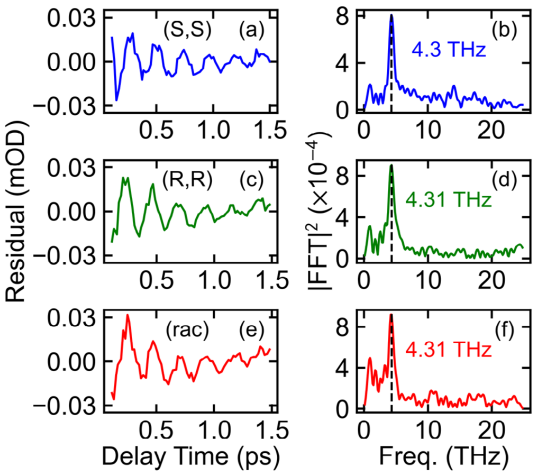


FIGURE 4 | Coherent oscillations in the residual of an exponential fit to the transient dynamics at 1.65 eV (a,c,e) and the corresponding Fourier-transform frequency spectra (b,d,f). The dynamics were obtained at the photon energy showing the most pronounced oscillations ((*S,S*): 1.625 eV; (*R,R*): 1.616 eV; (*rac*): 1.636 eV).

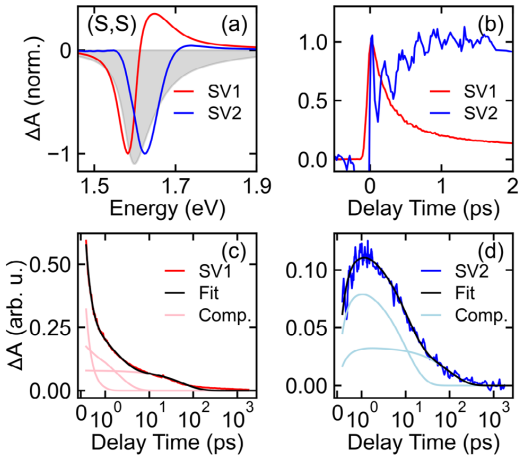


FIGURE 5 | Spectra and dynamics of the two relevant singular values obtained from the transient absorption data of the (*S,S*)-ProSQ-C16 thin film excited at 1.65 eV with a fluence of 400 W/cm². (a) Spectra of the first two singular values (SV), both demonstrating shifts of the negative features with respect to the inverted absorption maximum indicated by the gray shading. (b) Time traces associated with the singular values. (c) Fit of the dynamics of the first singular value dynamics using three exponential decay components, each shown. (d) Fit of the second singular value dynamics, with a function containing two initially rising and decaying components.

performed for a series of high fluence measurements, yielding characteristic time-independent singular value spectra as well as wavelength-independent singular value dynamics of different transient processes [41]. The results for the (*S,S*)-ProSQ-C16 thin film is shown in Figure 5, the corresponding results for the (*R,R*)- and (*rac*)-ProSQ-C16 thin films can be found in Figure S4 in Section S4.

For datasets obtained with J-band excitation, the first two singular values have a large impact on the transient absorption data. For datasets obtained with H-band excitation, the singular value decomposition did not yield constructive results, neither for the

26924560, 2025, 3, Downloaded from https://onlinelibrary.wiley.com/doi/10.1002/agt2.698, Wiley Online Library on [27/06/2025]. See the Terms and Conditions (https://onlinelibrary.wiley.com/terms-and-conditions) on Wiley Online Library for rules of use; OA articles are governed by the applicable Creative Commons License

26924560, 2025, 3, Downloaded from https://onlinelibrary.wiley.com/doi/10.1002/agt2.698, Wiley Online Library on [27/06/2025]. See the Terms and Conditions (https://onlinelibrary.wiley.com/terms-and-conditions) on Wiley Online Library for rules of use; OA articles are governed by the applicable Creative Commons License

TABLE 1 | Fitting results of singular value dynamics of the transient absorption spectrum of (*S,S*)-ProSQ-C16.

Data	A_1	t_1 (ps)	A_2	t_2 (ps)	A_3	t_3 (ps)
SV1	0.342 ± 0.007	0.242 ± 0.009	0.176 ± 0.007	1.75 ± 0.12	0.0796 ± 0.0024	57.1 ± 3.5
SV2	0.133 ± 0.004	0.364 ± 0.021	0.524 ± 0.095	0.452 ± 0.046	—	50.2 ± 7.2

racemic nor the enantiopure films, and therefore will not be discussed. For the enantiopure films, the spectral shape is consistent (Figures 5a and S4a): the first singular value largely resembles the J-aggregate-like transient absorption spectra after relatively short delay times and shows both bleach and photoinduced absorption signals. Its spectral shape is in line with the spectral signature of J-band occupation. The spectral response of the second singular value is dominated by a bleach signal, which has a similar spectral shape to the J-band absorption maximum but is blue-shifted, alongside a minuscule photoinduced absorption signal. This spectrum on the other hand might belong to the population of the intermediate state. The apparent spectral shift of the ground state bleach might be simply related to the absence of stimulated emission, which is commonly red-shifted with respect to the ground state bleach signal. Alternatively, a spectral shift of the absorbance line due to the population of other states or even a non-negligible transient reflectance contribution might be responsible for the spectral discrepancy [42, 43].

Similar to the spectral components, singular value dynamics differ significantly from each other (Figures 5b and S4b). Note that the strong negative feature of the second singular value dynamics is a decomposition artifact due to dynamical dispersion. While the dynamics of the first singular value are of purely decaying nature, a distinct growth can be seen for the second singular value. Additionally, the first singular value dynamics show a smooth decay, while the second dynamics clearly contain oscillations that echo the coherent oscillations observed in the dynamics of certain regions of the TA spectra. The spectral position of the coherent oscillations and the second singular value demonstrate a high degree of overlap.

To quantify the dynamics of the singular values and their relationship to each other, we fitted the dynamics considering two different fit functions. For the first singular value, at least three exponential decays are needed to fit the dynamics

$$f_1(t) = A_1 \cdot e^{\frac{-t}{\tau_1}} + A_2 \cdot e^{\frac{-t}{\tau_2}} + A_3 \cdot e^{\frac{-t}{\tau_3}}, \quad (1)$$

while for the second, the growing and decaying dynamics required a fit function with at least one growing component and two considered exponential decay functions

$$f_2(t) = A_1 \cdot \left(1 - e^{\frac{-t}{\tau_1}}\right)\left((1 - A_2) \cdot e^{\frac{-t}{\tau_2}} + A_2 \cdot e^{\frac{-t}{\tau_3}}\right). \quad (2)$$

The fit results are summarized in Table 1 and can be seen in Figure 5c,d for the (*S,S*)-ProSQ-C16 thin film (see Figure S4c,d,g,h and Tables S7 and S8 for the fit results of (*R,R*)- and racemic ProSQ-C16 thin films).

The multiple exponential decays of the SV1 dynamics indicate multiple relaxation channels and sub-populations of the initially excited states over a variety of time scales. While the shortest component (≈0.24 ps) makes the dominant contribution, a considerable fraction of the excited states relaxes more slowly (≈1.75 ps), while an even smaller fraction decays only after ≈57 ps. Similar to the SV1 dynamics, the decay of the SV2 dynamics requires two components after the signal rises for about 0.36 ps, with a fast ($1 - A_2$, ≈0.5 ps) and slow (A_2, ≈50 ps) decay of equal amplitude.

The time scales of both the fastest and slowest components of each SV dynamics are closely related. The rapid growth of SV2 coincides with the decay of SV1, suggesting a fast transition from one state represented by the first singular value to another associated with the second singular value. The long-time component indicates that both underlying excitonic states also possess a slowly decaying sub-population.

For the racemic thin film (see Figure S4e–h), the spectrum of SV1 resembles the initial transient absorption spectra, similar to the enantiopure thin films. On the other hand, the spectrum of SV2 deviates from a simple bleach profile, as the width of the negative feature is much narrower than the absorption line. Moreover, the side peak of the SV2 spectrum does not match the steady-state absorption spectrum, neither in relative position nor in relative amplitude. In addition to the spectral discrepancies, the SV2 dynamics of the racemic layer cannot be fitted with the fit functions applied to the enantiopure SV2 dynamics. This implies that these functions, which describe the dynamics of the enantiopure film, must be extended with more complex contributions to accurately represent the racemic thin film's behavior.

3 | Discussions

From the transient absorption spectra, the J-like character of the enantiopure thin films becomes more evident. The presence of stimulated emission and photoinduced absorption features next to the ground state bleach and their spectral shape are clear indications that the bright state observed as the J-band is indeed at the minimum of the exciton band, which is the fundamental requirement for a J-aggregate. Additionally, the appearance of a J-like transient signal after photoexcitation of the H-band represents compelling evidence for the J-band being the lowest exciton-band state.

Our data strongly support a "single-type-of-aggregate" picture for enantiopure thin films, in which only one single aggregate type is responsible for the light-matter interactions at visible-light frequencies. This is in line with the theoretical groundwork of Painelli and coworkers [32] that a single enantiopure aggregate

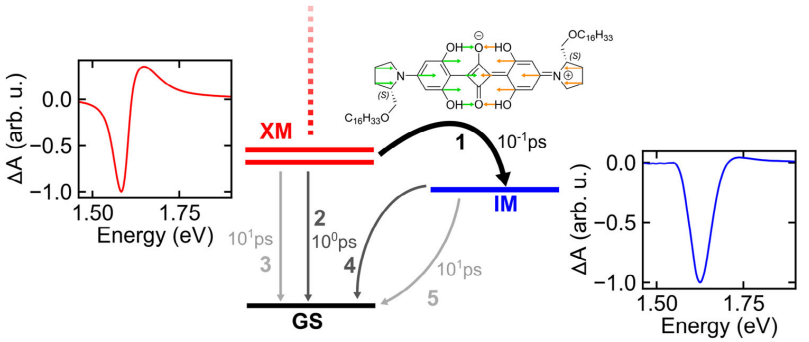


FIGURE 6 | Sketch of the exciton relaxation channels of enantiopure ProSQ-C16 aggregates. The fastest exciton dynamics are observed for a transition from the initially excited state at the low energy edge of the exciton band (XM) into the intermediate state (IM) (**1**), which might be mediated by vibronic coupling to collective molecular vibrational modes [40] (as indicated by the arrows attached to the molecular structure showing the (*S,S*)-ProSQ-C16). This migration happens extremely fast, while the transition to the ground state (GS) takes significantly longer (**4**,**5**). On longer time scales, excitons can also directly transition back into the ground state (**2**,**3**).

can lead to two absorptive peaks due to intermolecular charge transfer hybridization of excitons in dispersed colloidal ProSQ aggregates. Moreover, after some recent dispute [12], such charge-transfer Frenkel hybrid excitons were confirmed for non-chiral anilino-squaraine compounds in uniaxial and crystalline textured thin films by conclusive theoretical and experimental studies [11, 13].

Some of the observations made above partially also hold for the racemic thin film, even though the steady-state and transient spectra appear to be more convoluted. The transient response at the J-band deviates from a perfect J-aggregate-like ("J-like") response, especially for the PIA signal. Furthermore, the spectral shape and amplitude of the PIA signal depend on whether the J-band or the H-band is excited. This is a strong indication that, in contrast to the enantiopure thin films, multiple exciton bands must be responsible for the transient properties of the racemic thin film, and therefore multiple types or fractions of racemic aggregates must be present.

To understand the dynamics of all spectral features, multiple relaxation channels have to be considered, which is consistent with the dynamics obtained from SVD. We associate the first singular value signal with the occupation of the exciton band minimum (XM), and the second singular value signal with occupation of an intermediate dark state (IM), as sketched in Figure 6. The coinciding decay of the XM-related signal and growth of the IM-related signal (see Figure 5c,d) strongly suggests an excitonic transition from the XM to the IM state, which is consistent with the mismatch between the bleach and PIA dynamics. However, the XM → IM transition (**1**) cannot rationalize all facets of the dynamics, and multiple slower relaxation dynamics of both XM (**2**,**3**) and IM (**4**,**5**) have to be considered. The low fluorescence yield of the thin films suggests that the slower relaxation channels are mostly non-radiative. These dynamics might arise from recombination at traps or interfaces, or exciton-exciton annihilation processes [38, 44–49].

The nature of the reported intermediate state cannot be resolved by our study. However, considering the theoretical work done by Painelli and coworkers [32], an intermolecular charge transfer state, which is optically dark on its own [13, 14], represents a suitable candidate. Moreover, a dark state was recently experimentally evidenced by transient absorption spectroscopy in non-chiral anilino-squarain thin films, which are known to form charge-transfer Frenkel hybrid excitons [37].

The short lifetime of the excitons and their rapid transition into a dark state before relaxing back to the ground state deserves special attention. As this transition happens on the sub-ps scale, and is dressed with a strong vibronic coupling, it could possibly be mediated by a conical intersection [50, 51] that outperforms the radiative transition back to the ground state. Dynamics mediated by conical intersections have been demonstrated and hinted at for various molecular aggregates, including squaraines [19, 52, 53]. Conical intersections play an important role in biological systems as the relaxation channels act as energy scavengers to prevent photo damage [54] or they funnel efficient conversion from a reactant to a photochemical reaction product [55]. For chiral molecular systems, Berry forces occurring near a conical intersection have been predicted to enable sizable chiral-induced spin selectivity (CISS) effects [56]. While experimentally reported time scales are still sparse, both intra- and intermolecular conical intersection mediated dynamics have been reported in the timescale between 20-100 fs [50, 51, 57], which is close to the fast mechanism observed in this study. Note that the actual time scale of this process might be faster than the observed value, as the value approaches the time-resolution of the experiment.

So far, most studies on supramolecular conical intersections were focused on higher energy diatomic vibrational modes in dimer systems with highly localized states, leaving intermolecular charge transfer states largely unexplored [19, 50–53, 57–59]. In contrast, the conical intersection in the ProSQ-C16 system at hand might be characterized by a low energy vibrational mode (see Figures 4 and 6), delocalized excitonic states, and probably a large degree of intermolecular charge transfer. It will be highly valuable to further investigate these ProSQ-C16 system as well as to explore other (donor-acceptor-donor) molecular systems which could potentially help clarify the role of lower energy

26924560, 2025, 3, Downloaded from https://onlinelibrary.wiley.com/doi/10.1002/agt2.698, Wiley Online Library on [27/06/2025]. See the Terms and Conditions (https://onlinelibrary.wiley.com/terms-and-conditions) on Wiley Online Library for rules of use; OA articles are governed by the applicable Creative Commons License

26924560, 2025, 3, Downloaded from https://onlinelibrary.wiley.com/doi/10.1002/agt2.698, Wiley Online Library on [27/06/2025]. See the Terms and Conditions (https://onlinelibrary.wiley.com/terms-and-conditions) on Wiley Online Library for rules of use; OA articles are governed by the applicable Creative Commons License

vibrations, exciton delocalization, and intermolecular charge transfer in influencing conical intersections and macroscopic properties such as circular dichroism.

4 | Conclusions

Our study employs steady-state and ultrafast transient absorption spectroscopy to investigate the nature and dynamics of excitons in enantiopure and racemic aggregates in ProSQ-C16 thin films. We observe transient spectra originating from a single type of aggregate in the enantiopure thin films of both handednesses. Our data show that the optical response of these thin films in the form of a dominant J-band and a weaker H-band originates from the hybridization of a Frenkel with a charge transfer exciton. We report a multitude of dynamical contributions, led by an efficient transition of the photoexcited exciton band within the J-aggregate of the enantiopure thin films into an optically dark intermediate state, which explains the faint fluorescence observed for these systems. We conclude that this intermediate state is of intermolecular charge transfer nature. Based on the time scales and coherent oscillations observed in the transient response of all systems, we propose that a conical intersection towards the intermediate CT state could constitute an efficient non-radiative relaxation channel. Steady-state and transient optical properties of the racemic thin film deviate significantly from a typical J-aggregate-like behavior. This highlights the added value of chirality in general and enantiopurity in particular not only for the optical activity but also for the linear and transient optical properties. Our study provides fundamental insights into the excitonic properties of a family of chiral ProSQ aggregates based on the chiral arrangement of quadrupolar anilino-squaraine backbones. These findings are key to understanding and ultimately exploiting the giant circular dichroism of a molecular system on a scale relevant for future technological applications.

5 | Materials & Methods

5.1 | Samples

The squaraine dyes (*S,S*)- and (*R,R*)-ProSQ-C16 used for thin film preparation were synthesized following literature procedures [32, 33]. As starting material, *N*-Boc-D-prolinol (Fluorochem, 99% purity) or *N*-Boc-L-prolinol (chemPUR, 99% purity) was used as received. Thus, the chiral starting materials have a comparable purity to achieve a comparable enantiomeric purity of the target compounds, which was not the case in a previous study [33]. Thin films of ProSQ-C16 were processed on pieces of float glass (25 × 25 mm^2, VWR objective slides) similar to previously established procedures [33]. Both (*S,S*)-enantiopure, (*R,R*)-enantiopure as well as racemic (one-to-one (*S,S*) and (*R,R*) mixture; (*rac*)) ProSQ-C16 solutions in amylene stabilized chloroform (concentration = 3 mg/mL) were used to produce thin films in ambient atmosphere by spincasting (1000 rpm/s acceleration to 3000 rpm kept for 60 s; 400 rpm/s acceleration to 2000 rpm kept for 60 s), followed by thermal annealing on a hotplate (surface temperature 180°C) for 30 min to ensure thermodynamically stable aggregation.

ProSQ-C16 layer thicknesses were determined by variable angle spectroscopic ellipsometry (see Section S1 for details): (*S,S*) = 22 nm (±4 nm); (*R,R*) = 28 nm (±4 nm); (*rac*) = 29 nm (±4 nm).

5.2 | Circular Dichroism

A single rotating compensator J.A. Woollam M2000-DI ellipsometer with CCD-based detection was used for a partial Mueller matrix measurement (first three rows of the Mueller matrix) at normal incidence transmission. The beam diameter is approximately 2 mm, effectively averaging over nano- and microscaled domains. Data were recorded with CompleteEASE version 5 and exported for further analysis with Matlab. The full Mueller matrix is reconstructed by an algebraic procedure before the the matrix logarithm is calculated [60]. The CD spectra are the average of the l_{14} and l_{41} elements of the differential Mueller matrix and are divided by the respective layer thickness obtained from the ellipsometric analysis (see Section S1 for further details).

5.3 | Steady-State and Transient Absorption

Both steady-state and transient absorption spectroscopy measurements were conducted using a setup based on a 150 kHz, 15 W Yb:KGW regenerative amplifier laser system (PHAROS, Light Conversion) [61]. All transmission spectra are recorded at normal incidence. For transient measurements, band-pass filtered pulses from a non-collinear optical parametric amplifier (TOPAS, Light Conversion) were used for pumping the sample with a temporal width of 100–150 fs at 1.65 eV (750 nm) and 2.25 eV (550 nm). To prevent laser-induced degradation of the aggregated films, we allowed fluences of 20 to 800 W/cm^2 and loosely focused the pump beam onto the sample with a spot size of around 160 μm in diameter. For both the probe and (quasi-)steady-state measurements, a 1450 nm pulsed laser beam was tightly focused into a 2 mm thick sapphire plate (EKSMA) to generate a white light supercontinuum. The white light beam was spectrally filtered, limiting the range to 1.37–2.48 eV (500–900 nm). Spectra were detected using a silicon-based diode array mounted in a polychromatic spectrometer (HARPIA, Light Conversion; SHAMROCK, Andor; Hamamatsu S8380-256Q with a readout circuit c7884). To minimize pump beam scattering into the detector, the polarization of the pump beam was set to be perpendicular to that of the probe, and a polarizer was placed in front of the detector to filter out most of the residual intensity of the pump beam.

Author Contributions

Robin Bernhardt and Manuela Schiek conceived the project. Robin Bernhardt, Lukas Rieland and Tianyi Wang performed the steady-state and transient optical experiments and analyzed the experimental results. Marvin F. Schumacher and Arne Lützen synthesized the squaraine molecules. Marvin F. Schumacher prepared the thin film samples. Marvin F. Schumacher and Manuela Schiek performed and analyzed the ellipsometry and polarimetry experiments. Paul H. M. van Loosdrecht

supervised the project. Robin Bernhardt, Manuela Schiek and Tianyi Wang wrote the manuscript with contributions from all authors.

Acknowledgements

The authors gratefully acknowledge support from the Deutsche Forschungsgemeinschaft (DFG, RTG–2591 "TIDE – Template–designed Organic Electronics"). Manuela Schiek thanks the Linz Institute of Technology (LIT-2019-7-INC-313 SEAMBIOF and LI1013770001- 2D3M) for funding. Marvin F. Schumacher thanks the Manchot Foundation for a doctoral scholarship.

Conflicts of Interest

The authors declare no conflicts of interest.

Declaration of Content

This work is part of a thesis prepared toward the completion of a doctoral degree at University of Cologne and has not been published elsewhere in any peer-reviewed journals.

Data Availability Statement

The supporting data for this article are available from Zenodo via the following link: 10.5281/zenodo.14013785.

References

1. S. K. Saikin, A. Eisfeld, S. Valleau, and A. Aspuru-Guzik, "Photonics Meets Excitonics: Natural and Artificial Molecular Aggregates," *Nanophotonics* 2, no. 1 (2013): 21–38, https://doi.org/10.1515/nanoph-2012-0025.

2. A. M. Valencia, D. Bischof, S. Anhäuser, et al., "Excitons in Organic Materials: Revisiting Old Concepts With New Insights," *Electronic Structure* 5, no. 3 (2023): 033003, https://doi.org/10.1088/2516-1075/acf2d4.

3. M. Kasha, H. R. Rawls, and M. A. El-Bayoumi, "The Exciton Model in Molecular Spectroscopy," *Pure and Applied Chemistry* 11, no. 3 (1965): 371–392, https://doi.org/10.1351/pac196511030371.

4. A. S. Davydov, "The Theory of Molecular Excitons," *Soviet Physics Uspekhi* 7, no. 2 (1964): 145, https://doi.org/10.1070/PU1964v007n02ABEH003659.

5. N. J. Hestand and F. C. Spano, "Expanded Theory of H- and J-Molecular Aggregates: The Effects of Vibronic Coupling and Intermolecular Charge Transfer," *Chemical Reviews* 118, no. 15 (2018): 7069–7163, https://doi.org/10.1021/acs.chemrev.7b00581.

6. K. Ilina, W. M. MacCuaig, M. Laramie, J. N. Jeouty, L. R. McNally, and M. Henary, "Squaraine Dyes: Molecular Design for Different Applications and Remaining Challenges," *Bioconjugate Chemistry* 31, no. 2 (2020): 194–213, https://doi.org/10.1021/acs.bioconjchem.9b00482.

7. J. Zablocki, O. Arteaga, F. Balzer, et al., "Polymorphic Chiral Squaraine Crystallites in Textured Thin Films," *Chirality* 32, no. 5 (2020): 619–631, https://doi.org/10.1002/chir.23213.

8. G. de Miguel, M. Ziółek, M. Zitnan, et al., "Photophysics of H- and J-Aggregates of Indole-Based Squaraines in Solid State," *Journal of Physical Chemistry C* 116, no. 17 (2012): 9379–9389, https://doi.org/10.1021/jp210281z.

9. C. Lambert, F. Koch, S. F. Völker, et al., "Energy Transfer Between Squaraine Polymer Sections: From Helix to Zigzag and All the Way Back," *Journal of the American Chemical Society* 137, no. 24 (2015): 7851–7861, https://doi.org/10.1021/jacs.5b03644.

10. G. M. Paternò, L. Moretti, A. J. Barker, et al., "Near-Infrared Emitting Single Squaraine dye Aggregates With Large Stokes Shifts," *Journal of Materials Chemistry C* 5, no. 31 (2017): 7732–7738, https://doi.org/10.1039/C7TC01375B.

11. F. Balzer, N. J. Hestand, J. Zablocki, G. Schnakenburg, A. Lützen, and M. Schiek, "Spotlight on Charge-Transfer Excitons in Crystalline Textured n-Alkyl Anilino Squaraine Thin Films," *Journal of Physical Chemistry C* 126, no. 32 (2022): 13802–13813, https://doi.org/10.1021/acs.jpcc.2c03665.

12. R. Bernhardt, M. Manrho, J. Zablocki, et al., "Structural Disorder as the Origin of Optical Properties and Spectral Dynamics in Squaraine Nano-Aggregates," *Journal of the American Chemical Society* 144, no. 42 (2022): 19372–19381, https://doi.org/10.1021/jacs.2c07064.

13. N. J. Hestand, C. Zheng, A. R. Penmetcha, et al., "Confirmation of the Origins of Panchromatic Spectra in Squaraine Thin Films Targeted for Organic Photovoltaic Devices," *Journal of Physical Chemistry C* 119, no. 33 (2015): 18964–18974, https://doi.org/10.1021/acs.jpcc.5b05095.

14. C. A. Shen, D. Bialas, M. Hecht, V. Stepanenko, K. Sugiyasu, and F. Würthner, "Polymorphism in Squaraine Dye Aggregates by Self-Assembly Pathway Differentiation: Panchromatic Tubular Dye Nanorods versus J-Aggregate Nanosheets," *Angewandte Chemie International Edition* 133, no. 21 (2021): 12056–12065, https://doi.org/10.1002/ange.202102183.

15. H. Chen, M. S. Farahat, K. Y. Law, and D. G. Whitten, "Aggregation of Surfactant Squaraine Dyes in Aqueous Solution and Microheterogeneous Media: Correlation of Aggregation Behavior with Molecular Structure," *Journal of the American Chemical Society* 118, no. 11 (1996): 2584–2594, https://doi.org/10.1021/ja9523911.

16. A. T. Rösch, Q. Zhu, J. Robben, et al., "Helicity Control in the Aggregation of Achiral Squaraine Dyes in Solution and Thin Films," *Chemistry A European Journal* 27, no. 1 (2021): 298–306, https://doi.org/10.1002/chem.202002695.

17. J. Selby, M. Holzapfel, B. K. Lombe, et al., "Chiroptical Properties of Indolenine Squaraines With a Stereogenic Center at Close Proximity," *Journal of Organic Chemistry* 85, no. 19 (2020): 12227–12242, https://doi.org/10.1021/acs.joc.0c01422.

18. O. A. Mass, C. K. Wilson, S. K. Roy, et al., "Exciton Delocalization in Indolenine Squaraine Aggregates Templated by DNA Holliday Junction Scaffolds," *Journal of Physical Chemistry B* 124, no. 43 (2020): 9636–9647, https://doi.org/10.1021/acs.jpcb.0c06480.

19. E. Freytag, L. Kreimendahl, M. Holzapfel, et al., "Chiroptical Properties of Planar Benzobisthiazole-Bridged Squaraine Dimers," *Journal of Organic Chemistry* 88, no. 15 (2023): 10777–10788, https://doi.org/10.1021/acs.joc.3c00821.

20. J. R. Brandt, F. Salerno, and M. J. Fuchter, "The Added Value of Small-Molecule Chirality in Technological Applications," *Nature Reviews Chemistry* 1, no. 6 (2017): 1–12, https://doi.org/10.1038/s41570-017-0045.

21. B. P. Bloom, Y. Paltiel, R. Naaman, and D. H. Waldeck, "Chiral Induced Spin Selectivity," *Chemical Reviews* 4, no. 124, (2024): 1950–1991, https://doi.org/10.1021/acs.chemrev.3c00661.

22. N. S. S. Nizar, M. Sujith, K. Swathi, C. Sissa, A. Painelli, and K. G. Thomas, "Emergent Chiroptical Properties in Supramolecular and Plasmonic Assemblies," *Chemical Society Reviews* 50, no. 20 (2021): 11208–11226, https://doi.org/10.1039/D0CS01583K.

23. F. Bertocchi, C. Sissa, and A. Painelli, "Circular Dichroism of Molecular Aggregates: A Tutorial," *Chirality* 35, no. 10 (2023): 681–691, https://doi.org/10.1002/chir.23565.

24. M. Mitov, "Cholesteric Liquid Crystals With a Broad Light Reflection Band," *Advanced Materials* 24, no. 47 (2012): 6260–6276, https://doi.org/10.1002/adma.201202913.

25. B. Gompf, J. Braun, T. Weiss, H. Giessen, M. Dressel, and U. Hübner, "Periodic Nanostructures: Spatial Dispersion Mimics Chirality," *Physical Review Letters* 106, no. 18 (2011): 185501, https://doi.org/10.1103/PhysRevLett.106.185501.

26. Z. Wang, F. Cheng, T. Winsor, and Y. Liu, "Optical Chiral Metamaterials: A Review of the Fundamentals, Fabrication Methods and Applications," *Nanotechnology* 27, no. 41 (2016): 412001, https://doi.org/10.1088/0957-4484/27/41/412001.

26924560, 2025, 3, Downloaded from https://onlinelibrary.wiley.com/doi/10.1002/agt2.698, Wiley Online Library on [27/06/2025]. See the Terms and Conditions (https://onlinelibrary.wiley.com/terms-and-conditions) on Wiley Online Library for rules of use; OA articles are governed by the applicable Creative Commons License

27. Y. Yang, R. C. de Costa, M. J. Fuchter, and A. J. Campbell, "Circularly Polarized Light Detection by a Chiral Organic Semiconductor Transistor," *Nature Photonics* 7, no. 8 (2013): 634–638, https://doi.org/10.1038/nphoton.2013.176.

28. M. Schulz, F. Balzer, D. Scheunemann, et al., "Chiral Excitonic Organic Photodiodes for Direct Detection of Circular Polarized Light," *Advanced Functional Materials* 29, no. 16 (2019): 1900684, https://doi.org/10.1002/adfm.201900684.

29. G. Albano, G. Pescitelli, and L. D. Bari, "Chiroptical Properties in Thin Films of pi-Conjugated Systems," *Chemical Reviews* 120, no. 18 (2020): 10145–10243, https://doi.org/10.1021/acs.chemrev.0c00195.

30. J. Wade, J. N. Hilfiker, J. R. Brandt, et al., "Natural Optical Activity as the Origin of the Large Chiroptical Properties in Pi-Conjugated Polymer Thin Films," *Nature Communications* 11, no. 1 (2020): 6137, https://doi.org/10.1038/s41467-020-19951-y.

31. Y. Deng, M. Wang, Y. Zhuang, S. Liu, W. Huang, and Q. Zhao, "Circularly Polarized Luminescence From Organic Micro-/Nano-Structures," *Light: Science & Applications* 10, no. 1 (2021): 76, https://doi.org/10.1038/s41377-021-00516-7.

32. D. Giavazzi, M. F. Schumacher, L. Grisanti, et al., "A Marvel of Chiral Squaraine Aggregates: Chiroptical Spectra Beyond the Exciton Model," *Journal of Materials Chemistry C* 11, no. 24 (2023): 8307–8321, https://doi.org/10.1039/D2TC05555D.

33. M. Schulz, J. Zablocki, O. S. Abdullaeva, et al., "Giant Intrinsic Circular Dichroism of Prolinol-Derived Squaraine Thin Films," *Nature Communications* 9, no. 1 (2018): 2413, https://doi.org/10.1038/s41467-018-04811-7.

34. T. Quenzel, D. Timmer, M. Gittinger, et al., "Plasmon-Enhanced Exciton Delocalization in Squaraine-Type Molecular Aggregates," *ACS Nano* 16, no. 3 (2022): 4693–4704, https://doi.org/10.1021/acsnano.1c11398.

35. M. S. Vezie, S. Few, I. Meager, et al., "Exploring the Origin of High Optical Absorption in Conjugated Polymers," *Nature Materials* 15, no. 7 (2016): 746–753, https://doi.org/10.1038/nmat4645.

36. R. K. Hylton, G. J. Tizzard, T. L. Threlfall, et al., "Are the Crystal Structures of Enantiopure and Racemic Mandelic Acids Determined by Kinetics or Thermodynamics?," *Journal of the American Chemical Society* 137, no. 34 (2015): 11095–11104, https://doi.org/10.1021/jacs.5b05938.

37. T. J. Wiegand, J. S. Sandoval, J. A. Cody, D. W. McCamant, and C. J. Collison, "Directional Exciton Diffusion, Measured by Subpicosecond Transient Absorption as an Explanation for Squaraine Solar Cell Performance," *Journal of Physical Chemistry C* 128, no. 11 (2024): 4616–4630, https://doi.org/10.1021/acs.jpcc.3c06361.

38. C. Zheng, M. F. Mark, T. Wiegand, et al., "Measurement and Theoretical Interpretation of Exciton Diffusion as a Function of Intermolecular Separation for Squaraines Targeted for Bulk Heterojunction Solar Cells," *Journal of Physical Chemistry C* 124, no. 7 (2020): 4032–4043, https://doi.org/10.1021/acs.jpcc.9b11816.

39. L. D. Bakalis and J. Knoester, "Pump-Probe Spectroscopy and the Exciton Delocalization Length in Molecular Aggregates," *Journal of Physical Chemistry B* 103, no. 31 (1999): 6620–6628, https://doi.org/10.1021/jp990354g.

40. D. Timmer, F. Zheng, M. Gittinger, et al., "Charge Delocalization and Vibronic Couplings in Quadrupolar Squaraine Dyes," *Journal of the American Chemical Society* 144, no. 41 (2022): 19150–19162, https://doi.org/10.1021/jacs.2c08682.

41. C. Ruckebusch, M. Sliwa, P. Pernot, A. de Juan, and R. Tauler, "Comprehensive Data Analysis of Femtosecond Transient Absorption Spectra: A review," *Journal of Photochemistry and Photobiology C: Photochemistry Reviews* 13, no. 1 (2012): 1–27, https://doi.org/10.1016/j.jphotochemrev.2011.10.002.

42. H. P. Pasanen, R. Khan, J. A. Odutola, and N. V. Tkachenko, "Transient Absorption Spectroscopy of Films: Impact of Refractive Index," *Journal of Physical Chemistry C* 128, no. 15 (2024): 6167–6179, https://doi.org/10.1021/acs.jpcc.4c00981.

43. A. Ashoka, R. R. Tamming, A. V. Girija, et al., "Extracting Quantitative Dielectric Properties From Pump-Probe Spectroscopy," *Nature Communications* 13, no. 1 (2022): 1437, https://doi.org/10.1038/s41467-022-29112-y.

44. P. Malý, J. Lüttig, P. A. Rose, et al., "Separating Single- From Multi-Particle Dynamics in Nonlinear Spectroscopy," *Nature* 616, no. 7956 (2023): 280–287, https://doi.org/10.1038/s41586-023-05846-7.

45. D. Fazzi, M. Barbatti, and W. Thiel, "Unveiling the Role of Hot Charge-Transfer States in Molecular Aggregates via Nonadiabatic Dynamics," *Journal of the American Chemical Society* 138, no. 13 (2016): 4502–4511, https://doi.org/10.1021/jacs.5b13210.

46. R. Binder, M. Polkehn, T. Ma, and I. Burghardt, "Ultrafast Exciton Migration in an HJ-Aggregate: Potential Surfaces and Quantum Dynamics," *Chemical Physics* 482 (2017): 16–26, https://doi.org/10.1016/j.chemphys.2016.09.037.

47. A. Schubert, V. Settels, W. Liu, et al., "Ultrafast Exciton Self-Trapping Upon Geometry Deformation in Perylene-Based Molecular Aggregates," *Journal of Physical Chemistry Letters* 4, no. 5 (2013): 792–796, https://doi.org/10.1021/jz4000752.

48. B. Manna, R. Ghosh, and D. K. Palit, "Exciton Dynamics in Anthracene Nanoaggregates," *Journal of Physical Chemistry C* 119, no. 19 (2015): 10641–10652, https://doi.org/10.1021/acs.jpcc.5b00469.

49. X. Fan, A. Wei, T. Klamroth, Y. Zhang, K. Gao, and L. Wang, "Ultrafast Multiexciton Dynamics in Molecular Systems: Inclusion of Exciton-Exciton Annihilation," *Physical Review B* 107, no. 13 (2023): 134301, https://doi.org/10.1103/PhysRevB.107.134301.

50. A. De Sio, E. Sommer, X. T. Nguyen, et al., "Intermolecular Conical Intersections in Molecular Aggregates," *Nature Nanotechnology* 16, no. 1 (2021): 63–68, https://doi.org/10.1038/s41565-020-00791-2.

51. A. J. Musser, M. Liebel, C. Schnedermann, et al., "Evidence for Conical Intersection Dynamics Mediating Ultrafast Singlet Exciton Fission," *Nature Physics* 11, no. 4 (2015): 352–357, https://doi.org/10.1038/nphys3241.

52. M. J. Paterson, L. Blancafort, S. Wilsey, and M. A. Robb, "Photoinduced Electron Transfer in Squaraine Dyes: Sensitization of Large Band Gap Semiconductors," *Journal of Physical Chemistry A* 106, no. 47 (2002): 11431–11439, https://doi.org/10.1021/jp026418w.

53. G. de Miguel, M. Marchena, M. Zitnan, S. S. Pandey, S. Hayase, and A. Douhal, "Femto to Millisecond Observations of Indole-Based Squaraine Molecules Photodynamics in Solution," *Physical Chemistry Chemical Physics* 14, no. 5 (2012): 1796–1805, https://doi.org/10.1039/C1CP22864A.

54. B. G. Levine, M. P. Esch, B. S. Fales, D. T. Hardwick, W. T. Peng, and Y. Shu, "Conical Intersections at the Nanoscale: Molecular Ideas for Materials," *Annual Review of Physical Chemistry* 70 (2019): 21–43, https://doi.org/10.1146/annurev-physchem-042018-052425.

55. D. Polli, P. Altoé, O. Weingart, et al., "Conical Intersection Dynamics of the Primary Photoisomerization Event in Vision," *Nature* 467, no. 7314 (2010): 440–443, https://doi.org/10.1038/nature09346.

56. Y. Wu and J. E. Subotnik, "Electronic Spin Separation Induced by Nuclear Motion Near Conical Intersections," *Nature Communications* 12, no. 1 (2021): 700, https://doi.org/10.1038/s41467-020-20831-8.

57. M. S. Schuurman and A. Stolow, "Dynamics at Conical Intersections," *Annual Review of Physical Chemistry* 69 (2018): 427–450, https://doi.org/10.1146/annurev-physchem-052516-050721.

58. V. Settels, A. Schubert, M. Tafipolski, et al., "Identification of Ultrafast Relaxation Processes As a Major Reason for Inefficient Exciton Diffusion in Perylene-Based Organic Semiconductors," *Journal of the American Chemical Society* 136, no. 26 (2014): 9327–9337, https://doi.org/10.1021/ja413115h.

59. H. G. Duan, P. Nalbach, R. J. D. Miller, and M. Thorwart, "Ultrafast Energy Transfer in Excitonically Coupled Molecules Induced by a

26924560, 2025, 3, Downloaded from https://onlinelibrary.wiley.com/doi/10.1002/agt2.698, Wiley Online Library on [27/06/2025]. See the Terms and Conditions (https://onlinelibrary.wiley.com/terms-and-conditions) on Wiley Online Library for rules of use; OA articles are governed by the applicable Creative Commons License

Nonlocal Peierls Phonon," *Journal of Physical Chemistry Letters* 10, no. 6 (2019): 1206–1211, https://doi.org/10.1021/acs.jpclett.9b00242.

60. O. Arteaga and R. Ossikovski, "Complete Mueller Matrix From a Partial Polarimetry Experiment: The 12-Element Case," *Journal of the Optical Society of America A* 36, no. 3 (2019): 416–427, https://doi.org/10.1364/JOSAA.36.000416.

61. E. Jung, K. Budzinauskas, S. Öz, et al., "Femto- to Microsecond Dynamics of Excited Electrons in a Quadruple Cation Perovskite," *ACS Energy Letters* 5, no. 3 (2020): 785–792, https://doi.org/10.1021/acsenergylett.9b02684.

Supporting Information

Additional supporting information can be found online in the Supporting Information section.

26924560, 2025, 3, Downloaded from https://onlinelibrary.wiley.com/doi/10.1002/agt2.698, Wiley Online Library on [27/06/2025]. See the Terms and Conditions (https://onlinelibrary.wiley.com/terms-and-conditions) on Wiley Online Library for rules of use; OA articles are governed by the applicable Creative Commons License

Supplementary Information for: Ultrafast Excitonic Transitions in Enantiopure and Racemic Squaraine Thin Films

Robin Bernhardt,[*,†] Lukas Rieland,[†] Tianyi Wang,[*,†] Marvin F. Schumacher,[‡] Arne Lützen,[‡] Manuela Schiek,[*,¶] and Paul H. M. van Loosdrecht[*,†]

†*II. Institute of Physics, University of Cologne, Cologne, Germany*

‡*Kekulé-Institute for Organic Chemistry and Biochemistry, University of Bonn, Bonn, Germany*

¶*Center for Surface- and Nanoanalytics (ZONA), Institute for Physical Chemistry (IPC) & Linz Institute for Organic Solar Cells (LIOS), Johannes Kepler University, A-4040 Linz, Austria*

E-mail: bernhardt@ph2.uni-koeln.de; twang@ph2.uni-koeln.de; manuela.schiek@jku.at; pvl@ph2.uni-koeln.de

S1 Complex Refractive Index and Circular Dichroism Spectra

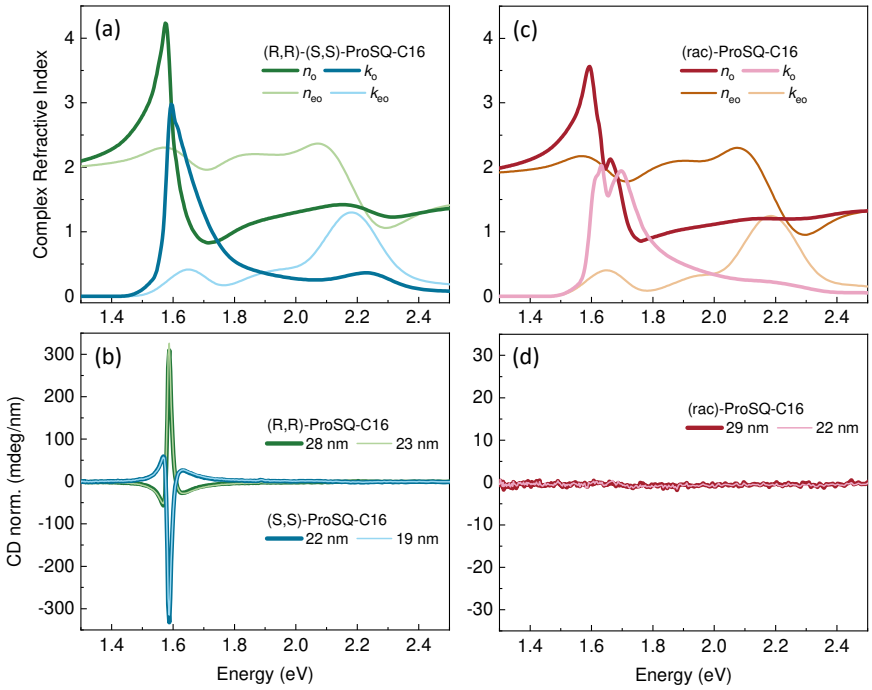


Figure S1: Steady-state optical characterization using a single rotating compensator J.A. Woollam M2000-DI ellipsometer with CCD-based detection. Upper row: Effective uniaxial complex refractive indices obtained via a combined multi-sample analysis of Ψ and Δ VASE scans in reflection and normal incidence transmission intensity scans of (a) enantiopure ProSQ-C16 and (c) racemic ProSQ-C16 spincasted and annealed thin films. The ordinary (in-plane) real and imaginary part, n_o and k_o, and the extra-ordinary (out-of-plane) real and imaginary part, n_{eo} and k_{eo}, are plotted. Lower row: Thickness normalized CD spectra extracted from the matrix logarithm of reconstructed normal incidence transmission Mueller matrix measurements of (b) (*R,R*)- and (*S,S*)-ProSQ-C16 as well as (d) (*rac*)-ProSQ-C16 spincasted and annealed thin films. Layer thicknesses used for the normalization are obtained from standard ellipsometric analysis and are indicated in the legend.

Steady-state optical characterization was performed using a single rotating compensator J.A. Woollam M2000-DI ellipsometer with CCD-based detection including the software CompleteEASE for data acquisition (version 5) and evaluation (version 6). The uniaxial anisotropic complex refractive indices were obtained by a multi-sample analysis combining variable angle

spectroscopic ellipsometry (VASE) scans recording Ψ and Δ for angles of incidence from 45° to 75° in steps of 5° as well as normal incidence transmission intensity scans in the spectroscopic range from 192 nm to 1688 nm following a previously described procedure.[1] Note that the float-glass substrate is opaque for wavelength below 350 nm.

The enantiopure thin films, (*R,R*)- and (*S,S*)-ProSQ-C16, are expected to have the same linear optical properties, and therefore, are evaluated jointly to give an effective complex refractive index, as is shown in Figure S1(a). Three measurements per sample (2x ellipsometry with 90° azimuthal sample rotation, 1x transmission intensity) from two sets of samples, i.e. two samples with different layer thicknesses for each handedness (N=12) have been fitted simultaneously.

For the racemic thin film (*rac*)-ProSQ-C16, two samples with different layer thicknesses were evaluated jointly (N=6) to obtain the complex refractive index plotted in Figure S1(c). For both the enantiopure and the racemic thin films, the extinction maximum (J-like band) is oriented within the plane of the film (ordinary components) in the deep-red spectral range, while their second spectral signature (H-like band) within the green is weaker and broader and mainly oriented out of the film plane (extra-ordinary components). The extinction maximum of the racemic thin film is split into two subbands and the values are considerably lower compared to the enantiopure films: (*rac*)-$n_o \approx 3.6$ (2.1) at 778 nm (745 nm) and versus enantiopure-$n_o \approx 4.3$ at 786 nm; (*rac*)-$k_o \approx 2.0$ (1.95) at 760 nm (730 nm) versus enantiopure-$k_o \approx 3.0$ at 778 nm.

The circular dichroism (CD) was obtained from a partial Mueller matrix measurement (first three rows of the Mueller matrix) at normal incidence transmission similar to the previously described procedure.[2] This time, however, the full Mueller matrix is reconstructed by an algebraic procedure before the differential Mueller matrix is calculated.[3] The CD spectra shown in Figure S1(b,d) are thickness normalized given in millidegree per nanometer (mdeg/nm) as the average of the l_{14} and l_{41} divided by the respective layer thickness obtained from the ellipsometric analysis. Note that CD is not equal to the ellipticity θ, which

is the typical output of a conventional "CD"-spectrometer, but instead equals CD = $2 \cdot \theta$, in the range of validity of low-value approximation for ellipticity. As expected, the racemic thin film is CD-silent, as shown in Figure S1(d), while the enantiopure thin films exhibit a strong conservative CD signal of opposite sign peaking at 780 nm. Since the CD signal scales linearly with layer thickness, it is of intrinsically excitonic nature, and is not overlaid by structural effects.

It should be noted that its maximum value around ± 330 mdeg/nm is clearly lower than the record value approaching ± 1000 mdeg/nm reported earlier.[2] This is mainly due to the considerably lower spectral resolution of the CCD-based detection of the M2000 instrument (5 nm bandwidth) used in this study compared to the monochromator-based VASE instrument with adjustable slit-width (less than 2 nm bandwidth) used previously.[2] Furthermore, processing under ambient conditions (instead of inert glove-box conditions previously) can affect the film quality.

S2 Fluence Dependence of Transient Signal Strengths

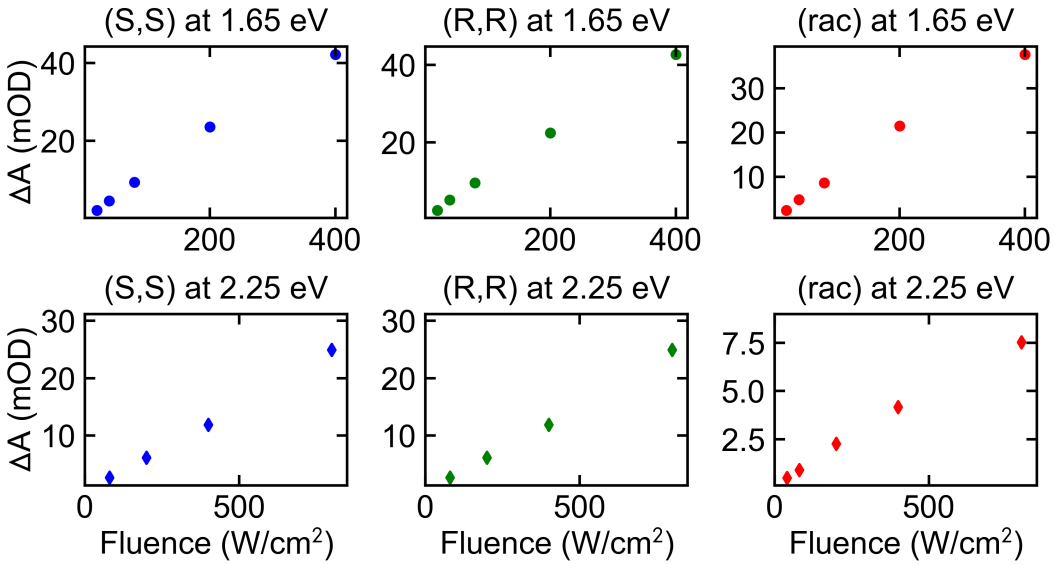


Figure S2: Amplitude of the bleach signal as a function of pump pulse fluence for all shown measurements.

S3 Fit Results of Bleach and Photoinduced Absorption Signals

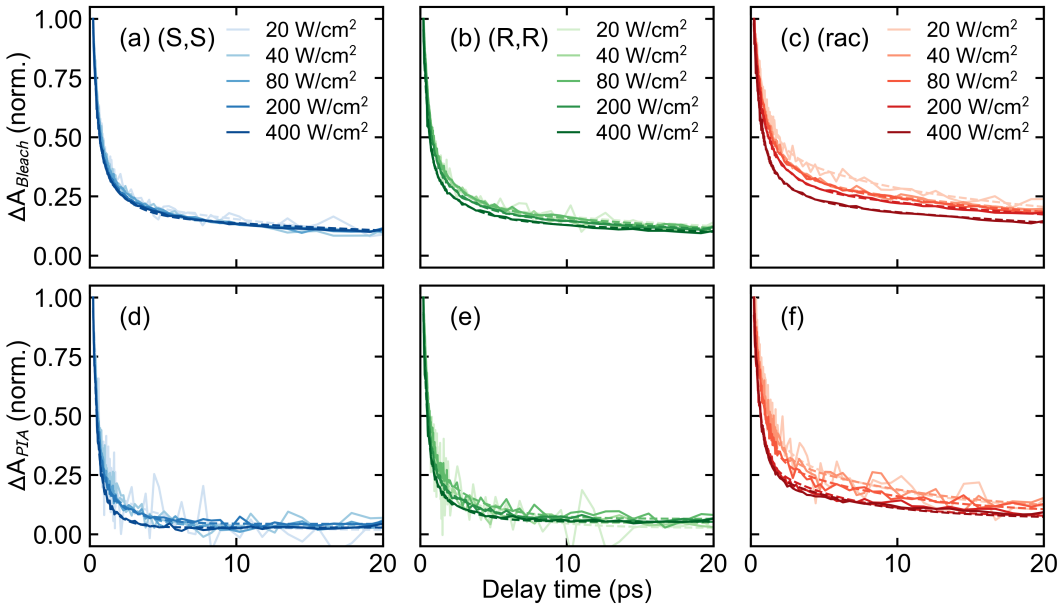


Figure S3: Fitting results (dashed) of the bleach (top) and PIA (bottom) signals for all samples after photoexcitation at 1.65 eV.

Fitting of the bleach dynamics reveals the origin of the fluence dependence. Since dynamics obtained from H-band excitations are distorted by the initial transition into the J-band, only data from J-band excitation is considered. Tables with the fit results are presented below. PIA fits are also added, even though they do not show any consistent patterns. Best fits were obtained by least-squares minimization using a trust region reflective algorithm.

S3.1 Bleach Dynamics

The bleach dynamics were fitted using the following formula

$$f_1 = A_1 \cdot e^{\frac{-t}{\tau_1}} + A_2 \cdot e^{\frac{-t}{\tau_2}} + A_3 \cdot e^{\frac{-t}{\tau_3}}. \tag{1}$$

This formula accounts for three contributions to the dynamics with different decay times. As seen in the tables below, the fluence dependent acceleration of dynamics is not rooted in an increase of the kinetic rates ($1/\tau_i$), but in an increase of the exciton population undergoing the fast relaxation (A_1), at the expense of the slower transitions (A_2, A_3).

Table S1: Bleach dynamics fit results of (*S,S*)-ProSQ-C16.

Fit parameter	**20 W/cm^2**	**Δ**	**40 W/cm^2**	**Δ**	**80 W/cm^2**	**Δ**
A_1	0.672	0.00783	0.935	0.000611	0.961	0.00024
t_1 (ps)	0.236	0.00461	0.368	0.000392	0.348	0.000132
A_2	0.546	0.0113	0.34	0.000604	0.33	0.000215
t_2 (ps)	1.05	0.0349	2.24	0.0781	2.18	0.0283
A_3	0.244	0.000239	0.166	0.000124	0.171	4.38e-05
t_3 (ps)	21.7	5.76	37.8	22.1	38.2	7.78
Fit parameter	**200 W/cm^2**	**Δ**	**400 W/cm^2**	**Δ**		
A_1	1.01	0.000361	1.17	0.000643		
t_1 (ps)	0.311	0.00014	0.256	0.000104		
A_2	0.32	0.000295	0.363	0.000367		
t_2 (ps)	1.92	0.0259	1.56	0.0121		
A_3	0.173	3.83e-05	0.177	2.63e-05		
t_3 (ps)	39.7	8.47	39.3	6.4		

Table S2: Bleach dynamics fit results of (*R,R*)-ProSQ-C16.

Fit parameter	**20 W/cm^2**	**Δ**	**40 W/cm^2**	**Δ**	**80 W/cm^2**	**Δ**
A_1	0.941	0.00232	0.857	0.000689	0.899	0.000308
t_1 (ps)	0.341	0.00129	0.379	0.000508	0.348	0.00019
A_2	0.323	0.00245	0.326	0.000782	0.347	0.000355
t_2 (ps)	1.99	0.221	2.1	0.0827	1.95	0.0248
A_3	0.213	0.00032	0.204	0.00013	0.21	4.26e-05
t_3 (ps)	37.5	37.0	31.1	8.06	33.9	3.61
Fit parameter	**200 W/cm^2**	**Δ**	**400 W/cm^2**	**Δ**		
A_1	0.93	0.000256	1.03	0.000471		
t_1 (ps)	0.36	0.00016	0.308	0.000169		
A_2	0.306	0.000261	0.283	0.00033		
t_2 (ps)	2.16	0.0347	2.08	0.0563		
A_3	0.182	4.23e-05	0.161	6.7e-05		
t_3 (ps)	40.9	8.46	42.7	21.2		

Table S3: Bleach dynamics fit results of (*rac*)-ProSQ-C16.

Fit parameter	**20 W/cm^2**	**Δ**	**40 W/cm^2**	**Δ**	**80 W/cm^2**	**Δ**
A_1	0.642	0.00212	0.478	0.00235	0.624	0.00075
t_1 (ps)	0.791	0.00699	0.474	0.00315	0.528	0.000965
A_2	0.345	0.00347	0.389	0.00281	0.307	0.000865
t_2 (ps)	37.6	61.6	1.85	0.0624	2.32	0.0732
A_3	0.158	0.00194	0.321	7.42e-05	0.304	5.76e-05
t_3(ps)	5.0	12.5	38.1	3.97	40.5	3.62
Fit parameter	**200 W/cm^2**	**Δ**	**400 W/cm^2**	**Δ**		
A_1	0.656	0.000857	0.799	0.00108		
t_1 (ps)	0.377	0.000795	0.387	0.000664		
A_2	0.393	0.00126	0.294	0.00144		
t_2 (ps)	1.69	0.0271	1.8	0.0773		
A_3	0.29	4.19e-05	0.239	7.27e-05		
t_3(ps)	38.9	3.24	37.5	6.99		

S3.2 PIA Dynamics

The PIA dynamics were fitted using the following formula

$$f_1 = A_1 \cdot e^{\frac{-t}{\tau_1}} + A_2 \cdot e^{\frac{-t}{\tau_2}} + A_3. \tag{2}$$

Note that just like the bleach signal, the dynamics of the PIA signals do not portray a single exponential decay but need at least two components to be fitted.

Table S4: PIA dynamics fit results of (*S,S*)-ProSQ-C16.

Fit parameter	**20 W/cm^2**	**Δ**	**40 W/cm^2**	**Δ**	**80 W/cm^2**	**Δ**
A_1	1.44	0.0177	1.2	0.00493	1.32	0.00149
t_1 (ps)	0.335	0.002	0.328	0.00151	0.317	0.000308
A_2	0.222	0.00244	0.341	0.00518	0.288	0.00103
t_2 (ps)	4.09	3.78	1.91	0.191	2.09	0.0803
A_3	0.0171	0.000339	0.0346	4.83e-05	0.0278	1.54e-05
Fit parameter	**200 W/cm^2**	**Δ**	**400 W/cm^2**	**Δ**		
A_1	1.4	0.000933	1.55	0.00185		
t_1 (ps)	0.285	0.000132	0.26	0.000253		
A_2	0.277	0.000623	0.324	0.00371		
t_2 (ps)	1.77	0.0314	1.06	0.0189		
A_3	0.0439	6.38e-06	0.0285	5.35e-06		

Table S5: PIA dynamics fit results of (*R,R*)-ProSQ-C16.

Fit parameter	**20 W/cm^2**	**Δ**	**40 W/cm^2**	**Δ**	**80 W/cm^2**	**Δ**
A_1	1.14	0.0163	1.16	0.00269	1.17	0.0011
t_1 (ps)	0.348	0.00374	0.31	0.000619	0.357	0.000342
A_2	0.287	0.00345	0.347	0.00137	0.298	0.000538
t_2 (ps)	3.69	2.12	2.34	0.118	2.89	0.118
A_3	0.0263	0.000327	0.0473	3.46e-05	0.065	2.09e-05
Fit parameter	**200 W/cm^2**	**Δ**	**400 W/cm^2**	**Δ**		
A_1	1.18	0.000455	1.34	0.00108		
t_1 (ps)	0.347	0.000132	0.274	0.000148		
A_2	0.242	0.000219	0.268	0.000604		
t_2 (ps)	2.89	0.0773	1.83	0.0391		
A_3	0.0523	9.36e-06	0.0532	8.14e-06		

Table S6: PIA dynamics fit results of (*rac*)-ProSQ-C16.

Fit parameter	**20 W/cm^2**	**Δ**	**40 W/cm^2**	**Δ**	**80 W/cm^2**	**Δ**
A_1	0.775	0.00201	0.787	0.000498	0.877	0.000233
t_1 (ps)	0.827	0.0115	0.809	0.00298	0.66	0.000824
A_2	0.311	0.00232	0.272	0.000461	0.26	0.000202
t_2 (ps)	8.22	6.6	10.7	5.37	8.37	1.18
A_3	0.0928	0.000381	0.0824	0.000221	0.0821	5.73e-05
Fit parameter	**200 W/cm^2**	**Δ**	**400 W/cm^2**	**Δ**		
A_1	0.965	0.000347	1.08	0.000325		
t_1 (ps)	0.436	0.000262	0.443	0.000181		
A_2	0.259	0.000118	0.227	8.18e-05		
t_2 (ps)	5.39	0.254	6.25	0.365		
A_3	0.0724	2.21e-05	0.0642	2.18e-05		

S4 Singular Value Decomposition of (*R,R*)- and Racemic ProSQ-C16 Thin Films and Fit Results

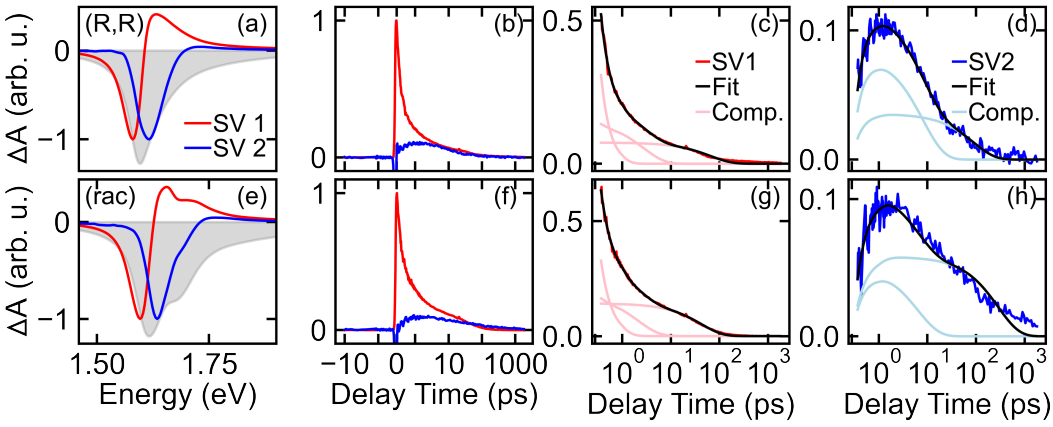


Figure S4: Spectra and dynamics of the two relevant singular values obtained from the transient absorption data of the (*R,R*)-ProSQ-C16 thin film (a-d) and the racemic thin film (e-h), in accordance with Fig. 5 in the main text. Note that the fitting function has been the same for all three samples, and that the racemic singular value dynamics yield a less matching fit to the model.

Table S7: Fit results of SV1

Data	A_1	t_1 (ps)	A_2	t_2 (ps)	A_3	t_3 (ps)
(*S,S*)	0.342	0.242	0.176	1.75	0.0796	57.1
Δ	0.007	0.009	0.007	0.12	0.0024	3.5
(*R,R*)	0.323	0.338	0.139	2.72	0.0735	65.1
Δ	0.006	0.011	0.006	0.23	0.0029	4.8
(*rac*)	0.339	0.399	0.165	2.13	0.141	42.4
Δ	0.013	0.018	0.012	0.23	0.004	1.9

Table S8: Fit results of SV2

Data	A_1	t_1 (ps)	A_2	t_2 (ps)	t_3 (ps)
(*S,S*)	0.133	0.364	0.524	0.452	50.2
Δ	0.004	0.021	0.095	0.046	7.2
(*R,R*)	0.118	0.344	0.817	0.3	90.7
Δ	0.002	0.015	0.087	0.037	16.6
(*rac*)	0.11	0.432	0.64	0.53	286
Δ	0.004	0.032	0.122	0.024	30

References

(1) Zablocki, J.; Schulz, M.; Schnakenburg, G.; Beverina, L.; Warzanowski, P.; Revelli, A.; Grüninger, M.; Balzer, F.; Meerholz, K.; Lützen, A.; Schiek, M. Structure and Dielectric Properties of Anisotropic n-Alkyl Anilino Squaraine Thin Films. *J. Phys. Chem. C* **2020**, *124*, 22721–22732.

(2) Schulz, M.; Zablocki, J.; Abdullaeva, O. S.; Brück, S.; Balzer, F.; Lützen, A.; Arteaga, O.; Schiek, M. Giant intrinsic circular dichroism of prolinol-derived squaraine thin films. *Nat. Commun.* **2018**, *9*, 2413.

(3) Arteaga, O.; Ossikovski, R. Complete Mueller matrix from a partial polarimetry experiment: the 12-element case. *J. Opt. Soc. Am. A* **2019**, *36*, 416–427.

APPENDIX G

From Proline to Indoline: Extending π-Conjugation for Enhancing Optical Properties and π-π-Interactions

G.1 Additional Spectra in Solution and Thin Film

Aggregated Solutions:

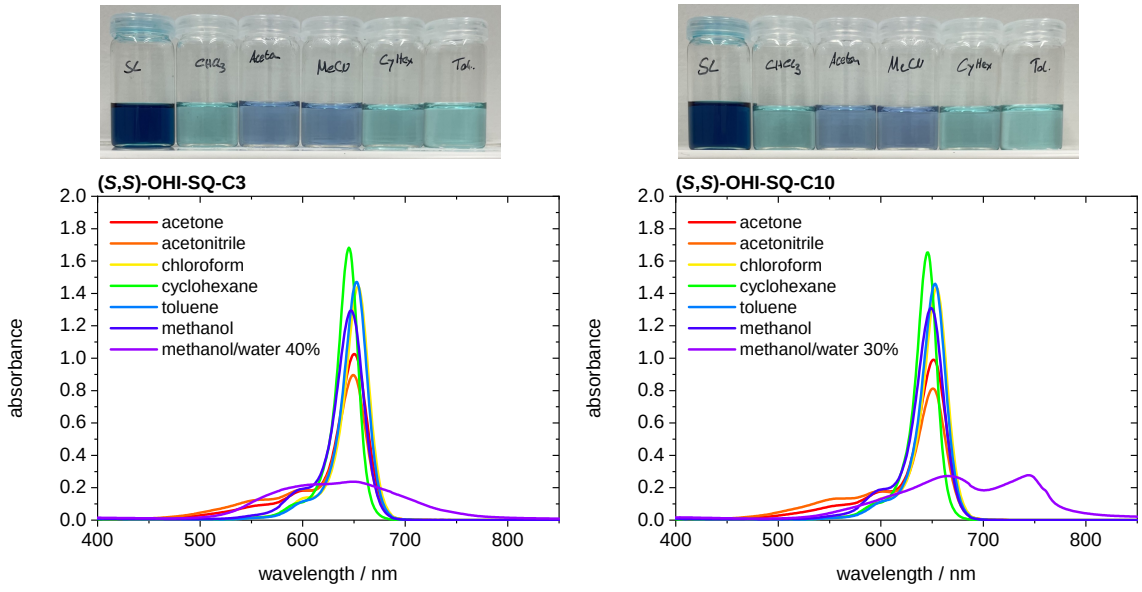


Figure G.1: UV/Vis absorbance spectra of **(*S*,*S*)-OHI-SQ-C3** (bottom left) and **(*S*,*S*)-OHI-SQ-C10** (bottom right) in different solvents and corresponding pictures of the visible changes in color (top). The solutions were prepared from a chloroform stock solution (c = 2.31 × 10^{-4} M) and therefore contain an additional 1.7% chloroform (50 µL in 3 mL) with an final concentration of the sample of c = 3.84 µM.

Thermally Annealed Thin Films:

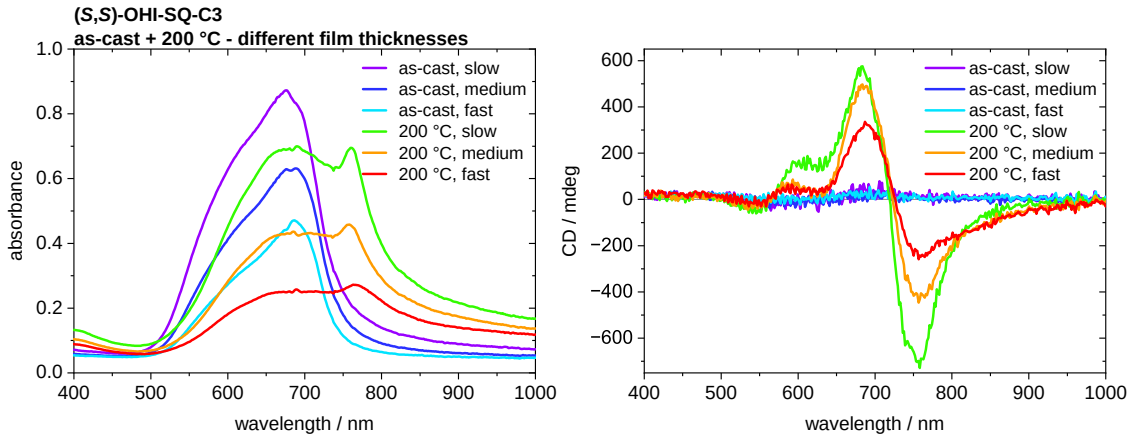


Figure G.2: UV/Vis absorbance (left) and corresponding CD spectra (right) of as-cast and thermally annealed **(*S*,*S*)-OHI-SQ-C3** thin films with varying thickness. Thin films were prepared by spin coating 120 µL of a chloroform solution with a dye concentration of 6 mg squaraine per mL, for 60 s at different rotation speeds and acceleration (1500 rpm, 750 rpm/s (slow); 3000 rpm, 3000 rpm/s (medium); 6000 rpm, 6000 rpm/s (fast)) on the glass substrate and – if noted – subsequent thermally annealed at 200 °C for 30 minutes.

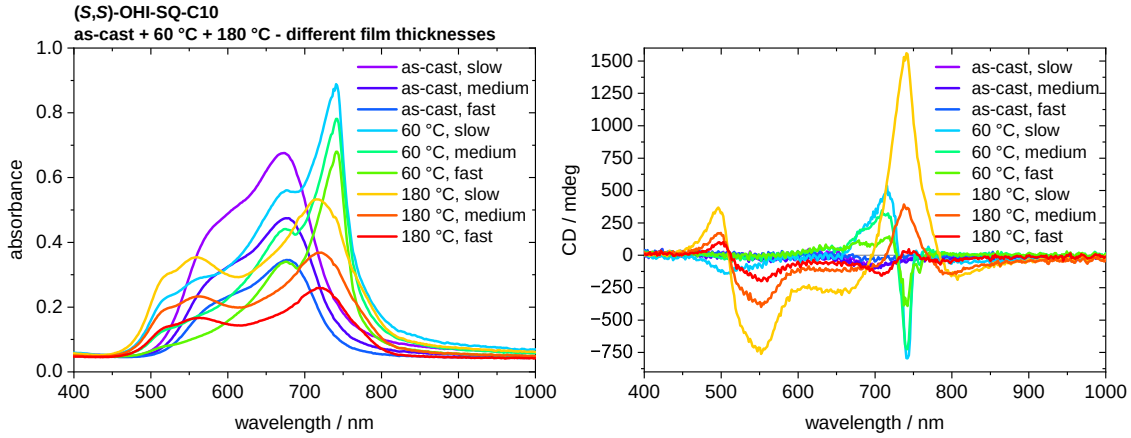


Figure G.3: UV/Vis absorbance (left) and corresponding CD spectra (right) of as-cast and thermally annealed **(*S*,*S*)-OHI-SQ-C10** thin films with varying thickness. Thin films were prepared by spin coating 120 µL of a chloroform solution with a dye concentration of 6 mg squaraine per mL, for 60 s at different rotation speeds and acceleration (1500 rpm, 750 rpm/s (slow); 3000 rpm, 3000 rpm/s (medium); 6000 rpm, 6000 rpm/s (fast)) on the glass substrate and – if noted – subsequent thermally annealed at 60 °C or 180 °C for 30 minutes.

G.2 Additional Information on Single-Crystal Structure

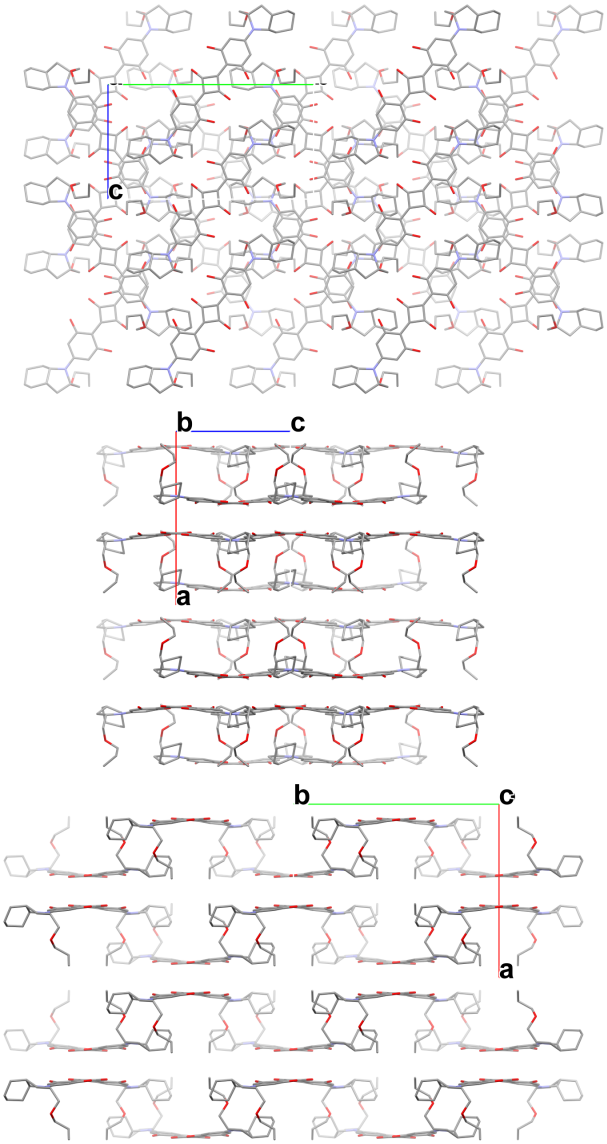


Figure G.4: Crystal structure of **(*S*,*S*)-OHI-SQ-C3** in a 2×2×2 unit cell (orthorhombic, space group = $C222_1$, a = 16.4987(6) Å, b = 19.5419(7) Å, c = 10.8616(3) Å, α = 90°, β = 90°, γ = 90° and Z = 4). Hydrogen was removed and depth perception was activated for clarity. Nitrogen is represented by blue, carbon by gray and oxygen by red.

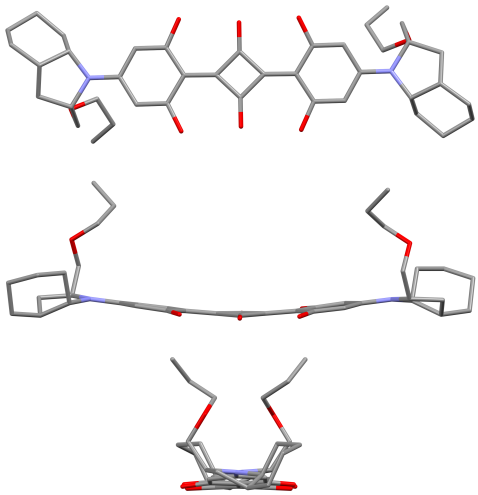


Figure G.5: Molecular geometry of **(*S*,*S*)-OHI-SQ-C3** from the orthorhombic crystal structure.

7912

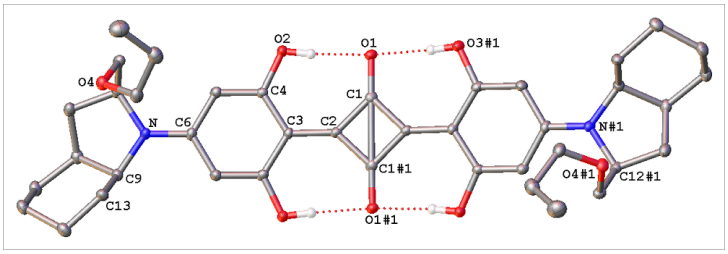


Table 1 Crystal data and structure refinement for 7912.

Identification code	GLUE259, MFS-143 // GXray7912
Crystal Habitus	metallic yellowish brown plank
Device Type	STOE STADIVARI
Empirical formula	$C_{40}H_{52}N_2O_8$
Moiety formula	C40 H52 N2 O8
Formula weight	688.85
Temperature/K	100
Crystal system	orthorhombic
Space group	$C222_1$
a/Å	16.4987(6)
b/Å	19.5419(7)
c/Å	10.8616(3)
α/°	90.00
β/°	90.00
γ/°	90.00
Volume/Å^3	3501.96(20)
Z	4
ρ_{calc}g/cm^3	1.307
μ/mm^{-1}	0.73
F(000)	1480.0
Crystal size/mm^3	0.2 × 0.04 × 0.03
Absorption correction	multi-scan
Tmin; Tmax	0.8133; 0.9187
Radiation	CuKα (λ = 1.54186)
2Θ range for data collection/°	7.012 to 141.226°
Completeness to theta	0.999
Index ranges	$-20 \le h \le 19$, $-23 \le k \le 23$, $-5 \le l \le 12$
Reflections collected	48012
Independent reflections	3345 [R_{int} = 0.0841, R_{sigma} = 0.0295]
Data/restraints/parameters	3345/0/229
Goodness-of-fit on F^2	1.086
Final R indexes [I>=2σ (I)]	R_1 = 0.0355, wR_2 = 0.0773
Final R indexes [all data]	R_1 = 0.0476, wR_2 = 0.0850
Largest diff. peak/hole / e Å^{-3}	0.19/-0.20
Flack parameter	-0.10(12)

Table 2 Bond Lengths for 7912.

Atom	Atom	Length/Å	Atom	Atom	Length/Å
O1	C1	1.256(3)	C5	C6	1.416(4)
O2	C4	1.363(3)	C6	C7	1.421(4)
O3	C8	1.353(3)	C7	C8	1.367(4)
O4	C17	1.427(3)	C9	C10	1.540(4)
O4	C18	1.426(3)	C9	C13	1.532(4)
N	C6	1.354(3)	C10	C11	1.525(4)
N	C9	1.472(3)	C10	C16	1.539(4)
N	C12	1.490(3)	C11	C12	1.527(4)
C1	C1[1]	2.013(5)	C12	C17	1.525(4)
C1	C2	1.459(4)	C13	C14	1.532(4)
C1	C2[1]	1.449(4)	C14	C15	1.527(4)
C2	C3	1.410(4)	C15	C16	1.529(4)
C3	C4	1.433(4)	C18	C19	1.499(5)
C3	C8	1.442(4)	C19	C20	1.510(5)
C4	C5	1.363(4)			

[1]+X,1-Y,-Z

Table 3 Bond Angles for 7912.

Atom	Atom	Atom	Angle/°	Atom	Atom	Atom	Angle/°
C18	O4	C17	114.0(2)	C5	C6	C7	118.7(2)
C6	N	C9	124.2(2)	C8	C7	C6	120.6(2)
C6	N	C12	123.7(2)	O3	C8	C3	122.0(2)
C9	N	C12	111.3(2)	O3	C8	C7	116.2(2)
O1	C1	C1[1]	177.39(15)	C7	C8	C3	121.8(2)
O1	C1	C2	133.9(2)	N	C9	C10	102.2(2)
O1	C1	C2[1]	133.8(2)	N	C9	C13	111.8(2)
C2[1]	C1	C1[1]	46.39(15)	C13	C9	C10	113.0(2)
C2	C1	C1[1]	46.00(14)	C11	C10	C9	102.4(2)
C2[1]	C1	C2	92.3(2)	C11	C10	C16	116.3(2)
C1[1]	C2	C1	87.6(2)	C16	C10	C9	114.1(2)
C3	C2	C1	136.5(2)	C10	C11	C12	104.7(2)
C3	C2	C1[1]	135.8(2)	N	C12	C11	103.7(2)
C2	C3	C4	121.6(2)	N	C12	C17	113.7(2)
C2	C3	C8	122.7(2)	C17	C12	C11	112.7(2)
C4	C3	C8	115.7(2)	C9	C13	C14	111.4(2)
O2	C4	C3	121.9(2)	C15	C14	C13	109.9(2)
O2	C4	C5	115.4(2)	C14	C15	C16	110.0(2)
C5	C4	C3	122.6(2)	C15	C16	C10	113.4(2)
C4	C5	C6	120.4(2)	O4	C17	C12	111.9(2)
N	C6	C5	120.3(2)	O4	C18	C19	113.4(3)
N	C6	C7	121.0(2)	C18	C19	C20	113.1(3)

[1]+X,1-Y,-Z

APPENDIX **H**

From the Idea to the Device – 2-Methylbutyl-Derived Anilino Squaraines

H.1 Synthesis

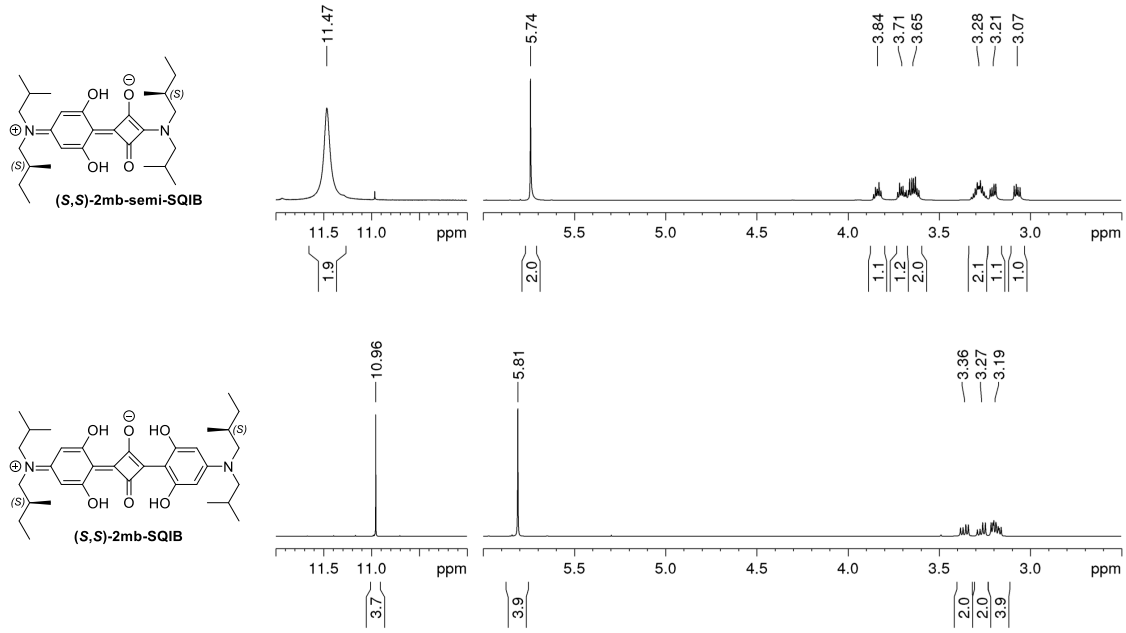


Figure H.1: Selected ^{1}H-NMR spectral region of **(*S*,*S*)-2mb-semi-SQIB** (top) and **(*S*,*S*)-2mb-SQIB** (bottom). Measured at 500 MHz, Chloroform-*d*, 298 K.

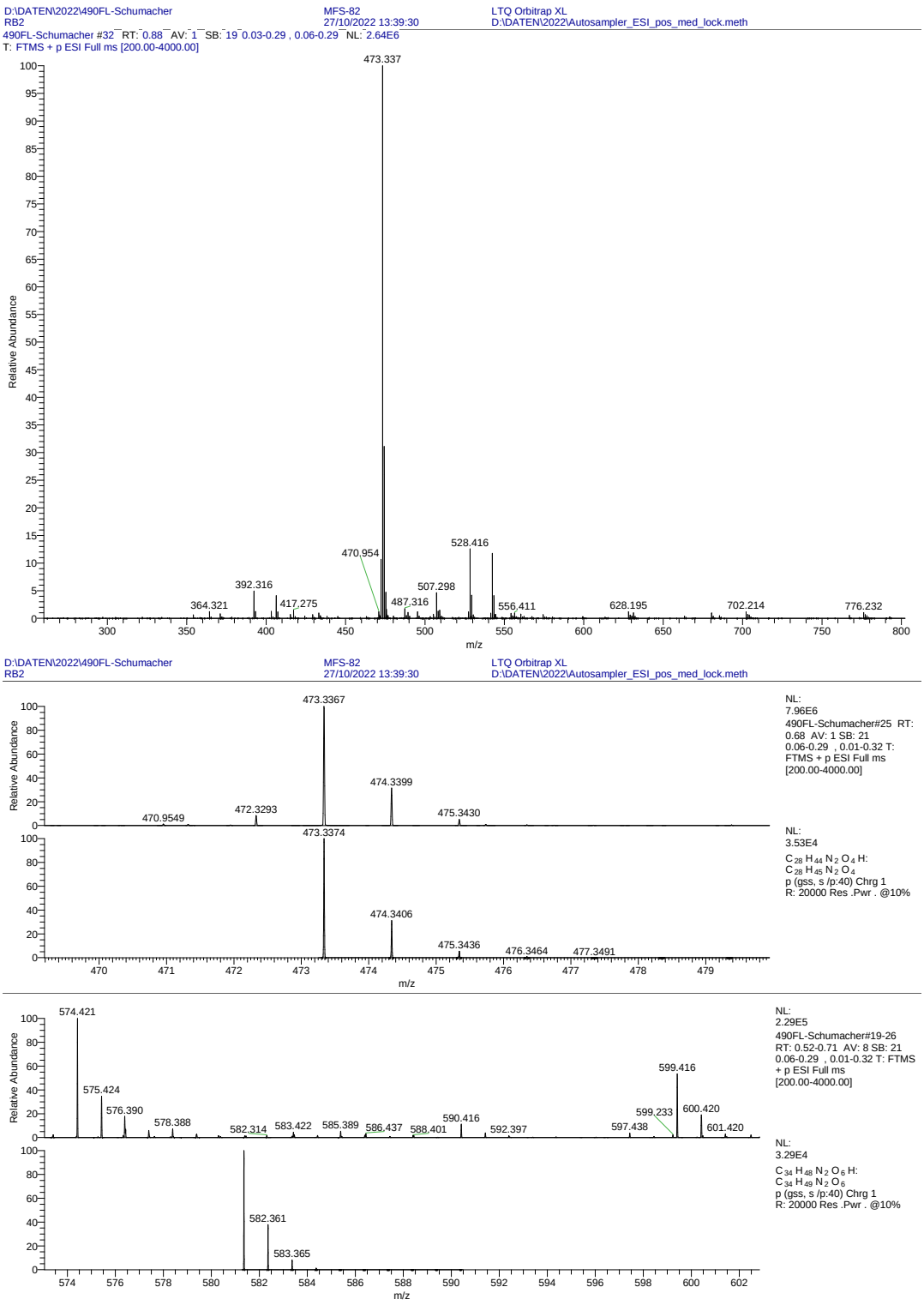


Figure H.2: ESI(+) Mass spectra of **(*S*,*S*)-2mb-semi-SQIB** ($[M+H]^+ = C_{28}H_{44}N_2O_4H = 473.3374$ m).

H.2 Additional Information on Single-Crystal Structures

(*S*,*S*)-2mb-SQIB:

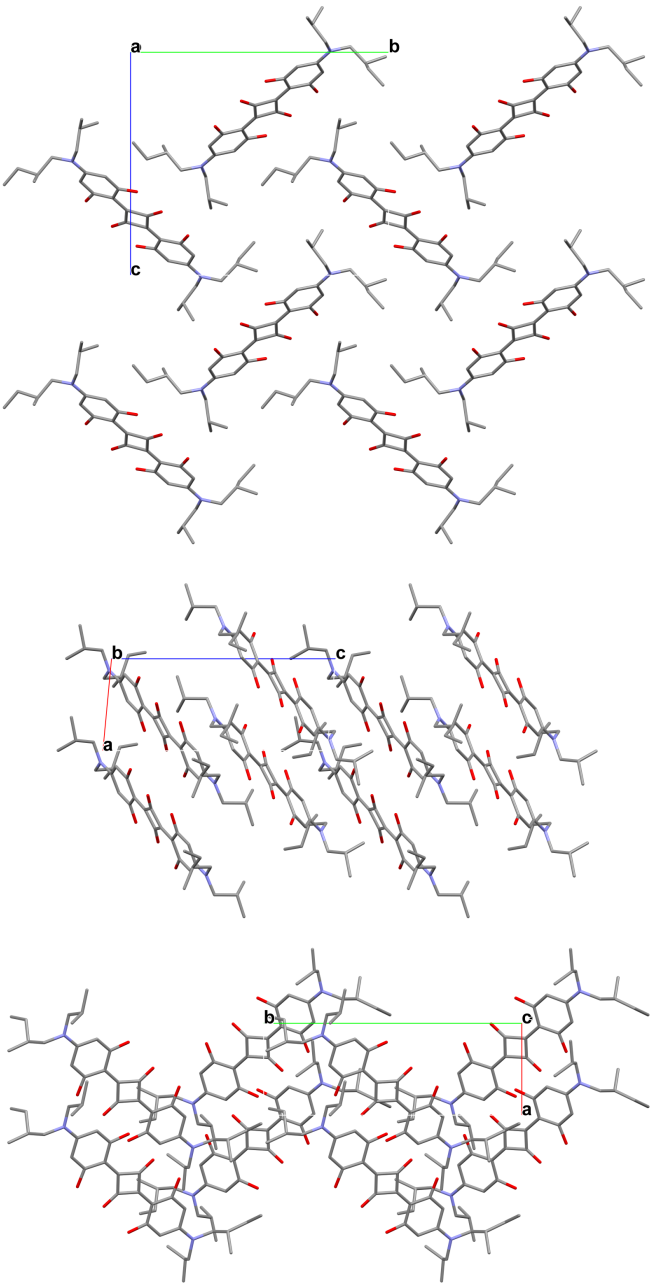


Figure H.3: Crystal structure of **(*S*,*S*)-2mb-SQIB** in a 2×2×2 unit cell (monoclinic, space group = $P2_1$, a = 6.1340(2) Å, b = 17.1614(4) Å, c = 14.9058(5) Å, α = 90°, β = 95.361(2)°, γ = 90° and Z = 2). Hydrogen was removed for clarity. Nitrogen is represented by blue, carbon by gray and oxygen by red. Top image: View of the unit cell along the a-axis. Middle image: View of the unit cell along the b-axis. Bottom image: View of the unit cell along the c-axis.

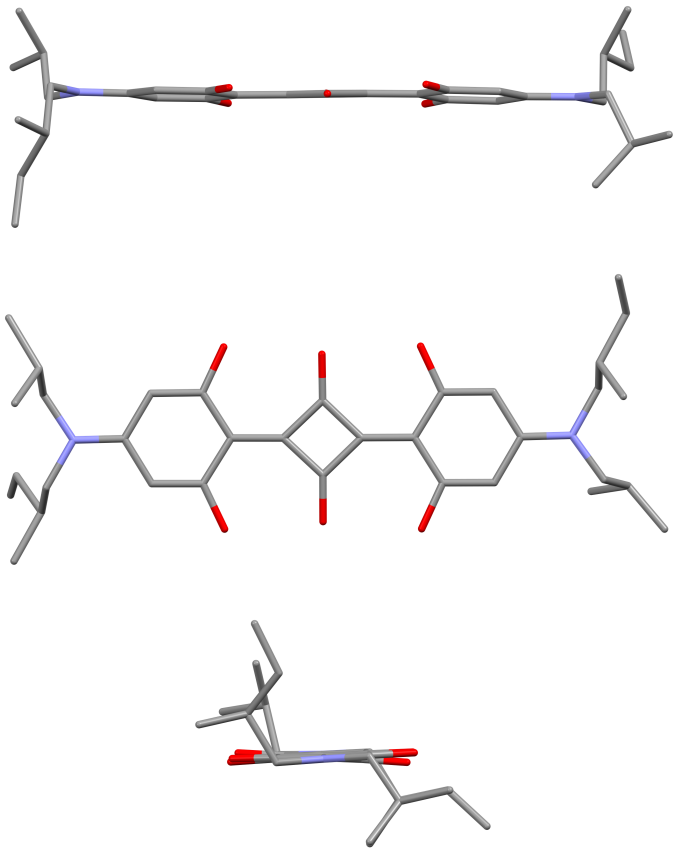


Figure H.4: Molecular geometry of **(*S*,*S*)-2mb-SQIB** from the monoclinic crystal structure.

7104

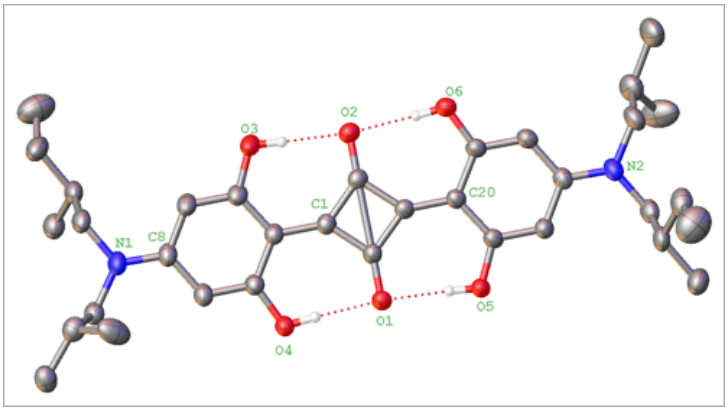


Table 1 Crystal data and structure refinement for 7104.

Identification code	MFS-70 // GXray7104
Crystal Habitus	clear greenish violet needle
Device Type	STOE STADIVARI
Empirical formula	$C_{34}H_{48}N_2O_6$
Moiety formula	C34 H48 N2 O6
Formula weight	580.74
Temperature/K	100(2)
Crystal system	monoclinic
Space group	$P2_1$
a/Å	6.1340(2)
b/Å	17.1614(4)
c/Å	14.9058(5)
α/°	90
β/°	95.361(2)
γ/°	90
Volume/Å^3	1562.24(8)
Z	2
ρ_{calc}g/cm^3	1.235
μ/mm^{-1}	0.673
F(000)	628.0
Crystal size/mm^3	0.4 × 0.15 × 0.02
Absorption correction	multi-scan
Tmin; Tmax	0.6079; 0.9748
Radiation	Cu Kα (λ = 1.54186)
2Θ range for data collection/°	5.956 to 141.476°
Completeness to theta	0.995
Index ranges	$-7 \le h \le 4$, $-20 \le k \le 19$, $-18 \le l \le 18$
Reflections collected	42828
Independent reflections	5441 [R_{int} = 0.0270, R_{sigma} = 0.0142]
Data/restraints/parameters	5441/352/422
Goodness-of-fit on F^2	1.049

Final R indexes [I>=2σ (I)]	R_1 = 0.0562, wR_2 = 0.1576
Final R indexes [all data]	R_1 = 0.0613, wR_2 = 0.1661
Largest diff. peak/hole / e Å^{-3}	0.62/-0.33
Flack parameter	0.2(2)

Table 2 Bond Lengths for 7104.

Atom	Atom	Length/Å	Atom	Atom	Length/Å
O1	C2	1.262(5)	C9	C10	1.381(6)
O2	C4	1.252(5)	C11	C12	1.519(7)
O3	C6	1.358(5)	C12	C13	1.532(6)
O4	C10	1.356(5)	C12	C15	1.533(6)
O5	C21	1.351(5)	C13	C14	1.443(9)
O6	C25	1.347(5)	C16	C17	1.523(6)
N1	C8	1.358(5)	C17	C18	1.519(6)
N1	C11	1.473(6)	C17	C19	1.505(7)
N1	C16	1.464(5)	C20	C21	1.443(6)
N2	C23	1.360(5)	C20	C25	1.444(5)
N2	C26	1.465(6)	C21	C22	1.371(5)
N2	C31	1.469(5)	C22	C23	1.413(5)
C1	C2	1.449(6)	C23	C24	1.413(6)
C1	C4	1.450(5)	C24	C25	1.376(6)
C1	C5	1.415(6)	C26	C27	1.531(7)
C2	C3	1.457(5)	C27	C28	1.541(6)
C2	C4	2.017(4)	C27	C30	1.518(7)
C3	C4	1.467(6)	C28	C29	1.483(9)
C3	C20	1.393(5)	C31	C32	1.462(10)
C5	C6	1.421(6)	C31	C32A	1.654(15)
C5	C10	1.437(5)	C32	C33	1.504(13)
C6	C7	1.373(6)	C32	C34	1.585(11)
C7	C8	1.417(6)	C32A	C33A	1.532(16)
C8	C9	1.423(6)	C32A	C34A	1.57(3)

Table 3 Bond Angles for 7104.

Atom	Atom	Atom	Angle/°	Atom	Atom	Atom	Angle/°
C8	N1	C11	120.8(4)	C9	C10	C5	122.2(4)
C8	N1	C16	124.2(4)	N1	C11	C12	114.8(4)
C16	N1	C11	115.0(3)	C11	C12	C13	107.0(4)
C23	N2	C26	121.3(4)	C11	C12	C15	112.9(4)
C23	N2	C31	122.0(4)	C13	C12	C15	111.8(4)
C26	N2	C31	116.7(4)	C14	C13	C12	115.6(5)
C2	C1	C4	88.2(3)	N1	C16	C17	114.2(3)
C5	C1	C2	135.9(4)	C18	C17	C16	108.5(3)
C5	C1	C4	135.9(4)	C19	C17	C16	113.7(4)
O1	C2	C1	134.1(4)	C19	C17	C18	112.3(4)
O1	C2	C3	133.4(4)	C3	C20	C21	121.9(3)
O1	C2	C4	179.6(3)	C3	C20	C25	122.6(4)
C1	C2	C3	92.5(3)	C21	C20	C25	115.5(3)
C1	C2	C4	45.9(2)	O5	C21	C20	122.5(4)
C3	C2	C4	46.6(2)	O5	C21	C22	115.6(4)
C2	C3	C4	87.2(3)	C22	C21	C20	121.8(4)
C20	C3	C2	136.8(4)	C21	C22	C23	121.6(4)
C20	C3	C4	136.0(4)	N2	C23	C22	120.2(4)
O2	C4	C1	134.7(4)	N2	C23	C24	122.0(4)
O2	C4	C2	178.7(3)	C24	C23	C22	117.8(4)
O2	C4	C3	133.2(4)	C25	C24	C23	121.4(4)
C1	C4	C2	45.9(2)	O6	C25	C20	122.2(4)
C1	C4	C3	92.1(3)	O6	C25	C24	115.9(3)
C3	C4	C2	46.2(2)	C24	C25	C20	121.8(4)
C1	C5	C6	121.9(4)	N2	C26	C27	115.6(3)
C1	C5	C10	122.0(4)	C26	C27	C28	110.9(4)
C6	C5	C10	116.1(4)	C30	C27	C26	108.4(4)
O3	C6	C5	123.2(4)	C30	C27	C28	113.1(4)
O3	C6	C7	114.8(4)	C29	C28	C27	115.8(5)
C7	C6	C5	122.0(4)	N2	C31	C32A	108.3(6)
C6	C7	C8	121.5(4)	C32	C31	N2	117.7(5)
N1	C8	C7	120.3(4)	C31	C32	C33	108.9(8)
N1	C8	C9	121.9(4)	C31	C32	C34	110.4(7)
C7	C8	C9	117.8(4)	C33	C32	C34	111.7(7)
C10	C9	C8	120.4(4)	C33A	C32A	C31	107.7(10)
O4	C10	C5	122.9(4)	C33A	C32A	C34A	109.1(14)
O4	C10	C9	114.9(4)	C34A	C32A	C31	112.4(13)

Table 4 Torsion Angles for 7104.

A	B	C	D	Angle/°	A	B	C	D	Angle/°
O1	C2	C3	C4	-179.4(4)	C5	C1	C4	C3	178.2(4)
O1	C2	C3	C20	1.8(8)	C5	C6	C7	C8	-0.7(6)
O3	C6	C7	C8	179.4(4)	C6	C5	C10	O4	179.9(3)
O5	C21	C22	C23	179.7(4)	C6	C5	C10	C9	0.5(6)
N1	C8	C9	C10	178.5(4)	C6	C7	C8	N1	-178.2(4)
N1	C11	C12	C13	-177.3(4)	C6	C7	C8	C9	1.2(6)
N1	C11	C12	C15	59.2(5)	C7	C8	C9	C10	-0.9(6)
N1	C16	C17	C18	173.4(4)	C8	N1	C11	C12	75.6(5)
N1	C16	C17	C19	-60.9(6)	C8	N1	C16	C17	104.9(5)
N2	C23	C24	C25	179.2(4)	C8	C9	C10	O4	-179.4(4)
N2	C26	C27	C28	-57.1(5)	C8	C9	C10	C5	0.0(6)
N2	C26	C27	C30	178.2(3)	C10	C5	C6	O3	179.7(4)
N2	C31	C32	C33	-61.4(9)	C10	C5	C6	C7	-0.2(6)
N2	C31	C32	C34	175.6(5)	C11	N1	C8	C7	0.1(6)
N2	C31	C32A	C33A	-175.2(11)	C11	N1	C8	C9	-179.3(4)
N2	C31	C32A	C34A	64.7(15)	C11	N1	C16	C17	-72.9(5)
C1	C2	C3	C4	-0.5(3)	C11	C12	C13	C14	162.7(5)
C1	C2	C3	C20	-179.4(4)	C15	C12	C13	C14	-73.2(6)
C1	C5	C6	O3	1.5(6)	C16	N1	C8	C7	-177.6(4)
C1	C5	C6	C7	-178.5(4)	C16	N1	C8	C9	3.0(6)
C1	C5	C10	O4	-1.8(6)	C16	N1	C11	C12	-106.5(4)
C1	C5	C10	C9	178.8(4)	C20	C3	C4	O2	0.4(8)
C2	C1	C4	O2	178.4(4)	C20	C3	C4	C1	179.4(4)
C2	C1	C4	C3	-0.5(3)	C20	C3	C4	C2	178.8(6)
C2	C1	C5	C6	172.5(4)	C20	C21	C22	C23	0.6(6)
C2	C1	C5	C10	-5.7(7)	C21	C20	C25	O6	-178.5(3)
C2	C3	C4	O2	-178.4(4)	C21	C20	C25	C24	0.4(5)
C2	C3	C4	C1	0.5(3)	C21	C22	C23	N2	-179.8(4)
C2	C3	C20	C21	3.8(7)	C21	C22	C23	C24	0.4(6)
C2	C3	C20	C25	-177.1(4)	C22	C23	C24	C25	-1.0(6)
C3	C20	C21	O5	-0.9(6)	C23	N2	C26	C27	-78.7(5)
C3	C20	C21	C22	178.2(4)	C23	N2	C31	C32	-77.4(6)
C3	C20	C25	O6	2.4(6)	C23	N2	C31	C32A	-111.2(9)
C3	C20	C25	C24	-178.8(4)	C23	C24	C25	O6	179.5(4)
C4	C1	C2	O1	179.4(4)	C23	C24	C25	C20	0.6(6)
C4	C1	C2	C3	0.6(3)	C25	C20	C21	O5	-180.0(4)
C4	C1	C5	C6	-5.8(7)	C25	C20	C21	C22	-1.0(5)
C4	C1	C5	C10	176.0(4)	C26	N2	C23	C22	1.8(6)
C4	C2	C3	C20	-178.8(6)	C26	N2	C23	C24	-178.4(4)
C4	C3	C20	C21	-174.5(4)	C26	N2	C31	C32	103.4(6)
C4	C3	C20	C25	4.6(7)	C26	N2	C31	C32A	69.5(9)
C5	C1	C2	O1	0.6(8)	C26	C27	C28	C29	179.0(5)
C5	C1	C2	C3	-178.2(4)	C30	C27	C28	C29	-59.0(6)
C5	C1	C2	C4	-178.8(6)	C31	N2	C23	C22	-177.4(4)
C5	C1	C4	O2	-2.8(8)	C31	N2	C23	C24	2.4(6)
C5	C1	C4	C2	178.8(6)	C31	N2	C26	C27	100.6(4)

H.2.1 (*S*,*S*)-2mb-SQPE:

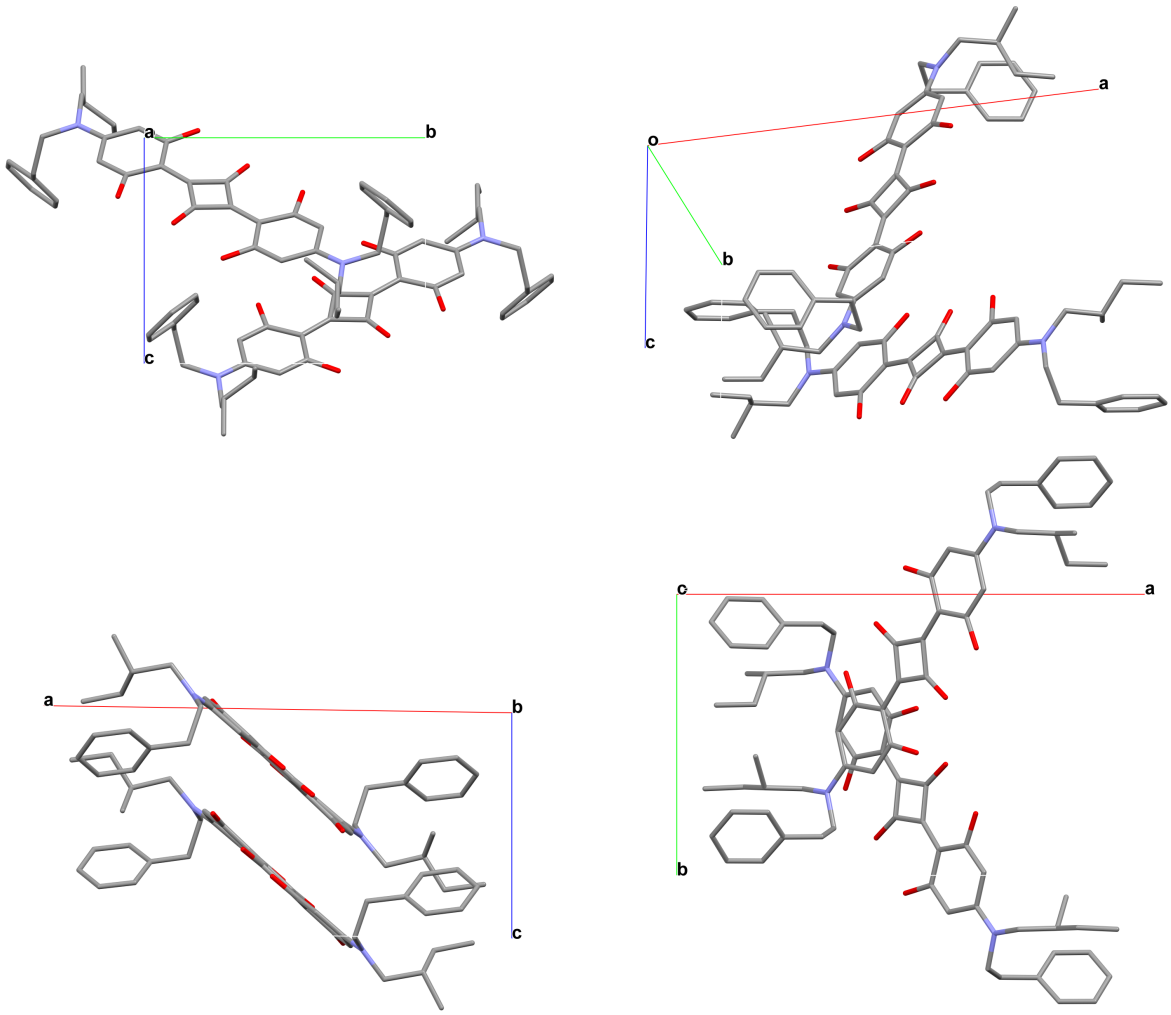


Figure H.5: Crystal structure of **(*S*,*S*)-2mb-SQPE** (monoclinic, space group = $P2_1$, a = 18.1776(10) Å, b = 10.9141(4) Å, c = 8.7563(5) Å, α = 90°, β = 90.869(4)°, γ = 90° and Z = 2). Hydrogen was removed for clarity. Nitrogen is represented by blue, carbon by gray and oxygen by red. Top left image: View of the unit cell along the a-axis. Top right image: View of the unit cell along no specific axis. Bottom left image: View of the unit cell along the b-axis. Bottom right image: View of the unit cell along the c-axis.

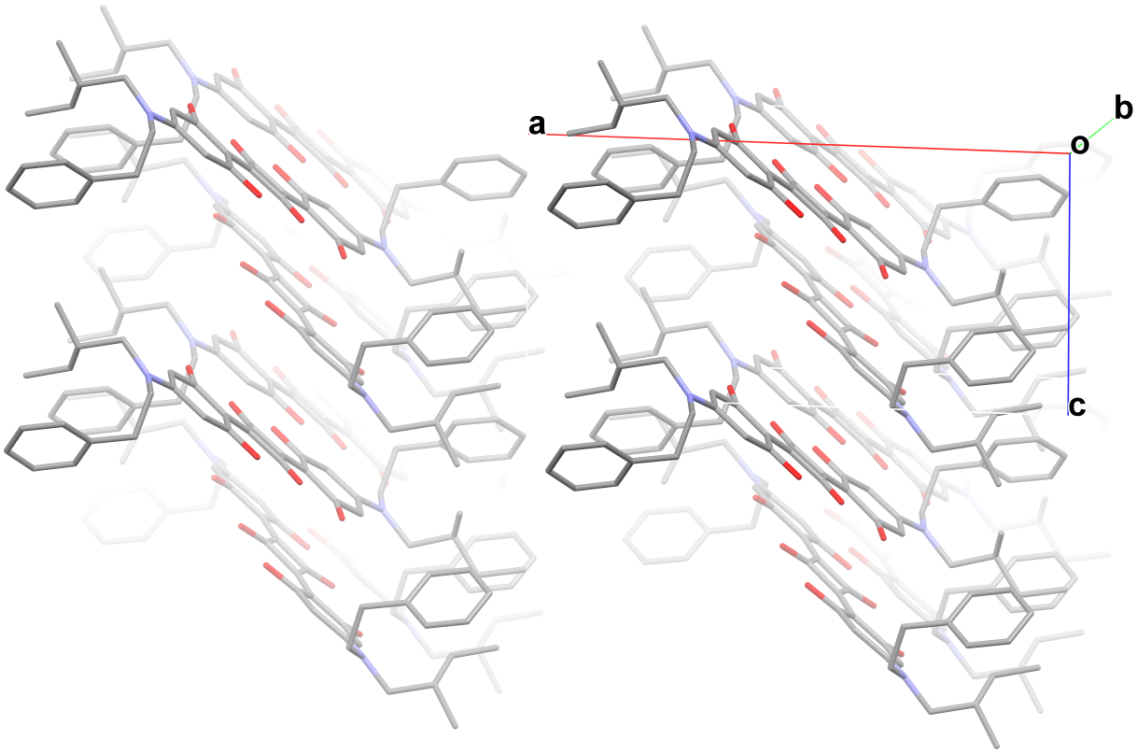


Figure H.6: Visualization of the dimers in the crystal structure of monoclinic **(*S*,*S*)-2mb-SQPE** in a 2×2×2 unit cell. Hydrogen was removed and depth perception was activated for clarity. Nitrogen is represented by blue, carbon by gray and oxygen by red.

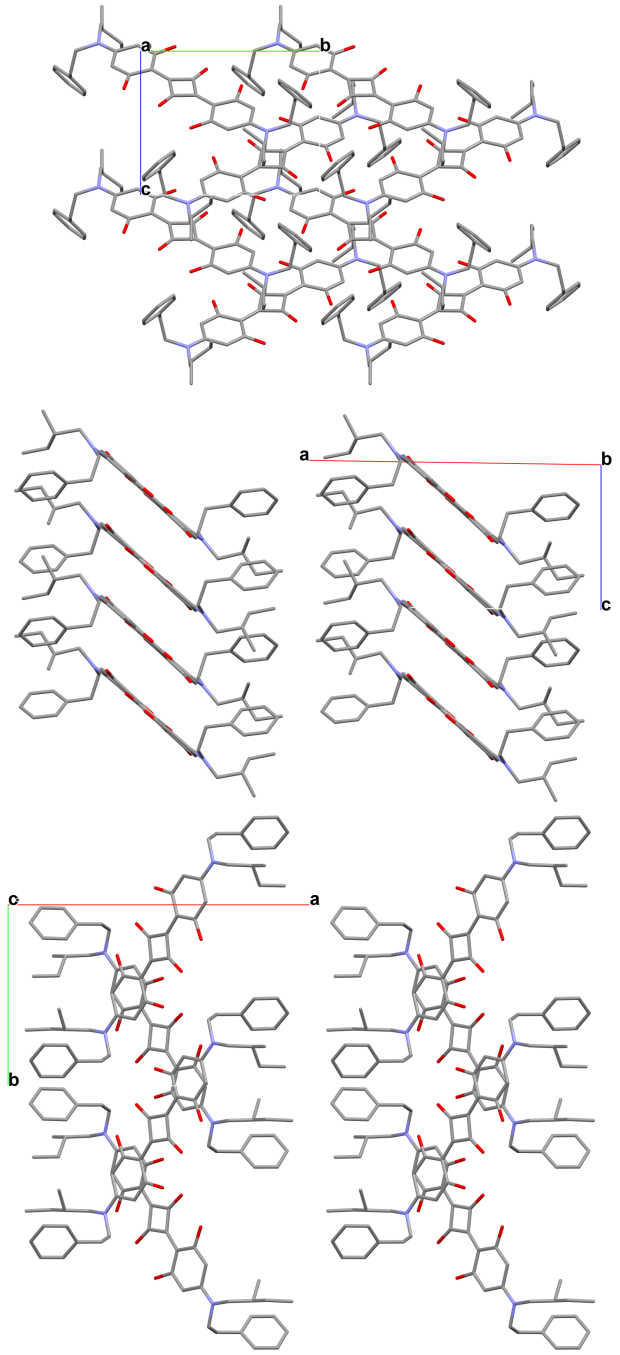


Figure H.7: Crystal structure of **(*S*,*S*)-2mb-SQPE** in a 2×2×2 unit cell (monoclinic, space group = $P2_1$, a = 18.1776(10) Å, b = 10.9141(4) Å, c = 8.7563(5) Å, α = 90°, β = 90.869(4)°, γ = 90° and Z = 2). Hydrogen was removed and depth perception was activated for clarity. Nitrogen is represented by blue, carbon by gray and oxygen by red. Top image: View of the unit cell along the a-axis. Middle image: View of the unit cell along the b-axis. Bottom image: View of the unit cell along the c-axis.

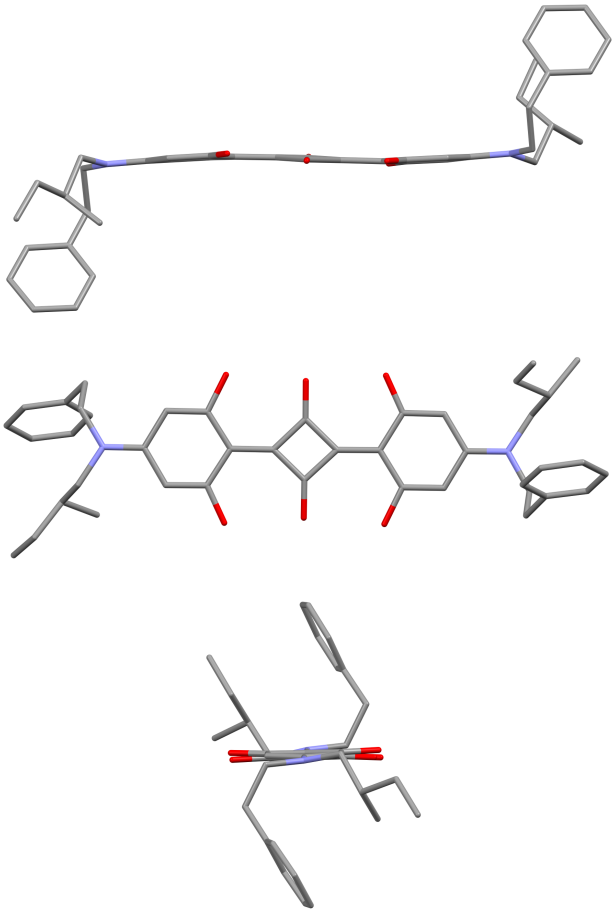


Figure H.8: Molecular geometry of **(*S*,*S*)-2mb-SQPE** from the monoclinic crystal structure.

8516

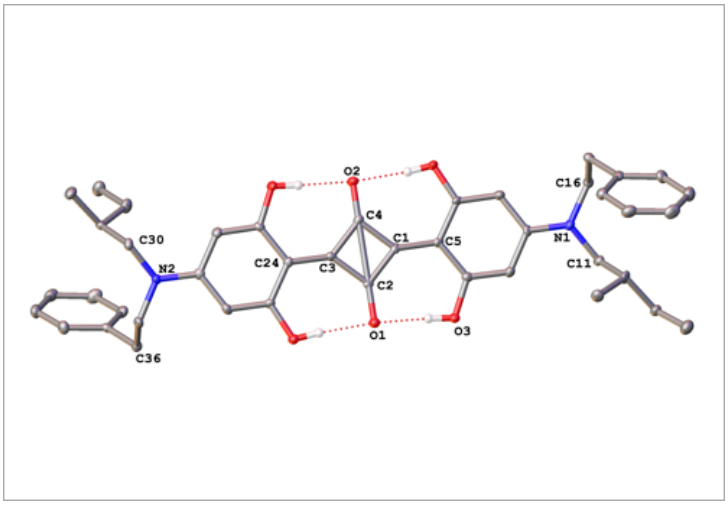


Table 1 Crystal data and structure refinement for 8516.

Identification code	GLUE273, MFS-179 #1 // GXray8516_3dn
Crystal Habitus	clear green plate
Device Type	STOE STADIVARI
Empirical formula	$C_{42}H_{48}N_2O_6$
Moiety formula	C42 H48 N2 O6
Formula weight	676.82
Temperature/K	100
Crystal system	monoclinic
Space group	$P2_1$
a/Å	18.1776(10)
b/Å	10.9141(4)
c/Å	8.7563(5)
α/°	90
β/°	90.869(4)
γ/°	90
Volume/Å^3	1736.98(15)
Z	2
ρ_{calc}g/cm^3	1.294
μ/mm^{-1}	0.688
F(000)	724.0
Crystal size/mm^3	0.22 × 0.14 × 0.02
Absorption correction	multi-scan
Tmin; Tmax	0.5201; 0.9503
Radiation	Cu Kα (λ = 1.54186)
2Θ range for data collection/°	9.452 to 141.02°
Completeness to theta	0.998
Index ranges	-22 ≤ h ≤ 20, -4 ≤ k ≤ 12, -10 ≤ l ≤ 10
Reflections collected	20351

Independent reflections	4193 [R_{int} = 0.0629, R_{sigma} = 0.0487]
Data/restraints/parameters	4193/2/460
Goodness-of-fit on F^2	1.043
Final R indexes [I>=2σ (I)]	R_1 = 0.0493, wR_2 = 0.1137
Final R indexes [all data]	R_1 = 0.0788, wR_2 = 0.1315
Largest diff. peak/hole / e $Å^{-3}$	0.27/-0.21
Flack parameter	0.3(6)

Table 2 Bond Lengths for 8516.

Atom	Atom	Length/Å	Atom	Atom	Length/Å
O1	C2	1.255(9)	C13	C14	1.535(8)
O2	C4	1.257(9)	C16	C17	1.558(8)
O3	C6	1.356(10)	C17	C18	1.498(9)
O4	C10	1.362(8)	C18	C19	1.391(11)
O5	C25	1.353(8)	C18	C23	1.400(11)
O6	C29	1.343(10)	C19	C20	1.386(10)
N1	C8	1.354(10)	C20	C21	1.387(12)
N1	C11	1.487(8)	C21	C22	1.382(12)
N1	C16	1.465(11)	C22	C23	1.382(10)
N2	C27	1.370(10)	C24	C25	1.435(12)
N2	C30	1.466(8)	C24	C29	1.443(9)
N2	C35	1.475(10)	C25	C26	1.374(10)
C1	C2	1.436(12)	C26	C27	1.417(10)
C1	C4	1.461(10)	C27	C28	1.415(12)
C1	C5	1.408(10)	C28	C29	1.371(11)
C2	C3	1.458(10)	C30	C31	1.533(9)
C2	C4	2.010(5)	C31	C32	1.517(11)
C3	C4	1.457(12)	C31	C34	1.542(9)
C3	C24	1.410(10)	C32	C33	1.514(8)
C5	C6	1.437(9)	C35	C36	1.527(8)
C5	C10	1.439(12)	C36	C37	1.506(9)
C6	C7	1.361(11)	C37	C38	1.392(10)
C7	C8	1.418(12)	C37	C42	1.396(10)
C8	C9	1.429(9)	C38	C39	1.391(10)
C9	C10	1.354(10)	C39	C40	1.381(12)
C11	C12	1.528(8)	C40	C41	1.391(11)
C12	C13	1.519(9)	C41	C42	1.382(10)
C12	C15	1.538(11)			

Table 3 Bond Angles for 8516.

Atom	Atom	Atom	Angle/°	Atom	Atom	Atom	Angle/°
C8	N1	C11	122.1(7)	C13	C12	C15	110.8(7)
C8	N1	C16	121.6(6)	C12	C13	C14	113.7(5)
C16	N1	C11	115.6(6)	N1	C16	C17	114.2(6)
C27	N2	C30	121.9(6)	C18	C17	C16	115.2(6)
C27	N2	C35	119.9(6)	C19	C18	C17	121.7(7)
C30	N2	C35	117.1(6)	C19	C18	C23	117.6(7)
C2	C1	C4	87.9(6)	C23	C18	C17	120.6(7)
C5	C1	C2	136.6(7)	C20	C19	C18	122.1(8)
C5	C1	C4	135.5(7)	C19	C20	C21	119.1(8)
O1	C2	C1	133.6(7)	C22	C21	C20	120.0(7)
O1	C2	C3	133.4(8)	C23	C22	C21	120.5(8)
O1	C2	C4	179.2(4)	C22	C23	C18	120.7(8)
C1	C2	C3	93.0(6)	C3	C24	C25	121.9(6)
C1	C2	C4	46.6(4)	C3	C24	C29	121.4(7)
C3	C2	C4	46.4(5)	C25	C24	C29	116.6(7)
C4	C3	C2	87.2(6)	O5	C25	C24	122.3(7)
C24	C3	C2	136.9(7)	O5	C25	C26	115.7(7)
C24	C3	C4	135.9(7)	C26	C25	C24	122.0(7)
O2	C4	C1	133.7(8)	C25	C26	C27	120.7(7)
O2	C4	C2	179.2(5)	N2	C27	C26	121.1(7)
O2	C4	C3	134.3(7)	N2	C27	C28	121.0(7)
C1	C4	C2	45.6(5)	C28	C27	C26	118.0(7)
C3	C4	C1	92.0(6)	C29	C28	C27	122.2(7)
C3	C4	C2	46.4(4)	O6	C29	C24	123.6(7)
C1	C5	C6	121.9(7)	O6	C29	C28	115.9(6)
C1	C5	C10	123.3(6)	C28	C29	C24	120.5(7)
C6	C5	C10	114.8(7)	N2	C30	C31	116.7(5)
O3	C6	C5	122.0(7)	C30	C31	C34	107.4(5)
O3	C6	C7	115.1(6)	C32	C31	C30	113.7(6)
C7	C6	C5	122.9(8)	C32	C31	C34	112.1(6)
C6	C7	C8	120.6(7)	C33	C32	C31	113.4(7)
N1	C8	C7	121.1(7)	N2	C35	C36	115.6(6)
N1	C8	C9	120.7(7)	C37	C36	C35	115.0(6)
C7	C8	C9	118.2(7)	C38	C37	C36	121.7(7)
C10	C9	C8	120.4(7)	C38	C37	C42	117.7(7)
O4	C10	C5	121.2(7)	C42	C37	C36	120.6(7)
C9	C10	O4	115.8(7)	C39	C38	C37	121.0(8)
C9	C10	C5	123.1(7)	C40	C39	C38	120.7(8)
N1	C11	C12	116.1(5)	C39	C40	C41	118.8(7)
C11	C12	C15	111.9(6)	C42	C41	C40	120.5(8)
C13	C12	C11	108.4(5)	C41	C42	C37	121.3(7)

Table 4 Torsion Angles for 8516.

A	B	C	D	Angle/°	A	B	C	D	Angle/°
O1	C2	C3	C4	179.0(5)	C10	C5	C6	O3	-177.7(6)
O1	C2	C3	C24	-2.4(14)	C10	C5	C6	C7	4.5(9)
O3	C6	C7	C8	-179.5(6)	C11	N1	C8	C7	11.7(9)
O5	C25	C26	C27	179.0(5)	C11	N1	C8	C9	-167.8(5)
N1	C8	C9	C10	-178.2(6)	C11	N1	C16	C17	-116.7(6)
N1	C11	C12	C13	-174.7(7)	C11	C12	C13	C14	175.6(7)
N1	C11	C12	C15	62.9(9)	C15	C12	C13	C14	-61.3(8)
N1	C16	C17	C18	68.1(9)	C16	N1	C8	C7	-178.1(6)
N2	C27	C28	C29	-177.6(6)	C16	N1	C8	C9	2.5(9)
N2	C30	C31	C32	-62.2(9)	C16	N1	C11	C12	86.1(8)
N2	C30	C31	C34	173.2(7)	C16	C17	C18	C19	64.6(11)
N2	C35	C36	C37	-66.0(9)	C16	C17	C18	C23	-113.4(8)
C1	C2	C3	C4	0.0(7)	C17	C18	C19	C20	-178.2(7)
C1	C2	C3	C24	178.6(6)	C17	C18	C23	C22	178.0(7)
C1	C5	C6	O3	2.9(9)	C18	C19	C20	C21	0.2(12)
C1	C5	C6	C7	-174.9(6)	C19	C18	C23	C22	-0.1(11)
C1	C5	C10	O4	-3.2(10)	C19	C20	C21	C22	-0.1(12)
C1	C5	C10	C9	175.2(6)	C20	C21	C22	C23	-0.1(12)
C2	C1	C4	O2	-179.5(6)	C21	C22	C23	C18	0.2(12)
C2	C1	C4	C3	0.0(7)	C23	C18	C19	C20	-0.1(11)
C2	C1	C5	C6	4.0(12)	C24	C3	C4	O2	0.8(14)
C2	C1	C5	C10	-175.4(7)	C24	C3	C4	C1	-178.6(6)
C2	C3	C4	O2	179.5(6)	C24	C3	C4	C2	-178.6(11)
C2	C3	C4	C1	0.0(7)	C24	C25	C26	C27	-0.2(10)
C2	C3	C24	C25	-3.4(12)	C25	C24	C29	O6	178.5(6)
C2	C3	C24	C29	-179.8(7)	C25	C24	C29	C28	-1.5(9)
C3	C24	C25	O5	6.0(10)	C25	C26	C27	N2	177.9(6)
C3	C24	C25	C26	-174.8(6)	C25	C26	C27	C28	-1.7(9)
C3	C24	C29	O6	-4.9(9)	C26	C27	C28	C29	1.9(10)
C3	C24	C29	C28	175.1(6)	C27	N2	C30	C31	104.3(8)
C4	C1	C2	O1	-179.0(5)	C27	N2	C35	C36	-73.8(8)
C4	C1	C2	C3	0.0(7)	C27	C28	C29	O6	179.7(6)
C4	C1	C5	C6	-179.3(7)	C27	C28	C29	C24	-0.3(10)
C4	C1	C5	C10	1.3(12)	C29	C24	C25	O5	-177.4(5)
C4	C2	C3	C24	178.6(11)	C29	C24	C25	C26	1.8(9)
C4	C3	C24	C25	174.6(7)	C30	N2	C27	C26	165.3(5)
C4	C3	C24	C29	-1.8(12)	C30	N2	C27	C28	-15.1(9)
C5	C1	C2	O1	-1.3(14)	C30	N2	C35	C36	117.9(6)
C5	C1	C2	C3	177.7(6)	C30	C31	C32	C33	178.3(6)
C5	C1	C2	C4	177.7(11)	C34	C31	C32	C33	-59.7(8)
C5	C1	C4	O2	2.8(14)	C35	N2	C27	C26	-2.4(8)
C5	C1	C4	C2	-177.7(11)	C35	N2	C27	C28	177.1(6)
C5	C1	C4	C3	-177.7(5)	C35	N2	C30	C31	-87.6(8)
C5	C6	C7	C8	-1.5(10)	C35	C36	C37	C38	116.6(8)
C6	C5	C10	O4	177.3(5)	C35	C36	C37	C42	-66.0(10)
C6	C5	C10	C9	-4.3(9)	C36	C37	C38	C39	177.9(7)
C6	C7	C8	N1	178.4(6)	C36	C37	C42	C41	-178.9(7)
C6	C7	C8	C9	-2.1(10)	C37	C38	C39	C40	0.7(13)
C7	C8	C9	C10	2.3(10)	C38	C37	C42	C41	-1.4(11)
C8	N1	C11	C12	-103.1(8)	C38	C39	C40	C41	-0.9(13)

A	B	C	D	Angle/°	A	B	C	D	Angle/°
C8	N1	C16	C17	72.4(8)	C39	C40	C41	C42	-0.1(12)
C8	C9	C10	O4	179.5(5)	C40	C41	C42	C37	1.2(12)
C8	C9	C10	C5	1.0(10)	C42	C37	C38	C39	0.5(11)

H.3 Additional Spectra in Solution and Thin Film

H.3.1 Solution:

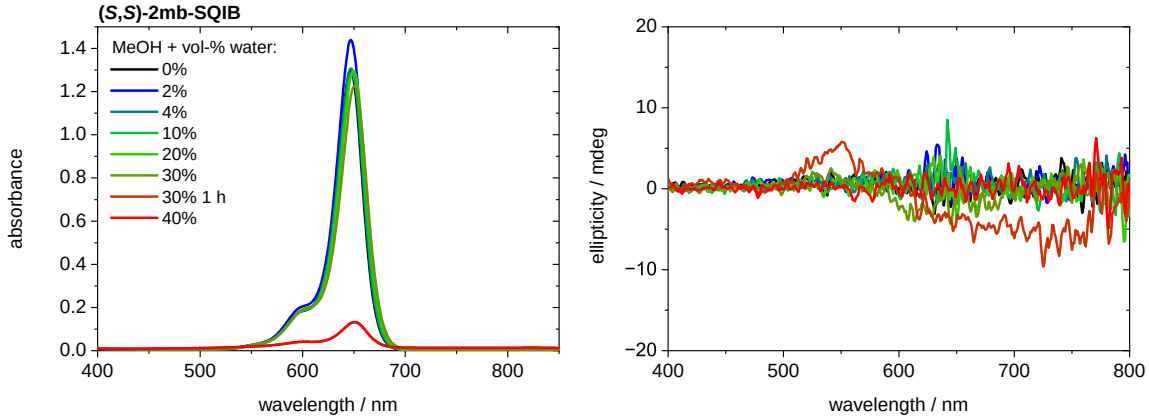


Figure H.9: Early stage aggregation experiments in solution with UV/Vis absorbance (left) and corresponding ellipticity spectra (right) of **(*S*,*S*)-2mb-SQIB** (c = 3.85 µM). The legend indicates the volume-percentage of water in the methanol-water mixture and applies to all plots. The solutions were prepared from a chloroform stock solution (c = 2.31 × 10^{-4} M) and therefore contain an additional 1.7% chloroform (50 µL in 3 mL).

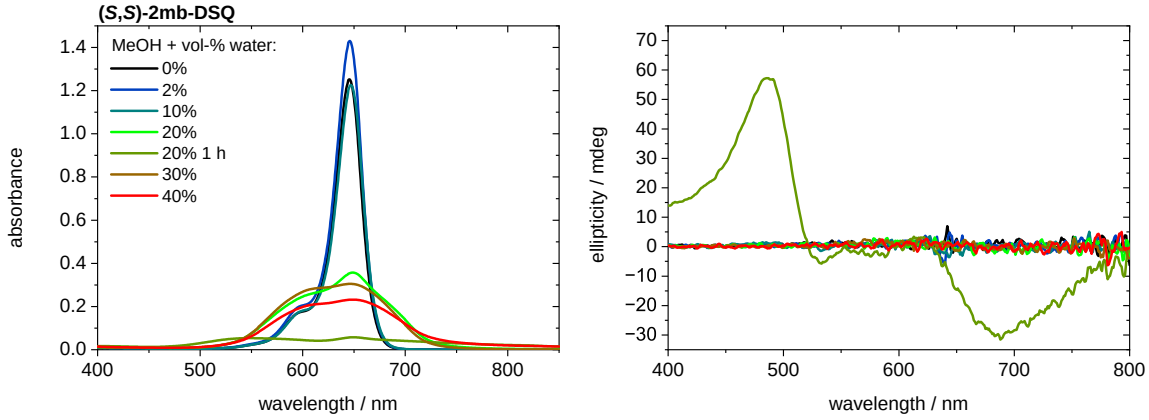


Figure H.10: Early stage aggregation experiments in solution with UV/Vis absorbance (left) and corresponding ellipticity spectra (right) of **(*S*,*S*)-2mb-DSQ** (c = 3.84 µM). The legend indicates the volume-percentage of water in the methanol-water mixture and applies to all plots. The solutions were prepared from a chloroform stock solution (c = 2.31 × 10^{-4} M) and therefore contain an additional 1.7% chloroform (50 µL in 3 mL).

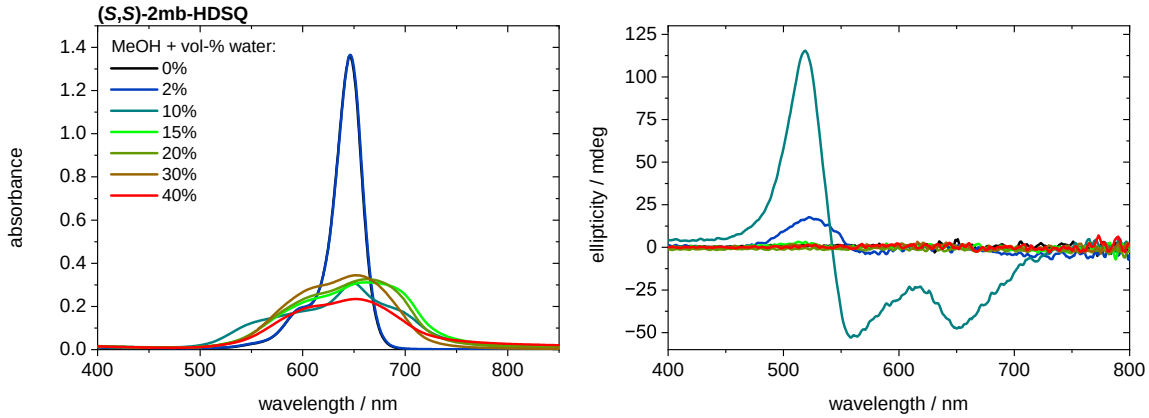


Figure H.11: Early stage aggregation experiments in solution with UV/Vis absorbance (left) and corresponding ellipticity spectra (right) of **(*S*,*S*)-2mb-HDSQ** (c = 3.84 µM). The legend indicates the volume-percentage of water in the methanol-water mixture and applies to all plots. The solutions were prepared from a chloroform stock solution (c = 2.31 × 10^{-4} M) and therefore contain an additional 1.7% chloroform (50 µL in 3 mL).

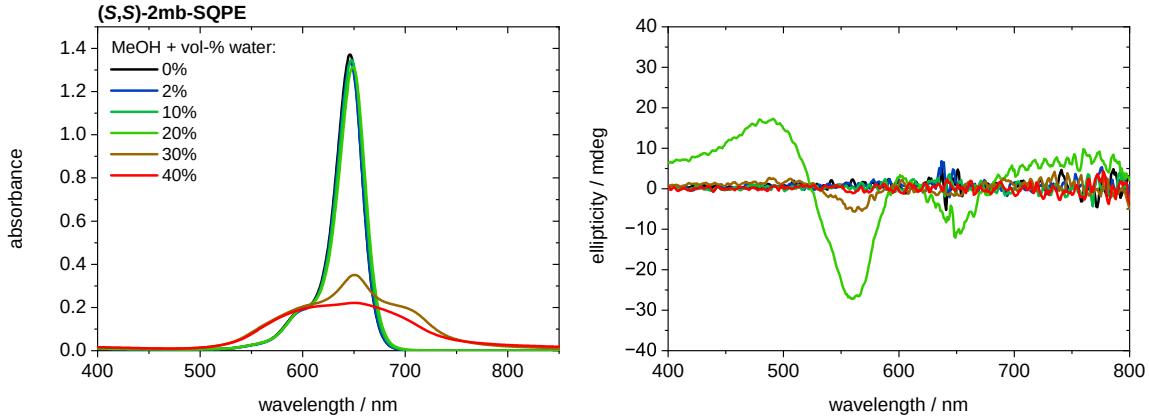


Figure H.12: Early stage aggregation experiments in solution with UV/Vis absorbance (left) and corresponding ellipticity spectra (right) of **(*S*,*S*)-2mb-SQPE** (c = 3.84 µM). The legend indicates the volume-percentage of water in the methanol-water mixture and applies to all plots. The solutions were prepared from a chloroform stock solution (c = 2.30 × 10^{-4} M) and therefore contain an additional 1.7% chloroform (50 µL in 3 mL).

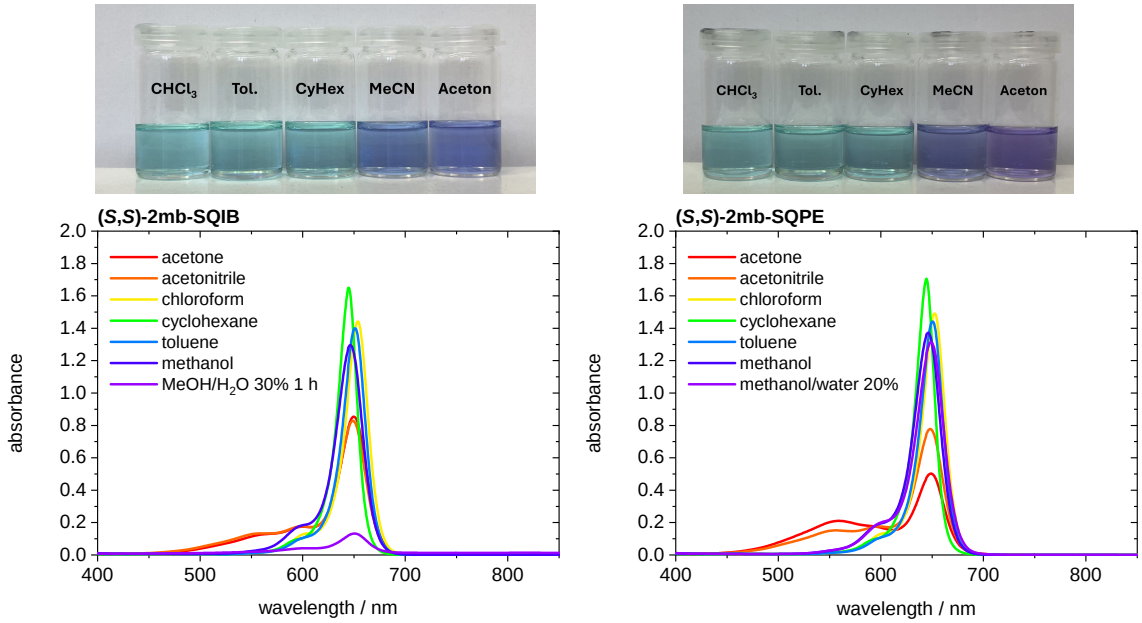


Figure H.13: UV/Vis absorbance spectra of **(*S*,*S*)-2mb-SQIB** (left) and **(*S*,*S*)-2mb-SQPE** (right) in indicated solvents with the corresponding picture on top. The solutions were prepared from a chloroform stock solution (c = 2.31 or 2.30 × 10^{-4} M) and therefore contain an additional 1.7% chloroform (50 µL in 3 mL) with an final concentration of the sample of c = 3.85 or 3.84 µM.

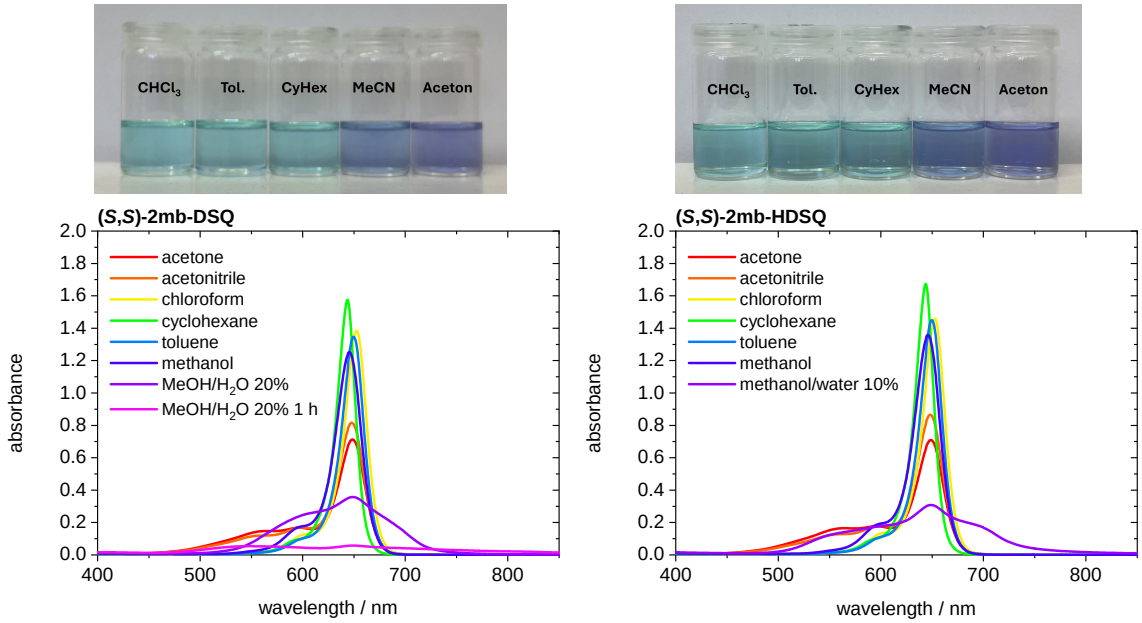


Figure H.14: UV/Vis absorbance spectra of **(*S*,*S*)-2mb-DSQ** (left) and **(*S*,*S*)-2mb-HDSQ** (right) in indicated solvents with the corresponding picture on top. The solutions were prepared from a chloroform stock solution (c = 2.31 × 10^{-4} M) and therefore contain an additional 1.7% chloroform (50 µL in 3 mL) with an final concentration of the sample of c = 3.84 µM.

H.3.2 Aggregated Thin Films:

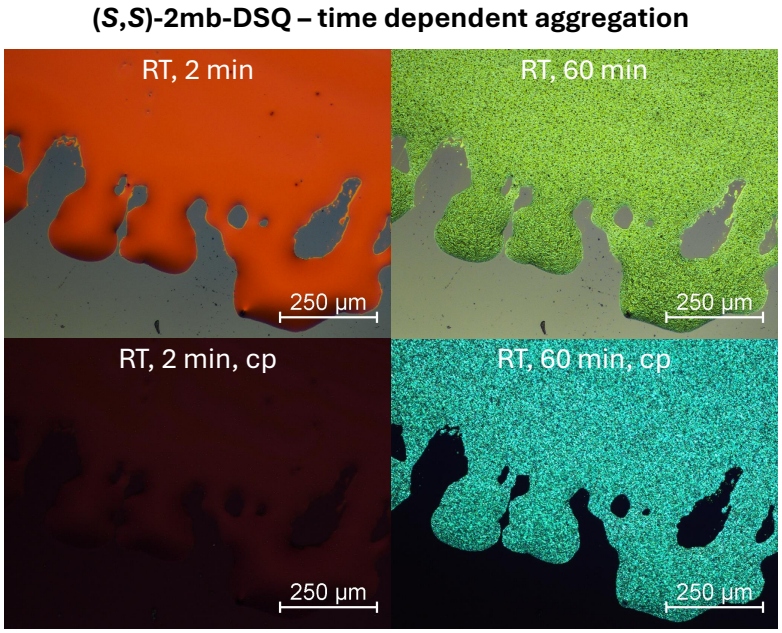


Figure H.15: Optical microscopy images (top) and corresponding images between crossed polarizers (bottom) at indicated times of drop-casted films of **(*S*,*S*)-2mb-DSQ** from a chloroform solution, highlighting the time dependent aggregation behaviour of this dye.

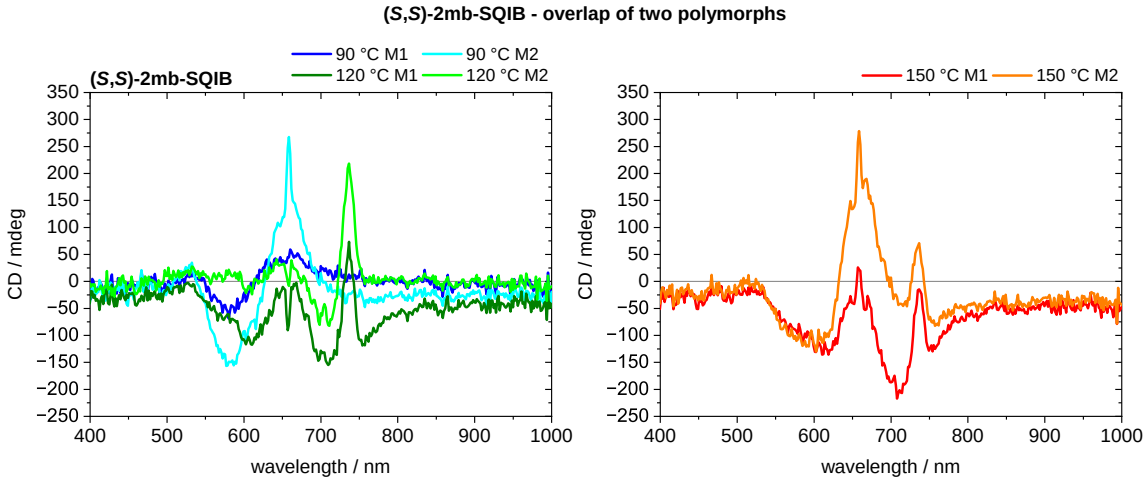


Figure H.16: Selected CD spectra of **(*S*,*S*)-2mb-SQIB**, spin-coated from a chloroform solution under the same conditions and thermally annealed at at indicated temperatures for 30 minutes. Each sample was measured twice (M1 and M2) at approximately the same position, with a 90° rotation between measurements. The resulting spectra differ significantly, highlighting the influence of the coexistence of two polymorphs within the sample and the effect of the macroscopic beam size (approx. 2 mm). Consequently, the recorded signal represents varying relative contributions from the monoclinic and the presumed orthorhombic polymorphs, leading to non-reproducible spectral features between measurements.

H.4 Additional Information on the Characterisation and Fabrication of the OPVs

H.4.1 Characterisation:

The characterisation of photovoltaic (PV) devices is of critical importance, as it should allow the evaluation of performance under standardized condition to enable direct comparison between different device compositions. To ensure such comparability, the *American Society for Testing and Materials* (ASTM) has established certain laboratory conditions for performance testing. The most widely used test environment – or more precisely, the most common reference spectrum – is *AM 1.5 G*. This spectrum represents the annual average global solar irradiance after passing through 1.5 times the Earth's atmosphere and corresponds to an incident power density of 1000 W·m^{-2}, which is typical for mid-latitude solar irradiation. Photovoltaic performance measurements are carried out by applying a series of voltages to the device under illumination and recording the corresponding output current. The resulting data are plotted to produce a current-voltage (I-V) curve characteristic of the device. Since the measured current I depends on the active layer dimensions, the results are typically normalised to a current density-voltage (J-V) plot. Figure H.17 shows an example of a J-V curve for an **(*S*,*S*)-2mb-DSQ** based OPV device (see Section 10.5) under illumination. Because this curve does not depend on the solar cell size and is measured under standardised *AM 1.5 G* conditions, comparability between different devices is possible.

The J-V curve contains all key photovoltaic parameters, including the maximum power point (MP or P_{max}),short-circuit current density (J_{SC}), open-circuit voltage (V_{OC}), voltage at the maximum power point (V_{MP}) and current density at the maximum power point (J_{MP}). From these values, the fill factor (FF) and the power conversion efficiency (PCE) can be calculated.[111, 189]

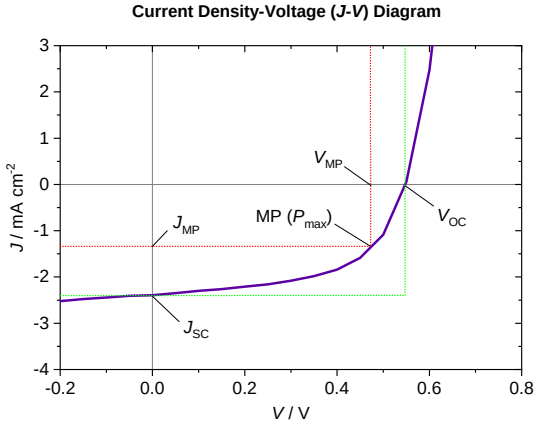


Figure H.17: Current density-voltage (J-V) diagram of a **(*S*,*S*)-2mb-DSQ** based OPV under illumination.

From the physical definition of power (voltage multiplied by current), the maximum power point (MP or P_{max}) occurs where the product of the current density and voltage is maximized. It represents the highest output power the solar cell can deliver and defines V_{MP} and J_{MP} on the J-V diagram. Under short-circuit conditions (no applied bias), the measured current is purely photogenerated and corresponds to

the short-circuit current density (J_{SC}). In this case, charge carriers are driven to the electrodes solely by the built-in electric field of the device. The magnitude of J_{SC} is primarily determined by the absorption properties of the photoactive layer and by the efficiency of each stage of the photovoltaic process. In contrast, open-circuit conditions yield the open-circuit voltage (V_{OC}), which represents the maximum electrochemical potential of the solar cell. Here, the externally applied voltage cancels the built-in electric field, eliminating all driving forces for charge carrier extraction and resulting in zero current flow. To a first approximation, V_{OC} depends linearly on the energy difference between the donor HOMO and acceptor LUMO levels, allowing for a straightforward estimation. However, the number of photoinduced charges also influences V_{OC}, meaning that the value is additionally affected by the absorption efficiency of the active layer. Furthermore, the work functions of the electrode materials play a role, as the donor and acceptor layers are not directly used as electrodes.[111, 189]

$$\text{Fill Factor} \quad FF = \frac{J_{MP} \cdot V_{MP}}{J_{SC} \cdot V_{OC}} \tag{H.1}$$

$$\text{Power conversion efficiency} \quad PCE: \eta_e = \frac{P_{max}}{P_{in}} = \frac{J_{SC} \cdot V_{OC} \cdot FF}{P_{in}} = \frac{J_{MP} \cdot V_{MP}}{P_{in}} \tag{H.2}$$

With these parameters defined, the fill factor (FF) can be calculated according to Equation H.1 as the ratio of the maximum power (MP = $J_{MP} \cdot V_{MP}$) of the photovoltaic device to the product of J_{SC} and V_{SC}. Graphically, this value corresponds to the ratio of the two rectangular areas in Figure H.17 (red area divided by green area), which is why the fill factor is sometimes referred to as the "squareness" of the J-V curve. It serves as a measure of the overall device performance – in other words, how efficiently charges can be extracted from the device – and should ideally approach unity.

Beyond these characteristics, the most important performance metric for solar cells is the efficiency with which incident light is converted into electrical power. This parameter, known as the power conversion efficiency (PCE), is defined as the ratio of the electrical output power to the incident light power (Equation H.2). Another important parameter, which cannot be derived from the J-V diagram, is the external quantum efficiency (EQE). This value represents the probability that the absorption of a single photon will generate a free charge carrier capable of flowing through an external circuit. Thereby, EQE is wavelength-dependent and is defined as the ratio of the number of collected charges (resulting from photoinduced electron transfer) to the number of incident photons on the solar cell. Thus, EQE provides a measure of the overall efficiency of the device, encompassing all four stages of the photovoltaic process in PVs.[111, 189] For further information please consider the cited literature.

H.4.2 Fabrication:

Table H.1: Details on the physical vapor deposition (PVD) parameters for the fabrication of the **(*S*,*S*)-2mb-DSQ** based OPV. Performed in collaboration with Otgonbayar Erdene-Ochir (group of Prof. Klaus Meerholz, University of Cologne).

Substance	Pressure / mbar	Power / %	T / °C	deposition rate / Ås^{-1}	Thickness / nm
MoO_3	$2.0 \cdot 10^{-7}$	34 (126 Amps)	–	0.1–0.15	8
C60	$2.0 \cdot 10^{-6}$	2.4 (≈ 8 Apms)	330	0.2	30
BPhen	$2.0 \cdot 10^{-6}$	0.7 (≈ 3 Apms)	110	0.29	6
Silver	$2.2 \cdot 10^{-7}$	36.8 (127 Amps)	–	0.05–0.5	100

APPENDIX I

Excursus – Synthesis of Chiral π-Conjugated Polymers Exhibiting the CISS Effect for Advanced Optoelectronic Applications

I.1 Equations for gel permeation chromatography (GPC) analysis

The following equations were used to define different average parameters, thereby allowing quantification of the chain-length distribution in a polymer sample:

$$\text{Number average molar mass} \quad M_{\mathrm{n}} = \frac{\sum M_i N_i}{\sum N_i} \tag{I.1}$$

$$\text{Mass average molar mass} \quad M_{\mathrm{w}} = \frac{\sum M_i^2 N_i}{\sum M_i N_i} \tag{I.2}$$

$$\text{Z(centrifugation)-average molar mass} \quad M_{\mathrm{z}} = \frac{\sum M_i^3 N_i}{\sum M_i^2 N_i} \tag{I.3}$$

$$\text{Polydispersity Index} \quad PDI = \frac{M_{\mathrm{w}}}{M_{\mathrm{n}}} \tag{I.4}$$

$$\text{Degree of Polymerization} \quad DP = \frac{M_{\mathrm{n}}}{\text{Molecular weight of the repeating unit}} \tag{I.5}$$

I.2 Information on Single-Crystal Structure of (*S*)-Binol-DibromoBT

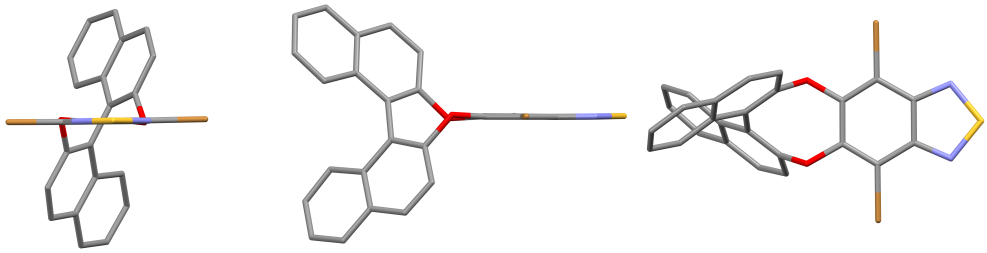


Figure I.1: Molecular geometry of **(*S*)-Binol-DibromoBT** from the monoclinic crystal structure.

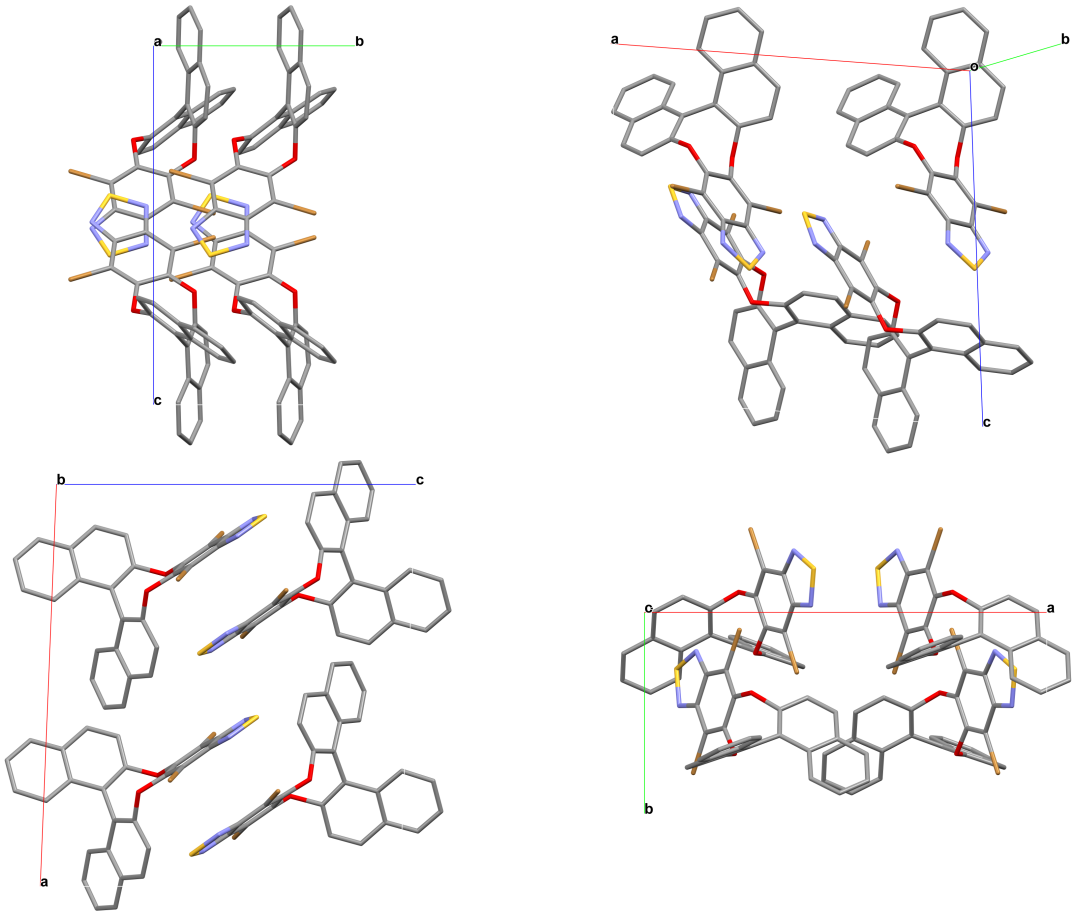


Figure I.2: Crystal structure of **(*S*)-Binol-DibromoBT** (monoclinic, space group = C2, a = 17.0199(5) Å, b = 8.5131(2) Å, c = 15.1950(4) Å, α = 90°, β = 92.305(2)°, γ = 90° and Z = 4). Hydrogen was removed for clarity. Nitrogen is represented by blue, carbon by gray, oxygen by light red, bromine by drak red and sulfur by yellow. Top left image: View of the unit cell along the a-axis. Top right image: View of the unit cell along no specific axis. Bottom left image: View of the unit cell along the b-axis. Bottom right image: View of the unit cell along the c-axis. Detailed characteristics and additional figures of the single-crystal X-ray structure can be found below.

8515_pl

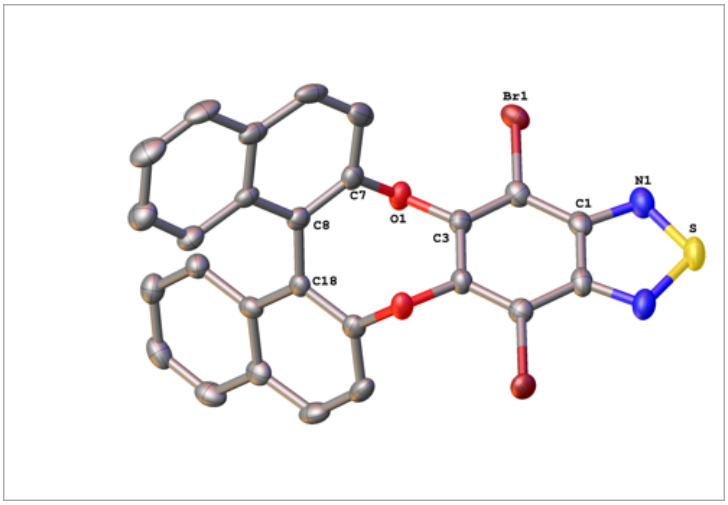


Table 1 Crystal data and structure refinement for 8515_pl.

Identification code	GLUE272, MFS-136 // GXray8515_pl
Crystal Habitus	clear colourless block
Device Type	STOE STADIVARI
Empirical formula	$C_{26}H_{12}Br_2N_2O_2S$
Moiety formula	C26 H12 Br2 N2 O2 S
Formula weight	576.26
Temperature/K	100
Crystal system	monoclinic
Space group	C2
a/Å	17.0199(5)
b/Å	8.5131(2)
c/Å	15.1950(4)
α/°	90
β/°	92.305(2)
γ/°	90
Volume/Å^3	2199.85(10)
Z	4
ρ_{calc}g/cm^3	1.740
μ/mm^{-1}	5.80
F(000)	1136.0
Crystal size/mm^3	0.28 × 0.167 × 0.06
Absorption correction	multi-scan
Tmin; Tmax	0.1233; 0.2039
Radiation	Cu Kα (λ = 1.54186)
2Θ range for data collection/°	5.822 to 140.784°
Completeness to theta	1.000
Index ranges	-20 ≤ h ≤ 20, -10 ≤ k ≤ 9, -12 ≤ l ≤ 18
Reflections collected	18795

Independent reflections	3710 [R_{int} = 0.0242, R_{sigma} = 0.0131]
Data/restraints/parameters	3710/1/299
Goodness-of-fit on F^2	1.076
Final R indexes [I>=2σ (I)]	R_1 = 0.0220, wR_2 = 0.0571
Final R indexes [all data]	R_1 = 0.0222, wR_2 = 0.0572
Largest diff. peak/hole / e $Å^{-3}$	0.24/-0.69
Flack parameter	0.028(17)

Table 2 Bond Lengths for 8515_pl.

Atom	Atom	Length/Å	Atom	Atom	Length/Å
Br1	C2	1.877(4)	C9	C10	1.423(5)
Br2	C5	1.867(4)	C9	C13	1.422(5)
S	N1	1.616(3)	C10	C11	1.419(6)
S	N2	1.621(4)	C10	C16	1.421(5)
O1	C3	1.370(4)	C11	C12	1.371(6)
O1	C7	1.415(4)	C13	C14	1.377(5)
O2	C4	1.377(4)	C14	C15	1.406(5)
O2	C17	1.411(4)	C15	C16	1.374(6)
N1	C1	1.351(5)	C17	C18	1.382(5)
N2	C6	1.344(5)	C17	C22	1.398(5)
C1	C2	1.420(5)	C18	C19	1.431(5)
C1	C6	1.434(6)	C19	C20	1.428(4)
C2	C3	1.362(5)	C19	C23	1.417(5)
C3	C4	1.443(5)	C20	C21	1.419(5)
C4	C5	1.366(5)	C20	C26	1.418(5)
C5	C6	1.427(5)	C21	C22	1.362(5)
C7	C8	1.372(5)	C23	C24	1.381(5)
C7	C12	1.404(5)	C24	C25	1.404(5)
C8	C9	1.439(5)	C25	C26	1.369(6)
C8	C18	1.477(4)			

Table 3 Bond Angles for 8515_pl.

Atom	Atom	Atom	Angle/°	Atom	Atom	Atom	Angle/°
N1	S	N2	101.53(16)	C13	C9	C8	122.2(3)
C3	O1	C7	119.0(3)	C13	C9	C10	118.9(3)
C4	O2	C17	116.1(3)	C11	C10	C9	119.8(3)
C1	N1	S	105.8(3)	C11	C10	C16	121.3(3)
C6	N2	S	105.7(3)	C16	C10	C9	118.9(3)
N1	C1	C2	127.0(4)	C12	C11	C10	121.1(3)
N1	C1	C6	113.2(3)	C11	C12	C7	118.2(3)
C2	C1	C6	119.8(3)	C14	C13	C9	120.3(3)
C1	C2	Br1	120.2(3)	C13	C14	C15	121.1(4)
C3	C2	Br1	121.2(3)	C16	C15	C14	119.7(4)
C3	C2	C1	118.6(4)	C15	C16	C10	121.1(3)
O1	C3	C4	119.8(3)	C18	C17	O2	118.8(3)
C2	C3	O1	118.2(3)	C18	C17	C22	123.2(3)
C2	C3	C4	121.8(3)	C22	C17	O2	118.0(3)
O2	C4	C3	119.1(3)	C17	C18	C8	117.8(3)
C5	C4	O2	119.8(4)	C17	C18	C19	118.0(3)
C5	C4	C3	121.0(3)	C19	C18	C8	124.1(3)
C4	C5	Br2	121.5(3)	C20	C19	C18	119.0(3)
C4	C5	C6	118.3(4)	C23	C19	C18	122.1(3)
C6	C5	Br2	120.2(3)	C23	C19	C20	118.8(3)
N2	C6	C1	113.7(3)	C21	C20	C19	119.6(3)
N2	C6	C5	125.8(4)	C26	C20	C19	118.8(3)
C5	C6	C1	120.5(3)	C26	C20	C21	121.5(3)
C8	C7	O1	117.6(3)	C22	C21	C20	120.7(3)
C8	C7	C12	124.1(3)	C21	C22	C17	119.5(3)
C12	C7	O1	118.1(3)	C24	C23	C19	120.3(3)
C7	C8	C9	118.0(3)	C23	C24	C25	120.9(3)
C7	C8	C18	117.8(3)	C26	C25	C24	119.9(3)
C9	C8	C18	124.1(3)	C25	C26	C20	121.2(3)
C10	C9	C8	118.8(3)				

Table 4 Torsion Angles for 8515_pl.

A	B	C	D	Angle/°	A	B	C	D	Angle/°
Br1	C2	C3	O1	4.2(4)	C7	C8	C18	C19	-119.8(4)
Br1	C2	C3	C4	179.6(3)	C8	C7	C12	C11	-0.3(5)
Br2	C5	C6	N2	0.1(5)	C8	C9	C10	C11	-2.1(5)
Br2	C5	C6	C1	-179.7(2)	C8	C9	C10	C16	-179.8(3)
S	N1	C1	C2	178.0(3)	C8	C9	C13	C14	179.0(3)
S	N1	C1	C6	-0.4(3)	C8	C18	C19	C20	178.5(3)
S	N2	C6	C1	0.4(4)	C8	C18	C19	C23	1.7(6)
S	N2	C6	C5	-179.4(3)	C9	C8	C18	C17	-119.1(4)
O1	C3	C4	O2	-7.5(5)	C9	C8	C18	C19	65.3(5)
O1	C3	C4	C5	176.4(3)	C9	C10	C11	C12	2.0(5)
O1	C7	C8	C9	-174.5(3)	C9	C10	C16	C15	1.7(5)
O1	C7	C8	C18	10.3(4)	C9	C13	C14	C15	-0.1(6)
O1	C7	C12	C11	174.3(3)	C10	C9	C13	C14	1.4(5)
O2	C4	C5	Br2	2.5(4)	C10	C11	C12	C7	-0.8(5)
O2	C4	C5	C6	-176.7(3)	C11	C10	C16	C15	-176.0(3)
O2	C17	C18	C8	5.1(5)	C12	C7	C8	C9	0.1(5)
O2	C17	C18	C19	-179.0(3)	C12	C7	C8	C18	-175.1(3)
O2	C17	C22	C21	176.5(3)	C13	C9	C10	C11	175.5(3)
N1	S	N2	C6	-0.6(3)	C13	C9	C10	C16	-2.2(5)
N1	C1	C2	Br1	0.9(5)	C13	C14	C15	C16	-0.5(6)
N1	C1	C2	C3	-179.2(3)	C14	C15	C16	C10	-0.3(6)
N1	C1	C6	N2	0.0(4)	C16	C10	C11	C12	179.7(3)
N1	C1	C6	C5	179.8(3)	C17	O2	C4	C3	61.5(4)
N2	S	N1	C1	0.6(3)	C17	O2	C4	C5	-122.4(3)
C1	C2	C3	O1	-175.6(3)	C17	C18	C19	C20	2.9(5)
C1	C2	C3	C4	-0.3(5)	C17	C18	C19	C23	-173.9(3)
C2	C1	C6	N2	-178.5(3)	C18	C8	C9	C10	176.0(3)
C2	C1	C6	C5	1.3(5)	C18	C8	C9	C13	-1.6(5)
C2	C3	C4	O2	177.2(3)	C18	C17	C22	C21	-0.1(6)
C2	C3	C4	C5	1.2(5)	C18	C19	C20	C21	-0.9(5)
C3	O1	C7	C8	-103.9(4)	C18	C19	C20	C26	-179.5(4)
C3	O1	C7	C12	81.1(4)	C18	C19	C23	C24	178.0(3)
C3	C4	C5	Br2	178.5(2)	C19	C20	C21	C22	-1.7(6)
C3	C4	C5	C6	-0.7(5)	C19	C20	C26	C25	2.9(6)
C4	O2	C17	C18	-103.1(4)	C19	C23	C24	C25	0.0(6)
C4	O2	C17	C22	80.2(4)	C20	C19	C23	C24	1.2(5)
C4	C5	C6	N2	179.3(3)	C20	C21	C22	C17	2.2(6)
C4	C5	C6	C1	-0.5(5)	C21	C20	C26	C25	-175.7(4)
C6	C1	C2	Br1	179.2(2)	C22	C17	C18	C8	-178.3(3)
C6	C1	C2	C3	-0.9(5)	C22	C17	C18	C19	-2.4(5)
C7	O1	C3	C2	-127.6(4)	C23	C19	C20	C21	176.0(4)
C7	O1	C3	C4	57.0(4)	C23	C19	C20	C26	-2.6(5)
C7	C8	C9	C10	1.1(5)	C23	C24	C25	C26	0.2(6)
C7	C8	C9	C13	-176.5(3)	C24	C25	C26	C20	-1.7(6)
C7	C8	C18	C17	55.8(5)	C26	C20	C21	C22	176.8(4)

I.3 Additional Information on Selected Chiral π-Conjugated Polymers

I.3.1 Additional Information on (*S*)-c_xF8BT

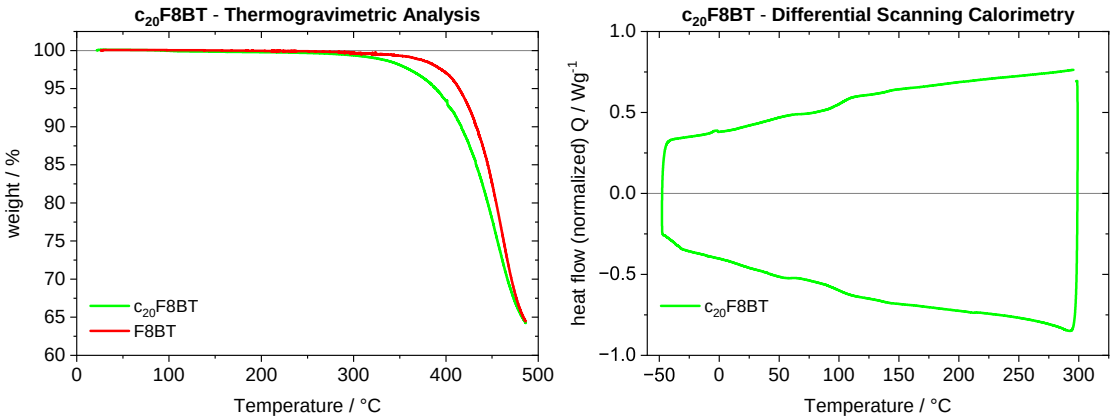


Figure I.3: Left: Thermogravimetric analysis (TGA) of **F8BT** and **(*S*)-c_{20}F8BT**. Note: both polymers are stable until ca. 375 °C, while BINOL substitution slightly lowers the thermal decomposition temperature. Right: Differential scanning calorimetry (DSC) of **(*S*)-c_{20}F8BT**. Note: T_g (glass transition temperature) is ca. 125 °C. BINOL substitution slightly lowers T_g (literature reported values for **F8BT** between 135–140 °C).

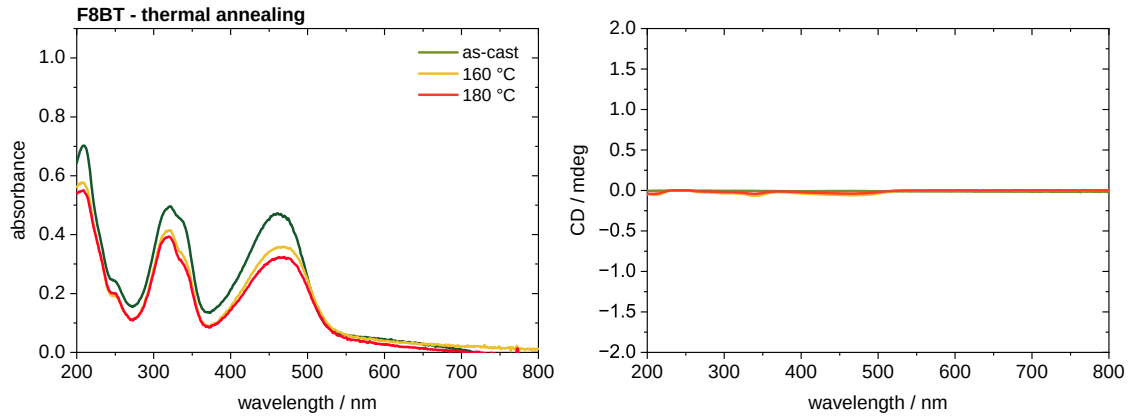


Figure I.4: UV/Vis absorbance (left) and corresponding CD spectra (right) of **F8BT**, spin-coated from a toluene/chloroform 5:3 (v/v) solution under the same conditions and thermally annealed at indicated temperatures for 10 minutes. Thin films were prepared by spin coating 25 µL of the spin-on solution with a polymer concentration of 12.5 mg per mL, for 60 s at 1000 rpm with 550 rpm/s + 10 s at 4000 rpm with 1450 rpm/s on a fused silica substrate and – if noted – subsequent thermally annealed.

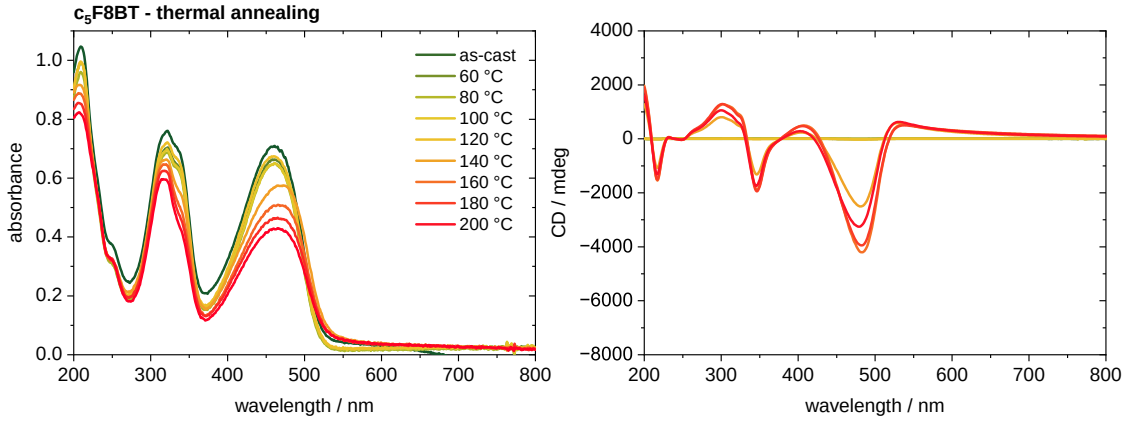


Figure I.5: UV/Vis absorbance (left) and corresponding CD spectra (right) of **(*S*)-c$_5$F8BT**, spin-coated from a toluene/chloroform 5:3 (v/v) solution under the same conditions and thermally annealed at indicated temperatures for 10 minutes. Thin films were prepared by spin coating 25 µL of the spin-on solution with a polymer concentration of 12.5 mg per mL, for 60 s at 1000 rpm with 550 rpm/s + 10 s at 4000 rpm with 1450 rpm/s on a fused silica substrate and – if noted – subsequent thermally annealed.

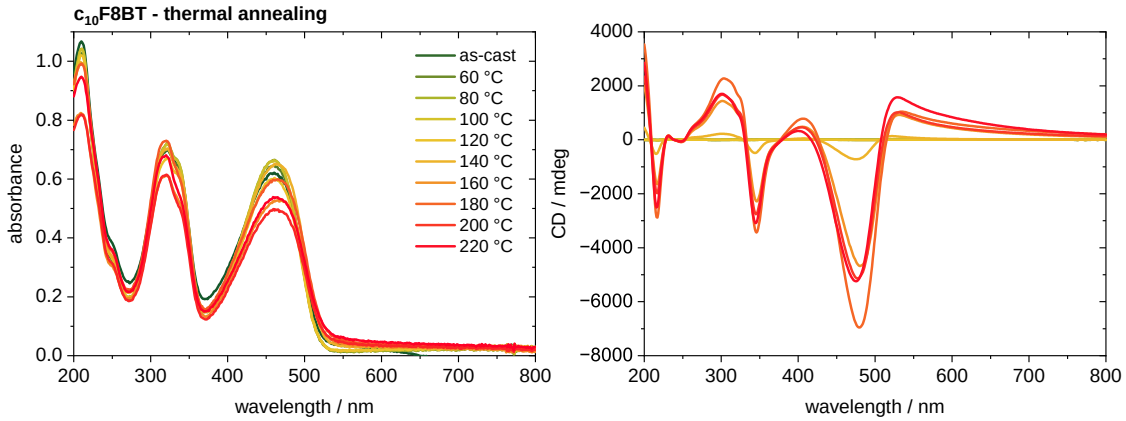


Figure I.6: UV/Vis absorbance (left) and corresponding CD spectra (right) of **(*S*)-c$_{10}$F8BT**, spin-coated from a toluene/chloroform 5:3 (v/v) solution under the same conditions and thermally annealed at indicated temperatures for 10 minutes. Thin films were prepared by spin coating 25 µL of the spin-on solution with a polymer concentration of 12.5 mg per mL, for 60 s at 1000 rpm with 550 rpm/s + 10 s at 4000 rpm with 1450 rpm/s on a fused silica substrate and – if noted – subsequent thermally annealed.

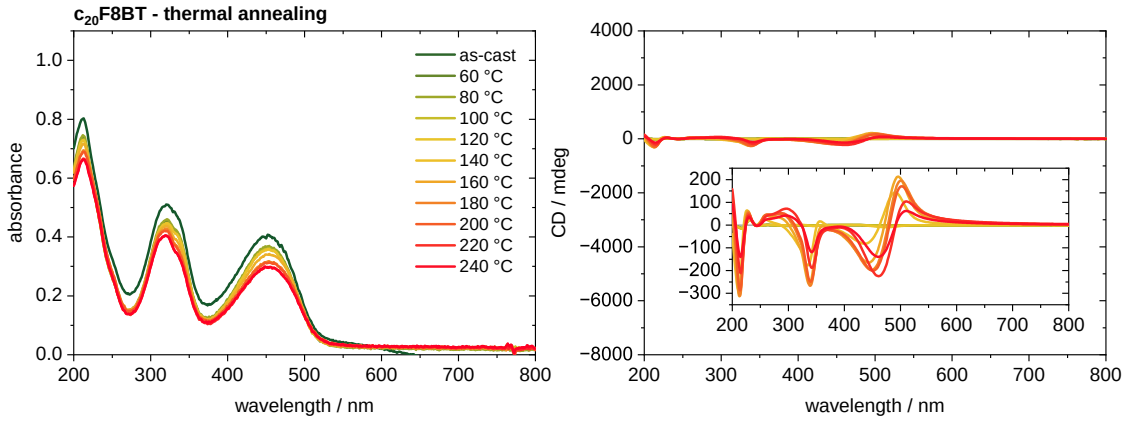


Figure I.7: UV/Vis absorbance (left) and corresponding CD spectra (right) of **(*S*)-c_{20}F8BT**, spin-coated from a toluene/chloroform 5:3 (v/v) solution under the same conditions and thermally annealed at indicated temperatures for 10 minutes. Thin films were prepared by spin coating 25 µL of the spin-on solution with a polymer concentration of 12.5 mg per mL, for 60 s at 1000 rpm with 550 rpm/s + 10 s at 4000 rpm with 1450 rpm/s on a fused silica substrate and – if noted – subsequent thermally annealed.

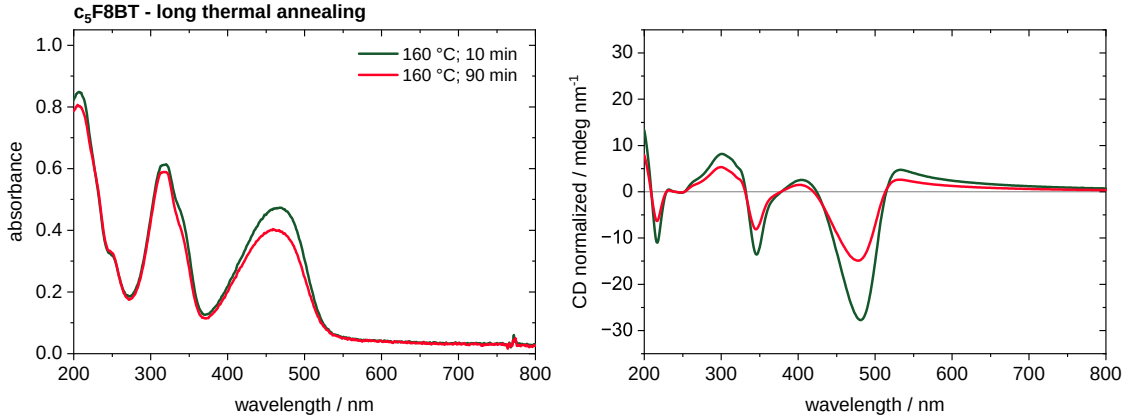


Figure I.8: UV/Vis absorbance (left) and corresponding normalized[a] CD spectra (right) of **(*S*)-c_5F8BT**, spin-coated from a toluene/chloroform 5:3 (v/v) solution under the same conditions and thermally annealed at 160 °C (corresponding to the optimal annealing temperature, measured by the highest CD value – see Figure I.5) for an indicated amount of time. Thin films were prepared by spin coating 25 µL of the spin-on solution with a polymer concentration of 12.5 mg per mL, for 60 s at 1000 rpm with 550 rpm/s + 10 s at 4000 rpm with 1450 rpm/s on a fused silica substrate.

[a] Please note: Normalized CD values are shown to allow a better comparison between the samples, as deviations in film thickness due to the extended thermal annealing process would otherwise make a direct comparison of the raw data difficult.

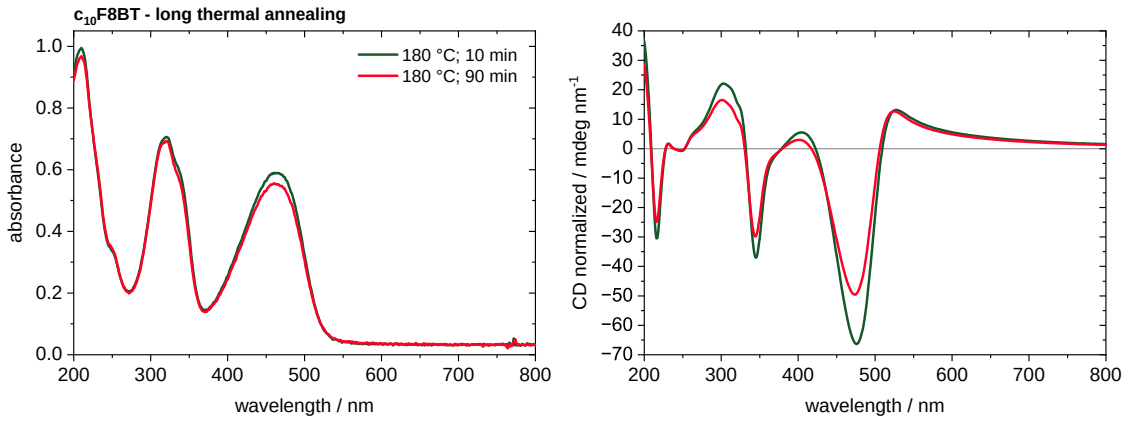


Figure I.9: UV/Vis absorbance (left) and corresponding normalized[a] CD spectra (right) of **(*S*)-c$_{10}$F8BT**, spin-coated from a toluene/chloroform 5:3 (v/v) solution under the same conditions and thermally annealed at 180 °C (corresponding to the optimal annealing temperature, measured by the highest CD value – see Figure I.6) for an indicated amount of time. Thin films were prepared by spin coating 25 µL of the spin-on solution with a polymer concentration of 12.5 mg per mL, for 60 s at 1000 rpm with 550 rpm/s + 10 s at 4000 rpm with 1450 rpm/s on a fused silica substrate.

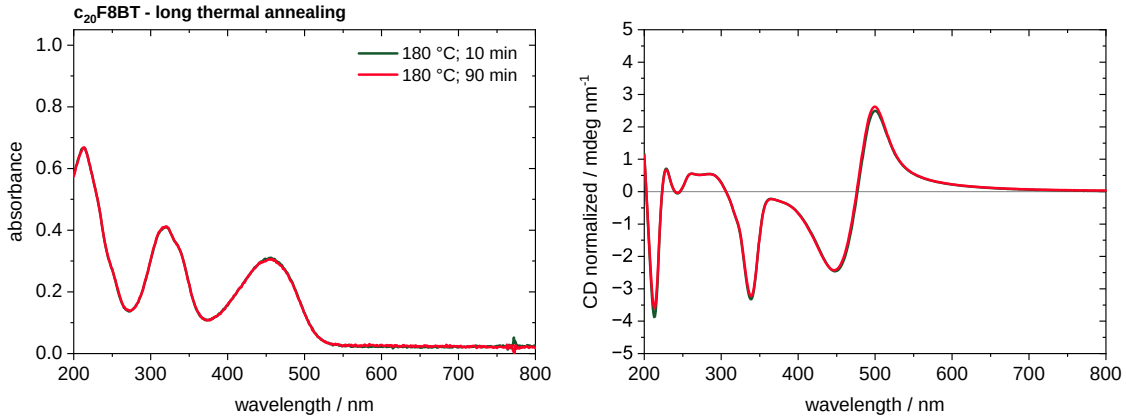


Figure I.10: UV/Vis absorbance (left) and corresponding normalized[a] CD spectra (right) of **(*S*)-c$_{20}$F8BT**, spin-coated from a toluene/chloroform 5:3 (v/v) solution under the same conditions and thermally annealed at 180 °C (corresponding to the optimal annealing temperature, measured by the highest CD value – see Figure I.7) for an indicated amount of time. Thin films were prepared by spin coating 25 µL of the spin-on solution with a polymer concentration of 12.5 mg per mL, for 60 s at 1000 rpm with 550 rpm/s + 10 s at 4000 rpm with 1450 rpm/s on a fused silica substrate. Note: Although the sign of the Cotton effect remains the same, the relative intensities of the two maxima of the bisignate signal differ. Interestingly, the asymmetry seen in **(*S*)-c$_5$F8BT** and **(*S*)-c$_{10}$F8BT** appears to vanish when 20% of the **(*S*)-Binol-DiBr-BT** building block is incorporated, resulting in a symmetrical bisignate signal with a zero-crossing shifted to approximately 475 nm. However, a detailed investigation of this phenomena lies beyond the scope of the corresponding chapter and was therefore not further intensified.

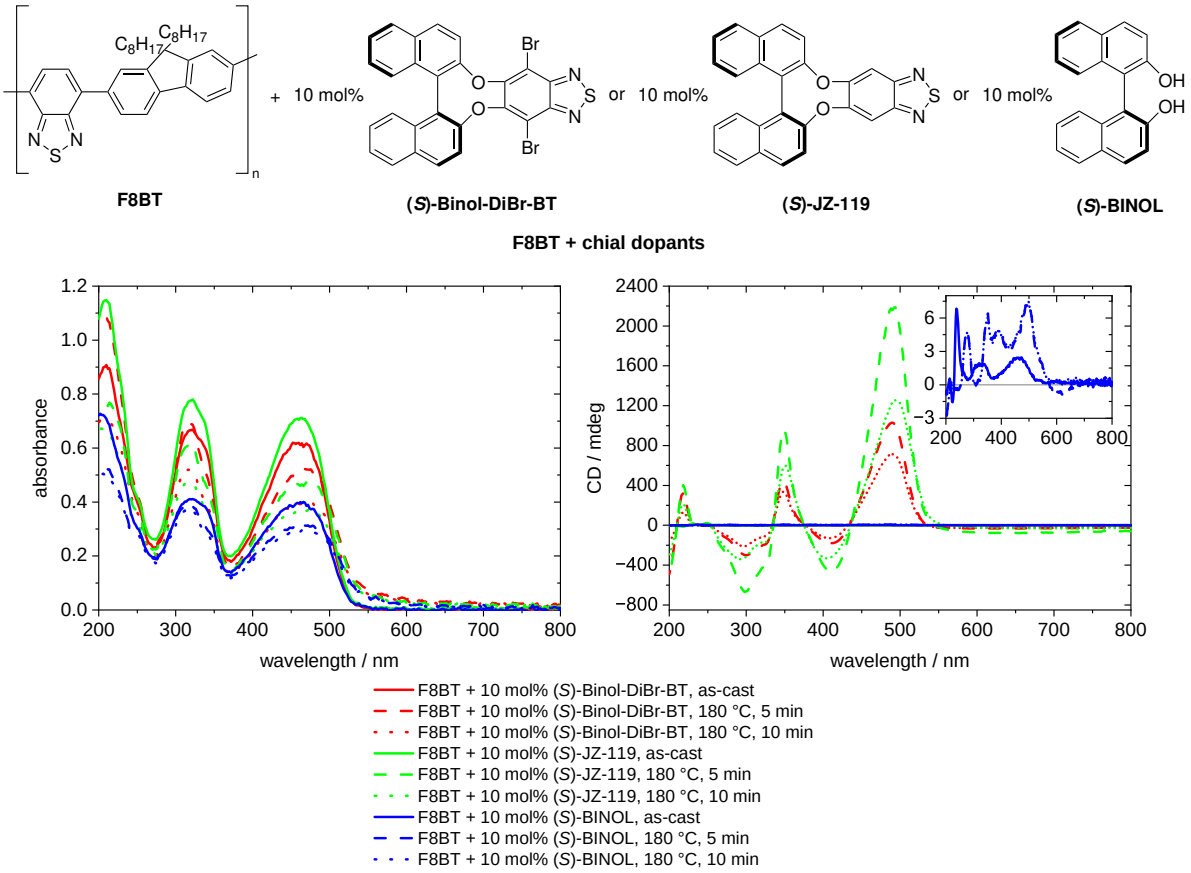


Figure I.11: Additional UV/Vis absorbance (left) and corresponding CD spectra (right) of **F8BT** mixed with 10 mol-% of different chiral dopants based on structurally similar molecules, thermally annealed at indicted temperatures and times. Thin films were prepared by spin coating 25 µL of the spin-on solution with a concentration of 12.5 mg polymer + dopant mix per mL, for 60 s at 1000 rpm with 550 rpm/s + 10 s at 4000 rpm with 1450 rpm/s on a fused silica substrate. Note: The CD signals of the doped systems exhibited an inverted sign compared to the intrinsically chiral polymers, despite the same stereogenic configuration. This interesting observation is still under active investigation, so a definitive explanation cannot be provided at this point. A comparison with the unnormalized CD values of the chiral polymers is provided in the main Chapter 11 - Figure 11.9.

I.3.2 Additional Information on MFS-125 – *poly*-(*S*)-Binol-BTQT

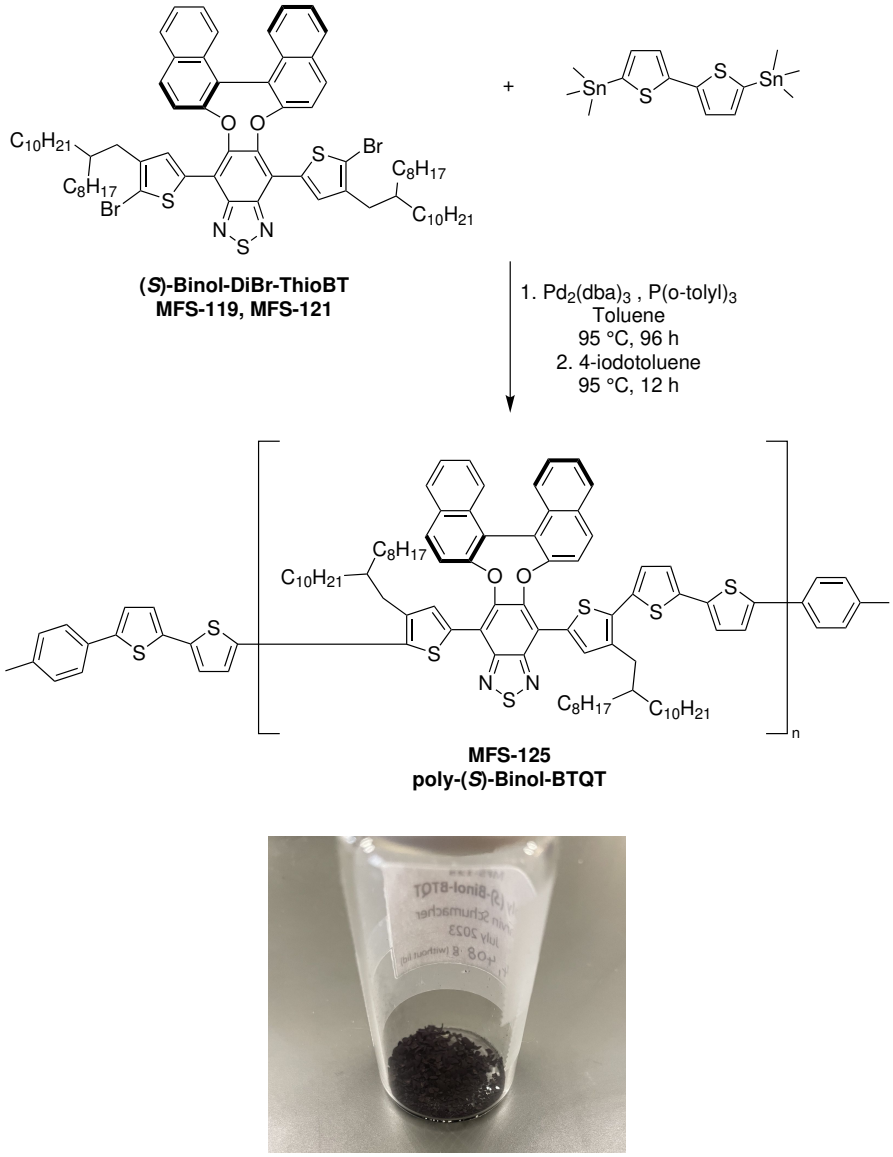


Figure I.12: Top: Synthesis of **poly-(*S*)-Binol-BTQT**, starting from enantiopure **(*S*)-Binol-DiBr-ThioBT** and 5,5'-Bis(trimethylstannyl)-2,2'-bithiophene. Bottom: Picture of the obtained dark red solid under normal light.

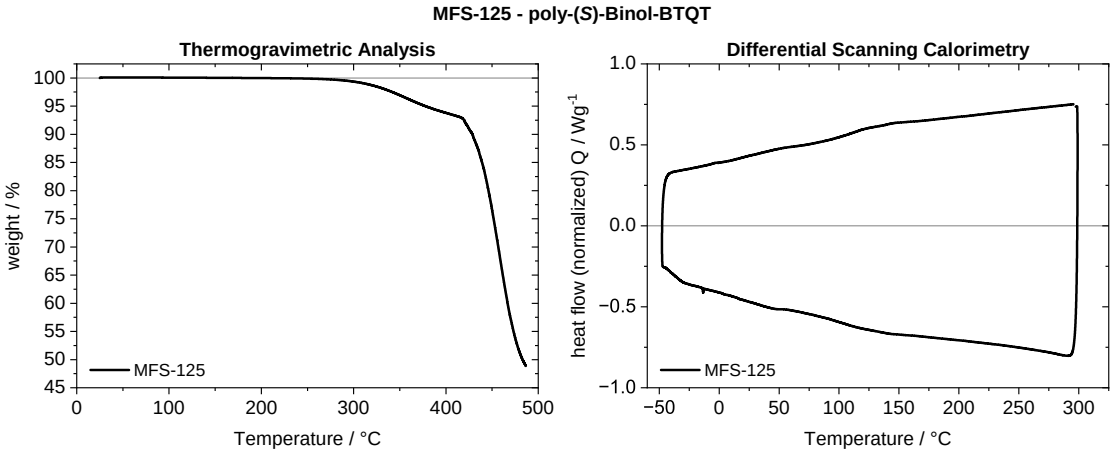


Figure I.13: Thermogravimetric analysis and differential scanning calorimetry of **poly-(*S*)-Binol-BTQT**. Note: the polymer is stable until ca. 325 °C with faster decomposition over 425 °C, T_g (glass transition temperature) is ca. 120 °C.

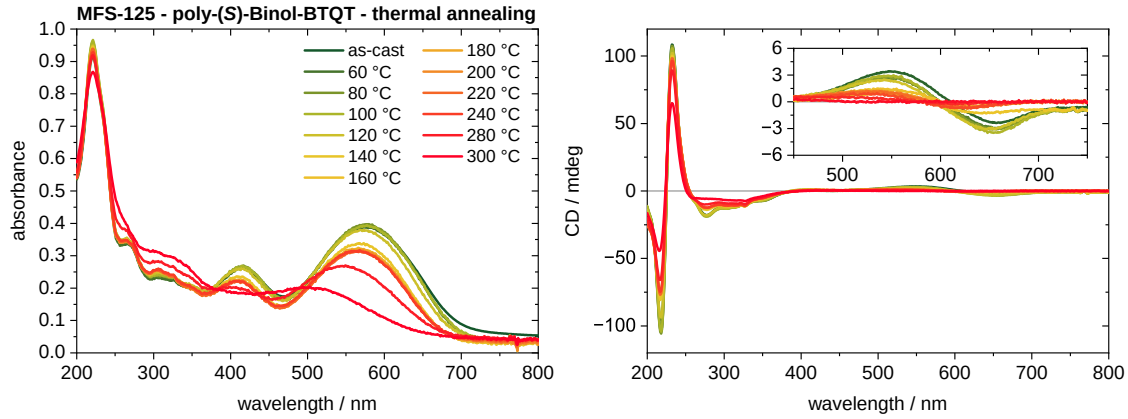


Figure I.14: UV/Vis absorbance (left) and corresponding CD spectra (right) of **poly-(*S*)-Binol-BTQT** spin-coated from a toluene/chloroform 5:3 (v/v) solution under the same conditions and thermally annealed at indicated temperatures for 10 minutes. Thin films were prepared by spin coating 25 µL of the spin-on solution with a polymer concentration of 12.5 mg per mL, for 60 s at 1000 rpm with 550 rpm/s + 10 s at 4000 rpm with 1450 rpm/s on a fused silica substrate and – if noted – subsequent thermally annealed.

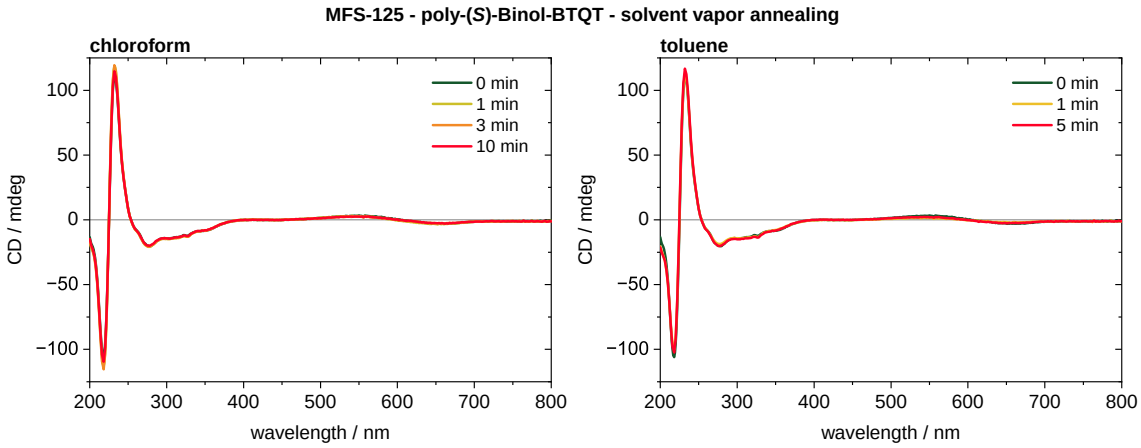


Figure I.15: CD spectra of **poly-(*S*)-Binol-BTQT**, spin-coated from a toluene/chloroform 5:3 (v/v) solution under the same conditions and solvent vapor annealed in a chloroform (left) or toluene (right) atmosphere for an indicated amount of time. Thin films were prepared by spin coating 25 µL of the spin-on solution with a polymer concentration of 12.5 mg per mL, for 60 s at 1000 rpm with 550 rpm/s + 10 s at 4000 rpm with 1450 rpm/s on a fused silica substrate.

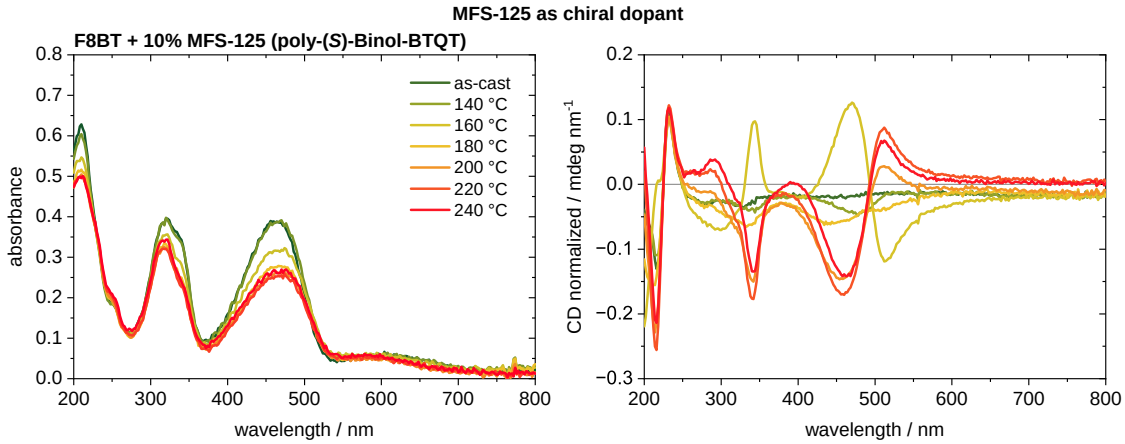


Figure I.16: UV/Vis absorbance (left) and corresponding normalized[b] CD spectra (right), where **poly-(*S*)-Binol-BTQT** was used as a polymeric chiral dopant for **F8BT**. A mixture of **F8BT** + **poly-(*S*)-Binol-BTQT** was spin-coated from a toluene/chloroform 5:3 (v/v) solution under the same conditions and thermally annealed at indicated temperatures for 10 minutes. Thin films were prepared by spin coating 25 µL of the spin-on solution with a polymer concentration of overall 12.5 mg per mL, for 60 s at 1000 rpm with 550 rpm/s + 10 s at 4000 rpm with 1450 rpm/s on a fused silica substrate and – if noted – subsequent thermally annealed.

[b] Please note: Normalized CD values are shown to enable an unbiased assessment of the influence of the polymeric chiral dopant and to allow a better comparison between MFS-125 (**poly-(*S*)-Binol-BTQT**) and MFS-131 (**(*S*)-F8TBT**, shown in Figure I.21) as such dopants.

I.3.3 Additional Information on MFS-131 – (*S*)-F8TBT

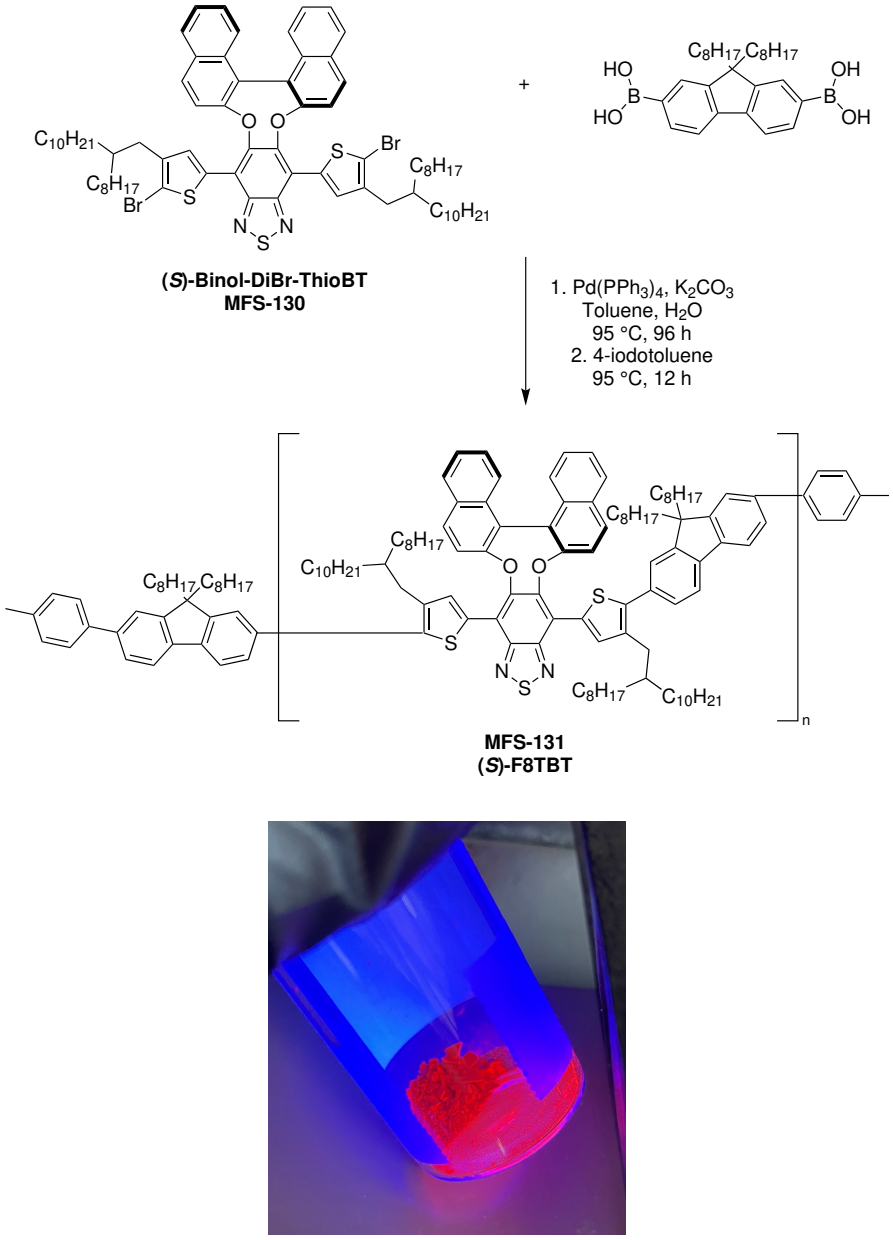


Figure I.17: Top: Synthesis of **(*S*)-F8TBT**, starting from enantiopure **(*S*)-Binol-DiBr-ThioBT** and 9,9-dioctylfluorene-2,7-diboronic acid. Bottom: Picture of the obtained red solid under UV-light.

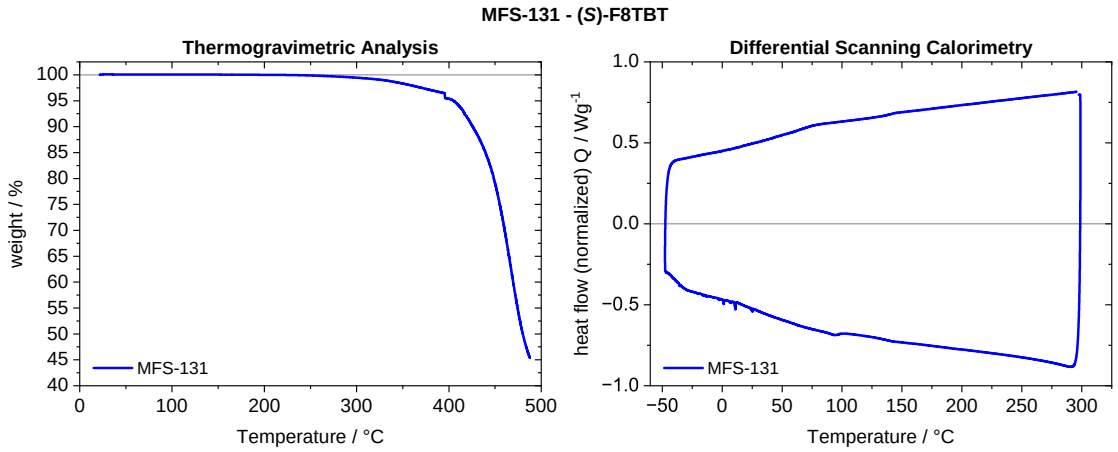


Figure I.18: Thermogravimetric analysis and differential scanning calorimetry of **(*S*)-F8TBT**. Note: the polymer is stable until ca. 400 °C, T_g (glass transition temperature) is ca. 75 °C.

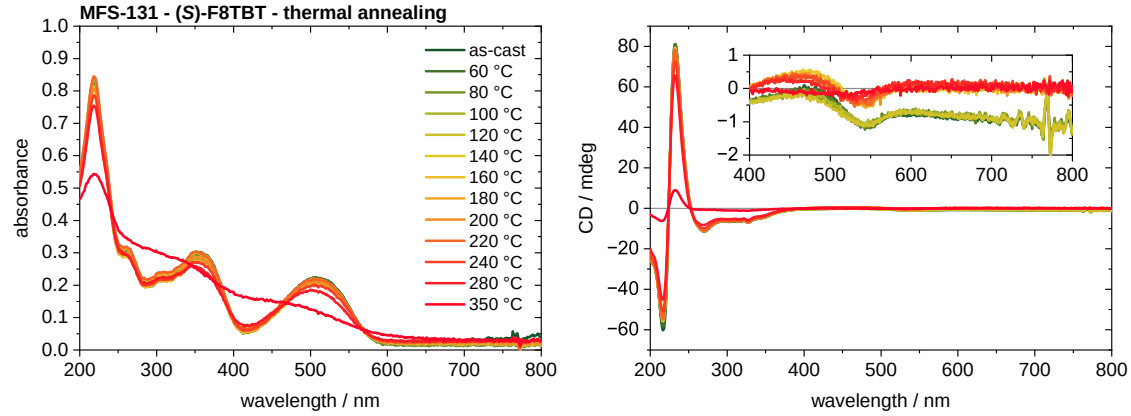


Figure I.19: UV/Vis absorbance (left) and corresponding CD spectra (right) of **(*S*)-F8TBT**, spin-coated from a toluene/chloroform 5:3 (v/v) solution under the same conditions and thermally annealed at indicated temperatures for 10 minutes. Thin films were prepared by spin coating 25 µL of the spin-on solution with a polymer concentration of 12.5 mg per mL, for 60 s at 1000 rpm with 550 rpm/s + 10 s at 4000 rpm with 1450 rpm/s on a fused silica substrate and – if noted – subsequent thermally annealed.

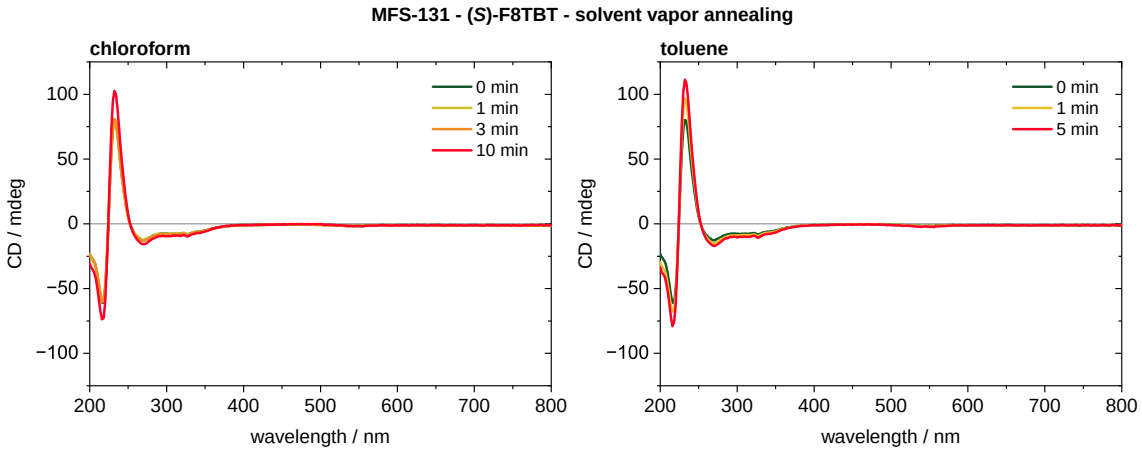


Figure I.20: CD spectra of **(*S*)-F8TBT**, spin-coated from a toluene/chloroform 5:3 (v/v) solution under the same conditions and solvent vapor annealed in a chloroform (left) or toluene (right) atmosphere for an indicated amount of time. Thin films were prepared by spin coating 25 µL of the spin-on solution with a polymer concentration of 12.5 mg per mL, for 60 s at 1000 rpm with 550 rpm/s + 10 s at 4000 rpm with 1450 rpm/s on a fused silica substrate.

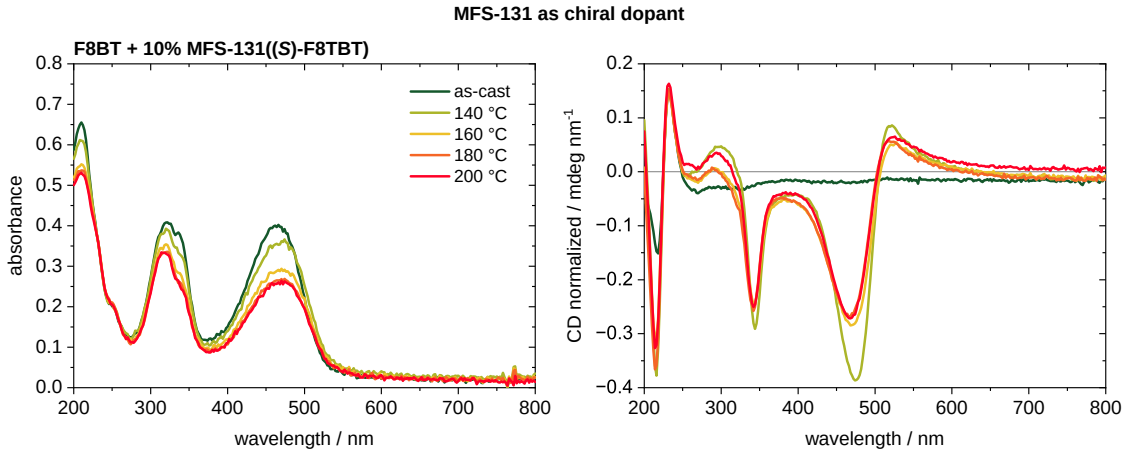


Figure I.21: UV/Vis absorbance (left) and corresponding normalized[c] CD spectra (right), where **(*S*)-F8TBT** was used as a polymeric chiral dopant for **F8BT**. A mixture of **F8BT** + **(*S*)-F8TBT** was spin-coated from a toluene/chloroform 5:3 (v/v) solution under the same conditions and thermally annealed at indicated temperatures for 10 minutes. Thin films were prepared by spin coating 25 µL of the spin-on solution with a polymer concentration of overall 12.5 mg per mL, for 60 s at 1000 rpm with 550 rpm/s + 10 s at 4000 rpm with 1450 rpm/s on a fused silica substrate and – if noted – subsequent thermally annealed.

[c] Please note: Normalized CD values are shown to enable an unbiased assessment of the influence of the polymeric chiral dopant and to allow a better comparison between MFS-131 (**(*S*)-F8TBT**) and MFS-125 (**poly-(*S*)-Binol-BTQT**„ shown in Figure I.16) as such dopants.

I.3.4 Additional Information on MFS-134 – (*S*)-c_{20}Binol-PCE11

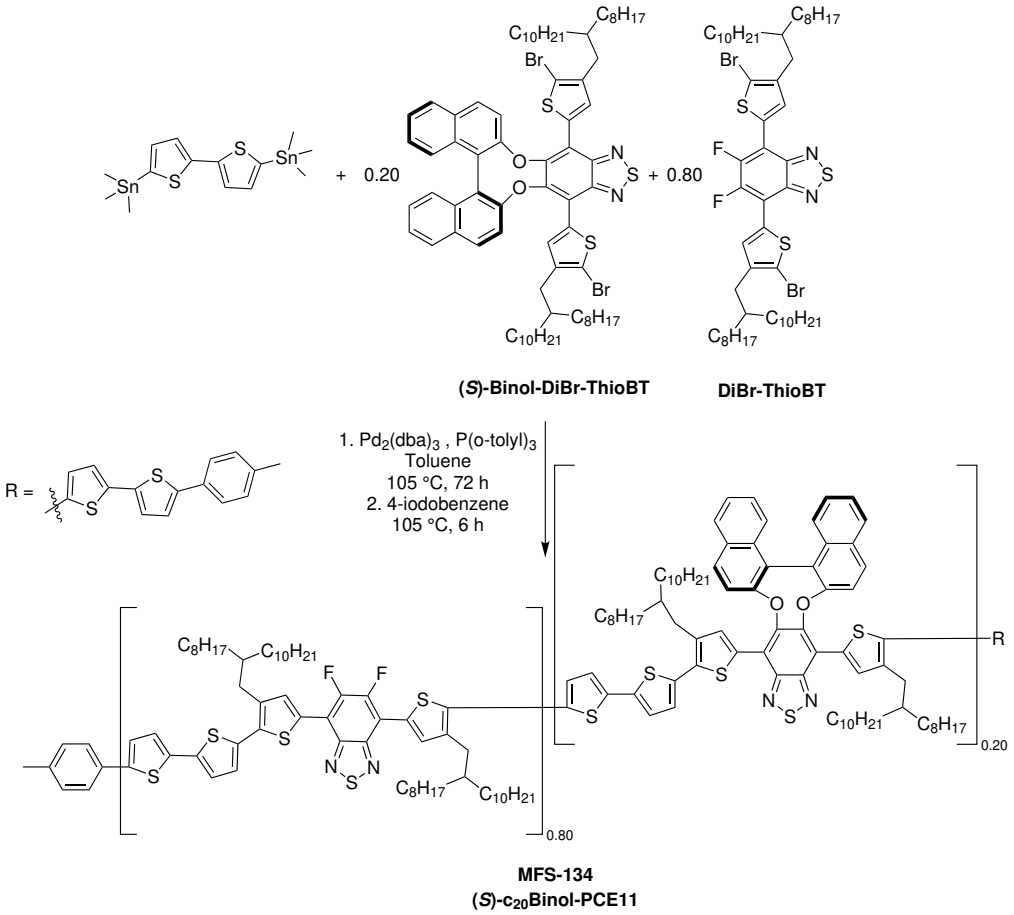




Figure I.22: Top: Synthesis of **(*S*)-c_{20}Binol-PCE11**, starting from **DiBr-ThioBT**, enantiopure **(*S*)-Binol-DiBr-ThioBT** and 5,5'-Bis(trimethylstannyl)-2,2'-bithiophene. Bottom: Picture of the obtained dark red to black solid under normal light (left) and solved in toluene at stated temperatures (right).

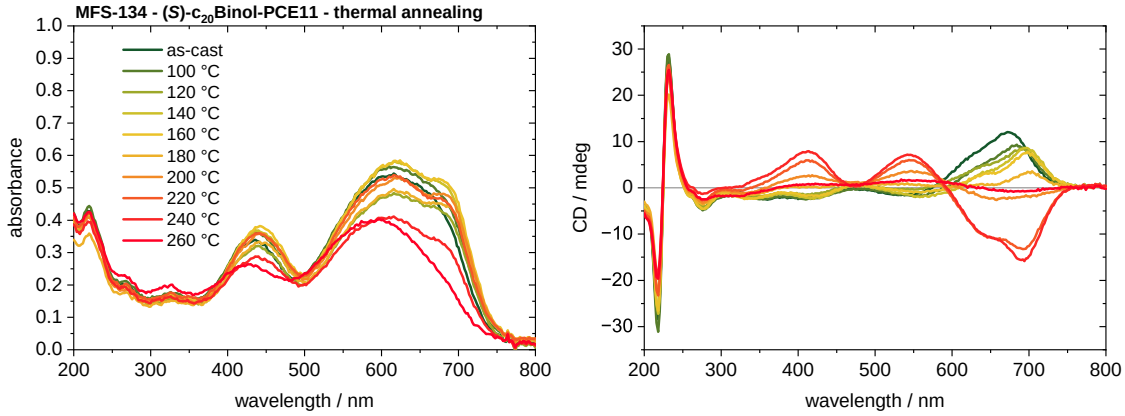
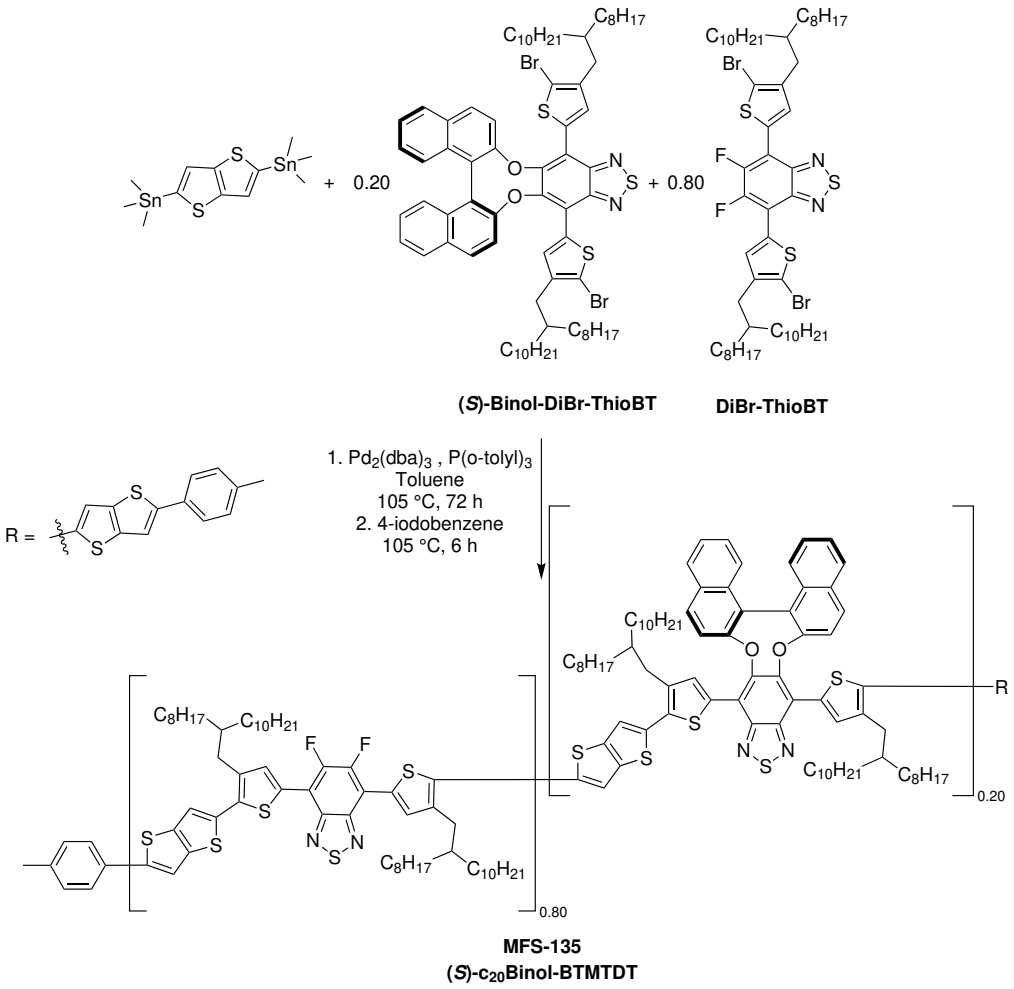


Figure I.23: UV/Vis absorbance (left) and corresponding CD spectra (right) of **(*S*)-c_{20}Binol-PCE11**, spin-coated from a toluene/chloroform 5:3 (v/v) solution under the same conditions and thermally annealed at indicated temperatures for 10 minutes. Thin films were prepared by spin coating 25 µL of the spin-on solution with a polymer concentration of 12.5 mg per mL, for 60 s at 1000 rpm with 550 rpm/s + 10 s at 4000 rpm with 1450 rpm/s on a fused silica substrate and – if noted – subsequent thermally annealed.

I.3.5 Additional Information on MFS-135 – (*S*)-c_{20}Binol-BTMTDT



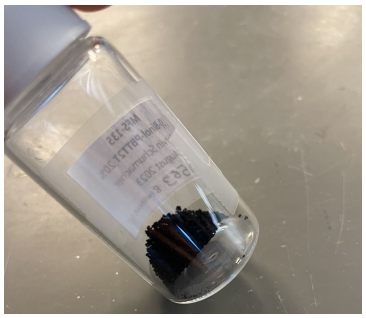


Figure I.24: Top: Synthesis of **(*S*)-c_{20}Binol-BTMTDT**, starting from **DiBr-ThioBT**, enantiopure **(*S*)-Binol-DiBr-ThioBT** and 2,5-Bis(trimethylstannyl)-thieno[3,2-*b*]thiophene. Bottom: Picture of the obtained dark red to black solid under normal light.

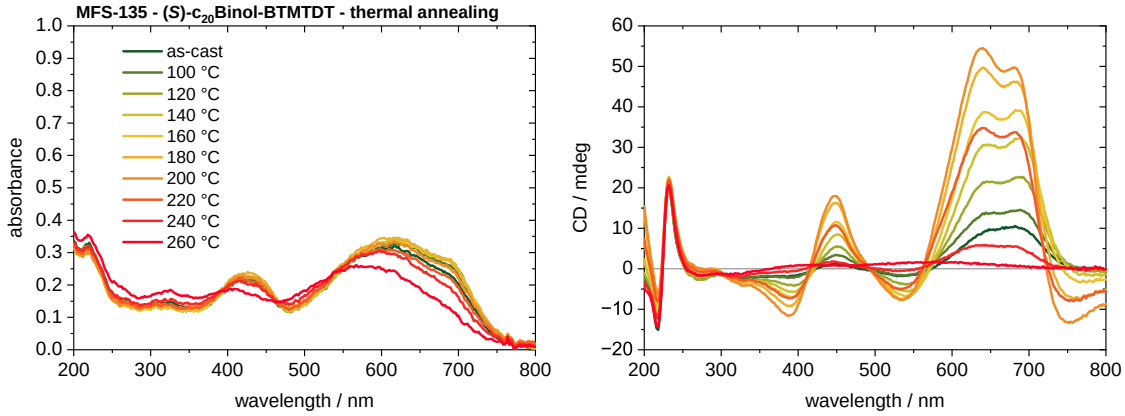


Figure I.25: UV/Vis absorbance (left) and corresponding CD spectra (right) of **(*S*)-c$_{20}$Binol-BTMTDT**, spin-coated from a toluene/chloroform 5:3 (v/v) solution under the same conditions and thermally annealed at indicated temperatures for 10 minutes. Thin films were prepared by spin coating 25 µL of the spin-on solution with a polymer concentration of 12.5 mg per mL, for 60 s at 1000 rpm with 550 rpm/s + 10 s at 4000 rpm with 1450 rpm/s on a fused silica substrate and – if noted – subsequent thermally annealed.

APPENDIX J

Substance/Reaction-Index + NMR and Mass Spectra

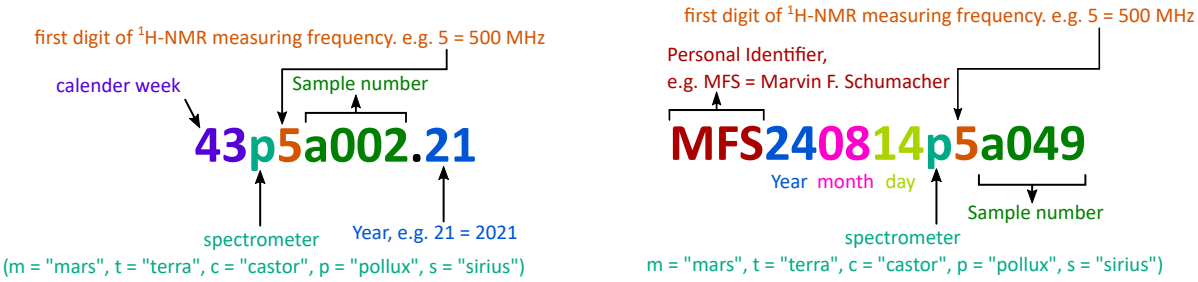


Figure J.1: Naming scheme of NMR identifiers. The scheme applied until the end of 2022 is shown on the left, while the scheme introduced in 2023 is shown on the right. Further details on the NMR instruments are provided in Chapter 13 - Materials and Methods.

Table J.1: Overview of substance abbreviations, reaction IDs, and NMR codes.

Abbreviation	Reaction-ID	full NMR-Code
Chapter 4 - Citronellyl-Functionalized Squaraines:		
(*S*)-Ci-N-IB	MFS-45	43p5a022.21
(*S*)-nCi-N-IB	MFS-47	47c5a026.21
(*S*)-Ci-N-O	*Supervised work*	43c5a011.21
(*S*)-nCi-N-O	*Supervised work*	49s7a021.21
(*S*)-Ci-N-NP	MFS-161	MFS240426c5a036
(*S*)-Ci-N-Ad	MFS-149/MFS-155	MFS240131c5a010
(*S*)-nCi-N-Ad	MFS-150	MFS240213p5a018
(*S*,*S*)-nCi-SQIB	MFS-48	51s7a014.21
(*S*,*S*)-nOnCi-SQ	*Supervised work*	50s7b008.21

Continued on next page

Abbreviation	Reaction-ID	full NMR-Code
(*S*,*S*)-Ci-SQNP	MFS-166	MFS240619p5a035
Chapter 7 - ProSQ-C1:		
(*S*)-Boc-Pro-C1	MFS-93	MFS230208c5b022
(*S*)-Pro-C1	MFS-94	MFS230214c5a016
(*S*,*S*)-ProSQ-C1	MFS-95	MFS230418c5a025
Chapter 9 - OHI-SQs:		
(*S*)-TIQ-C10	MFS-92	MFS230214c5a017
Boc-(*S*)-2mb-isoindole	MFS-172	MFS240813p5a028
(*S*)-2mb-isoindole	MFS-181	MFS240813p5a029
(*S*)-OHI-OH	MFS-98	MFS230320p5a015
(*S*)-Boc-OHI-OH	MFS-101	MFS230330c5a007
(*S*)-Boc-OHI-C3	MFS-140	MFS231027c5a015
(*S*)-OHI-C3	MFS-142	MFS231116c5a060
(*S*)-Boc-OHI-C10	MFS-102	MFS230411p5a012
(*S*)-OHI-C10	MFS-105	MFS230414c5a031
(*S*,*S*)-2mb-isoindole-SQ	MFS-182	not possible
(*S*,*S*)-OHI-SQ-C3	MFS-143	MFS240209s7a007
(*S*,*S*)-OHI-SQ-C10	MFS-106	MFS231024p5a019
Chapter 10 - 2mb-SQs:		
(*S*)-2mb-COOH	MFS-54/MFS-75	14s7a021.22
(*S*)-2mb-CON-IB	MFS-55/MFS-167	MFS240513p5a022
(*S*)-2mb-CON-C10	MFS-63	15t4a081.22
(*S*)-2mb-CON-C16	MFS-55/MFS-167	30c5a060.22
(*S*)-2mb-CON-PE	MFS-153	MFS240321c5a037
(*S*)-2mb-N-IB	MFS-168	MFS240516p5a051
(*S*)-2mb-N-C10	MFS-64	17p5a037.22
(*S*)-2mb-N-C16	MFS-80	44p5a024.22
(*S*)-2mb-N-PE	MFS-157	MFS240612t4a018
(*S*,*S*)-2mb-SQIB	MFS-180	MFS240814p5a049
(*S*,*S*)-2mb-DSQ	MFS-65	21s7a014.22
(*S*,*S*)-2mb-HDSQ	MFS-89	MFS230313p5a009
(*S*,*S*)-2mb-SQPE	MFS-179	MFS240808p5a030
Chapter 11 - Chiral Polymers:		
(*S*)-Binol-DiBr-BT	MFS-116/MFS-120	*Measured at CU Boulder*

Continued on next page

Abbreviation	Reaction-ID	full NMR-Code
DiBr-ThioBT	MFS-122	*Measured at CU Boulder*
(*S*)-Binol-ThioBT	MFS-117/MFS-124	*Measured at CU Boulder*
(*S*)-Binol-DiBr-ThioBT	MFS-119/MFS-130	*Measured at CU Boulder*
F8BT	MFS-126	*Measured at CU Boulder*
(*S*)-c_5F8BT	MFS-127	*Measured at CU Boulder*
(*S*)-c_{10}F8BT	MFS-128	*Measured at CU Boulder*
(*S*)-c_{20}F8BT	MFS-129	*Measured at CU Boulder*
(*S*)-F8TBT	MFS-131	*Measured at CU Boulder*
poly-(*S*)-Binol-BTQT	MFS-125	*Measured at CU Boulder*
(*S*)-c_{20}Binol-PCE11	MFS-134	*Measured at CU Boulder*
(*S*)-c_{20}Binol-BTMTDT	MFS-135	*Measured at CU Boulder*

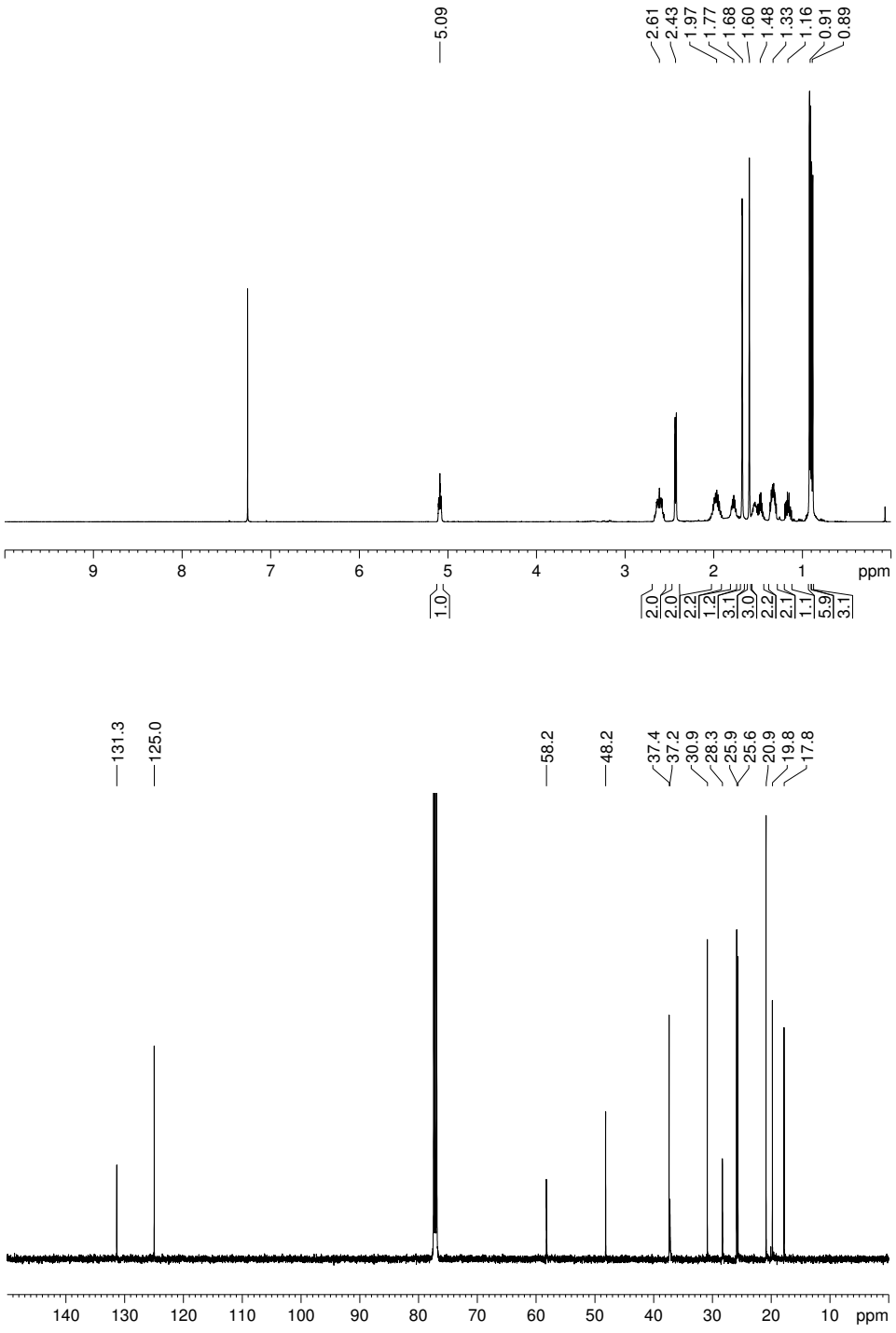


Figure J.2: ^{1}H- (top, 500 MHz) and ^{13}C-NMR (bottom, 125 MHz) spectrum of **(*S*)-Ci-N-IB**; $CDCl_3$, 298 K.

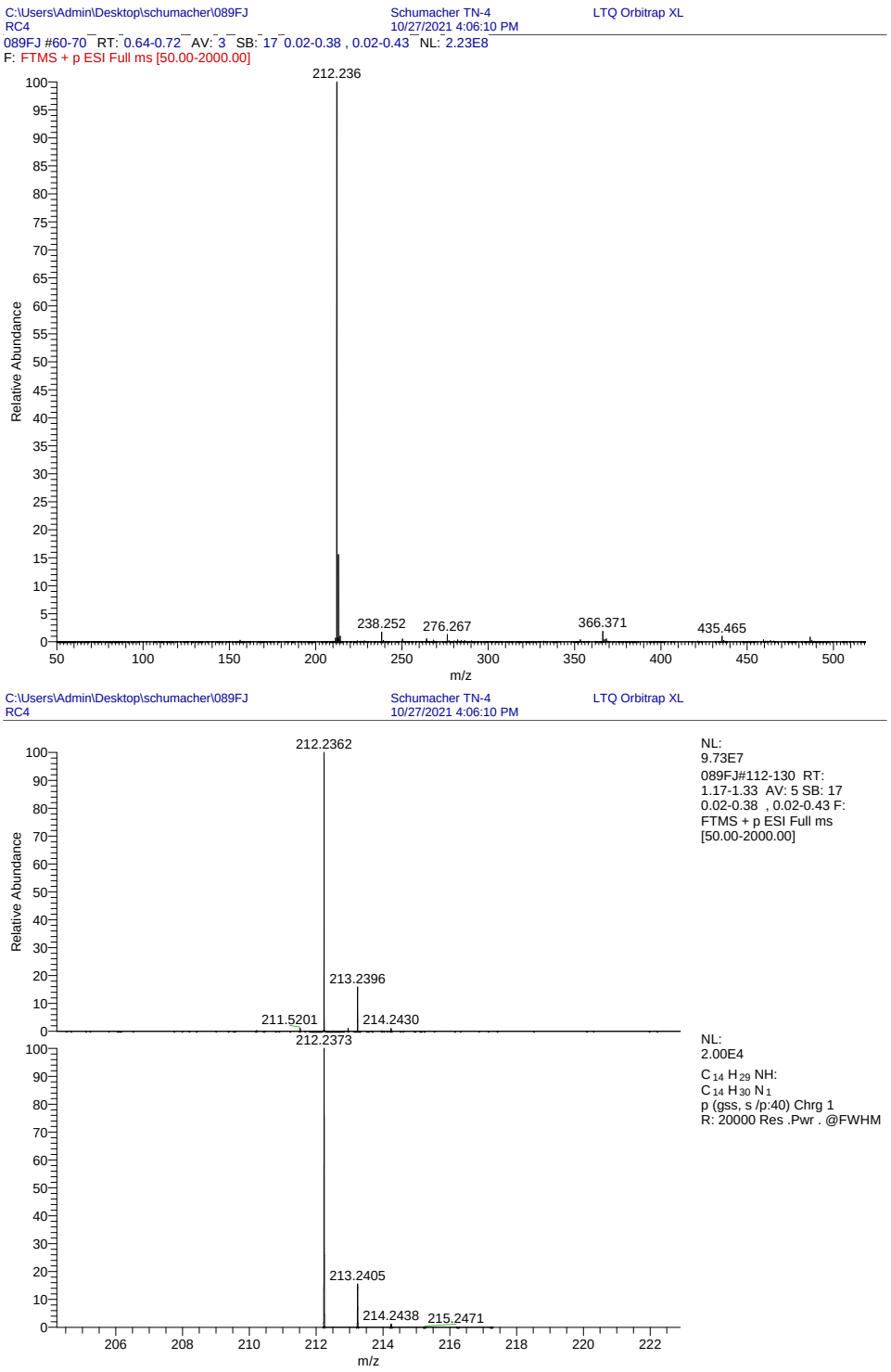


Figure J.3: ESI(+) Mass spectra of **(*S*)-Ci-N-IB**.

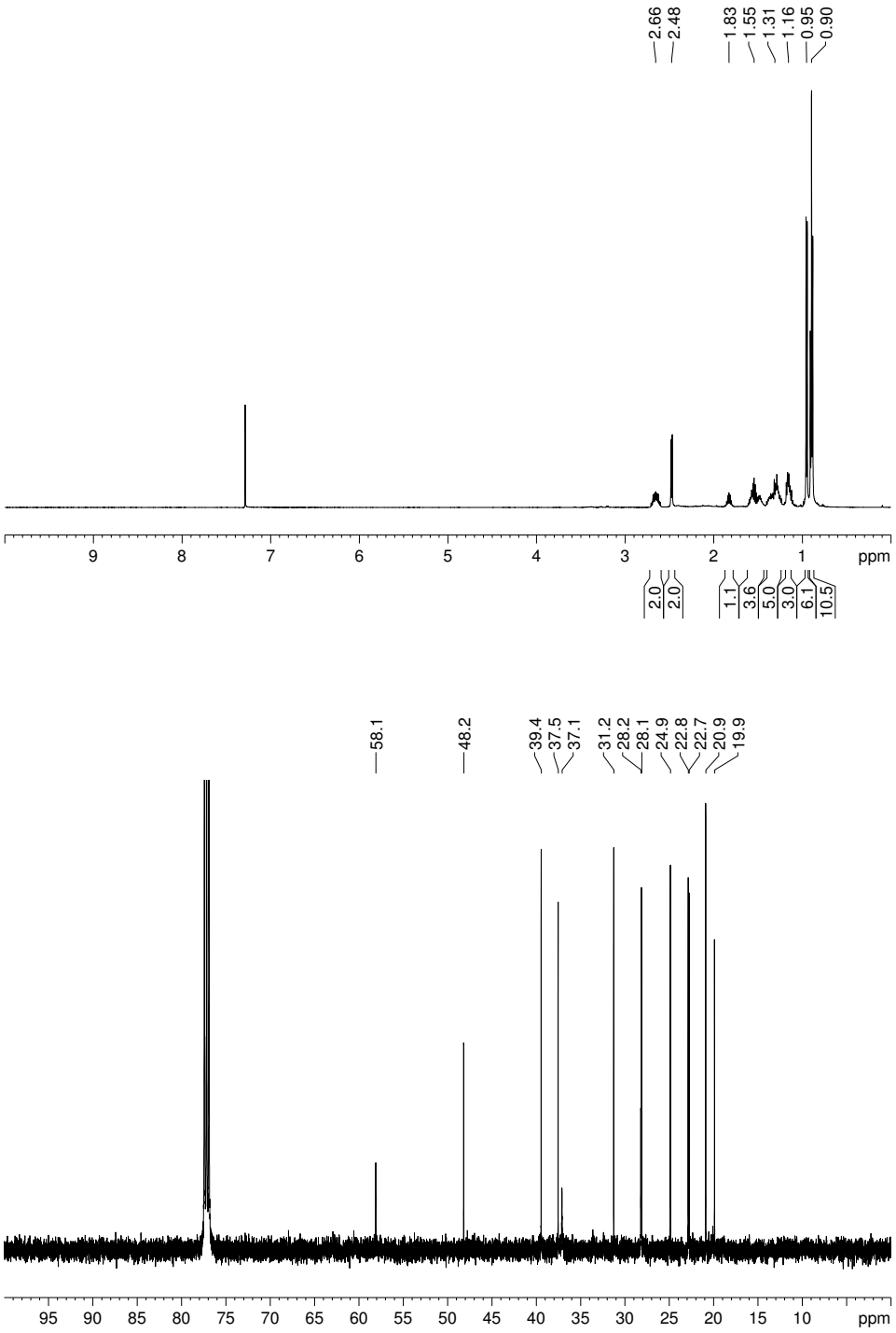


Figure J.4: ^{1}H- (top, 500 MHz) and ^{13}C-NMR (bottom, 125 MHz) spectrum of **(*S*)-nCi-N-IB**; $CDCl_3$, 298 K.

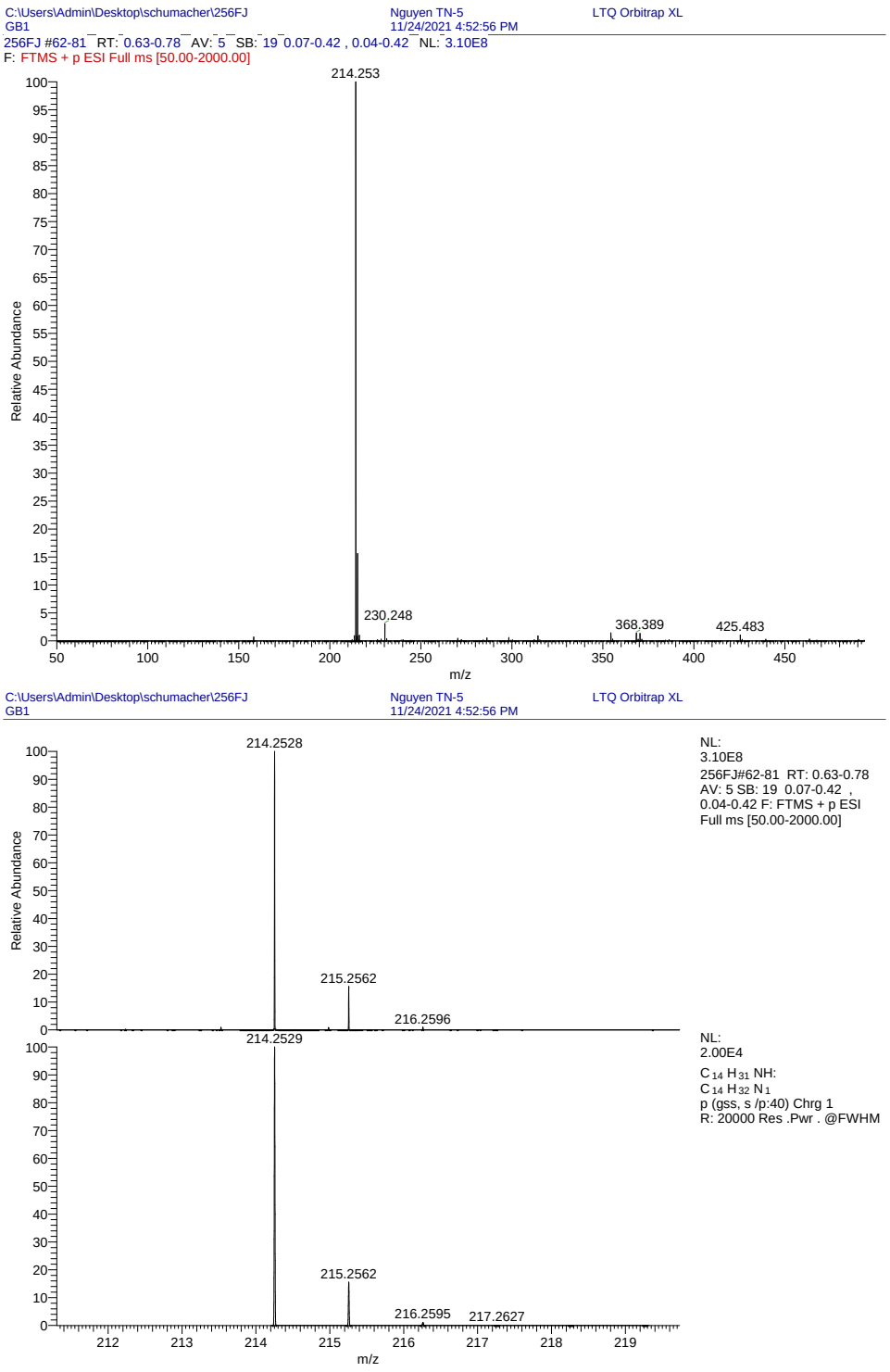


Figure J.5: ESI(+) Mass spectra of **(*S*)-nCi-N-IB**.

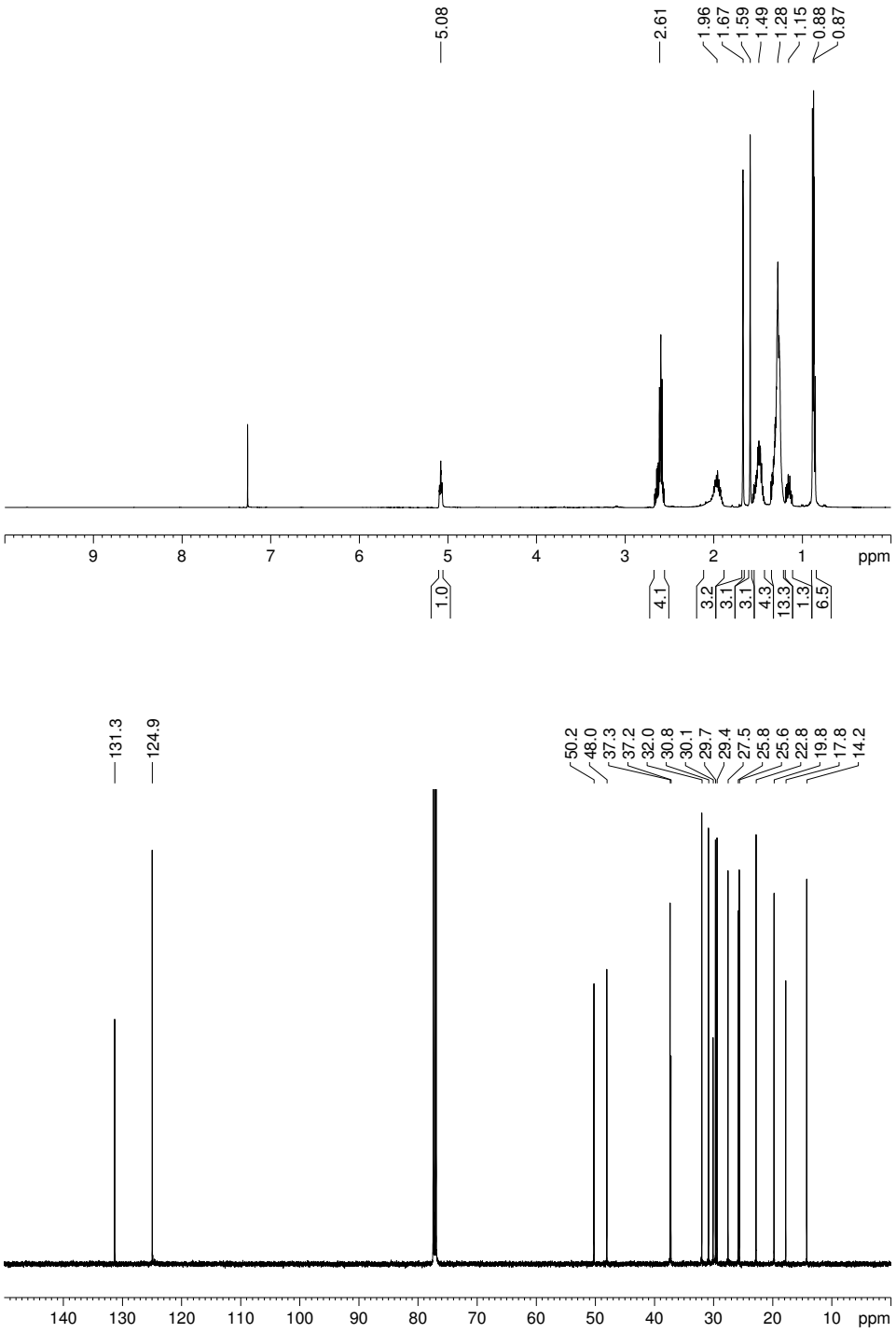


Figure J.6: ^{1}H- (top, 500 MHz) and ^{13}C-NMR (bottom, 125 MHz) spectrum of **(*S*)-Ci-N-O**; $CDCl_3$, 298 K.

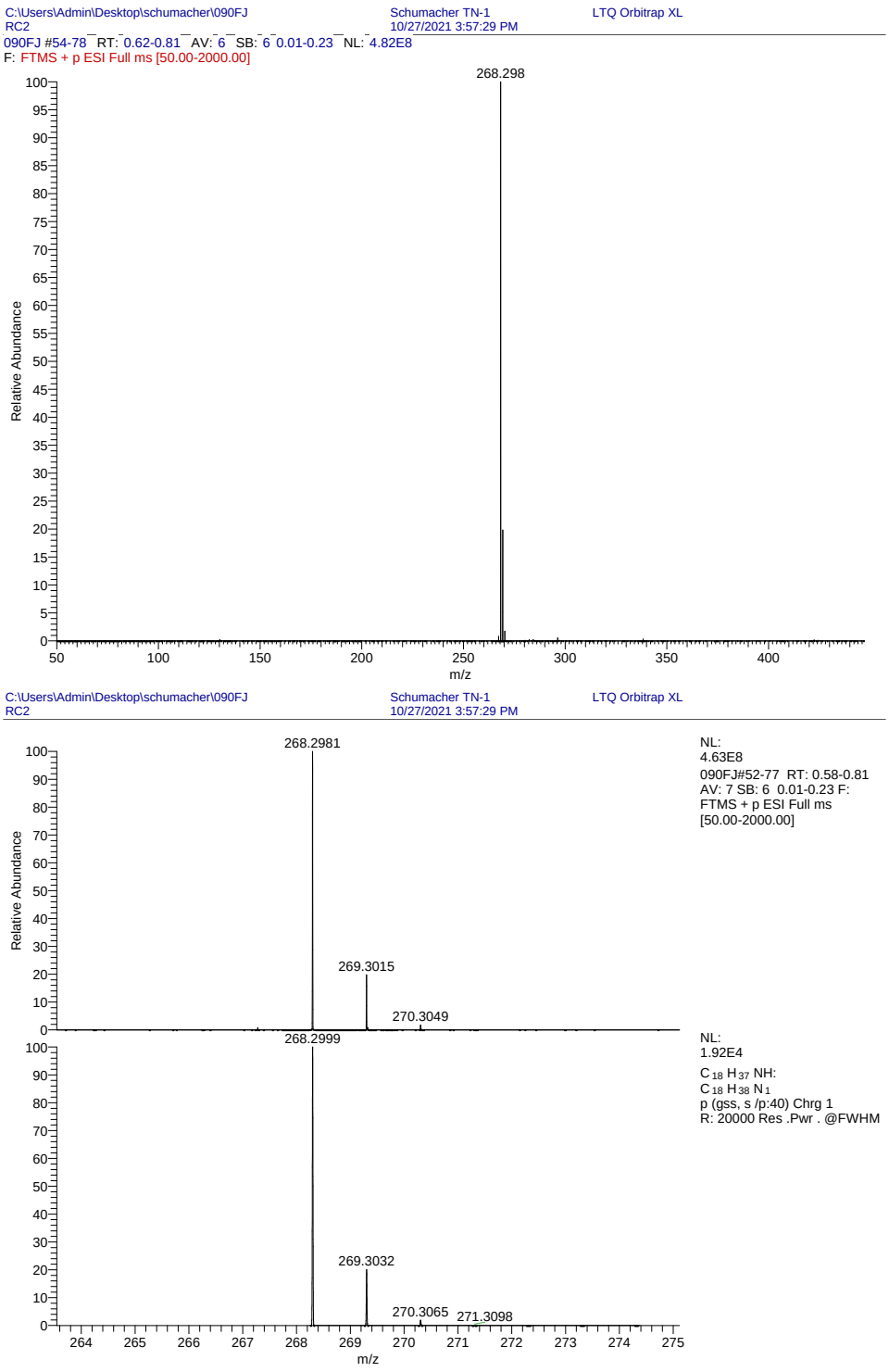


Figure J.7: ESI(+) Mass spectra of **(*S*)-Ci-N-O**.

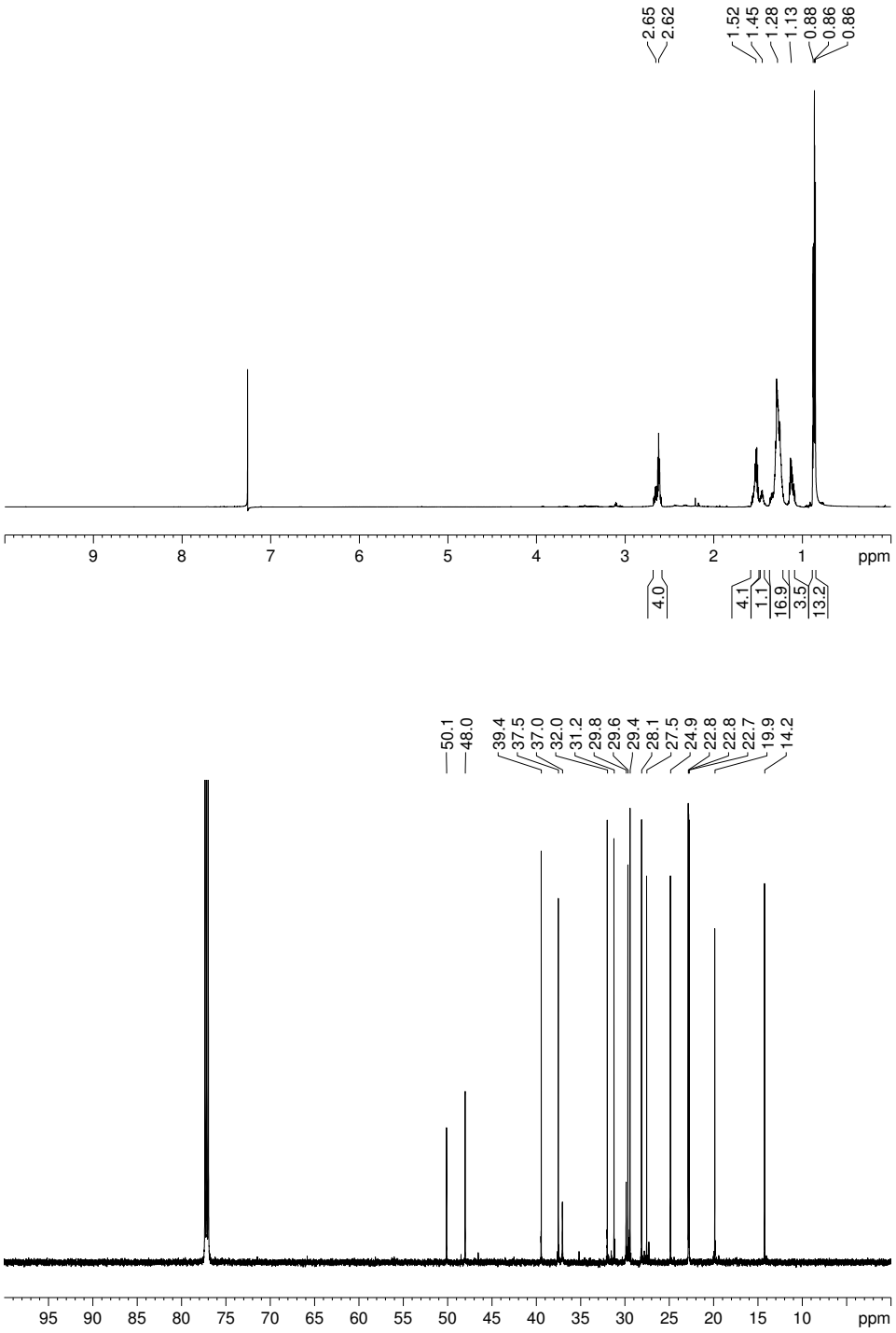


Figure J.8: ^{1}H- (top, 700 MHz) and ^{13}C-NMR (bottom, 176 MHz) spectrum of **(*S*)-nCi-N-O**; $CDCl_3$, 298 K.

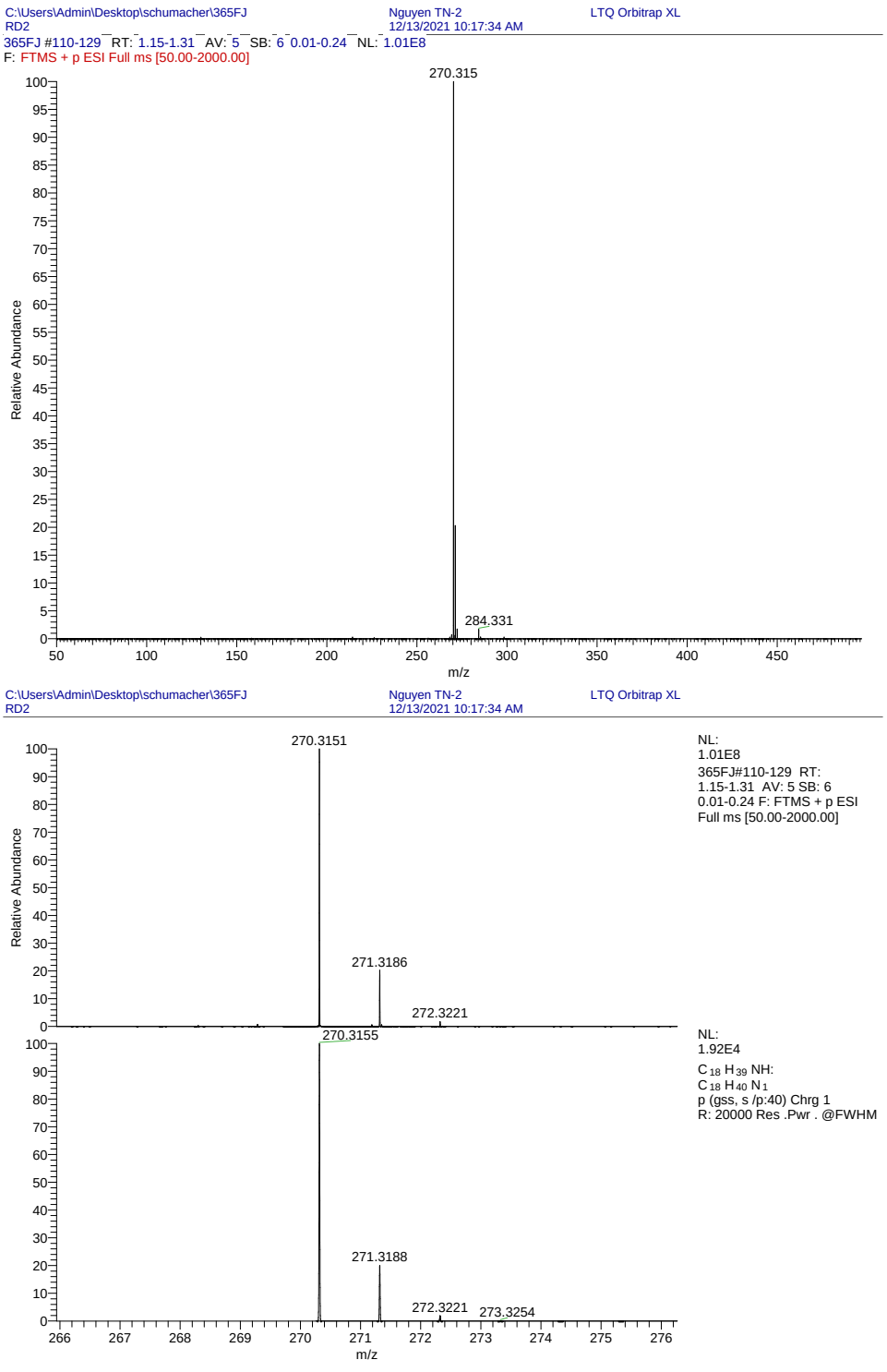


Figure J.9: ESI(+) Mass spectra of **(*S*)-nCi-N-O**.

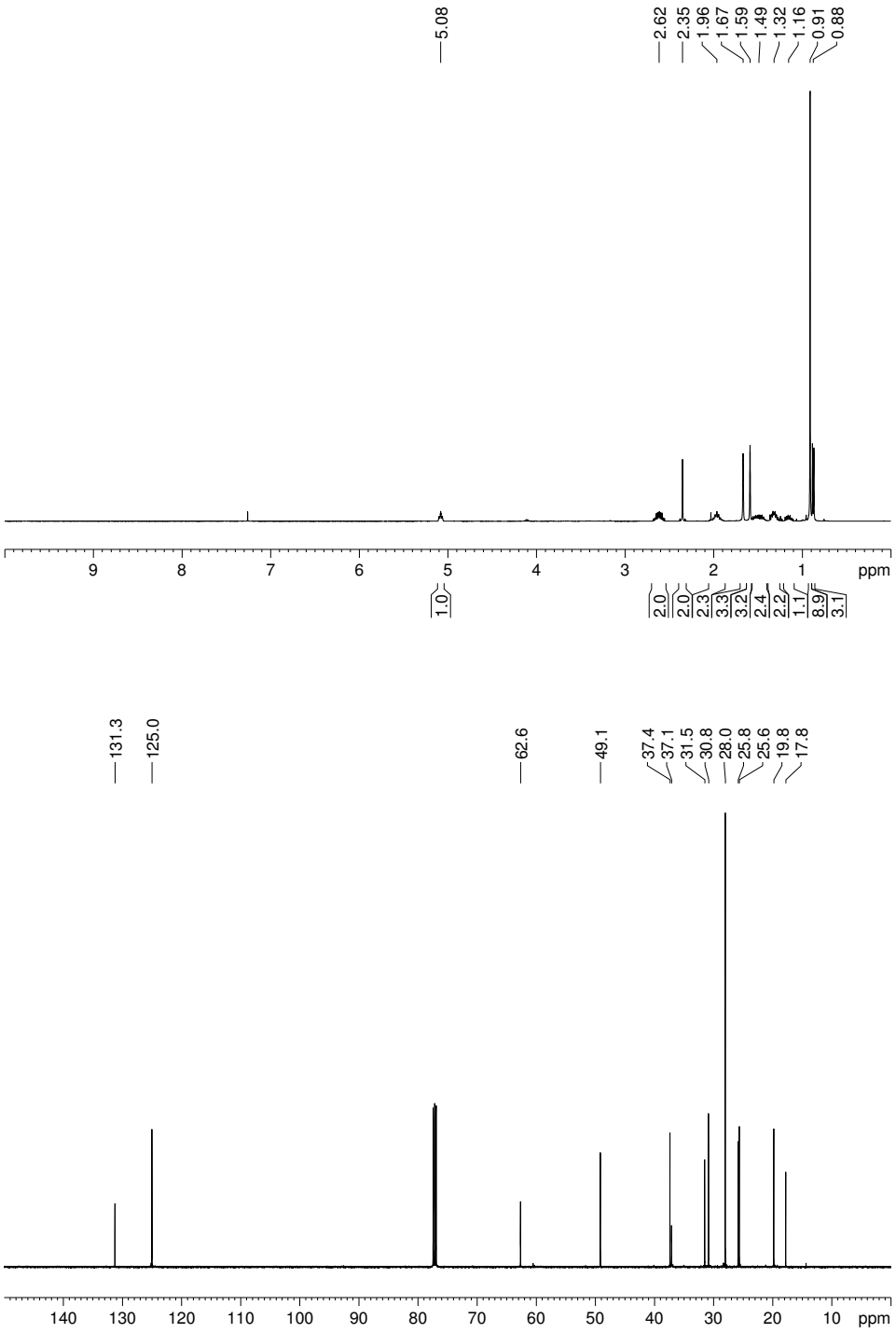


Figure J.10: ^{1}H- (top, 500 MHz) and ^{13}C-NMR (bottom, 125 MHz) spectrum of **(*S*)-Ci-N-NP**; $CDCl_3$, 298 K.

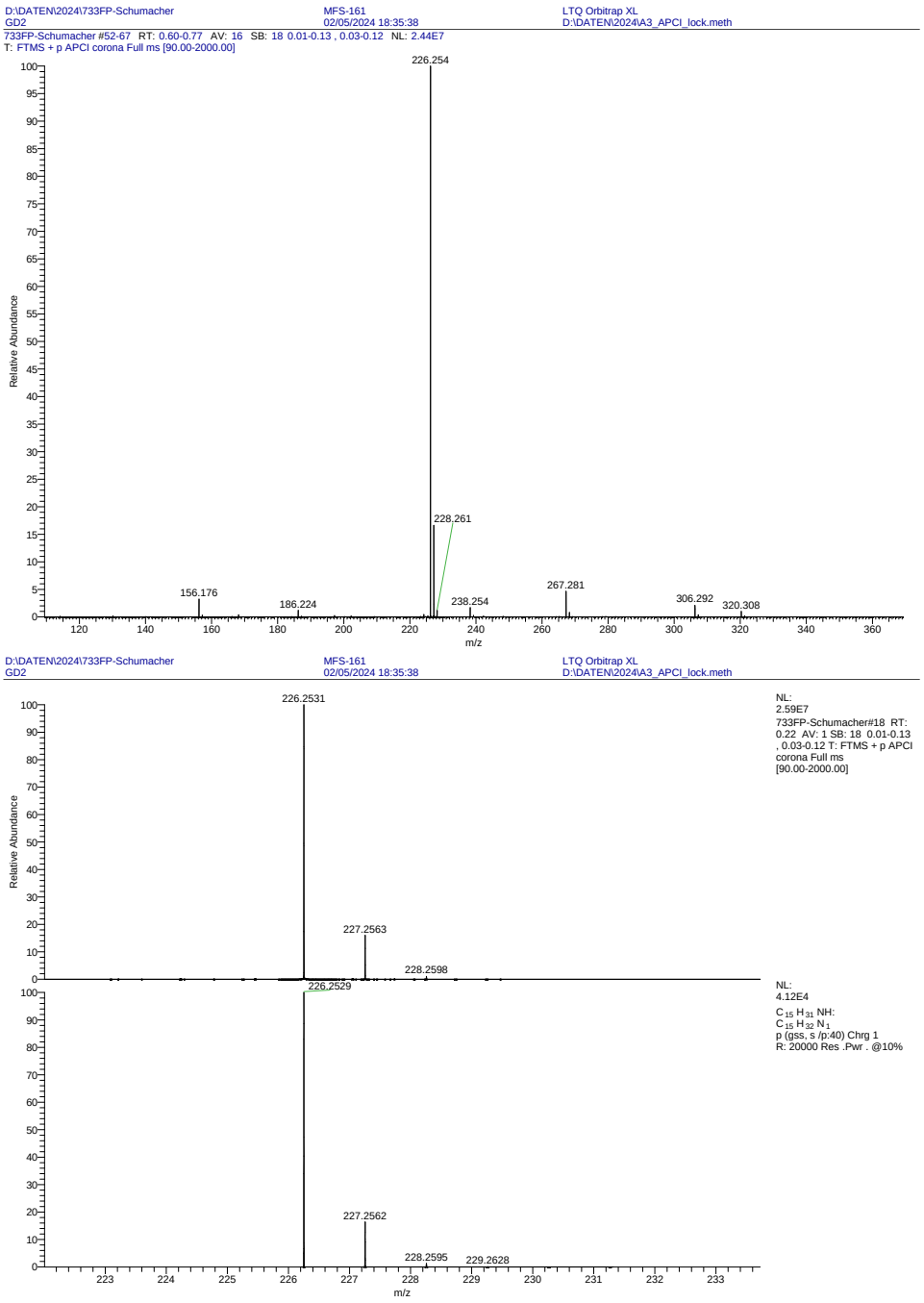


Figure J.11: APCI Mass spectra of **(*S*)-Ci-N-NP**.

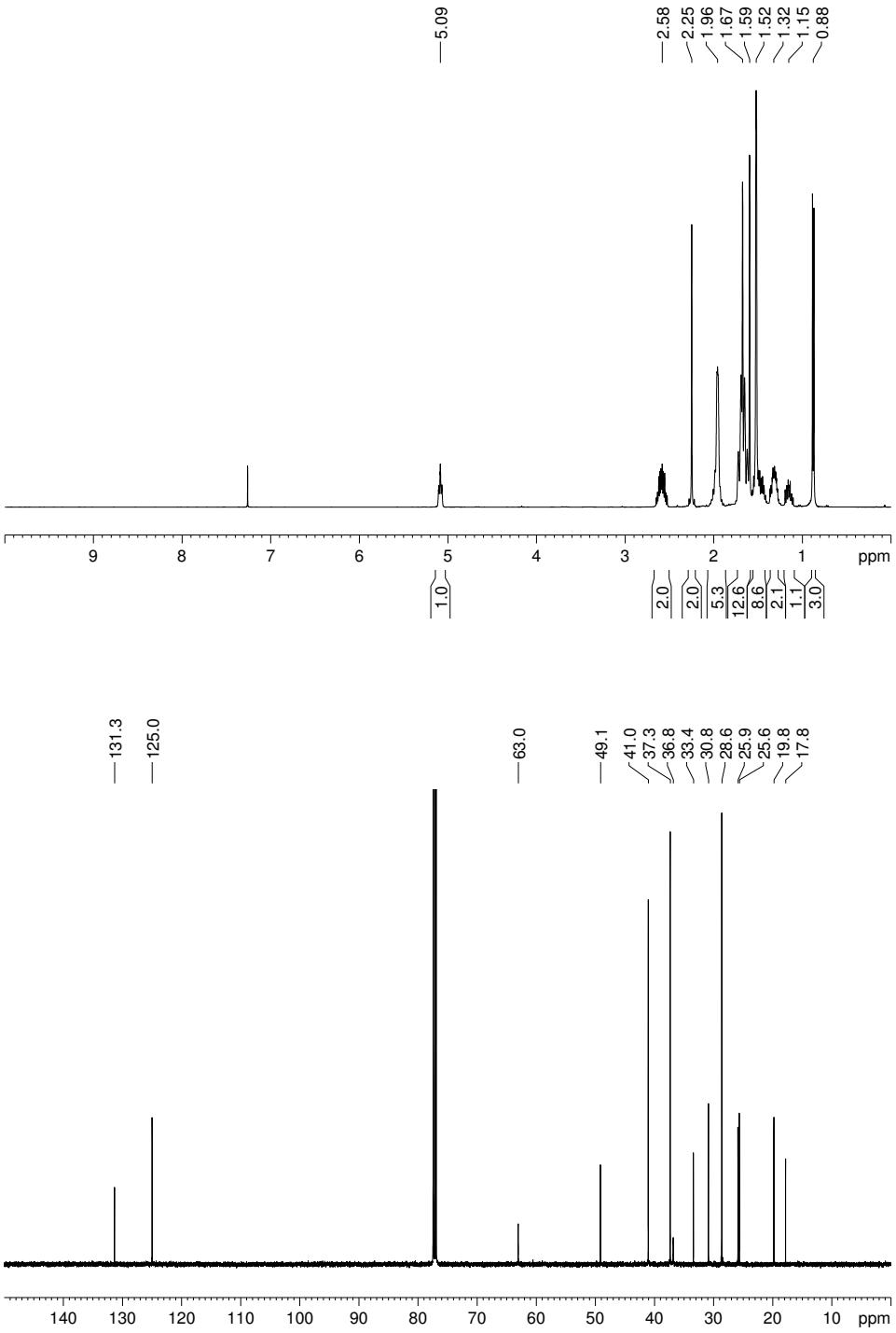


Figure J.12: ^{1}H- (top, 500 MHz) and ^{13}C-NMR (bottom, 125 MHz) spectrum of **(*S*)-Ci-N-Ad**; $CDCl_3$, 298 K.

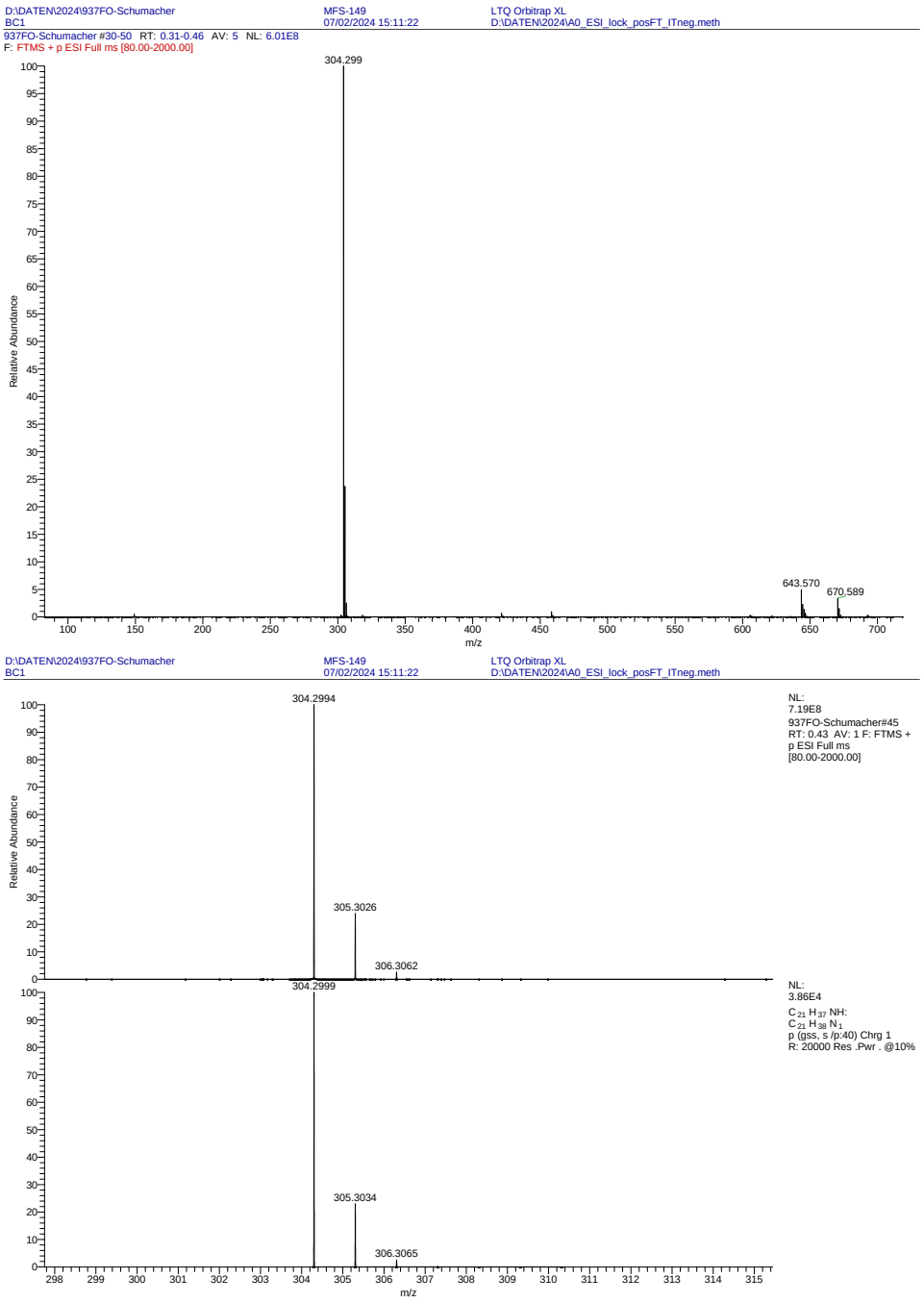


Figure J.13: ESI(+) Mass spectra of **(*S*)-Ci-N-Ad**.

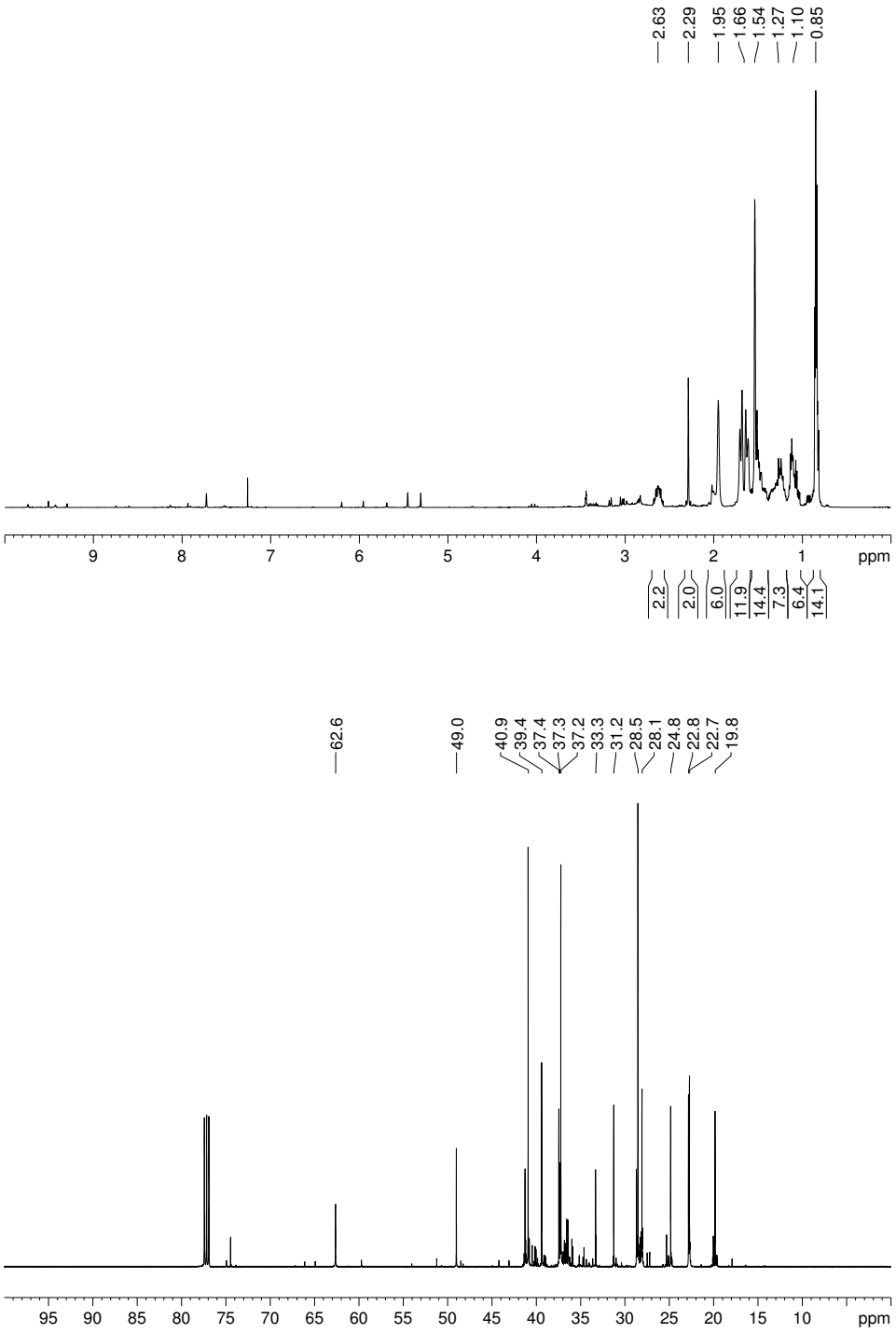


Figure J.14: ^{1}H- (top, 500 MHz) and ^{13}C-NMR (bottom, 125 MHz) spectrum of **(*S*)-nCi-N-Ad**; $CDCl_3$, 298 K.

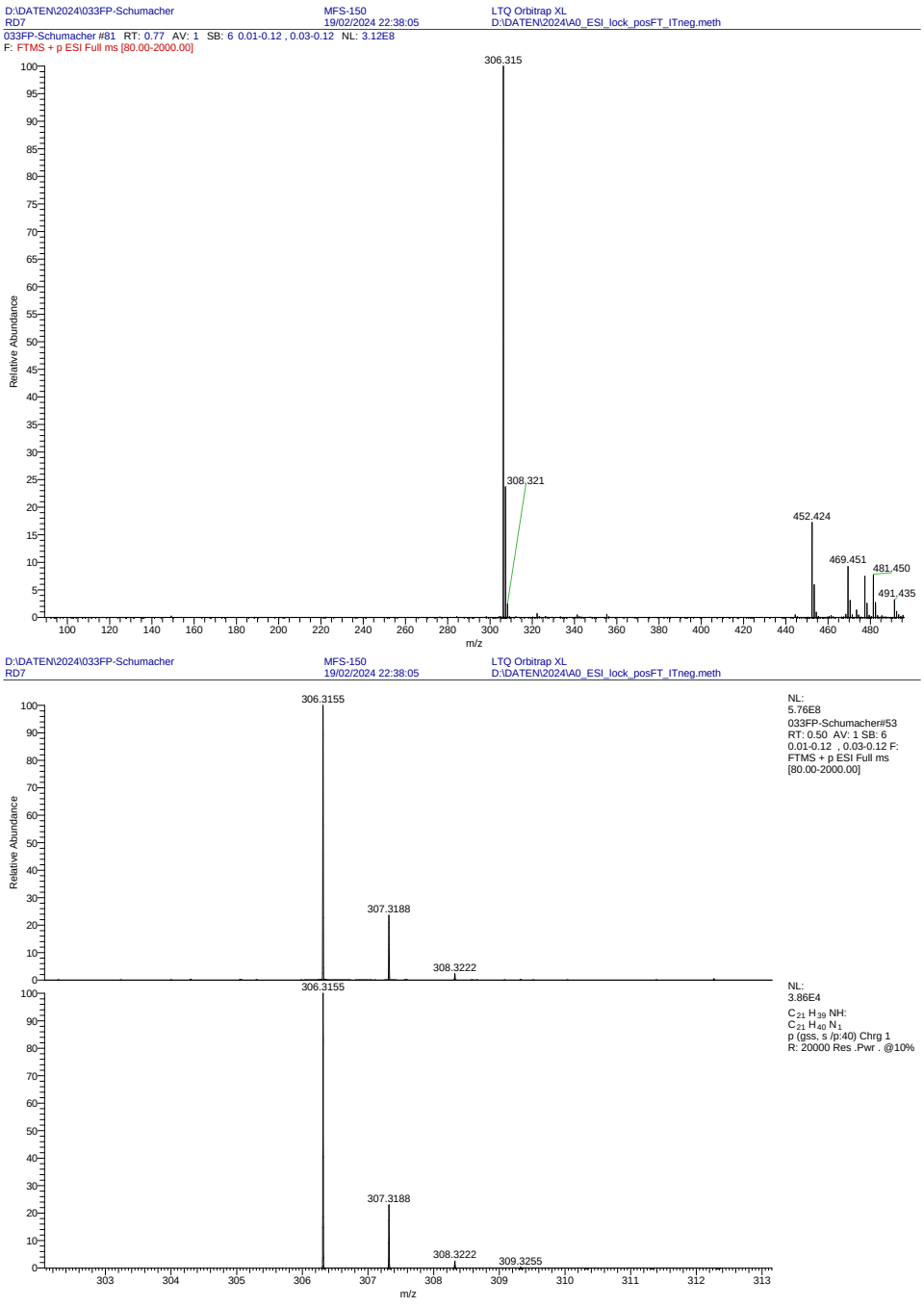


Figure J.15: ESI(+) Mass spectra of **(*S*)-nCi-N-Ad**.

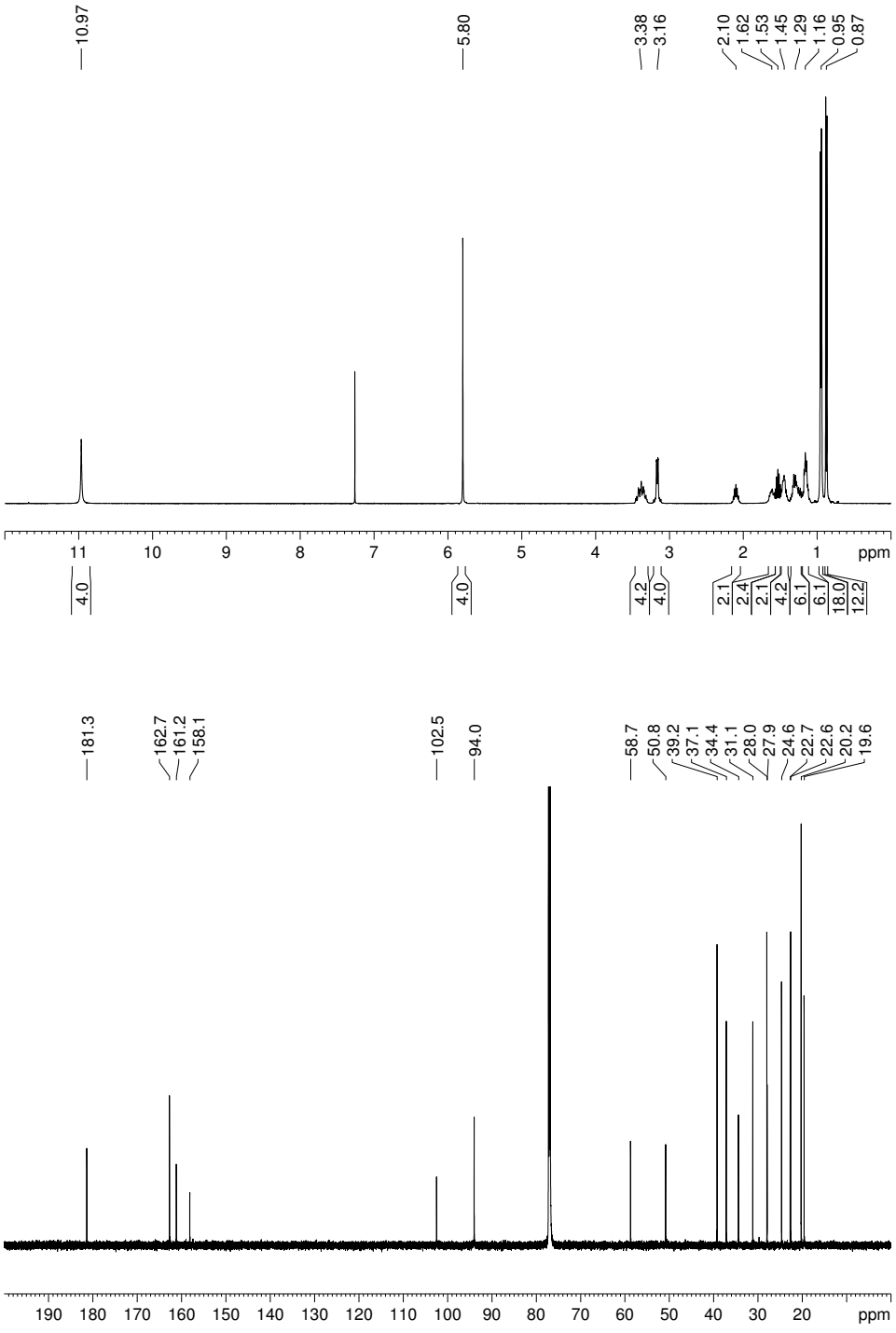


Figure J.16: ^{1}H- (top, 700 MHz) and ^{13}C-NMR (bottom, 176 MHz) spectrum of **(*S*,*S*)-nCi-SQIB**; $CDCl_3$, 298 K.

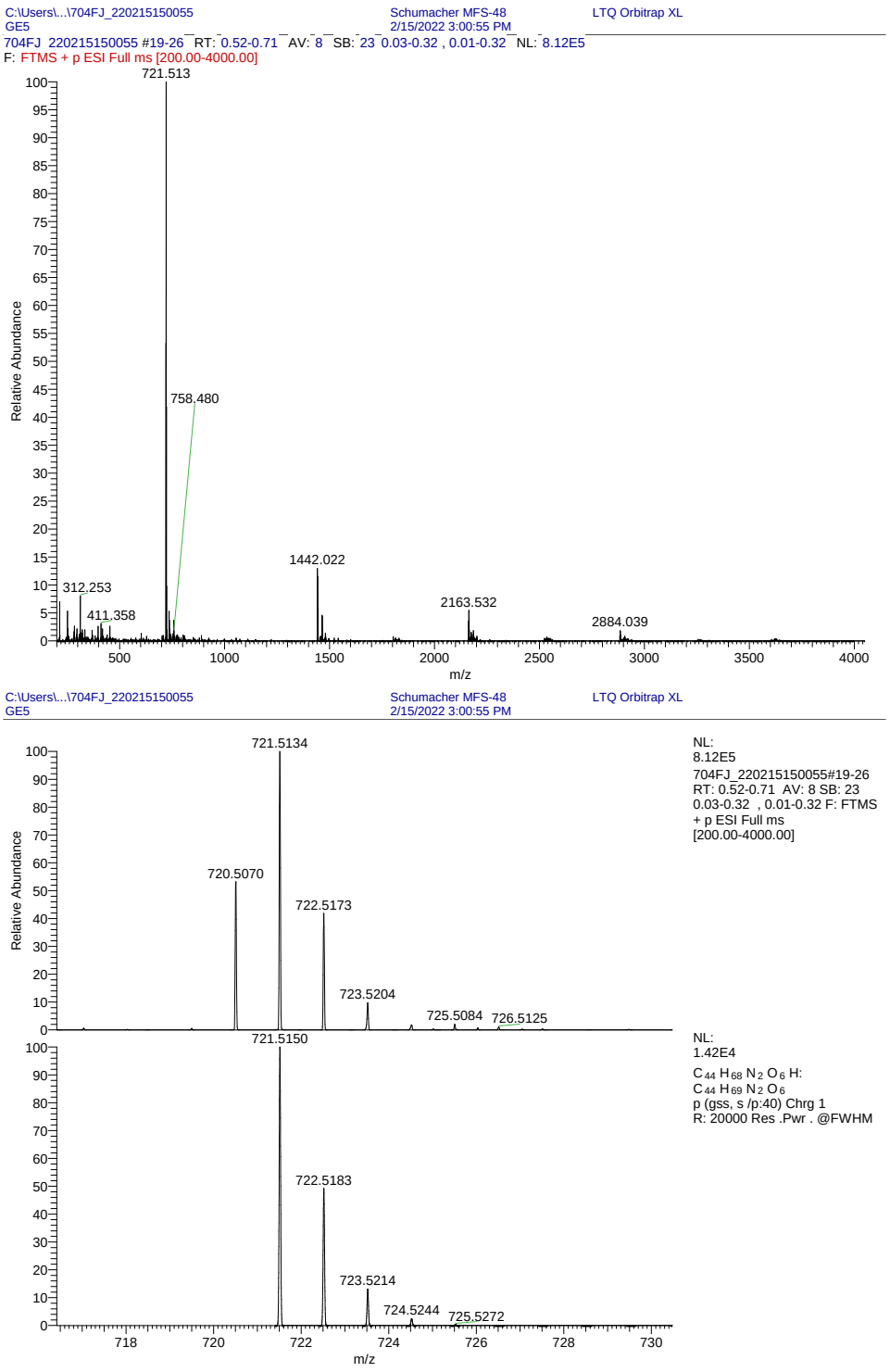


Figure J.17: ESI(+) Mass spectra of **(*S*,*S*)-nCi-SQIB**.

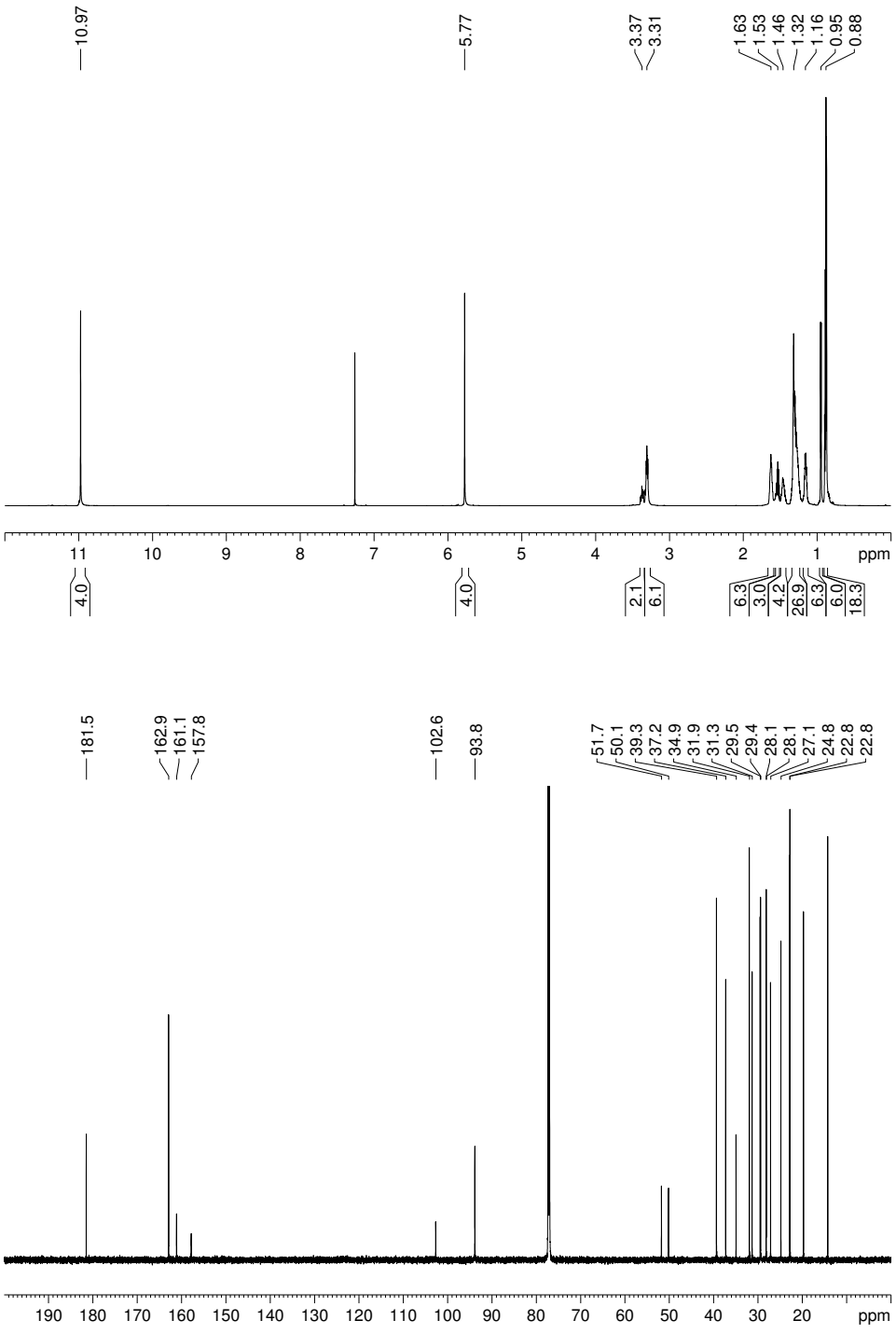


Figure J.18: ^{1}H- (top, 700 MHz) and ^{13}C-NMR (bottom, 176 MHz) spectrum of **(*S*,*S*)-nOnCi-SQ**; $CDCl_3$, 298 K.

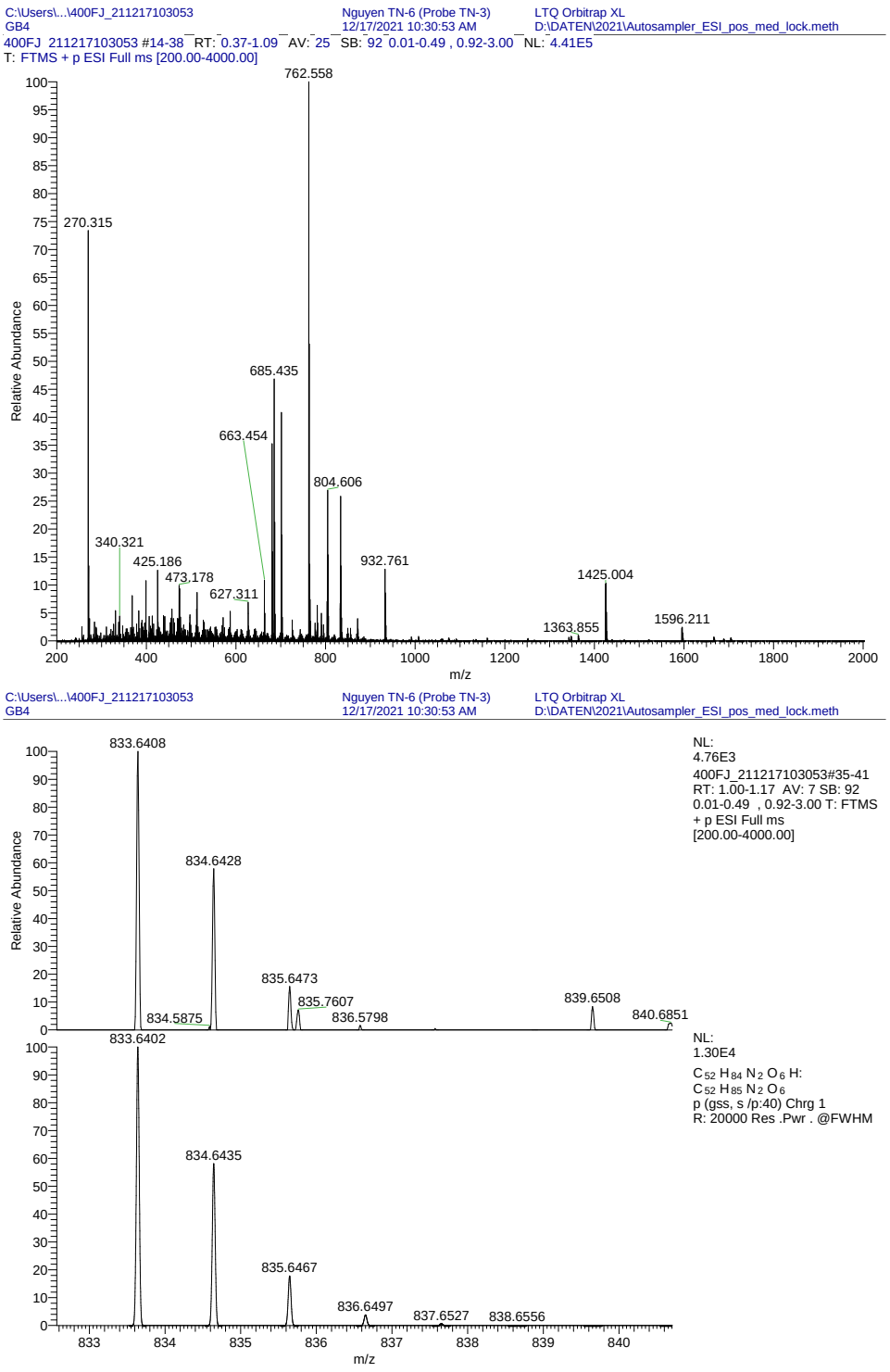


Figure J.19: ESI(+) Mass spectra of **(*S*,*S*)-nOnCi-SQ**.

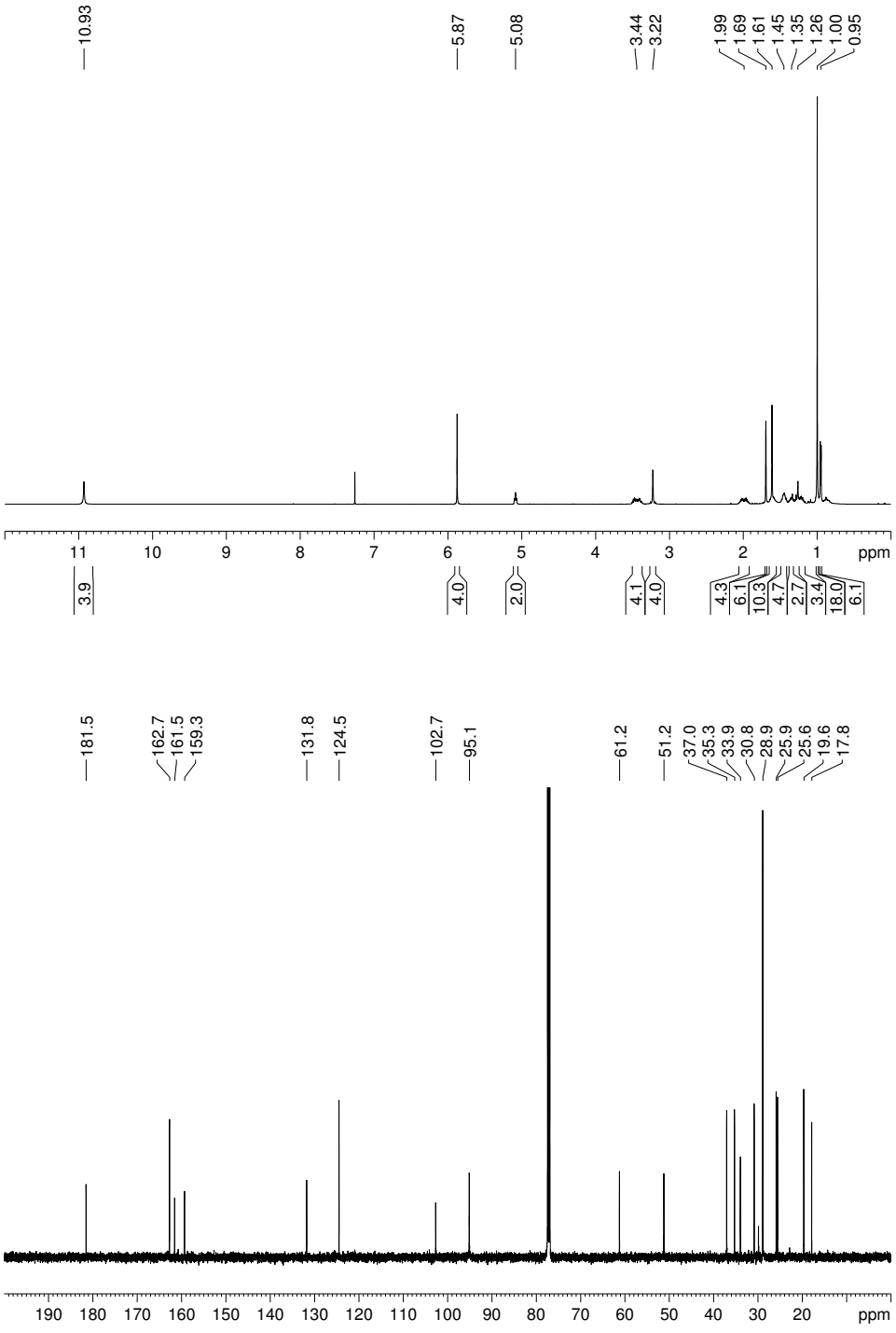


Figure J.20: ^{1}H- (top, 500 MHz) and ^{13}C-NMR (bottom, 125 MHz) spectrum of **(*S*,*S*)-Ci-SQNP**; $CDCl_3$, 298 K.

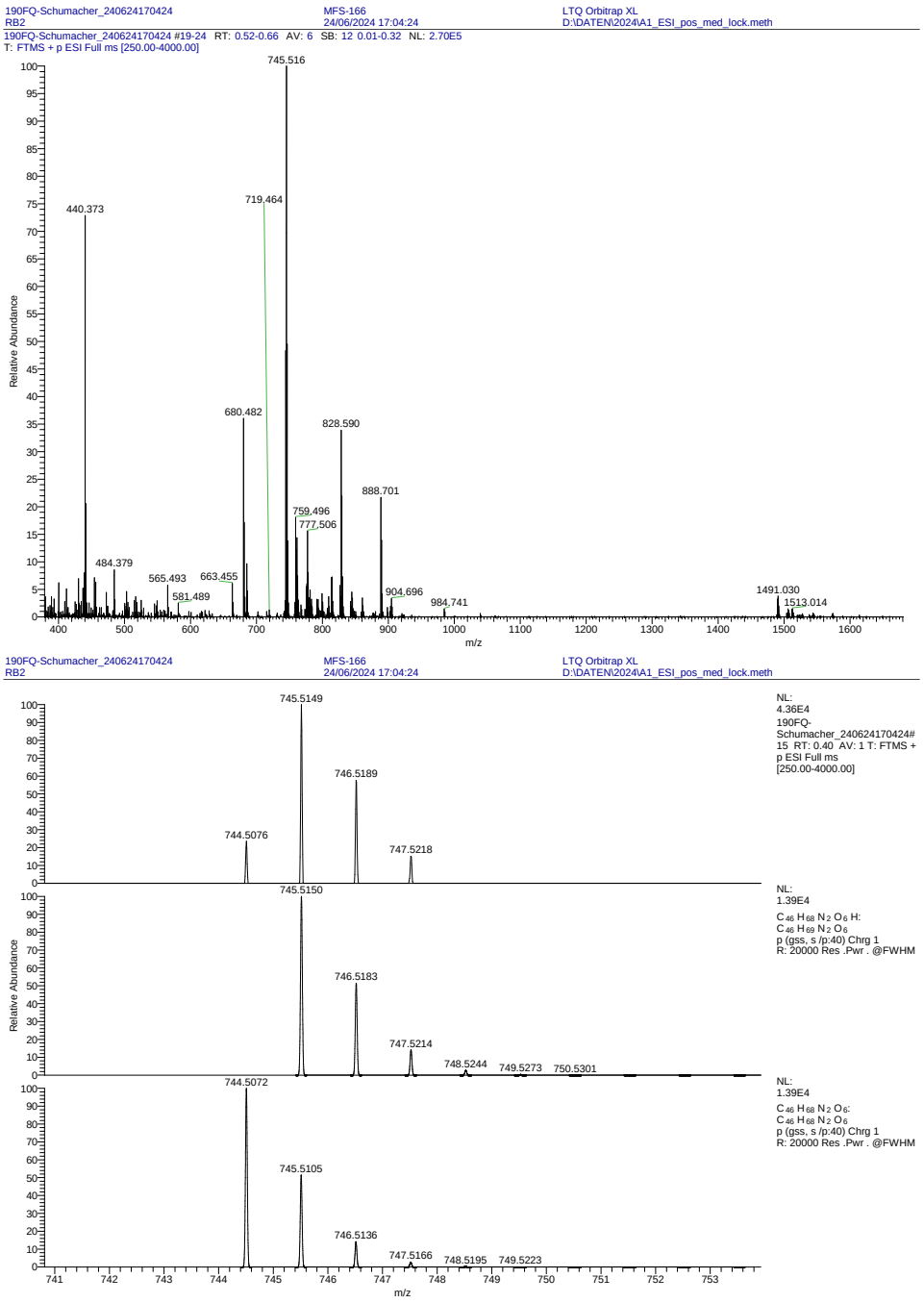


Figure J.21: ESI(+) Mass spectra of **(*S*,*S*)-Ci-SQNP**.

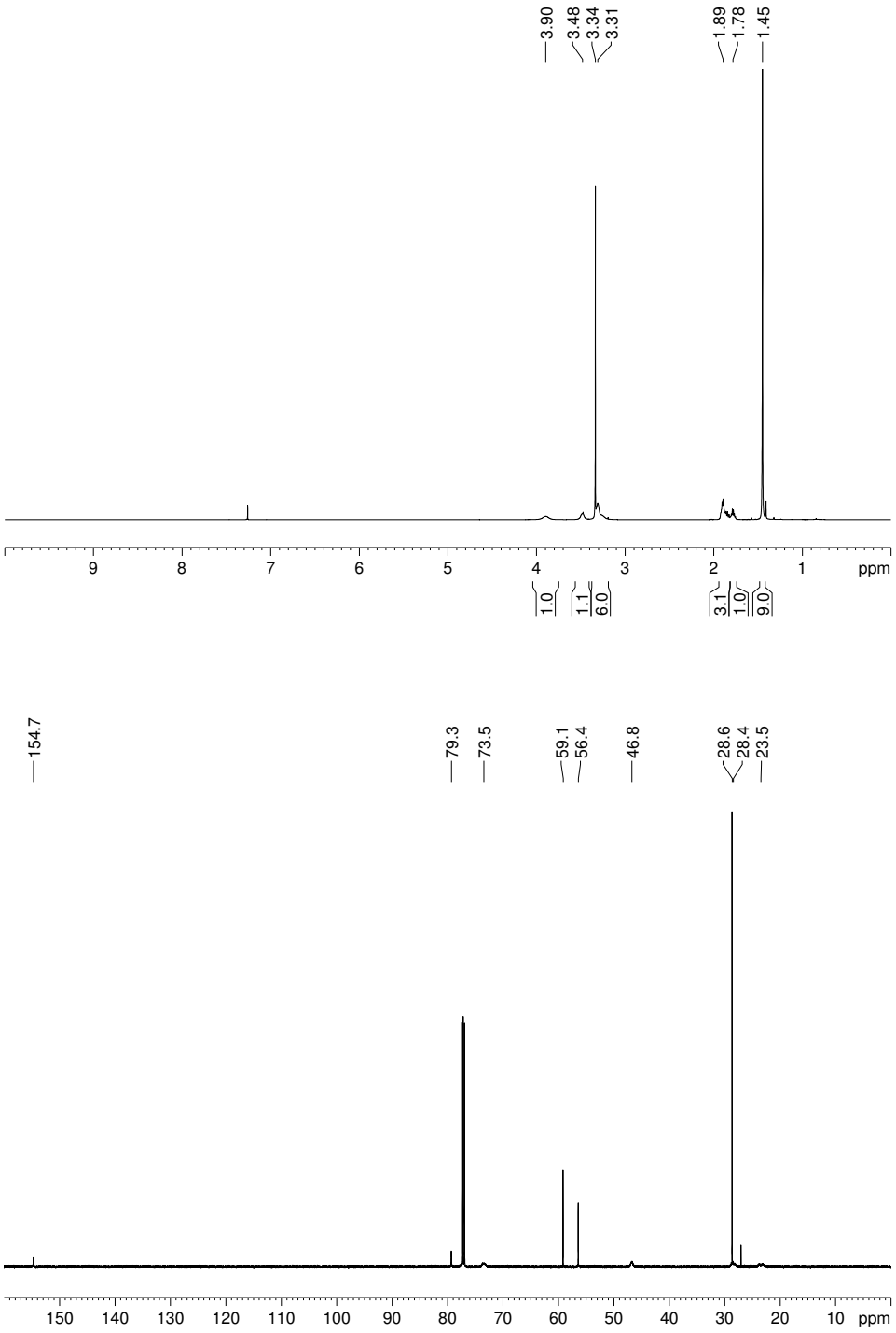


Figure J.22: ^{1}H- (top, 500 MHz) and ^{13}C-NMR (bottom, 125 MHz) spectrum of **(*S*)-Boc-Pro-C1**; $CDCl_3$, 298 K.

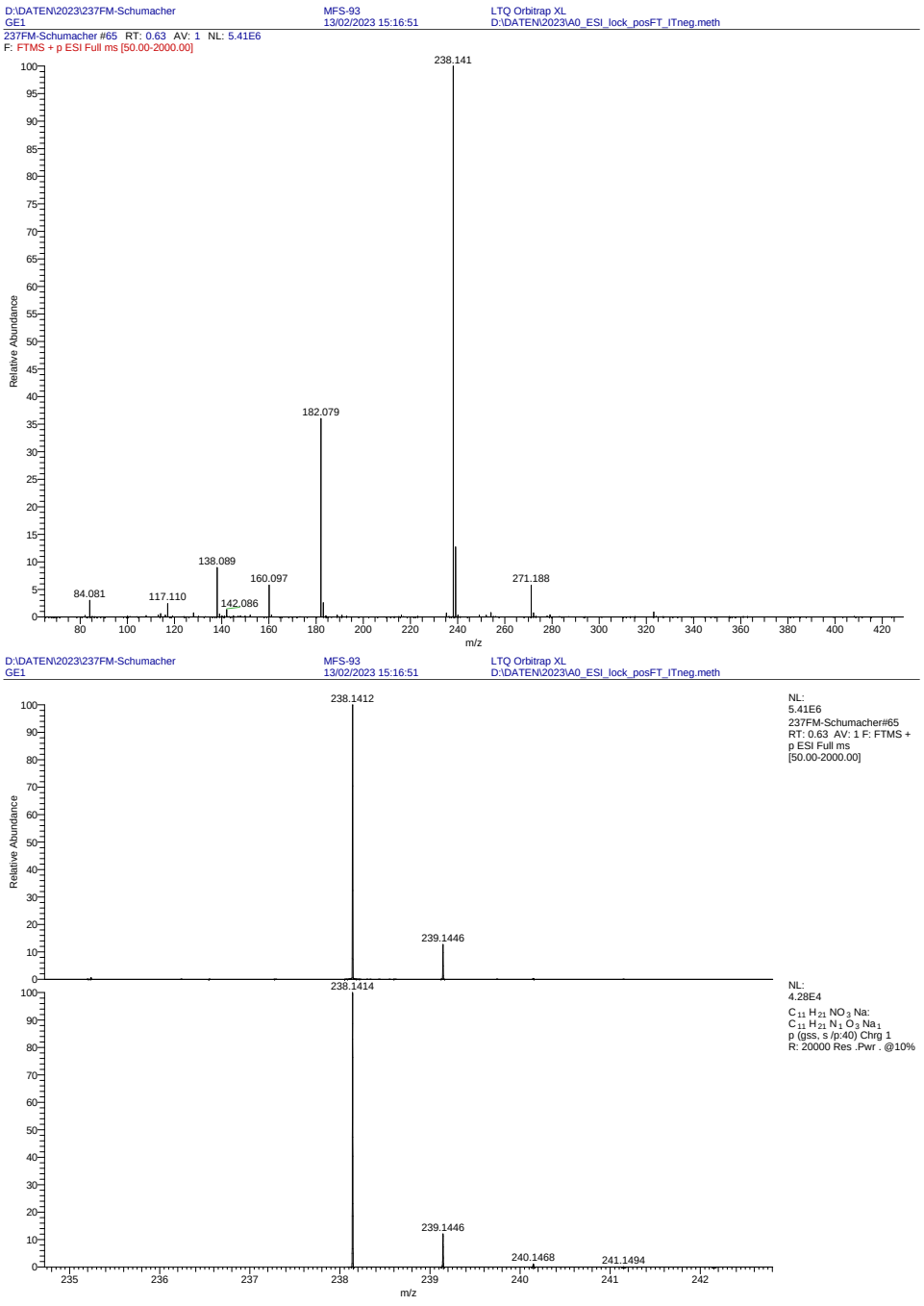


Figure J.23: ESI(+) Mass spectra of **(*S*)-Boc-Pro-C1**.

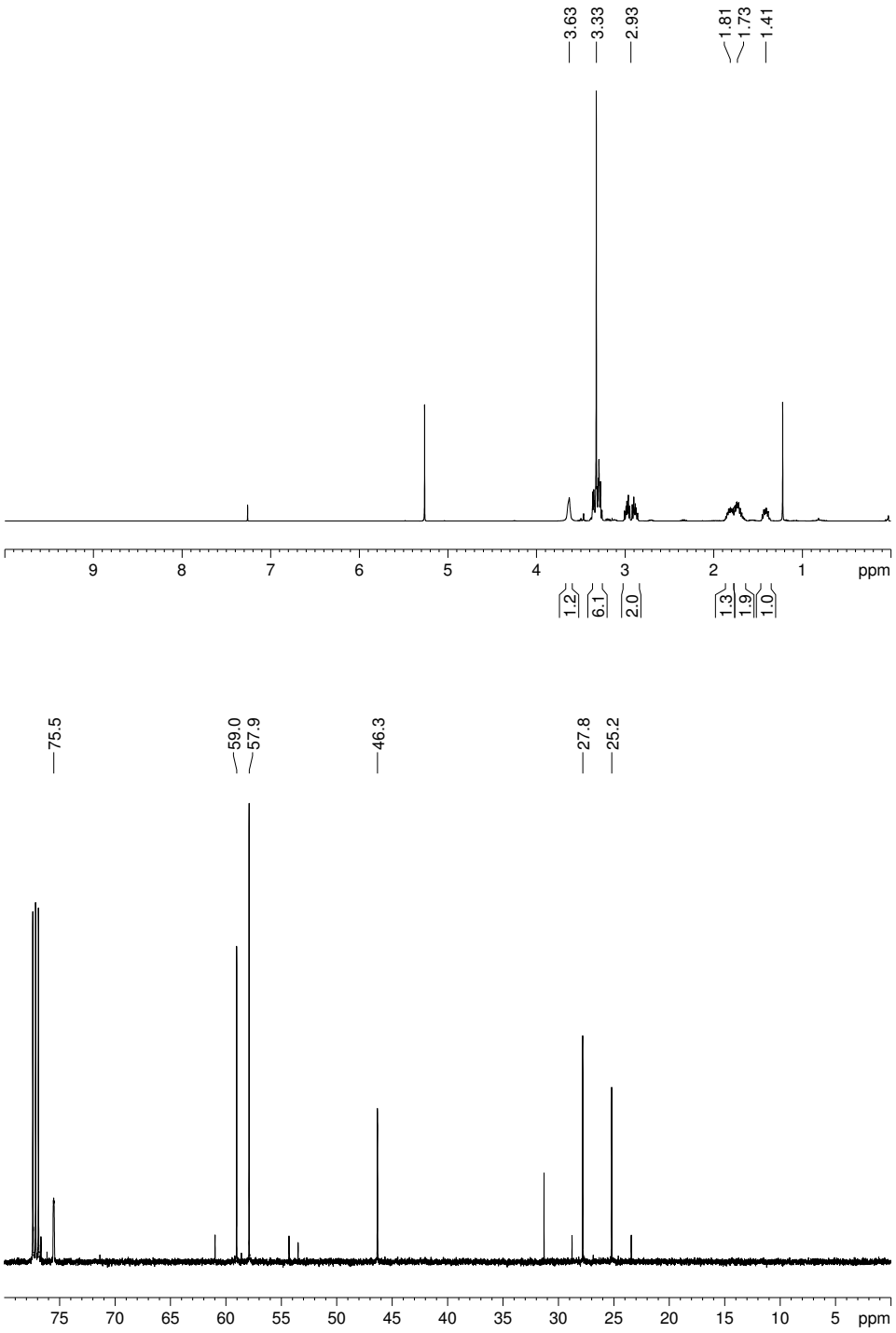


Figure J.24: ^{1}H- (top, 500 MHz) and ^{13}C-NMR (bottom, 125 MHz) spectrum of **(*S*)-Pro-C1**; $CDCl_3$, 298 K.

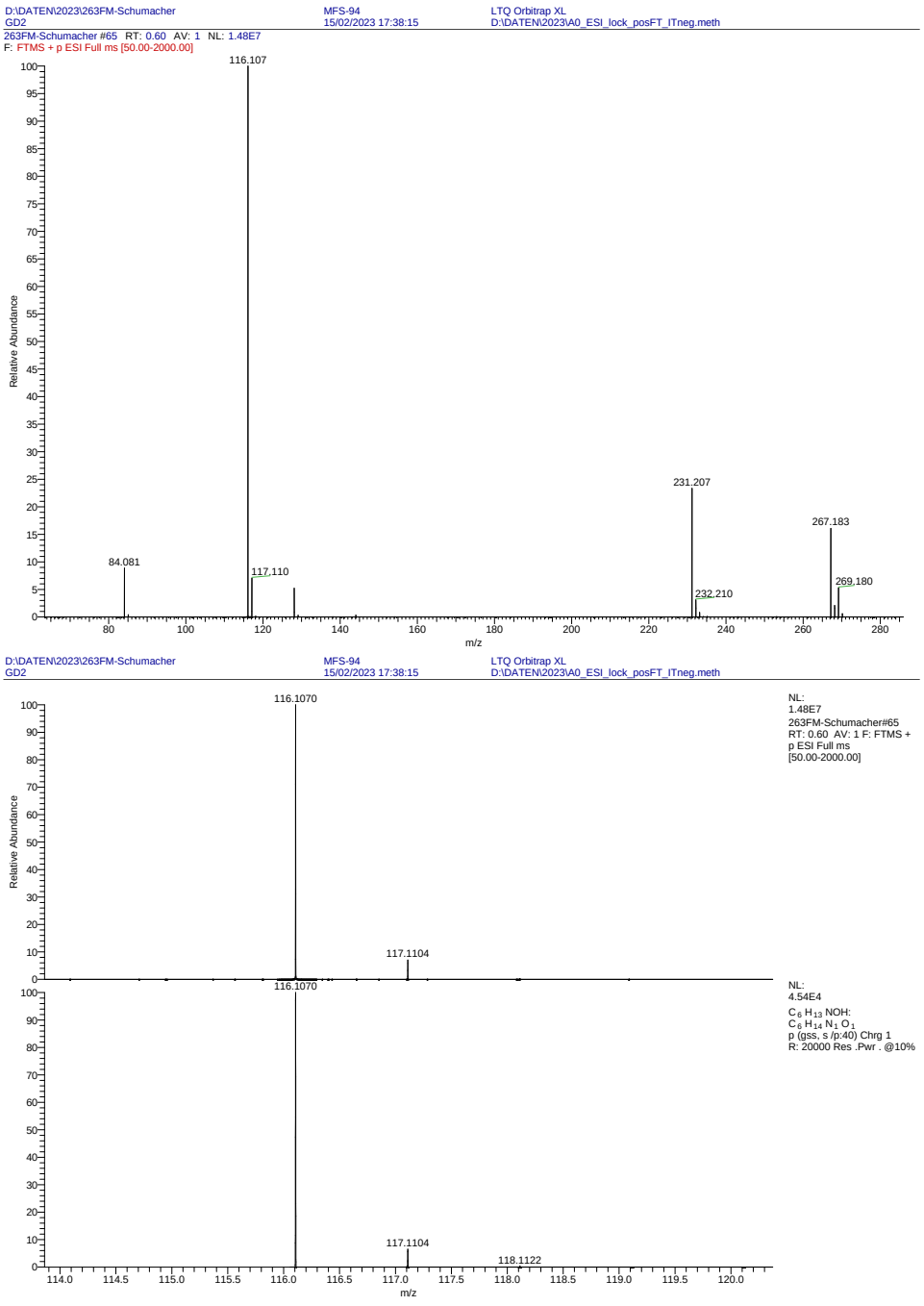


Figure J.25: ESI(+) Mass spectra of **(*S*)-Pro-C1**.

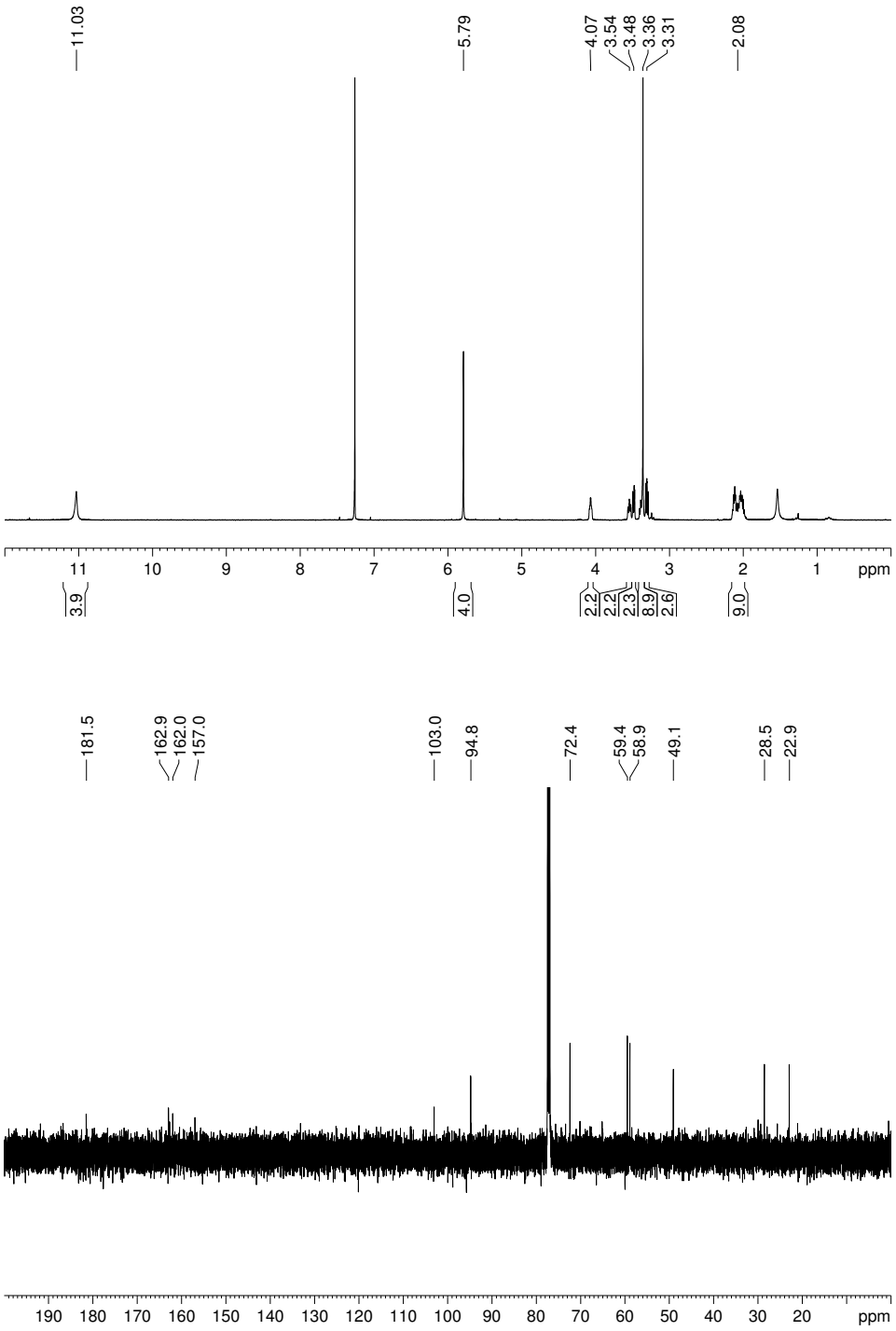
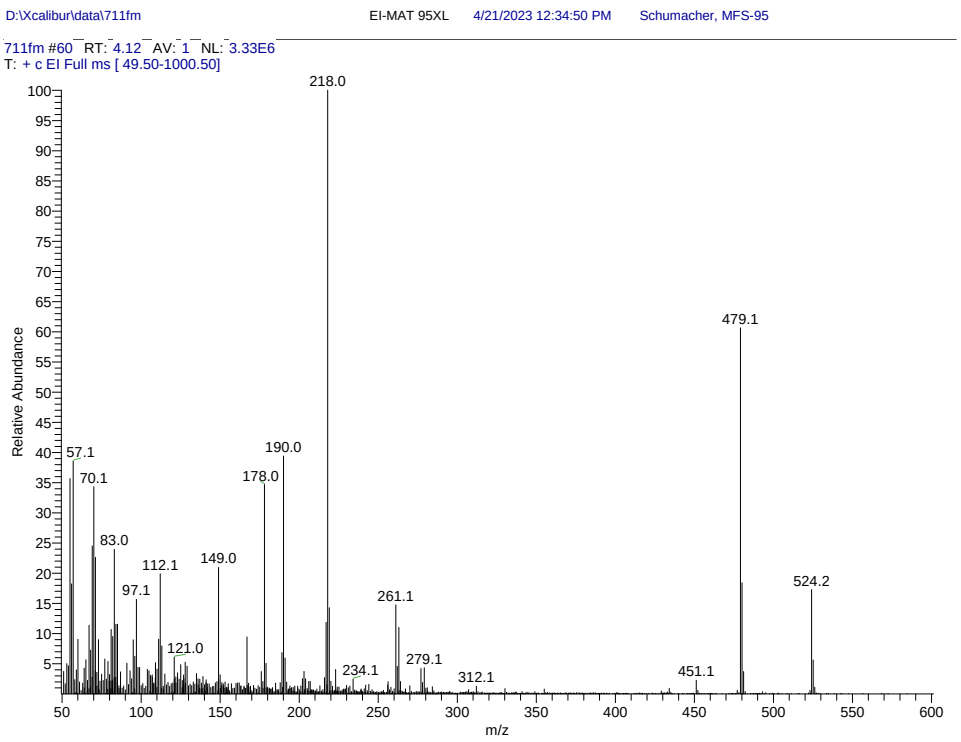


Figure J.26: ^{1}H- (top, 500 MHz) and ^{13}C-NMR (bottom, 125 MHz) spectrum of **(*S*,*S*)-ProSQ-C1**; $CDCl_3$, 298 K.



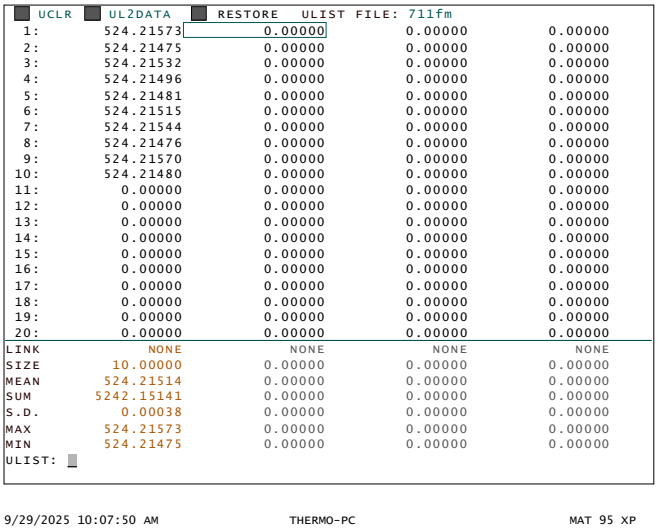


Figure J.27: EI Mass spectra of **(*S*,*S*)-ProSQ-C1**.

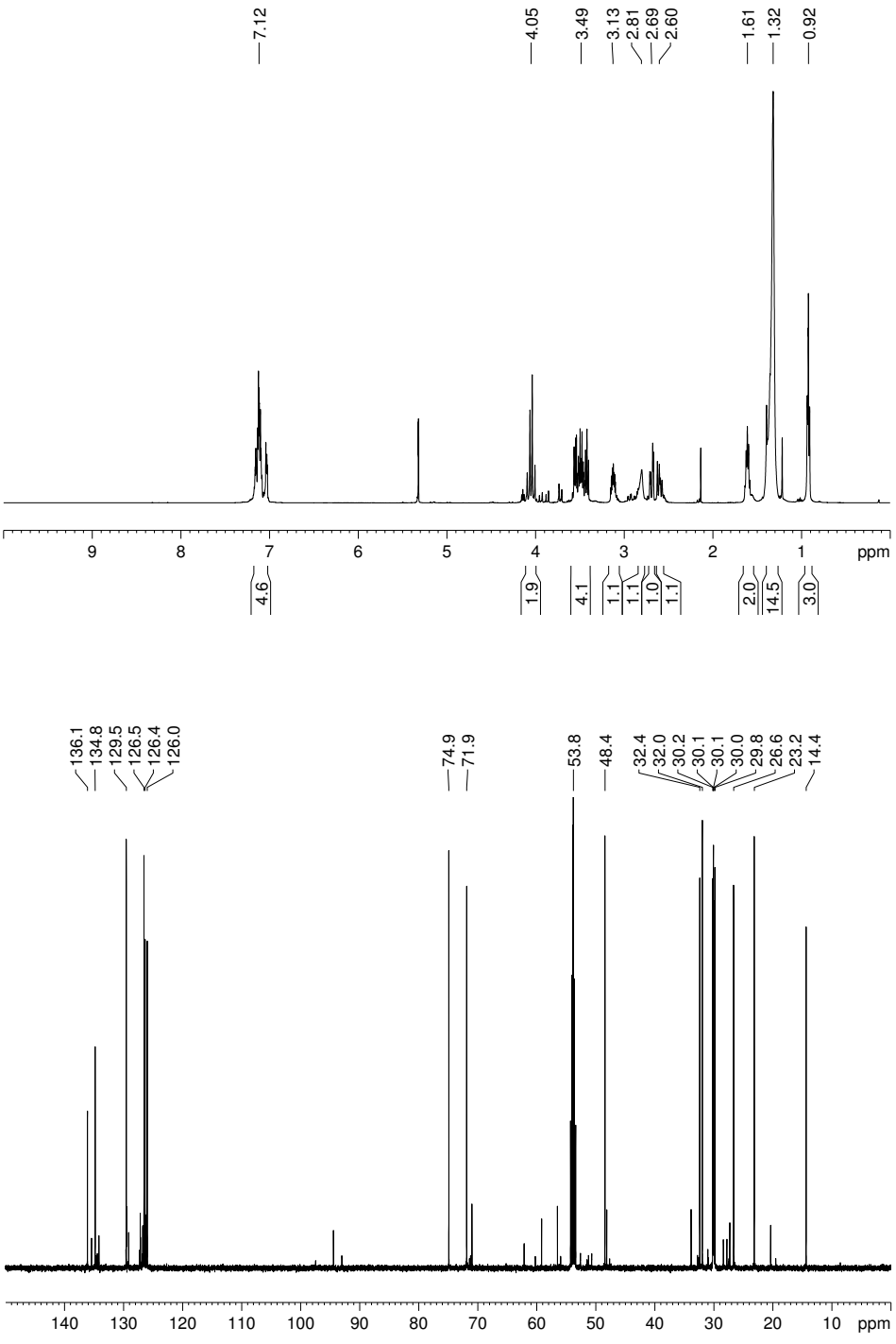


Figure J.28: ^{1}H- (top, 500 MHz) and ^{13}C-NMR (bottom, 125 MHz) spectrum of **(*S*)-TIQ-C10**; $CDCl_3$, 298 K.

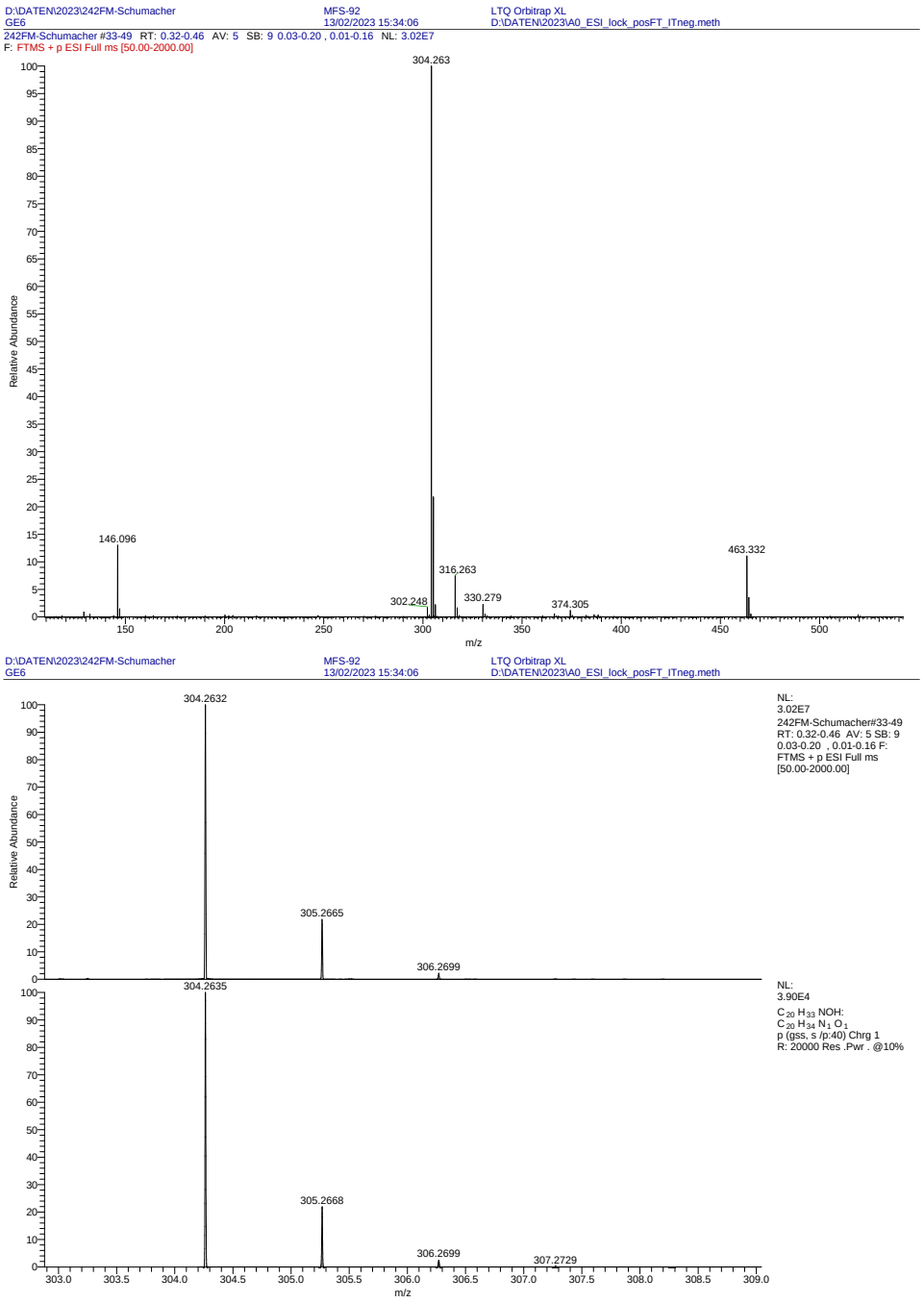


Figure J.29: ESI(+) Mass spectra of **(*S*)-TIQ-C10**.

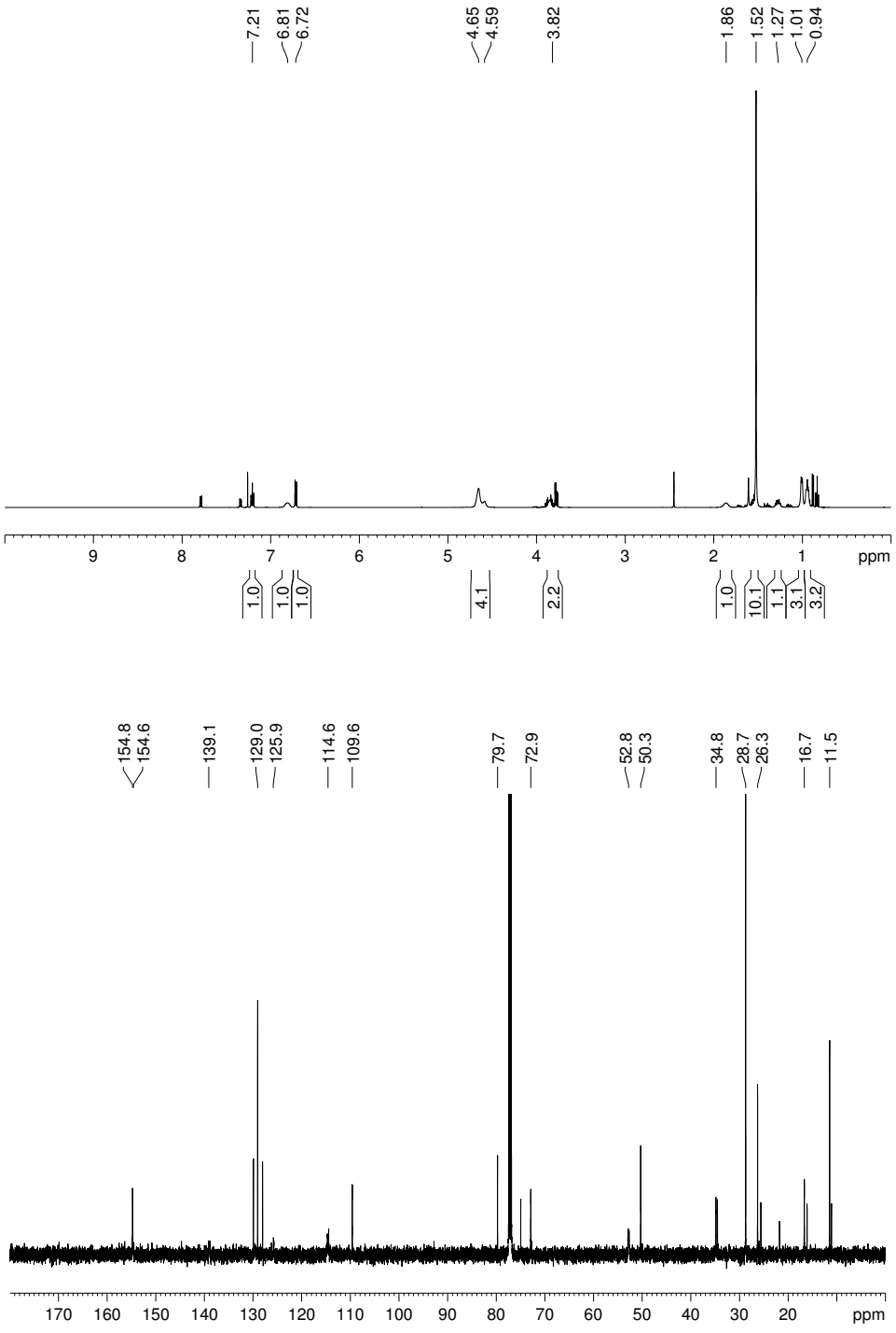


Figure J.30: ^{1}H- (top, 500 MHz) and ^{13}C-NMR (bottom, 125 MHz) spectrum of **Boc-(*S*)-2mb-isoindole**; $CDCl_3$, 298 K.

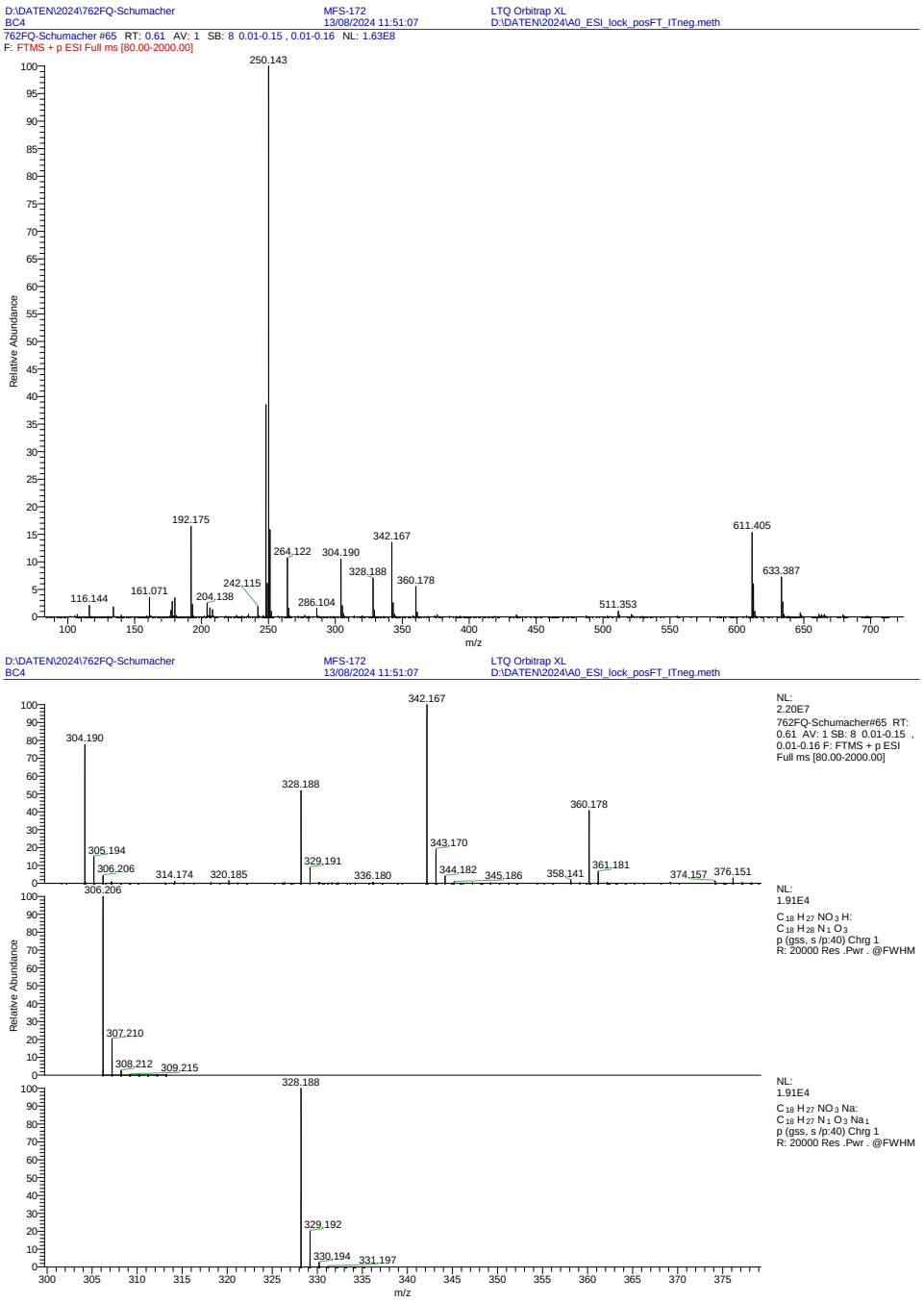


Figure J.31: ESI(+) Mass spectra of **Boc-(*S*)-2mb-isoindole**.

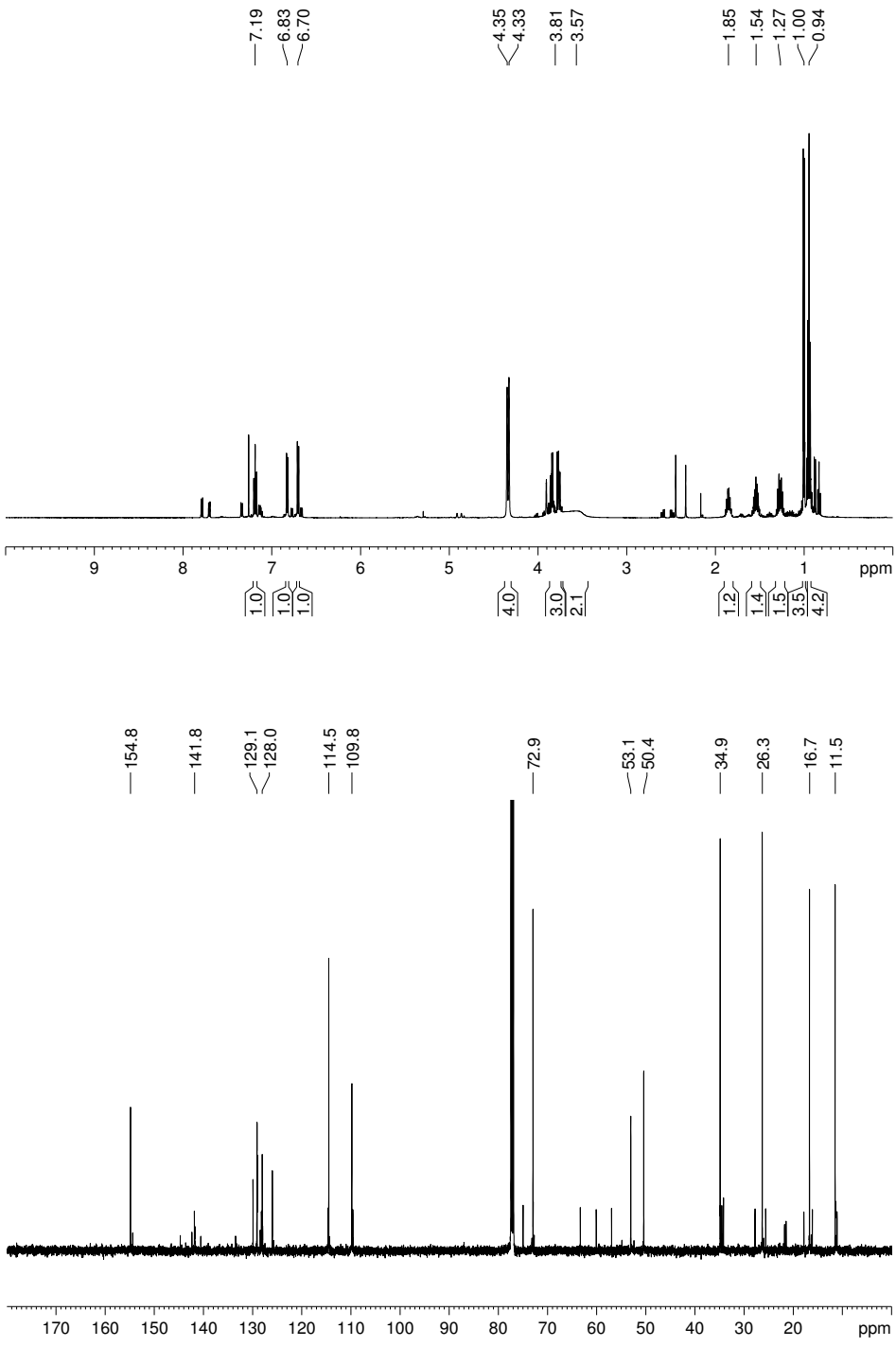


Figure J.32: ^{1}H- (top, 500 MHz) and ^{13}C-NMR (bottom, 125 MHz) spectrum of **(*S*)-2mb-isoindole**; $CDCl_3$, 298 K.

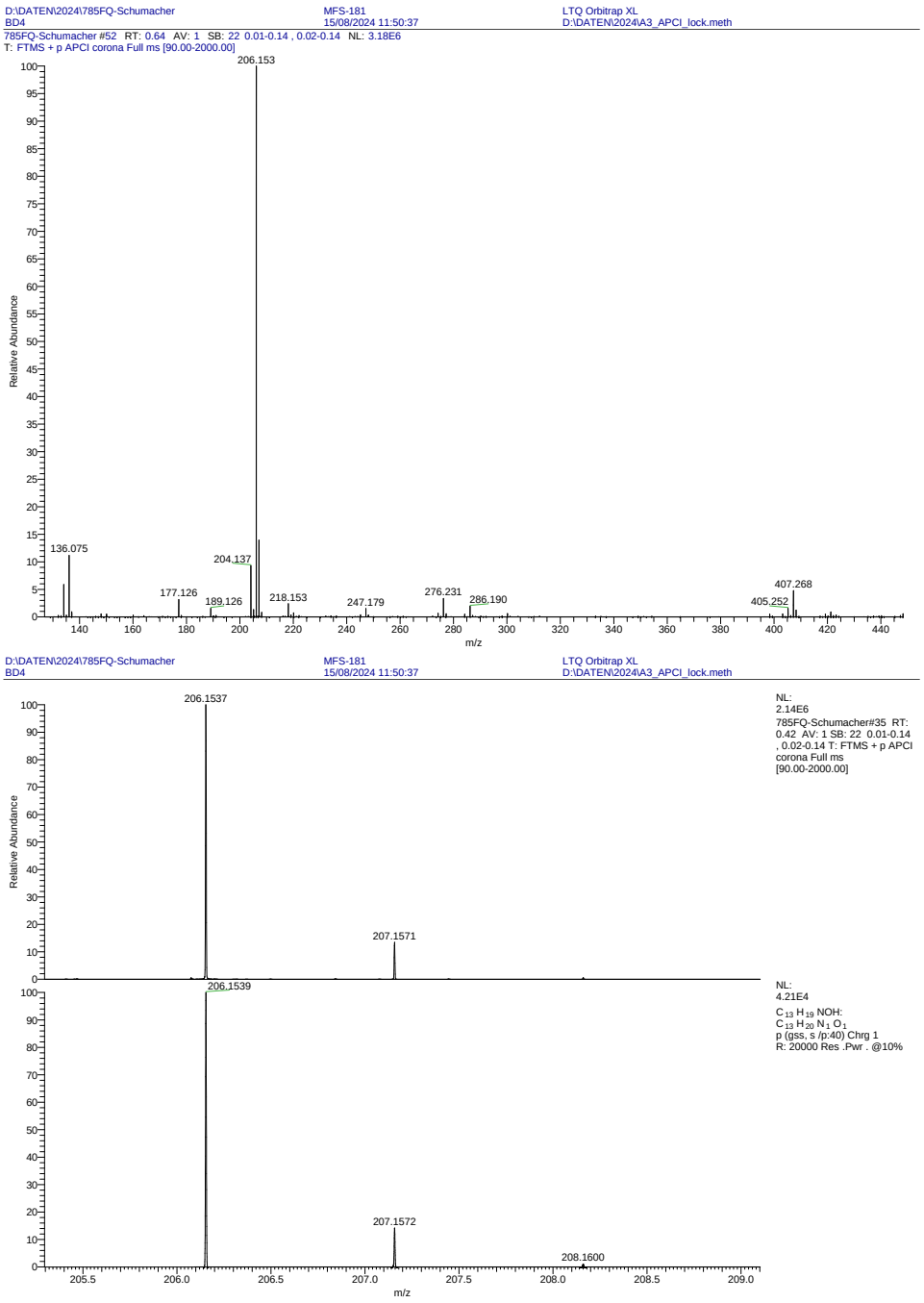


Figure J.33: APCI Mass spectra of **(*S*)-2mb-isoindole**.

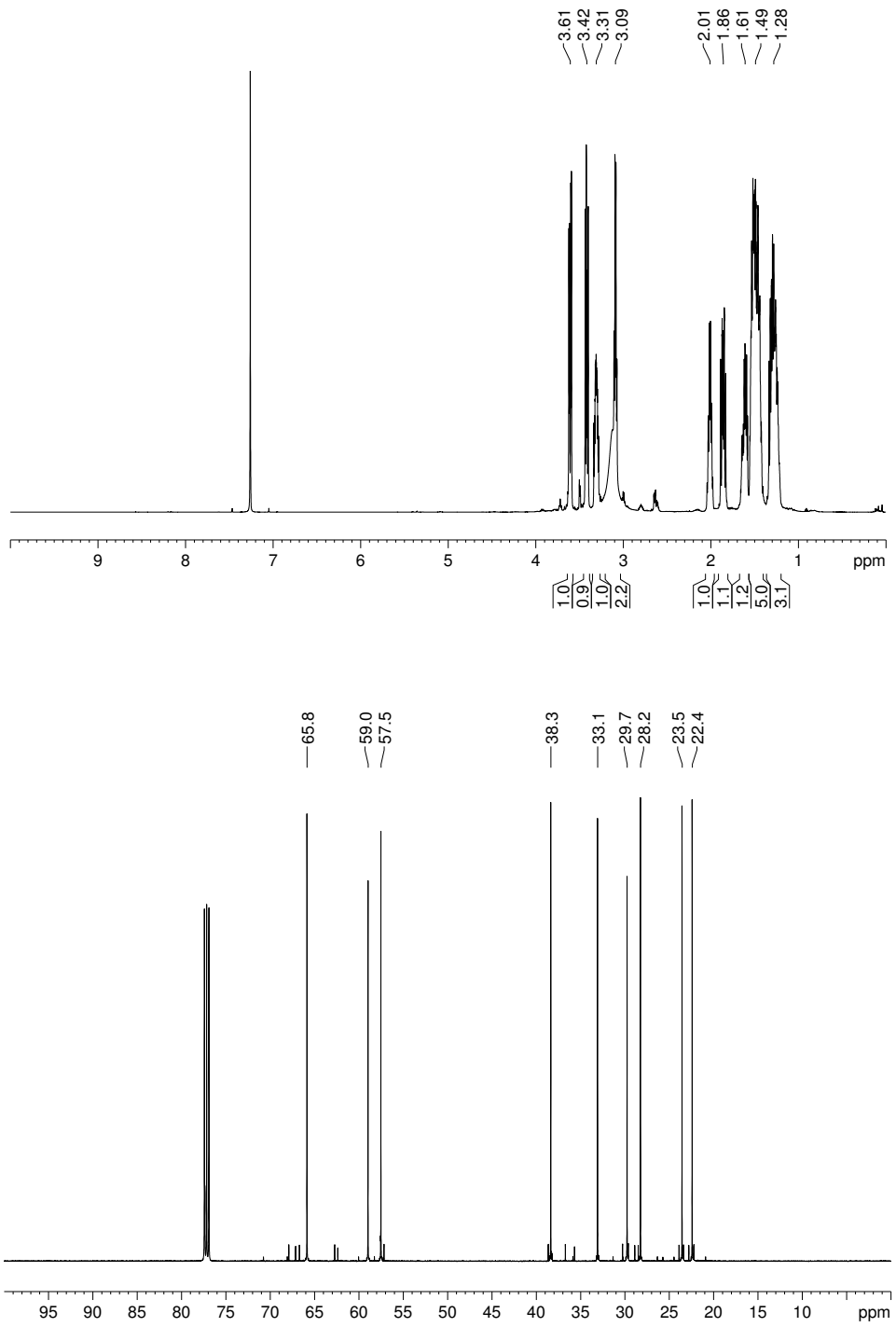


Figure J.34: ^{1}H- (top, 500 MHz) and ^{13}C-NMR (bottom, 125 MHz) spectrum of **(*S*)-OHI-OH**; $CDCl_3$, 298 K.

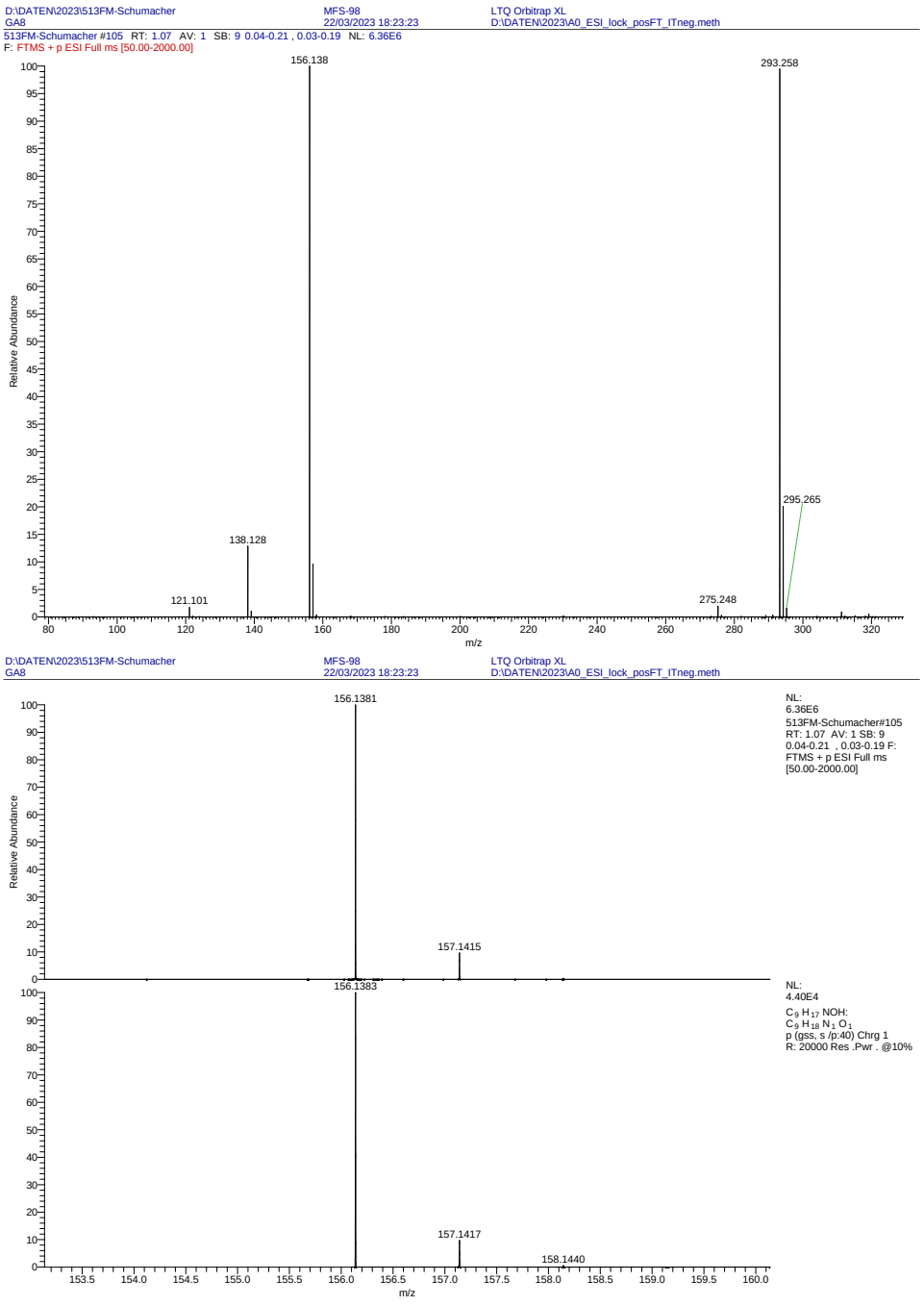


Figure J.35: ESI(+) Mass spectra of **(*S*)-OHI-OH**.

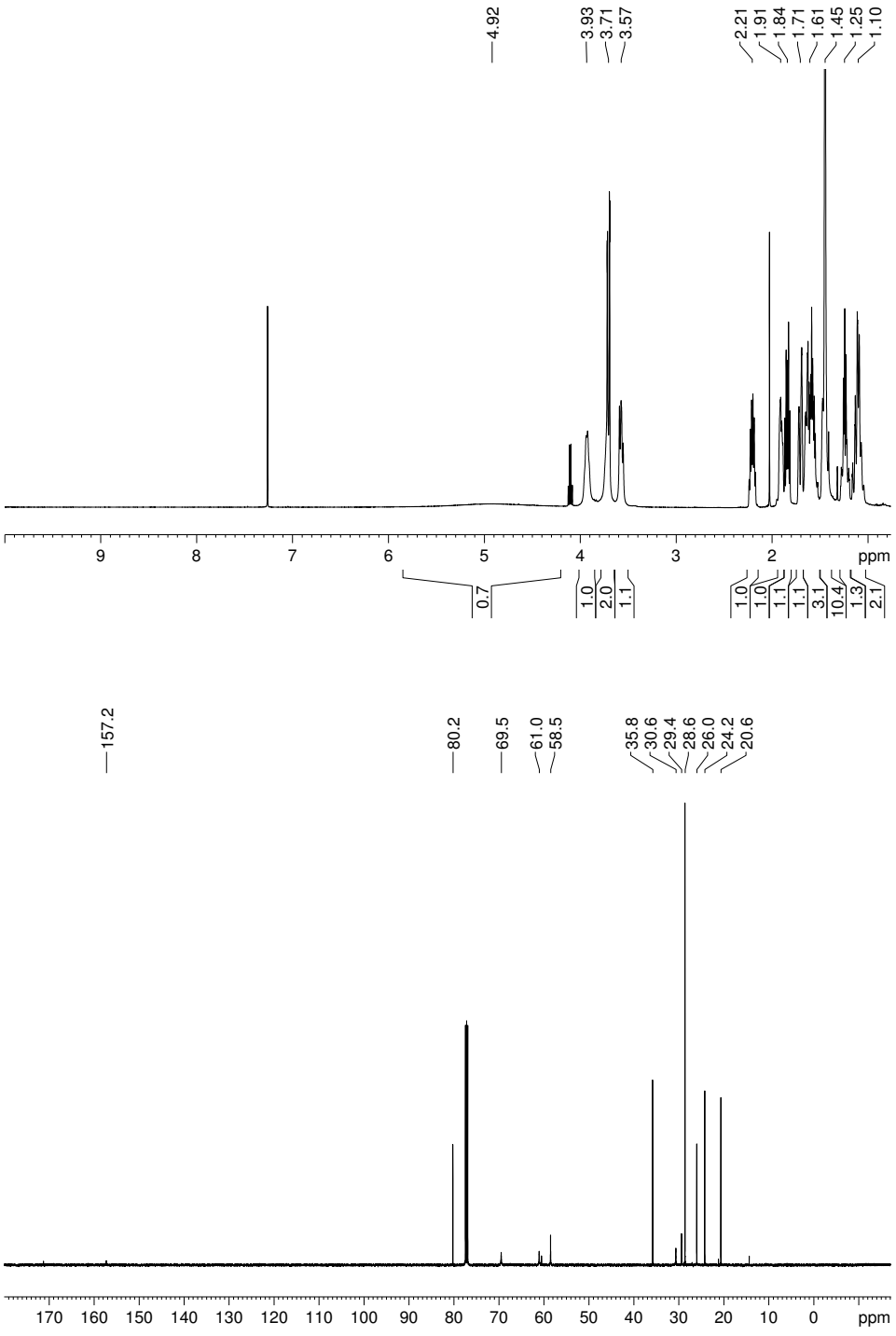


Figure J.36: ^{1}H- (top, 500 MHz) and ^{13}C-NMR (bottom, 125 MHz) spectrum of **(*S*)-Boc-OHI-OH**; $CDCl_3$, 298 K.

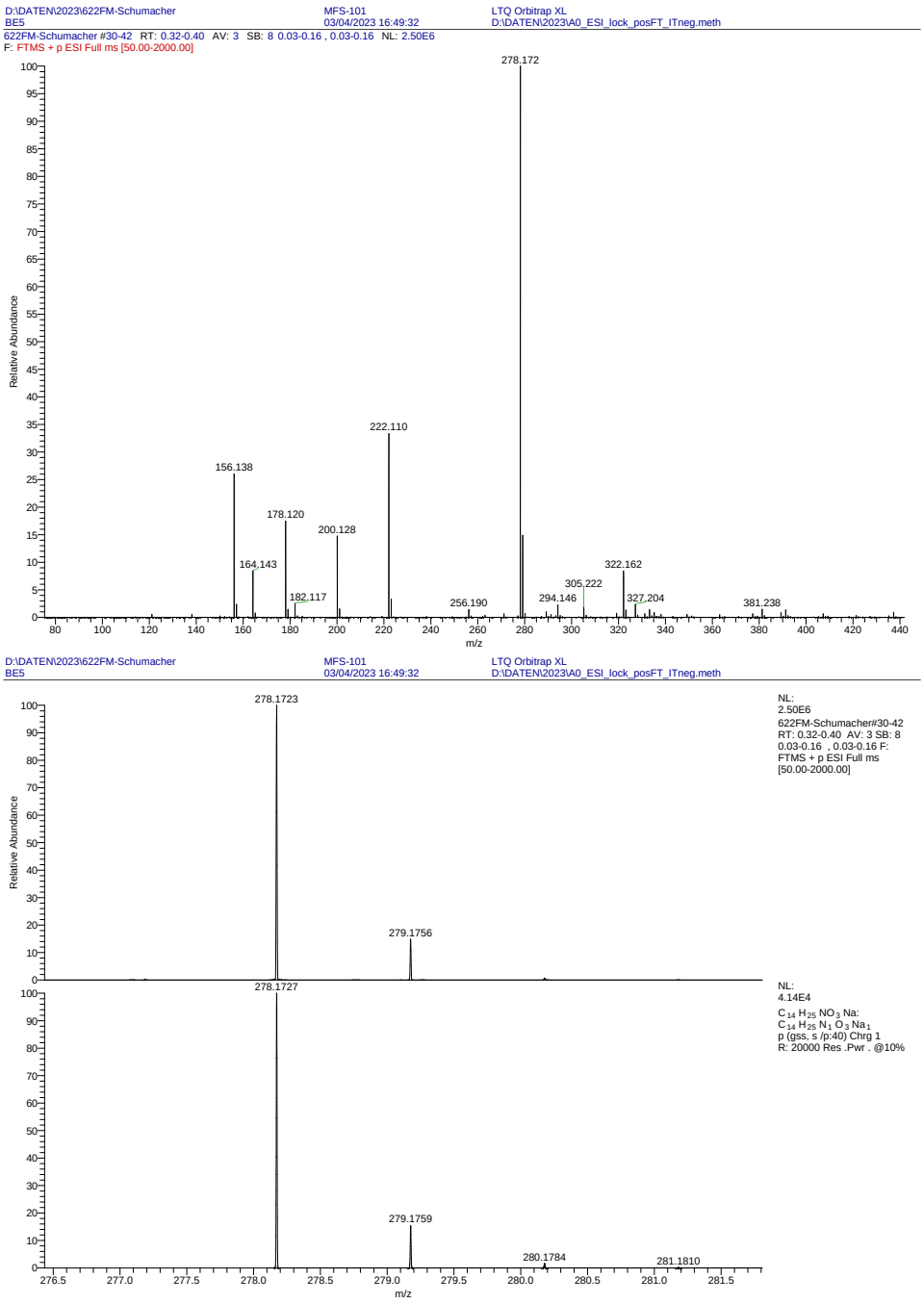


Figure J.37: ESI(+) Mass spectra of **(*S*)-Boc-OHI-OH**.

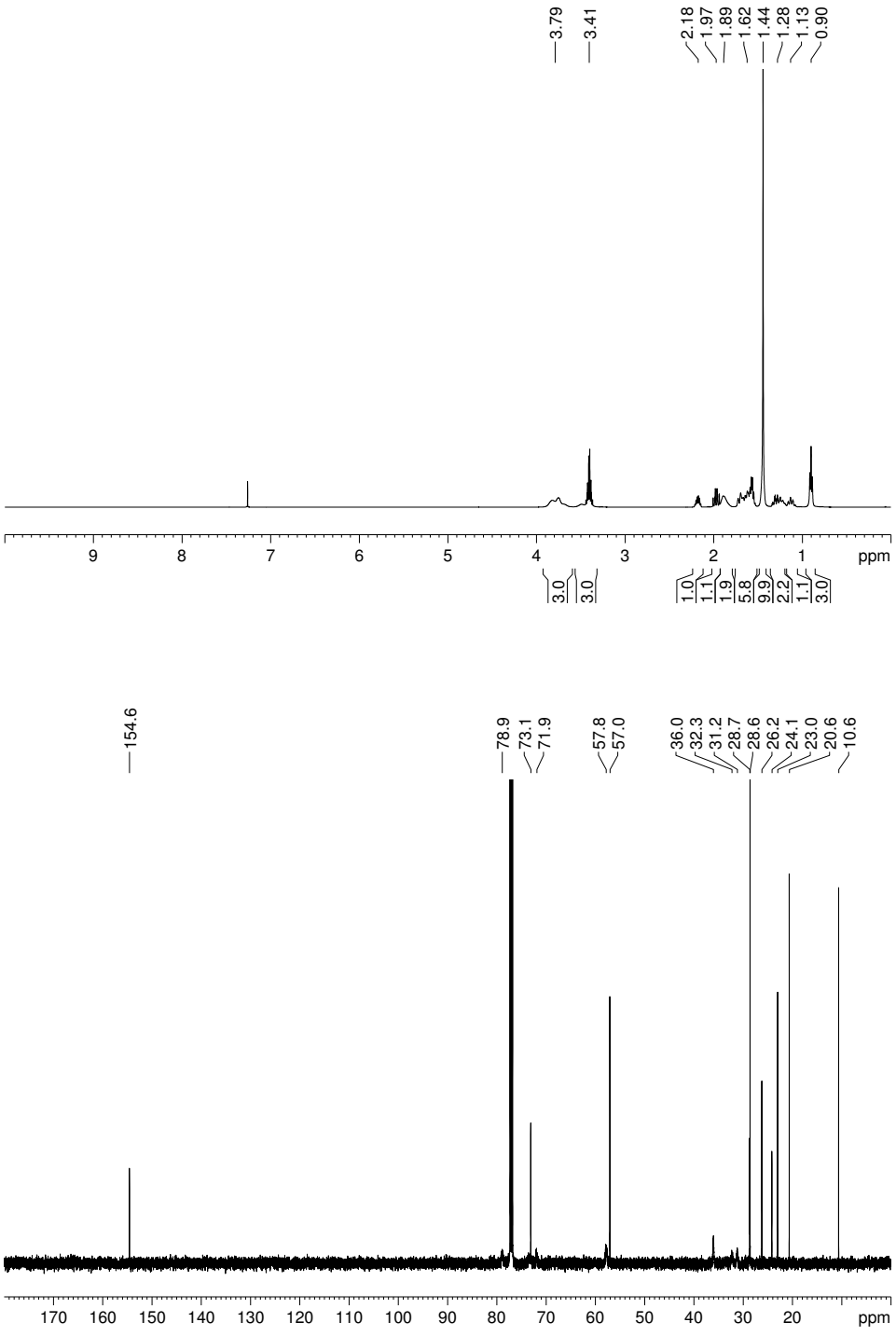


Figure J.38: ^{1}H- (top, 500 MHz) and ^{13}C-NMR (bottom, 125 MHz) spectrum of **(*S*)-Boc-OHI-C3**; $CDCl_3$, 298 K.

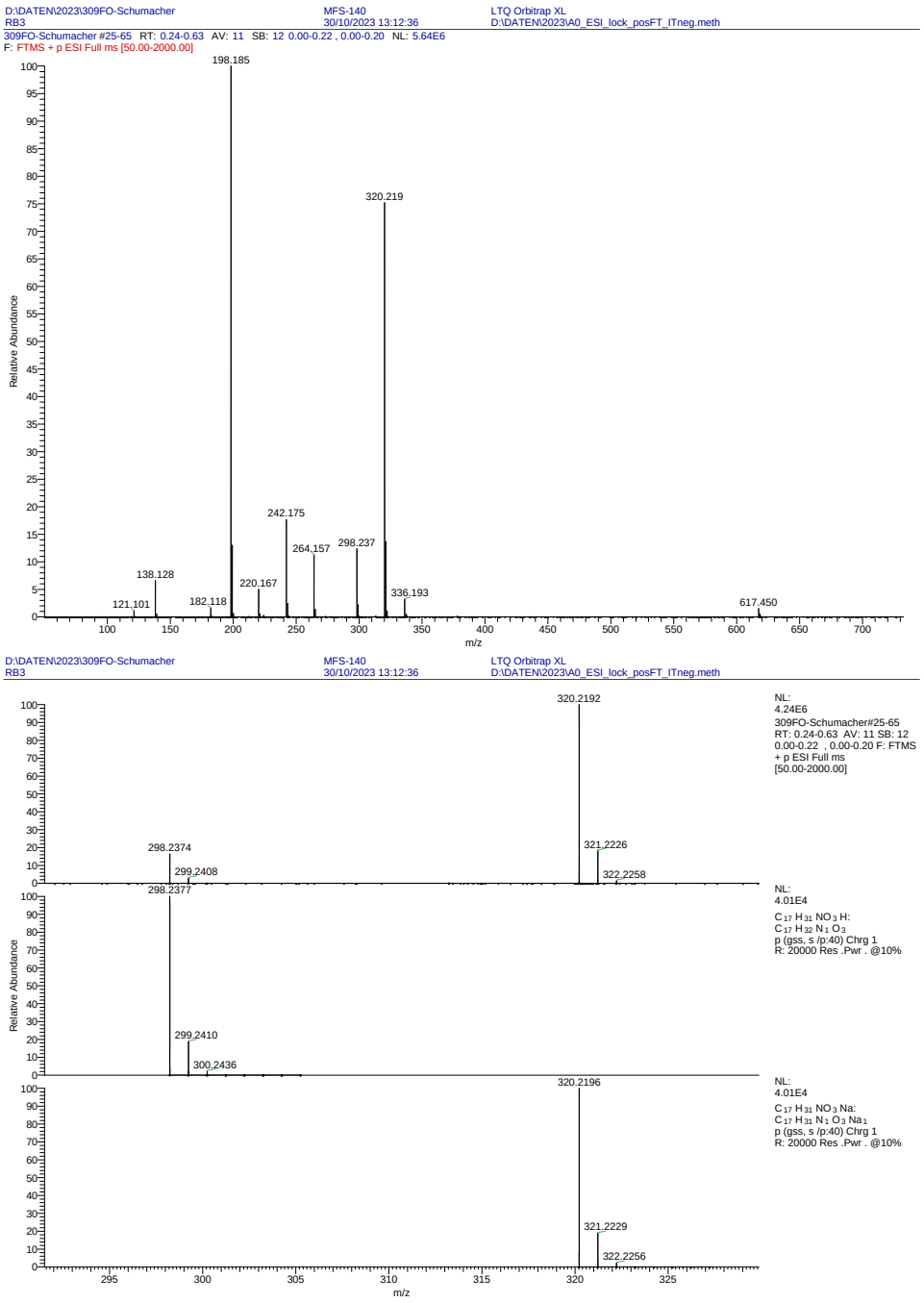


Figure J.39: ESI(+) Mass spectra of **(*S*)-Boc-OHI-C3**.

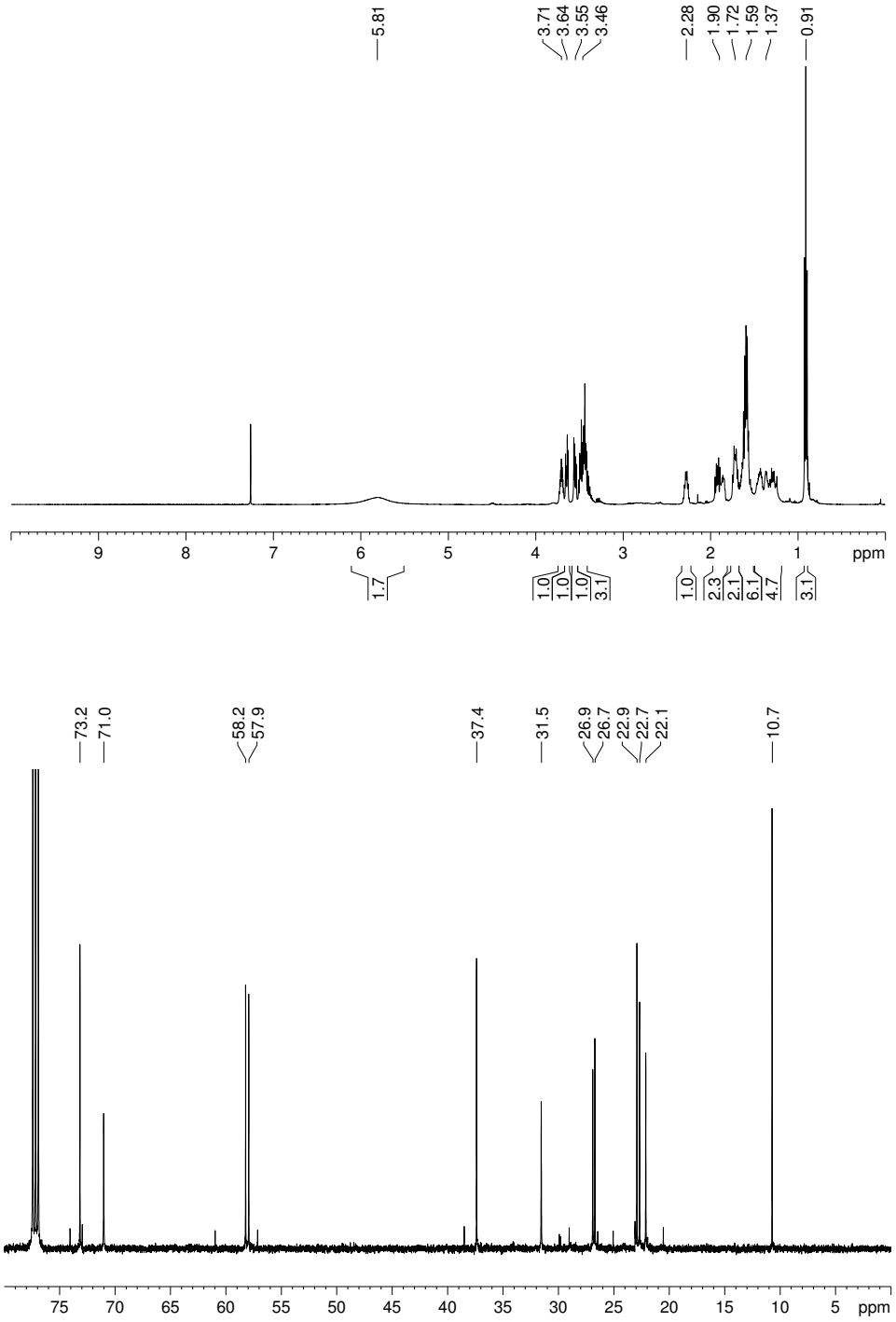


Figure J.40: ^{1}H- (top, 500 MHz) and ^{13}C-NMR (bottom, 125 MHz) spectrum of **(*S*)-OHI-C3**; $CDCl_3$, 298 K.

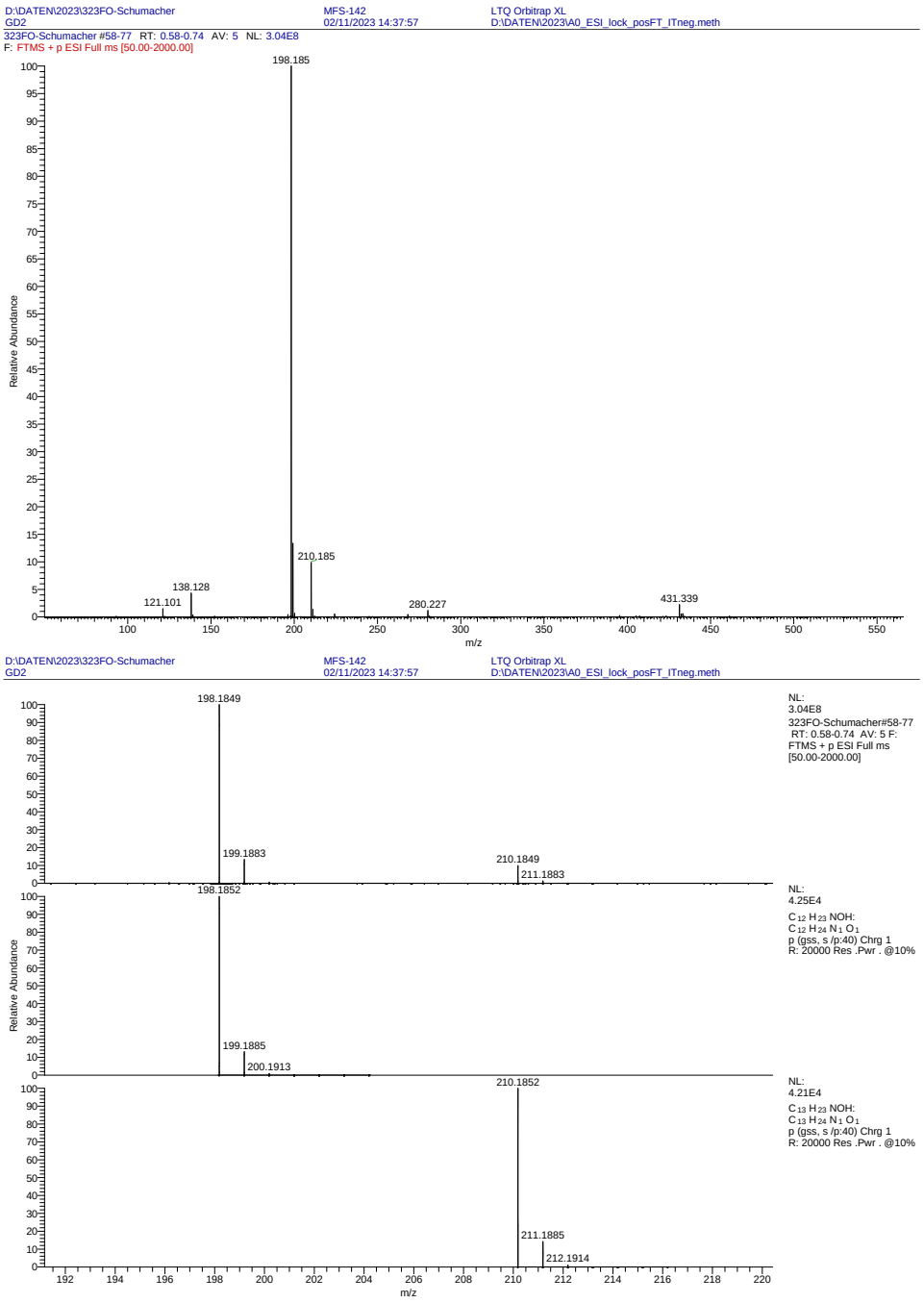


Figure J.41: ESI(+) Mass spectra of **(*S*)-OHI-C3**.

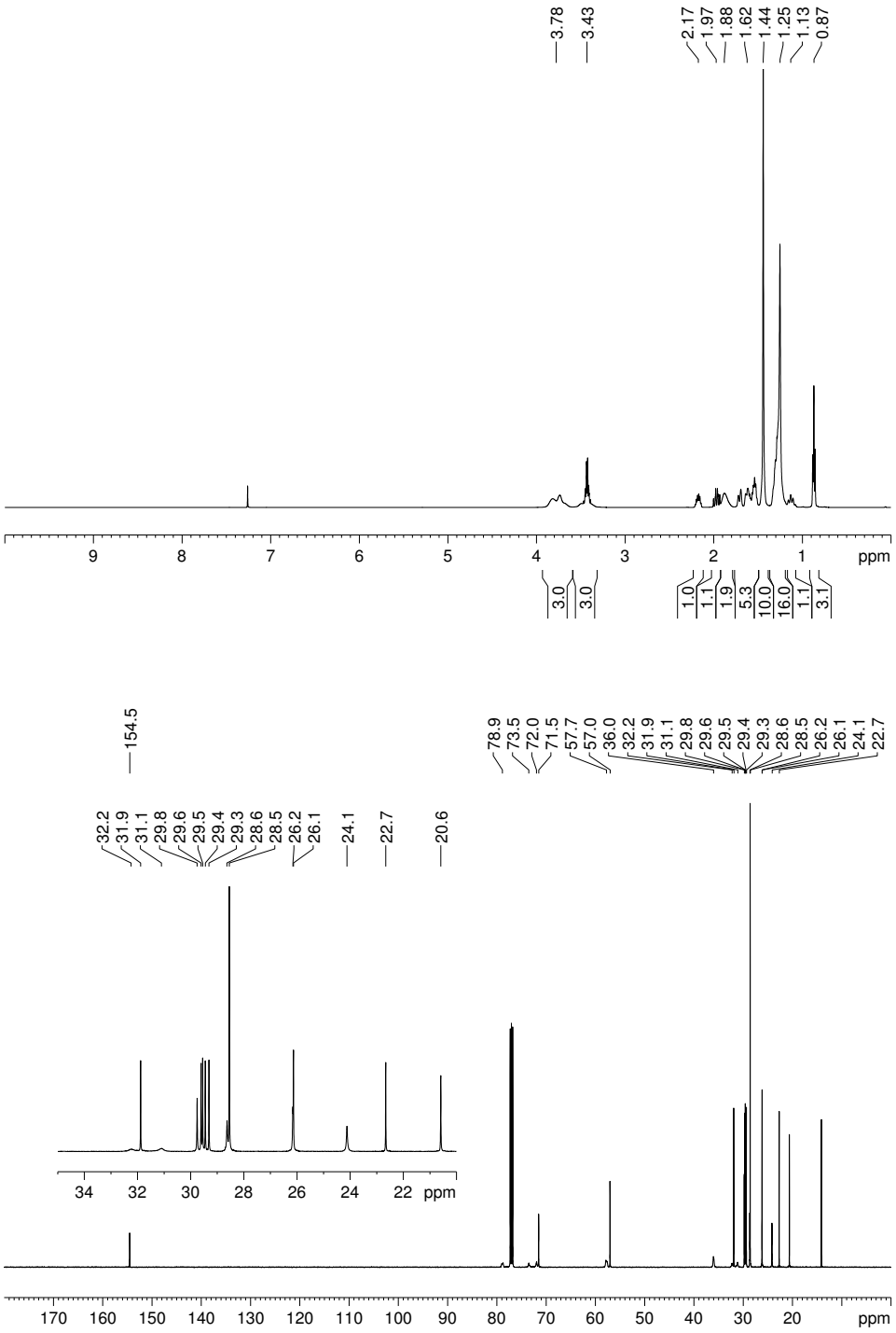


Figure J.42: ^{1}H- (top, 500 MHz) and ^{13}C-NMR (bottom, 125 MHz) spectrum of **(*S*)-Boc-OHI-C10**; $CDCl_3$, 298 K.

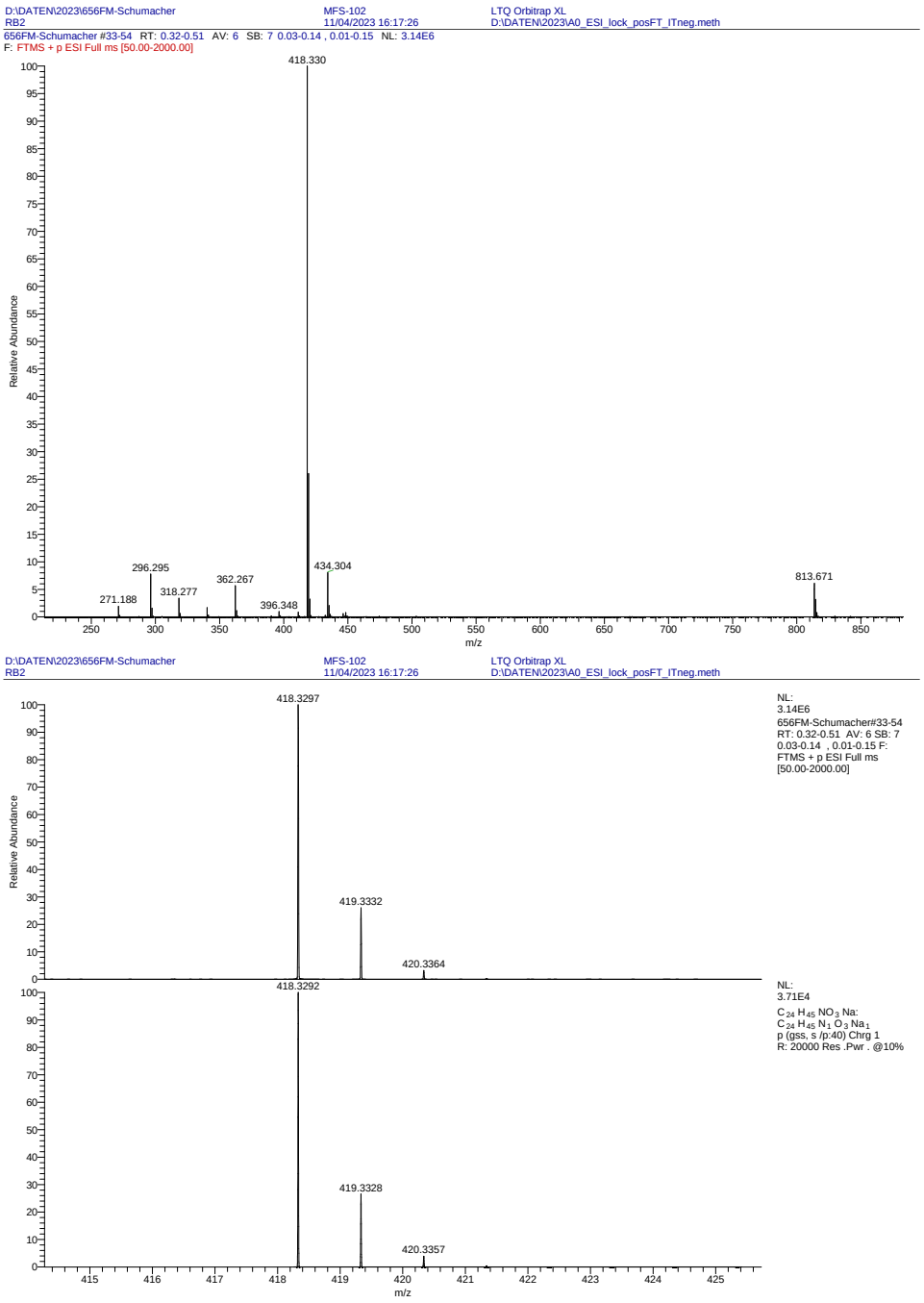


Figure J.43: ESI(+) Mass spectra of **(*S*)-Boc-OHI-C10**.

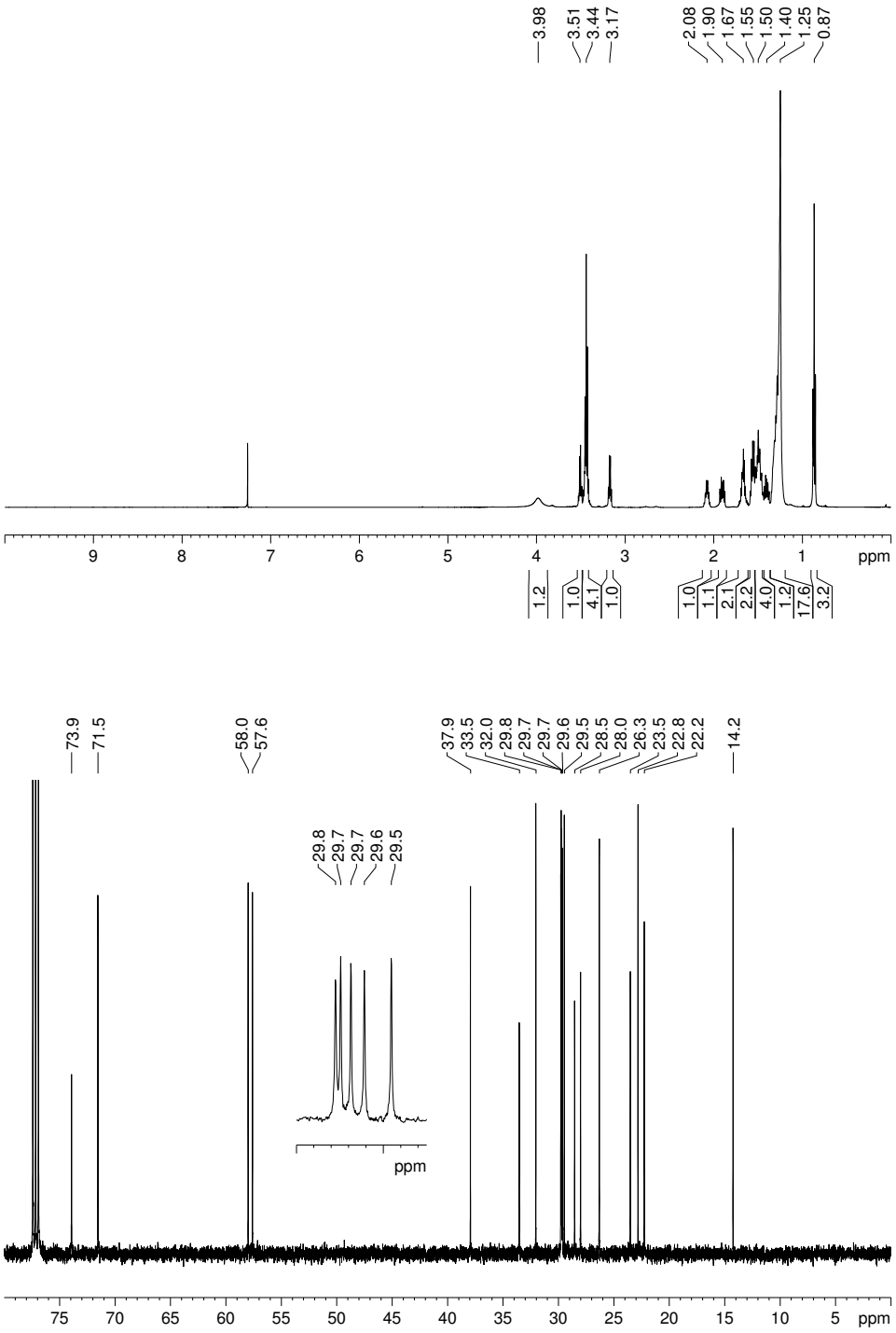


Figure J.44: ^{1}H- (top, 500 MHz) and ^{13}C-NMR (bottom, 125 MHz) spectrum of **(*S*)-OHI-C10**; $CDCl_3$, 298 K.

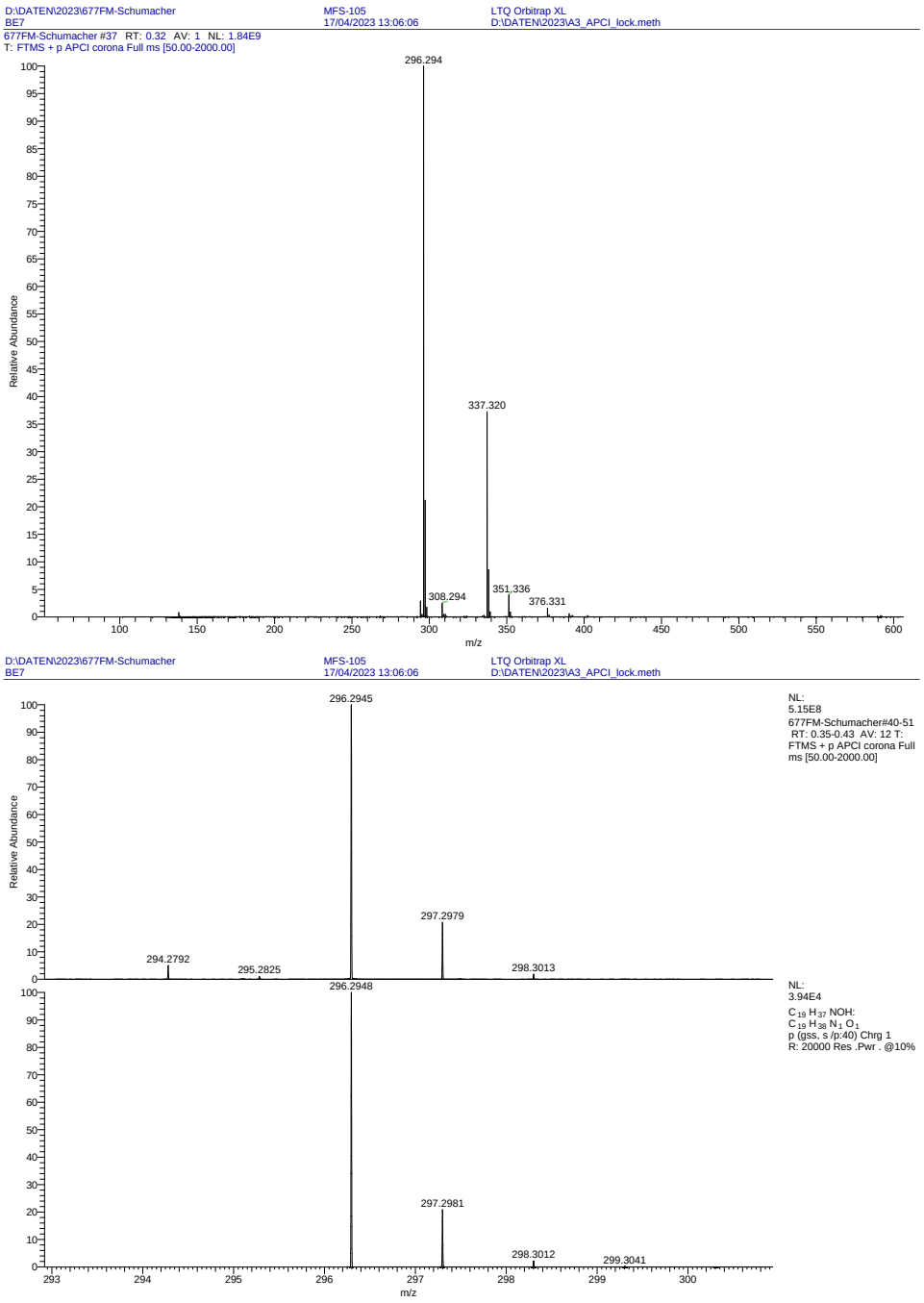


Figure J.45: APCI Mass spectra of **(*S*)-OHI-C10**.

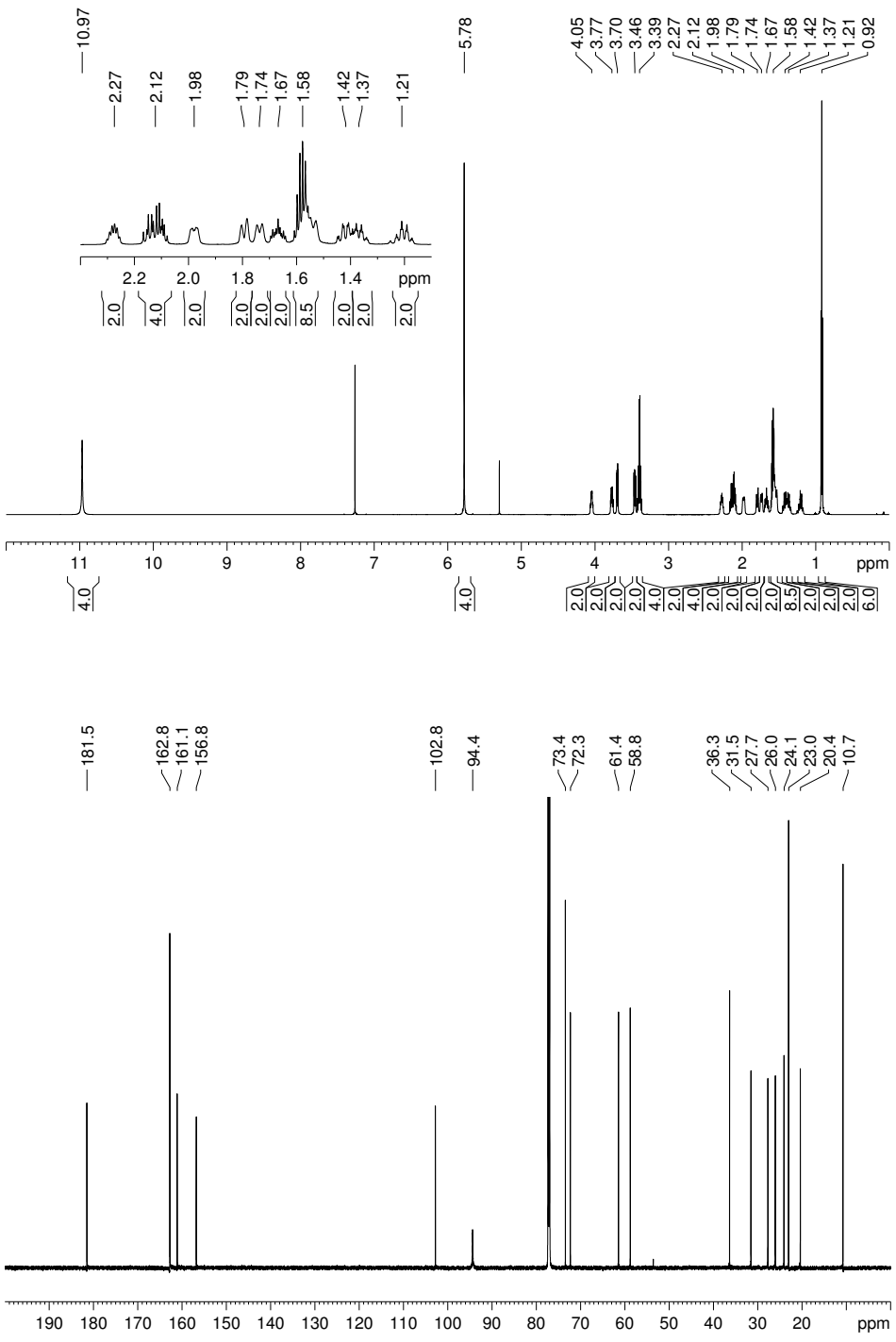


Figure J.46: ^{1}H- (top, 700 MHz) and ^{13}C-NMR (bottom, 176 MHz) spectrum of **(*S*,*S*)-OHI-SQ-C3**; $CDCl_3$, 298 K.

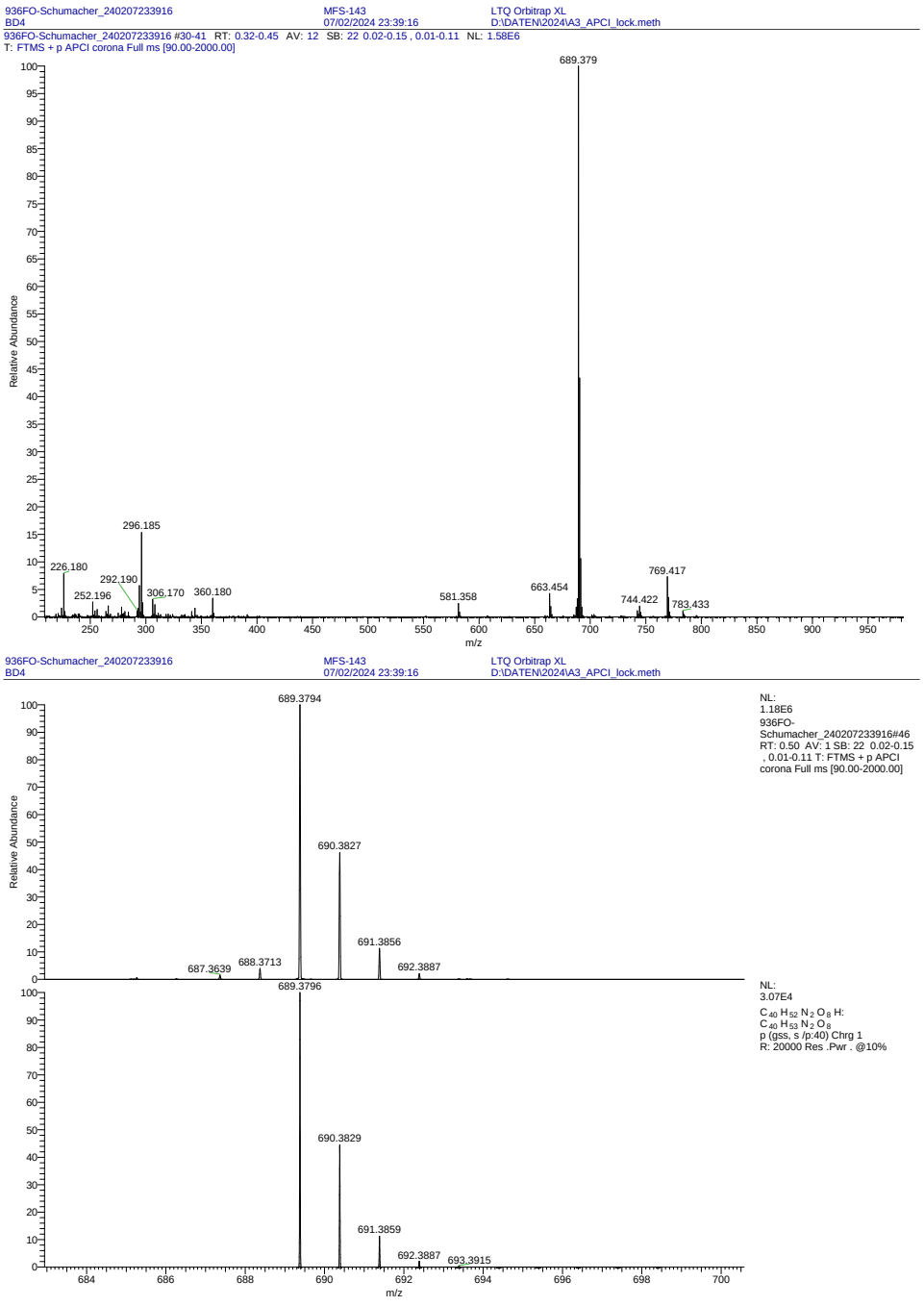


Figure J.47: APCI Mass spectra of **(*S*,*S*)-OHI-SQ-C3**.

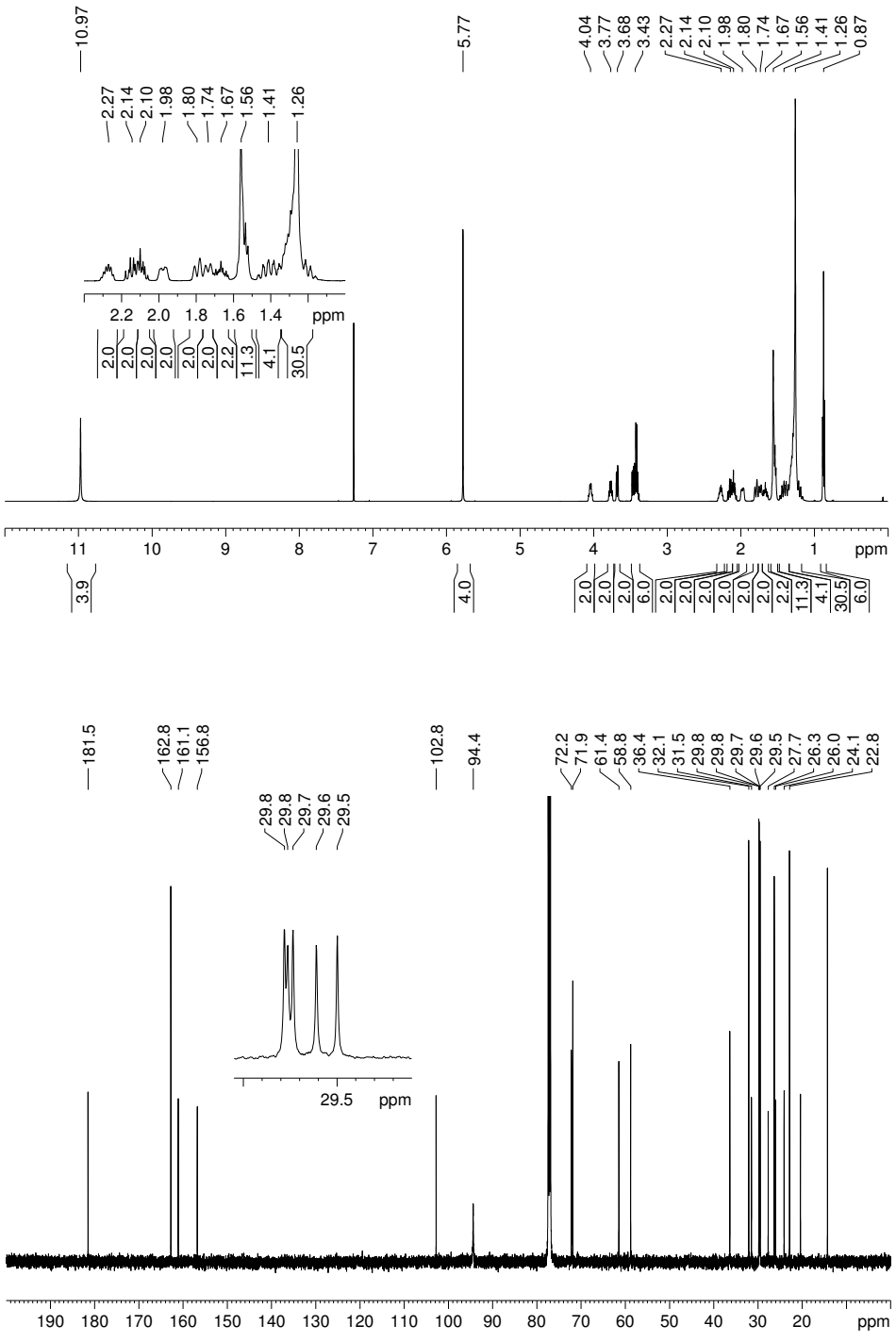


Figure J.48: ^{1}H- (top, 500 MHz) and ^{13}C-NMR (bottom, 125 MHz) spectrum of **(*S*,*S*)-OHI-SQ-C10**; $CDCl_3$, 298 K.

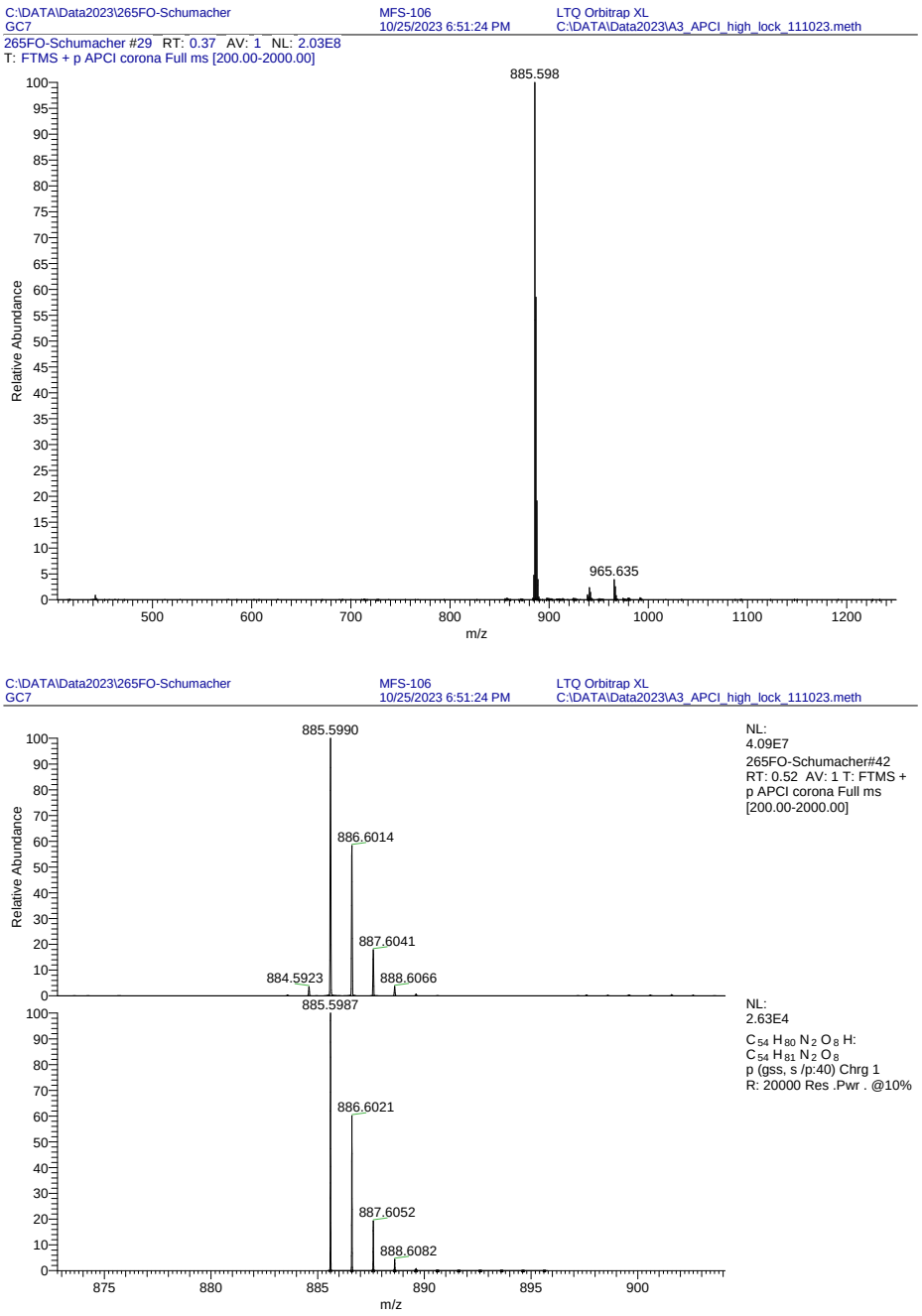


Figure J.49: APCI Mass spectra of **(*S*,*S*)-OHI-SQ-C10**.

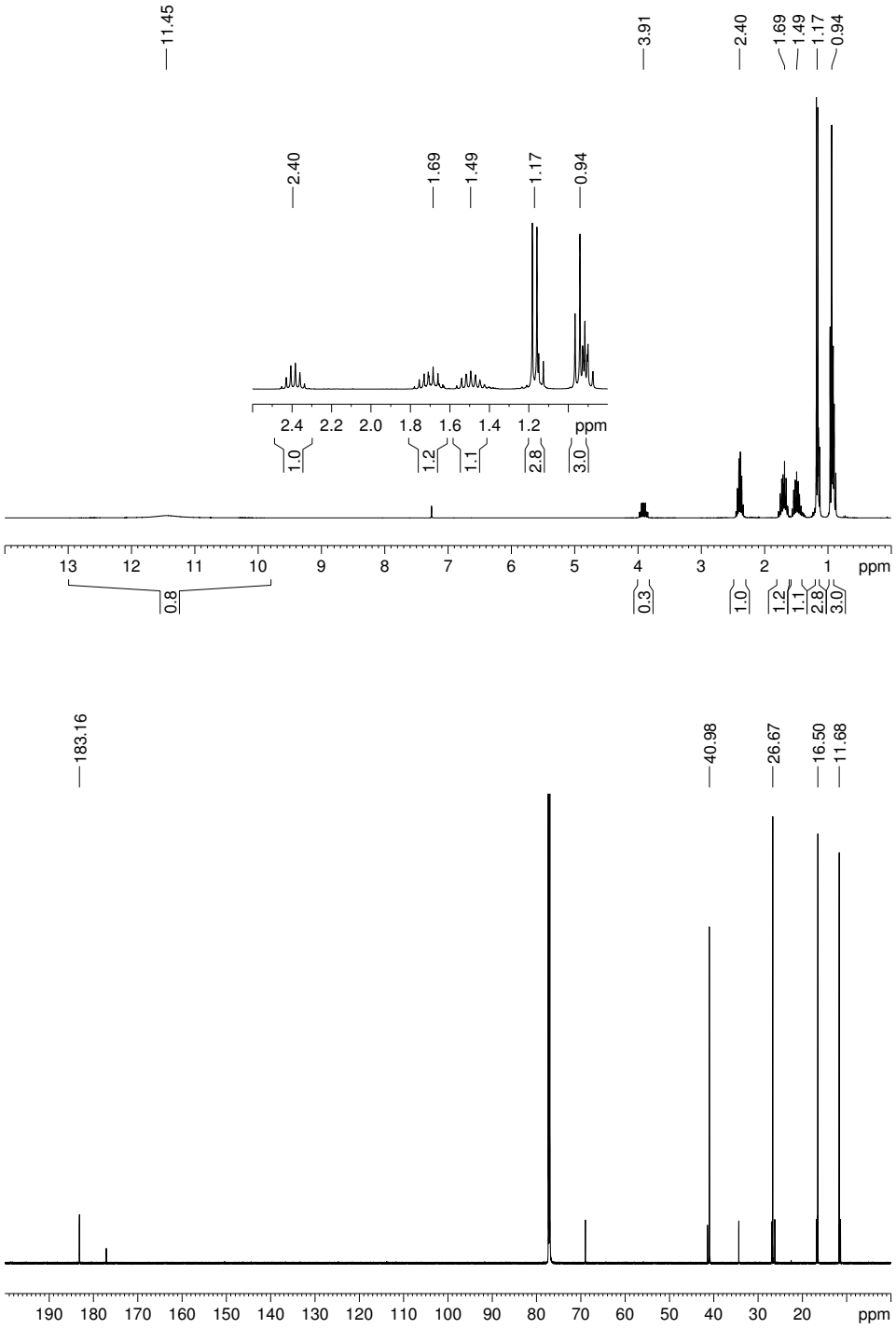


Figure J.50: ^{1}H- (top, 700 MHz) and ^{13}C-NMR (bottom, 176 MHz) spectrum of **(*S*)-2mb-COOH**; $CDCl_3$, 298 K.

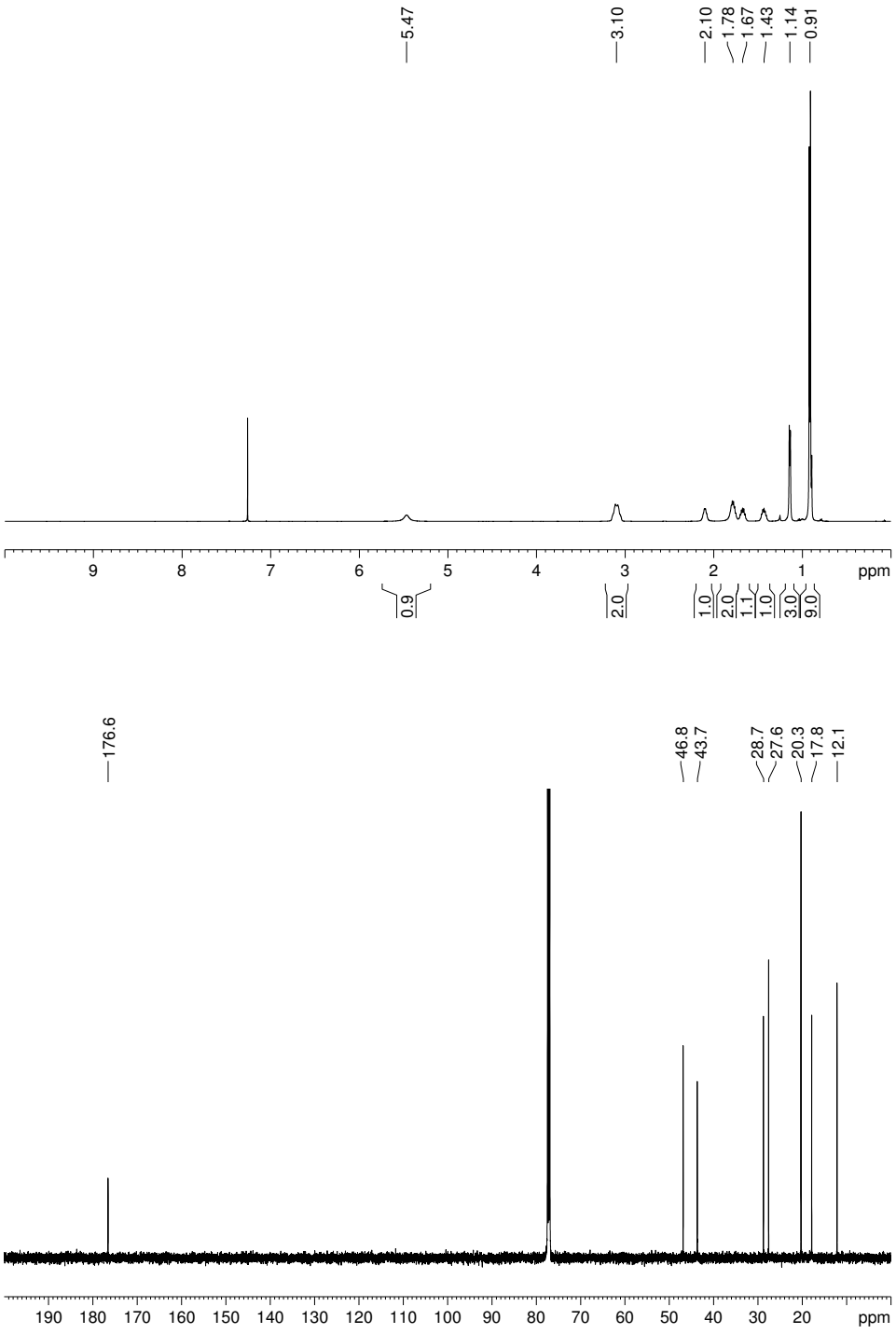


Figure J.51: ^{1}H- (top, 500 MHz) and ^{13}C-NMR (bottom, 125 MHz) spectrum of **(*S*)-2mb-CON-IB**; $CDCl_3$, 298 K.

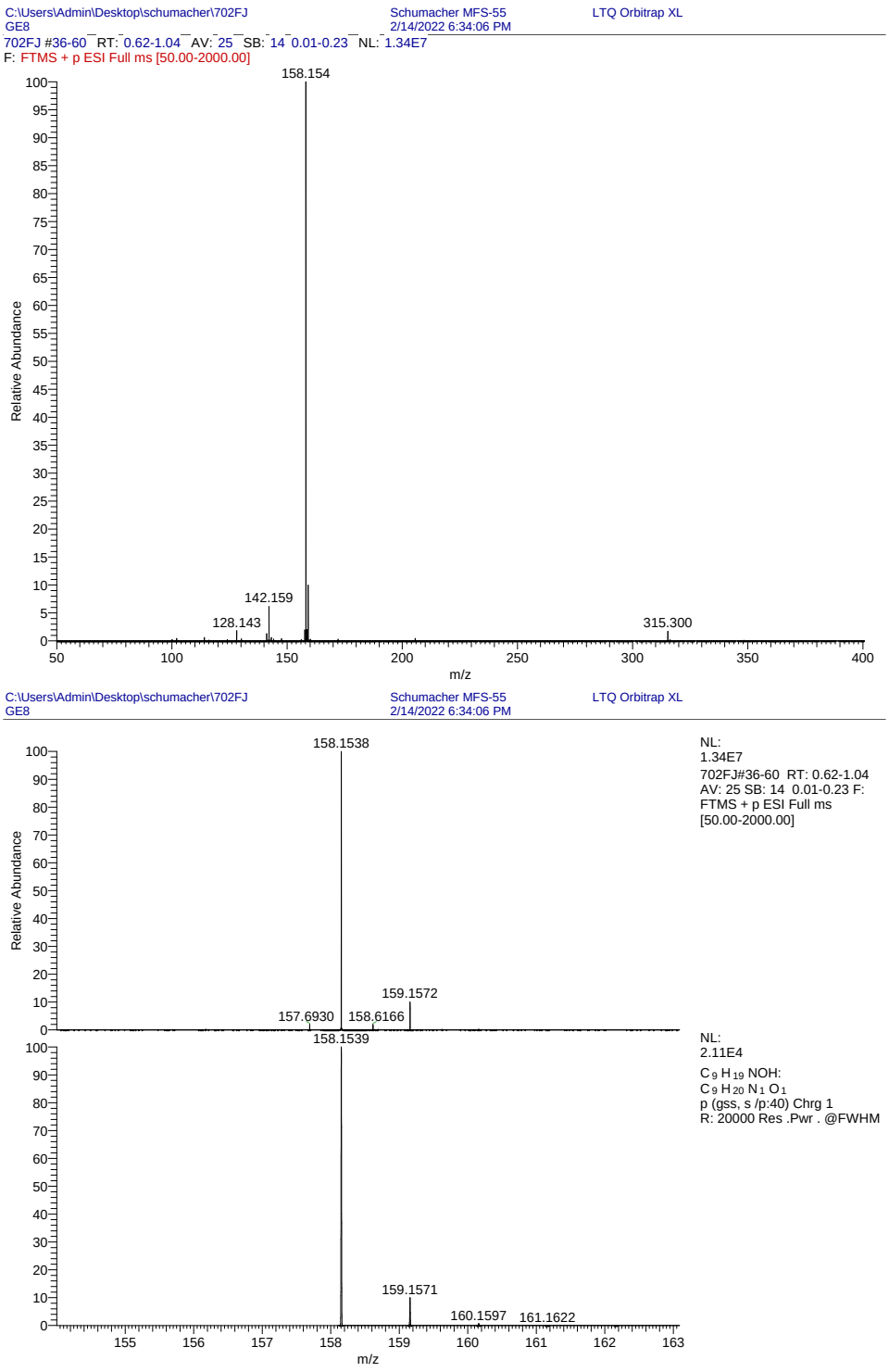


Figure J.52: ESI(+) Mass spectra of **(*S*)-2mb-CON-IB**.

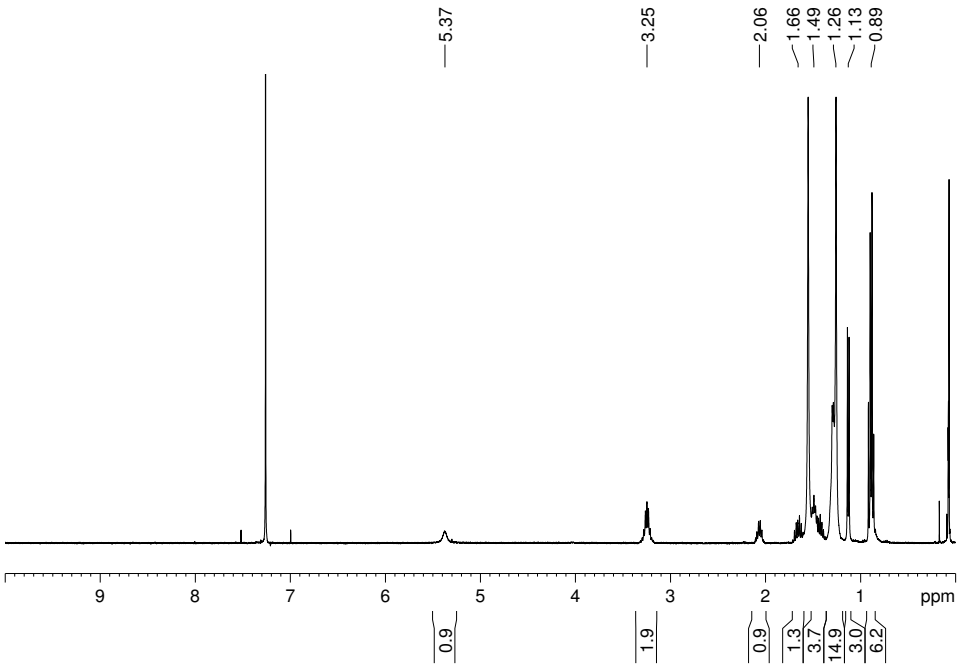


Figure J.53: ^{1}H-NMR (500 MHz) spectrum of **(*S*)-2mb-CON-C10**; $CDCl_3$, 298 K.

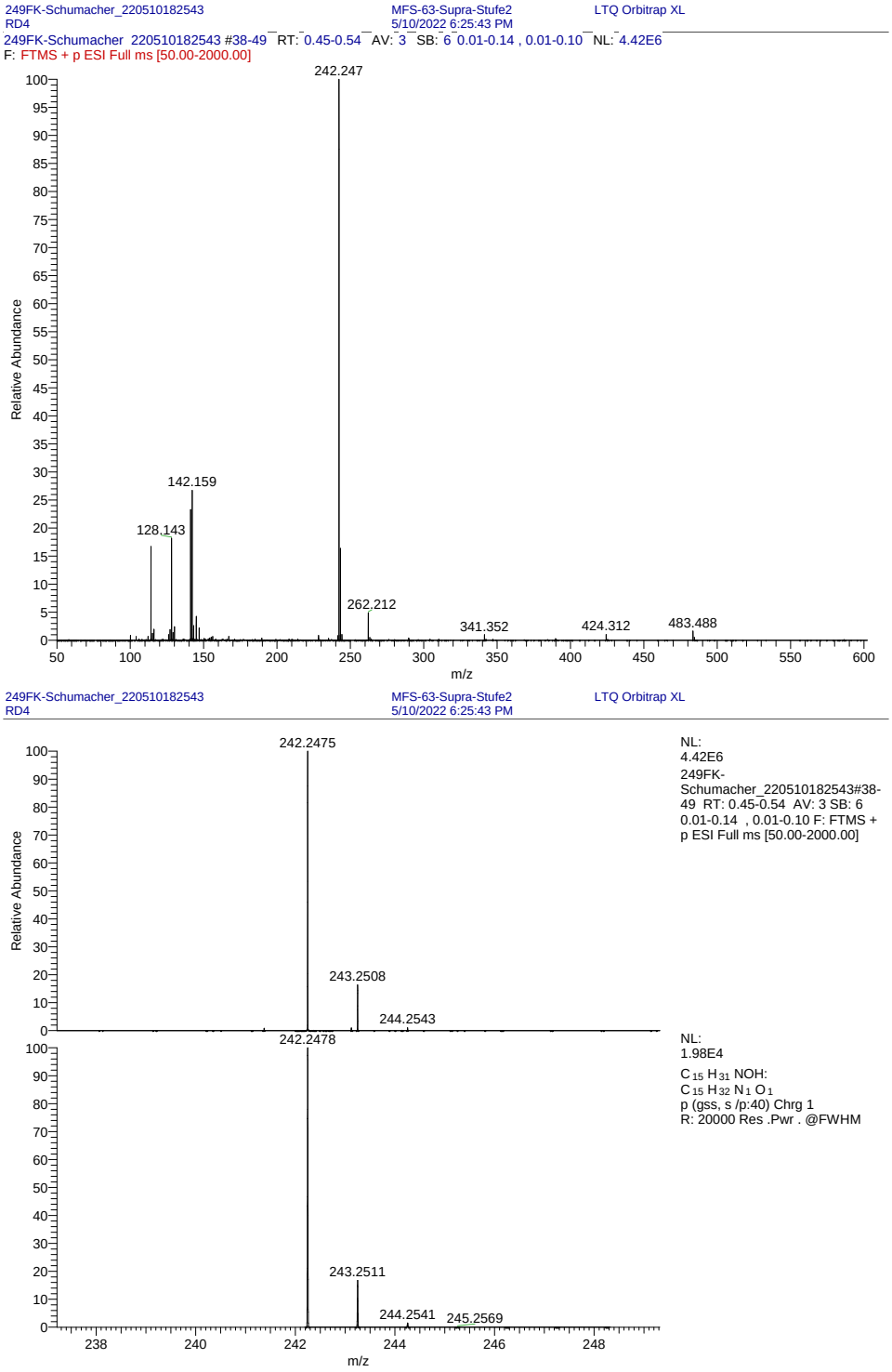


Figure J.54: ESI(+) Mass spectra of **(*S*)-2mb-CON-C10**.

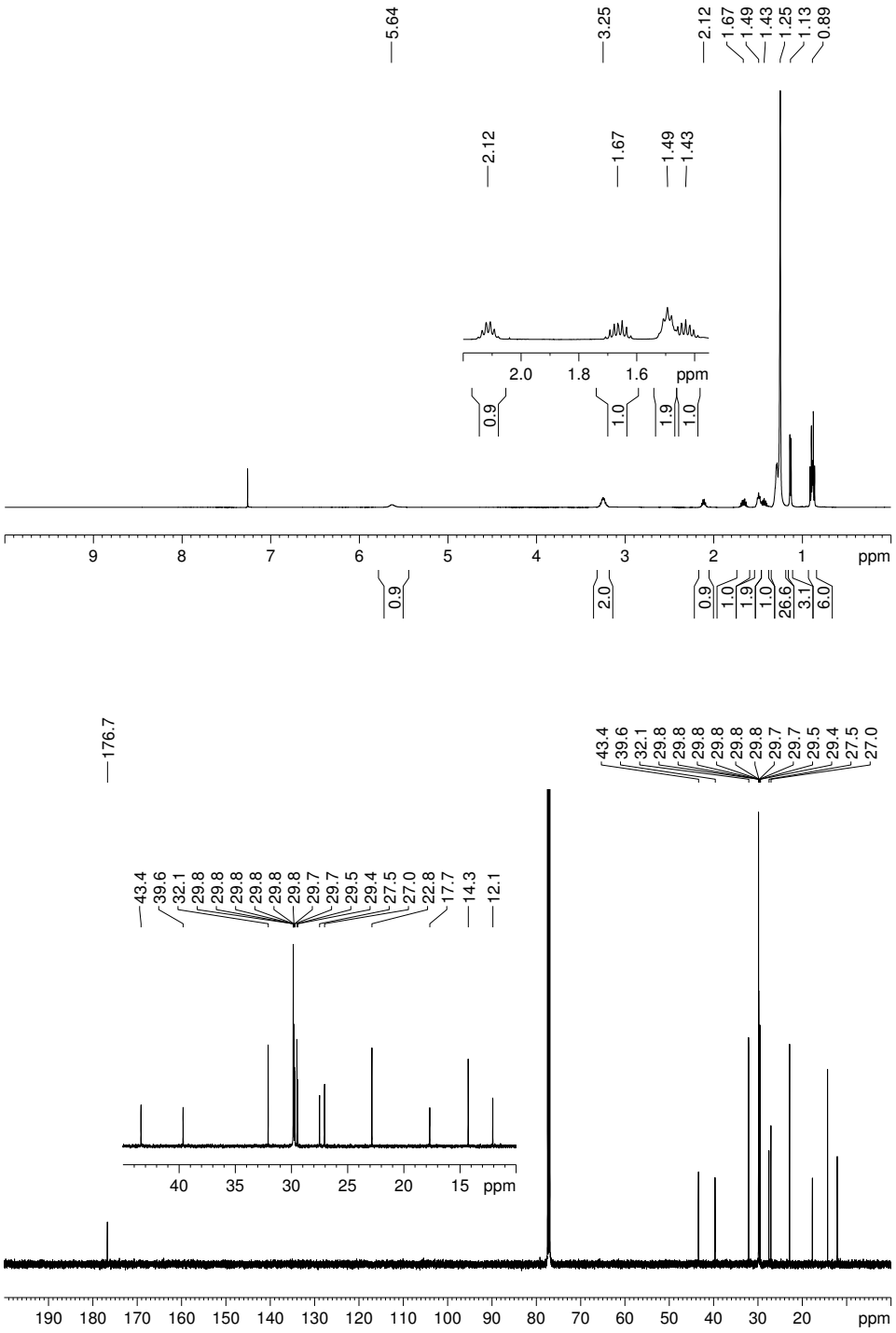


Figure J.55: ^{1}H- (top, 500 MHz) and ^{13}C-NMR (bottom, 125 MHz) spectrum of **(*S*)-2mb-CON-C16**; $CDCl_3$, 298 K.

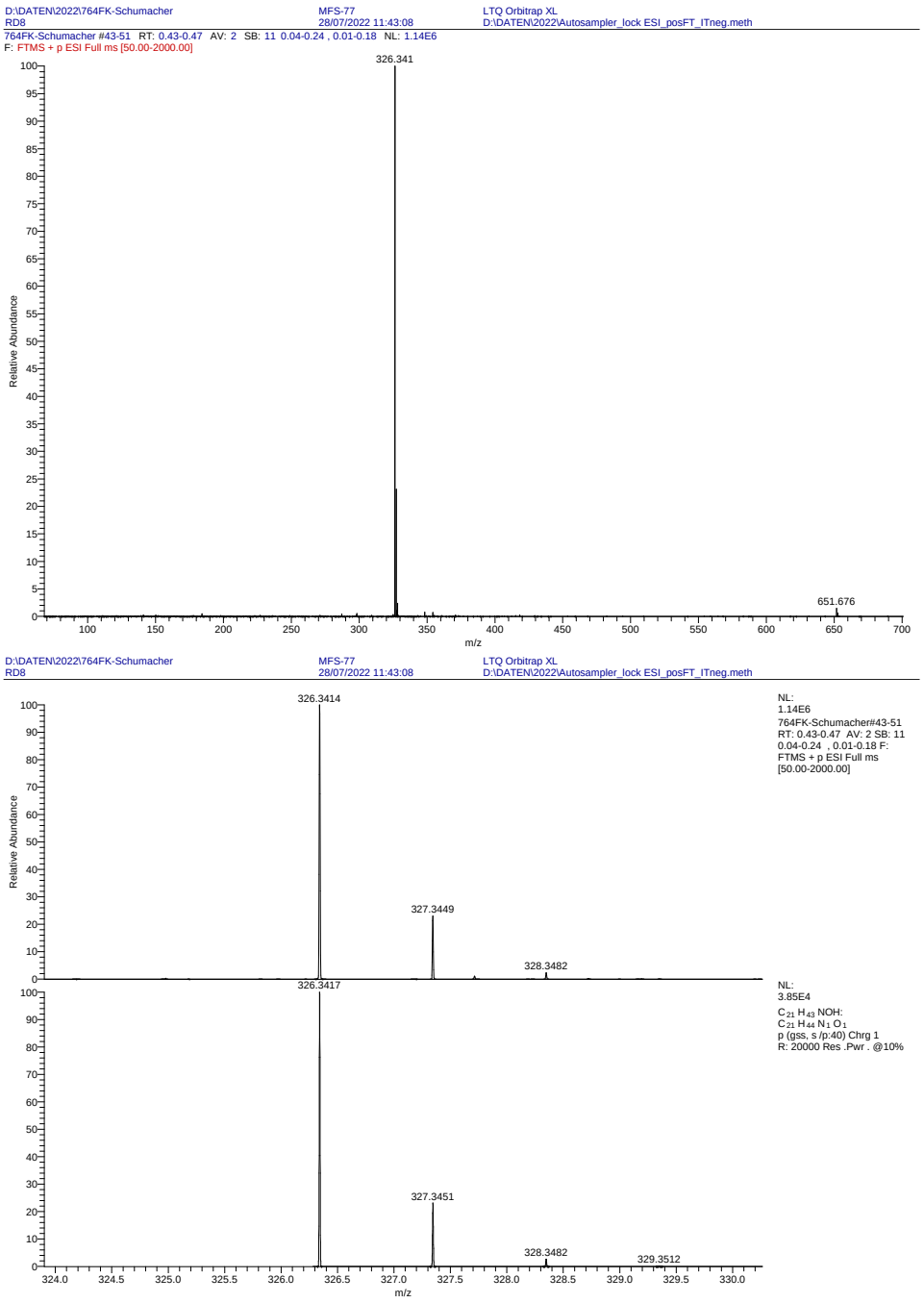


Figure J.56: ESI(+) Mass spectra of **(*S*)-2mb-CON-C16**.

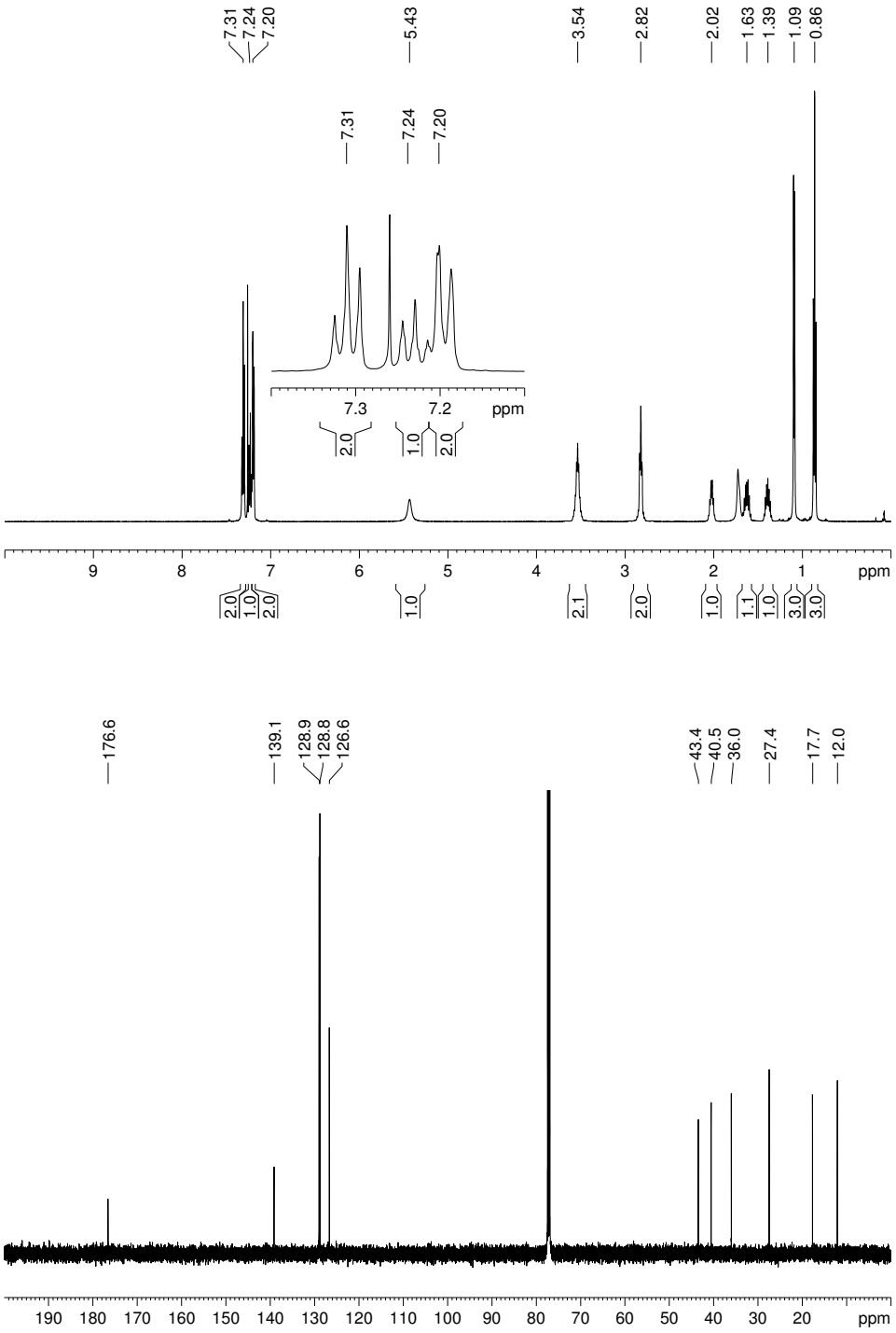


Figure J.57: ^{1}H- (top, 500 MHz) and ^{13}C-NMR (bottom, 125 MHz) spectrum of **(*S*)-2mb-CON-PE**; $CDCl_3$, 298 K.

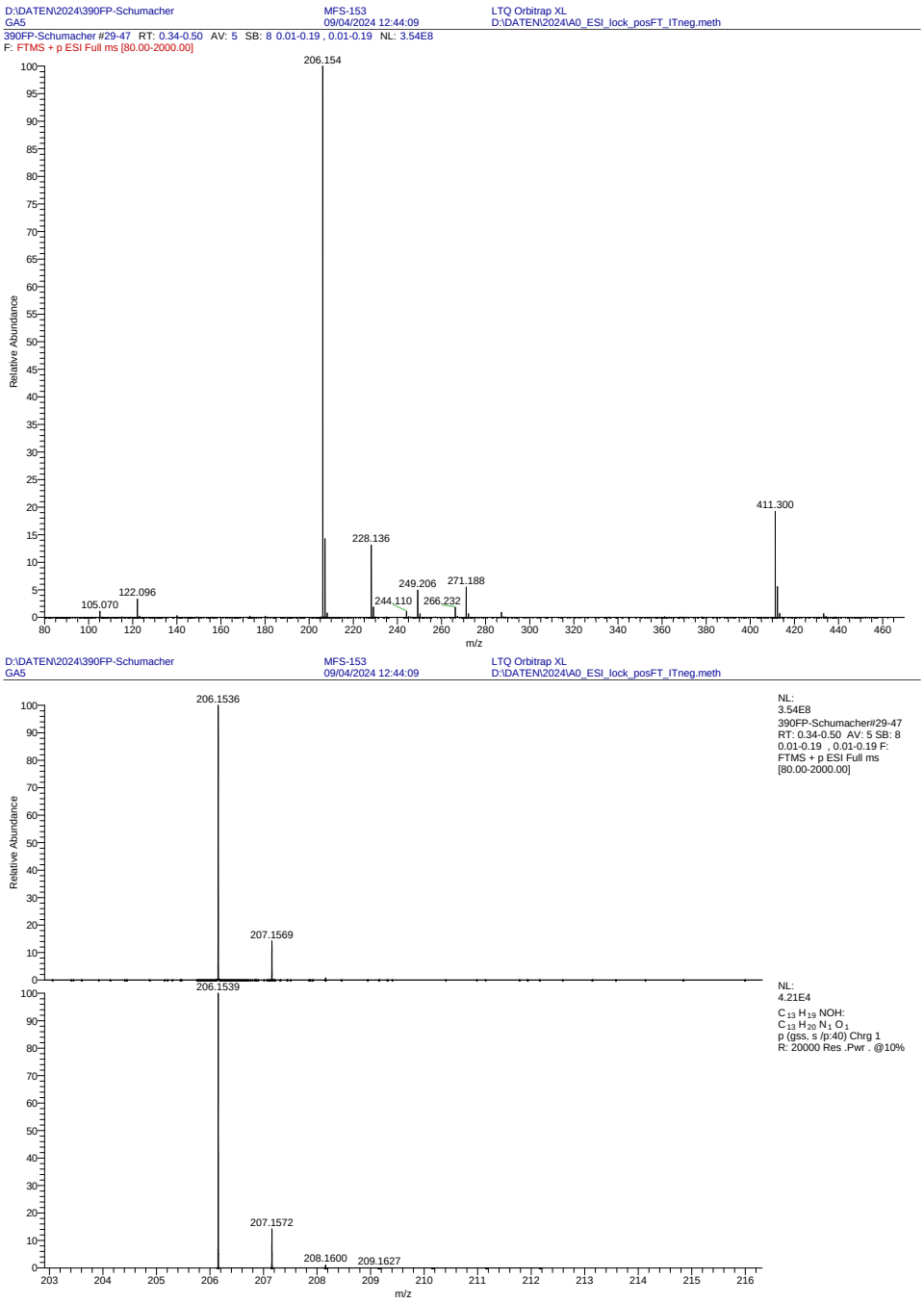


Figure J.58: ESI(+) Mass spectra of **(*S*)-2mb-CON-PE**.

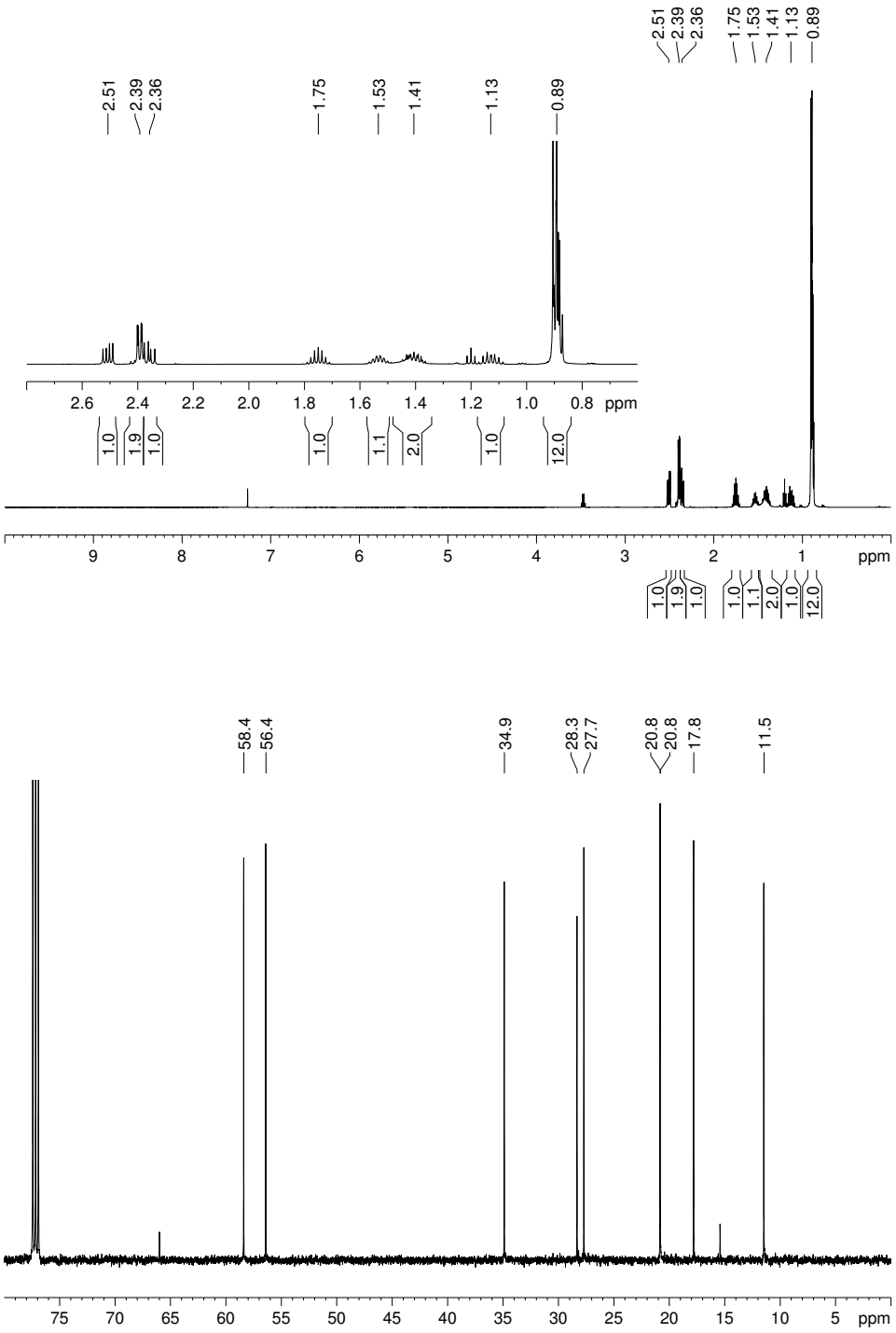


Figure J.59: ^{1}H- (top, 500 MHz) and ^{13}C-NMR (bottom, 125 MHz) spectrum of **(*S*)-2mb-N-IB**; $CDCl_3$, 298 K.

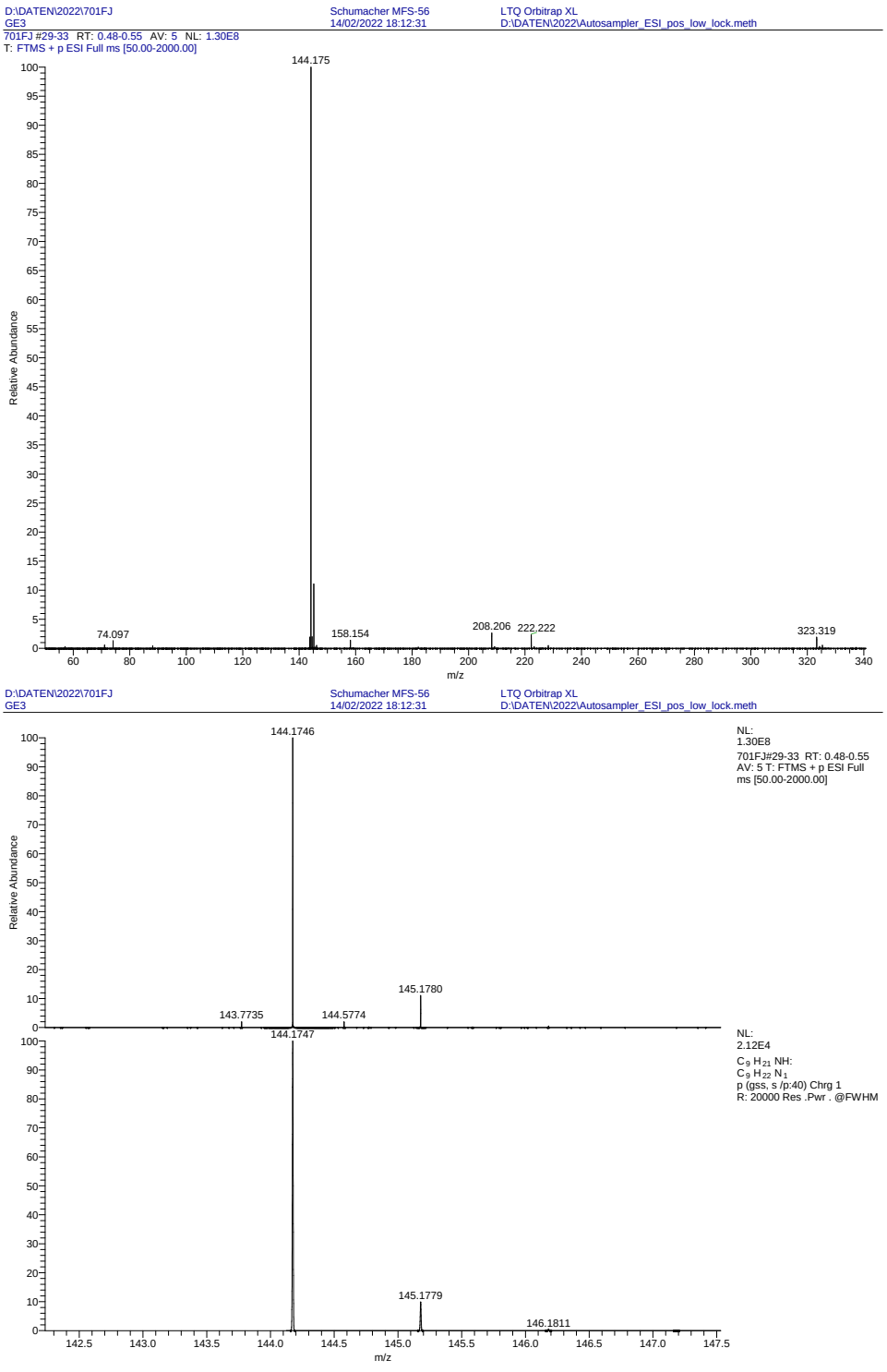


Figure J.60: ESI(+) Mass spectra of **(*S*)-2mb-N-IB**.

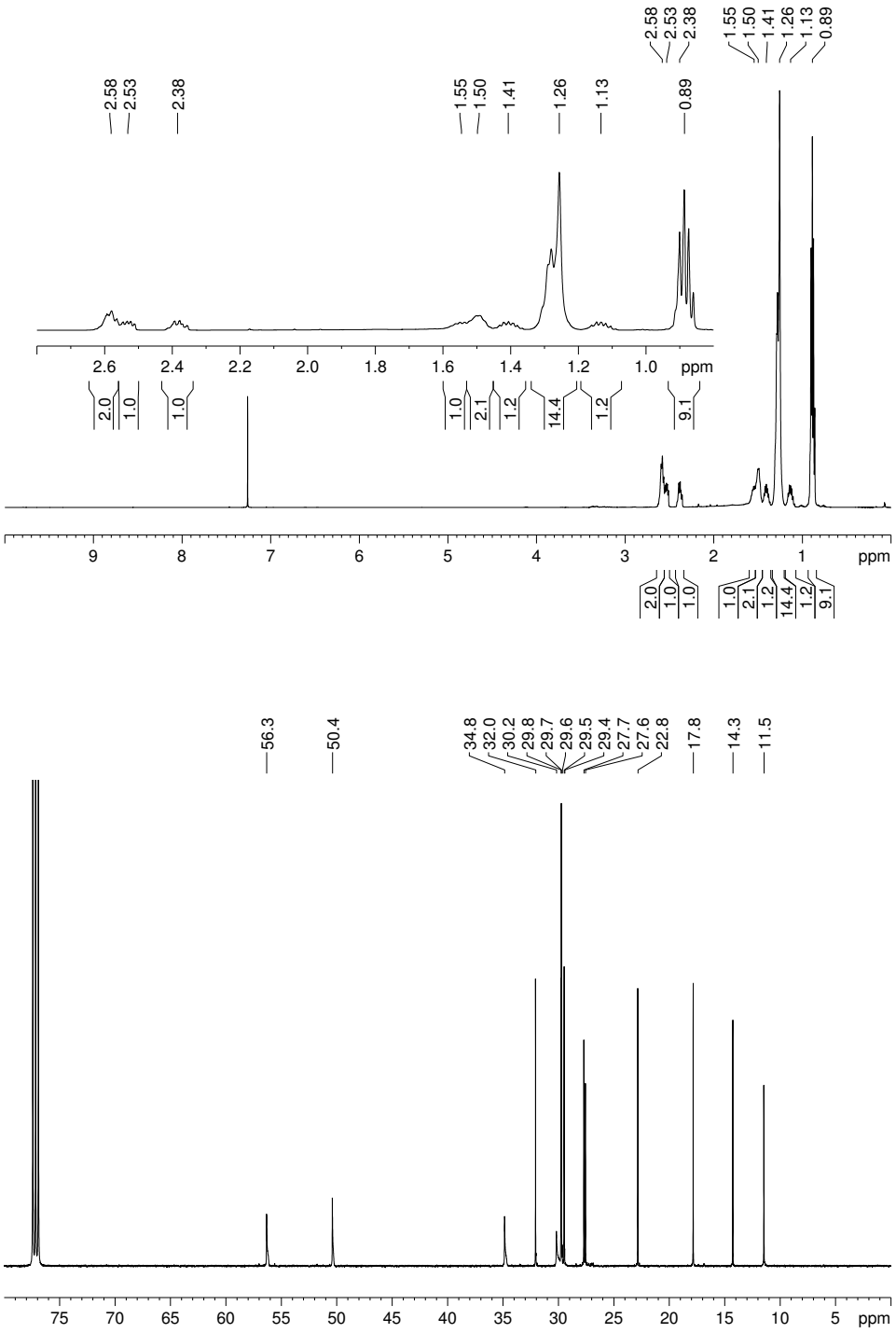


Figure J.61: ^{1}H- (top, 500 MHz) and ^{13}C-NMR (bottom, 125 MHz) spectrum of **(*S*)-2mb-N-C10**; $CDCl_3$, 298 K.

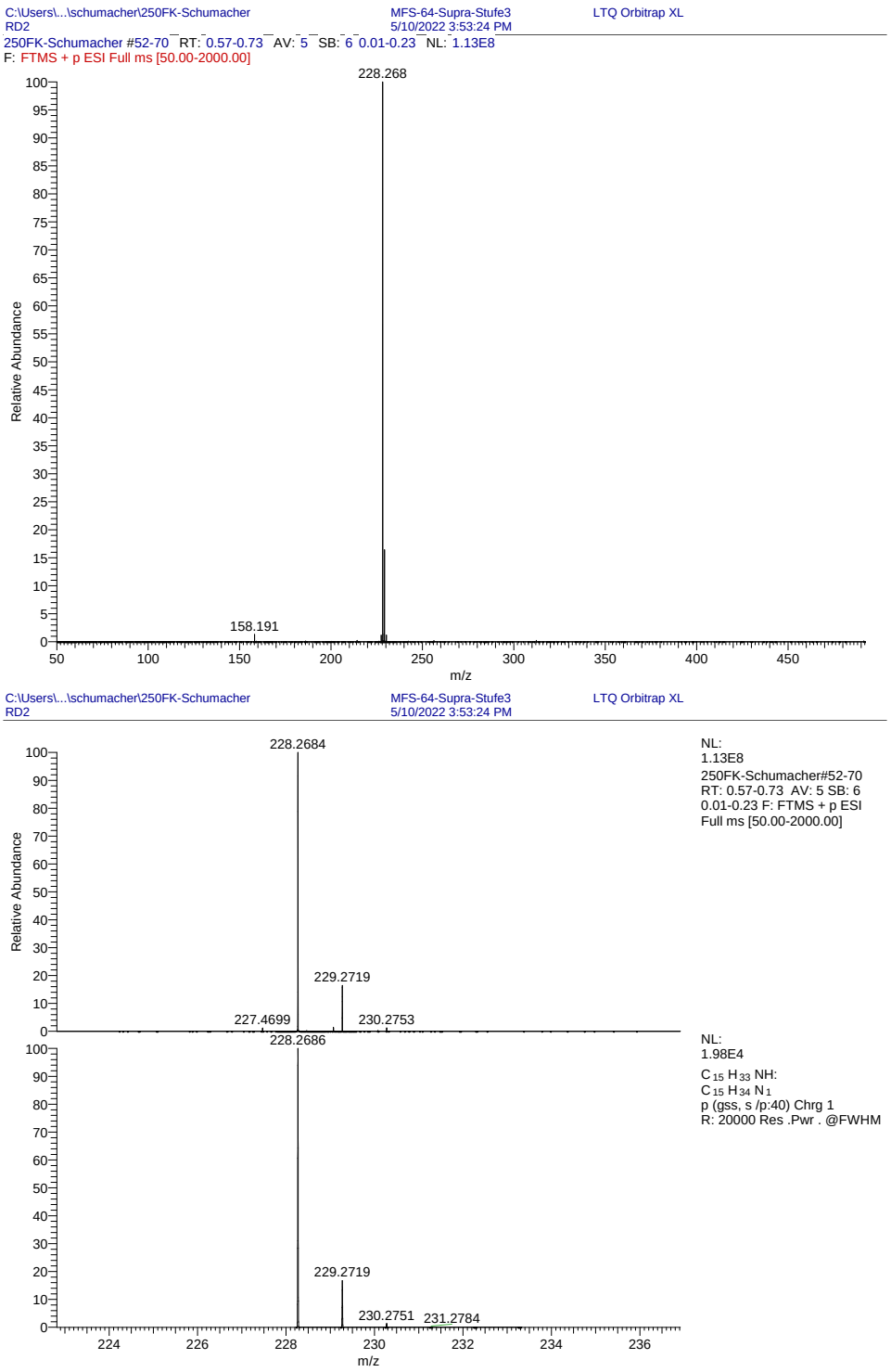


Figure J.62: ESI(+) Mass spectra of **(*S*)-2mb-N-C10**.

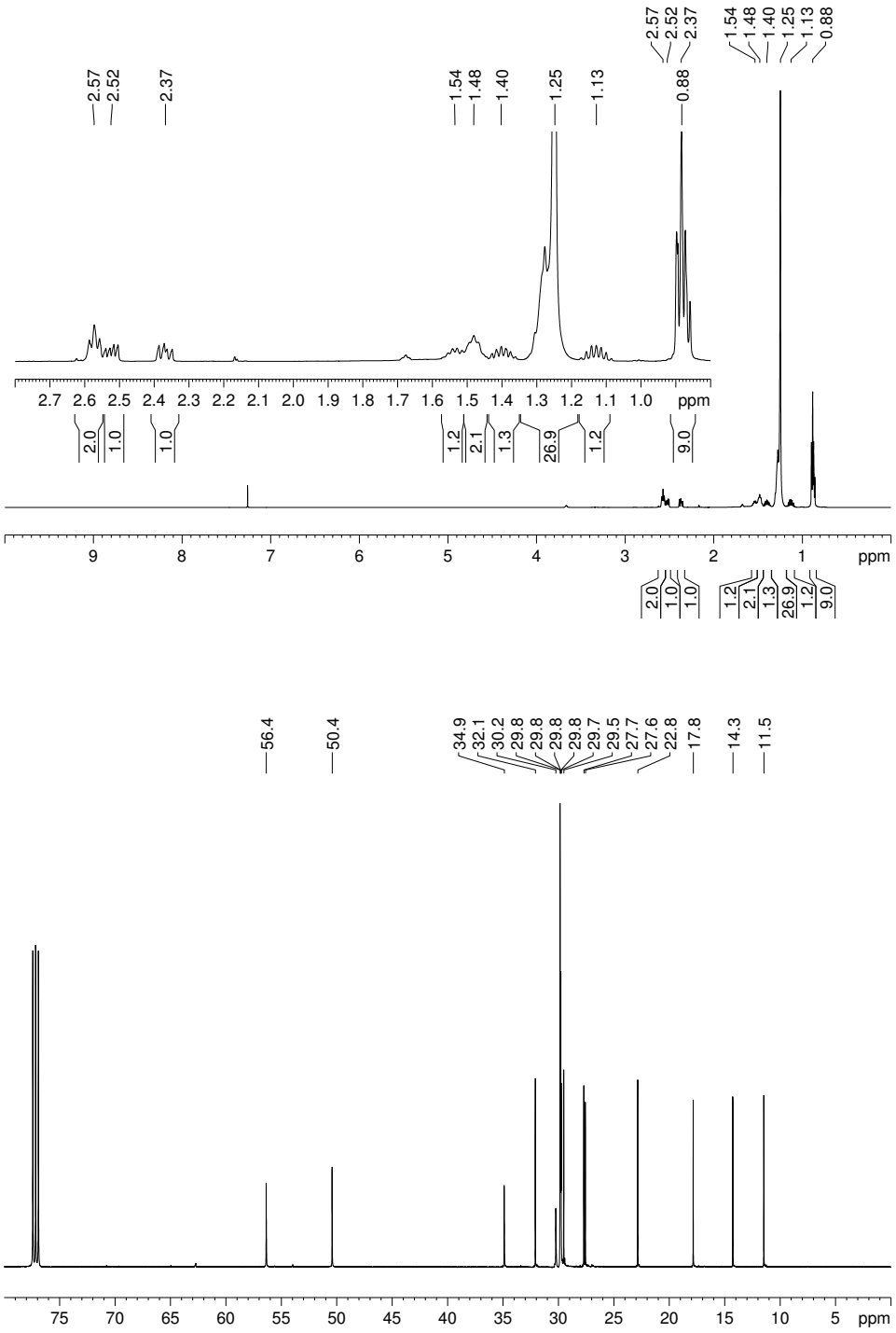


Figure J.63: ^{1}H- (top, 500 MHz) and ^{13}C-NMR (bottom, 125 MHz) spectrum of **(*S*)-2mb-N-C16**; $CDCl_3$, 298 K.

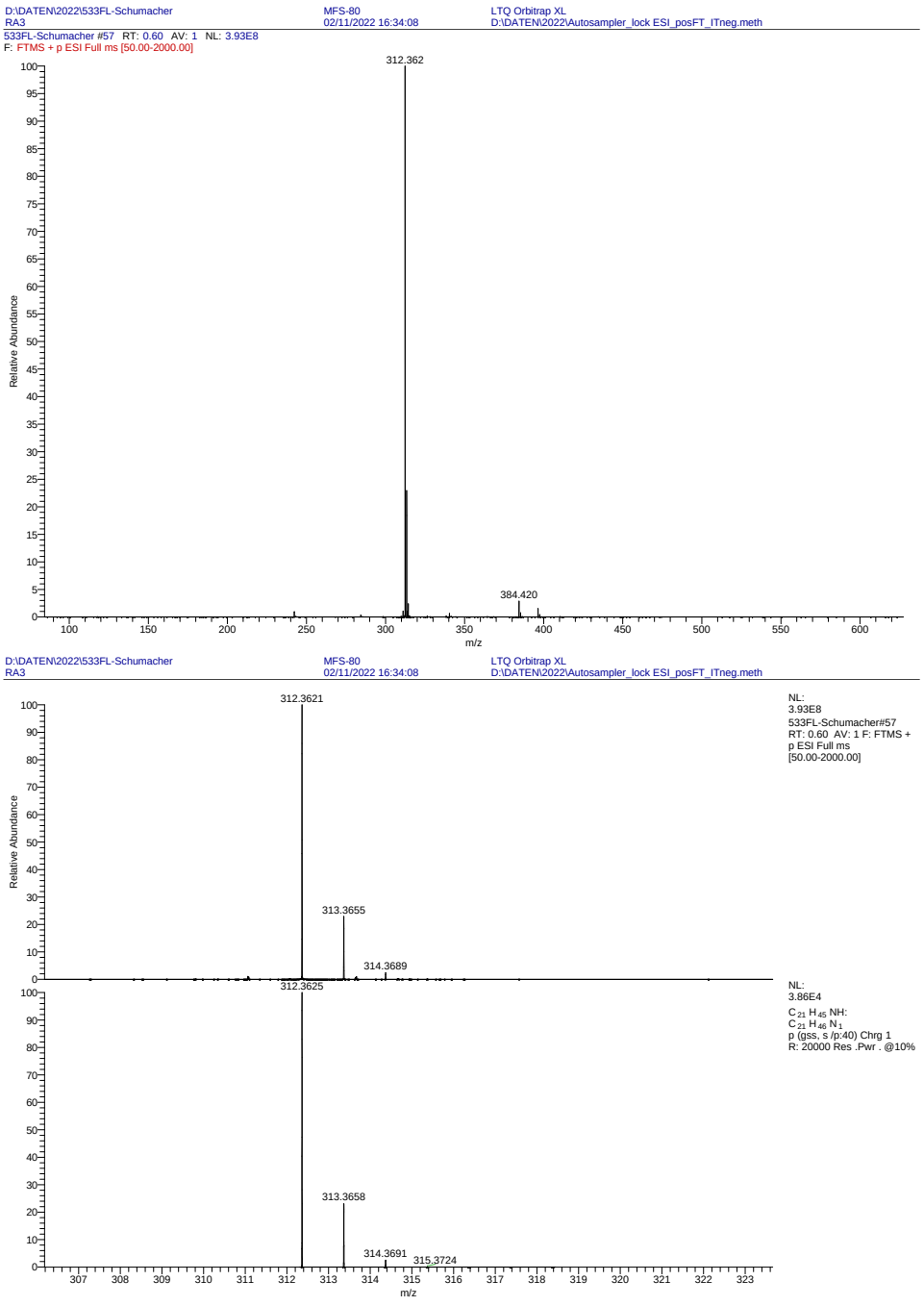


Figure J.64: ESI(+) Mass spectra of **(*S*)-2mb-N-C16**.

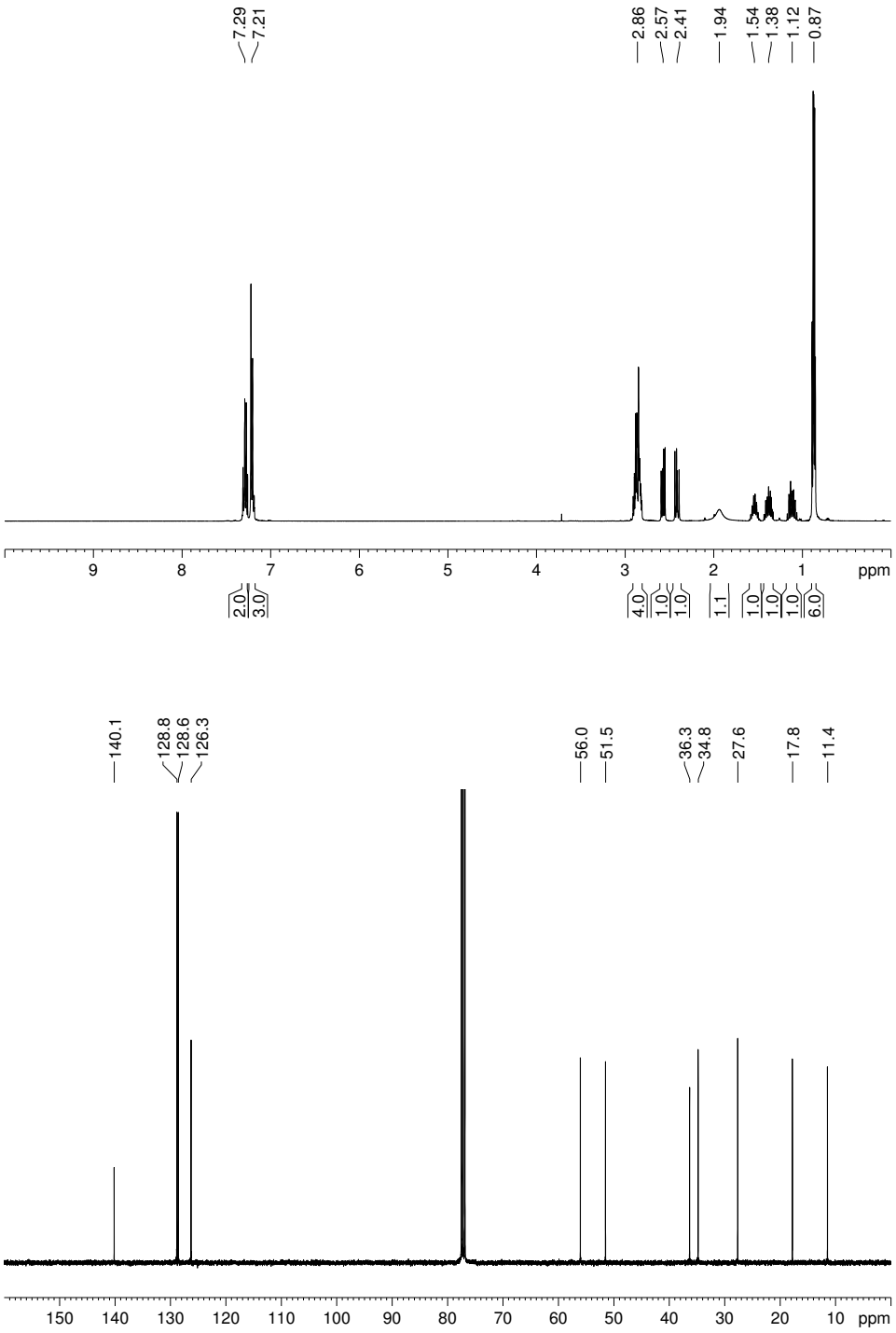


Figure J.65: ^{1}H- (top, 500 MHz) and ^{13}C-NMR (bottom, 125 MHz) spectrum of **(*S*)-2mb-N-PE**; $CDCl_3$, 298 K.

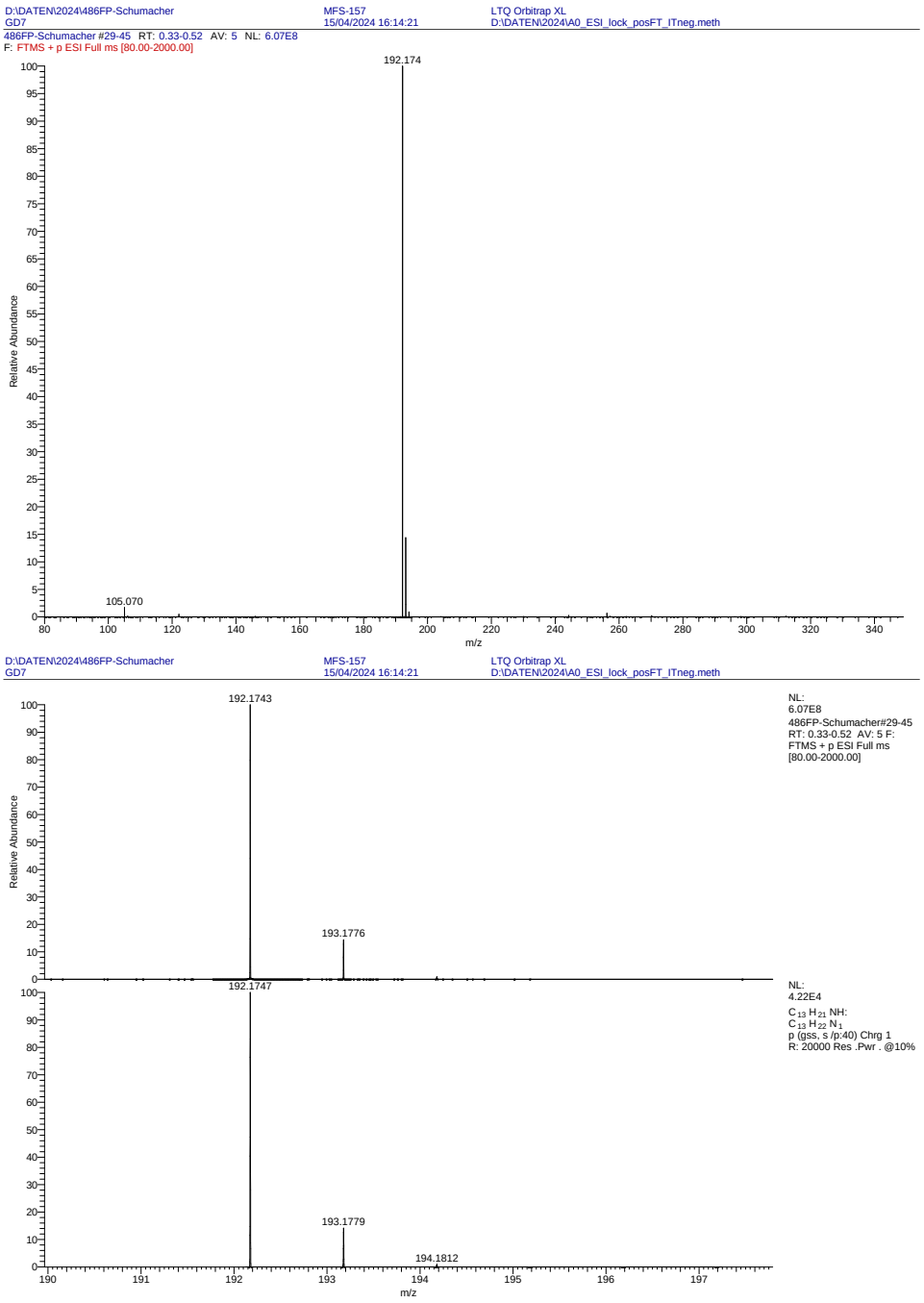


Figure J.66: ESI(+) Mass spectra of **(*S*)-2mb-N-PE**.

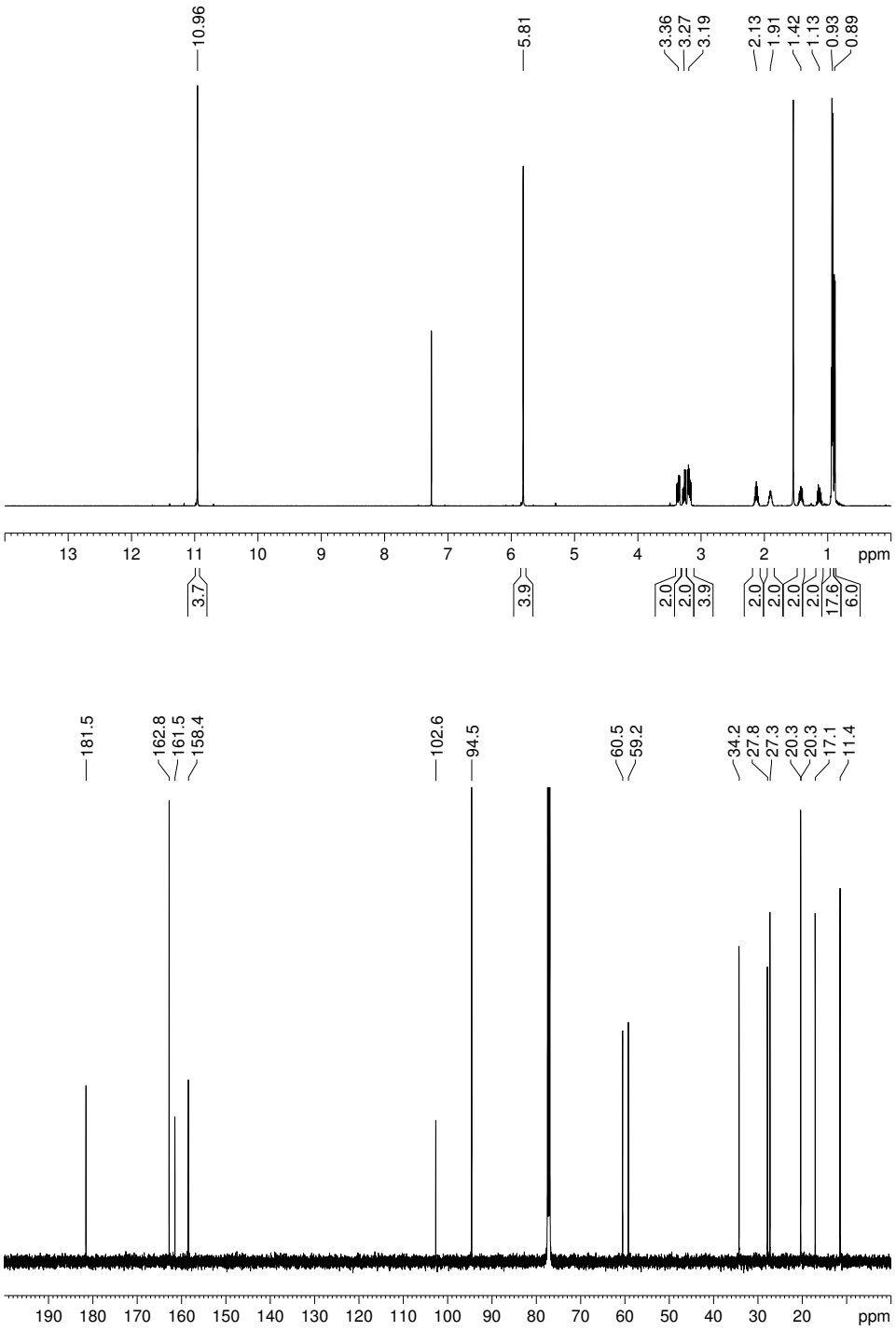


Figure J.67: ^{1}H- (top, 500 MHz) and ^{13}C-NMR (bottom, 125 MHz) spectrum of **(*S*,*S*)-2mb-SQIB**; $CDCl_3$, 298 K.

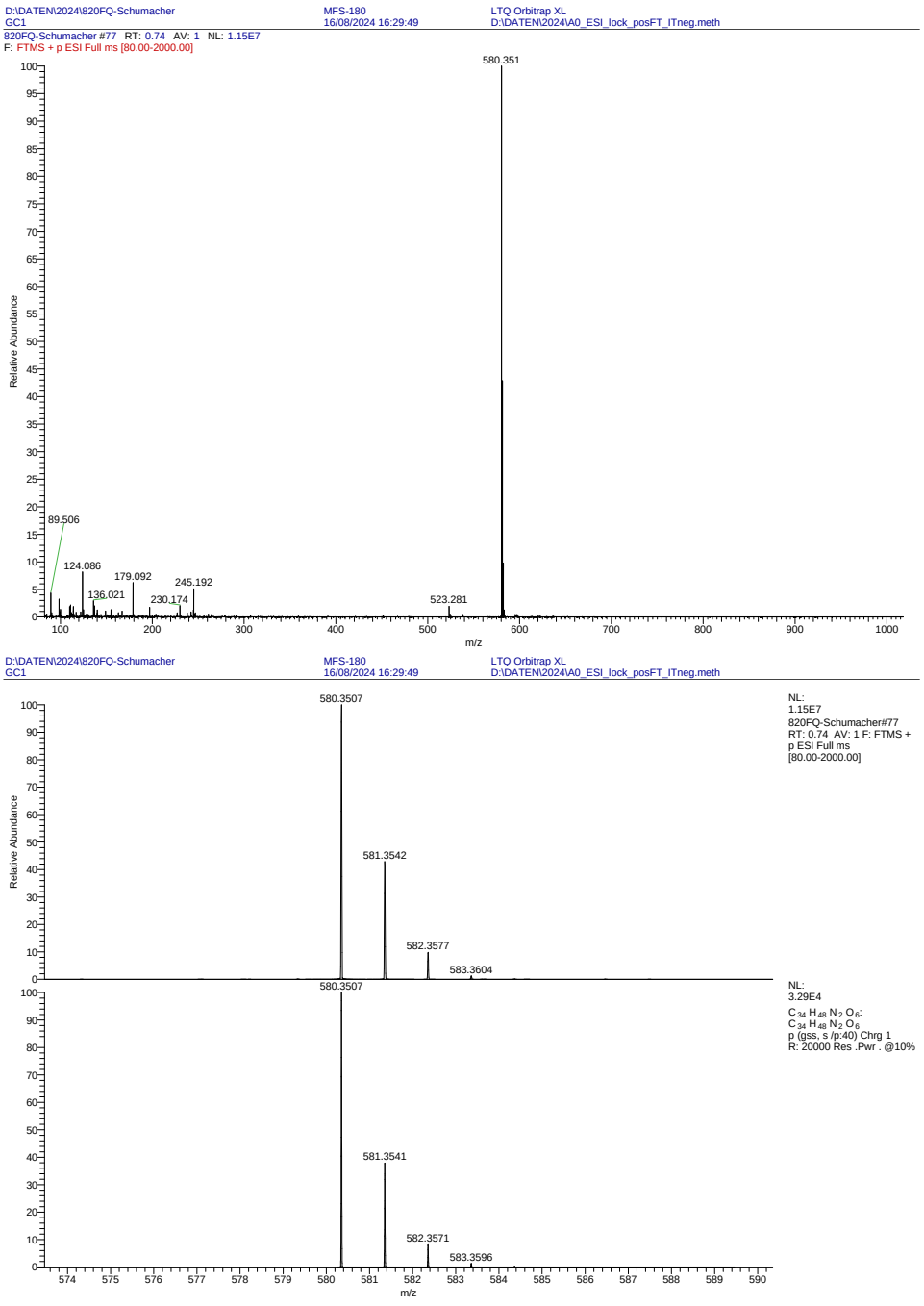


Figure J.68: ESI(+) Mass spectra of **(*S*,*S*)-2mb-SQIB**.

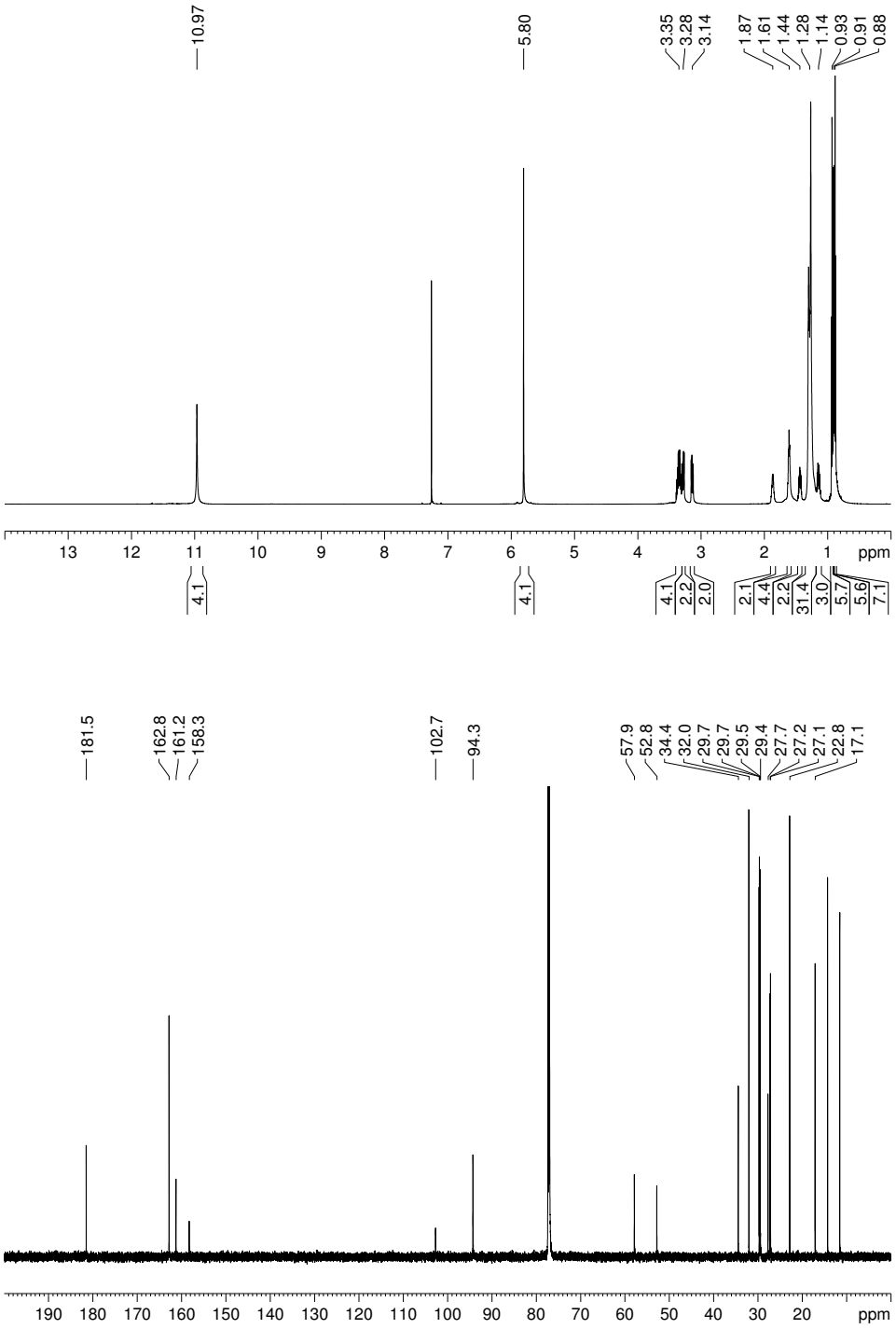


Figure J.69: ^{1}H- (top, 700 MHz) and ^{13}C-NMR (bottom, 176 MHz) spectrum of **(*S*,*S*)-2mb-DSQ**; $CDCl_3$, 298 K.

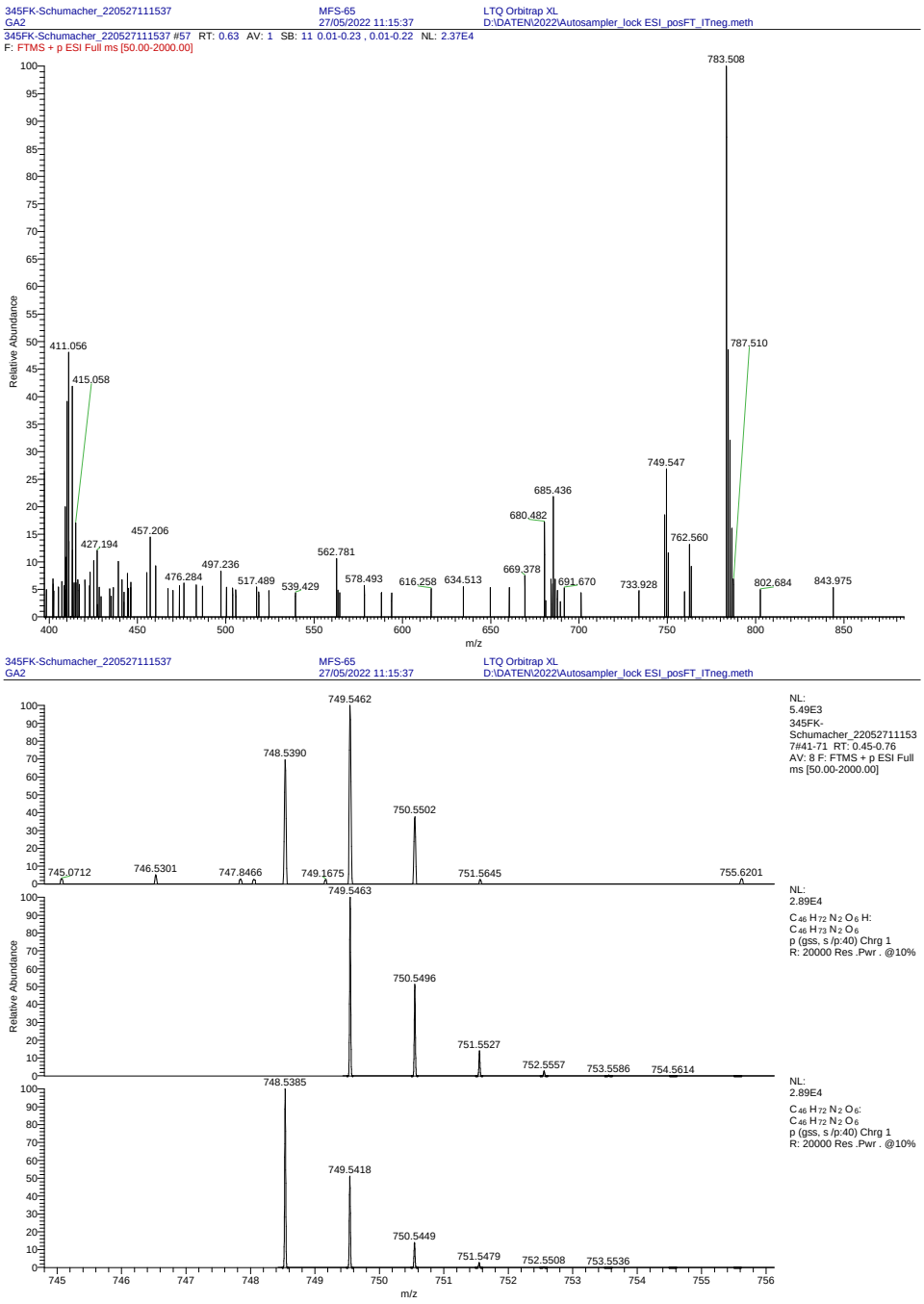


Figure J.70: ESI(+) Mass spectra of **(*S*,*S*)-2mb-DSQ**.

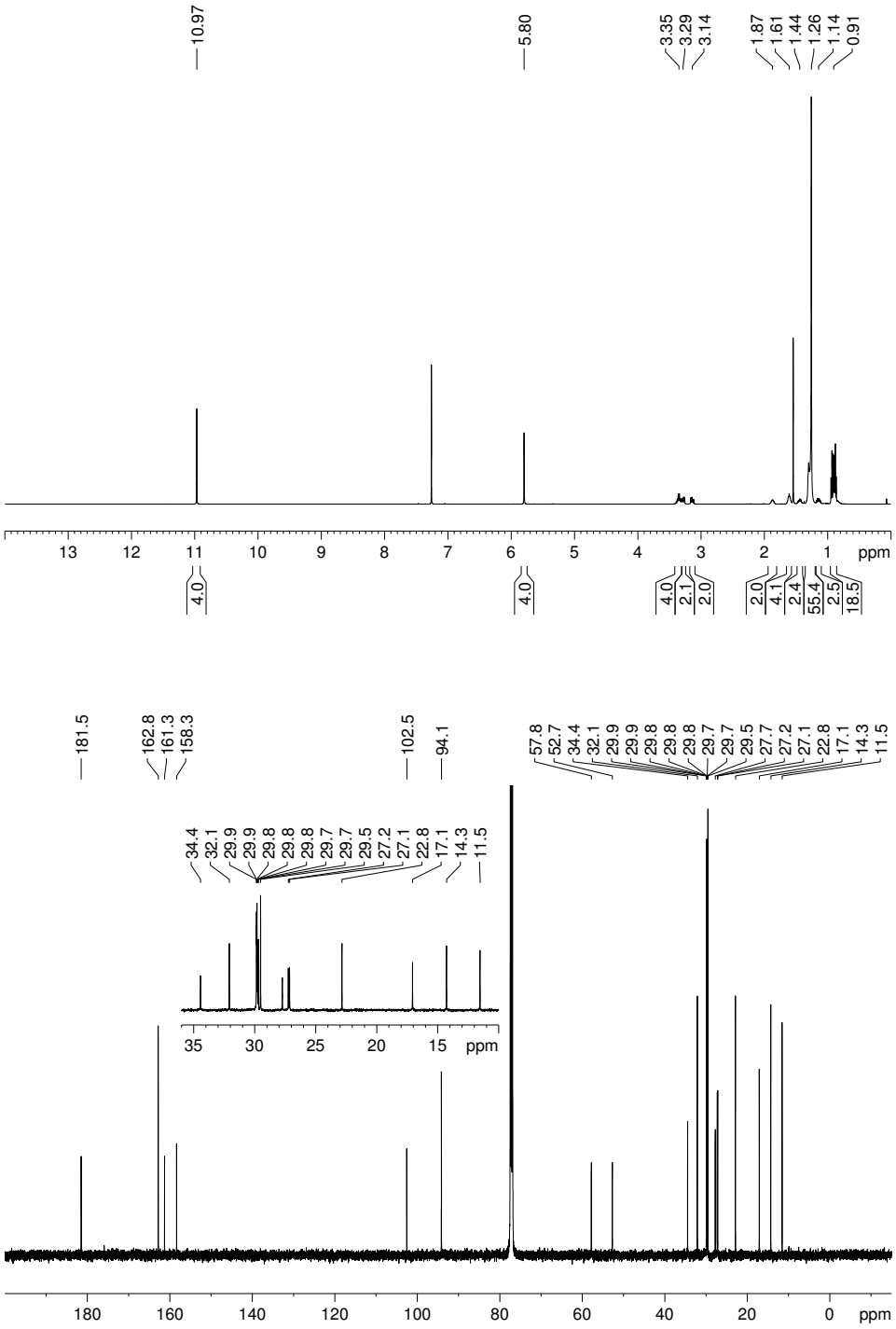


Figure J.71: ^{1}H- (top, 500 MHz) and ^{13}C-NMR (bottom, 125 MHz) spectrum of **(*S*,*S*)-2mb-HDSQ**; $CDCl_3$, 298 K.

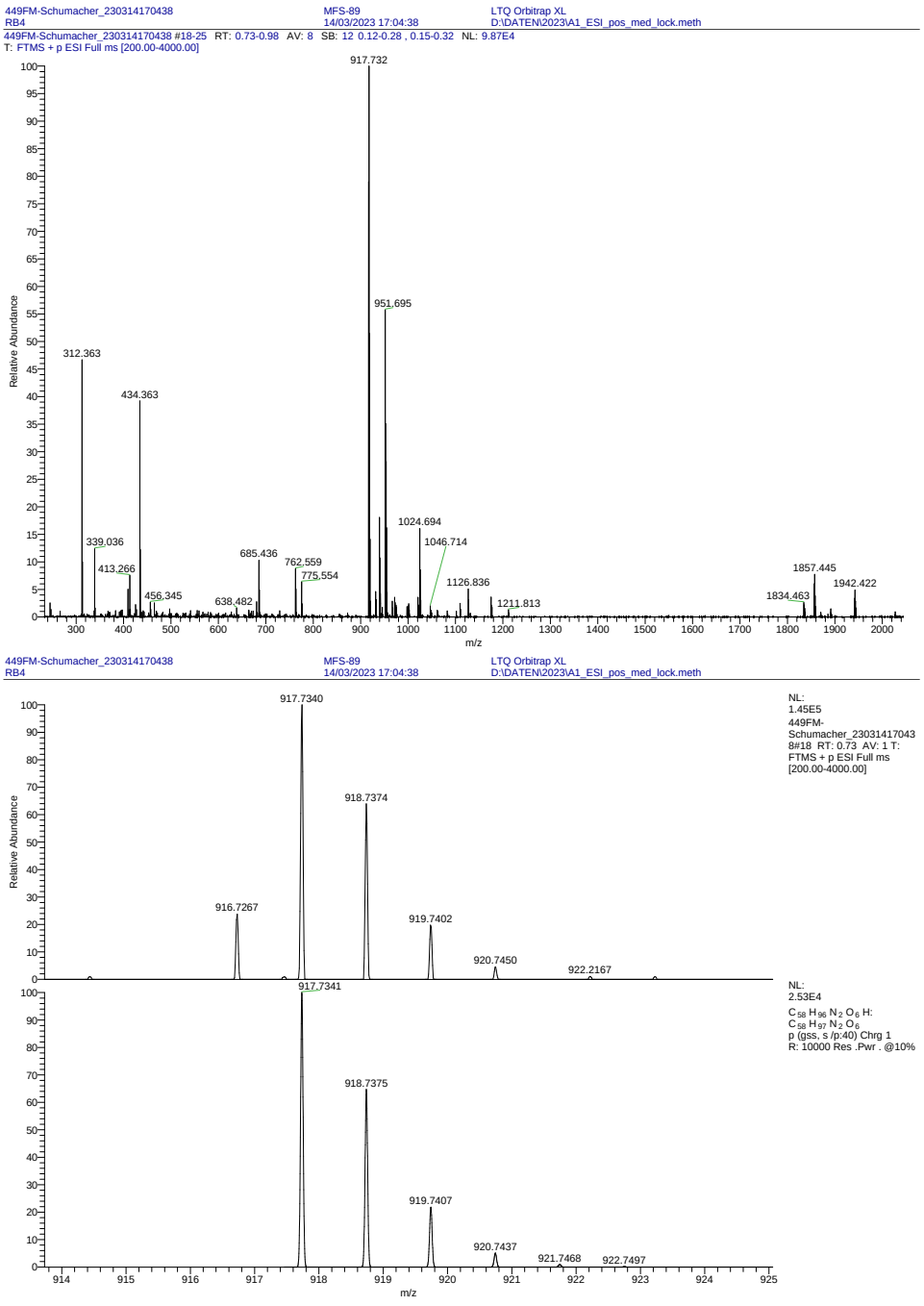


Figure J.72: ESI(+) Mass spectra of **(*S*,*S*)-2mb-HDSQ**.

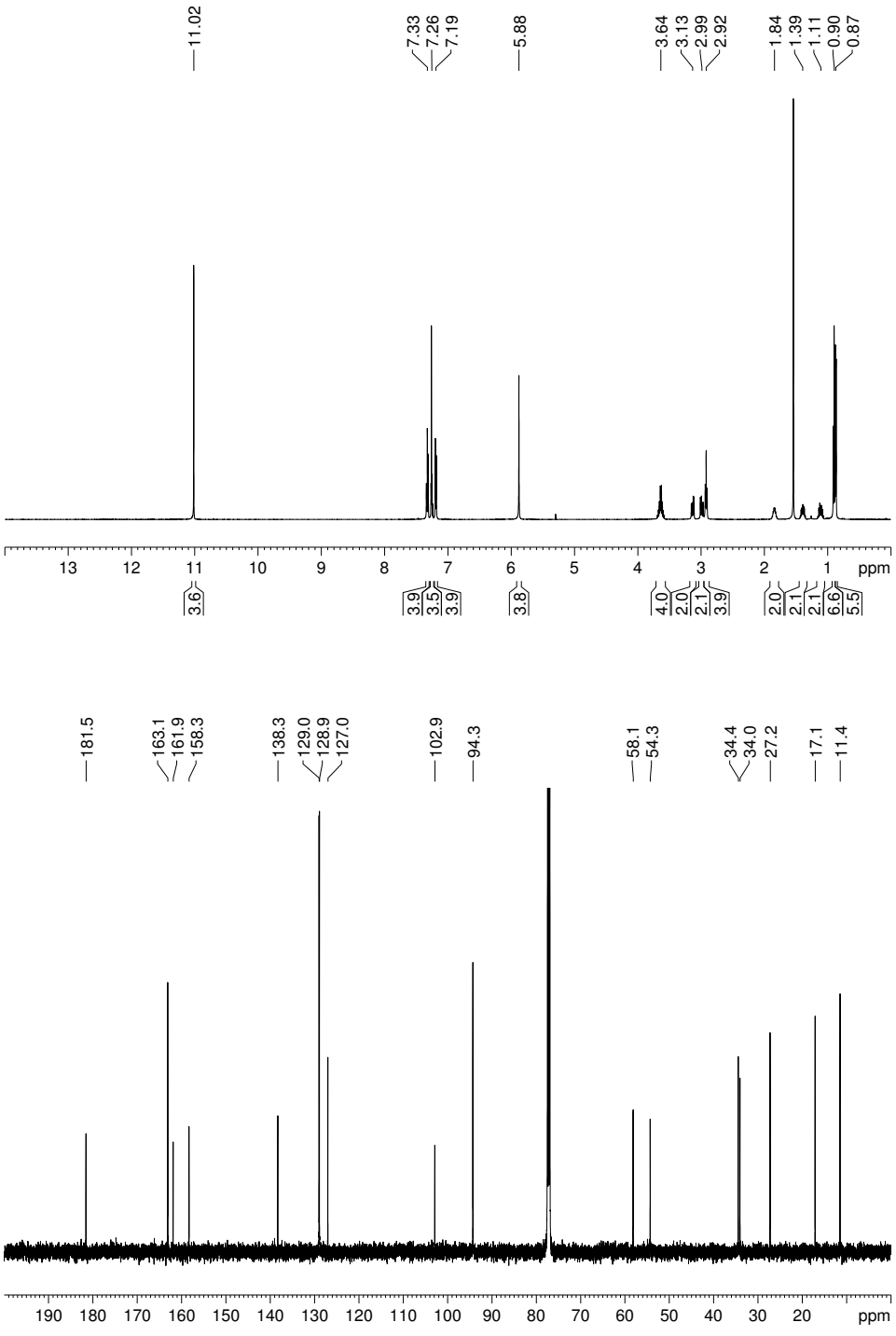


Figure J.73: ^{1}H- (top, 500 MHz) and ^{13}C-NMR (bottom, 125 MHz) spectrum of **(*S*,*S*)-2mb-SQPE**; $CDCl_3$, 298 K.

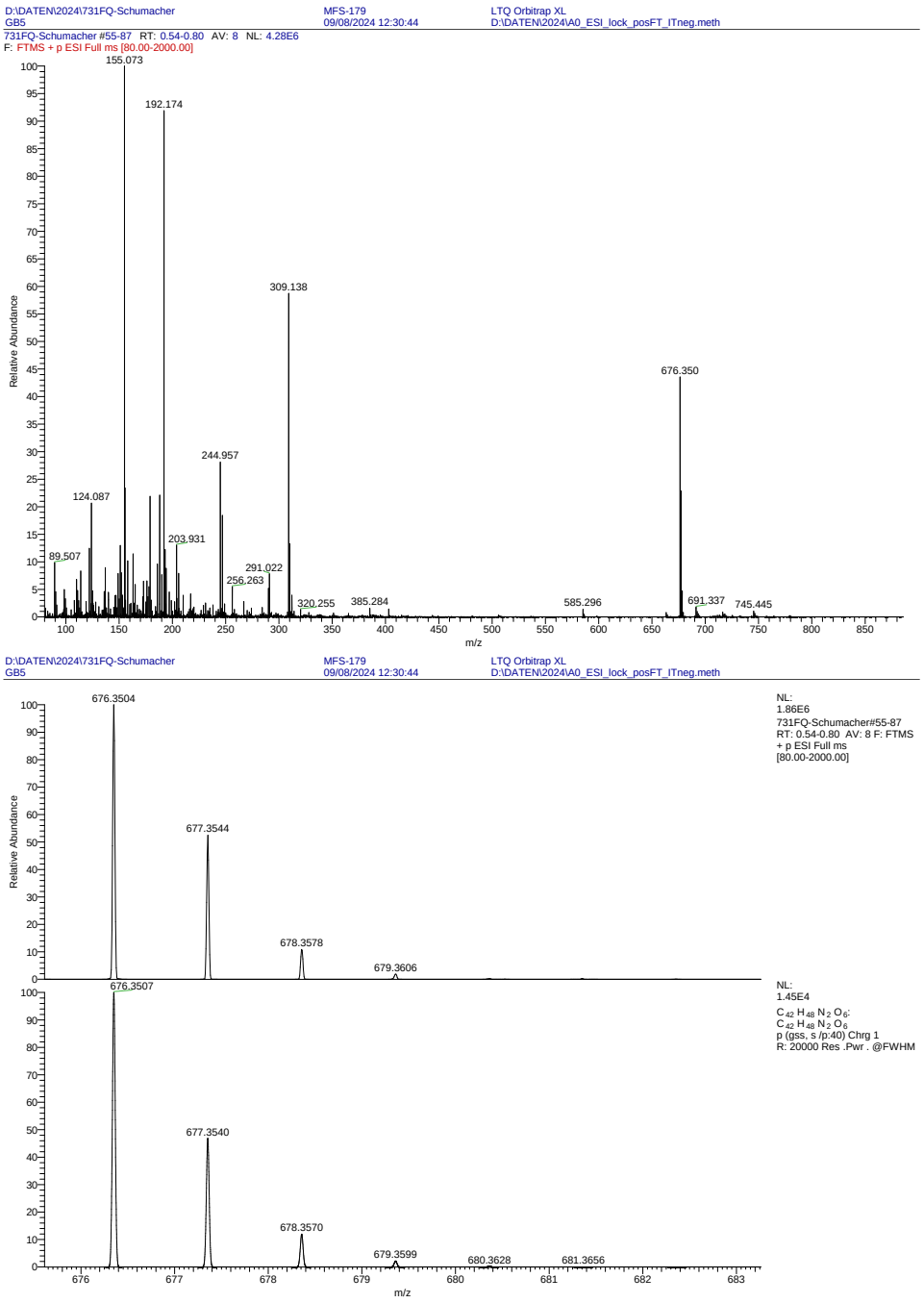


Figure J.74: ESI(+) Mass spectra of **(*S*,*S*)-2mb-SQPE**.

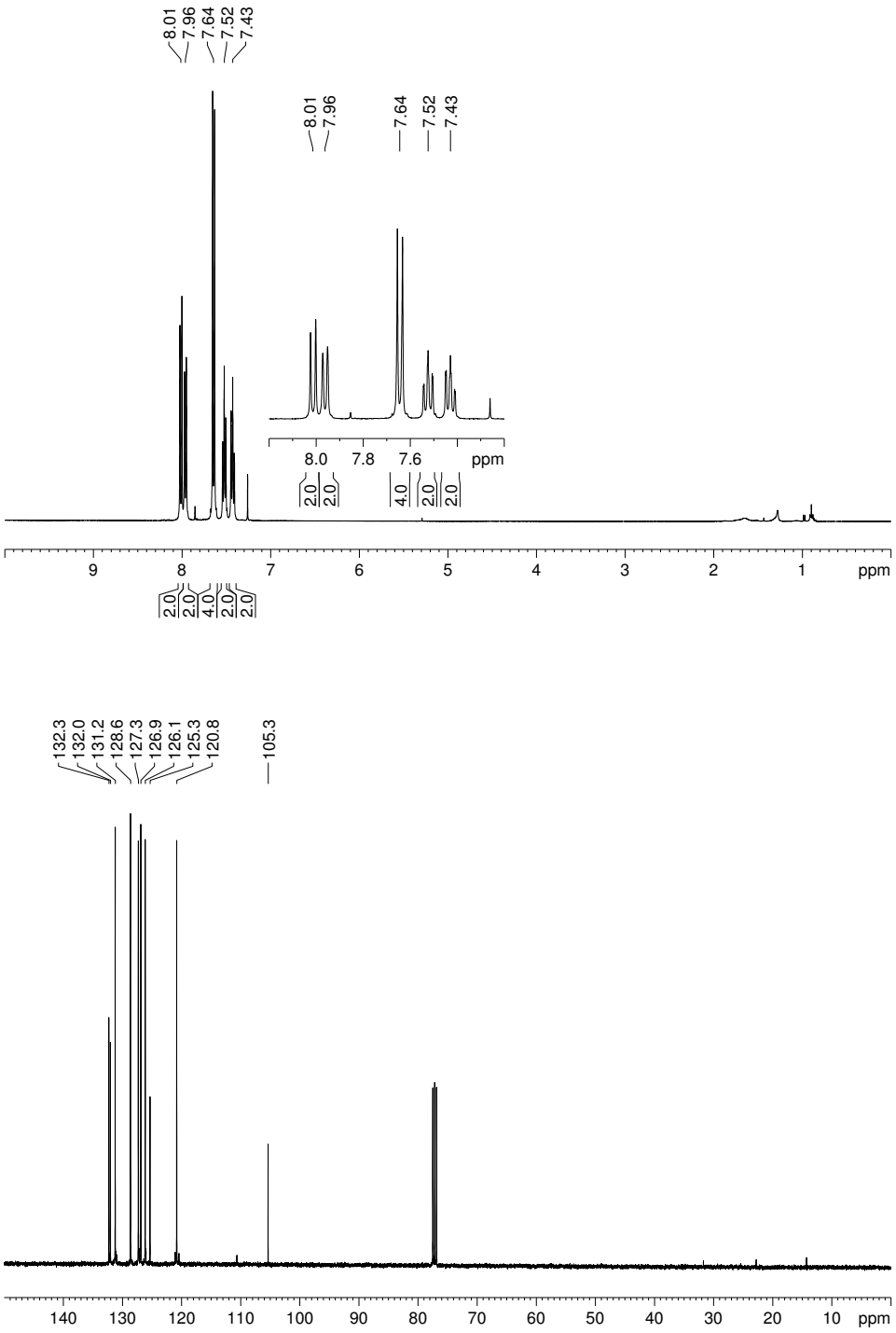


Figure J.75: ^{1}H- (top, 400 MHz) and ^{13}C-NMR (bottom, 100 MHz) spectrum of **(*S*)-Binol-DiBr-BT**; $CDCl_3$, 298 K.

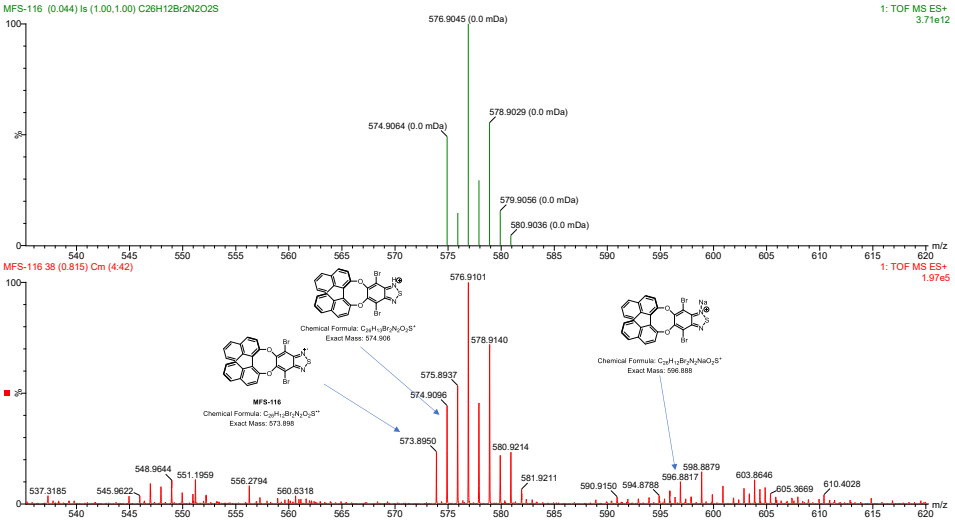


Figure J.76: ESI(+) Mass spectra of **(*S*)-Binol-DiBr-BT**.

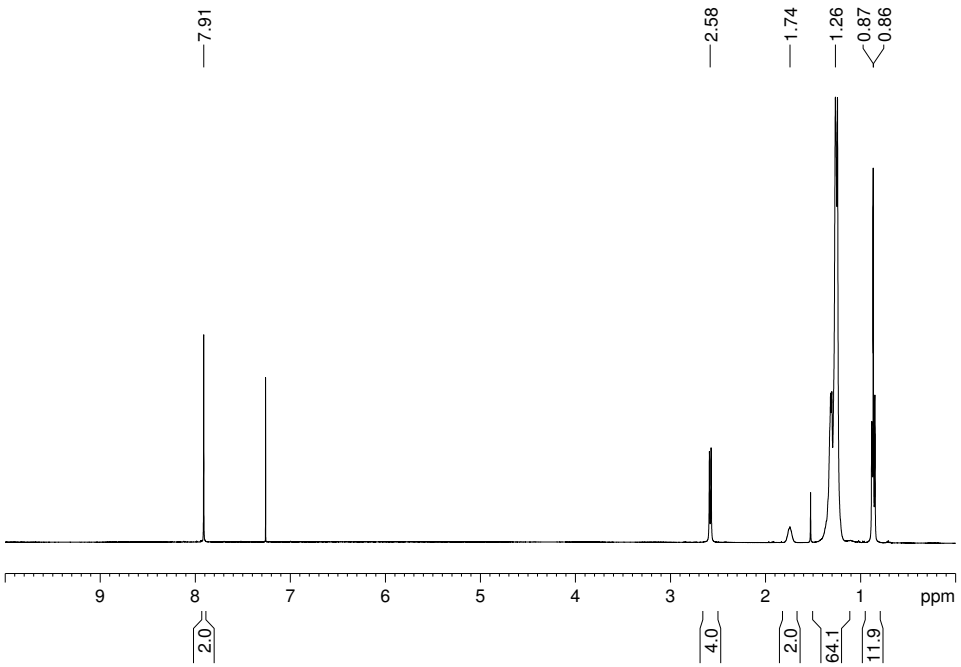


Figure J.77: ^{1}H-NMR (400 MHz) spectrum of **DiBr-ThioBT**; $CDCl_3$, 298 K.

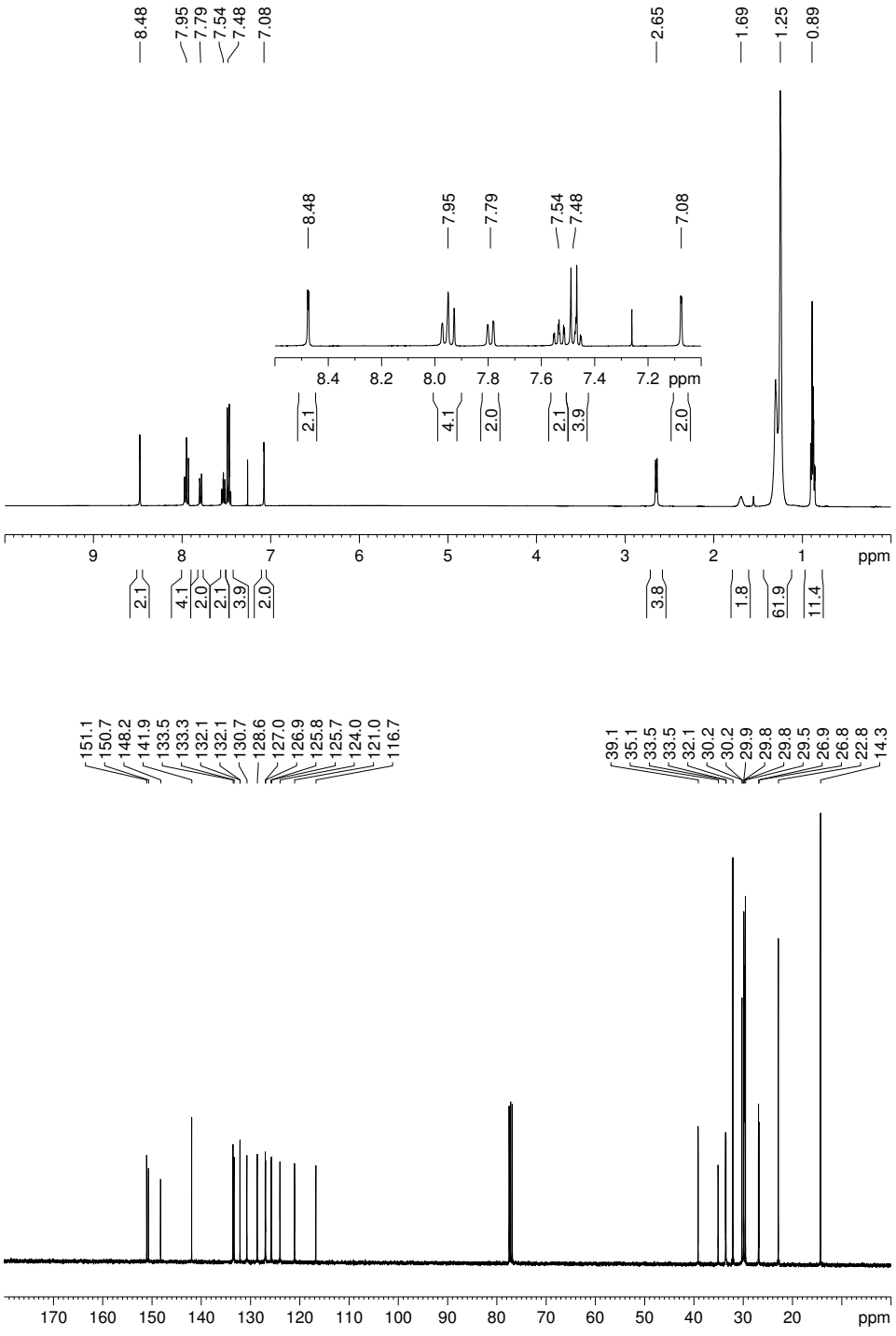


Figure J.78: ^{1}H- (top, 400 MHz) and ^{13}C-NMR (bottom, 100 MHz) spectrum of **(*S*)-Binol-ThioBT**; $CDCl_3$, 298 K.

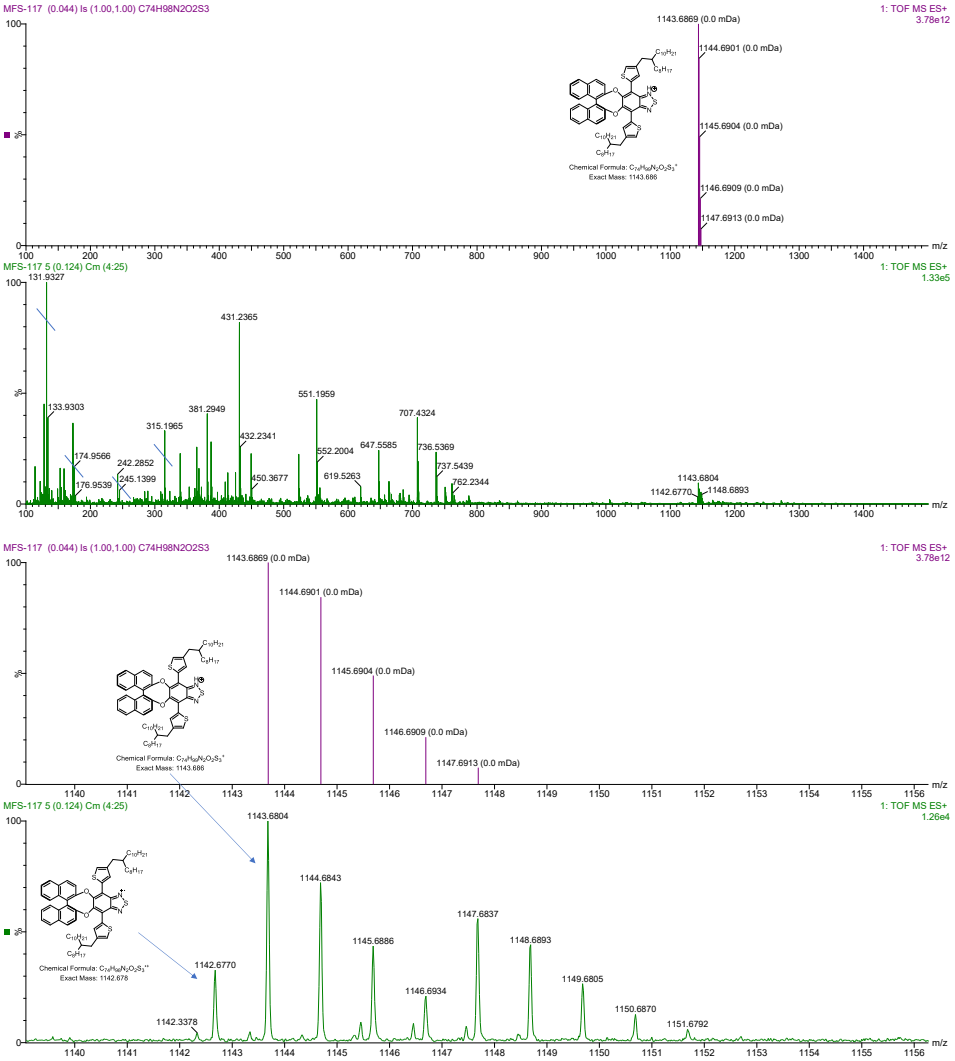


Figure J.79: ESI(+) Mass spectra of **(*S*)-Binol-ThioBT**.

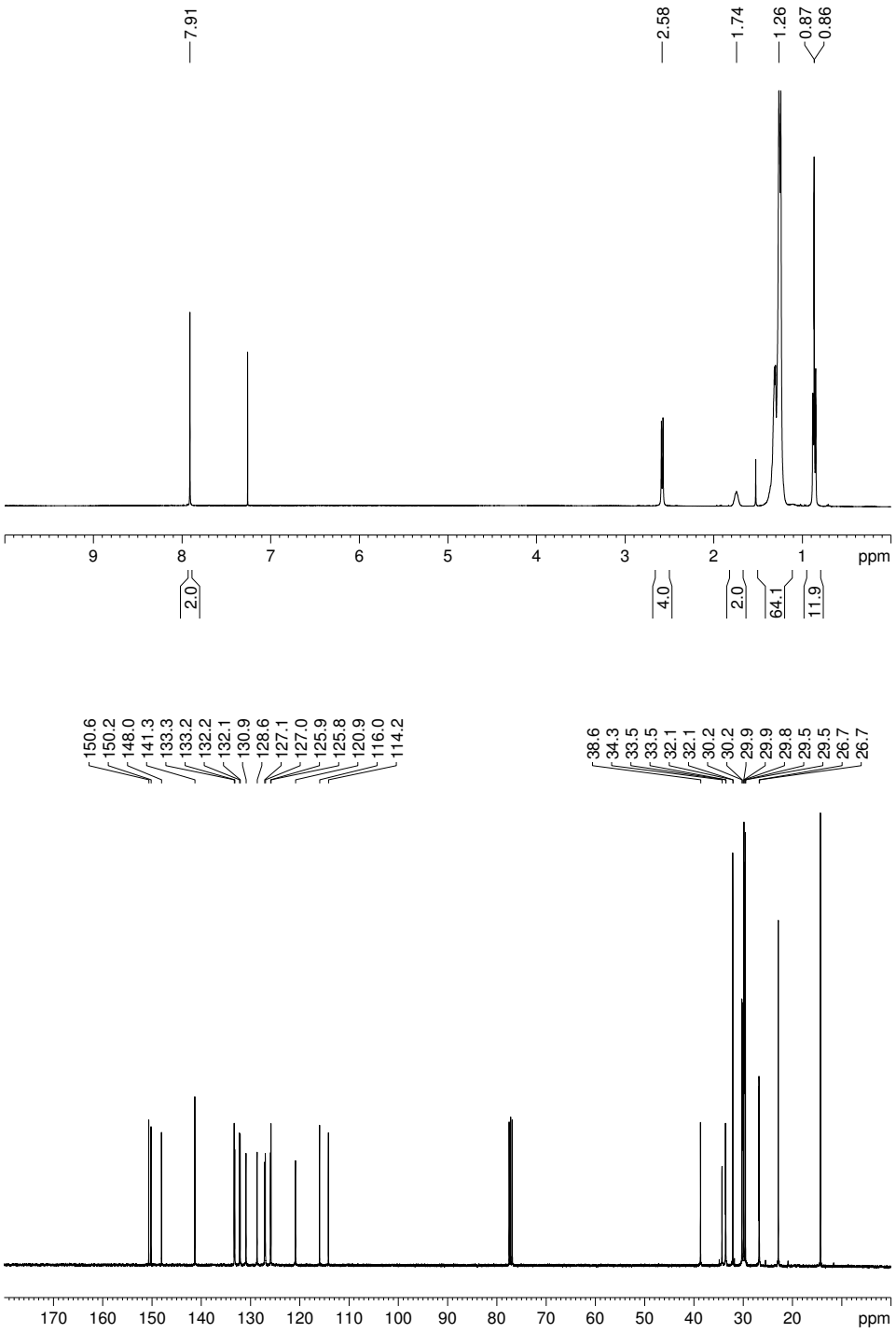


Figure J.80: ^{1}H- (top, 400 MHz) and ^{13}C-NMR (bottom, 100 MHz) spectrum of **(*S*)-Binol-DiBr-ThioBT**; $CDCl_3$, 298 K.

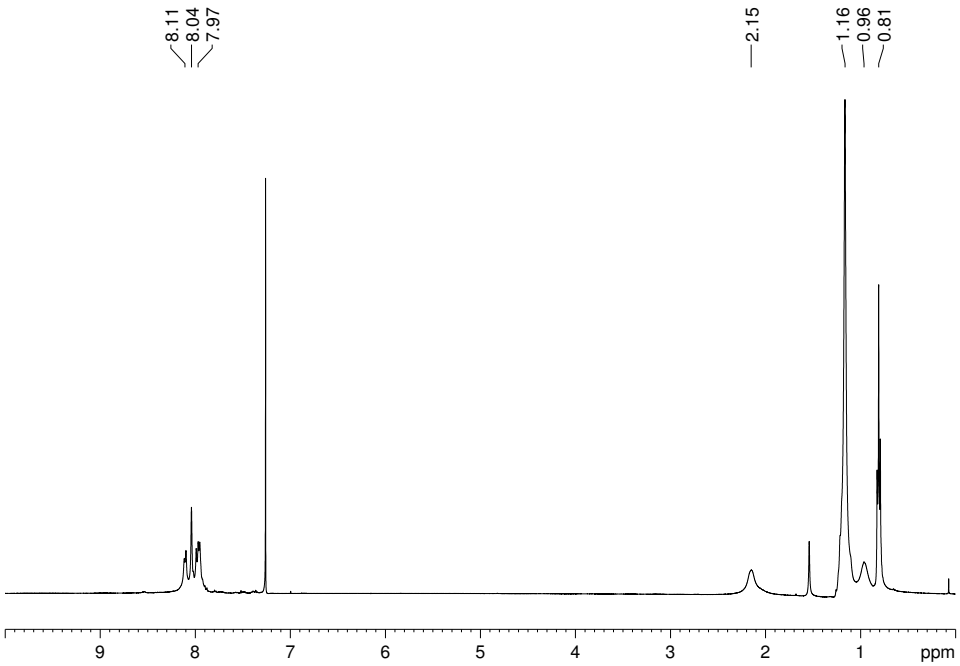


Figure J.81: ^{1}H-NMR (400 MHz) spectrum of **F8BT**; $CDCl_3$, 298 K, 1024 scans.

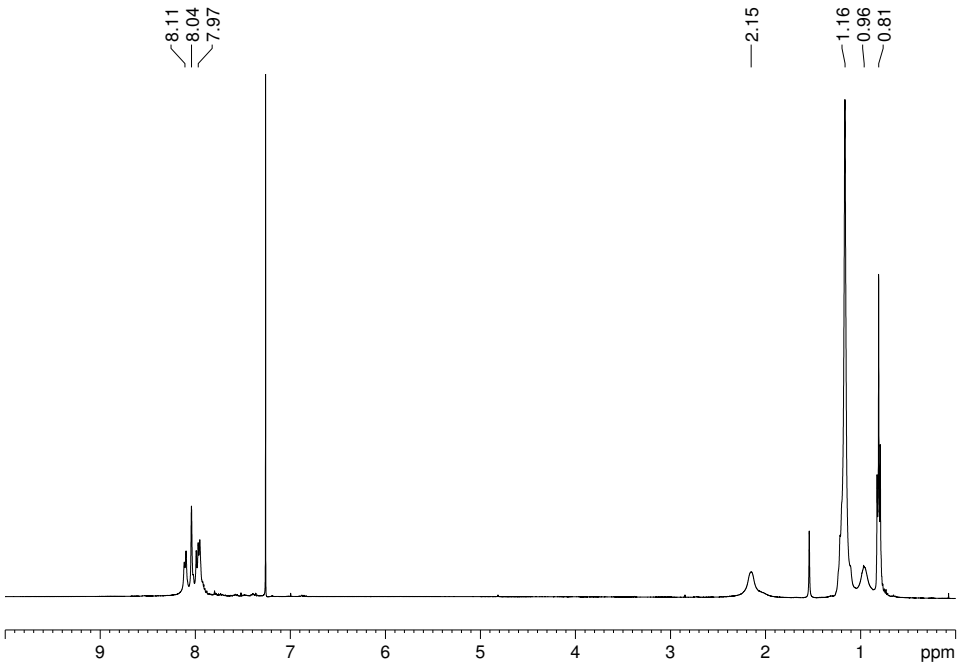


Figure J.82: ^{1}H-NMR (400 MHz) spectrum of **(*S*)-c$_5$F8BT**; $CDCl_3$, 298 K, 1024 scans.

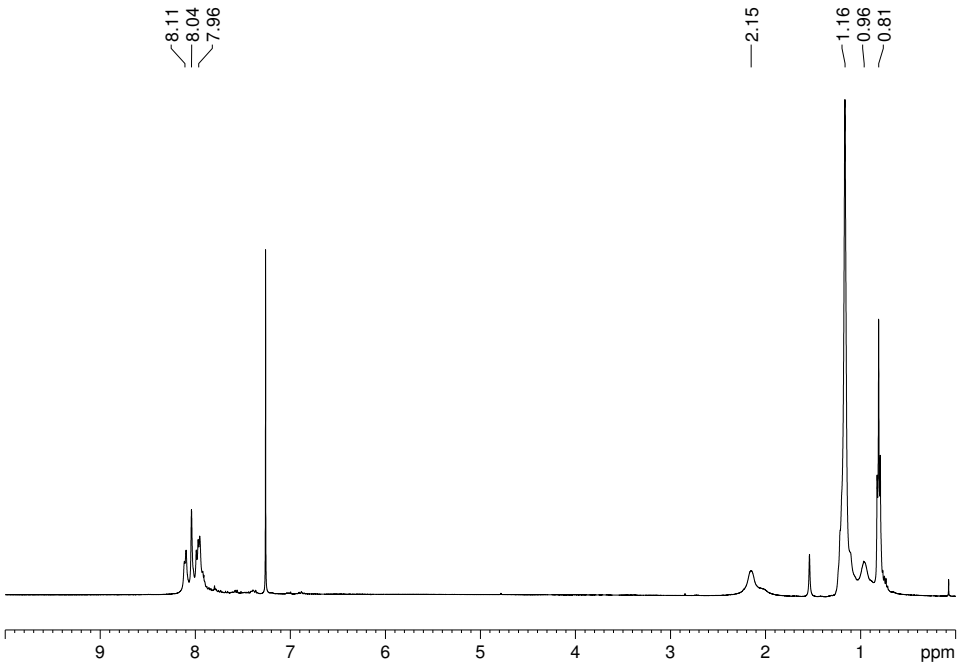


Figure J.83: ^{1}H-NMR (400 MHz) spectrum of **(*S*)-c$_{10}$F8BT**; $CDCl_3$, 298 K, 1024 scans.

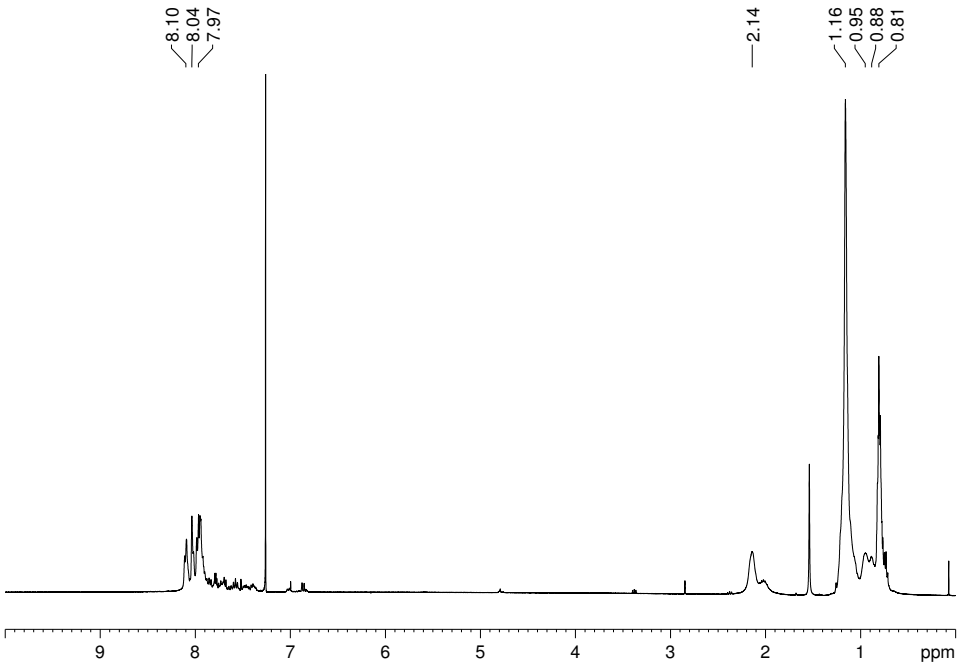


Figure J.84: ^{1}H-NMR (400 MHz) spectrum of **(*S*)-c$_{20}$F8BT**; $CDCl_3$, 298 K, 1024 scans.

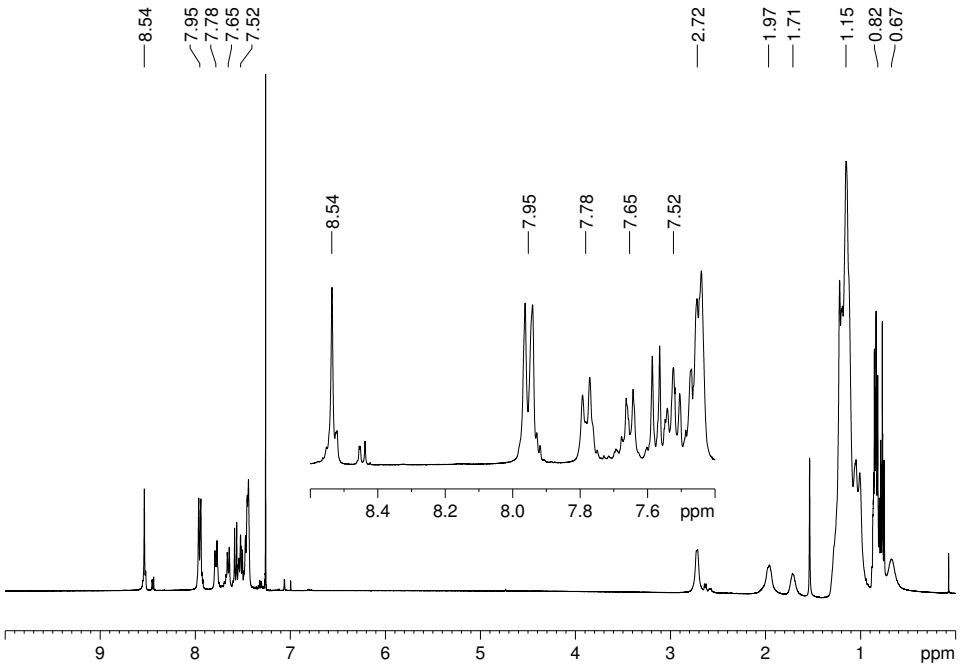


Figure J.85: ^{1}H-NMR (400 MHz) spectrum of **(*S*)-F8TBT**; $CDCl_3$, 298 K, 1024 scans.

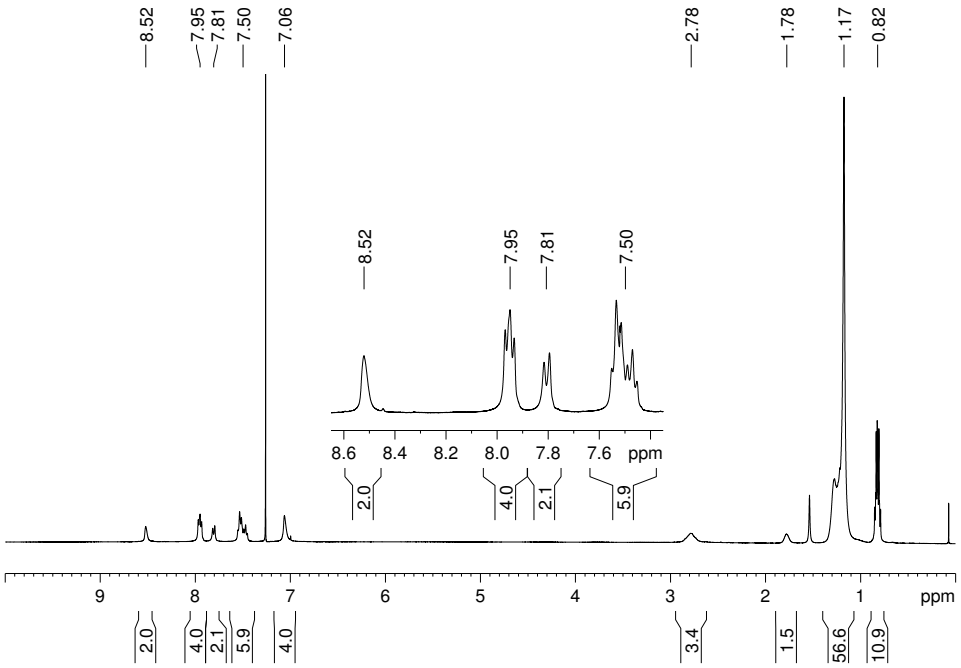


Figure J.86: ^{1}H-NMR (400 MHz) spectrum of **poly-(*S*)-Binol-BTQT**; $CDCl_3$, 298 K, 1024 scans.

List of Abbreviations and Acronyms

A absorption
Abs absorbance
EQE external quantum efficiency
FF fill factor
J_{MP} current density at the maximum power point
J_{SC} short-circuit current density
PCE power conversion efficiency
R rotational strength
$Refl$ reflection
S scattering
T transmission
V_{MP} voltage at the maximum power point
V_{OC} open-circuit voltage
ε_r relative permittivity or dielectric constant
$\vec{\mu}$ electric transition dipole moment
$\vec{m}$ magnetic transition dipole moment
M Molar i.e. mol/L
PCBM [6,6]-phenyl-C_{61}-butyric acid methyl ester
ProSQs proline-derived anilino squaraines
R_f-value retention factor
k_e extraordinary extinction coefficients
k_o ordinary extinction coefficients
k isotropic extinction coefficients
n_e extraordinary refractive index
n_o ordinary refractive index
n isotropic refractive index
2PA two-photon absorption

AFM atomic force microscopy

BHJ bulk heterojunction
borsm based on recovered starting material

CB circular birefringence
CD circular dichroism
CISS chiral induced spin selectivity
CP-PL circularly polarized photoluminescence
CPL circularly polarized light
CS charge separated
CT charge transfer

D-A-D Donor-Acceptor-Donor
DSC differential scanning calorimetry

E-Aff. electron affinity
EA elemental analysis
ee enantiomeric excess
ES electrostatic
ESM essential state models
ESM-CT essential state model including intermolecular charge transfer interactions
ESM-ES essential state model accounting for just electrostatic intermolecular interactions
ETL electron transporting layer

FRET Förster resonance energy transfer

g-value dissymmetry factor
GPC gel permeation chromatography

HOMO highest occupied molecular orbital
HPLC high-performance liquid chromatography
HTL hole transporting layer

ICT intermolecular charge transfer
IP ionization potential
IPV inorganic photovoltaic
IR infrared
ITO indium tin oxide

LB linear birefringence
LB' 45° linear birefringence
LD linear dichroism
LDC lower Davydov component
LD' 45° linear dichroism
LUMO lowest unoccupied molecular orbital

MD molecular dynamics
mdeg millidegree
mL milliliter
MM or M Mueller matrix
MP or P_{max} maximum power point

OLED organic light-emitting diode
OPV organic photovoltaic

Pd/C palladium on carbon
PDT photodynamic therapy
PEM photoelastic modulator
PHJ planar heterojunction
PIA photo-induced absorption
PTT photothermal therapy
PV photovoltaic
PVD physical vapor deposition

S/N ratio signal-to-noise ratio
S_NAr nucleophilic aromatic substitution
SC-XRD single-crystal X-ray diffraction
SI Supporting Information
SQ squaraine
SVD singular value decomposition

TA transient absorption
TGA thermogravimetric analysis
TLC thin-layer chromatography

UDC upper Davydov component

VASE variable angle spectroscopic ellipsometry

XRD X-ray diffraction

Diese Dissertation ist im Zeitraum 05/2021 – 11/2025
entstanden am

Kekulé-Institut für Organische Chemie und Biochemie
der Mathematisch-Naturwissenschaftlichen Fakultät
der Rheinischen Friedrich-Wilhelms-Universität Bonn